



TNT 2009

Trends in NanoTechnology

Barcelona (Spain)
September 07-11, 2009



PHANTOMS
foundation



Universidad
de Oviedo

UA

UNIVERSIDAD AUTONOMA
DE MADRID

UAB

Universitat Autònoma de Barcelona



CSIC

CONSEJO SUPERIOR DE INVESTIGACIONES CIENTÍFICAS



UNIVERSITAT DE BARCELONA



CIC
nanogUNE
nanoscience cooperative research center

**Georgia
Tech**



NIMS
Nanoscale Laboratory



Parc Científic
de Barcelona



UNIVERSITÄT
FRIBURGENSIS



leti

cea

CONDISTIA INTERNATIONAL
PHYSICS CENTER



Adsorption of Functionalized Fullerene Molecules on Different Noble Metal Substrates: An STM Study

Z. M. Abd El-Fattah¹, M. Corso², L. Fernández², F. Schiller¹, A. El-Sayed³, D.G. de Oteyza², N. Martín⁴, and J. E. Ortega^{1,2,3}

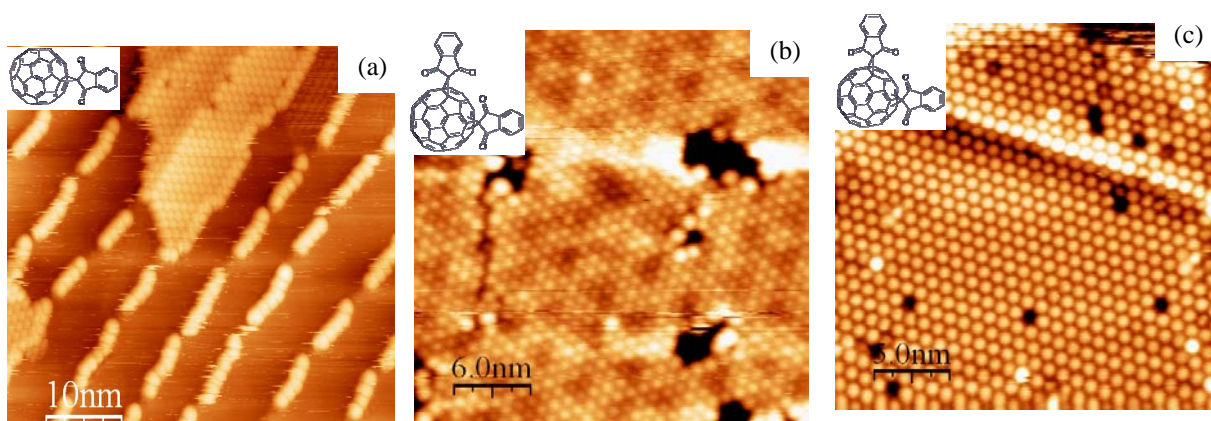
¹Centro de Física de Materiales CSIC/UPV-EHU, Materials Physics Center-MPC, San Sebastián, Spain

²Donostia International Physics Center DIPC, San Sebastián, Spain

³Departamento de Física Aplicada I, Universidad del País Vasco, San Sebastián, Spain

⁴Departamento de Química Orgánica, Facultad de Ciencias Químicas, Universidad Complutense, E-28040 Madrid, Spain

Functionalized fullerenes are actively tested as electron acceptors in optoelectronic devices and organic solar cells. For efficient charge transfer processes, it is of fundamental importance the ability to tailor molecular levels in the fullerene and their line-up with the contacting metal electrode. Hereby, by means of scanning tunneling microscopy (STM) we have investigated the adsorption of two types of functionalized C₆₀ fullerenes, namely BINDAN and INDAN, on top of different noble metal substrates, i.e., stepped Au (788), a Gd-Au surface alloy and stepped Ag(111). None of the adsorbed species revealed a specific role associated to the functional groups, such that the motifs were the same found for C₆₀ fullerenes on top of the same substrates, previously investigated with STM. This fact, together with the absence of 1s oxygen peak in x-ray photoemission spectra, suggests that the functional groups are lost at any stage from their synthesis to the adsorption on the surface top.



STM images showing (a) step decoration of INDAN molecules on Au(788) and structure of a closed packed island ($50 \times 50 \text{ nm}^2$), (b) the close-packing of BINDAN on GdAu₂ substrate with the Moiré reconstruction behind ($30 \times 30 \text{ nm}^2$), and (c) close-packing of BINDAN on Ag (111) ($25 \times 25 \text{ nm}^2$)

ELECTROLUMINESCENCE IN CARBON NANOTUBE NETWORK FIELD-EFFECT TRANSISTORS

Élyse Adam, Carla M. Aguirre, Matthieu Paillet, Benoit Cardin St-Antoine, David Ménard and Richard Martel

*Regroupement québécois sur les matériaux de pointes (RQMP) and Département de Génie Physique, École Polytechnique de Montréal, Québec, Canada and Département de Chimie, Université de Montréal, Québec, Canada.
elyse.adam@polymtl.ca*

Since the first report in 2003 [1], the electroluminescence properties of carbon nanotube field-effect transistors (FETs) have been explored with channels made of individual and bundle of carbon nanotubes (CNT) deposited on oxide layers or suspended over trenches. [2,3] These studies revealed electroluminescence from both ambipolar as well as unipolar p-type FETs. Two possible emission mechanisms have been proposed: direct bipolar recombination and impact excitation. [1,2] More recently, light emission from metallic nanotubes has also been reported and emission was discussed in terms of a thermally driven mechanism. [4,5] So far, there has been no report on the electroluminescence properties of CNT networks.

In this work, we explore the light emission properties of carbon nanotube network FETs. The channels consist of carbon nanotubes taken from different nanotube sources (laser ablation and CVD) and assembled in thin layers at densities near the metallic percolation threshold. We show that the emission of unipolar p-type network FETs is located at the drain (see figure below). This behavior is similar to what was already measured in long and individual nanotube FETs [6] and suggests that the emission involves bipolar recombination. Impact excitation thus appears to be negligible in those network FETs. Moreover, the light emission spectra show large resonance peak emission (~180 meV) that is consistent with excitonic radiation processes in CNTs. By comparing the spectra linewidths of the network FETs with that of individual carbon nanotubes (~80 meV), we proved that many nanotubes having different diameters emit simultaneously in network devices.

In order to investigate the population of CNTs that contributes to electroluminescence of network FETs, we compared the emission spectra of different sources with that of their corresponding absorption spectra. The figure below shows typical electroluminescence spectra and their corresponding absorption spectra for two sources (laser ablation and CoMoCAT). These results show an important red-shift between the emission maximum compared to that of the absorption spectrum, which is explained by energy or carrier transfer to the large diameter carbon nanotubes. [7] This important conclusion was also confirmed for network FETs made with double-wall carbon nanotubes. For the latter, additional peaks are also observed at higher energy. Possible explanations on the origin of this will be discussed.

Last, we also perform experiments on bundle FETs consisting of a mixture of metallic and semiconducting CNTs on an oxide. Our measurements revealed that only semiconducting carbon nanotubes produce a significant electroluminescent signal. To investigate further light emission of metallic nanotubes, we fabricated thick (100 nm) metallic carbon nanotube films. We observed that the spectral light emission response of these films is consistent with classical blackbody emission.

References:

- [1] Misewich, J. A.; Martel, R.; Avouris, Ph.; Tsang, J. C.; Heinze, S.; Tersoff, J., *Science*, **300**, 783 (2003).
- [2] Chen, J.; Perebeinos, V.; Freitag, M.; Tsang, J.; Fu, Q.; Liu, J.; Avouris, Ph. *Science*, **310**, 1171 (2005).
- [3] Marty, L.; Adam, E.; Albert, L.; Doyon, R.; Ménard, D.; Martel, R. *Phys. Rev. Lett.* **96**, 136803 (2006).
- [4] Mann, D.; Kato, Y. K.; Kinkhabwala, A.; Pop, E.; Cao, J.; Wang, X.; Zhang, L.; Wang, Q.; Guo, J.; Dai, H. *Nature Nanotech*, **2**, 33 (2007).
- [5] Xie, L.; Farhat, H.; Son, H.; Zhang, J.; Dresselhaus, M. S.; Kong, J.; Liu, Z. *Nano lett, article ASAP* (2009).
- [6] Freitag, M.; Chen, J.; Tersoff, J.; Tsang, J. C.; Fu, Q.; Liu, J.; Avouris, Ph. *Phys. Rev. Lett.*, **93**, 076803 (2004).
- [7] Adam, E.; Aguirre, C.M.; Marty, L.; St-Antoine B.C; Meunier F.; Desjardins, P.; Ménard D.; Martel R., *Nano Lett*, **8**, 2351 (2008).

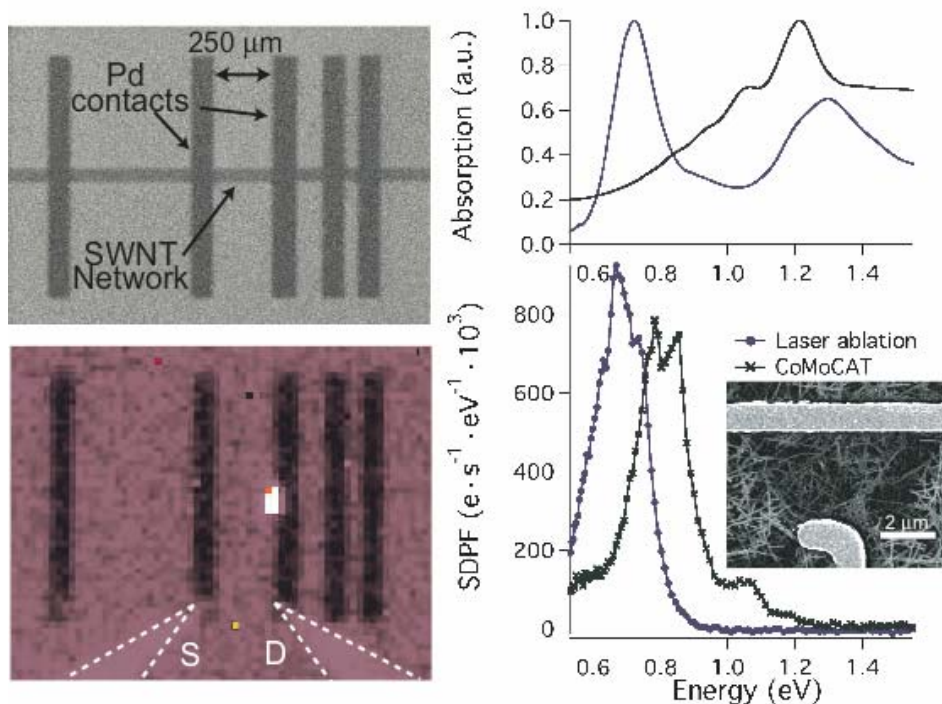


FIGURE Left-Top: SEM images of a long channel (250 μm) network FET made from laser ablation nanotubes. The width of the SWNT network is 100 μm. Left-down: near-infrared image of the light emission in a typical long channel unipolar p-type transistor. The light emission zone is always located at the drain (D) contact region. Right-Top: Absorption spectra recorded from networks made with CoMoCAT and laser ablation sources. Right-Down: corresponding electroluminescence spectra of the networks FETs from the same CNT sources. These spectra were acquired for $t_{\text{exp}}=2$ min using $V_d = -25$ V, $V_g = -20$ V and $V_d = -55$ V, $V_g = -20$ V for the laser ablation and CoMoCAT spectra, respectively. The electrode spacing is 3 μm for the laser ablation network and 1 μm for the CoMoCAT network device. Insets: SEM image of the device made with laser ablation nanotube.

On the Electrical properties of the C/Au thin film electrode deposited Over LTCC substrate

Fatemeh Afshar, Soroush Nazarpour, Jose Maria Lopez Villegace, Albert Cirera
Department of Electronics, University of Barcelona, Spain, 08028
Fafshar@el.ub.es

In last few years the increase in the level of functions required of wireless communications has necessitated the use of higher frequency ranges. As a result of this progress a very rapid growth of applications of Low Temperature Co-fired Ceramics in wireless communications has been observed recently. The Low Temperature Co-fired Ceramic (LTCC) Technology has been extensively explored in the microelectronics industry as a ceramic packaging technology for integrated microcircuits [1-2]. Additionally, LTCC was applied for the production of sensors and actuators due to its very good electrical and mechanical properties, high reliability and stability as well as possibility of making three dimensional (3D) integrated microstructures. A typical LTCC module consists of dielectric tapes, connecting vias, external and internal conductors and passive components [3].

Thin-film science and technology also play a crucial role in the high-tech industries and the major exploitation of thin films has been in microelectronics. Microelectronic packages for high frequency application require conductive materials with high conductivity. Lower temperature firing of ceramic blocks of about 850°C allows utilization of highly conductive and low resistive metals such as gold. Gold produces a very high definition and reliable circuit [4]. However, some restrictions limited these advantages like high diffusion coefficient [5] and poor adhesion of the Au metallic films on the substrates which hamper specific applications extensively.

Many transmission lines and electrodes used in microelectronics have conductors deposited directly on a substrate. Therefore, two Au thin films with different thicknesses 50 and 100 nm were deposited with DC sputtering technique over the LTCC substrate. Then by considering aforementioned problems of using metallic thin films as electrodes, a 100 nm C thin film layer has been deposited on Au/LTCC layer with Au 50 nm in order to avoid Au adhesive problem. Finally samples were annealed in Ar ambient for 1, 5, 10, 15 and 20 min. Thermal treatment has been done in order to make solid state reaction for mixing the layers to increase adhesive characteristics and observe possible modification of the conductive properties. We explored the obtained results of electrical property to improve functionality of the circuits in terms of the Au conductors.

Surprisingly, it was found that C/Au/LTCC bilayer annealed for 1 min shows more desirable conductance behavior in compare with as deposited sample and those annealed for higher annealing times. It can be due to improving interfacial contact between 2 layers by diffusing some atoms through the interface and avoiding sharp interface effect which may scatter electrons when are passing along. In addition, it was expected that sample with carbon layer have less conductance in compare with Au/LTCC samples (due to the low conductivity of C), but interestingly it could be observed that the conductance of the C/Au/LTCC bilayer with 1 min annealing time is comparable with the Au/LTCC which the thickness of gold is 100 nm. Therefore, in this study we could improve adhesion of Au thin film electrodes over LTCC substrates without losing electrical property and strong film stability has been seen with applying C layer over Au/LTCC. Thereafter, the conductance of annealed bilayers at 500°C for 1 min reached to the maximum which may be owing to improved contact between the layers which could be a solution to overcome low conductance of the deposited bilayers.

References:

- [1] J. Mazierska, M. V. Jacob. A. Haring, J. Krupka, P. Barnwell, T. Sims, J. Eur. Ceram. Soc. 23 (2003) 2611.
- [2] Y. Higuchi, Y. Sugimoto, J. Harada, H. Tamura, J. Eur. Ceram. Soc. 27 (2007) 2785.
- [3] L.J. Golonka. Bulletin Of The Polish Academy Of Sciences Technica Sciences. 54 (2006) 221.
- [4] J. b. Jarvis, M. D. Janezic, B. Riddle, CH. L. Holloway, N .G. paulter, J. E. Blendell. NIST technical note 1520 (2001).
- [5] B. Okkerse. Phys. Rev. 103 (1956) 1246.

Figures:

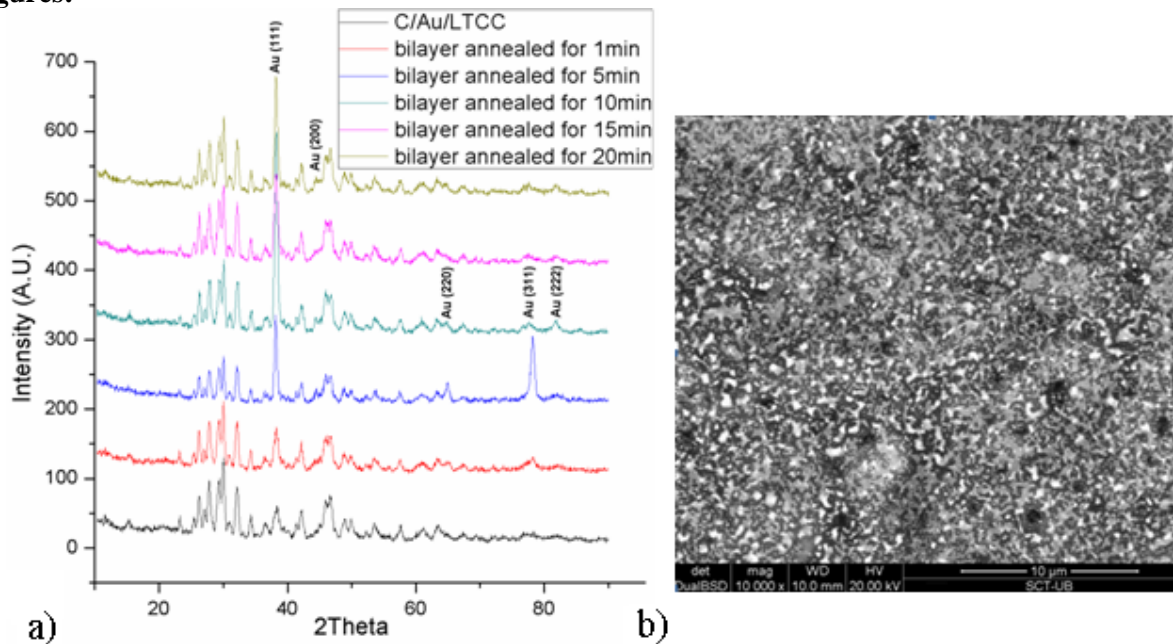


Fig 1. a) XRD results of C/Au/LTCC in which being textured along (111) crystal direction is noticeable. b) SEM image of C/Au/LTCC bilayer annealed for 10 min at 500°C.

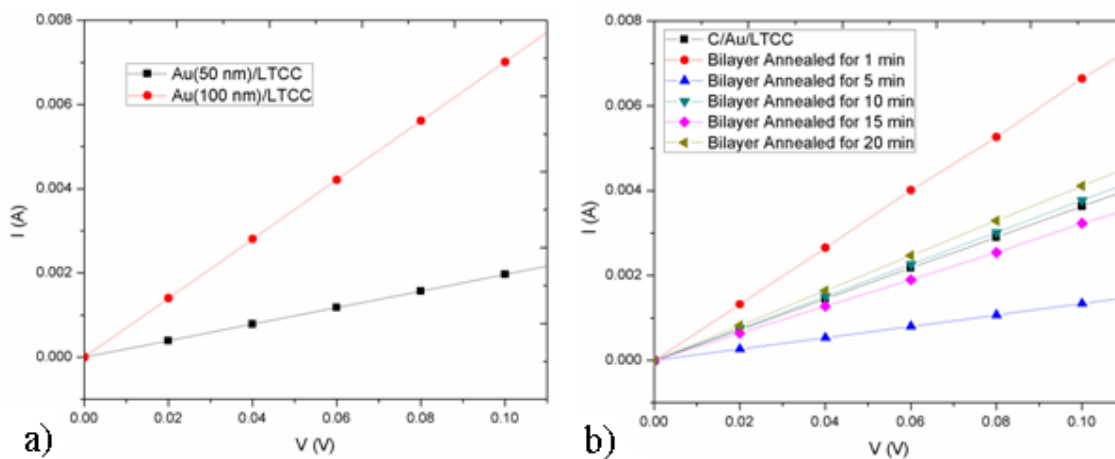


Fig 2. a) I- V plot of Au/LTCC with 50 nm and 100 nm thicknesses. b) I- V plot of C/Au/LTCC as deposited and annealed at 500°C for 1, 5, 10, 15, 20 min. Maximum conductance of the C/Au bilayer has been seen after 1 min annealing.

Investigation of NanoTechnological Capability of Diatomites in Nano-Industry

Masoud Aghabeigi¹ – Parmis Sepanloo²

*1 - Islamic Azad university – Mashhad Branch - Faculty of science - Geology department
(Young Researchers Club)*

*2 - Islamic Azad university – Mashhad Branch - Faculty of science – Biochemistry Department
M.Aghabeigi@gmail.com*

Abstract

The purpose of this investigation , is studing communication between morphological properties of diatomites and their constractive particulars (Diatoms) with many applications of these rocks in nano-industry. Increasing additive of diatomites uses in nano-industry. Which are commercial rocks with biogenic origin , has related with their particular properties. Indexes of study diatomites and their specific factors in determine of qualification as we investigate, it is our purposes in this article .These factors help us to understand the concepts of their communications. An important class of low permeability rock that remains relatively unstudied is diatomite . Diatomite is a hydrous form of silica or opal composed of the remains of microscopic shells of diatoms , which are single-celled aquatic plankton. Diatomites are very porous with high internal surface area but they are exceptionally impermeable . permeabilities range from 0.1 to 10 mD. Diatomites are fine-size rocks , irregular porous noncaking particles with a high liquid absorption capacity. They are relatively inert chemically , have a refractive index are mildly abrasive , have a low thermal conductivity with a reasonably high fusion point , can be slightly pozzolanic water imbibition is fundamental to both water flood and steamdrive performance in low permeability reservoir rocks such as diatomite . This phenomenon is caused by capillary suction and the differential attraction forces between the pore walls and fluids. The most important use of diatomite , in a great variety of grades , is as a filtration medium for beverages (especially beer and wine) , sugar and sweetener liquors , oils and fats , petroleum and chemical processing (including waste drycleaning fluids) , pharmaceuticals , and water (potable, industrial process , waste and swimming pool). A large and growing application is diatomite's use as an absorbent for industrial spills (oil and toxic liquids) and for pet litter. Another important broad category of use is as a filler , commonly serving a dual purpose , such as an extender and flattening agent in granular materials , a multieffect component in plastics (including the prevention of films from sticking) , and an extender/ absorbent carrier for dry pesticides , pharmaceuticals , catalysts and other chemicals. Other significant uses are as an insulation material in bulk (loose) and in molded forms, in other insulation products that include calcium silicate as a compounds , including mortar and portland cement , where it is also used for its pozzolanic properties. Emerging markets for diatomite include use in biotechnology and pharmaceuticals and as a nontoxic insecticide. Fundamental factors in diatomites's studies, for determinate of their quality , will mention below: Diatoms's shapes which make sample, Size of Diatoms, Rate of filling up the internal sediments into diatoms's chambers, Calculate of diatoms's percent. to make sample so we can study diatomites , according to our point of view which are: Lightness, High percent of moisture, To be soft, Clinkered fracture and to be powdering, Microscopic stud. From commercial point of view the most important of diatomite products, in a great variety of grades are such as: According to porosity and lightness factors; In nano-filtration medium for beverages , sugar , oil , Pharmaceuticals , wasts- In making lightweight bricks-In papermill- In drilling mud. According to ability of fillering; In nano-fillers , plastics, papers , paints , Films ,bricks , ceramics soaps , pharmaceuticals , dry trash , paint making , mortar and Portland cements , pozzolanic Materials. According to ability insulation; In thermal nano-insulation , fireproof's materials, dynamite , welding , electrodes , minning explosions. According to alternative of viscosity and be absorbent; In liquid nano-absorbents, fruit – juices, alcohol laquers and in environmental

filtrations According to contain of silica in diatomite's; In acids , calcium silicates , abrasives , resistance of lastics , metals , catalysts, Bricks. Existence of spontaneous water imbibition, fluid flow state , existence of high internal surface area associated with high porosity in diatoms's structure low permeability , function of capillary forces and creates of interfacial tension , existence the high amount of silica to be reason lightness , be soft , fillering ability, Power of high absorption , wettability , abrasive resistance in diatomites , as because of it , increase of nano-industrial usages of these rocks with a great development . circumstance of study , Identification and determinate of diatomites quality according to the indexes wich have mentioned above , are the most important ground in their nano-industrial uses. Main commercial resrvoirs diatomites in Iran , is located in northwest regions (Azarbajejan and Ardabil provinces).

Keywords : Diatomite – Nanofossils – Nano industry - spontaneous water imbibition – multi phase Flow.

References :

- 1) Black , R.M.1988, The Elements of palaentology. Second editon . cambridge university press.404p.
- 2) Brasier , M. D. 1988 , Microfossils. Unwin Hyman. London.
- 3) Burckle , L .H. 1978, Marine diatoms. In: Haq, B.U.
- 4) Cojan , I and Renard , M, 2002, Sedimentology . oxford & IBH publishing co (kolkata) .483p.
- 5) Dean , W. E and Leinen , M and stow , D.A.V , 1985. Classification of deep sea , fine - grained sediments. Jour, sed. Petrology , 55, p 250_256
- 6) Dolley , T.P and Moyle , P.R. 2003 . History and overview of the U.S.Diatomite . chapter E of conterbutions to industrial - Mineral Research. (Bulletin 2209 -E) . 8p
- 7) Milson , C and Rigby , S . 2004 . Fossils at A Glance . Blackwell publishing . 155P.
- 8) Schember, J. M and Akin , S and castanier , L . M and Kovscek , A . R.1997. Spontaneous water imbibition in to diatomite, Jur. Soc. Pet geology,9P.
- 9) Tucker , Me. E. 1981. Sedimentology Petrology An introduction, black well scientific pub 252P.
- 10) Wilkinson , M. H.F and Droop , S. 2002. Diatom contour Analysis using Morphological curvature scale spaces.

CARBON NANOTUBE PROGRAMMABLE DEVICES FOR ADAPTIVE ARCHITECTURES

*G. Agnus^a, W. Zhao^b, V. Derycke^a, A. Filoramo^a, S. Lenfant^c, D. Vuillaume^c,
C. Gamrat^b and J-P. Bourgoin^a*

^aLaboratoire d'Electronique Moléculaire, Service de Physique de L'Etat Condensé (CNRS URA 2464), CEA, IRAMIS F-91191 Gif sur Yvette, France

^bLaboratoire d'Intégration des Systèmes et des Technologies, CEA, F-91191 Gif sur Yvette, France

^cMolecular Nanostructures and Devices Group, IEMN, CNRS, BP 60069, Avenue Poincaré, 59652 Villeneuve d'Ascq, France

guillaume.agnus@cea.fr

Nano-objects with well defined structures and original electronic properties are of great interest for the development of new generation circuits. Their intrinsic nanometer scale, potentially associated with novel functionalities, is particularly interesting to complement CMOS. However, it is very unlikely that conventional architectures developed so far for the CMOS technology will be ideally suited for these new objects. These architectures can barely cope with any significant variation in either electrical characteristics or placement of individual devices, which are an inherent particularity of most nano-devices. On the other side, adaptive circuits such as neural networks represent a challenging approach which intends to take advantage of the rich functionality of nano-size building blocks and at the same time to manage variability.

In this context, functionalized carbon nanotube field effect transistors are of special relevance as they combine exceptional electrical performances with additional functionalities such as sensing and memory capabilities. In particular, coating such transistors with a thin film of photoconductive polymer adds decisive improvements in terms of optoelectronic properties: upon light excitation, we showed that these devices present large changes in conductance associated with a well controlled and non-volatile memory effect [1]. We established the critical role of charge trapping at the polymer-dielectric interface [2] in these memory-FETs.

In the present study, we show that Optically Gated Carbon Nanotube Field Effect Transistors (OG-CNTFETs) have all the required characteristics of a synapse, the basic building block for adaptive circuits. It requires demonstrating operation as 2-terminal devices with a memory effect, programmability, large dynamics and tolerance to variability. The capability to program multiple devices is also established and a way to implement these nano-synapses in large circuits is proposed.

Multiple OG-CNTFETs based on carbon nanotube networks and sharing the same output electrode were fabricated (Fig. 1). The use of nanotube networks allows the fabrication of reliable circuits with reasonable dispersion of their transfer characteristics. The conductivity of each device can be tuned over several orders of magnitude using both light and electrical pulses on the input electrode [3]. Using a global illumination step followed by electrical stimuli at the input electrodes, the conductance of multiple devices can be very precisely programmed to arbitrary values as shown in figure 2. No-cross-talk between neighboring devices was observed at the considered scale.

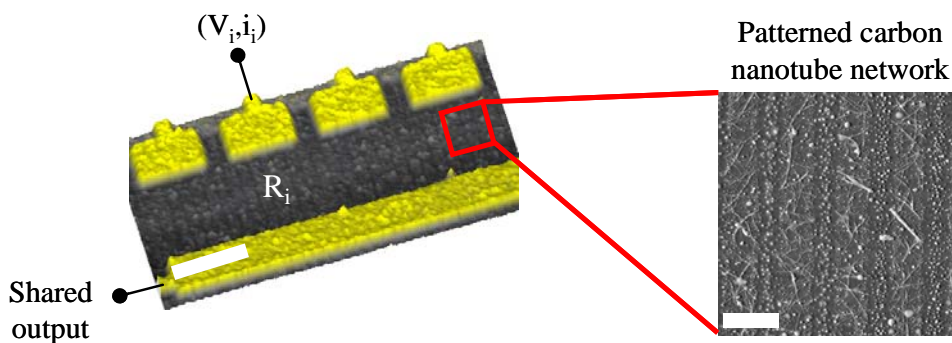


Figure 1: 3D view AFM image of a 4 OG-CNTFETs sharing the same output electrode. AFM image showing the CNT network used as transistor canal. Scales bars are respectively 4 μm and 800 nm.

We thus demonstrated that OG-CNTFETs act as 2-terminal like programmable resistor the resistivity of which can be adjusted within 3 orders of magnitude and then maintained in a non volatile way. Such programming scheme allows coping with the crucial issue of variability among as-built devices. Using experiments with aggressively scaled devices, we recently established that this programming step can be performed within the μs time range, thus allowing high speed writing. Detailed characterization of these scaled devices also brings new information on the charges trapping/detrapping mechanism and dynamics.

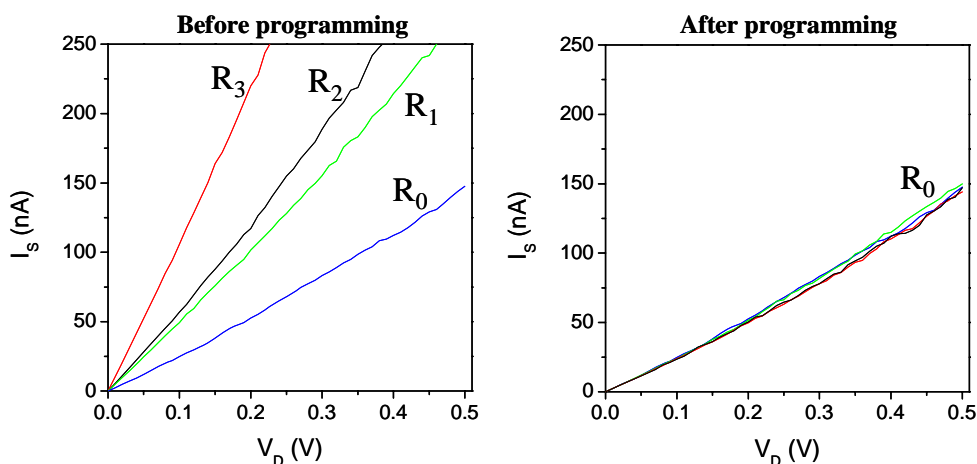


Figure 2: $I_s(V_{DS})$ characteristic of multiple OG-CNTFETs sharing the same output electrode. After the illumination step, each device has different conductance value. Using input electrode programming pulses, each device conductance is set to the same value.

As the process is compatible with integration above a CMOS layer, this strategy could allow implementing simple neural network-like architectures in which the nanotubes would play the role of synapses and the neurons would be implemented within the CMOS layer [4]. We will propose an original architecture based on OG-CNTFET synapses compatible with a massively parallel learning procedure.

References:

- [1] J. Borghetti, V. Derycke, S. Lenfant, P. Chenevier, A. Filoramo, M. Goffman, D. Vuillaume, and J.-P. Bourgoïn, *Advanced materials*, **18** (2006) 2535.
- [2] C. Anghel, V. Derycke, A. Filoramo, S. Lenfant, B. Giffard, D. Vuillaume and J.-P. Bourgoïn, *Nano Letters*, **8** (2008) 3619.
- [3] G. Agnus et al., submitted
- [4] W. Zhao, C. Gamrat, G. Agnus, V. Derycke, J.-P. Bourgoïn, European Patent 09305240.5.

STATISTICS-BASED EXPERIMENTAL DESIGN TO STUDY THE FORMATION OF CARBON-COATED MAGNETIC NANOPARTICLES BY PLASMA ARC

*Noemí Aguiló-Aguayo, Maria José Inestrosa-Izurrieta, Eric Jover, Enric Bertran
FEMAN Group, IN²UB, Martí i Franquès 1, Barcelona, Catalonia, Spain
noemiaguilo@gmail.com*

Statistics-based experimental designs have been usually exploited in fields related to biology such as agriculture, biochemistry or medicine, where a great number of parameters are involved in the processes under study [1]. In contrast, fields where physical factors are implicated, the systematic studies are carried out varying one of the process parameter and maintaining the rest of them constant.

Carbon-coated nanoparticles have been a focus of interest due to their advantageous properties over other coatings, such as their higher chemical and thermal stability and compatibility, very suitable for biological applications [2]. However, the understanding of the formation mechanism of this kind of structures is still unknown and remarkable field of research.

In an attempt to use the potential of statistics tools above mentioned, here we report, for the first time, the Plackett-Burman (PB) design was applied in order to study the formation process of carbon-coated magnetic nanoparticles by using a plasma arc technique, which is the most common technique to produce this kind of nanostructures.

The plasma arc reactor used is described elsewhere in the literature [3]. A schematic picture of the experimental apparatus is shown in Fig. 1. The parameters employed for the PB study are the following ones: pressure (evaluated from 500 mbar to 200 mbar), current applied (from 5 A to 55 A), amount of iron material (from 0.05 g to 0.17 g), helium flow (from 800 sccm to 1800 sccm), electrode diameters (from 0.9 mm to 7 mm), plasma time duration (from 180 s to 420 s) and flow geometry (gas flow coaxial nozzle or surrounding gas flow). All parameters were varied within the scope to our system and taking into account the values used in the literature [4-6].

In particular, there are three common problems in carbon-coated magnetic nanostructured products. On one hand, the poor yield achieved. A great quantity of nanoparticles is required for the commercialization and to produce enough signals for some measurements, such as, magnetization responses. The second problem is the fabrication of smaller nanoparticles. Ultrafine nanoparticles are very suitable for some activities, for example, in biomedical applications where superparamagnetic behaviour is requested. The last problem is about the polydispersity of the samples, which is one of the challenges in this field.

Pareto charts in PB design show the most influential control parameters in each case. The main factor to control the yield of nanoparticles is the flow geometry; gas flow coaxial nozzle allows obtaining higher yields. Smaller diameters are obtained using higher intensities and a surrounding gas flow. In addition, lower dispersions are also achieved with surrounding gas flow.

Fig. 2 shows TEM images of some samples obtained in PB experimental designs. Nanoparticles from 3 to 30 nm core diameters with dispersions from 20 % to 50 % were obtained.

The screening Plackett-Burman experimental design in 12 runs has been used to identify the most influent control parameters in the plasma arc method. As it is shown, geometry flow is a crucial parameter to control diameters and dispersions of nanoparticles. We conclude that this fact is related with the residence time of the nanoparticles in the plasma region. Surrounding

gas flow implies lower residence time, which involves minor diameters and dispersions. On the other hand, higher concentration of nanoparticles in the plasma region causes higher yields, but a gas flow coaxial nozzle is required. It means that the quality and quantity of nanoparticles are in competition. It is essential to find an intermediate point where yield, small diameters and minor dispersion are optimized.

This study was supported by projects CSD2006-12 and DPI2006-03070 of MEDU of Spain. The authors thank Serveis Científico-tècnics of the Universitat de Barcelona (SCT-UB) for measurements facilities.

References:

- [1] Vanaja, K., Shobha Rani, R. H., *Clinical Research and Regulatory Affairs*, **24** (2007) 1-23.
- [2] Corti, M., Lascialfari, A., Micotti, E., Castellano, A., Donativi, M., Quarta, A., Cozzoli, P. D., Manna, L., Pellegrino, T., Sangregorio, C., *Journal of Magnetism and Magnetic Materials* **320** (2008) 320-323.
- [3] Aguiló-Aguayo, N., Inestrosa-Izurieta, M. J., García-Céspedes, J., Bertran, E. *Journal of Nanoscience and Nanotechnology* (in press).
- [4] Bystrzejewski, M., Huczko, A., Lange, H., *Sensors and Actuators B* **109** (2005) 81-85.
- [5] Chazelas, C., Coudert, J. F., Jarrige, J., Fauchais, P., *Journal of the European Ceramics Society* **26** (2006) 3499-3507.
- [6] Hao, C., Xiao, F., Cui, Z., *Journal of Nanoparticle Research* **10** (2008) 47-51.

Figures:

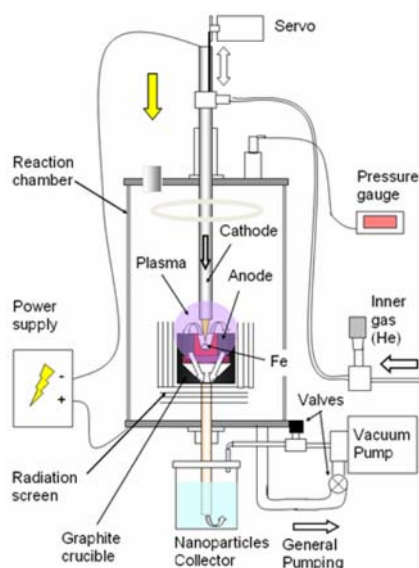


Fig. 1 Schematic picture of the experimental setup.

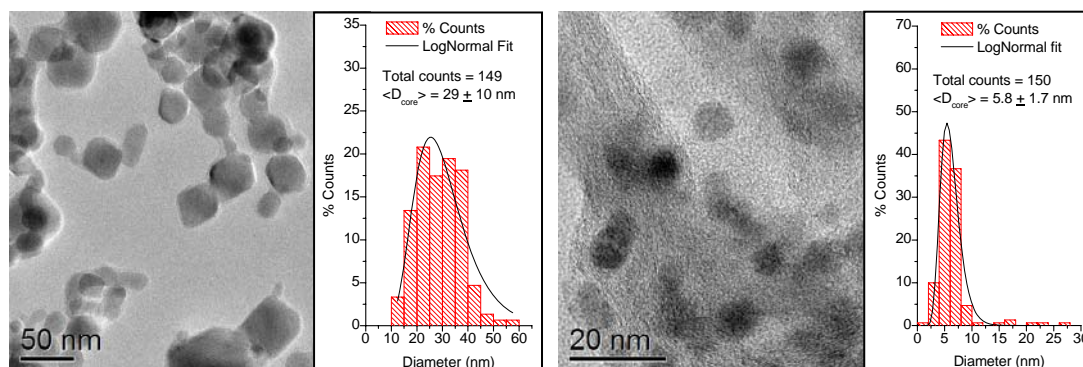


Fig. 2 TEM images of carbon-coated iron nanoparticles obtained in Plackett-Burman experimental design. Histograms are represented in both cases.

Explicit computation of Coulomb and exchange interactions for N-electrons in open quantum systems using Bohm trajectories

A.Alarcón , X.Cartoià and X.Oriols

*Departament d'Enginyeria Electrònica,
Universitat Autònoma de Barcelona, 08193, Bellaterra, SPAIN
Contact E-mail: Alfonso.Alarcon@uab.es*

From a computational point of view, the direct solution of the many-particle Schrödinger equation is inaccessible for more than very few electrons. This issue is at the heart of almost all the unsolved problems in quantum transport. Recently, a novel many-particle quantum transport formalism using Bohm trajectories has been presented for dealing with Coulomb and exchange interaction among electrons [1]. We discuss the computational burden associated with the explicit consideration of the electron spin in the previous formalism [1]. In particular, we provide a numerical justification that shows the viability of the previous formalism for a system with a large ($N \approx 100$) number of electrons. We consider a system of N electrons described by a many-particle wave-function $\Psi(\vec{r}_1, \vec{r}_2, \vec{r}_3 \dots \uparrow_1, \downarrow_2, \downarrow_3 \dots; t)$ with \vec{r}_i the electron position and $\uparrow_i / \downarrow_i$ its (up/down) spin. We use an uncoupled spin-base which is adequate for (non-conservative spin) open systems. In the previous formalism [1], the Bohm velocity of each electron has to be computed directly from the many-particle wave-function. Since this formalism is intrinsically time-dependent [1], the standard simplifications in the computation of the many-particle wave-function, obtained from Hamiltonian (orthogonal) eigenstates, cannot be used. In addition, the explicit evaluation of $N!N!$ products of permutations for the computation of the many-particle system is intractable for more than very few electrons because of computational limitations (note that $8!^2 = 40320^2$). The previous computational limitation is overcome by computing the many-particle velocity with the assumption that the many-particle wave-function can be separated into a product of spin-up (\uparrow) and spin-down (\downarrow) many-particle wave functions:

$$\Psi(\vec{r}_1, \vec{r}_2, \vec{r}_3 \dots \uparrow_1, \downarrow_2, \downarrow_3 \dots, t) \approx \Psi(\vec{r}_1, \vec{r}_4 \dots \uparrow_1, \uparrow_4 \dots, t) \cdot \Psi(\vec{r}_2, \vec{r}_3 \dots \downarrow_2, \downarrow_3 \dots, t). \quad (1)$$

Then, the numerical difficulties in the computation of the many-particle Bohm velocity disappear because it can be computed from a complex matrix (Slater) determinant. In order to numerically verify the correctness of our assumption, we compute the Bohm velocity associated to electron 1 in four different (exchange-interacting) situations. We have defined the parameter d as a normalized (i.e. without units) phase-space distance [2] between electron 1 and the others (see insets in all Figures). We have chosen arbitrary initial Gaussian wave-packets. In Fig. 1, we show the Bohm velocity (with an approximate value of 6×10^4 m/s) for one independent (spin-up) electron. In Fig. 2, we plot the same Bohm velocity for the same electron when other 4 exchange-interacting electrons are present. As we decrease the distance d among electrons, the Bohm velocity becomes very different from Fig. 1 as a consequence of the Pauli (Exclusion) Principle. In Fig. 3, we show one spin-up electron and two spin-down electrons. Surprisingly, when Fig. 3 is compared with Fig. 1, an exchange interaction between spin-up and spin-down electrons is present due to the non-orthogonal spatial behavior of our "arbitrary" wave-functions. However, the effect of such spin-up-spin-down interaction in the Bohm velocity is quite small when compared to its effect with the spin configuration of Fig. 4, where the 3 spin-up electrons of Fig. 2 are considered. The strong resemblance between the Bohm velocities of Figs. 2 and 4 for the different values of d provides a numerical justification

of expression (1) for the computation of many-particle Bohm velocities. The same result is obtained for many other spin schemes.

In conclusion, we present a powerful proposal to study quantum transport with the explicit consideration of Coulomb and exchange interaction among electrons. We show the practical numerical viability of our proposal for large, $N \approx 100$, number of electrons. Since the algorithm deals with time-dependent Schrödinger equations in terms of quantum trajectories, it can be applied for the computation of the average current or its fluctuations [3] in zero or high frequency [4] quantum scenarios.

This work was supported through Spanish MEC project TEC2006-13731-C02/MIC.

References:

- [1] X.Oriols, Physical Review Letters, 98, 066803 (2007).
- [2] X.Oriols, Nanotechnology 15, S167- S175 (2004).
- [3] G. Albareda, J.Suñe, X. Oriols, Phys. Rev. B 79, 075315 (2009).
- [4] A.Alarcon, X.Oriols, J. Stat. Mech, 2009 (P01051) (2009).

Figures:

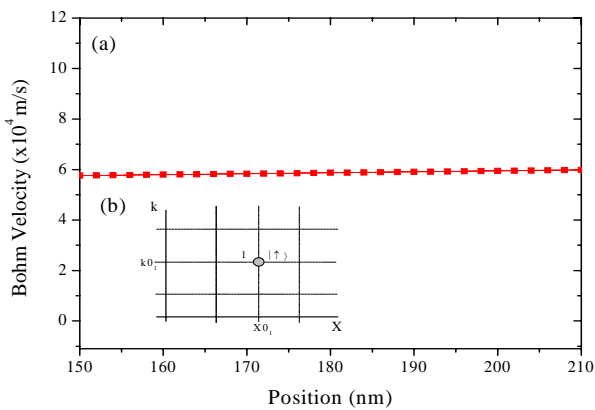


Fig. 1. (a) Bohm velocity for an independent electron. (b) Schematic representation of the system for an electron where we indicate the central value of the X₀ and wave-vector K₀.

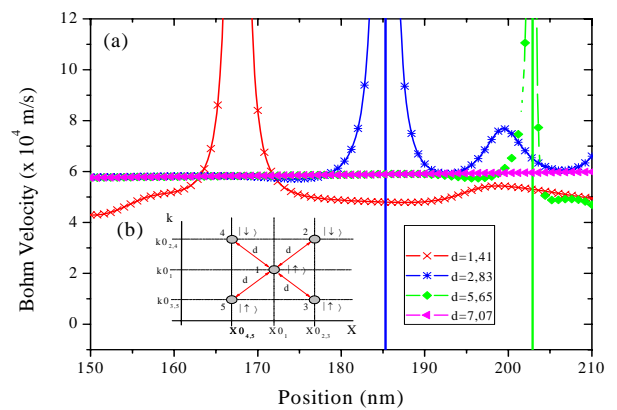


Fig. 2. (a) Bohm velocities for 1-electron using different values of d for a system of 5 electrons (3 spin-up and 2 spin-down). (b) In this scheme we indicate the central value of the X₀ and wave-vector K₀ of these electrons.

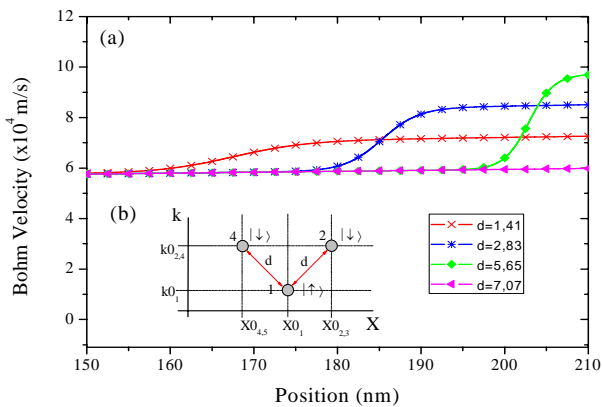


Fig. 3. (a) Bohm velocities for 1-electron using different values of d for a system of 3 electrons (1 spin-up and 2 spin-down). (b) In this scheme we indicate the central value of the X₀ and wave-vector K₀ of these electrons.

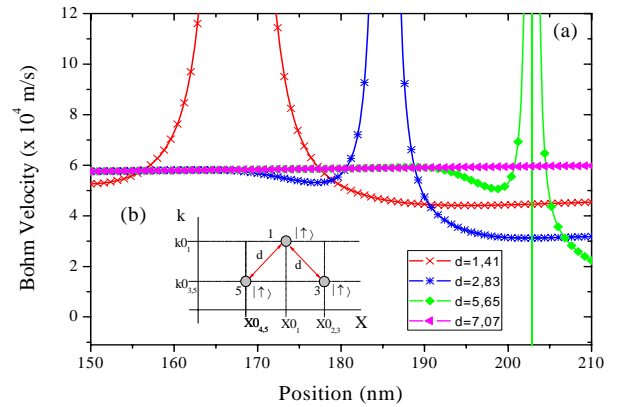


Fig. 4. Bohm velocities for 1-electron using different values of d for a system of 3 electrons (spin-up). (b) In this scheme we indicate the central value of the X₀ and wave-vector K₀ of these electrons.

TECHNOLOGICAL DEVELOPMENT FOR STEP AND REPEAT IMPRINT LITHOGRAPHY

*Nerea Alayo*¹, *Irene Fernández-Cuesta*^{1,*}, *Libertad Solé*^{1,2}, *Xavier Borrisé*^{1,2},
*Francesc Pérez-Murano*¹

¹ Instituto de Microelectronica de Barcelona (IMB-CNM, CSIC)

² Centre d'Investigaciones en Nanociencia i Nanotecnologia (CIN2, ICN-CSIC)

Campus de la Universitat Autònoma de Barcelona, E-08193 Bellaterra. SPAIN

Nerea.Alayo@imb-cnm.csic.es

* Present address: DTU-Nanotech

The possibility of replication of the nanostructures of a hard stamp into a polymer was first proposed by S. Chou et. al. in 1995 [1]. Since then, nanoimprint lithography (NIL) has evolved from being a promising alternative method for nanofabrication [2, 3], to be, nowadays, a mature technique that allows obtaining nanometer scale features at wafer scale, with high reproducibility and throughput [4]. The applications taking advantage of NIL fabricated structures covers from micro/nano electronics, material sciences, or biology, just to cite some examples. In this communication, we will show several technological developments for the fabrication of interdigitated nano-electrodes using different imprinting-based approaches.

Two different NIL methods have been developed. **Thermal NIL** process consists on embossing a deformable polymer above its glass transition temperature (T_g) with a hard stamp, cooling-down the system and releasing the pressure when the polymer is solid again. In **UV-NIL**, a transparent stamp is approached to the substrate, which is coated with a liquid photocurable pre-polymer or a very low molecular weight resist, so just a soft pressure is needed to fill the cavities with the liquid, that then is cured with UV light, so after releasing the stamp, the features are replicated in the polymer. On the other hand, the imprinting processes can be performed in a single imprint step of the whole sample (parallel printing) or by **step and repeat**, using smaller stamps and doing multiple replications in the wafer.

We are developing processes for thermal and UV step and repeat imprint lithography using an NPS 300 system from SET [5], recently installed at the IMB-CNM clean room. It is able to perform alignment with an accuracy of few hundreds of nanometers, which is important not only to carry out multiple step and imprint processes, but also to make structures in different layers. Several imprinting parameters are being optimized, such as the temperature of the stamp and chuck during imprinting. In the case of UV-NIL, the resist is dispensed locally for each imprinting step, so that it is cured at each local site. The imprinting process parameters needs to be studied and optimized according to the stamp geometry, structures depth and filling factor.

Several technological processes for **stamp fabrication** are also being developed. Figure 2 shows a silicon stamp fabricated by electron-beam lithography and reactive ion etching. Figure 3 shows an image of a transparent stamp, made in a novel polymer [7], for UV-NIL. More examples will be presented at the conference.

Acknowledgements

This work is partially financed by NILSIS (TEC2006-13910-C03-01/MIC) and Consolider-Nanobiomed (CSD00C-06-04615) projects. We thank Santos Merino and Aritz Retolaza from Fundación Tekniker for the reactive ion etching processes.

References:

- [1] Chou, S.Y., Krauss, P.R. and Renstrom, P.J., Applied Physics Letters, 1995 **67**, 3114.
- [2] Chou, S.Y. and Krauss, P.R., Microelectronic Engineering, 1997 **35**, 237.
- [3] Guo, L.J., Krauss, P.R. and Chou, S.Y., Applied Physics Letters, 1997. **71**, 881
- [4] Luesebrink, H. Microlithography World, 2006. **15**, 4
- [5] SET-Smart Equipment Technology. France. www.set-sas.fr
- [6] Fernandez-Cuesta, Irene. *Nanoimprint lithography: developments and nanodevice fabrication*. PhD Thesis. Universitat Autònoma de Barcelona. 2009
- [7] ORMOSTAMP from micro resist technology GmbH, Berlín. www.microresist.com

Figures:

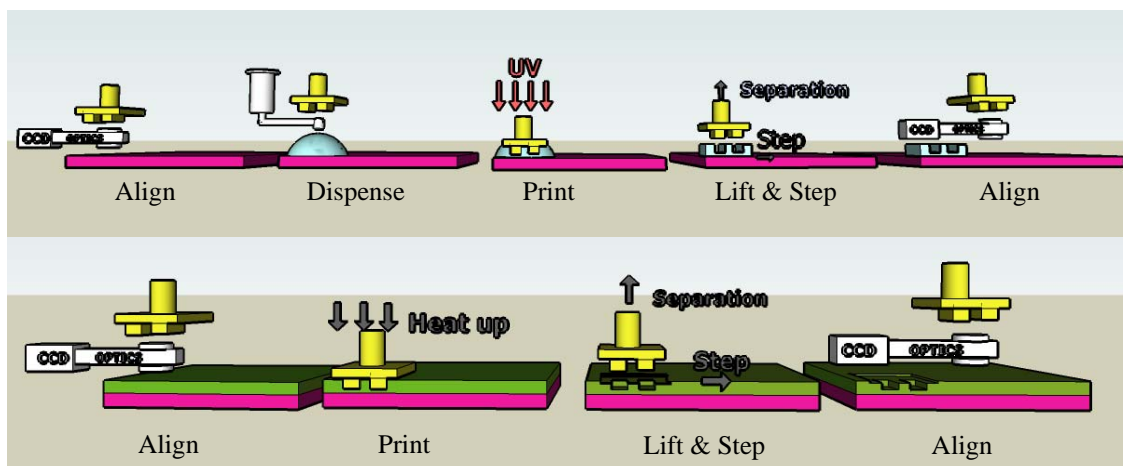


Figure 1. Scheme of UV-NIL process: align stamp and substrate, dispense the resist, print and UV cure, lift&step and align for a new imprint. Scheme of Hot Embossing process: align stamp and substrate, print applying pressure and heating up above the T_g of the polymer, lift&step and align for a new imprint.

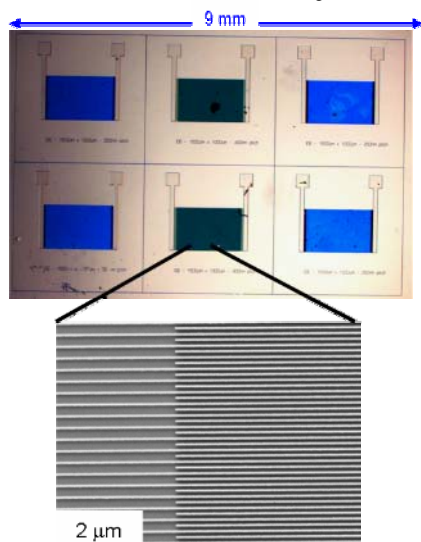


Figure 2. Silicon stamp containing six individual chips with structures of nanometric interdigitated electrodes. The stamp was fabricated by electron beam lithography, metal, lift-off, and reactive ion etching. The effective area of the digits is 1 mm x 1.5 mm. The pitch is varied from 250 nm to 400 nm, the electrode width is fixed at 150 nm, and the depth is 180 nm, as evaluated from AFM measurements.

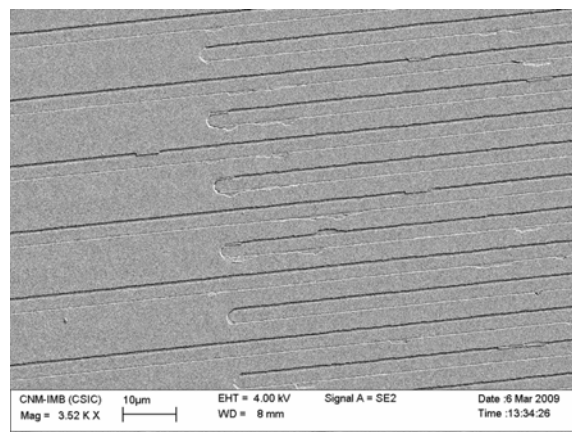


Figure 3. SEM image of the detail of one polymer stamp made of ORMOCOMP by replication from a silicon stamp. Depth of the features is 150 nm. Good uniformity is observed at chip level. The surface is covered with a gold layer to allow the SEM imaging. Process details will be shown at the conference.

MANY-PARTICLE EFFECTS IN THE ELECTRIC POWER OF NANOSCALE OPEN SYSTEMS

G.Albareda and X.Oriols

Departament d'Enginyeria Electrònica, Universitat Autònoma de Barcelona, 08193 Bellaterra, Spain

guillem.albareda@uab.cat

Due to computational limitations, one necessary strategy to study nanoscale structures is to reduce, as much as possible, the simulated degrees of freedom. This necessary separation of degrees of freedom is always traumatic because, in general, a subcomponent of the whole system cannot be described independently of the rest (See Fig. 1). The openness of classical and quantum systems has been studied extensively in the literature, but few works are devoted to discuss its effect on the computation of electric power. Here, we provide a novel expression for accurate estimation of the electric power in nanoscale open systems using a many-particle electron transport formalism that goes beyond the standard “mean field” approximation [1]. Surprisingly, we show that the usual expression of the electric power, as the product of the (time-averaged) current $\langle I \rangle_T$ and the voltage $\langle V \rangle_T$, is not accurate in nanoscale systems.

In order to provide a common classical and quantum language for our argumentation, we formulate the problem in terms of the de Broglie–Bohm approach of quantum mechanics for an open system of non-relativistic (spinless) Coulomb-interacting electrons [1,2]. Then, it can be shown that the mean electric power, P , for the $N(t)$ electrons inside the open system (see Fig. 1b) is:

$$P = \sum_{i=1}^{N(t)} q_i \langle \vec{v}_i(t) \vec{E}_i(t) \rangle_B, \quad (1)$$

where $\vec{v}_i(t)$ is the (Bohm) velocity of the i electron and $q_i \vec{E}_i(t)$ is the electrostatic force made by the rest of electrons of the whole (closed) system on it. Here, $\langle \dots \rangle_B$ is the de Broglie-Bohm averaging that can be converted into time averaging $\langle \dots \rangle_T$ under standard ergodic argumentations. After some straightforward development, the final value of the mean electric power P of expression (1) can be written as:

$$P = \langle I \rangle_T \cdot \langle V \rangle_T - \left\langle \sum_{i=1}^{N(t)} \sum_{\substack{j=1 \\ j \neq i}}^M \vec{\nabla}_{\vec{r}_j} W_i(\vec{r}_1, \dots, \vec{r}_j, \dots, \vec{r}_i(t), \dots, \vec{r}_M) \Big|_{\vec{R}_i = \vec{R}_i(t)} \cdot \vec{v}_j(t) \right\rangle_T, \quad (2)$$

where $W_i(\vec{r}_1, \dots, \vec{r}_j, \dots, \vec{r}_i(t), \dots, \vec{r}_M)$ is the i -th electrostatic potential defined in Ref. [1] that depends on the M electrons present in the close (whole) system (see Fig. 1a) and $\vec{R}_i(t) = (\vec{r}_1(t), \dots, \vec{r}_j(t), \dots, \vec{r}_{i-1}(t), \vec{r}_{i+1}(t), \dots, \vec{r}_M(t))$. The first term on the right side of (2) is the standard $\langle I \rangle_T \cdot \langle V \rangle_T$ power expression, while the second term represents the “unexpected” effects of the many-particle correlations on the electric power.

In order to show the relevance of the many-particle power correlations, we have simulated a nanoscale resistance using, both, a standard single-particle semiconductor Monte Carlo simulator and a many-particle electron transport approach explained in Ref. [1].

In fig. 2a, we have represented the current-voltage characteristic for a nanoscale resistance using a single-particle (i.e. time-independent electric-field) electron transport approach. We define the correlation power factor as the following (dimensionless) parameter, $G = (\langle I \rangle_T \cdot \langle V \rangle_T) / P$. As expected, the value of G reduces to unit, i.e. $P \approx \langle I \rangle_T \cdot \langle V \rangle_T$, indicating that many-particle Coulomb-interaction effects in the power computation are not accessible with single-particle electron transport simulations (Fig.2b). On the contrary, when the many-particle electron transport formalism explained in Ref. [1] is used, then, the relevance of correlations in the average power becomes evident (at low bias) in the correlation power factor G depicted in Fig. 3b.

The physical explanation of our “unexpected” many-particle corrections on the electric power is that the computation of power in numerical simulators has to account only for the (non-conservative) energy associated to the $N(t)$ electrons inside the open system, rather than the (conservative) energy of the M electrons inside the whole system (see Fig. 1). From a practical point of view, the relevance of our work is due to the fact that the small many-particle correction that appears on the electric power in a single state-of-the-art device ($\ll \mu\text{W}$) become dramatically huge when we multiply it by the number of transistors ($\ll 10^9$ transistors) present in modern computers.

References:

[1] G. Albareda, J. Suñé and X. Oriols, Physical Review B, **79** (2009) 075315.
 [2] X. Oriols, Physical Review Letters, **98** (2007) 066803.

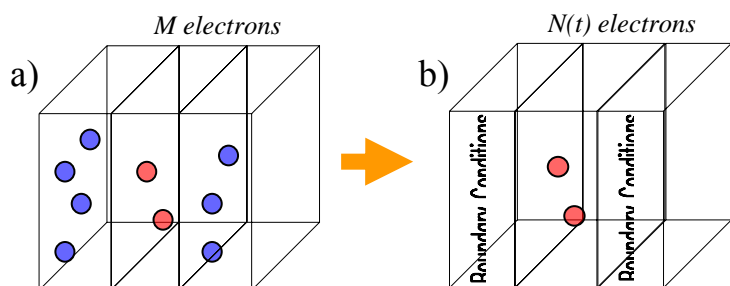


Fig.1. Schematic representation of the electrons in an electron device. a) A closed (whole) system of M electrons in the active region and the reservoirs and b) the open system of $N(t)$ electrons in the active region.

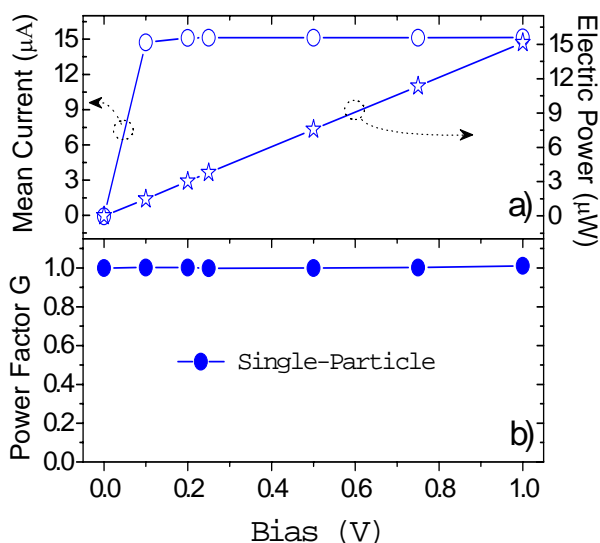


Fig.2. a) Average current, electric power, and b) correlation power factor, G , defined in the text as a function of bias. Electron transport is computed from a single-particle approach.

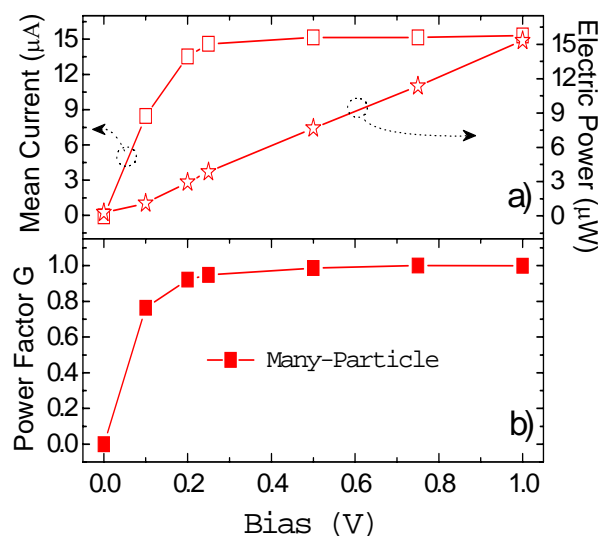


Fig.3. a) Average current, electric power, and b) correlation power factor, G , defined in the text as a function of bias. Electron transport is computed from the many-particle approach described in [1].

Recyclable Catalytically Active Superparamagnetic Polymer-Metal Nanocomposites with Enhanced Structural Parameters

A. Alonso, D.N. Muraviev, M. Muñoz, A. Vallribera, A. Shafir

Departament de Química, Universitat Autònoma de Barcelona, 08193 Bellaterra, Barcelona, Spain

amanda.alonso@uab.cat

The Metal Nanoparticles (MNPs) have found numerous applications lasting recent years due to their unique physical and chemical properties. One of the routes to overcome the high instability of MNPs (resulting in their agglomeration and aggregation) lies in the use of polymeric materials for the synthesis and stabilization of MNPs [1, 2]. Additionally, a serious concern associated with the growing production and the use of MNPs deals with a possibility of their uncontrollable release to the medium under treatment. A possible solution to this problem can be based on: 1) the immobilization of MNPs in polymers and 2) the synthesis of superparamagnetic MNPs, which would allow both the prevention of their escape and MNPs recovery and reuse by simply using a magnetic trap. This is particularly important in the case of catalytically-active nanoparticles containing platinum group metals (mainly for economical reasons).

In this presentation we report the synthesis, characterization and application of superparamagnetic core-shell MNPs with a Co-core and a functional Pd-shell. The MNPs were synthesized by using Intermatrix Synthesis (IMS) technique within the matrix of functional polymer [3,4]. The final material was characterized by ICP-OES, SQUID techniques and Electron Microscopy to determine the total metal content, the magnetic properties of polymer-metal nanocomposite and the size of nanoparticles and their distribution inside the polymeric matrix, respectively.

It has been shown that MNP-polymer nanocomposites are characterized by superparamagnetic properties and MNPs are distributed on the periphery of the fibers as shown in Fig. 1 (a, b) and also illustrated by EDS measurements presented in Fig. 1 (c). The distribution of Pd@Co core-shell MNPs at the surface of polymer fibres (the most favourable site for catalytic applications) can be explained by the action of Donnan-exclusion effect [5] during the reduction step (by using NaBH₄ as reducing agent) in the IMS of metal nanoparticles.

One of the applications of this material is as a nanocatalyst in some organic Cross-Coupling reactions [6] (e.g. Suzuki reaction in our case, see Scheme 1). In our presentation we report also some advantages of the use of this new nanocomposite in catalytic reactions, which follow from the results of studying the most important experimental parameters affecting in the efficiency of reaction (temperature, time, catalyst loading, solvents, catalytic cycles, etc.).

References:

- [1] J. Macanas, J. Parrondo, M. Muñoz, S. Alegret, F. Mijangos, D.N. Muraviev, *Phys. Stat. Sol. (a)* 204, 1699-1705 (2007).
- [2] D.N. Muraviev, P. Ruiz, M. Muñoz, J. Macanás, *Pure Appl. Chem.*, 80(11), 2425-2437 (2008).
- [3] D.N. Muraviev, *Contrib. Sci.* 3 (1), 19-32 (2005).
- [4] V. S. Soldatov, *Solvent Extraction and Exchange*, 26, 457-513 (2008).
- [5] F.G. Donnan, *Journal of Membrane Science* 100, 45-55 (1995).
- [6] S. Niembro, A. Safhir, A. Vallribera, R. Alibés, *Organic Letters*, 10, 3215-3218 (2008).

Figures:

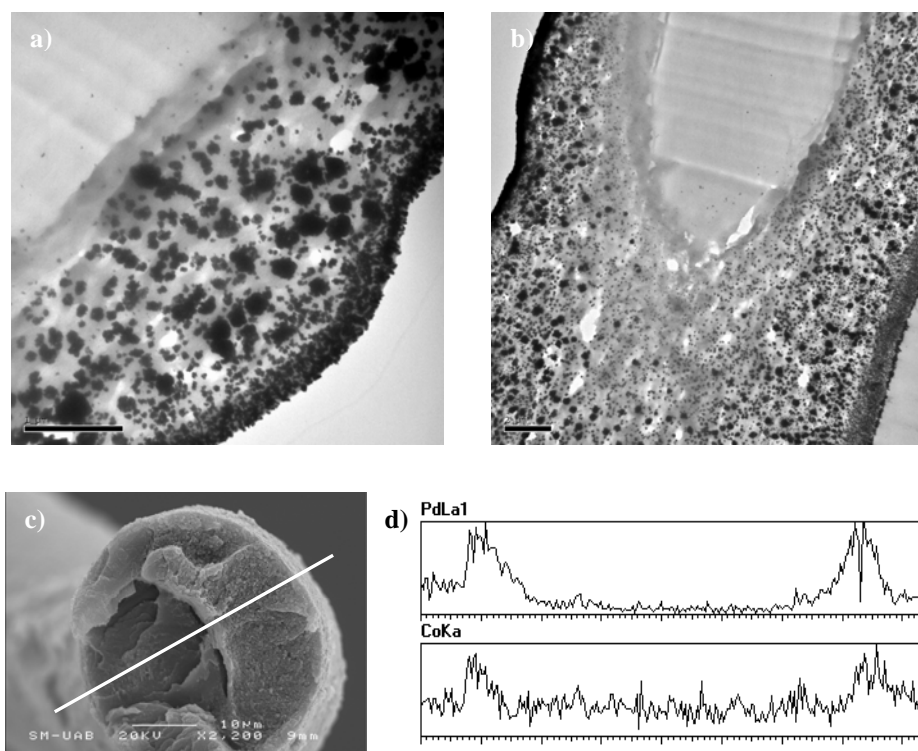
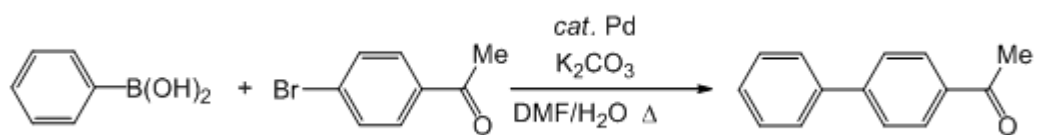


Fig 1. TEM images of fibre cross section after loading with Pd@Co nanoparticles (a, b), SEM image of fibre cross section after loading with Pd@Co nanoparticles (c) and Pd and Co LineScan EDS spectra (d).



Scheme 1. Suzuki Cross-Coupling reaction and the experimental conditions.

Collective magnetic behaviors in $\text{Fe}_x\text{Ag}_{100-x}$ granular thin films ($25 < x < 55$)

J. Alonso¹, M.L. Fdez-Gubieda¹, J.M. Barandiaran¹, L. Fernández-Barquín³, I. de Pedro³, I. Orue², A. Svalov¹

¹*Dpto. Electricidad y Electrónica, Universidad del País Vasco, Bilbao, Spain.*

²*SGIKER, Servicios Generales de medidas magnéticas, Universidad del País Vasco, Bilbao, Spain.*

³*CITIMAC, Universidad de Cantabria, Santander, Spain.*

jalonsomasa@gmail.com

The study of the magnetic behaviour of assemblies of interacting nanoparticles has attracted great attention from material scientists for many years. The understanding of these interactions is important not only from a theoretical point of view, but also for various technological applications.[1] Depending on the Fe content one can obtain very different magnetic collective behaviours, from an interacting superparamagnet (ISPM) at low enough concentrations to a superferromagnet (SFM) or a correlated superspin glass (CSSG) at higher volume fractions. Binary Fe-Ag alloys are ideal systems to study such phenomena since Fe and Ag are highly immiscible, and so, it is viable to produce samples consisting of Fe nanoparticles embedded in a diamagnetic Ag matrix. In our case, we have focused on the study of Fe-Ag thin films with Fe concentrations above 25 at. % prepared both by pulsed laser deposition (PLD) and sputtering techniques.

We have prepared Fe-Ag thin films (~100-200 nm) in the range of 25-55 at.% of Fe. Their composition was determined by energy dispersive X-ray analysis (EDX). Both PLD and sputtered films were coated with ~ 10 nm silver and gold capping layers, respectively. They were deposited at room temperature onto Si(100) substrates with a native oxide layer. The microstructure was studied by X-ray diffraction (XRD) and Transmission Electron Microscopy (TEM), and DC and AC magnetic characterization was performed using VSM and SQUID magnetometers as a function of temperature (5-350 K) and with frequencies in the range 0.01-1000 Hz.

X-Ray diffraction spectra have revealed the presence of small Fe bcc nanoparticles (~3 nm) inside a granular Ag fcc matrix (~7-9 nm). They also have suggested the presence of a certain amount Fe-Ag alloy, more noticeable for PLD samples. This has been corroborated by HRTEM analysis (see Fig. 1 left), which clearly shows an extended amorphous Fe-Ag interphase among the grains for PLD thin films, and which is called to be relevant in order to understand the magnetic behaviours observed in our samples. In these films we have found a rich variety of collective magnetic states modulated by the competition between interparticle interactions, mainly of dipolar and direct exchange character and the intraparticle anisotropy energy. These findings have demonstrated that even weak changes in the size and the compaction of the magnetic particles greatly modify the magnetic response of the films. Samples deposited by PLD show an increase of the susceptibility up to ~50 K, followed by a smooth variation characteristic of a ferromagnetic state up to 150-200 K, where the susceptibility decreases in a Curie-Weiss type decay. As the volume fraction changes, these phases evolve and even new phases as a spin-glass like state at low temperatures emerge (see Fig 1, bottom-right). On the other hand, for the sputtered sample a clear Curie transition at 310 K, with the susceptibility dropping to zero, has been found for the lowest composition studied (30 at. % of Fe). A slight increase of the Fe content can suppresses this transition (see Fig 1, top-right).

In order to get deeper insight of the magnetic behaviour, we have also performed zero field cooled AC magnetization measurements. Concerning sputtered thin films, both χ' and χ'' curves show a pronounced maximum (near 140 K, for $\text{Fe}_{25}\text{Ag}_{75}$), indicating a magnetic transition

similar to that presented by cluster spin glasses, probably mediated by magnetic dipolar interactions. For PLD thin films, AC susceptibility measurements have revealed a magnetic behavior analogous to the corresponding ZFC curve, showing χ' the presence of a magnetic phase transition with a Curie temperature due to the magnetic interactions (~ 185 K for $\text{Fe}_{51}\text{Ag}_{49}$). Below the transition temperature, χ' presents a smooth variation characteristic of a ferromagnet freezing. A similar magnetic behaviour has been found in discontinuous metal-insulators multilayers [2].

To sum up, these measurements have shown different and interesting non previously observed collective magnetic behaviours for sputtered and PLD thin films in the same range of compositions, mediated by differences in Fe grain sizes and spatial arrangements, and the Fe-Ag interface (as observed, more relevant for PLD samples).

References:

- [1] G. A. Prinz, **Science** 282, (1998) 1660
 [2] W. Kleemann, O. Petracic, Ch. Binek, G. N. Kakazei, Yu. G. Pogorelov, J. B. Sousa, S. Cardoso and P. P. Freitas, **Phys. Rev. B** 63, (2001) 134423

Figures:

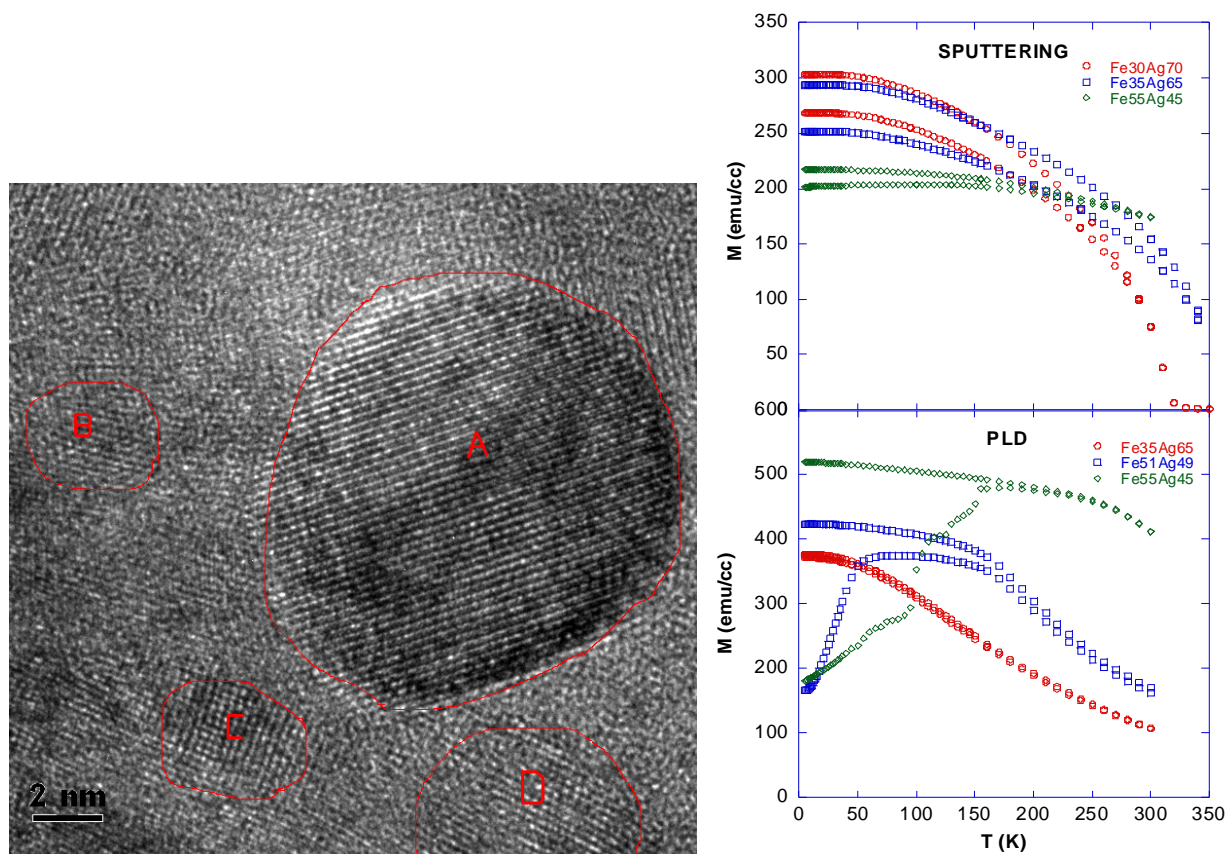


Fig1: (left) HRTEM image of a $\text{Fe}_{55}\text{Ag}_{45}$ PLD thin film. A is an Ag fcc grain, and B, C and D are Fe bcc iron grains (right) ZFC-FC curves for (top) sputtered $\text{Fe}_x\text{Ag}_{100-x}$ ($x=30, 35, 55, h=1$ Oe) and (bottom) PLD $\text{Fe}_x\text{Ag}_{100-x}$ ($x=51, 53, 55, h=5$ Oe) samples.

POLYMER CONDUCTOR AS TUNING OF THE POROUS SILICON PHOTONIC BANDGAP NANOSTRUCTURES

P. Altuzar-Coello^a, J. A. del Río^a, M.E. Nicho^b, Hailin Hu^a, M. Guizado^b, R. Cruz-Silva^b, M. García-Rocha^c, J. Gpe. Bañuelos^d, M. Reyes-Salas^e, C. Linares^f.

^a Centro de Investigación en Energía, Universidad Nacional Autónoma de México, Temixco, Morelos, México. E-mail: peac@cie.unam.mx

^b Centro de Investigación en Ingeniería y Ciencias Aplicadas, Universidad Autónoma del Estado de Morelos, Cuernavaca, Morelos, México.

^c Departamento de Materiales, CINVESTAV, Instituto Politécnico Nacional, México, D.F. México.

^d Centro de Ciencias Aplicadas y Desarrollo Tecnológico, Universidad Nacional Autónoma de México, México, D.F. México.

^e Instituto de Geología, Universidad Nacional Autónoma de México, México, D.F. México.

^f Instituto de Geofísica, Universidad Nacional Autónoma de México, México, D.F. México.

Nanostructures composites based on porous silicon (PSi) and conducting polymer (CP) excite interest due to the solution-based processing technology by which the cost can be reduced when compared with the conventional semiconductor. Devices like polymer light-emitting diodes, photo-voltaic cells, solution-based light-emitting devices, have already achieved practical success. In the present research effect of conducting polymer on photoluminescence characteristics of PSi-CP composites has been studied.

The poly(3-hexylthiophene)(P3OT) and poly(3-octylthiophene)(P3HT) were deposited on the surface p-type(100) PSi (85%-97% porosity) by spin coating method. The PL emission excited by HeCd lamp at 441 nm wavelength laser line was used. Obtained structures were studied by FT-IR spectroscopy, Atomic force microscopy and Scanning electronic microscopy and examined on the ability to photoluminescence (PL).

It has been found that presence of conducting polymer integrated to porous silicon has a different influence on the visible luminescence of PSi. In both P3OT-PSi composite (85%-97% porosity) and P3HT-PSi show an displacement of the maximum PL to higher energies and higher intensity PL in comparison with P3OT and P3HT respectively. Tunable emission at green wavelength are demonstrated. The efficiency ratios greater can be achieved by modifying the porous silicon size (~ 100 nm) and morphology. SEM images shows 1,5 and 10 μm of thickness porous silicon cross-section at an etching current density of 20, 50 and 100 mA/cm^2 during 35s. The analysis of PL spectra of the composites is complex and can be decomposed into two elementary luminescence bands: an band peaked

at 6200-6500 nm, and an band, centred at 5400-5700 nm. The PL spectra of both types of composites(P3OT-PSi and P3HT-PSi) with 97% porosity shows two new PL bands: peaked at 670-690 and an band at 520 nm.

PL measurements of the P3OT/PSi and P3HT/PSi suggest that there is a carrier mediated component to the excitation mechanism. The band gap (E_g) of porous silicon is 1.8 eV. The E_g of P3HT is 1.67-2.14 eV and E_g of P3OT is 1.96-2.4 eV. HOMO of P3HT and P3OT are clearly higher in energy than the PSi HOMO. On these conditions it is energetically favorable for the photoexcited P3HT or P3OT to transfer an electron to PSi. Therefore, conductor polymer can be used as an electron donor with PSi as an electron acceptor. The tunable porous silicon microcavities can serve as active building blocks for microelectronics and microphotonics technologies.

TNT2009

September 07-11, 2009

Barcelona-Spain

TNT2009

September 07-11, 2009

Barcelona-Spain

THE ROLE OF REACTION TEMPERATURE ON THE GROWTH OF CARBON NANOMATERIALS

Issam Thaher Amr, Muataz Ali Atieh, Adnan Al-Amer, Mamdouh Al-Harhi, Khaled Mezghani
King Fahd University of Petroleum & Minerals, P.O. Box 5050, Dhahran-31261, Saudi Arabia

esamamr@kfupm.edu.sa

motazali@kfupm.edu.sa

alamer@kfupm.edu.sa

mamdouh@kfupm.edu.sa

mezghani@kfupm.edu.sa

Well aligned multi wall carbon nanotubes (MWCNTs), carbon nanofibers (CNFs) and other type of carbon nanostructure materials have been synthesized by a fabricated floating catalyst chemical vapor deposition (FC-CVD) method. This involved the pyrolysis of benzene-ferrocene vapor mixture. Carbon nanotubes films with a diameter of 2-50 nm and nanofiber with a diameter range from 100-300 nm were synthesized in a benzene/hydrogen atmosphere. Furthermore vapor grown carbon fibers have been synthesized with different diameters and lengths. Iron clusters that were produced from the thermal decomposition of ferrocene films were used as catalyst for the synthesis of the carbon structures.

The effect of the reaction temperature on the production of carbon nanomaterials was investigated. The reaction temperature was varied from 500 °C to 1200 °C. By controlling the growth temperature, carbon nanotubes (CNTs), carbon nanofibers (CNFs) and vapor grown carbon fiber with different structures were produced. Increasing the temperature has a remarkable effect on the size and shape of the catalyst and this in turn affected the diameter distribution and structure of the carbon materials. The carbon nanotubes were produced from 600 °C to 850 °C with maximum yield at 850 °C, while for the production of carbon nanofibers the reaction temperature was from 900 °C to 1000 °C with a maximum yield at 1000 °C. Vapor grown carbon fibers were produced at 1050 °C to 1200 °C with maximum yield at 1050 °C.

STRUCTURAL AND MAGNETIC PROPERTIES OF Cu-Co NANOPARTICLES PREPARED BY MECHANOCHEMICAL SYNTHESIS

J. Angeles Islas¹, G. Alvarez², H. Montiel³, H. A. Calderón¹

¹Depto. Ciencia de Materiales, ESFM, Instituto Politécnico Nacional, Ed. 9 UPALM, México 07338 México D.F. México

²Depto. de Materiales Metálicos y Cerámicos, IIM, Universidad Nacional Autónoma de México, México D.F., 04510, México.

³Depto. de Tecnociencias, CCADET, Universidad Nacional Autónoma de México, México D.F., 04510, México.

E-mail: jangelesislases@yahoo.com.mx, hcalder@esfm.ipn.mx

Keywords: Mechanical Alloying; Nanoparticles; Magnetic Properties.

Abstract:

In the present work, we report the synthesis of nanoparticles of Cu-Co with 5, 20 and 50 % at Co, which are obtained by the reduction reaction between metallic chlorides in solid state, $\text{CuCl}_2 + \text{CoCl}_2 + 4\text{Na} \rightarrow \text{Cu/Co} + 4\text{NaCl}$, and that these are activated via the mechanical synthesis in a mill SPEX-D8000 of high energy. Additionally, NaCl is added as an environment to disperse the particles, and obtaining sizes below 5 nm; and that these are dependent on the time of the alloyed mechanic.

The nanoparticles are characterized by X-Ray diffraction (DRX), these indicate a reduction of the lattice parameters, and these suggest the formation of a solid solution between both metals. The images of electronic microscopy of high-resolution (HR-TEM) show his morphology (Fig.1) and also they indicate a homogeneous distribution of sizes. The previous results show that this synthesis method is useful for obtaining of nanoparticles with an alone metallic component, but it is also useful in the synthesis of particles in a solid solution.

A study of vibrant sample magnetometry (VSM) shows a typical magnetic response, that it is characteristic of a solid solution formed by nanometric particles [1]. These results show a narrow relation with the spectra of non-resonant microwave absorption, see Fig. 2, which are obtained in an electron paramagnetic resonance (EPR) spectrometer modified [2]; where this non-resonant signal is associated with magnetic order of the material [3]. Also, we compare the results for Cu and Co particles, which are synthesized by the same procedure, with the nanoparticles of the solid solution in order to highlight differences.

References

[1] Xu Fan et al. *Phys. Rev. B* **69** (2004) 094432.

[2] G. Alvarez et al. *J. Alloys Compd.* **369** (2004) 231.

[3] G. Alvarez and H. Montiel, *Magneto-sensitive techniques based on modulated microwave power absorption for detection of phase transitions*, in: Israel Betancourt (Ed.), *Magnetic Materials: Current Topics in Amorphous Wires, Hard Magnetic Alloys, Ceramics, Characterization and Modeling*, Research SignPost, Kerala, India, 2007.

Figures

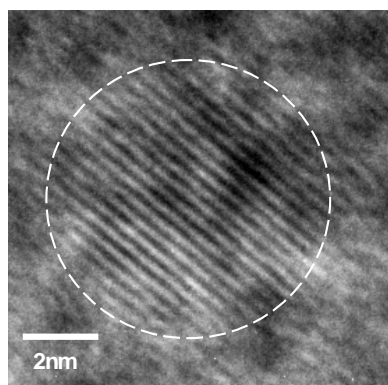


Fig. 1.- HR-TEM image of nanoparticles in the solid solution of Cu-Co with 20 % at Co.

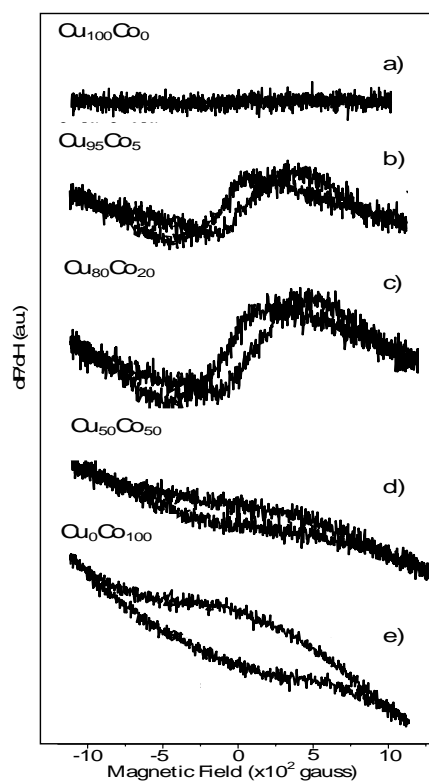


Fig. 2.- Non-resonant microwave absorption spectra for nanoparticles of Cu (a) and Co (e), and the solid solution of Cu-Co (b-d).

STUDY OF NANOROBOTS AS USEFUL THERAPEUTICALLY DEVICE IN NANOMEDICINE

Sahar Ardalan Khales^{1,*}, Sima Ardalan Khales¹

¹Genetic Students, members of young research club, Islamic Azad University branch of
Tonekabon, Iran

*saardalan2007@yahoo.com

Abstract

Nanorobotic artificial phagocytes called “microbivores” could patrol the bloodstream, seeking out and digesting unwanted pathogens including bacteria, viruses, or fungi. Microbivores would achieve complete clearance of even the most severe septicemic infections in hours or less. This is far better than the weeks or months needed for antibiotic-assisted natural phagocytic defenses. The nanorobots do not increase the risk of sepsis or septic shock because the pathogens are completely digested into harmless sugars, amino acids and the like, which are the only effluents from the nanorobot.

Key words: nanorobots, microbivores, Nanomedicine

DEVELOPMENT OF NANOTECHNOLOGIES FOR DRUG DELIVERY ACROSS THE BLOOD BRAIN BARRIER (BBB)

Sima Ardalan Khales^{1,*}, Sahar Ardalan Khales¹

¹Genetic Students, members of young research club, Islamic Azad University branch of
Tonekabon, Iran

*siardalan2008@yahoo.com

Abstract

Nanotechnology-based approaches to targeted delivery of drugs and other compounds across the BBB may potentially be engineered to carry out specific functions as needed. The drug itself – in other words the biologically active component being delivered, whatever that may be – constitutes one element of a nanoengineered complex. The rest of the complex is designed to carry out other key functions, including shielding the active drug from producing systemic side effects, being prematurely cleared or metabolized, crossing the BBB, and targeting specific cells after it has gained access to the CNS. Implicitly, all of this must be achieved by any drug intended to have CNS effects, regardless of whether it is part of a nanoengineered complex. An important advantage of a nanotechnological approach, as compared with the administration of free drug or the drug associated with a nonfunctional vehicle, is that these critical requirements do not need to be carried out by the active compound, but by supporting parts of the engineered complex. This allows the design of the active drug to be tailored for maximal efficacy. Currently, most nanoengineered systems for crossing the BBB take advantage of drugs that are already in clinical use and therefore have greater potential for reaching the clinic relatively quickly. This review discusses some of the main technical challenges associated with the development of nanotechnologies for delivery across the blood brain barrier.

Keywords: blood brain barrier, nanoengineered complex, drug delivery

Thermodynamic properties of Au-Pd nanostructured surfaces studied by atomic scale modeling

Ivailo Atanasov, Marc Hou

Physique des Solides Irradiés et des Nanostructures CP234, Université Libre de Bruxelles, Bd du Triomphe, 1050 Brussels, Belgium
iatanaso@ulb.ac.be

The understanding of equilibrium Au-Pd nanostructures is important in view of catalytic applications. The composition and ordering properties in the vicinity of Au-Pd cluster surfaces at equilibrium are studied using the Metropolis Monte Carlo importance sampling and a popular version of the embedded atom method (EAM). The clusters contain about 1000 atoms.

The thermodynamic stability of the ordered phases in the bulk and at the cluster surfaces is discussed on the basis of simulations in the semi-grand canonical ($\Delta\mu$, NPT) statistical ensemble. A stable ordered phase in this case is evidenced by a constant composition within a certain interval of values of the chemical potential difference $\Delta\mu = \mu_{\text{Au}} - \mu_{\text{Pd}}$. (Fig. 1)

Surface enrichment in Au is systematically predicted, accompanied by partial sub-surface enrichment in Pd, best enhanced around the equiatomic overall composition. Clusters display similar segregation and ordering properties as flat infinite surfaces. However, no thermodynamic stability of the ordering at cluster surfaces could be evidenced.

We also address the question about the sensitivity of the segregation and ordering properties on the surface energy. To this purpose, the parameterization of the EAM potential used has been modified in order to predict surface energies closer to the experimentally measured ones, 1.5 J/m² and 2.0 J/m² for Au and Pd respectively, as shown in the following table.

Surface	Standard EAM, J/m ²	Modified EAM, J/m ²	
Au	{111}	0.884	1.407
	{100}	0.973	1.497
	{110}	1.027	1.582
Pd	{111}	1.610	1.903
	{100}	1.722	2.011
	{110}	1.841	2.148

The new parameterization does not induce significant changes with regard to the results shown in Fig. 1. It is therefore concluded that surface energy is not of a major importance in segregation and ordering properties of nanostructured Au-Pd alloy surfaces.

Figures:

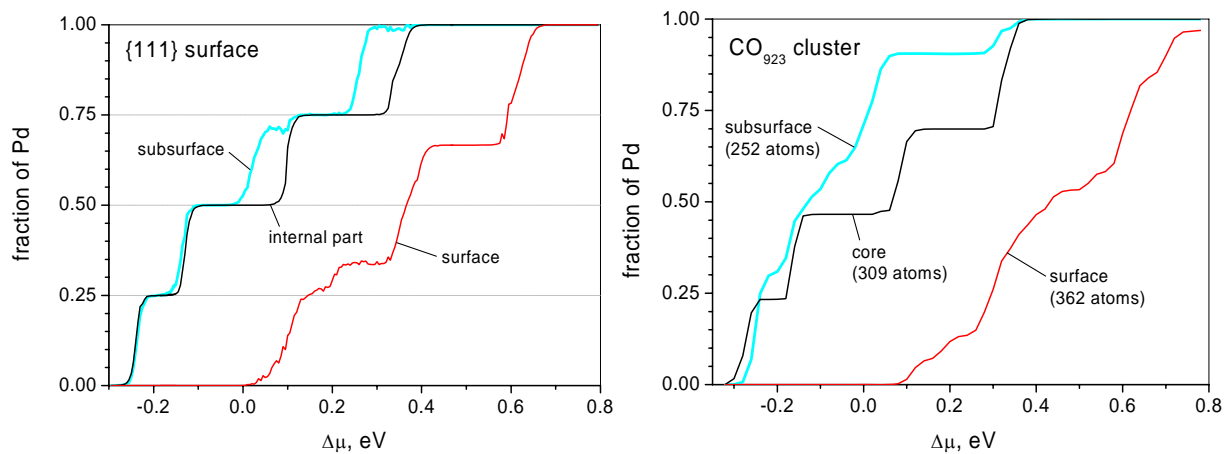


Figure 1. Composition versus $\Delta\mu$ in an infinite {111} surface and in a cuboctahedral cluster containing 923 atoms at $T = 100$ K. The surface, subsurface and the internal part of the system are separately shown.

NEAR FIELD OBSERVATION OF SURFACE PLASMONS GENERATED ELECTRICALLY

A. Babuty, Y. De Wilde

Institut Langevin, ESPCI Paristech, CNRS UMR7587, Laboratoire d'Optique Physique, 10 rue Vauquelin, 75231 Paris, France.

A. Bousseksou, J.-P Tetienne, Y. Chassagneux, R. Colombelli

Institut d'Electronique Fondamentale, Université Paris-Sud and CNRS, UMR8622, 91405 Orsay, France.

Contact : arthur.babuty@espci.fr

Surface plasmons are electromagnetic waves originating from electrons and light oscillations at metallic surfaces. These electromagnetic waves which propagate in a direction parallel to the metal/dielectric interface can be used to detect molecular species in functionalized biosensors. There are three main techniques for the excitation of surface plasmons. The first technique uses a prism and total internal reflection, the second one involves scattering from a topological defect like small holes in a thin film and the third technique makes use of periodic corrugations in the metal's surface.

In situ generation of surface plasmons using an active device would clearly be advantageous.

We will present near-field measurements highlighting a new method for the generation of surface plasmons via a quantum cascade laser (QCL), operating in the mid infrared ($\lambda = 7,7\mu\text{m}$), whose metallic top cladding has been periodically structured with a gold grating [1].

We give a direct proof of surface plasmons generation by measuring with an apertureless near-field scanning optical microscope (NSOM) the presence of an intense, evanescent electric field above the metal grating upon electrical injection into the device.

Our efforts are currently devoted to launching those surface plasmons into a passive waveguide.

[1] A. Bousseksou, R. Colombelli, A. Babuty, Y. De Wilde, Y. Chassagneux, C. Sirtori, G. Patriarche, G. Beaudoin, I. Sagnes. *Optics Express*, **17**, (2009), 9391-9400.

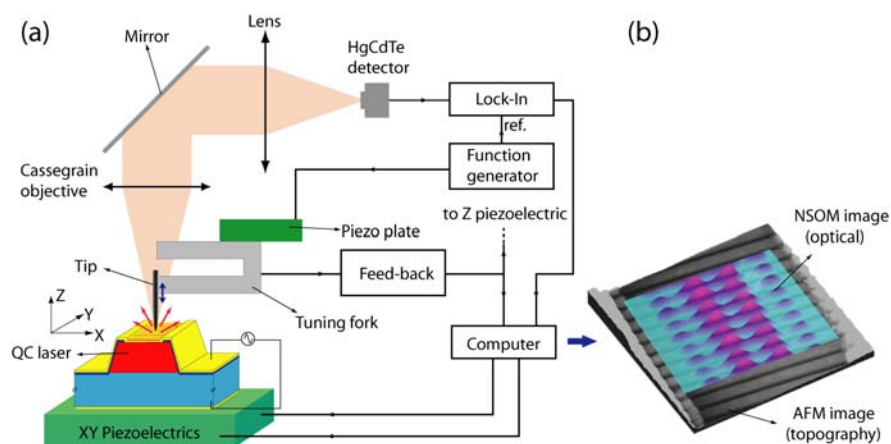


Figure 1: (a) Schematic of the apertureless near field optical microscope setup using a tungsten atomic force microscope tip to scatter the near-field at the surface of a quantum cascade laser with metallic grating. (b) Three dimensional experimental images obtained with this set-up, showing surface plasmons on the metallic fingers of the grating.

Experimental design data processing for optimal synthesis of TiO₂ nano photocatalyst

Amir Bagheri Garmarudi^{1,2}, *Mohammadreza Khanmohammadi*¹, *Nafiseh Khodami*¹

1) *Chemistry Department, Faculty of Science, IKIU, Qazvin, Iran.*

2) *Department of Chemistry & Polymer Laboratories, Engineering Research Institute, Tehran, Iran.*

violamir@gmail.com

Utilizing experimental factor design, it was tried to optimize the effective parameters in synthesis of nano TiO₂ in order to achieve the best results in particle size. Nanocrystalline TiO₂ has been extensively investigated in recent years because of its potential application in photovoltaics, gas sensing, and photo catalysis [1]. Sol-gel method has been successfully adopted to prepare film-like irod-silica substrates for large scale growth of highly aligned multi-walled carbon nanotube arrays [2-4]. TiO₂ nano structure has been proved to be an excellent catalyst in the photocatalytic degradation of organic pollutants, because it is an effective, photo stable, reusable, inexpensive, non-toxic and easily available catalyst. Sol-gel processing is a common chemical approach to produce high purity materials shaped as powders, coatings, fibers, monoliths, and self-supported bulk structures. The main issues, affecting the particle size and catalytic efficiency would be the stoichiometric portions of chemical, aging condition and sintering. Through controlled hydrolysis and polycondensation reactions of a precursor (e.g. metal alkoxide) a three dimensional network structure can be developed in the form of a gel. Subsequent drying and calcinations steps may result in an oxide structure, which consolidates at sintering temperatures much lower than that of materials derived from conventional methods.

Analysis of variance (ANOVA) is one of the most useful statistical data processing techniques which can be used in many situations to determine the significance of factors or terms in models. ANOVA is a useful technique for comparing more than two methods or treatments. The variation in the sample responses (treatments) is used to decide whether the sample treatment effect is significant. Analysis of variance ANOVA is similar to regression in that it is used to investigate and model the relationship between a response variable and one or more independent variables. Several analytical experiments e.g SEM, TGA and XRD were performed to characterize the synthesized nano particles. The main inputs for decision on the optimized condition were the experimental results. Finally the photocatalytic activity and efficiency of the optimized nano structure was also investigated via degradation monitoring of organic pollutant in environmental samples e.g. waste water.

References:

- [1] B. Huber, G. Hubert, C. Ziegler, *Surface Science* 566-568 (2004) 419.
- [2] W.Z. Li, S.S. Xie, L.X. Qian, B.H. Chang, B.S. Zhou, W.Y. Zhou, R.A. Zhao, G. Wang, *Science* 274, 1701-1703
- [3] Z.W.Pan, S.S. Xie, B.H.Chang, C.Y.Wang, L.Lu, W.Liu, W.Y.Zhou, W.Z.Li, L.X.Qian, *Nature* 394, 631-632
- [4] Z.W. Pan, S.S. Xie, B.H. Chang, L.F. Sun, W.Y. Zhou, G. Wang, *Chern. Phys. Lett.* 299,97 102 (1999).

SELF-ASSEMBLED MULTIFUNCTIONAL Fe/MgO NANOSPHERES FOR MRI AND HYPERTHERMIA

C. Martinez-Boubeta, LI. Balcells, R. Cristófol, C. Sanfeliu, E. Rodríguez, R. Weissleder, S. Lope-Piedrafita, K. Simeonidis, M. Angelakeris, F. Sandiumenge, A. Calleja, LI. Casas, C. Monty, and B. Martínez

*Institut de Ciència de Materials de Barcelona (ICMAB-CSIC), Spain
IN²UB, Dept. Electrònica, Univ.Barcelona, Spain
IIBB, CSIC-IDIBAPS, Barcelona, Spain*

*Center for Molecular Imaging Research, MGH-Harvard Medical School, Boston, US
Servicio de Resonancia Magnética Nuclear, Universidad Autónoma de Barcelona, Spain*

*Department of Physics, AUTH, Thessaloniki, Greece
Unitat de Cristal·lografia i Mineralogia, Dept. Geologia-UAB, Spain
CNRS/Procédés, Matériaux et Energie Solaire, Font Romeu, France*

We report on the fabrication of nearly spherical crystalline Fe particles covered by a uniform 3 nm thick MgO epitaxial shell (Figure), presenting advanced magnetic properties, and their potential forthcoming exploitation as contrast agents for magnetic resonance diagnosis and heating mediators for cancer therapy through hyperthermia.

Herein, We explored the potential use of the ferromagnetic properties of the Fe/MgO particles for cancer therapy by carrying out heating experiments. We found that under field amplitude $H = 250$ Oe and frequency $f = 765$ kHz nanoparticles solutions exhibited significant temperature increases over time (Figure). A very high specific absorption rate (SAR) in the order of 450 W g^{-1} (per Fe gram) was found. Typically, ferrofluid samples investigated in literature show SAR values in the order of 100 W g^{-1} . This demonstrated Fe/MgO NPs as high performance therapy vectors capable of induce heat at lower doses than existing materials.

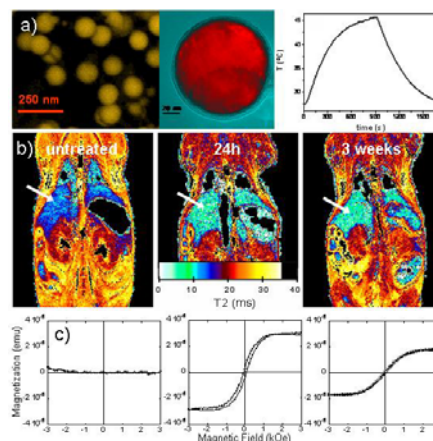
We also present results on particles biodistribution. In preliminary *in vivo* animal experiments, we intravenously injected $10 \mu\text{l g}^{-1}$ of saline solution at 1 mM Fe^0 molar concentration into mice (total iron dose about 0.6 mg kg^{-1}). No apparent acute toxicity or side-effects health problems were observed over a monitoring period of 3 weeks, though of fear of raising the likelihood of blood vessel blockage due to particles-cluster formation by magnetic interaction. Animals were imaged using MRI (Figure). The distribution of particles in the mouse 24 h post injection is similar to that reported previously for iron oxides particles with similar physical characteristics.^[1] This particles display a tendency to undergo phagocytic system clearance in the liver, spleen and kidneys. Significantly, the values measured for MRI are consistent with the magnetic data analysis of excised organs. The primary accumulation in liver, kidneys and spleen showed a gradual decrease within the 3 weeks monitoring period, for which urinary, and eventually hepatobiliary excretion into the intestinal tract, are considered as possible clearance pathways. A remarkable result was that the hysteresis cycle taken from tissue several days after injection resembled that of the NPs powder, demonstrating the particle *in vivo* solidity. Even in case the magnetic nanoparticles start to break down, any Fe and Mg amount will be diluted and regulated within the body. Given that a clinical dose would likely include a few milligrams of Fe per kilogram body mass, the prospect of iron overload is highly unlikely.^[2] Although our studies may be considered as a first proof-of-principle approach, further work is still needed to investigate the biocompatibility of the nanocrystals in various *in vivo* applications.

Referentes

- (1) H. Pardoe et al. *Mag. Res. Imag.* **2003**, 21, 483
- (2) P. Gould, *Nanotoday*, **2006**, 1, 34

Figure

- a) Tem image of Fe/MgO particles, Heating performance of particles aqueous suspensions under 250 Oe and 765 kHz (right)
- b) T₂ MR images of mouse body before (left) and after injection of nanoparticles. MRI show a decrease in T₂ values in the liver after contrast administration (arrow).
- c) Comparison of magnetic signal from targeted liver at the same time points as imagined by MRI.



**PHOTOIONIZATION AND PHOTOABSORPTION IN QUANTUM-DOT
NANOARRAYS AND SINGLE-ELECTRON TRANSISTORS: THEORETICAL
RESULTS AND EXPERIMENTAL IMPLICATIONS**

Ioan Baldea, H. Köppel, and Lorenz S. Cederbaum*

*Theoretische Chemie, Physikalisch-Chemisches Institut, Universität Heidelberg, Im
Neuenheimer Feld 229, D-69120 Heidelberg, Germany*
ioan.baldea@pci.uni-heidelberg.de

In this contribution, we report results of the extensive recent and ongoing work done at the University of Heidelberg on nanoarrays of metallic quantum dots (QDs) and nanoelectronic devices.

Basically, regular nanoarrays of assembled QDs can be characterized by three parameters: the hopping integral t , the charging energy (self-elasticity) U , and the mutual elasticance V . They depend on the dot size $2R$ and the interdot spacing D , and can be tuned in broad ranges, especially because t exponentially decreases with $d=D/2R$ [1]. Our studies on QD-nanoarrays were mainly devoted to nanorings consisting of QDs of silver [2-7]. For potential applications, the broad tunability is important, because one can hope to fabricate nanodevices with designer specified functional properties. For the fundamental science, the tunability is important because it enables to *continuously* drive a nanosystem from a weak to a strong electron correlation regime by varying d from $d \approx 1$ to $d \approx 2$. In spite of the hard work in the last two decades, e.g., in connection with high- T_c -superconductivity, the latter regime is still confronted with numerous open issues, and tracing back continuously to the uncorrelated limit can offer very useful clues.

Our works on Ag-QD-nanorings demonstrated intriguing correlation effects: in spite of the strong correlations [2], the optical and ionization spectra are astonishingly scarce [3-7]. This points towards a hidden quasi-symmetry and suggests a generalization of the Landau theory of interacting many-electron system [4,6]. Besides, in this contribution we will emphasize a new aspect related to this issue, which has experimental implications: the scarce spectra are not confronted with the problem of resolving certain more or less intense signals from the background signal, and this can be exploited to accurately extract the parameters t , U , and V . This is schematically visualized in Figs. 1 and 2. At small d , correlations are weak, and the optical gap (Fig. 1) and the lowest (HOMO) ionization energy (Fig. 2) are determined by t , while at larger d , correlations become strong and they are determined by the electrostatic interactions (U , V). So, the parameters can be deduced from the limiting cases $d \approx 1$ and $d \approx 2$.

In addition to the aforementioned parameters, other parameters are also important for QDs embedded in a nanoelectronic device — e.g. single-electron transistor (SET) —, namely, the device-electrode coupling t_d and the energy of the dot level ϵ_d . The latter, which can be controlled by a gate potential V_g ($\epsilon_d = \alpha V_g + \text{const.}$), can be used to tune the number of electrons on the dot n_d . The values of the latter are important e.g., for the occurrence of the Kondo effect.

Based on our recent theoretical results, we proposed to investigate SETs by photoionization [8]. To avoid confusions, we note that the photoionization we consider amounts to eject an electron from the QD into vacuum, which is completely different from the widely studied photon-assisted tunneling through a QD. Importantly, the photoionization enables to *directly* determine the dot occupancy n_d (see Fig. 3), which is directly related to the total ionization intensity [8].

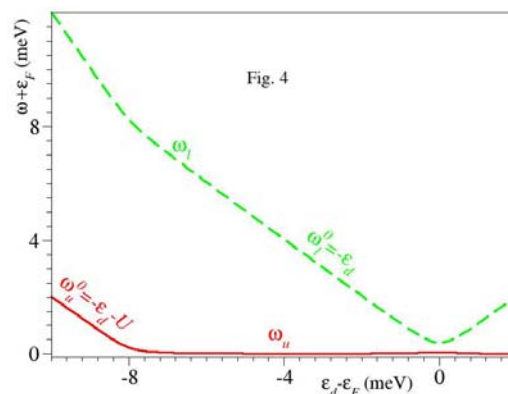
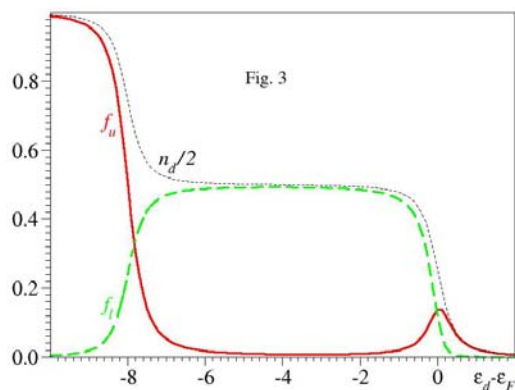
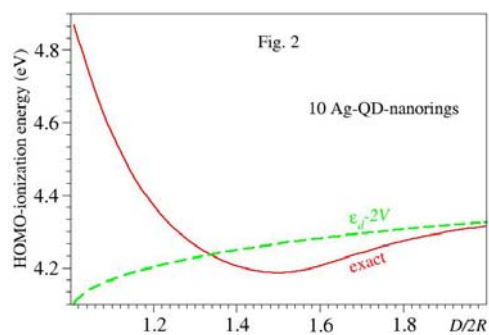
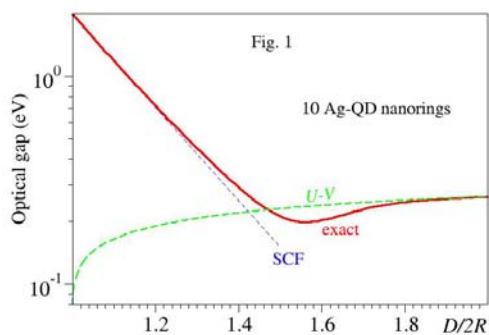
* Also at National Institut for Lasers, Plasmas and Radiation Physics, ISS, 077125 Bucharest, Romania

Moreover, photons with tunable frequency ω can be used to separately ionize from the lower ($\omega = \omega_l \approx \epsilon_d$) and the upper ($\omega = \omega_u \approx \epsilon_d - U$) Hubbard “bands” (see Figs. 3 and 4). As visible in Fig. 3, the spectroscopic factors $f_{l,u}$ [8] of the corresponding ionization signals are nonvanishing only in the ϵ_d -range where the corresponding band is occupied. The ionization energies $\omega_{l,u}$ can be employed to deduce the charging energy U and t_d . Noteworthy, this is a *direct* method to determine U . In the experiments proposed by us [8], the gate potential V_g must be also varied, like in dc-measurements, but the conversion factor α is not needed, in contrast to dc-transport experiments, where α is required, and its determination is affected by typical errors $\sim 20\%$ [9]. Besides the ZEKE-photoelectron spectroscopy, a combined photoionization–dc-transport can be conducted, which has the advantage that measuring the intensity of the ionized signals is *not* needed, a fact that makes the experimental task considerable easier [8]. We also suggest that far infrared absorption can be an even simpler method that ionization to investigate SETs [10].

References:

- [1] C. P. Collier et al, *Science* **277** (1997) 1978.
- [2] I. Baldea and L. S. Cederbaum, *Phys. Rev. Lett.* **89** (2002) 133003.
- [3] I. Baldea and L. S. Cederbaum, *Phys. Rev. B* **75** (2007) 125323.
- [4] I. Baldea and L. S. Cederbaum, *Phys. Rev. B* **77** (2008) 165339.
- [5] I. Baldea and L. S. Cederbaum, in *Frontiers Quantum Systems in Chemistry and Physics*, Springer series “Progress in Theoretical Chemistry and Physics”, vol. 18, edited by S. Wilson et al (2008) pp. 273-287, Springer Science + Business Media.
- [6] I. Baldea, L. S. Cederbaum, and J. Schirmer, *Eur. Phys. J. B* (2009) (in print).
- [7] I. Baldea and L. S. Cederbaum, *Quantum-Dot Nanorings*, in *Handbook of Nanophysics*, edited by K. Sattler, Boca Raton: Taylor & Francis (to appear).
- [8] I. Baldea and H. Köppel, *Phys. Rev. B* **79** (2009) 165317.
- [9] W. Liang et al, *Nature* **417** (2002) 725.
- [10] I. Baldea and H. Köppel, (submitted for publication).

Figures:



Langmuir and Langmuir-Blodgett Films Study of a New Phenylene Ethynylene Oligomer

L.M. Ballesteros, G. Pera, S. Martin, M. C. López, P. Cea, V. Perez-Gregorio
Departamento de Química Orgánica – Química Física, Área de Química Física,
Facultad de Ciencias, Universidad de Zaragoza, 50009, Zaragoza, Spain.
luzmabr@unizar.es

Miniaturization of electronic and mechanical devices at nanoscale level has grown rapidly in the last decades along with a social demand for tinier devices though keeping or increasing their efficiency. With the purpose of providing a complete study on molecules capable of becoming an active part of such devices, our investigation is focused on Langmuir-Blodgett (LB) films fabrication using a new oligo(phenylene-ethynylene) (OPE) derivative, 4-[4-(4-methylthioacetate-phenylethynyl)-phenylethynyl]-aniline, called NOPES (see Figure 1), being a molecule susceptible of acting as a molecular wire due to its conjugated structure. Surface pressure and surface potential, Vs., area isotherms were obtained on a pure water subphase and on HCl, pH 3.0, subphase to reduce the tridimensional molecules aggregation phenomenon (see Figure 2). Monolayers were characterized by Brewster angle microscopy and UV-vis reflection spectroscopy. The Langmuir films were transferred onto solid substrates at several surface pressures and analyzed by UV-vis absorption, and atomic force microscopy (AFM). Both of the spectroscopic studies confirmed the two-dimensional aggregation. AFM images show a high surface roughness at low surface pressures, but at 15 mN/M surface pressure AFM images show high homogeneity at monolayer formation. These results could make possible the use of NOPES in the production of molecular electronic devices.

References:

- [1] Ana Villares, Donocadh P. Lydon, Paul J. Low, Benjamin J. Robinson, Geoffrey J. Ashwell, Félix M. Royo, and Pilar Cea, *Chem. Mater.*, 20, (1), 2008, 258-264.
- [2] Ana Villares, Donocadh P. Lydon, Laurent Porrs, Andrew Beeby, Paul J. Low, Pilar Cea, and Félix M. Royo, *J. Phys. Chem. B*, 111, (25), 2007, 7201-7209.
- [3] Gorka Pera, Ana Villares, M^a. Carmen López, Pilar Cea, Donocadh P. Lydon, and Paul J. Low, *Chem. Mater.*, 19 (4), 2007, 857-864.

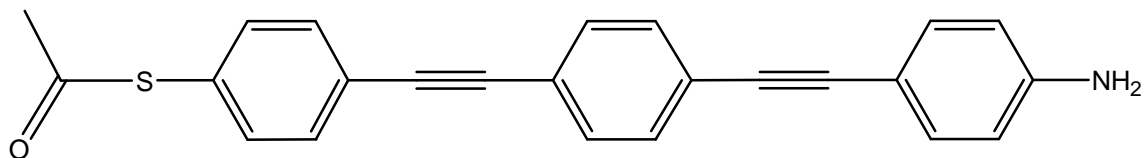


Figure 1. Chemical structure of the NOPES, new OPE derivate compound studied.

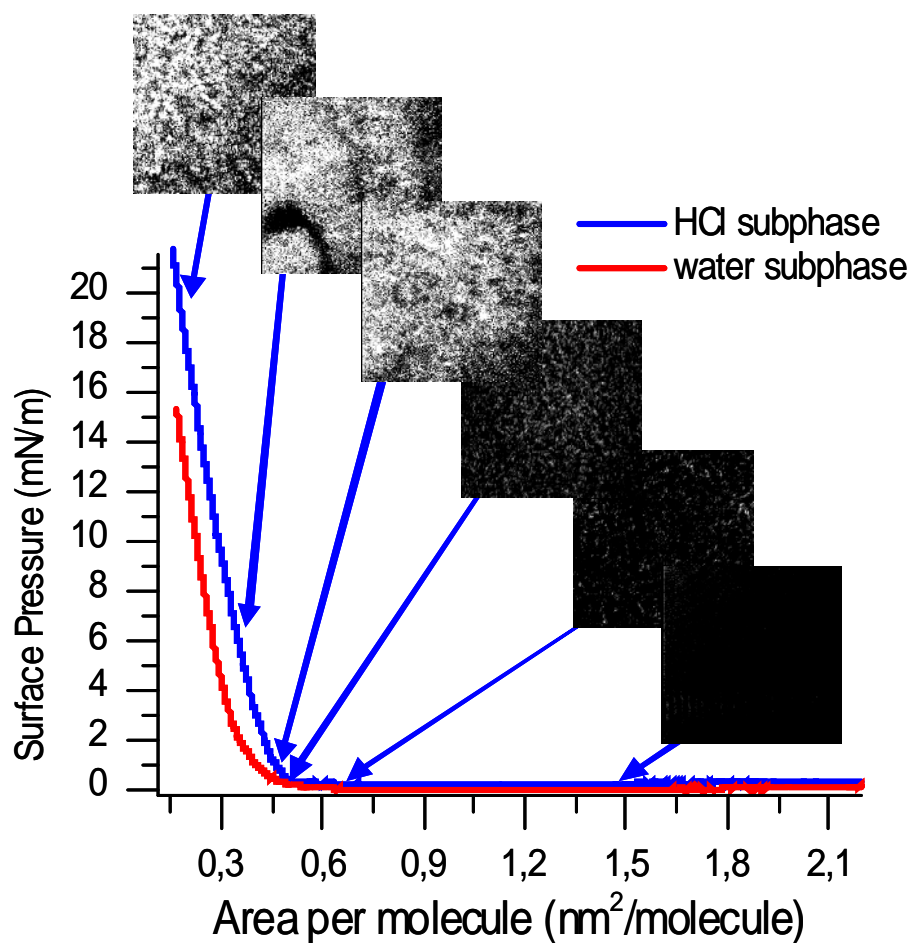


Figure 2. -A isotherm and BAM images of the Langmuir films at the indicated areas per molecule for NOPES.

Acknowledgement. The authors are grateful for financial assistance from DGA for its support through the interdisciplinary project CTQ2006-05236 (P.J.L., F.M.R. and P.C.). G. P., and L. M. B. thank their predoctoral DGA and BSCH-UZ.

Zero-bias anomalies in multisection carbon nanotube FETs

*Paola Barbara*¹, *Yanfei Yang*¹, *Georgy Fedorov*¹, *Serhii Shafraniuk*², *Rupert Lewis*³, *Benjamin Cooper*³, *Christopher Lobb*³

¹Department of Physics, Georgetown University, Washington, DC 20057, USA,

²Department of Physics and Astronomy, Northwestern University, Evanston, IL 60208, USA

³Center for Nanophysics and Advanced Materials, Department of Physics, University of Maryland, College Park, MD 20742-4111

barbara@physics.georgetown.edu

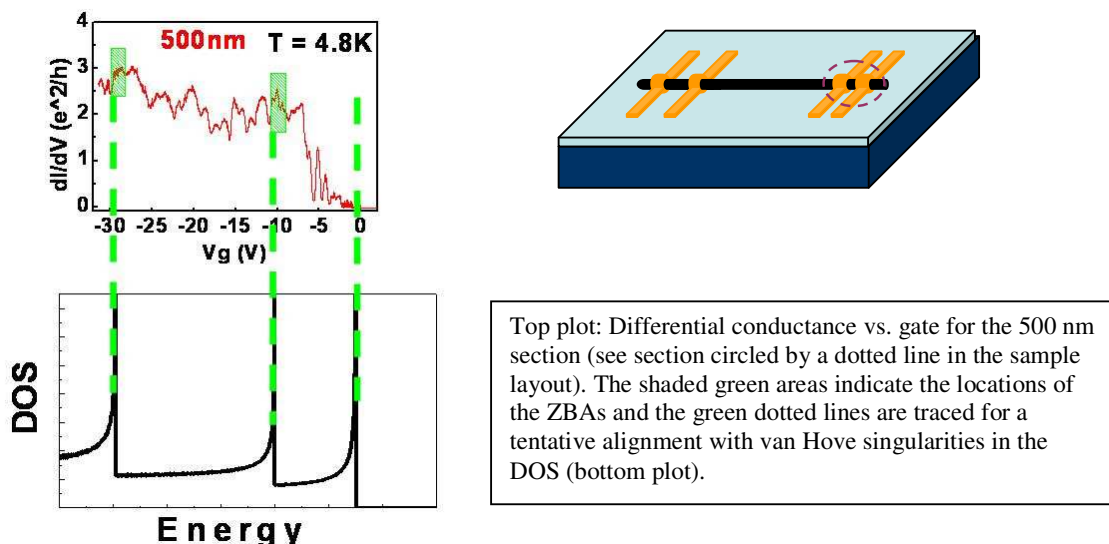
Carbon nanotube field effect transistors (CNFETs) with high transparency contacts show maxima of differential conductance at zero bias voltage [1]. These zero-bias anomalies (ZBAs) occur at large negative gate voltages and in narrow gate voltage ranges (about 1 V wide). Our proposed explanation is superconductivity in the nanotubes, occurring when the gate voltage shifts the Fermi energy into van Hove singularities of the electronic density of states. Here we probe this scenario using 3 FETs fabricated from different sections of one semiconducting carbon nanotube. Source and drain electrodes were patterned by e-beam lithography to achieve FET lengths of 500 nm, 1500 nm and 7000 nm, respectively. All devices showed high transparency contacts to their Pd electrodes. We report the observation of pronounced ZBAs in the multi-section CNFETs, their magnetic field (up to 7 T) and temperature evolution, and the modulation on the ZBAs by Fabry-Perot oscillation.

This work was supported by the NSF (DMR 0907220).

References:

[1] J. Zhang, A. Tselev, Y. Yang, K. Hatton, P. Barbara, and S. Shafraniuk, Zero-bias anomaly and possible superconductivity in single-walled carbon nanotubes, *Phys. Rev. B*, **74**, 155414 (2006).

Figures:



Structural characterization of nanogranular BaTiO₃-NiFe₂O₄ thin films deposited by laser ablation on Si/Pt substrates

J.R. Gonçalves, J. Barbosa, P. Sá, J.A. Mendes, A.G. Rolo, B.G. Almeida
 Dep. Física, Universidade do Minho, Campus de Gualtar, 4710-057 Braga, Portugal
 bernardo@fisica.uminho.pt

Multiferroic thin films constructed by mixing magnetostrictive and piezoelectric materials have attracted recently much scientific and technological interest [1]. In addition to possessing ferroelectricity and magnetism in each individual phase, they are shown to exhibit a stress mediated coupling between their magnetic and electric properties, the so called magnetoelectric effect [1]. Thus, the properties and performance of these nanostructures depend critically on the phase morphology and internal stress distribution, which, in turn, are determined by the elastic phase/phase and phase/substrate interactions. Here, nanogranular thin films composed by BaTiO₃ (piezoelectric) and NiFe₂O₄ (magnetostrictive) have been prepared, and their structural properties were characterized. The BaTiO₃-NiFe₂O₄ thin films were deposited by laser ablation, on platinum covered Si(001) substrates. The depositions were done with a KrF excimer laser (wavelength $\lambda = 248$ nm), at a fluence of 2 mJ/cm². The oxygen pressure was 1 mbar and the substrate temperature was 650°C. The ablation targets were obtained by sintering NiFe₂O₄ and BaTiO₃ powders with different concentrations. Structural studies were performed by X-ray diffraction (XRD), using a Philips PW-1710 diffractometer with CuK α radiation. Raman studies were performed using a Jobin-Yvon T64000 spectrometer.

Figure 1 shows the X-ray diffraction spectra measured on the nanocomposites with cobalt ferrite concentrations in the range 30% - 50%. For comparison, the end members BaTiO₃ and NiFe₂O₄ are also shown. The films are polycrystalline and composed by a mixture of tetragonal-BaTiO₃ and NiFe₂O₄ with cubic inverse spinel structure. As the concentration of the nickel ferrite increases the relative intensity of the (311) NiFe₂O₄ peak increases, indicating the progressive more oriented growth of this phase. The grain sizes, obtained from the fitted X-ray diffraction peak widths for both phases, were determined by using the Scherrer equation. They are in the range 20 - 71 nm for the barium titanate phase and 15 - 22 nm for the NiFe₂O₄ one.

The lattice parameters a and c of the tetragonal BaTiO₃ phase were obtained from the (200) and (002) peak positions. For the pure barium titanate film, a is slightly expanded and c is slightly contracted relative to the bulk, giving a lower tetragonal distortion of the BaTiO₃ structure. However, on the nanocomposites studied, the a and c lattice parameters of the BaTiO₃ phase are always above the bulk ones (but with c/a near the bulk one), indicating an overall expansion of the unit cell due to the presence of NiFe₂O₄. On the other hand, the lattice parameter of the NiFe₂O₄ phase, obtained from the (311) peak position, is always above the bulk value ($a_{\text{bulk}} = 4.339\text{\AA}$) and varies from 8.606 Å on the sample with lower cobalt ferrite concentration ($x=30\%$), to 8.624 Å on the sample with higher NiFe₂O₄ content ($x=50\%$). Comparing with the bulk NiFe₂O₄, in the films the nickel ferrite unit cell has an expansion strain that increases as its concentration increases, up to $x=50\%$.

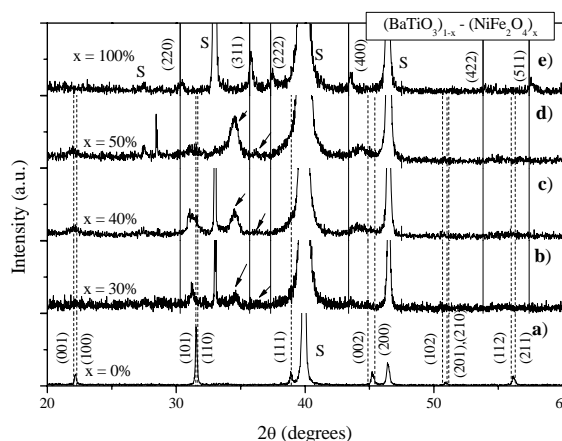


Figure 1: X-ray diffraction spectra of the samples deposited with nickel ferrite concentrations $x = 0\%$ - 50% and 100% . The peaks marked with an S are from the substrate.

Figure 2 shows the Raman spectra of the thin film samples deposited with cobalt ferrite concentrations in the range 30%-50%. Also shown are the individual BaTiO₃ and NiFe₂O₄ bulk reference powders, for comparison. In the BaTiO₃ case, the peak at 716 cm⁻¹, corresponds to the longitudinal optical (LO) vibration of the E phonon mode [2] and the decrease of its intensity with increasing nickel ferrite concentration reflects the corresponding decrease of the barium titanate content in the films.

The inverse spinel structure of AFe₂O₄ consists of AO₆ and FeO₄ octahedra and FeO₆ tetrahedra. The modes arising from the octahedra and tetrahedra can be easily distinguished in the Raman spectrum of ferrites. Raman peaks over the region 660-720 cm⁻¹ represent the modes of tetrahedra and those in 460-660 cm⁻¹ region correspond to modes of octahedra [3]. The nickel ferrite modes appearing at 570 cm⁻¹ and 700 cm⁻¹ can then be assigned to octahedral site (O-site) sublattice and tetrahedral site (T-site) sublattice vibration modes, respectively [3].

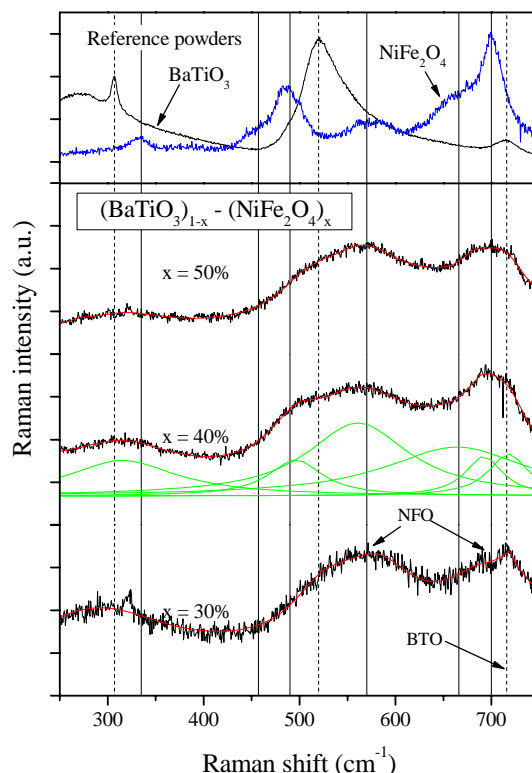


Figure 2: Raman spectra of the samples deposited with NiFe₂O₄ concentrations in the range 30%-50%, along with the corresponding fitting curves. Also shown are the BaTiO₃ and NiFe₂O₄ reference powders, and the Lorentzians obtained from the fit to the spectrum of the sample with $x = 40\%$.

Based on the peaks observed on the powders, the nanocomposite films spectra were

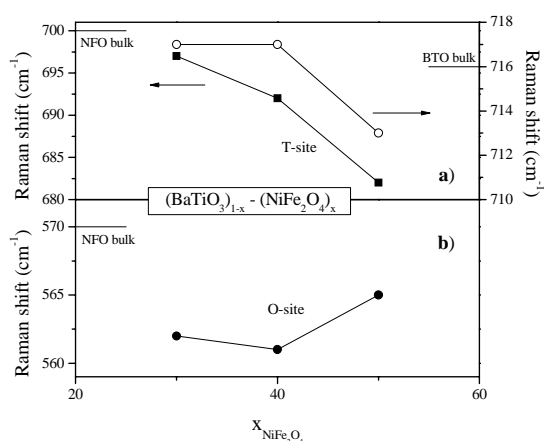


Figure 3: Raman shift as a function of the NiFe₂O₄ concentration, for the a) left: O-site and b) T-site modes. In the right axis of a) is the E mode of BaTiO₃ which appears at 716 cm⁻¹ in the bulk.

deconvoluted by using Lorentzian line-shape functions to least-squares fit the Raman peaks (fig. 2). Figure 3 shows the vibrational modes wavenumbers for the O-site and T-site Raman peaks of the NiFe₂O₄ phase as well as of the BaTiO₃ phase E peak near 716 cm⁻¹. As the nickel ferrite concentration increases, the barium titanate E peak of figure 3 is near and somewhat oscillates around the bulk value. On the other hand, the NiFe₂O₄ T-site mode has a redshift on the nanocomposites, with its wavenumber being systematically below the bulk value. A similar trend is observed for the O-site mode, for the films with 40% and 50% NiFe₂O₄ concentration. This redshift of the NiFe₂O₄ modes results from the expansion of the lattice parameter of the nickel ferrite, as was similarly observed from the X-ray diffraction results (fig. 1).

References:

- [1] - W. Eerenstein, N. D. Mathur, J. F. Scott, *Nature*, **442** (2006) 759
- [2] - U.V. Venkateswaran, V.M. Naik and R. Naik, *Phys. Rev. B*, **58** (1999) 14256
- [3] - S.P. Sanyal, R.K. Singh, "Phonons in condensed materials", Allied Publishers, (2004)

TRANSPORT PROPERTIES OF GRAPHENE IN THE HIGH-CURRENT LIMIT

*Amelia Barreiro*¹, *Michele Lazzeri*², *Joel Moser*¹, *Francesco Mauri*², *Adrian Bachtold*¹

¹*CIN2 Barcelona (ICN-CSIC), Campus UAB, E-08913 Bellaterra, Spain*

²*IMPMC-Université Pierre et Marie Curie-Paris 6, CNRS, F-75015 Paris, France*
amelia.barreiro.icn@uab.es

We present a detailed study of the high-current transport properties of graphene devices patterned in a four-point configuration [1]. The current tends to saturate as the voltage across graphene is increased but never reaches the complete saturation as in metallic nanotubes. The current in the saturation regime can be modulated by sweeping the backgate voltage. Measurements are compared to a model based on the Boltzmann equation, which includes electron scattering processes due to charged and neutral impurities, and graphene optical-phonons. The current saturation arises from the balance between elastic and optical-phonon scattering. Our work shows that the saturation current can be significantly increased by reducing disorder. This result holds promise for high-speed graphene electronics.

References:

[1] A. Barreiro, M. Lazzeri, J. Moser, F. Mauri, A. Bachtold, submitted to Phys. Rev. Lett.

Figures:

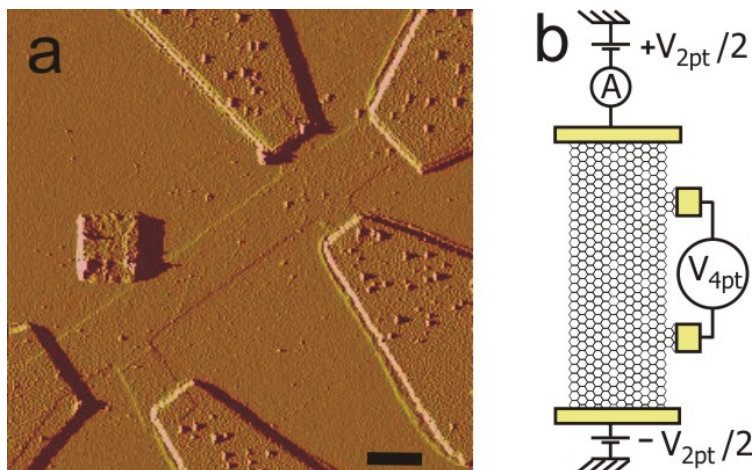


Fig. 1. Experimental setup. (a) Atomic force microscopy image of a graphene device. The scale bar is 1 μm. (b) Schematic of the set-up for the four-point measurement. The device is symmetrically voltage biased.

SYNTHESIS OF $\text{Tm}^{3+}:\text{Lu}_2\text{O}_3$ LAYERS ON SILICA SPHERES VIA MODIFIED PECHINI SOL GEL PROCESS

*E. W. Barrera*¹, *C. Cascales*², *M. C. Pujol*¹, *J. J. Carvajal*¹,
*X. Mateos*¹, *M. Aguiló*¹ and *F. Díaz*¹

¹*Física i Cristal·lografia de Materials i Nanomaterials (FiCMA-FiCNA), Universitat Rovira i Virgili (URV), Campus Sescelades, c/ Marcel·lí Domingo, s/n, E-43007 Tarragona, Spain*

²*Instituto de Ciencia de Materiales de Madrid, CSIC, Calle Sor Juana Inés de la Cruz, Cantoblanco, E-28049 Madrid, Spain*

elixirwilliam.barrera@estudiants.urv.cat

The importance in the last years of materials for optical applications has push the development of new class of structured materials in form of core-shell particles, used as activators or host materials in optical applications [1]. Many methods have been developed to fabricate core-shell structured materials such as sol-gel process, layer-by-layer technique [2], template-directed self assembly method [3], etc. One of the compounds more used as core is the amorphous silica, because the size and morphology could be controlled with reliability by the Stöber method [4]. For layer deposition, the Pechini method offers homogeneous mixing of the starting materials, good control of stoichiometry, fine particle size and uniform morphology [5]. In the modified Pechini method the chelating agent, the citric acid, is replaced by the ethylenediaminetetraacetic acid (EDTA), which poses a major chelating capacity forming stable metal ion-EDTA complexes [6].

Nanosize $\text{Tm}^{3+}:\text{Lu}_2\text{O}_3 @ \text{SiO}_2$ core-shell powder (5 at. %) have been prepared by the modified Pechini method. The complex gel was prepared by the evaporation of the water solvent, from the aqueous solution of the rare earth nitrates and EDTA as chelating agent. Amorphous spheres of silica with a mean size of 100 nm (Alfa Aesar) were used as core. By the pyrolysis of the gel at 573 K and sintering process at 973 K we obtain the nanostructured powder. The morphology was studied by Environmental Scanning Electron Microscopy (ESEM) showing fine particles and Transmission Electron Microscopy (TEM) shows the formation of the surrounding layer, and X-ray powder diffraction pattern shows the crystallization of the $\text{Tm}^{3+}:\text{Lu}_2\text{O}_3$ and the expected cubic structure and $Ia\bar{3}$ space group. The increased value of unit cell parameter indicates the substitution of Thulium ion in Lutetium sites.

References:

- [1] M. Yu, J. Lin, J. Fang, Chem. Mater, 17, 1783-1791, (2005).
- [2] P. Schuetzand, F. Caruso, Chem. Mater. 14, 4509, 2000
- [3] S. R. Hall, S. A. Davis, S. Mann, Langmuir 16, 1454, 2000
- [4] W. Stöber, A. Fink, E. Bohn, J. Colloid Interface Sci. 26, 62. 1968.
- [5] M. P. Pechini, US Patent Specification 3330697.
- [6] M. Galceran, M.C. Pujol, M. Aguiló, F. Díaz, Mat. Science Eng. B 146 (2008) 7–15

Figures:

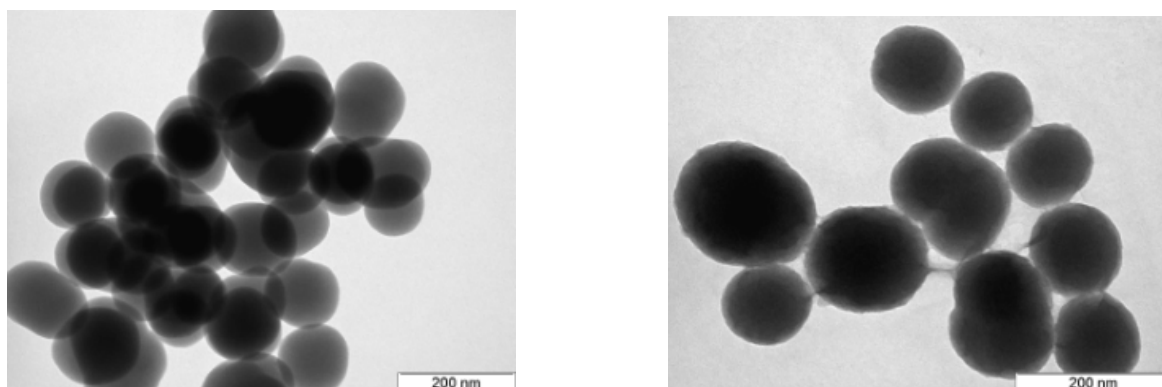


Figure 1 TEM graphs of silica nanospheres as obtained from the supplier (left), final core-shell structured nanoparticles (right).

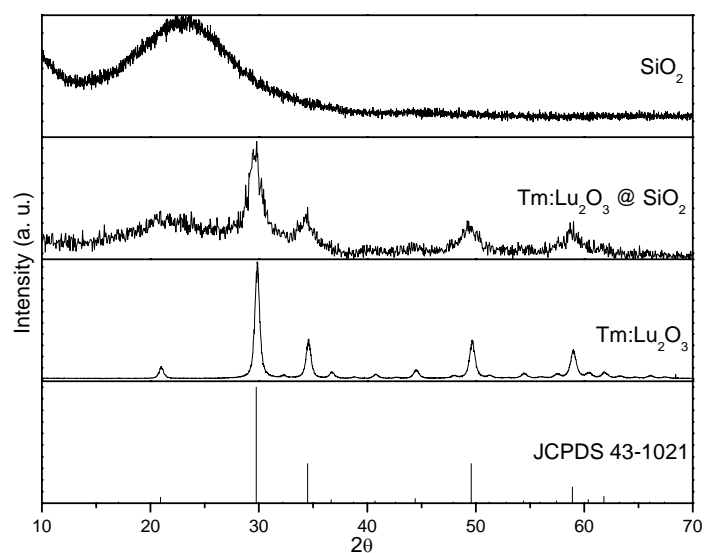


Figure 2 X-ray powder diffraction patterns for SiO_2 (no annealed) (a), $\text{Tm}^{3+}:\text{Lu}_2\text{O}_3@\text{SiO}_2$ core shell particles treated at 973 K (b), $\text{Tm}^{3+}:\text{Lu}_2\text{O}_3$ powder (c), and the JCPDS card 43-1021 for Lu_2O_3 (d).

Charge Transport in Plasmonic Nanocrystal-Molecule Nanostructures

Claire Barrett¹, Gaëtan Lévêque² and Aidan J. Quinn¹

¹Nanotechnology Group, Tyndall National Institute, Lee Maltings, Cork, Ireland.

²Photonics Theory Group, Tyndall National Institute, Cork, Ireland.

claire.barrett@tyndall.ie

We report on development of solution-based processes for assembly of plasmonic nanostructures through controlled mixing of citrate-stabilised gold nanocrystals and molecular linkers with isothiocyanate end groups; see Figure 1. Recent results on investigation of the novel plasmonic properties of these nanostructures via measurement and simulation are presented. We term these nanostructures “*n*-mers”, where *n* denotes the number of nanocrystals in the structure. Further, we report on directed assembly of nanostructures at contact nanoelectrodes and initial investigations of charge transport in these “few-molecule” devices.

Unmodified $d = 20$ nm Au nanocrystals showed the characteristic single nanocrystal absorbance with peak intensity, λ_{max} , at 523 nm, corresponding to the well-know plasmon resonance in gold nanocrystals; see Figure 2a. Bifunctional linker molecules were added to the nanocrystals over ~ 1 hour period (with a final molecule:nanocrystal ratio $\sim 500:1$), during which time 30 spectra were recorded. Figure 2a shows a subset of the recorded absorbance spectra ($A_1, A_2 \dots A_6$) chosen to show the evolution of the optical response. Almost immediately after addition of the linkers (A_1 , 2 minutes), a red-shift ($\Delta\lambda \approx 2$ nm) of the peak close to 523 nm could be observed, likely due to initial adsorption of the linkers at each nanocrystal surface. During the experiment the emergence of a second feature was observed close to 600 nm. The evolution of this shoulder can be highlighted by subtracting the absorbance data of unmodified Au nanocrystals, i.e., A_0 in Figure 2a, from the measured absorbance (A_i) at each time interval; see Figure 2b.

Figure 2c shows a histogram (dark blue data) of the *n*-mer nanostructure distribution for the solution whose absorbance (A_6) is shown in Figure 2a. The data, totalling >400 nanostructures, were extracted from analysis of >60 SEM images acquired at different locations across 4 substrates. The error bars, which show the 95% confidence interval for the analysis ($\pm 1.96\sigma$), confirm the reliability of the method to determine the distribution of nanostructures in a solution. The distribution comprises roughly 68% monomers, 20% dimers, 7% trimers and low incidences of higher order *n*-mers. Control experiments on unmodified nanocrystal solutions prepared in the same manner but without addition of linker molecules yielded the pale pink histogram data shown in Figure 2c (>100 nanostructures counted). Over 95% monomers were observed for the bare nanocrystals with a low incidence of dimers and negligible incidence of higher order *n*-mers. The statistics indicate that the nanostructures observed using SEM were formed in solution and not as a result of aggregation during drop-deposition onto the substrate or solvent evaporation.

The *n*-mer distribution extracted from SEM data suggests that the measured absorbance feature close to 600 nm in Figure 2 arises from the optical response of nanocrystal-molecule dimer or trimer nanostructures. Literature reports of simulations and optical scattering experiments on fabricated and synthesised dimer nanostructures have revealed the existence of a second peak, considerably red-shifted with respect to the plasmon peak for isolated spherical nanostructures. Simulations are currently being developed using the Generalised Multiparticle Mie method to model the optical extinction of nanocrystal dimers for electric field polarizations parallel (E_{\parallel}) and perpendicular (E_{\perp}) to the dimer axis, respectively. Initial results for dimers comprising $d = 20$ nm Au nanocrystals with edge-edge separation ~ 1.2 nm (expected length for Re linkers) show two main peaks: one close to 520 nm and a second longer-wavelength peak close to 600 nm; see Figure 3. This longer wavelength feature is more prominent for case where the field polarization is parallel to the dimer axis (E_{\parallel}), suggesting that the shoulder close to 600 nm in

the measured absorbance data shown in Figure 2a arises from a longitudinal excitation in the dimer nanostructures.

Full details of recent results from the plasmonics simulations, together with details of directed assembly of n -mers at contact nanoelectrodes and variable temperature (4 K – 300 K) charge transport in nanocrystal-molecule junctions will be presented at the meeting.

Figures:

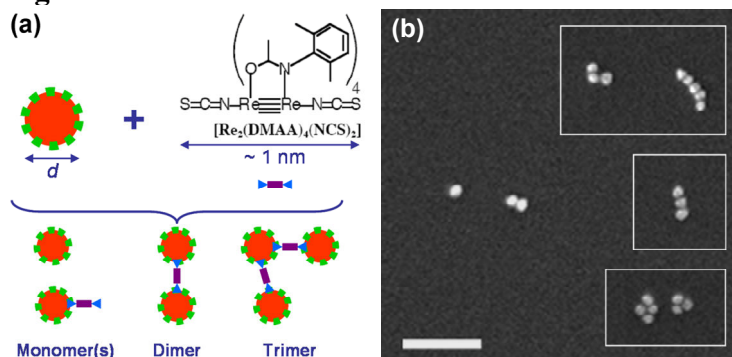


Figure 1 (a) Schematic (not to scale) of nanocrystal-molecule “ n -mer” nanostructures formed by mixing citrate-stabilised Au nanocrystals (core diameter $d = 20$ nm) with bi-functional linker molecules. (b) SEM image showing a monomer ($n = 1$) and a dimer ($n = 2$). Insets: Higher order n -mers ($3 \leq n \leq 5$). Scale bar: 150 nm.

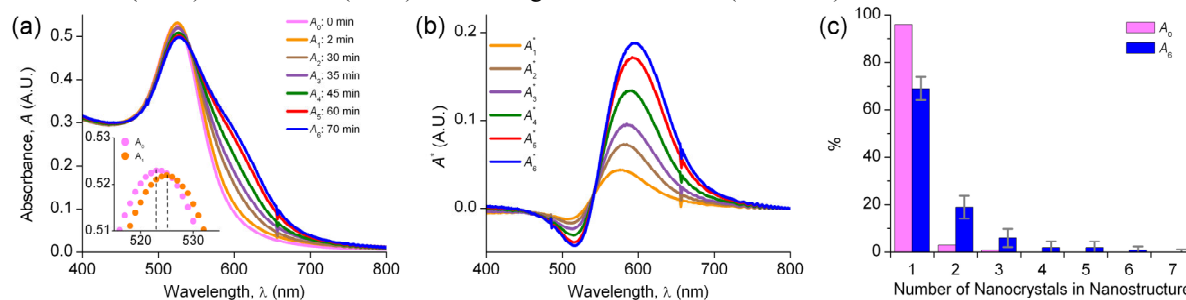


Figure 2 (a) Measured UV-Visible absorbance (A_1 - A_6) of a nanocrystal-molecule solution recorded versus wavelength (λ) over ~ 1 hour. A_0 is the absorbance measured for the starting solution of citrate-stabilised Au nanocrystals. The inset shows the peak positions of A_0 and A_1 , a 2 nm red-shift can be observed. (b) Relative absorbance (A^*) of the nanocrystal-molecule solutions shown in (a), following subtraction of the citrate spectrum according to: $A_i^*(\lambda) = A_i(\lambda) - A_0(\lambda)$, $i = 1..6$. (c) Histogram (dark blue) showing the distribution of n -mer nanostructures extracted from SEM data measured for the nanocrystal-molecule solution whose absorbance data (A_6) is shown in (a). Control data (pale pink) for an unmodified Au nanocrystal solution, A_0 from (a).

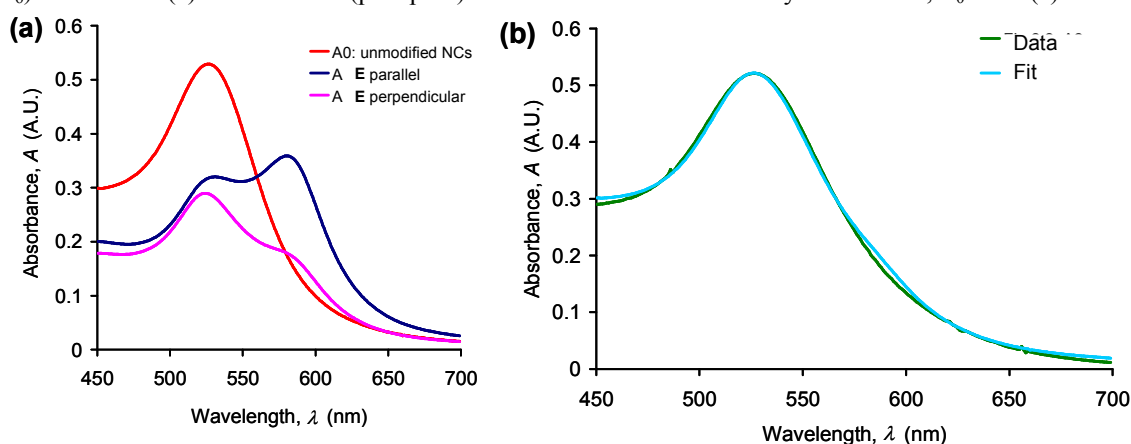


Figure 3 (a) Modelled extinction spectra for both $E_{//}$ and E_{\perp} field orientations for a dimer formed from $d = 20$ nm nanocrystals, where the edge-edge separation of the nanocrystals was fixed at 1.2 nm. Measured extinction spectrum of unmodified $d = 20$ nm Au nanocrystals (A_0) and (b) Fit using spectra shown in (a) to measured extinction data for nanocrystal-molecule nanostructures in the early stages of formation.

DISSECTING THE NANOWORLD: ATOMIC FORCE MICROSCOPY NANOSURGERY ON SINGLE CELLS

J.D. Beard, S.N. Gordeev, S.V. Smirnov, A. Mackenzie

University of Bath, Claverton Down, Bath, UK

jdb28@bath.ac.uk

“Nanosurgery” is the application of nanomanipulation techniques to individual cells or to intracellular structures, and provides a new route to investigate the organisation and properties of biological systems [1-6]. We have created novel tools for nanosurgical manipulation by using Electron Beam Induced Deposition (EBID) of carbon to modify AFM probes, and demonstrated their application to biological cells. The EBID process creates robust blade- or needle-like structures at the probe tip apex which we describe as “nanoscalpels”. The nanoscalpels consist of amorphous carbon and are much more durable than relatively brittle silicon AFM probes, allowing them to exert relatively large forces both vertically and laterally.

These nanoscalpels can be used for the manipulation and cutting of nanoscale biological structures, allowing the “dissection” of these structures so that their internal organisation can be observed *in situ* using AFM imaging. These experiments can be carried out under ambient conditions in air on fixed cells, or in fluid environments supporting living cells.

As an AFM-based technique, the scalpel also provides direct measurement of the applied cutting force. This gives precise control of the penetration depth into the cell, and allows the determination of the physical properties of intracellular structures by measuring the force on the scalpel blade during manipulation. Nanoscalpel blades can be fabricated with a uniform thickness ranging from 20 to 50nm and a typical length of ~500nm (see Fig 1); their small size and high aspect ratio allows cutting with high precision down to the chosen depth with an incision width of <50nm (see Fig 2). The high precision of the scalpel is much better than that attainable using other nanosurgical techniques such as laser microsclpels, and so inflicts less damage on the cell structure as a whole.

The nanoscalpel has the potential to be used for sophisticated investigation of the organization and physical properties of cells. Its potential applications include the removal of the cell membrane and outer layers from cells to reveal underlying structures (see Fig 3), dissection of small biological structures such as viruses, selective deletion of organelles or cytoskeleton filaments, as a probe of the physical properties of individual cellular components, and for the microinjection or recovery of substances to and from the cell. As such, it has the potential to become a widely used tool in many areas of biological and medical research.

References:

- [1] S.H. Chung, D.A. Clark, C.V. Gabel, E. Mazur and A. Samuel, *BMC Neurosci*, **7**, (2006) 30.
- [2] V. Kohli, A.Y. Elezzabi, and J.P. Acker, *Lasers Surg Med*, **37** (2005) 227.
- [3] R.W. Stark, F.J. Rubio-Sierra, S. Thalhammer, W.M. Heckl, *Eur Biophys J*, **32** (2003) 33.
- [4] N. Shen, D. Datta, C.B. Schaffer, P. LeDuc, D.E. Ingber, E. Mazur, *Mol Cell Biol*, **2** (2005) 17.
- [5] I. Obataya, C. Nakamura, S. Han, N. Nakamura, and J. Miyake, *Nano Lett*, **5** (2005) 27.
- [6] S. Han, C. Nakamura, Ikuo Obataya, N Nakamura, and J. Miyaka, *Biochem Biophys Res Commun* **332** (2005) 633.

Figures:

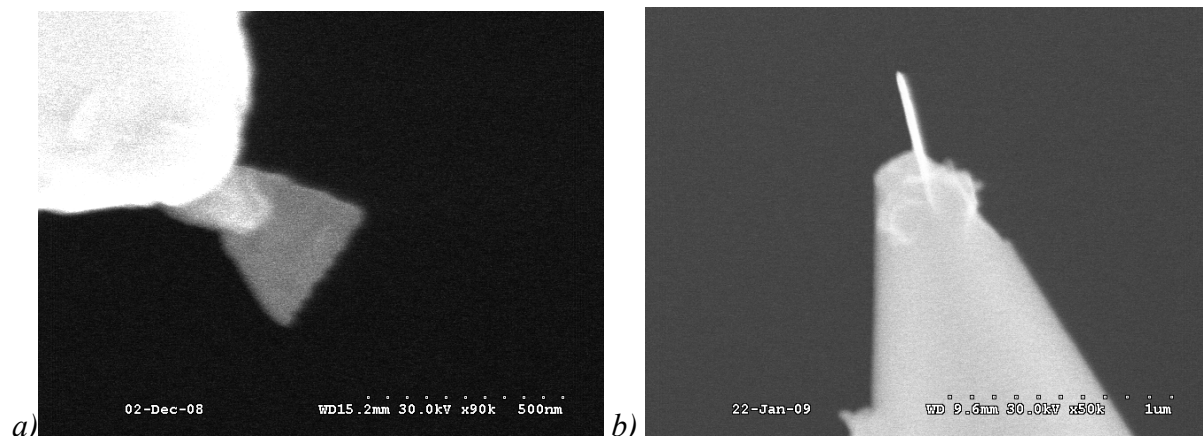


Fig 1: Two nanoscalpel blades at the apex of AFM probes, imaged from the side (a) and edge (b).

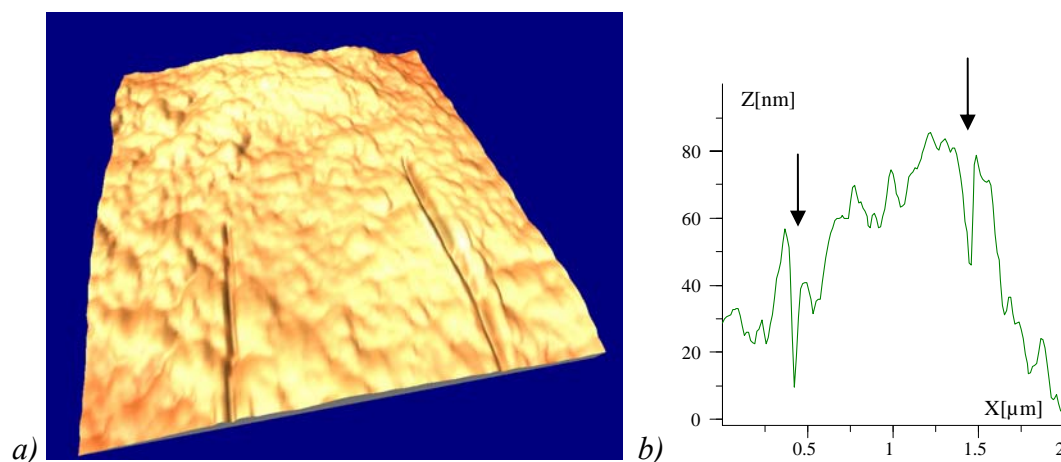


Fig 2: AFM images (a) and profile (b) of nanoscalpel incisions (arrowed) on aortic smooth muscle cell membrane. Imaged area is $1.5 \times 1.2 \mu\text{m}$.

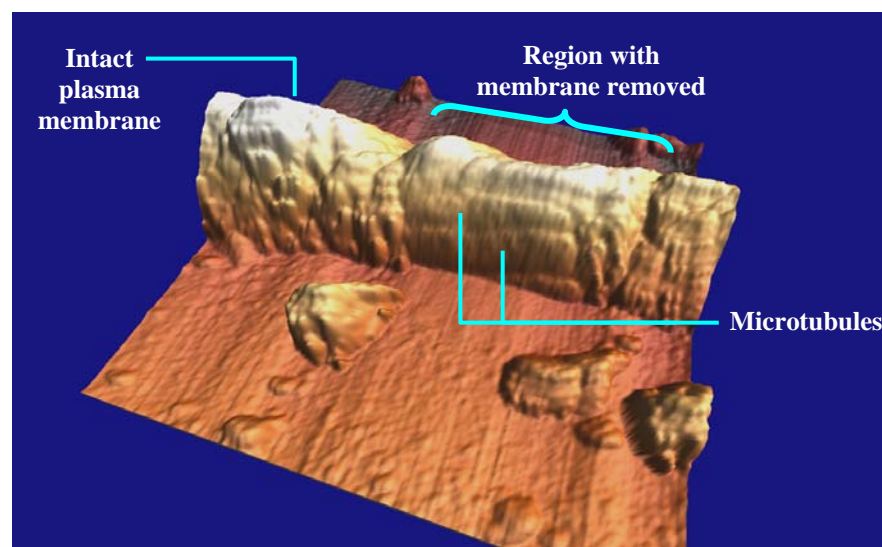


Fig 3: Proplatelet filament of a megakaryocyte, showing internal microtubules exposed by removing the cell membrane. Imaged area is $3.0 \times 3.0 \mu\text{m}$.

Cure and mechanical properties of styrene butadiene rubber-organomontmorillonite nanocomposites

*R.Bellas**, *J.Díez**, *A.Rodríguez***, *R. Bouza**, *B. Montero**

**Grupo de Polímeros, Universidad de A Coruña, E.U.P., Avda. 19 de Febrero s/n, 15405 Ferrol, Spain*

*** Instituto de Ciencia y Tecnología de Polímeros (CSIC), Juan de la Cierva 3, 28006 Madrid, Spain
labpolim@udc.es*

In recent years, rubber/clay nanocomposites have attracted much attention from researchers, because they show remarkable improvements in physical and chemical properties when they are compared with the pure rubbers or conventional filled rubbers [1, 2]. In fact, reinforcement can be achieved even at lower filler concentrations if the clay layers are able to disperse into the polymer matrix at nanoscale level.

This study is focused on the effect of octadecylamine-modified montmorillonite (OMMT) on the curing process, mechanical properties, hardness and viscoelastic properties of SBR vulcanizates. Organoclay was compounded with SBR using an internal mixer and cured by conventional sulphur curing system. The organoclay content was increased from 0 to 15 phr.

In presence of organoclay, the optimum cure time (t_{97}) is considerably reduced decreasing by almost 17 minutes for nanocomposite containing 15 phr of nanoclay. This accelerating effect has already been reported and traced to a transition complex formation with amines and sulphur-containing compounds, which facilitates the development of elemental sulphur [3]. Both minimum torque (ML) and maximum torque (MH) of the rheometer curves are increased by the presence of nanoclay (Figure 1). The values of the torque differences increases as the amount of added nanoclay is increased. Because the torque differences can be considered as a measure of crosslinking density and/or the interaction between organoclay and rubber, the results show that the crosslink density increased by the addition of nanoclay.

A sensible increase in the mechanical properties is obtained by adding organoclay, even at low percentages. The tensile strength and elongation at break values change from 1.75 to 2.85 MPa and from 189 to 347%, respectively, when 5 phr modified clay was added to unfilled SBR. Remarkably, the tensile strength and elongation at break of the 15 phr clay-filled SBR vulcanizates was 5.97 MPa and 516%, respectively. In addition, modulus at the elongation at 100% (M100) increases with the filler content and the maximum enhancement in modulus is shown by OMMT at 15 phr. The increase of tensile properties is related with the degree of dispersion of clay layers into the polymer matrix.

There is a significant change in Shore A hardness values with increasing the filler dosage. Improved hardness is also in concordance with tensile results.

On the other hand, the glass transition temperature of nanocomposites remains relatively unchanged with clay addition.

The authors gratefully acknowledge the financial support of the Xunta de Galicia (Axudas do Programa de Consolidación Expte. 2007/0008_0).

References:

- [1] R. Sengupta, S. Chakraborty, S. Bandyopadhyay, S. Dasgupta, R. Mukhopadhyay, K. Auddy, A.S. Deuri, *Polymer Engineering and Science* **47(11)** (2007) 1956.
- [2] Y. Ma, Y-P. Wu, L-Q. Zhang, Q-F. Li, *Journal of Applied Polymer Science* **109** (2008) 1925
- [3] S. Varghese, J. Karger-Kocsis, *Journal of Applied Polymer Science* **91** (2004) 813.

Figures:

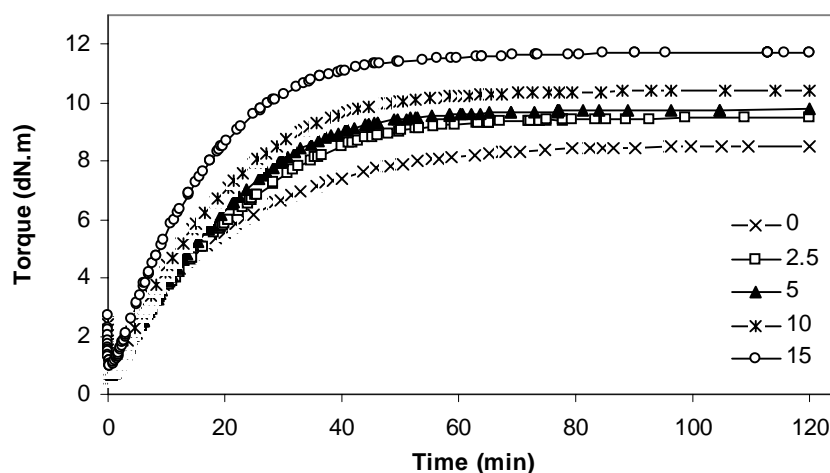


Figure 1. Cure curves of SBR/OMMT nanocomposites.

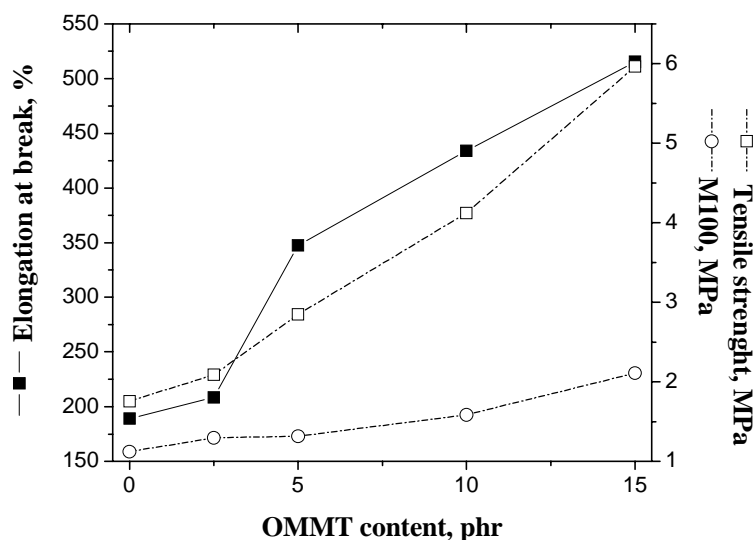


Figure 2. Variation of tensile strength, elongation at break and modulus at 100% elongation with filler content.

MAGNETIZATION OF DIAMOND-GRAPHENE FLAKES COMPOSITES

I.A. Denisov¹, P.I. Belobrov², S.S. Tsegelnik¹, K.A. Shaikhutdinov², D.A. Znak¹, D.A. Balaev²,
O.A. Bayukov², S.B. Korchagina³, E.A. Petrakovskaya², D.A. Velikanov², N.V. Volkov²,
S.K. Gordeev³

¹Siberian Federal University, 660074 Krasnoyarsk, Russia

²Kirensky Institute of Physics & Institute of Biophysics SB RAS, 660036 Krasnoyarsk, Russia

³Central Research Institute of Material, 191014 St. Petersburg, Russia

peter.belobrov@gmail.com

Magnetic properties of composites from nanodiamond and pyrocarbon (NDC) with the factor γ = mass ratio of sp²/sp³ phases have been studied. Solid bulk porous NDC is made as described in [1]. NDC is semiconductor with the electrical conductivity has changed by 12 orders of magnitude that are controlled by the ratio γ from 0 to 80 % [2]. NDC has intrinsic paramagnetic properties that are permanent for all values of γ [3].

Taking into attention the recent analysis of experimental errors in the observation of nanoscale magnetism [4] we report here the results detailed study the magnetization of NDC by a few methods: wide-angle X-ray diffraction, EPR, Mossbauer, Raman and FTIR spectroscopy. Magnetic measurement was made on the different type of magnetometers (vibration, SQUID, PPMS). The bulk magnetization and ¹³C NMR spin-lattice relaxation of nanodiamond powder samples have been studied [5] and nonaromatic core-shell structural model of nanodiamond particles has been proposed recently [6].

The total magnetization of NDC can be explained in terms of contributions from (1) the temperature independent different diamagnetic and paramagnetic effects of nanodiamond and graphene flakes χ_{Σ} , (2) the strong temperature dependent paramagnetic effect of unpaired electrons of nanodiamond and tetrahedral Fe-centers into nanodiamond structure, and (3) ferromagnetic-like contributions from magnetic impurities M_{ferro} . The results are shown in the figures 1 and 2 and table 1.

Main our result is following: NDC is magnetic semiconductor with phantom doping by Fe of nanodiamond. The principal possibilities of doping by Cr and S using porous structure of NDC have been illustrated here in the first time.

Recent synthesis of luminescence nanodiamonds from carbon black of 99.9 % purity [7] shows useful method to delete impurities naturally present in detonation nanodiamond.

This research was supported by RFBR Grants 07-04-01340-a and 08-02-00259-a, ME&S of RF Grant No. 2.2.2.2/5309 and U.S. CRDF Grant RUX0-002-KR-06/BP4M02.

References:

- [1] S. K. Gordeev, S. G. Zhukov, P. I. Belobrov, A. N. Smolianinov, and Ju. P. Dikov, U.S. Patent No. 6 083 614 (4 July 2000), Russian Patent No. 95116683 (27 September 1995).
- [2] S.K. Gordeev, P.I. Belobrov, N.I. Kiselev, E.A. Petrakovskaya, T.C. Ekstrom, Mat. Res. Soc. Proc., **638** (2001) F18.4.1-6.
- [3] P.I. Belobrov, S.K. Gordeev, E.A. Petrakovskaya and O.V. Falaleev, Doklady Physics, **46** (2001) 459.
- [4] M. A. Garcia, E. Fernandez Pinel, J. de la Venta, A. Quesada, V. Bouzas, J. F. Fernández, J. J. Romero, M. S. Martín González, and J. L. Costa-Krämer, J. Appl. Phys. **105** (2009) 013925.
- [5] E. M. Levin, X. W. Fang, S. L. Bud'ko, W. E. Straszheim, R. W. McCallum, and K. Schmidt-Rohr, Phys. Rev. B. **77** (2008) 054418.

[6] XiaoWen Fang, JingDong Mao, E. M. Levin and Klaus Schmidt-Rohr, J. Am. Chem. Soc., **131** (2009) 1426.

[7] S. Hua, F. Tian, P. Bai, S. Cao, J. Sun and J. Yang, Mater. Sci. Engin.: B., **157** (2009) 11.

Figures:

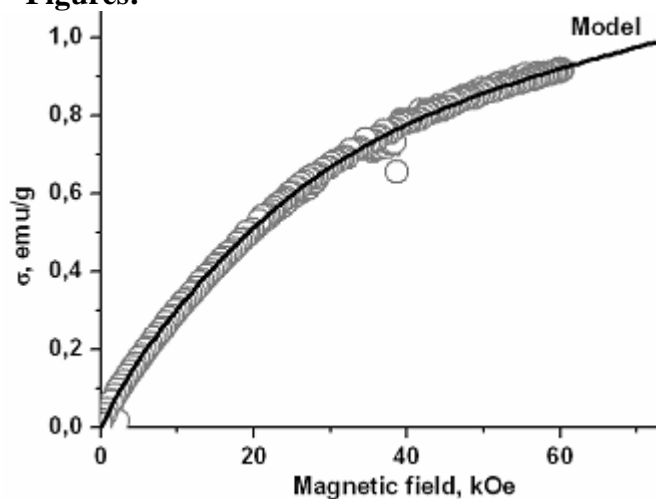


Fig. 1. Magnetization of NDC sample #1.

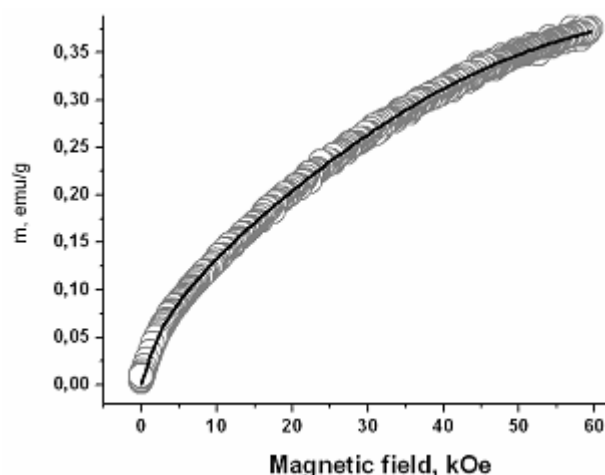


Fig. 2. Magnetization of NDC sample #7.

Table 1 – The results of magnetic measurement of diamond-graphene flakes composites

#	γ , %	H, Oe	T, K	Doped by	M_{ferro} , emu/g	N, spin/g	N/N _m	g	spin	χ_{Σ}
1	0	var	4,2	Fe*	0,05	3,00E+19	1600	4,4	0,5	4,37E-06
2	10	var	4,2	Fe	0,1	5,46E+19	835,16	2	0,5	-1,58E-06
3	20	var	4,2	Fe	0,1	5,81E+19	719,80	2	0,5	-2,14E-06
4	20	500	var	Cr		4,50E+19	261,38	2	0,5	2,40E-06
5	30	var	4,2	Fe	0,08	5,46E+19	706,67	2	0,5	-1,55E-06
6	40	var	4,2	Fe	0,07	6,60E+19	543,12	2	0,5	-2,00E-06
7	40	var	4,2	Fe	0,04	6,95E+19	515,77	2	0,5	-2,33E-06
8	40	500	var	S		3,60E+19	995,72	2	0,5	-1,20E-07
9	50	var	2	Fe	-	2,00E+20	167,28	2	0,5	1,52E-05
10	60	500	var	SiO ₂ **		9,26E+18	3388,28	2	0,5	4,30E-07
11	80	var	4,2	Fe	0,04	6,58E+19	423,85	2	0,5	-3,85E-06

Notes: *There are Fe < 0.4% in all samples except #1 where Fe < 4.3 mass %.

**NDC where nanodiamond was substituted by SiO₂ completely.

EXPERIENCE APPLICATION OF MAGNETITE NANOPARTICLES IN MEDICINE

Andrey N. Belousov

Laboratory of Applied Nanotechnology

pr. Lenina, 31-v, fl. 32

Kharkov, 61072 Ukraine

E-mail: anb@vlink.kharkov.ua

Web site: www.nanolab.com.ua

Nowadays nanotechnology as a new direction of science allows to develop therapeutic methods of the endogenous intoxication syndrome and to create a new class of biocompatible sorbents. In Ukraine first preparations of medical nanotechnology were produced and patented in 1998. These are “IKBB” intracorporeal biocorrector, magnetically controlled sorbent (MCS-B), and “Micromage-B”. The preparations are based on colloid magnetite particles (Fe_3O_4) from 6 to 12 nm. Adsorption layer provides a high sorption activity to magnetite nanoparticles. Total activity of their sorption surface is 800 – 1200 m^2/g , magnetic field intensity produced by each particle is 300 - 400 kA/m, ζ – potential is – 19 mV. Each magnetite particle is a subdomain elementary magnetite of a sphere shape. The main biological action of nanotechnology preparations is direct to regulation of cell metabolism. Therapeutic effect of this preparation is based on the influence of adsorption process and of constant magnetic field that surrounds colloid magnetite particle on cellular and subcellular structures. Point of attack is surface proteins of cell membranes. Colloid magnetite particles modify composition of protein molecules thereby effecting transport of substances to a cell. Using magnet-controlled sorbent the method of extracorporeal hemocorrection on the whole is rather the method of effective and reliable way to activate natural processes of detoxication of organism, than the method of artificial detoxication. The absence of contra-indication and incidental effects (haematic, haemodynamic, hormone, electrolytic, immune) creates real predisposition for using this method in intensive therapy of intoxication syndrome.

Keywords: magnetite nanoparticles; medical nanotechnology; regulation of cell metabolism; intensive therapy; intoxication syndrome.

HIGH FREQUENCY MODELING OF CLASSICAL AND QUANTUM NANOSCALE ELECTRON DEVICES

A.Benali, G.Albareda*, A.Alarcón*, M.Aghoutane** and X.Oriols**

**Departament d'Enginyeria Electrònica, Universitat Autònoma de Barcelona
08193, Bellaterra, Spain*

***Facultad de Ciencias, Universidad Abdelmalek Essaâdi, Tetuán, Marruecos
Abdelilah.benali@campus.uab.es*

One of the main interests for decreasing electron device dimensions towards nanoscale dimensions is the possibility of dealing with very short transit times, on the order of few picoseconds or less, envisaging either digital or analog THz applications [1,2]. At these frequencies, the total current depends not only on the rate of electrons crossing a particular surface (i.e. the conduction component), but also on the time-dependent variations of the electric field on that surface (i.e. the displacement current) [3,4]. Thus, the computation of THz currents is a quite difficult challenge because it needs the explicit consideration of the (“many-body” problem) Coulomb interaction among electrons.

We have recently showed a novel accurate method to solve the “many-body” problem in either classical [5] or quantum [6] scenarios. In order to improve our understanding of the total (particle plus displacement) current in nanoscale electron devices, we use our extension of the Ramo-Shockley theorem [3]. Then, the computation of the total current takes into account the whole active region (rather than just a particular surface) through the definition of a new vector function $\vec{F}_i(\vec{r})$ in the volume of the active region [4]. This new vector function provides an additional source of valuable information for understanding and predicting the behavior of THz currents. In particular, the total (particle and displacement) current through a surface “i” of volume of Fig. 1 can be written as:

$$I_i(t) = \Gamma_i^q(t) + \Gamma_i^e(t) = \sum_{a=1}^N \vec{F}_i(\vec{r}_a[t]) \cdot q \cdot \vec{v}_a(\vec{r}_a[t]) + \int_s \vec{F}_i(\vec{r}) \cdot \varepsilon(\vec{r}) \cdot \frac{\partial V(\vec{r}, t)}{\partial t} \cdot d\vec{s} \quad (1)$$

The first term, $\Gamma_i^q(t)$, relates the macroscopic THz current with the microscopic electron dynamics where q is the electron charge, $\vec{v}_a(\vec{r}_a[t])$ the a-electron (classical[5] or Bohm[6]) velocity and N is the number of electrons inside the whole active region. The second term, $\Gamma_i^e(t)$, provides information on the temporal variations of the scalar potential $V(\vec{r}, t)$ with $\varepsilon(\vec{r})$ the (time-independent) electric permittivity.

In this work, we have simulated the electron transport through a nanoscale resistor drawn in Fig. 1 within a time-dependent semiconductor Monte Carlo simulation of electron transport. The Coulomb interaction among electrons is computed through the novel many-particle algorithm presented in Ref. [5]. In Figs. 2,3 we show (in solid blue line) the power spectral density of the current fluctuations computed from the Monte Carlo results. In order to improve our understanding of each terms of expression (1), we have developed analytical expressions for the temporal behavior of $\Gamma_i^q(t)$ associated with a transmitted electron (see dashed red line in Fig. 4) and the term $\Gamma_i^e(t)$ associated to the temporal variations of the scalar potential $V(\vec{r}, t)$ (see dashed red line in Fig. 5) and compared them with the time-dependent Monte Carlo results. We do also Fourier transform these analytical expressions to compare them with the numerical Monte Carlo results mentioned before (see Figs. 2 and 3) showing an excellent agreement.

This work is a first step towards an accurate understanding of the behavior of THz currents in nanoscale (ballistic) devices that will become a very relevant issue for next generation of THz electronics.

References:

[1] X. Oriols, F. Boano, and A. Alarcón, Applied Physical Letters, **92**, (2008) 222107.
 [2] X. Oriols, A. Alarcón, and L. Baella, Solid-State Electron. 51, 1287, 2007.
 [3] A. Alarcón and X. Oriols, J. Stat. Mech. **2009** (2009) P01051.
 [4] A. Alarcón, A. Benali, G. Albareda and X. Oriols, CDE 2009
 [5] G. Albareda, J. Suñé and X. Oriols, Physical Review B, **79** (2009) 075315.
 [6] X. Oriols, Physical Review Letters, **98** (2007) 066803.

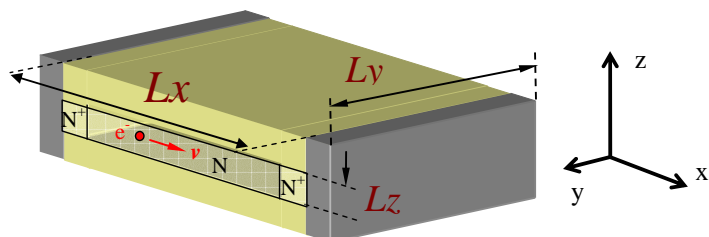


Fig.1. Schematic representation of a two-terminal nano-resistor with doping $N^+ = 2.2 \cdot 10^{19} \text{ cm}^{-3}$ and $N = 1 \cdot 10^{10} \text{ cm}^{-3}$. The dimensions of the active region of the device are $Lx \cdot Ly \cdot Lz = 20 \times 6 \times 6 \text{ nm}$. The total time-dependent current is computed through Monte Carlo simulations during 1.5 ns ($2 \cdot 10^6$ time steps) when a 1V bias is applied.

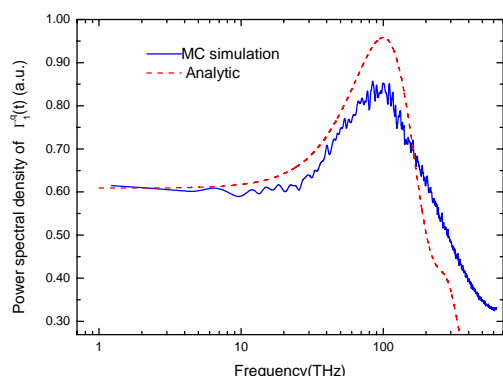


Fig.2. In solid line, power spectral density of the fluctuations of the first term of expression (1) for the device of Fig. 1. In dashed line, analytical approximation obtained from dashed line in Fig 4.

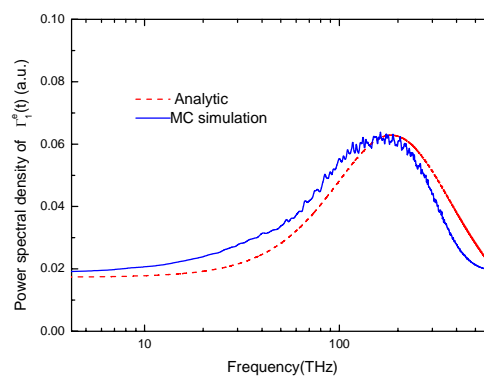


Fig.3. In solid line, power spectral density of the fluctuations of the second term of expression (1) for the device of Fig. 1. In dashed line, analytical approximation obtained from dashed line in Fig 5.

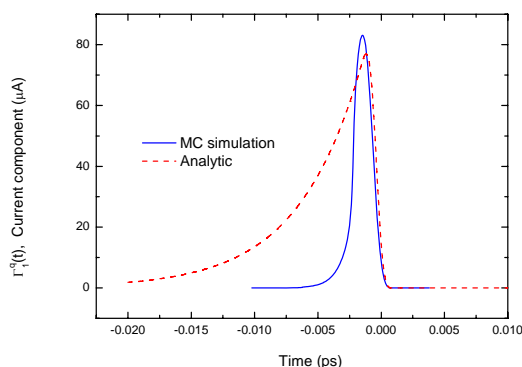


Fig.4. In solid line, zoom of the first term of the time dependent current of expression (1) for the results of Fig. 2. In dashed line, analytical approximation.

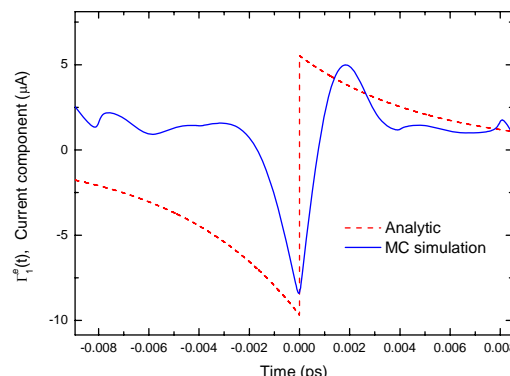


Fig.5. In solid line, zoom of the second term of the time dependent current of expression (1) for the results of Fig. 3. In dashed line, analytical approximation.

Spectroscopic evidences of Nanocrystallization in oxyfluoride Nd³⁺ doped glass due to laser irradiation

S. González-Pérez,¹ A. Benayas², D. Jaqué², I. Martín¹

¹Departamento de Física Fundamental y Experimental, Electrónica y Sistemas, Universidad de La Laguna, E-38200 San Cristóbal de La Laguna, Santa Cruz de Tenerife, Spain

²GIEL, Departamento de Física de Materiales, Facultad de Ciencias, Universidad Autónoma de Madrid, 28049 Madrid, Spain

antonio.benayas@uam.es

A local crystalline formation in a Neodymium doped oxyfluoride glass has been obtained using laser irradiation. It has been studied the intense emission around 880 nm originated from the ⁴F_{3/2} (Nd³⁺) level when the glass structure changes to a glass ceramic structure due to the irradiation of the laser beam. The emission spectra and the lifetime values obtained before and after the irradiation with 500 mW (effective power at sample surface) reveal that the devitrification process made by the laser power beam has been successfully achieved. Our micro-luminescence results shows that nanocrystals of βPbF₂ have been created by the laser action, confirming in this way that the transition from glass to glass ceramic has been completed.

Introduction

The lanthanide ion Nd³⁺ is one of the most interesting luminescent ions to be used for their laser applications due to the ⁴F_{3/2} → ⁴I_{11/2} transition centred at about 1064 nm.. Rare-earth doped transparent oxyfluoride glass ceramics, in which rare-earth ions are selectively incorporated into the fluoride nanocrystals embedded among the oxide glassy matrix, possess great potential applications in the field of solid luminescence due to the combination of the advantages of both fluorides and oxides: low phonon energy environment of fluoride crystalline for luminescent ions, and desirable mechanical and chemical properties of oxide glasses. This new material has attracted great attention in the continuous research for the novel photoelectric devices, and is usually fabricated by controlled crystallization of fluoride phase in oxide glassy matrix through thermal process using a furnace. Recently, laser irradiation to glass has received much attention as a new tool of micro and nanofabrication. Compared with current techniques such as photolithography and reactive ion etching, which requires numerous processing steps and fabrication masks, laser induced micro and nanofabrication have the advantage of being mask less, allowing single step and very fast processing.

Experimental

The transparent glass sample was prepared starting with the following composition in mol%: 30 SiO₂, 15 Al₂O₃, 29 CdF₂, 22 PbF₂, (4-x) YF₃ and 1 NdF₃. The glasses were obtained by melting the components at 1050 °C for 2 hours and finally casting the melt into a slab on a stainless steel plate at room temperature. One of the glasses was heated at 470 °C for 36 h to obtain a transparent glass ceramic for comparison purposes of the irradiated zone.

For laser irradiation we have used an Argon laser on multiline emission configuration. Laser beam was focused with a 10x microscope objective, and the effective power that arrived into the sample was 500 mW. The motorized stage speed was fixed on 125 μm/s. After irradiation process, the damaged zone has 100 μm of width in the orthogonal direction to “burning path”.

Results and Discussion

On Fig. 1 we can clearly appreciate an intermediate appearance of irradiated area emission spectra, between glass sample (outside damage area) and from glass ceramic 1% Nd mol sample. Our micro-luminescence measurements give us quantitative information about two kind of spectroscopic changes associated to laser irradiation process. Fig. 2 shows the deep contrast between spectroscopic signal from damage area (narrower emission line, a clear signal of crystallization) and non-irradiated areas that keep their glass-like spectrum. In the same way, we have measured a relevant red shift of the emission line collected on irradiated area with respect to non-damaged areas.

With that kind of spectroscopic data, we have proofs of laser induced nano-crystallization process within oxyfluoride glass sample.

Conclusions

On summary, a crystalline environment has been created in the 1 mol% Nd³⁺ doped glass by laser irradiation at 500 mW since the laser intensity is high enough to stimulate the formation of a glass ceramic structure. The rise of temperature in the irradiated zone due to the increasing laser power produces a local redistribution of the glass structure and leads to a permanent modification of the micro and nanostructure and its properties. The optically active rare earth ions are majority hosted in precipitated fluoride nanocrystals.

References:

- W. Höland, G. Beall, Glass-Ceramic Technology, Am. Ceram. Soc. Bull , **81**, 1–50 (2002). M. J. Dejneka, "Transparent oxyfluoride glass ceramics," MRS Bull. 23, 57-62 (1998). M. Abril, J. Méndez-Ramos, I. R. Martín, U. R. Rodríguez-Mendoza, V. Lavín, A. Delgado-Torres, V. D. Rodríguez, P. Núñez and A. D. Lozano-Gorrín, Optical properties of Nd³⁺ ions in oxyfluoride glasses and glass ceramics comparing different preparation methods, J. Appl. Phys., **95**, 5271-5279 (2004). S. González-Pérez, I. R. Martín, D. Jaque and P. Haro-González, Growth of Nanocrystals in Nd³⁺-Yb³⁺ codoped oxyfluoride glass by laser irradiation, J. Nanosci. Nanotechnol., **8**, 1-4 (2008). S. González-Pérez, I. R. Martín, F. Lahoz, P. Haro-González, J. Herreros, Local crystallization in an oxyfluoride glass doped with Er³⁺ ions using a continuous argon laser, Appl. Phys. A, **93**, 983-986 (2008).

Figures

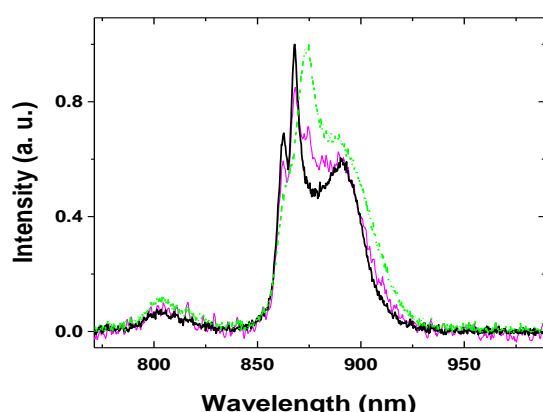


Fig 1: Emission spectra of the $^4F_{3/2}$ and $^4F_{5/2}$ levels of Nd³⁺ ions of the irradiated point (narrow magenta line), outside the damage (dashed green line) and from a 1 mol% of Nd³⁺ oxyfluoride glass ceramic sample (wide black line).

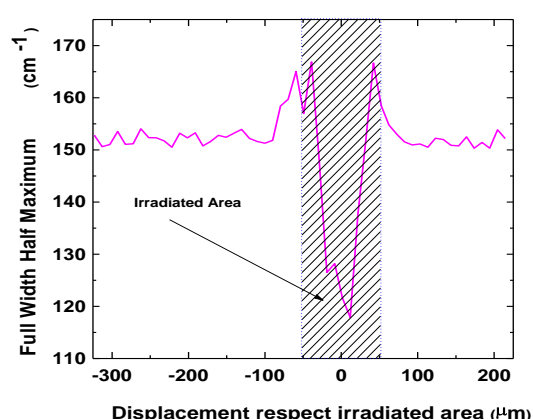


Fig. 2: Full Width Half Maximum data obtained from luminescence signal ($^4F_{3/2}$ to $^4I_{9/2}$ transition line) of a scan transversal to irradiated line direction. So it's possible to compare -on the same data set-, irradiated and non-irradiated areas.

NOVEL ONE-POT SYNTHESIS OF ORGANIC-FUNCTIONALIZED SILICA NANOPARTICLES

G. Berriozabal,^{a,b} Y. R. de Miguel^{a,c}

(a)LABEIN-Tecnalia, Centre for Nanomaterials Applications in Construction (NANOC), Calle Geldo, Edificio 700, Parque Tecnológico de Bizkaia, 48160 Derio (Spain) (b) CIC-NanoGUNE

Nanoscience Cooperative Research Center, Calle Tolosa 76, Donostia (Spain)

(c) Nanostructured and Eco-efficient Materials for Construction Unit, Associated Unit LABEIN-Tecnalia/CSIC, 48160 Derio, Bizkaia (Spain)

gberriozabal@labein.es

This research project focuses on the study and development of novel synthetic methodologies for the obtention of nanoparticles. In this poster, a convenient single step (one-pot) method is described for the preparation of nanoparticles bearing a wide range of organic functional groups.

Our route is based on well-known Sol-Gel methodology, particularly the Stöber method,¹ which is widely used to obtain silica nanoparticles under specific conditions involving base catalysis (Scheme 1).² For this, we have undertaken a study of methodology for the synthesis and functionalization of nanoparticles with a variety of functionalities (amine, phenyl, vinyl, etc.), comparing the novel one-pot method to the previously reported two-stage method,³ which requires an initial step for nanoparticle synthesis followed by functionalization in a second stage.

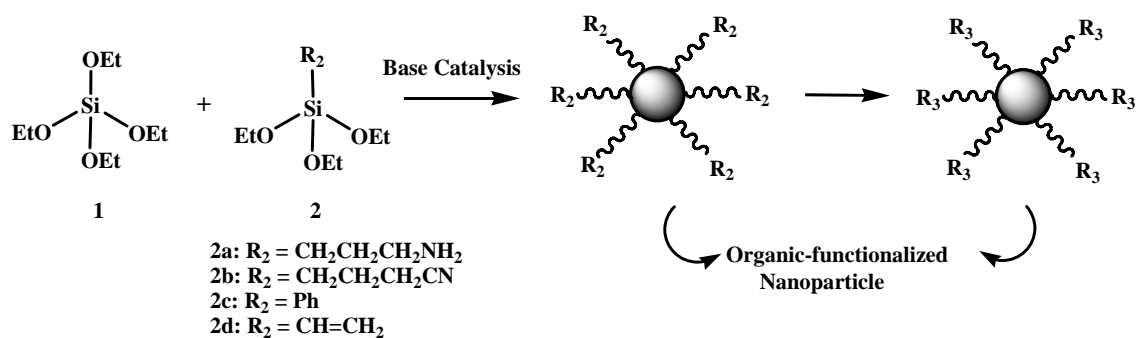
As a result of this novel method, stable colloidal suspensions of monodisperse silica nanoparticles with pendant organic moieties were successfully obtained; the size of these nanoparticles being in the range of 50 to 130 nm, as can be observed in the images obtained by Transmission Electron Microscopy (TEM) and Atomic Force Microscopy (AFM) (Fig 1).

In addition, ²⁹Si and ¹³C CP/MAS NMR spectra of these nanoparticles have been obtained in order to demonstrate the presence of the covalent bonding between the organic group and the silica nanoparticle (Fig 2).

References:

- [1] Stöber. W.; Fink. A.; Bohn. E.; *J. Colloid Interface Sci.*, **26** (1968) 62.
- [2] Brinker C.J.; Scherer G.W. (Eds.), “*Sol-Gel Science. The Physics and Chemistry of Sol-Gel Processing*”, Academic Press, San Diego (1990)
- [3] Yanqing, A.; Miao, C.; Qunji, X.; Weimin. L.; *J. Colloid Interface Sci.*, **311** (2007) 507.

Figures:



Scheme 1. Novel one-pot synthesis of organic-functionalized silica nanoparticles

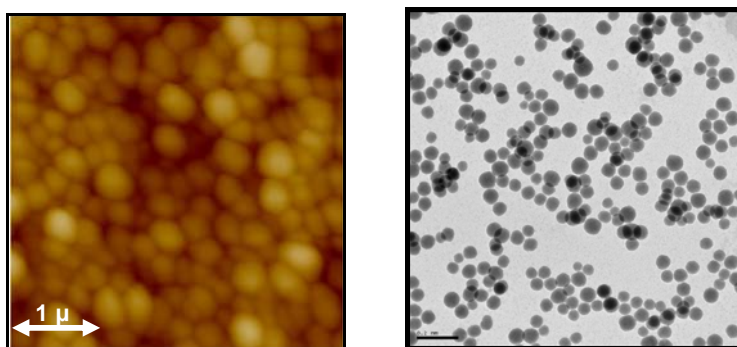
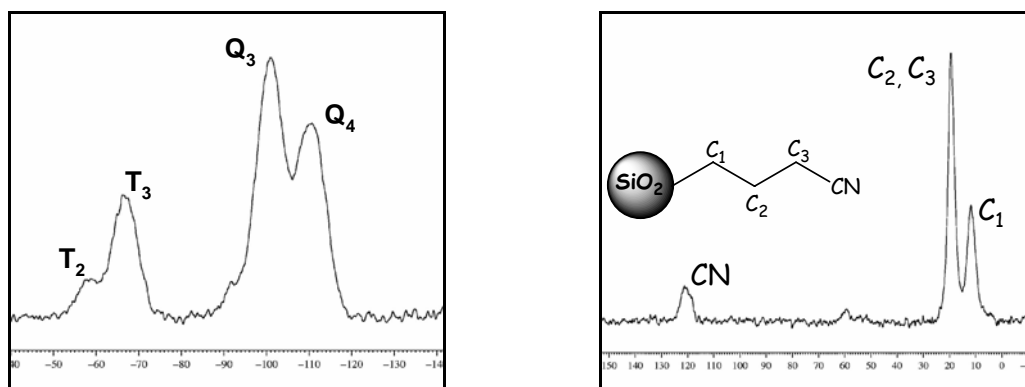


Fig. 1. AFM and TEM images of Ciano-functionalized silica nanoparticles

Fig. 2. ^{29}Si and ^{13}C CP/MAS NMR spectra of Ciano-functionalized silica nanoparticle

The Synthesis of Transition Metal Sulfide Catalysts for H₂S-Powered Solid Oxide Fuel Cells

Berçeste BEYRİBEY, Zehra ALTIN, Burcu ÇORBACIOĞLU, Seyfettin ERTURAN
Yıldız Technical University, Chemical Engineering Department, Istanbul, Turkey
b_berceste@hotmail.com, gulden@yildiz.edu.tr, burcucorbacioğlu@yahoo.com, erturan@yildiz.edu.tr

Currently over 40×10^6 tons of hydrogen sulfide are generated world-wide as by-product from the petroleum, natural gas and coal gasification industries. Its concentration ranges from a few ppm to above 80% in refining and natural gas industries. The adverse effects of H₂S on industrial processes, human health and the environment make it necessary to remove it from all effluent streams [1]. Many processes have been developed to remove and/or recover H₂S, including adsorption, absorption, hydrogen production and conversion to elemental sulfur via the two-step Claus process [2]. There are few direct commercial uses for H₂S; hence most of it is converted to sulfur [1]. The overall reaction is highly exothermic and although some of the heat can be recovered as steam it would be far more desirable to either directly recover hydrogen or to electrochemically oxidize H₂S in situ at the anode of a solid oxide fuel cell (SOFC).

It is well known that H₂S decomposes at high temperatures into hydrogen and sulfur via the general equilibrium reaction



Therefore, it would be highly desirable if hydrogen originating from this reaction could be electrochemically oxidized in a SOFC to generate electrical energy, leaving sulfur and water as exclusive anode reaction products. Thus utilization of H₂S in solid oxide fuel cells provides a potentially economical and powerful alternative for concurrent chemical conversion and power generation [2].

One of the major technical challenges in the development of H₂S/O₂ SOFC is to identify anode materials that are conductive, chemically and electrochemically stable, and catalytically active in H₂S-rich environments. In the last 20 years many groups have investigated several materials as potential candidates as anodes for SOFC operated on H₂S. Unfortunately, none of these materials fully satisfies criteria required for a successful and effective anode [1].

It is well known that catalytic activity of metals is strongly dependent on shape, size and size distribution of the metal particles [3]. Smaller particles are more desirable for electrodes in fuel cells because the smaller the particles, the greater the particle surface area to reduce hydrogen.

This paper is reported that vanadium molybdenum sulfur particles were synthesized using H₂S as reducing agent by chemical reduction of ammonium monovanadate and ammonium heptamolybdate tetrahydrate. The aim of this study was to investigate effects of temperature, pH and rate of H₂S on the structure of vanadium molybdenum sulfur particles. In all experiments, deionized water was used as solvent. The morphology of vanadium molybdenum sulfur particles was investigated by JEOL JSM-5410LX scanning electron microscope (SEM). A further part of this study will be present results of anode performance at low operating temperatures.

References:

- [1] Vorontsov, V., Luo, J.L., Sanger, A.R. and Chuang, K.T., *Journal of Power Sources*, **183** (2008) 76-83.
- [2] Vorontsov, An, W., V., Luo, J.L., Sanger, A.R. and Chuang, K.T., *Journal of Power Sources*, **179** (2008) 9-16.
- [3] Wang, H., Sun, X., Ye, Y. and Qiu, S., *Journal of Power Sources*, **161**(2006) 839-842.

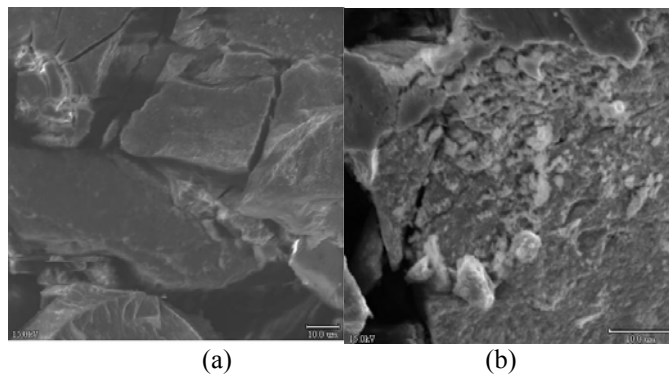
Figures:

Figure 1. Molybdenum vanadium sulfur particles synthesized at room temperature and (a) pH=6.0; (b) pH<1

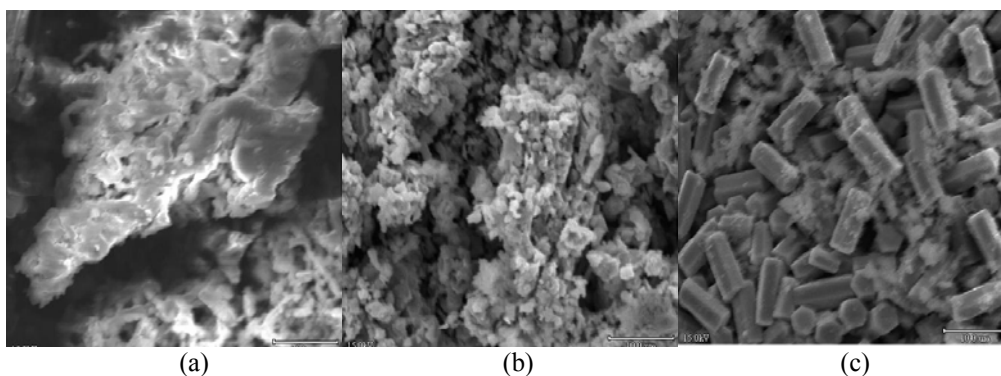


Figure 2. Molybdenum vanadium sulfur particles synthesized at pH<1 and (a) 0°C; (b) 40°C; (c) 80°C

Functional Model of Nanoparticle-Organic Memory Transistor for Use as a Spiking Synapse

O. Bichler^a, W. Zhao^a, F. Alibart^b, S. Pleutin^b, D. Vuillaume^b and C. Gamrat^a

^aEmbedded Computing Lab, CEA, LIST, F-91191 Gif sur Yvette, France

^bMolecular Nanostructures and Devices Group, IEMN, CNRS, BP 60069, Avenue Poincaré, 59652 Villeneuve d'Ascq, France

olivier.bichler@cea.fr

Emerging nanocomponents are of great interest to provide adaptability, high density and robustness for the development of new bio-inspired circuits or systems. Although CMOS Neuromorphic circuit was one of the most intense researches to bring the adaptability and robustness in the circuit beyond the conventional Von Neumann architecture in early 1990', CMOS technology could not provide the huge capacity to be scalable to biological levels because a great number of transistors are required to emulate the dynamical behaviors of biological synapse [1]. Nanoscale components are therefore of great interest to develop new neuromorphic circuits by replacing CMOS technology based synapse. The Nanoparticle–Organic Memory transistor (NOMFET) is one of the most promising candidates as it can exhibit dynamical behaviors similar to a biological synapse [2]. It could be very suitable to implement some natural synaptic learning mechanisms such as Spike-Time-Dependent-Plasticity (STDP) [3].

The NOMFET is composed of three terminals as the conventional MOSFET, Drain (D), Source (S) and Gate (G). The device is fabricated using a bottom-gate electrode configuration. Gold nanoparticles (NP) are immobilized on the surface of the inter-electrode gap before pentacene deposition. The conduction in the device is assured by holes, created in the thin film at the interface with the silicon oxide when a negative gate voltage is applied. In addition to rather classical transistor behavior, a negative gate voltage also positively charges the Au NPs. This has the effect of diminishing the channel conductivity of the device, because the charged NPs cause a repulsive electrostatic interaction between the holes trapped in the NPs and the ones created in the pentacene. The NOMFET therefore exhibits a short term memory and the charge retention time in the NPs can be as high as several thousand seconds [4].

A functional model is very useful for the design of hybrid Nano/CMOS circuit and architecture as it provides the interface between the fundamental physics and the electrical behaviors. We established the functional model of NOMFET for a two-terminal device configuration, as shown Fig. 1. The gate and the drain electrodes are driven by the same input voltage, a pulse train of a variable frequency. In this configuration, the dynamical behaviors of the NOMFET is a lot as a biological synapse: there is a competition between the charges provided to the NPs by the gate voltage pulses (resulting in a decrease of the drain-to-source current) and the natural NPs charge relaxation (which increases the current intensity until the NPs are fully discharged). When a new input pulse sequence occurs, the NOMFET exhibits either a depressing or a facilitating behavior, depending both on the duration between the pulses and on the charge level of the NPs. The current in the device is thus dependent on the history of the input signal; the maximum variation on our devices is close to 25% with 30V pulses amplitude.

Our model is iterative: the drain-to-source current response to a voltage pulse is calculated using essentially the width of the pulse, the current level at the previous pulse and the duration elapsed since then. Multiple measurements of the current response for voltage pulse sequences, including sequences with a variable frequency, are used to fit the model with experimental data,

to improve simulations accuracy. This iterative model has proved to be fully functional to simulate the dynamic behavior of NOMFET as a synaptic device (see Fig. 2). It is implemented in the Verilog-A analog hardware description language, which can be incorporated into the Spectre circuit simulator from Cadence to simulate mixed Verilog-A component and SPICE-level device circuits. This implementation also allows the model to easily integrate new experimental results.

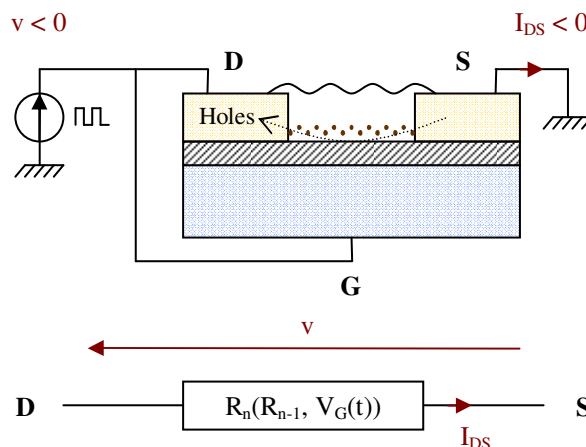


Figure 1: Device configuration used to establish our model and its electrical equivalent circuit (in linear regime). Input voltage v is a sequence of pulses of amplitude 30V. R_n is the equivalent drain-to-source resistance at the n -th pulse. R_n is dependent on the bias of the device and on the charge level of the NPs, reflected by the value of R_{n-1} .

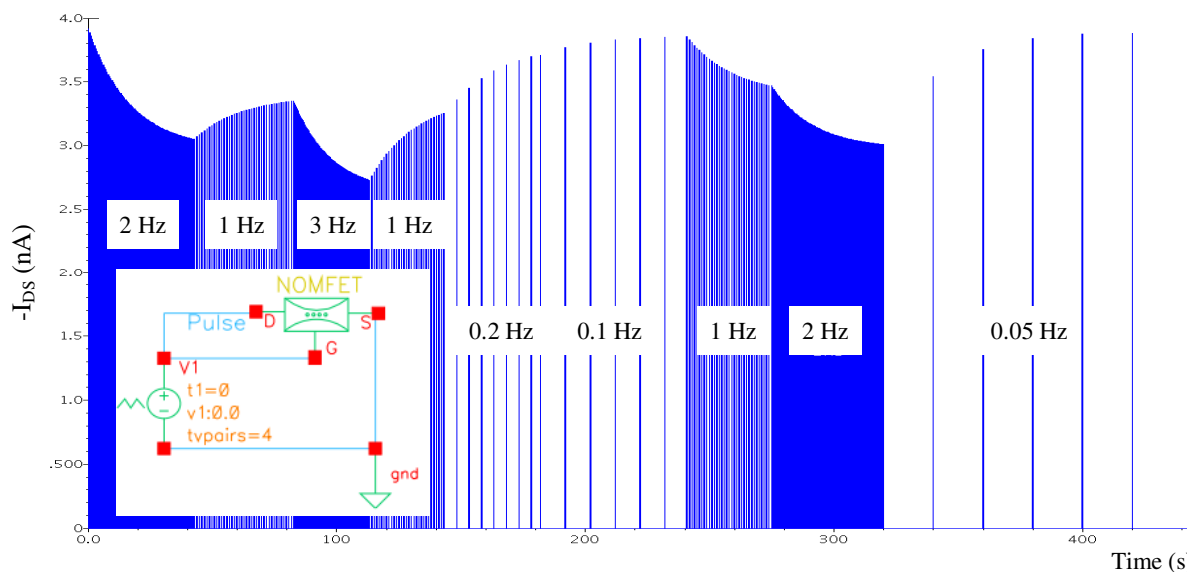


Figure 2: Transient simulation of spice NOMFET model with different input pulse train sequences (0.05 Hz – 3 Hz). Depending on the frequency and the historical weight or current level, depressing and facilitating behaviors can be simulated. NOMFET symbol and its test bench in the schematic editor of Cadence are shown as well.

Hybrid NOMFET/CMOS neuromorphic architectures are under investigation in our laboratory and future work will include model refinement, synapse-to-neuron interfacing and neuronal architecture simulation.

References:

- [1] K.M.Hynna and K.Boahen, *Neural Computation*, **19**, pp.327-350(2007)
- [2] F. Alibart, S. Pleutin, D. Guérin, C. Gamrat, and D. Vuillaume, *Nature Precedings* (2009)
- [3] H. Markram, J. Lübke, M. Frotscher, and B. Sakmann, *Science*, **275**, pp. 213-215(1997)
- [4] C. Novembre, D. Guérin, K. Lmimouni, C. Gamrat, and D. Vuillaume, *Applied physics letters*, **92**, 103314 (2008)

CHEMICALLY-INDUCED MOBILITY GAPS IN GRAPHENE NANORIBBONS: UPSCALING DEVICE PERFORMANCES

Blanca Biel, François Triozon, Xavier Blase, Stephan Roche
Departamento de Electrónica y Tecnología de Computadores, Facultad de Ciencias,
Universidad de Granada E18071 Granada, Spain
Biel@ugr.es

The rise of graphene-based science has been driven by the huge charge mobilities measured in undoped two-dimensional (2D) graphene materials close to the Dirac point [1]. However, owing to its zero energy bandgap, the 2D graphene-based field effect transistor (FET) has shown relatively poor field effect efficiency, with ON versus OFF current ratio (I_{on}/I_{off}) that can be tuned no more than a small factor (less than one order of magnitude). By using graphene nanoribbons with reduced lateral sizes, more efficient graphene-based FETs can be designed with enlarged energy bandgaps and more reasonable I_{on}/I_{off} characteristics, provided their lateral size is reduced to a few nanometers width. This, however, strongly reduces charge mobilities and ultimate device performances, and disallows the recourse to conventional lithographic techniques to massively integrate active devices and circuits at the wafer scale.

We present an *ab initio*-based study of mesoscopic quantum transport in chemically doped graphene nanoribbons with a width up to 10 nm and variable lengths up to the micron scale. The occurrence of quasibound states related to boron impurities results in mobility gaps as large as 1 eV (see figure), driven by strong electron-hole asymmetrical backscattering phenomena [2]. This phenomenon opens new ways to overcome current limitations of graphene-based devices through the fabrication of chemically-doped graphene nanoribbons with sizes within the reach of conventional lithography. Our study shows that, due to chemical doping impurities, a marked electron-hole asymmetry develops, and results in charge mobility gaps of up to one eV in nanoribbons whose electronic bandgaps before doping are only a few tens of meV large [3]. Such transport gaps should likely result in strong improvement of I_{on}/I_{off} ratio of doped graphene-FETs, without the need to use very narrow ribbons beyond the reach of current lithography.

Our theoretical results, based on first-principles and mesoscopic transport calculations, clearly evidence the potential of chemically doped graphene nanoribbons as a new material for designing performant graphene-FETs.

References:

- [1] A. Cresti, N. Nemeč, B. Biel, G. Niebler, F. Triozon, G. Cuniberti and S. Roche, *Nano Research*, **1** (2008) 361.
- [2] B. Biel, X. Blase, F. Triozon and S. Roche, *Phys. Rev. Lett.*, **102** (2009) 096803.
- [3] B. Biel, F. Triozon, X. Blase and S. Roche, (submitted)

Figures:

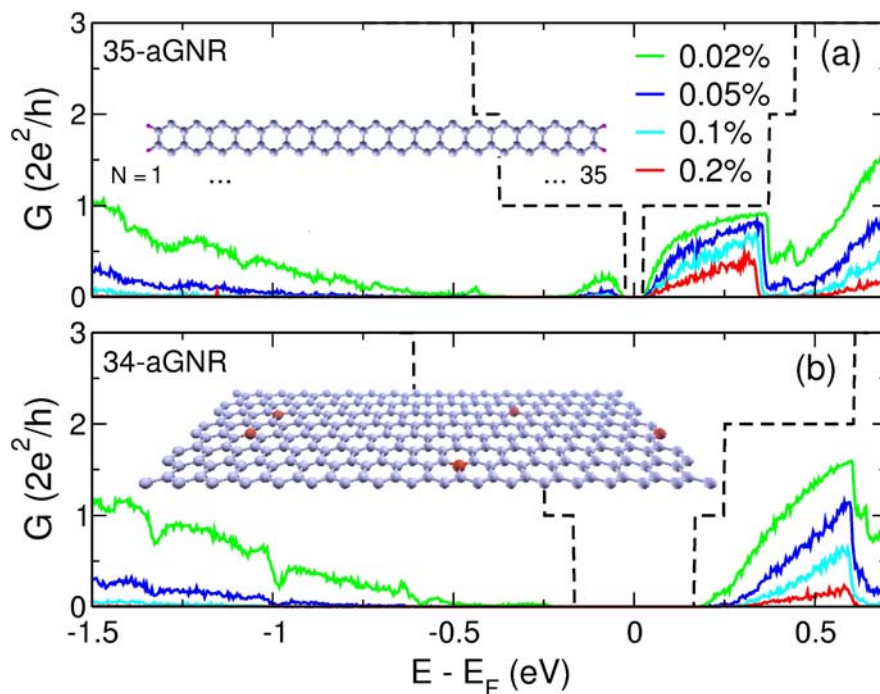


Figure: (a) Average conductance as a function of energy for a pseudo-metallic armchair GNR with $N=35$ (35-aGNR) for doping rates 0.02%, 0.05%, 0.1% and 0.2% (from top to bottom). The dashed black line corresponds to the ideal (undoped) case. The averages have been performed over 500 disorder realizations with a ribbon length of 1 micron. The inset shows the unit cell of the 35-aGNR with passivating H atoms. N indicates the number of dimer chains in a N -aGNR. (b) Same as in (a, main frame) for the semiconducting 34-aGNR. Inset: Schematic view of a randomly doped GNR.

PYRROLO-TTF-BASED MOLECULAR ELECTRONICS

S. Bilan¹, L.A. Zotti¹, F. Pauly², J.O. Jeppesen³, H. Riel⁴, and J.C. Cuevas¹

¹*Departamento de Física Teórica de la Materia Condensada, Universidad Autónoma de Madrid, E-28049 Madrid, Spain.*

²*Institut für Theoretische Festkörperphysik and DFG Center for Functional Nanostructures, Universität Karlsruhe, D- 76128 Karlsruhe, Germany.*

³*University of Southern Denmark, Campusvej 55, DK-5230 Odense M, Denmark.*

⁴*IBM Research GmbH, 8803 Rüschlikon, Switzerland.
stefan.bilan@uam.es*

In the last decade we have witnessed the development of a variety of experimental techniques that enable us to sandwich single molecules between metallic electrodes and to measure their transport properties [1]. Moreover, different groups have already demonstrated that certain molecules can perform functions analogous to those of the key microelectronics components such as switches, rectifiers and electronic mixers [1]. These results have triggered the hope that maybe molecules could be used as basic building blocks for future nanoelectronics. However, although the initial results in the field of *molecular electronics* have been quite promising, there are still many basic challenges and open problems. For instance, most molecular junctions exhibit a very low conductance that decreases exponentially with the length of the molecule, i.e. it seems to be very difficult to find the simplest electronic component, namely a good molecular wire. Another important problem is that little is still known about the relation between the structure and chemistry of the molecules and the transport properties of the junctions in which they are embedded. This is partly due to the fact that experiments probing systematically such relationship are scarce [2].

In this work we address the two fundamental problems described explicitly in the previous paragraph. In particular, we present here a comprehensive theoretical study of the transport properties of molecular junctions based on single bis(pyrrolo)tetrathiafulvalenes [bis(pyrrolo)-TTF] derivatives. These chemical compounds have several properties that make them very interesting for molecular electronics. Thus for instance, they are known to be excellent donors, they have several accessible red-ox states and a rather small HOMO-LUMO gap [3]. Using a combination of *ab initio* density function theory (DFT) calculations and nonequilibrium Green's functions techniques [4], we have studied the electronic structure and low-bias conductance of single-molecule junctions formed by gold electrodes and up to 20 different bis(pyrrolo)-TTF derivatives. The main conclusions of this study are:

- The electron-donating character of bis(pyrrolo)-TTF leads to a significant charge transfer between the molecules and the metallic leads, which in turn results in a unique level alignment that gives rise to very high conductance at low bias.
- The fact that the transport is dominated by resonant tunneling is manifested in a very slow decay of the low-bias conductance with molecular length. This is clearly at variance with the exponential behavior typically observed in most molecular junctions.
- We also show that the low-bias transport, which is completely dominated by the HOMO of the molecules, can be tuned to a large extent by means of the inclusion of appropriate side-groups.

In summary, our study suggests that due to the intrinsic properties of bis(pyrrolo)-TTF derivatives, they are excellent candidates for molecular wires and they are also ideal test-bed systems to study the structure-function relationship in molecular electronics. Let us finally say that experiments to test the main ideas presented in this work are currently under progress.

References:

- [1] N. J. Tao, Nature Nanotech. **1** (2006) 173.
- [2] L. Venkataraman, J.E. Klare, C. Nuckolls, M.S. Hybertsen and M. L. Steigerwald, Nature **442** (2006) 904.
- [3] J.O. Jeppesen and J. Becher, Eur. J. Org. Chem. (2003) 3245.
- [4] F. Pauly, J.K. Viljas, U. Huniar, M. Häfner, S. Wohlthat, M. Bürkle, J.C. Cuevas, Gerd Schön, New J. Phys. **10** (2008) 125019.

Figures:

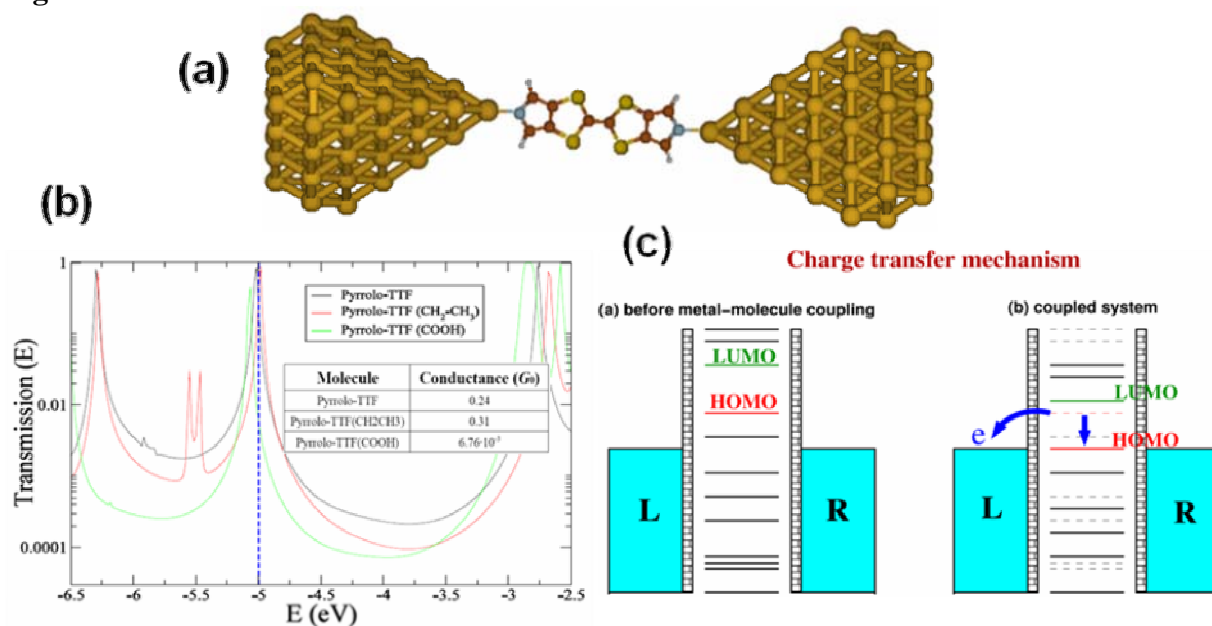


Figure 1: (a) Schematic representation of a gold-bis(pyrrolo)-TTF-gold junction studied in this work. (b) Transmission as a function of energy for single-molecule junctions formed with gold electrodes and several bis(pyrrolo)-TTF derivatives. Notice that the transmission is very high at the Fermi energy, the position of which is indicated by vertical dashed line. (c) Schematic description of the charge transfer mechanism that leads to the striking level alignment in these molecular junctions.

**ENVIRONMENTAL IMPACTS OF THE SYNTHESIS OF
PHOTOCATALYTIC FUELS AND SOLUTIONS**

Abram F. Bishay
Nuclear Materials Authority
PO / 530 El_maadi Kattamyia Road, Cairo (Egypt)

Email: abram_bishay2002@yahoo.com

A simple process was applied to acquire different fossil fuels, water and solutions a photocatalytic property using TiO_2 or its bearing ores such as ilmenite directly. The fuels and solutions are effective under broad spectrum of the ultraviolet light sources. The nano-particles in the photocatalyzed fuels may reduce the effect of their hazardous component on air pollution through destruction under ultraviolet rays in the upper atmosphere. However, the photocatalytic solutions and water can be used to decontaminate waste water and industrial effluent solutions under ultraviolet light.

Magneto-photonic properties of Nickel inverse opals

A. Blanco¹, J.B. González-Díaz², J.F. Torrado², A. Altube¹, V. Canalejas¹,
G. Armelles², C. López¹, A. García-Martín²

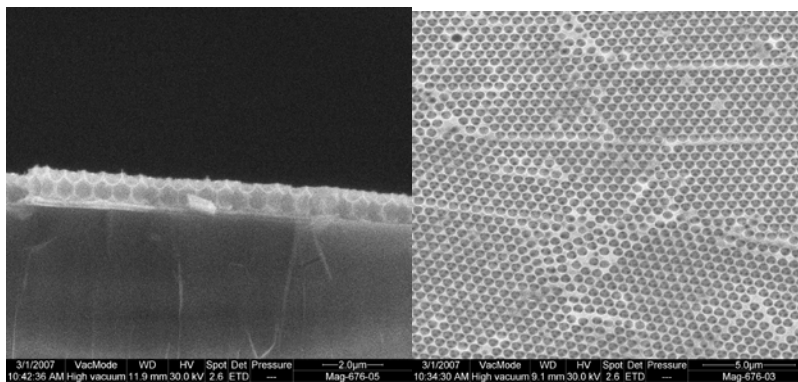
1. Instituto de Ciencia de Materiales de Madrid (CSIC) and CSIC-UVigo. C/ Sor Juana Inés de la Cruz 3 E-28049 Madrid

2. Instituto de Microelectrónica de Madrid. Centro Nacional de Microelectrónica (CSIC). C/ Isaac Newton 8 (PTM) E-28760 Tres Cantos, Madrid, Spain

Abstract

Photonic Crystals are a new class of materials where the dielectric constant is periodically modulated. This peculiar structuration provokes the appearance of allowed and forbidden states for photons, creating what have been called photonic bands and gaps, in analogy with their electronic counterparts. Generally these materials are passive, their properties only given by the structuration. However, introducing active elements it is possible to tune their photonic properties by external stimuli. Following this idea, we have fabricated three-dimensional photonic structures based on self-assembled colloidal crystals and replicated on Nickel to actuate on their photonic properties via magnetic fields.

Thin artificial opal films with sphere diameters ranging from 200-700 nm have been infiltrated with Ni by means of electrodeposition (ED) and Atomic Layer Deposition (ALD). The former yields homogeneous infiltration that floods the inner pores of the structure while the latter provides homogeneous conformal growth (shells) around the spheres with atomic precision. The magneto-photonic properties of these two Nickel nanostructures have been studied both experimentally and theoretically, performing a thorough analysis of the Magneto-Optical Kerr Effect spectra. We have found a clear dependence of the MO response as a function of the sphere size as well as on the Ni growth method, implying thus that local properties are of great importance. This is also corroborated when comparing ordered vs. disordered structures. Our ansatz is based in the fact that, due to the metallic character of Ni, there is a plasmon-like excitation that modifies the distribution of the electromagnetic field inside the system, responsible of the MO response.



Nickel inverse opals grown by ED on 670 nm polystyrene opals.

Yttria totally stabilized zirconia nanoparticles obtained through the pyrosol method

*B.S. Vasile**, *Otilia-Ruxandra Vasile***, *Cristina Ghitulica**, *Ecaterina Andronescu**, *Raluca Dobranis*, *Elena Dinu**, *Roxana Trusca****

**University POLITEHNICA from Bucharest, Faculty of Applied Chemistry and Material Science, No. 1-7 Polizu Street, Postal Code 011061, Bucharest, Romania*

*** National Research Institute for Electrochemistry and Condensed Matter, No. 202 Splaiul Independentei street, Postal Code 060021, Bucharest, Romania*

**** Metav C.D., No. 31 C.A. Rosesti Street, Postal Code 020015, Bucharest, Romania*
bogdan.vasile@upb.ro

It is well known that zirconia based ceramics, partially or totally stabilised, have a wide use in many fields, such as biomedical, sensors, catalysts, cutting tools and abrasives, components with high thermo-mechanical properties, filters or solid oxide fuel cells technologies. The use of totally stabilised zirconia in fuel cells technologies is due mainly to the very good ionic conductivity of cubic zirconia at medium and high temperature [1, 2, 3].

The pyrosol method consists in the formation of an aerosol from a diluted solution of precursors, using a high frequency ultrasounds generator. The formed aerosol is carried through a furnace, in a quartz tube, by a carrier gas. During the passage of the aerosol through the furnace, some reactions occur such as evaporation, calcination and densification of the powder. At the end of the tube, a high voltage wire collects the powder.

In this work, 10 mole percent yttria stabilised cubic zirconia is obtained through the pyrosol method, starting from a diluted solution of zirconia nitrate ($\text{N}_2\text{O}_7\text{Zr} \times 6\text{H}_2\text{O}$) and yttrium nitrate ($\text{Y}(\text{NO}_3)_3 \times 4\text{H}_2\text{O}$) [1]. The pyrosol method was used in order to obtain reactive powders, with dimensions in the nanometers range.

The main factors which are influencing the parameters of the obtained powders are concentration of the precursors' solutions, soluble salts type, synthesis temperature, vibration frequency, etc. In the present paper, it was investigated the influence of the concentration of solutions (5×10^{-2} M, 2.5×10^{-2} M and 1.25×10^{-2} M) and of the thermal treatment temperature (700, 800 and 900°C) on the dimensions, morphology and composition of powders.

The analyses used to characterise the obtained powders were X-ray diffraction, scanning electron microscopy (SEM), atomic force microscopy (AFM) and high resolution transmission electron microscopy (HRTEM).

The only crystallographic phase identified through X-ray diffraction, for powders prepared at 800°C and higher and for all concentrations, is cubic zirconia.

From SEM images it was observed that there were obtained perfect spherical particles. By increasing the thermal treatment temperature the particle sizes increases, reaching 0.6 microns, but by decreasing the concentration of the precursors' solutions, the particle size reaches a medium size of approximately 85 nm.

The profiles extraction of topography images from AFM reveal that more than 90 % of particles are below 90 nm.

From HRTEM images it can be seen that the spherical particles are formed from an agglomeration of nanocrystalites, reaching even a mean dimension of 4 nm for 1.25×10^{-2} M concentration of the starting solutions, which is the lowest concentration used, synthesized at 800°C . The maximum size of nanocrystalites is of approximately 9 nm, for the 5×10^{-2} M starting solutions, treated at 900°C .

We may conclude that the pyrosol process is a relatively simple method, which is allowing the preparation of reactive cubic zirconia powders, with dimensions in the nano domain and spherical morphology, with valuable application in main industrial fields.

References:

- [1] Chih-Wei Kuo, Yueh-Hsun Lee, Kuan-Zong Fung, Moo-Chin Wang, *Journal of Non-Crystalline Solids*, 2005, 304–311;
 [2] Christel Laberty-Robert, Florence Ansart, Simone Castillo, Guillaume Richard, *Solid State Sciences*, 4 (2002), 1053–1059;
 [3] Yueh-Hsun Lee, Chih-Wei Kuo, I-Ming Hung, Kuan-Zong Fung, Moo-Chin Wang, *Journal of Non-Crystalline Solids*, 351 (2005), 3709–3715.
 [4] Manuel Gaudona, Elisabeth Djurado, Norbert H. Menzler, Morphology and sintering behaviour of yttria stabilised zirconia (8-YSZ) powders synthesised by spray pyrolysis, *Ceramics International* 30 (2004) 2295–2303.

Figures:

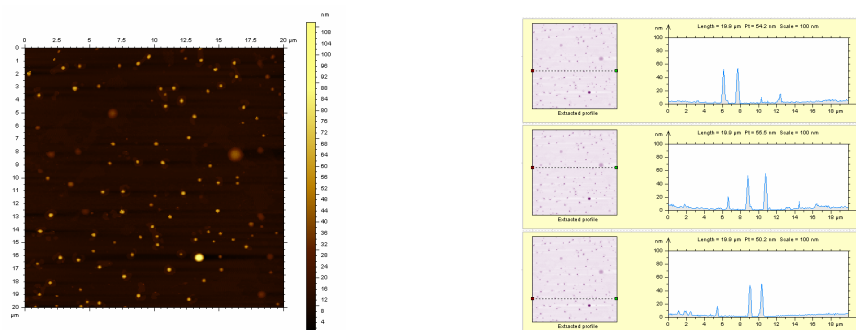


Figure 1 – A topography AFM image of 20µm and the extracted profile obtained on cubic yttria stabilised zirconia synthesised from the concentration of precursor solution of $1.25 \times 10^{-2} \text{M}$ at 800°C

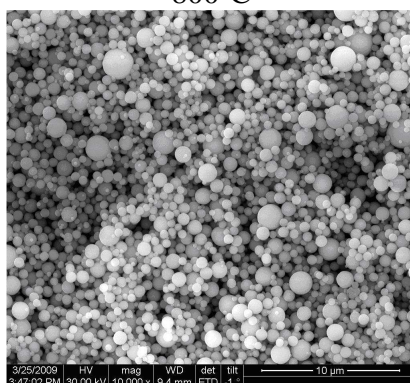


Figure 2 – SEM image on cubic yttria stabilised zirconia synthesised from the concentration of precursor solution of $1.25 \times 10^{-2} \text{M}$ at 800°C

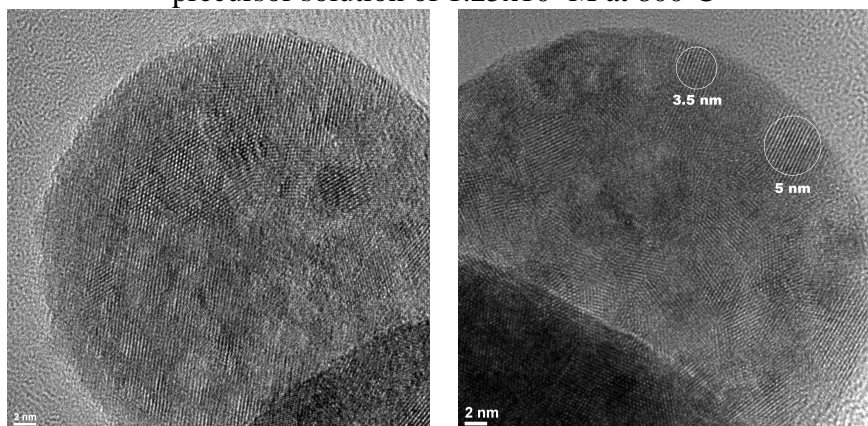


Figure 3 – TEM (HRTEM) image obtained on cubic yttria stabilised zirconia synthesised from the concentration of precursor solution of $1.25 \times 10^{-2} \text{M}$ at 800°C

Test and Modeling of the Electronic Behavior of Carbon Nanotubes High Performances Transistors obtained using Air-Brush Deposition Technique

P. Bondavalli¹, L. Gorintin¹, P. Legangneux¹, D. Pribat²

¹Nanocarb Lab, Thales Research and Technology, Palaiseau, France

²Lpicm, Ecole Polytechnique, Palaiseau, France

paolo.bondavalli@thalesgroup.com

Abstract

Using one Single-Walled-Carbon-Nanotube (SWCNT) to achieve high performances transistors presents two important issues. Firstly, we can not predict if SWCNTs are metallic or semiconducting before electrical tests. Secondly, it is quite difficult to identify the position of one single SWCNT using Atomic Force Microscope (AFM) technique and then to depose metal electrodes. For these reasons, this is not a suitable solution for batch fabrication. Thus, we have focused our work on carbon nanotube field effect transistors (CNTFETs) obtained using SWCNT mats as channels. Indeed, as far as random networks are concerned, it has been shown that, through a percolation effect, overall semiconductor behavior can be obtained for carefully controlled surface densities [1-4]. Only two conditions must be fulfilled: the distance between the two electrodes must be larger than the SWCNT average length (1 μ m), otherwise metallic nanotubes could cause short-circuit, and the surface density of the SWCNT mat has to exceed slightly the percolation threshold. For too high densities, the conduction reaches an ohmic trend with no gating effect [5]. Our contribution deals with the modeling and the test of CNTFETs obtained using SWCNTs networks as channels. To achieve these ones, we have deposited SWCNT mats using an improved air-brush technique. Firstly, gold electrodes were fabricated using common metal deposition methods on an oxidized Si substrate (used as the gate). The electrodes were designed using interdigitated configuration in order to maximize the chance to have SWCNT chains linking the two electrodes, with different channel width D (2, 5, 10 and 15 μ m). Secondly, using commercial SWCNTs from SouthWestNanoTechnologies, CoMoCat SG65 (90% of semiconducting SWCNTs), we have achieved, after a sonication and a centrifugation step as described in [6 -7], stabilized solutions using N-Methyl-pyrrolidone (NMP) as solvent. These solutions are deposited on the substrate, where the electrodes have been fabricated, using a spray-gun (Fig.1). The substrate is heated at a temperature higher than 202°C (evaporation point for NMP) in order to evaporate instantaneously the solvent droplets hitting the substrate. This last detail allows us to dramatically improve the uniformity of the SWCNTs mats preventing the so-called “coffee ring effect” (deposition of SWCNTs on the borders of the drops evaporated at room temperature) achieving mats with state of the art reproducible characteristics [8]. After electrical test, we have modeled the On/Off current ratio variation of CNTFETs as a function of the electrodes distance, and obtained the formula (1).

$$(1) \ln(I_{On}/I_{Off}) = \pi^{1/2}/4.236 (L_c/L_t) \ln((x/(1-x)))$$

L_c= channel length

L_t=SWCNT average length

x=Semiconducting Nanotubes percentage

This last was defined supposing that the current between electrodes is mainly due to the all semiconducting or all metallic SWCNT chains linking the two electrodes: the mixed paths (composed by semiconducting and metallic SWCNTs) minimally influence the final On/Off current ratio. Finally we have compared the theoretical results with experimental ones and found a close agreement. This result has confirmed that mixed paths have no effect on the overall current flowing in the mat. This is the first time that this hypothesis is confirmed. The impact of our model could be really huge to tailor electronic characteristics of SWCNT mat based devices for industrial applications.

References:

- [1] S. Kumar, N. Pimparkar, J. Y. Murthy, A. A. Alam, Theory of transfer characteristics of nanotube networks transistors, *Appl.Phys.Lett.* 88 (12) (2006), 123505
- [2] S. Kumar, G. B. Blanchet, M. Hybertsen., J. Y. Murthy, and M. A. Alam, Performance of carbon nanotube-dispersed thin-film transistors, *Appl.Phys.Lett* 89 (2006), 143501
- [3] S. Kumar, J. Y. Murthy, and M. A. Alam, Percolating Conduction in Finite Nanotube Networks *Phys. Rev. Lett.*, vol. 95 (2005), 066802
- [4] S. Kumar, Electrical and thermal transport in nanotubes based thin film transistors, PhD Thesis, Purdue Lafayette, Indiana (US), 2007
- [5] E. Berkyarova, M. E. Itkis, N. Cabrera, B. Zhao, A. Yu, J. Gao, R. C. Haddon, Electronic properties of Single-walled carbon nanotube networks, *J.Am.Chem.Soc.* 127 (16) (2005), pp. 5990-5995

Figures:

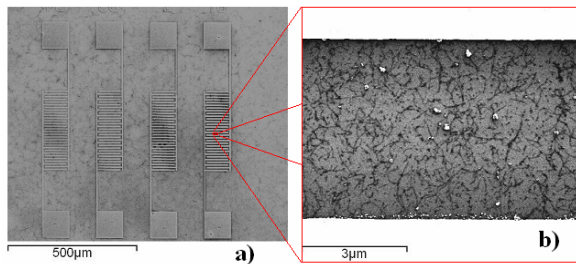


Fig. 1: Palladium interdigitated electrodes (a) with SWCNT networks deposited by spray gun technique (b).

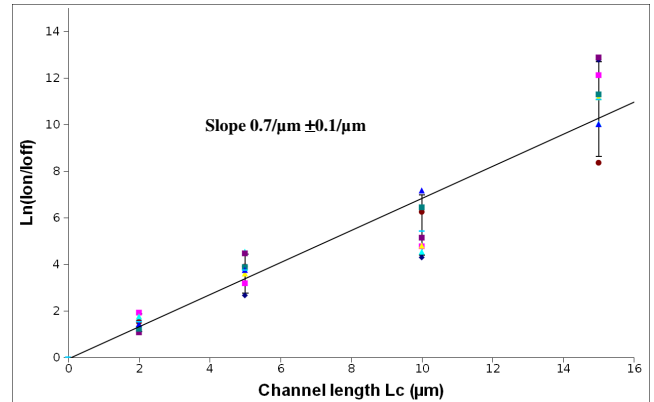


Fig. 3: $I_{\text{on}}/I_{\text{off}}$ natural logarithm as a function of the channel length L_c .

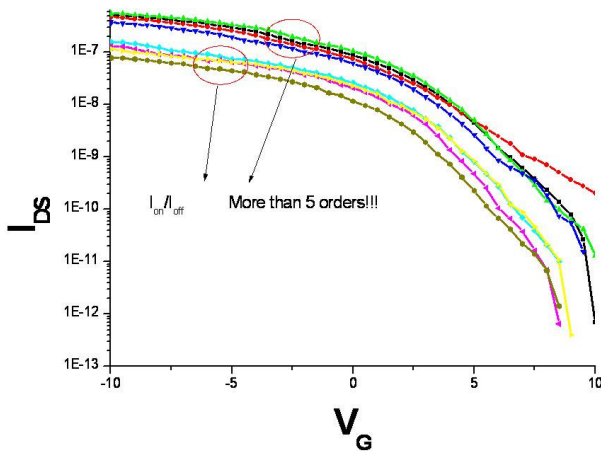


Fig. 2: Transfer Characteristics for CNTFETs obtained using Air-Brush technique.

ELECTROSTATIC PROPERTIES OF DOPED SILICON NANOCRYSTALS PROBED BY KELVIN FORCE MICROSCOPY

Lukasz BOROWIK, Koku KUSIAKU, Didier THERON, Heinrich DIESINGER, Dominique DEREMES, Thierry MELIN
INSTITUT D'ELECTRONIQUE, DE MICROÉLECTRONIQUE ET DE NANOTECHNOLOGIE
CNRS-UMR 8520, AVENUE POINCARÉ, BP 60069,
59652 VILLENEUVE D'ASCQ CEDEX, France

Thuat NGUYEN-TRAN, Pere ROCA i CABARROCAS
LABORATORIE DE PHYSIQUE DES INTERFACES ET DES COUCHES MINCES, UMR
7647 DU CNRS, ECOLE POLYTECHNIQUE
91128 PALAISEAU CEDEX, France
lukasz.borowik@isen-lci.iemn.univ-lille1.fr

We present ultra-high vacuum (UHV) atomic force experiments performed on doped silicon nanocrystals fabricated by plasma enhanced chemical vapour deposition [1]. The aim of this work is to study the doping properties and charge transfers from doped nanocrystals using amplitude modulation Kelvin force microscopy (AM-KFM).

Intrinsic, p- and n-type doped silicon nanocrystals have been deposited on silicon surfaces (p or n-type), passivated using diluted hydrofluoric acid, and then measured in UHV conditions using a home-made AM-KFM, in which the surface potential is measured using an electrostatic excitation of the cantilever at its second resonance (f_1 , here $\sim 450\text{kHz}$), while the topography is acquired in non-contact mode using a mechanical excitation of the cantilever at its first resonance (f_0 , here $\sim 70\text{kHz}$) [2].

The doping properties of nanocrystals are studied by monitoring the nanocrystal surface potential V_S as a function of the nanocrystal and substrate doping, and also as a function of the nanocrystal size. The case of intrinsic nanocrystals is illustrated in Figure 2 (left), in which the surface potential V_S of the nanocrystals is plotted as a function of their height, showing - in average - positive or negative charge transfer from the p-doped and n-doped substrate, together with strong potential fluctuations attributed to the variation of the nanocrystal surface states. This situation is then compared to the case of n-doped nanocrystals Figure 2 (right), for which much lower potential fluctuations can be observed, and for which the nanocrystal surface potential V_S is found almost independent of the doping level.

These two effects are understood as stemming from the doping of the nanocrystal, which provides the necessary charge to compensate for the nanocrystal surface states, and induce a charge transfer to the substrate. The interpretation of the charge transfer equilibrium will be detailed quantitatively [3], using numerical simulations of the KFM signals taking into account capacitance averaging effects known to occur in AM-KFM [4]. It will be shown that the charge transfer is enhanced due to the quantum confinement in nanocrystals with size $< 10\text{nm}$ in quantitative agreement with Ref [5].

References:

- [1] N. Chaabane et al, Applied Physics Letters, **88** (2006)
 [2] H. Diesinger et al, Ultramicroscopy, **108** (2008)
 [3] L. Borowik et al, submitted (2009)
 [4] F. Krok et al, Phys. Rev. B, **77** (2008)
 [5] Y. M. Niquet et al, Phys. Rev., B, **62** (2000)

Figures:

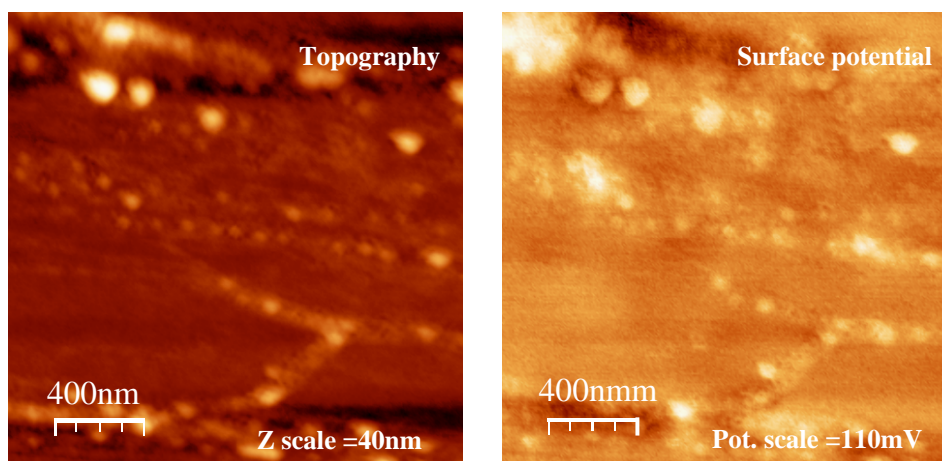


Figure 1: Images of n-doped silicon nanoparticles (topography and surface potential).

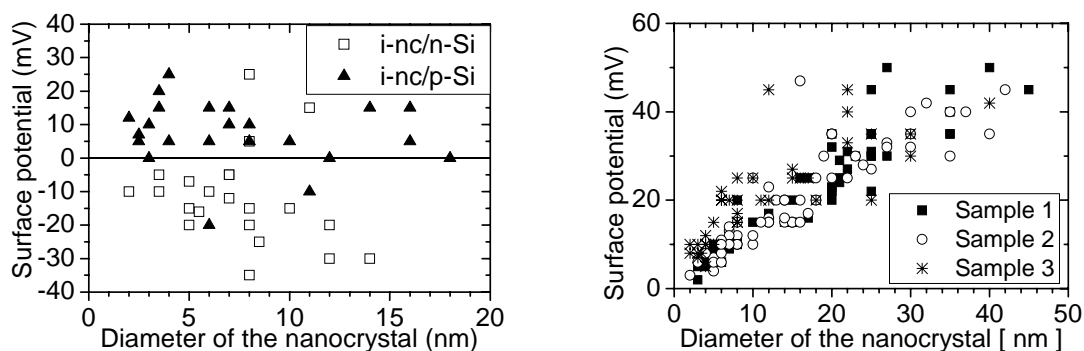


Figure 2: Left: surface potential of the intrinsic Si nanocrystals deposited on p- or n- doped substrates. Right: surface potential of the n-doped Si nanocrystals deposited on a n-doped Si substrate. The three samples correspond to SiH₄:PH₃ flux ratios of 5:1, 5:5 and 5:10 respectively.

Carbon nanotube-based MEMS devices : Gas sensor application

B. Bourlon¹, J. Wong², K. Danaie¹, K. Nacheff¹, F. Marty³, P. Guieze⁴, and M. Bockrath⁵

¹Schlumberger MEMS-TC, 10b rue Blaise Pascal, 78990 Elancourt, France

²Schlumberger-Doll Research, 1 Hampshire Street, MD-B453, Cambridge, MA 02139, USA

³ESIEE Paris, 2 boulevard Blaise Pascal, 93162 Noisy le Grand, France

⁴Schlumberger Riboud Product Center, 1, rue Becquerel, Clamart, France

⁵California Institute of Technology, Mail Stop 128-95 Pasadena, CA 9112, USA

bbourlon@slb.com

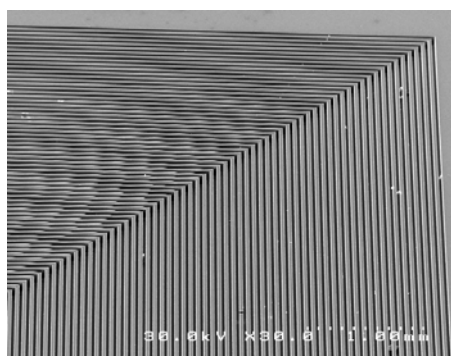
Taking advantage of the technology developed for integrated circuits during the past few decades, MEMS technology has allowed the development of innovative sensors, with an increase in microsystems miniaturization and complexity [1].

Chromatography is a laboratory technique that covers a wide range of applications in liquid or gas analysis from pharmaceutical to oilfield industries. Since the late 1970s, efforts have been directed towards the fabrication of on-chip gas chromatography sensors. While performances are improved with the miniaturization of MEMS chromatography columns, the deposition of uniform and well-controlled stationary phases inside these microscale silicon channels has remained challenging [2].

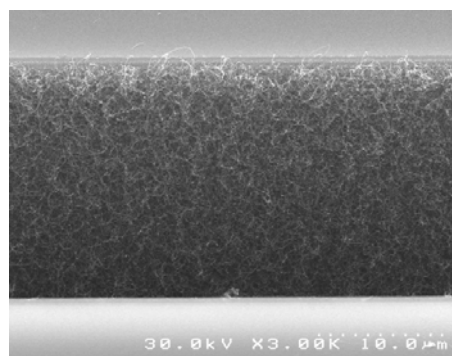
Self-assembling nanomaterials are particularly interesting for the purpose of coating and functionalization of microstructures. As part of the development of a MEMS gas chromatograph, our on-going work concerning nanotubes coated micro-columns will be presented. With their gas adsorption properties and high surface/volume ratio, nanotubes are indeed an excellent alternative material to replace some of the classical stationary phases used today [3,4]. Using microfabricated channels covered with carbon nanotubes mats, we have demonstrated separation of light hydrocarbons as well as some of the permanent gases in few tens of seconds [5].

References:

- [1] K. D. Wise, *Sens Actuators A*, **136** (2007) 39-50
- [2] M. A. Zareian-Jahromi et al., *J. Microelectromech. Syst.*, **18** (2009) 28-37
- [3] Q. Li and D. Yuan, *J. Chromatogr. A*, **1003** (2003) 203–209
- [4] M. Stadermann et al., *Anal. Chem.*, **78** (2006) 5639-5644
- [5] B. Bourlon, J. Wong and P. Guieze, Patent pending (U.S. Application Serial No. 12/503,902.)



Microfabricated Si channels



Nanotube mat on channel walls

Probing nanoscale fluid environment around individual carbon nanotube

B. Bourlon^{1,2}, *J. Wong*^{3,1}, *C. Mikó*⁴, *L. Forró*⁴, and *M. Bockrath*¹

¹ *California Institute of Technology, Mail Stop 128-95 Pasadena, CA 9112, USA*

² *Schlumberger MEMS-TC, 10b rue Blaise Pascal, 78990 Elancourt, France*

³ *Schlumberger-Doll Research, 1 Hampshire Street, MD-B453, Cambridge, MA 02139, USA*

⁴ *EPFL, CH-1015, Lausanne, Switzerland*

bbourlon@slb.com

With recent advances in nanofabrication and simulation techniques, the study of fluid properties in or around nanoscale size objects, or nanofluidics, is a subject of growing interest [1]. However, obtaining a nanoscale probe to study experimentally such fluid properties remains challenging. Our proposed approach is based on electrolytically gated single nanotube devices in electrolyte solutions [2]. Such devices integrated in microfluidic channels have been demonstrated to probe electrokinetic phenomena and also function as nanoscale flow sensors [3]. As a next step, our on-going work focuses on the nanoscale fluid properties surrounding the single nanotube device. To that end, we study transconductance of multiwalled carbon nanotube devices. Indeed, the nanotube transconductance depends on the geometrical capacitance set by the ionic distribution surrounding the nanotube [2]. We demonstrate that the ionic distribution depends on the sign of the surface charge as well as on the nature of the solvent used. Moreover, at the charge neutrality point we observe reproducible changes of the nanotube conductance as a function of ionic concentration. These results contrast with symmetric properties expected from a continuum Poisson-Boltzmann approach. However, similar asymmetric behaviors were predicted by molecular dynamic simulations [4,5] that more specifically take into account the molecular ion-surface and ion-solvent interactions. Based on our experimental results, a description of the nanotube surface fluid environment in response to different ionic and solvent environments is proposed.

References:

- [1] R. B. Schoch, *Rev. Mod. Phys.*, **80** (2008) 839
- [2] M. Kruger et al., *Appl. Phys. Lett.*, **78** (2001) 1291
- [3] B. Bourlon, J. Wong, C. Miko, L. Forro, and M. Bockrath, *Nat. Nanotechnol.*, **2** (2007) 104
- [4] R. Qiao and N. R. Aluru, *J. Chem. Phys.*, **118** (2003) 4692
- [5] R. Qiao and N. R. Aluru, *Nano Lett.*, **3** (2003) 1013-1017

TEMPLATED SYNTHESIS OF AGCN AND AG NANOWIRES

Gilles R. Bourret,^{†,‡} Thomas Dominic Lazzara,^{†,‡} R. Bruce Lennox,^{*,†} and Theo G.M. van de Ven^{*,†}

[†] Department of Chemistry, McGill University, 801 Sherbrooke St. West, Montreal, Quebec, H3A 2K6, Canada

[‡] These authors equally contributed to this work

Introduction

Fabrication of one-dimensional metallic nanostructures is an important activity within nanoscience. Their ability to absorb and scatter light has led to numerous studies in plasmonics, spectroscopy and biosensing[1].

Silver is a low cost and highly conductive metal, well known for the intense and tunable optical properties of its nanostructures.

Unlike direct wet chemical methods which are usually complex, templating processes are versatile and have been shown to be particularly successful in nanocomposite synthesis.

We present here, a simple, reproducible, high yield and inexpensive route to produce silver nanowire arrays from AgNO₃ precursor and poly(styrene-alt-maleic anhydride; SMA) polymer. Recently it has been showed that SMA self-assembles to form nanotubes in aqueous media[2]. Our technique takes advantage of this property to guide silver cyanide (AgCN) growth into very high aspect ratio nanowires (5 to 100 nm wide, > 50 μm long) [3]. Subsequent chemical reduction of the composite with sodium borohydride leads to the formation of a conductive porous metallic silver nanowire network. It is the first time to our knowledge that such long AgCN nanowires have been synthesized.

Experimental

Materials

Poly(styrene-alt-maleic anhydride) was purchased from SP² Scientific Polymer Source(1.6 kDa and 50 kDa). Silver nitrate (>99%), sodium borohydride and cyanoborohydride were purchased from Aldrich, potassium cyanide was purchased from Anachemia, and used as received.

SMA nanotube preparation

The SMA polymer nanotube preparation method (in deionized water) was the same for the two different M_w samples. An SMA solution of 0.1% wt. was prepared in deionized water. The maleic anhydride groups of SMA were hydrolyzed using an excess of NaOH, to obtain a pH beyond the second pKa. 3 mole equivalents of NaOH (by weight, relative to SMA monomer) was added. A 50% degree of protonation was achieved by dialysing the basic solution against 2 L of deionized water, using 1000 Da cut-off membranes (SpectraPore). When the solution inside

the dialysis bag reached pH 7.5 – 8, the dialysis was stopped.

AgCN-SMA composite preparation

AgCN-SMA nanowires were prepared by dissolving AgNO₃ in deionized water, added dropwise to the SMA nanotube solution. NaBH₃CN was dissolved in deionized water and added dropwise to the solution while stirring. The solution turned dark brown and opaque upon addition. During the course of 2 days, the bundles of nanotubes precipitated from solution as a white fibrous material.

Molecular modeling

Hydrolyzed SMA polymers have an increased persistence length and are stiffer when 50% protonated. Molecular modeling of the association properties of SMA in this protonation state has shown that the polymers associate sideways to form rigid association complexes bent by 130 degrees[2]. Multiple rigid associations form a minimum energy closed tubular structure involving eight SMA polymers (see Figure 1).

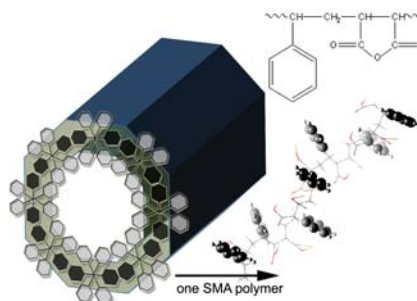


Figure 1: Schematic of the polymer nanotube formed by a process where 8 SMA polymer chains self-associate using π -stacking of the styrene groups.

The nanotube structure grows linearly by the addition of further polymers along the edges of the tube. Additional π -stacking at the periphery of the nanotubes drive sideways aggregation, giving SMA nanotube bundles. Modelling predicts that the SMA nanotubes have an outer diameter of 4.4 nm \pm 0.2 nm and an inner diameter of 2.0 nm \pm 0.2 nm.

Results and discussion

SMA nanotubes prepared by dialysis were used to template the growth of silver cyanide via the reduction of silver nitrate with sodium

cyanoborohydride. A fibrous composite results. The nanowires precipitate in bundles with various aggregation numbers and lengths, dependant on the molecular weight of the SMA polymer and whether sonication was employed. Figure 2 is a SEM scan showing extremely long nanowires formed using 50 kDa SMA.

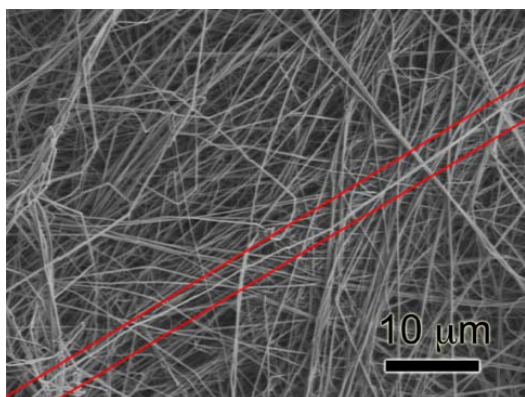


Figure 2: SEM scan of AgCN-SMA50K composite showing really long nanowires (up to 65 microns long)

1.6 kDa SMA forms bundles of 5-20 nanowires, which are joined together at one end. Performing the reaction while sonication leads to single nanotubes, as shown in figure 3.

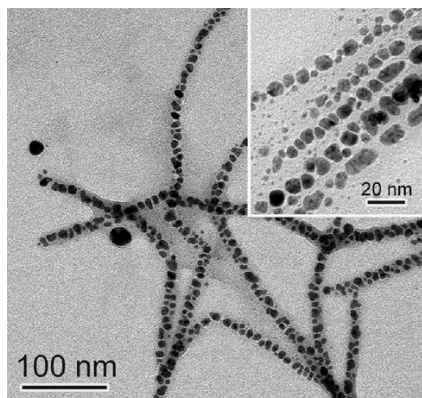


Figure 3: TEM scan of AgCN-SMA1.6K (reaction performed with sonication). Inset: High Resolution TEM showing single nanotubes.

A mechanism leading to the formation of these nano-composites can be described by a two step process. First, silver ions are quickly reduced to form silver nanoparticles (Ag NP), until the reducing power of NaBH_3CN is depleted, turning the solution into the characteristic orange color of Ag NP in water. This step is rapid and takes place in solution as typical for water phase nanoparticle synthesis.

The second step is slow and involves the growth of silver cyanide along the polymer nanotubes, forming AgCN-SMA nanowires that precipitate. Over the two day formation of the precipitate, CN^- is released, scavenging silver from the NP and reacting with free Ag^+ ions to form AgCN with the SMA nanotubes. The

AgCN nanowire structure becomes insoluble and precipitates out of solution as a white yellowish fibrous aggregate. The yellowish tint disappears upon washing, and likely arises from adsorbed silver NP within the nanowire network.

CN^- reacts with Ag^+ and Ag^0 forming different complex ions such as $\text{Ag}(\text{CN})_2^-$, and a silver cyanide precipitate in aqueous medium[4]. Ag^0 dissolution in an O_2 containing CN^- solution is a 4 electron oxidation process, involving the reduction of O_2 adsorbed on the metal surface. Reduction of silver nitrate with NaBH_3CN in presence of SMA in an Ar atmosphere did not form any wires after 4 days, in agreement with the proposed mechanism involving the oxidation of the Ag NP by O_2 in presence of CN^- , to form AgCN.

Like the other metal cyanides AuCN and CuCN, AgCN forms infinite $-\text{M}(\text{CN})-$ 1D chains, packed through argentophilic interactions into a trigonal structure[4]. The presence of silver cyanide is verified by IR spectroscopy and X-Ray diffraction [4]. Moreover, selected area electron diffraction pattern and the absence of the SPR peak characteristic of Ag NP (ca. 400 nm) supports the case for formation of AgCN rather than Ag(0) at this stage.

Subsequent reduction of the composite deposited on a nylon filter forms a conductive network of silver nanowires. Two-point probe measurements were performed on the dried sample at multiple locations. The resistance measurements ranged from 100-300 Ω (distances from 1-10 mm) on the remaining pattern, and showed huge resistance outside the array.

Conclusion

We have shown that SMA nanotubes can be used as templates to form stable networks of organic nanotubes with a high metal content. Lateral and longitudinal dimensions of the tubes can be tuned by modifying the M_w of the polymer and by sonication to prevent stacking between nanotubes. Silver cyanide is believed to occur along the length of the nanotubes and its reduction to metallic silver may be supported by the polymer scaffold of the SMA template.

Our work interest is three-fold: *first* it presents SMA as a new and an appropriate templating material, *secondly* it describes the synthesis of a new AgCN-SMA composite with genuine interesting geometry and *finally* it supports AgCN-SMA to be a suitable material for making silver nanostructures that would not be directly possible to make with pure AgCN.

References

- [1] C. Burda, X. Chen, R. Narayanan, M. A. El-Sayed, *Chemical Reviews (Washington, DC, United States)* **2005**, *105*, 1025.
- [2] C. Malardier-Jugroot, T. G. M. van de Ven, T. Cosgrove, R. M. Richardson, M. A. Whitehead, *Langmuir* **2005**, *21*, 10179.
- [3] T. D. Lazzara, G. R. Bourret, R. B. Lennox, T. G. M. van de Ven, *Chemistry of Materials*, **2009**, ASAP.
- [4] G. A. Bowmaker, B. J. Kennedy, J. C. Reid, *Inorganic Chemistry* **1998**, *37*, 3968.

CONTROLLING THE ORGANIZATION AND HEAT INDUCED COUPLING OF BIPHENYL DERIVATIVES ON METAL SURFACES

Serpil Boz¹, Meike Stöhr¹, Umut Soydaner², Marcel Mayor²

¹ *University of Basel, Department of Physics, Klingelbergstrasse, CH-4056 Basel, Switzerland*

² *University of Basel, Department of Chemistry, St. Johannisring 19, CH-4056 Basel, Switzerland*

serpil.boz@stud.unibas.ch

The development of scanning probe methods enabled the investigation of molecules on surfaces with impressive resolutions. A delicate balance between molecule - substrate and intermolecular interactions such as van der Waals interactions, H-bonding or dipolar coupling guides the arrangement of the molecules in well ordered patterns. A very appealing concept is to profit from the order of these pre-organized structures and to interlink the molecular building blocks to macromolecules.

Previously, we presented our new concept to control both, the molecular self-assembly and the subsequent intermolecular coupling reactivity by protection group chemistry and described the heat induced formation of individual polymeric structures from a biphenyl derivative on single crystal Cu (111) and Ag (111) substrates.

Here we would like to present how to control the arrangement and the size of the resulting polymeric structures by modification of the end groups of the previously presented biphenyl unit.

HYDROTHERMAL SYNTHESIS AND CHARACTERIZATION OF ONE-DIMENSIONAL TITANATE-BASED NANOSTRUCTURES

Ines Bračko¹, Boštjan Jančar¹, Danilo Suvorov¹

*¹“Jozef Stefan” Institute, Advanced Materials Department, Ljubljana, Slovenia
ines.bracko@ijs.si*

Typical hydrothermal reaction of TiO₂ and aqueous solution of NaOH yields formation of one-dimensional titanate-based nanostructures. Formation of one-dimensional titanate based nanostructures such as nanotubes, nanobelts and nanorods depends on the synthesis conditions. The layered, lamellar materials such as layered titanates with general formula A₂Ti_nO_{2n+1} (A = H, Na, K and n = 2-6) and A_xTi_{2-x/4}□_{x/4}O₄ (A = Na, H, Cs □ = vacancy) commonly undergo two kinds of topochemical reactions. In the first type of reaction, the layered structure of titanates enables intercalation of various species into interlayer galleries, while the morphology is preserved. The second type of reaction is exfoliation of sheets of the host material due to the intercalation. Based on known photocatalytic properties of TiO₂, many investigations have been initiated to study nanostructured titanates for similar photocatalytical processes. Intercalation of various species (alkaline, earth alkaline and transition metal cations, semiconductive nanoparticles) enables functionalization of one-dimensional titanates for possible applications in photocatalysis, in photodecomposition of water, as a gas sensors etc.. Hydrothermally synthesized one-dimensional nanostructures were used as a template in further hydrothermal ion-exchange reactions. The morphology, the composition and the crystal structure of hydrothermally synthesized one-dimensionally nanostructured products were determined using high-resolution transmission electron microscopy (HRTEM), energy-dispersive x-ray spectroscopy (EDS) and electron diffraction (ED).

CARBON NANOELECTRONICS: UNZIPPING TUBES INTO GRAPHENE RIBBONS

H.Santos, L.Chico and Luis Brey.

Instituto de Ciencia de Materiales de Madrid, (CSIC), Cantoblanco, 28049 Madrid SPAIN.

brey@icmm.csic.es

Quite recently, two experimental groups announced simultaneously a promising way to fabricate narrow graphene nanoribbons (GNR) using carbon nanotubes as starting material[1,2]. These two groups propose to longitudinally unzip carbon nanotubes (CNTs) to make nanoribbons, either by chemical attack[1] or by plasma etching[2], with very high yields. Unzipping carbon nanotubes appears as a promising way to fabricate narrow nanoribbons needed for nanoelectronic applications. Also, a partially unzipped carbon nanotube, Fig.1, can be regarded as a seamless junction of a tube and a nanoribbon.

In this communication, we report on the transport properties of unzipped carbon nanotubes[3]. We find that graphene nanoribbons act at certain energy ranges as a perfect valley filters for carbon nanotubes, with the maximum possible conductance. Our results show that a partially unzipped carbon nanotube is a magnetoresistive device, with a very large value of the magnetoresistance. We explore the properties of several structures combining nanotubes and graphene nanoribbons, demonstrating that they behave as optimal contacts for each other, and opening a new route for the design of mixed graphene/nanotube devices.

[1] D. V. Kosynkin, A. Higginbotham, A. Sinitskii, J. R. Lomeda, A. Dimiev, B. K. Price, and J. M. Tour, *Nature* 458, (2009), 872.

[2] L. Jiao, L. Zhang, X. Wang, G. Diankov, and H. Dai, *Nature* 458, (2009),877.

[3]H.Santos, L.Chico and L.Brey, arXiv:0904.3676

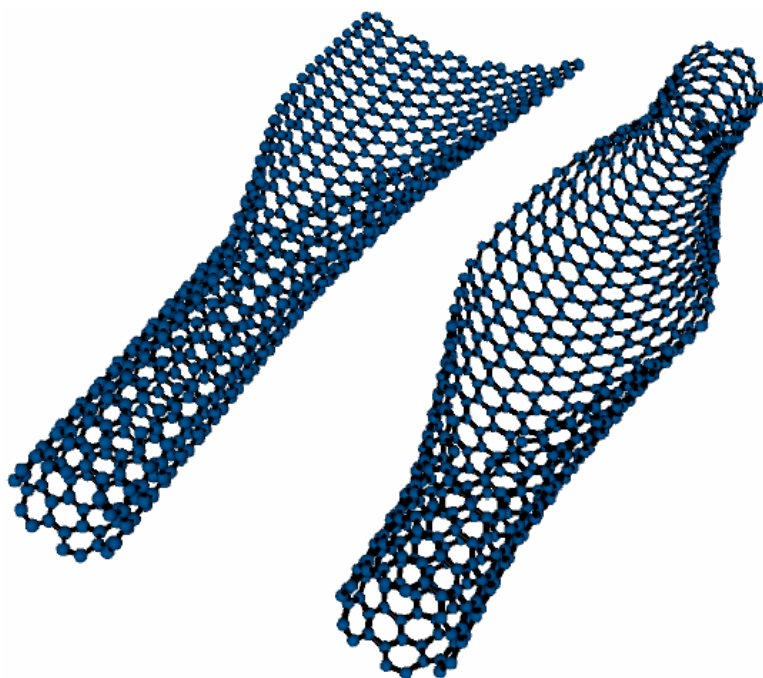


Fig.1. Geometry of two partially unzipped nanotubes. Left: a (6,6) armchair nanotube unzipped into a 12-ZGNR, making a CNT/GNR single junction. Right: the same nanotube unzipped in its central part, yielding a zigzag nanoribbon quantum dot connected to armchair nanotube contacts.

OPTICAL PROPERTIES OF CHIRPED NANO STRUCTURES

D.J. Brink, N.G. Van Der Berg and L.C. Prinsloo

Physics Department, University of Pretoria, Pretoria 0002, South Africa.
E-mail: johan.brink@up.ac.za

It is well known that a stack of ultra-thin (1 – 10 nm) birefringent layers twisted into a helicoidal structure (similar to a cholesteric liquid crystal) can act as a highly efficient reflector for circularly polarised light[1, 2, 3]. One disadvantage of these reflectors is their rather limited bandwidth. In this work we investigated the feasibility of broadening the reflectance bandwidth by applying a thickness chirp to the pitch of the structure. The paper will discuss the theory and optical properties of these structures. An example from the animal kingdom, the scarabus beetle *Gymnopleurus humanus*, which uses this concept will also be discussed. The exocuticle of this insect exhibits roughly a four fold increase in reflectance bandwidth compared to that of a normal helicoidal structure.

- [1] A.C. Neville and S. Caveney, “Scarab beetle exocuticle as an optical analogue of cholesteric liquid crystals” *Biol. Rev.*, vol 44, pp. 531-568, 1969.
- [2] D. J Brink, N. G. van der Berg, L. C. Prinsloo, and I.J. Hodgkinson, “Unusual coloration in scarabaeid beetles” *J. Phys. D: Appl. Phys.*, vol 40, pp. 2189-2196, 2007.
- [3] I. Hodgkinson and Q. Wu, “inorganic chiral optical materials”, *Adv. Mater.* vol 13, pp 889-897, 2001.

**UNEXPECTED PERSISTENCE OF MAGIC CLUSTER STABILITY IN
ULTRATHIN SEMICONDUCTOR NANORODS**W. Sangthong,^{1,2,3} J. Limtrakul,^{2,3} F. Illas¹, S.T. Bromley^{1,4*}

¹⁾ *Departament de Química Física & Institut de Química Teòrica i Computacional (IQTCUB),
Universitat de Barcelona, C/ Martí i Franquès 1, E-08028 Barcelona, Spain*

²⁾ *Center of Nanotechnology, Kasetsart University, Bangkok 10900, Thailand*

³⁾ *Department of Chemistry, Kasetsart University, Bangkok 10900, Thailand*

⁴⁾ *Institució Catalana de Recerca i Estudis Avançats (ICREA), 08010 Barcelona, Spain*

1

* Corresponding author

From cluster beam experiments excess abundances of particularly stable ‘magic’ clusters of the compound semiconductors CdS, CdSe and ZnS have been identified at well-defined sizes (e.g. (CdS)₁₃, (CdS)₃₃)¹. Based upon our bottom-up approach to predicting novel semiconductor structures², we have employed large-scale density functional calculations to investigate the stability and structures of magic cluster-based CdS and CdSe nanorods and nanowires. Both CdS and CdSe exhibit either the zincblende or wurtzite crystal structure in the bulk and have often been assumed in numerous studies to retain such structures down to a small size (e.g. nanoclusters or nanorods). Conversely, we show that ultrathin CdS nanorods (approx. 1 nm diameter) having structures based upon the assembly of magic (CdS)₁₃ nanoclusters are more stable than nanorods possessing the wurtzite or zincblende structure up to a length of approximately 11 nm. Further, the electronic structure of the nanorods reveals a progressive band gap reduction with respect to the band gap of the infinite nanowire providing evidence of both the influence of surface states and 1D quantum confinement effects³ in a realistic semiconducting nanowire model.

¹ A. Kasuya et al. *Nature Mater.* 3, 99 (2004).

² J. Carrasco, F. Illas, S. T. Bromley, *Phys. Rev. Lett.* 99, 235502 (2007).

³ S. -H. Kan, T. Mokari, E. Rothenberg, U. Banin, *Nature Mater.* 2, 155, (2003).

DESCRIPTION OF CNTS INTERCALATED STRUCTURES OBTAINED BY CVD

Eric Jover, Burak Caglar, Toygan Mutlu, Enric Bertran
FEMAN group, IN2UB, Dep. de Física Aplicada i Òptica, Universitat de Barcelona, Martí i
Franqués 1, E-08028 Barcelona, Spain
ebertran@ub.edu

From their discovery in 1991, carbon nanotubes (CNTs) have been an attractive research topic due to their original properties. Although much has been said on CNTs, new applications and new research perspectives are discovered everyday. In this way, publications on all the fundamental areas related to this topic continue to increase.

Growing CNTs is normally carried out on metallic catalyst such as Fe, Ni, Co, ... From a catalyst layer, after an annealing step, a CNT is grown from each resulting particle being different growing mechanisms possible. Catalyst thickness layer and the diameter of the Fe particles, after annealing, have been correlated with the diameter of the obtained CNTs.

In this work, we reported the growing of CNTs on SiO₂ substrate following a Chemical Vapour Deposition (CVD) and showing a non normal configuration. In our working conditions CNTs grow intercalated between the substrate and a non-homogeneous catalyst layer (Fe) (Figure 1). Annealing step was carried out in a H₂ reductive atmosphere. CNTs growing take place under an ammonia/C₂H₂ atmosphere.

The correlation between the appearance of this phenomenon, the catalyst layer thickness and the CVD deposition temperature has been assessed using a box-Wilson experimental design. The obtained samples have been characterized by means of SEM and SEM-EDX.

Figures:

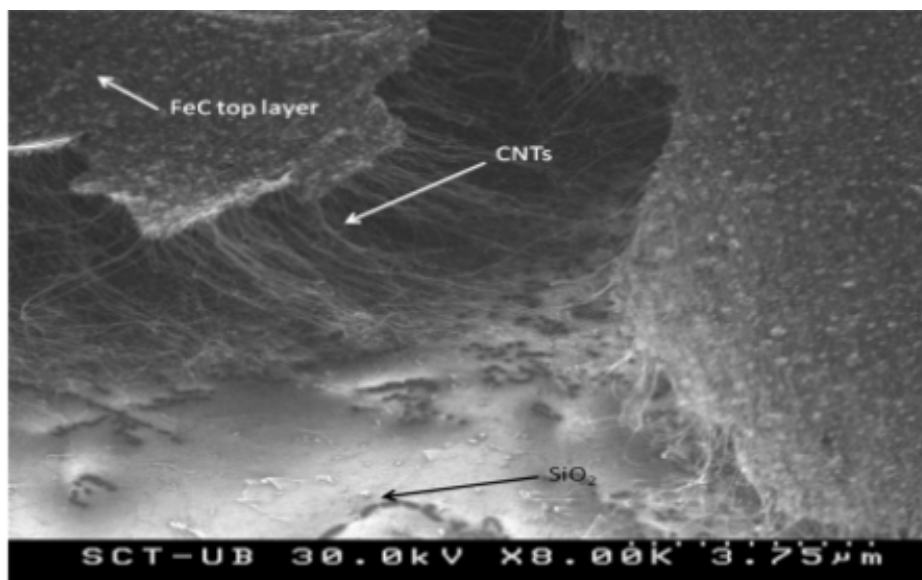


Figure 1. SEM image of a CVD sample where the intercalated CNTs structure could be observed.

Enhancement of Tribological Properties in Steel by Using a [TiCN/TiNbCN]_n Multilayer Nanostructured System

J. C. Caicedo¹, C. Amaya^{1,2}, M. E. Gómez¹, N. A. de Sánchez³, L. Yate⁴, A. Lousa⁴ and P. Prieto^{1,5}

¹ *Departamento de física, Universidad del Valle, Ciudad Universitaria Meléndez, Calle 13 #100-00 Edificio 320, A.A. 25360 Cali, Colombia*

² *Laboratorio de Recubrimientos Duros DT-ASTIN SENA, Cali, Colombia*

³ *Grupo Ciencia e Ingeniería de Materiales -GCIM, Universidad Autónoma de Occidente. Cali, Colombia*

⁴ *Departament de Física Aplicada i Òptica, Universitat de Barcelona. Martí i Franquès 1, E-08028 Barcelona, Catalunya, Spain*

⁵ *Centro de Excelencia en Nuevos Materiales, Calle 13 #100-00 Edificio 320, espacio 1026, Cali, Colombia*

jcaicedoangulo@gmail.com

[TiCN/TiNbCN]_n multilayers were grown onto silicon and steel substrates by reactive r.f. magnetron sputtering technique using two targets (TiC and Nb) and alternating deposition conditions. The multilayer period (λ) was varied from the micrometric to the nanometric range, maintaining the total thickness of the coatings in the range of a few microns by depositing a suitable number of bilayers (n). The coatings were characterized by x-ray diffraction (XRD), optical reflectance spectroscopy, and scanning electron microscopy (SEM). The tribological properties were determinate via dynamic contact test using a Microtest MT 4001–98 tribometer and Scratch Test Microtest MTR2 system; from them we measure friction coefficient and critical load for the different samples. The stress was calculated by measuring the curvature of the films onto Si substrates with a profilometer. An enhancement of both hardness and elastic modulus was observed as the number of bilayers (n) in the coating was increased. Sample with length period (λ) of 15 nm (n=200 bilayers) showed the lowest friction coefficient (~0.1) and the highest critical load (80 N), corresponding to 2.2, and 1.6 times better than those values for the coating with n=1, respectively. The enhancement effects in this [TiCN/TiNbCN]_n multilayer coatings can be attributed to the Hall Petch effect in multilayered coatings, in which the interfaces act as a barrier against the movement of the dislocations and the bilayers of materials having different mechanical properties generate an inhomogeneous system prohibiting the advancement of potential micro-cracks.

Preparation and characterization of hydrophobic polysaccharide derived nanoparticles obtained in O/W nano-emulsions by low-energy methods

Gabriela Calderó^{1,2}, M^a José García-Celma^{3,1}, Conxita Solans^{2,1}

¹*CIBER-BBN, Barcelona, Spain.*

²*Institut de Química Avançada de Catalunya (ICAQ). Jordi Girona 18-26, 08034 Barcelona, Spain*

³*Departament de Farmàcia i Tecnologia Farmacèutica. Univ. de Barcelona. Unitat Associada d'I+D al CSIC- Av Joan XXIII, s/n, 08028 Barcelona, Spain*

gabriela.caldero@iqac.csic.es

The development of nanostructured systems, is emerging as a novel approach to confer improved or new physical, chemical or biological properties to materials, ranging over optical, magnetic, electrical, interfacial, self-aggregating, catalytic, synthetic or pharmacologic features among others. Polymeric nanoparticles can be prepared by a broad variety of procedures, among which the nano-emulsion template approach offers interesting advantages for toxicological, economical and environmental reasons [1-3]. The aims of this work were the preparation of hydrophobic polysaccharide nano-emulsions by low-energy methods employing biocompatible components, and the use of these nano-emulsions as templates for the obtention of nanoparticles. Nano-emulsions were prepared in water / nonionic surfactant / hydrophobic polysaccharide organic solution systems by a low-energy method, consisting of changing composition at constant temperature. Nano-emulsions obtained were characterized by dynamic light scattering (DLS) and their stability was studied by means of backscattering. Nano-emulsions obtained showed mean droplet sizes around 200nm, low polydispersity (below 0.2) and good kinetic stability. In a second step, the organic solvent of these nano-emulsions was removed by evaporation, to obtain globular nanoparticles with mean sizes below 100nm. The nanoparticles shape, average sizes and polydispersity were assessed by DLS as well as scanning and transmission electron microscopy (SEM and TEM respectively) and related to the template nano-emulsion system.

References:

- [1] Solans C., Izquierdo P., Nolla J., Azemar N, García-Celma MJ. *Current Opinion in Colloid and Interface Science* **10** (2005)102-110
- [2] Asua J.M. *Prog Polym Sci* **27** (2002)1283-1346
- [3] Desgouilles S., Vauthier Ch., Bazile D., Vacus J., Grossiord JL, Veillard M, Couvreur P *Langmuir* **19**, (2003) 9504-9510

Aharonov-Bohm oscillations in the local density of states

A. Cano^{1,*} and I. Paul^{2,3,†}

¹ *European Synchrotron Radiation Facility, 6 rue Jules Horowitz, BP 220, 38043 Grenoble, France*

² *Institut Néel, CNRS/UJF, 25 avenue des Martyrs, BP 166, 38042 Grenoble, France*

³ *Institut Laue-Langevin, 6 rue Jules Horowitz, BP 156, 38042 Grenoble, France*

The density of states of an electronic system describes the number states available for putting electrons within a given energy range [1]. This quantity can be probed directly by scanning tunneling microscopy (STM) [2]. The scattering of electrons with inhomogeneities is known to modify the corresponding density of states producing local modulations [3]. These modulations were first probed by STM with atomic resolution in [4], where standing-wave patterns in the local density of states originated by the scattering of electrons with impurities and step edges were observed on the surface of Cu(111). Interference contributions to these modulations are affected by the magnetic field via the Aharonov-Bohm effect [5]. In the talk, I shall discuss how this phenomenon can be exploited in a simple STM setup that serves as an Aharonov-Bohm interferometer at the nanometer scale [5].

* Electronic address: cano@esrf.fr

† Electronic address: indranil.paul@grenoble.cnrs.fr

- [1] See e.g. C. Kittel *Introduction to Solid State Physics* (Wiley, 1996); N.W. Ashcroft and N.D. Mermin, *Solid State Physics* (Harcourt, New York 1976).
- [2] C.J. Chen, *Introduction to Scanning Tunneling Microscopy*, (Oxford, New York, 1993).
- [3] G.A. Fiete and E.J. Heller, *Rev. Mod. Phys.* **75**, 933 (2003).
- [4] M.F. Crommie, C.P. Lutz and D.M. Eigler, *Nature (London)* **363**, 524 (1993); Y. Hasegawa and Ph. Avouris, *Phys. Rev. Lett.* **71**, 1071 (1993).
- [5] A. Cano and I. Paul, to be published.

WEAR BEHAVIOUR OF CARBON NANOFIBER-EPOXY COMPOSITES

P. Carballeira, F. Hauptert
Institut für Verbundwerkstoffe GmbH,
Erwin-Schrödinger-Straße, 67663 Kaiserslautern, Deutschland
pablo.carballeira@ivw.uni-kl.de

Carbon nanofibers (CNFs) have been used in recent times to increase the mechanical properties of polymer matrices [1-3], the use of CNFs provide several advantages compared with the use of micro-sized fillers; they allow the production of micromechanical components and thin coatings and they do not cause embrittlement and deterioration of strength as microscopic fillers often do. These nanofillers also exhibit excellent thermal and electrical properties which make them excellent candidates for the production of conductive polymer composites, capable of dissipating electrostatic charges or even act as shielding devices from electromagnetic radiation. To benefit from the good reinforcing properties of the CNFs a good dispersion of the fibers in the polymer matrix is crucial since a well dispersed filler network results in a more uniform stress distribution within the composite. A good dispersion also minimizes the presence of agglomerates that can act as centres for stress-concentration which decrease the general strength and modulus of the composite.

This work deals with the effect of carbon nanofiber reinforcement on the performance of epoxy resin against sliding wear. Samples containing different volume concentrations of carbon nanofibers were systematically manufactured and tested under uniform sliding against a martensitic steel ring (100Cr6) in a block-on-ring configuration. Tested composite surfaces were analyzed by means of electronic microscopy in order to study the observed effects on the wear behaviour of the polymer matrix.

In our research nanofibers were dispersed in the polymer matrix with the aid of a three roll calender (**Fig. 1**). The use of this device for the dispersion of carbon nanotubes in an epoxy matrix was first reported by F.H. Gojny et al. [4]. This technology achieved excellent dispersion results without reducing the aspect ratio of the fillers which is important to enable a good load transfer from the polymer matrix to the nanofillers. One further advantage of the calendaring method is the possibility of up-scaling the manufacturing process to meet technical demands. The manufactured composites, containing different volume concentrations of carbon nanofibers, were characterized by tribological analysis in order to study the effects that the nanofibers had on the wear resistance of the epoxy resin.

(**Fig.2** left) depicts the results of the wear experiments conducted on a block on ring machine. The rotation speed was chosen to be 1 m/s and two different forces 15 N and 20 N were applied on the samples during testing. The specific wear resistance is documented as a function of the filler content. Low wear rates represent a high material resistance against wear. As Fig 2 shows the addition of CNF to the epoxy resin does not significantly affect the tribological performance of the matrix. (**Fig. 2** right) shows the evolution of the friction coefficient of the nanocomposites with increasing filler contents. A small decrease in the friction was observed with the addition of 0.05 vol % of carbon nanofibers. Further increase of fillers resulted in a minimal increase in the friction coefficient of the composites.

Scanning electron microscopy examinations were used to study the morphology of the tested surfaces (**Fig.3**). The aim was to study the role of the added carbon nanofibers in the measured tribological properties of the samples. The main features of the worn surface of the epoxy resin (**Fig.3** left) are smooth areas showing triangular scratches opening in the wear direction. The

morphology of the worn surface of the sample containing 1.5 vol. % CNF (**Fig.3 right**) does look quite similar to the one observed for the neat epoxy verifying the test data. Only a slight reduction in the size of the wear cracks might be appreciated.

References:

[1] B. Bai, A. Allaoui, Composites Part A **34(8)** (2003), 689–694.
 [2] T. Prasse, J.-Y. Cavaille, W. Bauhofer, Composites Science and Technology. **63(13)** (2003), 1835–1841
 [3] P. Richard, T. Prasse, J.-Y. Cavaille, L. Chazeau, C. Gauthier, J. Duchet, Materials Science and Engineering. A **352(1–2)** (2003), 344–348.
 [4] F.H. Gojny, M.H.G. Wichmann, U. Köpke, B. Fiedler, K. Schulte, Composites Science and Technology **64** (2004) 2363–2371.

Figures:

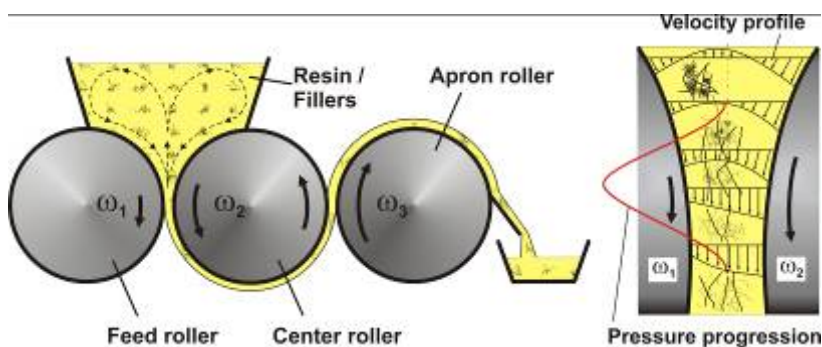


Fig. 1. Schematic view of the three roll calender and its working principle.

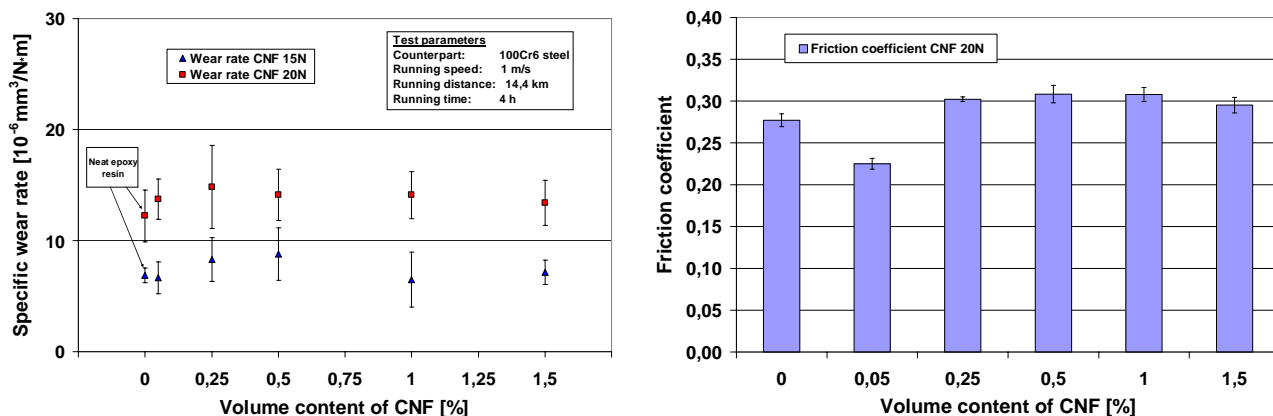


Fig.2 Specific wear rate (left) and friction coefficient (right) of the epoxy/CNF nanocomposites as a function of nanofiber volume content

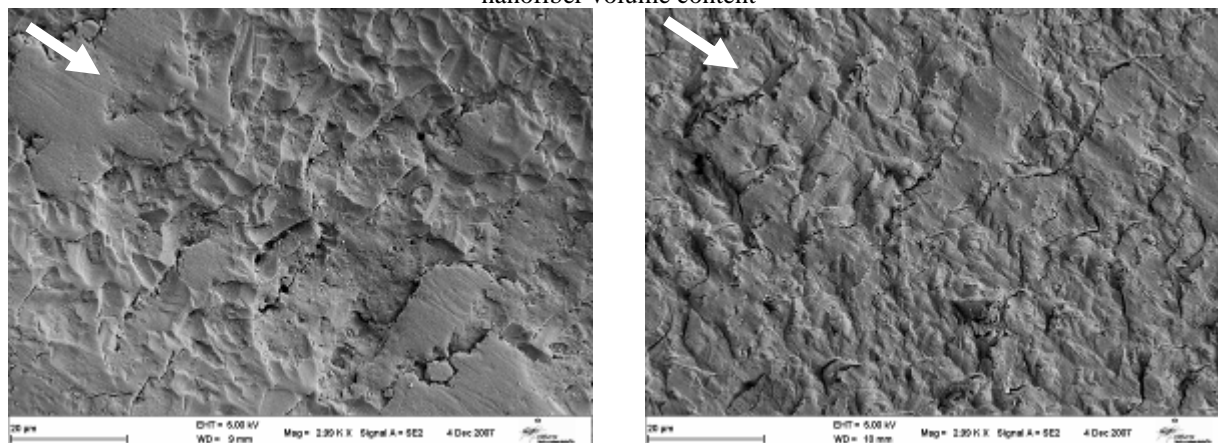


Fig.3 (Left) Neat epoxy surface from tribological testing.. (Right) Nanocomposite (1.5 % vol. of CNF) test surface surface. White arrows indicate the sliding wear direction.

Quantification of elastic energy of InAs QD in InGaAs/GaAs QW structures.

J. L. Casas Espínola, E. Velázquez Lozada, T. V. Torchynska.

ESFM - Instituto Politécnico Nacional, D.F. 07738, México,

The photoluminescence, its temperature dependence and scanning photoluminescence spectroscopy have been investigated for InAs quantum dots embedded in asymmetric GaAs/In_xGa_{1-x}As/GaAs quantum wells (DWELL structures) as a function of the indium content x ($x = 0.10 - 0.25$) in the capping In_xGa_{1-x}As layer. Photoluminescence (PL) enhancement and red shift of the QD ground state peak position have been observed as x increases from 0.10 to 0.15. Significant degradation of the PL intensity is accompanied by a blue shift of the peak position and its broadening when $x = 0.20$ or 0.25. In content increasing in the capping InGaAs layer results in the lattice mismatch and stress decreasing at the QD InAs/InGaAs interface and simultaneously the lattice mismatch and stress increasing at the QW InGaAs/GaAs spacer interface. The estimation of the elastic energy revealed that capping layer composition with $x = 0.15$ corresponds to the minimum value of elastic energy in studied QD structures.

This work was partially support by SIP - IPN Mexico.

Morphology controlled hydrothermal synthesis processes and emission near 2 μm of Tm^{3+} - doped Lu_2O_3 nanostructures

C. Cascales, F. Esteban-Betegón and C. Zaldo

Instituto de Ciencia de Materiales de Madrid, Consejo Superior de Investigaciones Científicas, c/Sor Juana Inés de la Cruz, 3. E-28049 Cantoblanco, Madrid, Spain.

ccascales@icmm.csic.es

Due to the conjunction of excellent thermo-mechanical properties, high optical cross-sections and high doping potential for rare-earth laser cations, the sesquioxides Sc_2O_3 , Y_2O_3 and Lu_2O_3 are attractive hosts for high power solid-state lasers [1]. Giving its very similar mass and size the latter is the choice material for the favorable incorporation of the highest concentration of Tm^{3+} . The 1.95 μm eye-safe laser emission operating in the $^3\text{F}_4 \rightarrow ^3\text{H}_6$ of Tm^{3+} can advantageously replace the traditionally used Ho^{3+} -doped analogue crystal, in the same spectral range, when pumping with high power AlGaAs diode lasers.

However, the high melting temperature, ~ 2500 °C, of Lu_2O_3 supposes serious difficulties for the production of bulk crystals. As an alternative, diverse low temperature methodologies have been extensively applied to prepare nanocrystals of this phase, mainly intended for fabricating transparent laser ceramics [2]. Another possibility to be explored is the incorporation of these nanoparticles in hybrid composites. A first step in this direction is the synthesis of Tm^{3+} - Lu_2O_3 nanocrystals with size and morphologies suitable for dense sintering or for infiltration or merging with other materials also transparent in the mid-infrared.

In this work a simple hydrothermal route to synthesize nanoparticles of $\text{Lu}_{2-x}\text{Tm}_x\text{O}_3$ is presented. Hydrothermal processes benefit not only of much lower temperatures than other preparation methods but also of being advantageous for homogeneous nucleation of nanocrystals with well-defined morphologies. Two distinct shapes such as micron size rods with ~ 90 nm \varnothing and nanosquare sheets have been obtained for Tm^{3+} concentrations ranging from 50% mol to 0.2% mol Tm (i.e., $1.0 \geq x \geq 0.004$) by choosing the starting reagents and adjusting the pH value, 7.5 and 12 respectively, of the reacting solution, which lasted in all cases the same time, 24h. Powder X-ray analyses indicate that both prepared structures are the pure cubic $Ia\bar{3}$ phase, see Figures 1a and 2a, while FESEM and TEM images confirm the formation of different morphologies, as shown in Figures 1b-c and 2c-d. The photoluminescence at ~ 1.95 μm of Tm^{3+} and emission lifetimes in these materials have been measured, and the dependence with the concentration and morphology is analyzed.

Consequently, the control of the hydrothermal reaction conditions open the possibility for obtaining the most adequate morphology for a same $\text{Lu}_{2-x}\text{Tm}_x\text{O}_3$ material to be incorporated in a given hybrid composite: given the near uniform distribution of sizes for nanosquare sheets they can be the choice for dispersing in transparent polymers, or used as precursors for transparent laser ceramics, while micron size rods will allow their incorporation in 2D and 3D patterned structures.

References:

- [1] A. Giesen, H. Hügel, A. Voss, K. Witting, U. Brauch, H. Opower, Appl. Phys. B **58** (1994) 365.
- [2] M. Tokurakawa, K. Takaichi, A. Shirakawa, K. Ueda, H. Yagi, S. Hosokawa, T. Yanagitani, A.A. Kaminskii, Opt. Express **14** (2006) 12832.

Figures:

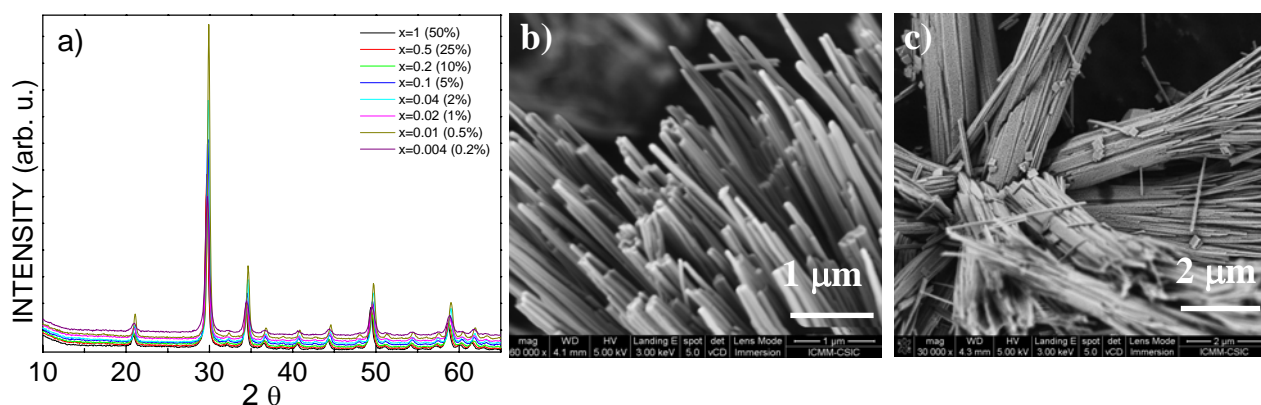


Figure 1. Hydrothermally prepared $\text{Lu}_{2-x}\text{Tm}_x\text{O}_3$ from chloride precursors ($\text{pH}=7.5$ and 185°C during 24 h, followed by annealing at 800°C during 30 min): a) XRD patterns showing the pure cubic $Ia\bar{3}$ phase for all Tm^{3+} concentrations, $1.0 \geq x \geq 0.004$, the FWHM of peaks indicating ~ 25 nm size for particles; b) FESEM image of micron size nanowires constituting the product of the hydrothermal synthesis ($x=0.04$); c) FESEM image of the final calcined product ($x=0.04$), where the predominant morphology consists of rods $15\mu\text{m} \times 90\text{ nm } \varnothing$

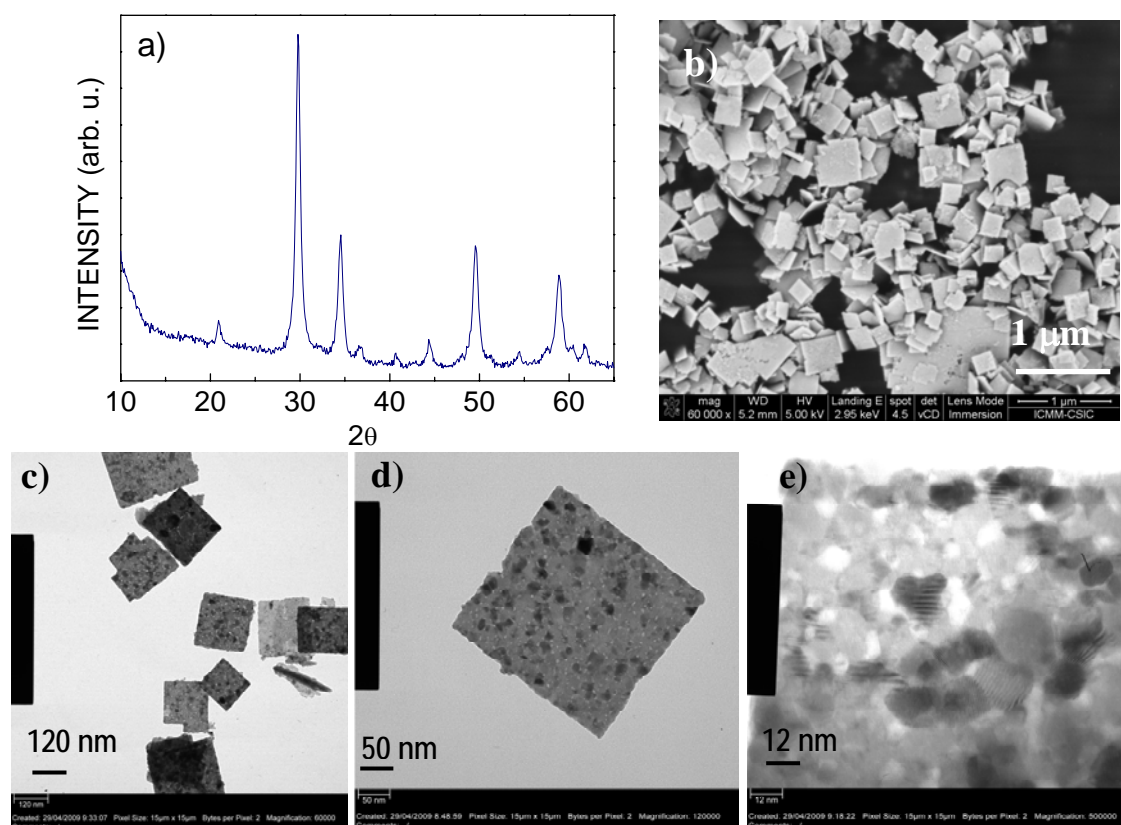


Figure 2. $\text{Lu}_{2-x}\text{Tm}_x\text{O}_3$ ($x=0.1$) hydrothermally prepared from nitrate precursors ($\text{pH}=12$ and 185°C during 24 h, followed by annealing at 600°C during 1 h): a) XRD pattern showing the pure cubic $Ia\bar{3}$ phase of the final product, the FWHM of peaks indicating ~ 10 nm size for particles; b) FESEM micrograph of final product consisting of ~ 150 nm square nanosheets; c), d) and e) TEM images of square nanosheets, the latter showing the elemental ~ 10 nm particles within square nanosheets.

RAMAN SPECTROSCOPY OF GRAPHENE EDGES

C. Casiraghi^{1*}, A. Hartschuh², H. Qian², S. Piscanec¹, C. Georgi², A. Fasoli¹,
K. S. Novoselov³, D. M. Basko⁴, and A. C. Ferrari¹

1 Engineering Department, Cambridge University, Cambridge, U.K.

** Present address: Physics Department, Free University, Berlin, Germany*

2 Chemistry and Biochemistry Department, LMU, Munich, Germany

3 Department of Physics and Astronomy, Manchester University, U.K.

4 Laboratoire de Physique et Modélisation des Milieux Condensés, Université Joseph Fourier and CNRS, Grenoble, France

Contact email: cinzia@physik.fu-berlin.de

Graphene edges are of particular interest since their orientation determines the electronic properties [1]. Furthermore edges are preferred doping sites [2].

Here we present a detailed Raman investigation of graphene flakes with edges oriented at different crystallographic directions. Very large graphene flakes (up to 100 μm^2) with sharp edges are produced by micromechanical cleavage of graphite. Single-layer flakes are then identified by Raman Spectroscopy [3]. The angle between the edges is determined by optical microscopy and atomic force microscopy. The position, width, and intensity of G and D peaks are studied as a function of the incident light polarization. The D-band is strongest for polarization parallel to the edge and minimum for perpendicular [4]. Raman mapping shows that the D peak is well localized in proximity of the edge, while the D peak intensity is very small or absent inside graphene flakes [4].

For ideal edges, the D peak is zero for zigzag orientation and large for armchair [5], allowing in principle the use of Raman spectroscopy as a sensitive tool for edge orientation. However, here we show that for our samples, the D to G ratio does not show a significant dependence on edge orientation [4]. Here we show that the D to G peak ratio strongly depends on polarization, relative position of the laser spot with respect to the edge, and amount of edge disorder. Thus, even if edges can appear macroscopically smooth and oriented at well-defined angles, graphene edges are often mixed and disordered, at least on the laser spot scale. This shows that Raman spectroscopy is able to probe the degree of disorder of an edge.

References:

- [1] Nakada, K et al. Phys. Rev. B, **54** (1996) 17954
- [2] Cervantes, F et al. Phys. Rev. B, **77** (2008) 165427
- [3] Ferrari, A. C. et al. Phys. Rev. Lett. **97** (2006) 187401
- [4] Casiraghi C et al. Nano Letters, **9** (2009) 1433
- [5] Cancado, L. G. et al. Phys. Rev. Lett. **93** (2004) 247401.

EXTRACELLULAR BIOSYNTHESIS OF GOLD NANOPARTICLES USING SUGAR BEET PULP

L. Castro, M.L. Blázquez, A. Ballester, F. González and J.A. Muñoz
Department of Materials Science and Metallurgical Engineering,
Complutense University of Madrid, Avda. Complutense s/n 28040 Madrid, Spain.
lauracr84@hotmail.com

Nowadays precious metal recovery technologies use harmful chemicals that may represent a risk to the environment and public health. This is the reason why it is necessary to develop clean, non-toxic and environmentally friendly procedures to recover precious metals. The use of biological organisms in synthesis and assembly of nanoparticles has received increasing attention. There are eco-friendly “green” methods for the synthesis of noble metal nanoparticles using bacteria, actinomycetes, yeast, fungi, and plant extracts. Sugar beet pulp, an industry waste, has been shown effective in the reduction of Au(III) to Au(0) and extracellular synthesis of nanoparticles.

The interest in nanoparticles synthesis research is now focused on the shape selectivity and size monodispersity. In this work, we report on the biological synthesis of several shape gold nanoparticles. Many properties of metal nanoparticles such as optical, electronic, magnetic and catalytic properties strongly depend on their size and shape.

It is shown that nanoparticles shape can be controlled by varying the initial pH value. The shape varies from triangular and geometrical nanoparticles to nanorods and nanowires. For long reaction times, gold biosorption instead of nanoparticle formation took place. UV-vis spectra and transmission electron micrographs showed nanoparticles of several shapes and sizes. Gold biosorption on biomass surface was detected by scanning electron microscopy. In order to resolve the mechanism of reduction of gold (III), the evolution of pH and potential was measured.

References:

Chandran, S. P.; Chaudhary, M.; Pasricha, R.; Ahmad, A.; Sastry, M. Synthesis of gold nanotriangles and silver nanoparticles using *Aloe vera* plant extract. *Biotechnol. Prog.* 2006, 22, 577-583.

Mohanpuria, P.; Rana, N. K.; Yadav, S. K. Biosynthesis of nanoparticles: technological concepts and future applications. *J. Nanopart. Res.* 2008, 10, 507-517.

He, S. Y.; Zhang, Y.; Guo, Z. R.; Go, N. Biological synthesis of gold nanowires using extract of *Rhodospseudomonas capsulate*. *Biotechnol. Prog.* 2008, 24, 476-480.

Figures:

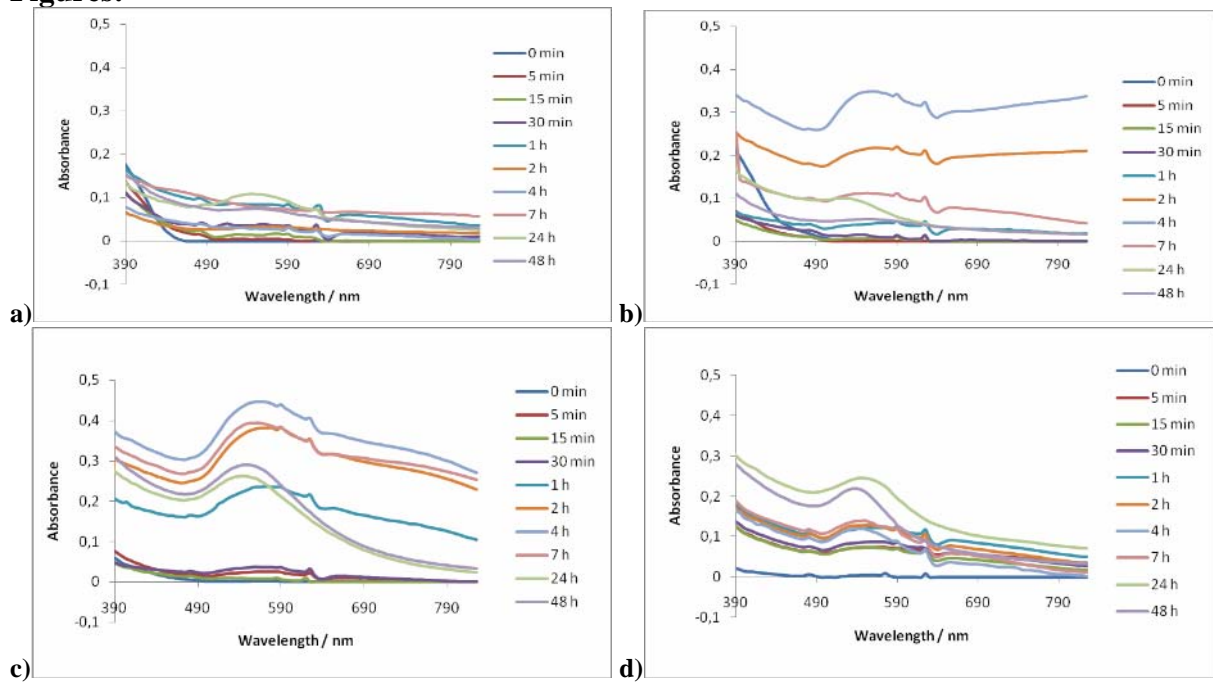


Figure 1. UV-Visible spectra as a function of time at different pH: a) pH 2, b) pH 4, c) pH 7; d) pH10.

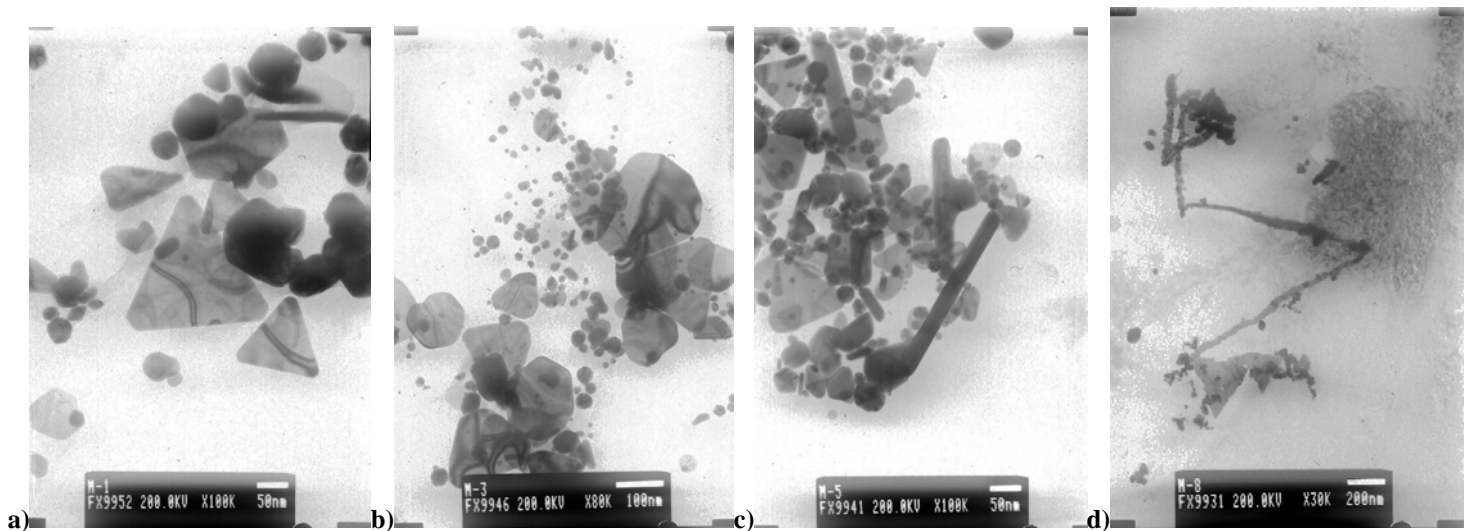


Figure 2. TEM images of gold nanoparticles synthesized using sugar beet pulp at different pH: a) pH 2, b) pH 4, c) pH 7, d) pH 10.

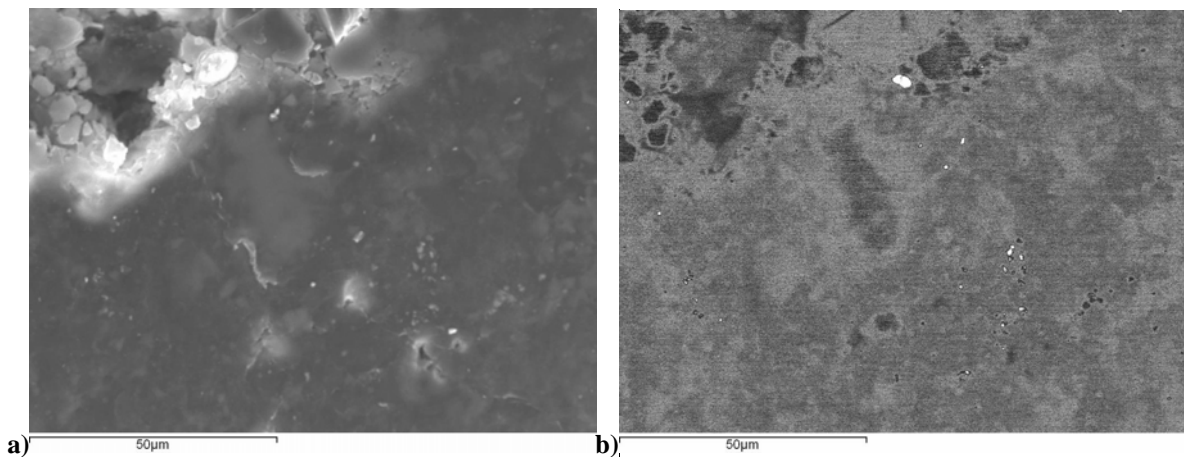


Figure 3. Secondary (a) and backscattered (b) scanning electron micrographs.

Structural and compositional properties of Sm-Fe-Ta magnetic nanospheres prepared by pulsed-laser deposition at 157 nm in N₂

S. Šturm¹, K. Žužek Rožman¹, E. Sarantopoulou², Z. Kolli², S. Kobe¹, A.C. Cefalas²

¹Theoretical and Physical Chemistry Institute, National Hellenic Research Foundation, TCPI, Athens 11635, Greece

²Jožef Stefan Institute, Nanostructured materials, 1000 Ljubljana, Slovenia

Sm-Fe-Ta-N magnetic nanodroplets were fabricated by pulse laser deposition at 157 nm at low laser energy of 10 mJ per pulse in nitrogen background pressure. The target intermetallic alloy with the composition of Sm_{13.8}Fe_{82.2}Ta_{4.0} was fabricated by arc-melting and further annealing to achieve homogeneity. The nanodroplets were deposited on a Si substrate coated with a ~ 100 nm thick layer of Ta to avoid chemical reaction between the highly reactive Sm and Si substrate.

The average composition of the deposited material reflected the stoichiometry of the initial target. As prepared droplets were analyzed by the magnetic measurements using SQUID, nano-structures observation was performed by using field emission gun scanning electron microscope (FEG SEM) imaging equipped by electron dispersive X-ray spectroscopy (EDXS), which at the same time allows for the chemical analysis of the composition of the films. The surface morphology of the films was investigated also with AFM and MFM.

For more detailed analyses nano-spheres were examined by a field-emission electron-source high-resolution transmission electron microscope HR-TEM Jeol 2010F equipped with an energy dispersive x-ray spectroscopy (EDXS) (LINK ISIS EDS 300) and electron energy-loss spectroscopy (EELS) (Gatan PEELS 667). The magnetic response on individual nanospheres was detected and quantified for the first time in this system by applying **Electron Holography**.

Nanodroplets with the diameter between 5 nm up to 130 nm were observed with the HRTEM (Figure 1). Small spheres (<50 nm) were mainly amorphous, while larger spheres have a core-shell structure with a crystalline nucleus surrounded by an amorphous layer. (Fig2). The combined EDXS and EELS analysis confirmed that the composition of the inner crystalline part corresponded to the Sm₂(Fe,Ta)₁₇ phase ($\text{Sm}_{(\text{at.}\%)} / (\text{Fe} + \text{Ta})_{(\text{at.}\%)} = 0.11$) enriched with nitrogen. The outer amorphous layer was oxygen-rich with no detectable amounts of nitrogen and significantly different ratio of $\text{Sm}_{(\text{at.}\%)} / (\text{Fe} + \text{Ta})_{(\text{at.}\%)} = 0.64$ (Fig. 3).

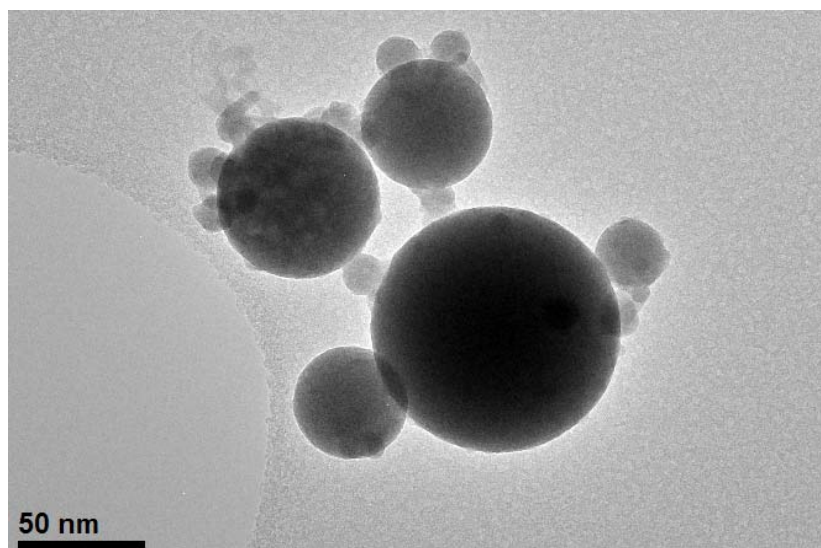


Figure 1. Core-shell structured Sm-Fe-Ta-based nano-spheres in-situ nitrified in Pulsed Laser Deposition at 157 nm.

These analytical results prove that nitrifying of nanodroplets was taken place already in the plume and thus further post ablation annealing of the films was unnecessary for ferromagnetic response. The liquid nanodroplets solidify on the surface of a Si-Ta substrate in two phases. One is a crystalline nucleus, which is surrounded by an amorphous one. The bi-phase spherical nanostructure retains its ferromagnetic response of its crystal nucleus far more efficiently than the high porosity crystal structures grown at higher laser energies because of their accelerated oxidization.

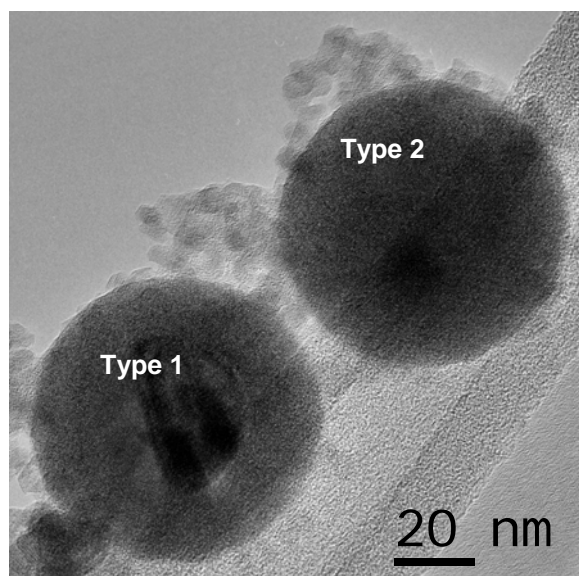


Fig. 2. Nanospheres obtained by in-situ nitrogeneration in PLD processing

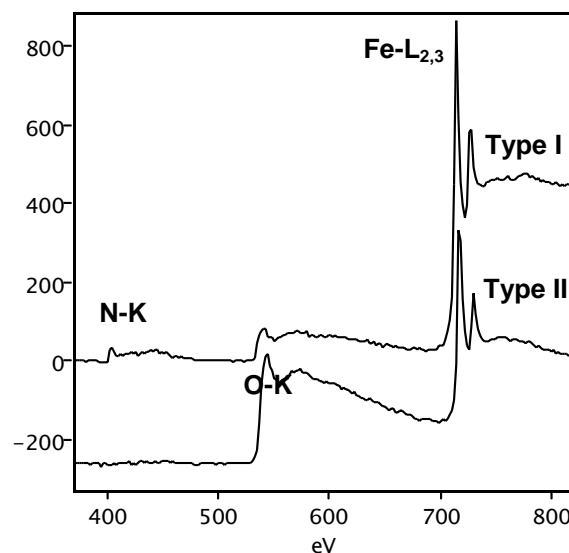


Fig. 3. EELS spectra of type I and Type II nano-spheres

The Mechanism of Methanol Decomposition. A Theoretical Study Based on the Reaction Force Analysis

María Luisa Cerón^{†,‡}, Barbara Herrera[‡], Paulo Araya[†], Francisco Gracia[†] and Alejandro Toro-Labbé[‡].

[†]Laboratorio de Catálisis, Facultad de Ciencias Físicas y Matemáticas, Universidad de Chile,

[‡]Laboratorio de Química Teórica Computacional (QTC), Facultad de Química, Pontificia Universidad Católica de Chile, Casilla 306, Correo 22, Santiago, Chile. CIMAT

Abstract.

A theoretical study of methanol decomposition using a model system that represents the initial step of the reaction $CH_3OH + CuO \rightarrow CH_2O + H_2O + Cu$ is presented. Theoretical calculations using B3LYP/6-21G along with Lan12DZ pseudopotentials on metallic centers were performed and discussed within the framework of the reaction force analysis. It has been found that the reaction takes place following a stepwise mechanism, in which electron transfer effects are predominant at the initial step of the reaction, whereas polarization effects takes over in the second step to promote a proton transfer that leads to the product formation.

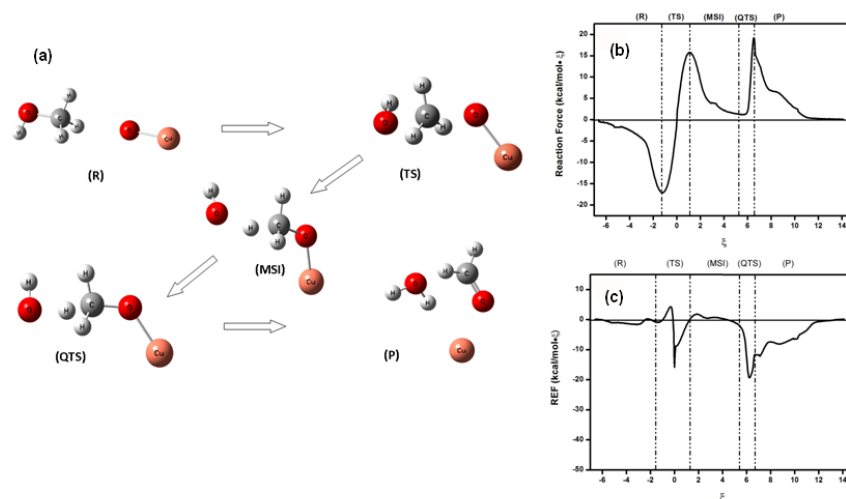


Figure 1: (a) Methanol Decomposition Reaction. (b) Reaction Force. (c) Reaction Electronic Flux

Acknowledgments This work was supported by FONDECYT under grants N° 1090460 and N° 11080002, FONDAP Project N°11980002 (CIMAT) and Proyecto VRAID 01/2008. María Luisa Cerón wants to thank Santander-Universia and Conicyt for Doctoral fellowships.

THE DESIGN AND FABRICATION OF A TIP-ON-APERTURE NEAR-FIELD SCANNING OPTICAL MICROSCOPE PROBE FOR HIGH RESOLUTION PATTERNING

Won Seok Chang¹, Seok-Joo Na², Mun Seok Jeong³

¹Nano-Mechanical Systems Research Division, Korea Institute of Machinery and Materials, 171 Jang-dong Yuseong-gu, Daejeon, Korea 305-343

²Dept. Mech. Eng., Korea Advanced Institute of Science and Technology

*³Advanced Photonics Research Institute, Gwangju Institute of Science and Technology
paul@kimm.re.kr*

The resolution of commercial optical system is limited to about the wavelength of incident light by the refraction limit. However, a resolution beyond the diffraction limit can be achieved at near-field. Near-field scanning optical microscope (NSOM) is a kind of scanning probe microscope; it can realize a sub-wavelength scale resolution. In NSOM, light is illuminated through an aperture smaller than the wavelength of incident light, and then the small aperture is used as an excitation source. The resolution of the NSOM is determined by the size of the aperture; to achieve a higher resolution, a smaller aperture is required. However, when the diameter of an aperture is smaller than the wavelength of the incident light, the transmission efficiency is proportional to the sixth power of the diameter of the aperture. Thus, a smaller aperture greatly reduces the transmission efficiency. To obtain a sufficiently strong signal from a small aperture, high-intensity light is needed¹. However, high-intensity light can damage the metal layer of the probe. The typical resolution of aperture NSOM is about 50 nm – 100 nm. In this work, the shape of a NSOM probe was modified using the resolution of numerical analysis based on a finite-difference time-domain (FDTD) algorithm. This probe has a narrow slit or small tip on its aperture. Especially in the near-field area, the electric field intensity distribution is heavily dependent on the polarization of incident light. In the plane of polarization, the electric field intensity of the NSOM aperture probe is strongly enhanced at the edge of the aperture. Simulation results show that this enhancement can be totally or partially removed according to the size of the slit, if the slit carved on the probe is aligned with the polarization direction of the incident light. When a long slit is carved on the probe (slit-on-aperture probe), the electric field intensity of the NSOM aperture probe in the plane of polarization shows a Gaussian distribution because the points of enhanced electric field intensity are totally removed. However, when a short slit is carved on the probe, the point of enhanced electric field intensity is removed at one edge of the aperture, and consequently the electric field intensity is enhanced only at the other edge. Moreover, when a tip is put on the probe (tip-on-aperture probe), the electric field intensity is enhanced only near the tip. This means that a higher intensity electric field can be obtained on the surface to be processed in an area smaller than the aperture size.

The tip of a tip-on-aperture (TOA) probe is illuminated through an aperture at the near-field of the probe and electromagnetic interaction between the structure sharp tip at the end of the probe and the surface is used for measurements and materials processing. A novel TOA probe is described, which has a polygonal cross-sectioned tip that can make the strong and local enhancement of electromagnetic field^{2,3}. A right triangular pillar was selected as optimal shape of the tip among the several polygonal pillars. The electromagnetic energy distributions at the near-field of the probe and of a typical TOA probe (with circular tip) were calculated numerically, and the results were analyzed. The results show that a TOA probe with a triangle tip confines electromagnetic energy within the smaller area than a typical tip-on-aperture probe, and has 6.7 times the maximum intensity. Moreover, the electric field distributions at the near-field of a TOA probe were calculated numerically to analyze the effects of polarization direction on the characteristics of measurement and processing. A TOA probe is asymmetric

for the axis, since it has a probe at metal coated layer on the aperture. The geometrical relationship between this asymmetric shape and polarization direction is the reason for the change of the electromagnetic energy distributions. Numerical analysis shows that a TOA probe can make the best use of the tip for high resolutions when the tip is located on the parallel axis with the polarization direction. After analyzing the trend in the magnitude of the electric field, it was proposed that a localized, enhanced field at the tip apex was caused by the local electric field at the aperture and surface plasmons excited and propagating on the outer surface of the probe.

An NSOM probe is a tinned, metal coated optical fiber with an aperture. To fabricate a TOA NSOM probe, a tip is generated at the end of the probe. FIB processing is applied to the process to make an aperture and a tip, so the aperture and the tip are generated at the same time. With this process, possibilities to fabricate TOA probes with various tips and were shown. And resolution enhancement for optical measurement and patterning was verified using the TOA probe fabricated in this study.

References:

- [1] M. Stähelin, M. A. Bopp, G.. Tarrach, A. J. Meixner, and I. Zschokke-Gränacher: Appl. Phys. Lett. **68** (1996) 2603.
- [2] T. Matsumoto, T. Ichimura, T. Yatsui, M. Kourohi, T. Saiki, and M. Ohtsu: Opt. Rev. **5** (1998) No. 6, 369.
- [3] H. G. Frey, F. Keilmann, A. Kriele, and R. Guckenberger: Appl. Phys. Lett. **81** (2002) 5030.

Figures:

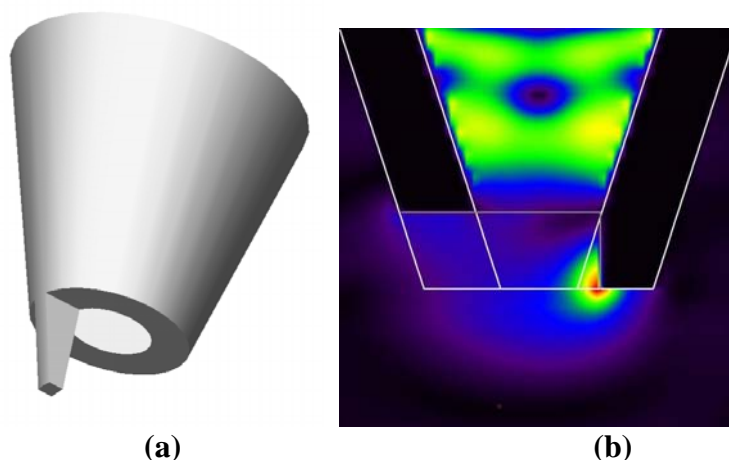


Fig.1 (a) Three dimensional modeling and (b) electric field distribution of TOP probe

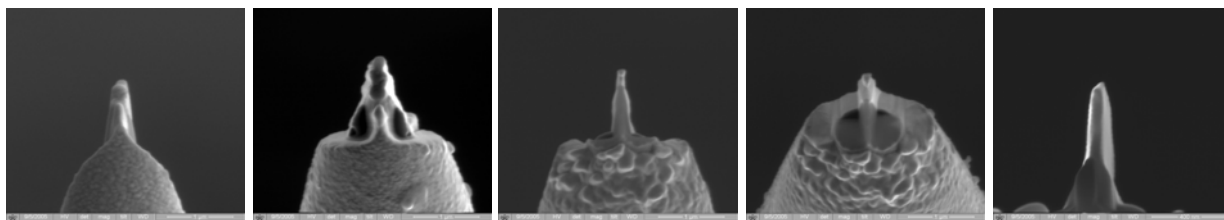


Fig. 2 FIB machined TOA probe

Fabrication of Multi-walled Carbon Nanotubes based Nanoelectrode Arrays for Bio Probe

Won Seok Chang¹, Dae. Geon Choi, Chang Soo Han

*¹Nano-Mechanical Systems Research Division, Korea Institute of Machinery and Materials,
171 Jang-dong Yuseong-gu, Daejeon, Korea 305-343
paul@kimm.re.kr*

Carbon nanotubes have began to attract enormous interest in electrochemistry because of their small size and good electrochemical properties. Gaining greater control over the distribution and amount of nanotubes to give a nanotube electrode has been attempted. The growth of aligned multi-wall carbon nanotubes (MWCNTs) directly onto an electrode surface has been performed. Among various synthesis methods for carbon nanotube growth, chemical vapor deposition (CVD) method has been widely used for various advantages such as high quality, vertical alignment, controlled diameter and length of nanotubes and so on. Especially, vertically aligned MWCNT arrays could be grown using plasma-enhanced chemical vapor deposition (PECVD)[1]. In this paper, the fabrication of nano-electrodes by the synthesis of multi-wall carbon nanotubes (MWCNTs) has been investigated for biological applications. To form Fe catalyst dots with diameter of 100 nm and thickness of 10 nm, nano holes patterned imprint resin with PMMA was used for lift-off process. Imprint lithography is easy and inexpensive to fabricate large areas of nano-patterns [2]. MWCNTs were grown on TiN electrode layer with Fe catalyst patterned by UV nano-imprint lithography (NIL) on quartz wafer. The proposed study is realization of a simple, inexpensive and reproducible method to produce nanoscale electrode arrays in large areas. The patterns were defined by an array of circle with 100 nm in diameter, and 200 nm in pitch. The nano-patterned master and Fe catalyst are observed with good pattern fidelity over a large area by atomic force microscope (AFM) and scanning electron microscopy (SEM).

Among various synthesis methods for carbon nanotube growth, plasma-enhanced chemical vapor deposition (PECVD) was used for the growth of vertically aligned multi-wall carbon nanotube arrays. Ammonia (NH₃) and acetylene (C₂H₂) were used as the etchant gases and carbon source. Nanoelectrodes of MWCNTs have diameters ranging from 20 nm to 40 nm and lengths of about 300 nm. The results showed that vertically aligned MWCNT electrodes into individually addressable probing elements could be applied for bio-compatible platforms for dynamic electrophysiological measurements in and around excitable cells.

References:

- [1] Meyyappan M, Delzeit L, Cassell A and David H, Plasma sources Sci. Technol. 12, 205 (2003).
- [2] W.M. Choi, O.O. Park, Microelectron. Eng. 70, 131 (2003).

3-omega measurements of thermal conductivities of materials for low thermal resistances

Pierre-Olivier Chapuis^a, Michael Schmidt^a, Nikos Kehagias^a, John Cuffe^a, Mika Prunnila^b, Jouni Ahopelto^b, Clivia Sotomayor Torres^a

*^aPhononic and Photonic Nanostructures (P2N) Group,
Institut Català de Nanotecnologia (ICN-CIN2), Edifici CM3
Campus de la Universitat Autònoma de Barcelona,
08193 Bellaterra (Barcelona), Spain*

*^bMicro and Nanoelectronics, P.O. Box 1000,
FI-02044 VTT, Espoo, Finland
olivier.chapuis@cin2.es*

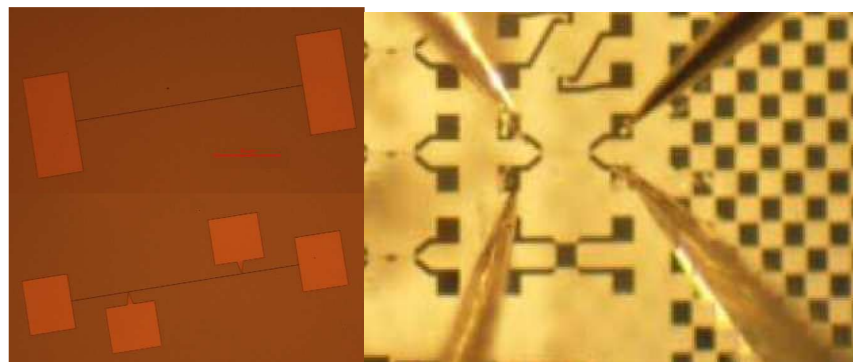
Thermal phenomena at nanometer-scale are being explored currently with great interest, as different behaviors are encountered when characteristic dimensions of the systems are approaching the energy carrier's mean free paths or their wavelengths. We have implemented a new 3-omega [1] method setup that enables to measure directly the thermal conductivity. The 3-omega method has been used for the last 20 years in order to determine the thermal conductivities of bulk materials, thin films and/or nanocomposites. We discuss issues related to the sensitivity of the method to anisotropy and how to improve the accuracy. We analyze also the classic design and show that it can be modified to take fewer approximations into account in the data analysis. In particular, we discuss possible improvements of this kind of setup in comparison to photo-thermal methods.

We have measured the conductivities of different samples to be used in the microelectronic industry, such as Thermal Interface Materials and silicon-based ones. These measurements have been done as a function of temperature in the range [10-300] K, enabling to probe different regime of the phonon Knudsen number.

Reference:

[1] D. Cahill, Review of Scientific Instruments, **61** (1990) 802

Figure:



Left: Optical microscope image of two different designs allowing for measurements with the 3-omega method. Right: Probes in contact with the metal design

single carbon nanotube transistor at GHz : a nanosecond electron sensibility

J. Chaste,^{1,2,3} G. Fève,^{1,2} T. Kontos,^{1,2} J.-M. Berroir,^{1,2} B. Plaçais,^{1,2,*} and D.C. Glattli^{1,2,4}¹*Ecole Normale Supérieure, Laboratoire Pierre Aigrain, 24 rue Lhomond, 75005 Paris, France*²*CNRS UMR8551, Laboratoire associé aux universités Pierre et Marie Curie et Denis Diderot, France*³*CIN2(CSIC-ICN), Barcelona campus UAB, E-08193 Bellaterra, Spain*⁴*Service de Physique de l'Etat Condensé, CEA Saclay, F-91191 Gif-sur-Yvette, France*

(Dated: 11 mai 2009)

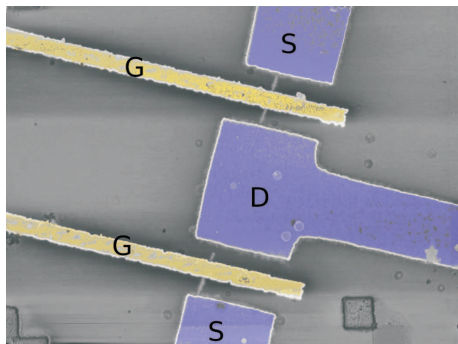
GHz electrometers are needed for promising applications in quantum physics. Typical electron detectors are limited either in sensibility for the quantum point contact (QPC-FET) or in frequency bandwidth for the single electron transistor (SET). Here, in order to detect electron in GHz regime we propose to use the field effect nanotransistor configuration (FET) where the gate voltage V_g module the semiconducting channel current I_{ds} through the transconductance $g_m = dI_{ds}/dV_g$. Increasing the sensibility of this system, means to have nanoscale dimension like our single-wall carbon nanotube transistor (NT-FET) with a top gate coupling (6 nm of AL_2O_3).

We have measured the transmission of our devices between 0.1-1.6GHz at 300K and 4K, obtained, in high frequencies, $g_m \sim 20 \mu S$ and gate capacitance of $C_g = 60 aF/\mu m$. Consequently, the cut-off frequency of our devices, $f_T = g_m/C_g$, which corresponds in the same time to the bandwidth of our system and to the charge amplification through the system, has values $f_T \sim 50 GHz$.

Due to our high bandwidth set-up, we are able to measure the noise of our NT-FET. The main contribution is a poissonian noise with fano factor ($F \sim 1$). The total electron sensibility of our nanotransistor is $q_{rms} = 20 \mu e/\sqrt{Hz}$. This performance is not so far than for better single electron transistor (SET). The high signal allowed us to say that this NT-FET is the best way to detect monocharge in GHz.

Adding to this, in the high energy regime, and for a complete on state of our nanotube, we have seen a pronounced saturation of noise which appeared at the energy of optical phonons in nanotube.

PACS numbers:

*Electronic address: julien.chaste@cin2.es

[1] J. Chaste, L. Lechner, P. Morfin, G. Fève, T. Kontos, J.-M. Berroir, D.C. Glattli, H. Happy, P. Hakonen and B.

Plaçais, *Nano Lett.*, **8** 525,(2008)

Nano Hall bar as a local probe to scan the density of states

*C. Chaubet, O. Couturaud, S. Bonifacie, A. Raymond and D. Mailly**

GES, Université UM2, Pl. E.Bataillon, 34095 MONTPELLIER cedex France

**LPN, Route de Nozay, 91460 Marcoussis, France*

chaubet@ges.univ-montp2.fr

We characterize the tunnelling processes between edge states in Hall bars at the mesoscopic scale.

We present a low temperature magnetoconductance study of several submicronic Hall bars (figure 1) made from an AlGaAs/GaInAs heterostructure having a gate on top, allowing to vary the electron density. Experiments were performed at very low temperature (80 mK-800 mK), under a magnetic field up to 13 T. Sharp fluctuations were observed in both longitudinal (R_L) and Hall (R_H) resistances. When plotting (see Figure 2) the conductance $G(V_g, B)$ on a color plot, groups of lines appear whose slope is quantized. Similar lines have been observed by Cobden et al.¹, and recently by Ilani et al.² who measured $d\mu/dV_g$ (μ is the chemical potential and V_g the gate voltage). In the latter case, lines appear at the center of the Hall plateaus where $d\mu/dn$ is high: they correspond to the charging of compressible puddles. Whereas in our case (we measure the conductance which is proportional to $dn/d\mu$), lines appear at the transition between plateaus and correspond to tunnelling processes between incompressible lakes of electrons.

All groups of lines are analysed via the classification proposed by C. Zhou and M. Berciu⁴: indeed the correlations⁵ between peaks in R_L and R_H , which is a signature of the symmetry of the conductance matrix, can be used to separate the lines in two groups of different slopes, corresponding to two kinds of tunnel effects (figure3). Thus, on the low field side of the transition, uncorrelated pics correspond to a double barrier tunneling⁶ which is identified by its correlations and its temperature dependence: pics diminish as the temperature increases like in coulomb blockade. On the high field side of the transition, we identify the peaks with single barrier tunnel processes between localized puddles of incompressible electrons, whose amplitude increase with the temperature.

At high magnetic field and very low temperature, the magnetoconductance does not vanish but exhibits a residual value (figure 4), which represents the recovering of electronic wave functions and which depends on the gate voltage. We argue that the background of this skeleton magnetoconductance is a direct image of the density of states, and that the nanoHall bar may be used as a local probe to scan the Landau levels density of states. We discuss the asymmetry of this density of states in disordered samples⁸.

References:

[1] D. H. Cobden, C. H. W. Barnes and C. J. B. Ford, Phys. Rev. Lett. 82, 4695 (1999).

[2] S. Ilani, J. Martin, E. Tetelbaum, J. H. Smet, D. Mahalu, V. Umanski and A. Yacobi, Nature 427, 328 (2004).

[3] C. Sohrmann and R.A. Römer, arXiv:cond-Mat/0612240v1 15 Dec 2006

TNT2009

September 07-11, 2009

Barcelona-Spain

[4] C.Zhou and M. Berciu, Phys. Rev. B 72, 85306 (2005).
 [5] E. Peled, D. Shahar, Y. Chen, E. Diez, D. L. Sivco and A. Cho, Phys. Rev. Lett. 91, 236802 (2003).
 [6] J. K. Jain and S. A. Kivelson, Phys. Rev. Lett., 1542 (1988)
 [7] B. Jouault, O. Couturaud, S. Bonifacie, D. Mailly, and C. Chaubet, Phys. Rev. B 76, 161302 (R) (2007)
 [8] S. Bonifacie, C. Chaubet, B. Jouault and A. Raymond, Phys. Rev. B 74, 245303 (2006)

Figures:

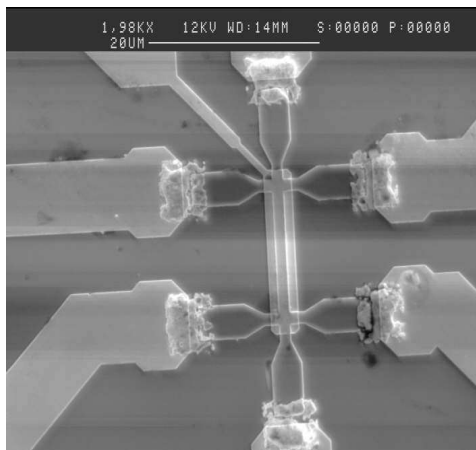


figure 1: the NanoHall bar

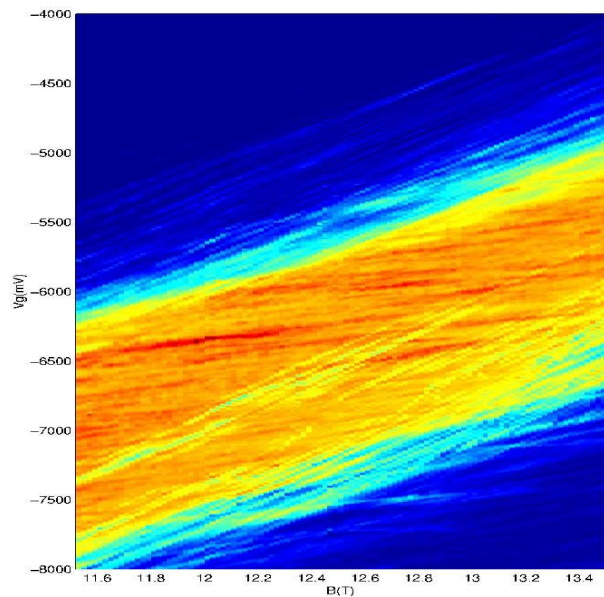


figure 2: $R_{xx}(N_s, B)$

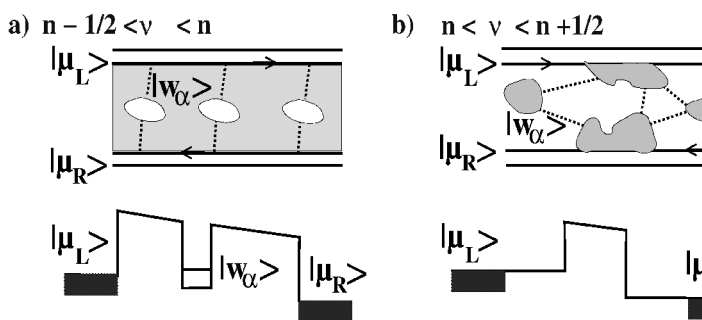


figure 3: two kinds of tunnel effects

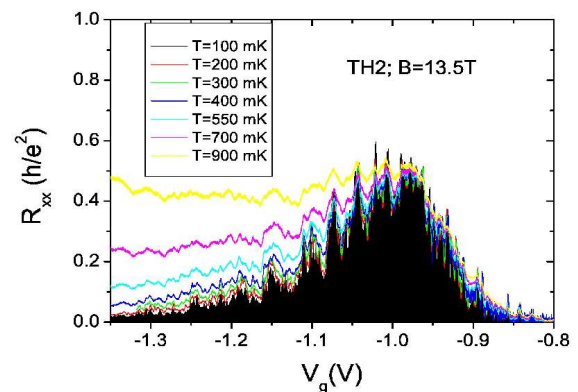


figure 4: the residual conductivity is the Density of States

Accurate prediction of the gate tunneling current for surrounding gate MOSFETs

Ferney Chaves*, David Jiménez^[a], Francisco Ruiz^[b], Andres Godoy^[c], Jordi Suñé^[d]

ferneyalveiro.chaves@uab.cat

^[*,a,d]Departament d'Enginyeria Electrònica, Escola Tècnica Superior d'Enginyeria
Universitat Autònoma de Barcelona, 08193 Bellaterra.

^[b,c]Departamento de Electrónica y Tecnología de Computadores
Universidad de Granada

ABSTRACT

We report on the calculation of quasi-bound states in ultra thin film Surrounding-Gate (SG) MOSFETs and their impact on the direct tunneling current through the SiO₂ layer. For typical device parameters, the gate leakage in inversion is dominated by this tunneling component. However, if the eigenvalues of the closed system are used to calculate quasi-bound state tunneling current, then strong inaccuracies can arise [1]. To account properly for eigenstates of an open system, Absorbing Boundary Conditions (ABCs) should be included, which are commonly used for simulating waves in unbounded domains [2]. As one of those approaches for designing ABCs, Perfectly Matched Layer (PML) method has achieved great success for both linear and nonlinear wave equations due to their effectiveness. In this work we apply PML method in a 2D self-consistent Schrödinger-Poisson solver on a Surrounding Gate MOSFET for gate tunneling current computation (Eq. 1). This technique accounts for the wave function penetration into the gate, thus allowing a more accurate estimation of the electrostatic potential, quasi-bound states, charge and carrier lifetime [3]. Our results are compared with other models based on the computation of bounded states assuming a closed system.

$$J = \frac{qkT}{\pi\hbar^2} \sum_{i,j} \frac{g_j m_{\parallel}}{\tau(E_{i,j}(m_q))} \ln \left(1 + \exp \left(\frac{E_f - E_{i,j}}{kT} \right) \right) \quad (1)$$

REFERENCES

- [1] M. Karner, A. Gehring, H. Kosina, and S. Selberherr, "Efficient Calculation of Quasi-Bound State tunneling in CMOS Devices", Simulation of Semiconductor Processes and Devices, 2005. SISPAD 2005. International Conference on. Vol. Issue, 01-03 Sept. 2005 Page(s): 35-38.
- [2] C. Zheng, "A perfectly matched layer approach to the nonlinear Schrodinger wave equations" Journal of Comp. Phys. 227 (2007) 537-556
- [3] N. Yang, W. K. Henson, J. R. Hauser, J. J. Wortman, "Modeling Study of Ultrathin Gate Oxides Using Direct Tunneling Current and Capacitance-Voltage Measurements in MOS Devices", IEEE Trans. Electron Devices 46 (1999) 1464-1471

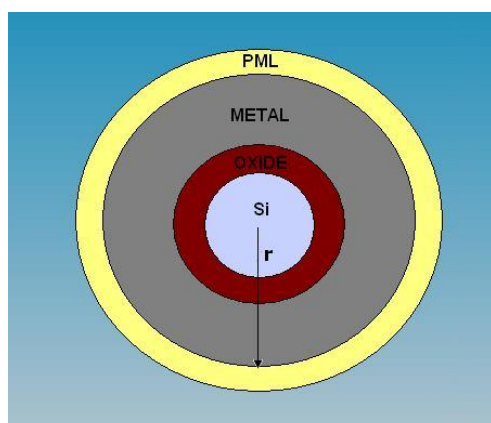


Fig 1a. Scheme of the cross section of Surrounding a Gate Mosfet.

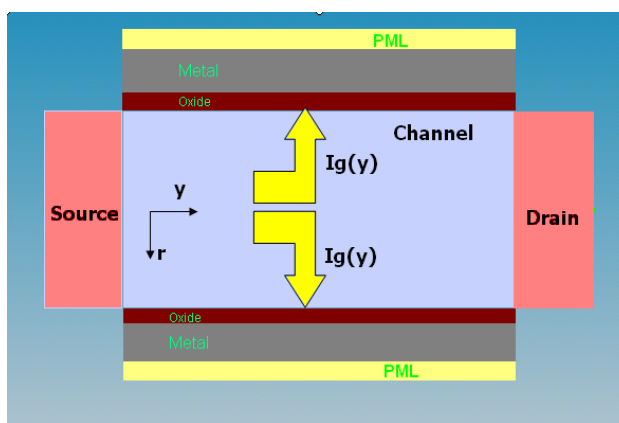


Fig 1b. Scheme of the longitudinal section of a Surrounding Gate Mosfet.

OPTIMUM POTENTIAL PROPERTIES OF Ag NANOSTRUCTURES: CONTROLLED SYNTHESIS AND CHARACTERIZATION

Nurul Akmal Che Lah, Mohd Rafie Johan

*Advanced Materials Research Laboratory, Department of Mechanical Engineering,
University of Malaya, 50603 Kuala Lumpur, Malaysia.
umieakmal@um.edu.my, mrafiej@um.edu.my*

The aim of this study is to obtain anisotropic and well dispersed shapes of silver (Ag) nanoparticles using controlled (isometric and anisotropic shapes) chemical reduction method. The characteristic absorption of Ag nanoparticles is approximately at the range of 420 – 450 nm (Fig.1). The spherical shape of Ag nanoparticles is observed at temperature of 80°C and the mean size is of approximately 5nm (Fig.2).

For the purpose, the experiments perform based on the combination factor design regarding some key factors involved in a general chemical reduction method. The optimum properties produced of Ag nanoparticles were governed by not only single or two prime factors but also interactions between them. In this controlled synthesis, the amounts of added chemicals and preparation conditions were varied. The presence of polyethylene glycol (PEG) as the reducing agent are described. Whereas the use of Daxad 19 in order to give better stable high concentration of Ag colloidal particles by prevention of particle interactions is introduced. Typically, 50 ml deionized water added into 100 ml beaker, maintained the temperature in the range of 78 - 80°C under magnetic stirring, dissolved 2.5 g of Daxad 19 as a stabilizer and then added 2 g of AgNO₃. To this solution, 4 g of PEG was added.

Relying on the experimental stipulations, Ag nanoparticles formed by directly or after the aging of reaction mixture for various period of time. By changing the amount of chemicals added, reactant temperatures, addition rates of reductant, and the aging time, particles of different structures were formed. Our observation can are agreement with the Lee et al. [1] statement where the reduction of silver nitrate with suitable reducing agent can lead not only to uniform, highly dispersed spheres in concentrated solutions, but also to isolated particles of other shapes.

The nanoparticles prepared were characterized by TEM, SEM and UV- vis absorbance for particle size, distribution, aggregation and anisotropy. The appropriate combination of the factors led to synthesize of varying in particle shapes, narrow distributed and non-aggregated of Ag nanoparticles. The sharp vertices of the elongated and hexagonal structures of Ag nanoparticles is expected to have optimum potential for enhancing the detection efficiency of SERS substrates and in current developing trends of the synthetic technology of Ag nanoparticles are also prospected.

References:

- [1] M.-H. Lee, S.-G. Oh, K.-D. Suh, D.-G. Kim, D. Sohn, Colloids Surf. A 210 (2002) 49.

Figures:

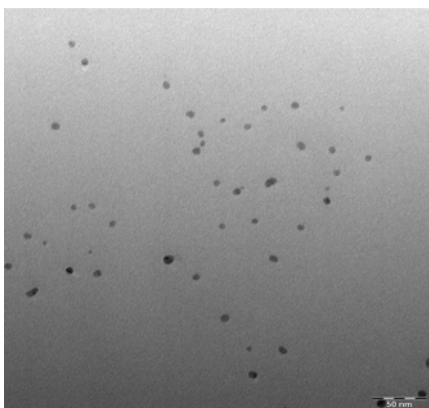


Figure 1: TEM micrograph of Ag nanoparticles obtained at temperature of 80°C.

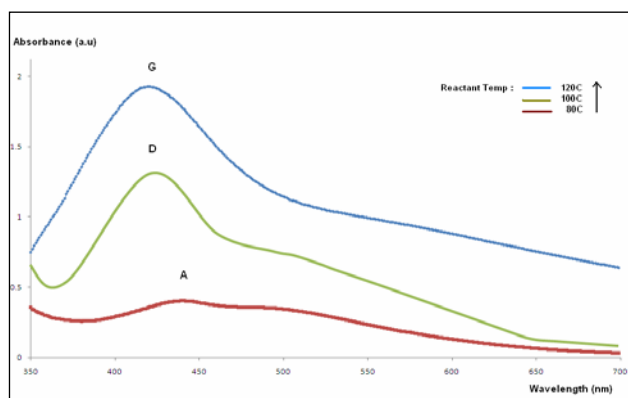


Figure 2: UV-vis absorbance spectra of Ag nanoparticles obtained at same concentration but different reactant temperatures.

Nanoelectronic biosensors to detect dynamic biological activities

Peng Chen

Division of Bioengineering, School of Chemical & Biomedical Engineering, Nanyang Technological University, Singapore

chenpeng@ntu.edu.sg

Nanostructured materials such as carbon nanotubes and nanowires are bringing unprecedented opportunities to biology. Their nanoscale dimensions allow them to interact intimately with and spy on the nanoscopic world of biomolecules and molecular machineries that mediates cellular functions. Here, we demonstrate several examples of using single walled carbon nanotubes (SWNTs) and silicon nanowire (SiNW) to interface with biomembranes for electrical detection of dynamic biological activities.

Thin-film network of SWNTs (SWNT-net) was fabricated using phase-separation facilitated self-assembly and subsequent drop-casting process. We demonstrate that SWNT-nets functionalized with bioactive monosaccharides were able to interface with living neuroendocrine PC12 cells and support their adhesion and growth. The glycosylated SWNT-net devices have been used to electrically detect dynamic vesicular release of catecholamine with millisecond resolution at single cell level [1]. In another effort, SWNT-nets functionalized with adhesion poly-peptides were able to interface with living neuroglial astrocytes and detect rapid release of ATP molecules [2]. Furthermore, we show that SWNT-net can integrate with biomemtic membrane (artificial lipid bilayers) to detect membrane insertion molecules.

Array of perfectly aligned long silicon nanowires were fabricated using top-down CMOS (complementary metal-oxide-semiconductor) compatible fabrication techniques standardized in large-scale production of microelectronics. SiNWs can interface with living excitable cells such as cardiac myocytes and smooth muscle cells, and detect cellular bioelectricity (action potentials) produced by these cells [3]. SiNWs have also been used to detect adipocytokines secreted by adipose cells with simple detection scheme, femtomolar sensitivity, high specificity, wide detection range, and ability for parallel multiplexed sensing. This development is of obvious scientific and clinical significance in terms of revealing the poorly understood signaling mechanisms of these newly recognized hormone molecules as well as their relevance in common diseases such as obesity, diabetes, cardiovascular disease, and so on.

The nanoelectric biosensing devices that we developed are not only instrumental for fundamental research but also useful for high throughput drug screening for critical diseases such as neurodegenerative diseases, hormone disorders, cardiovascular diseases, channelopathies, and so on.

References:

- [1] Sudibya HG, *Angew. Chem. Intl.*, **In press**, 2009.
- [2] Huang Y, *Biosen. Bioelec.*, **in press** 2009.
- [3] Pui TZ, *Small*, **5(2)** 2009 p.208-212.

PREPARATION AND CHARACTERIZATION OF COPPER (II) OXIDE NANOLAYER

Maryam Chenani, Abbas Honarbakhsh-Raouf, Ali Ghafari-Nazari
R&D Group, Rafsanjan Almas Kavir Tile Company, 7717577911 Rafsanjan, Iran
maryamchenani13@gmail.com

In recent years, nano-oxides layer were prepared for various applications by different method. They have unusual and strong physical and mechanical properties. Much interest focuses on the use of nano-layer copper oxide for optical use. In sol-gel method, copper oxide nanolayers have intense light absorption in wavelength of 400-700 nm. Absorption in rang of visible has very applications, for example, they are used in solar for light absorption from sun. Besides, copper oxide nanolayers prepared by sol-gel, have able to use in gas sensors due to high porosity. If they are compounded with zinc oxide, gas sensor efficiency will increase.

Here, we report on the preparation and characterization of CuO nanolayer by using the sol-gel technique. The precursor for sol preparation was copper chloride, copper acetate monohydrate and polyvinyl alcohol used as a solvent in various environments. Temperature (300-600 c), time, and atmosphere of heating were changed for finding role of them in structural, optical and electrical properties of CuO nanolayer. For the characterization of the obtained nanolayers, X-ray diffraction, SEM, and AFM were used. Optical properties of nanolayer was measured by UV-Visible absorption spectroscopy are also discussed. With varying heat treatment band gap energy will be changed.

References:

- [1] S. C. Ray, Solar Energy Materials & Solar Chemistry and Physics, **83** (2004) 307-312.
- [2] R. Boucher, J. Physic and Chemistry of Solids, **66** (2005) 1234-1239.

ASSESSMENT OF THE CARBON-NICKEL INTERACTION FOR ATOMISTIC SIMULATION OF CARBON NANOFIBER GROWTH

Daojian Cheng and Marc Hou

Physique des Solides Irradiés et des Nanostructures CP234, Faculté des Sciences, Université Libre de Bruxelles, Bd. du Triomphe, B-1050 Bruxelles, Belgium.

chengdaojian@gmail.com

Investigating the dynamics of carbon nanofiber growth is necessary for probing further which role the Ni catalysts play. One could use classical molecular dynamics simulations to this purpose and we explore the possibilities of simple carbon-metal interaction models fitted to experimental and *ab initio* data.

Regarding the initial steps of the catalysis of nanotubes on metal nanostructures, DFT shows the importance of the stability of adsorbed C at 5-fold symmetric Ni metallic sites [1]. Using classical molecular statics with a Lennard Jones, we show that this is impossible in the frame of Van der Waals interactions, strongly supporting the carbidic nature of bonding. By parameterizing the LJ potential for carbidic bonding (DFT-LJ), we find an energetic order of favored C adsorption sites consistent with experimental findings [2] and migration energies by means of Nudged Elastic Band calculations consistent with DFT [1]. Moreover, the reliability of the DFT-LJ potential for Ni-C is validated for single carbon on (322) and (111) Ni surfaces, as well as inside bulk Ni.

The parameters (ϵ, σ) of the 12-6 Lennard Jones potential (DFT-LJ) were fitted to: (1) The energetic order of favored C adsorption sites obtained from DFT calculations [1, 3] and experimental findings [2]. (2) The migration energies from DFT calculations [1] by means of Nudged Elastic Band calculations. By fitting to (1), we got $\sigma = 1.77 \text{ \AA}$. By fitting to (2), we got $\epsilon = 0.235 \text{ eV}$. In fitting to (2), the migration energies were calculated also by the Nudged Elastic Band method. The nickel atoms are modeled by the second moment approximation to the tight-binding potential (TB-SMA). Three energy barriers, $E_{diff}^1, E_{diff}^2, E_{diff}^3$, of C diffusion steps on the Ni(322) surface in this work, compared with the points calculated by DFT calculations [1], are shown in Figure 1. $E_{diff}^1, E_{diff}^2, E_{diff}^3$ correspond to “from step edge to clean surface”, “from clean surface to clean surface”, and “from clean surface to step edge”. It should be mentioned that fitting DFT-LJ parameters on E_{diff}^3 is sufficient to predict E_{diff}^1 and E_{diff}^2 correctly.

Regarding the weak interaction for the whole graphene-Ni(111), we model the graphene on Ni(111) with a van der Waals potential (VDW-LJ) for the Ni-C, with parameters from the Ref. [4]. The VDW-LJ is very weak, and is only about 1/10 of the DFT-LJ for Ni-C interactions. We found that, in order to describe the growth of graphene on a Ni stepped surface it is necessary to couple the DFT-LJ with VDW-LJ for Ni-C, suggesting the role of both graphitic and carbidic bonding.

References:

- [1] F. Abild-Pedersen, J.K Nørskov, J.R. Rostrup-Nielsen, J. Sehested, S. Helveg. *Phys. Rev. B* **73**(2006)115419
 [2] M. Moors, T. Visart de Bocarmé, and N. Kruse. *Ultramicroscopy* **109**(2008)381-384

[3] Li, Tao; Bhatia, Bhawna; Sholl, David S. *Journal of Chemical Physics* **121** (2004)10241-10249.

[4] Balbuena et al. *Surface Science* **545**(2003)163-179

Figures:

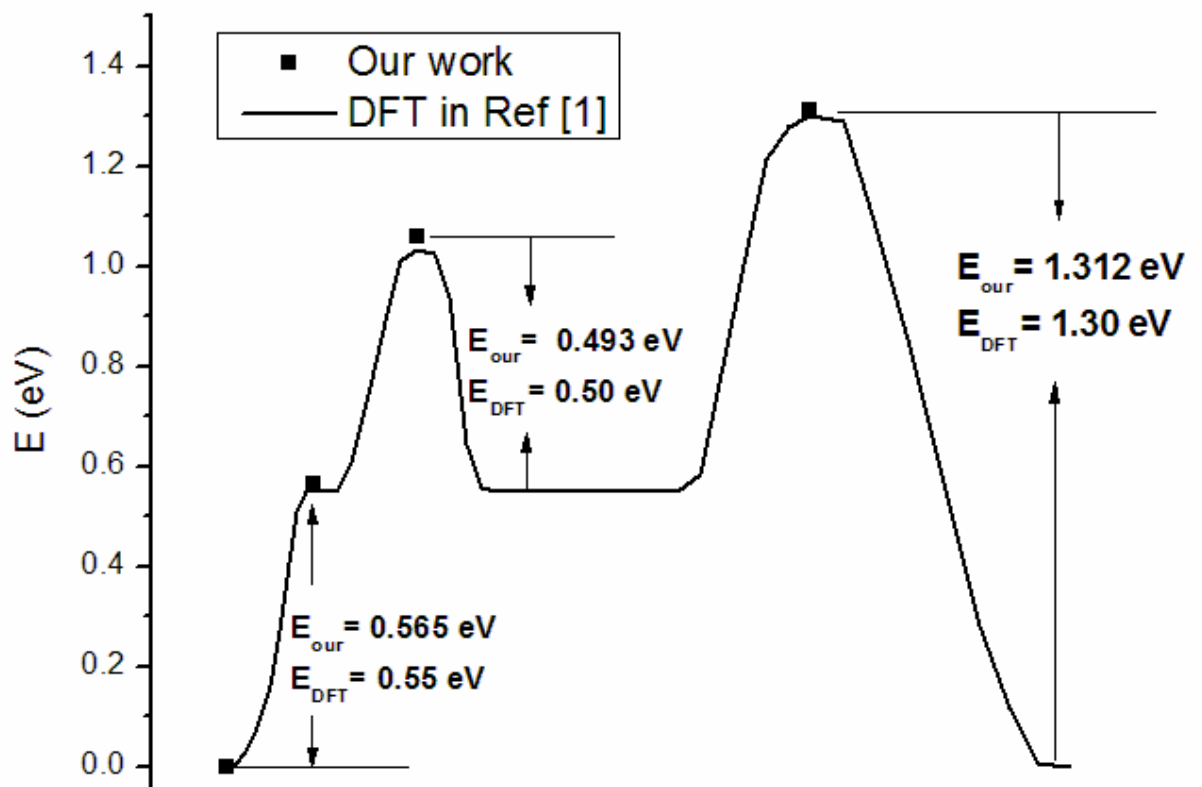


Figure 1 Three energy barriers, E_{diff}^1 , E_{diff}^2 , E_{diff}^3 , of C diffusion steps on the Ni(322) surface in this work, compared with the points calculated by DFT calculations [1]. E_{diff}^1 , E_{diff}^2 , E_{diff}^3 correspond to “from step edge to clean surface”, “from clean surface to clean surface”, and “from clean surface to step edge”.

MODELLING OF GRAPHENE-NANOTUBE STRUCTURES: ARCHITECTURE, PROPERTIES AND APPLICATIONS

L.A.Chernozatonskii*, A.A.Artyukh*, E.F.Sheka**, P. B. Sorokin*#

*Institute of Biochemical Physics RAS, 119334 Moscow, Russia

**Peoples' Friendship University of the Russian Federation, 117923 Moscow, Russia

#Siberian Federal University, Krasnoyarsk, 660041 Russia

cherno@sky.chph.ras.ru

New prospects related to the preparation and characterization of individual carbon nanotubes and graphenes (graphite sheets) have been currently developed in carbon nanotechnology during last years. The special graphene feature plays an important role in the electronic structure of carbon nanotubes (CNT) and graphene nanoribbons (GNR) whose conductivity type depends on the coincidence of the allowed wave vector with the Dirac points of graphene. CNT and GNR possess unique mechanic properties. That is why we began to study new symbiosis structures formed by CNT's and nanographenes/or GNR's [1].

We consider the reaction covalent addition zigzag (Z) edge or armchair (A) edge of GNR's to a single walled nanotube (SWNT) of different chirality. Between them more stable structures are Z-edged GNR covalent bonded (cb) with (n,n) SWNT's and A-edged GNR covalent bonded with (n,0) SWNT's. The covalent bonding change symmetry drastically both nanotubes and nanoribbons. Therefore, practically all cbGNR-SWNT structures are semiconductors. Each considered structure has "finger print" Van Hove peculiarities of electron spectrum similar separate SWNT's (or GNR's), and so they can be identified by Raman studies. We have studied free standing molecular bonded (mb) GNR -SWNT structures by molecular dynamic (MD) methods and showed that all nanoribbons align along nanotubes and take the form similar a part of cylinder. MD studies of considered quasi one-dimensional and two-dimensional cb-GNR-SWNT and mb-GNR-SWNT structures have showed high anisotropic elastic effects.

The calculations of reaction process were carried out in a single-determinant unrestricted Hartree-Fock approximation implemented in a semi-empirical version of the AM1 approach that is the most suitable for a thorough quantitative description of the odd-electron systems to which the above carbeneous composites belong [2]. The calculations of electronic properties were made by DFT method using SIESTA program [3].

We have modeled also multi-terminal (T- and X- types) mb -GNR -SWNT junctions and their electronic properties. These junctions can be used as nanoelectronic elements with nonlinear current-voltage characteristics.

Some applications these structures (as components of elastic and conducting composites, optics and electronic elements, and so on) are considered.

This work was supported by Russian Fund of Basic Research (grant 08-02-01096) and Russian Academy Program № 27.

References:

- [1] L.A. Chernozatonskii, E.F. Sheka, A.A. Artyukh. *JETP Lett.* **89**, (2009). 412.
- [2] E.F. Sheka, and L.A. Chernozatonskii. *J. Phys. Chem. C*, **111**, (2007) 10771.
- [3] E. Artacho, *at al. J. Phys.: Condens. Matter* **20**, (2008) 064208.

SUPERSATURATION INFLUENCE ON THE SYNTHESIS OF ULTRAFINE ARAGONITE. KINETIC PARAMETERS ESTIMATION

*Irinela Chilibon*¹, Carmencita D. Mateescu², Raluca Isopescu³, Mihaela Mihai³

¹*National Institute for Optoelectronics, INOE- 2000, 77125,409 Atomistilor Str., PO Box MG-5, Bucharest - Magurele, Romania, e-mail: gilib@yahoo.com*

²*National Institute for Materials Physics, 105- bis Atomistilor Str., Bucharest - Magurele, Romania*

³*“Politehnica” University of Bucharest, 303 Splaiul Independentei, Bucharest, Romania*

Precipitated calcium carbonate with nano- scale particles is interesting for many applications like composite materials or biomaterials.

The deposition of solid particles from the liquid phase through a precipitation reaction is a simple and reliable method for obtaining nanostructures with good control of particles' characteristics. Several studies have been published regarding to the synthesis of metal oxides, hydrous oxides and hydroxide particles by precipitation from aqueous solutions [1, 2]. The controlled double-jet precipitation method allows the production of colloidal particles with a good control of their monodispersity [3].

Calcium carbonate presents the phenomenon of polymorphism having at least three stable polymorphs: calcite with rhombohedra structure and cubic appearance, aragonite with orthorhombic structure and whiskers like crystals and vaterite with hexagonal structure and spherical appearance. Besides these there are two hydrated and an amorphous form. Calcite is the most stable form while aragonite is the high pressure polymorph. During the precipitation process, in the first moments, a mixture of polymorphs is formed followed by polymorphic transformations in the next stages of the process. These transformations are influenced by many parameters like: temperature, pH, presence/absence of additives or impurities, hydrodynamic conditions or super saturation, having more or less influence on the final characteristics of the material.

Precipitated calcium carbonate (PCC) with high purity as regarding the polymorphic form, with nano size particles and sharp particles size distribution was synthesized by the double jet precipitation method using either pure ethanol or solutions of ethanol in bi-distilled water as reaction medium. Calcium ions were provided by calcium nitrate solution and carbonate ions were supplied by a solution of potassium carbonate. In order to evaluate the supersaturation influence on the morphology, particle size and distribution of PCC, the concentration of the reagent solutions were varied from 0.1 M to 1 M.

All samples were characterized by FTIR spectroscopy, XRD, optical and electron microscopy, particle size distribution by laser granulometer, microscopic measurements and dynamic light scattering method (Figure 1). The results proved that a very small amount of the precipitated particles were agglomerated and the mean particle sizes were under 1 micron.

Particles size measured by a laser particle size analyser varied around 1 μm . These particles are formed by agglomeration of crystallites with sizes in the range 50-100 nm as resulted from XRD spectra and confirmed by TEM images (Figure 2a).

Particle size distribution (Figure 2b) measured in a mass base system was used for the kinetic parameter estimation considering that the final shape of the PSD is the result of overlapping primary and secondary crystallization mechanisms such as nucleation, growth and agglomeration. The population balance equation describing the precipitation process was integrated using the method of classes [4].

References:

- [1] J.E. Rodriguez-Paez, A.C. Caballero, M. Villegas, J. Eur. Ceram. Soc., **21**, (2001) 925
 [2] P.D. Southon, J.R. Bartlett, J.L. Woolfrey, B. Ben-Nissan, Chem. Mater., **14**, (2002) 4313
 [3] Q. Zhong, E. Matijevic, J. Mater. Chem., **6**, (1996) 443
 [4] P. Marchal, R. David, J. P. Klein, J. Villermaux, Chem. Eng. Sci., **43** (1988) 59-67

Figures:

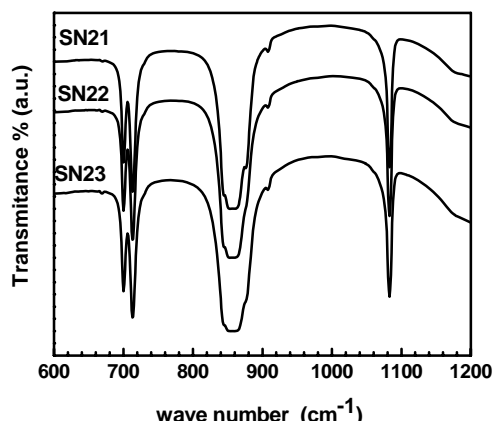


Figure 1. IR spectra of aragonite precipitated in the presence of alcohols (SN21- ethanol; SN22- 2-propanol; SN23-methanol)

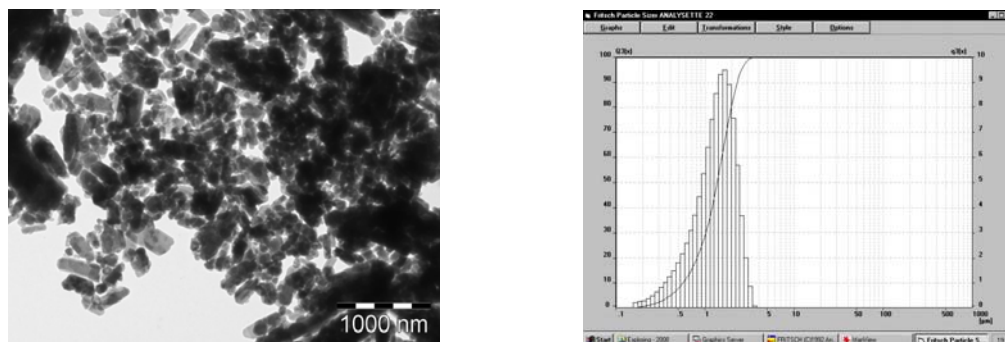


Figure 2. a) TEM image b) Particle size distribution of PCC in ethanol medium

EIS Biochips for studying cell cultures

Maria Serena Chiriaco*, Elisabetta Primiceri*, Addolorata Maria Luce Coluccia*, Elisabetta Tarentini*, Eliana D'Amone*, Roberto Cingolani*, Ross Rinaldi*, Giuseppe Maruccio*

*National Nanotechnology Lab of CNR-INFM, Lecce, Italy,
ISUFI-University of Salento

elisabetta.primiceri@unile.it

Biochips are attracting large interest in cell biology as functional tools to perform quick and extensive cell studies by integrating different functions in a single chip. In this respect, electrochemical impedance spectroscopy (EIS) is an emerging read-out technique since the immobilization/adhesion of cells on biofunctionalized electrodes alters the capacitance C and interfacial electron transfer resistance R_{ET} , which are correlated to cell number, adhesion and cytoskeleton organization [1-5].

Here an EIS Biochip for cell counting is demonstrated. Such device provides an easy tool to study cell attachment, spreading and to perform cell counting and viability tests. Specifically, the chips consist of a PDMS cell culture chamber on interdigitated electrodes. Cr/Au electrodes were fabricated by optical lithography on glass substrates. The PDMS chamber was realized by replica molding from a hard master.

These biochips are very cheap and reusable and represent a robust method to count cells with great sensitivity without detaching/destroying them (a crucial property for further assays such as migration tests and/or cytotoxicity tests):

With such a biochip we are able to count cells from several cell line (B104, HeLa, endothelial cells and others): in particular we report in fig.1 the results of some experiments with HeLa cells. These results show a linear relationship between the number of cells and the impedance measured and demonstrate that our chip is a powerful method for cell counting.

In addition we have used our biochip to monitor the adhesion between two different cell type, endothelial cells and leukaemia cells. We have evaluated the changes in adhesion as a consequence of an anti-leukaemia drug: SKI606 (fig.2). Ku812 leukaemia cells have a weak adhesion with endothelial cells because of a phosphorylation of β -catenin which in the phosphorylated form is located in the nucleus. SKI 606, a tyrosine-kinase inhibitor, blocks the β -catenin phosphorylation restoring cell adhesion. After the treatment with SKI606 the increase in impedance is bigger than in the control experiment demonstrating a stronger adhesion between the two cell types (fig.2).

The results reveal that our cell chip provides an easy and real-time monitoring tool to study cells and can be very useful in all biology laboratory. Our device is very cheap and reusable and allows us to perform automatic cell counting and other studies saving time and reagents. It joins a great sensitivity and low cost both for fabrication and usage.

1. E.Katz and I.Willner, *Electroanalysis* Vol 15, No. 11 pp 913-947, 2003.
2. X. Cheng et al., *Lab on a Chip*, Vol 7, pp 746-755, 2007.
3. C.Xiao et al., *Anal. Chem.* Vol 74, pp 1333-1339, 2002.
4. R. Ehret et al., *Biosens. Bioelectron.* Vol. 12, pp 29-41, 1997.
5. S. Arndt et al., *Biosensors and Bioelectronics* Vol. 19, pp 583-594, 2004

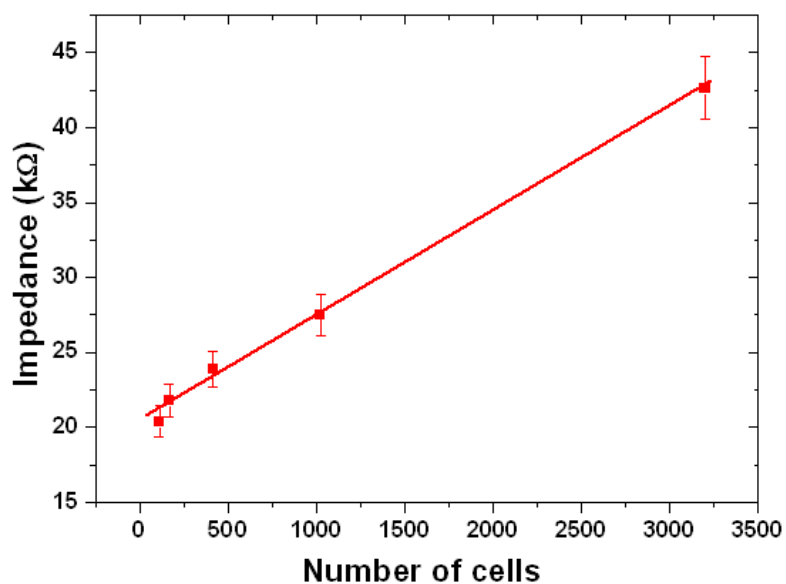


Fig. 1 Cell counting by EIS measurements. The relationship between the number of cells grown upon the device and the impedance values is linear.

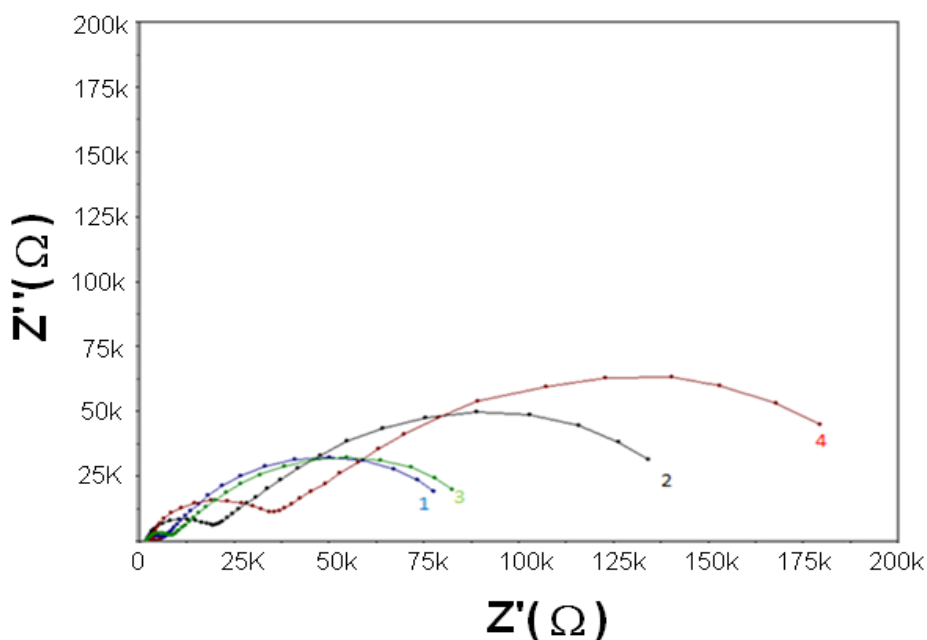


Fig. 2: EIS curves related to a co-culture of endothelial cells and leukaemia cells. The blue curve (1) and the black one (2) are related to a control experiment in which non treated leukaemia cells are seeded on a layer of endothelial cells. The curve 1 is referred to the impedance values measured for the monolayer of endothelial cells, while the curve 2 has been obtained after the addition of the Ku812 (leukaemia cells).

The same experiment has been carried out with leukaemia cells treated with a anti-cancer drug, SKI606, which restores the adhesive properties of lymphocytes. On the layer of endothelial cells (curve 3, green), Ku812 treated for 15 min with SKI606 have been seeded (red curve, 4). As we can see the impedance values after the treatment are bigger than in the control experiment (4 vs 2) demonstrating a stronger adhesion between the two cell type.

Synthesis and Characterization of Semiconducting Nanoparticles for Printing Process

Youngmin Choi*, Younghwa Bae, Wonwoo Lee, Beyongseok Lee,
Doohyoung Lee, Sunho Jung, Beyong-Hwan Ryu
Device Materials Research Center, Korea Research Institute of Chemical Technology
19 Sinseongno, Yuseong, Daejeon 305-600 Korea
*youngmin@kriect.re.kr

Semiconducting nanoparticles (SNPs) play a key role in the field of printed device application, such as electronics, solar cells, display. In this research, semiconducting nanoparticles (CIGS, Si, etc.) have been synthesized by using a simple solution method with various experimental conditions (e.g. concentrations, temperatures, pressures and time, etc.). Our method to synthesize SNPs is more simple compare to other methods [1-3].

X-ray diffraction (XRD), high-resolution transmission electron microscopy (HRTEM) and energy dispersive spectrum (EDS) are employed in order to characterize the physical and chemical properties of the SNPs. We will discuss the optimum synthetic conditions of SNPs, rheological and viscometric properties for their dispersion stability as a semiconductor ink. Furthermore, semiconducting properties of TFT prepared from semiconductor ink will also be discussed.

Keywords: semiconducting nanoparticles, solution method, printing process, semiconductor ink

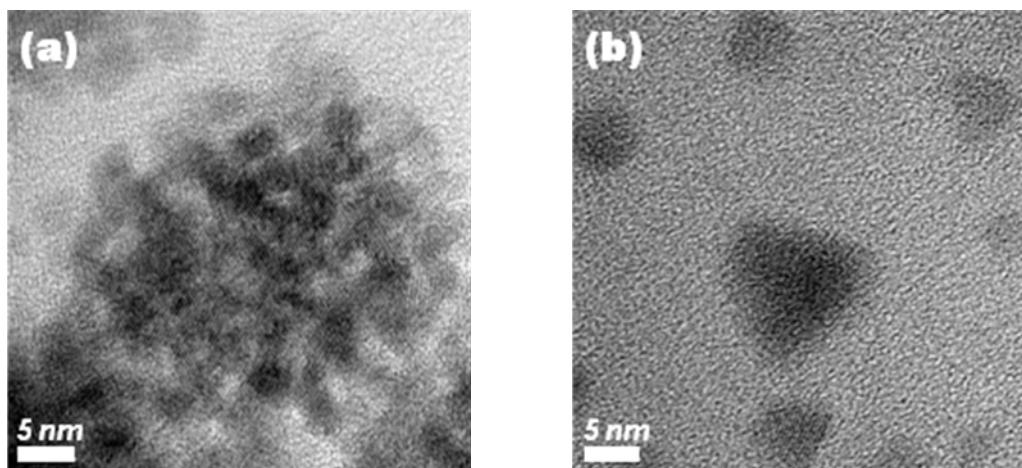


Fig. 1. HRTEM images of (a) CIGS and (b) Si nanoparticles.

Reference

1. Hsing-Yu Tuan, Doh C. Lee, and Brian A. Korgel, *Angew. Chem. Int. Ed.*, 45, 5184–5187 (2006)
2. Y.W. Chen¹, Y.H. Tang, L.Z. Pei, C. Guo, L.W. Lin, *Materials Science and Engineering B* 138, 189–192 (2007)
3. Rezan Demir Cakan,^a Maria-Magdalena Titirici, Markus Antonietti, Guanglei Cui, Joachim Maier and Yong-Sheng Hu, *Chem. Commun.*, 3759-3761 (2008)

Synthesis of Metal Nanoparticles in Solutions by γ -ray Illumination and Their Physical Properties

Sun-Woo Choi, Jae Young Park, Jin Zhang and Sang Sub Kim
School of Materials Science and Engineering, Inha University, Incheon 402-751, Korea

sangsub@inha.ac.kr

In recent years, metal nanoparticles have been actively studied because of their various potential applications including biomedical uses such as cell and DNA separation and drug delivery systems [1, 2].

One of the methods for synthesizing metal nanoparticles in solution is to use photon illumination. By applying photons in solutions containing metal precursors, they are likely to be easily reduced to their neutral atoms. The reduced atoms form clusters, finally generating nanosized particles. Recently, some research groups succeeded in synthesizing metal nanoparticles using γ -ray, which is one of high energy photons [3, 4].

In this work, we tried to synthesize metal nanoparticles including Pt and Au by γ -ray illumination. By changing the precursor contents in solution, intensity and exposed time of γ -ray, etc, different sizes and shapes of metal nanoparticles were obtained. The key processing parameters determining their growth behavior will be discussed.

References:

- [1] S. Seino, T. Kinoshita, T. Nakagawa, T. Kojima, R. Taniguci and S. Okuda, *J. Nanopart. Res.*, **10** (2008) 1076.
- [2] S. Seino, T. Kusunose and T. Sekino, *J. Appl. Phys.*, **99** (2006).
- [3] S-D. Oh, S. Lee, S-H. Choi, I-S. Lee, Y-M. Lee, J-H. Chun and H-J. Park, *Mater. Lett.*, **59** (2005) 1124.
- [4] S-H. Choi, S-H. Lee, Y-M. Hwang, K-P. Lee and H-D. Kang, *Colloid Surface A*, **256** (2005) 170.

Acknowledgement:

This work was financially supported by Korea Science and Engineering Foundation (KOSEF) grant funded by Ministry of Education Science and Technology (MEST) (M2AN01).

Figure :

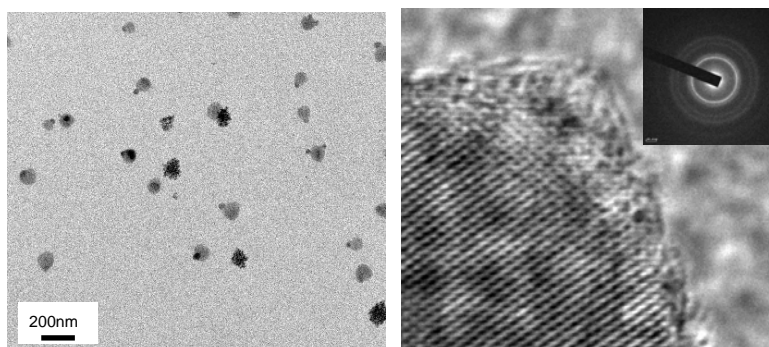


Figure 1 : Transmission electron micrographs of Pt nanoparticles synthesized by γ -ray illumination.

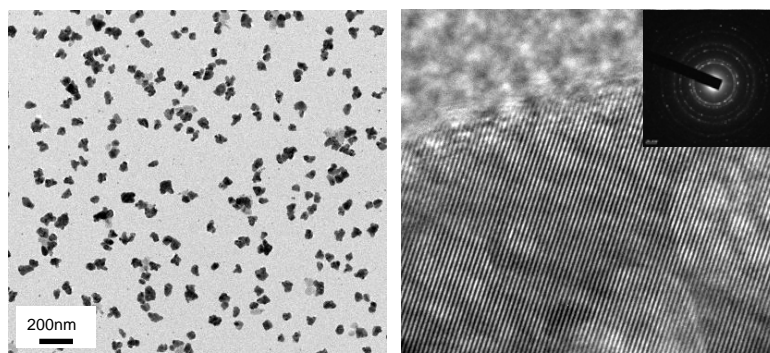


Figure 2 : Transmission electron micrographs of Au nanoparticles synthesized by γ -ray illumination.

MBE growth and properties of A3B5 nanowires on silicon substrates

G.E.Cirlin¹⁻³, Yu.B.Samsonenko¹⁻³, A.D.Bouravlev^{2,3}, N.V.Sibirev², V.G.Dubrovskii^{2,3},
M.Tchenycheva⁴, C.Sartel⁴, J.-C. Harmand⁴, G.Patriarche⁴, F. Glas⁴

¹Institute for Analytical Instrumentation RAS

²Ioffe Physical Technical Institute RAS

³St.-Petersburg Physics and Technology Centre for Research and Education RAS

⁴CNRS-LPN, Route de Nozay, 91460 Marcoussis, France

e-mail: cirlin@beam.ioffe.ru

Introduction. Over last few decades one of the most important tasks in optoelectronics is to merge Si-based microelectronics with A3B5 components serving as light emitters and/or detectors. Different approaches were examined so far, however with a limited success. In the case of direct growth of A3B5 on silicon several physical reasons (lattice mismatch, thermal expansion difference, phase-anti-phase boundary issues, different crystal structure etc.) are the key factors introducing structural defects at the A3B5 material/Si substrate interface. The way to decrease the sizes of A3B5 structures is now seen as one of the most promising to overcome the intrinsic problem. The object studied in this work is the A3B5 semiconductor NWs grown by MBE directly on Si substrates. It has been recently theoretically shown [1] that NWs can be grown on lattice mismatched surfaces without the formation of the structural defects (e.g., dislocations) due to the ability to accumulate for strain in two dimensions. We will also show that, together with commonly used external Au-catalyzed NWs formation, a self-catalyst Ga-terminated growth method can also be applied to A3B5 NWs fabrication directly on Si.

Experimental. Growth experiments are carried out using EP1203 and Riber 32P setups equipped with effusion Au cell to get Au-metal droplets at the high vacuum conditions. During the growth we have used Si(100) and Si(111). After the desorption of an oxide layer in the growth chamber we did not grow the buffer layer but, according to in situ reflection high energy electron diffraction (RHEED) patterns, the surface was atomically-smooth. After that, the deposition of Au or Ga layer (0.1 – 1 nm) was applied. In the case of nitrogen-content NWs, AlN nanoscale islands were deposited on Si(111) substrate prior to the NW growth. The substrate was then set above the eutectic melting point of a corresponding alloy with Au in order to form seed drops. After this stage the grown of NW with desirable chemical composition was initiated. The growth temperature of NWs, V/III flux ratio and growth rate were varied during our experiments depending on the material. Formation of cubic, polytype or wurzite crystal phases at different stages was clearly observed from RHEED patterns. After the growth, the samples were characterized by scanning electron microscopy (SEM) and photoluminescence (PL) methods.

Results and discussion. The temperature ranges for the growth of A3B5/Si NWs are found to be quite different for the different material systems. The broadest temperature range (380⁰C – 540⁰C) corresponds to the cases of GaAs/Si(111) and AlGaAs/Si(111). In opposite, InAs and InP NWs can be growth within a very narrow temperature windows, (370⁰C – 380⁰C) and (390⁰C – 410⁰C), respectively.

An interesting phenomenon has been detected from the dynamic monitoring of the RHEED patterns. At the beginning of growth, the NWs (independently on the material deposited) have a pure cubic phase, however, it has been rather quickly converted to the wurzite or polytype lattice. As the NWs growth continued, the RHEED pattern (at least, partially) has been transformed back to the cubic phase. This is in opposite to the case A3B5 NWs growth on the own substrates, e.g., GaAs/GaAs(111)B, where the wurzite phase does not change in time after the first transformation from cubic to wurzite (except for the very top of the NW) [2]. According to our preliminary PL measurements of GaAs/Si(111) and InAs/Si(111) NWs [3], the dominant PL peak can be attributed to the cubic phase. This is also confirmed by the transmission electron microscopy studies.

In addition, we have studied the possibility of NW formation using the self-catalized method, where one of the element of the NW (e.g., Ga) is used as a growth catalyst. The use of Ga instead of Au allows one to avoid an unintentional Au doping during the growth. It is well established that Au incorporates during the growth of Si NWs, for A3B5 materials this is still not obvious. In the case of GaAs/Si(111), we use Si substrate covered with a thin (~20 nm) oxide layer. The shape of these NWs is also different from those obtained on the GaAs(111)B surface. In particular, a negative tapering towards the NW foot is clearly seen in Fig.2. The density and diameter of NWs are determined by the density of the openings in SiO layer and can be controlled by the thickness of the latter as well as by the duration of deoxidation process.

Finally, we grow GaN NWs on Si(111) substrates with pre-deposited AlN nanoscale islands. These islands serve as the nucleation sites for the subsequent NWs growth. These NWs exhibit pure wurzite phase with a very low concentration of structural defects. GaN NWs has a strong PL up to the room temperature in spectral range of 3.4 – 3.6 eV.

In conclusion, we have demonstrated the possibility to grow epitaxial, dislocation-free A3B5 NWs on different Si substrates. All of them exhibit a bright light emission thus opening a new way for monolithic integration of A3B5 components on silicon substrates.

This work was partially supported by RFBR grants and scientific programs of Presidium RAS.

References

1. F.Glas. Phys. Rev. B 74, (2006) 121302(R)
2. I.P.Soshnikov, G.E.Cirlin, A.A.Tonkikh, Yu.B.Samsonenko, V.G.Dubrovskii, V.M.Ustinov, O.M.Gorbenko, D.Litvinov, D.Gerthen. Phys.Sol.St., 47, (2005) 2213.
3. Cun-Zheng Ning, private communication.

NANOFACETING OF VICINAL Ni SURFACES INDUCED BY Ag DEPOSIT

Carole Chambon^{1,2}, Alessandro Coati¹, Michèle Sauvage¹, Jérôme Creuze³, Yves Garreau^{1,2}

¹Synchrotron SOLEIL, l'Orme des Merisiers, Saint Aubin BP 48, 91192 Gif-sur-Yvette Cedex, France

²Université Paris Diderot, MPQ, Bâtiment Condorcet, Case courrier 7021, 75205 Paris Cedex 13, France

³LEMHE-ICMMO, Bâtiment 410, Université Paris Sud, 15, Rue Georges Clémenceau, 91405 Orsay Cedex, France

alessandro.coati@synchrotron-soleil.fr

The deposit of small amounts of atoms on surfaces may induce the formation of well organised nanostructures, which can present a long range order. In the case of Ag adsorption on a vicinal Cu surface [1], the deposit induces a periodic faceting of the surface, with well defined facets; moreover, in this case, the Ag coverage can be used to tune the periodicity and the orientation of facets. The Ag/Ni couple was thought to be very similar to Ag/Cu: Ag and Ni are not miscible in the bulk, their cohesive energies and atomic sizes are very different, leading to Ag segregation at the Ni surface and to an abrupt chemical interface. However, the faceting behaviour of vicinal surfaces under Ag adsorption is found different, as observed on Scanning Tunnelling Microscope STM images and confirmed quantitatively by Grazing incidence X-ray Diffraction (GIXD), performed on the ID03 beamline at ESRF.

Ni (322) is a surface presenting a miscut of 11.42° with respect to (111) planes and is constituted by a regular succession of (111) terraces of 1.03 nm width separated by {100}-type monatomic steps. When Ag is deposited on this surface, in the monolayer range, and after a thermal annealing, a periodic faceting of the surface is observed, covering the whole surface only within a very restricted coverage range around 0.6 monolayer (ML). Fig 1a and b show this "ideal" faceted surface observed by STM and the corresponding X-ray reciprocal space map recorded at $k=2$ around two nickel Bragg peaks, on which the scattering rods diffused by the facets are well defined. Two orientations are observed for the facets: (111) and (211); the comparison with a parallel map going through the relaxed silver Bragg peaks ($k=1.77$), fig.1c, which shows only (211) facet induced diffuse rods arising from the Bragg nodes, enables to conclude that the surface is made of (111) bare Ni facets and (211) Ag covered facets. The narrow (111) oriented diffuse features in fig.1c do not stem from silver Bragg peaks and are presumably linked to planar defects in the nickel near surface region.

For different coverages and particularly for lower ones like 0.3 ML, a surface phase separation between faceted regions similar to the case previously described (same facets with similar local periodicity) and bare vicinal nickel as shown in the STM image and the two corresponding maps in fig.1d, e and f. The energetics of the system needs to be further investigated to understand the unicity of the surface faceting decomposition.

In addition, as already visible in the STM image, fig.1a, one of the facets shows a reconstruction and indeed accurate GIXD data could be collected on the reconstructed Ag covered (211) facets (fig.2a) corresponding to a $(2 \times n)$ surface cell ($8 < n < 9$). A starting model sketched in fig.2b involving 6 silver rows on top of two successive (111) terraces of the (211) Ni substrate with $(n-1)$ Ag atoms for n Ni atoms along the $[01\bar{1}]$ direction has been used. When optimised by quenched molecular dynamics simulations involving about 60 bulk layers, this model renders satisfactorily the overall dynamics of the diffraction data but needs further

refinement to account for the whole in-plane and out-of plane measured structure factors. A mixture of different coverages of the individual terraces is presently investigated.

The knowledge of the system morphology and its surface structure are key parameters for its possible use as a nano-organized template for further growth of selected nano objects with magnetic or catalytic properties. This study shows how the coupling between GIXD, STM and atomistic simulations is fruitful as well as necessary to understand such phenomena.

References:

- [1] A. Coati, J. Creuze, and Y. Garreau, Phys. Rev. **B 72** (2005) 115424
 [2] Y. Garreau, A. Coati, A. Zobelli, J. Creuze, Phys. Rev. Lett. **91** (2003) 116101.

Figures:

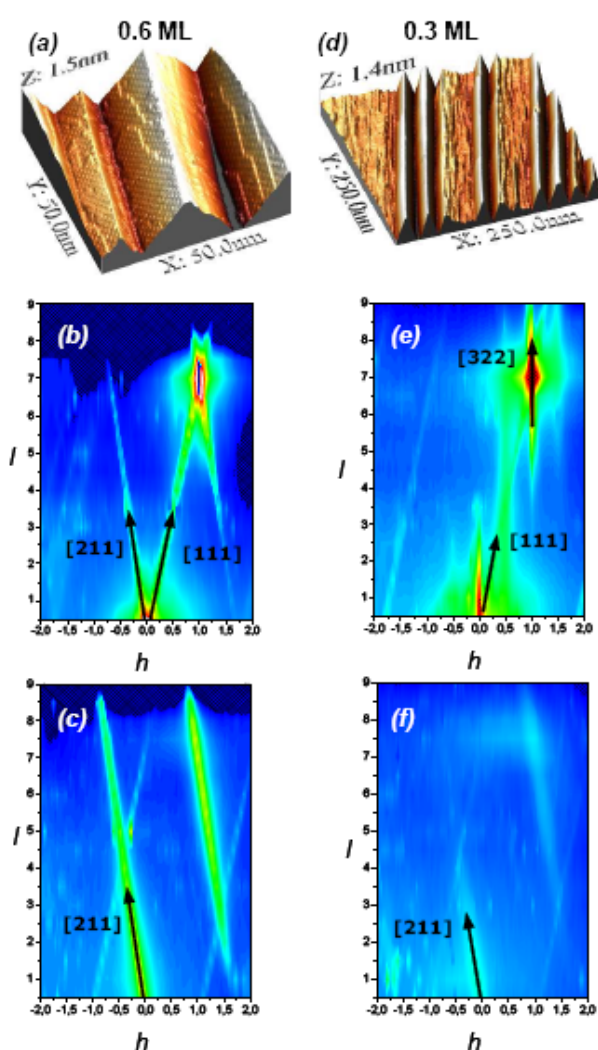


Fig. 1: Ni(322) surface after Ag deposit followed by annealing at 600 K. The Ag covered and bare Ni facets are clearly recognized: (a), (b) and (c) correspond to a 0.6 ML deposit, and (d), (e) and (f) to 0.3 ML. (a) 3D STM image (50x50) nm²; (b) (h , l) reciprocal space map at $k=2$; (c) (h , l) reciprocal space map at $k=1.77$; (d) 3D STM image (250x250) nm²; (e) (h , l) reciprocal space map at $k=2$; (f) (h , l) reciprocal space map at $k=1.77$.

TNT2009

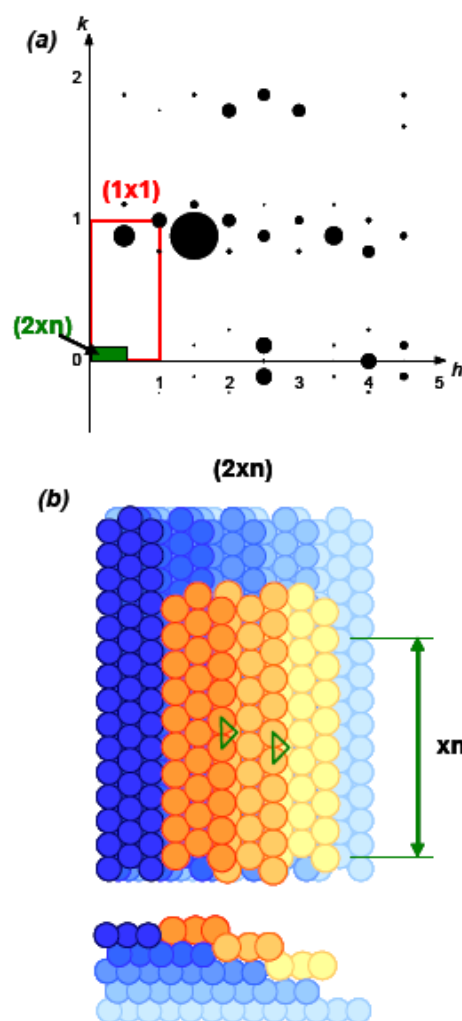


Fig. 2: Surface reconstruction induced by silver on the (211) facets. (a) GIXD in-plane data which shows the $(2 \times n)$ surface periodicity; (b) model of the surface structure used for QMD simulations (Ag atoms in orange, Ni atoms in blue).

September 07-11, 2009

Barcelona-Spain

EVALUATION OF TOXICITY ASSAYS ON AU, AG AND Fe_3O_4 NANOPARTICLES.

Joan Colón¹, Raquel Barrena¹, Eudald Casals², Xavier Font¹, Lucia Delgado¹, Antoni Sánchez¹, Víctor Puntès^{2,3}

¹*Composting Research Group. Department of Chemical Engineering. Universitat Autònoma de Barcelona. 08193-Bellaterra. Spain.*

²*Institut Català de Nanotecnologia. Campus de la Universitat Autònoma de Barcelona. 08193-Bellaterra. Spain.*

³*Institut Català de Recerca i Estudis Avançats. Passeig Lluís Companys, 23. 08010-Barcelona. Spain. Organization, Address, City, Country*

xavier.font@uab.cat

Since society realized about the use of nanomaterials in greater quantities in consumer products and their presence in the environment, the interest on the impact of this emerging technology has grown. The main concern is whether the unknown risks of engineered nanoparticles (NPs), in particular their health and environmental impact, outweighs their established benefits for society.

Therefore, a key issue in this field is to evaluate the potential toxicity of these engineered nanomaterials. In this context we evaluated the effects on plants and microorganisms of model nanoparticles, in particular of a stable metal (Au, 10 nm mean diameter), a well known bactericide (Ag, 2 nm mean diameter) and the broadly used Fe_3O_4 (7 nm mean diameter).

Toxicity of Ag, Au and Fe_3O_4 nanoparticles was assayed by using standard toxicity tests. Specifically germination test (cucumber and lettuce), bioluminescent test (Photobacterium phosphoreum) and anaerobic toxicity tests has been performed. Germination tests were conducted at a NP dose of 62, 100 and 116 $\mu\text{g ml}^{-1}$ for Au, Ag, and Fe_3O_4 respectively. Bioluminescent test (Photobacterium phosphoreum) was conducted at a dose of 28, 45 and 52 $\mu\text{g ml}^{-1}$ for Au, Ag, and Fe_3O_4 respectively. Finally anaerobic tests were conducted at a NP dose of 10, 16 and 18 $\mu\text{g ml}^{-1}$ for Au, Ag, and Fe_3O_4 respectively.

It has been observed that toxicity effects can be due to the presence of NPs solvent (stabilizers) and to the combined effect of NPs solvent and NPs. While no observed effect of NPs in the bioluminescent test, some effects were observed in the case of anaerobic bacteria (mainly in the case of NPs-solvents) and a modified root growth in the germination tests. Observed effects were either positive or negative.

In the germination tests, in some cases a slight positive effect of NPs was observed, which can be due to a hormesis effect, that is, a generally-favorable biological responses to low exposures to toxins and other stressors. Moreover, while the germination index was similar regardless of the NPs, the presence of them induced growth of larger roots as if the seeds were slightly stressed by the environment, which in the long term may be harmful, depending on the persistence of NPs in the environment.

In conclusion low or nil toxicity effect was observed for Au, Ag and Fe_3O_4 nanoparticles at the assayed concentrations. However some perturbation of the normal functions with respect to controls in germinating tests was observed, suggesting the necessity of further research in this

field. At the same time, the effect of NPs solvents (TMAOH, sodium citrate, NaBH₄) was in some cases more significant than that of NPs themselves, a point that is of special interest for future nanotoxicology studies.

At present, we are studying the toxicological effects of several inorganic nanoparticles using different biological tests.

Acknowledgment

The authors wish to thank the financial support received by the Spanish Ministerio de Medio Ambiente through the project NanoClean (Ref: 007/RN08/03.1). Joan Colón thanks to the Universitat Autònoma de Barcelona for the award of a pre-doctoral fellowship.

A DFT STUDY OF THE INTERACTION OF SULFURIC ACID WITH BILAYER GRAPHENE

Isabel G. Ayala¹ and Nicolas A. Cordero^{1,2}

¹ *Physics Department, University of Burgos, C/Villadiego s/n, E-09001 Burgos, Spain*

² *Department of Materials Science and Engineering, University of Pennsylvania, 3231 Walnut St, Philadelphia PA 19104, USA*

ncordero@ubu.es

One of the main problems for the industrial application of single-walled carbon nanotubes (SWCNTs) is their insolubility in either water or organic solvents. The available methods for the synthesis of carbon nanotubes produce bundles of SWCNTs. It is necessary to disentangle these bundles in order to separate the tubes. There are many surfactant molecules suitable for this task, but among the best are sodium dodecyl sulfate (SDS), sodium dodecylbenzene sulfonate (NaDDBS), and sodium polystyrene sulfonate (NaPSS), all of which have in common a sulfonate head group. In fact, sulfuric acid itself is a good nanotube disperser, the proposed reason being the protonation of SWCNTs by this acid. We had previously studied the interaction of H₂SO₄ with a single graphene sheet (that can be seen as a very large radius SWCNT) and found this to be true [1], but in order to understand the surfactant effect it is necessary to analyze the way these molecules behave when in between two carbon nanostructures. We have used density functional theory (DFT) within the local density approximation (LDA) to calculate the interaction between sulfuric acid and bilayer graphene (i.e. H₂SO₄ molecules between two graphene sheets), calculating equilibrium geometries, binding energies, charge transfers and densities of states.

We have studied four different concentrations of H₂SO₄ ranging from nearly isolated acid molecules (Fig. 1) to two layers of H₂SO₄ (Fig. 2) between the two graphene sheets, namely one sulfuric acid molecule per 64, 36, 16 and 8 carbon atoms, respectively. Hexagonal and orthorhombic cells were chosen to take advantage of both graphene and sulfuric acid crystal symmetries.

References:

[1] N.A. Cordero and J.A. Alonso, *Nanotechnology*, **18** (2007) 485705.

Figures:

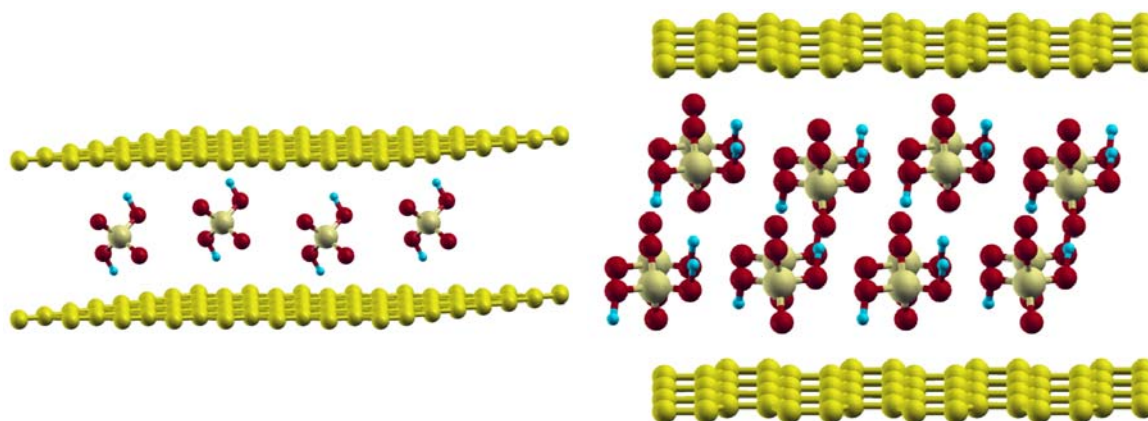


Figure 1

Figure 2

MAGNETIC PROPERTIES IN STRAINED DOUBLE EPITAXIAL NICKEL FILMS WITH PERPENDICULAR MAGNETIC ANISOTROPY.

Edna C. Corredor^{1,2}, *J. L. Diez-Ferrer*^{1,2}, *D. Coffey*^{1,2}, *J. I. Arnaudas*^{1,2} and *M. Ciria*^{2,3}

¹*Instituto Universitario de Nanociencia de Aragón, Universidad de Zaragoza.*

²*Departamento de Física de la Materia Condensada, Universidad de Zaragoza, Zaragoza, Spain.*

³*Departamento de Magnetismo de Sólidos, Instituto de Ciencia de Materiales de Aragón, Consejo Superior de Investigaciones Científicas, Zaragoza, Spain.*

Contact@E-mail

Magnetic films with perpendicular magnetic anisotropy (PMA) are used to improve some technology performances, such as areal density for magnetic recording [1] and are involved in the fabrication of planar nanowires because of their potential use in domain-wall devices proposed for data storage [2] and logic applications [3]. These devices may include several layers with PMA which made the knowledge of the magnetic properties in the resulting system an important issue to optimize device operation. The Cu/Ni/Cu system exhibits perpendicular magnetization for nickel thickness ranging from, approximately, 2 nm to 13 nm and has been a model for the technologically substantial phenomenon of perpendicular magnetization [4]. Here, we present a study of magnetic and structural properties in epitaxial double nickel films: Cu(5 nm)/Ni(3 nm)/Cu(t_{Cu})/Ni(3 nm)/Cu(100 nm)/Si(001), with the interleaving copper layer thickness t_{Cu} ranging between 0 nm and 6 nm. The results reveal the intimate relation between the strain state of the nickel block and its magnetic behaviour.

Figure 1 shows the coercive field H_c and the in-plane strain ϵ , determined by high resolution grazing incidence x-ray diffraction (GIXRD), done in the BM25B beamline of ESRF using a photon energy of $h\nu=15$ keV. Assuming the H_c depends on square root of the density of dislocations $\rho^{1/2}$ [5], the line in figure 1 is a fit of H_c to a law proportional to $a-b\epsilon^{1/2}$, where a and b are constants. A portion of the strain in the layer can be released by the formation of misfit dislocations. A mechanism proposed for the formation of dislocation is the glide of the existing threading dislocations in the layer, therefore the dislocation line forms a 90° angle at the Cu-Ni interface increasing the dislocation line and taking plastically a part of the misfit strain η . The dimension of the core of these misfit dislocations correspond to a few times the Burgers vector b , and the misfit strain between two materials is accommodated by elastic and plastic δ strain ($\eta=\epsilon+\delta$). The latter is given by $\rho b \sin\beta \sin\alpha$ [6], where β is the angle between the interfacial plane and the slip plane of the dislocation and α is the angle between the Burgers vector and dislocation lines. Thus the measurement of ϵ in the epilayer allows estimating ρ .

The correlation between K_{eff} and ϵ is presented in Fig. 2. Both quantities increases in value for $t_{\text{Cu}} < 1.8$ nm and remain roughly constant above that value. This fact clearly indentifies a magnetoelastic term, proportional to $B_{\text{eff}}\epsilon$ (B_{eff} is the effective magnetoelastic stress), in the magnetic anisotropy energy.

References:

- [1] S. N. Piramanayagam *J. Appl. Phys.* **102** (2007) 011301.
- [2] S. S. Parkin, M. Hayashi, and L. Thomas, *Science* **320** (2008) 190.
- [3] D. A. Allwood, G. Xiong, C. C. Faulkner, D. Atkinson, D. Petit, and R. P. Cowburn, *Science* **309**, (2005) 011301.
- [4] M. T. Johnson, P. J. H. Bloemen, F. J. A. den Broeder and J. J. de Vries, *Rep. Prog. Phys.* **59**, (1996) 1409.
- [5] H. Traible and A. Seeger, *Z. Angew. Phys.*, **21**, (1966), 299.

[6] J. Y. Tsao, Materials Fundamentals of Molecular Beam Epitaxy Academic, New York, (1993), p. 164.

Figures:

Figure 1

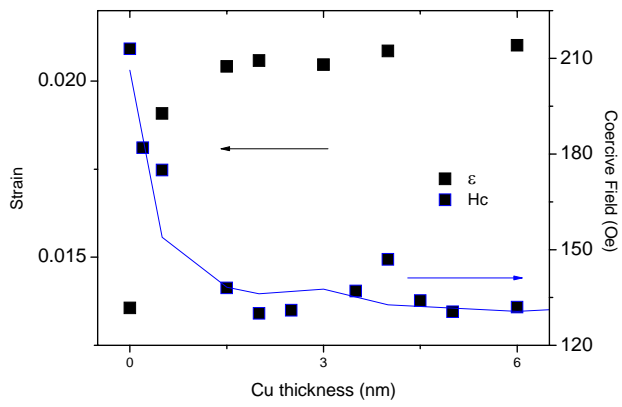
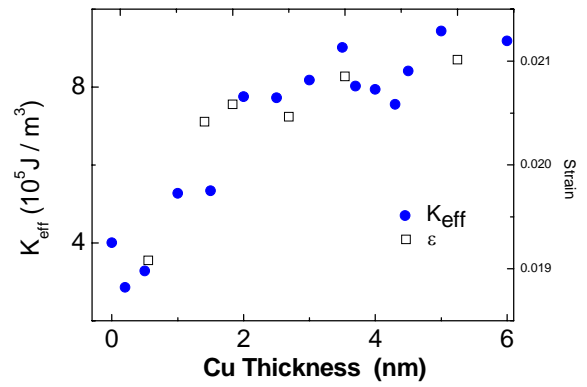


Figure 2



III-V semiconductor nanowires: structural vs. electrostatic properties

A.C.Narvaez, Th.Chiamonte, L.H.G.Tizei, K.O.Vicaro, J.H.Clerice,
D.Ugarte and M.A.Cotta
Instituto de Física Gleb Wataghin, Universidade Estadual de Campinas,
CP 6165, 13083-970, Campinas, SP, Brazil

monica@ifi.unicamp.br

Quasi-one-dimensional systems such as semiconductor nanowires (NWs) are considered as one of the main possible building blocks for nanoscale electronic and optoelectronic devices. From the possible choices of materials, InP and InAs NWs have been extensively investigated due to their large carrier mobilities and small surface recombination rates. Recent works evaluating possible nanoelectronics devices, however, have shown that the electrostatic characteristics of these nano-objects still need to be addressed.

We discuss here the synthesis and spatially-resolved characterization of nanowires based on III-V compounds. In particular, we have studied the growth evolution of InP and InAs NWs obtained using catalytic Au nanoparticles (NP) and the vapor-liquid-solid mechanism. Our results suggest the existence of different ‘incubation times’ for NP supersaturation prior to InP and InAs NW growth. For InP/InAs/InP heterostructured NWs, InP/InAs interfaces were well defined. However, InAs-rich regions were formed close to the NW/NP interface during sample cool down, indicating a stable phase in the NP not predicted from bulk phase diagrams.

The electrostatic characteristics of the NWs were investigated with spatial resolution by Kelvin Probe Force Microscopy (KPFM). This technique can provide information on the charge distribution and electronic structure of nano-objects. KPFM images show a variation of surface potential (SP) along individual NW's and a dependence on NW diameter. For heterostructured NWs, changes in SP values reflect the different materials and the presence of the nanoparticle (NP) used to catalyze the growth. Our results suggest there is an effective ‘electrical contact’ formed at the NW tip due to the presence of the metallic NP as well as a depletion region associated to the increasing surface to volume ratio at the thinner regions of the NW.

Figures:

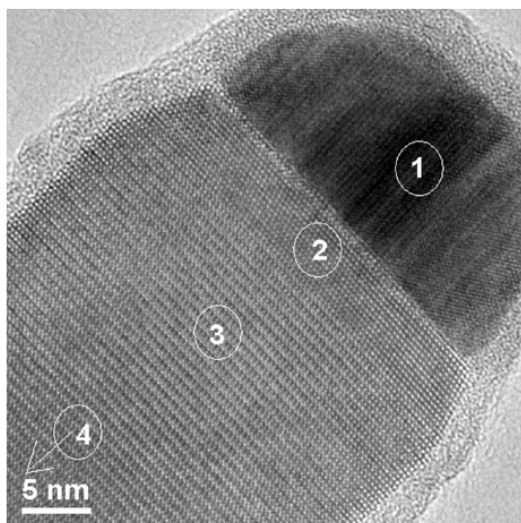


Fig.1 – High Resolution Transmission Electron Microscopy of the heterostructured InP/InAs/InP NW showing a wurtzite/zincblende structural transition. Energy Dispersive Spectroscopy measurements at the marked spots have shown the presence of up to 20% in As concentration near the NW/NP interface (neck region) while pure InP is at the NW body segment.

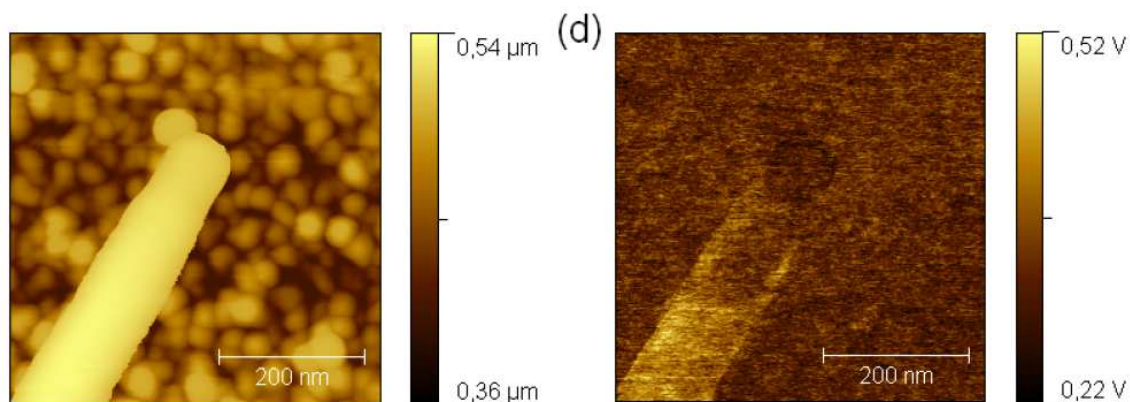


Fig.2 – Topography and Surface potential (SP) images of the heterostructured NW apex on top of a Pt film which acts as ground electrode.

MAGNETOSTATIC INTERACTION IN Fe-Co NANOWIRE ARRAYS

M^a Rosario D. Crespo^a, Laura Elbaile^a, Víctor Vega^b, and José A. García^a

a) Departamento de Física, Universidad de Oviedo, c/ Calvo Sotelo s/n, 33007 Oviedo, Spain

b) Unidad de membranas nanoporosas, SCTs Campus del Cristo, 33006 Oviedo, Spain

elbaile@uniovi.es

Recently, nanowire arrays of Fe-Co were being studied as potential materials for high-density magnetic recording due to its high coercivity and squareness resulting from shape anisotropy [1]. Besides this applied aspect, the nanowire arrays constitute one of the most important systems for studying the effect of magnetic interactions on the magnetization process in ordered systems. In this work, we have performed a study of the magnetic properties of Fe-Co nanowires with different lengths by analyzing the hysteresis loops and two different remanence curves, the isothermal remanent magnetization and the dc demagnetization remanence [2].

The arrays of Fe-Co nanowires have been prepared by coelectrodepositing Fe and Co into anodic aluminium oxide (AAO) membranes. The ordered porous alumina membranes with pore diameter about 35 nm and 105 nm interpore distance were prepared by anodic oxidation of 99.999% Al sheet at 40 Vcc in a 0.3M C₂H₂O₄ aqueous solution at 1-3 °C via two-step.

The Fe-Co nanowires were obtained by pulsed electrodeposition. The Fe and Co atoms were coelectrodeposited into the AAO membranes from an aqueous bath containing CoSO₄·7H₂O 0.045M, FeSO₄·7H₂O 0.18 M, boric acid 0.54 M, ascorbic acid 0.006M and NaOH to obtain a pH about 4.

Morphology of nanowire arrays of Fe₇₀Co₃₀ was characterized by SEM and TEM. Fig.1 shows a SEM image corresponding to Fe-Co nanowires of 8 μm length after dissolving the alumina using a 5 M NaOH solution for 30 min. The nanowires are clearly uniform in size. The average diameter of the nanowires has been measured from the TEM images and is ≈ 35 nm.

The hysteresis loops and remanence curves were measured using a VSM magnetometer at 300 K and at a maximum applied magnetic field of 20 kOe. Fig. 2 shows the magnetic hysteresis loops of Fe-Co nanowires array of 8 μm length with applied magnetic field parallel and perpendicular to nanowire axes. The experimental data can be explained using a quantitative description of interaction field obtained by treating the wire as a linear chain of several thousand point dipoles [3].

References:

- [1] Q. Zhan, Z. Chen, D. Xue and F. Li, *Phys. Rev. B* vol. 66 , pp.134436-1-134436-6, 2002.
- [2] P. S. Fodor, G. M. Tsoi and L. E. Wenger, *J. Appl. Phys.* 103, 07B713 (2008).
- [3] L. Clime, P. Ciureanu and A. Yelon, *J. Magn. Magn. Mater.*, 297 60 (2005).

Figure 1

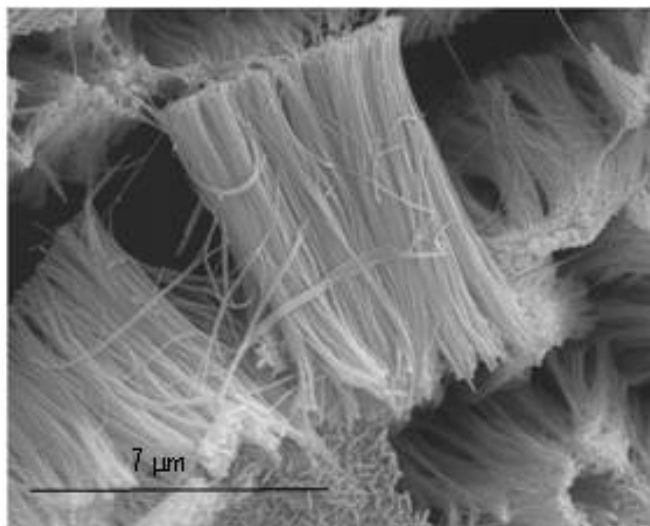
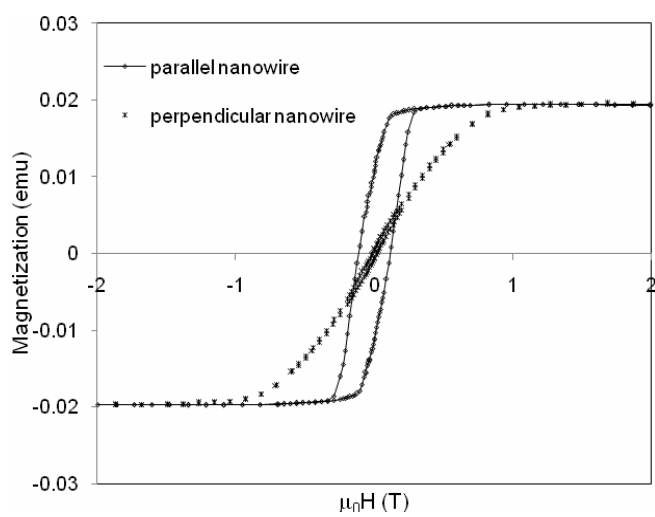


Figure 2



Nano scale surface and reaction mechanism study of (*R*)- and (*S*)-2-butanol over 100 surface alumina: Experimental vs. DFT

Hossein A. Dabbagh, Mehdi Zamani
dabbagh@cc.iut.ac.ir

*Catalysis Research Laboratory, Department of Chemistry, Isfahan University of Technology
 Isfahan, 841548311 Iran*

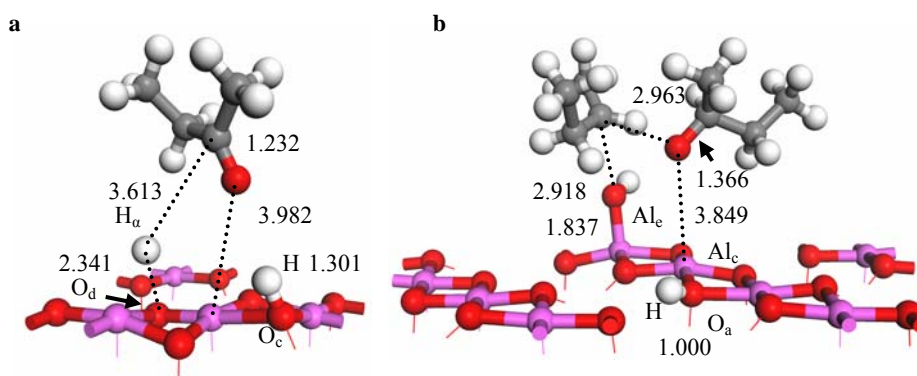
Reactions of 2-butanol over alumina were investigated under various conditions. The mechanism of dehydration, dehydrogenation, ether formation, hydrogen-shift, and the conformational analysis of adsorbed (*R*)- and (*S*)-2-butanol over the (100) surface of alumina was computed by Density Functional Theory (DFT). Adsorption, dissociation energy, and Mulliken charges were calculated for (*R*)- and (*S*)-2-butanol adsorbed on the surface (100) alumina. Mulliken atomic charges predict that selected basic sites play a major role in elimination reactions. Computed conformational analysis indicates that the (*S*)-isomer forms a stronger bond with the surface than the (*R*)-isomer. Migration of proton of (*S*)-isomer (sc-ap conformer) to oxygen O_c is an endothermic process ($+9.187 \text{ kcal mol}^{-1}$) with small activation energy ($13.560 \text{ kcal mol}^{-1}$). Transition state model, made of two layers of alumina is involved in anti elimination of the sc-sc conformer of (*S*)-2-butanol. E2 elimination with synclinal transition state is comparable with E2 antiperiplanar transition state (Figure 1).

The distance between basic sites of alumina and β , activation energy (E_a), and enthalpy (ΔH°) of the most stable conformers of adsorbed (*R*)- and (*S*)-2-butanol over the (100) surface were calculated to help shed light on the elimination reaction pathway. All basic oxygen sites of the surface at distances less than 4 \AA from β hydrogens were considered as a site for elimination and were included in our study.

References:

- [1] H. A. Dabbagh, J. Mohammad Salehi, J. Org. Chem. **63** (1998) 7619.
- [2] H. Pines, W. O. Haag, J. Am. Chem. Soc. **83** (1961) 2847.
- [3] H. Pines, C. N. Pillai, J. Am. Chem. Soc. **83** (1961) 3270.

Figure 1.



MULTIFUNCTIONAL ORGANIC FIELD-EFFECT TRANSISTORS BASED ON PENTYL-VINYL END-CAPPED OF ANTHRACENE AND TETRACENE**A.Dadvand,^{a,b} H.Meng,^c F.Cicoira,^d C.Santato,^e C.Harnagea,^a F.Rosei,^a D.F.Perepichka,^b**^a INRS-EMT, University of Quebec, ^b Department of Chemistry, McGill University, ^c DuPont Experimental Station, ^d Department of Materials Science, Cornell University, ^e Department of Physics, École Polytechnique de Montréal

Thin films of organic π -conjugated molecules are of great interest for devices such as field effect transistors (FETs), light emitting diodes, light emitting field effect transistors and photovoltaic cells.¹ Organic light emitting transistors (OLETs) have a similar architecture to organic field effect transistor (OFETs) and the intensity of electroluminescence (EL) is controlled by the drain and gate voltage. This structure is ideal for improving the EL quantum efficiency and lifetime of organic semiconductors (OSCs) due to the different driving conditions comparing to organic light emitting diodes OLEDs.²

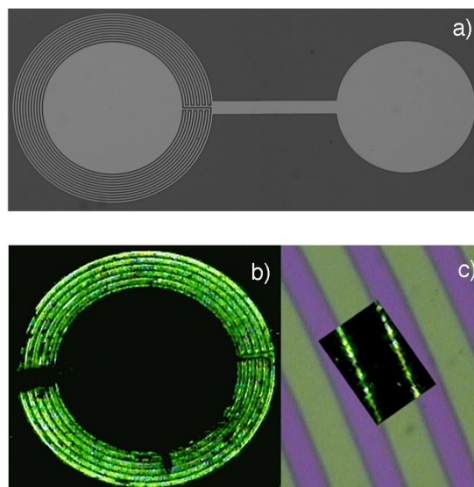
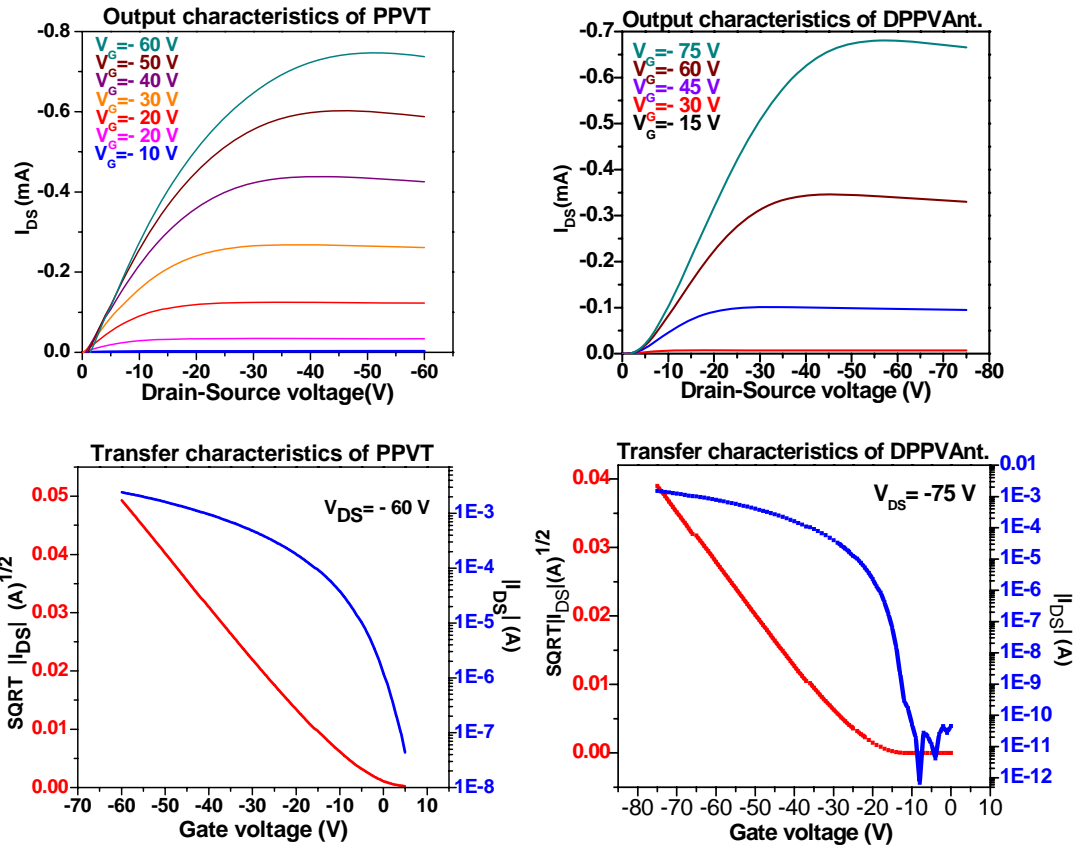
We compare new synthesized anthracene and tetracene derivative, 2,6-bis[2-(4-pentylphenyl)vinyl]anthracene (DPPVAnt) and 2-(4-pentylphenyl)vinyl tetracene] (PPVT)³, used as an active layer to fabricate OLETs. PPVT and DPPVAnt are conjugated trans-phenylvinylene substitutes linked to tetracene and anthracene cores, respectively, with a pentyl group as side chain.

For vacuum sublimated films of both compounds, we carried out optoelectronic characterisation in field effect transistor configuration and AFM study of the early stages of film growth. X-Ray diffraction (XRD) as well as various analytical techniques such as UV-Vis absorption and Fluorescence Spectroscopy was also used to study physical properties of the OSCs and thin film.

¹ C. Reese, M. Roberts, M. Ling, and Z. Bao, *Mater. Today*, **2004**, 7, 20; C. D. Dimitrakopoulos, and P. R. L. Malenfant, *Adv. Mater.*, **2002**, 14, 99; G. Horowitz, *Adv. Mater.*, **1998**, 10, 365; H.E. Katz, and Z. Bao, *J. Phys. Chem. B.*, **2000**, 104, 671; E. L. Williams, K. Haavisto, J. Li, and G. E. Jabbour, *Adv. Mater.*, **2007**, 19, 197

² C. T. Kuo, S. Z. Weng, *Adv. Tech.*, **2002**, 13, 753; H. Heil, W. Weise, M. Ahles, R. Schmechel, H. V. Seggern, *Phys. Rev. Lett.*, **2003**, 91, 157406-1; C. Rost, S. Karg, W. Riess, M. A. Loi, M. Murgia, M. Muccini, *Appl. Phys. Lett.*, **2004**, 85, 1613.

³ F. Cicoira, C. Santato, A. Dadvand, C. Harnagea, A. Pignolet, P. Bellutti, Z. Xiang, F. Rosei, H. Meng and D. F. Perepichka, *J. Mater. Chem.*, **2008**, 18, 158–160



Optical images of: a) Interdigitated bottom-contact device b) Green electroluminescence of PPVT-LET c) magnified contacts and localized light emission

SILICA-COATED COBALT BORIDE NANOPARTICLES SYNTHESIS, MAGNETIC CHARACTERIZATION AND FUNCTIONALIZATION

Ana B. Dávila Ibáñez,¹ Verónica Salgueiriño-Maceira*² José Rivas¹

¹Departamento de Física Aplicada, Universidade de Santiago de Compostela, 15782 Santiago de Compostela (Spain).

²Departamento de Física Aplicada, Universidade de Vigo, 36310 Vigo (Spain).

vsalgue@uvigo.es

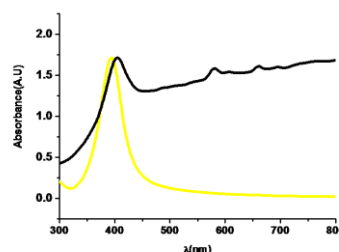
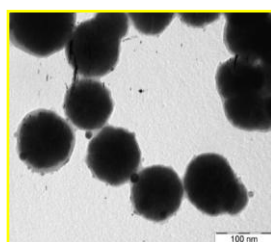
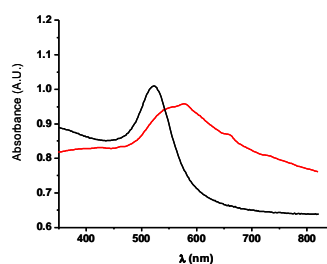
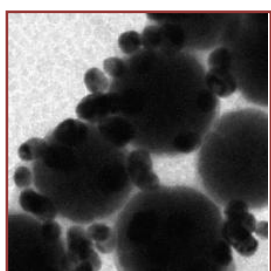
Herein we present a colloidal chemistry method for the synthesis of environmentally stable silica-coated cobalt boride nanoparticles, prepared combining the sodium borohydride reduction in aqueous solution and the silica precipitation in basic medium.^[1,2] Size of monodispersed silica-coated cobalt boride nanoparticles is controlled by this method. Additionally we highlight the further functionalization of the silica-coated cobalt nanoparticles using (3-aminopropyl) tris(trimethylsiloxy) silane. These attached amino groups are used as bridges (coupling chemistry) between the magnetic nanoparticles and gold and silver seeds, in such a way that we render the nanoparticles bifunctionalized (magnetic and optically active).

Figure 1 shows a TEM image of the gold/silver-decorated silica-coated cobalt boride nanoparticles and their UV-vis spectrum (red, yellow), maintaining the surface plasmon band of individual gold and silver nanoparticles (black) but red-shifted to 560 for gold (red) and 402 for silver (yellow).^[3]

References

- [1] V. Salgueiriño-Maceira, M. A. Correa-Duarte, *J. Mater. Chem.* **16**, 3593 (2006).
- [2] V. Salgueiriño-Maceira, M. A. Correa-Duarte, M. Farle, M. A. López-Quintela, K. Sieradzki, R. Díaz, *Langmuir* **22**, 1455 (2006).
- [3] Ana B. Dávila-Ibáñez, V. Salgueiriño-Maceira, J. Rivas, *in preparation* (2009).

Figures:



Fullerenes C₆₀ self-assembled on functionalized surfaces

Grégory Delafosse, Lionel Patrone, Didier Goguenheim
Institut Matériaux Microélectronique Nanosciences de Provence
CNRS IM2NP UMR 6242

ISEN-Toulon, Maison des Technologies, Place Georges Pompidou, F-83000 Toulon, France
gregory.delafosse@im2np.fr

Memory devices play an important role in electronics market leading to a growing research interest in the next generation of non-volatile memory cells. Numerous groups [1,2] work on top-down memory cells based on fullerenes C₆₀ that are generally embedded in insulating polymers where they act as storage sites. Beside these studies, a reaction path between amines and fullerenes [3] may be used to covalently bind C₆₀ on an amine-functionalized surface. Such an approach is interesting since it involves self-assembled monolayers (SAM) [4,5] which constitute a promising strategy to build molecular nano-devices. For applications compatible with microelectronics technology, it is very important to control first the formation of amine-terminated SAMs grafted on silicon, second the grafting of a C₆₀ monolayer on top of these SAMs. In this work, we studied these two steps in order to build memory cells using a bottom-up approach based on organic SAMs.

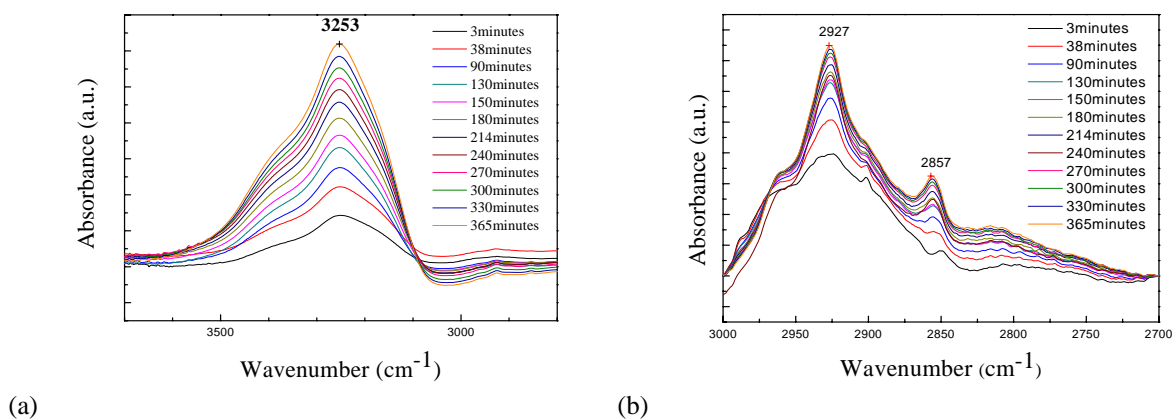
As substrates, we used silicon covered with its native oxide, and Au(111) for scanning tunnelling microscopy (STM) experiments. Surface modification is observed by contact angle measurements, ellipsometry, UV-visible and FTIR spectroscopy, and AFM/STM microscopy. Surface functionalization is performed using aminopropyltrimethoxysilane (APTMS) molecules for Si/SiO₂ surfaces, and aminothiophenol or aminoethanethiol for Au(111). We developed two methods to build APTMS SAMs on Si/SiO₂ substrates. Using APTMS in methanol solution, SAM formation was analyzed in order to obtain the right parameters leading to a single amine-functionalized monolayer. A second original way was studied using a dry deposition method. In the latest, freshly prepared clean substrates are exposed to APTMS vapor under a nitrogen flux, leading to the formation of APTMS SAM. This deposition method allowed us to show there is a minimum waiting time of ~4 hours under our conditions for the monolayer to be grafted on Si/SiO₂. APTMS SAM formation could be monitored using ATR-FTIR spectroscopy. Particularly, the increase of OH absorption band at ~3253 cm⁻¹ (Fig.1(a)) may be attributed to the formation of methanol due to the reaction between methoxysilane heads and silicon oxide. Moreover CH₂ band narrowing (Fig.1(b)) indicates the monolayer order is increasing during the grafting process. Fullerenes are then grafted from a toluene solution on these amine-functionalized SAMs. Two deposition conditions are compared: at room temperature and at high temperature under solvent reflux. AFM/STM experiments allowed monitoring fullerene deposition by either imaging (Fig.2) or I-V characteristics (Fig.3). Further studies are addressed such as thermal deposition of fullerenes [6], Surface Enhanced Raman Scattering on fullerenes grafted on nanostructured amine-modified gold substrates, and electronic transport properties of those C₆₀ SAMs via evaporated metallic contacts.

References:

- [1] A. Kanwal, M. Chowalla, "Stable, three layered organic memory devices from C60 molecules and insulating polymers", *Appl. Phys. Lett.* **89** (2006) 203103
- [2] H.S. Majumdar, J.K. Baral, R. Osterbacka, O. Ikkala, H. Stubb, "Fullerene-based bistable devices and associated negative differential resistance effect", *Organic Electronics* **6** (2005) 188
- [3] G.P. Miller, "Reactions between aliphatic amines and [60]fullerene: a review", *Comptes-Rendus Chimie* **9** (2006) 952

- [4] A. Ulman, "Formation and structure of self-assembled monolayers", Chem. Rev. **96** (1996) 1533
- [5] F. Schreiber, "Structure and growth of self-assembling monolayers", Progress in Surf. Sci. **65** (2000) 151
- [6] T.H. Hou, U. Ganguly, E.C. Kan, "Programable molecular orbital states of C₆₀ from integrated circuits", Appl. Phys. Lett. **89** (2006) 253113

Figures:



(a) (b)
Figure 1. ATR-FTIR spectra of dry-deposited APTMS SAM showing (a) the increase of OH absorption band, (b) the CH₂ band narrowing with time.

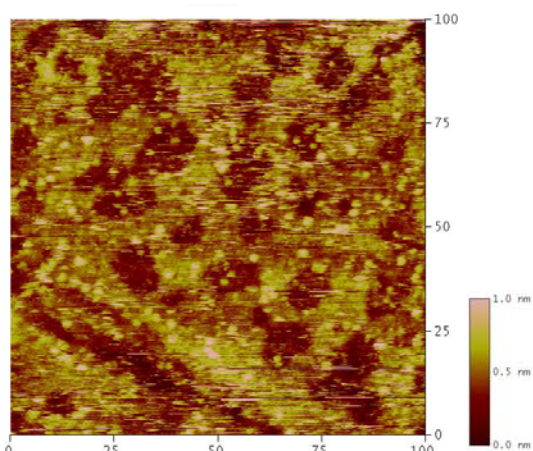


Figure 2. STM (100nm x 100nm) image of C₆₀ molecules grafted under reflux during 24 hours on NH₂ (aminoethanethiol) functionalized Au(111).

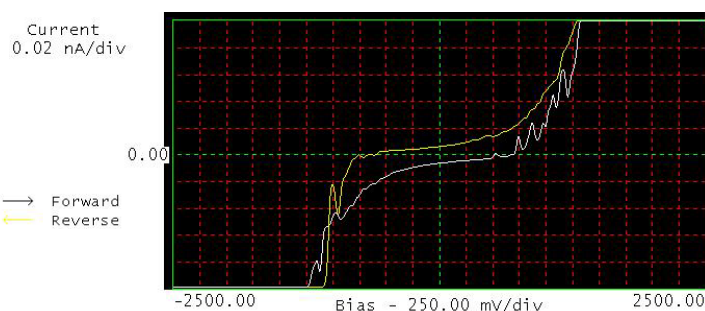


Figure 3. STM I-V characteristic of C₆₀ molecules grafted under reflux during 24 hours on NH₂ (aminoethanethiol) functionalized Au(111).

Electronic structure and inelastic transport through a single magnetic adatom

F. Delgado, J. Fernández-Rossier, and J. J. Palacios

Departamento de Física Aplicada, Universidad de Alicante, San Vicente del Raspeig, Alicante 03690, Spain

Recent works [1-7] show that inelastic electron scanning tunnelling microscope (STM) probes the elementary spin excitations of a single and a few magnetic atoms in a thin insulating layer as well as the interactions between spins in individual atomic-scale magnetic structures. The experimental data have been successfully explained in terms of a phenomenological model in which both, the tunnel process and the electronic structure of the magnetic atom, are described with spin operators [8]. Here we provide a microscopic understanding of these phenomenological spin-models. This is done in two steps.

We study the energy spectra of a magnetic atom embedded in an insulating layer. Configuration interaction (CI) method is used as a computational tool to study the system. In our approach, only electrons belonging to the incomplete d-shell of the magnetic ion (Mn^{2+} , Fe^{2+}), are considered. Effects of the surrounding atoms are accounted for by a point charge model, which permits to simulate different environments and strengths of this interaction. The model also includes Coulomb repulsion and spin orbit coupling. The combination of spin orbit and crystal field is crucial to derive the single ion magnetic anisotropy observed experimentally. The spectra of the magnetic atoms as a function of the intensity and direction of the magnetic field compare well with the simpler phenomenological single ion spin models.

Within this approach, inelastic spin assisted transport is described with a generalized Anderson model, while current is calculated up to second order in the tunnelling Hamiltonian (cotunnelling) [9]. For that matter, we derive an effective cotunnelling Hamiltonian using degenerate second order perturbation theory. This permits us to derive an expression for the inelastic current based upon a theory without effective spins. Thus, our theory provides a complete microscopic understanding of the origin of the spin assisted tunnelling spectroscopy.

Referencies:

- [1] A. J. Heinrich, J. A. Gupta, C. P. Lutz, D. M. Eigler, *Science*, **306** (2004) 466 .
- [2] Cyrus F. Hirjibehedin, Christopher P. Lutz, Andreas J. Heinrich, *Science*, **312** (2006) 1021.
- [3] Cyrus F. Hirjibehedin, Chiung-Yuan Lin, Alexander F. Otte, Markus Ternes, Christopher P. Lutz, Barbara A. Jones, Andreas J. Heinrich, *Science*, **317** (2007) 1199.
- [4] Alexander F. Otte, Markus Ternes, Kirsten von Bergmann, Sebastian Loth, Harald Brune, Christopher P. Lutz, Cyrus F. Hirjibehedin, and Andreas J. Heinrich, *Nature Physics*, **4** (2008) 847.
- [5] Xi. Chen, Ying-Shuang Fu, Shuai-Hua Ji, Tong Zhang, Peng Cheng, Xu-Cun Ma, Xiao-Long Zou, Wen-Hui Duan, Jin-Feng Jia, and Qi-Kun Xue, *Phys. Rev. Lett.*, **101** (2008) 197208.

- [6] N. Tsukahara, K. Noto, M. Ohara, S. Shiraki, N. Takagi, Y. Takata, J. Miyawaki, M. Taguchi, A. Chainani, S. Shin, M. Kawai, Phys. Rev. Lett., **102** (2009) 167203.
 [7] T. Balashov, T. Schuh, A. F. Takacs, A. Ernst, S. Ostanin, J. Henk, I. Mertig, P. Bruno, T. Miyamachi, S. Suga, and W. Wulfhekel, arXiv:0903.3337.
 [8] J. Fernandez-Rossier, arXiv:0901.4839.
 [9] J. A. Applebaum, Phys. Rev., **154** (1967) 633.

Fig. 1 Schematic upper view of a CuN surface. The magnetic ion forming the last contact point of the STM tip (green circles) is positioned over a Cu atom (yellow circles).

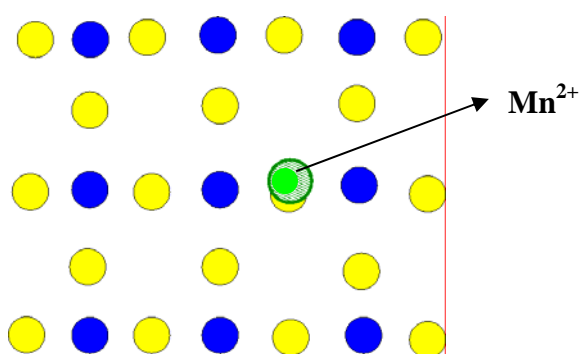
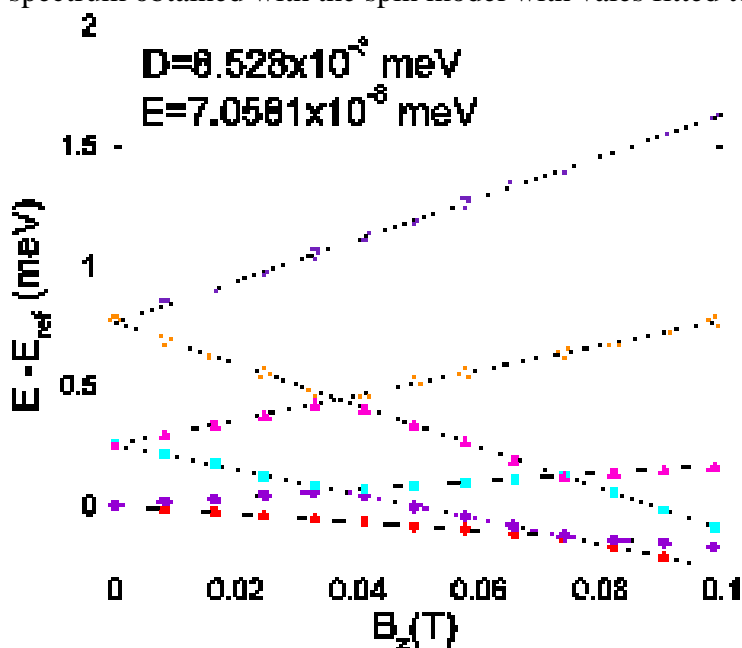


Fig. 2 Typical low energy spectrum of the Mn^{2+} ion in a tetragonal environment. Magnetic field is applied along the long axis (z-axis). Symbols correspond to the energy spectrum obtained with the spin model with vales fitted to the CI calculation at $B=0$.



ELECTRONIC TRANSPORT IN GOLD ELECTROMIGRATED NANOGAPS

M. L. Della Rocca, A. Mangin, A. Anthore, E. Boulat, P. Lafarge
Laboratoire Matériaux et Phénomènes Quantiques,
Université Paris Diderot-Paris 7, CNRS UMR 7162,
75205 Paris Cedex 13, France
maria-luisa.della-rocca@univ-paris-diderot.fr

Contacting nanometric objects between two metallic electrodes separated by a nanometric distance is the technological challenge at the basis of single molecular electronics. Among the different methods to realize single molecule device, such as scanning tunnel microscopy, mechanical controllable break junction, one of the most used is electromigration [1-3]. Electromigration takes place by applying a current ramp to a continuous nanowire; above a critical current density, the wind force resulting from momentum transfer from the electrons starts to displace gold atoms. A controlled electromigration technique can produce a nanogap, i.e. two electrodes separated by a distance even smaller than a nanometer.

A large number of phenomena have been observed in electromigrated single molecule quantum dot, like single electron effects such as Coulomb blockade and Kondo effect [4–6]. Anyway very often metallic clusters can remain in between the electrodes simulating a molecular behaviour [7]. This point raises the question of characterizing the nanogap even before inserting a molecule. An appropriate description of electron transport through the small space electrode separation, even in absence of molecules, can give a better control of the quality of the future device.

I will present a careful analysis of the current voltage characteristics (I/V) of fresh electromigrated nanogaps at low temperature. The I/V curves exhibit two transport regimes, direct tunneling with a linear dependence at low voltage and field emission with an exponential growth at higher voltage. We describe transport properties in the framework of electron tunneling through a trapezoidal barrier, showing that a 1D as well as a planar junction tunneling model can describe the whole curves for samples with very different tunnel resistances. We find that it is possible to quantitatively extract geometrical and physical parameters characteristics of these structures.

Knowing the size of fresh electromigrated nanogap is an essential precondition to obtain good quality single molecule devices. The quantitative description we propose could infer such properties more exactly.

References:

- [1] H. Park, A.K.L. Lim, A.P. Alivisatos, J. Park, P.L. McEuen, *Appl. Phys. Lett.*, **75** (1999) 301.
- [2] D. Strachan, D.E. Smith, D.E. Johnston, T.-H. Park, M.J. Therien, D.A. Bonnel, A.T. Johnson, *Appl. Phys. Lett.*, **86** (2005) 043109.
- [3] K. O'Neill, E.A. Osorio, H.S.J. van der Zant, *Appl. Phys. Lett.*, **90** (2007) 133109.
- [4] J. Park, A.N. Pasupathy, J.I. Goldsmith, C.Chang, Y. Yaish, J.R. Petta, M. Rinkoski, J.P. Sethna, H.D. Abruña, P.L. McEuen, D.C. Ralph, *Nature*, **417** (2002) 722.
- [5] J. Thijssen, H.S.J. van der Zant, *Physica Status Solid (b)*, **245** (2008) 1455.
- [6] E. Osorio, T. Bjornholm, J.M. Lehn, M. Ruben, H.S.J. Van der Zant, *Jour. Phys.: Cond. Mat.*, **20** (2008) 374121.
- [7] A. Mangin, A. Anthore, M.L. Della Rocca, E. Boulat, P. Lafarge, *Jour. Appl. Phys.*, **105** (2009) 014313.

IMPROVEMENT OF DYE SENSITIZED SOLAR CELLS (DSSCS) ENERGY EFFICIENCY BY CARBON NANOTUBES (CNTS) INCORPORATION IN THEIR ACTIVE LAYER.

Kadiatou Thérèse Dembélé; Federico Rosei, Enrico Traversa, Sylvia Licoccia, Clara Santato.

The sun is a most inexhaustible and available renewable energy source, it is why photovoltaic cells have attracted much interest in the scientific world. However, the first photovoltaic cells based on silicon have good energy efficiency but are expensive and are not very accessible because of their cost.

Graetzel cells commonly called DSSCs (Dye Sensitized Solar Cells) were studied and searched over the last decade as the third generation of photovoltaic cells because of their potential low-cost manufacturing based on printing technology. However, the energy efficiency of DSSCs remains low compared to those of conventional solar cells. To make DSSCs more competitive, it is important to study their characteristics and energy efficiency by incorporating in the active layer the materials which may improve the conduction and / or absorption in the cell.

Carbon nanotubes (CNTs) are very interesting materials because of their extraordinary physical properties. Some reports have shown that the incorporation of CNTs in a film of polymer poly (3-octylthiophène) increases the electrical conductivity of the film. A composite of poly (p-phenylene vinylene) with CNTs in a photovoltaic device shows good quantum efficiency.

However, this incorporation may be advantageous or not if we do not use good concentrations of these nanotubes. In this study we use MWCNTs (because of their electrical conductivity and low cost) in addition to titanium oxide (TiO_2) in the cell active layer and investigate the optimum condition of using these MWCNTs.

Design of New Polyaromatic Scaffolds for Nano-Scale Molecular Electronics

Paula de Mendoza, Thorsten Lauterbach, Catelijne H. M. Amijs, Antonio M. Echavarren
Institute of Chemical Research of Catalonia (ICIQ)
 Av. Països Catalans 16, 43007 Tarragona.
 pmendoza@iciq.es

In the last decade, design and synthesis of polyaromatic scaffolds have attracted much interest due to their exceptional properties and their potential applications in material science [1] and in molecular electronic devices. [2]

PicoInside, an integrated European project, aims at computing inside a single molecule using atomic scale technologies. [3] Our participation consists on the design and synthesis of Y-shaped polyaromatic molecules, like starphenes, that could be applied as molecular *OR logic gates* in an integrated intramolecular circuit.

Herein, we present divergent synthetic approaches for the synthesis of a series of three branched polyaromatic scaffolds that we have designed as promising candidates for their application as molecular switching units. Furthermore, preliminary studies carried out to investigate their properties towards their potential implementation, like deposition on isolating surfaces and LT-UHV-STM images, will be presented.

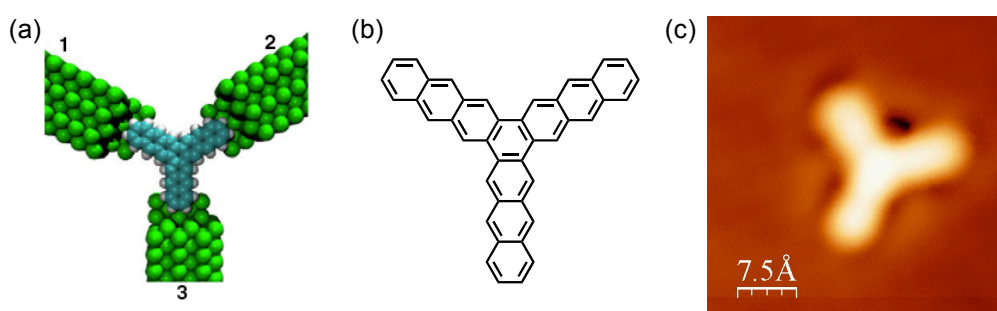


Figure 1: (a) Design, (b) synthesis and (c) LT-UHV-STM image of dianthra[a,c]naphthalene *OR logic gate* molecule.

Acknowledgements. We thank support by the MEC (CTQ2007-60745/BQU, Consolider Ingenio 2010, Grant CSD2006-0003), the AGAUR, European Commission (FP6-015847, Pico-Inside IST Integrated Project) and the ICIQ Foundation.

References:

- [1] Anthony, J. E. *Chem Rev.* **106** (2006) 5028
 [2] (a) Joachim, C. Gimzewski, J. K. Aviram. A. *Nature*, **408** (2000) 541. (b) Jlidat, N. Hilwa, M. Joachim, C. *Chem. Phys. Lett.* **470** (2009) 275.
 [3] Gourdon, A. *NanoLetters* **4** (2006) 22.

DE BROGLIE TAMM STATES OF DIAMOND QUANTUM DOT

I.A. Denisov¹, P.I. Belobrov², S.S. Tsegelnik¹, L.A. Solovyov³, N.P. Shestakov², D.A. Znak¹, V.A. Arbuзов¹, A.S. Krylov², S.B. Korchagina⁴, A.A. Latynina¹, N.V. Volkov², S.K. Gordeev⁴

¹*Siberian Federal University, 660074 Krasnoyarsk, Russia*

²*Kirensky Institute of Physics & Institute of Biophysics SB RAS, 660036 Krasnoyarsk, Russia*

³*Institute of Chemistry and Chemical Technology SB RAS, 660049 Krasnoyarsk, Russia*

⁴*Central Research Institute of Material, 191014 St. Petersburg, Russia*

d.ivan.krsk@gmail.com

The exact definition: thermodynamically stable diamond with size of 2-6 nm is called diamond quantum dot (DQD). DQDs with phantom (or random) doping were produced by the explosion method. These detonation DQDs are called with an uncertain word nanodiamond which is understood as DQD units more often. DQDs are widely used in biology and medicine, since the first pioneer works on interaction DQD with fibers [1, 2]. The recent review describes small toxicity of nanodiamond [3]. The production of DQD from high purity carbon black with the sizes of particles 2-6 nanometers proofs their thermodynamic stability. Such nanodiamonds possess a photoluminescence after simple surface passivation by polyethylene glycol [4].

DQD model has been offered for the first time in [5-7] on the basis of EPR, PEELS and Auger data and recently has been confirmed in [8, 9] by researches of magnetisation and ¹³C NMR spin-lattice relaxation. We offer following exact «watermelon» model of DQD based on representation about de Broglie Tamm states lie and detailed researches of magnetic properties of semiconductors made from DQD and graphen flakes [10].

Tamm has started the consideration of 3D structures on a diamond surface. Precisely having solved a problem about superficial electronic states in a perpendicular to section border dimension between dielectric and vacuum Tamm has suggested to consider for two-dimensional border of section electronic waves de Broglie with energy of an order of the diamond cohesion energy which size is 0.1 eV (800 cm⁻¹). The energy agrees with a 4 nm de Broglie wave length. These states we called de Broglie Tamm states (DBTS).

FTIR spectroscopy shows changes in a range 50-400 meV depending on surface states at (Fig.2). DQD model based on the assumption that DBTS is universal and has the identical nature in DQD and on a surface of diamond single crystal. In oscillatory system of DQD there is a set of harmonics on surface which their own frequencies of the complex self-consistent electronic-vibration structure of a shell and a core of DQD. The frequencies are deformation fluctuations of a 1 nm thickness surface of stable DQD that is agreed with a recent work [9] where it is offered core#shell model.

On model of Brillouin the analysis of the magnetisation data were made. By results of the analysis (Table 1) concentration of the paramagnetic centres have amount $\sim 5-7 \times 10^{19}$ spin/g that approximately means 7-10 free electronic spins on a particle. Diamond is diamagnetic but DQD are paramagnetic, and paramagnetism does not depend almost on temperature that is unusual. The assumption that DQD consists from ordered diamagnetic core defended by a weak-ordered paramagnetic shell take off this contradiction. The paramagnetic component is consist in collective electron oscillatory de Broglie Tamm states so the diamond crystal less big amount of this states. Additional argument is the given nuclear magnetic resonances ¹³C: 70% of the deformed communications sp³ and only 30 % normal sp³ [9].

The model allows estimating that several electrons participate in collective electron oscillation resonances of superficial de Broglie waves which are observed in a low-energy part of PEELS spectrum. The model qualitatively explains the existence of invariance in paramagnetic properties and Auger-process characteristics at X-ray excitation. Bioimaging and drug delivery is really to carry out by means of DQD. Magnetic tomography of DQD allows imaging of weakly-transparent objects. The management of the porous membrane molecular penetrability based on DQD-graphene flakes composite (Fig.1) properties is useful for steady-state drug delivery systems.

This research was supported by RFBR Grants 07-04-01340-a and 08-02-00259-a, ME&S of RF Grant No. 2.2.2.2/5309 and U.S. CRDF Grant RUX0-002-KR-06/BP4M02.

References:

- [1] V.A. Bondar, A.P. Puzyr. Doklady Biochemistry, **373** (2000) 129.
- [2] A.P. Puzyr, V.S. Bondar, P.I. Belobrov and A.A. Bukaemskii, Doklady Biochemistry, **373**, (2000) 139.
- [3] Y. Xing; L. Dai, Nanomedicine, **4** (2009) 207.
- [4] S. Hua, F. Tian, P. Bai, S. Cao, J. Sun and J. Yang, Mater. Sci. Engin.: B., **157** (2009) 11.
- [5] P.I. Belobrov, S.K. Gordeev, E.A. Petrakovskaya and O.V. Falaleev, Doklady Physics, **46** (2001) 459.
- [6] J.L. Peng, S. Bulcock, P. I. Belobrov, L.A. Bursill, Intern. J. Mod. Phys. B, **15** (2001) 4071.
- [7] P. I. Belobrov, L. A. Bursill, K. I. Maslakov and A. P. Dementjev, Appl. Surf. Sci., **210** (2003) 169.
- [8] E. M. Levin, X. W. Fang, S. L. Bud'ko, W. E. Straszheim, R. W. McCallum, and K. Schmidt-Rohr, Phys. Rev. B. **77** (2008) 054418.
- [9] XiaoWen Fang, JingDong Mao, E. M. Levin and Klaus Schmidt-Rohr, J. Am. Chem. Soc, **131** (2009) 1426.

Figures:

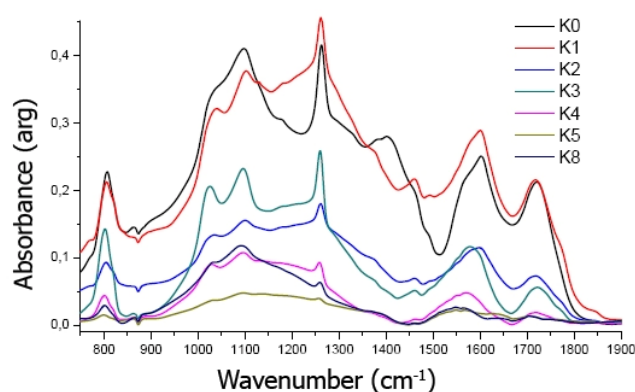
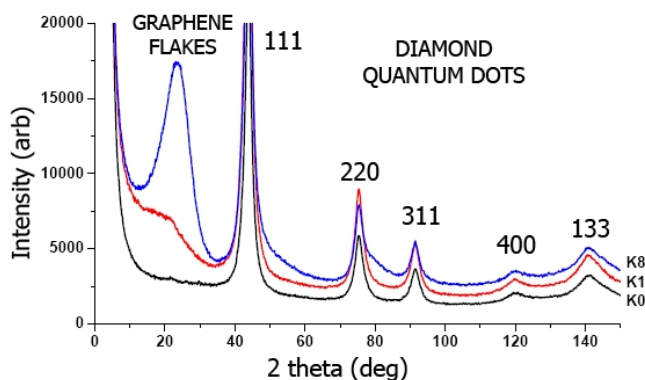


Fig.1. X-ray diffraction pattern of composites. Scherrer' coherent length is used in Tabl.1

Fig.2. FTIR spectrum of diamond-graphene flakes composites

Table 1. The results of X-rays and magnetism data analysis

No	Diamond, g	Graphene flakes, g	Spins per gramm	Susceptibility, χ	L, nm	C atoms in a particle	Spins per particle
0	1	0	$6,96 \times 10^{19}$	$4,15 \times 10^{-6}$	5,25	5113	7
1	0,91	0,09	$5,46 \times 10^{19}$	$-1,58 \times 10^{-6}$	4,96	4567	5,5
2	0,83	0,17	$5,81 \times 10^{19}$	$-2,14 \times 10^{-6}$	5,26	5130	7,1
3	0,77	0,23	$5,46 \times 10^{19}$	$-1,55 \times 10^{-6}$	5,38	5365	7,6
4	0,71	0,29	$6,60 \times 10^{19}$	$-2,00 \times 10^{-6}$	5,59	5787	10,6
8	0,56	0,44	$6,58 \times 10^{19}$	$-3,85 \times 10^{-6}$	4,81	4295	10,1

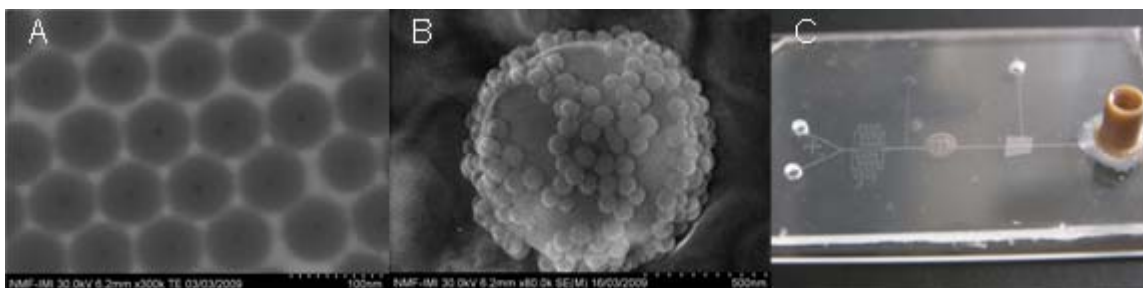
MULTIFUNCTIONAL NANOPROBES AND INTEGRATED MULTI-TRANSDUCTION SENSOR PLATFORM.

Céline Desvaux¹, Liviu Clime¹, Kebin Li¹ and Teodor Veres¹.

¹ Institut des matériaux industriels, NRC-CNRC, 75, boulevard de Mortagne, Boucherville, Québec, J4B 6Y4, Canada.

Rapid and reliable detection of pathogens is a key issue in a large number of domains including medicine, environment, food industry or military sector. We therefore developed in parallel multifunctional nanoprobess (MNPr) in order to label, confine and detect pathogens and a microfluidic chip to mix, incubate, concentrate and detect the pathogens.

The multifunctional nanoprobess were designed as follows. The core of the probe consisted of high magnetic FeCo nanoparticles for magnetic concentration mixed with Raman enhancing gold nanoparticles for SERS optical detection. This core was embedded into a silica shell, providing biocompatibility, loaded with nitrobenzenethiol, a fluorescent and Raman active molecule. The surface of the probe was amine functionalized and bio-conjugated to the appropriate antibody for specific detection of *Staphylococcus Aureus*. Incubation of the nanoprobess with simulated bacteria led to agglomeration of the probes on the surface of the bacteria. We also designed and fabricated a microfluidic chip as a platform for the integrated recognition-detection process. Basic microfluidic operations as mixing, incubation, capture and detection of bacteria can be integrally performed on this chip. It consists of two inlets, a meander mixer with three branches, an incubation chamber (reservoir with posts), a filtering module and three outlets. The manipulation of the liquid inside this chip is achieved by controlling the external pressure at the outlets. The multifunctional nanoprobess and bacteria are introduced by the two inlets, mixed together and incubated for a few tens of minutes into the reservoir. The separation of bonded from unbonded particles (elimination of the false positive signal) is achieved by forcing the liquid to pass from reservoir through the porous (filtering) membrane where the final detection takes place. This device allows us to effectively and selectively detect pathogens in very small volumes ($\sim 10\mu\text{L}$) and in few tens of minutes.



A- Multifunctional nanoprobess; B- MNPr agglomerated onto a simulated bacteria; C- Microfluidic chip.

Dynamic Behavior and Noise Propagation of Kelvin Force Microscopy

Heinrich Diesinger, Dominique Deresmes, Jean-Philippe-Nys, and Thierry Mélin
 Institut d'Electronique Microélectronique et Nanotechnologie, Av. Henri Poincaré,
 F-59652 Villeneuve d'Ascq, France
heinrich.diesinger@isen.iemn.univ-lille1.fr

The bandwidth of scanning probe control loops limits the sampling rate in data acquisition. In this work, the dynamic behavior of amplitude detection (AM) and frequency detection (FM) Kelvin force microscopy (KFM) setups is analyzed and optimized. Since enhanced bandwidth alone would increase speed at the expense of tolerating more noise, the origin of noise and its propagation within the control loops must be studied in parallel.

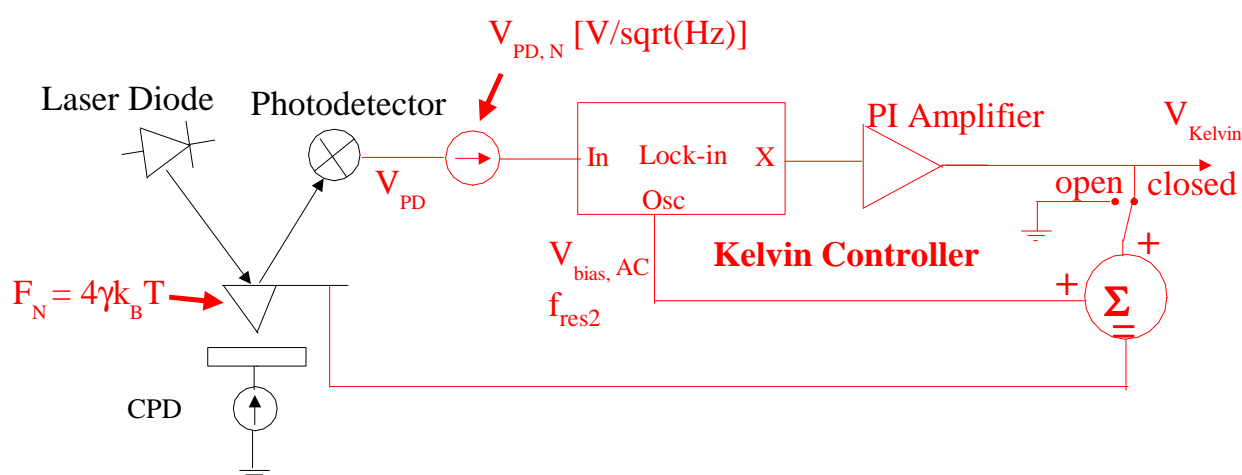


Figure 1: Setup of the Kelvin control loop of an AM-KFM, consisting of a lock-in amplifier exciting the probe electrostatically at its second resonance frequency, and a PI error amplifier that applies the Kelvin voltage to the probe. The loop can be opened. Main noise sources are the thermal probe excitation force and white noise at the output of the photodetector.

Fig. 1 shows the Kelvin control loop of an AM-KFM in ultrahigh vacuum, using the second cantilever resonance for KFM while distance control is based on the first, similar to the setup demonstrated by Kikukawa et al.[1]. The noise power spectral density of the Kelvin output signal can be modeled after the transfer functions of the different stages have been measured in open loop configuration. Criteria for comparing hardware from different manufacturers with respect to noise are proposed. An FM KFM setup close to the configuration suggested by Kitamura [2] is also analyzed. Advantages and drawbacks of both methods in terms of bandwidth and signal to noise are discussed.

References:

- [1] A. Kikukawa, S. Hosaka, and R. Imura, Appl. Phys. Lett., **66** (1995) 3510.
- [2] S. Kitamura and M. Iwatsuki, Appl. Phys. Lett., **72** (1998) 3154

MC SIMULATION OF WATER MENISCUS IN NANOCAVITIES

M. Douas^{1,2*}, P.A. Serena², M.I. Marqués¹

¹ *Departamento de Física de Materiales, C-IV, Facultad de Ciencias, Universidad Autónoma de Madrid, 28049 Madrid, Spain.*

² *Instituto de Ciencia de Materiales de Madrid, Consejo Superior de Investigaciones Científicas, Campus de Cantoblanco, 28049 Madrid, Spain..*

*e.mail: maysoun.douas@icmm.csic.es

The study of properties of water confined in complex systems with nanometric dimension is relevant to many important processes ranging from industrial applications (water membranes, filtering, etc) to biological processes (protein folding, ionic transport through membranes,...) [1]. In these systems, the water behavior is determined by the large surface/volume ratio as well as the non negligible interaction between water and container. Changes in thermodynamics, phase behavior and molecular mobility of water have been observed upon confinement [2].

In particular, we are interested in the behavior of the water menisci formed in different nanometric cavities. For example, in closed geometries, we have studied the structural effects of the capillary forces on viruses collapse during the final stage of desiccation see Figure 1. [3, 4]. Another interesting problem, with technological relevance, is how the formation of a nanometric water menisci may modify the light propagation in photonic waveguides formed by void structures (as inverse opals) and may change properties like the refraction index. These changes open a way for the design of photonic materials with controllable properties (for instance, under control of relative humidity).

In this paper we will show how lattice gas models used to mimic water behavior and solved by Monte Carlo calculations Figure 2[5] together with electromagnetic and finite element structural force calculations may be used to tackle a large variety of these interesting problems, as those mentioned above.

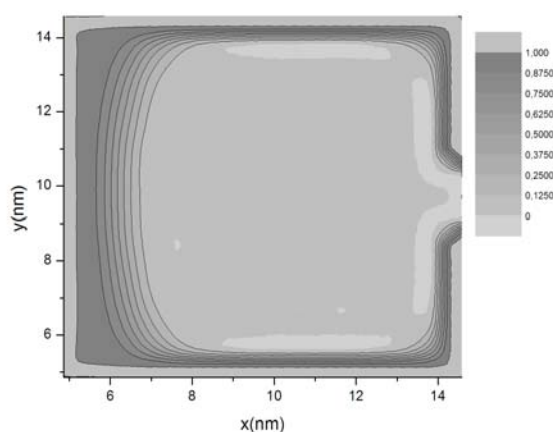


Figure 1. Last stage of the desiccation process for a simulated model virial capsid, over an average of 1000 viruses

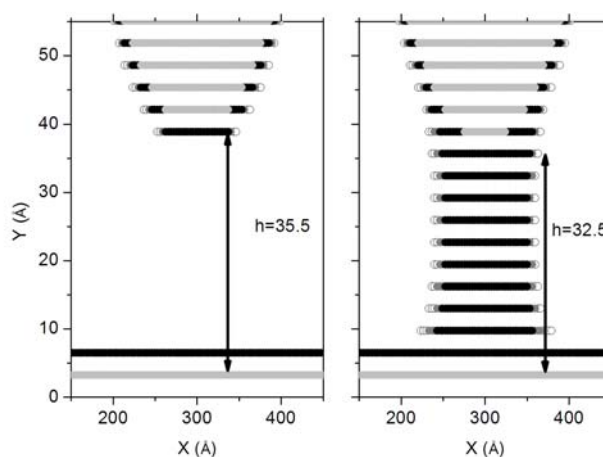


Figure 2. MC simulation of a water bridge formation between an AFM tip and a flat surface, both hydrophilic. Formation of the water nano-neck takes place at a distance of 33 Å for the set of parameters considered (T=294.62K, RH=70%).

References:

[1] Special issue on Nanoconfined water. *J. Phys. Condens. Matter.* 16 (2004) pp.S5257-S5470.

[2] See f.i. M. Rovere (ed.) *J. Phys.: Condens. Matter* 16, (45), (2004) 1.

[3] C. Carrasco, M. Douas, R. Miranda, M. Castellanos, P.A. Serena, J.L. Carrascosa, M.G. Mateu, M.I. Marqués, P.J. de Pablo, *Proceedings of the National Academy of Sciences.* 106, (14), (2009).

[4] P.A. Serena, M. Douas, M.I. Marqués, C. Carrasco, P. J. de Pablo, R. Miranda, J. L. Carrascosa, M. Castellanos, M. G. Mateu *Phys. Stat. Solidi C "Proceedings of TNT 2008 Trends in Nanotechnology"* (accepted).

[5] J. Y. Jang, G.C. Schatz, M.A. Ratner, *Phys. Rev. Lett.* 92, (8), (2004) 085504.

SELECTIVE GROWTH OF CARBON NANOTUBES BY MICROWAVE IRRADIATION

Tamara Druzhinina¹, Stephanie Hoepfener^{1,2}, Ulrich S. Schubert^{1,2}

¹*Laboratory of Macromolecular Chemistry and Nanoscience, Eindhoven University of Technology, P.O. Box 513, 5600 MB Eindhoven, The Netherlands*

²*Laboratory of Organic and Macromolecular Chemistry, Friedrich-Schiller-University Jena, Humboldtstr. 10, D-07743 Jena, Germany
t.s.druzhinina@tue.nl*

Microwave-assisted synthesis is of increasing interest. Besides the fact, that the reaction kinetics can be positively influenced by the use of microwave irradiation, advanced reaction conditions can be applied.[1,2] Moreover, the absorption of the microwave radiation depends on the material properties, thus resulting in a selective heating mechanism.[3-5] A detailed investigation of the selective heating of surface bound iron nanoparticles provided first experimental evidence for this effect by utilizing a self-assembled monolayer of *n*-octadecyltrichlorosilane (OTS), which acts as a sensitive indicator for locally elevated temperatures.

This selective heating process was furthermore used to grow carbon nanofibers and nanotubes on nickel catalyst. By using ethanol as a carbon source, provided by a liquid reservoir which is located beneath the sample, a flux of highly flammable and explosive feeding gas mixtures was avoided. As a result carbon nanotubes (CNTs) were synthesized in short times scales of a few minutes only. The synthetic approach can be applied also to obtain patterned carbon nanotube films which indicate a homogeneous growth of the tubes (Figure 1).

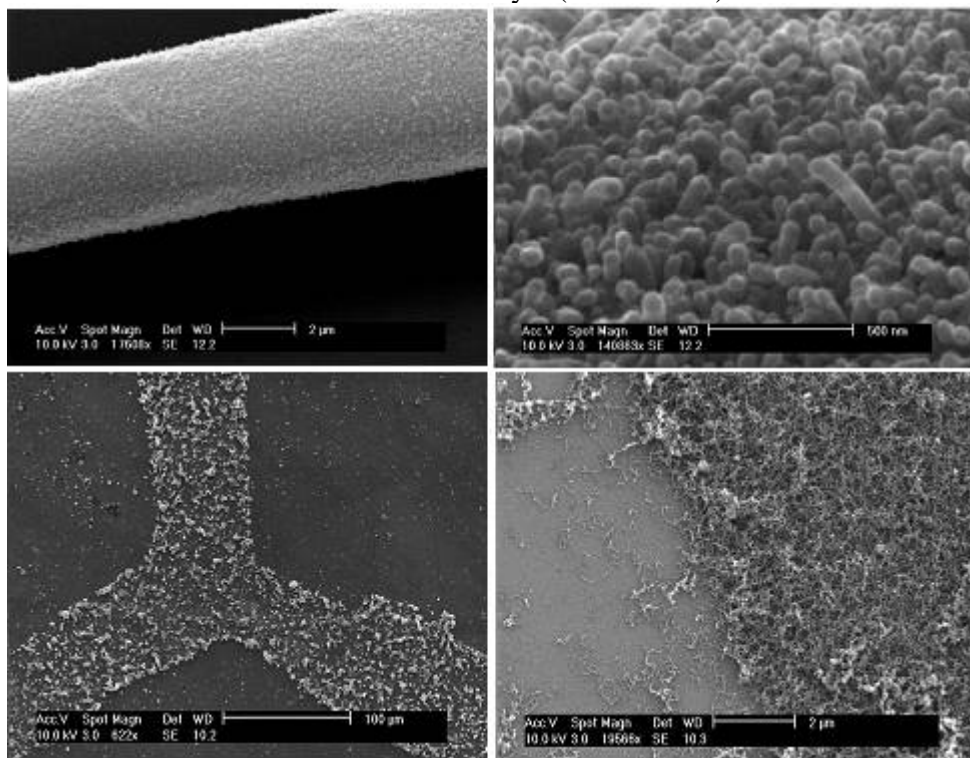
The investigation of the reaction conditions by analysis of temperature and pressure curves permitted [6] the determination of the reaction conditions. These investigations led to a significant improvement of the developed method and resulted into the controllable synthesis of defined carbon nanotubes and carbon nanofibers systems. This microwave-assisted method provides advantages over conventionally used methods, i.e., the reduced reaction time, the lower overall exposure temperature of the substrates and its potential for the integration of one-dimensional carbon material into predefined device frameworks consisting of different materials.

References:

- [1] Kappe, C.O. *Angew. Chem. Int. Ed.*, **43** (2004) 6250; Kappe, C.O. *Angew. Chem.*, **116** (2004) 6408.
- [2] Iannelli, M.; Alupei, V.; Ritter, H. *Tetrahedron*, **61** (2005) 1509.
- [3] Hong, E.H.; Lee, K.-H.; Oh S.H.; Park, C.-G. *Adv. Funct. Mater.*, **13** (2003) 961-966.
- [4] Hong, E.H.; Lee, K.-H.; Oh S.H.; Park, C.-G. *Adv. Mater.*, **14** (2002) 676-679.
- [5] Druzhinina T., Weltjens W., Hoepfener S., Schubert U.S. *Adv. Funct. Mater.*, **19** (2009) 1287-1292.
- [6] Druzhinina T., Hoepfener S., Schubert U.S. *Adv. Funct. Mater.*, (2009) in press

Figures:

Figure 1. SEM images of patterned growth of carbon nanofibers from iron catalyst (top row) and carbon nanotubes from nickel catalyst (bottom row)



**CHEMISTRY ON THE NANOMETER-SCALE – ELECTRO-OXIDATIVELY
GENERATED NANOMETER PATTERNS FUNCTIONALIZED BY SELF-
ASSEMBLED MONOLAYERS**

*Tamara Druzhinina¹, Stephanie Hoepfener^{1,2}, Claudia Haensch¹, Nicole Herzer¹, Ulrich
S. Schubert^{1,2}*

*¹Laboratory of Macromolecular Chemistry and Nanoscience, Eindhoven University of
Technology, P.O. Box 513, 5600 MB Eindhoven, The Netherlands*

*²Laboratory of Organic and Macromolecular Chemistry, Friedrich-Schiller-University
Jena, Humboldtstr. 10, D-07743 Jena, Germany
t.s.druzhinina@tue.nl*

The use of chemically active surface templates to perform chemical reactions and self-assembly on the nanoscale has been identified as a powerful approach towards nanofabrication. The structures are inscribed to a self-assembled monolayer of *n*-octadecyltrichlorosilane (OTS) by means of a conductive SFM tip, which locally initiates the electrochemical oxidation of the terminal –CH₃ groups of the monolayer into reactive –COOH groups.[1] They provide chemically active surface templates with a resolution down to ~ 10 nm and allow for the site-selective assembly of additional (functional) monolayers, the self-assembly of nanomaterials (e.g. nanoparticles and nanotubes) and the performance of chemical reactions directly on the structures.[2]

The combination of different modification schemes and the sequential patterning of the OTS monolayer represents a powerful toolbox for nanofabrication consisting of functionalization approaches that hold promises to develop strategies to assemble complex device features. We provide an overview about recently developed modification strategies, including click chemistry functionalization on nanometer scale patterns, the site-selective growth of polymer brushes on functional precursor monolayers and the combination of different monolayers to pattern surfaces sequentially with different chemical functionalities (Figure 1). Different examples will be highlighted.

These modification schemes are seen to be important building blocks towards the step-by-step fabrication of functional device features.

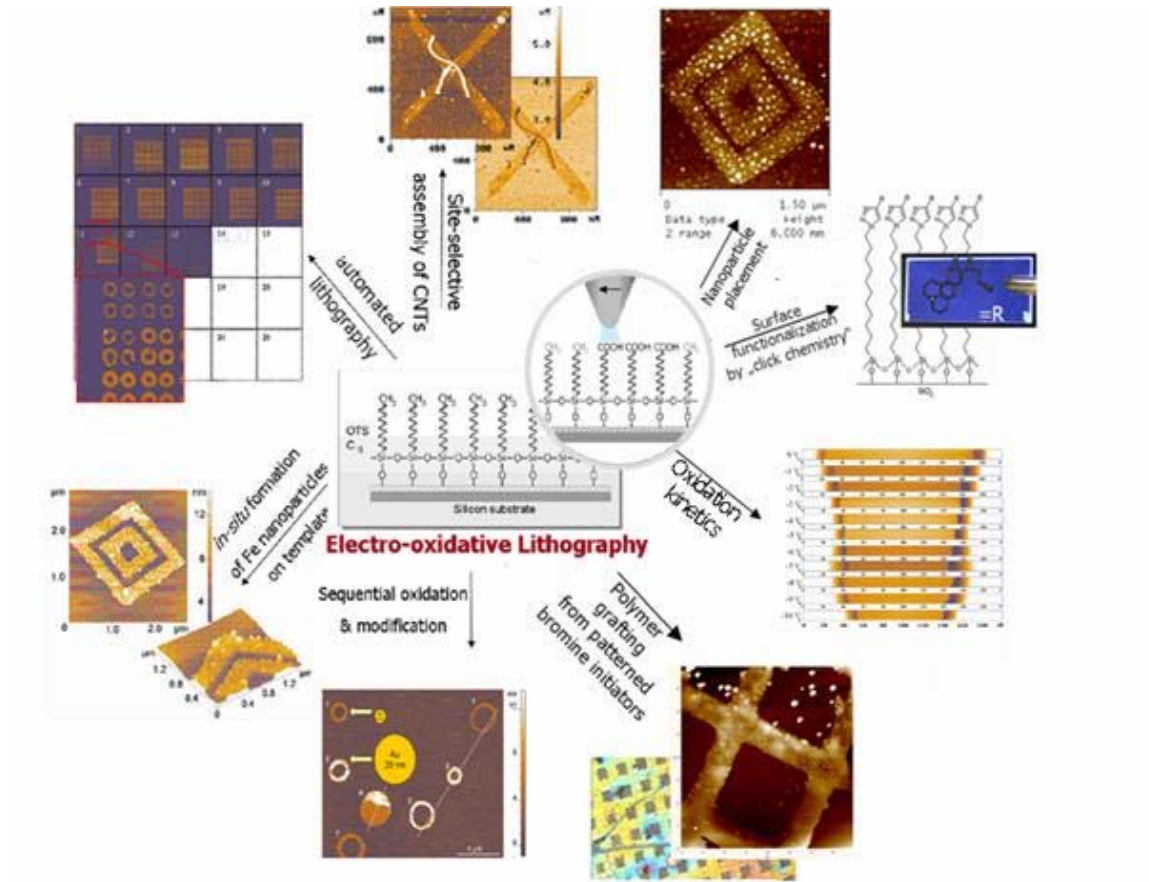
References:

[1] R. Maoz, E. Frydman, S.R. Cohen, J. Sagiv, *Adv. Mater.*, **12** (2000) 725

[2] D. Wouters, S. Hoepfener, U.S. Schubert, *Angew. Chem. Int. Ed.*, **48** (2009) 1732

Figures:

Figure 1. Different modification approaches to obtain functional nanostructures.



Structural phase transitions in zincblende III-V nanowires

V.G. Dubrovskii, G.E. Cirlin, N.V. Sibirev

Ioffe Physical Technical Institute RAS

St.-Petersburg Physics and Technology Centre for Research and Education RAS

C.Sartel, J.C. Harmand, J. Patriarche, and F. Glas

CNRS-LPN, Route de Nozay, 91460 Marcoussis, France

e-mail: dubrovskii@mail.ioffe.ru

Introduction. A rapidly growing interest in self-standing semiconductor NWs ranges from fundamental physics of their growth, transport and optical phenomena to many promising applications in nanoelectronics, nanophotonics and nanosensors. One of the most surprising features of these NWs is that their crystal structure may differ from that in bulk form. Recent studies demonstrate that III-V NWs of cubic (CUB) zinc blende (ZB) materials often adopt HEX wurtzite (WZ) structure. This phenomenon has been reported for most ZB compounds, both for Au-assisted [1-4] and selective area [5] growth. Recently, HEX diamond lattice was experimentally observed in Si NWs [6]. In many cases, the structure of NWs is not stable and exhibits a spontaneous switching between different phases, creating rotational twins and stacking faults. This clearly impedes material properties, so the control over the phase purity is now considered as one of the main challenges in NW technology.

Experimental facts. As shown in Refs. [7] and [3], given the prevalence of HEX phase in III-V NWs, CUB phase systematically appears at the initial and final stages of growth (Figs. 1 and 2). This strongly suggests that CUB phase forms when the supersaturation is less than some critical value and that HEX formation requires a *high supersaturation*. We therefore conclude that the nucleation kinetics plays an important role in crystal structure. The CUB to HEX transition can not be entirely determined by a lower surface energy of HEX NWs [8,9]. While the latter should be indeed smaller in HEX than in CUB phase, the estimates of Refs. [8] and [9] provide the values of critical radii of transition in order of magnitude smaller than the experimentally observed HEX NWs.

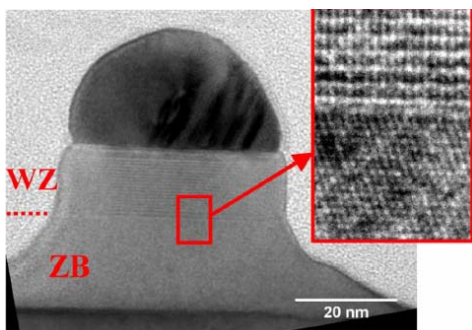


Fig. 1. TEM image of a short GaAs NW with high resolution close-up of transition zone between CUB ZB and HEX WZ [7].

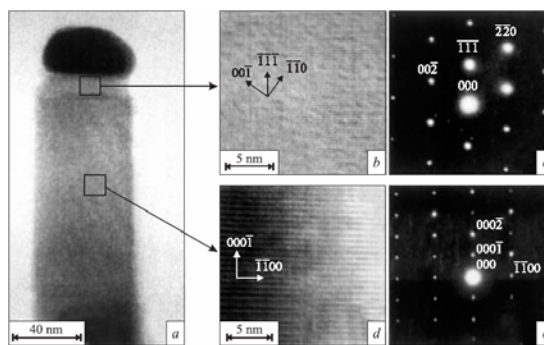


Fig. 2. TEM image of top section of GaAs NW (a, b, d) and electron diffraction patterns (c, e), showing the HEX (d, e) to CUB (b, c) transition at the NW top [3].

Theoretical model. To explain and analyze the peculiarities of CUB to HEX transformation in different III-V NWs, we have developed the model of NW growth and crystal structure [11]. The model accounts for the following

verified facts: (i) the formation of NWs is strongly influenced by the Gibbs-Thomson effect of elevation of chemical potential in the drop [9]; (ii) the growth of Si and III-V NWs is controlled by the diffusion of adatoms from the substrate surface to the NW top [2,10]; (iii) the VLS growth on the NW top is mediated by 2D nucleation, which often takes place at the triple line (TL) rather than in the centre I of the liquid-solid interface [7]. We also allow for the formation of NWs in CUB and HEX phase with different surface energies of lateral facets, characterized by coefficient $\tau \equiv \gamma_{HEX} / \gamma_{CUB}$. In view of fact (i), the chemical potential of semiconductor material in the liquid is modified by the radius-dependent correction. Fact (ii) gives the upper limit for the supersaturation of liquid phase, $\Delta\mu_{LS}$, below which the diffusion flux is directed from the surface to the NW top. Fact (iii) provides the lower limit for $\Delta\mu_{LS}$, above which the NW growth rate is larger than that of a non-activated surface. This lower limit is different, however, for CUB and HEX NWs as well as for nucleation at TL and C position. Typical structural diagram of NWs in normalized coordinated of liquid supersaturation, $f = \Delta\mu_{LS} / \psi$, and NW radius, $\rho \equiv R / R_0$, are presented in Fig.3, for typical MBE growth conditions of GaAs. In the latter, ψ stands for the difference of bulk cohesive energies of HEX and CUB phase (~ 24 meV per pair in GaAs [7-9]). Material-related parameter $R_0 = 2\gamma_{CUB}\Omega_s / \psi$ (Ω_s is the volume per pair in solid phase) determines the characteristic radius of CUB to HEX transition. Dashed regions indicate the prevalence of different phases. The obtained results demonstrate that (i) CUB to HEX structural transition onsets in the nanometer range for different III-V materials considered, (ii) TL nucleation is favourable in the most cases and (iii) the formation of HEX phase generally requires high supersaturations.

Formation of stacking fault free GaAs NWs. Based on the above model, the growth of stacking fault free CUB III-V NWs generally requires low supersaturation. In the case of Au-assisted molecular beam epitaxy (MBE) of GaAs NWs on the GaAs(111)B substrates, low supersaturation relates to a high surface temperature during the growth. It is known however that GaAs NWs can not be grown at temperature above 600 °C [12]. In order to overcome this, we have developed a special two-step growth procedure, where short NW seeds are prepared at a lower temperature (530-550 °C) and the upper part is grown at 630 °C [13]. We will demonstrate that such GaAs NWs can reach up to μm in length and that their crystal structure is pure CUB from base to top, as follows from our transmission electron microscopy measurements. The described approach therefore presents a new method to obtain rather thin ($\sim 30\text{-}50$ nm in diameter) stacking fault free GaAs NWs by Au-assisted MBE, which is of paramount importance for applications.

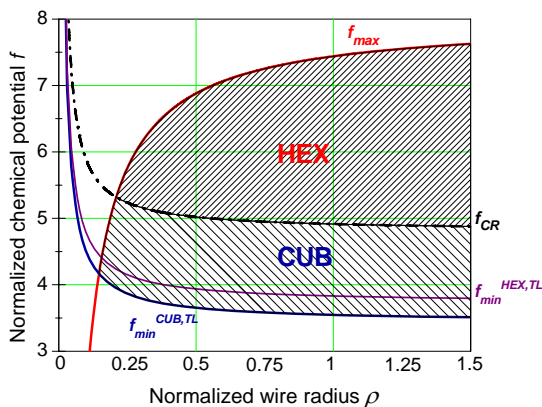


Fig. 3 Structural phase diagrams in the case of TL nucleation at $\tau=0.875$. Shaded domains, separated by the curve $f_{CR}(\rho)$, correspond to the prevalence of CUB or HEX phase.

References

- 1 A.I. Persson et al., Nature Mater. **3** (2004), 678.
- 2 J.C. Harmand et al., Appl. Phys. Lett. **87** (2005), 203101.
- 3 I.P. Soshnikov et al., Phys. Sol. State **47**, 2213 (2005).
- 4 L. C. Chuang et al., Appl. Phys. Lett. **92**, 013121 (2008).
- 5 P. Mohan et al., Nanotechnology **16**, 2903 (2005).
- 6 A. Fontcuberta i Morral et al., Adv. Mater. **19**, 1347 (2007).
- 7 F. Glas et al., Phys. Rev. Lett. **99**, 146101 (2007).
- 8 T. Akiyama et al., Jpn. J. Appl. Phys. **45**, L275 (2006).
- 9 V.G.Dubrovskii and N.V.Sibirev, Phys. Rev. B **77**, 035414 (2008).
- 10 V.G.Dubrovskii et al., Phys.Rev.B **71**, 205325 (2005).
11. V.G.Dubrovskii et al., Phys.Rev.B **78**, 235301 (2008).
12. J.C.Harmand et al., J.Cryst.Growth **301-302**, 853 (2007).
13. V.G.Dubrovskii et al., Phys.Rev.B, submitted.

Nanotube Substituted Source/Drain Regions for Carbon Nanotube Transistors for VLSI Circuits

Shibesh Dutta

Amrita Vishwa Vidyapeetham, Amritapuri, P.O. Clappana, Dist Kollam, Kerala 690525, INDIA shibeshdutta@ieee.org

Abstract-Aggressive scaling of silicon technology over the years has pushed CMOS devices to their fundamental limits. Pioneering works on carbon nanotube during the last decade, possessing exceptional electrical properties have provided an intriguing solution for high performance integrated circuits. So far, at best, carbon nanotubes have been considered only for the channel, with metal electrodes being used for source/drain. Here, alternative schemes of „All-Nanotube“ transistor are presented where even the transistor components are derived from carbon nanotubes which hold the promise for smaller, faster, denser and more power efficient electronics.

Index Terms: CMOS, carbon nanotubes and chirality

References

- [1] Hongjie Dai, Ali Javey, Eric Pop, David Mann “Electrical Transport Properties and Field-Effect Transistors of Carbon Nanotubes”, *NANO: Brief Reports and Reviews Vol. 1, (2006) 1–4*.
- [2] T Mizutani, Y Nosho and Y Ohno, “Electrical properties of carbon nanotube FETs,” *Journal of Physics: Conference Series 109 (2008) 012002*.
- [3] Rahmat Bin Sanudin, “Characterisation Of Ballistic Carbon Nanotube Field-Effect Transistor,” *M.S. Thesis*, Universiti Teknologi Malaysia, November 2005
- [4] Deanna Zhang Chuan-Lan Lin, “Carbon Nanotube Final Report,” May 14, 2003
- [5] Jing Guo, “Carbon Nanotube Electronics: Modelling, Physics, and Applications,” *Ph.D Thesis*, Purdue University, August 2004.
- [6] Jia Chen, “Carbon Nanotubes for Potential Electronic and Optoelectronic Application,” *ICCAD'06*, San Jose, November 2006.
- [7] Philip G. Collins and Phaedon Avouris, “Nanotubes for Electronics,” *Scientific American*, December 2000.
- [8] Julia Van Meter Cline, “Characterization of Schottky Barrier Carbon Nanotube Transistors and their Applications to Digital Circuit Design,” Brown University, June 2004.
- [9] J. Robertson, G. Zhong1, H. Telg, C. Thomsen, J. M. Warner, “Carbon nanotubes for interconnects in VLSI integrated circuits,” *phys. stat. sol. (b) 245, No. 10, 2303–2307 (2008) /pssb.200879553*.

Figures:

Proposed Model I

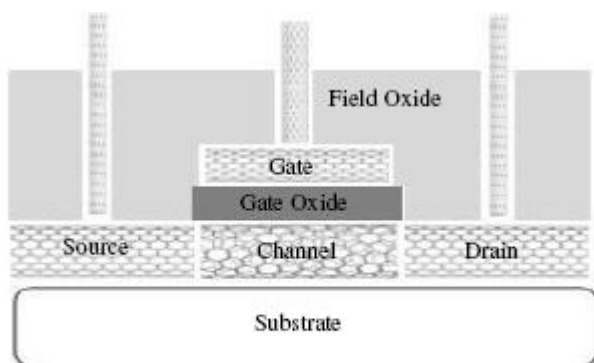


Figure 2(a): Sectional view of the proposed model I

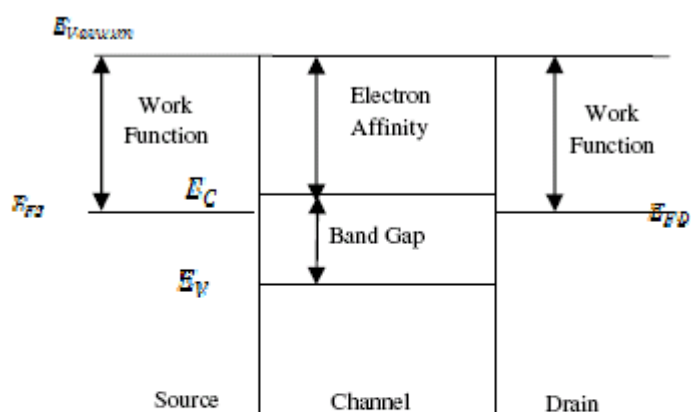


Figure 2(b): Band diagram before contact

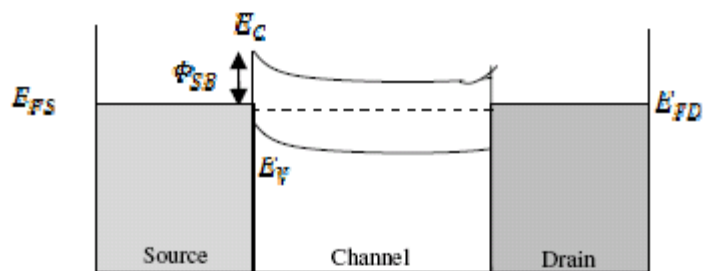


Figure 2(c): Band diagram after contact

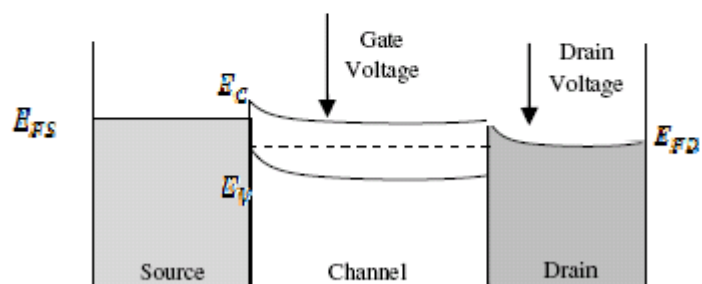


Figure 2(d): Band diagram with proper biasing

Proposed Model II

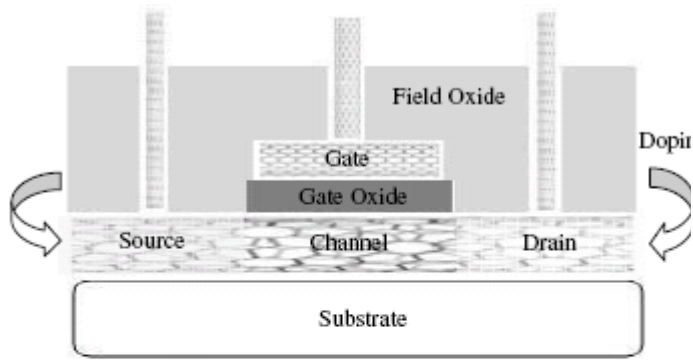


Figure 3(a) Sectional view of the proposed Model II

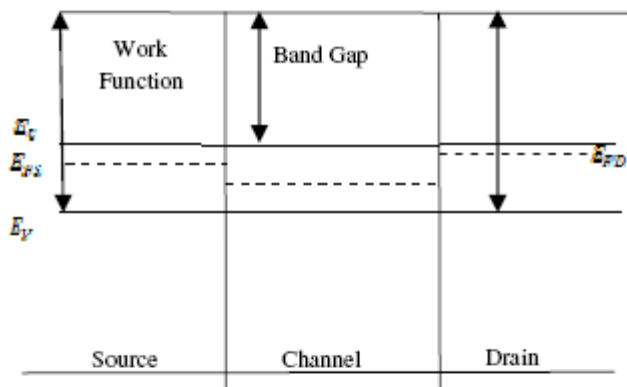


Figure 3(b): Band diagram before contact

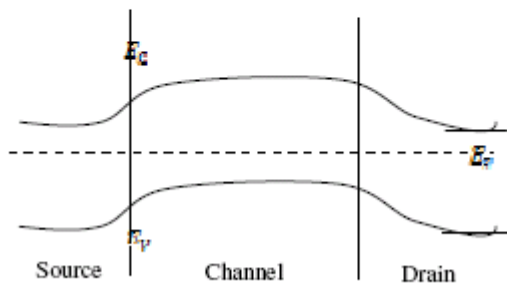
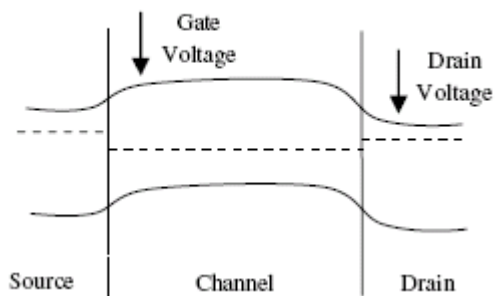


Figure 3(c): Band diagram after contact



SELF-CONSISTENT CALCULATIONS OF THE SURFACE ELECTRONIC EXCITATIONS IN K(110) ADSORBED LAYER ON Be(0001) SUBSTRATE

J. P. Echeverry^{1,2}, *V. M. Silkin*^{1,2}, *B. Hellsing*^{3,4}, *P. M. Echenique*^{1,2,5}, *E. V. Chulkov*^{1,2,5}

¹*Donostia International Physics Center (DIPC), P. Manuel de Lardizabal, 20018 San Sebastián, Basque Country, Spain*

²*Depto. De Física de Materiales, Facultad de Ciencias Químicas, Universidad del País Vasco, apto.1072, 20080 San Sebastián, Basque Country, Spain*

³*Department of Physics, Göteborg, Sweden*

⁴*Department of Applied Physics, Chalmers University, Göteborg, Sweden*

⁵*Centro Mixto CSIC-UPV/EHU, apto.1072, 20080 San Sebastián, Basque Country, Spain
Kutxatila, E-20080 Donostia, Basque Country*

juanpablo_echeverry@ehu.es

We investigate the collective surface excitations associated with an overlayer of K(110) atoms adsorbed on a Be(0001) substrate in the self-consistent jellium framework and with ab-initio pseudo-potentials calculations¹ in order to compare the results obtained from both approximations. We calculate the surface response function with energies and wave functions derived from the Kohn-Sham density-functional theory and from the non-conserving pseudo-potentials ab-initio calculations respectively. The dispersion relation for the plasmon modes², the real and imaginary part of the surface response function were obtained. A relation of the collective modes in Be surface and K/Be ad-layer surface is analyzed in terms of the contribution from each system.

References:

- [1] V.M. Silkin, E.V. Chulkov, and P.M. Echenique, *Phys. Rev. Lett*, **93**, 176801-1 (2004)
- [2] B. Diacunescu, K. Pohl, L. Vattuone, L. Savio, P. Hofmann, V.M. Silkin, J.M. Pitarke, E.V. Chulkov, P.M. Echenique, D. Farías & M. Rocca, *nature*, **448**, 57 (2007)

MAGNETIC BEHAVIOUR OF NON-CONTACTING NI NANOPARTICLES ENCAPSULATED IN VERTICALLY ALIGNED CARBON NANOTUBES

L. Elbaile^a, J.A. García^a, E. Bertran^b, J. García-Céspedes^b and A. Svalov^c

a Departamento de Física, Universidad de Oviedo, c/ Calvo Sotelo s/n 33007 Oviedo, Spain

b Grupo FEMAN, IN2UB, Universitat de Barcelona, Martí i Franquès 1, E08028 Barcelona Spain.

*c Ural State University, Institute of Physics and Applied Mathematics, Lenin Ave. 51 620083 Ekaterinburg, Russia
elbaile@uniovi.es*

Magnetic properties of carbon nanotubes (MF-CNT) obtained by plasma-enhanced chemical vapour deposition (PECVD) have been studied [1]. The growth of these nanotubes has been activated from Ni catalyst nanoparticles. Samples consist of Ni nanoparticles encapsulated at the tip of vertically aligned multiwalled carbon nanotubes (VACNTs) forming an homogeneous and dense large-area monolayer of magnetically isolated (non-contacting) nanoparticles. Figure 1 shows SEM micrograph of aligned CNTs grown on Si using Ni as catalyst and the diameter and mass distribution (normalised) histograms.

The magnetic characterisation has been performed by a Physical Property Measurement system (PPMS-14 T) in the temperature range of 5-300 K with magnetic fields up to 9 T. Figure 2 shows the hysteresis loops of the Ni particles in carbon nanotubes in the 5-300 K temperature range.

The results show that the wide size range (30-180 nm) of the particles originates the coexistence of blocked and superparamagnetic particles that leads into an intense ferromagnetic behaviour of the whole assembly [2]. At 5 K temperature the magnetization saturation is reached at an applied magnetic field of $\mu_0 H = 8\text{T}$. The coercivity decreases monotonically with increasing temperature and the value for the intrinsic coercivity is 250 Oe. The encapsulation of Ni nanoparticles by VACNTs preserves them from aggregation, this makes possible a tuning of the coercivity by controlling size distribution of particle monolayers. Torque measurements in the plane of the substrate and in the perpendicular plane, indicate the absence of preferential orientation of the Ni particles.

References:

- [1] H. Li, N. Zhao, Ch. He, Ch. Shi, X. Du and J. Li, *J. of Alloys and Compounds* 465 (2008) 51.
- [2] M.E. McHenry, *Phys. Rev. B*, 49 (1994) 11358.

Fig.1

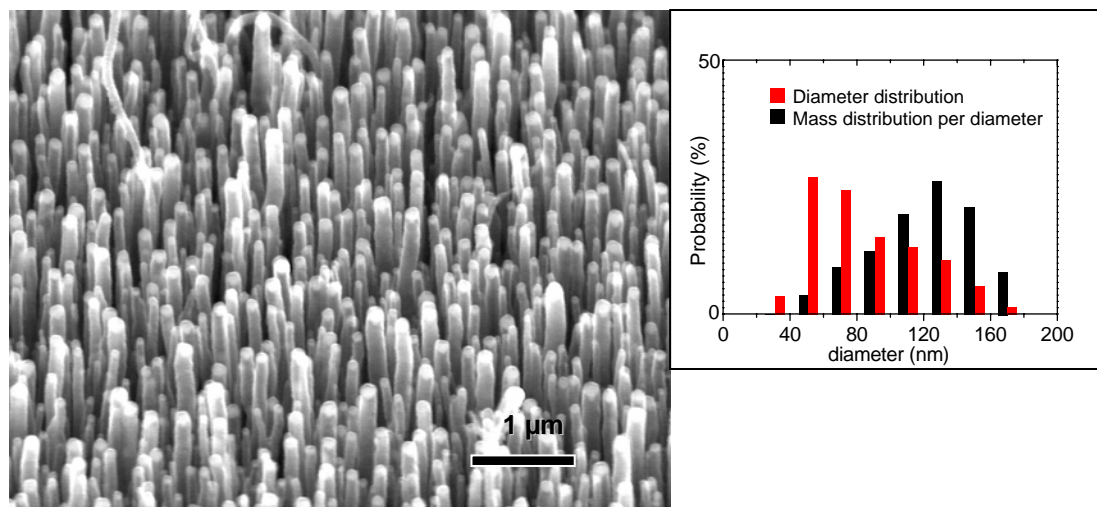
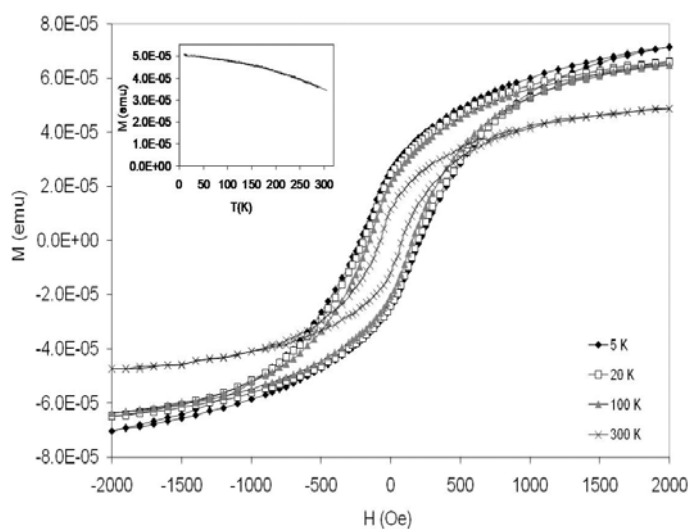


Fig.2



Synthesis and Characterization of Crosslinked (NIPA-co-AAc) Copolymer as a Thermoresponsive Nanohydrogel

Shimaa M. Elsaed* and Reem K. Farag
Egyptian Petroleum Research Institute, Nasr City, 11727 Cairo, Egypt
E.mail: shy_saeed@yahoo.com

Poly (*N*-isopropylacrylamide) (PNIPA) is the most popular synthetic polymer among the thermoresponsive polymers since it displays a sharp phase transition close to 32°C [1,2]. The crosslinked hydrogels obtained from this polymer swell under the LCST and shrink above it. When *N*-isopropylacrylamide (NIPA) copolymerized with other hydrophilic monomers with specific functional group such as acrylamide [3] and *N*-(hydroxymethyl) acrylamide [4] the obtained co-polymeric hydrogel may have better hydrophilicity and site-specific function compared to PNIPA itself. So that the applications of such gel usually involve the chemical modification of poly (NIPA). These modifications are usually performed to introduce functional groups that can increase the LCST towards body temperature to improve the mechanical properties [5,6,7]. So the thermoresponsive polymeric nanogels have been synthesized by inverse microemulsion polymerization of *N*-isopropylacrylamide (NIPA) and acrylic acid (AAc) in our study.

Microemulsions are thermodynamically stable mixtures of water, oil and surfactant that exhibit either a discrete micro droplet or a bicontinuous sponge-like structure. Most usually direct (o/w) or inverse (w/o) microemulsions are used for the synthesis of ultra small polymer particles. These nanoparticles are typically characterized by diameters between 5 and 100 nm, a narrow size distribution, and a small number of polymer chains per particle [8]. The synthesized nanogels were characterized by FTIR, ¹HNMR, TEM.

References:

- [1] Li SK, D'Emanuele A, Int J Pharm, 267 (2003) 27-34.
- [2] Schild HG, Prog Polym Sci., 17 (1992) 163-249.
- [3] D. E. Meyer and B. C. Shin, J. Control. Release., 74 (2001) 213.
- [4] C. S. Chaw, K. W. Chooi and X. M. Liu, Biomaterials, 25 (2004) 4297.
- [5] FeilH, Bae YH, Feijen J, Kim SW, Macromolecules, 25 (1992) 5528-30.
- [6] Park TG, Hoffman AS, J Appl Polym Sci, 46 (1992) 659-71.
- [7] Dong LC, Hoffman AS, J. Control. Release., 13 (1990) 21-31.
- [8] Co CC, CottsP, Burauer S, de Vries R, Kaler EW. Macromolecules, 34, (2001) 3245-54.

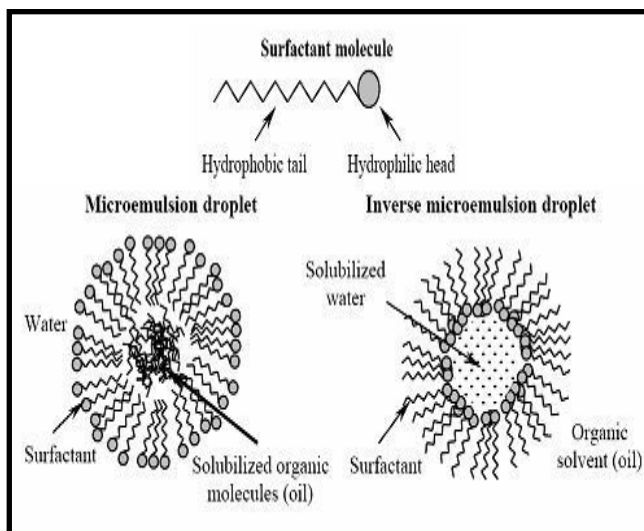


Figure (1): schematic diagram of micelles and microemulsions

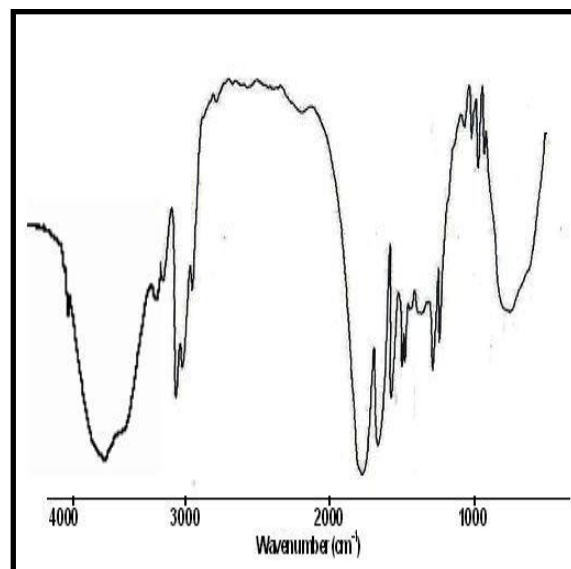


Figure (2): IR-Spectra of synthesized nanohydrogel

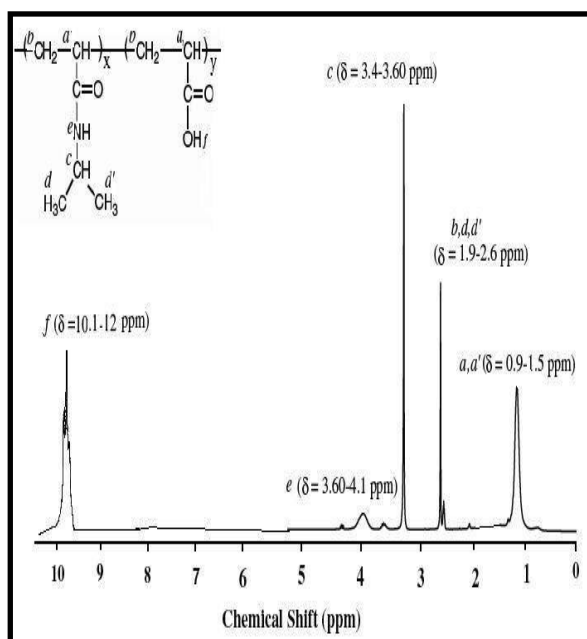


Figure (3): ¹HNMR-Spectra of synthesized nanohydrogel

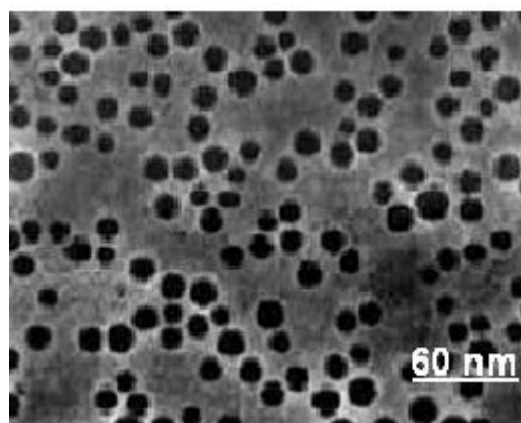


Figure (4): TEM of synthesized nanohydrogel

Wafer scale fabrication of AFM probes with carbon nanotube tips using a nanostencil

Daniel Engström^a, Veronica Savu^b, Jürgen Brugger^b, Ian Y. Y. Bu^c,
William I. Milne^d, Peter Bøggild^a

^a Department of Micro- and Nanotechnology, Technical University of Denmark, Lyngby, 2800, Denmark

^b Institut de Microtechnique, Ecole Polytechnique Fédérale de Lausanne, Lausanne, 1015, Switzerland

^c Department of Microelectronics Engineering, National Kaohsiung Marine University, 81157 Nanzih District, Kaohsiung City, Taiwan, Republic of China

^d Centre for Advanced Photonics and Electronics, Cambridge University, Cambridge, CB3 0FA, UK

e-mail: daniel.engstrom@nanotech.dtu.dk

Carbon nanotubes are used as tips for AFM probes in order to obtain high resolution¹ and to be able to image high aspect ratio structures². Many different methods have been proposed to integrate a carbon nanotube on the tip of an AFM cantilever. Some methods involve manual placement and in some cases gluing of the carbon nanotubes to the AFM tip², whereas other methods are based on the direct growth of a carbon nanotube on an AFM cantilever^{3,4}.

Direct growth of carbon nanotubes requires fabrication or placement of a catalyst particle on the AFM cantilever, at the location where the nanotube tip should have its base. The catalyst particle can either be incorporated as an integral part of the AFM cantilever fabrication before the AFM probe is released⁴ or as a separate add-on step after the release³. Integration of the catalyst particle with the AFM probe fabrication involves protecting the catalyst particle from wet and dry etches that would otherwise damage it. This becomes increasingly difficult with smaller catalyst particles or in the case where the catalyst particle has to be positioned at the apex of a silicon tip. Fabricating the catalyst particles after the release of the AFM cantilevers may on the other hand be difficult since deposition of resist by both spinning and spraying with a good edge coverage is at best very difficult.

The stencil technology provides a non-invasive, cheap and versatile way of transferring these catalytic nanostructures to a substrate. A stencil mask consists of a thin membrane in which apertures have been etched (figure 1a). By placing the stencil mask on top of a substrate and subsequently depositing a material through the openings in the membrane the structures are transferred (figure 1b). In addition to this, the stencil mask can be cleaned and reused⁵, which makes it a potentially cheap fabrication method. Stencil technology has proven useful for the transfer of structures from hundreds of micrometers⁶ to tens of nanometers⁷, and since the stencil mask only needs to touch the substrate on the periphery it is possible to transfer structures to 3D surfaces⁸. As an alternative to carbon nanotubes epitaxially grown nanowires can be formed from catalyst particles and here it is advantageous that no chemicals are needed which could damage the substrate.

In this work, we transferred catalyst particles for carbon nanotube growth at specific locations onto a wafer of released AFM probes (figure 2). The AFM probes are only attached by a single silicon beam so that after the catalyst deposition and carbon nanotube growth they can be picked out of the wafer by a pair of tweezers. It is shown that catalyst particles can indeed be transferred onto these free-hanging AFM probes on a wafer scale and that carbon nanotubes can be grown vertically on the tip using a PECVD process (figure 3). The alignment of the catalyst particle over the full wafer was done with an accuracy of $\pm 1\mu\text{m}$ or better, which allows the nanotubes to be placed close to the edge of the cantilever. In figure 4 an AFM cantilever with a single carbon nanotube placed $2\mu\text{m}$ from the edge is shown. The carbon nanotube was grown from the catalyst particle, which was deposited on the substrate through a 300 nm hole in the stencil. This project shows the way for a versatile and cheap method for wafer scale fabrication of AFM probes with carbon nanotube tips, while several other applications are possible; free-standing resonators, mechanical switches, electron field emitters.

[1] J. Hafner, C. Cheung, A. Woolley, C. M. Lieber, *Biophysics & Molecular Biology* 77 (2003) 73-110
 [2] K. Carlson, K. N. Andersen, V. Eichhorn, D. H. Petersen, K. Molhave, I. Y. Y. Bu, K. B. K. Teo, W. I. Milne, S. Fatikow, P. Boggild, *Nanotechnology* 18 (2007) 345501
 [3] C.L. Cheung, J. H. Hafner, C. M. Lieber, *PNAS* Vol. 97 No. 8 (2000), 3809-3813
 [4] Q. Ye, A. M Cassell, H. Liu, K.-J. Chao, J. Han, M. Meyyappan, *Nano Letters* Vol. 4, No. 7 (2004), 1301-1308
 [5] O. Vázquez-Mena, G. Villanueva, M. A. F. van den Boogaart, V. Savu, and J. Brugger, "*Microelectronic Engineering*", vol. 85 (2008), pp. 1237-1240
 [6] M. A. F. van den Boogaart, G. M. Kim, R. Pellens, J.-P. van den Heuvel, J. Brugger, *J. Vac. Sci. Technol. B* 22(6) (2004)
 [7] M. M. Deshmukh, D. Ralph, M Thomas, J. Silcox, *Applied Physics Letters* 75 No. 11 (1999) 1631-1633
 [8] R. R. Schlitter, J. K. Gimzewski, C. Durkan, M. S. M. Saifullah, M. E. Welland, *Science* 292 (2001) 1136

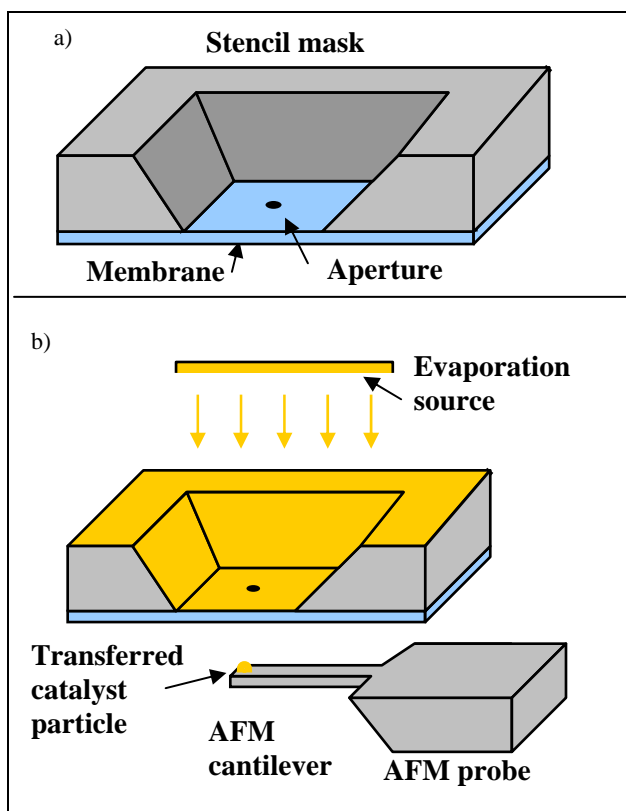


Figure 1. a) A stencil mask. b) The process of making a stencil transfer. Nickel was transferred to the AFM cantilever.

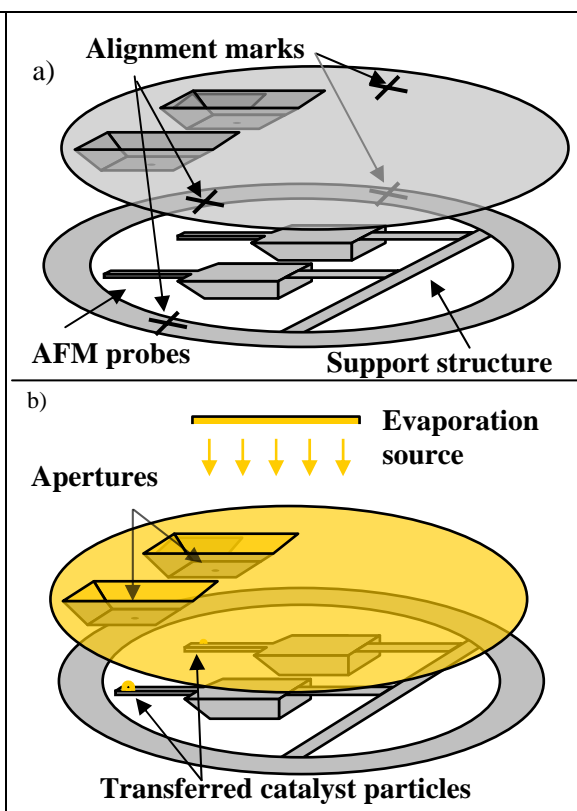


Figure 2. a) Stencil and wafer was aligned using alignment marks b) Nickel was evaporated through the apertures to the probes.

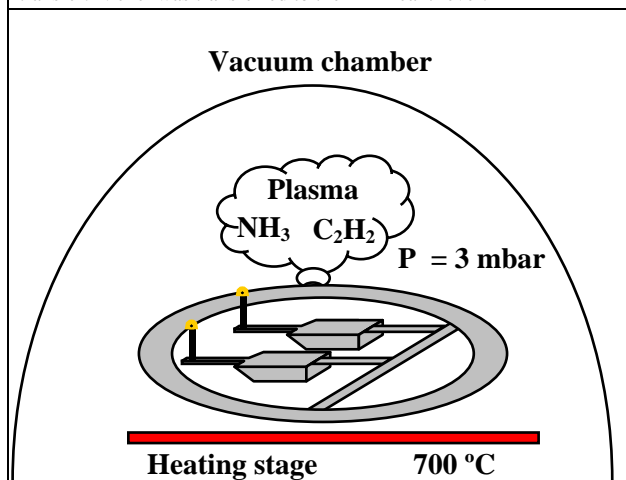


Figure 3. The carbon nanotubes were grown in a PECVD chamber which made them vertically aligned.

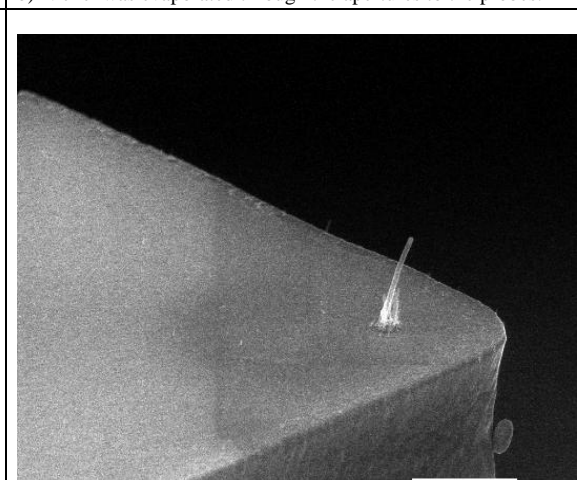


Figure 4. An electron micrograph of the end of an AFM cantilever with a carbon nanotube tip. Scale bar is 2 μm .

VIBRATIONS OF TETRAHEDRAL Co AND Cu CLUSTERS ON Cu(111) SURFACE

Sergey Ereemeev¹, Svetlana Borisova¹, Galina Rusina¹, and Eugene Chulkov^{2,3}

¹*Institute of Strength Physics and Materials Science, Siberian Branch, Russian Academy of Sciences, pr. Akademicheskoy 2/4, Tomsk, 634021, Russia*

²*Donostia International Physics Center (DIPC), Paseo de Manuel Lardizabal, 4, 20018 San Sebastián/Donostia, Spain*

³*Depto. de Física de Materiales and Centro Mixto CSIS-UPV/EHU, Facultad de Ciencias Químicas, Universidad del País Vasco/Euskal Herriko Unibertsitatea, Apdo.1072, 20018 San Sebastián/Donostia, Spain*

eremeev@ispms.tsc.ru

The epitaxial thin-film growth of Co on Cu substrates has been studied extensively during the last years. Because of the giant magnetoresistance observed in Co/Cu multilayer systems and its sensitivity to the atomic-scale morphology, extensive experimental studies have been devoted to their growth. These studies have revealed a variety of growth modes [1-6]. At the initial stages of growth some of the deposited Co atoms can exchange with Cu substrate atoms. This atomic exchange in conjunction with its coverage dependence leads to three different adatom species on the surface: substitutional Co, on-surface Co, and on-surface Cu, which can form compact clusters [1,6]. Numerous theoretical investigations have also been performed to study atomic structure as well as energetic and magnetic properties in Co/Cu system. Using density-functional theory calculations possible equilibrium structures for a monolayer coverage of Co on Cu(001) were analyzed [2]. Atomistic processes involved in the growth of Co on Cu surfaces were studied by employing static energy calculations and accelerated molecular dynamics simulations [7]. The interplay between structure and magnetic properties of small cobalt clusters on Cu surface were investigated by *ab initio* and tight-binding calculations [8]. Despite important role that vibrational properties of small clusters play in understanding of many phenomena such as adsorbate diffusion, island and film growth significantly less attention was paid to study adsorbate and cluster vibrations on Cu surfaces. Recently vibrational properties of a single adatom [9-11] as well as of a dimer, and trimer of Co on low-index Cu surfaces [11,12] have been thoroughly studied by using tight-binding second moment approximation interatomic interaction potentials. It was shown that structural and vibrational properties of the Co clusters strongly depend on the substrate orientation and the cluster size.

The simplest 3D clusters that can be formed in this system, tetrahedral Co₄ and Cu₄ clusters are considered in the present work. We study vibrational properties of these clusters on Cu(111) surface by using many-body interatomic potentials developed within tight-binding second moment approximation (TB-SMA) [13,14]. To determine the equilibrium atomic structure of free and supported clusters standard molecular dynamic technique based on the TB interaction potentials is applied. To simulate a semi-infinite Cu(111) surface with an adsorbed cluster a thin-film model of a two-dimensional periodic slab consisting of 31 atomic layers of Cu(111) with 5×5 supercell to exclude direct cluster-cluster interaction is used (see Fig. 1). The chosen thickness prevents interaction between two opposite surfaces of the copper film. The calculations of vibrational spectra are carried out by the dynamical matrix method. Diagonalizing the matrix gives the eigenfrequencies and the polarization vectors of vibrations. The local vibration densities of states were obtained by projecting these eigenmodes onto atoms of the cluster or the substrate in a given (*x+y* or *z*) direction. We also have done calculations of the equilibrium structure and vibrations of the free standing Cu₂ and Co₂ as well as Cu₄ and Co₄ clusters. The calculated Co₂ and Cu₂ bond lengths, binding energies, and the stretch mode frequencies are in close agreement with available experimental data.

In Fig. 2 we show the calculated local density of states (LDOS) for the Cu_4 (a) and Co_4 (b) cluster atoms and for the first and second Cu(111) layer atoms. Analysis of equilibrium structure of the adsorbed tetramers shows that in the case of Cu_4 the interaction with Cu(111) substrate leads to weakening Cu-Cu bonds within cluster while for the Co cluster interaction with the substrate affects only the Co-Co bonds between atoms closest to the surface. In both cases the clusters lose a high symmetry tetrahedral shape, which they have in a free standing state. The interaction of the Co and Cu clusters with the substrate leads to vibrations which correspond to translational and rotational degrees of freedom of the free clusters. These frustrated translation and frustrated rotation modes are in-plane polarized and lying in a low-frequency region. The frequencies of these modes in the Co cluster are ≈ 2 meV higher due to the stronger Co-Cu interaction in comparison with the Cu-Cu one. The vibrational modes of the free Cu_4 upon its adsorption on the Cu(111) surface mix with Cu bulk phonons and become almost delocalized. Contrary to that, in the Co_4 cluster on the surface the high frequency modes remain strongly localized and mixed with the nearest neighbor atoms vibrations only. Like vibrational modes of smaller Co clusters on low-index Cu surfaces, the highest frequency vibration of the Co_4 cluster splits due to different interactions with certain groups of nearest neighbor atoms of the substrate.

References:

- [1] M. T. Kief and W. F. Egelhoff, Phys. Rev. B **47** (1993) 10785.
- [2] R. Pentcheva and M. Scheffler, Phys. Rev. B **61** (2000) 2211.
- [3] J. Fassbender, R. Allenspach, and U. Dürig, Surf. Sci. **383** (1997) L742.
- [4] U. May, J. Fassbender, and G. Güntherodt, Surf. Sci. **377–379** (1997) 992.
- [5] T. Bernhard, R. Pfandzelter, and H. Winter, Nucl. Instrum. Methods Phys. Res. B **203** (2003) 111.
- [6] F. Nouvertné, U. May, M. Bammig, A. Rampe, U. Korte, G. Güntherodt, R. Pentcheva, and M. Scheffler, Phys. Rev. B **60** (1999) 14382.
- [7] Radu A. Miron and Kristen A. Fichthorn, Phys. Rev. B **72** (2005) 035415.
- [8] Š. Pick, V. S. Stepanyuk, A. L. Klavysyuk, L. Niebergall, W. Hergert, J. Kirschner, and P. Bruno, Phys. Rev. B **70** (2004) 224419.
- [9] Kai Liu and Shiwu Gao, Phys. Rev. Lett. **95** (2005) 226102.
- [10] Kai Liu and Shiwu Gao, Phys. Rev. B **74** (2006) 195433.
- [11] S. D. Borisova, S. V. Ereemeev, G. G. Rusina, V.S. Stepanyuk, P. Bruno, and E. V. Chulkov, Phys. Rev. B **78** (2008) 075428.
- [12] S.D. Borisova, G.G. Rusina, S.V. Ereemeev, and E.V. Chulkov, Phys. Solid State **51** (2009) 1271.
- [13] N. A. Livanov, V. S. Stepanyuk, W. Hergert, D. I. Bazhanov, P. H. Dederichs, A. Katsnelson, C. Massobrio. Phys. Rev. B **61** (2000) 2230.
- [14] V. S. Stepanyuk, D. V. Tsviline, D. I. Bazhanov, W. Hergert, and A. A. Katsnelson, Phys. Rev. B **63** (2001) 235406.

Figures:

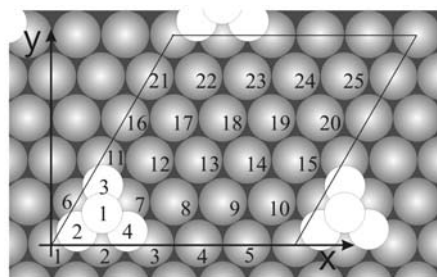


Figure 1 The atomic structure for adsorbed Cu_4 (Co_4) cluster on the Cu(111) surface. The computational 5×5 supercell is indicated by a rhombus, $x = [\bar{1}10]$ and $y = [11\bar{2}]$.

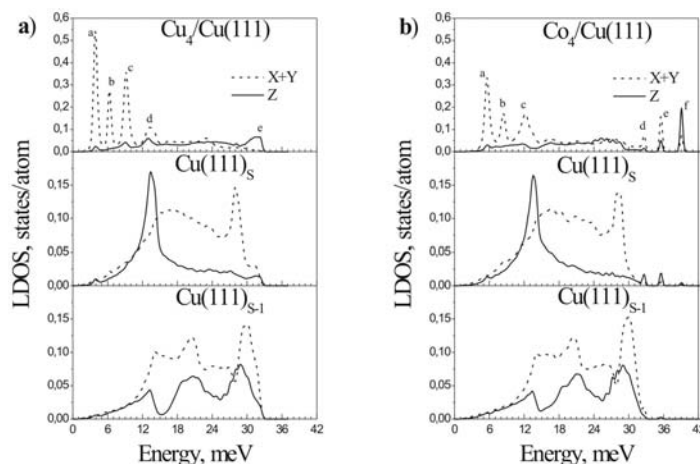


Figure 2 Local density of vibrational states for a tetrahedral clusters: a) Cu_4 and b) Co_4 as well as for the Cu(111) surface (S) and subsurface (S-1) atoms.

USE OF PHOTOLABILE OLIGONUCLEOTIDES IN THE FABRICATION OF PATTERNED SURFACES

Brendan Manning¹, Sonia Pérez-Rentero¹, Roger Ramos¹, Simon Leigh², Jon Preece², Ramon Eritja¹

¹*Institute for Research in Biomedicine, Institute for Advanced Chemistry of Catalonia (IQAC), CIBER-BBN Networking Centre on Bioengineering, Biomaterials and Nanomedicine. Helix Building, Baldori Reixac 15, E-08028 Barcelona, Spain.*

²*Nanoscale Chemistry Laboratory. School of Chemistry. The University of Birmingham, B15 2TT, United Kingdom.*

There is a large interest in the use of the self-assembly properties of biomolecules for electronic or biological or sensing applications. Among the biomolecules, oligonucleotides have been captured a large part of this interest^{1,3}. This is due to the existence of a robust method for the preparation of oligonucleotides that allows the production of these compounds carrying reactive groups needed to anchor these molecules to surfaces.

Recently it has been shown that is possible to modify a specific region of a surface introducing chemical functionality to direct the adsorption of particulate species⁴. As example self-assembled monolayers (SAMs) carrying 4-nitrophenoxy head-groups can be converted to 4-aminophenoxy groups by electron-beam and X-ray irradiation⁵. Selective deposition of citrate-passivated gold nanoparticles (NPs) to the chemically patterned surfaces can subsequently be achieved due to the affinity of negatively charged gold NPs to protonated amino groups at the surface.

In the present communication we study the use of oligonucleotides carrying photolabile groups in their sequence as a new kind of biological resist to form patterns on surfaces. To this end, a method for the fabrication of patterned surfaces using hairpin oligonucleotides carrying photolabile groups is described. A photolabile group has been introduced at the loop of an intramolecular oligonucleotide hairpin. The photolabile oligonucleotide was immobilized on glass and SiO₂ surfaces. Photolysis results on the formation of areas carrying single-stranded DNA sequences that direct the deposition of the complementary sequence at the photolyzed sites.

References

1. Aldaye, F. A., Palmer, A.L., Sleimar, H.F. *Science* **2008**, *321*, 1795-1799.
2. Seeman, N. C., Lukeman, P. S. *Rep. Prog. Phys.* **2005**, *68*, 237-270.
3. Gothelf, K.V., LaBean, T.H. *Org. Biomol. Chem.* **2005**, *3*, 4023-4037.
4. Mendes, P. M., Preece, J. A. *Curr. Opin. Coll. Inter. Sci.* **2004**, *9*, 236-248
5. Mendes, P. M., Jacke, S., Critchley, K., Plaza, J., Chen, Y., Nikitin, K., Palmer, R.E., Preece, J.A., Evans, S.D., Fitzmaurice, D. *Langmuir* **2004**, *20*, 3766-3768

Far-infrared spectrum of few-electron concentric quantum rings

José María Escartín¹, Francesc Malet², Manuel Barranco¹, and Martí Pi¹

¹*Dept. d'Estructura i Constituents de la Matèria, Facultat de Física, and IN²-UB, Universitat de Barcelona, Diagonal 647, Barcelona 08028, Spain*

²*Mathematical Physics, LTH, Lund University, Box 118, 22100 Lund, Sweden*
escartin@ecm.ub.es

Using an exact diagonalization technique [1], we address the far-infrared response of nanoscopic few-electron concentric double quantum rings (CDQR) [2-3].

We show that, in the presence of a perpendicularly applied magnetic field, CDQR display radially and azimuthally localized many-electron states whose fingerprint is the appearance of a very soft mode in the dipole infrared response at an energy that roughly corresponds to the absorption of a photon by a rigidly-rotating N -electron molecule [4]. This mode should be experimentally observable in CDQR far-infrared absorption spectroscopy [5].

The ground state energy as a function of the total angular momentum of the system (yrast line), two-electron densities (Fig. 1) and dipole infrared absorption spectra (Fig. 2) are discussed in detail for highly-symmetric configurations made of $N = 4$ and 6 fully-polarized electrons. We also discuss the charge-density response corresponding to monopole and quadrupole excitations, and show the existence in the quadrupole channel of excited states that can be identified with vibrational states arising in the N -electron molecule, thus strengthening the picture of an underlying electron-localized configuration.

References:

- [1] A. Emperador, E. Lipparini, and F. Pederiva, *Phys. Rev. B*, **72** (2005) 033306.
- [2] T. Mano, T. Kuroda, S. Sanguinetti, T. Ochiai, T. Tateno, J. Kim, T. Noda, M. Kawabe, K. Sakoda, G. Kido, and N. Koguchi, *Nano Lett.*, **5** (2005) 425.
- [3] A. Mühle, W. Wegscheider, and R. J. Haug, *Appl. Phys. Lett.*, **91** (2007) 133116.
- [4] J. M. Escartín, F. Malet, A. Emperador, and M. Pi, submitted to *Phys. Rev. B*.
- [5] A. Lorke and R. J. Luyken, *Physica B*, **256-258** (1998) 424.

Figures:

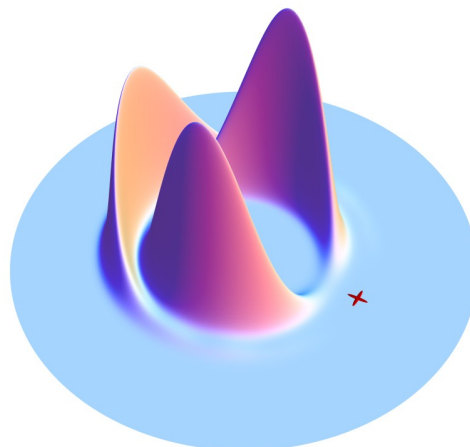


Figure 1: Two-body density for a circularly-symmetric state of four electrons. The position of one of the electrons is fixed at the point marked by the cross.

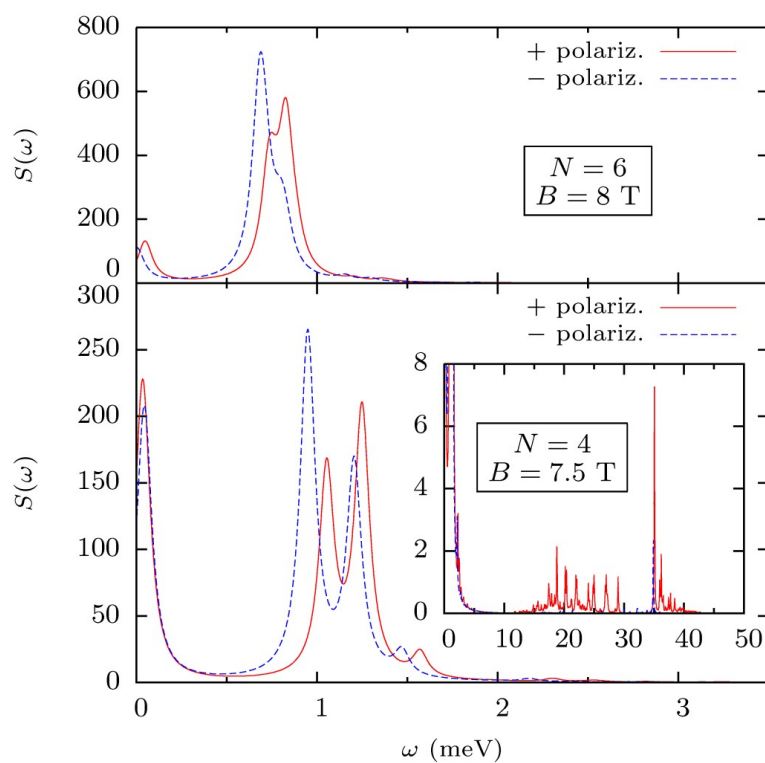


Figure 2: Low-energy dipole absorption spectrum (in arbitrary units), for CDQR ground states with $N = 4$ (bottom panel) and $N = 6$ (top panel) electrons. The inset in the bottom panel displays the whole spectrum (up to a 97% of the Thomas-Reiche-Kuhn sum rule). Peaks are represented by Lorentzians of 0.1 meV full width at half maximum.

PHASE DIAGRAMS AND SWITCHING OF VOLTAGE AND MAGNETIC FIELD IN DILUTED MAGNETIC SEMICONDUCTOR NANOSTRUCTURES

*R. Escobedo*¹, *M. Carretero*^{2,3}, *L. L. Bonilla*^{2,3}, *G. Platero*⁴

¹*Dpto. Matemática Aplicada y Ciencias de la Computación
Universidad de Cantabria, 39005 Santander – Spain*

²*G. Millan Institute, Fluid Dynamics, Nanoscience and Industrial Mathematics,
Universidad Carlos III de Madrid, 28911 Leganés, Madrid – Spain,*

³*Unidad asociada al Instituto de Ciencias de Materiales del CSIC, Madrid – Spain*

⁴*Instituto de Ciencia de Materiales de Madrid, CSIC, 28049 Cantoblanco, Madrid – Spain*

escobedo@unican.es

We investigate the response of a n-doped dc voltage biased II-VI multi-quantum well diluted magnetic semiconductor nanostructure having its first well doped with magnetic impurities (Mn) under both voltage and magnetic-field abrupt switching.

Transitions between stationary states and self-sustained current oscillations are systematically analyzed, obtaining the phase diagram of voltage versus level splitting induced by an external magnetic field. The phase diagram shows regions of stable self-sustained current oscillations immersed in a region of stable stationary states. Sudden voltage or magnetic field changes may switch or disconnect current oscillations from an initial stationary state, and reciprocally, current oscillations may disappear after sudden changes of voltage or magnetic field changes into the stable stationary states region.

Our results show how to design a device operating as a spin injector and a spin oscillator by tuning the Zeeman splitting (through the applied external magnetic field and the density of magnetic impurities) and the parameters determining the sample configuration (number of wells, doping density, barrier and well widths, . . .).

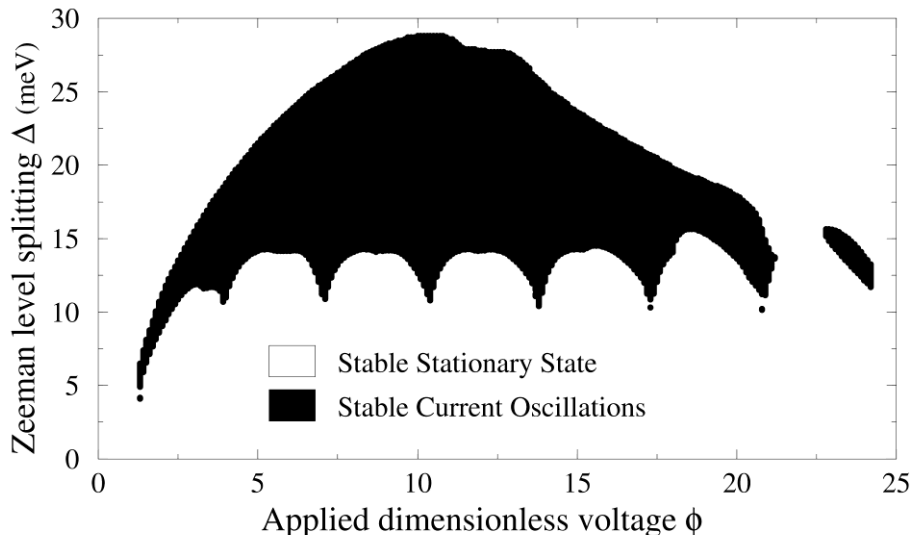


Fig. Phase diagram of Δ vs. ϕ showing regions of stable self-sustained current oscillations immersed in a region of stable stationary states in a 10-wells superlattice.

References:

- D. Sanchez, A.H. MacDonald, G. Platero, Phys. Rev. B **65**, 035301 (2002).
- M. Bejar, D. Sanchez, G. Platero, A. H. MacDonald, Phys. Rev. B **67**, 045324 (2003).
- L. L. Bonilla, R. Escobedo, M. Carretero, G. Platero, Appl. Phys. Lett. **91**, 092102 (2007).
- R. Escobedo, M. Carretero, L.L. Bonilla, G. Platero, New J. Phys. **11**, 013033 (2009).

NANOSCALE IMPEDANCE MICROSCOPY ON SINGLE BACTERIA. A THEORETICAL STUDY.

D. Esteban-Ferrer,¹ A. Juárez,² G. Gomila¹

¹*Institut de Bioenginyeria de Catalunya (IBEC) and Departament d'Electrònica Universitat de Barcelona, Baldori i Reixac 11-15, 08028-Barcelona (Spain)*

²*Institut de Bioenginyeria de Catalunya (IBEC) and Departament de Microbiologia, Universitat de Barcelona*

desteban@ibec.pcb.ub.cat, ggomila@ibec.pc.ub.cat

In recent years it has been recognized that single cell studies with microbial cells, as compared to the more common population based studies, may provide answers to some unresolved scientific questions [1]. Most of the advances reported until now have been produced with microorganisms with relatively large sizes (yeast cells, algae, amebae, etc.) of at least 5 μm in diameter and hence accessible by optical techniques and conventional micromanipulation technologies at the single cell level [2]. Much less has been done with small bacteria with typical sizes around 1 μm which lie at the frontier of conventional techniques and hence require more advanced (nano)techniques, essentially Atomic Force Microscopy (AFM). [3,4,5] This technique has allowed obtaining three dimensional images of the live bacterial cell surfaces with high spatial resolution as well as quantification of adhesion to molecules and surfaces, the study of the antibacterial effect of different compounds, evidence for horizontal genetic transfer through conjugative pili, DNA-protein interactions, etc. In spite of these results, still a lot remains to be explored in order to better understand the properties of these small single bacterial cells.

In our groups we are exploring novel applications of atomic force microscopy to the study of single bacterial cells to generate new biologically relevant knowledge not currently available by existing biotechniques. In particular, we aim to combine AFM and nanoscale impedance electrical measurements to rapidly discriminate between the most relevant and prevalent pathotypes of some pathogens. We present in this contribution a theoretical study to assess the experimental viability of this approach. The theoretical study has been performed at both the whole cell level and at the local cell level. In the former case (Fig. 1a) analytical parallel plate models have been used, while in the later case (Fig. 1b) finite element numerical simulations including the system geometry (AFM probe and bacteria) have been used. The bacteria have been simply modelled as a closed sphere of 500 nm in diameter surrounded by an insulating membrane 6 nm thick with intrinsic electric properties represented by the membrane dielectric constant, cytoplasm conductivity, and cytoplasm dielectric constant. The computed magnitude (in analogy to the experiments to be performed) consists of the difference in impedance corresponding to the electrode-bacteria and electrode-air system. The impedance differences as a function of frequency and for a range of physiologically relevant set of values of the intrinsic electric properties have been computed and compared to the specifications of our state of the art wide bandwidth high gain current sensor for impedance measurements [6].

The main conclusion of the study is that in the frequency range accessible to our measuring set up (100 Hz-1 MHz) and under the dry conditions considered, nanoscale impedance measurements are mostly sensitive to the dielectric properties of the bacterial membrane, and very little to the cytoplasm properties. This fact is illustrated in Fig. 2a where the capacitance difference is plotted as a function of the frequency for various membrane dielectric constants and in Fig. 2b (top) where the values at 100 KHz are plotted as a function of the dielectric constant of the membrane. Due to the high sensitivity of our measuring set up, relative variations as small as ~10-15% in the membrane relative dielectric constant might be detectable Fig. 2b (bottom), thus being sensitive enough for phenotype variation associated to membrane changes.

References:

- [1] S. V. Avery, "Microbial cell individuality and the underlying sources of heterogeneity", *Nature Reviews Microbiology* **4** (2006), 577.
- [2] B. F. Brehm-Stecher and E. A. Johnson, "Single cell microbiology: tools, Techniques and Applications", *Microbiology and molecular biology reviews* **68** (2004), 538.
- [3] Y. F. Dufrene, "Using nanotechniques to explore microbial surfaces", *Nature Reviews Microbiology* **2** (2004), 451.
- [4] D. Alsteens et al., "Nanomicrobiology", *Nanoscale Research Letters* **2** (2007), 365–372.
- [5] Y. F. Dufrene, "AFM for nanoscale microbe analysis", *The Analyst* **133** (2008), 297–301.
- [6] L. Fumagalli, G. Ferrari, M. Sampietro and G. Gomila, *Nano Letters* **9**(4) (2009), 1604-1608.

Figures:

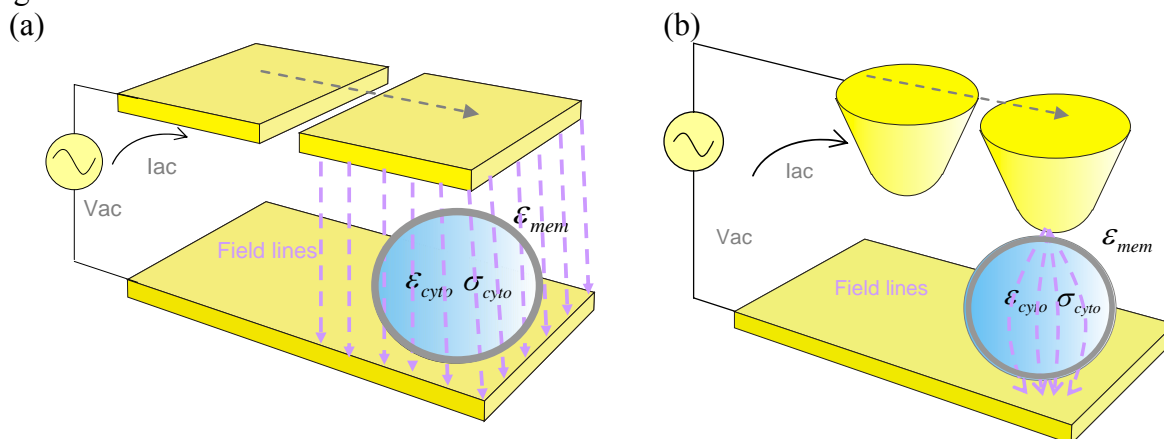


Figure 1: a) Schematic representation of the systems modelled. (a) Whole cell approach (parallel plate configuration), where analytical models can be used and (b) local cell approach (tip-substrate configuration) where finite element numerical simulations are used. The bacteria are simply modelled as a sphere of diameter 500 nm with a 6 nm membrane. The intrinsic electric properties of the membrane are represented by the membrane dielectric constant, cytoplasm conductivity and cytoplasm dielectric constant.

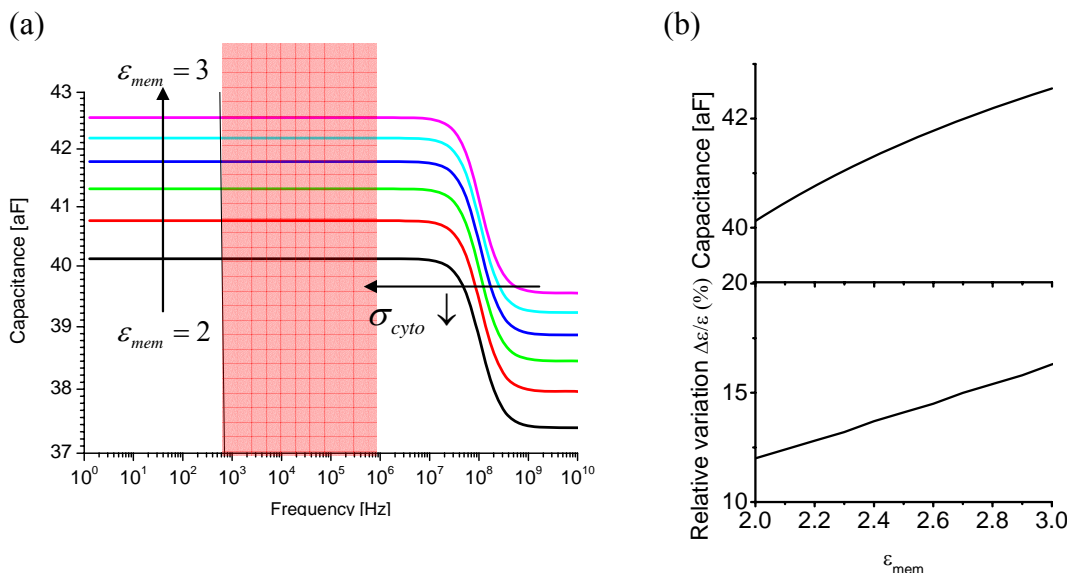


Figure 2: Change in the capacitance (imaginary part of the admittance divided by the frequency) as a function of frequency for different values of the dielectric constant of the membrane. The effect of reducing the cytoplasm conductivity is indicated schematically by the horizontal arrow. The shadow area corresponds to the measurable region. (b) Capacitance plateaux values in the range from 10 kHz to 1 MHz vs relative dielectric constant of the membrane for a cytoplasm conductivity of 0.1 [S/m] and cytoplasm permittivity of 80. (c) Minimum detectable variation in membrane dielectric constant (expressed in relative variation) for different values of the dielectric constant of the membrane (assumed experimental conditions: applied voltage 1 V_{rms}, measuring time per point 1 s, frequency range from 10 kHz to 1 MHz, detector capacitance noise under these conditions 0.83 aF).

EXCHANGE BIAS IN INVERTED ANTIFERROMAGNETIC-CORE|FERRIMAGNETIC-SHELL NANOPARTICLES

M. Estrader¹, A. López-Ortega¹, G. Salazar-Alvarez^{1,2}, D. Tobia³, E. Winkler³, S. Estradé⁴, I. Golosovsky⁵, J. Sort⁶, J. Arbiol⁴, F. Peiró⁴, S. Suriñach⁷, R.D. Zysler³, M.D. Baró⁷, J. Nogués⁸

¹Centre d'Investigació en Nanociència i Nanotecnologia, Campus UAB, Bellaterra, Spain.

²Materials Chemistry Group, Dept. of Physical, Inorganic and Structural Chemistry, Arrhenius Laboratory, Stockholm Univ., Stockholm, Sweden.

³Centro Atomico Bariloche, S.C. de Bariloche, Argentina

⁴MIND-IN2UB, Departament d'Electrònica, Universitat de Barcelona, Martí i Franquès 1, 08028 Barcelona, Spain

⁵St. Petersburg Nuclear Physics Institute, Gatchina, St. Petersburg, Russia

⁶ICREA and Dept. de Física, Univ. Autònoma de Barcelona, Bellaterra, Spain.

⁷Departament de Física, Universitat Autònoma de Barcelona, Bellaterra, Spain.

⁸ICREA and Centre d'Investigació en Nanociència i Nanotecnologia, Campus UAB, Bellaterra, Spain.

marta.estrader.icn@uab.cat

Passivated ferromagnetic (FM) nanoparticles coated with the corresponding antiferromagnetic (AFM) oxide shell have been extensively investigated [1]. However, studies of core-shell nanoparticles with AFM cores are rather scarce [2]. Here we present the study of inverted AFM-core|FiM-shell systems (MnO| γ -Mn₂O₃ and FeO|Fe₃O₄) as opposed to the typical FM-core|AFM-shell obtained from oxidation of transition metal cores. The nanoparticles have been prepared by thermolysis of the corresponding metal organic salt leading to the AFM-core (MnO or FeO) which is passivated under air yielding to the corresponding FiM-shell (γ -Mn₂O₃ or Fe₃O₄) [2,3]. The dependence of the magnetic properties of core-shell nanoparticles as a function of the AFM core size are systematically addressed for the first time, in contrast to the archetypical FM metal-core|AFM metal oxide-shell configuration where the magnetic properties are usually studied as a function of the FM size.

Narrowly size distributed MnO|Mn₃O₄ nanoparticles with different core sizes (2-20 nm) and fixed shell thickness (~3 nm) were synthesized. This system may be considered as *double inverted* since it is composed of a MnO-AFM core with $T_N = 122$ K and a γ -Mn₂O₃-FiM shell with $T_C = 39$ K (i.e., $T_C < T_N$, as opposed to conventional exchange biased systems). On the other hand, monodispersed 11nm FeO|Fe₃O₄ particles (Figure 1), with easily tuneable ratio between the core diameter and the shell thickness were prepared by controlling the passivation conditions. In this case $T_C(\text{Fe}_3\text{O}_4) > T_M(\text{FeO})$, thus the system can be considered *single inverted*. The samples were characterized by means of X-ray and neutron diffraction, transmission electron microscopy, electron energy loss spectroscopy and magnetic measurements.

In both systems the coupling at the AFM|FiM interface leads to strong exchange bias effects (e.g., large loop shift, H_E and coercivities, H_C) at low temperatures. Moreover, the magnetic properties depend in a complex way on the core and shell sizes. Interestingly, in both systems the temperature dependence of the exchange bias properties is mainly controlled by the counterpart with lowest critical temperature (γ -Mn₂O₃ or FeO).

References:

- [1] J. Nogués, et al. Phys. Rep. **422** (2005) 65.
[2] G. Salazar-Álvarez, et al. J. Am. Chem. Soc. **129** (2007) 9102.
[3] A. E. Berkowitz, et al. Phys. Rev. B. **77** (2008) 024403; A. E. Berkowitz, et al. J. Phys. D. **41** (2008) 134007; I. Djerdj, et al. J. Phys. Chem. C. **111** (2007) 3641; D. W. Kavich, et al. Phys. Rev. B. **78** (2008) 174414.

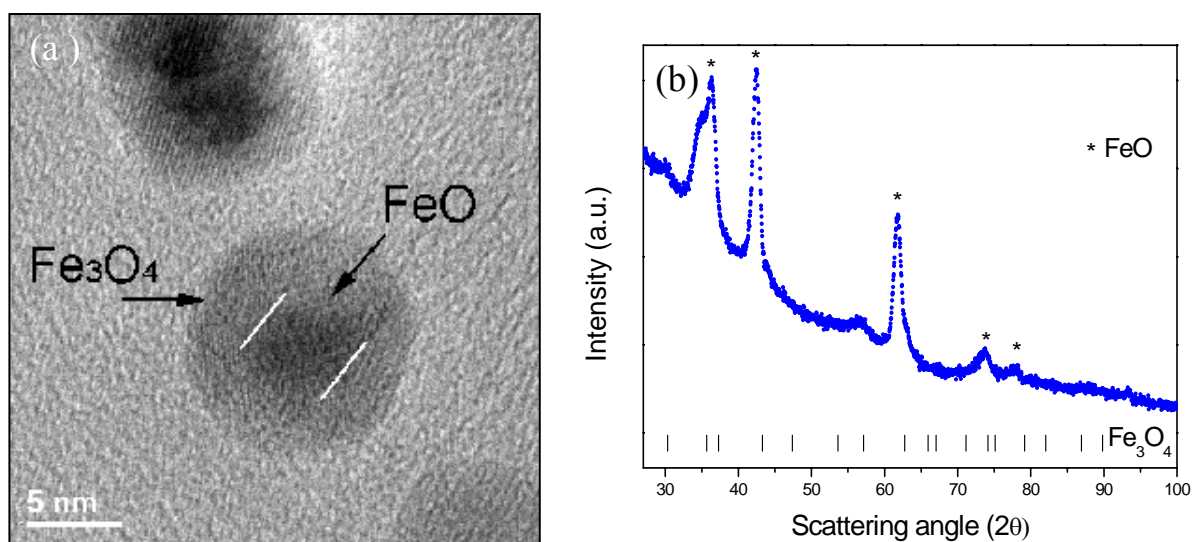
Figures :

Figure 1 : (a) HRTEM image of $\text{FeO}|\text{Fe}_3\text{O}_4$ core-shell nanoparticle. (b) XRD diffractogram of $\text{FeO}|\text{Fe}_3\text{O}_4$ core-shell particle. The lines below show the position of the reflections corresponding to cubic Fe_3O_4 phase.

NANOPARTICLE HETEROCOALESCENCE INDUCED BY DEPOSITION

J C Jiménez-Sáez¹, M S Ettaoussi², A M C Pérez-Martín³, M L Kerkeb² and J J Jiménez-Rodríguez³

¹*Dpto. de Física y Química Aplicadas a la Técnica Aeronáutica, E.U.I.T.Aeronáutica, Universidad Politécnica de Madrid (UPM), E-28040 Madrid, Spain.*

²*Dép. de Physique, Faculté des Sciences, Université Abdelmalek Essaâd, Tétouan, Maroc.*

³*Dpto. de Física Aplicada III (Electricidad y Electrónica), Facultad de Ciencias Físicas, Universidad Complutense de Madrid (UCM), E-28040 Madrid, Spain.*

jc.jimenez@upm.es

Cobalt in nanocrystalline form is an attractive system because it displays a wealth of size-dependent structural, magnetic, electronic, and catalytic properties [1]. From a technological viewpoint, Co nanoparticles have applications in magnetic storage media. Below a certain size (≤ 20 nm of diameter), clusters of cobalt crystallize in the face-centered cubic (fcc) phase and most particles possess crystalline structures made up of multiply-twinned icosahedra [2]. Besides, these nanoparticles are converted into single-crystal Wulff polyhedra above 300°C.

The general process of intercluster coalescence has been extensively studied using molecular dynamics [3-5] or by macroscopic models of sintering [6]. This process is driven by capillarity since it reduces the surface free energy. Specifically, the coalescence of supported clusters is of great importance in the field of surface nanostructuring [7]. Kellet and Lange [8, 9] indicated that, in the case of the presence of grain boundaries between particles, a further lowering of the free energy would require the recrystallization of some particles. Therefore, atomistic models describing coalescence must account for changing crystallographic mismatch. Many groups have performed crystallite rotation techniques in order to investigate the reorientation during sintering for metals [10-14] and oxide particles [15, 16]. For metals, the mechanism of reorientation may then include the formation or migration of grain-boundary dislocations.

In the present work, the coalescence between Co and Cu clusters on Cu(001) substrate is studied by constant-temperature molecular dynamics simulations. Cobalt clusters embedded or supported in a copper matrix constitute an attractive system, because it displays important magnetic properties [17,18]. Atomic interactions are mimicked by a many-body potential based on the second-moment tight-binding approximation (TB-SMA). Initially, Co clusters of about half a thousand of atoms in their more stable form were deposited on a Cu (001) substrate at 250 meV/atom and room temperature. Next, a randomly oriented Cu cluster of the same size at 250 meV/atom with icosahedral or cuboctahedral form and fcc phase was deposited on the former colliding with this at room temperature. The center-of-mass separation between the projectile and target clusters was varied uniformly. The degree of epitaxy of the two clusters has been investigated as a function of this separation, and of the type of material. The effect of the temperature as activation of grain-boundary movement to get the complete epitaxy has been also analyzed in the projectile cluster.

Nanoparticle coalescence has theoretically as well as experimentally been shown to be a two-step process: first a reorientation of adjacent nanoparticles, and second a complete or incomplete adhesion depending on the matching of the crystallographic orientations [16]. This work is mainly focused on the first process, since the appearance, movement, and disappearance of grains after the collision has been described. The evolution of the number of atoms and energy in each grain plays an important role in the alignment of the second cluster with the substrate [19], and define a trend in the final internal morphology of the system.

References:

- [1] V. F. Puentes, K. M. Krishnan, and A. P. Alivisatos, *Science*, **291** (2001) 2115.
- [2] O. Kitakami, H. Sato, Y. Shimada, F. Sato, and M. Tanaka, *Phys. Rev. B*, **56** (1997) 13849.
- [3] L. J. Lewis, P. Jensen, and J.-L. Barrat, *Phys. Rev. B*, **56** (1997) 2248.
- [4] S. Hendy, S. A. Brown, and M. Hyslop, *Phys. Rev. B*, **68** (2003) 241403-1.
- [5] S. Arcidiacono, N. R. Bieri, D. Poulidakos, and C. P. Grigoropoulos, *Int. J. of Multiphase Flow*, **30** (2004) 979.
- [6] F. A. Nichols and W. W. Mullins, *J. Appl. Phys.*, **36** (1965) 1826.
- [7] P. Jensen, *Rev. Mod. Phys.*, **71** (1999) 1695.
- [8] B. J. Kellett and F. F. Lange, *J. Am. Ceram. Soc.*, **72** (1989) 725.
- [9] F. F. Lange and B. J. Kellett, *J. Am. Ceram. Soc.*, **72** (1989) 735.
- [10] S.-W. Chan and R. W. Balluffi, *Acta Metall.*, **34** (1986) 2191.
- [11] M. Yeadon, J. C. Yang, R. S. Averback, J. W. Bullard, D. L. Olynick, and J. M. Gibson, *Appl. Phys. Lett.*, **71** (1997) 1631.
- [12] J. K. Bording, B. Q. Li, Y. F. Shi, and J. M. Zuo, *Phys. Rev. Lett.*, **90** (2003) 226104.
- [13] Y. Ashkenazy, R. S. Averback, and K. Albe, *Phys. Rev. B*, **64** (2001) 205409.
- [14] S. Arcidiacono, N. R. Bieri, D. Poulidakos, and C. P. Grigoropoulos, *Int. J. Multiphase Flow*, **30** (2004) 979.
- [15] J. Rankin and B. W. Sheldon, *Mater. Sci. Eng. A*, **204** (1995) 48.
- [16] R. Theissmann, M. Fendrich, R. Zinetullin, G. Guenther, G. Schierning, and D. E. Wolf, *Phys. Rev. B*, **78** (2008) 205413.
- [17] J. C. Cezar, H. C. N. Tolentino, M. Knobel, *Phys. Rev. B*, **68** (2003) 054404.
- [18] Š. Pick, V. S. Stepanyuk, A. L. Klavsyuk, L. Niebergall, W. Hergert, J. Kirschner, and P. Bruno, *Phys. Rev. B*, **70** (2004) 224419.
- [19] J. C. Jiménez-Sáez, M. S. Ettaoussi, A. M. C. Pérez-Martín, M. L. Kerkeb, and J. J. Jiménez-Rodríguez, *J. Nanosci. Nanotechnol.*, in press (2009).

Impact of agglomeration on the relaxometric properties of gadolinium oxide nanoparticles as a contrast agent for MRI

Luc Faucher¹, Yves Gossuin², Marc-André Fortin¹

¹*Université Laval et Centre hospitalier universitaire de Québec (CHUQ), Québec, Canada*

²*Université de Mons-Hainaut, Mons, Belgique*

luc.faucher.1@ulaval.ca

Context: Magnetic resonance imaging (MRI) is a non invasive biomedical imaging modality that allows high resolution diagnostics. The signal in MRI is provided by relaxing ^1H protons. In order to increase the efficiency of tissue differentiation, it is often necessary to increase the signal in specific organs or tissues. To date, contrast agents are used in 30% of all clinical scans and the most used are gadolinium chelates [1]. These chelates are referred to as “positive- T_1 ” contrast agents since they enhance the signal from relaxing ^1H protons. In the context of cellular imaging however, those chelates do not allow the study of cell migration in vivo since they are not efficiently retained within the cells. This is a niche application for which ultra-small gadolinium oxide nanoparticles (US-Gd₂O₃, \varnothing core = 3 nm) have been considered [2, 3]. Nanoparticles can be efficiently ingested and retained by cells, leading to improved contrast with T_1 -weighted MRI sequences [4, 5]. However, once internalised by the cells, the nanoparticles tend to agglomerate in endosomes [4]. The present study aimed at evaluating the impact of agglomeration on the relaxometric properties of Gd₂O₃ nanoparticles. In order to avoid interference with organic materials, here only aqueous suspensions of nanoparticles were characterized (without cells).

Materials and Methods: US-Gd₂O₃ were synthesized by hydrolysis in a polyol solvent [6, 7]. As-synthesized nanoparticles are covered with diethylene glycol (DEG-Gd₂O₃). Then, they were dialyzed against water. Due to the presence of contaminating DEG, the resulting nanoparticle suspensions tend to form nanoagglomerates of hydrodynamic size ranging from 3 nm (individual nanoparticles) to about 105 nm. The hydrodynamic radius of agglomerates was studied by dynamic light scattering (DLS), while longitudinal relaxivities (r_1) were measured on a Stellar field cycling relaxometer (NMRD) from 0.01 to 10 MHz. The relaxometric study was completed by using dedicated relaxometers (Bruker Minispec, 10, 20, 60 MHz) to measure ^1H longitudinal and transversal relaxation times (T_1 and T_2) at clinical fields. High resolution NMR spectrometers were used to characterize the suspensions at 300 and 500 MHz (high-field MRI). Gd concentration was measured by ICP-MS.

Results and conclusions: Agglomeration of DEG-Gd₂O₃ results in a slight decrease of both r_1 and r_2 . However, even 105 nm agglomerates still perform well as “positive- T_1 ” contrast agents, as suggested by r_2/r_1 ratios close to 1.5 at 60 MHz, compared to 1.3 for individual nanoparticles. The simulated signal intensity is 10.5% higher for individual nanoparticles. At clinical fields (~1.5 T, 60 MHz), NMRD curves indicate a promising maximum in r_1 relaxivity. This maximum occurs at magnetic fields six times higher than for individual ultra-small iron oxide nanoparticles (USPIOs). This result suggests that Gd₂O₃ nanoparticles are more suitable than USPIOs to provide positive contrast in clinical 1.5 to 3 T MRI [8, 9]. DEG-Gd₂O₃ could also be used in high-field pre-clinical MRI (at 4-7 T), a range of magnetic fields for which USPIOs cannot be used to provide positive contrast because the T_2^* effects become too important [8].

References:

- [1] Toth, É., L. Helm and A.E. Merbach, *Topics in Current Chemistry*, **221** (2002) 235.
- [2] Fortin, M.-A. et al., *Nanotechnology*, **18** (2007) 395501.
- [3] Bridot, J.-L. et al., *Journal of the American Chemical Society*, **129** (2007) 5076.
- [4] Fortin, M.-A. et al., *Proceedings of the ISMRM Conference 2009, Hawaii*, (April 2009) Abstract 6130.
- [5] Klasson, A. et al., *Contrast Media & Molecular Imaging*, **3** (2008) 106.

- [6] Bazzi, R. et al., *Journal of Luminescence*, **102-103** (2003) 445.
- [7] Söderlind, F. et al., *Journal of Colloid and Interface Science*, **288** (2005) 140.
- [8] Roch, A., R.N. Muller and P. Gillis, *The Journal of Chemical Physics*, **110** (1999) 5403.
- [9] Cunningham, C.H. et al., *Magnetic Resonance in Medicine*, **53** (2005) 999.
- [10] Weishaupt, D., V.D. Köchli and B. Marincek, *An Introduction to the Physics and Function of Magnetic Resonance Imaging*, Springer, Berlin, (2003) 169 p.

Figures:

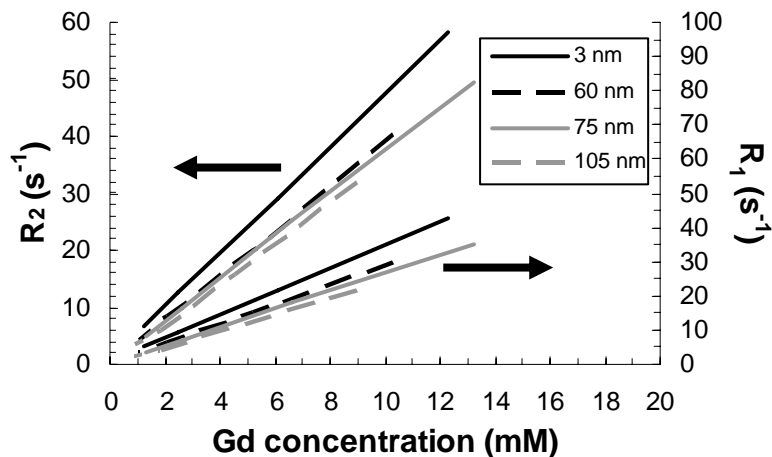


Figure 1: Longitudinal (R_1) and transversal (R_2) relaxation rates of DEG-Gd₂O₃ agglomerates

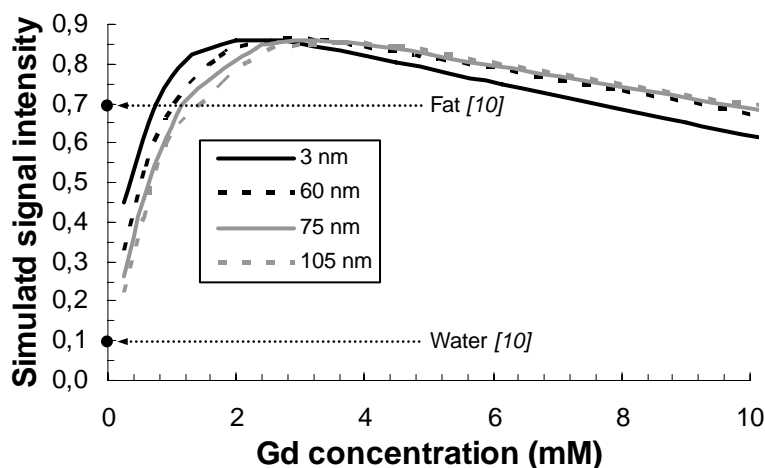


Figure 2: Simulated signal intensity for suspensions of Gd₂O₃-containing nanoagglomerates (based on measured T_1 and T_2 , and a spin-echo sequence with TE 10 ms, TR 400 ms)

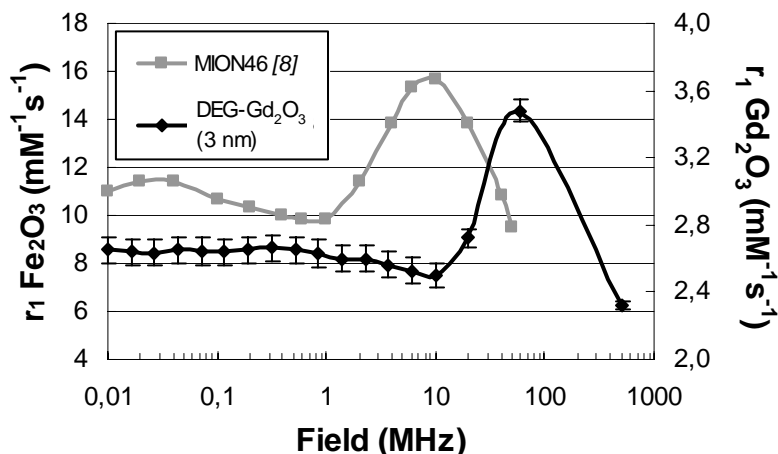


Figure 3: NMRD curves of Fe₂O₃ and DEG-Gd₂O₃ nanoparticles

Magnetoresistance and I-V characteristics of n-Si/SiO₂/Ni nanostructures

Fedotov A., Ivanou D., Ivanova Yu., Mazanik A., Svito I.

Belarusian State University, Independence av. 4, 220030 Minsk, Belarus

fedotov@bsu.by

Tyutyunnikov S.,

Joint Institute for Nuclear Research, Dubna, Russia

Demyanov S., Kanyukov E.

Scientific-Practical Material Research Centre NAS of Belarus, Minsk, Belarus

At the present times development of the methods to create spintronic nanostructures on the base of porous templates is of special interest. An electrochemical filling of pores requires no vacuum or expensive equipment and possesses several advantages over other processes like chemical deposition, sputtering, etc. Electrodeposition is a low-temperature technique permitting to avoid interdiffusion of the components of the formed heterostructures. Electrodeposition occurs only on conductive areas of the substrate.

In this work we used underpotential electrodeposition of Ni nanoparticles into mesopores in SiO₂ layer as template [1] created on n-Si(1 0 0) substrate with 4.5 Ω·cm resistivity to produce magneto sensitive nanostructures n-Si/SiO₂/Ni. SiO₂ layer with thickness of 700 nm was thermally grown by standard procedure (1100 °C, 10 hours, pure oxygen). To produce a mesoporous SiO₂ layer, scanned beams of 350 MeV ¹⁹⁷Au²⁶⁺ ions were employed for the bombardment of silicon oxide on Si(1 0 0) substrate with doses of 5·10⁸ cm⁻². Pores were formed by chemical etching of the irradiated SiO₂ layer with latent tracks in dilute HF on the whole depth of layer down to Si substrate. Etching resulted in the formation of the uniform mesopores randomly distributed over the surface and shaped like truncated cones with base diameters of 100 and 250 nm. Mesopores filled with Ni was nanostructured rods (nanorods).

Structure of Ni nanorods inside of SiO₂ was studied using SEM LEO-1455VP and AFM SolverPro. I-V characteristics and DC resistance of n-Si/SiO₂/Ni nanostructures were measured in the Close-Cycle Refrigerator System (Cryogenic Ltd.) in the temperature range 1.8 – 310 K and magnetic fields with induction up to 8 T. Electrical probes were prepared by ultrasound soldering of indium. Schematic sketch of the sample with pores and probes is shown in insert 1 in Fig. 1. As is seen, at such scheme of electric measurements the studied n-Si/SiO₂/Ni nanostructures present two sets of Ni nanorods embedded in SiO₂ layer (under two In probes) connected by Si substrate.

Temperature dependences of resistance R(T) of n-Si/SiO₂/Ni nanostructures in Arrhenius scale are presented in Fig. 1. The observed behavior of R(T) indicates that in the studied nanostructures at temperatures of 200 – 300 K (region 1 in Fig. 1) activation (exponential) carrier transport by Si substrate predominates having activation energy close to half of the gap width of Si. At the lowest temperatures (less than 20 K), when zone carrier transport by Si substrate is frozen-out, curves lg(R) -1/T are characterized by changing activation energies (region 3 in Fig. 1) that can be evidence of hopping conductance by localized states. This contribution in carrier transport can be attributed to the movement of electrons either along interface n-Si/SiO₂ (due to the band bending and formation of the layer enriched by electrons) or by thin parts of SiO₂ between Ni nanorods. The region 2 of R(T) in Fig. 1, having activation energy close to the ionization energy of phosphorus in Si, may be attributed to impurity conductance.

Inasmuch as junction of Si with Ni nanorods should result in energy band bending the nanostructure n-Si/SiO₂/Ni in electric sense will look like two Schottky barriers switched on oppositely to each other. Just due to this reason I-V characteristics shown in Insert 2 in Fig. 1 are non-linear and practically symmetrical.

As is seen from Fig. 2a, application of magnetic field both normally and along surface of n-Si/SiO₂/Ni nanostructures resulted in increase of resistance. As shown in Fig. 2b, the values of magnetoresistance $\Delta R(H)/R(0)$ were maximal at the temperature 25 K and dependent on measuring current (value of R estimated as V/I) reaching magnitudes of 800 – 12500 at the maximum point.

References:

[1] Yu. A. Ivanova, D. K. Ivanou, Ж. A. K. Fedotov, E. A. Streltsov, S. E. Demyanov, A. V. Petrov, E. Yu. Kaniukov, D. Fink, J. Mater. Sci., **42** (2007) 9163.

Figures:

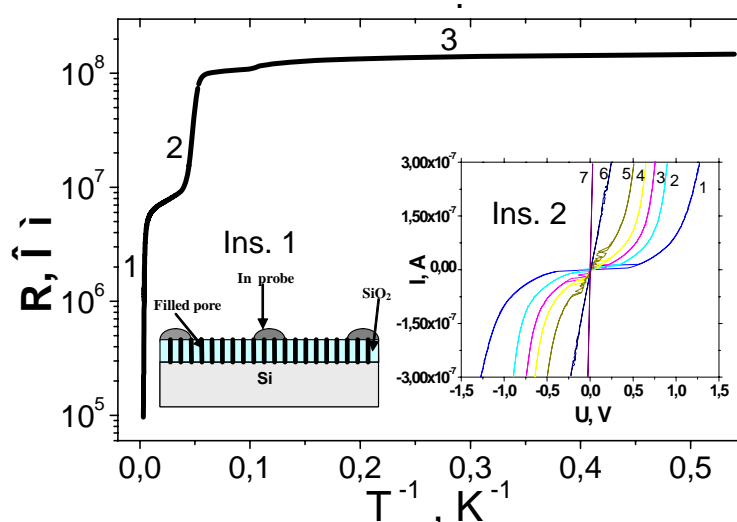


Fig. 1. Temperature dependence of resistance between two In-probes shown in Insert 1 at current 100 nA. Insert 1: A schematic sketch of the sample containing Si substrate, SiO₂ layer with filled pores and In probes. Insert 2: I-V characteristics for different temperatures in zero magnetic field: 1 – 25 K, 2 – 50 K, 3 – 100 K, 4 – 150 K, 5 – 200 K, 6 – 250 K, 7 – 300 K

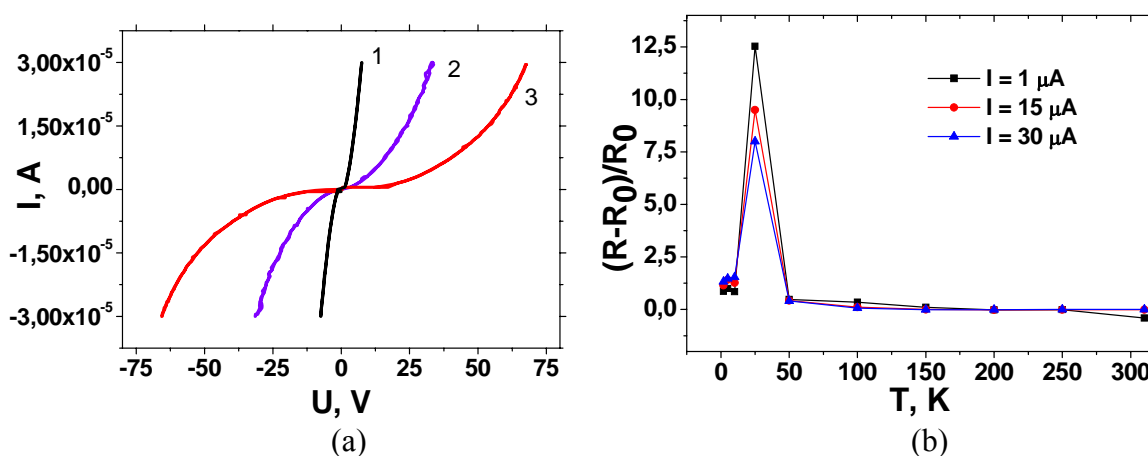


Fig. 2. I-V characteristics at 25 K for zero magnetic field (1) and fields 8 T directed normally (2) or along (3) sample surface (a) and temperature dependences of magnetoresistance $[R(8\text{ T}) - R(0)]/R(0)$ for 3 different measuring current I values (b)

Verification of coupling between negative magnetoresistance and magnetization in FeCoZr-Al₂O₃ granular nanocomposites

Fedotov Alexander¹, Kasiuk Julia², Fedotova Julia², Przewoznik Janusz³, Kapusta Czeslaw³

¹BSU, 4 Nezavisimostci av., 220030, Minsk, Belarus

²NC PHEP BSU, 153 M.Bogdanovich str., 220040, Minsk, Belarus

³Faculty of Physics and Applied Computer Science, AGH University of Science and Technology, 30-059, Cracow, Poland

Julia@hep.by

Granular metal-dielectric nanocomposites (Me_xD_{100-x} GNC) are characterized with change of electrical conductivity mechanism from variable-range hopping (VHR) onto metallic within percolation threshold, where current-conductive (percolative) cluster of metallic nanoparticles is formed ($X \approx 50$ at. %). Spin-dependent character of negative magnetoresistance (NMR) assumes correlation between magnetoresistivity $(\rho(B) - \rho(0)) / \rho(0)$ ($\Delta\rho/\rho$) and reduced magnetization $(M/M_S)^2$ [1]. Experimental observation of such correlation may serve as a criterion for VHR conductivity at applied magnetic field at definite Me_xD_{100-x} GNC composition. Obviously, size of Me nanoparticles is also one of factors influencing both $M(B)$ and $\Delta\rho/\rho$ curves and conductivity mechanisms in GNC. Present research is aimed on the joint analysis of $\Delta\rho/\rho$ and $(M/M_S)^2$ curves in order to investigate magnetotransport measurements in FeCoZr-Al₂O₃ GNC.

GNC films (FeCoZr)_x(Al₂O₃)_{100-x}, 38 ≤ x ≤ 63 at.% were sputtered in Ar ambient, $P_{Ar} = 6.7 \cdot 10^{-2}$ Pa, onto glass-ceramic substrates. Field cooled - zero field cooled (FC-ZFC) dc $M(T)$ and $M(B)$ magnetization curves as well as $\Delta\rho/\rho$ were measured in the temperature range of 4–300 K using a 9 T VSM-PPMS (Quantum Design).

Fig. 1 shows $\Delta\rho/\rho$ and $(M/M_S)^2$ curves plotted for (FeCoZr)₄₂(Al₂O₃)₅₈ and (FeCoZr)₅₀(Al₂O₃)₅₀ compositions. Observed coincidence between $\Delta\rho/\rho$ and $(M/M_S)^2$ for (FeCoZr)₅₀(Al₂O₃)₅₀ evidenced that magnetotransport is realized predominantly by spin-dependent VHR (see Fig. 1a). Increase of FeCoZr fraction draw to progressive deviation between $\Delta\rho/\rho$ and $(M/M_S)^2$ (see Fig. 1b) that correlates with the formation of current-conductive cluster and growing contribution of metallic conductivity.

FC-ZFC magnetization curves $M(T)$ are presented in Fig. 2a. Growth of metallic fraction draw to the broadening of ZFC $M(T)$ curves and shift of its maximum correspondent to blocking temperature (T_B) towards higher values. Sizes of weakly interacting (superparamagnetic, SP) FeCoZr nanoparticles were calculated using the relationship $25k_B T = KV$ between T_B and particles' volume V , where k_B is a Boltzmann constant, K is the magnetic anisotropy constant for FeCo nanoparticles (10^6 J/m³ [2]). Expectedly, growth of FeCoZr fraction in nanocomposites draw to the increase of SP nanoparticle sizes (see Table). Alternative estimation of nanoparticles size by fitting of $M(B)$ (see Fig. 3) curves with Langevin functions $M(B)/M_S = \coth(M_S V B / kT) - kT / M_S V B$, where M_S is saturation magnetization revealed quite similar values (see Table).

Table

Estimation of FeCoZr granules sizes based on ZFC $M(T)$ and $M(B)$ magnetization curves

Estimation method	Samples	(FeCoZr) ₄₂ - (Al ₂ O ₃) ₅₈	(FeCoZr) ₄₇ - (Al ₂ O ₃) ₅₃	(FeCoZr) ₅₀ - (Al ₂ O ₃) ₅₀
Maximum of ZFC curve, (T_B)		3 nm	3,5 nm	4 nm
Fitting of $M(B)$ using Langevin function		4,4 nm	5,8 nm	---

In doing so, spin-dependent *VRH* was proved to be the dominating mechanism of magnetotransport for $(\text{FeCoZr})_{42}(\text{Al}_2\text{O}_3)_{58}$ *GNC* containing totally isolated SP nanoparticles with medium sizes about 4,4 nm. Alternatively, deviation from *VHR* conductivity were observed for $(\text{FeCoZr})_{50}(\text{Al}_2\text{O}_3)_{50}$ *GNC* where nanoparticles size increased up to 5,8 nm.

References:

[1] Changzheng Wang et al., *J. Mater. Sci.*, **41** (2006) 3873.
 [2] N.M. Dempsey et al., *J. Appl. Phys.*, **90** (2) (2001) 6268.

Figures:

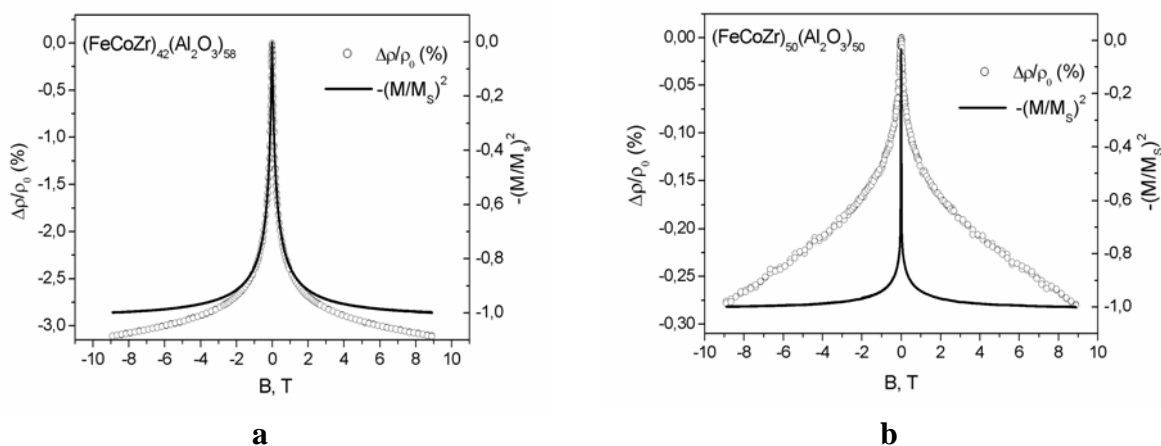


Fig. 1. NMR and reduced magnetization $(M/M_s)^2$ of $(\text{FeCoZr})_{42}(\text{Al}_2\text{O}_3)_{58}$ (a) and $(\text{FeCoZr})_{50}(\text{Al}_2\text{O}_3)_{50}$ (b) samples

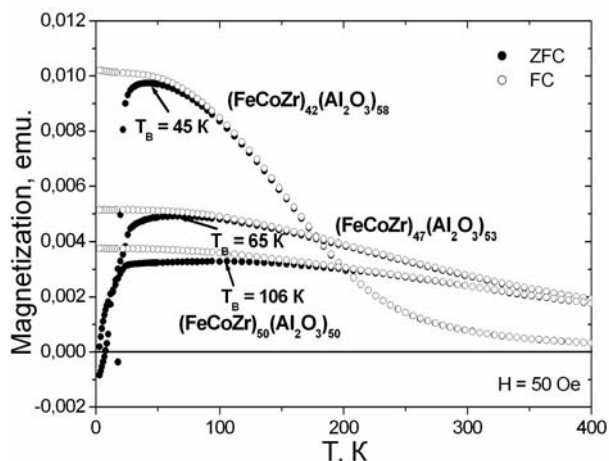


Fig. 2. FC-ZFC curves of samples with different concentration

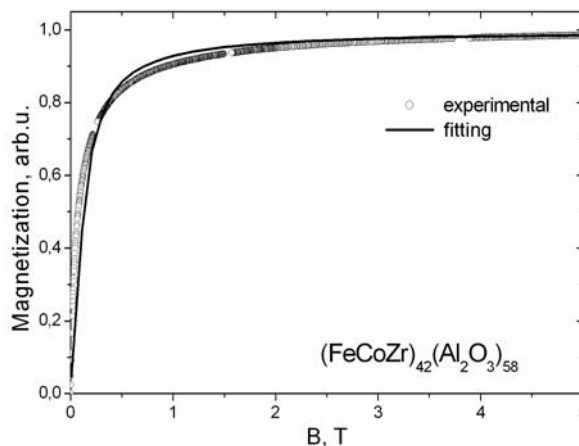


Fig. 3. Magnetization curve $M(B)$ and its fitting for $(\text{FeCoZr})_{42}(\text{Al}_2\text{O}_3)_{58}$ sample

Influence of sputtering ambient on impedance and magnetoimpedance of soft magnetic CoFeZr nanoparticles embedded in alumina matrix

J. Fedotova, A. Larkin, Yu. Kalinin, A. Sitnikov, V. Fedotova, Yu. Ilyashuk, A. Fedotov
Belarusian State University, Independence av. 4, 220030 Minsk, Belarus
fedotov@bsu.by

At the present time great interest is shown in granular composite materials which consist of Fe-Co-containing soft ferromagnetic nanoparticles, embedded in dielectric matrixes [1]. Their low coercivity along with high saturation magnetization and the observed GMR/TMR effects are beneficial for many of high-frequency applications of such composites. The aim of the present work is to investigate the influence of a sputtering ambient on the impedance and magnetoimpedance over a wide frequency range of the $(\text{Co}_{45}\text{Fe}_{45}\text{Zr}_{10})_x(\text{Al}_2\text{O}_3)_{100-x}$ composite films.

The films with the fractions of metallic alloy $20 < x < 70$ at.% were sputtered in the chamber evacuated either with pure Ar under pressure P_{Ar} of $6,7 \cdot 10^{-2}$ Pa (set 1 films) or Ar + O₂ mixtures with partial pressure $P_{\text{O}} = (1.3 \div 5.0) \cdot 10^{-3}$ Pa (set 2) or Ar + N₂ with $P_{\text{N}} = (1.31 \div 2.13) \cdot 10^{-2}$ Pa (set 3). For the films with thicknesses from 3 to 15 μm such properties as DC and AC resistance, magneto transport, Mössbauer spectra, magnetization were measured. Impedance measurements were carried out at the frequencies $f \approx 10^2 \div 2 \cdot 10^6$ Hz at $100 \div 340$ K. The real (μ') and imaginary (μ'') parts of magnetic permeability μ was measured at $f \approx 25 \div 200$ MHz. Magnetization, permeability, AFM in AC MFM regime and Mössbauer studies were performed at room temperatures. The presence of alloy nanoparticles with sizes of 2 - 10 nm in the studied samples was confirmed by TEM and PC AFM microscopies.

Analysing the Mossbauer and carrier transport data for the studied composites, we can conclude that the introduction of reactive gases into the argon sputtering atmosphere has resulted in the formation of oxide or nitride "shells" around the alloy nanoparticles. These "shells" led to an increase (approximately by 2-3 orders of magnitude) in the values of DC/AC resistance of the films in sets 2 and 3 as related to the set 1 at the comparable x values. Our measurements have also shown that introduction of reactive gas into the deposition atmosphere greatly increased inductive contribution into the low-frequency impedance of composite materials especially for the composites beyond the x_C . The presence of an inductive contribution in the equivalent circuits was explained by a phenomenological model [2]. According to this model, in real nanostructured composites, even below the x , the insulating layers (strata) separating single highly-conductive (metallic) nanoparticles can take part in the formation of the self-crossing current-conducting routes similar to inductive coils embedded in the dielectric matrix. The formation of the whole net of coil-like routes beyond the percolation threshold enhances this effect.

To understand the influence of reactive gases on the magnetic state of the studied nanocomposites, the magnetoimpedance was measured too. Comparison of Figs 1a-1d have shown that for the films of set 2 and 3 the region of superparamagnetic state was expanded far beyond the value of $x_C \approx 41-45$ at.% observed for the set 1 films (see, Fig. 1a). The last was confirmed in a lack of sextet in Mössbauer spectra, conservation of non-hysteresis behavior of magnetization curves higher than the blocking temperature [2-5] and lowering of real μ' and imaginary μ'' parts of magnetic permeability (compare Fig. 1a and Figs. 1b-1d) far beyond x_C in comparison with the films sputtered in pure argon (Fig. 1a). Mössbauer spectroscopy allowed to attribute such peculiarities to the formation of oxide or nitride shells around nanoparticles

preventing their magnetic interaction even at the direct electric contacting of nanoparticles covered with these shells [3-5].

Analysis of Fig. 1 and earlier results obtained in [1-5] allows to conclude that the values of complex magnetic permeability and magnetic state of the composites under study results in two their main features. Firstly, at room temperatures the low- x composites display superparamagnetic state which is not generally dependent on the composition of gaseous atmosphere during film deposition, although the x -values where the superparamagnetic state is observed are shifted to higher concentrations of metallic phase with the addition of reactive gases into the vacuum chamber. Secondly, for the studied nanocomposites with $x > x_c$ their magnetic state, including the AC MFM response [5] and values of high-frequency μ' and μ'' , is strongly dependent on the composition of gaseous atmosphere in the sputtering chamber. Specifically, the superparamagnetic state and labyrinth-like AC MFM contrast for the set 2 samples (see, [3,5]) were conserved even beyond the percolation threshold.

References:

- [1] A. Saad, A. Mazanik, Yu. Kalinin, J. Fedotova, A. Fedotov, S. Wrotek, A. Sitnikov and I. Svito, *Rev. Adv. Mater. Sci.*, **8** (2004) 152.
 [2] J. Fedotova, A.Larkin, A.Fedotov, A. Kalaev, A. Sitnikov, Yu. Kalinin, B. Andrievski, A. Patrin. *Physics, Chemistry and Application of Nanostructures: Reviews and Short Notes to NANOMEETING-2007* (Minsk, Belarus, May 22-25, 2009, Eds V.E. Borisenko, S.V. Gaponenko, V.S. Gurin). 2009 (in print).
 [3] A.M. Saad, A.K. Fedotov, J.A. Fedotova, I.A. Svito, B.V. Andrievsky, Yu.E. Kalinin, V.V. Fedotova, V. Malyutina-Bronskaya, A.A. Patryn, A.V. Mazanik and A.V. Sitnikov, *Phys. Stat. Solidi (c)*, **3** (2006) 1283.
 [4] Anis Saad, A.K. Fedotov, I.A. Svito, AV. Mazanik, B.V. Andrievski, AA. Patryn, Yu. Kalinin and AV. Sitnikov, *Progr. in Solid. State Chem.* **14** (2006) 139.
 [5] A.V. Sitnikov, *Proc. of Intern. Seminar on the Problems of Magnetism in Magnetic Films, Small Particles and Nanostructures* (Astrakhan, Russia, 2003), p. 75.
 [6] A.M. Saad, V.A. Kalaev, J.A. Fedotova, K.A. Sitnikov, A.V. Sitnikov, Yu. Kalinin, A.K. Fedotov and I.A. Svito, *Rev. Adv. Mater. Sci.*, **15** (2007) 208.

Figures:

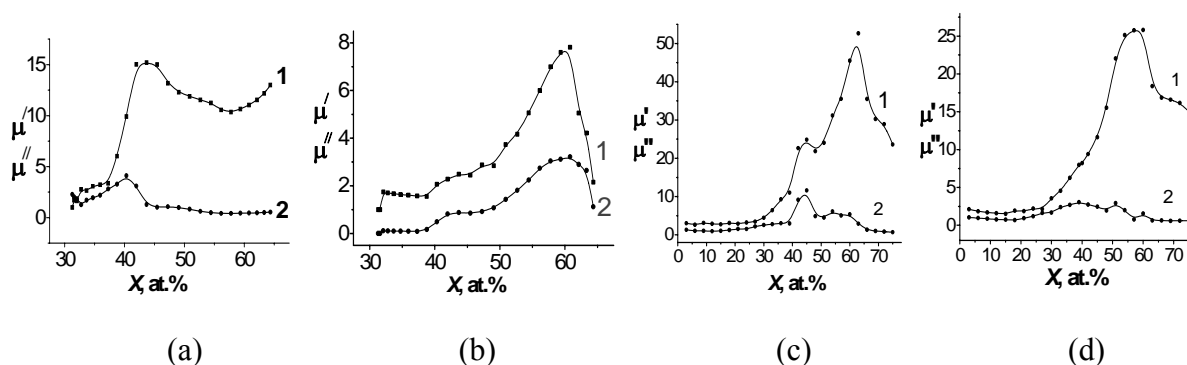


Fig. 1. Dependences of μ' (curves 1) and μ'' (curves 2) for $f = 25$ MHz vs concentration x in nanocomposites of set 1 deposited in Ar (a), in set 2 deposited in Ar + O₂ (b) and set 3 deposited in Ar + N₂ with $P_{N_1} = 1.31 \cdot 10^{-2}$ Pa (c) and $P_{N_2} = 2.13 \cdot 10^{-2}$ Pa (d).

Piezoresistive cantilevers based on Si nanowire array strain gauges

Marta Fernández-Regúlez, Jose Antonio Plaza, Álvaro San Paulo

Instituto de Microelectrónica de Barcelona,
Centro Nacional de Microelectrónica (CSIC)
Campus UAB, Bellaterra 08193, Barcelona, Spain.
Phone: (+34).93.594.77.00; E-mail: alvaro.sanpaulo@cnm.es

Silicon nanowires obtained via catalytic synthesis offer many extraordinary properties for applications in nanomechanical devices. In particular, their double-clamped horizontally self-assembled growth [1], together with their recently reported giant piezoresistance [2,3], enable an unprecedented approach to obtain highly sensitive piezoresistive nanomechanical cantilever sensors. The use of integrated piezoresistive sensors for detecting cantilever deflections implies important advantages with respect to conventional external optical detection, such as enabling applications where difficulties in laser alignment make optical detection inconvenient, or when sensitivity optimization via size reduction implies scaling dimensions far below the wavelength of the illumination used. Unfortunately, typical detection limits obtained with conventional Si thin film piezoresistive strain gauges are still below the values provided by optical detection. The integration of Si nanowire arrays as piezoresistive strain gauges in cantilevers will allow taking advantage of their giant piezoresistive coefficients, providing and improvement in sensitivity that could reach more than two orders of magnitude and become comparable to that of optical methods.

In this contribution, we present our conclusions concerning the design, fabrication technology and preliminary performance tests of piezoresistive cantilevers based on Si nanowire array strain gauges. Our design is based on the standard double-leg strain gauge cantilever. Finite elements simulations show that the nanowire array must be located only in one side of the neutral axis at the base of the cantilever, so that only tensile or compressive stresses occur in the nanowires when the cantilever is deflected. Fabrication of such structure can be achieved by lithography-guided growth of Si nanowires via the VLS mechanism [4]. Guided growth is possible by using a selective area Au catalyst deposition method that ensures nanoparticle deposition only at silicon exposed areas but not on oxide covered surfaces. The diameter, density and doping concentration of the nanowire arrays are all controlled by tuning the synthesis conditions.

The analysis of the device performance reveals that besides the high sensitivity provided by the large piezoresistive gauge factor of the nanowires, which increases with decreasing NW diameter, signal-to-noise ratio plays a dominant role on determining the deflection detection limit. We find that Hooge noise ($1/f$) is the dominant noise source, which is essentially due to the reduced volume of the nanowire array resistor and thus the low number of carriers. In consequence, a large number of small diameter nanowires minimizes the total noise while optimizes the piezoresistive sensitivity, resulting in a minimum detectable deflection that can reach the sub-picometer range, a factor 3 to 5 lower than previously reported state-of-the-art piezoresistive Si cantilevers.

- [1] A. San Paulo, et al. Appl. Phys. Lett. 87 (2005) 053111
- [2] R. He, et al. Nat. Nanotech.1(2006) 46
- [3] A.C.H. Rowe, Nat. Nanotech. 3(2008) 312
- [4] A. San Paulo, et al. Nano Lett. 7 (2007) 1100

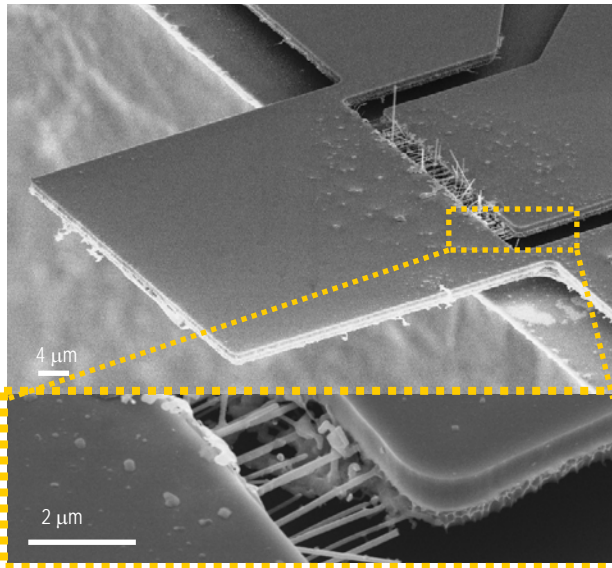


Fig 1. SEM image of the Cantilever

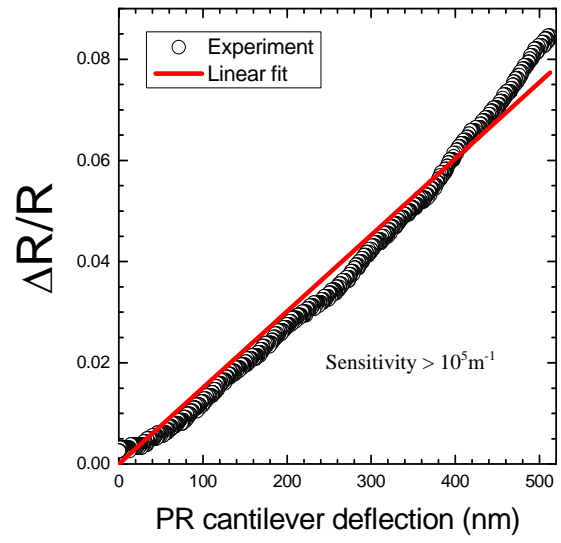


Fig 2. Relative change of resistance vs cantilver deflection.

INTERACTION BETWEEN LSP AND SPP IN MAGNETOPLASMONIC STRUCTURES

J. F. Torrado¹, J. B. González-Díaz¹, A. García-Martín¹, M. U. González^{1,2}, J. M. García-Martín¹, A. Cebollada¹, S. Acimovic², J. Cesario², R. Quidant², G. Badenes², G. Armelles¹.

¹Instituto de Microelectrónica de Madrid, IMM (CNM-CSIC), Tres Cantos, Madrid, Spain

²ICFO-The Institute of Photonic Sciences, Castelldefels, Barcelona, Spain

jftorrado@imm.cnm.csic.es

Purpose

It is well known that the fundamental optical properties of hybrid structures conformed by arrays of metallic nanoparticles, sustaining localized surface plasmons (LSP), and metallic films, which support propagating surface plasmons (SPP), are strongly influenced by their mutual electromagnetic coupling [1,2]. On the other hand, the inclusion of ferromagnetic materials in nanoparticles or metallic films allow us to control the respective excitation LSP and SPP by an external magnetic field [3,4]. In this work we analyze a system presenting both situations: LSP on gold nanoparticles over a continuous metallic trilayer exhibiting magneto-optical (MO) activity.

Methods

Figure A shows the configuration under study: a Au/Co/Au trilayer film over a glass substrate and below a thin SiO₂ spacer that has an array of gold nanoparticles on top of it. The magneto-optical response of samples with different thicknesses of SiO₂ and different array periodicities have been measured in the polar Kerr and the transverse Kerr configurations. In the polar Kerr configuration we analyze the polarization conversion (p-light into s-light) in the reflected light when a magnetic field is applied perpendicular to the sample plane and parallel to the incident light plane; and in transverse Kerr measurement, we study the modification of the reflected p-light intensity when the magnetic field is applied parallel to the sample plane and perpendicular to the incident light plane.

Results

The polar Kerr spectra show that the MO response differs from that of the trilayer alone due to the presence of LSP, even being physically separated. Moreover, we have determined that the electromagnetic field inside the trilayer is redistributed when the LSP is excited, resulting in an enhancement of the MO signal only for those energies where the electromagnetic field is increased [5].

In the transverse Kerr configuration both the LSP and SPP plasmons are excited, and from the dependence on the angle of incidence of the TMOKE spectra, we can reconstruct the SPP dispersion relation. Furthermore we have seen that the magnetic field modulates the SPP wavevector allowing us to use an external magnetic field as a tuning parameter of SPP properties.

Conclusions

We have studied the influence of LSP on the MO activity of the system, the effect of the magnetic field on both kind of plasmons, and the interaction between them.

References:

- [1] A. Christ, T. Zentgraf, S. G. Tikhodeev, N. A. Gippius, J. Kuhl, and H. Giessen, *Phys. Rev. B* 74, 155435 (2006).
- [2] J. Cesario, R. Quidant, G. Badenes, and S. Enoch, *Opt. Lett.* 30, 3404-3406 (2005).
- [3] J. B. Gonzalez-Díaz, A. Garcia-Martin, G. Armelles, J. M. Garcia-Martin, C. Clavero, A. Cebollada, R. A. Lukaszew, J. R. Skuza, D. P. Kumah, and R. Clarke, *Phys. Rev. B* 76, 153402 (2007).
- [4] J. B. González-Díaz, A. García-Martín, J. M. GarcíaMartín, A. Cebollada, G. Armelles, B. Sepúlveda, Y. Alaverdyan, and M. Käll, *Small* 4, 202-205 (2008).
- [5] G. Armelles, J. B. González-Díaz, A. García-Martín, J. M. García-Martín, A. Cebollada, M. U. González, S. Acimovic, J. Cesario, R. Quidant, and G. Badenes, *Opt. Express* 16, 16104-16112 (2008).

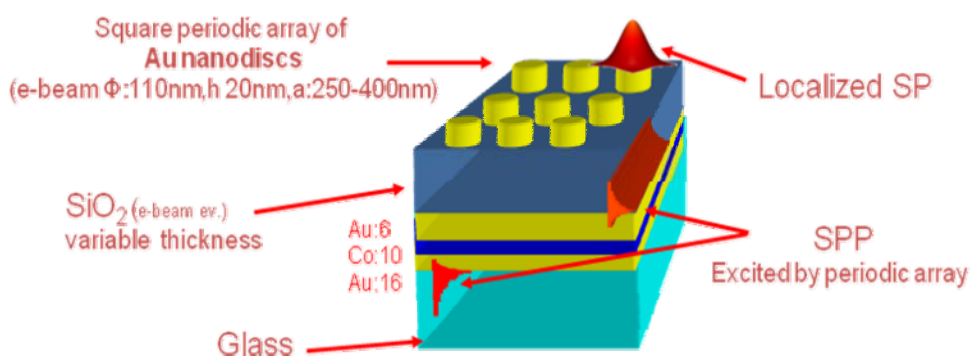
Figures:

Figure A. Configuration sustaining LSP, SPP and magneto-optical activity analyzed in this work

ENHANCED SPIN-VALVE EFFECT IN MAGNETICALLY DOPED CARBON NANOTUBES

D. F. Kirwan , V. M. de Menezes , C. G. Rocha , A. T. Costa, R. B. Muniz , S. B. Fagan and M. S. Ferreira

Trinity College Dublin (Ireland)

Spin valves made of nanotubes contacted to magnetic electrodes may display significant values of magnetoresistance but are limited by the restricted capacity for spin-injection into the tube and by the unwanted spin-flip scattering caused by magnetic impurities. We propose an alternative route to produce the spin-valve effect which (a) does not involve magnetic electrodes, avoiding the spin injection limitation, and (b) uses magnetically coupled impurities to generate an efficient spin filter that enhances the magnetoresistance by orders of magnitude. Furthermore, we predict that substitutional Mn impurities on metallic nanotubes will generate enormously large values of magnetoresistance.

Synthesis and microstructural investigation of $Mn_xZn_{1-x}Fe_2O_4$ magnetic fluids

Foca-nici Ecaterina, Nica Valentin, Creanga Dorina, Caltun Ovidiu

Faculty of Physics, University "Al.I.Cuza", 11A Carol I Blvd., 700506, Iasi, Romania

focanici@yahoo.com

Magnetic materials in the form of colloidal nanoparticles have received many attention because of their unique magnetic properties, which are dominated by superparamagnetism. These materials can be used in many applications, including magnetic fluids. For most biological purposes the magnetic nanoparticles should have between 5 and 15 nm in diameter that ensure their stable dispersion in normal environmental conditions [1-2]. There are many methods for the preparation of ferrite powders, such as: co-precipitation method [3], hydrothermal method [4], micro-emulsion method [5], the sol-gel method [6] and others. Co-precipitation from metal salts solutions is a rather simple and available method still widely applied. The purpose of this work was to prepare colloidal aqueous suspensions of $Mn_xZn_{1-x}Fe_2O_4$ ($x=0.9, 0.7, 0.5, 0.3$) and to study the structure, morphology as well magnetic properties of the obtained materials.

Ferrofluid preparation. Ferrophase particles were prepared by chemical precipitation from $FeCl_3 \cdot 7H_2O$ on a side and $MnSO_4 \cdot 6H_2O$ and $ZnSO_4 \cdot 6H_2O$ solutions on the other side, in the presence of NaOH under continuous magnetic stirring at constant temperature of about 80 °C for 1h. Sodium oleate in aqueous solution was used to coat the ferrophase particles. Coating of surfactant was carried out at 80 °C for 1h under continuous stirring.

Microstructural characterization. SEM device was used to characterize the shape and average size of submicron magnetic particles. AFM device, provided with commercial standard silicon nitride cantilevers (NSC21) having a force constant of 17.5 Nm^{-1} , 210 kHz resonance frequency and tips with radii between 10 and 20 nm (intermittent contact, tapping mode cantilevers) was utilized also to investigate nanoparticle and nanoparticle aggregation topology.

X-ray analysis. Shimadzu XRD 6000 device with $CuK\alpha$ radiation and corresponding soft package were utilized.

Magnetization measurements were performed using a vibrating sample magnetometer **Quantum Design, model 6000** on native ferrofluid samples.

Results and discussion. The magnetic fluid samples were dark brown materials that exhibited obvious magnetic behavior in the presence of a permanent magnet. The SEM micrographs revealed that the investigated colloidal magnetic particles are mostly spherical ranging between 0.1 μm and 1.7 μm for all three samples. AFM scanning provided additional data regarding the height of the investigated colloidal particles as well as for the rare aggregates or short chains evidenced within the samples - no more than 60 nm height. Typical hysteresis plot obtained from VSM measurement for $Mn_{0.3}Zn_{0.7}Fe_2O_4$ sample (for example) indicated the saturation value of 70 Am^2/kg (Fig. 2). Saturation magnetization is increasing with the Mn concentration due to the arrangement within the spinel structural units. Using magnetization data, the average sizes of magnetic diameter were calculated following Langevin's equation. The most relevant data regarding the influence of the ratio Mn:Zn were provided by the XRD analysis XRD graphs (Fig. 3) that allowed the calculation of the crystallite diameter in each case (applying the Debye- Scherrer equation)- that increased with the content of Mn.

Conclusion. The various ratios of Mn:Zn within the magnetic particles representing the ferrophase of several aqueous magnetic fluids led to the increase of the saturation magnetization as well as of the spinel crystallite diameter. Further applications in plant biotechnology are intended based on the magnetic properties and microstructural features (rather uniform granulation) of the discussed magnetic fluids.

References:

- [1] T. Neuberger, B. Schoepf, H. Hoffman, et al., J. Magn. Magn. Mater. 293, (2005), 483;
- [2] A.K. Gupta, M. Gupta, Biomater. 26 (2005), 3995;

- [3] E. Blums, M. Mihail, G. Kronkalns, J., IEEE Trans. Magn., 1993, 29 (6):3267-3269;
- [4] S. Verma, P.A. Joy, Y.B. Khollam, Mater. Lett., 2004, 1092- 1095;
- [5] A. Kosak, D. Makovec, A. Znidarsic, et al , J. Eur. Cer. Soc., 2004, 959-962;
- [6] Z.X. Yue, W.Y. Guo, J. Zhou, et al, J. Magn. Magn. Mater., 2004, 364-374;

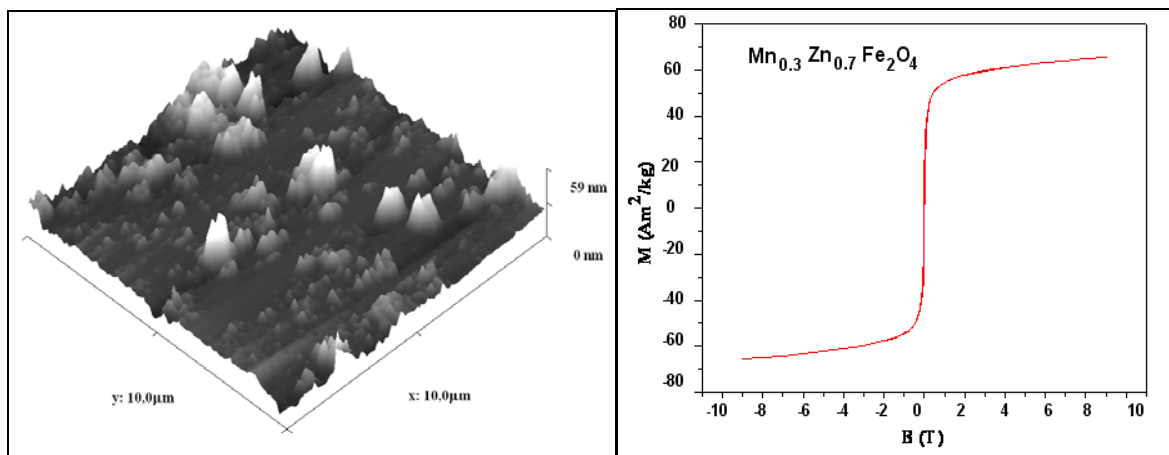


Fig. 1. AFM investigation result – 3D image (left); Fig. 2. Magnetization curve of MnZn ferrite colloidal particles (right)

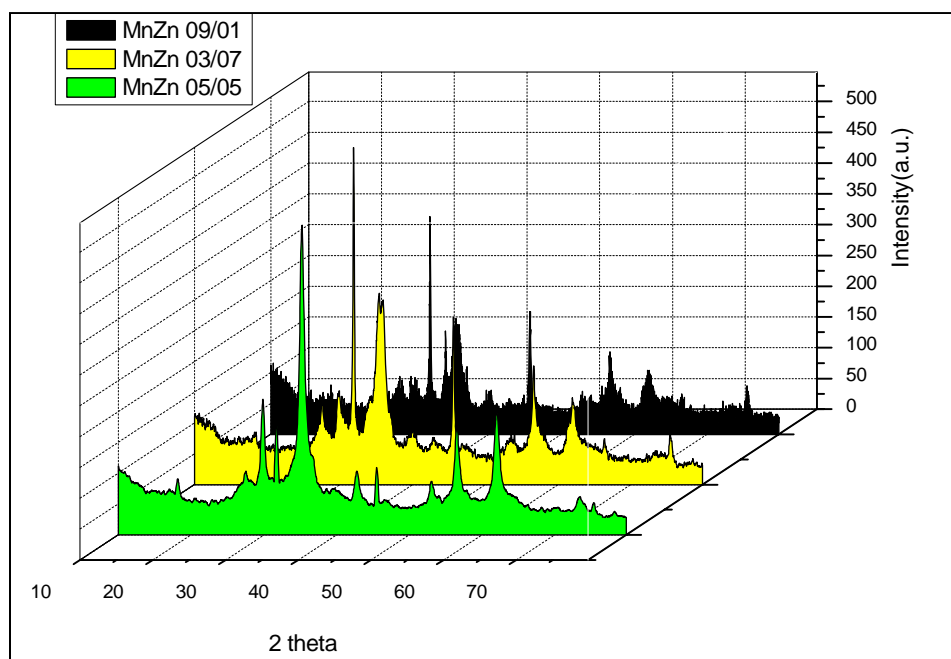


Fig. 3. XRD recordings for $Mn_xZn_{1-x}Fe_2O_4$ samples

APPLICATIONS IN MOLECULAR PHYSICS OF A BASIS IN THE SPACE OF PRODUCTS

D. Foerster and P. Koval
CPMOH, Universite de Bordeaux I

Previously we showed that our method [1] of basis set reduction allows relatively straightforward calculation of molecular spectra from the Petersilka-Gossmann-Gross equations [2].

Here we give further examples from molecular physics where our method simplifies and accelerates computations, building on data imported from the siesta code.

References:

[1] Foerster D, J. Chem. Phys. 128 034108 (2008) and P. Koval and D. Foerster, arXiv:0904.3834v1 (2009)

[2] Petersilka M, Gossmann U J and Gross E K U, Phys. Rev. Lett. 76 1212 (1996)

Nanoparticles at NANOPART

Antonio Fonseca, Janos B.Nagy
NANOPART, Kapeldreef 60, B-3001 Leuven, Belgium
fonseca@scarlet.be

NANOPART is a young Belgian SME active in research and development in the field of nanomaterials. It is open to collaboration with interested partners for national and international projects.

NANOPART is also active in the production and commercialization of nanoparticles, nanofilaments, nanofibres, organic and inorganic nanotubes and graphene sheets.

The monodisperse nanoparticles produced in microemulsions are either organic (i.e. cholesterol, retinol) or inorganic (i.e. AgBr, CdS). Other nanoparticles such as graphene sheets are also produced.

The nanofilaments produced range from carbon- and other organic- nanotubes to inorganic nanotubes, as well as carbon fibres and nanowires.

Composite materials based on carbon nanotubes such as buckypapers, infiltrated buckypapers and polymer based nanocomposites with improved flame retardant properties, are also part of new materials developed at NANOPART.

Strong dispersive effects in the light-scattering mean free path in photonic gaps

P. D. García, R. Sapienza, L. S. Froufe-Pérez, and C. López
 Instituto de Ciencia de Materiales de Madrid (CSIC) and Unidad Asociada CSIC-UVigo,
 Cantoblanco, 28049 Madrid, Spain
luis.froufe@icmm.csic.es

Light propagates along straight lines from the luminous body to the body illuminated and bends or breaks those lines (scatters) when passes out of one medium into another^[1]. Contemporary photonic science goes one step further and provides materials, like photonic crystals, in which light scattering is controlled through interference from the bulk nanostructure instead of the system boundaries. Photonic crystals modify the vacuum modes, change the available phase space for light propagation opening photonic gaps which inhibits some (or even all) directions, while increase the density of light states around the band-gap frequencies. We present here^[2] direct evidence of one order of magnitude variance in the scattering mean free path in photonic crystals for just ~ 25 nm wavelength shift around the band-gap. This dramatic and resonant dispersion is unique and comes from the light interference rather than from material properties. The co-existence of periodicity (the crystal) and disorder (structural imperfections) allows controlling light scattering and diffusion. In particular, light scattering enhancement at band-edge mode has been predicted to be the key for achieving Anderson localization of light. Relying on very high quality photonic crystals, with losses of ~ 100 dB/cm, we confirm that scattered photons dramatically feel the density of states when propagating through photonic crystals. We present a method that permits an accurate measurement of the light scattering mean free path and a precise assessment of the quality of photonic materials. A control of light diffusion in ordered dielectrics is an unexplored route to photonic devices based on disorder rather than order, in analogy to the majority of microelectronic devices that are based on the control of electron diffusion in atomic crystals^[3].

We show^[2] that a controlled smooth transition from ballistic to diffuse transport in photonic crystals can be induced by the introduction of extrinsic disorder. We find that the strength of scattering is strongly determined by the spectral function, which induces immense, up to 20-fold, variations in the scattering mean free path. We propose the scattering mean free path as a robust, easy to measure, figure of merit in assessing the quality of photonic crystals for technological applications. The possibility of controlling light scattering and diffusion in nanostructured optical media has important implications not only in testing the quality of photonic devices but also in properly addressing the proximity to the onset of Anderson in disordered lattices or for the spectral control of lasing emission from disordered/ordered active media^[4].

References:

- [1] I. Newton, A treatise of the reflections, refractions, inflections and colours of light (Opticks) (London, 1704; reprinted by Dover, New York, 1952).
- [2] P. D. García, R. Sapienza, L. S. Froufe-Pérez, and C. López, *Phys. Rev. B* **79** (2009) 241109R.
- [3] C. Kittel, Introduction to Solid State Physics (J. Wiley and sons, N. York, 1971).
- [4] D. S. Wiersma, *Nature Phys.* **4** (2008) 359; S. Gottardo, R. Sapienza, P.D. García, A. Blanco, D. S. Wiersma, and C. López, *Nature Phot.* **2** (2008) 429.

Observation of enhanced optical gain in photonic crystals

R. Sapienza¹, M. Leonetti^{1,2}, L. S. Froufe-Pérez¹, J. Galisteo-López¹, C. Conti³, and C. López¹

1 *Instituto de Ciencia de Materiales de Madrid (CSIC) and Unidad Asociada CSIC-UVigo, Cantoblanco, 28049 Madrid, Spain.*

2 *Dipartimento di Fisica, Università di Roma La Sapienza, I-00185, Roma, Italy.*

3 *Research Center INFM-CNR, c/o Università di Roma Sapienza, I-00185, Roma Italy.*

luis.froufe@icmm.csic.es

We present the measurement of gain length in photonic crystals doped with laser dye. A gain enhancement is experimentally observed for light propagating along the Γ -K symmetry direction in reciprocal space, while a strong inhibition is measured for directions characterized by a lower degree of crystal symmetry. These results are theoretically explained by comparing the optical gain to the calculated density of states along the crystal directions.

We find a six-fold increase of the gain in opal photonic crystal, as compared to the homogeneous film, and a more than 20-fold variation between Γ -K and less symmetrical directions, in the same photonic crystal. We explain this enhancement as due to a large increase of the density of the available modes around the Γ -K direction. Large variation of the gain in photonic crystal show the impact of the tailored density of states on light generation and amplification and open the way to enhancement of other phenomena like non-linear wave mixing and harmonic generation. Our result show how nanostructured media could be at the basis of the development of novel lasing sources with exceptional tunability, directionality and efficiency while being plastic photonics CMOS compatible, and candidates for in-board interconnections for future generation computers.

DEVELOPMENT OF NEW BIOLABELS BASED ON SILICON NANOCRYSTALS AND NANODIAMONDS

Fucikova Anna¹, Valenta Jan¹, Pelant Ivan², Brezina Vitezslav³,

¹Faculty of Mathematics and Physics, Charles University, Ke Karlovu 3, 121 16 Prague 2, Czech Republic

²Institute of Physics AS CR, v. v. i., Cukrovarnicka 10, 162 53 Prague 6, Czech Republic

³Institute of Systems Biology and Ecology AS CR, v. v. i., Zamek 136, 373 33 Nove Hradky, Czech Republic

anna.fucikova@email.cz

Commercially used semiconductor quantum dots (e.g. cadmium containing quantum dots like CdS, CdSe, CdTe etc.) are toxic according to the latest results. They cannot be used in long-term biological studies in vitro and there is no safe method how to remove them after application in vivo. We are developing new non-toxic nanocrystalline silicon (Si-NCs) fluorescence labels which are biodegradable in living body and fluorescent nanodiamonds which are long-term stable (mainly for in vitro use).

Si-NCs have a crystalline core with size between 1 to 5 nm and their surface is most often covered by SiO₂. Photoluminescence (PL) emission bands of Si-NCs are ranging from ultraviolet to near infrared spectral regions [1]. The PL depend not only on the Si-NC size but the surface of nanocrystal plays also a crucial role. We are mostly interested in yellow-orange luminescence band with slow stretched-exponential decay. Lifetime of excited state of Si-NCs is ranging from 10 to 100 μs at room temperature. In the yellow-orange spectral region, there is not so strong autofluorescence of animal cells that could interfere with luminescence of these labels. In addition we can use normally available microscopes without any special filters for observing yellow-orange Si-NCs. We study in details luminescence spectra of single nanocrystals at room temperature in various chemicals and also in animal cells. We determine the size and shape of nanocrystals using atomic force microscopy (AFM).

Nanodiamond (ND) samples are produced by NanoCarbon UDD-TAH, Diamond Centre, St. Petersburg, Russia. The product consists of a mixture of 10 nm (56.6 Vol %) and 460 nm (43.4 Vol %) diamonds in de-ionized water. We are mostly studying the properties of 10 nm NDs, They emit in the visible part of the spectrum with PL peak between 600-800 nm [2].

The interaction of nanoparticles with bio-environment is studied on two cell culture lines: L929 mouse fibroblast and HeLa cells (human cervical cancer cells). The bio-interaction of nanoparticles is studied by optical transmission microscopy, time-lapse microphotography of cell culture evolution, fluorescence microscopy, fluorescence micro-spectroscopy, and scanning electron microscopy. The first cytotoxic tests are showing that Si-NCs and NDs are biocompatible and no significant damage or changes in cell system was observed. In case of bigger (1 μm) particles we observe necrosis of cells due to mechanical damage of the cell membrane.

In case of Si-NCs we observe a slight shift of the PL emission in the spectra when Si-NCs is interacting with internal environment of the cell. Similar shifts are observed when Si-NCs is introduced into surroundings of various chemicals nature.

Optical properties of Si-NCs and NDs are showing promising application potential as fluorescent labels. The size of these nanoparticles is smaller than commercially used CdS-based quantum dots (e.g. EviTag® around 25 nm). The next steps towards applicable fluorescent labels is the development of bioactivation procedures and technology for large scale production of Si and nanodiamond particles.

Keywords: Silicon nanocrystals, nanodiamonds, biocompatibility, quantum dot, fluorescence label, micro-spectroscopy

References:

- [1] Canham, L. T. Silicon quantum wire array fabrication by electrochemical and chemical dissolution of wafers. **Applied Physics Letters**, 57, (1990), 1045.
- [2] Yu, S.J., Kang, M-W., Chang, H-CH., Chen K-M., Yu, Y-CH.. Bright fluorescent nanodiamonds: No photobleaching and low cytotoxicity. **J. Am. Chem. Soc.** 127, (2005), 17604- 17605.

Fabrication by Dip-Pen Nanolithography of Polypyrrole Nanowires for DNA biosensors

T. Galán^{1,3}, S. Oberhansl^{1,2}, E. Martínez^{1,2}, J. Samitier^{1,2,3}.

¹*Nanobioengineering group, Institute for Bioengineering of Catalonia (IBEC), Josep Samitier 1-5, 08028 Barcelona, Spain.*

²*Networking Research Center on Bioengineering, Biomaterials and Nanomedicine (CIBER-BBN), Barcelona, Spain.*

³*Department of Electronics, University of Barcelona, c/ Martí i Franquès 1, 08028 Barcelona, Spain.*

tgalan@ibec.pcb.ub.es

Conducting polymers constitute an attractive alternative to metals and semiconductors as sensing elements in biosensor devices. They are low cost, easy processing materials at the micro and the nanoscale with controllable mechanical and electrical properties and, particularly important in the biomedical field, they show high biocompatibility¹.

We propose the fabrication of conducting polymer nanowires, by the method of Dip-pen nanolithography, for the selective recognition of single-base mismatches through electrical measurements. This would be used further on in DNA sensor by depositing the polypyrrole nanowires between two metal contacts previously deposited on top of a silicon oxide substrate. To address these challenges, Dip-pen² and nanoimprint and focused ion beam (FIB) lithographies, combined to electrochemical deposition,³ will be used as main processing techniques. Once these challenges are met; a large reduction of the sequencing cost of the DNA can be achieved by using Conducting Polymer Nanowires as DNA sensors.

Dip-pen nanolithography is a technique developed in 1999 by C. Mirkin et al.⁴ where the ink is deposited onto a surface via cantilever. The use of the so called inkwells (microfluidic chips) enables the deposition of bio-molecules which are in a buffered solution. The cantilever is introduced in the wells, retracted abruptly and left drying to bring it into contact with the surface and write the nanosize pattern.

Dip-pen experiments have been performed with a NSCRIPTOR system from Nanoink (Skokie, USA) at room temperature (20°C ±1°C) and humidity ranging from 30% to 45% on silicon oxide. An image of the written nanowires at 21°C and 41% of humidity is shown in figure 1, done after writing with the same tip and Dip-pen equipment, just by changing the scan velocity. Higher humidity increases the nanowire dimensions, so it should be a parameter optimized when critical size tolerances are needed.

Another parameter influencing the nanowire dimensions is the deposition speed, which should be highly controllable with the technical set-up. Studies of the nanowire dimensions as a function of the deposition speed were performed in order to determine the optimum conditions and control the process of deposition. The figures 2 and 3 show the decay tendency of the size while increasing the speed, at 21°C and humidity within 32% and 34%. Similar results were obtained for different environment conditions.

In summary, we showed that it was possible to obtain nanowires with tailored dimensions (height and diameter) by controlling environmental conditions (temperature and humidity), and that we could deposit our structures in a certain location between electrodes for further processes.

References:

- ¹ Waneka AK, et.al. J. Phys Chem C 2007; 111: 5218.
- ² Tang Q, et.al. Sensor Actuat B-Chem 2008; 13: 379.
- ³ Yun M, et. al. Nanosensing: Materials and Devices. 2004; 5593: 200
- ⁴ C. Mirkin, et. al. Science. 1999; 283, 661

Figures:

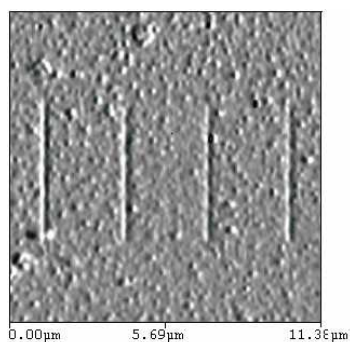


Fig.1.- LFM image in contact mode of Nanowires at different writing speeds.

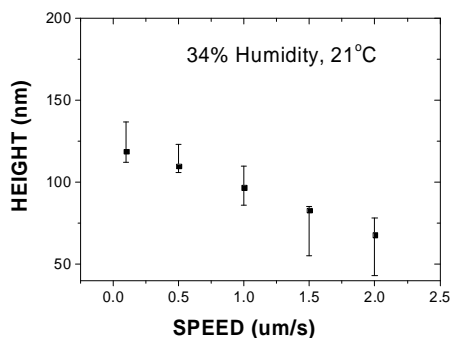


Fig.2.- Decrease in height with higher speed.

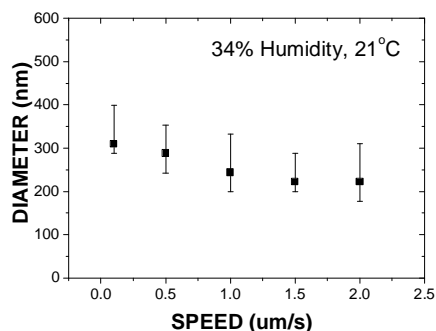


Fig.3.- Decrease in diameter of the Nanowire with increasing velocity.

Synthesis and characterization of Yb³⁺ doped scandium oxide nanocrystals

*M. Galceran*¹, M.C. Pujol¹, J.J. Carvajal¹, X. Mateos¹, M. Aguiló¹, F. Díaz¹, C. Zaldo²
¹*Física i Cristal·lografia de Materials i Nanomaterials (FiCMA-FiCNA), Universitat Rovira i Virgili (URV), Campus Sescelades, c/ Marcel·lí Domingo, s/n, E-43007 Tarragona, Spain*
²*Instituto de Ciencia de Materiales de Madrid, Consejo Superior de Investigaciones Científicas, c/ Sor Juana Inés de la Cruz 3, E-28049, Madrid, Spain*
montserrat.galceran@urv.cat

The rare earth sesquioxides are known as excellent hosts of laser ions due to their low thermal expansion, high thermal conductivity and large crystal field splitting of the electronic states of lanthanides [1] [2]. These suppose clear advantages over the classic YAG laser host, however single crystals of sesquioxides are difficult to grow due to the high melting temperature, ≈2700K. The synthesis of lanthanide-doped sesquioxide nanocrystals is of great interest as the first step for the preparation of ceramic lasers, an alternative to single crystalline lasers with improved thermal and mechanical properties.

Trivalent ytterbium (Yb³⁺) is an interesting laser active ion as an alternative to Nd³⁺ in 1 μm range. Yb³⁺ presents a simple energy level scheme leading to low quantum defect between the pump and the laser photons, a long radiative lifetime, no excited-state absorption or up-conversion losses, and weaker than Nd³⁺ cross-relaxation processes [3].

In the present study, the modified Pechini method was used to obtain Yb_x:Sc_{2-x}O₃ (x = 0.001 – 1) nanocrystals because of its several advantages such as low temperature processing, low cost and simplicity [4,5]. The structural characterization of Yb_x:Sc_{2-x}O₃ nanocrystals was carried out by powder X-ray diffraction, TEM studies and electron diffraction. Synthesized Yb_x:Sc_{2-x}O₃ nanocrystals belong to the cubic system with space group $Ia\bar{3}$.

Figure 1 shows a representative TEM image of the obtained nanocrystals to estimate the particle size and their dispersion. Most nanocrystals were in the range 15-25 nm with a mean and dispersion of 17.7 nm and 46 %, respectively. We applied two types of electron diffraction techniques: selected area electron diffraction (SAED) and convergent beam electron diffraction as nanobeam electron diffraction. Figure 2a shows the TEM image that consists in aggregates of Yb_x:Sc_{2-x}O₃ nanocrystals, the corresponding SAED pattern which confirms the no preferential orientation for the nanocrystals is shown in figure 2b. Each ring corresponds to a crystallographic plane, which can be indexed according with the space group ($Ia\bar{3}$). Figures 2c and 2d depict a TEM image of an individual Yb_x:Sc_{2-x}O₃ nanocrystal and its nanobeam electron diffraction pattern, it can be observed the presence of four equivalent reflections (the most closest to the central beam) corresponding to $\{2\bar{2}2\}$ with interplanar distance of 2.8425 Å. Two other equivalent reflections correspond to $\{004\}$ with an interplanar distance of 2.4616 Å. The last one is $\{4\bar{4}0\}$ and its inter-planar distance is 1.7406 Å. From these reflections, the orientation of these nanocrystals can be indexed in the [110] zone axis. Spectroscopic properties of nanocrystals have been measured and are equivalent respect to the bulk single crystal; this is a necessary condition to manufacture the laser.

References:

- [1] J. Lu, K. Takaichi, T. Uematsu, A. Shirakawa, M. Musha, K. Ueda, H. Yagi, T. Yanagitani, A.A. Kaminskii, *Appl. Phys. Lett.* **81** (2002) 43244326.
 [2] C.A. Morrison, R.P. Leavitt, *Handbook on the Physics and Chemistry of Rare Earths*, New York:1982.
 [3] L.D. Deloach, S.A. Payne, L.L. Chase, L.K. Smith, W.L. Kway, W.F. Krupe, *IEEE J. Quantum Electron.* **29** (1993) 1179
 [4] M. Galceran, M.C. Pujol, M. Aguiló, F. Díaz, *J. Sol-Gel Tech.* **42** (2007) 79.
 [5] M. Galceran, M.C. Pujol, M. Aguiló, F. Díaz, *Mater. Sci. Engineer. B* **146** (2008) 7.

Figures:

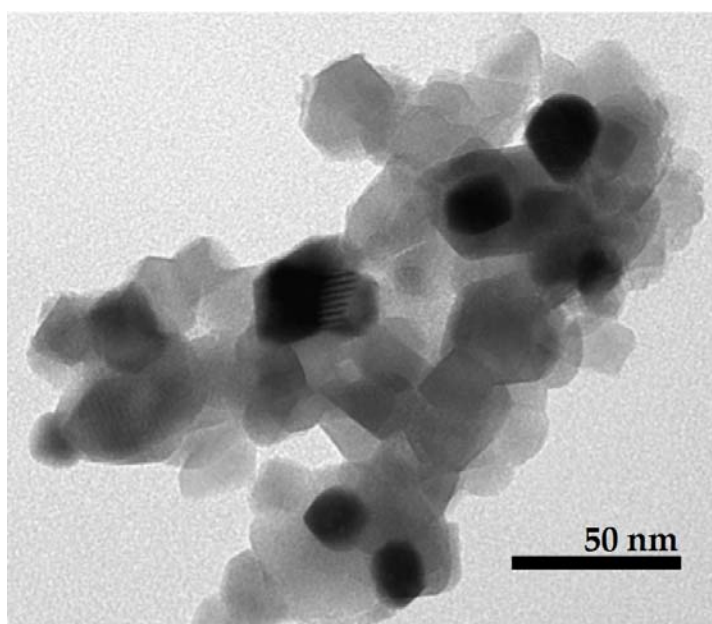


Figure 1. Representative TEM image of $\text{Yb}_x:\text{Sc}_{2-x}\text{O}_3$ nanocrystals

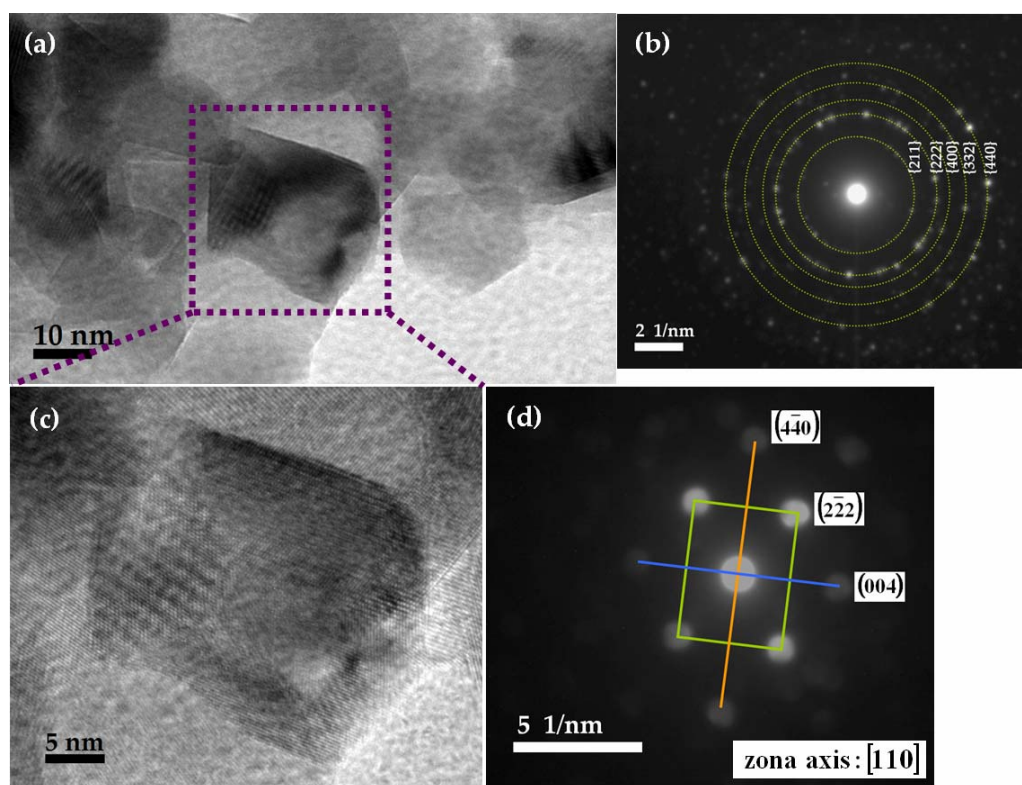


Figure 2. (a) TEM image of an aggregate of $\text{Yb}_x:\text{Sc}_{2-x}\text{O}_3$ nanocrystals, (b) SAED pattern of (a), (c) zoomed part of (a) showing a small nanocrystal with visible lattice planes and (d) Nanobeam electron diffraction pattern of (c).

Analysis of depth profile components at the Interface of Ti6242 Alloy and TiNi Coatings after High Temperature Oxidation in Air

A.Galdikas^a, J.P.Rivière^b, A.Petraitiene,^a T.Moskaliuviene^a, L.Pichon^b

^(a) Physics Department, Kaunas University of Technology, Kaunas (Lithuania)

^(b) Laboratoire de Physique des Matériaux, University of Poitiers, Poitiers (France),

We have analyzed the interfacial elemental depth profile evolution after high temperature isothermal oxidation of NiTi coatings deposited by dynamic ion mixing on a Ti6242 alloy (Ti-6Al-2Sn-4Zr-2Mo). NiTi coatings (thickness 0,4 μ m) were deposited at room temperature (RT) by ion beam sputtering using a Kaufman type ion source of 7.5 cm diameter and the samples are mounted on a rotating substrate holder. A water cooled Ti₅₀Ni₅₀ target of 10 cm diameter was sputtered with 1.2 keV Ar⁺ ions and ion beam mixing during the film deposition was performed with 120 keV Ar⁺ ions. High temperature isothermal oxidation tests in 1 atm flowing synthetic air (80% N₂, 20% O₂) have been conducted at 500°C and 600°C during 100 hours.

We have observed a non-monotonous depth distribution of nickel in GDOES depth profiles after oxidation of TiNi/Ti6242: nickel segregates to the surface of TiNi coating and to the interface between TiNi coating and Ti6242 alloy. We propose a kinetic model based on rate equations for analyzing the depth profile. This model includes microprocesses taking place during oxidation in air such as: adsorption of nitrogen and oxygen, diffusion of components through the film and interface, formation of chemical compounds. The calculations are based on a monolayer approach where the equations are written for each component in each monolayer. It is shown by modeling that non-monotonous depth profile of nickel occurs because nickel from TiNi coating is forming a nickel oxide compound when oxygen atoms reach the film/alloy interface. As a result the atomic concentration of nickel decreases at the interface which induces a diffusion flux of atomic nickel from the bulk to the interface. This process leads to the increase of the total amount of nickel at the film interface and at the surface of coating and thus formation of non-monotonous depth profile. It is shown that the process of nickel oxide formation at the interface plays an important role and acts as a protective barrier for further penetration of oxygen atoms into the Ti6242 alloy. XRD analysis confirms the presence of nickel oxide in the TiNi/Ti6242 interface after oxidation at both temperatures 500°C and 600°C.

YOUNG'S MODULUS FOR GRAPHITIC MONO-ATOMIC LAYER (GRAPHENE)

Eugene G. Gamaly

*Laser Physics Centre, Research School of Physics and Engineering, The Australian National University, Canberra ACT 0200, Australia
e-mail: gam111@rsphysse.anu.edu.au*

Recent discovery of perfect two-dimensional crystals [1] revealed a new way for obtaining the strong materials. The conventional wisdom dictates that the rise in a material hardness can be achieved by the increase in the internal energy density by transition to the high mass density phase state with shorter bond length under high pressure-temperature conditions. In 2D crystals the transition to high modulus state occurs in seemingly counter-intuitive way by the diminishing the effective volume per atom due to decrease in the layer thickness down to atomic level, the natural limit of compressibility. It appeared that stiffness of graphene is higher than that of diamond [2]. More than decade ago it was demonstrated that the Young modulus of graphitic monolayer exceeds that for bulk graphite [3]. Simultaneously the modulus of carbon nanotube then was obtained as that for the rolled-up monolayer in agreement with experiments [4].

In what follows the Young (bulk) modulus of a graphitic monolayer is derived from the semi-empirical inter-atomic pseudo-potential for covalently bounded 2D carbon with new experimental evidence taken into account [1,2]. The bulk modulus of a monolayer expresses in a general form through the cohesive energy and effective volume per atom. The extreme stiffness of a monolayer relates to the absence of defects, high cohesive energy and to the minimum effective volume per atom in 2D crystal. I also discuss how this approach applies to the mechanical properties of 2D crystals in general.

It is well known that the linear elasticity predicts well the elastic properties of fullerenes and carbon nanotubes in a good fit to MD calculations and experimental data. Here the modulus of a mono-atomic graphitic sheet is also calculated using the linear elasticity theory. In elasticity theory one can express the modulus through the thermodynamic parameters and the Poisson ratio. One can show that in deformation of a 2D monolayer the Poisson ratio is zero because an atom is incompressible under the force much smaller of atomic forces. Thus for 2D monolayer the homogenous (bulk) modulus, K , expresses through the internal energy, U , and volume of a system similar to [5] but with different coefficients as the following:

$$K = \frac{2V}{3} \left(\frac{\partial^2 U}{\partial V^2} \right)_{T=0} \quad (1)$$

Relation $K = Y/3$ now connects the bulk and the Young moduli in 2D layer. One can describe in-plane inter-atomic interactions by the simplified semi-empirical pseudo-potential [6] assuming the homogeneity in two dimensions:

$$\phi = Ae^{-\lambda_1 R} - Be^{-\lambda_2 R} \quad (2)$$

The potential (2) reproduces the most important parameters of 2D layer such as inter-atomic distance, R_0 , and the binding (cohesive) energy, ε_b , in equilibrium through the condition $(\partial\phi/\partial R)_{R=R_0} = 0$. A molecular volume is presented in the form $V = V_0 N$, where $V_0 = hR_0^2$ is volume per atom, N is the number of atoms in a structure, R_0 is in-plane inter-atomic distance in equilibrium and h is the effective “thickness” of monolayer that should be extracted from experiment [2]. The total internal energy of a system in equilibrium is $U = \phi(R_0)N$. Now the Young's modulus of a single monolayer expresses through repulsive and attractive gradient

space scales of the potential, the cohesive energy and through the effective “thickness” of monolayer in the following form:

$$Y_{mono} = \frac{\lambda_1 \lambda_2 |\varepsilon_{bind}|}{2h} \quad (3)$$

The physical meaning of (3) is obvious: the Young modulus directly relates to the internal energy density in the characteristic atomic volume. The Young modulus for any 2D crystal with in-plane isotropic properties and known potential can be calculated by formula (3).

Let us apply formula (3) for calculation the Young modulus of graphene taking the following parameters for the potential: $A = 1,753.438$ eV, $B = 452.2$ eV, $\lambda_1 = 3.488 \text{ \AA}^{-1}$, $\lambda_2 = 2.2 \text{ \AA}^{-1}$ [6]. Then the binding energy, $\varepsilon_{bind} = -7.56$ eV is close to the experimentally measured value for graphite. Taking $h \sim 2.5\text{-}4 \text{ \AA}$ from [2] one can calculate the Young’s modulus of a defectless mono-atomic graphite sheet, graphene, as $Y_{mono} = (1.856\text{-}1.16 \text{ TPa})$. One can see that the minimum value is just a little bit higher than that for graphite, $c_{11} = 1.06 \text{ TPa}$ in a direction while the maximum value exceeds that for diamond ($0.9\text{-}1.25 \text{ TPa}$) [7].

One can see that the effective thickness of a monolayer is a crucial parameter defining the strength of 2D crystal. The covalent diameter of carbon of 1.54 \AA perhaps gives the upper theoretical limit of the monolayer “thickness” and therefore upper limit for the Young modulus of 2D carbon of 3 TPa . Hopefully future smart experiments allow the direct measurement of the graphene Young modulus.

References:

- [1]. K.S. Novoselov, et al, PNAS, 102, 1051-1053 (2005)
- [2]. A.K. Geim & K.S. Novoselov, Nature Materials, 6, 183-191 (2007)
- [3]. E. Gamaly (1998) “*Young’s modulus of individual carbon nanotubes: comparing theory to observations*”, pp. 482-488, in Molecular Nanostructures, H. Kuzmany, J. Fink, M. Mehring, and S. Roth, Eds., World Scientific, Singapore.
- [4]. Treacy, M. M. J., Ebbesen, T.W., & Gibson, J. M. *Nature*, 381, 678-680, (1996)
- [5]. Landau, L.D., & Lifshitz, E. M., *The theory of elasticity*, (Oxford, 1960)
- [6]. Tersoff, J. *Phys. Rev. Lett.*, 61, 2879-2882, (1988)
- [7]. Hugh O. Pierson, 1993, “*Handbook of Carbon, Graphite, Diamond, and Fullerenes*”,

Distribution of Eu ion in nano-size $Y_2O_3:Eu$ Nanopowder prepared by solution combustion method

Yadolah Ganjikhanelou¹, Fereydoun Alikhani Hessari¹, Mahmood Kazemzad¹, Seyed Hamed Aboutalebi¹

1-Materials and Energy Research Center, P.O. BOX: 31787- 316, Tehran, Iran

yadolah1@gmail.com, kazemzad@gmail.com, hessarifa@gmail.com,

hamed.Aboutalebi@gmail.com

$Y_2O_3:Eu$ compound is known as the best red phosphor source for three color fluorescent lamps and color displays [1]. The chemical and thermal stability of this compound is better than sulfide based phosphors such as $Y_2O_2SO_4:Eu$ [2]. It also exhibits higher quantum efficiency and stability against high current densities [3]. Although, the optical properties of micron-size $Y_2O_3:Eu$ powder have been optimized [3], they are not optimized for nanosize $Y_2O_3:Eu$. In our previous work [4, 5], we demonstrated that quenching concentration of nanosize $Y_2O_3:Eu$ is about 5 percent of Eu concentration which had conflict with the result of Ye et al[6]. They believed that upon decreasing the size of $Y_2O_3:Eu$ compound the quenching concentration could be enhanced. In this work, we present solid reasons and mechanism in order to explain this phenomenon.

$Y_2O_3:Eu$ nanopowder was prepared by urea solution combustion method. The samples were then analyzed by X-ray diffraction (XRD), high resolution transmission electron microscopy (HRTEM) and energy dispersive X-ray analysis (EDX). Photoluminescence of the samples was measured employing 230 nm excitation. To analyze $Y_2O_3:Eu$ (3%) sample with Warren-Averbach (WA) method, the XRD pattern was taken with the step time of 5 sec. for 222 and 444 peak.

Fig. 1 shows HRTEM picture of $Y_2O_3:Eu$ (3%) sample. In inset of this figure, reduced FFT image of the selected area in HRTEM image is shown. It can be seen that good crystallinity was obtained by solution combustion synthesis method.

Result of WA analysis of $Y_2O_3:Eu$ (3%) sample is shown in Fig. 2 and 3. The trend of the micro-strain distribution (Fig. 3 b) is nearly proportional to $1/L$, indicating that defects (line and point) are preferentially localized along grain boundaries [7]. These result also showed that Eu is accumulated near the grain boundary of each crystallite and therefore quenching concentration decreased. This hypothesis was confirmed by EDX Analysis (Table 1). Moreover the distribution of crystallite size was computed by Bertout method [8]. The distribution of crystallite size was also computed from the HRTEM micrograph. Figure 4 shows the distribution of crystallites computed from HRTEM micrograph and Warren-Averbach method. It can be seen that there is good correlation between them. Mean value of crystallite size is about 5-7 nm which is much smaller than the one determined by Scherrer's formula (about 25 nm).

Scherrer's formula determines the crystallite size with the assumption that crystallites have uniform distribution. The difference between the result of WA and Scherrer's formula comes from this limitation of Scherrer's formula.

References:

- [1] S. Ekambaram, K.C. Patil, M. Maaza, *Journal of Alloys and Compounds*, **393** (2005) 81-92.
 [2] W.N. Wang, W. Widiyastuti, T. Ogi, I.W. Lenggoro, K. Okuyama, *Chem. Mater.* **19** (2007) 1723–1730.
 [3] W.M. Yen, S. Shionoya, H. Yamamoto 2006 *Phosphor Handbook* (Tokyo, Japan: The CRC Press).
 [4] F.A.Hessari, Y. Ganjkhanlou, M.Kazemzad, Chromaticity Dependence on Eu Concentration in $Y_2O_3:Eu$ Nanopowder, Nano Conference 2009, King Saud University, Riyadh, Saudi Arabia, 5-7 April 2009.
 [5] Y. Ganjkhanlou, M.Kazemzad, F.A.Hessari, S.H. Aboutalebi, Chromaticity Dependence on Eu Concentration in $Y_2O_3:Eu$ Nanopowders, submitted work to *Journal of alloys and compound*.
 [6] T. Ye, Z. Guiwen, Z. Weiping, X. Shangda, *Mater. Res. Bul.* **322** (1997) 501-506.
 [7] H. S. Nalwa 2007 *Nanoclusters and Nanocrystals* (New York: American scientific paplishers)
 [8] M. Birkholz 2006 *Thin Film Analysis by X-Ray Scattering* (Weinheim: Wiley-VCH)

Figures:

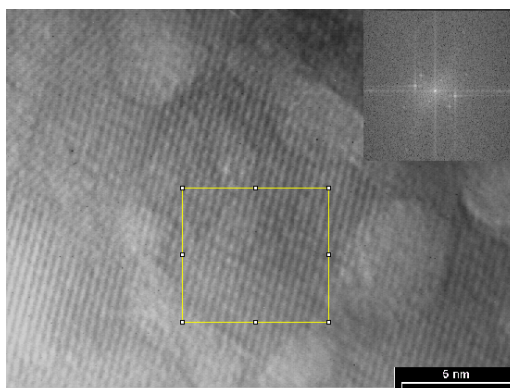


Fig. 1 HRTEM picture of $Y_2O_3:Eu$ (3%) sample, inset) reduced FFT of selected area in HRTEM image.

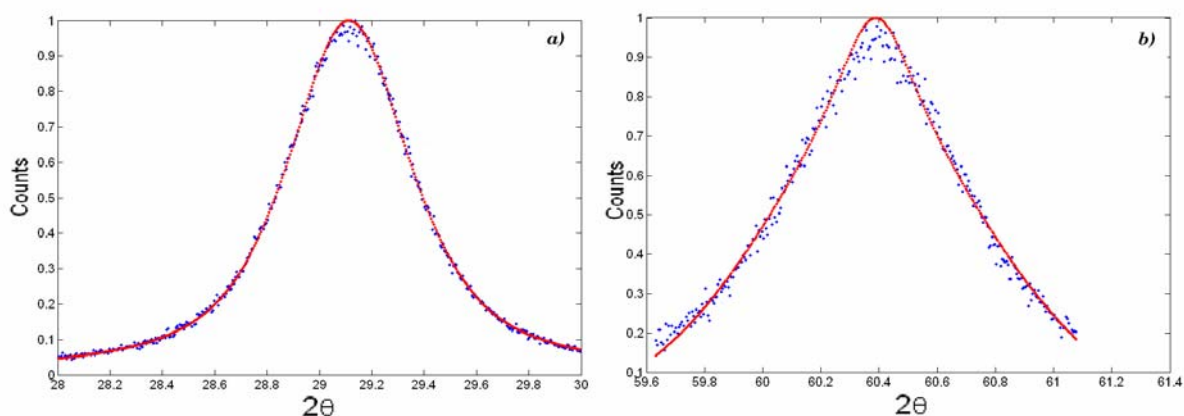


Fig. 2 Fitting by pseudo-Voigt functions of the a) (111), b) (222) peaks for the $Y_2O_3:Eu$ (3%) sample (step time 5 sec.)

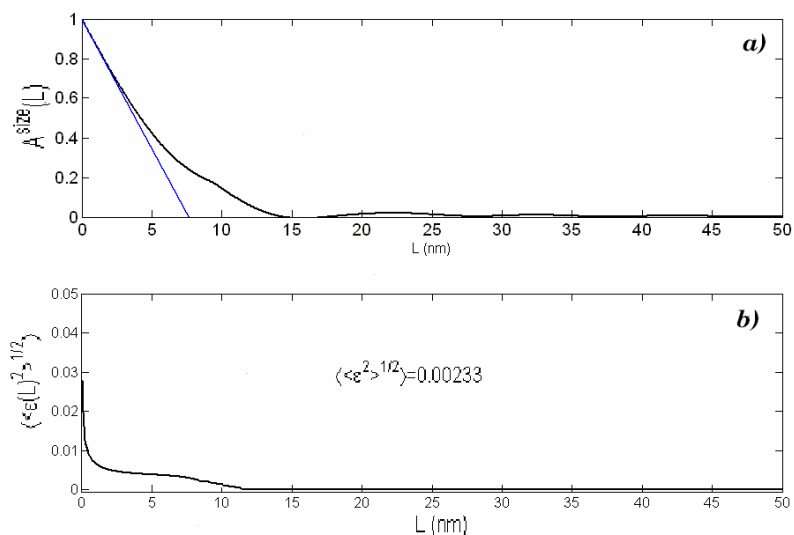


Fig. 3 Fourier transform coefficient of $Y_2O_3:Eu$ (3%) sample after correction for instrument broadening by stokes method and removing of strain broadening. b) distribution of micro-strain vs. correlation length.

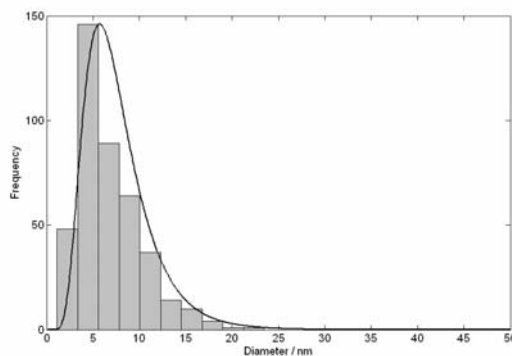


Fig. 4 Crystallite size distribution of $Y_2O_3:Eu$ (3%) sample determined by warren-averbach method and HTEM picture.

Table 1 EDX analysis of the $Y_2O_3:Eu$ (3%) in three different points

Point	1	2	3	AVE	STD DEV
Eu(% mol)	3.73	3.66	4.37	3.92	0.39
Y (% mol)	96.27	96.34	95.63	96.08	0.39

HIGH ANTIBACTERIAL EFFECT OF SILVER NANOPARTICLES PREPARED FROM AN ORGANOMETALLIC COMPOUND.

Jorge García-Barrasa,^a José M. López de Luzuriaga,^a Miguel Monge,^a Yolanda Sáenz,^{b,c} and Carmen Torres.^{b,c}

^aDepartamento de Química. Grupo de síntesis química de La Rioja, UA-CSIC. Universidad de La Rioja. Madre de Dios 51. E-26006 Logroño, Spain.

^bDepartamento de Agricultura y Alimentación, Universidad de La Rioja, Complejo Científico-Tecnológico, Madre de Dios 51. E-26006 Logroño, Spain.

^cUnidad de Microbiología Molecular, Centro de Investigación Biomédica de La Rioja (CIBIR). Piqueras 98. E-26006 Logroño, Spain.

Email: jorge.garcia@unirioja.es

Silver ions have long been known to have strong inhibitory and bactericidal effects,¹ however the antibacterial effect of Ag nanoparticles (NPs) has only been studied recently. The mechanism of action of the nanoparticles is not yet fully understood but it is believed that AgNPs appear attached at the bacteria cell membrane, disturbing its permeability and respiration like silver ions proceed, but whereas the silver ions coming from a salt like AgNO₃ show a bactericidal effect in micromolar concentrations, AgNPs show a similar effect in nanomolar concentrations.² In different studies it is observed a higher bactericidal effect using Ag NPs which size is in the 1–10 nm range.³

In order to gain more insight into this antibacterial property of AgNPs, we have prepared AgNPs in this size range (<10 nm) from organometallic compounds, like [Ag(C₆F₅)]. The use of these precursors allows to work under mild reaction conditions and permits a good control over the size and shape of the nanomaterials.

To control the growth of nanoparticles we use different stabilizers like long alkyl-chain amines or organic polymers. In this way, when hexadecylamine is used as stabilizer we have obtained small silver nanoparticles (~10 nm) that present an excellent antibacterial effect against *E. Coli*, *S. Aureus* and *L. Monocytogenes* bacteria.(Figure 1).⁴

When polyvinylpyrrolidone (PVP) is used as stabilizer, a polydisperse sample of silver nanoparticles displaying two size populations (~2-4 nm and ~12-15 nm) are obtained. We have checked through transmission electron microscopy (TEM) the interaction between the smaller nanoparticles and the bacteria, which does not happen with the bigger ones, proving that the higher bactericidal effect of silver nanoparticles arise from the small nanoparticles even in the presence of larger ones. We have tested these AgNPs against some usual microorganism like *E. Coli* and *S. Aureus*, and other bacteria important in food and health, obtaining very good results.

References:

- [1] T. J. Berger, J. A. Spadaro, S. E. Chapin, R. O. Becker, *Anti Microb Agents*. **9** (2), (1976), 357–358.
- [2] C. N. Lok, C. M. Ho, R. Chen, Q. Y. He, W. Y. Yu, H. Sun, P. K. H. Tam, J. F. Chiu, C. M. Che. *J Proteome Res*. **5**, (2006), 916-924.
- [3] J. R. Morones, J. L. Elechiguerra, A. Camacho, K. Holt, J. B. Kouri, J. T. Ramírez, M. J. Yacaman. *Nanotechnology*, **16**, (2005), 2346–2353.
- [4] E. J. Fernández, J. García-Barrasa, A. Laguna, J. M. López-de-Luzuriaga, M. Monge and C. Torres. *Nanotechnology*, **19**, (2008), 185602 (6pp).

Figures:

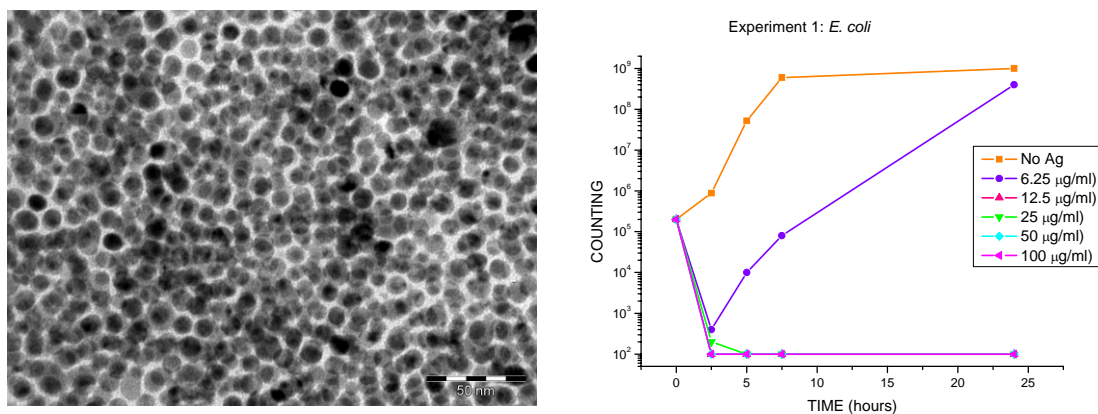


Figure 1. Silver nanoparticles obtained using hexadecylamine as stabilizing agent, and kinetic study of the bactericide effect of these AgNPs against *E. Coli*.

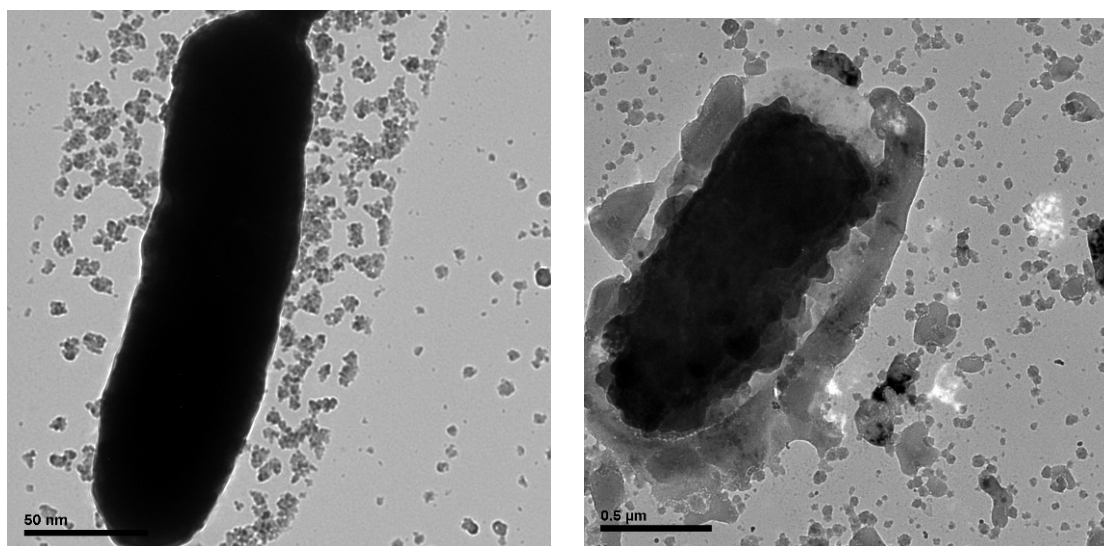


Figure 2. *E. Coli* bacterium a) without silver nanoparticles and b) with a concentration of 100 $\mu\text{g/mL}$ of silver nanoparticles prepared using PVP as stabilizer.

MERGING NANOWIRES BREAKAGE RESULTS FOR DIFFERENT STRETCHING DIRECTIONS TO COMPARE WITH EXPERIMENTAL ONES

S. Peláez¹, C. Guerrero², R. Paredes³, P. A. Serena¹, P. García-Mochales^{4,}*

¹ *Inst. de Ciencia de Materiales de Madrid, Consejo Superior de Investigaciones Científicas (CSIC),
c/ Sor Juana Inés de la Cruz 3, Cantoblanco, E-28049-Madrid, Spain*

² *Departamento de Física, Facultad Experimental de Ciencias, La Universidad del Zulia (LUZ),
Maracaibo, Venezuela*

³ *Centro de Física, Instituto Venezolano de Investigaciones Científicas (IVIC),
Apto. 20632, Caracas 1020A, Venezuela*

⁴ *Dept. Física de la Materia Condensada, F. de Ciencias, Universidad Autónoma de Madrid (UAM),
c/ Tomas y Valiente 7, Cantoblanco, E-28049-Madrid, Spain*

* *pedro.garciamochales@uam.es*

During the last two decades, the study of the properties of nanowires has been one of the keystones of the development of nanotechnology since these nanoobjects exhibit electrical and mechanical properties of interest in fundamental knowledge as well as technological applications [1]. In particular, many experimental studies of electrical and mechanical properties of metallic nanowires have been addressed in order to describe the quantum features appearing due to electron transversal confinement. The standard approximation for the experimental study of such metallic nanowires includes the formation, elongation and breakage of ultranarrow nanocontacts, as for instance, those formed between an STM tip and a metallic surface.

With the advent of powerful computational resources and realistic descriptions of the atomic interactions, it has been possible to reproduce many of such formation-breaking experiments “in silicon” [2]. An important part of these simulation studies have been done using Molecular Dynamics (MD) algorithms, allowing to elucidate how this formation-elongation-breakage occurs. Furthermore MD simulations allow us to determine the kind of structures that appear during the final stages of the breaking process. Getting insight of such structures is a crucial matter since they control the electron transport of the nanowire, allowing a comparison with the experimental data.

However, the comparison between experimental results and MD computational simulations requires an extra ingredient: statistics. It is necessary to statistically address the study of many nanowire breaking events, mimicking the experimental indentation-retraction cycles used to accumulate data. Statistic in this context implies take into account two facts: a) breaking events involving random stretching directions; b) given a particular initial geometrical configuration, each breakage event evolves differently. The last condition is easily achieved performing many simulations with the same initial structure at a given temperature [3]. Obtain an accurate statistic that take into account the first condition is tricky because it is not easy to perform simulations with arbitrary initial stretching directions. There is no reason that indicates that any particular orientation would be preferred, but the final stages and behaviour of the experimental nanowire break must be determined by the structure type closest to its elongation direction. Then, to achieve orientation statistic, results for the three main fcc directions [100], [110] and [111] (with a good samples statistic) have to be merged with weights proportional to their zone axis multiplicity (6, 12 and 8 respectively) [4].

References:

- [1] Agrait, N.; Levy Yeyati, A.; Van Ruitenbeek, J.M. *Physics Report*, **2003**, *377*, 81-279.
- [2] Barnet, R.N.; Landman, U.; *Nature* **1997**, *387*, 788. Hasmy, A.; Medina, E.; Serena, P. A. *Phys. Rev. Lett.* **2001**, *86*, 5574. Sen, P. et al.; *Phys. Rev. B* **2002**, *65*, 235433; Hasmy, A. et al.; *Phys. Rev. B* **2005**, *72*, 245405. Pauly, F. et al.; *Phys. Rev. B* **2006**, *74*, 235106. García-Mochales, P.; Paredes, R.; Peláez, S.; Serena, P.A.; *Nanotechnology* **2008**, *19*, 225704
- [3] García-Mochales, P. et al.; *Materials Science-Poland* **2005**, *23*, 413. García-Mochales, P.; Peláez, S.; Serena, P. A.; Medina, E.; Hasmy, A. *Appl. Phys. A* **2005**, *81*, 1545.
- [4] Rodrigues, V.; Fuhrer, T.; Ugarte, D. *Phys. Rev. Lett.* **2000**, *85*, 4124. González, J. C. et al.; *Phys. Rev. Lett.* **2004**, *92*, 126102

Figures:

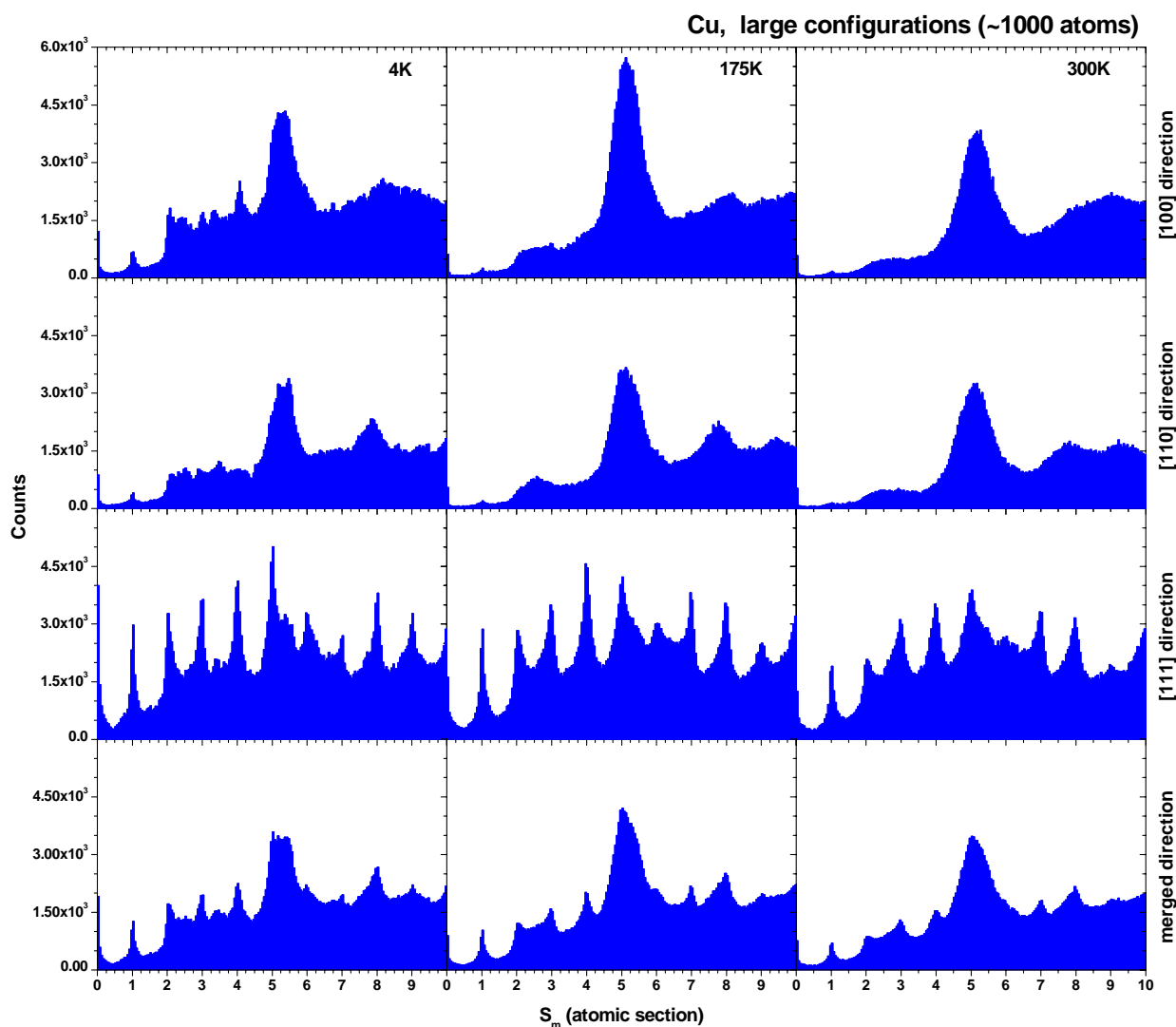


Figure 1: Minimum cross-section S_m histograms of Cu nanocontacts evolving under stretching at $T= 4, 175$ and 300 K. Histograms correspond to $[100]$, $[110]$ and $[111]$ orientation (built each with 300 independent ruptures), and a normalised average of the three orientation taking into account their axis multiplicity (6, 12 and 8 respectively) [4].

IN SITU TEM OBSERVATION OF NUCLEATION AND GROWTH OF Co NANOPARTICLES IN ZIRCONIA MATRIX

M. García del Muro, Z. Konstantinović, X. Batlle and A. Labarta

Dpt. de Física Fonamental i Institut de Nanociència i Nanotecnologia, Universitat de Barcelona, Martí i Franquès 1, 08020-Barcelona, Spain
montse@ffn.ub.es

Granular films of Co nanoparticles embedded in a zirconia matrix were prepared by KrF pulsed laser deposition (PLD). Zirconia was stabilized with 7 mol.% Y₂O₃, which provides the matrix with very good properties, such as good oxidation resistance, thermal expansion coefficient matching that of metal alloys and very high fracture toughness values. It has been observed that ZrO₂ matrix gives rise to sharper interfaces between the amorphous matrix and nanoparticles [1]. Besides, the high oxygen affinity of ZrO₂ prevents oxidation of the metallic nanoparticles. The samples were deposited at room temperature in a vacuum chamber with rotating composite targets made of sectors of ZrO₂ and pure cobalt. The distance between target and substrate was fixed at 30 mm. The laser fluency was typically 3 Jcm⁻². Average compositions were determined by microprobe analyses. The substrates for TEM experiments were silicon nitride membrane windows enabling direct observation of as-deposited samples.

We have previously shown [2] that for Co volume concentration $x < 0.31$, the particles have mostly spherical shape, while for $x \geq 0.31$, the neighboring particles start to coalesce, giving rise to larger, non spherical shape, indicating the rapid approach to the percolation threshold. About $x=0.35$, the size distribution broadens abruptly because of the massive coalescence of the nanoparticles that leads to percolation. In the present work, and in order to directly obtain information about particle growth mechanisms, we have performed TEM observations using a Hitachi 800MT electronic microscope equipped with a heating specimen holder. The selected samples are in the region $0.25 < x < 0.31$, so below the Co concentrations at which coalescence starts to be significant. The heating rate was about 50 °C/min from room temperature to 300 °C. TEM images were obtained after 15 min waiting for stabilization of both temperature and microscope electronics. Then we increased the heater power to reach 400 °C and waited again before obtaining new images.

Figure 1 shows TEM images of practically the same area of Co-ZrO₂ film before and during in situ heating at 300 °C. Comparing the two images we can observe, at a glance, a significant and new fact: the number of small particles has increased. Particle size distribution extracted from TEM images shows, on one hand, the appearance of small particles with annealing, and on the other hand, that the mean size of the particles slightly increases with annealing. After annealing at 400 °C, a bimodal particle size distribution has to be assumed to fit experimental data, demonstrating both effects of annealing: nucleation of new particles from Co atoms dispersed in the zirconia matrix, and growing of the previously existing particles by adhesion of neighbour atoms and by coalescence. Previous similar works have only shown the second effect (see for example [3]).

Magnetic characterization by measuring the temperature dependence of the magnetization after field cooling and zero-field cooling the samples was done with the as-prepared samples and after annealings at 300 °C and 400 °C. The experimental results are fitted assuming particle size distributions which confirm the observed by direct TEM imaging.

References:

- [1] Z. Konstantinović, M. García del Muro, X. Batlle, A. Labarta and M. Varela, *Nanotechnology*, **17** (2006) 21.
- [2] Z. Konstantinović, M. García del Muro, M. Kovylyna, X. Batlle and A. Labarta, *Phys. Rev. B*, **79** (2009) 094201.
- [3] G. Palasantzas, T. Vystavel, S.A. Koch and J.Th.M. De Hosson, *J. of Appl. Phys.*, **99** (2006) 024307.

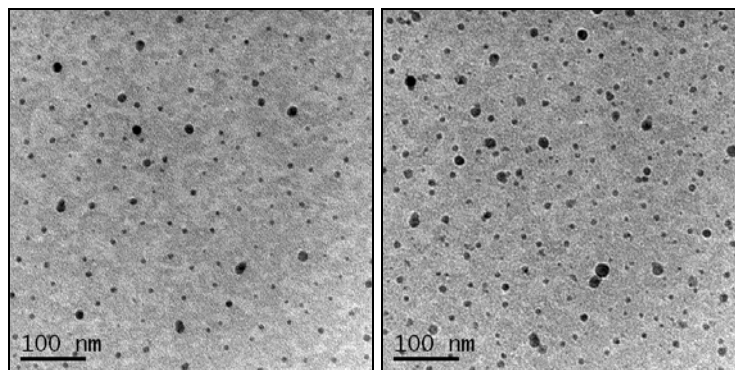
Figures:

Figure 1. Bright field TEM images of the same area of Co-ZrO₂ film before (left) and during heating (right) at 300 °C.

Integrated optical sensor using silicon ring resonators

J.G. Castelló, J. García, A. Griol, J. Hurtado, L. Belliers, J. Ayucar, J. Martí
Valencia Nanophotonics Technology Center, Universidad Politécnica de Valencia
Camino de vera s/n, 46022, Valencia
jagarcas@ntc.upv.es

We report an experimental demonstration of an integrated optical sensor based on ring resonators. The device is fabricated in a Silicon-On-Insulator (SOI) platform and operates at a wavelength of 1550 nm. The transmission spectrum of the device is measured for different substances on the top of the sample varying their refractive index. After measurements, a linear shift of the resonances of the ring resonator is observed, obtaining a sensitivity of 46 nm/RIU (Refractive Index Units) and a detection limit of $2.1 \cdot 10^{-3}$ RIU, which is in the order of other reported results for Silicon ring resonators [1], but this sensitivity is improved using slotted waveguides [2].

Label-free biosensors are becoming more stable and reliable with a high relying level [3]. So that, a biosensor based on integrated microring resonators in SOI is reported in this work. One of the main advantages of these devices is their size, giving structures with footprints in the order or tenths of μm^2 . Moreover, high sensitivities can be achieved. Fabrication process for devices in SOI technology is fully CMOS compatible, making it very profitable for mass production and achieving very cost-effective devices.

SOI wafers used in this work have a top 250nm-thick silicon layer of and an underlying $3\mu\text{m}$ -thick silicon oxide substrate. The structures were exposed using high resolution e-beam lithography and transferred to the silicon using an ICP (Inductive Coupled Plasma) etching. The fabricated ring resonator is shown in Fig. 1. The bent sections of the ring have a radius of 3 μm , the racetrack is 20 μm long and coupling regions of 1 μm have been created in the ring resonator. The coupling gap is around 75 nm. The waveguides' width is 500. A theoretical FSR (Free Spectral Range) of 13 nm is obtained for these parameters.

We coupled TE-polarized light from an ASE (Amplified Spontaneous Emission) source to the device using a lensed fiber, and a second lensed fiber was used at the output of the device to collect the light and display the spectrum in an optical spectrum analyzer. Different substances were dropped over the chip and the shift of the resonances was measured. We used different alcohols with different refraction indices: ethanol ($n=1.361$), isopropyl alcohol ($n=1.376$) and acetone ($n=1.359$). Spectra ranging from 1540 nm to 1560 nm were measured in order to see two resonances. The resolution was set to 20 pm.

Figure 3 shows the position of the resonance when depositing ethanol and isopropyl alcohol. Different measurements for each alcohol are depicted, showing a good repetitivity of the results. The detection limit achieved is $2.1 \cdot 10^{-3}$ RIU. Using the shift in the position of the resonances we can obtain the sensitivity curve plotted in Fig. 4, giving a value of sensitivity of 46 nm/RIU.

To conclude, in this work we have presented the experimental results of an integrated biochemical sensor based on a ring resonator on SOI technology, obtaining values of sensitivity of 46nm/RIU, what is in the same order of magnitude as for other recent works. Some improvements still to be included such as Peltier elements for temperature controlling or

combining a Mach-Zehnder structure with the rings in order to have an interferometric scheme. The main advantage of this device is the possibility of obtaining highly integrated and low cost sensors, with a high potential for several applications when combined with surface functionalization techniques.

References:

- [1] Katrien De Vos, Irene Bartolozzi, Etienne Schacht, Peter Bienstman, Roel Baets, “*Silicon-on-insulator microring resonator for sensitive and label-free biosensing*”, Optics Express, 11 junio 2007, nº 12 vol. 15.
- [2] Carlos A. Barrios, K. Gylfason, B. Sanchez, A. Griol, “*Slot-waveguide biochemical sensor*”, Optical Letters, 21 septiembre 2007.
- [3] Vittorio M. N. Passaro, Francesco Dell’Olio, Biagio Casamassina, Francesco De Leonardis, A. Griol, “*Guided-Wave Optical Biosensor*”, Sensors, 25 abril 2007, pags: 508-536.
- [4] Dominik G. Rabus, “*Integrated ring resonators, the compendium*” (Springer, 2007).

Figures:

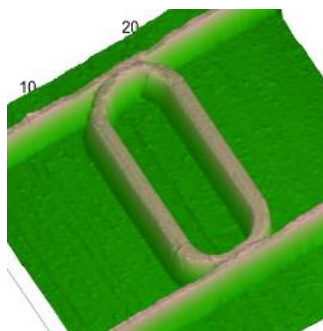


Figure 1) AFM picture of the fabricated ring resonator. The bent sections have a radius of 3 μm , the racetracks have a length of 20 μm , and a coupling region of 1 μm has been used.

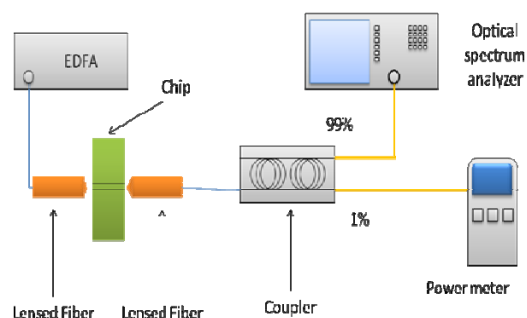


Figure 2) Scheme of the optical set-up used to carry out the measurements.

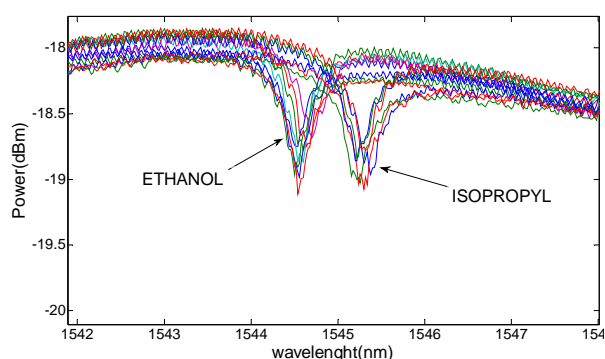


Figure 3) Transmission spectra of the ring resonator for two different alcohols. Several measurements are plotted for each substance, in order to depict the repetitibility of the measurements.

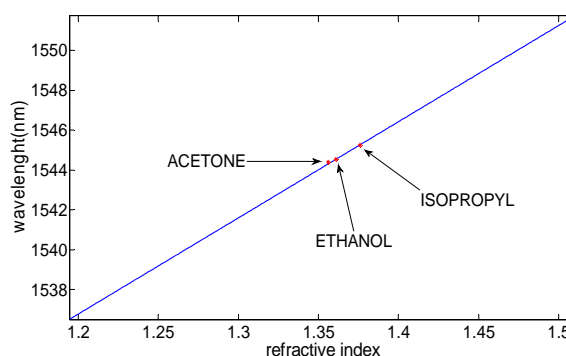


Figure 4) Resonance wavelength (nm) shift versus refractive index of the deposited substance.

Magnetism in TiO₂/ Co₃O₄ interfaces

M. A. Garcia^{1,2}, J. L Costa-Krämer³, M. S. Martín-González³ and J. F. Fernández²

¹Dpto. Física de Materiales Universidad Complutense de Madrid, Madrid, Spain

²Instituto de Cerámica y Vidrio, CSIC, Madrid, Spain

³Instituto de Microelectrónica de Madrid, CSIC, Tres Cantos, Madrid, Spain

ma.garcia@fis.ucm.es

The appearance and control of magnetism in traditionally non-magnetic oxides is nowadays one of the most active and pursued goals of material physics [1]. In the last few years, research has been focused mainly on oxides doped with magnetic ions (the so-called Diluted Magnetic semiconductors). Recent results [2-4] indicate that the appearance of magnetism in these oxides (mainly based in ZnO and TiO₂) is related to the presence of defects and surface/interface effects [2-4] but the origin of most of the experimental results is still unclear [5]. Actually, results are hardly reproducible and findings from different groups are commonly contradictory. Understanding this lack of reproducibility is probably one of the main challenges to determine the origin of this magnetism. A common feature of all the experimental observations of this magnetism is that signals are very weak, suggesting that only few atoms are involved in the magnetic response. Thus, it has been proposed that the emerging magnetism in oxides corresponds to surface/interface magnetism [6].

Here, we report the appearance of room temperature of ferromagnetism in mixtures of TiO₂ and Co₃O₄ despite the diamagnetic and antiferromagnetic character of both oxides separately [7]. The magnetic signal appears when both oxides are milled and disappears as they are annealed to promote the interdiffusion and reaction that forms the CoTiO₃ spinel. The magnetic features are found only when using TiO₂-anatase while no ferromagnetism is found for TiO₂-rutile mixtures (figure 1). This fact points towards a magnetic phase whose appearance depends delicately on the structure of the oxide host phases. Due to the difficulties in the measurement of these small magnetic signals [8] a full set of control experiments were performed, including sample preparation by three different groups and measurements in three different magnetometers. Results showed that the magnetic phase appears reproducibly although the amount varies up to a factor of 3 depending on the sample set. These differences are related to the distinct surface features and reactivity of the starting powders.

Optical and X-ray absorption spectroscopy (figure 2) evidenced that mixing TiO₂-anatase and Co₃O₄ led to a surface reaction consisting on a partial reduction of Co³⁺ ions in octahedral position to Co²⁺. The effect was not observed in the TiO₂-rutile samples suggesting that this reduction is in the origin of the observed ferromagnetism. In Co₃O₄, only Co²⁺ (in tetrahedral positions) holds a magnetic moment arising an antiferromagnetic behavior. However, a partial reduction of Co³⁺ in octahedral sites to Co²⁺, will lead to surface regions with magnetic moments in both tetrahedral and octahedral positions. This situation, can give rise to ferrimagnetic ordering (very similar to that of Fe₃O₄) with high T_C, explaining the observed magnetic behavior [9].

References:

- [1] K. Ando, Science 312 (2006) 1883. H. Ohno, Science 281 951 (1998).
- [2] K. R Kittilstved, N. S. Norberg and D. R. Gamelin, Phys. Rev. Lett. 94, 147209 (2005).
- [3] J. L. Costa-Krämer et al, Nanotechnology 16, 214 (2005)
- [4] M. A. García et al, Phys. Rev. Lett. 94 217206 (2005)
- [5] J. M. D. Coey, S. A. Chambers, MRS Bulletin 33, 1053 (2008)
- [6] M. A. Garcia et al, Nano Letters, 7 1489 (2007)
- [7] A. Serrano et al, Phys. Rev. B B 79, 144405 (2009)- (Editor Suggestion)
- [8] M.A. Garcia et al, J. Appl. Phys, 105, 013925 (2009)

Figures:

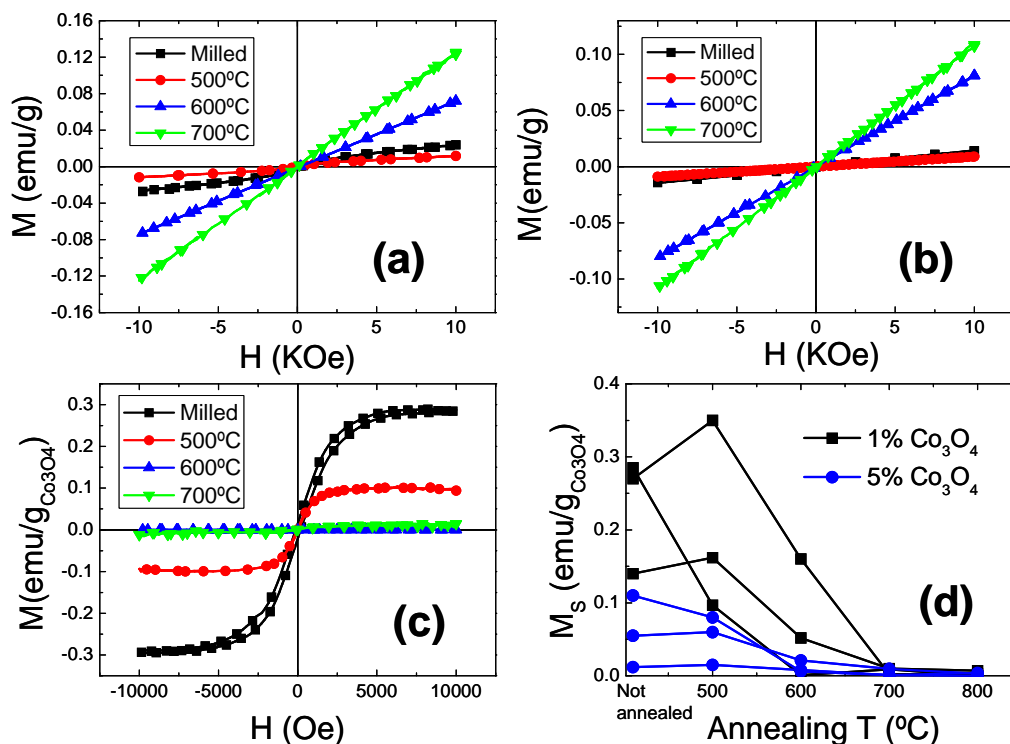


Figure 1. Magnetization curves for 99% TiO_2 - 1% Co_3O_4 samples annealed at different temperatures for (a) Anatase- TiO_2 and (b) Rutile- TiO_2 . (c) Curves for the samples with TiO_2 in anatase structure after subtraction of a paramagnetic (linear) component. (d) Saturation magnetization of the ferromagnetic component for the samples prepared with A- TiO_2 with 1% and 5% wt of Co_3O_4 . From [7]

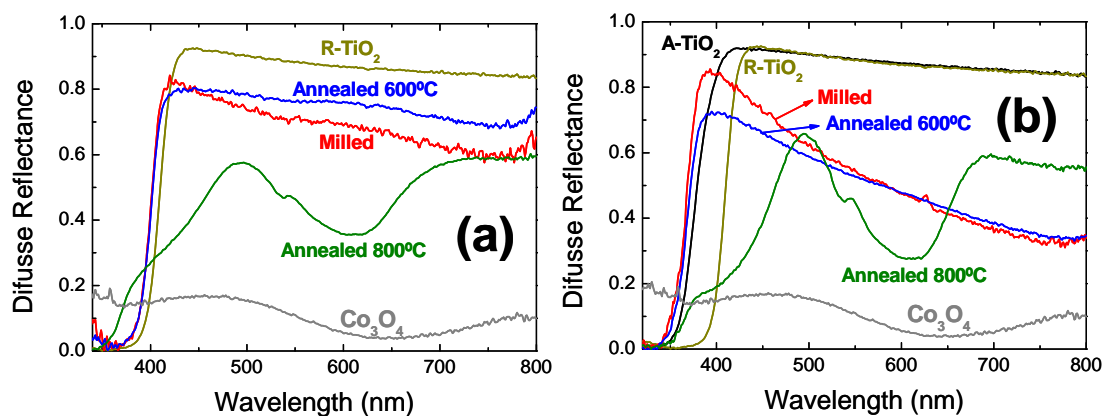


Figure 2. Diffuse Reflectance spectra for the samples containing 5% Co_3O_4 prepared with (a) rutile and (b) anatase TiO_2 . Spectra from Rutile- TiO_2 , Anatase- TiO_2 and Co_3O_4 are also presented for comparison purposes. . From [7]

SILVER NANOCOMPOSITES FOR ANTIBACTERIAL TILE

Ali Ghafari-Nazari, Mahmood Rabiee, Fath Allah Mostarzade, Ahmad Movlaei, Maryam Chenani
R&D Group, Rafsanjan Almas Kavir Tile Company, 7717577911 Rafsanjan, Iran
ali.ghafari@akt.ir

A most prominent nanoproduct is nanosilver. At nanoscale, silver exhibits remarkably unusual physical, chemical and biological properties. Due to its strong antibacterial activity, nanosilver coatings are used on various textiles but as well as coatings on certain implants. Further, nanosilver is used for treatment of wounds and burns and marketed as a sanitary ware, water disinfectant and room spray.

At this research, metallic silver was generated by ultraviolet radiation with 5% PVP as a surfactant from AgNO_3 . Silver nanoparticles were precipitated in deionized water and sulfuric acid (2M). Also, silver was doped on micro powder of Nepheline and micro/nanopowder of TiO_2 , SiO_2 in both of environments. All samples were produced 30 liters homogeny suspension in stank industrially. The relationships between the antibacterial activity of powders and the fabrication conditions were investigated by X-ray diffraction, SEM and UV-visible spectrophotometer. Opposite of other papers, composites TiO_2 were the worst matrix, because TiO_2 was absorbed energy of UV radiation that were never perfected precipitation. Beside, antibacterial activity was very increase in acidic environment.

After generated silver composites, they were coated on surfaces of raw glaze with spray. All kinds of tiles (floor, wall, opaque, luster etc) were cooked. Then, they were compared in basic and important tile factors (for examples: autoclave, corrosion and erosion resistant) after stabilized of tile conditions, they were compared them in antibacterial activity.

References:

- [1] X. Chen, H.J. Schluesener, *Toxicology Letters*, **176** (2008) 1–12.
 [2] P. Davide Cozzoli et al., *JACS*, **126** (2004), 3868-3879.

Figures:

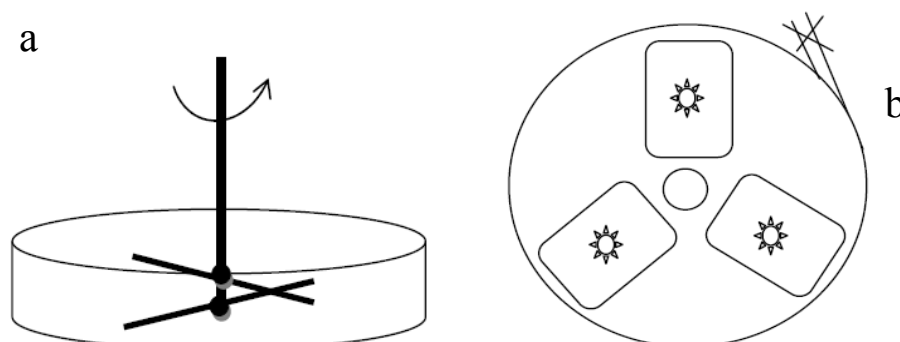


Figure 1. Schematic of used stank for production of nanosilver by UV. A) Under of stank with 2 wings. B) Head of stank with 3 lamps in projector (every ones: 250 v) and exit of production.

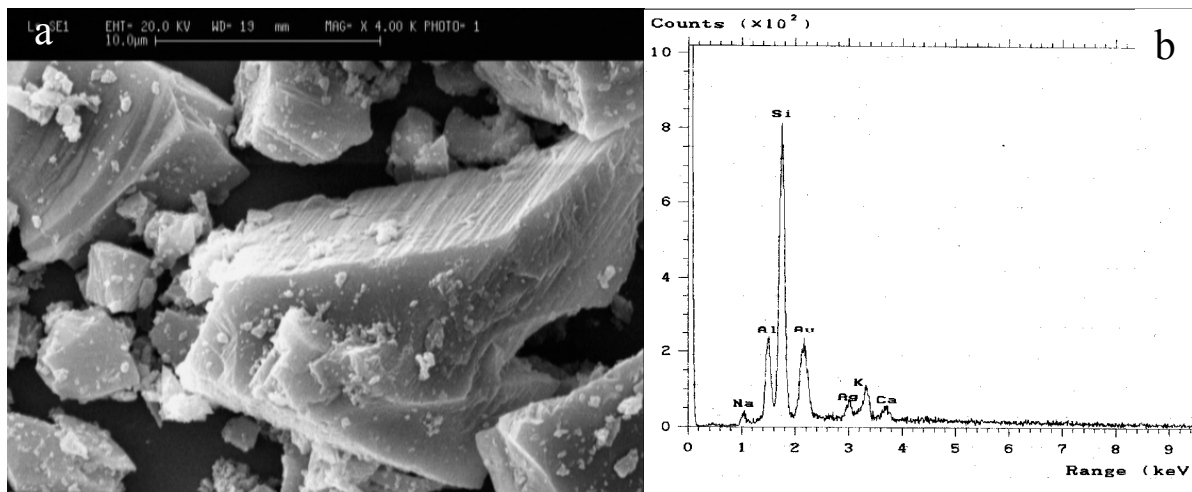


Figure 2. Nepheline nanocomposites were the best in antibacterial activity and tile productions. a) SEM micrograph of Nepheline in water, shows streaky surface that increases nucleation of reactions. b) EDX analysis estimates production of silver.

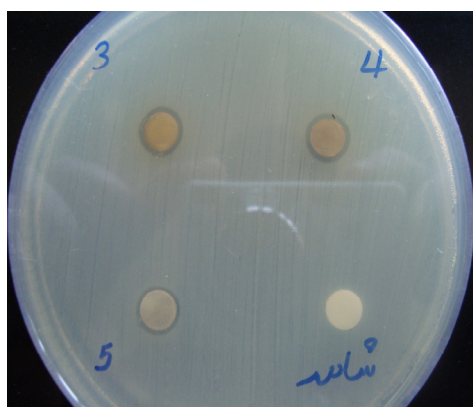


Figure 3. Antibacterial activity of nanocomposites on E.coli bacteria.

(3: Pure silver. 4: Doped on Nepheline. 5: Doped on micro-SiO₂. the other is control)

Insights in optical properties of bundled carbon nanotubes for telecommunications applications: a preliminary comparative study with individualized carbon nanotubes

M. Gicquel¹, P. Turban², A. Moréac², R. Fleurier³, A. Maalouf⁴, H. Nong¹, S. Loualiche¹

¹Laboratoire FOTON, UMR CNRS 6082, INSA, 20 Avenue des Buttes de Coësmes CS 14315
35043 Rennes Cedex, France

²IPR, UMR CNRS 6251, Université Rennes 1, 263 Avenue du Général Leclerc, 35 042 Rennes
Cedex, France

³Laboratoire d'Etude des Microstructures, ONERA, 29 Avenue de la division Leclerc, 92322
Châtillon Cedex, France

⁴Laboratoire FOTON, UMR CNRS 6082, ENSSAT, 6 Rue de Kerampont, BP 80518, 22305
Lannion Cedex, France

maud.gicquel@insa-rennes.fr

Contact author : maud.gicquel@insa-rennes.fr

Among nanomaterials with great potential for optical devices (light emitting diodes, lasers, semiconducting optical amplifiers, ultrafast switches), carbon nanotubes (CNT) take a particular place near classical semiconducting nanostructures (quantum wells and dots). Indeed, these 1D-nanomaterials demonstrate original and efficient excitonic optical properties [1,2], and the large-scale production of CNT, as well as the relative process simplicity required for CNT-based devices should most probably open the way towards low-cost devices. Finally, CNT-based devices are still research challenges in nanooptics and our work particularly aims at demonstrating ultrafast switches for telecommunication applications, in optical fiber networks.

Since the discovery in 2002 that CNT can emit light [3], an impressive number of research studies focused on their intrinsic optical properties [4]. This jump in optical research on CNT was made possible thanks to a powerful physico-chemical process that leads to CNT individualization. However, when CNT are in bundles (or in ropes), which is the naturally form of as-grown CNT, optical properties of CNT are drastically modified. We performed a structural analysis of spray-deposited bundled CNT films, using scanning tunnelling microscopy (STM). Figure 1A provides a (175X175 nm²)-sized STM image of our simple-processed bundled CNT-samples. In a rope, there are statistically 1/3 metallic and 2/3 semiconducting CNT, which are strongly linked by Van der Waals interactions, resulting in an intertube distance of ~0.3 nm [5]. We suggest below that this intertube narrow distance in CNT bundles is useful for ultrafast switching applications.

We present here a comparative study on linear optical properties of individualized CNT and bundled CNT. We use therefore visible-infrared absorption and Raman spectroscopies. Thus, highlighting the benefit of bundling for CNT-based ultrafast optical devices, which are simply processed in comparison with individualized CNT-based devices, we finally demonstrate the femtosecond-scale optical switch of bundled-CNT, at 1550-nm telecom wavelength.

In figure 1B, we present absorption spectra of both CNT types. We show that bundling effect induces redshifting and broadening of first optical transitions of semiconducting CNT, around 1300 nm. We suggest that both effects are advantageous for telecom applications, where 1550 nm-wavelength-window is exploited in long-haul optical fiber and, multiplexing-wavelength technique is used to enhance the high-bit-rate of telecom signal. Furthermore, the vibration modes of CNT were probed using Raman spectroscopy at 785nm-excitation wavelength. We focus on radial breathing modes (RBM), which highlights qualitatively the various CNT diameters in the samples [6]. Even if we find qualitatively the same diameters in individualized and bundled CNT-based samples (with diameter average of ~1 nm), Raman

spectra of both CNT types demonstrate typical features. Among them, we note the presence of a “roping peak” around 270 cm^{-1} for bundled CNT, confirming the strong extent of bundling in our samples [7], and we highlight modifications of phonons-excitons interactions and resonant probed-semiconducting CNT.

Finally, we tested the absorption dynamics of bundled CNT using femtosecond pulses in pump-probe experiments. We report a typical switching time of 0.41 ps at 1550 nm telecom-wavelength-excitation, which is suitable for 500 Gb/s bit-rate telecom signal treatment, far beyond the 160 Gb/s rate of test-systems. This ultrafast switching is most attributed to charge transfer from semiconducting to neighbouring metallic CNT [8]. The vicinity of CNT in bundles is also an asset for ultrafast all-optical telecom applications and insertion of bundled CNT in resonant optical microcavities are in progress, in order to enhance light-matter interaction.

References:

- [1] Tsuneya Ando, J. Phys. Soc. Jpn **66**, 1066 (1997).
- [2] O. J. Korovyanko, C. -X. Sheng, Z. V. Vardeny, A. B. Dalton and R. H. Baughman, Phys. Rev. Lett. **92**, 017403 (2004).
- [3] Michael J. O’Connell *et al.*, Science **297**, 593 (2002).
- [4] R. Bruce Weisman and Sergei M. Bachilo, Nanolett. **3**, 1235 (2003).
- [5] Y. J. Dappe, J. Ortega, F. Flores, Phys. Rev. B **79**, 165409 (2009).
- [6] M. S. Dresselhaus, G. Dresselhaus, R. Saito, A. Jorio, Phys. Rep. **409**, 47 (2005).
- [7] M. J. O’Connell, S. Sivaram and S. K. Doorn, Phys. Rev. B **69**, 235415 (2004).
- [8] J.-S. Lauret *et al.*. PRL **90**, 057404 (2003).

Figure:

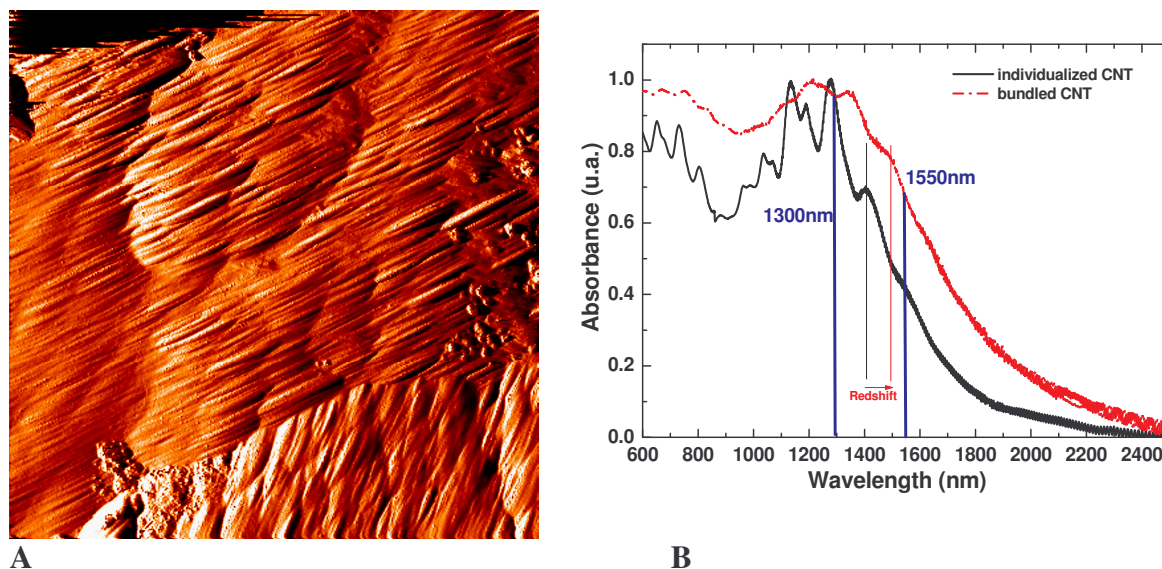


Figure 1: A) STM image of bundled CNT (175X175) nm², B) Normalized absorbance of individualized and bundled CNT in visible-infrared window.

FABRICATION OF LANGMUIR-BLODGETT FILMS INCORPORATING A BANANA-SHAPED MOLECULE

*Ignacio Giner, Ignacio Gascón, Héctor Artigas,
Isabel Bandrés, Diego F. Montaña, Hernando Guerrero*
Departamento de Química Orgánica y Química Física, Área de Química Física,
Facultad de Ciencias, Universidad de Zaragoza, 50009 Zaragoza, Spain
iginer@unizar.es

Bent-core or banana-shaped molecules are an active field of research in liquid crystals since the pioneering results by Niori et al¹. These molecules adopt a compact packing arrangement that restricts rotational freedom, thus allowing the molecules to organise into novel types of liquid crystalline phases with noticeable electro-optical responses, ferro- or antiferroelectric behaviour and high polarization values². In this work we have used the Langmuir-Blodgett technique to study a bent-core molecule (see Figure 1) which presents a tilted lamellar polar phase in the bulk. We show that the LB technique is a useful procedure to fabricate well-ordered films of bent-core molecules and also can give insight into their molecular packing³. Stable Langmuir films have been prepared and characterized onto an aqueous basic subphase (pH = 9). Monolayer phase transitions have been investigated using surface pressure-area (π -A) and surface potential-area (ΔV -A) isotherms and BAM images, showing that solid phase is achieved at $\pi = 20$ mN/m. UV-vis reflection experiments have shown that molecules are tilted up during compression, reaching a compact packing in the condensed phase. Langmuir films have been transferred onto solid substrates at $\pi = 25$ mN/m, resulting in formation of noncentrosymmetric LB layers (Z type transference). UV-vis spectra of the LB films confirm a constant transfer ratio during the LB fabrication. Moreover, one-layer LB films deposited onto Si (100) have been investigated using the XRR technique; the fitting of experimental data indicates that the monolayer has a height of 5.8 nm. This result shows that molecular orientation in the LB films is almost similar to the air-water interface.

References

1. Niori, T.; Sekine, T.; Watanabe, J.; Furukawa, T.; Takezoe, H., *J. Mater. Chem.* **1996**, 6, 1231.
2. Ros, M. B.; Serrano, J. L.; de la Fuente, M. R.; Folcia, C. L., *J. Mater. Chem.* **2005**, 15, 5093.
3. Ashwell, G. J.; Amiri, M. A., *J. Mater. Chem.* **2002**, 12, 2181.

Figures:

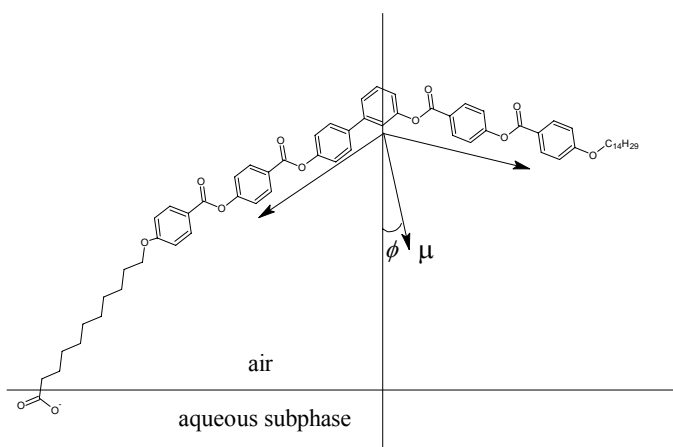


Figure 1: Chemical structure and molecular orientation at the air-water interface

of the banana-shaped molecule.

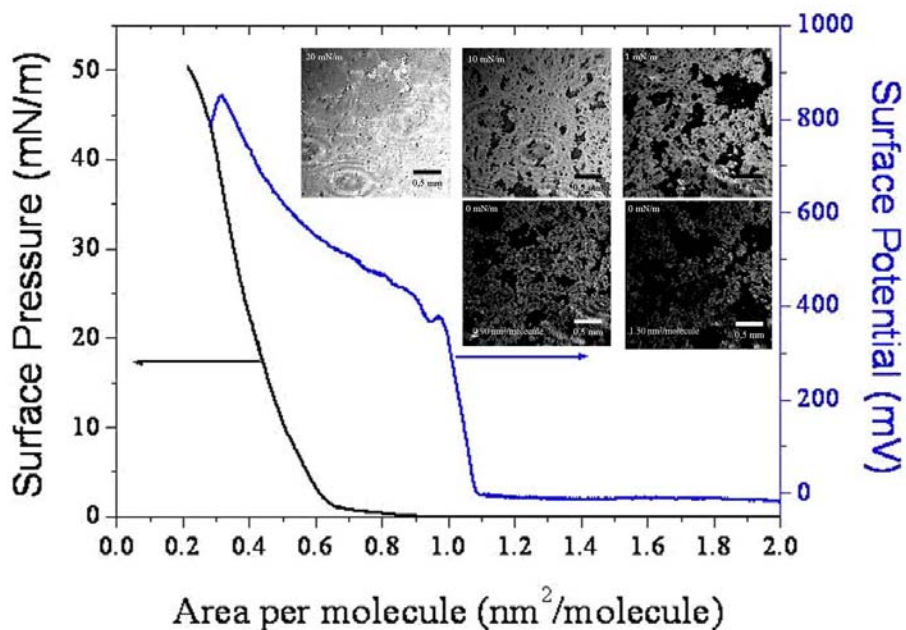


Figure 2: π -A and ΔV -A isotherms and BAM images obtained during compression.

Acknowledgements. The authors thank Dr. B. Ros and J. Vergara from Universidad de Zaragoza for the synthesis of the banana-shaped molecule. We are grateful for financial assistance from MEC and fondos FEDER in the framework of the project CTQ2006-05236. We are also indebted to D.G.A. for financial support. I. G., I. B. and D. M. thank their pre-doctoral DGA and BSCH grants, respectively.

GRAPHENE AT THE EDGE: STABILITY AND DYNAMICS

Çaglar Ö. Girit,^{1,2} Jannik C. Meyer,^{1,2} Rolf Erni,³ Marta D. Rossell,³
C. Kisielowski,³ Li Yang,^{1,2} Cheol-Hwan Park,^{1,2} M. F. Crommie,^{1,2}
Marvin L. Cohen,^{1,2} Steven G. Louie,^{1,2} A. Zettl^{1,2*}

¹ Department of Physics, University of California at Berkeley,
Berkeley, CA 94720, USA.

² Materials Sciences Division, Lawrence Berkeley National Laboratory,
Berkeley, CA 94720, USA.

³ National Center for Electron Microscopy, Lawrence Berkeley National
Laboratory, Berkeley, CA 94720, USA.

Although the physics of materials at surfaces and edges has been extensively studied, the movement of individual atoms at an isolated edge has not been directly observed in real time. With a transmission electron aberration-corrected microscope capable of simultaneous atomic spatial resolution and 1-second temporal resolution, we produced movies of the dynamics of carbon atoms at the edge of a hole in a suspended, single atomic layer of graphene. The rearrangement of bonds and beam-induced ejection of carbon atoms are recorded as the hole grows. We investigated the mechanism of edge reconstruction and demonstrated the stability of the "zigzag" edge configuration. This study of an ideal low-dimensional interface, a hole in graphene, exhibits the complex behavior of atoms at a boundary.

References:

Science 27 March 2009: Vol. 323. no. 5922, pp. 1705 - 1708
DOI: 10.1126/science.1166999

Photoluminescence of rare earth doped upconverting NaYF₄ nanoparticles

Goel, V., Lennox, R.B., Perepichka, D.F.

Department of Chemistry, McGill University, 801 Sherbrooke St. W., Montreal, Canada
vishya.goel@mail.mcgill.ca

Upconversion is a phenomenon in which multiple photons of lower energy are converted to higher energy light. This effect can be observed in systems of rare earth ions doped in an inorganic host matrix to convert near infrared light to visible photoluminescence. The photoluminescence is highly dependent on the rare earth ions and host matrix used. The wavelength of visible emission is tuned via the rare earth ion while the intensity is dependent on the phonon energy of the host. In this study, upconverting nanoparticles with improved photoluminescence have been prepared via a thermal decomposition preparation method.

The conversion of near infrared light to visible light is achieved using Er³⁺ and Yb³⁺ ions doped into an NaYF₄ lattice. The photoluminescence properties of the nanoparticles is dependent on the crystalline phase of the NaYF₄ lattice. The selective formation of the crystal phase is achieved via control of the reactant concentrations during the nucleation phase of nanoparticle formation. The optimized synthesis has been shown to create pure hexagonal nanoparticles with a high degree of crystallinity. The photoluminescence of the nanoparticles was studied using low power NIR light (980 nm) to excite emission in the red and green portions of the visible spectrum.

Growth and characterization of Mn- doped ZnO/TiO₂ multilayered nanostructures grown by pulsed laser deposition

A. Khodorov^a, S. Levichev^a, A. Chahboun^b, A.G. Rolo^a, N. P. Barradas^c, E. Alves^c,
M.J.M. Gomes^a

^a *Physics Centre, University of Minho, 4710-057, Campus de Gualtar, Braga, Portugal*

^b *Physics Department, Dhar Mehraz Sciences Faculty, BP 1796, Fès, Morocco*

^c *ITN, Ion Beam Laboratory, E. N. 10, 2686-953 Sacavém, Portugal*

mjesus@fisica.uminho.pt

During last years diluted magnetic semiconductors (DMS) caused considerable attention due to their possible application in spintronics. Spintronics with semiconductors is very attractive as it can combine the potential of semiconductors (control of current by gate, coupling with optics, etc.) with the potential of the magnetic materials (control of current by spin manipulation, nonvolatility, etc.) [1-3]. DMS is obtained by doping a non-magnetic semiconductor with transition-metal elements. In this aspect, ZnO doped with transition-metals as Mn, Co, V, Cr, etc has the especial interest. First of all, these materials are predicted to have the ferromagnetism above room temperature [4] that is a prerequisite for practical use. Moreover, being low-cost, wide-band gap semiconductor, ZnO itself has been focus of renewed research for applications such as UV light-emitters, transparent high-power electronics, surface acoustic wave devices, piezoelectric transducers and window materials for display and solar cells [5-6]. Whereas transition-metal doped ZnO multilayers have been extensively studied last years, the nanocrystals as well as multilayered structures based on these DMS have been away of interest, however, they have a strong potential from application point of view. In this work we prepared Mn-doped ZnO/TiO₂ multilayered structures and studied their structure properties.

The multilayered structures were prepared by pulsed laser deposition (PLD) techniques equipped with multitarget carousel system that allowed growing of alternating layers without breaking the vacuum. The deposition was performed with help of KrF laser (248 nm) in the oxygen atmosphere (10⁻³ mbar) and at substrate temperature of 300 °C. The used targets were TiO₂ of 99.99% pure (bought at KurtLesker Co.) and 2% Mn doped ZnO prepared follow the solid state reaction route. Post growing annealing was performed to improve the crystallization of ZnMnO nano-layers. The set of nanostructures with alternating MnZnO and TiO₂ layers (up to 20 layers) were prepared with different sets of thicknesses (from 1 to 3 for MnZnO and from 10 to 15 for TiO₂).

The samples were structurally characterized by Wide Angle X-ray Scattering (WAXS), Grazing Incidence Small angle X-ray Scattering (GISAXS) at SAXS beamline (with the energy of the beam of 8 keV) in the Elettra Synchrotron Facilities (Trieste, Italy). The Rutherford backscattering (RBS) measurements were made at 2 MeV with 4He as well as PIXE analyse was performed. The Raman scattering was performed with help of the Jobin–Yvon T64000 spectrometer equipped with a cooled CCD detector, using the 514.5 nm excitation wavelength of an Ar⁺ laser in the back scattering geometry.

The WAXS of as-deposited MnZnO/TiO₂ multilayer nanostructure showed pure crystallization of Mn-doped ZnO and amorphous TiO₂. The GISAXS illustrated well-resolved layered structure. The alternation of composition in the layers was confirmed by RBS study. The as grown sample shows low Raman signal. Annealing considerably improves the crystalline structure of MnZnO and leads to crystallization of TiO₂. The multilayer structure was maintained after annealing which was evidenced by GISAXS and RBS techniques. The analysis of annealing conditions on structure properties has been performed and the results will be reported.

References:

- [1] I. Žutić, J. Fabian, S. Das Sarma, Rev. Mod. Phys. **76** (2004) 323.
- [2] C. Felser, G.H. Fecher and B. Balke, Angew Chem. Int. Ed, **46** (2007) 668.
- [3] A. Fert, Rev. Mod. Phys. **80** (2008) 1517.
- [4] T. Dietl, H. Ohno, F. Matsukara, J. Cibert, D. Ferrand, Science **287** (2000) 1019.
- [5] Ü. Özgür et al., J Appl. Phys. **98** (2005) 041301.
- [6] C. Klingshirn, ChemPhysChem **8** (2007) 782

Figures:

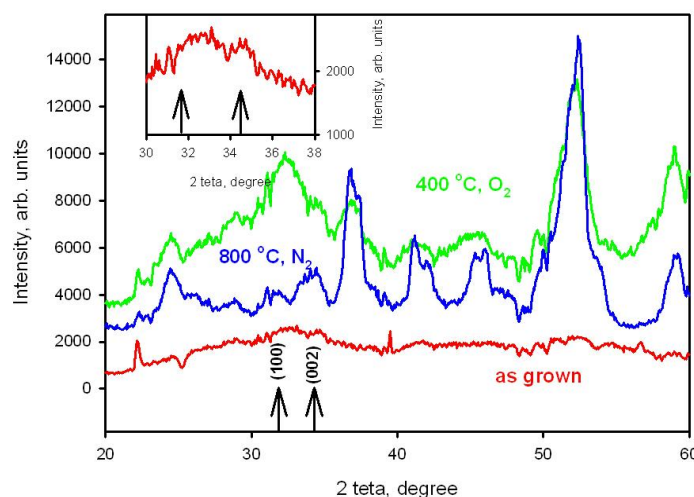


Fig.1. WAXS results of Mn-doped ZnO/TiO₂ multilayers annealed at different conditions

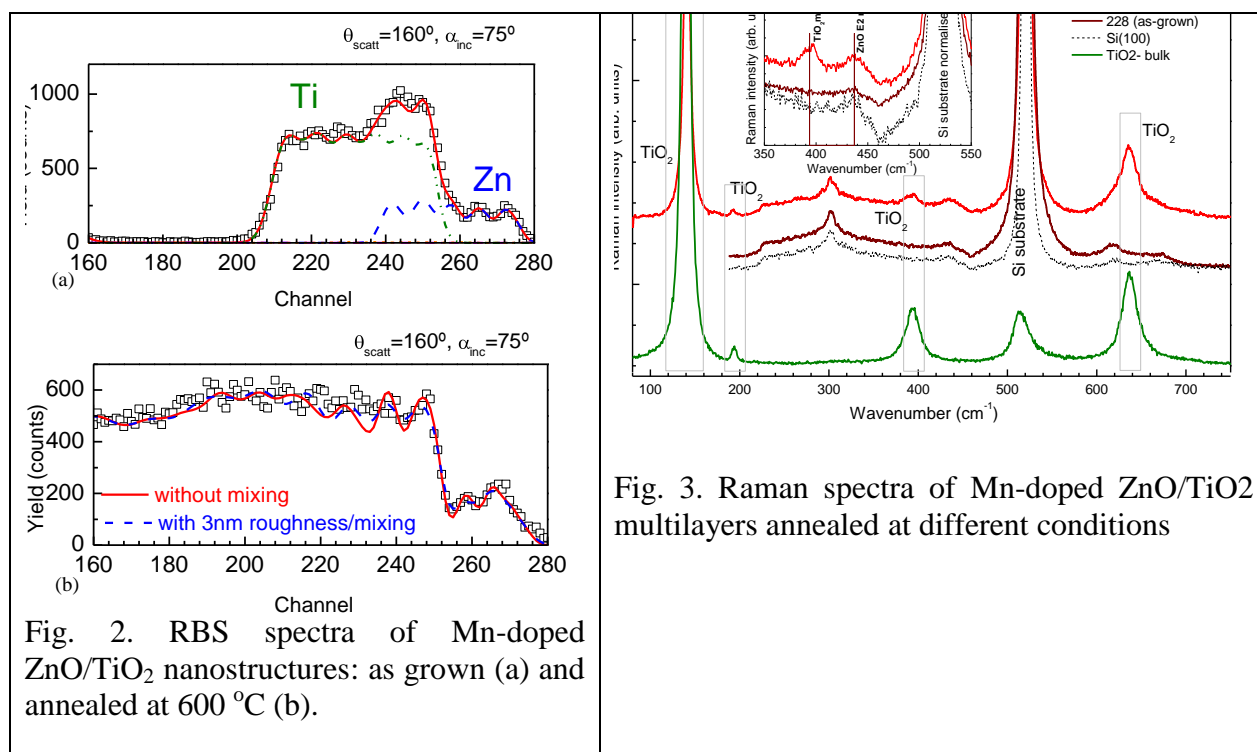


Fig. 2. RBS spectra of Mn-doped ZnO/TiO₂ nanostructures: as grown (a) and annealed at 600 °C (b).

Fig. 3. Raman spectra of Mn-doped ZnO/TiO₂ multilayers annealed at different conditions

THEORETICAL STUDY OF FUNCTIONALIZED NANOTUBES BETWEEN TRANSITION METAL ATOMS

S. Gómez-Coca and E. Ruiz

*Departament de Química Inorgànica and Institut de Química Teòrica i Computacional
(IQTCUB), Universitat de Barcelona, Diagonal 647, Barcelona 08028 Spain.*

silvia.gomez@qi.ub.es

Functionalized nanotubes [1] are interesting bridging ligands to comunicate paramagnetic transition metals, thus, we can solve the problem of the fast decay of the exchange coupling between this paramagnetic centres at long distance [2]. The mechanism of the exchange interaction is related with a charge transfer processes between the d orbitals of the metal and the π system of the nanotube. Previously, theoretical studies based on density functional theory predicted the presence of strong couplings at very long distances for this kind of systems. This coupling mainly depends of the chirality and nature of the nanotube and the oxidation state of the metal cation; it is stronger through metallic nanotubes than with semiconducting ones in similar length. Now we want to extend this previous work showing results for either metallic or semiconducting chiral nanotubes.

References:

- [1] S. Banarjee, M. G. C. Kahn, S. S. Wong, Chem. Eur. J., **9** (2003) 1898.
- [2] E. Ruiz, F. Nunzi, S. Alvarez, Nano Letters, **6** (2006) 380.

Highly luminescent Nanostructures of CdS and ZnS prepared by microwaves heating: effect of ions metal concentration

Samuel Martínez, Idalia Gómez, Perla Elizondo, J. L. Cavazos

Materials Laboratory I, Chemistry Sciences Faculty at University of Nuevo Leon, México

mgomez@fcq.uanl.mx

Colloidal semiconductor nanocrystals (NCs) are of great interest for fundamental studies^{1,2} and technical applications³⁻⁵ such as light-emitting devices, lasers, and fluorescent labels. Because of their size-dependent photoluminescence across the visible spectrum,¹ ZnS and CdS nanocrystals have become the most extensively investigated NCs. Besides the development of synthesis techniques to prepare samples with narrow size distributions,^{2,6} much experimental work is devoted to molecular surface modification aiming to improve the luminescence efficiency¹, the colloidal stability of the particles and developing a reliable processing chemistry.² This work presents the results of the study in the synthesis of CdS and ZnS in presence of cadmium citrate as stabilizer agent and processed by microwaves heating. Effect of concentration of Cd and Zn ions were studied in the luminescence property. RXD, AFM, TEM and UV-Vis were used too as analytical equipment for characterization.

Nearly monodisperse and highly luminescent ZnS and CdS NPs were obtained by microwave irradiation. The ZnS and CdS NPs solutions were prepared by adding freshly prepared ZnSO₄ or CdSO₄ solution to a thioacetamide solution at pH 8 in the presence of sodium citrate in solution used as stabilizer. The precursors concentration were such that the metal ion concentrations were [Zn-Cd] = 3x10⁻²M, [Zn-Cd] = 6x10⁻²M and [Zn-Cd] = 8x10⁻²M, for each of these [Zn] or [Cd] concentrations the [S] content was fixed at [S] = 3x10⁻²M. NPs were prepared under microwave irradiation for 1 min at 905 W of power. The NPs samples were taken when the temperature descended to ambient temperature for further analysis.

The UV-vis spectra of the nanoparticles synthesized by microwave heating shows a blue-shift due to the quantum confinement and the reduction of the particle size. This effect is due the increase of the concentration of metal ion. The band gap of the semiconductors increases when the particle size decreases. The crystal structure of the ZnS synthesized is cubic sphalerite form and for CdS was cubic type zinc blend according the XRD analysis, Fig. 2 and 3 respectively. The results of AFM of ZnS are in accordance with the XRD results, showing sizes of around 100nm. The morphology of the prepared ZnS shows islands with a nanocenter as well as nanoparticles of about 100 nm (Fig. 4). The ZnS NPs obtained shown high monodispersity according to PL analysis, see Fig. 1. The high luminescence is present when the NPs are irradiated with UV light using energy higher than the band gap value found for each sample, this property is due to the reduction of the particle at nanometer scale. Synthesis by microwave heating provides a very powerful option to prepare ZnS and CdS nanoparticles with highly luminescent properties.

This work was financial support by CONACYT and PAICYT under the projects #52797 and CA-1524-07 respectively.

References:

- [1] Paras N. Prasad, Nanophotonics, Wiley Interscience, **2004**.
- [2] Geoffrey A Ozin & André C Arsenault, Nanochemistry, RSC Publishing, **2005**.
- [3] Yury Gogotsi, Nanomaterials Handbook, Taylor & Francis, **2006**.
- [4] Edward L. Wolf, Nanophysics and Nanotechnology, Wiley-VCH, **2006**.
- [5] Guozhong Cao, Nanostructures and Nanomaterials, Imperial College Press, **2004**.
- [6] Thelma Serrano et al, Colloids and Surfaces A: Physicochem. Eng. Aspects **2009** 20-24

Figures:

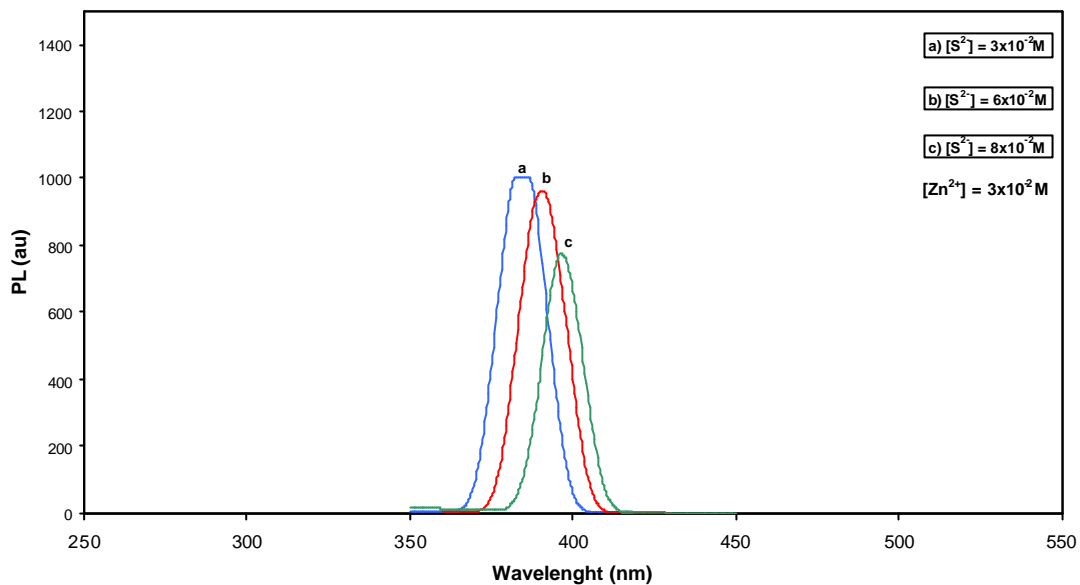


Fig. 1. Photoluminescence of ZnS nanoparticles.

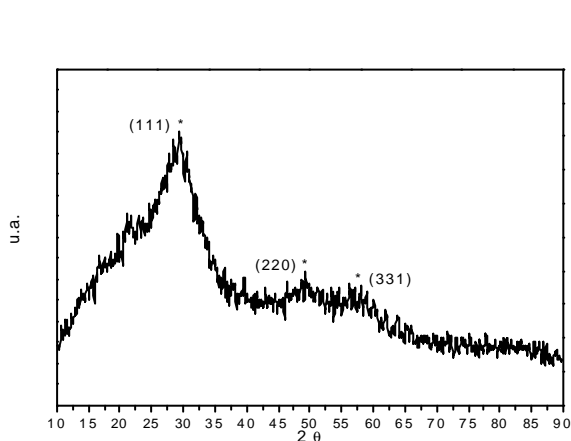


Fig. 2. XRD of ZnS nanoparticles.

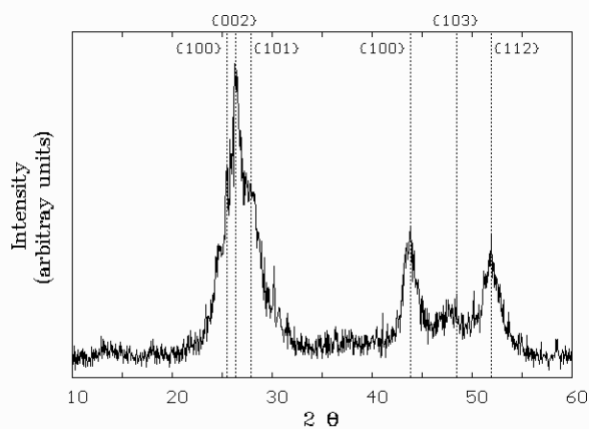


Fig. 3. XRD of CdS nanoparticles

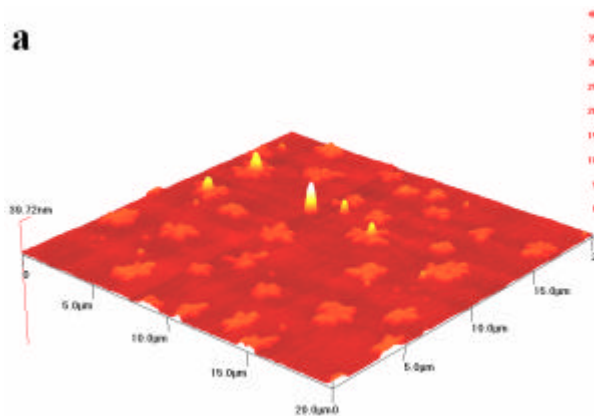


Fig. 4. AFM of ZnS nanoparticles.

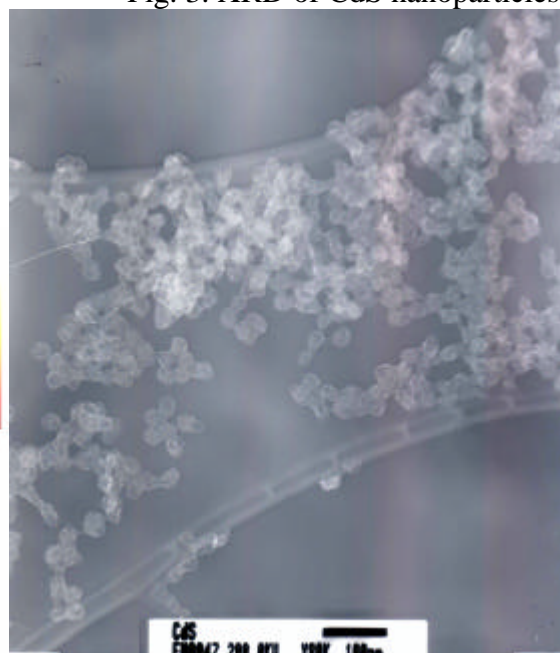


Fig. 5. TEM of CdS nanoparticles.

Supramolecular effects of chiral molecules on metallic surfaces: D-alaninol on Cu(100) as a case study

P. Gori¹, M. Aschi², G. Contini¹, T. Prosperi¹, N. Zema¹, A. Cricenti¹ and A. Palma³

¹*Istituto di Struttura della Materia, CNR, Via Fosso del Cavaliere 100, 00133 Rome, Italy*

²*Università L'Aquila, Dipartimento di Chimica,*

Ingegneria Chimica e Materiali - Coppito (AQ), Italy

³*Istituto per lo Studio dei Materiali Nanostrutturati, CNR, Via Salaria Km 29.3, 00016*

Monterotondo S. (RM), Italy

paola.gori@ism.cnr.it

Organic chiral molecules adsorbed on metallic surfaces provide a simple and flexible way to transfer chirality to achiral substrates. The beneficial quality of the resulting structures ranges from their practical use as stereospecific catalysts or as substrates for possible homochiral propagation to supramolecular gratings. Many works have been devoted to the adsorption of amino acids on metallic surfaces [1]. We address here instead the adsorption of a simple amino alcohol, alaninol (2-amino-1-propanol), on Cu(100) as a case study. The molecule's bifunctional nature permits a possible double interaction taking place between both amino and hydroxyl groups on one side and copper atoms on the other. Among the two functional groups, the amino group is the one that is most strongly involved in the binding with the surface, making the hydroxyl group more easily available to create lateral hydrogen-bonded interactions with other molecules of the same type in a possible self-assembled surface structure. In this respect, chirality plays an additional role in permitting the creation of clusters of molecules at the surface with complex relationships occurring between them, instead of a simple molecular packing.

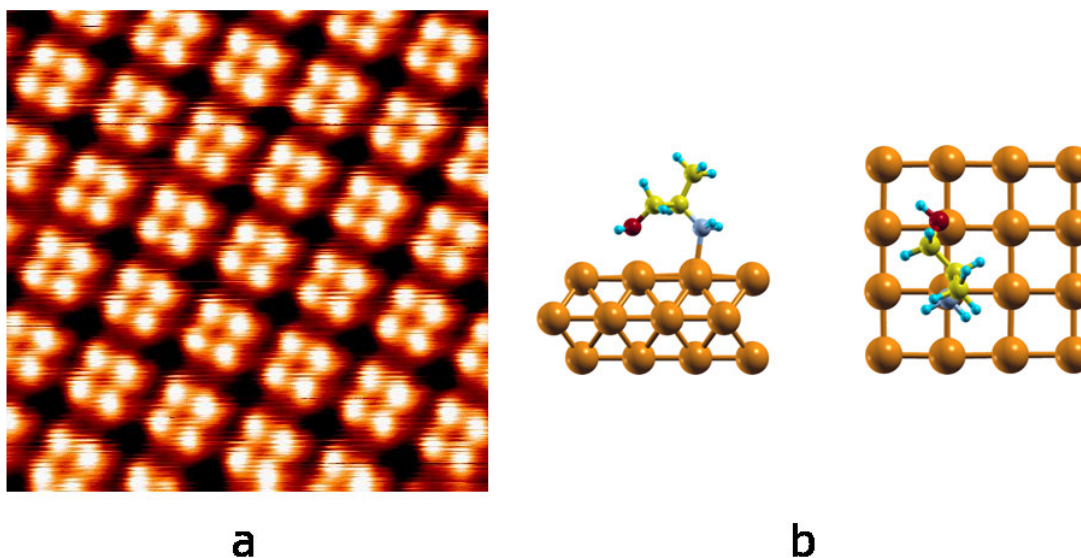
In order to investigate and possibly to enhance the achievable enantioselectivity, it is of primary importance to understand the mechanisms of adsorption at the surface. The practical use of such modified surfaces is made possible by the fact that a long-range ordered self-assembled molecular phase is formed upon adsorption. Experimentally [2], alaninol is found to self-assemble on Cu(100) forming, at monolayer coverage, a phase composed by tetrameric units. In particular, as shown by low energy electron diffraction (LEED), its D-enantiomer arranges in a square structure represented in matrixial form as (1,4|4,-1) leading to a 14 degrees clockwise rotation of the molecular phase with respect to the [011] direction of copper. The tetramers composing this phase are presumably due to four alaninol molecules [3], that appear not exactly equal when imaged by a scanning tunnelling microscope (STM, see Fig. 1a). A complex interaction among molecules and between molecules and surface is therefore to be expected and a mere systematic search of all possible combinations of four molecules can be not sufficient to devise the type of molecular structure describing the system. In this work we therefore address the problem employing a composite approach based on the interplay between density functional theory (DFT) calculations and classical molecular dynamics. DFT is employed for providing the starting point, *i.e.* the adsorption configurations of a single alaninol molecule on the Cu(100) surface [4]. This shows that the most stable adsorption geometry involves the amino group and a less strong interaction with the surface through the hydroxyl group (see Fig. 1b). A tetramer of alaninol molecules is then assumed as initial configuration to start molecular dynamics at room temperature, in which N-Cu bonds are fixed, whereas the hydroxyl end of the molecules are left free to rotate on the surface. The successive dynamics is carried on for a few tens of nanoseconds, which allows the exploration of a good portion of the configuration space. Two different situations are addressed in the simulations: a first case in which the dynamics of a single tetramer is analyzed and a second case in which nine tetramers on a square matrix are considered. This two step approach allows to assess the comparative

importance of intra- and inter-tetramer forces. One of the outcomes of such calculations is that it is essential to take into account the larger simulation cell, that best matches the experimental situation, and that quite different results are obtained when comparing the most sampled geometries in the two cases. This points to the important role of supramolecular interactions and highlights the cooperative effect that takes place, correlating even molecules that are located several angstrom apart, as is shown by performing an essential dynamics analysis [5]. As a final point, we resort again to DFT calculations applied to the central tetramer of the most sampled geometries, simulating STM images and comparing them with available experimental data.

References:

- [1] S.M. Barlow and R. Raval, *Current Opinion in Colloid & Interface Science* **13** (2008), 65.
- [2] S. Irrera, G. Contini, N. Zema, S. Turchini, J. Fujii, S. Sanna and T. Prospero, *J. Phys. Chem. B* **111** (2007), 7478.
- [3] P. Gori, G. Contini, T. Prospero, F. Ronci, S. Colonna, N. Zema, S. Turchini, D. Catone, A. Cricenti and A. Palma, *Superlattices and Microstructures*, in press (2009).
- [4] P. Gori, G. Contini, T. Prospero, D. Catone, S. Turchini, N. Zema and A. Palma, *J. Phys. Chem. B* **112** (2008), 3963.
- [5] A. Amadei, A. B. M. Linssen and H. J. C. Berendsen, *Proteins: Structure, Function, and Genetics*, **17**, (1993), 412.

Figure 1



- a) Experimental STM image of a $6 \times 6 \text{ nm}^2$ area ($V = 0.1 \text{ V}$; $I = 0.2 \text{ nA}$); b) Most stable adsorption configuration (side and top view) of a single D-alanine molecule adsorbed on Cu(100).

Nanoparticles with “onion-like” core (α -Fe) / double shell (γ -Fe/Fe-oxide) structure

M.P. Fernández ^a, P. Gorria ^a, R. Boada ^b, J. Chaboy ^b, M. Sevilla ^c, A.B. Fuertes ^c, J.-M. Greneche ^d, J.A. Blanco ^a.

^a Departamento de Física, Universidad de Oviedo, Calvo Sotelo s/n, 33007, Oviedo, SPAIN.

^b Instituto de Ciencia de Materiales de Aragón and Dpto. de Física de la Materia Condensada, CSIC-Universidad de Zaragoza, 50009, Zaragoza, SPAIN

^c Instituto Nacional del Carbón, CSIC, Ap. 73, 33080, Oviedo, SPAIN.

^d LPEC, UMR 6087, Université du Maine, 72085 Le Mans Cedex 9, FRANCE

pgorria@uniovi.es

The large variety of magnetic scenarios displayed by metal transition nanoparticle systems is greatly influenced by the reduced size and/or miscellaneous morphologies of the nanoparticles, because surface, interface or finite-size effects play an important role [1-3]. Nevertheless, the magnetic behaviour may depend on the surrounding media or matrix in which the nanoparticles are dispersed as well. The complete understanding of such behaviour is of major importance for any particular application from the technological point of view.

One of the most studied systems are those containing iron nanoparticles, which very often present a core-shell morphology due to the strong and fast reactivity of iron with oxygen. In this situation, strong magnetic interactions between the iron particle core and the iron oxide shell give rise to modifications of the coercivity, the magnetic anisotropy and to the appearance of an exchange bias effect [4]. Recently, exchange bias has been reported for iron nanoparticles coated by a thin ferrimagnetic iron oxide layer at temperatures much lower than that corresponding to the Néel temperature (T_N) of the iron oxide. This effect is originated by the freezing of the iron oxide spins due to low temperature spin-glass like behaviour. We will show in this contribution how the magnetic behaviour of iron nanoparticles, randomly dispersed in activated carbon, is strongly correlated with the microstructure and the complex nanoparticle morphology, through the combination of several experimental techniques such as x-ray powder diffraction, scanning and transmission electron microscopy, Fe-K edge x-ray absorption and Mössbauer spectroscopies and magnetic measurements.

The iron nanoparticles were randomly dispersed in a commercial porous carbon using a low cost and simple chemical synthesis route [5,6]. The process is based in a pyrolysis taken place at the intersections between the nanopores of the activated carbon (see Figure 1a) [7,8]. This method allows the fabrication of several grams of powder samples with iron weight percentages above 15 %. The NPs present a broad particle-size distribution (5-50 nm) with an atypical “onion-like” morphology: Core (α -Fe) – inner layer (γ -Fe) – outer layer (Fe-oxide) (see Figures 1b-1c). The estimated phase percentages (by combining XRD, Mössbauer and XANES spectroscopies) are around: 44% (α -Fe), 32% (γ -Fe) and 24% (Fe-oxides) (see Figures 2 and 3). The γ -Fe layer remains paramagnetic down to 77 K, while the whole system does not reach a fully superparamagnetic regime even at 750 K, probably due to the high blocking temperature of the largest NPs (see Figures 4a-4b). However, the nanoparticles exhibit exchange bias below 60 K ($H_{ex} \approx 150$ Oe at $T = 5$ K), a temperature much lower than T_N of Fe oxides (ferrimagnetic magnetite, maghemite or a non-stoichiometric mixture of them) (Figure 4b). Hence, we suggest that the existence of the exchange bias could be due to the combination of two effects, (i) the oxide shell-core interaction, governed by a spin freezing at the surface of the particles due to low-temperature spin-glass behaviour of the oxide layer, and (ii) the possible antiferromagnetic coupling between α -Fe core and γ -Fe layer.

The financial support for this research work provided from FEDER and the Spanish MICINN (MAT2008-06542-C04, MAT2008-00407) is acknowledged. One of us, M.P.F. thanks MICINN for the award of a FPI grant cofinanced by the European Social Fund.

References:

- [1] J.L. Dormann, D. Fioranni, E. Tronc, Magnetic relaxation in fine-particle systems, John Wiley & Sons, (1997).
- [2] P. Gorria, M. Sevilla, J.A. Blanco, A.B. Fuertes, Carbon **44** (2006) 1954.
- [3] P. Gorria, M.P. Fernández, M. Sevilla, J.A. Blanco, A.B. Fuertes, Phys. Status Solidi-RRL **3** (2009) 4.
- [4] J. Nogués, J. Sort, V. Langlais, V. Skumryev, S. Suriñach, J. S. Muñoz, Phys. Reports, **422** (2005) 65.
- [5] A.B. Fuertes, P. Tartaj, Chem. Mater. **18** (2006) 1675.
- [6] A.B. Fuertes, P. Tartaj, Small **3** (2006) 275.
- [7] M.P. Fernández, D.S. Schmool, A.S. Silva, M. Sevilla, A.B. Fuertes, P. Gorria, J.A. Blanco, J. Non-Cryst. Solids **354** (2008) 5219-5221.
- [8] M.P. Fernández, D.S. Schmool, A.S. Silva, M. Sevilla, A.B. Fuertes, P. Gorria, J.A. Blanco, J. Magn. Magn. Mater. DOI: 10.1016/j.jmmm.2009.04.058.

Figures:

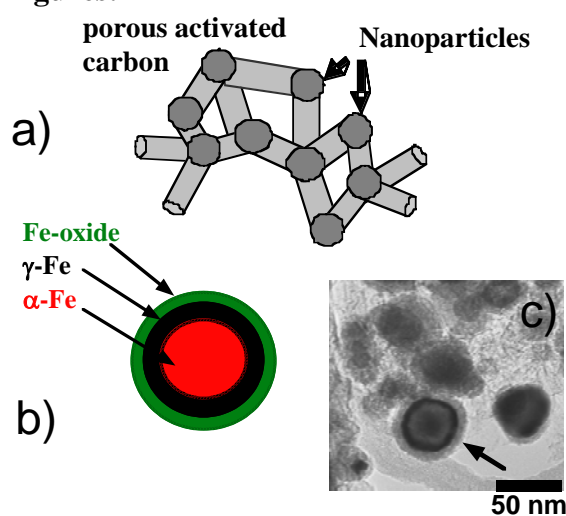


Figure 1. a) Schematic drawing of interconnected nanopores where Fe-NPs are deposited. b) "Onion-like" core (α -Fe) / double shell (γ -Fe/Fe-oxide) structure. c) TEM image of Fe-AC NPs. The arrow points an "onion-like" nanoparticle.

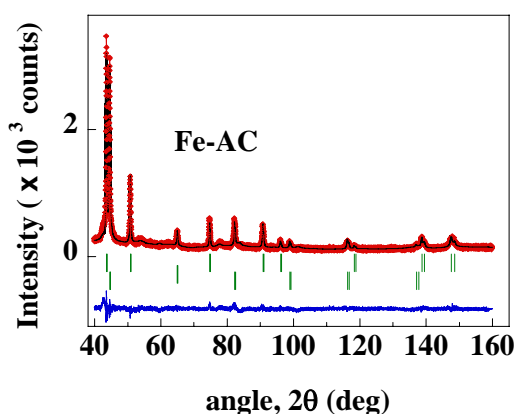


Figure 2. Observed (red points) and calculated (solid line) room temperature XRD pattern of Fe-AC sample. Positions of Bragg reflections are represented by vertical bars (first series correspond to γ -Fe and the second to α -Fe crystalline phases). The observed-calculated difference pattern is depicted at the bottom of the figure.

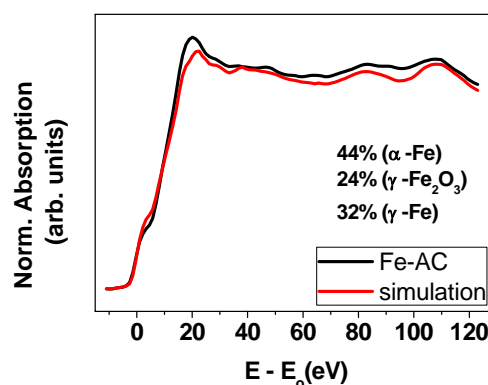


Figure 3. Fe K-edge XANES spectrum for Fe-AC composite (black line) together with the simulation (red line) considering a mixture of 44% (α -Fe) 24% (γ -Fe₂O₃) and 32% (γ -Fe).

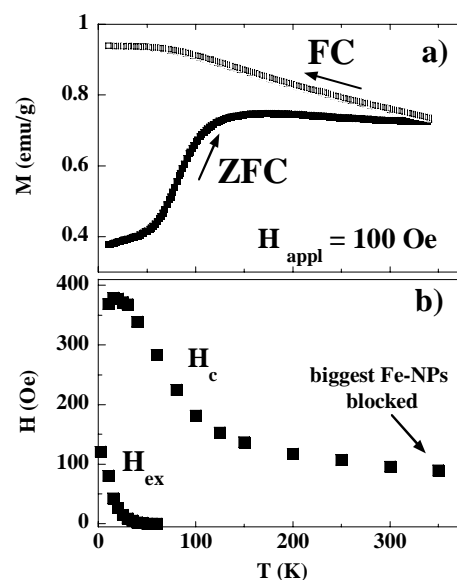


Figure 4. a) $M(T)$ ZFC-FC magnetization measurement under an applied magnetic field of 100 Oe. b) Temperature dependences of the coercive, H_c , and exchange bias, H_{ex} , fields.

THE USE OF INTRACELLULAR HYPERTHERMIA ON DENDRITIC CELLS LOADED WITH MAGNETIC NANOPARTICLES: A PROMISING WAY TO IMMUNOTHERAPY

G. F. Goya^{1,2}, I. Marcos-Campos^{1,3}, L. Asín¹, T. E. Torres^{1,2}, C. Marquina^{2,4}, A. Tres³, and M. R. Ibarra^{1,2}

1. Aragon Institute of Nanoscience (INA), University of Zaragoza- Zaragoza, Spain.

2 Condensed Matter Department, Sciences Faculty, University of Zaragoza, Spain.

3 Oncology Department, Hospital Universitario "Lozano Blesa", Zaragoza, Spain.

4 Instituto de Ciencia de Materiales de Aragón (ICMA), CSIC, Zaragoza, Spain

goya@unizar.es

The increasing synergy between biomedicine and nanosciences has its paradigm in the use of magnetic nanoparticles (NPs) in routine laboratory and clinical protocols, such as cell sorting, DNA separation, Magnetic Resonance Imaging (MRI) and gene therapy. [1] Among those applications of NPs currently in preclinical stages we can mention cell-targeted delivery of anticancer agents and molecular diagnosis. A key issue in the search for high-performance magnetic materials is the toxicity that a given element (or its oxides) has on the cellular metabolism.

Dendritic cells (DCs) are the most important antigen-presenting cells (APC), performing a key role at the first steps of most immune responses. [2] The main hallmarks of DCs are their high potential to capture, process and present antigens through MHC-I and MHC-II molecules to T cells. DCs are derived from bone marrow precursors and migrate to non-lymphoid tissues where they differentiate into dendritic cells. Once DCs are in the mature state, they express a lack of receptors, such as CCR7, which permits them to migrate to lymph nodes where take place the antigen presentation to T cells.[3]

In this presentation we show the first results on a new strategy, based in the use of dendritic cells as natural carriers of the NPs to the desired target tissue. The bottom line of using dendritic cells as carriers of NPs is to mimic biological units in order to elude the immune response of the body. The potential of this strategy is that the cargo of the DCs could be designed to be either 'nude' magnetic NPs for hyperthermia therapy, or functionalized magnetic NPs with specific drugs that could be released by application of time-varying magnetic fields. We also present an easy method to quantify the incorporation of magnetic NPs into DCs, which has the potential to quantify the amount of magnetic material absorbed.

The magnetic NPs (Micromod GmbH, Germany) used in this work were constituted by a magnetite (Fe_3O_4) core of c.a. 13-16 nm radii (Figure 1), and functionalized shell with positive/negative surface having NH_2 and COOH - groups. These samples were selected to test the effect of surface charge on the particle incorporation efficiency of the DCs. The nanoparticles were further characterized through Dynamic Light Scattering (DLS), and magnetization measurements.

We have observed that the nanoparticles had no effect in DC viability observed up to five days of co-culture. Moreover, these MNPs did not inhibit the differentiation process from blood monocytes into mature, fully functional DC cells. The total amount of MNPs was determined through magnetic measurements, yielding values of 2-5 pg/cell. The DCs already loaded with MNPs were exposed to rf magnetic fields to induce cellular death by local heating. We found clear evidence that only magnetically-loaded cells were killed when exposed to the magnetic field, yielding up to 90% of cell death. The high level of cell death observed in NP-loaded cells

after hyperthermia treatments suggests that this method could be a first step for assessing the feasibility of using DCs as vectors for NPs towards angioplastic areas for therapeutic purposes.

References:

- [1] G.F. Goya, V. Grazú and M.R. Ibarra, Current Nanoscience, **4** (2008), 1-16.
- [2] Adema GJ, Hartgers F, Verstraten R, De Vries E, Marland G, Menon S, Foster J, Xu Y, Nooyen P, McClanahan T, Bacon KB, Figdor CG. Nature **387** (1997) 713-7.
- [3] Cumberbatch M, Kimber I., Immunology 1995; 84:31–5.

Figures:

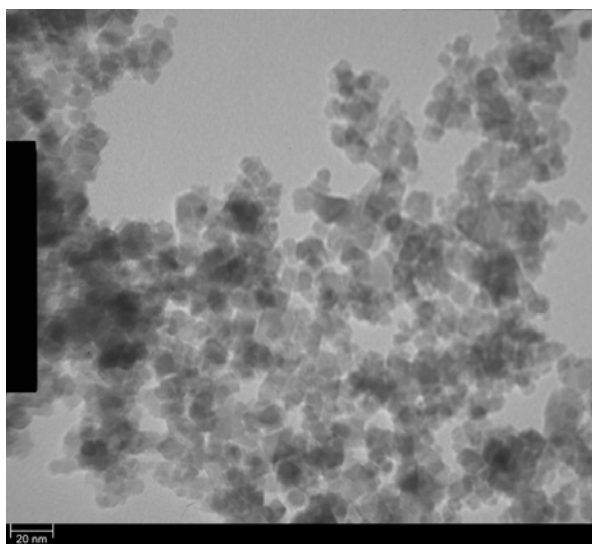


Figure 1: TEM image of Fe₃O₄ nanoparticles with magnetic cores of $\langle d \rangle = 13-16\text{ nm}$, functionalized with NH₂⁺ groups at the surface.

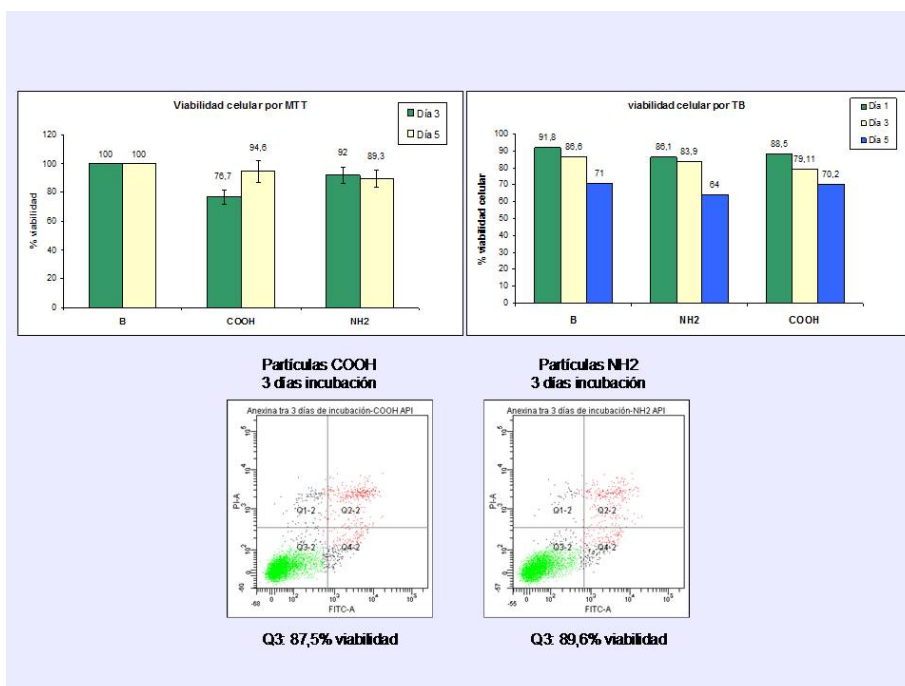


Figure 2: Cell viability verified for the two kind of NPs used. It can be seen that nearly 90% of the original cells remained viable after 3 day incubation with NPs. The three methods showed agreement within experimental error.

MODELLING ELECTRON CORRELATION EFFECTS IN MOLECULAR ELECTRONICS DEVICES

Francois Goyer, Matthias Ernzerhof

Department of Chemistry, University of Montréal, Montréal, Canada

francois.goyer@umontreal.com

Understanding electron transport through molecular electronic devices (MEDs) is essential for the conception of new types of circuits, i.e. quantum transistors. Presently, most theoretical approaches used to model these systems are based on effective one-electron theories. In these models, however, it is not possible to properly account for electron correlation effects.

We present our progress in including electron interaction effects in the description of MEDs. Starting from the Hubbard Hamiltonian¹, we describe an extension of the Source-Sink Potential (SSP)² method suitable for interacting systems. This multi-particle framework enables us to study systems in which electron interaction is the dominant factor. We investigate what impact electron correlation has on various recently discussed phenomena: interference effects present in cross-conjugated chains³ and circular current interference⁴⁻⁵ present in aromatic cycles such as benzene.

References:

- [1] Goker, Goyer and Ernzerhof, *The Journal of Chemical Physics* **129**, p 194901 (2008).
- [2] Goyer, Ernzerhof, and Zhuang, *The Journal of Chemical Physics* **126**, p 144104 (2007).
- [3] Solomon GC, Andrews DQ, Goldsmith RH, et al., *Journal of the American Chemical Society* **130**, p 17301 (2008).
- [4] Cardamone DM, Stafford CA, Mazumdar S, *Nano Letters* **6(11)**, p 2422 (2006).
- [5] Ernzerhof, M. Bahmann H. Goyer, F. Zhuang, M. Rocheleau, P, *Journal of Chemical Theory and Computation* **2(5)**; p 1291 (2006)

MAGNETIC CHARACTERISTICS OF MAGNETITE NANOCRYSTALS FORMED BY ESTUARY MAGNETOTACTIC BACTERIA FROM COLOMBIA

Sandra Grisales, Viviana Morillo, Marco Márquez

National University of Colombia, Medellín Campus, Medellín, 050034, Medellín, Colombia

sagris77@hotmail.com

Magnetotactic bacteria contain chains of magnetite nanocrystals that comprise a permanent magnetic dipole in each cell (Frankel *et al.* 2006; Fischer *et al.*, 2008). These nanocrystals fall within the stable single domain magnetic size range of between 30 and 120 nm, and are permanently magnetic. Smaller sizes crystals do not show persistent magnetization. In crystals larger than 120 nm, multiple magnetic domains of opposite magnetic orientation can be formed, which reduces the total magnetic remanence of the crystal (Lang and Shüler, 2006; Pósfai *et al.* 2006; Shuler, 2008). This means that magnetite nanocrystals of magnetotactic bacteria show superior magnetic properties (Arakaki *et al.* 2008; Frankel *et al.* 2006; Fischer *et al.*, 2008). In order to study the morphology, crystal size and elemental analysis of nanocrystals of magnetotactic bacteria, the cells were magnetically harvested and deposited on Cu TEM grids (Lins *et al.* 2003). The grids were analyzed using a TECNAI G2 20 D345 (FEI) transmission electron microscope operating at 200 kV, equipped with an EDX analysis system. For magnetic measurements, concentrated samples of bacteria were packed into paraffin blocks. Magnetic hysteresis loops were measured using a Quantum Design Vibrating Sample Magnetometer (VSM) in a magnetic field of 1 Tesla. The saturation magnetization (M_s), remanent magnetization after saturation (M_r), coercivity (H_c) and remanence coercivity (H_{cr}) were determined at room temperature (300 K) and lower temperatures (150 K and 80 K).

TEM images of magnetotactic bacteria showed that the nanocrystals are arranged in two pairs of parallel chains in each cell (Figure 1A). Each chain, containing about 6 to 8 elongated prismatic nanocrystals (Figures 1B and 1C), showed a size range between 30 and 110 nm, with the maximum of the size distribution at 80 – 110 nm (Figure 1D). These crystals were elongated (width/length ratio of 0.8) along [111] their axes. These particles fall within the single magnetic domain (SD) range. EDX analyses showed that the nanocrystals consist of magnetite (Figure 1E). Saturation magnetization, M_s , remanent magnetization after saturation, M_r , coercive force, H_c and coercivity of remanence, H_{cr} , and their ratios (M_r/M_s and H_{cr}/H_c) serve to define domain states. For single domain crystals of magnetite, the theoretical values of the remanence ratio and the coercivity ratio are $M_r/M_s \sim 0.5$ and $H_{cr}/H_c \sim 1.5$, respectively and these ratios are essentially temperature invariant (Davila, 2005). The hysteresis loops of magnetotactic bacteria at all temperatures showed a coercive force (H_c) ranging from 0.375 to 0.416 mT, and a coercivity of remanence (H_{cr}) ranging of 0.125 to 0.917. The remanence ratio (M_r/M_s) was 0.44 (300 K), 0.38 (150 K) and 0.4 (80 K), while the coercivity ratio H_{cr}/H_c was 0.5 (300 k), 0.58 (150 K) and 2.2 (80 K) (Figure 2). The samples were saturated at 100 mT, showed the presence of ferromagnetic minerals such as magnetite (Han *et al.* 2007). These results demonstrate that the nanocrystals of estuary magnetotactic bacteria consist of single domain magnetite. In a Day plot (remanence ratio, M_r/M_s versus coercivity ratio B_{cr}/B_c) the ratios of the hysteresis parameters M_r/M_s , M_s , B_{cr} and B_c are sensitive to the domain state of the particles (Davila, 2005). As can be seen, the Day plot parameters for the magnetotactic bacteria sample fall well within the single domain range ($M_r/M_s \sim 0.5$, $H_{cr}/H_c \sim 1.5$) (Figure 2D). The magnetite nanocrystals of magnetotactic bacteria are good candidates for the potential applications as single-domain nanomagnets in fields such as biomedical, electronics, catalysis, and magnetic recording.

References

- [1] Arakaki A, Nakazawa H, Nemoto M, Mori T and Matsunaga T. Journal of the Royal Society interface, 5, (2008). 977- 999.
- [2] Davila F. PhD work (2005) 3-37.
- [3] Frankel R, Williams T and Bazylinski D, Springer, Heidelberg, 3 (2006). 1 – 24.
- [4] Fischer H, Mastrogriacomo G, Löffler J, Warthmann R , Weidler P and Gehring A. Earth and Planetary Science Letters 270 (2008) 200–208

- [5] Han L, Li S, Yang Y, Zhao F, Huang J, Chang J, *Journal of Magnetism and Magnetic Materials* 313 (2007) 236–242.
- [6] Lang C. and Schüler D, *Journal of Physics: Condensed Matter*, 18 (2006)2815-2828.
- [7] Lins U, Freitas F, Keim C, Barros H, Esquivel D. And Farina M, *Brazilian Journal of Microbiology*, 34 (2003) 111-116.
- [8] Pósfai M, Moskowicz M, Arató B, Schüler D, Flies C, Bazyliniski D and Frankel B. *Earth and Planetary Science Letters* 249 (2006) 444–455.
- [9] Schüler D, *FEMS Microbiol Rev* 32 (2008) 654–672.

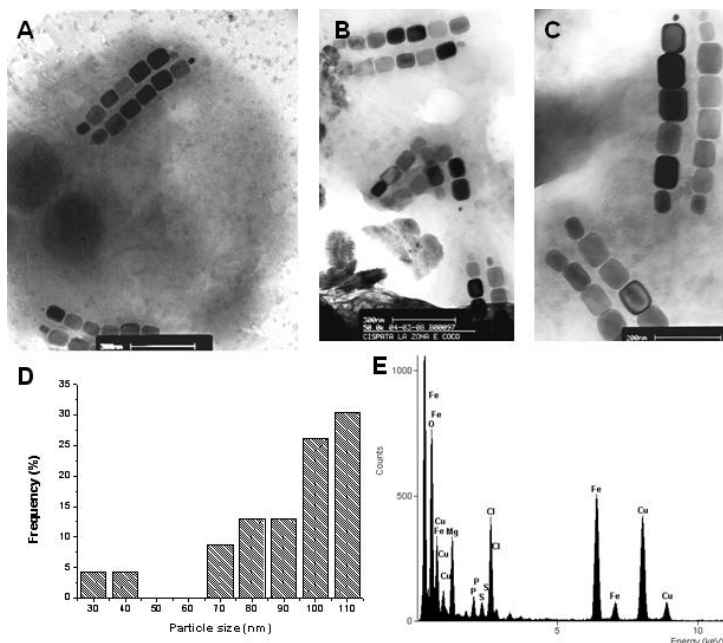


Figure 1. A. TEM Image of intact magnetotactic bacteria with two pairs of chains of magnetite nanocrystals. B and C. The pairs of chains of magnetite nanocrystals with elongated prismatic crystals. D. Crystal size distribution of intracellular magnetite nanocrystals of magnetotactic bacteria (120 crystals were measured). E. EDX spectrum of a nanocrystal showing mainly iron and oxygen peaks. Small Mg, P, S, and Cl peaks are derived from the cytoplasm and membranes surrounding the magnetosome. Cu peaks were derived from the supporting grid.

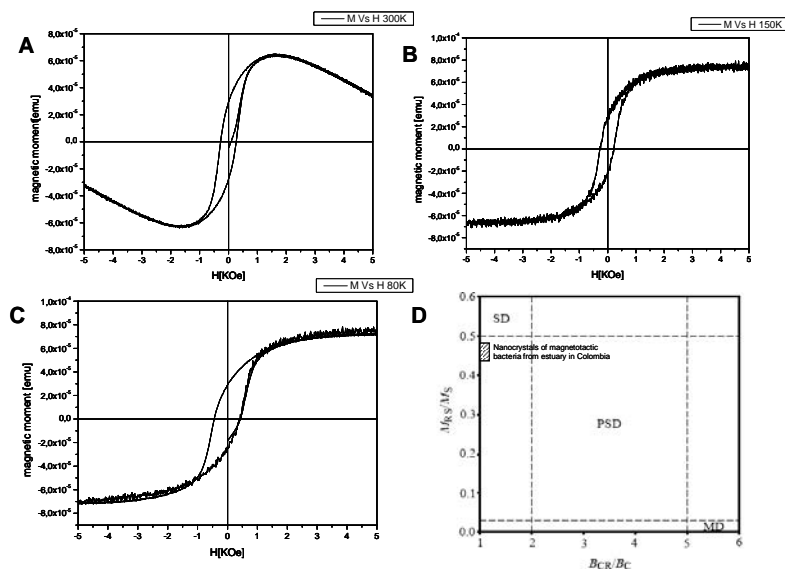


Figure 2. A. Hysteresis loops measured at 300 K. B. Hysteresis loops measured at 150 K. C. Hysteresis loops measured at 80 K. D. Comparison of the Day plot for the nanocrystals from estuary magnetotactic bacteria sample. (remanence ratio, M_{RS}/M_S) and coercivity ratio (B_{CR}/B_C). Single domain (SD), Pseudo-single domain (PSD) and Multi-domain (MD).

Epitaxy of ordered arrays of semiconductor nanostructures on substrates patterned by EUV interference and e-beam lithography

D. Grützmacher, C. Dais[#], G. Mussler, K. Sladek, and H. Hardtdegen

Institute for Semiconductor Nanoelectronics IBN-1, Forschungszentrum Jülich, Jülich, Germany and Jülich Aachen Research Alliance on Fundamentals of Future Information Technology (JARA-FIT), Germany

[#]Labor für Mikro- and Nanotechnology, Paul Scherrer Institute, Villigen Switzerland

Detlev.Gruetzmacher@fz-juelich.de

On the one hand side typical applications within nanoelectronics for semiconductor nanostructures, like quantum dots and nanowires, require precise control of the position, size and composition of the nanostructures. On the other hand side, commonly used bottom-up technologies for the fabrication of nanostructures, like self assembly, lead to arbitrary nucleation sites and a rather broad distribution of island sizes. Moreover, epitaxy of nanowires frequently involves the vapour liquid solid growth mode, employing metallic catalysts which potentially contaminate the semiconductor. Here we investigate the nucleation of nanostructures on predefined locations on the substrates. The patterns are produced by either EUV interference or by e-beam lithography. Two examples are presented, namely the growth of Ge quantum dots and quantum dot crystals on templated Si substrates and the growth of GaAs/AlGaAs core shell structures on GaAs/SiO₂ substrates.

Interference lithography using EUV light at a wavelength of $\lambda=13.5$ nm allows the fabrication of periodic patterns with a pitch of less than 20nm [1]. Using this technology Si (100) substrates have been patterned with 2-dimensional hole patterns with periodicities ranging from 35 to 100 nm. After EUV exposure and resist development the pattern was transferred to the Si substrate by reactive ion etching (RIE). Typically the holes were etched to a depth of 6-8 nm. Subsequently low temperature Molecular beam Epitaxy of a thin Si buffer layer was performed followed by the growth of a stack of Ge quantum dot layers separated by thin (5-10 nm) Si spacer layers. Fig. 1 shows AFM images of the top surface of quantum dot crystals (QDC) with lateral periodicities of 49, 42 and 35 nm fabricated by this technology. The QDC exhibit excellent ordering of the Ge dots and a very small size distribution as manifested by AFM, TEM as well as X-ray diffraction measurements. Moreover intense photoluminescence has been observed, which persists up to room temperature. Model calculations are in agreement with the structural and optical properties. These calculations indicate vertical and horizontal coupling of electronic states of neighbouring dots in the QDC.

In the second example presented in this study, GaAs (111) substrates have been coated with SiO₂ films. The SiO₂ film was patterned by means of e-beam lithography and subsequent RIE to open small windows with typical diameter of 50 nm into the SiO₂. These patterned wafers were subject to MOVPE growth using a selective mode to grow ordered arrays of GaAs nanowires. After the deposition of the GaAs wires the growth mode was switched by switching the precursors and a AlGaAs shell was deposited. Embedding a n-doped layer into the AlGaAs shell aims to the fabrication of a modulation doped 1-dimensional GaAs wire. Fig. 2 shows a) schematically of the structure of the grown core-shell structures and b) an SEM image of the MOVPE grown modulation doped AlGaAs/GaAs core-shell structures. First experiments on the transport in these wires are reported.

References:

[1] Y. Ekinici, H.H. Solak, C. Padeste, J. Gobrecht, M. P. Stoikovich, and P.F. Nealey, *Microelectronic Engineering* 84, 700 (2007).

Figures:

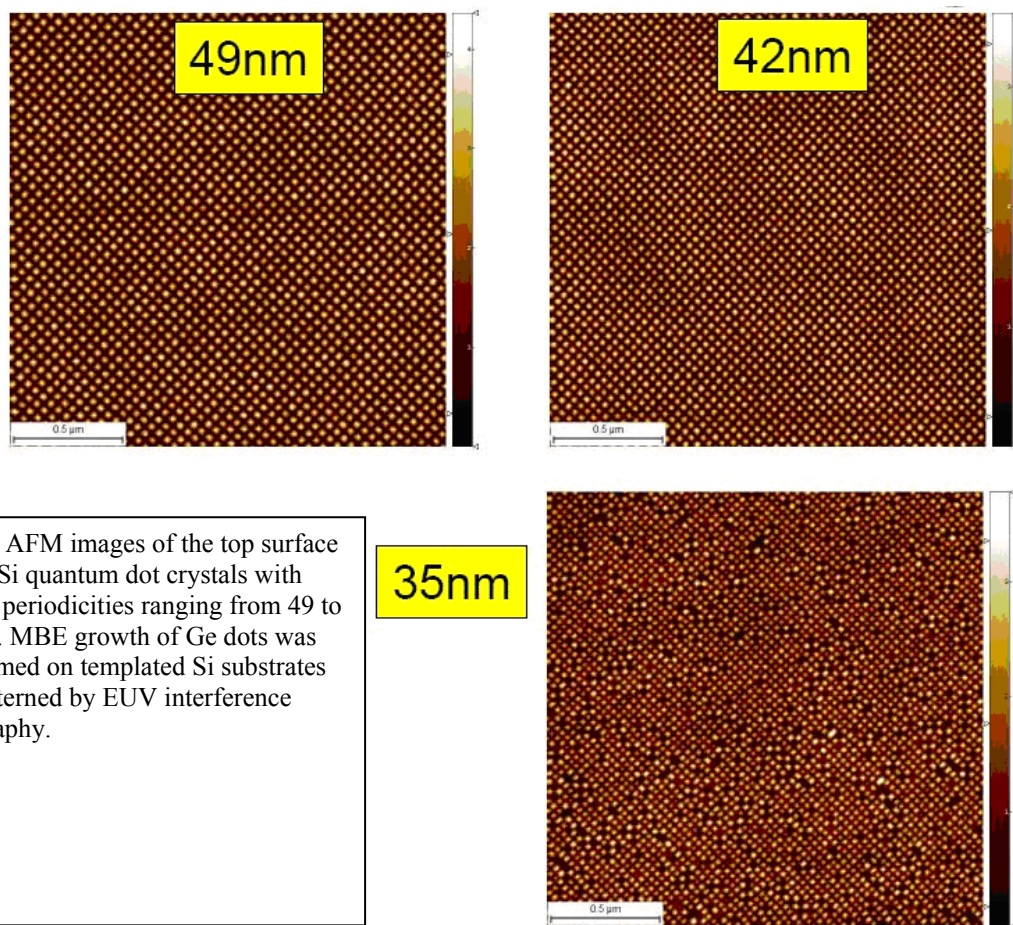


Fig. 1: AFM images of the top surface of Ge/Si quantum dot crystals with lateral periodicities ranging from 49 to 35 nm. MBE growth of Ge dots was performed on templated Si substrates prepatterned by EUV interference lithography.

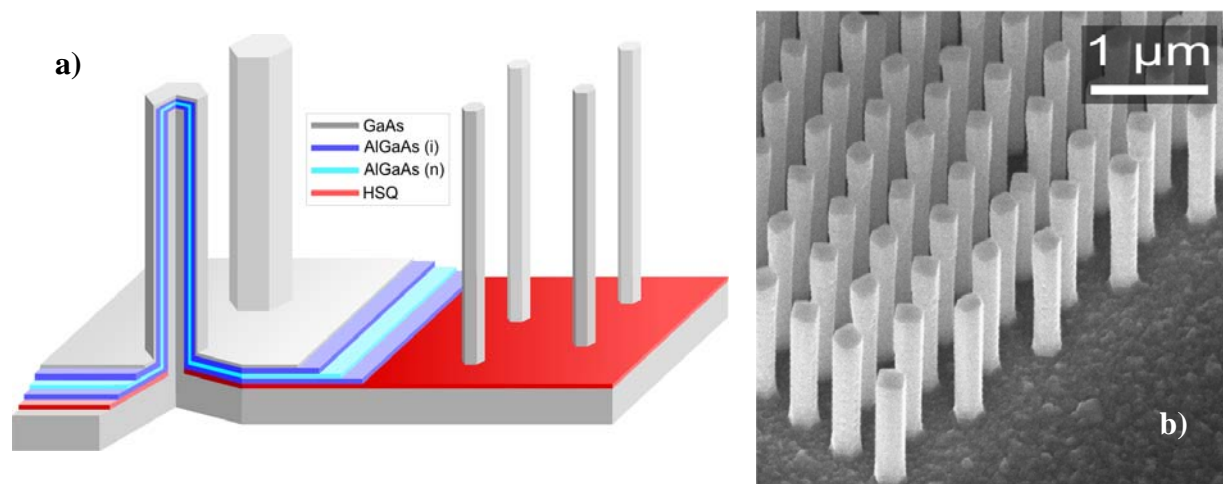


Fig. 2: a) schematic view and b) SEM image of GaAs/AIGaAs core-shell structures grown by MOVPE on GaAs (111) substrates. The nucleation of the GaAs wires was initiated in small windows opened in a SiO₂ layer at the surface of the GaAs substrate.

ELECTROPHORETIC DEPOSITION OF PALLADIUM NANOPARTICLES ON InP FOR HYDROGEN SENSORS

Jan Grym¹, Olga Procházková¹, Karel Zdánský¹, Roman Yatskiv¹, and Anton Fojtík²

¹Institute of Photonics and Electronics, ASCR, v.v.i. Czech Republic

²Faculty of Nuclear Sciences and Physical Engineering, CTU Prague, Czech Republic

grym@ufe.cz

Semiconducting, insulating, and metallic nanoparticles have attracted considerable interest due to their size-dependent, quantum confinement characteristics, which make them attractive for a wide range of optical, magnetic, and electronic devices. We report on the deposition of Pd nanoparticles prepared with reverse micellae of water/AOT/isooctane solution on the surface of n-type InP substrates and epitaxial layers. High quality metal/InP interfaces are essential for the fabrication of high-speed electronic devices, charge-control devices, optoelectronic and particle detectors. Thanks to catalytic activity of Pd, increasing number of papers has been devoted to hydrogen sensors based on Pd/InP interfaces [1]. Sensors based on Schottky diodes are capable of monitoring hydrogen and hydrogen-containing moieties in subppm and ppm range [2]. The hydrogen molecules are absorbed and dissociated at Pd surface, atomic hydrogen rapidly diffuses to the Pd/InP interface, where the dipole layer develops. Subsequently, the Schottky barrier height decreases and the electric current increases.

Pd nanoparticles with the diameters of 7 and 10 nm were prepared in isooctane colloid solution by the reverse micelle technique [3]. The electrophoretic deposition from the colloid solution took place in a cell with two parallel electrodes. The upper electrode was made from a high-purity graphite, the lower electrode was formed by an InP substrate or an InP substrate with an epitaxial layer, both of n-type conductivity with the background concentration of about $1 \times 10^{16} \text{ cm}^{-3}$. Liquid phase epitaxy from rare-earth treated melts was used to tune the background concentration in the epitaxial layers [4]. DC voltage was applied for a selected period of time to deposit a Pd-based nanolayer of about 100 nm in thickness. Pd nanoparticle shapes and sizes were observed by SEM and TEM, The deposited films were characterized by SEM, TEM, AFM, optical reflection spectroscopy, and SIMS. Several sets of samples were prepared by depositing different materials onto the nanolayer (spots of conductive Ag colloid paint, electrolytically deposited Pd, vacuum evaporated Pd followed by the evaporation of Au) serving as electrodes of a diode. The diodes were characterized by the measurement of I-V characteristics and their sensitivity towards hydrogen was tested.

We discuss the influence of particular combinations of (i) the substrate/epitaxial layer methods of preparation and surface treatment, (ii) conditions of the electrophoretic deposition, and (iii) methods of the electrical contact preparation on the performance of hydrogen detectors.

This work was supported by the Czech Science Foundation grant 102/09/1037 and grant KAN401220801 of the Academy of Sciences of the Czech Republic.

References:

- [1] H.-I. Chen, Y.-I. Chou, C.-Y. Chu, *Sensors and Actuators B* 85 (2002) 10-18.
- [2] Y.I. Chou, C.M. Chen, W.C. Liu, H.I. Chen, *IEEE Electron Device Letters* 26 (2005) 62-65.
- [3] K. Zdansky, P. Kacerovsky, J. Zavadil, J. Lorincik, A. Fojtik, *Nanoscale Research Letters* 2 (2007) 450-454.
- [4] J. Grym, O. Procházková, J. Zavadil, K. Zdánský, *Materials Science and Engineering B*, in print, corrected proof

NANOSTRUCTURED ANTITAGS-BASED BIOSENSORS FOR SENSITIVE PROTEIN DETECTION BY SERS ENHANCEMENT.

N. Guarrotxena^{1,2}, L. Fabris¹ and G.C. Bazan¹

¹ *Department of Chemistry / Biochemistry, Department of Materials, Institute for Polymers and Organic Solids, University of California, Santa Barbara, California 93106.* ² *Instituto de Ciencia y Tecnología de Polímeros (ICTP), CSIC, Juan de la Cierva, 3-28006, Madrid, Spain*

nekane@ictp.csic.es

The development of effective methods for the reliable and trace measurements of proteins are highly desired to facilitate the diagnosis disease states, improve drug discovery and defend against biological threats. Certainly, new methods that enable sensitive, selective, and rapid detection of proteins are essential. The potential benefits of protein biomarkers for disease detection and treatment have greatly motivated both academic and industry researchers to apply new proteomic technologies for biomarker discovery and to develop quantitative analytical methodologies for rapid and sensitive biomarker detection [1]. However, disease biomarkers and biological agents are often present at very low concentrations. Therefore, protein detection with high specificity and sensitivity is required.

Highly sensitive detection of proteins is commonly accomplished via antibody-based immunoassays, with the primary antibody is attached to a solid surface [2]. Based on this principle antibody-antigen interaction, the ELISA assay is one of the most important biochemical techniques used in immunology to detect the presence of an antibody or an antigen in a sample [3, 4].

However, the lack of amplification methods for protein detection, as compared to "PCR-like" amplification protocols for the case of nucleic acid detection limits the analysis and underscores, undoubtedly, the importance of new strategies for their detection and signal amplification that incorporate sensitive spectroscopic techniques and novel recognition systems.

Based on these considerations, while the majority of these bioassays, such as a sandwich ELISA (capture antibody and detector antibody involved), rely on the use of enzyme labels; our efforts have led to the development of a nanoparticle-based for immunoassays of proteins. The attractive amplification and multiplexing properties of metal nanoparticles make these suspensions of NP dimers and small aggregates ideal labels for immunoassays of proteins.

In this presentation, we disclose the design, preparation and function of *antitags*, which contain antibodies as the recognition element. These materials can be defined as nanostructured tools for developing ELISA analogues based on SERS concept [5]. SERS (Surface enhanced Raman spectroscopy) takes advantage of strongly increase Raman scattering signals generated by local field enhancements near metallic nanostructures. Since SERS retains the fingerprinting capabilities of Raman, the internal modes of a reporter molecules brought in close proximity to the metallic surface can be used as diagnostic signals for analyte detection.

In summary, the combination of opportunities given by nanotechnology and SERS enhancement together with the application of classic sandwich ELISA concept allow us to develop new sensitive protein detection. The main advantage of our method resides in the capability of the SERS-based techniques to allow multiplex detection not possible with the colorimetric and fluorometric ELISA analogue and in the creation of tags not dependent upon surface-specific enhancements. The use of antibodies should increase considerably the scope of targets, in comparison to recent reports of aptamer-based sensing [6].

References

- [1] C.G. Gunawardana, EP. Diamandis, *Cancer Lett.* **249** (2007) 110.
- [2] K.R. Rogers, *Molecular Biotechnol.* **14** (2000) 109.
- [3] (a) E. Engvall, P. Perlmann, *Immunochemistry* **8** (1971) 871. (b) R. Lequin, *Clin. Chem.* **51** (2005) 2415.
- [4] N. Guarrotxena, B. Liu, L Fabris, G.C. Bazan, *JACS* (2009) submitted.
- [5] M Moskovits, *J. Raman Spectrosc.* **36** (2005) 485.
- [6] L. Fabris, M. Dante, T.Q. Nguyen, JB. Tok, G.C. Bazan, *Adv. Funct. Mater.* **18** (2008) 2518.

Formulation of surfactant-polymer systems for the synthesis of hybrid organic-inorganic nanocomposites

L-H. Guillemot¹, C.E. Hoppe², C. Rodriguez-Abreu¹

1. Institut de Química Avançada de Catalunya. Consejo Superior de Investigaciones Científicas (IQAC- CSIC), Jordi Girona 18-26, 08034 Barcelona, Spain

2. Intema (Univ. Nacional de Mar del Plata - Conicet) – J. B. Justo 4302 - (7600) Buenos Aires, Argentina

craqci@iqac.csic.es

Nanocomposites consist of two or more segregated components incorporated in one material with characteristic lengths in the nanometer scale. They have attracted significant scientific and industrial interest due to their special optical, electronic, magnetic and chemical properties derived from the synergism between components. Applications such as detectors or optical waveguides in optoelectronics, among others, require the nanoparticles to be homogeneously dispersed in a polymeric matrix [1], leading to complex systems in which flocculation should be controlled.

In this work, bulk transparent, flocculation –free monolithic nanocomposites were synthesized by mixing a pre-synthesized colloid of surface-modified inorganic nanoparticles (NPs) with cross-linkable macromonomers, i.e. poly(dimethylsiloxane) (PDMS) containing reactive terminal groups (vinyl and hydroxyl). Nanoparticles dispersed in both organic and aqueous media were used; in the last case, an amphiphilic block copolymer (Polyoxyethylene grafted Polydimethylsiloxane, PEO-g-PDMS) was added to promote miscibility. To obtain such transparent monolithic nanocomposites, a phase behavior study was carried out at different temperatures on the crosslinkable mixtures to determine the regions of miscibility (see Fig.1).

It was also possible to obtain nanocomposites in the dispersed state by carrying out the crosslinking reaction using emulsions as templates to obtain microsized beads containing embedded nanoparticles (see Fig.2). Both bulk and particulate nanocomposites were characterized by several techniques such as spectrophotometry, microscopy, calorimetry and Small Angle X-ray Scattering (SAXS).

References:

[1] Pastoriza-Santos I., Pérez-Juste J., Kickelbick G., Liz-Marzán L., *Journal of Nanoscience and Nanotechnology*, **6** (2006) 1-6.

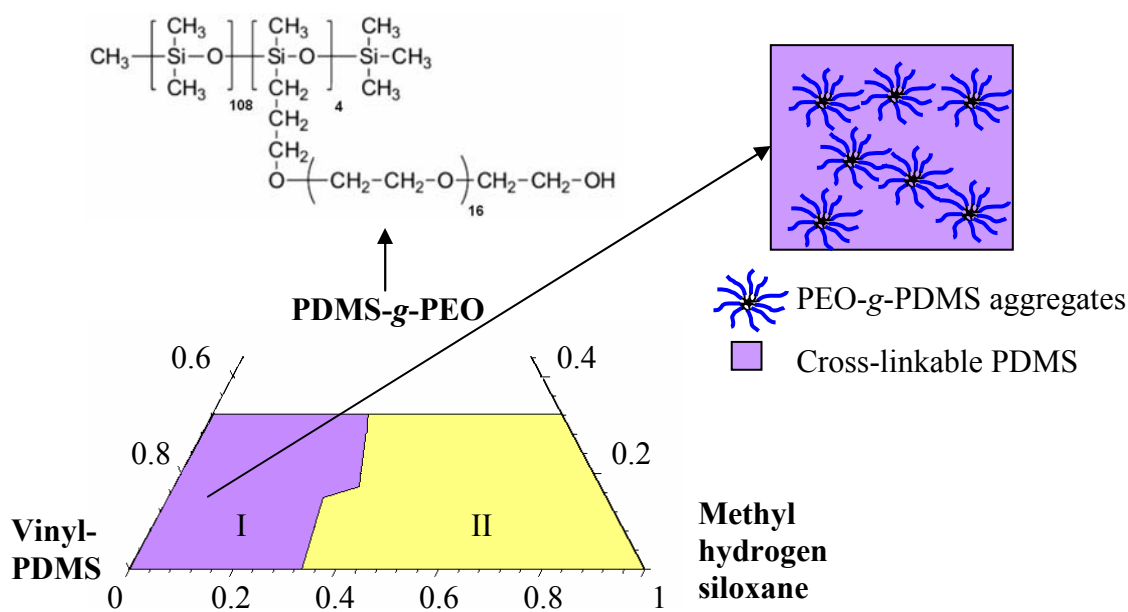


Figure 1: Partial ternary phase diagram of a Vinyl-PDMS/ PEO-g-PDMS/methyl hydrogen siloxane system at 50 °C. I: transparent isotropic single phase region; II: turbid multiphase region.

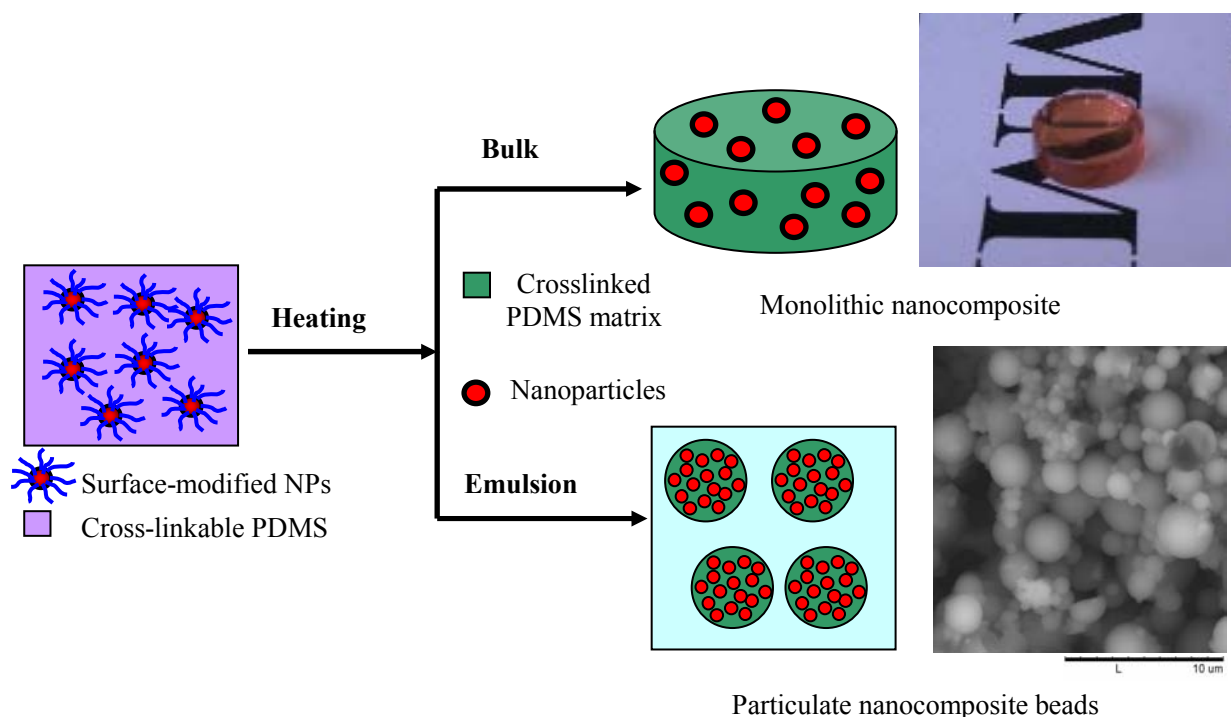


Figure 2: Schematic representation of the synthesis of nanocomposites in monolithic and particulate forms.

DEVELOPMENT OF BIOSENSORS BASED ON SINGLE WALL CARBON NANOTUBES AND APTAMERS

Saino Hanna Varghese, Y. Yoshida, T. Maekawa, D. Sakthikumar

*Bio Nano Electronics Research Center,
Graduate School of Interdisciplinary New Science, Toyo University,
350-8585, Kawagoe, Saitama, Japan
sainoshiju@gmail.com*

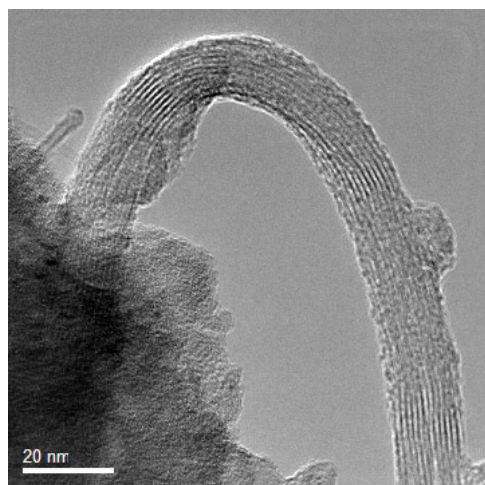
Single wall carbon nanotubes (SWCNTs) [1] based biosensors have received a great deal of attention due to their applications in disease diagnosis, environmental monitoring, food analysis etc. The development of an effective DNA-sensing system with the potential for genomic sequencing, mutation detection, and pathogen identification is extremely important. DNA immobilization on SWCNTs [2] can be considered as the fundamental methodology for the development of DNA biosensors. Covalent attachment of DNA primers to chemically functionalized SWCNTs has been used in the development of DNA biosensors [3]. In order to attach DNA molecules onto SWCNTs, we covalently functionalized SWCNTs with carboxylic acid groups [4] resulted in the “shortening” of SWCNTs (Figs. A&B). The products obtained were characterized by X-ray Photoelectron Spectroscopy (XPS) and Transmission Electron Microscopy (TEM). Single strands of DNA with a terminal primary amine group were covalently attached to these oxidized SWCNTs via an amide bond, after activating the carboxylic acid group on SWCNTs using two methods [5]. In the first method, carboxylic acid groups were activated using disuccinimide carbonate and in the second method the activation of carboxylic acid groups was achieved by 1-ethyl-(3-dimethyl amino-propyl) carbodiimide. XPS and TEM were used to characterize SWCNT samples for the presence of DNA. Thus, by chemically grafting single stranded DNA (ssDNA) on length-shortened SWCNTs resulted in the selective and sensitive detection of complementary DNA. The development of a bio carbon nanotube array in which SWCNTs were attached to an electrode through DNA could be used for the detection of complementary DNA which can be achieved by a methodology that involves the formation of an electric signal.

References:

- [1] Iijima, S, Ichihashi, T. Nature, **363** (1993) 603-605.
- [2] Wang, S. G et al. Biochem. Biophys. Res. Commun. **325** (2004), 1433-1437.
- [3] Baker, S. E et al. Nano Lett. **2** (2002), 1413-1417.
- [4] Liu, J. et al. Science, **280** (1998), 1253-1255.

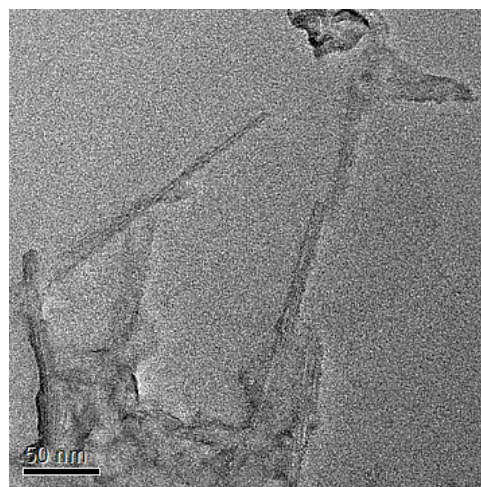
[5] Yang, W et al. Chemical Physics Letters, **443** (2007), 169-172.

Figures:



A

Fig A- TEM image of SWCNTs



B

Fig B- TEM image of isolated shortened SWCNTs

STUDY OF GELATION DURING THE FORMATION OF SOL-GEL FIBRES*Kelli Hanschmidt¹; Marko Part¹; Tanel Tättel¹; Uno Mäeorg²; Ants Lõhmus¹**¹Institute of Physics, University of Tartu, Riia 142, 51014, Tartu, Estonia,**²Institute of Organic and Bioorganic Chemistry, University of Tartu, Jakobi 2, 51014, Tartu, Estonia**kelli84@fi.tartu.ee*

Ceramic materials, including metal oxides, have wide range of outstanding properties like high hardness, refractive index, resistance for thermal shocks etc. Still, the promising real applications of the materials are often limited by their fragile nature and difficulties in preparing them in desired final shape structures. The origin of the problems is the fact that usually bulk ceramics decompose instead of melting at very high temperatures. Therefore melt molding is not suitable for shaping of metal oxides. The problems are classically overcome by using sintering of micro level compressed powders. Since early works in 1970`s, different sol-gel approaches have also become routine in many labs and industry in order to prepare ceramic materials [1].

Compared with powder ceramics sol-gel method has several advantages in preparation of low-dimensional materials. The main advantages like easiness to dope the materials by different additives (even viruses and DNA), structural homogeneity, low-cost is possible as preparation of these materials starts from fully homogeneous precursors. If the processes are carried out correctly then the homogeneity is not lost until reaching final dense materials. Real mastery of sol-gel technology is achieved if chemistry is combined with mechanical shape processing of the materials. Direct drawing of suitable sol-matters enables for example to prepare different shape nano and micro materials as nanofibres, microtubes and nanometer level sharp needles [2]. Tape casting enables to prepare micro stripes on flat surfaces [3]. Colloidal generation if applied at suitable conditions results in formation of oxide micro spheres.

However in our recent works we have introduced an alternative approach for alkoxide based sol-gel preparation: oligomeric concentrate route [4, 5]. It is based on utilizing solvent-free oligomeric concentrates of primary alkoxides such as Ti, Sn, Hf, Zr, Ce, etc. The materials that have viscous fresh honey-like nature are stable in dry atmosphere for a period longer than a year. Drawing of these materials enables to obtain optical quality nanocrystalline metal oxides in shape of microtubes, (micro)nanofibres and nanometrically sharp needles. Characteristic for these structures is their high uniformity. AFM measurements have proved that surface roughness of the fibres remains in 1-2 nm range. First test using some micron diameter fibres have proved that the structures are applicable as optical waveguides with possible sensor applications. Materials can be heat-treated for transforming to final dense ceramics.

Current presentation focuses on solidification kinetics of freshly formed sol-jet surfaces after pulling into humid air. Thickening of the shell-structure is directly measured and presented as a function of time in case of alkoxides of different metals. Evolution of elastic-plastic behavior of the core is monitored in-time by measuring the tensile strength of the structures. Calculations of the results show that shell thickening is limited by diffusion of water molecules that initiate polymerization reaction. Discrete transition of viscoelastic core into fragile shell proves that chemical reactivity is many orders of magnitude higher compared to diffusion of water in the core. Moreover, a method to reliquify the shell, giving therefore a possibility to joint the structures is introduced. Current project has great cognitive value as it enables to understand sol-gel processes more deeply, having also direct value for sol-gel synthesis of low dimensional structures.

This work was supported by the Estonian Science Foundation grant no 7612 and 6660 and by the Estonian Nanotechnology Competence Centre.

References:

- [1] Rosenblatt, G. M., Worrel, W. L., *An International Review Journal*, 18 (1988) 259-340.
- [2] Sakka, S., Yoko, T., *Journal of Non-Crystalline Solids*, 147&148 (1992) 394-403.
- [3] Kisand, V.; Shulga, J.; Tätte, T.; Visk, U.; Natali, M.; Mistura, G.; Paalo, M.; Lobjakas, M.; Kink, I., *Materials Science and Engineering B-Solid State Materials for Advanced Technology*, 137 (2007) 162 – 165.
- [4] Tatte, T., Jacobsen, V., Paalo, M., Branscheid, R., Kreiter, M., Maeorg, U., Saal, K., Lohmus, A., Kink, I, *NSTI Nanotech 2005*, 3 (May 8-12, 2005) 305-308.
- [5] Tatte, T., Talviste, R., Paalo, M., Vorobjov, A., Part, M., Kiisk, V., Saal, K., Lohmus, A., Kink, I., *NSTI Nanotech 2008*, 3 (June 1-5, 2008) 109-111.

Figures:

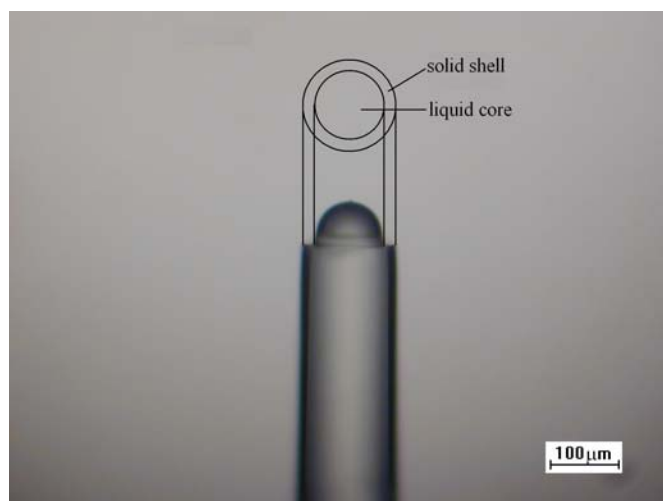


Image of core-shell sol-gel fiber structure
Sketch on the image illustrate structure of the fiber.

PERSISTENCE OF EDGE-STATE IN STACKED BILAYER NANOGRAFENE

Kikuo Harigaya

Nanotechnology Research Institute, AIST, Tsukuba 305-8568, Japan

k.harigaya@aist.go.jp

The graphite and single layer graphene materials have been studied intensively, since the electric field effect has been found in atomically thin graphene films [1]. These materials can be regarded as bulk systems. On the other hand, nanographenes with controlled edge structures have been predicted to have localized states along the zigzag edges [2]. The presence of the edge states have been observed by experiments of scanning tunneling spectroscopy [3,4]. Thus, the studies of the edge states are one of the interesting topic of the field.

Previously, the magnetic switching effect has been found in the process of insertion and extraction of molecules in activated carbon fibers [5]. The inserted molecules remain in nanometer size pores, and give effective pressure to the nanographite clusters. The Pauli susceptibility decreases due to the decrease of the magnetic moment magnitude. We have studied the magnetism of the nanographite using the tight binding model including the interlayer interaction between neighboring nanographene layers [6-8]. We have found that open shell nature of each layer might explain the experimental observations.

Recently, interlayer hopping interaction effects in stacked graphite have been investigated theoretically [9]. The electronic structures change dramatically including the massless Dirac cone and parabolic dispersions, depending on the layer numbers from a single graphene, bilayer graphene, to multi layers.

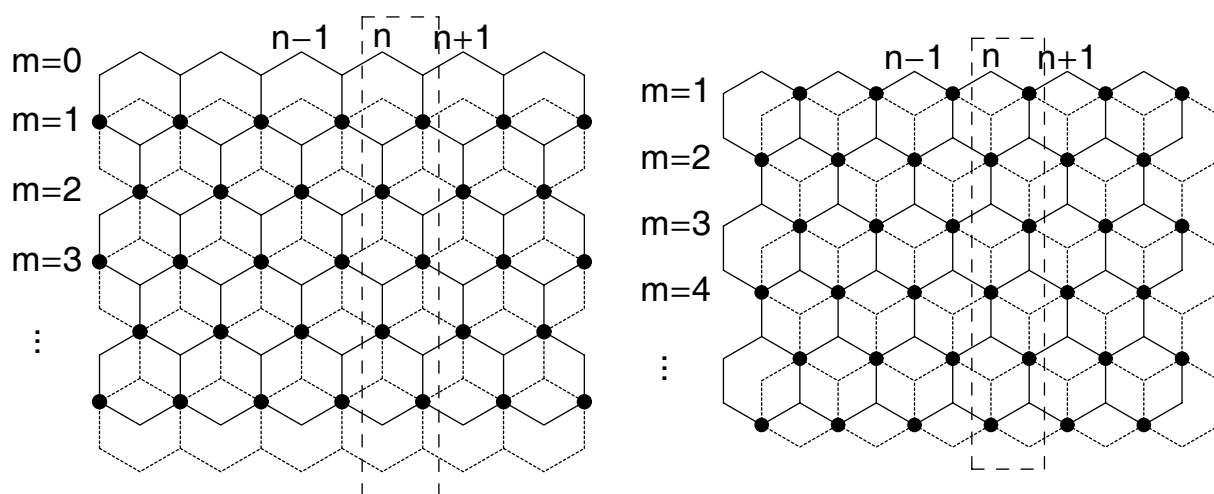
In this paper, we will study the edge-state in nanographene materials with zigzag edges including the inter-layer interactions, extending the work of a single layer [2]. We will prove that edge states exist at the energy of the Dirac point in the doubly stacked nanographene, and in the case of the infinitely-wide lower layer case. This property can be shown both for the A-B and A-C stackings. We also show that the correction by the interlayer interaction is of the order $r_1=t_1/t$ with respect to the intralayer term, where t_1 the interlayer hopping and t is the intralayer hopping. The recent report can be found, here [10].

References:

- [1] K. S. Novoselov, A. K. Geim, S. V. Morozov, D. Jiang, Y. Zhang, S. V. Dubonos, I. V. Grigorieva, and A. A. Firsov, *Science* **306**, 666 (2004).
- [2] M. Fujita, K. Wakabayashi, K. Nakada, and K. Kusakabe, *J. Phys. Soc. Jpn.* **65**, 1920 (1996).
- [3] Y. Kobayashi, K. Fukui, T. Enoki, and K. Kusakabe, *Phys. Rev. B* **73**, 125415 (2006).

- [4] Y. Niimi, T. Matsui, H. Kambara, K. Tagami, M. Tsukada, and H. Fukuyama, *Phys. Rev. B* **73**, 085421 (2006).
- [5] H. Sato, N. Kawatsu, T. Enoki, M. Endo, R. Kobori, S. Maruyama, and K. Kaneko, *Solid State Commun.* **125**, 641 (2003).
- [6] K. Harigaya, *J. Phys.: Condens. Matter* **13**, 1295 (2001).
- [7] K. Harigaya, *Chem. Phys. Lett.* **340**, 123 (2001).
- [8] K. Harigaya and T. Enoki, *Chem. Phys. Lett.* **351**, 128 (2002).
- [9] M. Koshino and T. Ando, *Phys. Rev. B* **73**, 245403 (2006).
- [10] K. Harigaya, arXiv:0904.4371 (2009).

Figures:



Bilayer graphene with parallel zigzag lines. The A-B stacking (left) and the A-C stacking (right) are shown. There are the zigzag edges at the top of the honeycomb lattice, and the system extends infinitely in the other directions. The upper layer is shown by the solid lines, and the lower layer (dotted line) is shift downward by the bond length. The number n ravel the n -th unit cell shown by the dashed line. The other label m indicates each zigzag line. At the circles, two carbon atoms overlap completely, and weak hopping interaction t_1 is assigned here.

Improvement of TFT properties by hydrogen defect passivation for high performance flexible electronics device application

Musarrat Hasan¹, Houk Jang², Sang-Hee Ko Park¹, Joon-Myong Lee³, Min-seok Jo³, Jae-Bon Koo¹,
Kyong-Ae Lee², Hyunsang Hwang³, Jong-Hyun Ahn², Yong Hae Kim¹, Seung Youl Kang¹

¹Electronics and Telecommunication Research Institute, Convergence Components & Materials Research Laboratory, Daejeon; ²Sung Kyun Kwan University, Suwon 440-746;

³Gwangju Institute of Science and Technology, Gwangju 500-712; Republic of Korea.
musarrat@etri.re.kr

Introduction: Electronic devices on flexible organic substrate have a huge market in the near future in the form of flexible display, RF ID tags, solar cells and various bio-systems.[1] But due to the limitation imposed by sustainable temperature it is a challenge to grow quality dielectric for transistor application for high mobility device. The dielectrics grown at low temperature (<200°C) contains lots of defect sites. To improve the device properties, successful defect passivation is absolute necessity. Hydrogen (H₂) has been known for years to passivate the defect sites far more effectively, especially near the interface region.[2,3] In this work we have investigated impact of H₂ annealing on the device performance of single-crystal Silicon active layer device on flexible substrate.

Experimental: The fabrication steps started with the doping process of phosphorous spin-on dopant at 950°C on SOI wafer. The underneath SiO₂ layer was etched out by HF solution (49%) and Si ribbons were detached. After that the Si layer of 290 nm was transferred to the polyimide (PI) plastic substrate via PDMS stamping process described in many other recent publications.[4] After the transfer process, Alumina (Al₂O₃=110nm) was deposited in an ALD system at 150°C. Chromium (Cr) and gold (Au), 5 nm and 100 nm respectively, were deposited to complete the TFT fabrication process (fig. 1). To improve the contact between the metal and S-D, a forming gas annealing process (FGA; H₂=3 wt%, rest N₂) was performed at 200°C and 1 atm pressure. To improve the oxide interface quality subsequent high pressure pure hydrogen annealing (HPHA) was performed for the same sample at 20 atm pressure where pure H₂ was used.

Results and discussions: Fig. 2 shows the transfer characteristics of the as deposited Al₂O₃ device at V_d of 0.1 volt. The threshold voltage (V_{th}) was calculated from the x-axis intersection of the square root of the transfer curve. Fig. 3 shows the I_d-V_g result at different gate voltage, but the output current is mere few microamperes. The sample was then annealed at 200°C in 1 atm pressure in FGA containing 3% H₂ and 97% N₂. The current increased over 100 times, giving an on/off ratio of >10⁵ (fig. 4). The mobility improved to 140 cm²/V.s. Hydrogen passivate the defects present at the metal-dielectric interface during metal deposition. This is known as the “Sintering” step in the silicon industry for long time.[5] The oxide defects present at the Si/oxide interface and also the bulk defects are also important and can be effectively passivated by H₂.

To passivate the defects more aggressively, H₂ annealing was done at pressure as high as 20 atm (HPHA) at 200°C of the same sample in pure H₂ atmosphere. A specially built chamber was used for this kind of experiment. Fig. 4 compared the HPHA data with that of as deposited and FGA data. Compared to the FGA sample further improvement especially in the off current has been observed. This indicates better passivation of the oxide defects by more injection of H₂ at a very aggressive manner. Fig. 5 shows transconductance curve (g_m) of devices after each step. Significant improvement of g_m is achieved after FGA and consequent HPHA step. Fig. 6 shows the output characteristics after FGA and subsequent HPHA treatment. All the properties are summarized and compared in table 1. The on/off ratio, g_m, mobility, subthreshold slope, all shows tremendous improvements after annealing in hydrogen atmosphere. These results are encouraging for low-temperature plastic TFT technology for flexible device application with mobility close to 200 cm²/V.s.

Next the interface charge density has been measured using the charge pumping (CP) method. Along with CP, the V_{th} shift was also monitored under constant voltage stress. The applied voltage stress was +10 V. The voltage sweep was performed from -10 V to +10 V with V_d 0.1 V. For the CP method a voltage pulse was applied from base voltage of -7 V to top voltage of -4.5 V. The falling and rising time was fixed to 100 ns. The pulse width was 1 μs. The stress was applied for 1000 s and both I_d-V_g and CP current was measured at different interval. With applied stress, the V_{th} shift in the positive direction and the total shift after certain stress time are depicted in Fig. 7 against time. Fig. 8 shows the interface charge density (N_{it}) after each stress cycle. A low N_{it} values in the range of 2x10¹¹ cm⁻² has been found. The N_{it} after each stress also does not change, which indicates the voltage shifts that is observed is not related to the interface charge traps. The hydrogen annealing effectively passivated the interface traps and the mobility improvement primarily is due to the interface charge passivation. The V_{th} shift may be mainly due to the traps in the bulk oxide region.

Conclusion: High mobility single crystal Silicon TFT with medium-k dielectric has been fabricated. The device performance was improved after H₂ passivation annealing. The maximum process temperature was 200°C suitable for flexible device applications. The understanding and improvement of higher-k device gate insulator by post metal annealing for flexible device technology performed in this study is promising for future.

References:

[1] R. H. Reuss, et. al.; Proceedings of the IEEE, v. 93, p. 1239 (2005) [3] P.J. Chen, et. al.; Jour. Appl. Phys. Vol. 86, p. 2237 (1999)
 [2] A. Kamgar, et.al.; IEEE Elec. Dev. Let. Vol. 24, p. 448 (2003) [4] D.-H. Kim, et. al.; IEEE Elec. Dev. Lett., Vol. 29, p. 73 (2008)
 [5] K. Onishi, et. al.; IEEE Trans. Elec. Dev., Vol. 50, p. 384 (2003)

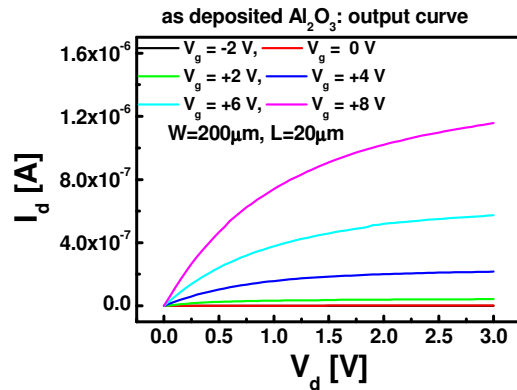
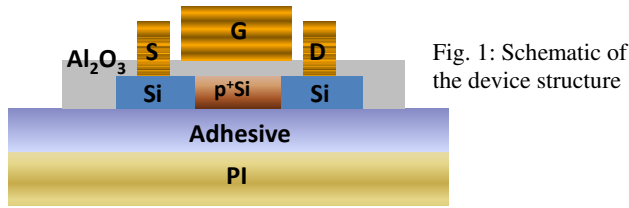


Fig. 3: I_d - V_d characteristics of the as-deposited Al_2O_3 device

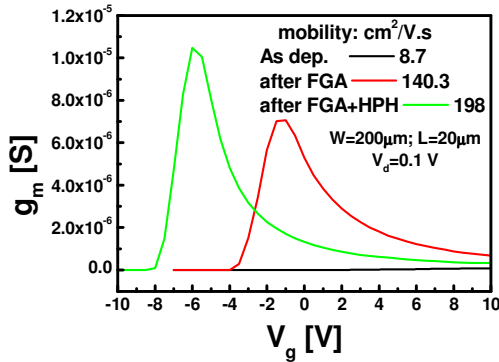


Fig. 5: Comparison of the g_m characteristics of the device data shown in fig. 4.

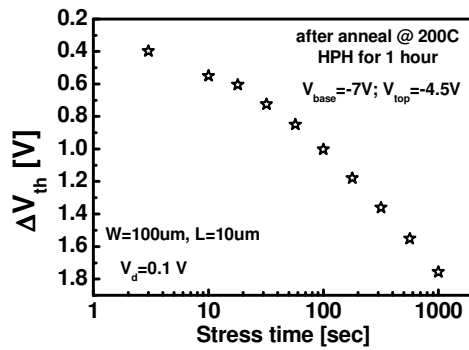


Fig. 7: Total V_{th} shift after HPHA measured at different time interval

Table 1	As dep.	FGA	HPHA
On/Off ratio	$>10^3$	$>10^6$	$>10^8$
$G_{m,max}$ (S)	8.2×10^{-8}	7.05×10^{-6}	1.2×10^{-5}
Mobility ($cm^2/V.s$)	8.7	140	198
SS (V/dec)	3.22	0.36	0.28
V_{th} (Volt)	0.2	-3	-7.3
Hysteresis (Volts)	8	7.5	3.1

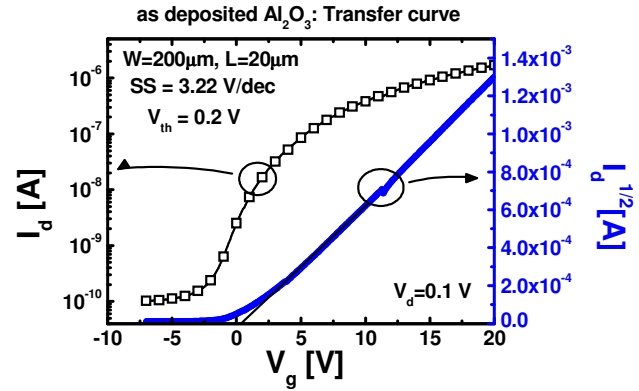


Fig. 2: I_d - V_g characteristics of the as-deposited Al_2O_3 device

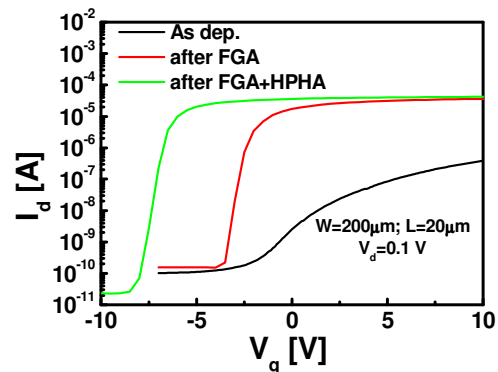


Fig. 4: Comparison of the I_d - V_d characteristics of the as-deposited and after different annealing steps.

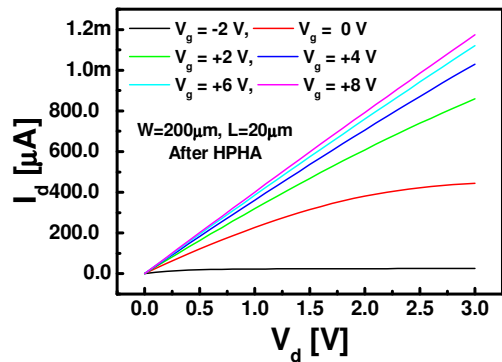


Fig. 6: Output curve after HPHA at 200°C

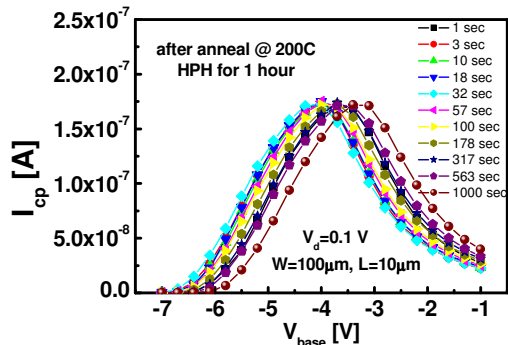


Fig. 8: Interface trap density measured in CP method does not change with stress implying V_{th} shift is not due to interface traps.

A molecular dynamics study on fullerene-implanted carbon nanotori as electromagnetic sensing and emitting devices

Authors: Michael Griebel, Frederik Heber

Affiliations: Institute for Numerical Simulation, Wegelerstrasse 6,
53115 Bonn, Germany, heber@ins.uni-bonn.de

Abstract

Open-ended carbon nanotubes have been found to form toroidal structures [1]. These specific structures bear striking resemblance to electrographic coils. Two modes of action can be thought of: Either the metallic conductivity of certain chiralities of the nanotorus configuration is exploited directly or fullerenes may be implanted into the torus' inner region [4]. Alone these fullerenes are charge-neutral, but they may easily be inoculated with metals carrying additional charges. Henceforth, currents would not act upon the electrons in the nanotorus' surface but also on the fullerene's surplus charges. This interplay may lead to very interesting applications. We have investigated the mechanical stability of these toroidal systems by molecular dynamics simulation [3], employing a potential by [2], well-suited for carbon. This research has significant importance on the frequency and quality for applications employing nanotori as tunable circuits. We report on the current status of our findings.

- [1] Liu, J. and Dai, H. and Hafner, J. H. and Colbert, D. T. and Smalley, R. E. and Tans, S. J. and Dekker, C.. Fullerene 'crop circles' *Nature*, 385:780–781, 1997.
- [2] Brenner, D. W.. Empirical potential for hydrocarbons for use in simulating the chemical vapor deposition of diamond films *Physical Review B*, 42:9458–9471, 1990.
- [3] M. Griebel and J. Hamaekers. Molecular Dynamics Simulations of the Mechanical Properties of Polyethylene-Carbon Nanotube Composites *Handbook of Theoretical and Computational Nanotechnology*, 8:409–454, American Scientific Publishers 2006.
- [4] T. A. Hilder and J. M. Hill. Orbiting atoms and C_{60} fullerenes inside carbon nanotori *Journal of Applied Physics*, 101:064319, 2007.

Materials for Energy

Dr. Regine Hedderich

*Forschungszentrum Karlsruhe, Netzwerk NanoMat, 76344 Eggenstein-Leopoldshafen,
Germany*

regine.hedderich@int.fzk.de / www.nanomat.de

The poster will cover current topics and recent progress in Germany in the science and technology of energy and new materials, including the nanoscale origin of macroscopic properties.

One challenge is avoiding negative effects from the current energy system on climate, environment and health and to find ways to replace fossil fuel supply.

New materials can contribute to a positive development in this direction in several ways, for instance by influencing the energy efficiency of industrial production and of household energy use (e.g., through fuel cells, catalysis, reduced friction losses), and by offering schemes to clean up harmful emissions resulting from various energy systems by contributing to more efficient harvesting of sun light, by providing thermoelectric materials to harvest energy from temperature gradients, by providing energy storage technology e.g. in batteries and for hydrogen storage, by enabling light-weight materials for transportation. Materials are central to every energy technology; the future will place increasing demands on materials performance with respect to extremes in stress, strain, temperature, pressure, chemical reactivity, photon or radiation flux, and electric or magnetic fields.

Quantitative Composition of a SWCNT-sample:

Raman Scattering vs. Photoluminescence

Sebastian Heeg, Cinzia Casiraghi, Stephanie Reich
Freie Universität Berlin, Arnimalle 14, 14195 Berlin, Germany
Sebastian.heeg@physik.fu-berlin.de

The different growth processes of Carbon Nanotubes (CNTs) yield samples containing tubes with a large variety of different chiralities. The qualitative composition of the CNTs product has been revealed by optical spectroscopy techniques such as Raman scattering [1] and Photoluminescence Excitation (PLE) measurements [2]. The quantitative composition, however, remains a task in CNT characterization.

We address this problem by comparing the relative PLE intensities of two families of single walled carbon nanotubes with the relative intensities of the corresponding Radial Breathing Modes measured by Raman scattering. The PLE measurements were performed by dissolving the HiPCO grown nanotubes in aqueous solution using sodium dodecylbenzene sulfonate as surfactant. Raman spectroscopy was performed by depositing the tubes from the solution on a silicon substrate by spin-coating. The presence of the CNTs was confirmed by atomic force microscopy.

We show that the two methods yield significantly different ratios [3]. We propose a simple model to obtain the relative abundance of the CNT species investigated. The Raman intensities are scaled with respect to the resonance conditions of Raman scattering on carbon nanotubes [1]. Further, we include excitonic transition probabilities [4] and electron-phonon coupling matrix elements [5]. By applying this model, we show that both the methods agree on one CNT species dominating the subset investigated.

In addition we analyse the effect of spectrometers, which use non-coherent light sources such as a *HgXe* lamp, on the PL and PLE intensities. We show that it is important to take into account both PL and PLE intensities [3] - rather than PL intensities only - in the interpretation of photoluminescence data of CNT.

References

- [1] J. Maultsch *et al.*, Phys. Rev B, **72** (2005) 205438
- [2] S. M. Bachilo *et al.*, Science, **298** (2002) 2361
- [3] S. Heeg *et al.*, PSS(b), 2009, submitted for publication
- [4] E. Malić *et al.*, PSS (RRL), **1** (2009)
- [5] J. Jiang *et al.*, Phys. Rev B, **72** (2005) 235408

Agarose optical fiber humidity sensor based on surface plasmon resonance in the infra-red region

M. Hernández, C. R. Zamarreño, I. R. Matías, F. J. Arregui

Sensor Research Laboratory, Electrical and Electronic Engineering Department, Public University of Navarra (UPNA), Campus de Arrosadía, Pamplona, SPAIN.

miguel.hernaez@unavarra.es

Here, it is presented a novel optical fiber humidity sensor based on surface plasmon resonance (SPR) spectroscopy in the infra-red region. Most of SPR optical fiber sensors proposed in previous works have been based in the utilization of noble metals, e.g. gold or silver, to create the SPR supporting layer [1-2], which limited the detection range to the visible spectrum. In this work, a 200 μm optical fiber is coated with an indium tin oxide (ITO) layer in order to achieve SPR recognition in the infra-red region [3]. Then, ITO-coated fibers are used as substrates to deposit a hydrogel (agarose) whose thickness and refractive index variations are related to the external relative humidity (RH) changes [4]. These refractive index variations shift the SPR maximum absorption peak to higher wavelengths when RH rises and to lower wavelengths when RH falls.

The sensors fabrication involves the deposition of two different layers. Firstly, 200 μm optical fiber claddings and jackets were removed and an ITO coating was deposited over the optical fiber core using a sol-gel dip-coating method, as described by Ota et al. [5]. Then, the ITO-coated fibers were perpendicularly cleaved to obtain 7 cm pieces. Both sides of these fragments were spliced to 200 μm optical fiber pigtailed. Finally, an agarose layer was created over the SPR supporting device using the boiling water bath method proposed by Arregui et al [4]. In Figure 1 are shown the different materials used in this work, all of them supplied by Sigma Aldrich.

The fabricated sensors were examined using the experimental setup shown in Figure 2, where the sensor structure is also schematically represented. In order to characterize the sensor to RH variations in the range from 20 to 80% it was placed into a climatic chamber (Angelantoni Inc.) meanwhile a spectrometer connected to a PC collected the spectra obtained at the end of the fiber. The absorbance spectra and maximum absorption wavelength (line) are represented in Figure 3, showing the variations with the RH. These variations are also represented in Figure 4, where the maxima absorption wavelength variation and the real RH obtained from the climatic chamber electronic sensor can be directly compared. In figure 4, it is observed the correspondence between the variations in RH and the SPR wavelength with a fast response of the sensor to small variations in RH. The sensor shows a dynamic range of 45 nm in this RH range.

References:

- [1] D. Monzón-Hernández, J. Villatoro, D. Talavera, D. Luna-Moreno, *Applied Optics*, **46**(3) (2004) 1216-1220
- [2] R. Slavík, J. Homola, J. Ctyroky, Eduard Brynda, *Sens. & Actuators B*, **74** (2001) 106-111.
- [3] M Y. Xu et al, QELS Conference, San Jose California 4 May (2008)
- [4] F. J. Arregui, Z. Ciaurriz, M. Oneca, I. R. Matías, *Sens. & Actuators B*, **96** (2003), 165-172.
- [5] R. Ota et al., *Thin Solid Films*, **411** (2002) 42-45.

Figures:

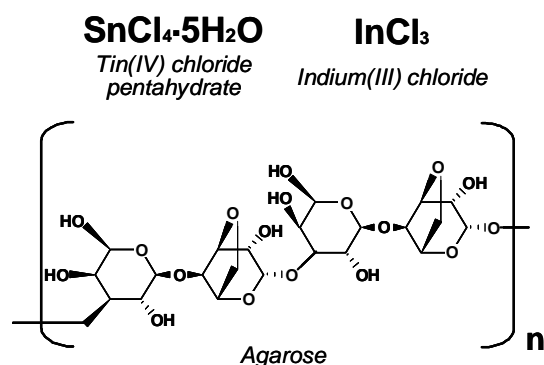


Figure 1. Molecules involved in the sensor fabrication process.

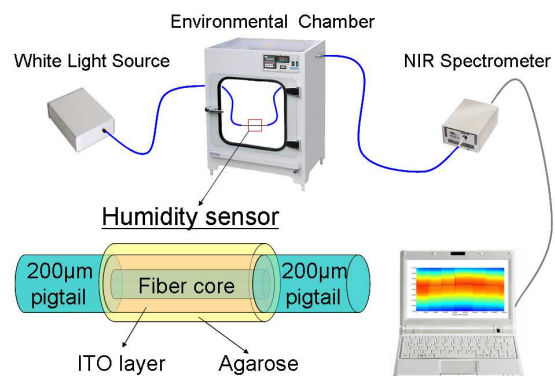


Figure 2. Experimental setup

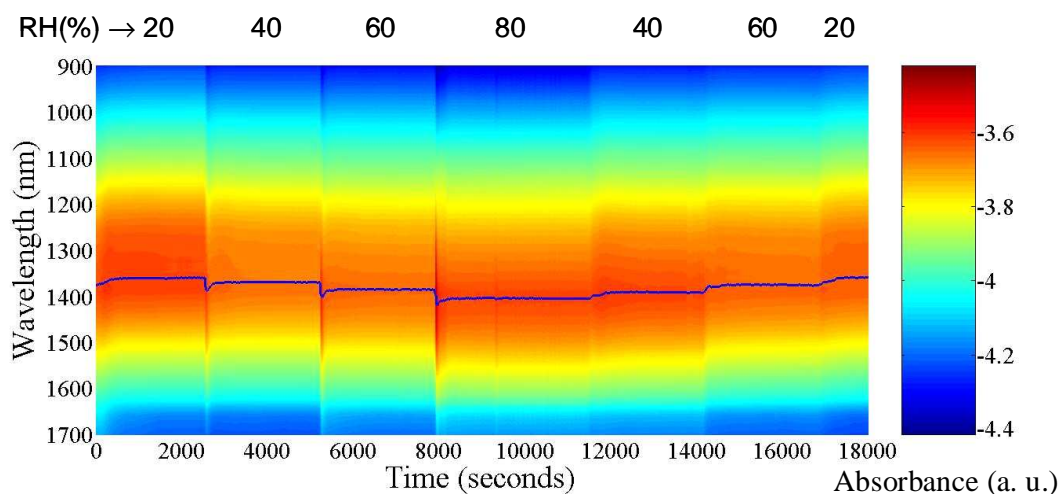


Figure 3. Spectral response and maxima absorption wavelength variations (line) at different RH values.

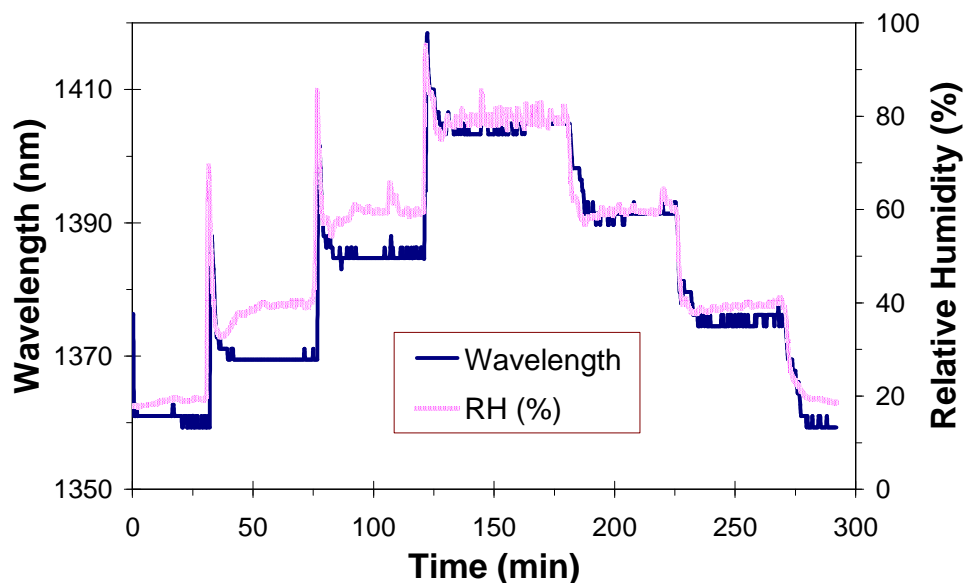


Figure 4. Wavelength variation at maximum absorbance when the sensor is subjected to RH changes.

Field induced phase transition and formation of microdomains from polar nanoregions in lead free ferroelectrics

Manuel Hinterstein¹, Michael Knapp², Jens Kling¹, Ljubomira Ana Schmitt¹, Markus Hölzel¹, Wook Jo¹, Jürgen Rödel¹, Hans-Joachim Kleebe¹, Hartmut Fuess¹

¹Institute for Material Science, University of Technology Darmstadt, Petersenstr. 23, 64287 Darmstadt, Germany

²ALBA Light Source, Carretera BP 1413, Km 3.3, 08290 Cerdanyola/Barcelona, Spain
manuel.hinterstein@desy.de

Lead containing oxides with perovskite structure are widely used as sensors and actuators. Among those materials lead titanate zirconate $\text{PbZr}_{1-x}\text{Ti}_x\text{O}_3$ (PZT) and lead magnesium niobate-lead titanate, PMN-PT are the most prominent ones. The possible environmental hazard connected with lead has driven research of novel materials with comparable electrical and mechanical properties as PZT. For the dielectric properties of such materials the microstructure plays a crucial role. In PZT the domain structure diminishes to the scale of several nanometres in the vicinity of the morphotropic phase boundary, where the dielectric properties have a maximum [1].

Lead-free piezoelectric ceramics $(1-x-y)\text{Bi}_{0.5}\text{Na}_{0.5}\text{TiO}_3-x\text{BaTiO}_3-y\text{K}_{0.5}\text{Na}_{0.5}\text{NbO}_3$ ($0.05 \leq x \leq 0.07$ and $0.01 \leq y \leq 0.03$) (BNT-BT-KNN) have been synthesized by the mixed oxide route and sintering. Preliminary electromechanical characterization revealed a remarkable strain of approximately 0.4 % at an electric field of 8 kV/mm close to the boundary between two compositions with dominant ferroelectric and antiferroelectric properties [2, 3, 4].

In the unpoled state BNT-BT-KNN exhibits a pseudocubic symmetry in high resolution X-ray diffraction, performed at the MS synchrotron beamline at the SLS (Switzerland). However, high resolution neutron diffraction at the SPODI neutron diffractometer at the FRM II (Germany) showed superstructure reflections, which were indexed based on the tetragonal space group $P4bm$ [5] and the rhombohedral one $R3c$ [6]. No prominent domain structure as commonly seen in PZT polycrystals ceramics was observed in transmission electron microscopy (TEM) experiments. In contrast, electron diffraction revealed weak superlattice reflections in prominent zone axes. Temperature dependent Raman spectroscopy indicated a relaxor like behaviour, indicated by noncubic symmetry stable at the local scale and far above the Curie temperature. Therefore, in unpoled samples it can be deduced that ferroelectric distortions are present in polar nanoregions.

By applying an electric field *in situ* with synchrotron and neutron powder diffraction the former pseudocubic diffraction patterns show pronounced splitting of reflections and nanoscale domain structures become visible in TEM.

[1]K.A. Schoenau, L.A. Schmitt, M. Knapp, C. Baetz, H. Fuess, S. Wagner, T. Fett, M.J. Hoffmann, Phys. Rev. B, **75** (2007) 184117.

[2]S.-T. Zhang, A. B. Kounga, E. Aulbach, H. Ehrenberg, J. Rödel, Appl. Phys. Lett., **91** (2007) 112906.

[3]S.-T. Zhang, A. B. Kounga, E. Aulbach, T. Granzow, Wook Jo, H.-J. Kleebe, J. Rödel, J. Appl. Phys., **103** (2008) 034107.

[4]S.-T. Zhang, A. B. Kounga, E. Aulbach, Wook Jo, T. Granzow, H. Ehrenberg, J. Rödel, J. Appl. Phys., **103** (2008) 034108.

[5]G.O. Jones, P.A. Thomas, Acta Cryst. B, **56** (2000) 426.

[6]G.O. Jones, P.A. Thomas, Acta Cryst. B, **58** (2002) 168.

**FABRICATION AND CHARACTERIZATION OF HIGH PERFORMANCE CERAMIC
MEMBRANE HAVING NANOMETRIC PORES**

Ali A Hosseini*, A Sadigzadeh, R Soltani, and S Mohammadi

Mazandaran University (Iran)

In this study, CNTs were grown directly in the pores of microporous Pyrex membranes and ceramic membranes with very fine pores and high porosity were achieved. The experiment was done in two stages. Initially cobalt powder was homogeneously mixed with Pyrex powder in different percent. In order to produce row membranes, each of these mixtures were compacted in the form of tablet by use of an uniaxial press and a stainless steel mould and then the tablets were sintered in an electric furnace. In second stage thermal chemical vapor deposition (TCVD) method was used to grown nanotubes within pores of the membranes. Argon and ammonia were used as carrier gas and reaction control and acetylene was used as the carbon feedstock. Morphology of the membranes before and after CVD process was studied by scanning electron microscopy. With our developed method, the Pores size are decreased but total porosity of membrane is not change considerably after growth of nanotubes. In this way a strong membrane with high porosity and fine pores is produced.

INVESTIGATION OF PHYSICAL AND MECHANICAL PROPERTIES OF AL NANOCOMPOSITE REINFORCED WITH CNTs

Ali.A. Hosseini¹, F. Ghaharpour¹, H. Rajaei¹, M. Abbasi¹

Hos-a-pl@umz.ac.ir

^a Physics Department, Faculty of Sciences, Mazandaran University, Babalsar, Iran, P.O.Box:47416-95447

^b Metallurgy and Material Engineering Department, Iran University of Science and Technology, Tehran, Iran

Abstract: In this paper the physical and mechanical properties of Al nanocomposite reinforced with CNTs were investigated. Al powders with high purity and Carbon Nanotubes (CNTs) with different percentage were mixed by ball milling method and the composite was fabricated by cold pressing followed by sintering technique. The variation of density and hardness of composite with CNT content were investigated. The microstructure of composite was evaluated by SEM (Scanning Electron Microscope) and XRD (X-Ray Diffraction). The results show that the density and hardness increase with CNT percentage.

Keywords: Carbon Nanotube, Nanocomposite, Cold Pressing, Sintering.

**EFFECT OF REACTION TEMPERATURE ON THE PRODUCTION OF
CARBON NANOTUBES ON A SILICON DIOXIDE WAFER**

Muataz Ali Atieh

Department of Chemical Engineering,
Centre of Research Excellent in Nanotechnology
King Fahd University of Petroleum and Minerals
P.O. Box 5050, Dhahran-31261, Saudi Arabia
motazali@kfupm.edu.sa

Floating catalyst chemical vapor deposition (FC-CVD) method has been to synthesize carbon nanotubes (CNTs) on silicon dioxide substrate at different reaction temperature. The effect of the reaction temperature on the purity and the yield of carbon nanotubes were studied. Increasing the temperature has a remarkable effect on the size and shape of the catalyst and this in turn affected the diameter distribution and structure of the carbon materials. The carbon nanotubes were produced from 600 °C to 900 °C with maximum yield at 900 °C.

Keyword: CNTs, FC-CVD, Reaction Temperature.

Enhancement of electrochromic durability of polyaniline using the inorganic-organic hybrid nanostructure in form of nanoparticles

HeungYeol Lee, Taejin Hwang, Hohyeong Kim, GyunTak Kim
Surface Technology and Heat Treatment R&D Division

Korea Institute of Industrial Technology (KITECH), 7-47 Songdo-Dong, Yeonsu-Gu, Incheon
406-840, Korea

Contact@E-mail

Enhancing the operation life time or the electrochemical durability is one of the key issues in the electrochromic material studies. Recently, the flexible display devices are drawing much attention since they can facilitate new technological demands such as bending and folding of paper-like displays. For these applications high electrochromic efficiency, short response time, long operating life time are the most important requisites of the material [1,2]. Recently conducting polymers are considered as more competitive material than the inorganic transition metal oxides for the display applications because of their faster response and longer operating life time the operating. However, life time of electrochromic conducting polymers is still limited to 10^6 cycles while more than 10^8 cycles are preferably required for an acceptable display material.

As it is generally accepted, the inorganic-organic hybrid structure is one of the effective ways to enhance the chemical stability of the material [3,4]. In this study, an electrochromic film made of silica-polyaniline core-shell nanoparticles was prepared on an Indium Tin Oxide (ITO)-coated glass substrate and the operation life time of the film was investigated.

Through a chemical polymerization of polyaniline in a colloidal solution of silica, nanoparticles of silica-polyaniline were obtained. In the core-shell structure the inorganic silica was incorporated to enhance the chemical durability of the organic moiety, polyaniline (Fig. 1). The synthesized particles were then dispersed into ethanol and were deposited onto glass substrate in the form of thin film. For a better adhesion to the substrate, small amount of tetraethoxysilane (TEOS) and HCl aqueous solution was added to the dispersion solution, and the prepared film showed strong adhesion to the ITO-coated glass substrate (Fig. 2).

The electrochromic characterization on the prepared films was performed using the cyclic voltammetry and the optical response to the electrical potential change, and it showed an enhanced electrochromic operation life time (Fig. 3,4).

The material characterization results showed that the life time enhancement is possibly due to the enhanced chemical stability of the inorganic-organic core-shell hybrid nanoparticles. The developed hybrid material could readily be applied to the production of variable reflectance room-mirrors for automobiles.

References:

- [1] M. Mastragostino, Electrochromic devices, in Applications of Electroactive Polymers, B. Scrosati, Editor. Chapman & Hall: London (1993) 223-249.
- [2] P.R. Somani and S. Radhakrishnan, Materials Chemistry and Physics **77** (2002) 117-133.
- [3] L. Hou, H.K. Schmidt, B. Hoffmann, and M. Mennig, Journal of Sol-Gel Science and Technology **8** (1997) 927-929.
- [4] H.K. Schmidt, Journal of Sol-Gel Science and Technology **1** (1994) 217-231.

Figures:

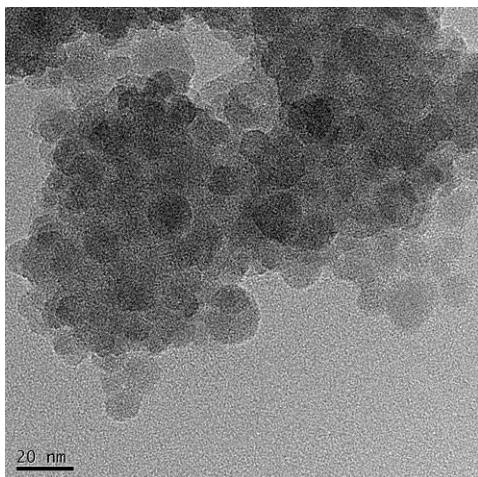


Fig. 1 Silica-polyaniline core-shell nanoparticles.

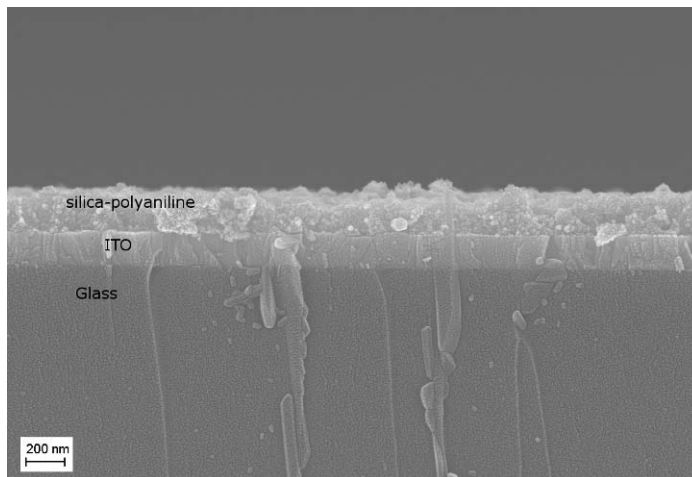


Fig. 2 Prepared composite film on the ITO-coated glass substrate.

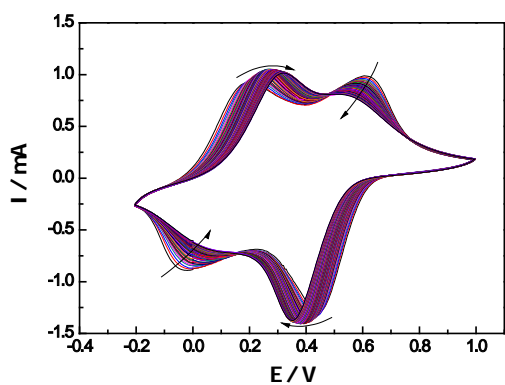


Fig. 3 Cyclovoltammogram of the prepared composite electrochromic film.

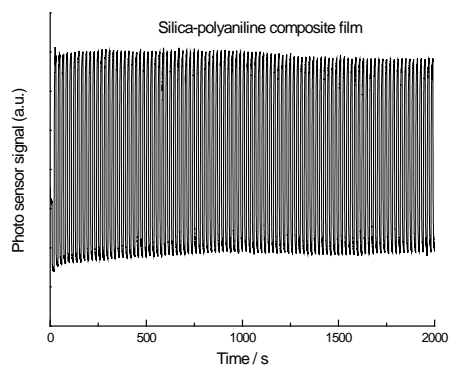


Fig. 4 The optical switching curves between colored and bleached state for the prepared composite film.

**PREPARATION AND CHARACTERIZATION OF LAYERED DOUBLE
HYDROXIDES THROUGHOUT DETERMINATION OF SIZE CONTROLLABLE
SYNTHETIC PARAMETERS**

Sanghee Kim, Sung-Ho Hwang, Sang Kyoo Lim, Soo-Keun Lee

*Advanced Nano-Materials Research Team, Division of Nano & Bio Technology, Daegu
Gyeongbuk Institute of Science & Technology, 5th Floor, Daegu Technopark Venture 2 Plant,
75 Gongdanbuk2gil, Dalseo-gu, 704-230, Daegu, Republic of Korea*

hsungho@dgist.ac.kr

Layered double hydroxide(LDH) compounds have attracted a great attention because of their layered structure and high anion exchange capacity, which can make various technical applications. LDHs are the only known inorganic materials with positive layer charge, in which the interlayer anions can be replaced by ion-exchange processes. Their structural units are made from stacks of positively charged octahedral sheets. The net positive charge, which is due to substitution of divalent ions with trivalent ones in the brucite-like metal hydroxide $M(OH)_2$, is balanced by an equal negative charge from the interlayer anion. The structure is also stabilized by hydrogen bonds among interlayer water molecules, anions and the hydroxyl slabs as well as by electrostatic interactions between the layer and the anions. Owing to their high anion exchange capacity, high surface area, physical strength and layered structure, LDHs have many potential applications, including pharmaceuticals, adsorbents, catalysts, catalyst supports, etc.. In recent, much attention have also been paid for the fabrication of organic-inorganic composites containing LDHs as eco-friendly materials due to their heat resistant and flame retardant properties. Especially, it is very important to how to control its particle size, which plays a critical role in such industrial applications. In this work, the synthetic parameters affecting the particle size have been investigated on the basis of crystal growth mechanism. Based on crystal growth mechanism, the total metal ion concentration, which may influence the nucleation rate, can be considered as one of the size controlling parameters. In addition, since aging time and reaction temperature could influence the crystal growth kinetically or thermodynamically, we have also considered them as the parameter to control the particle size. And two bases such as NaOH and urea were selected to determine the effects of precipitation rate on particle size, because urea shows slow hydrolysis resulting in slow precipitation. On the other hand, NaOH gives fast precipitation. Two different synthetic methods such as hydrothermal treatment and urea hydrolysis were chosen to compare the difference of basicity between strong and weak bases. In addition, we would intend to apply this technology, in more industrial point of view, to the fabrication process of the organic-inorganic composites. The nano-sized LDHs were dispersed in polyethyleneterephthalate(PET) resin, which formed master batch by using compounding technique in order to produce organic-inorganic hybrid film or fiber.

The layered double hydroxide particles of $Mg_2Al(OH)_6(CO_3)_{1/2} \cdot 0.1H_2O$ have been prepared by two different methods: (1) direct coprecipitation of aqueous solution of $Mg(NO_3)_2 \cdot 6H_2O$, $Al(NO_3)_3 \cdot 9H_2O$ upon hydrolysis of urea, and (2) hydrothermal aging of the same nitrate solution after NaOH titration. In order to control the particle size and morphology of LDH, various parameters such as metal ion concentration, aging time, reaction temperature are systematically studied. According to the powder X-ray diffraction, all the samples turn out to be well crystallized with an average basal spacing of 7.6 Å corresponding to the LDH crystal. From the SEM images, the coprecipitates are found to be hexagonal in shape and are controlled in the particle size range of 0.9–2.2 and 1.2–4.5 μm depending on aging time (6–69 h) and metal ion concentration (0.87–0.065 M), respectively. However, the particle size of the hydrothermally prepared samples increase in proportion to aging time (12–72 h ; 85–120 nm) and reaction temperature (100–180 °C; 115–340 nm). The effect of such parameters upon the particle size was rationalized on the basis of crystal growth mechanism.

References:

- [1] F. Cavani, F. Trifiro, A. Vaccari, *Catal. Today*, 11, 173 (1991)
- [2] C. O. Oriakhi, I.V. Farr, M.M. Lerner, *J. Mater. Chem.*, 6, 103 (1996)
- [3] J.H. Choy, S.Y. Kwak, Y. J. Jeong, J. S. Park, *Angew Chem. Int. Ed.* 39, 4041 (2000)
- [4] F. Leroux, J.-P. Besse, *Chem. Mater.* 13, 3507 (2001)
- [5] N.S. Puttasway, P. Vishnu Kamath, *J. Mater. Chem.* 7, 1941 (1997)

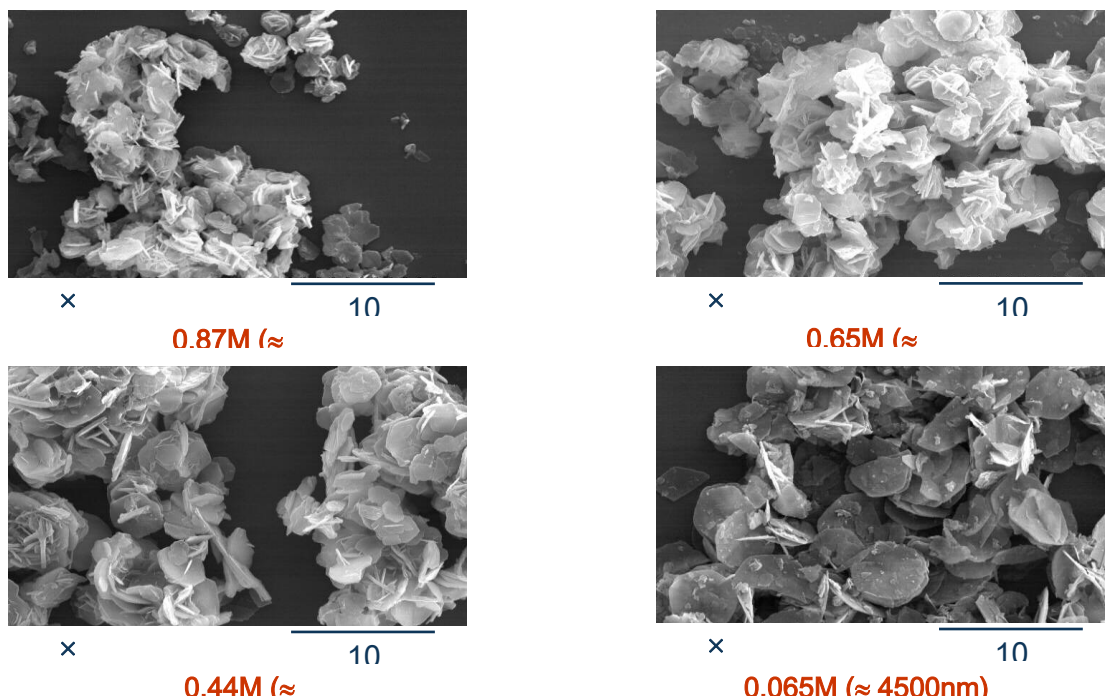


Figure 1. FE-SEM images of LDH particles prepared by urea hydrolysis method

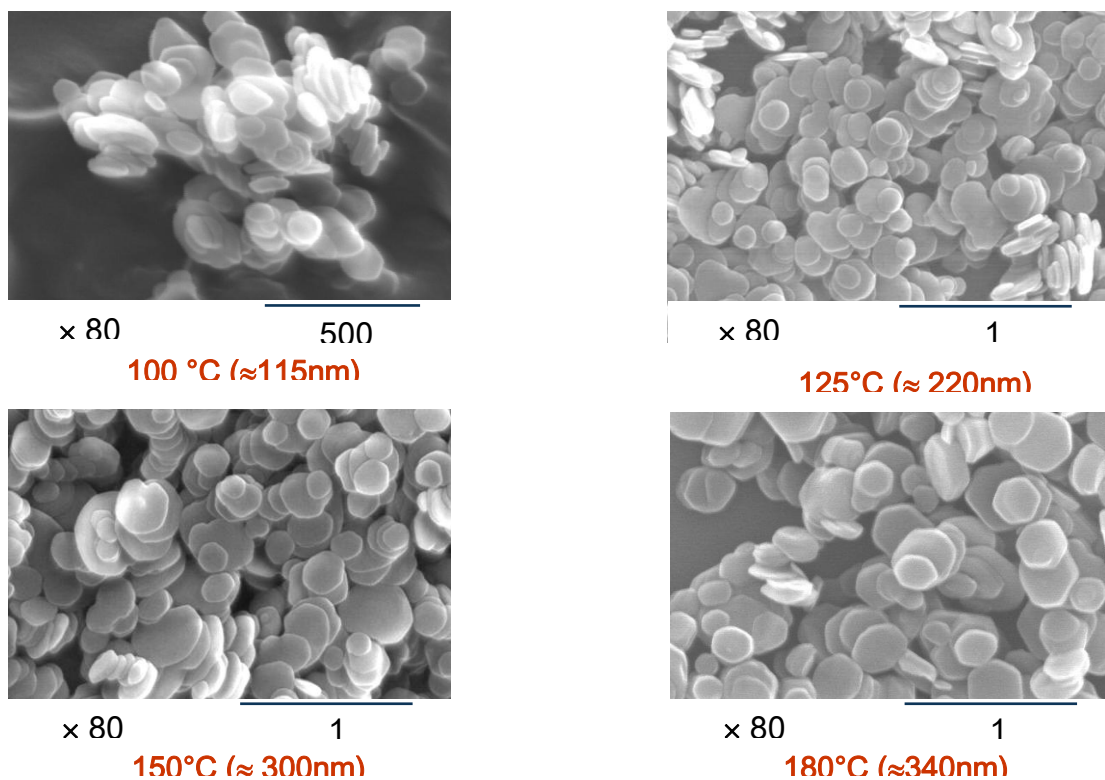


Figure 2. FE-SEM images of LDH particles prepared by hydrothermal method

Effect of nanoparticle addition on the mechanical protection properties of pure inorganic layer on the titanium and the stainless steel surfaces by a sol-gel coating method

Hohyeong Kim, GyunTak Kim, HeungYeol Lee, Taejin Hwang
Surface Technology and Heat Treatment R&D Division

Korea Institute of Industrial Technology (KITECH), 7-47 Songdo-Dong, Yeonsu-Gu, Incheon
406-840, Korea
greathtj@kitech.re.kr

As the mobile devices markets are growing, demand on the new materials for the new high-end cases of the products is also growing very fast. The metallic titanium and stainless steel are the most attractive candidates. Unlike the other devices, mobile device case requires high standard on the mechanical resistance to scratches from outside. In terms of that the metallic cases have found no noticeable solution yet. Therefore, it is urgently required to provide a protective layer for the new metallic cases [1-4].

In this study, we tried pure inorganic layer on the titanium and the stainless steel surfaces using the sol-gel coating method, and tested the mechanical properties. The inorganic layers were prepared by spraying the sol-gel coating solution on the metallic substrates. The coating solution was synthesized by the hydrolysis and condensation of tetraethoxysilane (TEOS) and methyltriethoxysilane (MTES) in ethanol, and by mixing colloidal silica nanoparticle.

It was clearly shown that the inorganic protection layers both on the titanium and stainless steel plate enhanced the scratch resistance dramatically (Fig. 1). It was also shown that the addition of silica colloidal nanoparticle is helpful to enhance the film hardness of the inorganic layer. However, the addition of the nanoparticle more than 2 wt% decreased the hardness of the film (Fig. 2). Since the coating layers were prepared by the spray coating method which is most frequently used in the mass production field, the production technology developed in this study would readily be applied to the mobile device case production lines.

References:

- [1] F. Feil, W. Fürbeth, M. Schütze, *Electrochimica Acta* 54 (2009) 2478–2486
- [2] D. Pech, P. Steyer, J.-P. Millet, *Corrosion Science* 50 (2008) 1492–1497
- [3] J. Ballarre, D.A. López, A.L. Cavalieri, *Thin Solid Films* 516 (2008) 1082–1087
- [4] H.K. Schmidt, *Journal of Sol-Gel Science and Technology* 1 (1994) 217–231.

Figures:



Fig.1 Scratch test results for a) the titanium and b) the stainless steel plates.

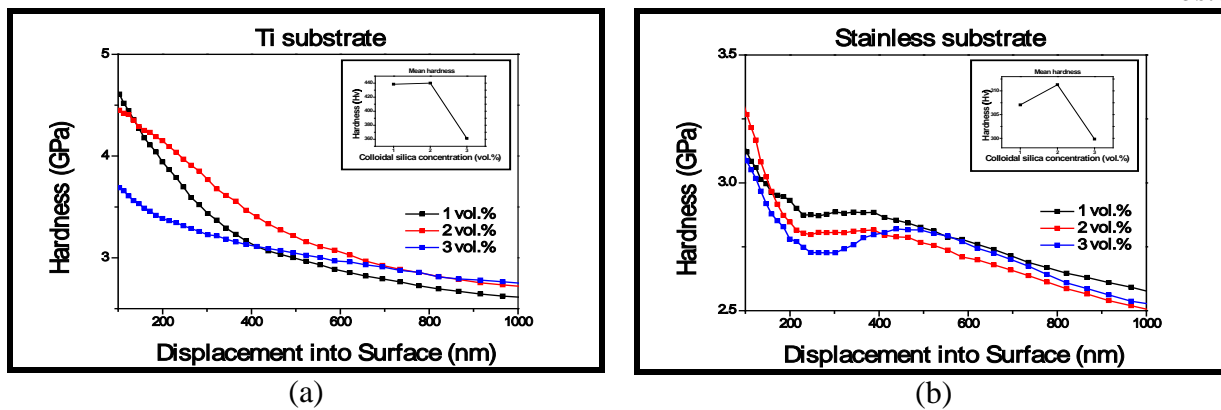


Fig. 2 Film hardness for a) the titanium and b) the stainless steel plates.

SCANNING PHOTOELECTRON MICROSCOPY FOR NANOMATERIALS AND NANODEVICE CHARACTERIZATION

Hyun-Joon Shin¹, Jaeyoon Baik¹, Ki-jeong Kim¹, Bongsoo Kim¹, Hyunseob Lim², Hyeon Suk Shin³, and Hee Cheul Choi²

¹Pohang Accelerator Laboratory, Pohang University of Science and Technology, Pohang, Kyungbuk, 790-784, Korea

²Department of Chemistry, Pohang University of Science and Technology, Pohang, Kyungbuk, 790-784, Korea

³School of Mechanical and Advanced Materials Engineering, Ulsan National Institute of Science and Technology, Ulsan, 681-800, Korea

shj001@postech.ac.kr

A scanning photoelectron microscope (SPEM) was installed at the 8A1 undulator beamline at the Pohang Light Source in Korea. The best space resolution of the SPEM in practical application is yet about 0.5 micrometer, which is much larger than the need of nanotechnology community. Nevertheless, the SPEM has been applied to nanomaterials and nanodevices in order to provide the chemical state information on domains of specific interest, such as graphene layers of several micrometers wide (single-, double-, and multi-layered graphenes) [1] and intentionally fabricated nanodevice patterns having micrometer size electrodes and bunch of Li-atom-intercalated Pyrene-functionalized carbon nanotubes dispersed between the electrodes [2]. In the former application, SPEM was applied to provide photoelectron spectral shape or chemical shift as a fingerprint of graphene thickness. In the latter application, SPEM was applied to identify the location of Li atoms along the conduction path that could explain the origin of diode characteristics. In this presentation, we will also introduce the limitation and the applicability of the SPEM for investigating the nanomaterials and the nanodevices.

References:

- [1] K. Kim, H. Lee, J.-H. Choi, Y.-S. Youn, J. Choi, et al., *Adv. Meter.* **20**, (2008) 3589.
- [2] H. Lim, H. S. Shin, H.-J. Shin, and H. C. Choi, *J. Am. Chem. Soc.* **130**, (2008) 2160.

Kerr microscopy studies of magnetization reversal uniformity in thin Co-films

O. Idigoras, P. Vavassori, J. M. Porro, and A. Berger
CIC nanoGUNE Consolider
E-20018 Donostia-San Sebastian, Spain
o.idigoras@nanogune.eu

We have studied the magnetization reversal of thin Co-films as a function of film thickness by means of magneto-optical Kerr effect microscopy. While all films exhibit uniaxial in-plane anisotropy and very sharp magnetization reversal at their respective coercive fields H_c , we also observe distinct differences in the overall reversal process for films of different thickness. Specifically, we find thinner films with a thickness of 15 nm or less to produce non-uniform magnetization states on the 1 - 10 micron lateral length scale, while thicker films of 30 nm thickness and more are characterized by domain wall motion and uniformly magnetized domains.

Thin Co-films were grown by means of e-beam evaporation onto naturally oxidized silicon (110) wafers. Our Oerlikon UNIVEX 350 deposition system is equipped with a 6 pocket rotary system for e-beam evaporation and 2 pockets for thermal evaporation. It also allows for substrate rotation during deposition to achieve excellent film uniformity and it enables substrate temperatures of up to 850°C. During the cobalt deposition, the vacuum pressure was better than 10^{-5} mbar. The deposition rate was continuously monitored and controlled by a quartz crystal sensor and held constant at 0.5 ± 0.1 Å/sec for all films. The accuracy of the deposition rate and total film thickness was furthermore corroborated by means of ellipsometry measurements. Magnetic measurements were performed using an advanced wide-field EVICO® Kerr-microscope for magnetic domain imaging and magnetic hysteresis measurements. Our system is equipped with a custom-build rotatable electromagnet for in-plane fields of up to 150 Oe (12 kA/m) and allows for the simultaneous measurement of local $M(H)$ -curves and recording of underlying domain processes, with a lateral resolution down to the limit of optical microscopy (approximately 500 nm). The magnetic field can be varied in steps of down to 0.1 Oe.

Figure 1 shows measurements obtained for a 15 nm thick Co-film with the external field applied along the easy magnetization axis. The Kerr microscope image illustrates the non-uniform magnetization state that occurs upon relaxing the magnetic field from positive saturation. The local $M(H)$ -curves show that the large area hysteresis loop corresponds to the average of two main types of local hysteresis loops, which can be observed on the micron scale. Some parts of the sample show very rectangular hysteresis loops with nearly full remanence, while other parts exhibit a rather substantial reduction of the remanent magnetization, even though the large magnetization jump at H_c is synchronized for both areas. The easy axis magnetic behaviour of a 30 nm thick Co-film is substantially different, as shown in Figure 2. In this case the magnetization relaxes into a uniform state as the external field is reduced to zero from positive saturation. In contrast to the thinner Co-films, for which the magnetization switching occurred in a single avalanche given our field resolution, thicker films show a more gradual magnetization reversal, as illustrated by the sequence of Kerr-microscope images shown in Fig. 2. Here, the reversal is dominated by the motion of domain walls in between macroscopically large and uniform domains.

The difference in behavior can be understood by the different role the exchange energy has. Due to substrate roughness and the polycrystalline nature of the films, inter-granular exchange coupling is weak in the initial onset layer during growth. Thus, on average thinner films exhibit a lower level of inter-granular exchange coupling,

enabling them to exhibit non-uniform magnetization states at low fields, in which the local magnetization follows the easy axis distribution of the grains. For thicker films, this non-uniformity is more strongly suppressed due to the more prominent role of the inter-granular exchange coupling, which forces the magnetization to align throughout the sample. This physical picture is supported by model calculations.

We acknowledge funding from the Department of Industry, Trade, and Tourism of the Basque Government and the Provincial Council of Gipuzkoa under the EROTEK Program, Project No. IE06-172, as well as from the Spanish Ministry of Science and Education under the Consolider-Ingenio 2010 Program, Project No. CSD2006-53. P.V. also acknowledges support through 7th European Community Framework Programme (Grant Agreement No. PIEF-GA-2008-220166).

Figures:

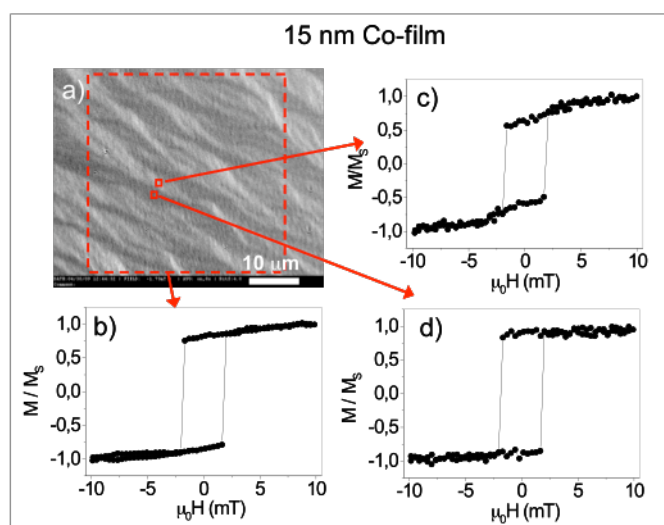


Figure 1 Panel a): Kerr microscope image (55 mm x 42 mm) of a 15 nm thick Co-film taken at remanence upon field reduction from saturation along the magnetic easy axis. Panel b): Easy axis MOKE hysteresis loop measured within the area of 40 μm x 40 μm marked in Panel a). Panels c) and d): MOKE hysteresis loops measured within the two regions of 1 μm x 1 μm marked in Panel a).

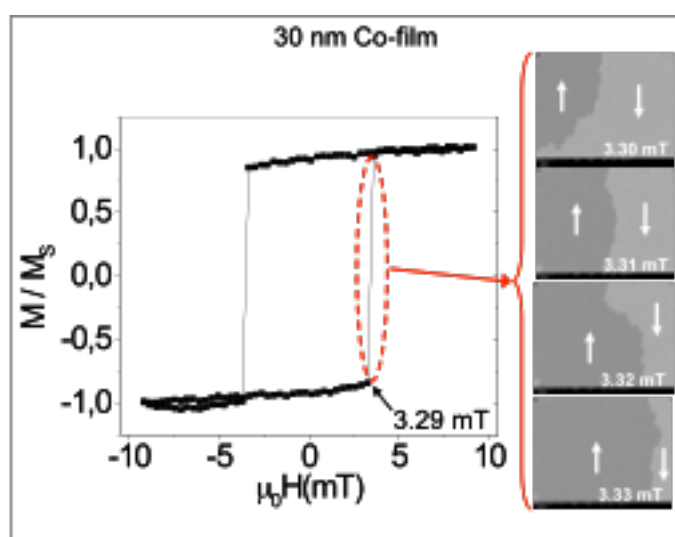


Figure 2 MOKE hysteresis loop recorded with the external field applied along the magnetic easy axis for a 30 nm thick Co sample. The insets display a sequence of Kerr microscope images (435 μm x 330 μm) illustrating the domain reversal pattern in the sample.

MICROSCOPIC ORIGIN OF EXCHANGE BIAS IN INVERTED CORE/SHELL MAGNETIC NANOPARTICLES

Òscar Iglesias and Amílcar Labarta

*Departament de Física Fonamental and IN2UB, Universitat de Barcelona, Av. Diagonal 647,
08028 Barcelona, Spain
oscar@ffn.ub.es*

The exchange bias (EB) phenomenon has been reported in a variety of nanoparticle systems with core/shell structure until its first report in the 50's. In most of the cases, this phenomenology has been observed in the paradigmatic case of a nanoparticle consisting of a ferromagnetic (FM) core surrounded by an antiferromagnet (AFM) with Néel temperature (T_N) lower than the Curie temperature (T_C) of the FM. However, there have been recent studies [1] reporting the observation of EB in nanoparticles with doubly inverted composition: an AFM core (MnO) surrounded by a ferrimagnetic shell (Mn_3O_4) and with a T_C much lower than the T_N of the core. These unusual observations, together with the peculiar magnetic properties of these systems [1], remain a challenge for the current proposed models of EB in nanoparticles.

We present results of Monte Carlo (MC) simulations based on a classical Heisenberg model of lattice spins for a core (AFM)/shell (FM) nanoparticle in which the values of microscopic parameters such as anisotropy K and exchange constants J can be tuned in the core, shell and at the interfacial regions, offering new insight on the microscopic origin of the experimental phenomenology [2]. To this end, we have computed low temperature equilibrium magnetic configurations (see Fig. 1) in the presence of a magnetic field and at zero field for different values of the K 's and J 's in order to study the magnetic order established at the core/shell interface, which is essential to understand EB. We have also simulated hysteresis loops after field cooling as a function of the exchange coupling at the interface (see Fig. 2) and K for a range of particle diameters similar to the experimental systems. The simulated loops display shifts along the field axis with a nonmonotonous dependence on the core diameter in qualitative agreement with the experimental observation. A detailed analysis of the interfacial spin configurations along the loops have allowed us to quantify the magnitude of the loop shifts with striking agreement with the macroscopic observed values and to give compelling evidence of the relevant role of the uncompensated net magnetization at the interface to explain the observed phenomenology.

Financial support of the Spanish MEyC (MAT2006-03999), Consolider-Ingenio 2010 CSD2006-00012 and Catalan CURSI (2005SGR00969) is acknowledged. We acknowledge CESCA and CEPBA under coordination of C4 for computer facilities.

References:

- [1] G. Salazar-Alvarez *et al.*, J. Am. Chem. Soc. 129 (2007) 9102; A. E. Berkowitz *et al.*, Phys. Rev. B 77 (2008) 024403.
- [2] O. Iglesias, X. Batlle and A. Labarta, Phys. Rev. B 72 212401 (2005), J. Nanosci. Nanotechnol. 8 (2008) 2761.

Figures:

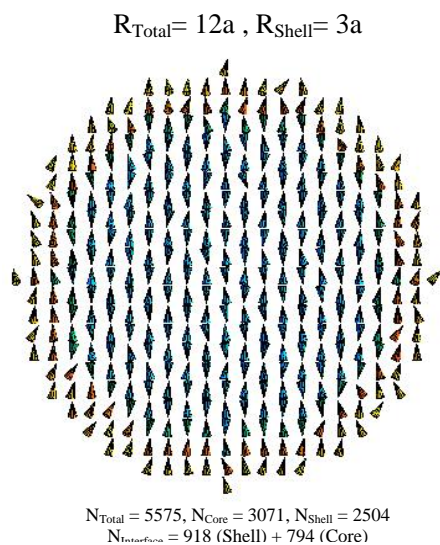


FIGURE 1: Magnetic configuration of a nanoparticle with AFM core/FM shell structure after a field cooling process.

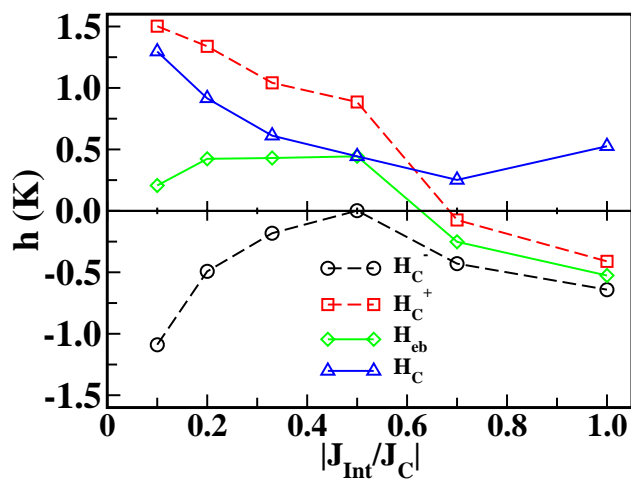


FIGURE 2: Dependence of the coercive field and exchange bias fields on the exchange coupling constant at the interface for antiferromagnetic interfacial coupling.

Structural phase Transition of Low-coverage Pentacene on SiO₂ and Au surfaces

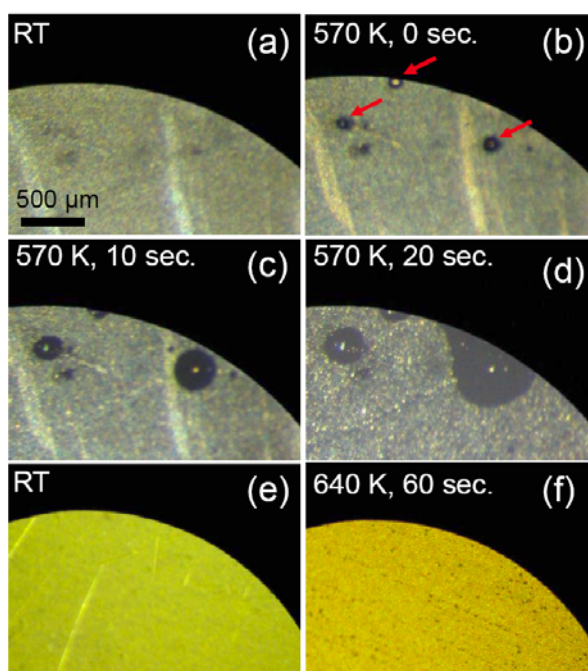
Kyuwook Ihm,¹ Kyoung-Jae Lee,² Tai-Hee Kang,¹ Sukmin Chung,² and M. Y. Choi³

¹Beamline research division, Pohang Accelerator Laboratory, Pohang, Kyungbuk 790-784, Korea

²Department of Physics, POSTECH, Pohang, Kyungbuk 790-784, Korea

³Department of Physics and Astronomy and Center for Theoretical Physics, Seoul National University, Seoul 151-747, Korea

Thermodynamic behaviors of low-coverage pentacene molecules on both silicon oxide (SiO₂) and gold (Au) surfaces have been observed via x-ray absorption spectroscopy. It reveals intriguing structural transitions with temperature: For the SiO₂ surface, monotonic decrease in the mean tilt angle of the pentacene layer is observed as the temperature is increased. For the Au surface, three different structural regimes are found, indicating double transitions. Such contrasting thermodynamic behaviors are explained in terms of a spin-1 Ising model, which includes three structural states: standing-up, lying-down, and desorbed.



Oxygen sensor based on the thermoelectric effect

I. Iraizoz¹, A. Martinez Mariñelarena¹, I. R. Matias¹, J. Maset², M. A. Arangoa², S. Azkoiti³,
F. J. Arregui¹

¹Public University of Navarra, Pamplona, SPAIN

²Laboratorios CINFA

³IDEN Biotechnology

E-mail: parregui@unavarra.es

There are many techniques utilized for the synthesis and fabrication of thick and thin films for chemical sensing. Among others, methods like spin coating, dip coating or screen printing have been already successfully used for the fabrication of oxygen sensors [1]. Most of these techniques are limited for the fabrication of thick films or are not suitable to control the thickness of the coating on the nanometer scale. On the other hand, there are techniques, like the Layer-by-Layer Electrostatic Self Assembly (LbL) method, which are suitable for the deposition of diverse nanostructured materials (ceramics, semiconductors, metals, biomaterials and others) on many types of substrates of even complex surfaces with convex, concave or even conical shapes [2]. Due to this the LbL method can be successfully used for the synthesis and deposition of sensing thin films. More specifically, we propose here the utilization of the LbL method for the fabrication of a new sensor based on the thermoelectric effect for the measurement of oxygen. Basically, nanofilms of Yttria-stabilized zirconia (YSZ) have been deposited by means of the LbL on alumina substrates with interdigitated platinum electrodes. The interdigitated electrodes device consists on a 300 μm thick alumina substrate with platinum interdigitated electrodes (250 μm width and spacing) and a platinum resistance detector (RTD) on one side and a platinum heater (microhot plate) on the other side. The overall dimensions of the alumina are 15mm x 13 mm (see Fig. 1).

In opposition to classic oxygen sensors based on changes of the electrical impedance of YSZ films in presence of oxygen at high temperature [3], this sensor is based on the voltage generated between electrodes due to a temperature gradient [4]. This voltage between the interdigitated electrodes will change depending of the oxygen concentration. See Fig. 2 where the gradient of temperature introduced by the heater can be clearly appreciated.

In Fig. 3, an AFM image of the YSZ films is plotted, it can be seen that these films are homogeneous. The sensing film synthesized for the experiments had a thickness of 150 nm and an average RMS roughness of 49 nm. In Fig. 4 a SEM image of the YSZ deposition onto the interdigitated electrodes device is also shown. In Fig. 5 the response of the sensor at different oxygen concentrations (from 2% to 100%) is plotted. Fig. 6 shows the dynamic response of the sensor when is submitted to repetitive cycles of 100% Nitrogen and 100% Oxygen. To our knowledge, this is the first time that the LbL method has been used for the fabrication of oxygen sensors based on the thermoelectric effect.

References:

- [1] N. Izu, W. Shin, I. Matsubara and N. Murayama, *Sens Actuator, B Chem.* (2009) vol. 139, pp. 317-321.
- [2] D. Galbarra, F. J. Arregui, I. R. Matias and R. O. Claus, *Smart Mater. Struct.* (2005) vol.14, pp. 739-734.
- [3] S. YU, Q. Wu, M. Tabid-Azar and C. -C. Liu, *Sens Actuators, B Chem.* (2002) vol. 85, pp. 212-218.
- [4] U. Röder-Roith, F. Rettig, T. Röder, J. Janek, R. Moos and K. Sahner, *Sens Actuators, B Chem* (2009) vol. 136, pp. 530-535.

Figures:

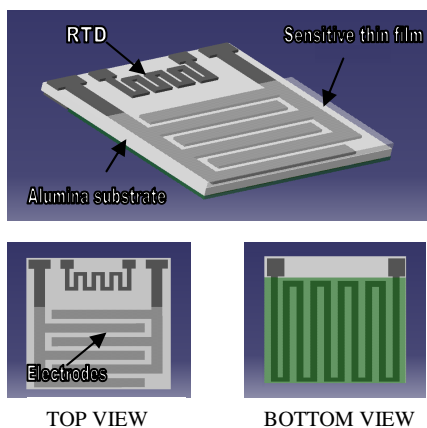


Fig. 1: Setup of the LbL fabricated Oxygen sensor.



Fig. 2: IR image of the temperature gradient induced in the device.

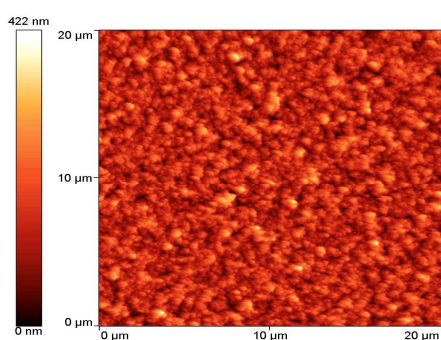


Fig. 3: AFM image of an YSZ layer deposited onto a glass microscope slide.

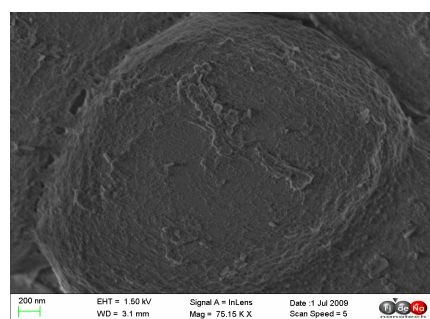


Fig. 4: SEM image of the YSZ layer deposited onto the interdigitated electrodes device.

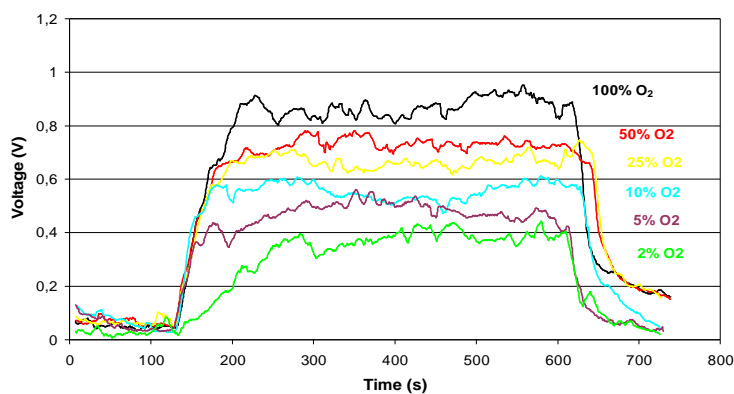


Fig. 6: Typical sensor response to oxygen at different concentrations.

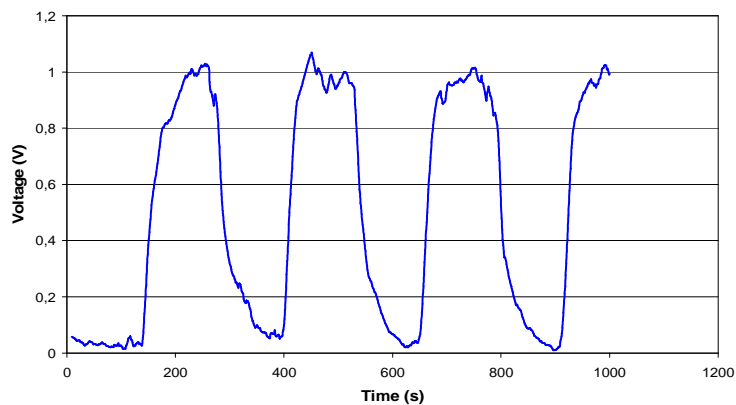


Fig. 5: Sensor response changing Oxygen concentration from 0% to 100%.

Paramagnetic Gd-based Gold Glyconanoparticles as MRI Contrast Agents for Brain Tumor Detection

Ainhoa Irure,^{1,2} Marco Marradi,^{1,2} Ana Paula Candiota,^{2,3} Rui Simões,^{2,3} Teresa Delgado,^{2,3} Milena Acosta,^{2,3} Carles Arus,^{2,3} and Soledad Penadés^{1,2}

¹Lab. of GlycoNanotechnology, CIC biomaGUNE, P^o Miramon 182, 20009 San Sebastián

²Centro de Investigación Biomédica en Red en Bioingeniería, Biomateriales y Nanomedicina (CIBER-BBN)

³Department de Bioquímica i Biologia Molecular, Unitat de Bioquímica de Biociències, Edifici Cs, Universitat Autònoma de Barcelona, Cerdanyola del Vallés, Spain

airure@cicbiomagune.es

Nanoparticles for Magnetic Resonance Imaging (MRI) have attracted much attention in the last years.[1] Most of them consists in magnetic iron oxide nanoparticles (T₂ agents) which have some disadvantages that limit their extensive clinical applications. For example, they are negative imaging agents (signal-decreasing effect) and their high susceptibility induces distortion of the magnetic field on neighbouring normal tissues. Because of this, most extensively and clinically used MRI contrast agents are T₁ agents (signal-increasing effect) based on gadolinium complexes.[2] Many research groups are devoting their work to develop nanoparticle-based T₁ contrast agents, in which the core material is composed by Gd (III) salts.[1] Recently, the synthesis of gold nanoparticles capped with a Gd-based contrast agent (DTDTPA) has been reported.[3] Our laboratory has a great expertise in preparing gold nanoclusters and semiconductor nanocrystals functionalized with carbohydrate antigens (glyconanoparticles, GNPs).[4] These gold GNPs have been shown to be excellent platforms for basic studies of carbohydrate interactions and potential tools for biotechnological and biomedical applications. GNPs are multivalent sugar-coated gold nanoclusters. The sugar coat confers water solubility and biological activity to the nanoclusters. GNPs are biocompatible and non-toxic to cellular lines or mice,[5] thus being good candidates for in vivo use. The methodology developed in our laboratories allows us to introduce multifunctionality in a controlled way.[6]

We herein present hybrid GNPs having on the same gold nanopatform sugar conjugates and Gd(III) chelates for converting GNPs into new paramagnetic probes for MRI. The insertion of both Gd-complex derivatives and suitable glycoconjugates in a one-step process onto the same gold nanocluster can enhance the relaxation properties of the Gd-chelate. Both sugar stereochemistry and the relative position of the sugar with respect to the Gd(III) ion seem to control the relaxivity values of these GNPs. The paramagnetic gold GNPs were prepared using different ratios of thiol-ending sugar (glucose, galactose, mannose, cellobiose, maltose or lactose) conjugates and tetraazacyclododecane triacetic acid (DO3A) ligands (Scheme 1). DO3A-ligands were selected to chelate the Gd(III) cation. Twenty hybrid GNPs were prepared by reducing a gold salt in the presence of a mixture of glycoconjugate and ~10% of DO3AC₅S or DO3AC₁₁S, following our methodology.[7] Transmission electron microscopy (TEM), UV-Vis, IR, ¹H NMR, and elemental analysis were used for their characterization (Scheme 1). The prepared GNPs were incubated with GdCl₃. The amount of Gd³⁺ present in the GNPs has been measured by ICP and by UV complexometric titration (xylenol orange test). One important characteristic of these GNPs is the number of water molecules coordinated directly to the Gd(III) (q) which was measured using ¹⁷O NMR resonance.

The longitudinal and transversal relaxation times (T₁ and T₂) of our GNPs were measured to confirm their potentiality as MRI contrast agents. They showed very good relaxivities values (r₁ and r₂), even better than commercial available contrast agents. Gluco-GNPs have been used as in vivo contrast agents for detection of brain tumours (GL261 brain glioma in mice) using a 7 T horizontal magnet. Commercial Dotarem[®] was used as reference at the same dose (0.04 mmol Gd/Kg, i.v. injection in the tail vein). Dynamic Contrast Enhanced T₁ images (DCE-T₁) and

relative contrast enhancement (RCE) are shown in Fig. 1. Gluco-GNPs reached brain tumours and accumulate there, allowing their visualization by MRI.

The promising results of the contrast enhancement observed with the evaluated GNP suggest that Gd-based GNPs could be used as new nano-probes for brain tumour detection *in vivo*. Besides, GNPs can be further derivatized to improve targeting.

References:

- [1] For a recent review, see: H. B. Na, I. C. Song, T. Hyeon, *Adv. Mater.*, **21** (2009) 1.
- [2] P. Hermann, J. Kotek, V. Kubicek, I. Lukes, *Dalton Trans.*, **23** (2008) 3027.
- [3] a) P.-J. Debouttière, S. Roux, F. Vocanson, C. Billotey, O. Beuf, A. Favre-Réguillon, Y. Lin, S. Pellet-Rostaing, R. Lamartine, P. Perriat, O. Tillement, *Adv. Funct. Mater.*, **16** (2006) 2330; b) C. Alric, J. Taleb, G. Le Duc, C. Mandon, C. Billotey, A. Le Meur-Herland, T. Brochard, F. Vocanson, M. Janier, P. Perriat, S. Roux, O. Tillement, *J. Am. Chem. Soc.*, **130** (2008) 5908.
- [4] J. M. de la Fuente, S. Penades, *BBA-Gen. Subjects*, **4** (2006) 636.
- [5] J. Rojo, V. Díaz, J. M. de la Fuente, I. Segura, A. G. Barrientos, H. H. Riese, A. Bernad, S. Penadés, *ChemBioChem*, **5** (2004) 291.
- [6] R. Ojeda, J. L. de Paz, A. G. Barrientos, M. Martin-Lomas, S. Penadés, *Carbohydr. Res.*, **342** (2007) 448.
- [7] A. G. Barrientos, J. M. de la Fuente, T. C. Rojas, A. Fernández, S. Penadés, *Chem. Eur. J.*, **9** (2003) 1909.

Figures:

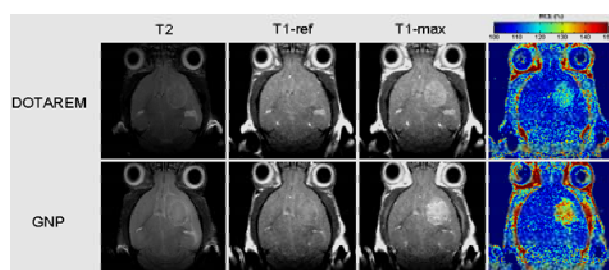
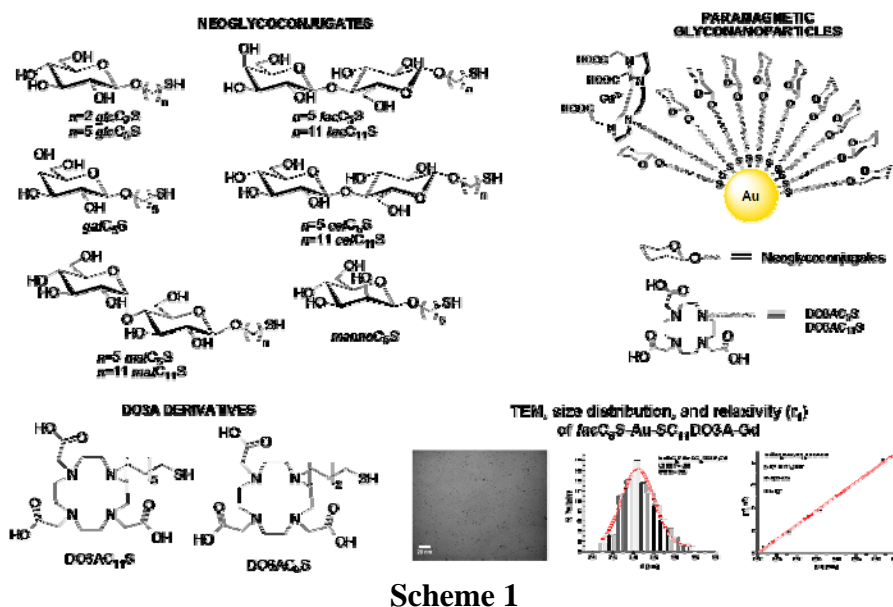


Fig. 1: Left to right, axial T2-weighted images, DCE-T1 images and RCE maps of 2 mouse brains with a GL261 glioma. One animal was studied with Dotarem (top row) and the other with the GNP (bottom row). T1-ref images were acquired before injecting the agent, T1-max images correspond to the point of maximum contrast enhancement after Dotarem or GNP administration.

Surface and volume plasmons in metallic nanospheres in semi-classical RPA-type approach; near field coupling of surface plasmons with semiconductor substrate

W. Jacak, J. Krasnyj, J. Jacak, L. Jacak

Institute of Physics, Wrocław University of Technology

Wyb. Wyspińskiego 27, 50-370, Wrocław, Poland

witold.aleksander.jacak@pwr.wroc.pl

Recently there have been reported experimental data on giant enhancement of photoluminescence and absorption of light by semiconductor surface (of photo-diode) covered with metallic (gold, silver, or copper) nanospheres, with sphere radius of order of several to several tens of nanometers [1]. These phenomena are considered as a perspective for efficiency enhancement of solar cells by application of special metallic nanoparticle coverings of photo-active surfaces. Metallic nanospheres (or nanoparticles of other shapes) can act as light converters, collecting energy of incident photons in surface plasmon oscillations. This energy can be then transferred to semiconductor substrate in a more efficient manner in comparison to the direct photo-effect. This phenomenon is not described in detail as of yet, moreover some other convergent mechanisms apparently contribute, manifesting themselves in strong sensitivity of the effect to size and shape of metallic nanocomponents, type of the material and dielectric coverings of nanoparticles. Nevertheless, one can argue generally that due to nanoscale of the metallic components the momentum is not conserved which leads to the allowance of all indirect optical interband transitions in semiconductor layer, resulting in enhancement of a photo-current in relation to the ordinary photo-effect where only direct interband transitions are admitted. We formulate a theoretical model in which these phenomena can be described. The random-phase-approximation semi-classical scheme for metallic nanosphere is formulated in all-analytical version. The spectrum of plasmons in metallic nanosphere is determined including both surface and volume type excitations and their mutual connections. It is also demonstrated that the surface plasmons in nanosphere can be incited by the volume ones, while conversely not. Various channels for damping of surface plasmons on nanosphere are evaluated and the relevant resonance shifts are compared with the experimental data for metallic nanoparticles of different dimensions, located in dielectric medium or on the semiconductor substrate. The described above strong enhancement of the energy transfer from surface plasmon oscillations to the substrate semiconductor is explained in the regime of a near field coupling in agreement with the experimental observations for metallic nanomodified photo-diode systems.

References:

[1] S. Pillai, et al., Appl. Phys. Lett. **88** (2006) 161102; H. R. Stuart and D. G. Hall, Appl. Phys. Lett. **73** (1998) 3815, Phys. Rev. Lett. **80** (1998) 5663; D. M. Schaadt, B. Feng, and E. T. Yu, Appl. Phys. Lett. **86** (2005) 063106; K. Okamoto, et al., Nature Mat. **3** (2004) 661;

NQD-SWNT FETs Assembled using Dielectrophoresis

*Sohee Jeong**, *Hyung Cheoul Shim[†]*, *Soohyun Kim[†]*, *Chang-Soo Han**

**Nanomechanical Systems Research Division, Korea Institute of Machinery and Materials
171 Jang-dong, Yuseong-gu, Daejeon 305-343, Korea*

*[†]Department of Mechanical Engineering, Korea Advanced Institute of Science and Technology
Guseong-dong, Yuseong-gu, Daejeon 305-343, Korea
sjeong@kimm.re.kr*

Semiconductor nanocrystal quantum dots (NQDs) have attracted considerable interest for use in photovoltaics and optoelectric sensor applications. The ability to transport extracted carriers from the NQDs is essential for the development of NQD incorporated device applications. Coupling of NQDs to one-dimensional nanostructures such as single wall carbon nanotubes (SWNTs) is expected to produce a composite material which facilitates selective wavelength absorption, charge transfer to 1-D nanostructures, and efficient carrier transport. Both covalent and non-covalent routes to assemble NQDs to SWNTs have been reported.

In this paper, we actively assembled CdSe/ZnS nanocrystal quantum dots on CNTs using AC electric fields. Photoluminescence coming from NQDs allowed us to monitor the assembled structures on CNTs aligned in between the electrodes. We further fabricated FETs using NQD/SWNT hybrid nanostructures using dielectrophoresis to monitor the carrier transfer behavior upon photoexcitation.

Assembly of NQDs on SWNTs using Dielectrophoresis

DEP is the electrokinetic motion of dielectrically polarized materials in non-uniform electric fields and is currently an active area of research for manipulation of biological materials such as cells, bacteria and DNA. [2] The polarized material is driven towards (positive DEP) or away from (negative DEP) the high field region depending on the complex dielectric permittivity of the particle and its surrounding medium.

Generally for the particles smaller than 500 nm, the dielectrophoretic force is negligible compared to the Brownian motion due to their small size. When CNT is used as an electrode, independent of the position along the CNTs, dielectric force F_{DEP} can be described as followed;

$$\nabla(E_{rms}^2) \approx -2[V_{rms}/\{\ln(4h/d)\}]^2(r^{-3})\mathbf{r} \quad [2]$$

For the positive DEP force, AC sinusoidal wave was applied and NQDs were assembled on the aligned CNTs on Pt electrode with 2 μm gap. Resulting assembly was viewed under the confocal microscope where the excitation wavelength was 458 nm and photoluminescence (PL) emitting at the maximum wavelength of 550 nm was collected. (Fig. 2, middle) Decrease in PL intensity was observed due to the photobleaching of NQDs. Around after 4 minutes, no observable PL signal was obtained. (Fig. 2, right)

Optical/Electrical Characterizations of NQD/SWNT Hybrid Nanostructures

Further to verify the charge transfer mechanism of the NQD-CNT hybrid nanostructures, we assembled the NQDs to SWNTs first then assemble the FET device using dielectrophoresis. Attaching NQDs to SWNTs were performed via non-covalent attachment where both NQD and SWNTs retain their electronic structures before and after the attachment. [3, 4] PL intensity measurements expect us to the extent of charge transfer in core and core/shell NQDs to SWNTs. More efficient charge transfer is expected in core NQD-SWNTs system.

The assembled CdSe-SWNTs which resulted in photoluminescence quenching confirmed optically was fabricated into the FET using dielectrophoresis. We used n-doped silicon substrate as back gate, and the aligned the CdSe-SWNTs hybrid nanostructures between microelectrodes function as a channel in FET structure. We then packaged CdSe-SWNT device into conventional chip using wire bonding for the convenience of measurement of electrical properties. With the fabricated FET device, we measured the resistance between source and drain with gate voltage of 100 mV using digital multimeter (Fulke, 189) in real-time. The resistance starts to decrease when the light was on and increase when the light was off.

In this paper, we assembled prepared CdSe (core and core/shell with ZnS) semiconductor nanocrystal quantum dots on single walled carbon nanotubes using dielectrophoresis (DEP). Confocal imaging confirmed the assembled hybrid nanostructures. To further characterize the charge transfer from photoexcited NQDs to SWNTs, FETs were fabricated. We monitored the electrical signatures from NQD decorated SWNTs upon photoexcitation and were able to elucidate the carrier transfer mechanism.

References:

- [1] K. S. Leschkies, et al., *Nano Lett.*, 7 (2007) 1793
- [2] M. P. Hughes, *Nanotechnology* 11, (2000) 124
- [3] S. Banerjee, and S. S. Wong, *JACS*, 125 (2003) 10342
- [4] B. Landi et al., *Mat. Lett.*, 60 (2006) 3502

Figures:

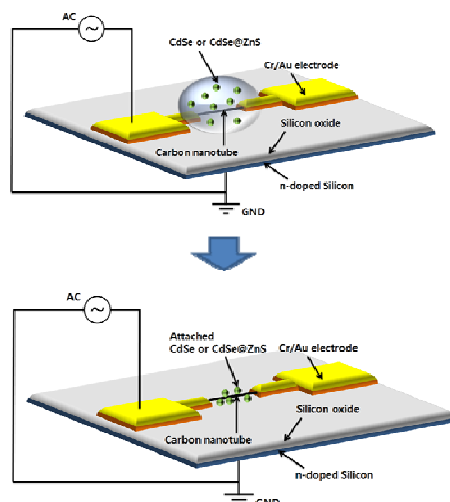


Figure 1 DEP assembly of NQDs on CNTs

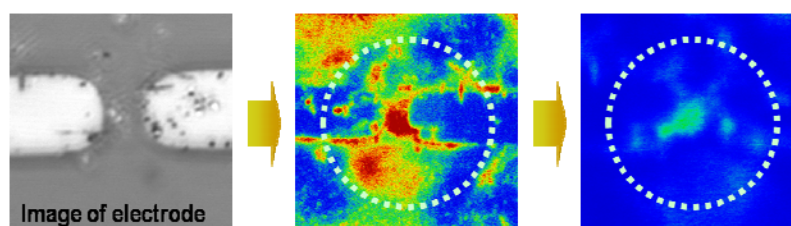


Figure 2 Microscope images of nanocrystal quantum dots assembled on carbon nanotubes (left: transmission image of electrode, middle 550 nm emitting dots assembled on carbon nanotubes aligned in between the electrodes, right: PL from the NQDs were photo-bleached)

SPIN-RESOLVED STM SIMULATION OF GRAPHENE NANORIBBON

Wei Ji^{1,2}, *Werner A. Hofer*³, *Hong-Jun Gao*², and *Hong Guo*¹

*Centre for the Physics of Materials and Department of Physics, McGill University,
Montreal, Quebec, Canada H3A 2T8*

*Department of Chemistry, The University of Liverpool, Liverpool L69 LBX, UK
Institute of Physics, Chinese Academy of Sciences, Beijing 100080, China*

wei.ji@mcgill.ca

Graphene nanoribbon was predicted by previous literature to exhibit ferromagnetic magnetism at its zig-zag edge and anti-ferromagnetic coupling between the two edges of the ribbon [1]. Spin-polarized scanning tunneling spectroscopy (SPSTM) may be able to experimentally verify this prediction. In this work, we report a calculated spin contrast in SPSTM setup from atomic first principles. Using a DFT based scattering states method [2], we calculate a series of SPSTM images of grapheme nanoribbons having zig-zag edges. A free-standing ribbon, a ribbon on a free-standing two dimensional graphene sheet, and a ribbon on a SiC(0001) supported (C terminated) two dimensional grapheme sheet, have been investigated. It was found that the spin-contrast at zig-zag edges should be detectable. The contrast can also be enhanced or suppressed by interlayer interactions of graphene ribbon and the graphene sheet underneath.

References:

- [1] Y.-W. Son, M. L. Cohen, and S. G. Louie, *Nature*, **444** (2006), 347.
- [2] Werner A. Hofer, Adam S. Foster and Alexander L. Shluger *Rev. Mod. Phys.* **75** (2003), 1287-1331.

FORMATION OF OLIGOTHIOPHENES FROM TERTHIOPHENES CATALYSED BY GOLD NANOPARTICLES

Xiuqian Jiang, Ashton Partridge and Mark Waterland

MacDiamid Institute, Massey university, Private Bag 11222, Palmerston North, New Zealand

E-mail address: L.Jiang@massey.ac.nz

The use of gold nanoparticles has been demonstrated to catalyse the formation of oligothiophenes from terthiophene in solution using ferric chloride as the oxidizing agent. The structures of the resulting core-shell materials have been confirmed by electron microscopy and surface-enhanced Raman spectroscopy. Due to the lengthening of the conjugated backbone upon polymerization the SERS enhancement of the polymer increases as the interband electronic transition approaches resonance with the laser excitation. We believe that it should be possible to perform the polymerization of terthiophene *in solution* on the surface of AuNPs, the very high surface area of nanoparticles allows a much larger amount of material to be prepared.

EXPLOITING THE NEGATIVE CAPACITANCE REGION OF FERROELECTRIC OXIDES FOR SURFACE POTENTIAL AMPLIFICATION IN METAL-FERROELECTRIC-INSULATOR-SEMICONDUCTOR DEVICES

David Jiménez^{1}, Enrique Miranda¹, Francesca Campabadal², Joan Marc Rafi², and Florencio Sánchez³*

¹*Departament d'Enginyeria Electrònica, Escola d'Enginyeria, Universitat Autònoma de Barcelona*

²*Instituto de Microelectrónica de Barcelona (IMB-CNM-CSIC)*

³*Instituto de Ciencia de Materiales de Barcelona (ICMAB-CSIC)*

(*) david.jimenez@uab.es

One of the most severe problems pointed out by the microelectronics industry in the *International Technology Roadmap for Semiconductors* is the increasing power dissipation at the chip level due to the relentless scaling down of the transistors dimensions [1]. This problem has been referred to as the **power crisis** in the microelectronics industry and the main reason behind can be traced back to the difficulty of reducing the transistor inverse subthreshold slope (S), which shows an *apparent* limit (because of thermodynamics constraints) of 60 mV/decade. Nevertheless, theoretical studies show the feasibility of achieving **S<60 mV/decade** by replacing the gate insulator dielectric with a **ferroelectric material** [2]. This kind of materials exhibits a **negative capacitance** region that, according to theoretical considerations, could result in surface potential amplification. This approach presents two important advantages: the transistor operation principle is retained as well as the potential compatibility with CMOS (Complementary Metal-Oxide-Semiconductor) fabrication technology.

From a practical viewpoint, integration of a ferroelectric oxide film directly on silicon is extremely difficult because of the mismatch between lattice parameters, interdiffusion, and chemical reactions that degrade the properties of the oxide, the underlying silicon, or both, yielding electrically active defects at the semiconductor interface [3]. To our knowledge, only a very recent publication has reported the growth of a good quality ferroelectric layer of SrTiO₃ on silicon [4]. To overcome the integration problem, the usual approach consists in using a thin insulating buffer layer that almost perfectly matches the silicon substrate with the ferroelectric oxide film [5]. Considering the state of the art on ferroelectric oxide integration, we have focused our research on a Metal-Ferroelectric-Insulator-Semiconductor (MFIS) gate stack. In this work, we have theoretically investigated the referred system, and explored the optimal geometrical parameters needed for the experimental observation of the surface potential amplification effect (Figure 1).

References:

- [1] International Technology Roadmap for Semiconductors. Available: public.itrs.net
- [2] S. Salahuddin and S. Datta, Nano Letters 2008, no. 2, 405
- [3] D. Schlom, J. Am. Ceram. Soc 2008, vol. 91, 2429
- [4] M. P. Warusawithana et al., Science 2009, vol. 324, 367
- [5] R. A. McKee, Science 2001, vol. 300, 1726

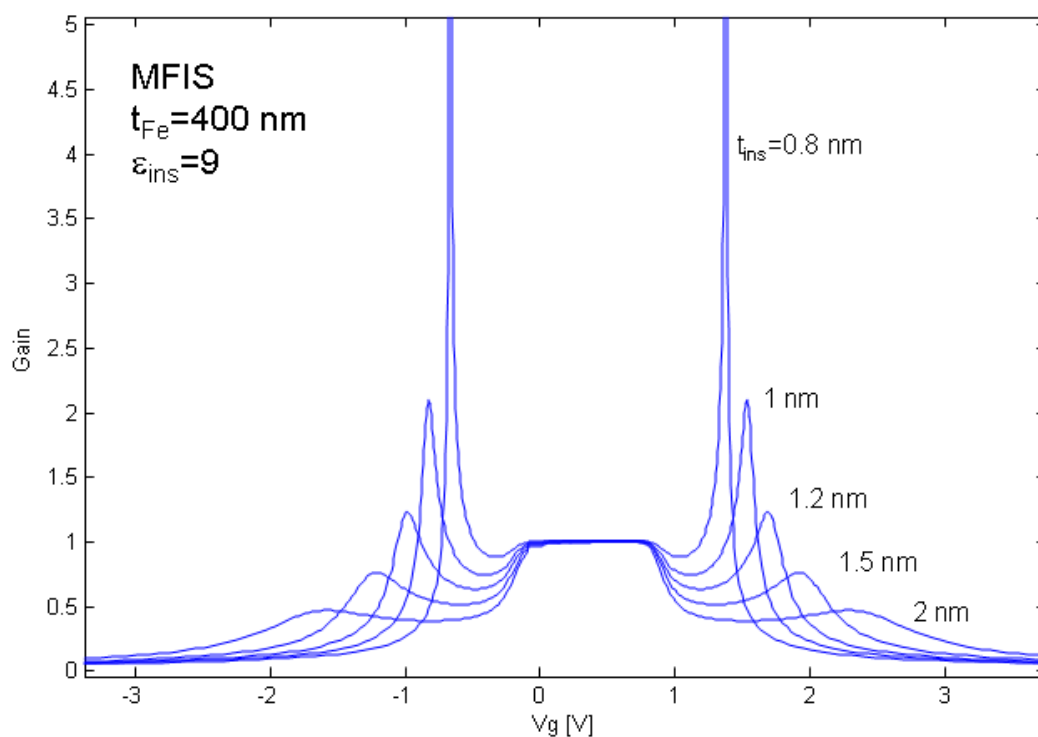


Figure 1. Predicted gain of a MFIS gate stack, looking for surface potential amplification. A large gain (~ 5) should be possible with an insulator buffer layer 0.8 nm-thick and dielectric permittivity of 9. As shown in this figure, degradation of the gain is severe as the insulator thickness increases. Above 1.2 nm the gain turns out to be smaller than unity for any applied gate voltage. At this critical value the surface potential amplification would not be observable

Individual Nanowires Contacted onto Microhotplates: A Strategy for Improving the Performance of Gas Nanosensors

R. Jiménez-Díaz⁽¹⁾, J. D. Prades⁽²⁾, F. Hernandez-Ramirez^(2,3), J. Santander⁽⁴⁾, C. Calaza⁽⁴⁾, L. Fonseca⁽⁴⁾, J. R. Morante^(2,5), C. Cané⁽⁴⁾, S. Barth⁽⁶⁾, S. Mathur⁽⁷⁾, A. Romano-Rodríguez⁽¹⁾

⁽¹⁾ *MIND-IN2UB, Departament d'Electrònica, Universitat de Barcelona, c/Martí i Franquès 1, E-08028 Barcelona, Spain*

⁽²⁾ *IREC, Catalonia Institute for Energy Research, E-08019, Barcelona, Spain*

⁽³⁾ *Electronic Nanosystems, S.L., E-08028, Barcelona, Spain*

⁽⁴⁾ *Instituto de Microelectrónica de Barcelona, IMB-CNM-CSIC, E-08193 Bellaterra, Spain*

⁽⁵⁾ *M2E, Departament d'Electrònica, Universitat de Barcelona, E-08028 Barcelona, Spain*

⁽⁶⁾ *Department of Chemistry, University College Cork, Cork, Ireland*

⁽⁷⁾ *Institute of Inorganic Chemistry, University of Cologne, D-Cologne, Germany;*

rjimenez@el.ub.es

Solid state devices based on metal oxides are amongst the most popular types of gas sensors for monitoring toxic species, such as carbon monoxide (CO) and nitrogen oxide (NO_x) [1]. In the last years, significant research efforts have been devoted to extend their fabrication to the nanoscale, using nanowires and nanotubes as building-blocks, because of their excellent sensing properties related to the high surface-to-volume ratio. The final aim of this new field of research is to improve the performance of current sensors by taking advantage of the unique and intrinsic properties of nanomaterials.

Up to now, the feasibility of using nanowires as basic elements of electronic devices, such as gas and optical sensors have been demonstrated, being possible the modeling of their electrical properties [2]. Nevertheless, the fabrication of these nanodevices has been hindered because of the manifold problems which arise to electrically access these nanostructures in a controlled and reproducible way. That is to say, the fabrication of electrical nanocontacts with high stability, low contact resistances and ohmic behaviour remains a challenge. To overcome this limitation, some fabrication strategies have been reported [3], demonstrating that reliable, reproducible and low-cost prototypes based on individual nanowires can be attained [2]. Nevertheless, most of these new technologies are still in their infancy.

In particular, the efficiency of Focused Ion Beam (FIB) lithography has been demonstrated elsewhere [4]. Using the abovementioned technique, the electrical access to individual nanomaterials is achieved fabricating metal nanocontacts according to a process which combines both electron and ion assisted platinum deposition. The resulting devices provide an excellent opportunity to study the electrical, optical and gas sensing properties of individual metal oxide nanowires [5].

Metal oxides' gas sensing characteristics are usually temperature-dependant; being the optimal working conditions unique for each material and gas molecule to be detected. Thus, the integration of nanowires in sensing devices requires the possibility of modulating their temperature with an easy-to-control and low power consumption system. Therefore, the combination of nanowires and suspended microhotplates is a promising solution. Microhotplates include microheaters that allow setting the working temperature up to 600 K. Their reduced dimensions guarantee thermal dynamics response much faster than the bulky counterparts, as well as having extremely low power consumption requirements. In this experimental approach, individual nanowires are placed onto a microhotplate, and contacted with FIB assisted techniques. In these sensing platforms, the size-reduction of the microhotplates, which are suspended by a few arms contribute to an important reduction in the

power consumption. For this reason, present development efforts are focused on the fabrication of even smaller hotplates with ultra-low power consumption.

In this contribution, our work to achieve this ambitious goal will be presented. Furthermore, these first prototypes can be combined with energy-scavenging technologies to have ultrafast circuits based on nanomaterials. In particular, we will discuss the possibility to develop self-powered gas sensing nanosystem. Despite the research and development of these devices are still ongoing, these technologies may overcome cost and size limitations of lab-class equipments, which are usually needed to work with nanomaterials.

References:

- [1] B. Hoffheins, in: R.F. Taylor, J.S. Schultz (Eds.), Handbook of Chemical and Biological Sensors, IOP Publishing, Bristol, 1996, pp. 371–397.
- [2] A. Kolmakov and M. Moskovits, *Annu. Rev. Mater. Res* **34** (2004) 151–180.
- [3] F. Hernandez-Ramirez, J. D. Prades, R. Jimenez-Diaz, O. Casals, A. Cirera, A. Romano-Rodriguez, J. R. Morante, S. Barth and S. Mathur, “Fabrication of Electrical Contacts on Individual Metal Oxide Nanowires and Novel Device Architectures” *Nanotechnology: Nanofabrication, Patterning, and Self Assembly*, Ed. C. J. Dixon and O. W. Curtines, Announced Novapublisher 2009 1st Quarter
- [4] F. Hernandez-Ramirez, A. Tarancon, O. Casals, J. Rodriguez, A. Romano-Rodriguez, J. R. Morante, S. Barth, S. Mathur, T. Y. Choi, D. Poulidakos, V. Callegari and P. M. Nellen, *Nanotechnology* **17** (2006) 5577-5583.
- [5] F. Hernandez-Ramirez, J. Rodriguez, O. Casals, E. Russinyol, A. Vila, A. Romano-Rodriguez, J.R. Morante, M. Abid, *Sens. Actuators, B, Chem* **118** (2006) 198–203.

Figures:

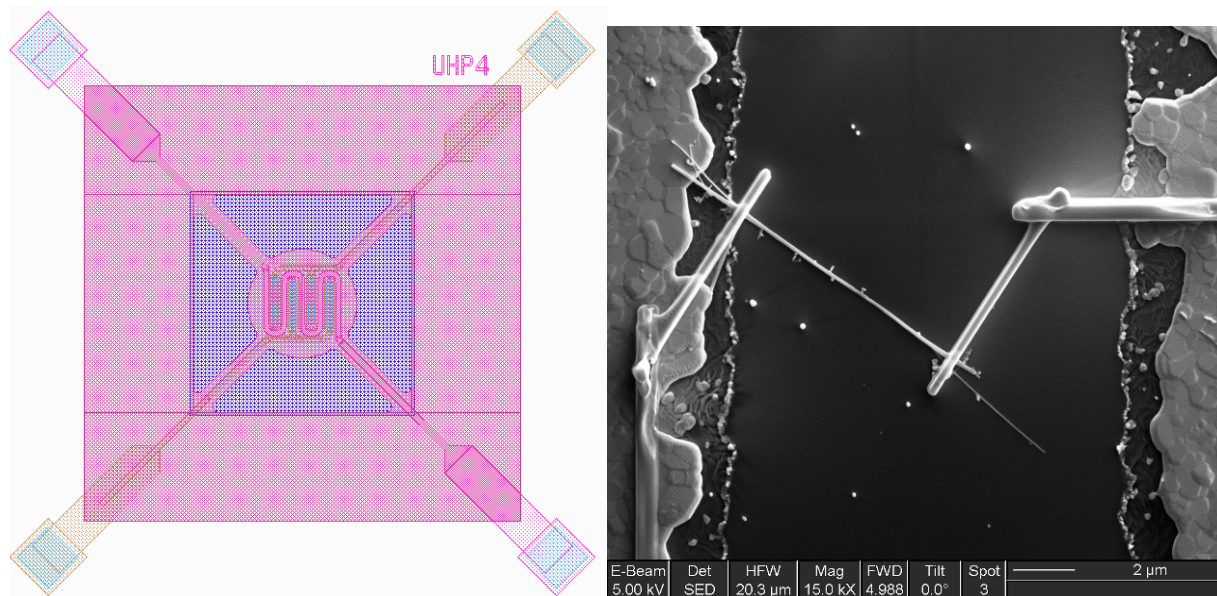


Figure 1. Left: Schematic of the design of a microhotplate with integrated heaters. Right: SEM micrograph of a single nanowire contacted on a microhotplate.

NANOBIOTECHNOLOGIES: TECHNOLOGY TRANSFER AND COMMERCIALIZATION IN SPAIN

Esteve Juanola-Feliu¹, Josep Samitier^{1,2}

¹CEMIC-Universitat de Barcelona, Martí i Franquès 1, Planta 2, Barcelona, Spain,

ejuanola@el.ub.es

²IBEC-Institute for Bioengineering of Catalonia, Baldiri Reixac 10-12, 08028 Barcelona,

Spain, jsamitier@ub.edu

This paper analyses the state of the art for nanobiotechnology commercialization, focusing on the scientific and economic challenges arising from nanomedicine.

Nanotechnology is an endless source of innovation and creativity at the intersection of medicine, biotechnology, engineering, physical sciences and information technology, and it is opening up new directions in R+D, knowledge management and technology transfer. Nanotechnology has already penetrated the market and, consequently, the competitive advantages of the more developed economies are threatened.

Nanotechnology is expected to make a rapid impact on society [1]: creation of future economic scenarios, stimulation of productivity and competitiveness, converging technologies, and new education and human development. Evidence for the rapid impact of nanotechnology can be gleaned from figures for government investment in nanotechnology R+D activities, facilities and workforce training. The 2008 USA National Nanotechnology Initiative budget request for nanotechnology R+D across the Federal Government was over US\$1.44 billion [2]. In Europe, the VIIth Framework Programme (FP) will contribute about €600 million per year to nanotechnology research until 2013, with an additional, similar amount being provided by individual countries. This gives Europe a larger yearly spend on nanotechnology than the United States or Japan [3].

Scientific papers and patents in the nanotechnology sector have grown exponentially over the last two decades. Products based on nanotechnology are already in use and analysts expect markets to grow by hundreds of billions of euros during the present decade. After a long R+D incubation period, several industrial segments are already emerging as early adopters of nanotech-enabled products [4]; in this context, surprisingly rapid market growth is expected and high mass market opportunities are envisaged for targeted research sub-segments (Figure 1). Findings suggest that the Bio&Health market is among the most challenging ones during the next years.

By the end of April 2009, the NanoSpain Network was up to 273 research groups and companies accounting over 1500 researchers. In 2007, there were 211 Spanish projects in the nano field (including 567 subprojects), involving 294 industries as partners or end users, as well as 5,000 researchers (2,400 doctors) [5]. Over 100 companies, research centres, technology centres and hospitals are currently members of the Spanish Nanomedicine Platform. Since 2004 the Spanish NanoTechnology Think Tank has sought to link public research institutions and private companies by exploiting innovative market opportunities from nanotechnologies. Over fifty applications in biomedicine and pharmacology, energy, electronics, ICT, aeronautics, chemistry and advanced materials have been launched onto the market in the search for development agreements [6]

Nanobiotechnology is a rapidly advancing area of scientific and technological opportunity that provides advances into the food industry, energy, environment and medicine. In the nanomedicine case, there is a wide range of technologies that can be applied to medical devices, materials, procedures, and treatment modalities. A closer look at nanomedicine introduces emerging nanomedical techniques such as nanosurgery, tissue engineering,

nanoparticle-enabled diagnostics, and targeted drug delivery. According to an expert group of the European Medicines Evaluation Agency (EMA), the majority of current commercial applications of nanotechnology to medicine are devoted to drug delivery. On the other hand, novel applications of nanotechnology include tissue replacement, transport across biological barriers, remote control of nanoprobes, integrated implantable sensory nanoelectronic systems and multifunctional chemical structures for targeting of disease.

In summary, a survey about nanobiotechnology commercialization is given laying emphasis on nanomedicine and its Spanish context, where research and medical applications are heavily funded by governments and private sector. Thus, Spain could strengthen its networks of science and technology parks, institutes and research centres, hospitals, technology platforms and incubators to meet the new scientific and market challenges provide by nanotech-related life sciences .

References:

- [1] Roco M.C., Bainbridge W.S. (2005). « Social implications of nanoscience and nanotechnology: Maximising human benefit », *Journal of Nanoparticle Research*, Vol. 7, p.1-13.
- [2] NNI (2007). « Research and Development Leading to a Revolution in Technology and Industry ». National Nanotechnology Initiative, Supplement to the President's 2008 Budget
- [3] Swarup A. (2007). « How Will Nanotech Fare in Europe? » http://sciencecareers.sciencemag.org/career_development/previous_issues/articles/2007_09_21/caredit_a0700136
- [4] Fuji-Keizai USA (2007). « Worldwide Market Research: Nanotechnology-based Product Market and Business Opportunities-Current & Future Outlook », February 2007
- [5] Spanish Strategic Action for Nanoscience and Nanotechnology, Ministry of Science and Innovation
- [6] Juanola-Feliu E. et al. (2004). « Spain Nanotechnology Think Tank 2004 », Fundación Española para la Ciencia y la Tecnología, ISBN 84-689-2723-6

Figures:

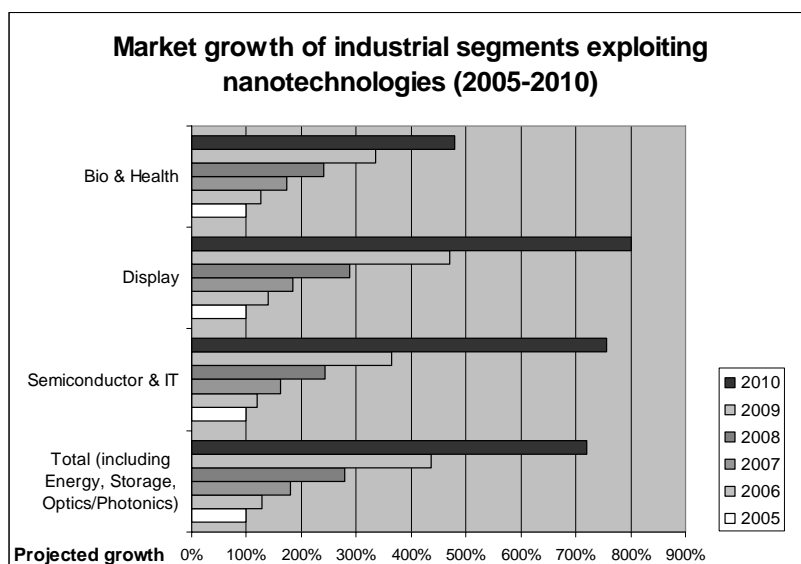


Figure 1: Chart based on Fuji-Keizai USA market research

ELECTROCHEMICAL CHARGING OF SINGLE WALLED CARBON NANOTUBES: AN IN-SITU RAMAN SPECTROELECTROCHEMICAL STUDY

Martin Kalbac,^{a,b,*} Ladislav Kavan^a, Lothar Dunsch^b

^a *J. Heyrovský Institute of Physical Chemistry, Academy of Sciences of the Czech Republic, v.v.i., Dolejškova 3, CZ-18223 Prague 8, Czech Republic. Fax: 420 2 6605 3804; Tel: 420 2 8658 2307; E-mail: kalbac@jh-inst.cas.cz*

^b *Leibniz Institute of Solid State and Materials Research, Dep. Electrochemistry and Cond. Polymers, Helmholtzstr. 20, D - 01069 Dresden, Germany. Fax: 49 351 4659 811 ; Tel: 49 351 4659 660*

In-situ Raman spectroelectrochemistry is a well established method to study the electronic structure of carbon nanostructures such as SWCNTs, DWCNTs and peapods. In contrast to chemical doping, electrochemistry allows a precise and well controlled doping of carbon nanostructures. The Raman spectra of SWCNTs are resonantly enhanced and thus by selection of the appropriate laser excitation energy an array of tubes is chosen which appear in the spectra. This allows a study of the effects of doping on metallic or semiconducting tubes in a separate way, even if the tubes are mixed in a sample. Recently, a number of spectroelectrochemical studies of SWCNTs was published both on bundles and individual tubes, which confirm the importance of Raman spectroelectrochemistry for the evaluation of the changes in electronic structure of carbon nanotubes upon doping. In general, the doping (electrochemical charging) of SWCNTs leads to a shift of the Fermi level. When the Fermi level reaches the energy of the Van Hove singularity, it suppresses the electronic transitions from/to this particular singularity. If the Raman signal is in resonance with this optical transition including such a singularity (E_{ii}^R) a strong bleaching of the Raman intensity for this feature is expected. However, we have recently shown that this simple model must be revisited.^[1]

We have inspected the Raman spectra of SWCNTs during electrochemical doping and focused the study on the detailed development of the radial breathing mode (RBM) of SWCNTs under precise control of the electrochemical charging. We show that the RBM band is changed already at early stages of the electrochemical doping, well before the Fermi level of the electrode reaches the energy of the Van Hove singularity which is responsible for resonance enhancement (optical transition E_{ii}^R). The intensity of the RBM changes for both the semiconducting and metallic tubes, but the dependence on the electrode potential has been found to be different for metallic and semiconducting tubes, due to the different electronic structure of these types of carbon nanotubes.

We found that the bleaching of the RBM band starts to occur at the potential where the first available electronic states are affected. This happens when the potential is changed from $E = 0$ V (in case of metallic tubes) or with a delay of about 0.5 or -0.5 Volts (in case of semiconducting tubes). It is important to emphasize that this in contrast to the general assumption that the spectra should be affected only if the Fermi level reaches the energy of the Van Hove singularity which is in resonance with excitation laser energy. Therefore, even at a low level of doping, significant changes in the electronic structure of carbon nanotubes occur and the electronic states cannot be considered as rigid if the SWCNTs are doped. The electronic conditions at the electrode surface with a nanotube layer are discussed in detail.

[1] M. Kalbac, L. Kavan, L. Dunsch. *J. Phys. Chem. C* **2008**, 112(43), 16759-16763.

STUDY ON THE EFFECT OF SOL-GEL PARAMETERS ON THE SIZE AND MORPHOLOGY OF SILICA MICROCAPSULES CONTAINING DIFFERENT ORGANIC COMPOUNDS

Idurre Kaltzakorta, Edurne Erkizia

*Labein-Tecnalia, Calle Geldo, Edificio 700, Parque Tecnológico de Bizkaia, Derio 48160,
BIZKAIA-SPAIN
ikaltzakorta@labein.es*

Microcapsules can be considered as small containers filled of active compounds that depending on the final application can contain a very wide range of different materials.

In the last years the importance of silica microcapsules has grown considerably due to their great chemical resistance, thermal stability, biocompatibility and environmental-friendliness.¹

Silica microcapsules with diameters in the range of nano, micro, and in some cases almost in the millimetre scale containing different organic compounds have been synthesized combining the sol-gel chemistry with the oil in water microemulsion technology.²

In the current study we have observed that variations in the pH of the reaction during the hydrolysis step, modifications in the silica/water ratio, or even the nature of the encapsulated organic compound, have dramatic effects in the type of shell obtained, the morphology and also in the particle size distribution.

References:

[1] C. J. Barbé, L. Kong, K.S. Finnie, S. Calleja, J.V. Hannah, E. Drabarek, D.T.Cassidy, M.G. Blackford, J. Sol-Gel Sci. Technol., **46** (2008) 393-409.

[2] B.Y. Ahn, S.I. Seok, I.C. Baek, S.I. Hong, Chem. Commun., **2** (2006) 189-190 and references therein.

Figures:

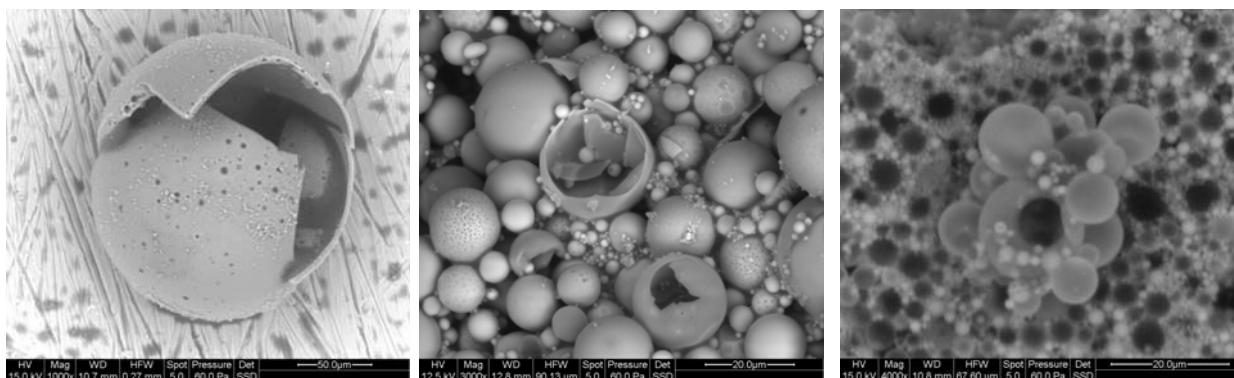


Fig. 1 Different capsules synthesized at different pH. The first image corresponds to a synthesis carried out at a pH of 2.2, the second one at pH 3.2 and the last one at pH 4.2.

Novel nano-template based quantum dot devices

A. Kam, P. J. Poole, D. Dalacu, G. Granger, S.A. Studenikin, R.L. Williams, G.C. Aers, A.S. Sachrajda
 Institute for Microstructural Sciences, National Research Council, Ottawa, Canada
alicia.kam@nrc.gc.ca

Semiconductor quantum dots have widely been viewed as a route to enabling quantum computing algorithms. For laterally gated quantum dots, one of the fundamental challenges towards realizing this goal has been the fabrication and integration of reproducible solid state qubits. Limitations arise from the inherent inhomogeneities that fabrication processes impart on these devices which in turn influence the wavefunctions required in quantum computing [1]. The implementation of nanotemplated structures, such as ridges and wires, for the fabrication of transport quantum dots structures is a novel technique which provides an avenue to addressing device reproducibility and scalability by confining 2DEG systems with minimized fabrication steps.

A series of quantum dot structures have been fabricated utilizing nanotemplate grown InP ridges with two types of embedded quantum wells: $\text{In}_x\text{Ga}_{1-x}\text{As}$ and $\text{InAs}_x\text{P}_{1-x}$ [2]. The electrostatic confinement of these dots was achieved by using various combinations and spacing of finger gates (Figure 1), while attenuation and optimization of the electron density and mobility in the 2DEG ridge structures were accomplished by varying the ridge width and growth parameters. Preliminary results indicate that electron mobility values of these ridges approach that of planar InGaAs/InP 2DEG structures, $\sim 100000 \text{ cm}^2/\text{Vs}$. Moreover, gated ridges exhibit mesoscopic characteristics, while transport data demonstrate Coulomb blockade peaks (Figure 2) – a clear indication of quantum dot formation.

It is envisioned that by designing and fabricating progressive 2DEG based controllable multiple quantum dot devices, as demonstrated, these structures can be integrated into functional quantum dot circuits with minimal effort. The devices presented would help to elucidate the confinement and transport properties of quantum dots in pre-patterned substrates.

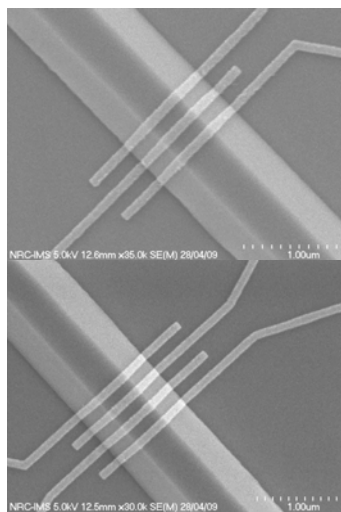


Figure 1: Gated ridges illustrating two types of gate combinations.

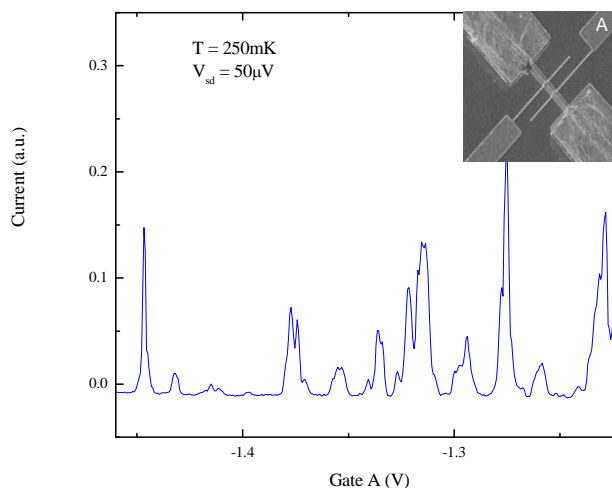


Figure 2: Coulomb blockade peaks through a quantum dot formed in ridge. Inset: gated ridge, $W=0.7 \mu\text{m}$, $L=5 \mu\text{m}$.

[1] R.W. Keyes, IEEE Computer Society, Computer, **38**, (2005) 65-69

[2] P.J. Poole, G.C. Aers, A. Kam, D. Dalacu, S. Studenikin and R.L. Williams, J. Crystal Growth, **310**, (2008)1069-1074

THE CHARACTERISTICS OF SILC IN SILICON OXIDE FOR SoC

Chang Soo Kang

Department of Electronic & Information Engineering, Yuhan University
185-34, Kwoiandong, Sosaku, Pucheon City, Kyunggido, 422-749, KOREA

E-mail cskang@yuhan.ac.kr

The traps are generated inside the oxides and at the oxide interfaces by the applied electric fields across the oxide and the flowing currents through the oxides in the nano scale structure for SoC. The trap charging and discharging currents can be explained by the flow of electrons into and out of traps generated by the stress high electric field. The traps are negatively charged near the cathode and positively charged near the anode respectively in the condition. The charge state of the traps can easily be changed according to the application of repetitively low electric fields after the stress high electric fields. Measurements have shown that the traps are relatively uniformly distributed throughout 113.4 to 814 silicon oxide thicknesses. In this study we present evidence that shows to the difference trap densities near anodes and cathodes of thicker oxides in the nanoscale structure. It was due to the charging and discharging after high electric field stressing.

The current was composed of three regions, the low level, pretunneling region, the tunneling region and the breakdown region. Onset tunneling voltage was measured 7.2[V] 9.2[V] 10.2[V] with fluence $1.07 \times 10^{-8} [\text{C}/\text{cm}^2]$, $1.02 \times 10^{-11} [\text{C}/\text{cm}^2]$, $1.19 \times 10^{-13} [\text{C}/\text{cm}^2]$ in the oxide thickness between 41 , 86 , 112 respectively. Prior to the onset of tunneling the currents were in the low ampere range. The current density according to the gate bias voltage was measured in the oxide thickness between 41 , 86 , 113.4 respectively has been shown Fig. 1.

The stress currents through an unstressed oxide measured during application of constant positive gate voltage and the transient currents through an unstressed oxide measured after application of constant positive gate voltage has been shown in Fig. 2.

The capacitor in this case was stressed at -17[V] for 100[sec] respectively. The transient currents were measured after the stress at 5[V] for 100[sec]. The transient currents after application of a voltage pulse for an oxide that had been stressed with either positive stress voltage or negative voltage has been shown in Fig. 3.

After the oxides had been stressed and traps had been generated in the oxides, the pretunneling currents and the discharge currents rose. The discharge currents have been adequately explained in terms of the tunneling front model. The pretunneling currents that flowed when the low measurement voltages were applied were also related to the charging of the stress generated traps. difference in these two charging currents had the $1/t$ time dependence that had previously been associated with the discharging of these traps by the tunneling front. Thus, by fitting the difference in the currents to a $1/t$ dependence, the charging of the traps in the oxide could also be explained by the tunneling front model.

Whenever the measurement polarity was changed, it was necessary that the one time only leakage current caused by the transient tunneling charging discharging of the traps. The stress induced leakage currents were measured on an 113.4 thick oxide fabricated on n type silicon after positive gate voltage stressing at 13V has been shown in Fig. 4.

The stress induced leakage currents measured after a high electric field stress showed a higher stress induced leakage currents than subsequent stress induced leakage currents.

The stress induced leakage currents showed a one time only leakage current whenever the measurement polarity was changed. This one time only leakage current was caused by the transient tunnel charging discharging of the traps near the interfaces. The stress induced leakage currents depend on trap location. The decay of the low electric field tunneling current was decided to use the increase in the stress induced leakage currents as a measure of trap distributions in the oxides. The stress induced leakage currents are related to trap assisted tunneling processes in thin oxides. The stress induced leakage currents are proportional to the

stress induced trap densities. The negative measurement electric fields sampled the traps near the substrate and the positive measurement electric fields sampled the traps near the gate.

The transient currents associated with low voltage pulses applied to thin oxide of the polysilicon gate Metal Oxide Semiconductor capacitors have been analyzed in terms of the charging and discharging of stress generated traps in the oxide. The tunneling front model was used to explain the $1/t$ time dependence of the decay current after application of a low voltage pulse. The transient currents were dependent on the stress polarity. The stress generated transient currents were relatively uniform the order of 10^{-11} - 10^{-15} [A] after a high field stress voltage.

The stress anode and cathode were used to attempt to find the differences in trap densities of silicon oxides for the nano scale structure. The traps are negatively charged near the cathode and positively charged near the anode respectively. The charge state of the traps can easily be changed according to the application of repetitively low electric fields after the stress high electric fields.

References

[1] J.C. Jackson, D.J. Dumin, "Electric breakdowns and breakdown mechanisms in ultrathin silicon oxides", Microelectronics Reliability, Vol. 39, pp. 171-179, 1999
 [2] B. De Salvo, G. Reimbold, "Study of stress induced leakage current by using high resolution measurements", Microelectronics Reliability, Vol. 39, pp. 797-802, 1999
 [3] E. Miranda, J. Sune, R. Rodriguez, M. Nafria, X. Aymerich, L. Fonseca, F. Campabadal, "Soft Breakdown Conduction in Ultrathin Gate Dielectrics", IEEE Transactions on Electron Devices, Vol. 47, No. 1, pp. 82 - 89, 2000

Figures

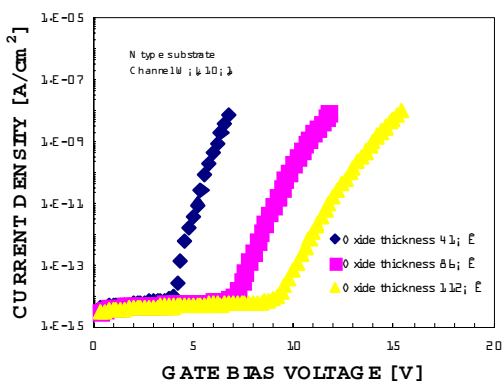


Fig. 1

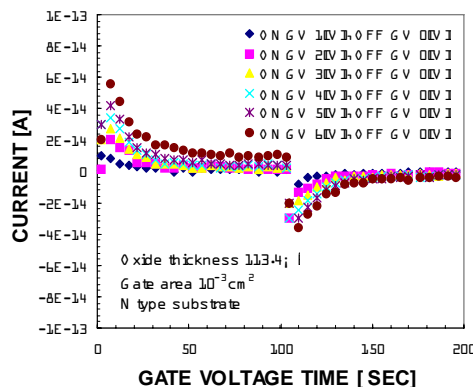


Fig. 2

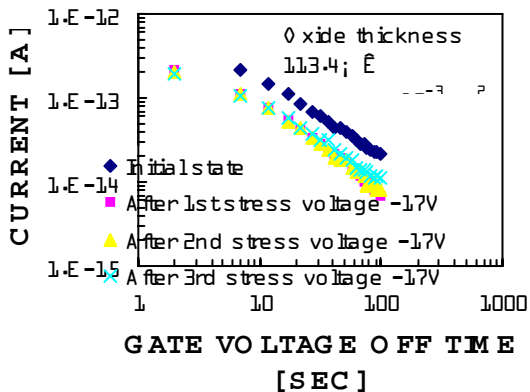


Fig. 3

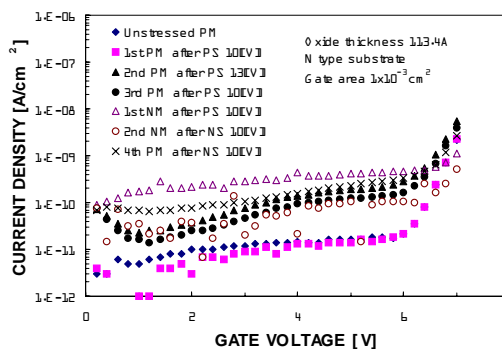


Fig. 4

CATALYTIC APPLICATION OF MESOPOROUS SILICAS IN SYNTHESIS OF SUBSTITUTED IMIDAZOLES UNDER MICROWAVE IRRADIATION AND SOLVENT-FREE CONDITIONS

Mahmood Kazemzad¹, Amir Ali Yuzbashi¹, Saeed Balalaie²

1. Materials and Energy Research Center, P.O.Box 14155-4777, Tehran, Iran

2. Department of Chemistry, K.N. Toosi University of Technology, PO Box 15875-4416, Tehran, Iran

kazemzad@gmail.com, a-yuzbashi@merc.ac.ir, balalaie@kntu.ac.ir

Mesoporous compounds, founded in 1992, are of great interest because of their remarkable properties, such as their large surface area and pore volume, narrow pore size distribution, and the ease with which their surface can be functionalized. There are many applications for these compounds namely hard template for nanopowder synthesis [1], molecular sieves [2], catalysis [3] and catalyst support [4]. Microwave-assisted rapid organic reactions, on the other hand, constitute an emerging technology, that make organic syntheses more effective and more eco-friendly than conventional reactions. Microwave-assisted synthesis of heterocyclic compounds is also being attended in combinatorial chemistry synthesis of fine chemicals and pharmaceuticals.

This report is focused on application of this technique for environmentally friendly synthesis of substituted imidazoles using SBA-15 mesoporous silica as an efficient catalyst. Some of tri and tetra substituted imidazoles have been known for several years in agrochemicals as herbicide, fungicide [5-6], and also in photography as photosensitive compound [7]. Moreover, compounds with the imidazole ring system have many pharmacological properties and play important roles in biochemical processes. In addition imidazole is the basic skeletal of imidazolium salts, well known as ionic liquids. The use of ionic liquids, composed entirely of ions with a melting point below 100 °C, has become one of the most prolific areas of research, due to their unique properties, including low volatility, high polarity, and good stability over a wide temperature range, as well as selective dissolving capacity with proper selection of cation and anion.

Mesoporous silica was briefly synthesized using a block copolymer as structure directing surfactant in aqueous solution of 2M HCl and Tetraethyl orthosilicate (TEOS) as silica source in hydrothermal condition. The catalytic reactions were done using a domestic microwave oven and a home made Teflon pot as reaction vessel. The reaction progress has been tracked by thin layer chromatography (TLC) and products were extracted by solvent following by crystallization in ethanol. Materials have been characterized using Fourier Transform Infrared (FT-IR), and Nuclear Magnetic Resonance (NMR) spectroscopies and BET surface area measurement methods.

All of the chemicals used were from MERCK, but block copolymers being an industrial co-emulsifier from Clariant and have been used without further purification. General procedure for imidazole synthesis started with 1 mM benzyl and equimolar amount of aldehyde in the presence of 4 times of stoichiometric amount of ammonium acetate as ammonia source. These substances were completely mixed together with 250 mg of the catalyst in a Teflon vessel and the mixture was irradiated by 2 minute microwave energy pulses up to elimination of aldehyde as limiting reagent. The total reaction time was between 6-10 min for different aldehydes.

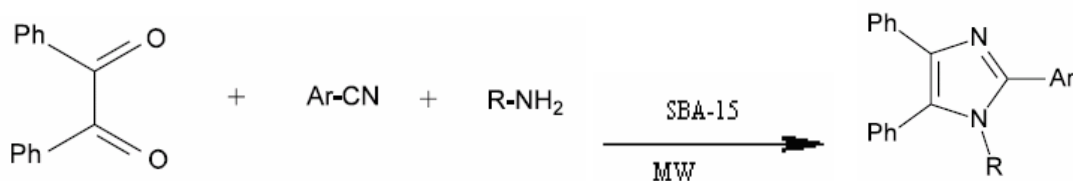
From our results, we can conclude that SBA-15 mesoporous silica is an efficient catalyst for synthesis of imidazoles. The surface area measured by BET nitrogen absorption method was in the range of 690-730 m²/g which is greater than that of silica gel used in our previous work as

catalyst for this reaction. Its pore volume is also larger than HY zeolite, we applied for the same reaction [8]. The melting point and TLC of products confirm the catalytic effect of mesoporous silica. Moreover, NMR and IR spectroscopy results obtained in this work is in good agreement with our previous experiments and further study on application of this catalyst is under investigation in our laboratory.

References:

- [1] Anhui Lu, Andreas Kiefer, Wolfgang Schmidt, and Ferdi Schth, Chem. Mater.(2004) 16(1), 100-103
 [2] M. Rozwardowski, M. Lezanska, K. Erdmann, Adsorption 11 (2005) 363–377
 [3] C.C. Pavel, R. Palkovits, F. Schüth, W. Schmidt, Journal of Catalysis 254 (2008) 84–90
 [4] Shih Yin Liu, Sze Ming Yang , Applied Catalysis A: General 334 (2008) 92–99
 [5] Liebl R, Handte R, Mildenberger H, Bauer K, Bieringer H (1989) Ger Offen DE 3,604,042
 [6] Pozhershkii AF, Soldatenkov AT, Katritzki AR, Hetrocycles in Life and Society. Wiley, NY pp 179-180
 [7] Satoru I (1989) Japan Kokkai Tokyo Koho JP 01, 117,867 [89,117,867]
 [8] Saeed Balalaie, Armin Arbanian, Mehri S. Hashtroudi; Monatschefte fur chemie, 131(2000) 945-948

Figures:



Non-Equilibrium Vertex Correction Theory in First Principle: From Specular to Diffusive Scattering in Fe/MgO/Fe Magnetic Tunnel Junction

Youqi Ke[1], Ke Xia[2], Hong Guo[1]

1, Physics Department of McGill University, Montreal, QC, H3A 2T8, Canada,

2, Department of Physics, Beijing Normal University, Beijing 100875, China

All realistic device properties are strongly influenced by or even built on these impurities. Examples are electron scattering by dopants in semiconductor nano-wires, spin scattering by disorder in magnetic tunnel junctions, and spin polarized current in dilute magnetic semiconductors. However, the presence of random impurities destroys the translational invariance, and the theoretical transport quantities must be averaged over all possible impurity configurations. The first principle analysis of nano-device is therefore seriously limited to the perfectly ordered systems. In this Poster, we present our recently developed formalism and numerical implementation of non-equilibrium vertex correct (NVC) theory which is a first principle solution of the *nonequilibrium* impurity average problem for quantum transport; and its applications to oxygen vacancy effect in Magnetic Tunneling Junction (MTJ) Fe/MgO/Fe.

For treating nonequilibrium quantum transport properties of nanoelectronic devices having atomistic substitutional disorder under external bias potential, our first principle formalism is developed based on carrying out density functional theory (DFT) within the Keldysh non-equilibrium Green's function (NEGF) framework, where the configurational average over random disorder is handled by a nonequilibrium vertex correction (NVC) theory at the density matrix level [1,3]. We use Coherent Potential Approximation to reconstruct translational invariance in the disordered Hamiltonian and one-particle Green's function; and use NVC to perform disorder average for the nonequilibrium density matrix that is determined by NEGF. the NEGF-DFT-NVC formalism is implemented within a tight-binding linearized Muffin tin orbital(TB-LMTO) electronic package. By using the NEGF-DFT-NVC theory, disorder effect to nonlinear and non-equilibrium quantum transport can be calculated from atomic first principles in a self-consistent and efficient manner.

The NEGF-DFT-NVC theory has been applied to investigate the significant physics of diffusive impurity scattering happening in the realistic Nano-Devices[1,2,3]. In this poster, as an application, we show some new results of the barrier defect scattering in the MTJ Fe/MgO/Fe. The roles of Oxygen Vacancy has been investigated in Fe/MgO/Fe Junction, in

which the Oxygen Vacancy is the major defect but is entirely neglected in all the previous first principle calculations. Our calculation shows a dramatic effect of oxygen vacancy scattering in the MgO barrier. the vacancies next to the interfaces can effectively scatter the electrons of d states in minority spin in electrodes into the s states with Delta 1 symmetry which can tunnel through MgO by suffering lowest decay rate, resulting in the huge increase in the Anti parallel conductance which reduces the TMR very much. Furthermore, the vacancy diffusive scattering inside the MgO barrier significantly increase the decay of s state with Delta 1 symmetry, which enhances the device resistance dramatically. So far, Our calculation has shown excellent agreement with the experiment of G.X.Miao et al (PRL,2008) by including oxygen vacancies in MgO barrier, the understanding about the big discrepancy between previous first principle calculations and experiments has been improved.

Reference:

- 1, Youqi Ke, Ke Xia and Hong Guo, *Phys. Rev. Lett.* 100, 166805 (2008).
- 2, Youqi Ke, Ferdows Zahid, V. Timoshevskii, Ke Xia, D. Gall, and Hong Guo, *Phys. Rev. B* 79, 155406 (2009)
- 3, *theoretical issues related to multiple impurity scattering in solid state devices (a book chapter to be published by Springer-Verlag).*

Specular to Diffusive Scattering in Fe/MgO/Fe Magnetic Tunnel Junctions

Youqi Ke[1], Ke Xia[2], Hong Guo[1]

1, Physics Department of McGill University, Montreal, QC, H3A 2T8, Canada,

2, Department of Physics, Beijing Normal University, Beijing 100875, China

Nanoelectronic device properties are usually influenced rather strongly by impurities and atomistic disorder. Examples are electron scattering by dopants in semiconductor nano-wires, spin scattering by disorder in magnetic tunnel junctions, and spin polarized current in dilute magnetic semiconductors. Theoretically, any calculated transport quantity must be averaged over the ensemble of possible impurity configurations. There has been no theoretical formalism and computational tool that can effectively carried out disorder averaging for nonequilibrium quantum transport problems. In this poster presentation, we report our recently developed formalism and numerical implementation of the non-equilibrium vertex correction (NVC) theory which is a first principles solution of the *nonequilibrium* impurity average problem for quantum transport. We apply this theory to investigate effects due to oxygen vacancy to spin polarized quantum transport in magnetic tunneling junction (MTJ) Fe/MgO/Fe.

To treat nonequilibrium quantum transport properties of nanoelectronic devices having atomistic substitutional disorder under external bias potential, our first principle formalism is based on carrying out density functional theory (DFT) within the Keldysh non-equilibrium Green's function (NEGF) framework, where the configurational average over random disorder is handled by a nonequilibrium vertex correction (NVC) theory at the density matrix level [1,3]. We use Coherent Potential Approximation to reconstruct translational invariance in the disordered Hamiltonian and one-particle Green's function; and use NVC to perform disorder average for the nonequilibrium density matrix that is determined by NEGF. The NEGF-DFT-NVC formalism is implemented within a tight-binding linearized Muffin tin orbital (TB-LMTO) electronic package. By using the NEGF-DFT-NVC theory, disorder effect to nonlinear and non-equilibrium quantum transport can be calculated from atomic first principles in a self-consistent and efficient manner.

The NEGF-DFT-NVC theory has been applied to investigate the significant physics of diffusive impurity scattering in the realistic nano-devices[1,2,3]. In this poster, as an application, we show new results of the barrier defect scattering in MTJ Fe/MgO/Fe. The

oxygen vacancy has been the major defect but is entirely neglected in all the previous first principle calculations. Our results show a dramatic effect of oxygen vacancy scattering in the MgO barrier. The vacancies next to the interfaces can effectively scatter electrons of d states in the minority spin channel of Fe into the s states with $\Delta-1$ symmetry which can tunnel through MgO by suffering the lowest decay rate. This leads to a huge increase of anti-parallel conductance and reduces the TMR significantly. Furthermore, the vacancy diffusive scattering inside the MgO barrier significantly increase the decay of s-state with $\Delta-1$ symmetry, which enhances the device resistance dramatically. By including oxygen vacancies in the MgO barrier, our calculated results are found to be in excellent agreement with the experimental data of G.X. Miao *et al* (PRL,2008).

Reference:

- 1, Youqi Ke, Ke Xia and Hong Guo, *Phys. Rev. Lett.* 100, 166805 (2008).
- 2, Youqi Ke, Ferdows Zahid, V. Timoshevskii, Ke Xia, D. Gall, and Hong Guo, *Phys. Rev. B* **79**, 155406 (2009)
- 3, *Theoretical issues related to multiple impurity scattering in solid state devices (a book chapter to be published by Springer-Verlag).*

NANOCLUSTERS IN TSALLIS NON-EXTENSIVE STATISTICAL MECHANICS

Ezat Keshavarzi^{*1,2} Mozhgan Sabzevari¹

¹*Department of Chemistry, Isfahan University of Technology, Isfahan, Iran, 8415683111*

²*Center of Excellence on Environmental Nanotechnology, Isfahan University of Technology, Isfahan, Iran, 8415683111*

* Corresponding author:

E-mail: keshavrz@cc.iut.ac.ir

Fax: +98-311-391-2350

Tel: +98-311-391-3281

Abstract

The mechanical and thermodynamic properties of nanoclusters, of much concern to nanotechnology, do not obey macroscopic thermodynamic principles. There are currently three approaches to Nano-thermodynamics of nanosystems (1) a modification of the Boltzmann–Gibbs statistics (BGS) adding subdivision energy, i.e., Hill's nanothermodynamics (2) non-equilibrium thermodynamics including work fluctuations and (3) the non-extensive statistics (NES) generalizing the BGS so as to take account of the non-extensive feature of such systems. In this study, we intend to investigate nanoclusters in the Tsallis nonextensive statistical mechanics while also defining the parameter q for them. The nonextensive entropy generalization in the classical thermo-statistics proposed by Tsallis [5] takes the following form

$$S_q = k_B \frac{1 - \sum_i P_i^q}{q - 1} \quad (1)$$

where, P_i is the probability of the i -th microstate, k_B is Boltzmann's constant, and q is an entropic index. In this study, we have shown that the non-extensivity in nanoclusters (L.J nanoclusters) may be categorized in the Tsallis statistical mechanics with an entropic index, q , slightly greater than unity. We have selected the L.J nanoclusters to study the problem of non-extensivity, due to its simplicity and the availability of molecular dynamic simulation results for them. For a typical nanocluster at a very low temperature, we may assume each atom to vibrate about its equilibrium position point with a nearly small amplitude (this assumption is, of course, only valid for a temperature range far below the melting points). Since nanoclusters do not rotate or translate, the complete partition function is:

$$Z_N = \dots \prod_{j=1}^{3N-6(5)} z_{vib,j} \quad (2)$$

where, $z_{vib,j}$ is the vibration partition function associated with the j th vibration frequency. The analytical form for $z_{vib,j}$ may be obtained via Tsallis statistical mechanics as :

$$z = \sum_{i=1}^w [1 + \beta(q-1)\varepsilon_i]^{-\frac{1}{1-q}} \quad (3)$$

$$\varepsilon_{i,j} = (i + \frac{1}{2})h\nu_j \quad (4)$$

Therefore the exact solution of the partition function of the vibration motion using the harmonic oscillator is:

$$z_{vib,j} = [(q-1)\beta h\nu_j]^{-\frac{1}{1-q}} \xi\left(\frac{1}{q-1}, \frac{1}{(q-1)\beta h\nu_j} + \frac{1}{2}\right) \quad (5)$$

In fact, the vibration partition function for such a system has been obtained using the harmonic oscillator approximation. The internal energy has been calculated and, as we expected, the internal energy of the nanoclusters is sub-extensive according to the results of the Molecular Dynamic Simulations. The temperature dependency of the internal energy and heat capacity has been investigated to show that the internal energy and its slope are different from those for macroscopic values, when ($q=1$).

An interesting finding in our work is that the result of internal energy of a nanocluster may be fitted in our derived equation by assuming $h\nu/k$ to be a temperature-dependent parameter. Finally, we have shown that ($q-1$) is related to the non-negligible surface effect in nanoclusters and that it approaches zero for very large clusters in which surface effect has no important role.

Processing, Fabrication and Mechanical Properties of Polymer Composites Filled With Covalently Functionalized Carbon Nanotubes

Valery N. Khabashesku¹, Merlyn X. Pulikkathara², Oleksandr V. Kuznetsov³

¹Department of Chemical and Biomolecular Engineering, University of Houston, Houston, TX, 77204, USA; ²Department of Chemistry, Rice University, Houston, TX, 77005, USA; ³Department of Physics and Astronomy, Rice University, Houston, TX, 77005, USA
valery@uh.edu

Remarkable mechanical strength and high aspect ratio of single walled carbon nanotubes (SWNTs) make them a highly attractive nanoscale materials for applications as a reinforcing fillers for structurally weaker polymers. Extensive research efforts are on dispersion and processing of SWNTs with different polymer materials and fabrication of SWNT-nanocomposites. Major challenge in these efforts is presented by the need to overcome strong Van der Waals forces between the individual nanotubes causing the formation of large bundles and ropes within which nanotubes tend to slide and decrease the strength of polymer composites filled with the SWNTs. This challenge is being addressed by adopting the nanotube sidewall functionalization through non-covalent and covalent methods. Besides debundling and improved dispersion, specific functional groups attached to the SWNTs can also provide for interfacial covalent bonding of the SWNTs to the polymer during the processing of the nanocomposites.

In the series of recent works [1-3], an array of methods of covalent functionalization to enable solubilization and dispersion of SWNTs in different solvents and polymer matrixes have been developed by the presenting author and his coworkers. SWNT derivatives carrying fluorine, short and long chain alkyls or perfluoroalkyl groups, terminal amino, amide, thioamide, hydroxyl, thiol and carboxyl moieties have been synthesized and characterized. Water soluble SWNTs functionalized with biomolecules, such as urea [4], aminoacids [5], glucose and sucrose [6], have also been prepared. These “tailored“ chemical modifications were shown to be particularly useful for creating multiple sites for covalent bonding of nanotubes to host matrices for enhancement of mechanical properties of thermoset (epoxy [7]), and thermoplastic (polyethylene [8], polypropylene [9] and Nylon-6 [10]) polymers. In the most of chemical modifications, fluorinated nanotubes (F-SWNTs) were used as precursor for subsequent sidewall functionalization. In our works, we have used the F-SWNTs either prepared in our lab by direct fluorination of purified SWNTs in a custom-built Monel apparatus or acquired from Carbon Nanotechnologies, Inc. (now Unidym).

Depending on the purity and aspect ratio of starting nanotubes, nature of functional group attached to the SWNTs, type of polymer, composite processing technique and fabrication temperature, and nanofiller (SWNT) content, enhancements of the tensile strength of composites filled with functionalized SWNTs were achieved in the range of 22% to 231 %. The highest strength increase (231%) was achieved with the functionalized nanotubes (F-SWNT) loading content into polymer matrix (Nylon 6) being as low as 0.5 wt.%. Evidences of in situ interfacial covalent bonding of SWNTs to the polymer have been obtained from Raman spectra demonstrating the shifts of the sp^3 C-C “D” mode in SWNT-nanocomposites in comparison with the unprocessed SWNTs and SEM images of composite fracture surfaces after the tensile test. The images (Figures 1 and 2) showed the ends of the polymer-coated nanotube ropes broken rather than pulled out which would be the case for composites filled with non-modified SWNTs. The broken tubes appear on these images as bright spots, some of which are shown on

the yellow circles. These results and the most recent data on polyethylene composites filled with “bi-functionalized” SWNTs will be presented and discussed.

The research was supported by Carbon Nanotechnology, Inc., NASA, Air Force, Navy, and in part by Awards No. RUE2-2659-MO-05 and No. RUE2 – 2894 – TI – 07 of the U.S. Civilian Research & Development Foundation for the Independent States of the Former Soviet Union (CRDF).

References:

- [1] V. N. Khabashesku, W. E. Billups, J. L. Margrave, *Acc. Chem. Res.* **35** (2002), 1087-1095.
- [2] V. N. Khabashesku, M. X. Pulikkathara, *Mendeleev Comm.* (2006), 61-66.
- [3] V. N. Khabashesku, O. V. Kuznetsov, M.X. Pulikkathara, *Carbon Nanotubes: Fluorinated Derivatives*, in *Nanomaterials: Inorganic and Bioinorganic Perspectives*. Ed. C.M. Lukehart and R.A. Scott, John Wiley & Sons, Ltd, , (2009), 856 p.
- [4] M. X. Pulikkathara, O. V. Kuznetsov, V. N. Khabashesku, *Chem. Mater.* **20** (2008), 2685-2695.
- [5] M. X. Pulikkathara, V.N. Khabashesku, *Izvestia Akad Nauk. Ser. Khim.* **57** (2008), 1035-1043 (Russ.); *Russ. Chem. Bull.* **57** (2008), 1054-1062 (Engl.).
- [6] O. V. Kuznetsov, M. X. Pulikkathara, R.F. M. Lobo, V. N. Khabashesku. *Russ. Chem. Bull.* (2009), in press.
- [7] J. Zhu, J. D. Kim, H. Peng, J.L. Margrave, V.N. Khabashesku, E.V. Barrera, *Nano Lett.* **3** (2003), 1107-1113.
- [8] M.X.Pulikkathara, O.V.Kuznetsov, I.R.G.Peralta, X.Wei, V.N.Khabashesku, *Nanotechnology*, **20** (2009), 195602-15.
- [9] D. McIntosh, V. N. Khabashesku, E. V. Barrera, *J. Phys. Chem. C*, **111** (2007), 1592-1600; *Chem. Mater.* **18** (2006), 4561-4569.
- [10] V. K. Rangari, M.Yousuf, S. Jeelani, M. X. Pulikkathara, V. N. Khabashesku. *Nanotechnology*, **19** (2008), 245703-12.

Figures:

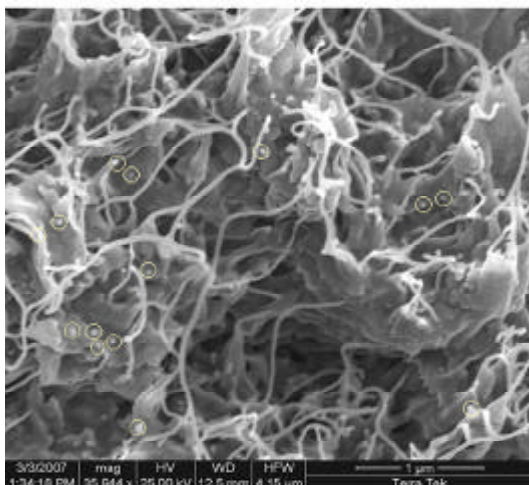


Figure 1. SEM image of the fractured surface of 0.5 wt% F-SWNT/Nylon-6 composite fiber showing the ends of the polymer-coated nanotube ropes broken rather than pulled out during the tensile test.

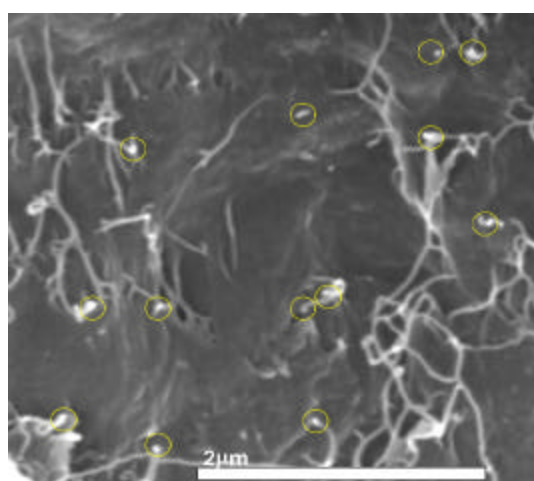


Figure 2. SEM image of the fracture surface of medium density polyethylene composite sample filled with 1 wt. % “bi-functionalized” F-SWNT-C₁₁F₃H₂ Derivative.

SYNTHESIS AND CHARACTERIZATION OF TITANIUM OXIDE – LEAD SULFIDE NANO HYBRID

Mohammadreza Khanmohammadi¹, Amir Bagheri Garmarudi^{1,2}, Nafiseh Khodami¹

1) Chemistry Department, Faculty of Science, IKIU, Qazvin, Iran.

2) Department of Chemistry & Polymer Laboratories, Engineering Research Institute, Tehran, Iran.

[*mrkhanmohammadi@gmail.com*](mailto:mrkhanmohammadi@gmail.com)

Sol-gel method has found increasing attention during recent years according to its high variety for the synthesis of materials. The nano materials synthesized via a sol-gel method exhibit high surface area and hence have an advantage over conventional materials for potential applications as catalyst or semiconductor [1-4]. In the other hand, semiconductor nanocrystals in transparent media have been the focus of attention due to their promising applications in non-linear optics and optical switches [5-6]. TiO₂ has been applied to a variety of environmental problems especially in water and air purification. It has antibacterial properties and is useful in the purification of water against different bacteria. One of the limiting factors, associated with the efficiency of photocatalysis is the fast recombination of charge carriers in the system. To challenge with this problem, it has been suggested that the coupling of semiconductors with appropriate energy levels can produce a more efficient photocatalyst via better charge separation. The SNCs like PbS or CdS have been introduced into TiO₂/SiO₂ matrix, although the content of NCs is lower (5–10 mol%). PbS is the most interesting for this aim. As the direct band gap energy of the bulk lead sulfide is 0.41 eV, this characteristic makes PbS clusters a good material for high-speed photonic switch applications. PbS NCs are suitable as saturable absorbers in Q-switched or mode-locked lasers. Composite SNCs in TiO₂ matrix are considerable because of their application in solar cells and optoelectronic devices. In this research a binary phase material was prepared by sol-gel via: hydrolysis, sol formation, condensation to gel, un-reacted material removing and finally calcinations. Titanium oxide and lead sulfide were the ingredients of synthesized nano hybrid. TiO₂-PbS nanocomposite was prepared by tetraisopropyl orthotitanate (TIPT) and lead acetate precursors. Liquid state sol and chemical changes during the hydrolysis and polycondensation processes were also monitored. Mechanism of sol-gel formation has been also investigated by several spectroscopic techniques but FTIR spectroscopy seems to be of interest because of its sensitivity and selectivity, while no sample preparation step is required prior to analysis. Thus, the sol-gel synthesis of PbS–TiO₂ nanocomposite has been monitored by FTIR spectroscopy.

References:

- [1] A. Fujishima, T.N. Rao, D.A. Tryk, J. Photochem. Photobiol. C: Photochem. Rev. 1, 1–21 (2000).
- [2] M. Gartner, R. Scurtu, A. Ghita, M. Zaharescu, M. Modreanu, C. Trapalis, M. Kokkoris, G. Kordas, Thin Solid Films, 455–456, 417–421 (2004).
- [3] S.G. Deng, Y.S. Lin, AIChE J., 41, 559 (1995).
- [4] L.L. Hench, J. West, Chem. Rev., 90, 33 (1990).
- [5] J. Fick, in: H.S. Nalwa (Ed.), Handbook of Surfaces and Interfaces of Materials, Vol. 3, Academic, San Diego, 2001.
- [6] A.D. Yoffe, Adv. Phys. 50, 1 (2001).

SINGLE-WALLED CARBON NANOTUBES: GROWTH OVER VARIOUS CATALYSTS AND ELECTRONIC PROPERTIES

*I.I. Khodos¹, O.V. Kononenko¹, V.T. Volkov¹, V.N. Matveev¹, Yu.A. Kasumov¹, A.A. Firsov¹,
D.V. Matveev², M.A. Knyazev¹*

¹Institute of Microelectronics Technology and High Purity Materials, Russian Academy of Sciences (RAS), 142432 Chernogolovka, Moscow Region, Russia

²Institute of Solid State Physics, Russian Academy of Sciences (RAS), 142432 Chernogolovka, Moscow Region, Russia

khodos@iptm.ru

A task of obtaining identical carbon nanotubes by chemical vapour deposition (CVD) requires careful study of catalytic nanoparticles used for nanotube growth, because a nanotube structure is largely defined by that of a catalytic particle [1]. It is also generally accepted that in order to use the nanotubes as building blocks for electronic devices, it is necessary to incorporate the nanotube growth or deposition into standard CMOS technological chain [2]. This means in particular that the nanotubes should be grown on silicon wafers with a SiO₂ layer. But a question emerges: how to assess the state of the catalyst on such a substrate? In this work we present a technique allowing to study the structure of both catalytic nanoparticles and nanotubes on SiO₂ with high spatial resolution. The technique is based on using a thin SiO₂ membrane. 20 nm SiO₂ film is deposited by electron beam evaporation onto freshly cleaved NaCl crystals. The crystals are then dissolved in water, leaving the SiO₂ film floating on the surface. The film is then transferred onto common transmission electron microscopy copper grids by dipping them into the water. Resulting SiO₂ membranes are then used for thin intermediate Al buffer layer and islanded catalytic film deposition. Our studies revealed to our surprise that these membranes sustain carbon nanotube growth, and can also be used to study the grown nanotubes and the state of catalytic nanoparticles after the CVD nanotube synthesis.

An islanded iron film (catalyst for nanotube synthesis) on an intermediate 10 nm thick Al film [3] were deposited on SiO₂ membranes by two ways: electron beam evaporation and rf-sputtering. The thickness of the Fe film was 0.5 nm and 2 nm. After the catalyst deposition samples were annealed in the vacuum furnace at the temperatures of 100°C and 800°C. Then the nanotubes were synthesized by a method of single injection of acetylene [4] at the pressure of 2.5 mbar and temperature of 950°C.

The membranes were studied in a transmission electron microscope immediately after the nanotube synthesis. It was found that such parameters as the size, and density of catalytic particles, the type and diameter of carbon nanotubes, and even amorphous carbon coating of nanotubes and nanoparticles depend on catalyst deposition technique (fig.1). The narrowest diameter distribution of catalytic particles, and, accordingly, nanotube diameters was observed in case of deposition of 0.5 nm Fe/Al bilayer using electron beam evaporation and subsequent annealing at 100°C (fig.1c).

Using the optimized catalyst the single-walled carbon nanotubes (SWNT) were grown on oxidized silicon substrates selectively on 10x30 μm² catalyst patterned rectangles. Pd electrodes were subsequently deposited onto the surface of the samples with the synthesized nanotubes using electron beam lithography. The example of six nanotubes lying between two Pd electrodes is shown in Fig. 2. Resistance of four two-terminal structures containing from three to eight SWCNTs connected in parallel between Pd contacts was measured. The resistance was in the range from 15 to 50 kOhm. The electrodes to individual nanotubes were also prepared (fig.3) using a bilayer of 3 nm Pd / 50 nm Al, but in this case the resistance was much higher (200 kOhm and more).

This work has been supported by the International Science and Technology Center, grant no. 3836.

References:

- [1] Y. Zhang, Y. Li, W. Kim, D. Wang, H. Dai, *Appl. Phys. A* 74 (2002) 325.
 [2] Y.-C. Tseng, P. Xuan, A. Javey, R. Malloy, Q. Wang, J. Bokor and H. Dai, *Nano Lett.*, 4 (2004) 123.
 [3] L. Delzeit, B. Chen, A.M. Cassel, R. Stevens, C. Nguyen, M. Meyyappan M, *Chem. Phys. Lett.* 348 (2001) 368.
 [4] Yu. A. Kasumov et al, *Appl. Phys. A* 88 (2007) 687.

Figures:

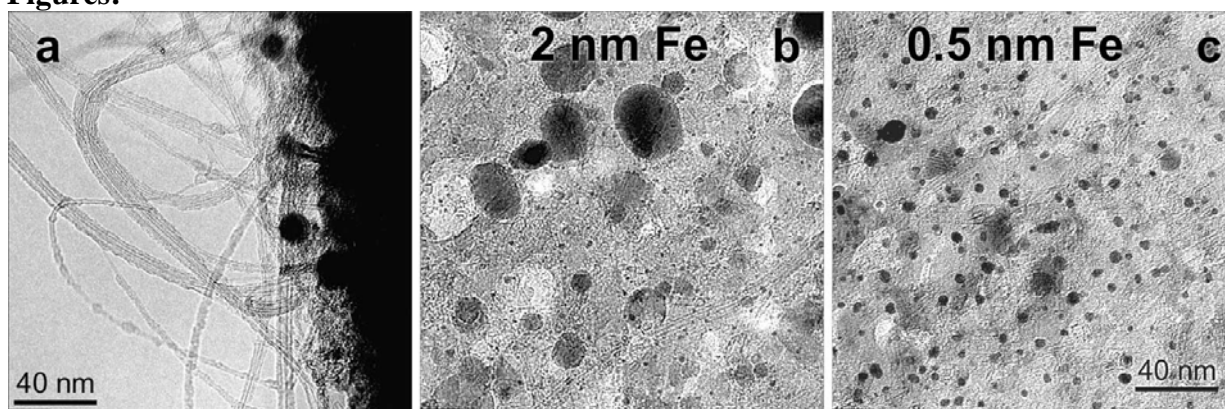


Figure 1: **a)** TEM image of single-walled carbon nanotubes on the edge of a folded SiO_2 membrane. **b,c)** TEM image of Fe particles on alumina over thin SiO_2 membranes after synthesis of carbon nanotubes. Catalyst (Fe) film thickness - 2 nm **(b)**, 0.5 nm **(c)**.

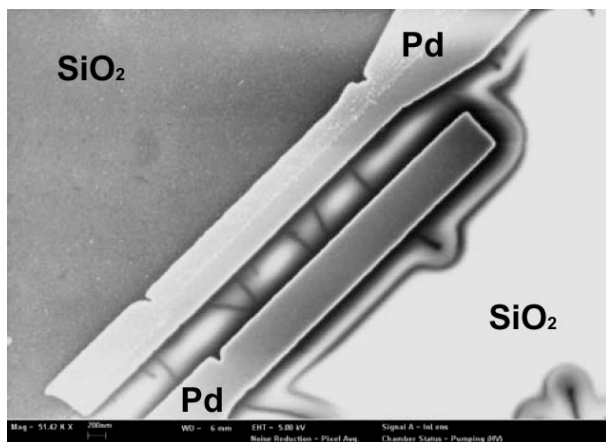


Figure 2: SEM image of two-terminal structure for electrical characterization of SWNTs. Six nanotubes contacted by two Pd electrodes. Difference in brightness of SiO_2 substrate is due to charging.

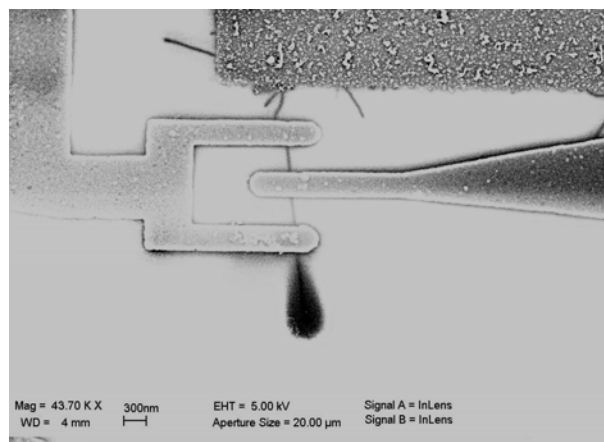


Figure 3: SEM image of a carbon nanotube grown from a large catalyst Al/Fe pad (top right). The nanotube lying on an insulating surface (SiO_2) is contacted by two electrodes. The end of the nanotube is charged. A Si substrate below SiO_2 film acts as a back gate.

NEXAFS and Photoemission Spectroscopy Study for O-Phthalaldehyde (OP) molecule on the H-terminated Si(001) Surface.

Ki-jeong Kim, Bongsoo Kim

Beamline Research Division, Pohang Accelerator laboratory (PAL), POSTECH, Pohang, Kyongbuk 790-784, Republic of Korea

The organic layers and lines on silicon surfaces has been very interesting research subject with scientific point of view as well as technological point of view. The hybrid between the organic materials and the silicon surface provides pathways of the molecular electronics.

1D self-directed line growth through radical chain reactions is particular interest since the line growth could provide the connecting wire in molecular devices and the patterning of molecular nano scale devices.

Density functional calculation tells that O-Phthalaldehyde (OP) grows self-directly 1D molecular lines on the H-terminated Si(001) surface. The bonding mechanism between Op molecule and Si surface atoms is studied using Near Edge X-ray Fine Structure (NEXAFS) and photoemission spectroscopy.

CONDUCTION AND ELECTROLUMINESCENCE FROM ORGANIC CONTINUOUS AND NANOFIBER THIN FILMS

Xuhai Liu¹, Jakob Kjelstrup-Hansen¹, Kasper Thilsing-Hansen¹, Henrik H. Henrichsen², and Horst-Günter Rubahn¹

¹NanoSYD, Mads Clausen Institute, University of Southern Denmark, Alsion 2, DK-6400 Sønderborg, Denmark

²DTU Nanotech, Department of Micro- and Nanotechnology, Technical University of Denmark, Building 345Ø, DK-2800 Kgs. Lyngby, Denmark
jkh@mci.sdu.dk

Organic nanofibers and thin films made from para-hexaphenylene (p6P) molecules exhibit a range of extraordinary properties with application potential, such as the ability to emit intense blue light after either UV excitation or electron and hole injection, while the semiconducting properties enable field-effect transistor (FET) applications. Organic nanofibers have been shown to act as optical waveguides and random lasers, while chemical functionalization of the molecular building blocks can be used to tailor the nanofiber optoelectronic properties for a given application [1]. Connection to electrodes makes the probing of their electrical properties possible [2] and represents an important step towards the realization of a nanoscale organic light-emitting device.

The nanofibers are grown by physical vapour deposition of p6P onto a specific growth substrate, where the organic molecules self-assemble into a discontinuous thin film, made of straight, mutually parallel and crystalline, fiber-like nanostructures [3]. Following the growth process, the nanofibers are transferred to a pre-fabricated device substrate by gentle stamping, which does not destroy the otherwise fragile van der Waals bonded molecular crystals. The device substrate consists of an interdigitated array of gold electrodes placed on a 200 nm thick layer of silicon dioxide on highly doped silicon as shown in fig. 1. The underlying silicon acts as a backgate electrode in a FET configuration. In order to allow for quantitative evaluation of the effect of crystalline nanofiber growth on the electric and electroluminescence properties of the resulting device, thin film devices have also been fabricated by deposition of the p6P molecules directly on the device substrate. This procedure leads to a non-singlecrystalline thin film with arbitrarily oriented molecular absorbers and emitters.

The devices have been characterized both in terms of their electrical transport properties and their ability to emit light. Both the nanofiber and the thin film devices exhibit a clear influence of the backgate voltage on the current-voltage characteristics. Biasing such organic semiconductor devices in a FET configuration with an AC signal applied to the backgate electrode enables efficient injection of both carrier types into the organic material and thereby results in emission of light through radiative electron-hole recombination [4]. In this paper, parameters for distinctive blue light emission and for charge transport from continuous thin film devices (fig. 1) as well as from discontinuous nanofiber arrays are discussed.

References:

- [1] M. Schiek, F. Balzer, K. Al-Shamery, J. R. Brewer, A. Lützen, and H.-G. Rubahn, *Small*, **4** (2008) 176
- [2] H. H. Henrichsen, J. Kjelstrup-Hansen, D. Engstrøm, C. H. Clausen, P. Bøggild, and H.-G. Rubahn, *Org. Electron.*, **8** (2007) 540
- [3] F. Balzer and H.-G. Rubahn, *Appl. Phys. Lett.*, **79** (2001) 3860
- [4] T. Yamao, Y. Shimizu, K. Terasaki, and S. Hotta, *Avd. Mater.*, **20** (2008) 4109

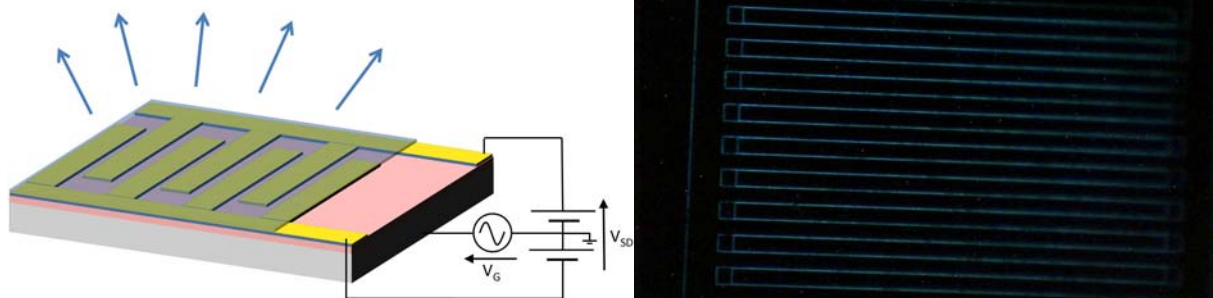
Figures:

Figure 1 (left): Device structure consisting of a silicon substrate with a 200 nm silicon dioxide layer and an interdigitated array of gold electrodes upon which the organic material is placed. (Right): Blue light is observed from the device upon application of a DC source-drain voltage and an AC gate voltage.

RAMAN SPECTROSCOPY OF GRAPHENE IN DIFFERENT DIELECTRIC ENVIRONMENTS

Ph. Klar and C. Casiraghi

Freie Universität Berlin, Arnimallee 14, Berlin, Germany

Philipp.Klar@FU-Berlin.de

Graphene, a monolayer of sp^2 hybridized carbon atoms, has a unique electronic structure with a zero gap and quasiparticles behaving like massless Dirac fermions [1]. Its extremely high carrier mobility makes it a promising candidate for future electronics [1]. However, its carrier mobility has been shown to vary from sample to sample and to be limited to $\sim 10000 \text{ cm}^2/\text{Vs}$ [2,3]. Furthermore, unintentional doping and excess charges up to 10^{13} cm^{-2} have been reported for pristine graphene, deposited on silicon substrate covered with silicon oxide (Si/SiO_x), [4]. Thus, charged impurities seem to be the dominant source of charge scattering in graphene. For this reason, it is fundamental to investigate the origin of charged impurities. Since graphene is unprotected from the environment, the strength of scattering by charged impurities should be strongly dependent on the dielectric environment [3]. On the other side, charged impurities could be in the substrate. Indeed, the highest carrier mobility ($2 \times 10^5 \text{ cm}^2/\text{Vs}$) has been measured on suspended graphene [5].

Raman spectroscopy is a widely used method for the study of graphene: it can identify graphene [6], monitor the charge carrier concentration [7,8] and probe disorder [9] and edges [10]. In particular, the Raman G and 2D bands positions and intensities are sensitive to the amount of excess charges [4,11] and they can be used to distinguish between disorder and doping effects [9].

Here we use Raman spectroscopy in order to investigate the effect of the dielectric environment and the substrate on the charged impurities of graphene. Graphene samples were produced by micro-mechanical exfoliation of graphite and deposited on Si/SiO_x and Calcium Fluoride (CaF_2) substrates. Water, ethanol and chloroform, which have a relative permittivity of 80, 30 and 4.8 respectively, have been used as a top dielectric layers: a drop of dielectric was placed on graphene deposited on Si/SiO_x , and then the sample was covered with a glass slide to avoid evaporation of the dielectric during the Raman measurement. We observed strong variations in the Raman spectra during the first 30 minutes after immersion; then the spectra stabilize and no variations are observed until evaporation of the dielectric. We show that ethanol mainly introduces disorder in graphene, since graphene tends to roll and wrinkle, after interaction with ethanol; water and chloroform, in contrast, mainly produce chemical doping. In particular a strong p-doping has been observed in the case of chloroform, where an upshift of 15 cm^{-1} has been measured for the 2D peak position. Thus, a change in the environment can produce strong variations in the Raman spectrum, but the strength of this variation is not directly correlated with the change in permittivity.

We finally show the Raman spectrum of graphene deposited on CaF_2 . The analysis of the Raman fit parameters shows that graphene deposited on CaF_2 is un-doped and without disorder, and virtually comparable with suspended graphene. This suggests that the charged impurities are mainly related with the Si/SiO_x substrate.

References:

- [1] A. K. Geim and K. S. Novoselov, *Nature Materials* **6**, 183 (2007).
- [2] Y.-W. Tan *et al.*, *Physical Review Letters* **99**, 246803 (2007).
- [3] Ponomarenko L. A *et al.*, *Phys. Rev. Lett.* **102**, 206603 (2009).
- [4] C. Casiraghi *et al.*, *Applied Physics Letters* **91**, 233108 (2007).
- [5] K.I. Bolotin *et al.*, *Sol. State Comm.* **146**, 351 (2008)
- [6] A.C.Ferrari *et al.*, *Phys. Rev. Lett.* **97**, 187401 (2006)
- [7] S. Pisana *et al.*, *Nat. Mater.* **6**, 198 (2007)
- [8] A. Das *et al.*, *Nature Nanotech.* **3**, 210 (2008)
- [9] C. Casiraghi, rapid PSS, in press
- [10] C. Casiraghi *et al.*, *Nano Lett.* **9**, 1433 (2009)
- [11] D. M. Basko *et al.*, arXiv:0906.0975v2 (2009)

ICOSAHEDRAL Ti-Zr-Ni THIN FILMS

¹A. Kocjan, ¹G. Dražič, ¹P. McGuinness, ²E. Sarantopoulou, ²Z. Kollia, ²A.C. Cefalas, ¹S. Kobe

¹*Jozef Stefan Institute, Department for Nanostructured Materials, Jamova 39, SI-1000 Ljubljana, Slovenia*

²*National Hellenic Research Foundation, TPCI, Athens 11635 Greece*

Icosahedral (i-phase) quasicrystals have many tetrahedral interstitial sites, which are structurally favourable for hydrogen absorption, making them good candidate as a hydrogen-storage material. It has been reported [1, 2] how Ti–Zr–Ni quasicrystals can absorb large amounts of hydrogen, equivalent to an M/H value of 1.7. Qiang et al. [3] reported that single-phase quasicrystals can be obtained by the casting method at the compositions of $Ti_{40}Zr_{40}Ni_{20}$ and $Ti_{33}Zr_{44}Ni_{18}Cu_5$, and a bulk glassy alloy is formed at the composition of $Ti_{12}Zr_{55}Ni_{13}Cu_{20}$. In our previous work we have demonstrated that it is possible to store up to 2 % of hydrogen to the nanocrystalline powder with the composition of $Ti_{40}Zr_{40}Ni_{20}$ prepared by melt-spinning followed by crushing the ribbons and subsequent hydrogenation [4].

In the present work we report the results of analytical electron microscopy study of $Ti_{40}Zr_{40}Ni_{20}$ based thin films, prepared by pulsed laser deposition at 157 nm.

Precursors for pulsed laser deposition were prepared by arc-melting of $Zr_{65,9}Ni_{34,1}$ alloy and Ti powder in such a ratio, that final material composition should be close to $Ti_{40}Zr_{40}Ni_{20}$. Sample was heated up to 1400°C by RF induction and melt was injected through the nozzle by 200 mbar of argon over-pressure on rotating copper wheel of 200 mm diameter. For pulsed laser deposition Fluorine laser (wavelength 157 nm) was used with energy of 20 mJ/pulse, repetition rate of 15 Hz and ablation time of 2 hours. Distance to the substrate was 0.5 cm and alumina, graphite and sapphire were used as a substrate. Nanoparticles, prepared with pulsed laser deposition were transferred to lacy-carbon copper grid. Analytical work was done on a Jeol 2010 F field-emission gun TEM equipped with a Link ISIS EDXS system (UTW Si(Li) detector) and Gatan PEELS.

In samples prepared by pulsed laser deposition (on sapphire substrates) nanosized particles, with a diameter up to 5 nm were observed (Fig. 1a). On HRTEM images we could not detect any particle with 5 or 3-fold symmetry, characteristic for quasicrystals (Fig. 1b). To establish if this lack of i-phase is the consequence of chemical composition we performed quantitative EDXS analysis on numerous particles. The spread of the results (defined as relative standard deviation of measurements) was 9% in the case of Ti, 8% in the case of Zr and 25% in the case of Ni. Using standards for quantitative analysis and all precautions during spectra collection (absorption correction was neglected due to very small thickness of the particles) the relative standard deviation of the measurement should not exceed 5 %. We could state that the particles inside the sample prepared with pulsed laser deposition were chemically not homogeneous. In the continuation of our experiments we calculated the composition of the basic target alloy on the basis of Ni losses and we succeeded in the preparation of films much closer to the ideal composition for the processing of i-phase ($Ti_{40}Zr_{40}Ni_{20}$). In the present paper the results of high resolution analytical microscopy and EDXS analyses will be presented.

References:

1. Viano, A.M., Majzoub, E.H., Stroud, R.M., Kramer, M.J., Misture, S.T., Gibbons, P.C., Kelton, K.F., *Phil. Mag. A* 78 (1998) 131–141
2. Kelton K. F. and Gibbons, P. C., *MRS Bulletin* 22(11) (1997) 69
3. Qiang, J., Wang, Q., Wang, Y., Huang, H., Wu, J., Dong, C., *Materials Science and Engineering A* 448-451, (2007) 565–568
4. A. Kocjan, P.J. McGuinness, A. Recnik, S. Kobe, Direct production of the Ti-Zr-Ni-Cu icosahedral phase for hydrogen-storage applications by rapid quenching from the melt, in press *JALCOM*.

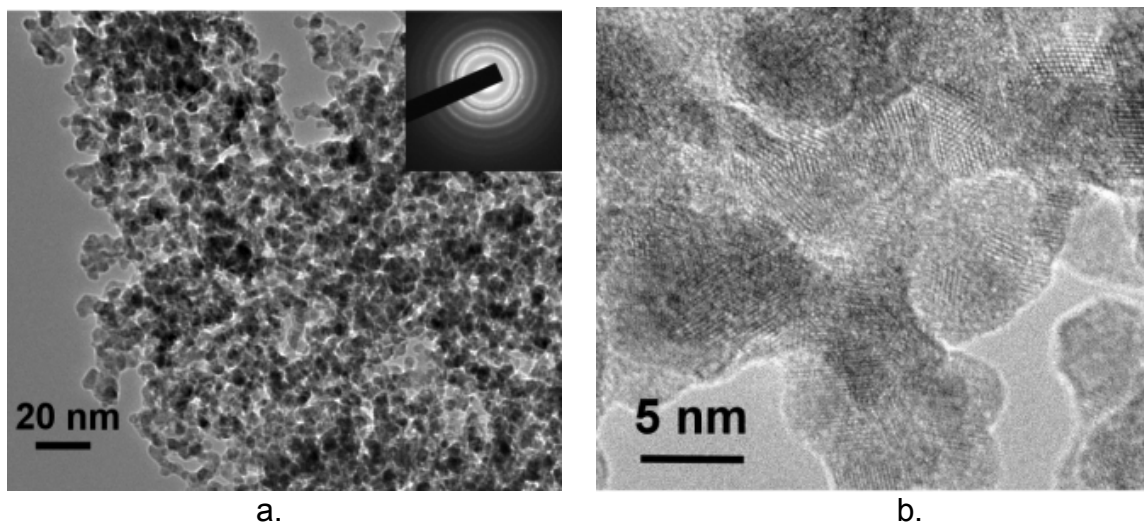


Fig 1. a – TEM micrograph and SAED pattern (inset) of the sample prepared with pulsed laser deposition, b - HRTEM image of the particles

Spin-atomic vibration interaction and spin-flip Hamiltonian of a single atomic spin

*Satoshi Kokado*¹, *Kikuo Harigaya*², and *Akimasa Sakuma*³

¹*Faculty of Engineering, Shizuoka University, Hamamatsu, Japan*

²*Nanotechnology Research Institute, AIST, Tsukuba, Japan*

³*Graduate School of Engineering, Tohoku University, Sendai, Japan*

tskokad@ipc.shizuoka.ac.jp

Recently, magnetic properties for molecular magnets and atomic spins have been extensively studied toward the development of ultimate microscopic elements for mass-storage devices and quantum information devices [1-3]. In the field of data storage, quantum spin systems with bistable states, which contribute to 1 bit of information storage, are expected to be an ideal memory element. A typical energy producing the bistable states is a uniaxial anisotropy energy, $-|D|S_z^2$, with D being the uniaxial anisotropy constant. Materials with such an energy are Mn_{12} of $S=10$ [4] with $|D|=0.06$ meV and a single Fe atom on a CuN surface of $S=2$ with $|D|\simeq 1.55$ meV [1]. In particular, this Fe atom may have the potential of a single atomic memory.

Regarding the spin system with $-|D|S_z^2$, it is known that the spin relaxation has a strong influence on the spin switching time (i.e., the writing time of data), and so on [3]. An origin of the spin relaxation is considered to be the spin-atomic vibration interaction V_{SA} , because the atomic vibration energy is usually in the range of 0.041 meV - 41 meV (10^{10} s^{-1} - 10^{13} s^{-1}) which is comparable to energy-level spacings of spin systems. To our knowledge, however, the concrete expression of V_{SA} has not been reported so far.

In this paper, we derived V_{SA} and the spin-flip Hamiltonian V_{SF} of a single atomic spin in the crystal field, using the perturbation theory for the spin-orbit (SO) interaction in which the difference of displacement between the nucleus and the electron, $\Delta\vec{r}$, is taken into account (see Fig. 1). For the case of Fe^{2+} , we investigated the presence or absence of V_{SA} and V_{SF} for any parameter sets. In addition, the magnitude of their coefficients was roughly estimated.

The perturbation energy for the SO interaction is obtained as, $V = V_A + V_{SA} + V_{SF}$, with

$$V_A = DS_z^2 + E(S_x^2 - S_y^2), \quad (1)$$

$$V_{SA} = \sum_{\mu,\nu=x,y,z} S_\mu \left(\Lambda_{\mu,\nu}^{(1)} a_\nu + \Lambda_{\mu,\nu}^{(2)} a_\nu^\dagger \right) + \sum_{\mu,\nu,\xi=x,y,z} S_\mu S_\nu \left(\Lambda_{\mu,\nu,\xi}^{(1)} a_\xi + \Lambda_{\mu,\nu,\xi}^{(2)} a_\xi^\dagger \right), \quad (2)$$

$$V_{SF} = \sum_{\mu,\nu=x,y,z} \Gamma_{\mu,\nu} S_\mu S_\nu. \quad (3)$$

Here, V_A is the so-called anisotropy spin Hamiltonian [5], where E is the biaxial anisotropy constant. The operator S_μ is the spin operator in the direction of μ , and a_ν^\dagger (a_ν) is the creation (annihilation) operator of the atomic vibration in the direction of ν . The coefficients $\Lambda_{\mu,\nu}^{(i)}$, $\Lambda_{\mu,\nu,\xi}^{(i)}$, and $\Gamma_{\mu,\nu}$ contain the matrix element of the orbital angular momentum, and so on.

We now focus on Fe^{2+} ($3d^6$) in a crystal field of the tetragonal symmetry. In this case we consider only one down-spin electron because the up-spin shell is filled. The above-

mentioned coefficients are therefore calculated by using the following orbital state:

$$|\phi_i\rangle = C_i \left(|d_i\rangle + \sum_{d_j(\neq d_i)} c_{d_j}^{(i)} |d_j\rangle + \sum_p c_p^{(i)} |p\rangle \right), \quad (4)$$

with $C_i = (1 + \sum_{d_j(\neq d_i)} |c_{d_j}^{(i)}|^2 + \sum_p |c_p^{(i)}|^2)^{-1/2}$, $|c_{d_j}^{(i)}|^2 \ll 1$, and $|c_p^{(i)}|^2 \ll 1$, where the energy level for $|\phi_i\rangle$ is written as E_i . Here, $|d_i\rangle$ is the dominant d orbital, while $|d_j\rangle$ and $|p\rangle$ are the other d orbital and the p orbital in the atom, respectively. Owing to the d-d and d-p hybridizations in the atom, $|d_j\rangle$ and $|p\rangle$ are included in $|\phi_i\rangle$. The hybridizations originate from, for example, the mixing of atomic orbitals via the surrounding ions.

On the basis of expressions of the coefficients, we investigate the presence or absence of V_{SA} and V_{SF} , where $c_{d_j}^{(i)} = c_d$ and $c_p^{(i)} = c_p$ are set (see Table 1). The interaction V_{SA} exists for $\Delta\vec{r} \neq 0$ and $c_p \neq 0$, although it vanishes for $\Delta\vec{r} = 0$. Namely, the d-p hybridizations as well as $\Delta\vec{r} \neq 0$ play an important role in the presence of V_{SA} . On the other hand, V_{SF} is present for $c_d \neq 0$ even when $\Delta\vec{r} = 0$. The d-d hybridization is essential for the presence of V_{SF} .

When $|\Delta\vec{r}|/|\Delta\vec{r}_n| = 0.5$, $c_d = c_p$, and $\sum_d |c_d|^2 + \sum_p |c_p|^2 = 0.2$ are set, where $\Delta\vec{r}_n$ is the displacement of the nucleus, we estimate the magnitude of the coefficients of V_{SA} and V_{SF} as follows: The largest coefficient of V_{SF} divided by $|D|$ is 0.2, while that of the second term of V_{SA} divided by $|D|$ is 0.1. Also, the largest coefficient of the first term of V_{SA} divided by $|\lambda|$ is less than 10^{-4} , where λ is the SO interaction constant.

References:

- [1] C. F. Hirjibehedin, C.-Y. Lin, A. F. Otte, M. Ternes, C. P. Lutz, B. A. Jones, A. J. Heinrich, *Science* **317** (2007) 1199.
- [2] S. Kokado, K. Ueda, K. Harigaya, and A. Sakuma, *Phys. Rev. B* **76** (2007) 054451.
- [3] S. Kokado, K. Harigaya, and A. Sakuma, *phys. stat. solidi (c)*, in press.
- [4] A. Caneschi, D. Gatteschi, and R. Sessoli, *J. Am. Chem. Soc.* **113** (1991) 5873.
- [5] K. Yosida, *Theory of Magnetism* (Springer Series, New York, 1998) chap. 3.

Figure and Table:

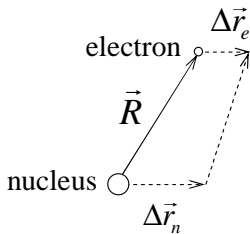


Fig. 1 : Positions and displacements of the nucleus (large circle) and the electron (small circle). The difference of displacement between the nucleus and the electron is given by $\Delta r = \Delta\vec{r}_e - \Delta\vec{r}_n$, where $\Delta\vec{r}_n$ is the displacement of the nucleus, and $\Delta\vec{r}_e$ is that of the electron. In addition, \vec{R} is the position vector of the electron measured from the nucleus.

Table 1 : The presence or absence of V_{SA} and V_{SF} for each set of $\Delta\vec{r}$, c_d , c_p . The presence and absence are represented by \bigcirc and \times , respectively.

		V_{SA}	V_{SF}
$\Delta\vec{r}=0$	$c_d=0, c_p=0$	\times	\times
	$c_d=0, c_p \neq 0$	\times	\times
	$c_d \neq 0, c_p=0$	\times	\bigcirc
	$c_d \neq 0, c_p \neq 0$	\times	\bigcirc
$\Delta\vec{r} \neq 0$	$c_d=0, c_p=0$	\times	\times
	$c_d=0, c_p \neq 0$	\bigcirc	\times
	$c_d \neq 0, c_p=0$	\times	\bigcirc
	$c_d \neq 0, c_p \neq 0$	\bigcirc	\bigcirc

PREPARATION OF SIZE-CONTROLLED SILVER NANOPARTICLES BY THE HYDROTHERMAL METHOD

Noritsugu Kometani, and Takeshi Teranishi
 Department of Applied Chemistry, Osaka City University
 3-3-138 Sugimoto, Sumiyoshi-ku, Osaka, Japan
kometani@a-chem.eng.osaka-cu.ac.jp

Noble metal nanoparticles (NPs) have been extensively studied owing to many intriguing properties such as high catalytic activity, remarkable optical properties arising from the localized surface plasmon resonance, and so on. In recent years, Ag NPs have been drawing much attention as a new material for constructing the wiring patterns on electric circuit boards by means of the printing technology. From the viewpoint of such applications, developing the cost-effective method to produce a large quantity of size-controlled Ag NPs is an important subject for study. We recently examined the hydrothermal synthesis of Ag NPs by using the flow-type high-temperature high-pressure reactor and demonstrated that it would be promising for the large-scale synthesis of Ag NPs [1]. Here, we report that the size and morphology of Ag NPs produced by this method can be controlled by adjusting the reaction conditions such as temperature, pressure and flow rate.

Fig. 1 shows the schematic diagram of the flow-type high-temperature high-pressure reactor system used in this study. This reactor system was designed to allow the rapid mixing of two kinds of solutions under hydrothermal conditions. Two kinds of aqueous solutions containing 1.5 mM AgNO₃ and 30 g dm⁻³ polyvinylpyrrolidone (PVP) (solution A) or 15 mM sodium citrate and 30 g dm⁻³ PVP (solution B) were prepared with a distilled water. These solutions were individually fed into the tubular reactor made of stainless steel (1/8 inch o.d and 1.755 mm i.d) by two intelligent high pressure pumps (Jasco co. Pu-2080) and mixed at a T-shaped junction (SS-200-3, Swagelok) inside of the reactor. An orifice having a pinhole with 0.5 or 1.0 mm diameter was installed inside the T-shaped junction if needed. The reactor was immersed in a thermostated salt bath to control reaction temperature between 200–350°C and pressure was adjusted between 15–40 MPa by a back-up pressure regulator. The produced Ag NPs were analyzed by an optical absorption spectroscopy with a V-530 UV-vis spectrophotometer (Jasco co.) and a transmission electron microscopy (TEM) with an H-7000 microscope (Hitachi).

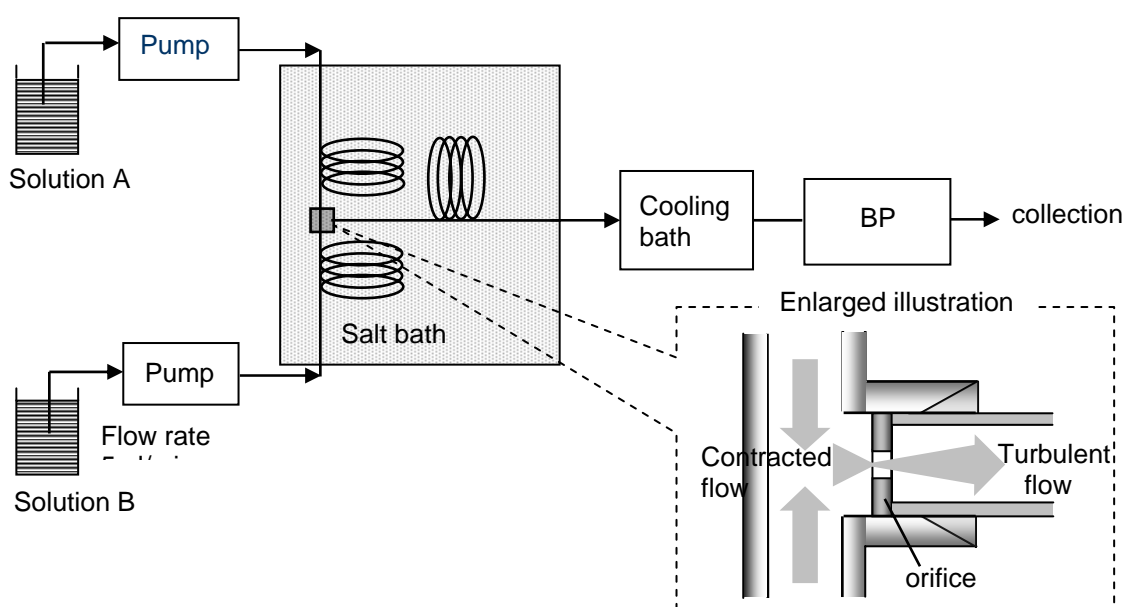


Figure 1: Schematic diagram of experimental reactor system used in this study.

We began with synthesizing Ag NPs at different pressures (15, 20, 23, 30, 40 MPa) and at fixed temperature, 300°C. The absorption spectra of obtained colloidal solutions were characterized by a distinct band at about 400 nm for all pressures, which was attributed to the localized surface plasmon (LSP) resonance of Ag NPs. The intensity of LSP band increased with pressure from 15 MPa to 20 MPa while it turned to decrease above 23 MPa. It was found that yellow precipitate was accumulated inside the filter at pressures above 30 MPa, indicating the considerable aggregation of Ag NPs. The TEM image and size distribution of Ag NPs obtained under typical condition (23 MPa) were shown in Fig. 2. The average diameters of Ag NPs estimated from TEM images are 13.8 ± 5.3 , 17.5 ± 6.8 , and 18.1 ± 6.6 nm for 15, 20, and 23 MPa, respectively. At 30 and 40 MPa, most of NPs are larger than 100 nm and the size was rather inhomogeneous.

Next, Ag NPs were synthesized at fixed pressure, 20 MPa, and at different temperatures, 200, 250 and 350°C. For all temperatures, the sizes of obtained Ag NPs were less homogeneous than those for 300°C. In particular, the colloidal solution obtained at 200°C showed no distinct SP band, suggesting that only small amount of Ag NPs were produced. It is interesting that Ag NPs obtained at 350°C have a variety of shapes like rods, triangles and squares, implying a possible control of morphology by tuning the reaction condition. However, most of Ag NPs obtained at this temperature were larger than 100 nm. Based on the above observations, it is concluded that the optimal reaction conditions for the synthesis of fine and homogeneous Ag NPs are $T=300^\circ\text{C}$ and $P=20\sim 23$ MPa, respectively.

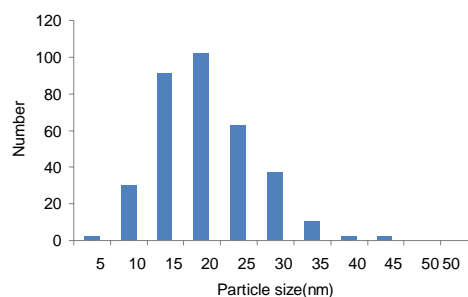
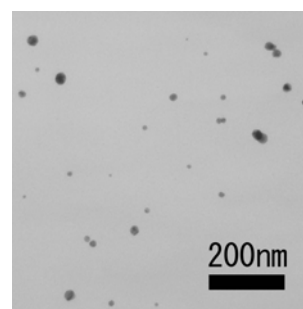
We finally examined the effect of an orifice installed inside the reactor. As seen in Fig. 1, the flow path is narrowed by the orifice. This causes the contracted and turbulent flow before and after the orifice, resulting in the effective mixing of two reaction solutions at the T-shaped junction. When the orifice with 0.5 or 1.0 mm diameter was installed, the average sizes of Ag NPs produced at 300°C and 20 MPa were 13.7 and 16.4 nm, respectively. These values are significantly smaller than that without the orifice inside the reactor (17.5 nm). Furthermore, the size distribution became more homogeneous when we used the orifice. It is thus obvious that the use of orifice is of benefit for the synthesis of fine and homogeneous Ag NPs by the present method.

Acknowledgment:

This work is a part of the Osaka Central Area Industry-Government-Academia Collaboration Project on “City Area Program” sponsored by MEXT (Ministry of Education, Culture, Sports, Science & Technology, Japan), 2007–2009. This work is also partially supported by KAKENHI (20510079), MEXT.

References:

[1] N. Kometani, et al., *J. Soc. Mater. Sci. Jpn. (Zairyo)*, **58** (2009) 481-485.



Figures: TEM image and size distribution of Ag NPs prepared at 300°C and 23 MPa.

Band selection and disentanglement using maximally-localized Wannier functions: the cases of Co impurities in bulk copper and the Cu (111) surface

Richard Korytár¹, Miguel Pruneda¹, Javier Junquera², Pablo Ordejón¹, Nicolás Lorente¹

¹*Centro de investigación en nanociencia y nanotecnología (CSIC - ICN),
Campus de la UAB, E-08193 Bellaterra, Spain*

²*Departamento de ciencias de la Tierra y física de la materia condensada,
Universidad de Cantabria, E-39005 Santander, Spain*

rkorytar@cin2.es

We have adapted the maximally-localized Wannier function approach of [1] to the density functional theory based **Siesta** method[2] and applied it to the study of Co substitutional impurities in bulk copper as well as to the Cu (111) surface. In the Co impurity case, we have reduced the problem to the Co d-electrons and the Cu sp-band, permitting us to obtain an Anderson-like Hamiltonian from well defined density functional parameters in a fully orthonormal basis set. An important insight into the impurity problem is provided by the projected density of states onto the impurity Wannier functions (Fig. 1), showing sharp spin and crystal field polarized peaks. This confirms the picture of a localized state weakly perturbed by the continuum.

In order to test the quality of the Wannier approach to surfaces, we have studied the electronic structure of the Cu (111) surface by again transforming the density functional problem into the Wannier one. This can be in turn diagonalized (Fig. 2), showing that an excellent description of the Shockley surface state is attained, permitting us to be confident in the application of this method to the study of magnetic adsorbates in the presence of an extended surface state.

[1] I. Souza, N. Marzari, and D. Vanderbilt, Phys. Rev. B **65**, 035109 (2001).

[2] J. M. Soler et al., Journal of Physics: Condensed Matter **14**, 2745 (2002).

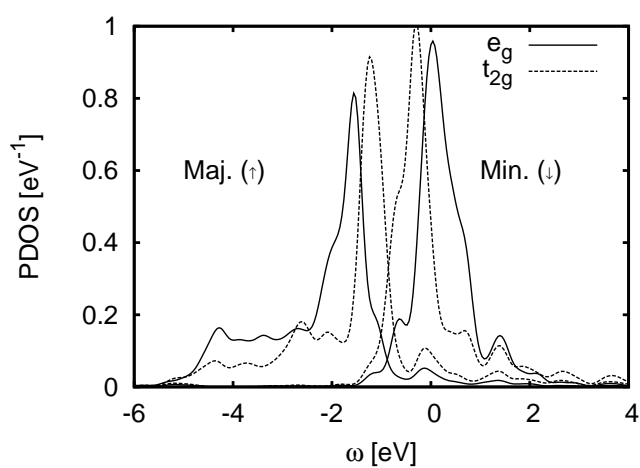


FIG. 1: Cobalt Wannier-function projected density of states for both spins. Zero energy coincides with Fermi level.

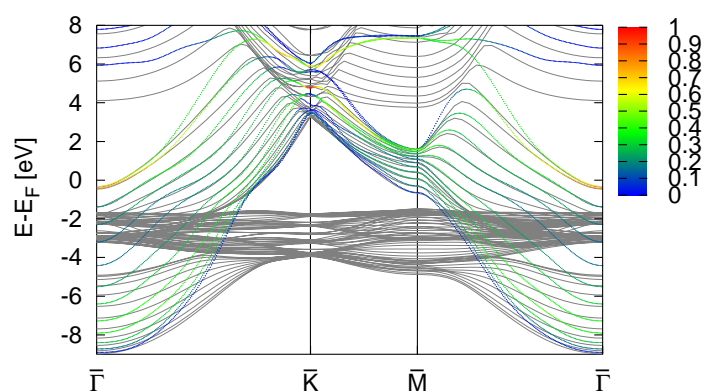


FIG. 2: Comparison of ab-initio band structure (grey) with the Wannier (color) of a Cu (111) slab. Color indicates the admixture of surface Wannier functions to the eigenstate.

**PRODUCT BASIS SET IN TDDFT: MOLECULAR ABSORPTION SPECTRA
WITHIN LINEAR RESPONSE.**

Peter Koval and Dietrich Foerster
CPMOH - France

We propose a new basis set [1] and corresponding method [2] to calculate of the Kohn-Sham density response function.

Computational cost of our method scales comparatively cheaply with the number of atoms N .

Here we discuss the application of our technique to the computation of molecular absorption spectra. Spectra are calculated directly in $O(N^2)$ operations from the Gross-Petersilka-Gossmann equations [3].

References:

[1] Foerster~D, J. Chem. Phys. 128 034108 (2008)

[2] Foerster~D, Phys. Rev. B 72 073106 (2005)

[3] Petersilka M, Gossmann U J and Gross E K U, Phys. Rev. Lett. 76 1212 (1996)

Magnetoresistance in positive and negative exchange bias Ni/FeF₂ bilayered antidots

M. Kovyлина¹, M. Erekhinsky², R. Morales³, J.E. Villegas⁴, I. K. Schuller², A. Labarta¹ and X. Batlle¹

¹ *Departament de Física Fonamental and Institut de Nanociència i Nanotecnologia (IN2UB), Universitat de Barcelona, 08028 Barcelona, Catalonia, Spain*

² *Physics Department, University of California-San Diego, La Jolla 92093, California, USA*

³ *Departamento de Física, Universidad de Oviedo-CINN, Oviedo 33007, Spain*

⁴ *Unite Mixte de Physique CNRS/Thales, Universite Paris Sud, 91405 Orsay, France*

miroslavna@ffn.ub.es

The comprehensive explanation of the exchange bias phenomenon (EB) in nanostructured materials still remains a challenge, despite the number of experimental and theoretical investigations [1]. We used focused ion beam lithography to fabricate a series of ordered arrays of antidots, as a function of the antidot-antidot distance in the x - y plane (Fig.1). The fabrication was performed on bilayered samples prepared by electron beam evaporation consisting of antiferromagnetic (AF) FeF₂ (70nm), ferromagnetic (FM) Ni (50nm) and Al (4nm) as a protective layer. FeF₂ was epitaxially grown on top of single crystalline MgF₂, while the FM layer was polycrystalline. The antidots were fabricated in a square/rectangular array, with antidot size of 200 nm and x and/or y antidot-antidot distances within the range 120-900 nm. The antidot density was set within 5% and 55%. Atomic force and scanning electron microscopy were used to characterize the quality of the nanostructures. Magnetoresistance (MR) measurements were carried out to determine the exchange bias field (loop shift) in both continuous thin films and nanostructures. MR was measured with the standard four probe technique in the temperature range 4.2 K – 300 K up to 50 kOe. The magnetic field was applied either parallel or transversal to the in plane easy magnetization axis of the AF, while the in plane current was set parallel to the latter. The resistivity was measured at various field cooling conditions (from 100 Oe to 50 kOe). The measuring field was applied parallel the cooling field.

Three types of behaviour were observed: for small cooling fields, MR curves display a shift towards negative field values (negative EB), while for large cooling fields the shift is positive (positive EB) (Fig.2). At intermediate cooling fields, two MR peaks are observed (one shifted to negative fields; the other one shifted to positive fields), whose relative height and area depend on the cooling field. However, in all cases the absolute value of the exchange bias field is almost independent of the cooling field, at a given antidot density. Consequently, the AF domain size is suggested to be comparable to or larger than the FM domain size, such that each FM domain couples only to one AF domain with a particular direction of the EB [2]. Therefore, for small/large cooling fields we have only one EB direction, while two directions appear for intermediate cooling fields. Finally, it is worth stressing that both the magnetization reversal mechanisms (domain nucleation and propagation and non-uniform rotation) and switching from positive to negative EB depend on the antidot density. We have developed a model based on the micromagnetic simulations that allow accounting for all the foregoing results.

The funding from the Spanish MEC through a FPU grant, Spanish CICYT project MAT2006-03999 and from the Catalan DURSI (2005SGR00969) are acknowledged.

References:

[1] O. Iglesias, A. Labarta, X. Batlle, *Journal of Nanoscience and Nanotechnology*, **8** (2008) 2761; J. Nogués and I. K. Schuller, *J. Magn. Magn. Mater.*, **192**, (1999) 203.

[2] O. Petravic, Z.P. Li, I. V. Roshchin, M. Viret, R. Morales, X. Batlle, and I. K. Schuller, *Appl. Phys. Lett.*, **87** (2005) 222509; I. V. Roshchin, O. Petravic, R. Morales, Z.P. Li, X. Batlle and I.K. Schuller, *Euro. Phys. Lett.*, **71** (2005) 297; R. Morales, Z.P. Li, O. Petravic, X. Batlle, and I.K. Schuller, *Appl. Phys. Lett.*, **89** (2006) 072504.

Figures:

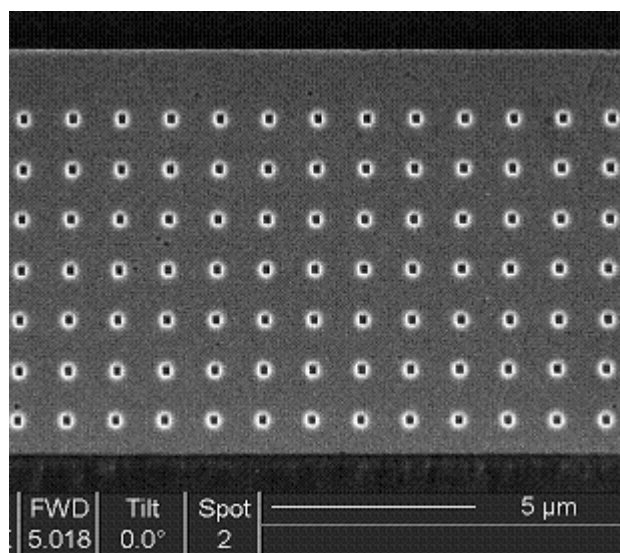


Fig.1. SEM image for square array antidots.

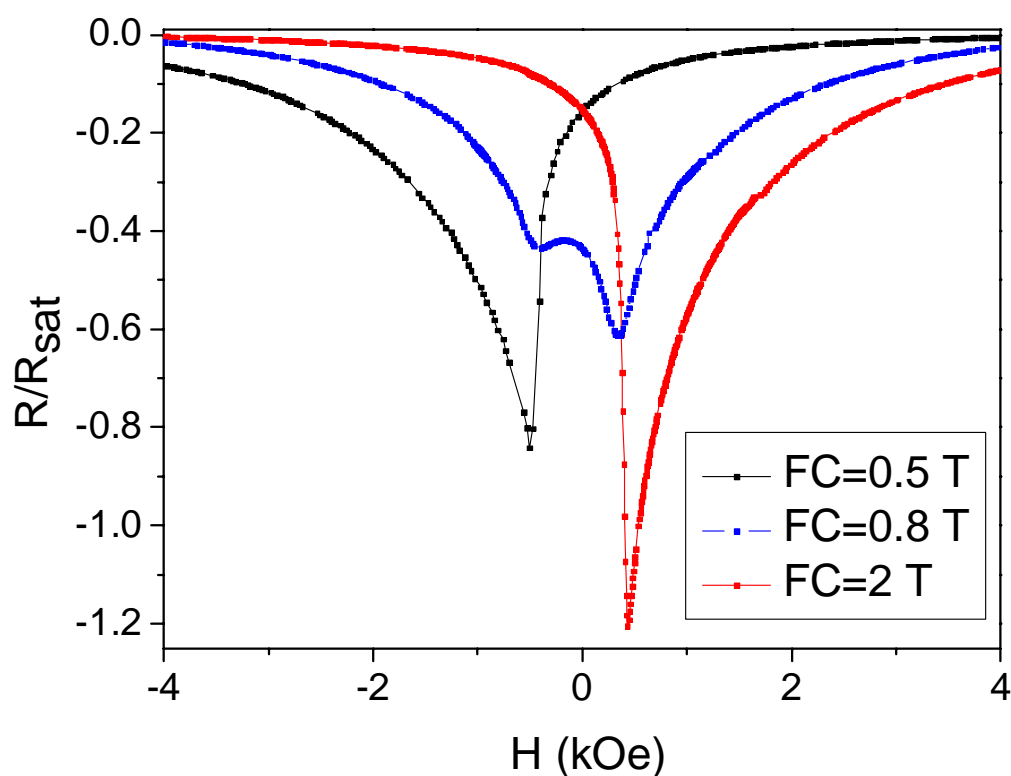


Fig.2. (Colour online) Example of the ratio of the resistance R to the minimum resistance $R_{\text{saturation}}$, $R/R_{\text{saturation}}$, as a function of magnetic field, H , measured at 4.2 K after a field cooling process at the following cooling fields FC = 0.05 (black squares), 0.08 (blue triangles), 2 T (red circles) for antidot density = 0.06.

Homochiral monolayers of Cu-Phthalocyanine driven by adsorption induced electronic chirality

A. Mugarza¹, N. Lorente¹, C. Krull¹, S. Stepanow¹, G. Ceballos¹, J. Fraxedas¹, P. Ordejón¹, M. L. Bouquet², and P. Gambardella¹

¹Centre d'Investigació en Nanociència i Nanotecnologia (ICN-CSIC), Campus UAB Bellaterra, Barcelona

²Laboratoire de Chimie, UMR 5532, Ecole Normale Supérieure, Lyon, France, and Department of Chemistry
cornelius.krull.icn@uab.cat

The most efficient route to imprint chirality to surfaces is the adsorption of molecular layers [1]. However, when the molecule is adsorbed on a surface chirality can be induced [2], eliminated [3], or even switched [4]. Hence the molecule-substrate interaction plays a fundamental role in the growth of chiral surfaces.

In the adsorption of Cu-Phthalocyanine (CuPc) on Ag(100), both with four-fold symmetry, the molecule-surface interaction azimuthally rotates the molecule generating a mismatch between the symmetry axes of molecule and substrate and thereby imprinting chirality to the system. Fig. 1 (a) shows scanning tunneling microscopy (STM) images of the two molecular enantiomers. However, in this case the molecule-substrate interaction is not strong enough to induce conformational distortions in the molecule but induces a large charge transfer that imprints chirality to the molecular orbitals. The purely electronic origin of chirality is confirmed by voltage dependent STM topographic and conductance images (Fig. 1 (b)-(e)), where chirality is observed only for negative bias voltage. The energy dependence of the chirality is due to the different contribution of the HOMO/LUMO orbitals, as confirmed by density functional theory (DFT) calculations.

The electronic chirality observed in isolated molecules extends to the nearby surface atoms inducing an asymmetric potential. This breaks the symmetry between otherwise equivalent intermolecular bonding configurations, leading to the growth of one type of cluster for each molecular configuration, as can be seen in Fig. 2. At increasing coverage, the coexistence between the two cluster domains is inhibited by the high energy of domain walls and a single domain is efficiently propagated creating μm -size homochiral layers.

References:

- [1] S. M. Barlow, and R. Raval, Surf. Sci. Rep. **50** (2003) 201
- [2] M. Parschau, R. Fasel, K.-H. Ernst, O. Gröning, L. Brandenberger, R. Schillinger, T. Greber, A. P. Seitsonen, Y.-T. Wu, and J. Siegel, Angew. Chem. Int. Ed. **46** (2007) 8258
- [3] J. Zhang, A. Gesquière, M. Sieffert, M. Klapper, K. Müllen, F. C. De Schryver, and S. De Feyter, Nano Letters **5** (2005) 1395
- [4] S. Weigelt, C. Busse, L. Petersen, E. Rauls, B. Hammer, K. V. Gothelf, F. Besenbacher, and T. R. Linderoth, Nature Materials **5** (2006) 112

Figures:

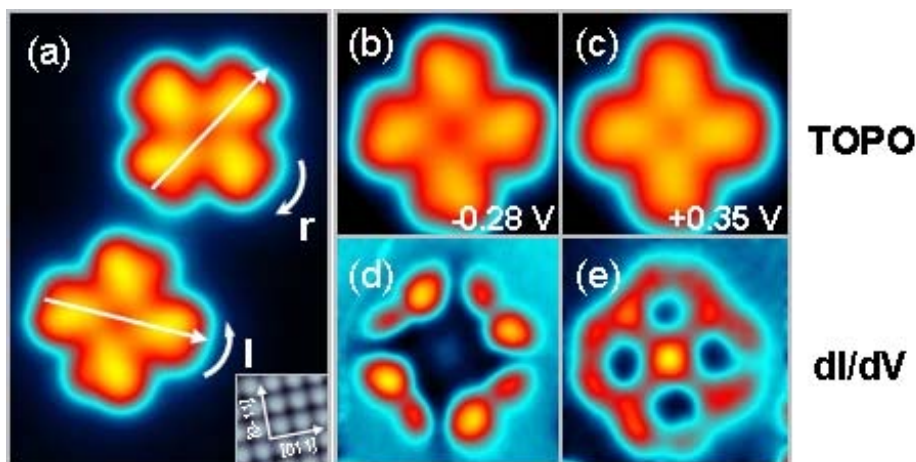


Fig. 1: a) STM image of individual CuPc molecules adsorbed on Ag(100), showing the two type of chiral configurations (r/l), rotated $\pm 30^\circ$ with respect to the $[011]$ surface crystallographic direction. b)-e) Topographic and conductance images of a CuPc molecule at -0.28 V (b and d) and $+0.35$ V (c and e). The electronic chirality, which depends on the molecular resonance where electrons tunnel into at each voltage, is present both in the topographic and conductance images at negative voltage and disappears at positive voltage.

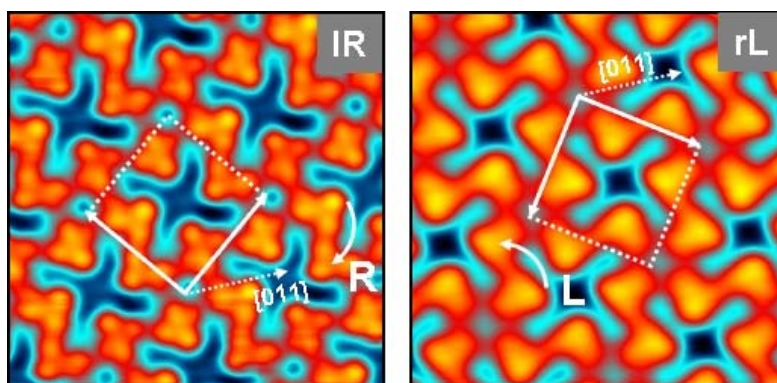


Fig. 2: STM images showing disconnected patches with the two possible chiral assembly configurations of the first CuPc monolayer on Ag(100). Chirality is effectively transferred from molecule to array by a unequivocal assembling relation (lR/rL).

Preparation and metrology of nanoparticles

Kyumin LEE, Andrzej J. Kulik, László Forró

Institut of Physics of Condensed Matter, EPFL-FSB, Lausanne, Switzerland
andrzej.kulik@epfl.ch

Study of the individual nanoscale objects on the substrate ask for reliable method of their deposition, insuring that they remain single and isolated. We developped boil-off method which guarantee uniform distribution and is very simple to implement [1]. Boil-off method provides regular distribution of nanoparticles, nanotubes and nanorods on the subtrate.

In most of cases, non-contact or tapping mode of AFM operation have to be used, to avoid lateral displacements of particles during scanning. Usually, small amplitudes of cantilever oscillations are preferred, to avoid errors due to particle deformation and to protect the AFM tip. In such practical condidtions we observed that AFM mode of operation is switching between non-contact and tapping, while passing between the substrate and particle. This may lead to errors in height measurement of the order of few nm. [2]

Experiments with analysis and interpretation will be presented.

References

- [1] Kyumin LEE et al, Appl Phys Lett 91, 173112 (2007). DOI: 10.1063/1.2803320
- [2] Kyumin LEE, PhD thesis EPFL: <http://library.epfl.ch/theses/?nr=4042>

CONDUCTIVE AFM ANALYSIS OF THE TRAPPING PROPERTIES OF SiO₂ TUNNEL LAYERS FOR
NON-VOLATILE MEMORY DEVICES

M.Lanza¹, M.Porti¹, M.Nafría¹, X. Aymerich¹, A. Sebastiani², G. Ghidini²

¹Dept. Eng. Electrònica, Universitat Autònoma de Barcelona, 08193, Bellaterra, Spain

²Numonyx, Via Olivetti 2, 20041 Agrate Brianza, Italy

Phone: 0034935813513; fax: 0034935812600; e-mail: mario.lanza@uab.cat

Abstract

In this work, the impact of an electrical stress on MOS structures with a 9.8nm thick SiO₂ layer has been investigated at device level and at the nanoscale with Conductive Atomic Force Microscopy (CAFM). The goal is to correlate both kinds of measurements when studying the degradation of tunnel oxides of non-volatile memory devices. In particular, the generation of defects and its impact on leakage current and charge trapping have been analyzed through spectroscopic measurements and current images.

Keywords: Conductive Atomic Force Microscopy, electrical characterization, non-volatile memory devices.

1. Introduction

To continue with the scaling down of the dimensions of memory devices, their electrical properties and reliability have to be further investigated. In particular, the degradation of the tunnel oxide due to the programming operations (which leads to a reduction of the device reliability) must be studied in detail. However, standard characterization techniques only give averaged information of the electrical properties of the devices. To obtain more detailed information, new techniques with higher spatial resolution must be considered. In this work, a CAFM (Conductive Atomic Force Microscope) [1,2] has been used to investigate, at the nanoscale, the electrical properties of SiO₂ tunnel oxides that have been previously subjected to an electrical stress using standard characterization techniques at wafer level.

2. Experimental

The samples are MOS capacitors (2.5µm x 2.5µm sized) with a 9.8nm thick SiO₂ dielectric and polysilicon gate. These capacitors have been stressed by applying constant current stresses (CCS). In particular, CCS of $J=10^{-2}$ A/cm² and $J=10^{-1}$ A/cm² during 100 seconds have been applied to different structures. Some of the capacitors, without being stressed, will be considered as reference. In the V-t curves measured during the stress, an increase of the applied voltage has been observed, which suggests trapping of negative charge in the oxide. In the harder stress, some structures experienced breakdown (BD), registering a sudden drop in the V-t curve. After the stress, the polysilicon layer has been removed with a very selective etching to avoid any damage of the oxide. Afterwards, the AFM tip was located on the gate area and CAFM measurements have been performed. When the tip scans the surface, simultaneously to the topography, current maps are obtained by applying a constant voltage between the tip and the sample and I-V curves can be measured on particular oxide locations (area of ~300nm²).

3. Results

We will start investigating the nanoscale electrical conduction of the different samples from spectroscopic measurements. I-V characteristics were measured at different positions with the tip of the AFM. Low voltages have been applied during these monitors in order to modify the less as possible the previously induced degradation. Figure 1 shows the statistical distribution of the onset voltage (voltage needed to measure a current of 10pA) for the different structures after measuring I-V curves on several positions. Note that the mean value of the onset voltage does not show significant differences between the samples, although it is slightly larger for those previously stressed. Since the larger the onset voltage, the lower the conductivity, this slight increase of the onset voltage could be attributed to the charge trapped in the oxide during the pre-stress (as already observed in the V-t measurements at device level). On the other hand, the rms value of the onset voltage increases with the stress, which suggests that the electrical conduction is less homogeneous in stressed structures than in fresh oxides. This behavior can be related to the generation of defects during the pre-stress. In those positions with a larger concentration of defects, the conduction could be increased due to trap assisted tunneling (TAT) or decreased due to charge trapping after stress, leading to a larger dispersion of the onset voltage and therefore, to a larger rms value. Note that, although the global electrical conduction decreases (as observed in the poly-gated devices during the stress), the inhomogeneity of electrical conductivity

increases. It is important to emphasize that this inhomogeneity can not be detected from standard techniques: only AFM techniques allow these observations due to its nanoscale spatial resolution.

To perform a more detailed analysis, the electrical conduction has been further studied from current images obtained with the CAFM. To investigate the electrical homogeneity, images were obtained by applying the gate voltage necessary to measure current just above the noise level (that is, by applying the same electrical field). Figure 2 shows current images obtained by scanning the surfaces of, (a) a reference oxide and (b) and (c) oxides stressed at $J=10^{-2}$ A/cm² and $J=10^{-1}$ A/cm², respectively. The voltages needed were 10.2 V for figures 2a and b, and 10.7 V for figure 2c. In (c) no BD spots were observed (in case they were triggered) since the scanned area is much smaller than the capacitor size and BD is a local phenomenon. Due to charge trapping, after the stress, higher voltages are necessary to measure the same current for the samples subjected to the larger CCS stress. However, this is not the case of the sample stressed at $J=10^{-2}$ A/cm²; this effect could be attributed to the fact that there can be other experimental factors (changes on the tip conductivity, contact area, small local variations of the oxide thickness...) that can have a larger impact on the electrical conduction. The statistical analysis of these images allows to compare the homogeneity of each sample. Note that the rms value of the current is larger on stressed samples (as already observed from the I-V curves). In these samples, some leaky sites appear which show larger currents than the rest of the oxide (darker areas in the images). A statistical analysis of the leaky sites with a current 1pA above the background has been done (fig.2 table). Note that the number, the mean current and the mean area of the leaky sites after the stress are larger than in the fresh structure. This result suggests that, although there is a certain amount of trapped charge in the oxide after the stress, which leads to smaller average currents when applying the same gate voltage, at some sites, the stress also leads to an increase of current related to TAT through the generated defects.

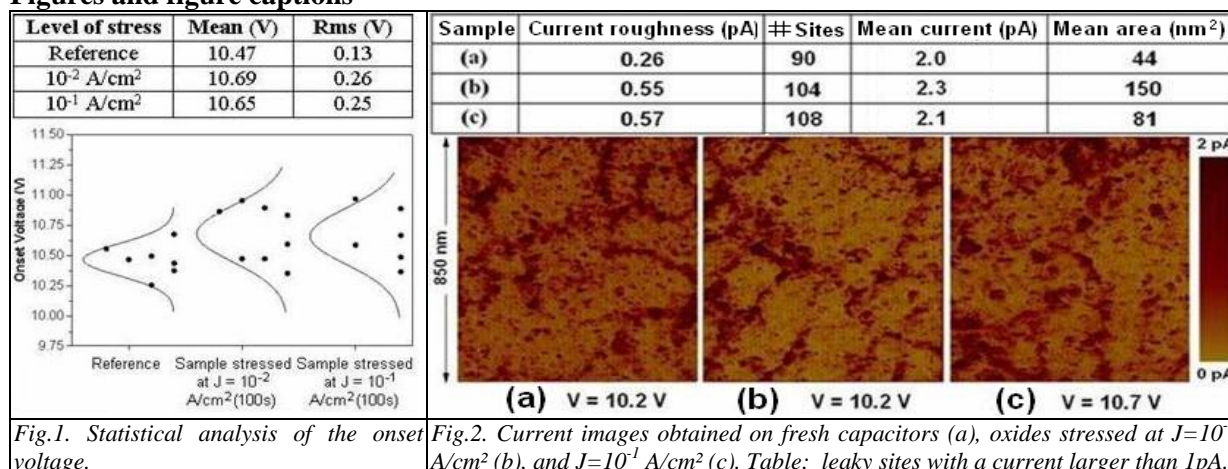
4. Conclusion

The electrical properties of SiO₂ tunnel oxides of non-volatile memory devices subjected to different device level stresses have been studied at nanometer scale using a CAFM after poly-silicon gate removal. I-V curves have been measured with the CAFM at different oxide locations. In the stressed samples, smaller conductivities but larger inhomogeneities are observed. These results are further supported by the current maps measured at the nanoscale with the CAFM. Additionally, the current images show that although after the stress the mean current decreases, some leaky sites appear. Therefore, most of the defects generated during the stress act as trapping sites (which lead to the increase of voltage during the CCS), but some of them locally increase the conductivity of the sample leading to Stress Induced Leakage Current (SILC). At device level, however, SILC is masked by the decrease of the conductivity due to trapping, since standard tests are only able to measure average properties of the layer.

References

- [1] A. Paskaleva, V. Yanev, M. Rommel, et al., J. of App Phys, Vol. 104(2) 024108 (2008).
 [2] M Porti, M Avidano, M Nafria, et al., J. App Phys 101(6) 064509 (2007).

Figures and figure captions



PROPERTIES OF COPPER COATED WITH CARBON NANOTUBES

Tahar Laoui

Mechanical Engineering Department/Center of Excellence in Nanotechnology
KFUPM, Dhahran, Saudi Arabia

Abstract

A thick layer of multi-wall carbon nanotubes (CNTs) was deposited on copper surface by gravity from a solution containing dispersed CNTs in water. Scanning electron microscopy (SEM) was utilized to characterize the morphology, uniformity and thickness of the CNTs coating. A low magnification examination shows a uniform coating. However, a close look at the SEM images reveals that the coating consists of clumps of CNTs deposited rather irregularly on the surface. The Vickers microhardness values measured using a 300 gf load for copper (Cu) and CNT coated Cu samples were 103 and 111 HV respectively. This indicates that the CNT coating yielded a relatively softer surface than Cu. A corrosion test was carried out to investigate the effect of CNTs coating on the corrosion performance of copper. The corrosion resistance (R_p) calculated from the linear polarization resistance results yielded 585 Ohms for Cu and 26,460 Ohms for the CNT coated Cu indicating an increase in the corrosion resistance of about 45 times. In other words, the corrosion rate of Cu has been greatly reduced by the deposited CNT coating allowing a longer lifetime.

H₂O INDUCED STRUCTURAL MODIFICATION OF PENTACENE CRYSTAL

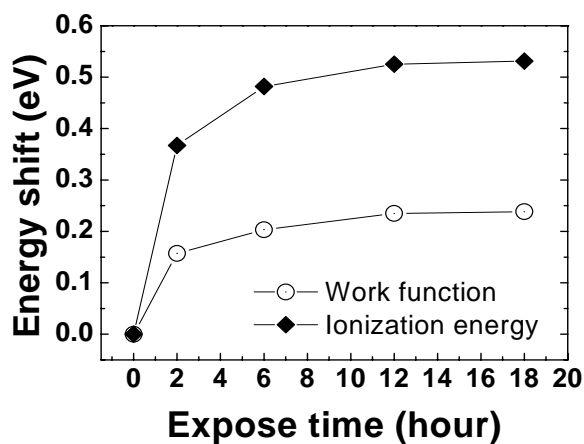
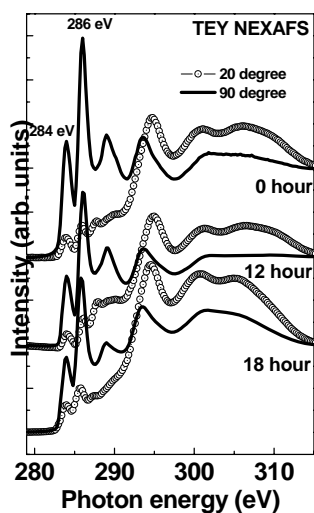
Kyoung-Jae Lee,¹ Kyuwook Ihm,² Tai-Hee Kang,² Sukmin Chung,¹

¹*Department of physics, POSTECH, Pohang, Kyungbuk 790-784, Korea*

²*Pohang Accelerator Laboratory, Pohang, Kyungbuk 790-784, Korea*

Atmospheric H₂O has been known as one of the obstacles for prolonged life time of organic devices. Pentacene have been widely studied as a model system of simple organic based field effect transistors (OFETs). Here, we show the evolution of the electronic and geometric structure of the pentacene crystal driven by the adsorption of H₂O molecules. Core level, valence band, and x-ray absorption spectra support that H₂O molecules physisorb on the pentacene surface, which form a strong dipole layer which increases the ionization energy by about 0.5 eV. It reflects the increase of hole injection barrier. In addition, we made another discovery that the crystallinity of the pentacene layer is deteriorated by the diffused H₂O molecules, which reflect the weakening intermolecular interactions of pentacene crystal.

Figures:



HYDROTHERMAL SYNTHESIS AND CHARACTERIZATION OF NANO-FLAKE MAGNESIUM HYDROXIDES FROM MAGNESIUM OXIDE

Soo-Keun Lee, Seong Hui Hong, Sung-Ho Hwang, Sang Kyoo Lim

Division of Nano-Bio Technology, Daegu Gyeongbuk Institute of Science and Technology (DGIST), Samsung Financial Plaza, Duksan-dong 110, Jung-gu, Daegu 700-010, Korea
laser@dgist.ac.kr

Magnesium hydroxide [Mg(OH)₂] has been extensively studied with regard to its application in desulfurization [1], flame retardant [2], foodstuff [3], smoke letting [4], water treating [5] and so on. During the past decades, nanostructured Mg(OH)₂ has received a considerable interest due to their potential property modification and been supposed to apply in more areas. In general, Mg(OH)₂ have been synthesized by a coprecipitation reaction between magnesium salt and sodium hydroxide. Some additives, such as surface modified agent [6], polymer [7] and copolymer [8] were employed in most of the nanostructured Mg(OH)₂ preparation processes. They remained in the final products and acted as baleful impurity in its application. Here, a simple, mild and environment-friendly hydrothermal method was suggested, where magnesium oxide [MgO] was used alone as a reactant without further additives.

In this work, Mg(OH)₂ was prepared by a simple hydrothermal reaction of bulk magnesium oxide, which shows random size distribution and micro size. Magnesium oxide, 5, 10, and 20 wt%, respectively, were dispersed and agitated in 50 ml of distilled water were agitated and then heated up to 150°C in the Teflon-lined stainless steel hydrothermal reactor for 3, 6, 10, 12, and 24 hours, respectively. The obtained powder was rinsed with distilled water and dried at 80°C. The obtained Mg(OH)₂ product was hexagonal shaped nano-flake. Crystalline structure of Mg(OH)₂ samples was analysed by XRD and shape and size of Mg(OH)₂ samples were confirmed by SEM. Relative surface areas of samples were calculated from the isotherm nitrogen adsorption-desorption experiments. The primary particle size of samples was in the range of several hundreds of nano meters and the thickness of samples under 100 nano meter (Fig.1). The thickness of nano-flake Mg(OH)₂ were varied with the change of reaction time. Thus, the thickness of nano-flake (below 100 nm) is controllable by changing the reaction time. Relative surface area of the Mg(OH)₂ (20% MgO, 10hrs) was calculated to 26 m²/g by BET equation. In conclusion, the mass production of the nano-flake Mg(OH)₂ has been achieved by the simple hydrothermal reaction.

This work was supported by DGIST basic research program of the MOST.

References:

- [1] H.S. Shin and S.M. Lee, Environ. Technol. **19** (1998) 283.
- [2] J. Ok and K. Matyjaszewski, J. Inorg. Organ. Polym. Mater. **16** (2006) 129.
- [3] Alfonso De Sande Moreno, US Patent 5,955,004 (1999).
- [4] L. Shi, D. Li, J. Wang, S. Li, D.G. Evans and X. Duan, Clays Clay Miner. **53** (2005) 294.
- [5] Y. Zhao, Y. Tan, F.-S. Wong, A.G. Fane and N. Xu, Desalination **191** (2006) 344.
- [6] B. Li, Y. Zhang, Y. Zhao, Z. Wu and Z. Zhang, Mater. Sci. Eng. A **452/453** (2007)v302.
- [7] L. Qiu, R. Xie, P. Ding and B. Qu, Comp. Struct. **62** (2003) 391.
- [8] Z.G. Zhao, F.X. Geng, H.T. Cong, J.B. Bai and H.M. Cheng, Nano **1** (2006) 185.

Figures:

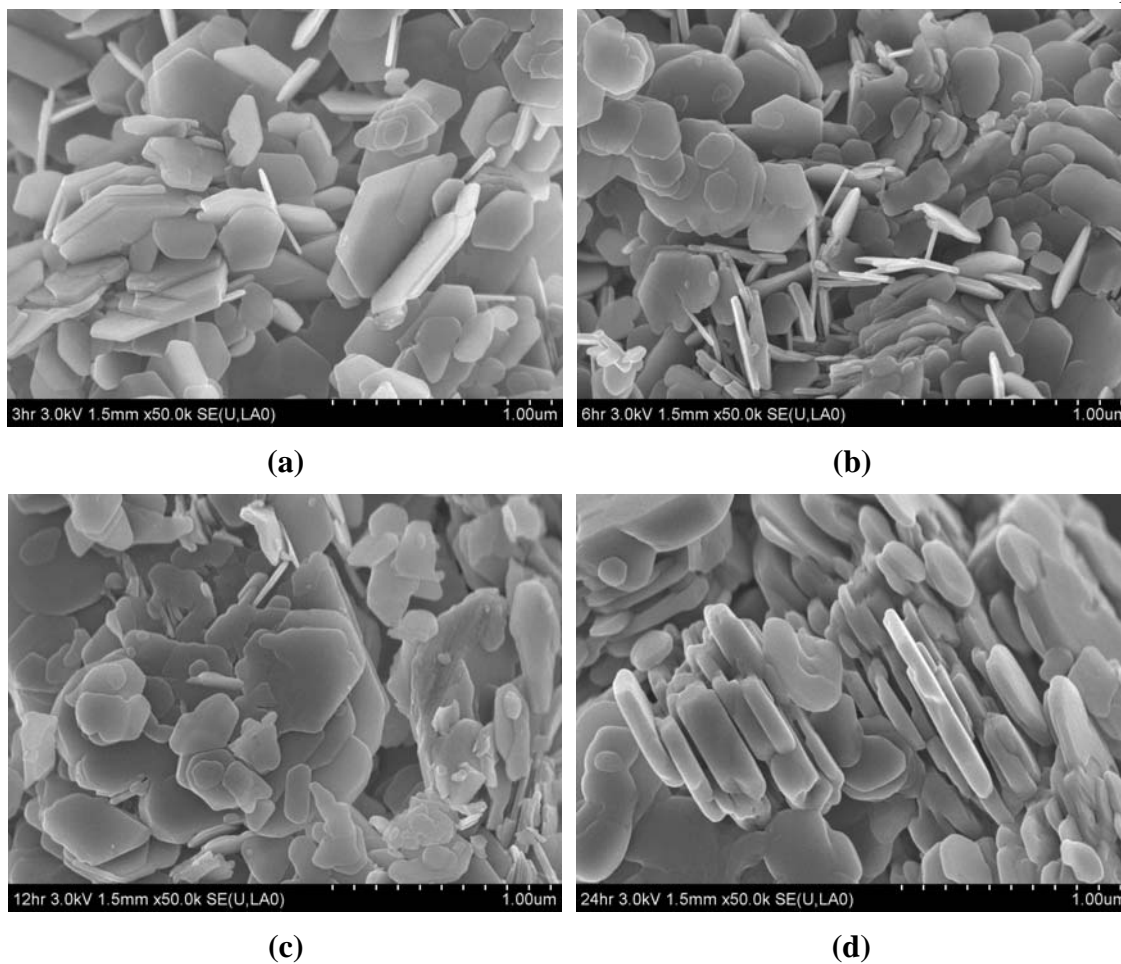


Fig. 1 SEM images of various $\text{Mg}(\text{OH})_2$ samples. (a) 3 (b) 6 (c) 12 (d) 24hours hydrothermal reaction(20% MgO).

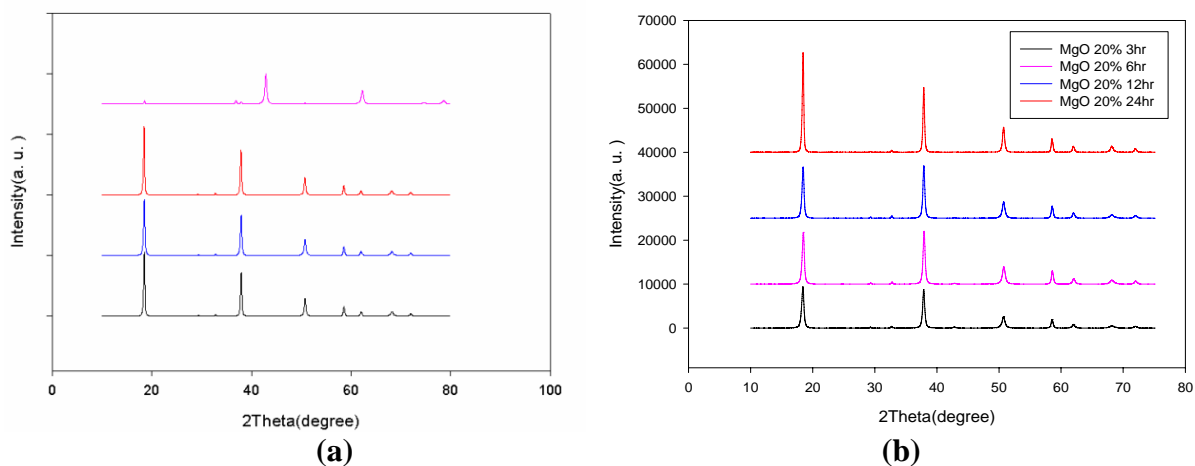


Fig. 2 XRD spectra of the samples (a) MgO, $\text{Mg}(\text{OH})_2$ (5% MgO, 24h), $\text{Mg}(\text{OH})_2$ (10% MgO 24h) $\text{Mg}(\text{OH})_2$ (20% MgO 24h); from top to bottom (b) various reaction time.

Enhancement of electrochromic durability of polyaniline using the inorganic-organic hybrid nanostructure in form of nanoparticles

HeungYeol Lee, Taejin Hwang, Hohyeong Kim, GyunTak Kim
Surface Technology and Heat Treatment R&D Division

Korea Institute of Industrial Technology (KITECH), 7-47 Songdo-Dong, Yeonsu-Gu, Incheon
406-840, Korea

Contact@E-mail

Enhancing the operation life time or the electrochemical durability is one of the key issues in the electrochromic material studies. Recently, the flexible display devices are drawing much attention since they can facilitate new technological demands such as bending and folding of paper-like displays. For these applications high electrochromic efficiency, short response time, long operating life time are the most important requisites of the material [1,2]. Recently conducting polymers are considered as more competitive material than the inorganic transition metal oxides for the display applications because of their faster response and longer operating life time the operating. However, life time of electrochromic conducting polymers is still limited to 10^6 cycles while more than 10^8 cycles are preferably required for an acceptable display material.

As it is generally accepted, the inorganic-organic hybrid structure is one of the effective ways to enhance the chemical stability of the material [3,4]. In this study, an electrochromic film made of silica-polyaniline core-shell nanoparticles was prepared on an Indium Tin Oxide (ITO)-coated glass substrate and the operation life time of the film was investigated.

Through a chemical polymerization of polyaniline in a colloidal solution of silica, nanoparticles of silica-polyaniline were obtained. In the core-shell structure the inorganic silica was incorporated to enhance the chemical durability of the organic moiety, polyaniline (Fig. 1). The synthesized particles were then dispersed into ethanol and were deposited onto glass substrate in the form of thin film. For a better adhesion to the substrate, small amount of tetraethoxysilane (TEOS) and HCl aqueous solution was added to the dispersion solution, and the prepared film showed strong adhesion to the ITO-coated glass substrate (Fig. 2).

The electrochromic characterization on the prepared films was performed using the cyclic voltammetry and the optical response to the electrical potential change, and it showed an enhanced electrochromic operation life time (Fig. 3,4).

The material characterization results showed that the life time enhancement is possibly due to the enhanced chemical stability of the inorganic-organic core-shell hybrid nanoparticles. The developed hybrid material could readily be applied to the production of variable reflectance room-mirrors for automobiles.

References:

- [1] M. Mastragostino, Electrochromic devices, in Applications of Electroactive Polymers, B. Scrosati, Editor. Chapman & Hall: London (1993) 223-249.
- [2] P.R. Somani and S. Radhakrishnan, Materials Chemistry and Physics **77** (2002) 117-133.
- [3] L. Hou, H.K. Schmidt, B. Hoffmann, and M. Mennig, Journal of Sol-Gel Science and Technology **8** (1997) 927-929.
- [4] H.K. Schmidt, Journal of Sol-Gel Science and Technology **1** (1994) 217-231.

Figures:

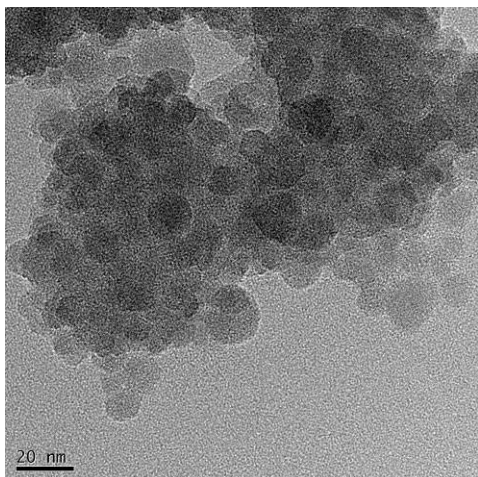


Fig. 1 Silica-polyaniline core-shell nanoparticles.

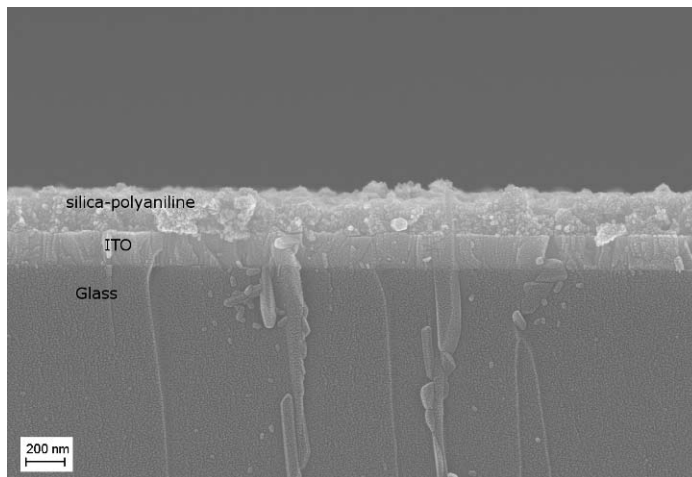


Fig. 2 Prepared composite film on the ITO-coated glass substrate.

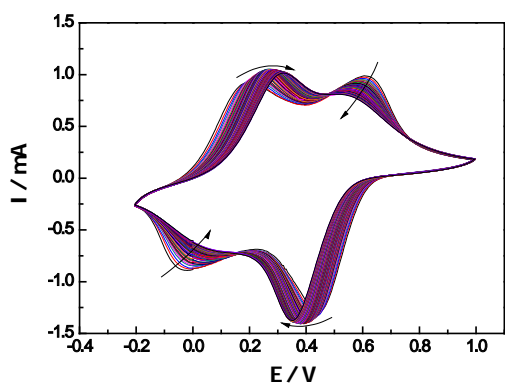


Fig. 3 Cyclic voltammogram of the prepared composite electrochromic film.

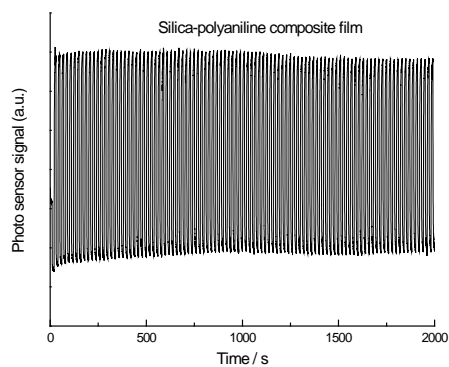


Fig. 4 The optical switching curves between colored and bleached state for the prepared composite film.

CARBON NANOTUBE BASED PHOTOCATHODES FOR X-RAY SOURCES AND MICROWAVE AMPLIFIERS

P. Legagneux¹, N. Le Sech¹, L. Gangloff¹, J-P Schnell¹, C-S Cojocar¹, P. Guiset¹, K B K Teo², J. Robertson³, W. I. Milne³, C. Bourat², P. Ponard², M. Châtelet¹, L. Hudanski¹ and D. Pribat¹

¹ *Nanocarb Lab., Thales—Ecole Polytechnique, Palaiseau, France*

² *Thales Electron Devices, Thonon-les-Bains*

³ *Electrical Engineering Division, University of Cambridge, UK*

Compared to thermoionic cathodes used in most electron tubes, carbon nanotube (CNT) based cathodes enable to easily modulate the emitted electron beam. This can be performed using an integrated or external extraction grid. This can also be performed using a new method that we recently proposed: the optical control of a CNT photocathode [1].

This photocathode is an array of vertically aligned multiwall CNTs, each CNT being associated to a semiconducting p-i-n photodiode. The p-i-n element acts as an optically controlled current source that imposes the current that can be emitted by the CNT emitter. The envisaged applications are 3D X-ray imaging using computed tomography and microwave amplification.

Computed tomography enables the reconstruction of a 3D image of an object by collecting many 2D projection images. Using multiple X-ray sources and a 2D X-ray sensor, low cost, light and efficient stationary scanners can be fabricated. CNT based X-ray sources are currently studied because they operate at low temperature and enable pulsed operation. However the control of the emission through a control circuit is complicated, especially if the cathode is biased at high voltage (50 to 200 kV). CNT photocathodes are particularly attractive for this application because the laser source is electrically insulated from the cathode and also because the emission current is proportional to the laser power. To demonstrate this approach, we will present the performances of a CNT photocathode based on silicon p-i-n photodiodes and multiwall CNTs. The CNTs have been grown by plasma enhanced chemical vapour deposition using C₂H₂ and NH₃ gases. Using a 532 nm laser, this photocathode delivers 0.5 mA with an internal quantum efficiency of 10% and an I_{ON}/I_{OFF} ratio of 30. With a 658 nm laser source, the electron beam was modulated at frequencies up to 300 MHz.

The second application relates to microwave amplifiers and particularly to the large bandwidth travelling wave tubes (TWTs) which are used on satellites for telecommunication. These TWTs are based on thermoionic cathodes that emit a continuous electron beam. The post modulation of the beam that is required to amplify the microwave signal takes roughly half of the tube length. The use of a photocathode directly delivering a modulated electron beam would enable the fabrication of light, compact and efficient amplifiers. For this purpose, we are currently studying CNT photocathodes based on GaInAs p-i-n photodiodes operating at 1.55 μ m. To prevent dopant diffusion during CNT growth, we have developed a new water-based growth process where H₂O is employed (instead of NH₃) [2]. The growth temperature is then reduced to 550°C. First experiments of high frequency modulation of the CNT photocathodes will be presented.

[1] L. Hudanski et al, *Nanotechnology* **19**, 105201 (2008).

[2] C. Cojocar, D. Pribat, A.Caillard et al., to be published

Top-down Silicon Nanowire Field-Effect Transistors for Real-Time Biological Detection

*G. Lehoucq¹, S. Xavier¹, P. Abbyad², M. Fromant³, L. Mugheri³, P. Bondavalli¹,
P. Legagneux¹, P. Plateau³, D. Pribat⁴*

¹Thales Research and Technology, Palaiseau, France

²Laboratoire d'Optique et Biosciences, Palaiseau, France

³Laboratoire de Biochimie de l'Ecole Polytechnique, Palaiseau, France

*⁴Laboratoire de Physique des Interfaces et des Couches Minces, Palaiseau, France
gaelle.lehoucq@thalesgroup.com*

Silicon Nanowire Field-Effect Transistors designed for biological detection exploit what is commonly called the “molecular gate” effect : the detection is based on the extremely sensitive change of the conductivity of the FET channel as a function of the variation of the electric field resulting from charged species binding to the wires. These devices are particularly interesting for biosensing for several reasons :

- sensitivity : using nanowires enables a huge increase in sensitivity (compared to the so-called planar CHEM-FETs, studied three decades ago), which is intuitively related to their one-dimensional morphology and nanometer-scale cross-section
- selectivity : the nanowires can be functionalized using opportunely chosen bioreceptors for highly selective biosensing
- rapid analysis : this technique is not based on amplification and don't require to extract DNA from targeted molecules if the suited functionalization is developed. Moreover, it is a label-free method contrary to optical devices. As a result, it is a time-saving technique.

High sensitivity and detection limit to low concentration has already been demonstrated with bottom-up Si nanowires devices [1]. However, considerable problems remain like depositing the nanowires at defined position on chips properly and achieving high quality contacts. This results in severe integration issues that hinder large-scale application. That is why we propose to fabricate nanowire FETs with a top-down approach, which consists in patterning and dry etching a Silicon On Insulator wafer. Our transistors are based on nanowires whose section ranges from 100 to 200nm (*fig 1*). The sensor is integrated with a microfluidic device allowing a good control of liquid flow over nanowires and real-time measurements during functionalization.

In a first step, the device was used as a hydrogen ion sensor (*fig 2*). These measurements show reproducible, reversible results with a high sensitivity and a short response time. We also demonstrate that the conductance of nanowires can be tuned for optimal sensitivity using the back-gate voltage.

In a second step, we studied the activity of an aminoacyl tRNA synthetase (precisely the Methionyl tRNA synthetase (MetRS)). This enzyme is a small ribonucleic acid that transfers a specific active amino acid to a growing polypeptide chain at the ribosomal site of protein synthesis during translation. We functionalized nanowires with two different linkage chemistries, allowing regular [2] or random [3] attachment of the enzyme. The functionalization was characterized using atomic force microscopy to obtain the thinnest layers as possible in order to avoid Debye screening. As it can interact with positively or negatively-charged substrates, MetRS shows its particular interest to assess the potential of our sensor.

References:

- [1] F. Patolsky, G. Zheng, C.M. Lieber, Nature Protocols, **vol. 1 n°41** (2006), 1711
- [2] T. Cha, A. Guo, X-Y. Zhu, Proteomics, **5** (2005), 416
- [3] G. MacBeath, S. Schreiber, Science, **289** (2000), 1760

Figures:

Fig. 1: Top-down field-effect transistors based on a 150nm-wide silicon nanowire

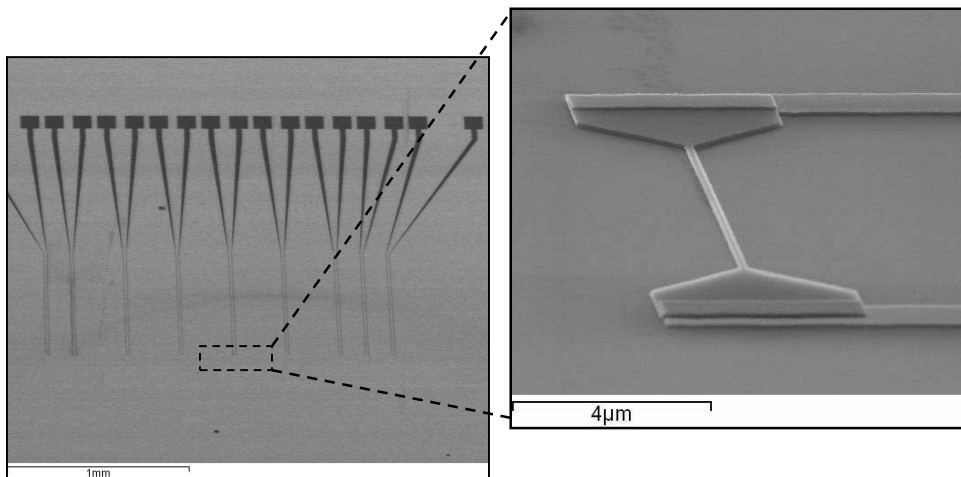
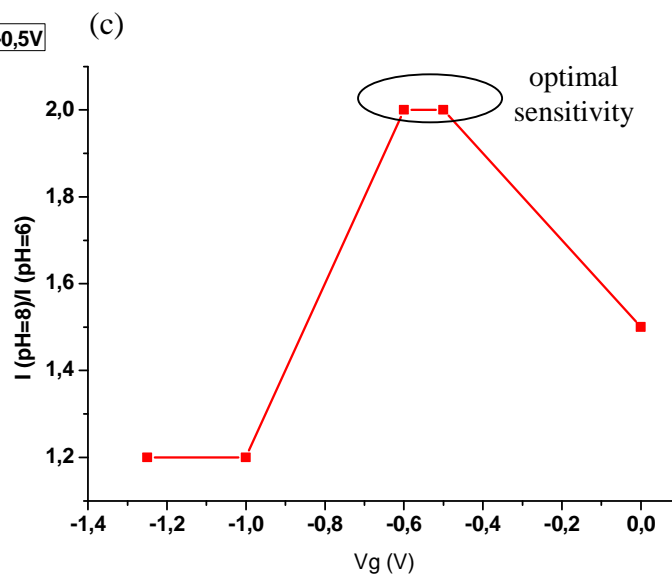
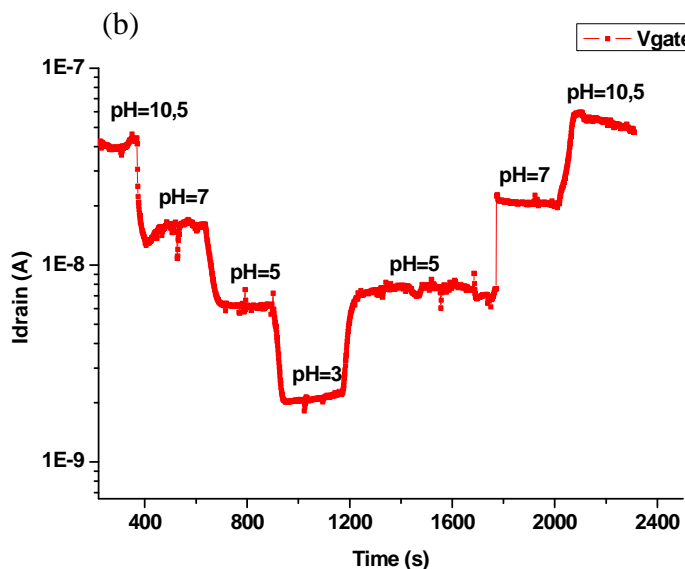
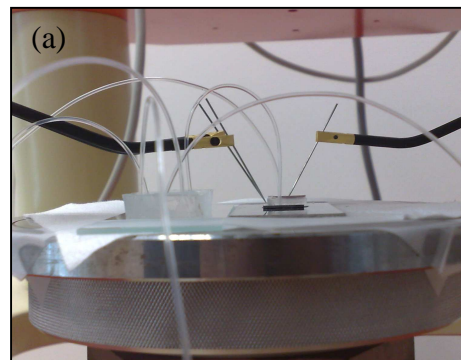


Fig. 2 : Real-time measurement of the conductance of a nanowire FET

- (a) Experimental setup with integrated microfluidics
- (b) Real-time measurement of the conductance of a nanowire FET for pH from 3 to 10,5 (acetate and phosphate buffer)
- (c) Study of the sensitivity (current ratio) for a pH variation from 6 to 8 as a function of backgate voltage V_g



Surface plasmon effects induced by uncollimated emission of semiconductor microstructures

D. Lepage, J.J. Dubowski*,

Department of Electrical and Computer Engineering,
Université de Sherbrooke, Québec J1K 2R1, Canada

The inherent surface sensitivity of the surface plasmon resonance (SPR) effect has made it highly attractive for biochemical analysis of processes localized on metal surfaces. Many SPR devices have been developed and made commercially available for that purpose in the past 20 years. However, most of them are relatively bulky and a monolithically integrated SPR microchip, which could be easily integrated with specimen processing hardware for a wholly automated analysis, has yet to be demonstrated. We have recently proposed an innovative SPR microstructure comprising a metal coated SiO₂ layer deposited on top of a photoluminescence (PL) emitting quantum well (QW) wafer. Nano-scale grating fabricated in the metal layer allows for the extraction of the SPR signal. The entire device, thanks to the built-in light source and the application of a SPR imaging technique, has the potential to become a highly compact SPR biosensor for simultaneous detection of numerous biomolecules. Although the proof of concept of the QW-SPR device has already been demonstrated [1], a full understanding of its operation has yet to be developed, a step critical to our ability in designing a fully optimized and functional integrated SPR architecture for specific biosensing applications.

The functioning of the QW-SPR device is based on the uncollimated, and usually incoherent, emission of QW. Therefore, any given point of the metal-dielectric interface is exposed to the whole range of wavevector spectra and thus, coupling of all the SPR modes supported by the architecture is expected to take place. The multiple SPR coupling along the metal-dielectric interfaces distinguishes our QW-SPR device from other “macro” SPR devices, where only one wavevector is excited at a time.

In this communication, we discuss the results of our calculations aimed at the description of surface plasmons generated at SiO₂/Au/Photoresist (PR) interfaces irradiated by an uncollimated emission from a semiconductor QW [1]. The calculations were carried out using a Rigorous Coupled-Wave Analysis (RCWA) algorithm and a scattering matrices approach. This allowed us to predict the coupling of QW PL and describe the

propagation of SP in both the Near- and Far-Fields. It has been determined that the two SPs (Au/PR and Au/SiO₂) could couple in the 0th and higher diffraction orders where the injected in-plane wavevectors from the GaAs-AlGaAs QW structure can always meet SPR conditions. As a dramatic result, the coupling efficiency of SPs can be up to 10² times higher when coupling of all SPs occurs in the 0th diffraction order.

An $\omega(k_{||})$ map (angular frequency versus in-plane wavevector) of the analytical far-field dispersion relation for the investigated microstructure is shown in Fig. 1. Such a map could be determined experimentally using, e.g., a spectro-angular SPR system [2]. A normalized QW PL intensity at 820 nm for this microstructure [1] has been plotted in Fig. 2 and compared with calculated values. A very good agreement has been achieved, which provides validation of our calculations. In addition, our calculations enabled us to provide accurate interpretation of experimental data concerning other semiconductor-based SPR microstructure, with PL emission from Si nanocrystals [3]. We will discuss the perspective of the reported approach for designing a monolithically integrated SPR device for specific bio-sensing applications.

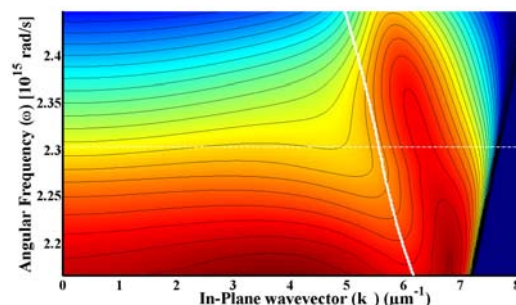


Fig 1. Dispersion relation map (angular frequency versus in-plane wavevector) for the QW-SiO₂/Au/Photoresist microstructure. SPR follows the white solid line.

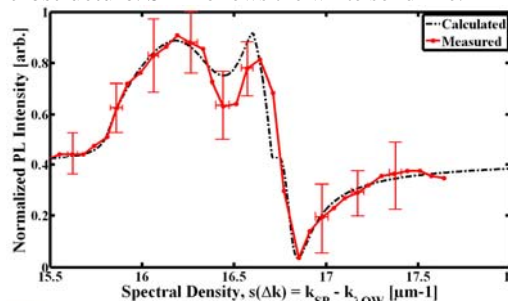


Fig 2. A QW PL emission at 820nm illustrating a match in calculated and measured in [1] intensity modulation.

- [1] D. Lepage et al, APL **91**, 163106 (2007)
- [2] C.J. Alleyne et al, Opt. Exp. **16**, 19493 (2008)
- [3] E. Takeda et al, APL **89**, 101907 (2006)

* E-mail: jan.j.dubowski@usherbrooke.ca

Compact modeling of Optically-Gated Carbon NanoTube Field Effect Transistor

Si-Yu Liao, Cristell Maneux, Vincent Pouget, Sébastien Frégonèse, and Thomas Zimmer

Université Bordeaux, CNRS, UMR 5218, 351 Crs de la Libération, TALENCE, France

siyu.liao@ims-bordeaux.fr

Background

Carbon Nanotube Field Effect Transistors (CNTFETs) have high charge sensitivity at room temperature [1]. By using this sensitivity, some nonvolatile memory devices have been demonstrated with charge trapping in SiO₂ gate insulator [2, 3]. Besides, a new design of synapse-like circuit requires a multi-level nonvolatile memory [4]. For this application, and according to its high charge sensitivity, Optically-Gated Carbon Nanotube Field Effect Transistor (OG-CNTFET) appears as a good candidate thanks to optical writing and electrical erasing abilities both with single and multiple drain current levels [5, 6].

By coating a thin layer of photosensitive polymer such as poly3-octylthiophene-2,5-diyl (P3OT) over the nanotube, a CNTFET becomes an OG-CNTFET [5], as presented in Fig. 1a. Compared to the conventional CNTFET, the OG-CNTFET reveals a significant increase of the drain current below the threshold gate bias voltage. If this device is under significant powerful illumination, the gate bias will no longer control the conductivity of the CNT channel, and the optical gate will dominate the functionality. This property of variable conductance is of particular interest for neural network designs to define a third logic level. In this work, we present a compact model for OG-CNTFET. Indeed, compact modeling (i.e. SPICE-like) is a key issue for predicting the ultimate performances of these novel nano-devices in a circuit environment using standard simulation tools.

Electron trapping/releasing mechanism

When a thin film of P3OT coats on a CNTFET, this polymer acts as a p-type doping under no illumination condition [5]. We suppose that the CNT channel is electrostatically doped due to negative charges trapped at the polymer/SiO₂ interface in the nanotube vicinity [1].

When an OG-CNTFET is under illumination with a wavelength that can be absorbed by the polymer, electron-hole pairs are generated in the P3OT layer, and a minor part of them can be separated [7]. This polymer is known for trapping only electrons [8]. If the gate is biased positively, these trapped electrons can be homogeneously attracted by the electrostatic field to the P3OT/SiO₂ interface. The resulting charge density contributes to modulate the channel conductivity by screening the back gate bias. Fig. 1b describes this so-called optical gating effect. When the light is turned off, the trapped electrons are not released immediately; they are hold for about ten hours [5, 7].

The optical gating effect can be removed more rapidly by applying a negative gate voltage or a positive drain-source one [5-6, 9]. The negative gate bias provides an electrostatic field that contributes to release the trapped electrons at the P3OT/SiO₂ interface. Concerning the effect of the positive V_{ds}, we assume that it creates an electric field close to the drain electrode that contributes to sweep away the trapped carriers according to the field magnitude distribution as a function of the distance to the drain electrode (c.f. Fig. 1c).

Modeling of OG-CNTFET

Since the OG-CNTFET is a modification of the conventional CNTFET, we developed the compact model of OG-CNTFET based on the one of CNTFET. In previous works, we have presented a physics-based CNTFET electrical model [10]. It computes the relationship between the electrostatic capacitances C_{OX}, C_{SE}, and C_{DE}, the quantum charges Q_S and Q_D and the intrinsic channel potential V_{CNT} on one hand, and the channel charge density on the other hand. The OG-CNTFET model takes into account the additional electrostatic capacitances C_{SO} and C_{DO} and the doping charges due to P3OT coating. When a laser spot illuminates the device, the intrinsic channel potential V_{CNT} is directly affected by the trapping of electrons represented as a laser-power-controlled current source charging a pair of trap capacitors: C_{Optic1} and C_{Optic2} (c.f. Fig 2). These capacitors hold trapped electrons when the illumination stops. The natural recombination mechanism of traps has been taken account in this current source I_{Optic}. The release of the optical gating effect via V_{ds} is achieved by commanding the variable resistor R_{Vds}. When V_{ds} is negative, this resistor is infinite, whereas for positive V_{ds} bias, R_{Vds} becomes a finite value which depends on the amplitude of V_{ds}.

Simulation results

The calculation of internal potential V_{CNT} is self-consistent through Kirchoff's laws. The DC simulation results present good agreement with the measurements in the dark of the I_d-V_{gs} characteristics of a single CNTFET and the same one with coated P3OT, as shown in Fig. 3a.

The model also gives a good estimation of the gate bias voltage influence after laser illumination for positive values. Fig. 3b presents typical transient simulation results. Our model clearly exhibits optical writing and electrical erasing dynamics via V_{ds} bias that are close to experimental results presented in [5] and [9].

Hence, the model results present good agreement with previously published experimental results. Future work will include specific experiments to get accurate values of the model physical parameters such as the optical gate capacitance.

References:

[1] H. B. Peng et al., Appl. Phys. Lett. 89, (2006), 243502.
 [2] M. S. Fuhrer et al., Nano Letters, 2(7), (2002), 755-759.
 [3] M. Radosavljevi et al., Nano Letters, 2(7), (2002), 761-764.
 [4] M. He et al., IEEE Electronics Letters, vol. 44, issue 9, (2008), 575-576.
 [5] J. Borghetti et al., Adv. Mater. 18, (2006), 2535-2540.
 [6] J.P. Bourgoin et al. Electron Devices Meeting, IEDM '06. International, (2006), 11-13.
 [7] C. Anghel et al., Nano Letter, 8 (11), (2008), 3619-3625.
 [8] C. D. Dimitrakopoulos, P. R. Malenfant, Adv. Mater. 14, (2002), 99-117.
 [9] G. Agnus et al., Nano Letter, submitted.
 [10] S. Fregonese et al., IEEE Transaction on Electron Devices, vol. 55, issue 6, 2008, 1317-1326.

Figures:

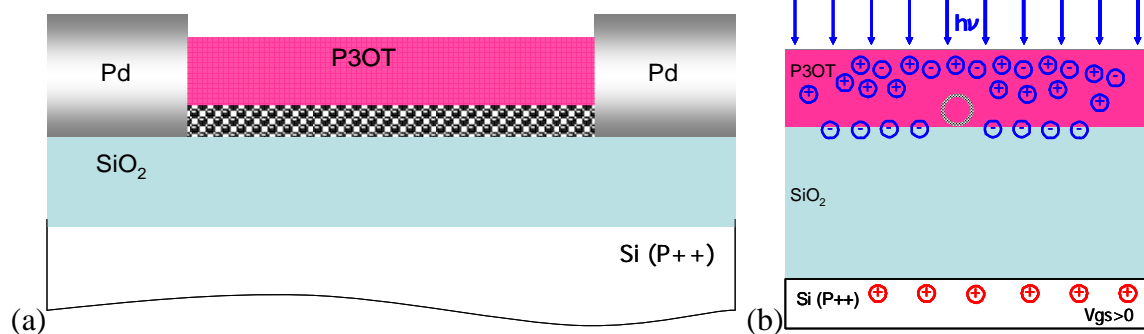


Figure 1. a). Schematic structure of OG-CNTFET. b). Schematic cross-section on the carbon nanotube axis of OG-CNTFET under illumination.

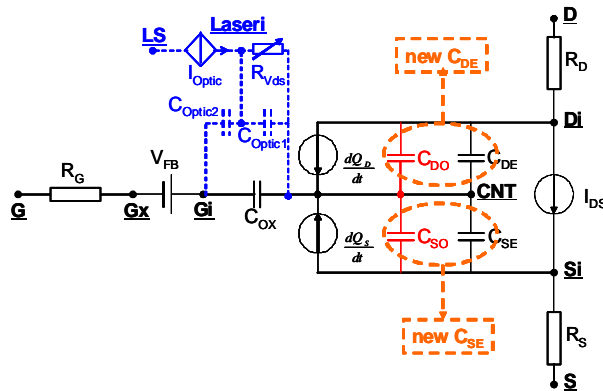


Figure 2. Electric equivalent circuit of OG-CNTFET. In black, the conventional CNTFET. In red, the P3OT influence on electrostatic capacitors. In blue, the photo-charging and discharging sub-circuit.

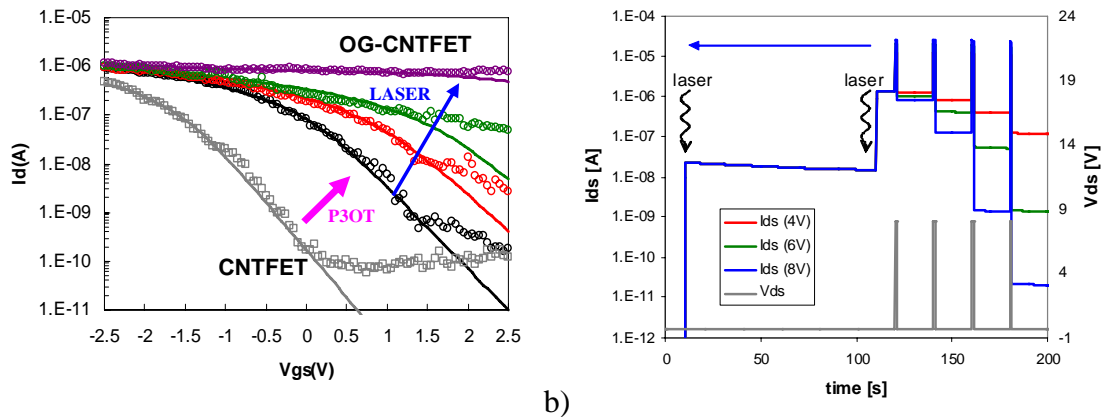


Figure 3. Simulation results. a). I_d - V_{gs} transfer characteristics. The solid lines are simulation results, and the symble are measurements in ref. 5. The gray curves are CNTFET in dark; the black ones are OG-CNTFET in dark; the red ones are OG-CNTFET under laser of 6nW in the spot (2 μ m); the green ones are under laser of 60nW; and the purple ones are under laser of 6 μ W. b). Transient simulation results of optical writing and electrical erasing operations. The drain current I_d is controlled by pulsed V_{ds} of 4 V (red curve), of 6 V (green curve) and of 8 V (blue curve). The gray curve is V_{ds} command. Each laser pulse is 150ms long, each V_{ds} one is 1s long.

Application of Flexible Field-Effect Transistor Device with Nanoscale Zinc Oxide as Active Semiconductor Material

Sang Chul Lim, Ji Young Oh, Seong Youl Kang, Jong Hyurk Park, Yong Suk Yang, Jae Bon Koo, and Kyoung Ik Cho

*IT Convergence and Components & Materials Research Laboratory, Electronics and Telecommunications Research Institute 138, Gajeongno, Yuseong-gu, Daejeon 305-700, Korea
lsc@etri.re.kr*

For solution processed ZnO field-effect transistor (FET) devices, the highest electron mobility values are currently $1.65 \text{ cm}^2/\text{Vs}$, however obtainable only after annealing at temperatures $>300 \text{ }^\circ\text{C}$. Here we report our investigation on the formation, characterization, room temperature processing and spin-casting, printing behavior of a molecular precursor and adherence of such films in an FET device. ZnO nanoparticles were synthesized using a facile sonochemical method with modification of previously conditions. Firstly, zinc acetate dehydrate $[\text{Zn}(\text{CH}_3\text{COO})_2 \cdot 2\text{H}_2\text{O}]$ and potassium hydroxide $[\text{KOH}]$ were dissolved into methanol. The reaction mixture was sonicated for one hour. Currently the utmost challenge in the field is to gain a most complete understanding of the interplay between the parameters synthesis, processing and semiconductor performance for future development of printable electronic devices based on inorganic semiconductors such as ZnO. This work showed that the ink-jet printing technique was a convenient and low cost method to prepare films with controlled film thickness. The typical FETs exhibited a mobility of $0.86 \text{ cm}^2/\text{Vs}$, on/off current ratio of 10^5 , and the threshold voltage of -4V .

PREPARATION OF ELECTRICALLY CONDUCTIVE PET FILM WITH AL-DOPED ZINC OXIDE NANORODS

Sang Kyoo Lim, Sung-Ho Hwang, Hyun Jung Choi, Soonhyun Kim and Soo Keun Lee
Advanced Nano-Materials Research Team, Division of Nano & Bio Technology, Daegu
Gyeongbuk Institute of Science & Technology, 5th Floor, Daegu Technopark Venture 2 Plant,
75 Gongdanbuk2gil, Dalseo-gu, 704-230, Daegu, Republic of Korea
limsk@dgist.ac.kr

Transparent conductive oxides (TCOs) films are of considerable interest for many electrical and photoelectrical applications such as various conductive oxide electrodes, gas sensor, photoelectronic display devices, solar cells and energy efficient windows. There are various techniques to deposit TCO film on a substrate surface including chemical vapor deposition, physical vapor deposition, electron beam evaporation, sputtering and wet coating. Recently, wet coating has been much attention which is an easy way to fabricate large-area film and simple process and cost effective compare to dry coating methods. Among the various transparent and conductive oxides for antistatic coating materials, zinc oxide has possibility of transparent conducting material in place of indium tin oxide (ITO), if we could control its performance and stability. Zinc oxide is a versatile material with many applications including transparent electrode in solar cells, gas sensors and photo-luminescence devices. Generally, Zinc oxide nano particles are prepared by two methods, traditional solid state reaction and wet chemical methods. Also, the benefits of a utilizing solution-based method have also involved the considerable influence of reaction species on the size and morphology. In this aspect, many of the previous investigations on pure and transition metal doped ZnO prepared by solution based method, mainly utilized zinc hydroxide or salt as precursors and water or organic solvent as reaction media. Herein, we present microemulsion method toward the growth of well-proportioned and crystallized pure and aluminum doped ZnO nanorods using amphiphile as the modifying and protecting agent. The synthesis of aluminum doped ZnO nanorod was carried out in microemulsions, which were consisting of 5g of amphiphile such as dodexyl benzene sulfonate and 2 mmol of $ZnAc_2 \cdot 2H_2O$ both dispersed in 60 ml xylene by stirring until a homogenous slightly-turbid appearance of mixture was obtained. After aluminum precursor (aluminum nitrate nonahydrate) was added depend on the doping ratios. Then hydrazine monohydrate 2 ml and ethanol 8 ml mixture solution was added drop-wisely to the well-stirred mixture at room temperature by simultaneous agitation. The resulting precursor-containing mixture was subsequently heated to the 140°C for refluxing. After refluxing for 5 hours, a milky-white suspension was obtained and centrifuged to separate the precipitate, which was rinsed with absolute ethanol and distilled water for several times and dried in vacuum oven at 70°C for 24 hours. In the present study, a conductive film was fabricated using aluminum doped zinc oxide nanorods by the wet coating method. We investigated electrical and optical properties of the film.

References:

- [1] Y. Cho, Gi. Yi, J. Hong, S. H. Jang and S. Yang, *Thin Soild Films*. 515, 1864, (2006).
- [2] Z. W. Pang, Z. R. Dai and Z. L. Wang, *Science*, 291, 1947, (2001).
- [3] E. Comini, D. Faglia, G. Sberveglier, Z. Pan and Z. L. Wang, *Appl. Phys. Lett.* 81, 1869, (2002).
- [4] W. C. Shih and M. S. Wu, *J. Cryst. Growth*, 137, 319, (1994).
- [5] M. H. Huang, S. Mao, H. Feick, H. Q. Yan, Y. Y. Wu, H. Kind, R. Russo and P. D. Yang, *Science*, 292, 1897, (2001).
- [6] T. Izumi, K. Izumi, N. Kuroiwa, A. Fujimoto, M. Adachi and T. Yamamoto, *J. Alloys*

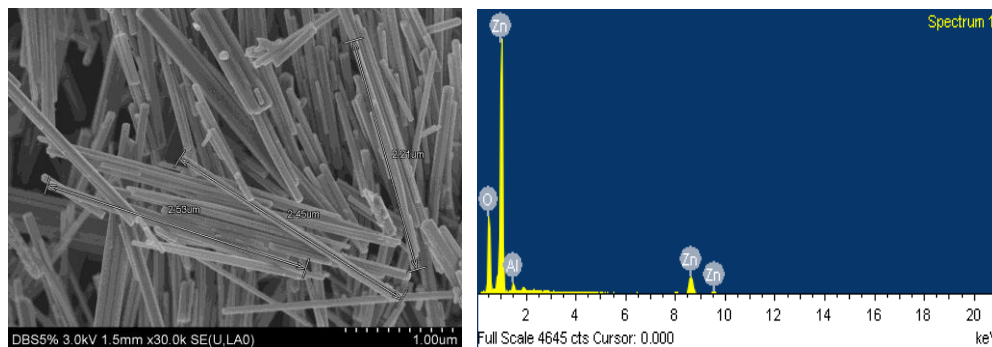


Figure 1. FE-SEM and EDX images of AZO nanorods.

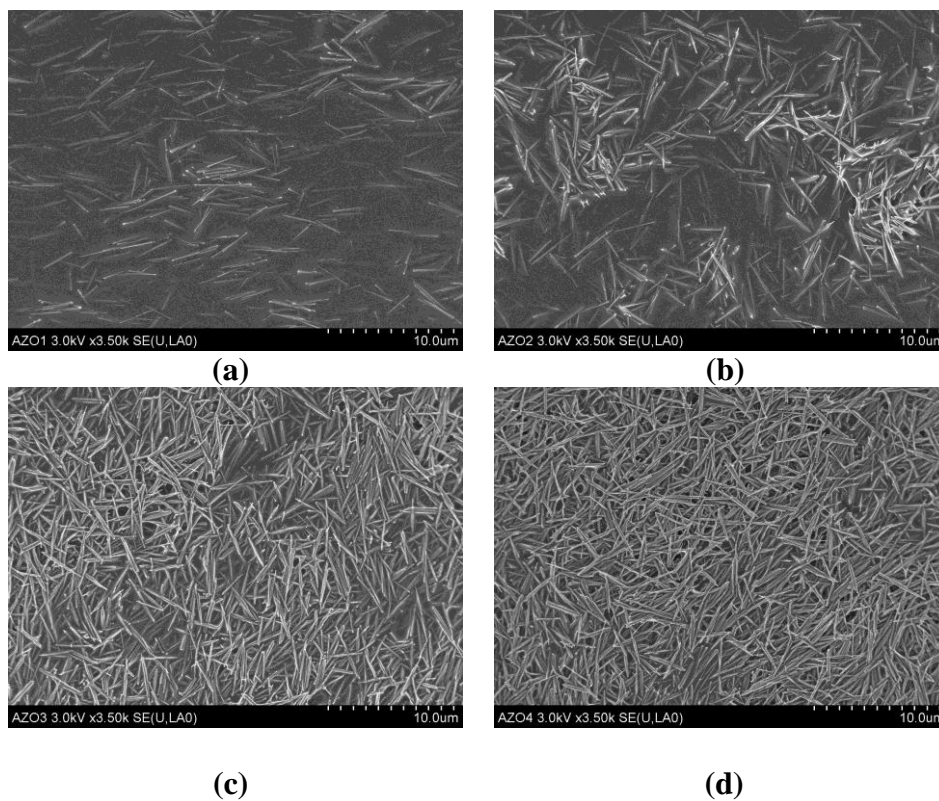


Figure 2. FE-SEM images of surface morphology of AZO nanorods coated film. (a) 3 wt.%, (b) 5 wt.%, (c) 7 wt.%, (d) 10 wt.%.

Magneto-optical study of single InAs/GaAs quantum rings

Ta-Chun Lin¹, Hong-Shi Ling¹, Sheng-Di Lin¹, Chien-Ping Lee¹,

Chia-Hsien Lin², Wen-Hao Chang²

¹*Department of Electronic Engineering, National Chiao Tung University, Hsinchu 300, Taiwan*

²*Department of Electrophysics, National Chiao Tung University, Hsinchu 300, Taiwan*

dajin6@yahoo.com.tw

Abstract—The magneto-optical properties of self-assembled InAs/GaAs quantum rings are investigated by the single ring spectroscopy in this work. The emissions of the single excitons and the biexciton complexes in individual rings are unambiguously identified by the power dependence of their emission intensity. In magneto-photoluminescence spectra, unlike quantum dots, where the diamagnetic shift of the biexciton emission is smaller than or equal to that of the exciton emission, quantum rings reveal surprisingly large diamagnetic coefficient for biexcitons, about twice as large as that of the single excitons, implying the large spatial extent of biexciton wave function. The magnetic response probes the considerable difference of the electronic structures between excitations and biexciton confined in quantum rings.

Self-assembled quantum dots (QDs) have attracted great interest in the field of photonic devices and quantum computing applications. Recently, a growth process involving partially capping and in-situ annealing has succeeded in transforming InAs QDs into quantum rings (QRs). The detailed morphological evolution and the associated optical properties have been carefully studied by atomic force microscopy (AFM) and conventional photoluminescence (PL) [1]. However, the magneto-optical properties of QRs have yet to be completely studied. So far only the diamagnetic properties of the neutral and the negatively charged excitons have been discussed [2]. In this work, with magnetic field up to 6 T, the diamagnetic shifts and Zeeman splittings of the neutral single excitons and biexcitons are investigated. The diamagnetic energy shift reveals the spatial distribution of the excitonic wave function which in turn provides informations on the QR's confinement potential and the Coulomb interactions.

The QRs used in this study were fabricated by a Varian Gen-II molecular beam epitaxy (MBE) system on a GaAs (001) substrate. Two monolayers of InAs were first deposited at a substrate temperature of 520 °C to form the precursor QDs. The substrate temperature was then lowered to 490 °C. A thin GaAs layer of 1.7 nm was next deposited to cover the QD sidewalls, and a growth interruption of 50 seconds was performed for a dewetting process which expels the indium atoms from the center of the QDs to move outwards for the QR formation.[1] The single ring PL studies were achieved in a low-temperature micro-photoluminescence (μ -PL) setup. The PL was excited with a 633 nm He-Ne laser and dispersed by a 750 mm monochromator into a silicon charge coupled device.

The AFM image of the QR on the surface is shown in the inset of fig. 1. The height of the rim including the capped region and the outer diameter are around 3 nm and 70 nm, respectively. The area density of QRs is estimated to be about $1 \times 10^7 \text{ cm}^{-2}$. Figure 1 reveals the conventional PL and the single ring spectra. The conventional PL spectrum shows an emission peak at 1329 meV with a 26 meV line width arising from the size fluctuation of the QRs. In the μ -PL spectrum, there is one sharp emission line at 1320 meV with the narrow line width around 50 μeV which is limited by the resolution of the measurement system.

A series of PL spectra were taken from the single QR over a range of excitation power as shown in Fig. 2. At low excitation powers, one emission line at 1320 meV dominates the spectrum and is associated with the neutral single exciton emission (X). Its intensity increases linearly with excitation power before it saturates. As the excitation power increases, a second emission line at 0.51meV below the X emission peak appears. Fig. 2(b) depicts the integrated intensity of both signals as function of the excitation power. The second line shows a nearly

quadratic increase with power and is therefore attributed to the biexciton emission (XX). For seven measured rings, the emission energies of X range from 1320 to 1328 meV, and the biexciton binding energies (defined as $E_X - E_{XX}$) are estimated to be 0.2 ~ 0.7 meV.

When an external magnetic field is applied along the growth direction, each of X and XX lines shifts and splits into two emission lines with opposite circular polarizations, as presented in Fig. 3. The Zeeman splitting values of X and XX are the same and equal to 120 $\mu\text{eV}/\text{T}$, corresponding to an exciton g-factor of $|g| = 2.1$. The identical splitting of X and XX confirms that the origin of XX is the optical transition of the biexciton into an exciton [3]. Furthermore, the energy shift of the center of the Zeeman doublet, the black solid line in Fig. 3(b), shows the quadratic dependence on magnetic field. This shift is fitted to βB^2 , and the average β_X is 6.8 $\mu\text{eV}/\text{T}^2$, while β_{XX} is 14.8 $\mu\text{eV}/\text{T}^2$, which is two times more than β_X .

The diamagnetic coefficient is proportional to the square of the radius of the excitonic wave function extension. The biexciton complexes in rings have wider in-plane extension of wave functions. This is different from the case of QDs [3-5], where the extension of the biexciton wave function is smaller than or equal to that of the exciton due to the electron-hole Coulomb attractive force. This striking result in QRs tells us that the Coulomb interactions inside the biexciton complex are much more complicated than that in QDs, where the electrons and holes are strongly confined in the center of QDs. We built up a three-dimensional finite element model based on Hartree approximation. The calculation result agrees reasonably well with our experimental finding. This theoretical study will be published elsewhere.

In brief, single quantum ring spectroscopy was studied. The exciton and the biexciton emission lines were assigned by power-dependent PL. The biexciton emission showed twice larger diamagnetic coefficient than the exciton, implying wider extension of wave functions for the biexciton complexes. The results indicate the novel magneto-optical responses of QRs.

This work was financially supported by the National Science Council under Contract Nos. NSC97-2120-M-009-002, NSC97-2120-M-009-004, and National Nano Device Laboratories.

References:

- [1] H. S. Ling, C. P. Lee, J. Appl. Phys. 102, 024314 (2007)
- [2] D. Haft, C. Schulhauser, A.O. Govorov, R.J. Warburton, K. Karrai, J.M. Garcia, W. Schoenfeld, P.M. Petroff, Physica E 13, 165 (2002)
- [3] A. Babinski, S. Awirothananon, J. Lapointe, Z. Wasilewski, S. Raymond, M. Potemski, Physica E 26, 190 (2005)
- [4] A. Kuther, M. Bayer, A. Forchel, A. Gorbunov, V. B. Timofeev, F. Schäfer, and J. P. Reithmaier, Phys. Rev. B. 58, R7508 (1998)
- [5] R.M. Stevenson, R.J. Young, P. See, I. Farrer, D.A. Ritchie, A.J. Shields, Physica E. 21, 381 (2004)

Figures:

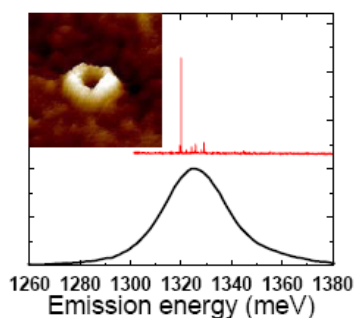


Fig. 1. PL spectra from conventional PL and μ -PL. The inset is the AFM image of the surface QR.

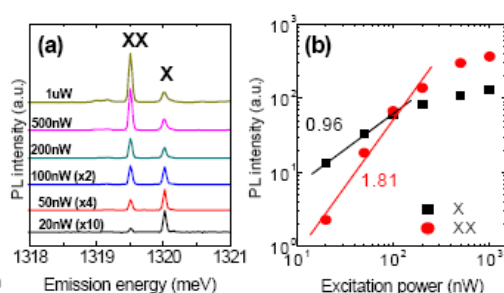


Fig. 2. (a) Power dependent PL spectra of single QR. (b) The integrated intensity versus the excitation power. The straight lines are the fitting results. The slope equals to 0.96 for the excitation (X, square) and 1.81 for the biexcitron (XX, circle)

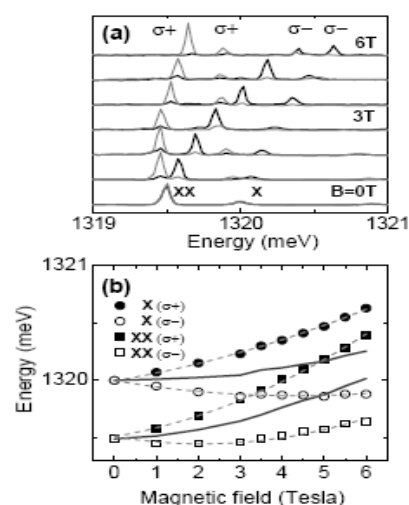


Fig. 3. (a) Magneto-optical spectra of the exciton and the biexciton emissions. (b) Peak positions as a function of the magnetic field. The diamagnetic coefficient of the exciton (biexciton) is 7.1 (14.6) $\mu\text{eV}/\text{T}^2$.

Nanoindentation fatigue of Diamond-Like Carbon and TiN hard coatings

E. Jiménez-Piqué, E. Tarrés, G. Ramírez and L. Llanes

Departament de Ciència dels Materials i Enginyeria Metal·lúrgica / CrNE,

ETSEIB, Universitat Politècnica de Catalunya, 08028 Barcelona, SPAIN

The tribomechanical response of diamond-like carbon (DLC) and TiN hard coatings has been extensively documented in the literature. However, most of this work has been mainly conducted on the basis of indentation, scratch or well-established tribological (e.g. pin-on-disc or abrasive wheel) testing techniques. On the other hand, knowledge on their behavior under repetitive contact loading is rather scarce. Considering that there is an increasing usage of DLCs in applications where contact loads of cyclic nature between curved surfaces are common, e.g. cold forming tools and machine components; such information on both mechanical response and damage mechanisms involved during contact fatigue of diamond-like carbon coated systems is required if they want to be used effectively. It is important to tests these systems at the micro and nano-levels, in order to understand the behaviour of the coatings without influence of the substrate.

In this investigation this is approached by assessing the contact fatigue behavior of a multilayer WC/C coating, with both amorphous WC and C lamellas, deposited on a fine-grained hardmetal by means of indentation testing techniques at both micro- and nano- scales. Spherical indentation tests at the micro-level indicate that the DLC multilayer exhibit a pronounced susceptibility to fatigue degradation in terms of emergence of circular cracks. Attempting to analyze and understand the reasons behind this response, the intrinsic fatigue behavior and implicit deformation and failure mechanisms of the DLC coating under consideration are then assessed by nanoindentation (both monotonic and cyclic) and microscopic techniques (AFM and FIB for cross-section inspection). The experimental findings are finally discussed in terms of the changes on mechanical response and damage evolution observed as applied contact stress and number of cycles increase for the different films.

Hetero-Onion-like, multilayered, core-Fe₃O₄|shell1-MnFe₂O₄|shell2-γ-Mn₂O₃ nanoparticles

A. López-Ortega¹, M. Estrader¹, G. Salazar-Alvarez^{1,2}, S. Estradé³,
J. Sort⁴, J. Arbiol³, F. Peiró³, S. Suriñach⁵, M.D. Baró⁵, J. Nogués⁶

¹Centre d'Investigació en Nanociència i Nanotecnologia, Campus UAB, Bellaterra, Spain.

²Materials Chemistry Group, Dept. of Physical, Inorganic and Structural Chemistry, Arrhenius Laboratory, Stockholm Univ., Stockholm, Sweden.

³MIND-IN2UB, Departament d'Electrònica, Universitat de Barcelona, Martí i Franquès 1, 08028 Barcelona, Spain

⁴ICREA and Dept. de Física, Univ. Autònoma de Barcelona, Bellaterra, Spain.

⁵Departament de Física, Universitat Autònoma de Barcelona, Bellaterra, Spain.

⁶ICREA and Centre d'Investigació en Nanociència i Nanotecnologia, Campus UAB, Bellaterra, Spain.

alo.icn@gmail.com

The interest in bi-magnetic core-shell nanoparticles is steadily increasing due to the possibility to obtain enhanced magnetic properties. Particularly, since the report on the use of exchange bias to overcome the superparamagnetic limit [1], the amount of experimental and theoretical work on passivated ferromagnetic (FM) nanoparticles coated with the corresponding antiferromagnetic (AFM) oxide layer has increased in the recent years [2]. Most of these systems are obtained by a simple chemical treatment of the core (e.g., oxidation), thus both core and shell contain the same transition metal. The synthesis of new hetero-core-shell systems, composed of different transition metal materials, would lead to a new degree of freedom to control the magnetic properties [3] and is thus of great interest. In this work we present the study of tri-magnetic hetero-onion nanoparticles composed by core-Fe₃O₄(ferrimagnetic, FiM)|shell1-MnFe₂O₄(FiM)|shell2-γ-Mn₂O₃ (FiM).

The synthesis of the onion particles was carried out following a multi-step procedure where preformed iron oxide nanoparticles were used as seeds for the subsequent growth of manganese (II) oxide and its passivation to form γ-Mn₂O₃. [4] Briefly, the Fe₃O₄ seeds were prepared by thermolysis of the iron (III) oleate [5] leading to an average particle size of 6.5 ± 1 nm. The manganese oxide layers were laid on the iron oxide-based nanocubes modifying an earlier reported procedure used for the synthesis of MnO|γ-Mn₂O₃ nanoparticles [6], leading to an interface MnFe₂O₄ layer of roughly 2 nm and an outer γ-Mn₂O₃ shell of 1nm. The morphology and compositions were determined through X-ray diffraction, transmission electron microscopy (Fig. 1(a)) and electron energy loss spectroscopy (EELS). The quantitative analysis of the EELS spectra and the simulations of the dependence of the percentage of each element on the position along the particle diameter, shown in Fig. 1(b), were performed using the home-made software package MANGANITAS [7].

Magnetic measurements reveal that onion nanoparticles exhibit an extra transition at the known T_C of γ-Mn₂O₃ ($T_C \sim 40$ K) and an increase in T_B , where the latter is consistent with the creation of a Mn-ferrite interface layer. The results show that the coercivity increases significantly while M_S decreases compared with Fe₃O₄ seeds magnetic data. Both effects are consistent with the incorporation of γ-Mn₂O₃ which has a much larger anisotropy and smaller M_S than Fe₃O₄. Interestingly, the hysteresis loop the onion nanoparticles shows a two stage behavior, implying that the core and the shell switch independently. This is probably due to a spring-magnet [8] effect given the diameter-thickness of the constituents. Also, the core-shell nanoparticles show

larger exchange bias than the seeds, which is expected since the seeds should only have surface effects while the core-shell should have FiM-FiM coupling [2].

References:

- [1] V. Skumryev, et al. *Nature*. **423** (2003) 850.
- [2] J. Nogués, et al. *Phys. Rep.* **422** (2005) 65.
- [3] O. Iglesias, et al. *J. Nanosci. Nanotechnol.* **8** (2008) 2761; W. Liu, et al. *J. Nanosci. Nanotechnol.* **8** (2008) 2781.
- [4] G. Salazar-Alvarez, et al. to be submitted (2009).
- [5] J. Park, et al. *Nat. Mater.* **3** (2004) 891.
- [6] G. Salazar-Alvarez, et al. *J. Am. Chem. Soc.* **129** (2007) 9102.
- [7] S. Estradé et al, *Appl. Phys. Lett.* **91** (2007) 252503.
- [8] E.E. Fullerton, et al. *J. Magn. Magn. Mater.* **200** (1999) 392.

Figures:

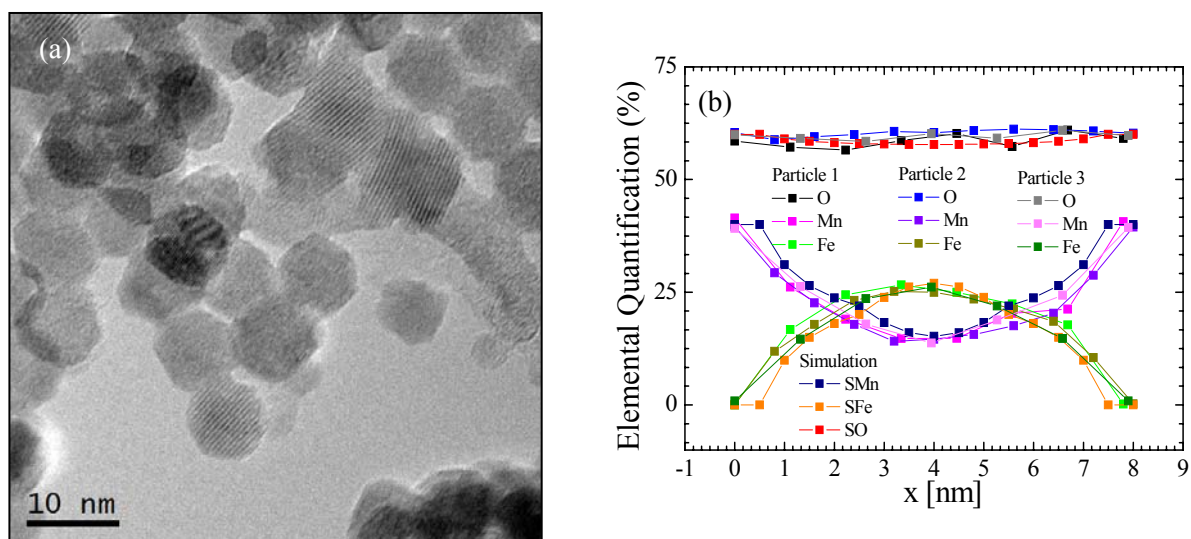


Figure 1 (a) TEM Image of $\text{Fe}_3\text{O}_4|\text{MnFe}_2\text{O}_4|\gamma\text{-Mn}_2\text{O}_3$ hetero-core-shell nanoparticles. (b) Elemental quantification for three different core-shell particles and simulation considering a 1 nm Mn_2O_3 /2 nm MnFe_2O_4 /5 nm Fe_3O_4 core.

Numerical simulation of Dielectrophoresis and AC Electroosmosis for DNA trapping including the particle steric effect

Neophytos Loucaides¹, Antonio Ramos², George E. Georghiou³

^{1,3}*University of Cyprus, Department of Electrical and Computer Engineering, 75 Kallipoleos Str., Nicosia, Cyprus*

²*University of Seville, Department of Electronics and Electromagnetism, Faculty of Physics, 41012 Avenida Reina Mercedes, Sevilla, Spain*

¹leep4nl1@ucy.ac.cy

Dielectrophoresis (DEP) is a very promising method for nanoparticle manipulation [1]. It has already been used in order to trap, separate or manipulate many types of nanoparticles, such as DNA [2], carbon nanotubes [3], viruses [4] and many more. Nanoparticle dielectrophoresis is usually performed in microfluidic channels above electrode formations that induce an AC electric field. However, the process is very complex due to the interactions between the fluid, the particles and the electric field [5].

A physical model is presented here that includes the AC electroosmotic motion of the fluid, the dielectrophoretic force [6], the steric effect on the particle concentration [7] and on the fluid motion, as well as other parameters affecting the system (such as buoyancy, gravity, drag etc). This model, which is solved by the finite element method, is considered as the most complete to date for the characterisation and understanding of the processes encountered in such devices.

Results are presented for the specific case of the dielectrophoretic trapping of 12kb pTA250 DNA using parallel electrodes. The numerical predictions are subsequently compared with experimental results, demonstrating qualitative agreement with many observations. Furthermore, this model allows the investigation of device parameters which are very difficult or impossible to study under experimental conditions and provides new insights into the operation of such systems.

References:

- [1] Hughes MP. *Nanotechnology*. **11**(2000):124-132.
- [2] Bakewell DJ, Ermolina I, Morgan H, Milner J, Feldman Y. *Biochimica et Biophysica Acta*. **1493**(2000):151-158.
- [3] Dimaki M, Boggild P. **15**(2004):1095-1102.
- [4] Hughes MP, Morgan H. 21st Annual International Conference of the IEEE Engineering in Medicine and Biology Society. Atlanta; 1999.
- [5] Ramos A, Morgan H, Green NG, Castellanos A. *J Phys D*. **31**(1998): 2338-2353.
- [6] Loucaides N, Georghiou GE, Charalambous CD. *J Phys: Conf Ser*. **61**(2007): 718-723.
- [7] Kumar A, Qiu Z, Acrivos A, Khusid B, Jacqmin D. *Phys Rev E*. **69**(2004):021402.

Figures:

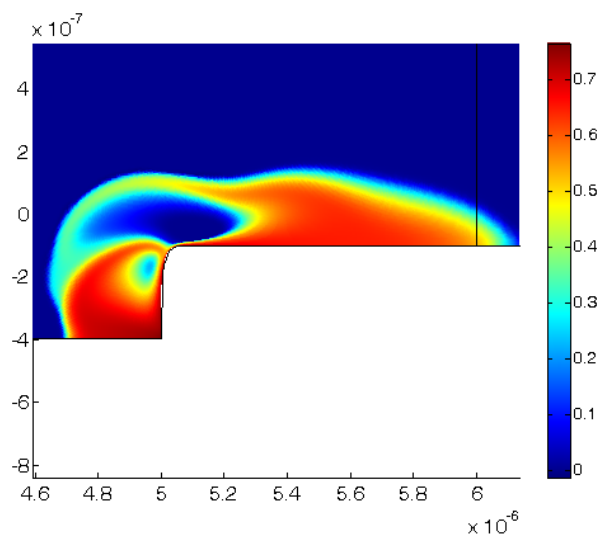


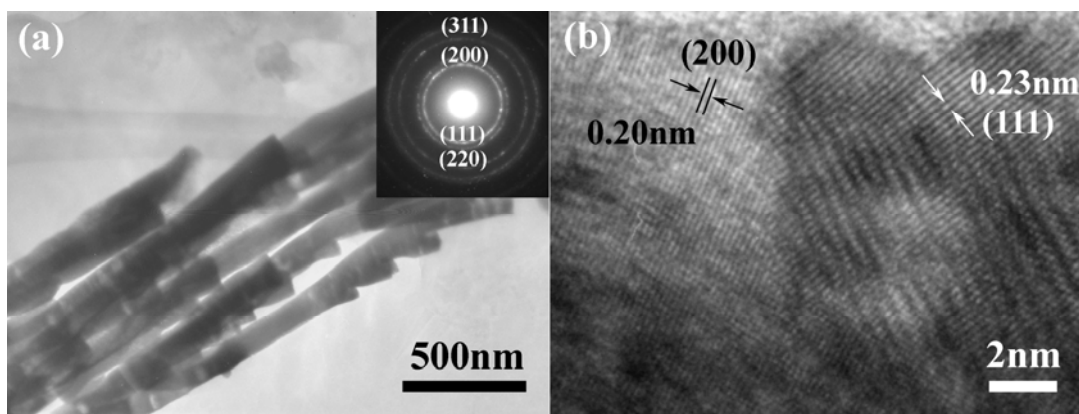
Figure 1. Steady state concentration over the electrode edge for 12kb pTA250 DNA under Dielectrophoresis and ACEO.

Self Assembly of Periodic Serrated Nanostructures

Dongdong Li and Jia G. Lu*

Departments of Physics & Astronomy and Electrical Engineering
University of Southern California
Los Angeles, CA 90089-0484 (USA)

Anodic aluminum oxide membranes with serrated nanochannels have been successfully fabricated via a two-step anodization method. The serrated channels with periodic intervals are aligned at an angle of $\sim 25^\circ$ along the stem channels. The formation of the serrated channels is attributed to the generation of oxygen gas bubbles and the resulted compressive stress on the oxide membrane. Via electrodeposition, serrated Pt nanowires are formed, as shown in the figure below. The as-synthesized nanowires demonstrate a superior electrocatalytic activity compared to the conventional straight nanowires. Moreover, three-dimensional hierarchical serrated/straight hybrid structures is constructed using this simple and novel self assembly technique.



(a) A TEM image of serrated Pt nanowires. Inset: corresponding polycrystalline electron diffraction pattern. (b) A high-resolution TEM image of Pt nanowire. The lattice fringes of Pt (111) and (200) planes are labeled with the interplane distances of 0.23 and 0.20 nm, respectively.

Electronic Properties of Organic Photovoltaic rr-P3HT/C₆₀ Ordered Blend

Arnaud Maillard and Alain Rochefort

*Département de génie physique, École Polytechnique de Montréal,
and Regroupement Québécois sur les Matériaux de Pointes (RQMP), Montréal, Canada*

arnaud.maillard@polymtl.ca

The need for clean and renewable energy sources has recently promoted research on organic photovoltaic cells (OPCs) to reduce the cost of solar energy by exploiting the large-scale and low-cost fabrication techniques associated with polymers. Photon absorption, occurring in an electron donor material, creates excitons which are dissociated into free charge carriers when encountering an interface with an electron acceptor material. Bulk heterojunctions of donor and acceptor are used to reduce exciton recombination in the donor and to achieve power conversion efficiencies up to 5% [1,2]. However, the efficiency of OPCs has to reach 10% before they can be competitive in the solar cell market which is currently dominated by polycrystalline silicon [3]. One possible way to achieve such target is through the engineering of the donor-acceptor structure, which requires a better fundamental understanding of the physical processes taking place in these organic systems.

A computational study on a promising donor-acceptor system is performed to investigate the influence of structural order within the blend on the resulting electronic properties. The donor is regioregular head-to-tail poly(3-hexylthiophene-2,5-diyl) (rrP3HT), which self-assemble into microcrystalline domains [4] of high charge carrier mobility [5], while the acceptor is buckminsterfullerene (C₆₀), allowing an ultrafast charge transfer between the donor and the acceptor [1]. First principles DFT computations were performed with SIESTA [6] within the local density approximation (LDA) using periodic boundary conditions, norm-conserving Troullier-Martins pseudopotentials and linear combination of numerical atomic orbitals basis sets. The molecular geometries were optimized using the DFT calculated forces and stresses in a quasi-Newton method following the Broyden-Fletcher-Goldfarb-Shanno (BFGS) procedure to update the Hessian matrix. The optimization was stopped when the maximum force in the system was less than 10⁻² eV/Å and the total energy variation between two iterations was less than 5 × 10⁻⁴ eV.

Bulk donor-acceptor heterojunctions were studied by diluting a rrP3HT crystal network by C₆₀s. The geometric and electronic properties of the rrP3HT crystal used as reference were obtained in previous work [7]. Multiple configurations with various positions and orientations of the C₆₀s (Fig. 1(A)) were optimized as a function of distance between the C₆₀s and the rrP3HT chains (Fig. 1(B)). The first configuration, where the C₆₀ pentagonal face is between two hexylthiophene monomers, is slightly more stable than the second and third configurations. The inclusion of C₆₀s in the rrP3HT crystal also reduces the HOMO bandwidth in the π -stacking and backbone direction compared to the rrP3HT crystal by respectively annihilating the interchain π - π coupling, and by lifting the degeneracies at the Brillouin zone edge. The LUMO of the heterojunction is formed of one of the C₆₀ triply degenerated states and exhibits very small dispersion. The HOMO wavefunction is similar to the HOMO of the rrP3HT crystal, while the LUMO is strongly localized on the C₆₀ (Fig. 1(C)).

The influence of the distance between the C₆₀s and the rrP3HT chains in the π -stacking direction on the band structure was also studied (Fig. 1(D)). An increased pressure, reducing this distance,

causes a small decrease of the HOMO bandwidth in both the π -stacking and backbone directions, while it causes a small increase of the LUMO bandwidth in these two directions. Furthermore, the increased pressure stabilizes in energy the HOMO and destabilizes the LUMO, resulting in a marked augmentation of the bandgap. Finally, the number of rrP3HT chains between C_{60} s in the π -stacking direction was varied. Adding rrP3HT chains in the heterojunction pushes the LUMO band down and reduces the bandgap.

The results discussed above were obtained in the ground state picture. The next step in our study is to use time-dependent DFT to compute the excited states of these systems. These excited states should include an electronic bridging state overlapping the rrP3HT and the C_{60} [8]. Nevertheless, the results presented here clearly reveal that the positions of the band levels can be modulated by pressure or by the dilution degree of C_{60} s in the rrP3HT crystal network. This important observation will lead to the engineering of the band alignment of future OPCs to optimize their power conversion efficiencies.

References:

- [1] N. S. Sariciftci, *et al.*, Science, **258**, (1992), 1474.
- [2] N. S. Sariciftci, Materials Today, **7**, (2004), 36.
- [3] A. C. Mayer, *et al.*, Materials Today, **10**, (2007), 28.
- [4] T. J. Prosa, *et al.*, Macromolecules, **25**, (1992), 4364.
- [5] H. Sirringhaus, *et al.*, Nature, **401**, (1999), 685.
- [6] J.M. Soler *et al.*, Journal of Physics: Condensed Matter, **14**, (2002), 2745.
- [7] A. Maillard and A. Rochefort, Physical Review B, **79**, (2009), 115207.
- [8] Y. Kanai and J. C. Grossman, Nano Letters, **7**, (2007), 1967.

Figures:

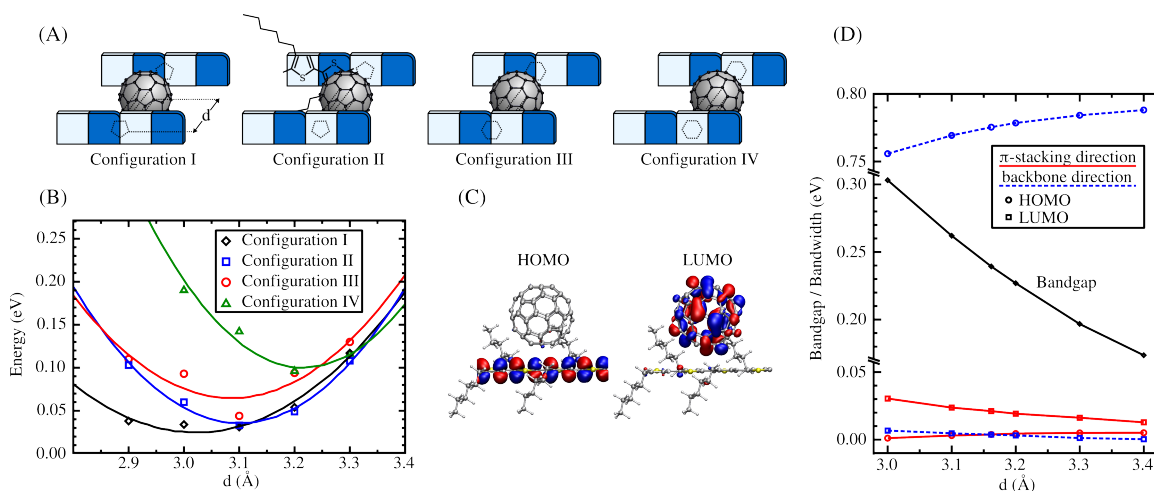


FIG. 1 – (A) Considered configurations of donor-acceptor bulk heterojunctions. (B) Total energy of the configurations as a function of distance between the C_{60} s and the rrP3HT chains. (C) HOMO and LUMO wavefunctions. (D) Variation of the band structure properties as a function of distance between the C_{60} s and the rrP3HT chains.

CARBON NANOTUBES FILMS FOR THE DETECTION OF MID-INFRARED LIGHT

*Sylvain Maine, C. Koechlin, R. Haidar, B. Tretout, J. Deschamps, A. Loiseau, and J.-L. Pelouard**

ONERA, Chemin de la Hunière, F-91761 Palaiseau, France

**LPN-CNRS, Route de Nozay, F-91461 Marcoussis, France*
sylvain.maine@onera.fr

Carbon nanotubes CNT behave as a direct gap semiconductor, with a band-gap energy depending on their structure (single or multi-wall) and geometry (diameter, chirality). Typically, single-walled CNT present a bandgap energy between 0.1eV and 1.5eV, thus they are well suited for opto-electronic applications in visible to the infrared range, such as bolometric light detectors [1] or phototransistors [2].

Following these pioneering works, we propose to study bolometers based on CNT films with extended detection range to the mid-infrared spectrum (8-12 μm), in band III of atmospheric transparency. As shown in Figure 1, thin CNT films may present constant and highly efficient absorption in this spectral range, demonstrating their high potential for band III applications.

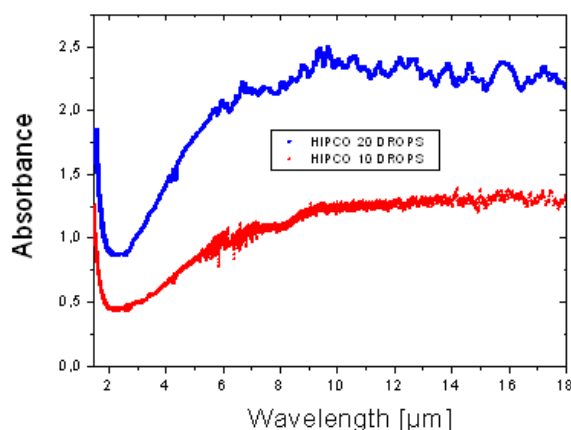


Figure 1 : absorption spectra of thin HiPCO CNT films (density expressed in drops, corresponding to typical thicknesses of 100nm and 200nm).

Studied devices are made of a suspended CNT film over platinum interdigit electrodes (Figure 2), using a technique based on cellulose filters [3]. The electrode interdigital pitch can be of 1 μm , 2 μm , 5 μm or 10 μm .

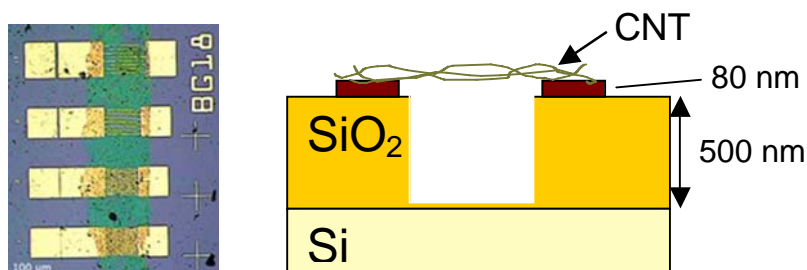


Figure 2 : Photo and Schematic diagram of the CNT films suspended on 80nm thick platinum electrodes.

In the 100-300K temperature range, measured I - V characteristics denotes a slight nonlinearity for bias voltages larger than 0.5V as already been noted for thin CNT films [4]. Measurements of the low voltage resistance of various geometry devices give reach to the resistance square which proves to follow a quadratic temperature law (Figure 3a):

$$R_{square} = \frac{R_0}{T^2} \text{ where } R_0 \approx 10^{12} \Omega$$

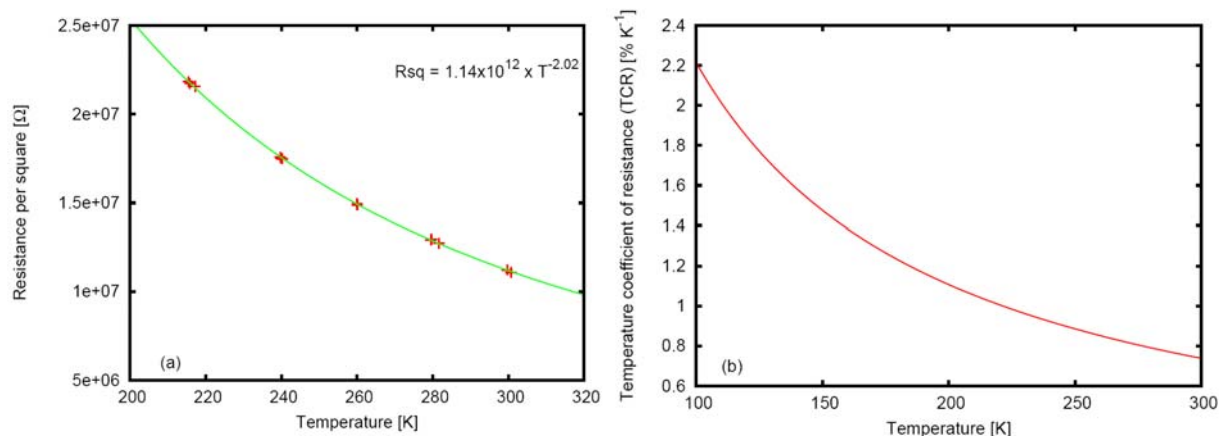


Figure 3 : (a) Resistance per square of the CNT film versus temperature for various geometry devices ; (b) TCR as a function of temperature.

One can also extract the temperature coefficient of resistance TCR which is a sizing parameter for bolometric devices based on semiconductor material (Figure 3b):

$$TCR = - \frac{\Delta R}{R \Delta T}$$

We find out a TCR of $\sim 1\%$ at ambient temperature, which is slightly below the usual value of materials used for bolometric applications (2.5% in amorphous silicon). Let us point out that this promising value is obtained on non-optimised structures: indeed, scanning electron microscope (SEM) images show that the CNT films presents textural defects and/or embeds remaining cellulose impurities. Work is in progress to address this specific matter as well as the architecture of the devices, in order to achieve the best possible electrical contact on the CNT.

References:

- [1] M.E. Itkis et al., "Bolometric Infrared Photoresponse of Suspended Single-Walled Carbon Nanotube Films", *Science* **312**, p 413 (2006)
- [2] M. Freitag et al., "Photoconductivity of Single Carbon Nanotubes", *NanoLetters* **3**, 8 (2003)
- [3] Z. Wu et al., "Transparent, Conductive Nanotube Films", *Science* 305, p 1273 (2004).
- [4] V. Skalavova et al., "Electronic transport in carbon nanotubes: From individual nanotubes to thin and thick networks", *Phys. Rev. B* 74, 085403 (2006).

**IN SITU POLYMERIZATION AND COMPOSITE FORMATION: AN
EFFICIENT SYNTHESIS TECHNIQUE FOR NEW GENERATION
NANOMATERIALS**

Kaushik Mallick^{1,3}, Michael Witcomb², André Strydom³

¹ Advanced Materials Division, Mintek, Private Bag X3015, Randburg 2125,
South Africa.

² Microscopy and Microanalysis Unit, University of the Witwatersrand, Private
Bag 3, WITS 2050, South Africa.

³ Physics Department, University of Johannesburg, PO Box 524, Auckland Park
2006, South Africa.

Nanotechnology is a rapidly growing area of material science because of their numerous applications in various fields such as catalysis, sensor, electronics and optics as well as in the application of medical science. The unique properties of metal nanoparticles are directly related to their size and are significantly different from those of the corresponding bulk materials. Besides precise control over the size and shape, the stability of nanoparticles is an extremely important issue. Surfactants, polymer and thiol functionalized molecules have also been used in the synthesis of particles to promote stabilization. The advantage of polymer as a stabilizer is due to its robust nature which could give the metal particles additional stability.

'*In situ* polymerization and composite formation' (IPCF) types of reactions, specifically for the synthesis of 'metal-polymer composite material' [1-4], have potential advantage in the area of 'synthetic material science' because both the polymer and the nanoparticles are produced simultaneously which facilitate an intimate contact between the particles and the polymer through functionalization. The resultant material, which shows interesting catalytic, electrical and magnetic property, would acquire the quality of both components, such as, good stability, conductivity, optical property and catalytic activity from the metal and easy processing, light weight and also tunable conductivity from the polymer. We synthesized a series of composite materials exploiting the IPCF approach and used them for catalytic application that showed tremendous potential of these kinds of materials. We report on our results of conductivity and magnetic investigations on nano-structured composites, which highlight the potential of this type of material for versatile applications.

We believe that an ideal composite material having a higher degree of nano-level interaction between two components might be expected to exhibit an improved performance with wider applications in various systems of basic science and engineering.

References:

- [1] K. Mallick, M. Witcomb, A. Dinsmore, M. Scurrrell, *Langmuir*, 21 (2005) 7964.
- [2] K. Mallick, M. Witcomb, M. Scurrrell, *Eur. Phys. J. E*, 20 (2006) 347.
- [3] S. Scalzullo, K. Mondal, M. Witcomb, A. Deshmukh, M. Scurrrell, K. Mallick, *Nanotechnology*, 19 (2008) 075708.
- [4] K. Mallick, M. Witcomb, M. Scurrrell, A. Strydom, *J. Phys. D: Appl. Phys.*, 42 (2009) 095409.

Length dependence of half-metallicity on zigzag carbon nanotubes

P. Alonso-Lanza¹, A. Mañanes¹, M. J. López² and J. A. Alonso^{2,3}

¹Departamento de Física Moderna, Universidad de Cantabria, 39005 Santander, Spain

²Departamento de Física Teórica, Atómica y Óptica, Universidad de Valladolid,
47011 Valladolid, Spain

³Donostia International Physics Center DIPC, 20018 San Sebastián, Spain

angel.mananes@unican.es

It has been established, by first principles calculations, that carbon nanostructures with zigzag boundaries, like graphene nanoribbons and nanoflakes or finite zigzag nanotubes, present the property of half-metallicity under the influence of an intense external electric field [1, 2]. Half metals are materials which filter the electronic current into a single spin channel, so that they are metals for one spin and semiconductors for the other spin orientation. These materials are the cornerstone for the implementation of spintronic devices [3].

In the present work we analyze the half-metallicity of finite (7,0) zigzag carbon nanotubes of four different lengths, in order to study the evolution of the property with the actual length of the finite nanotube. The nanotubes considered have different number, n , of zigzag carbon chains: $n=8$, $C_{112}H_{14}$; $n=10$, $C_{140}H_{14}$; $n=12$, $C_{168}H_{14}$ and $n=14$, $C_{196}H_{14}$. The corresponding lengths are: $L_8=15.537$ Å, $L_{10}=19.790$ Å, $L_{12}=24.234$ Å and $L_{14}=28.513$ Å. Both open ends of the nanotubes were saturated with hydrogen atoms (seven H on each side).

The electronic structure is calculated by solving the Kohn-Sham equations of density functional theory, DFT, within both the Local Spin Density Approximation, LSDA, and the Generalized Gradient Approximation, GGA, for the exchange-correlation energy, using the Amsterdam Density Functional, ADF 2008.01, code [4]. The method uses Slater type orbitals localized at the atoms as basis sets, and a frozen core approximation, so only the electronic structure of the valence electrons is optimized in the calculation. The basis set is triple- ζ with polarization. The code makes full use of the symmetry of the system, C_{7v} and D_{7h} depending on the spin state of the nanotube, and it calculates bonding energies with respect to restricted atomic fragments. Geometry optimization is based on a quasi Newton approach, using the Hessian for computing changes in the geometry so as to make the gradients vanish.

The ground state for the four tubes considered is the antiferromagnetic, AFM, state with spin $S=0$ and C_{7v} symmetry. This means that one extreme of the nanotube is dominated by spin alpha density, $\rho_\alpha(\vec{r})$, and the other extreme by spin beta density, $\rho_\beta(\vec{r})$. This localization is due to the structure of the highest occupied molecular orbital, HOMO, of each spin which is a localized edge state for all the tubes considered. However, the lowest unoccupied molecular orbital, LUMO, is a delocalized state for all the nanotubes, and this is different with respect to the results obtained in the (14,0) finite nanotubes [1], for which the LUMO state was also localized at the edges. The nonmagnetic, NM, state, also with $S=0$ but with D_{7h} symmetry so $\rho_\alpha(\vec{r}) = \rho_\beta(\vec{r})$ at any point of the nanotube, is always higher in energy than the AFM state. There is also a local minimum at $S=2$, a ferromagnetic state, FM, which is lower in energy than the NM and that is nearly degenerate with the AFM state for the longest nanotube considered. For this FM state the net spin density is localized at the edges of the nanotube.

Starting from the relaxed ground state AFM structures, a static electric field of increasing intensity was applied along the axis of the nanotube and the electronic structure was selfconsistently recalculated without allowing for any geometrical distortion. The results indicate that the property of half-metallicity is obtained for all the nanotubes considered, in spite of the very small initial gaps, and of the delocalized nature of the LUMO states, which, consequently are much less affected by the external electric field. So even if the LUMO states do not modify their energies, the eigenvalues of the localized HOMO states are modified by the

electric field thus producing half-metallicity. The dependence of the critical electric field with the nanotube length is analyzed from the results.

Acknowledgments: Work supported by MEC of Spain (Grants MAT2008-06483-C03-01/-03). MPAL acknowledges a “Beca-colaboración” fellowship of the Spanish MEC.

References:

- [1] A. Mañanes, F. Duque, A. Ayuela, M. J. López, J.A. Alonso, Phys. Rev. B **78** (2008) 35432
 [2] A.J. Du, Z.H. Zhu, C.H. Sun, Y. Chen, G.Q. Lu, S.C. Smith, Chem. Phys. Lett., **468** (2009) 257
 [3] J.R. Hauptmann, J. Paaske and P.E. Lindelof, Nature Phys. **4** (2008) 373
 [4] G. te Velde, F.M. Bickelhaupt, S.J.A. van Gisbergen, C. Fonseca Guerra, E.J. Baerends, J.G. Snijders and T. Ziegler, J. Comp. Chem. **22** (2001) 931; C. Fonseca Guerra, J.G. Snijders, G. te Velde and E.J. Baerends, Th. Chem. Acc. **99** (1998) 391; <http://www.scm.com>

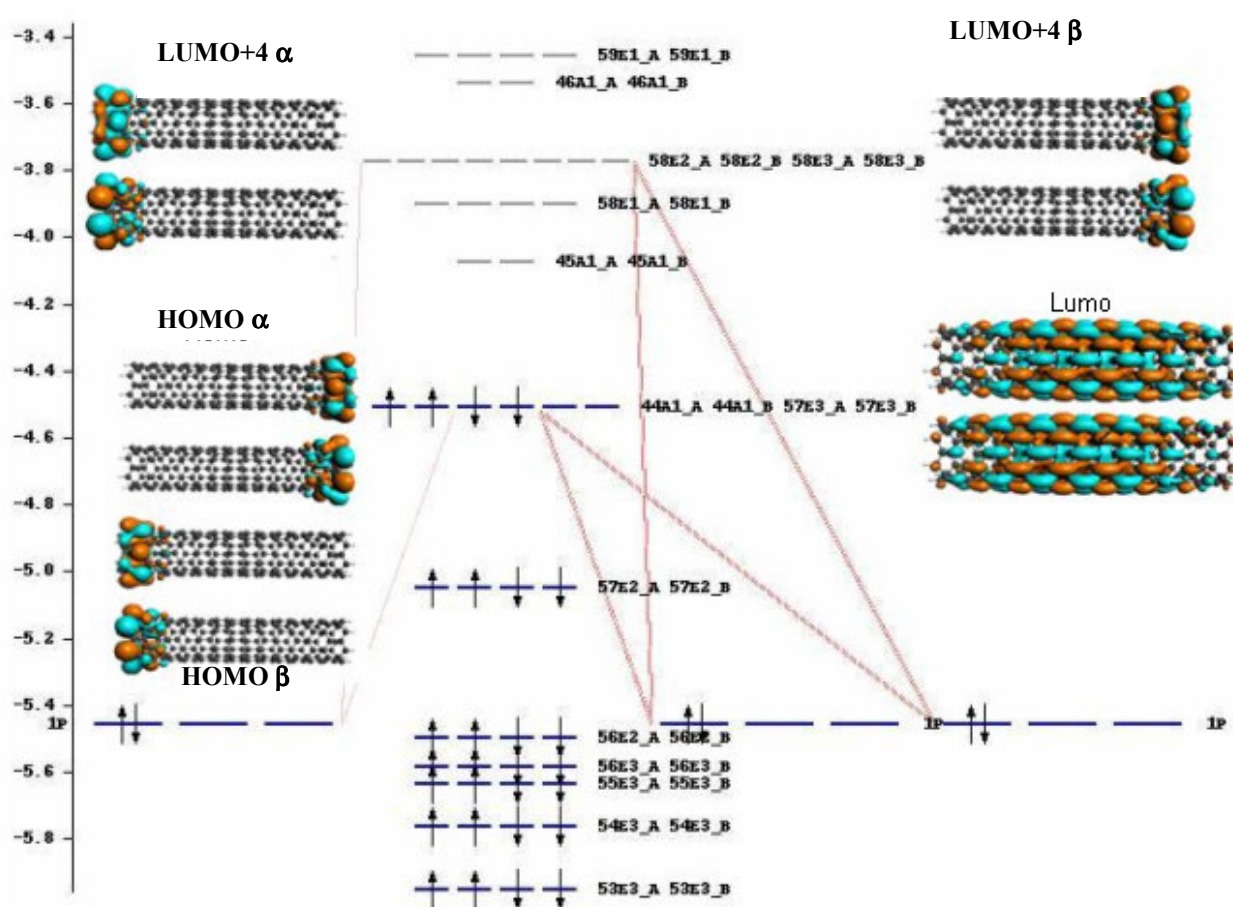


Figure 1.- Energy eigenvalues and wave functions for the frontier orbitals, orbitals near the HOMO and LUMO, for the AFM ground state of the longest nanotube $n=14$, C₁₉₆H₁₄. The vertical scale gives the energy in eV; the labels correspond to the C_{7v} symmetry of the system. The red lines indicate the atomic orbitals that dominate the corresponding molecular orbital. The two colours of the wave functions indicate positive and negative values.

Aggregate model for the vibrational properties of hydroxyapatites

M. Vallejo¹, M. Rada², L. Buelta³, I. Cabria⁴, F. Rodríguez⁵, and A. Mañanes¹

¹Departamento de Física Moderna, Universidad de Cantabria, 39005 Santander, Spain

²Instituto Cántabro de Estadística ICANE, 39008 Santander, Spain

³Departamento de Ciencias Médicas y Q., Universidad de Cantabria, 39011 Santander, Spain

⁴Departamento de Física Teórica, Atómica y Óptica., Universidad de Valladolid, 47011

Valladolid, Spain

⁵Departamento CITIMAC, Universidad de Cantabria, 39005 Santander, Spain

angel.mananes@unican.es

The infrared spectrum, IR, of the relevant biological material hydroxyapatite HA, $\text{Ca}_{10}(\text{PO}_4)_6(\text{OH})_2$, is calculated using Density Functional Theory DFT to describe the electronic structure of the compound. The inorganic component of human bone is not pure HA but a poorly crystalline biological apatite containing numerous trace ions, the most abundant of which are carbonate, $(\text{CO}_3)^{2-}$ and acid phosphate, $(\text{HPO}_4)^{2-}$. It is then relevant to characterize the changes in the infrared spectra of pure HA due to the substitution of some phosphate groups by carbonate, for example, a process which is related with bone maturity.

As has been indicated in previous works [1, 2], the crystalline solid HA can be considered as a solid “made of clusters”, like for example some intermetallic compounds [3]. In the case of HA, the relevant structures are the, approximately tetrahedral, phosphate groups, with a charge $-3e$ and that maintain their structure inside the crystal, which are surrounded by the Ca^{2+} ions and the hydroxyl groups, OH^- . Following this suggestion, we have considered different finite clusters, which involve always six phosphate groups but different numbers of Ca and OH ions, to calculate the vibrational spectrum to be compared with the measured infrared spectra. To calculate the vibrational properties, a complete relaxation of the geometrical structure of the clusters has been performed by steepest descent methods.

The electronic structure is calculated by solving the Kohn-Sham equations of DFT, within the Local Spin Density Approximation, LSDA, for the exchange-correlation energy, using the Amsterdam Density Functional, ADF 2008.01, code [4]. This method uses Slater type orbitals localized at the atoms of the aggregate as basis sets, and it calculates bonding energies with respect to restricted atomic fragments. The dynamical matrix is obtained using analytical first derivatives of the binding energy.

Firstly, we have calculated the electronic structure of the cluster $\text{Ca}_{10}(\text{PO}_4)_6(\text{OH})_2$, in the geometry of the unit cell, and with a field of point charges located at the lattice points of the nearest 26 unit cells of hydroxyapatite surrounding the cluster, and considering in these extra unit cells charge $+2e$ at the Ca atoms, charge $-3e$ at P and charge $-1e$ at the O atom of the OH group. The electronic density of states DOS shows in this model the same main features which have been obtained in DFT calculations of the crystalline solid [1]. Secondly, the following free clusters have been considered as a model for the vibrational properties of HA: c1) $\text{Ca}_{24}(\text{PO}_4)_6(\text{OH})_4$, c2) $\text{Ca}_{14}(\text{PO}_4)_6(\text{OH})_4$, c3) $\text{Ca}_{12}(\text{PO}_4)_6(\text{OH})_4$, c4) $\text{Ca}_{12}(\text{PO}_4)_6(\text{OH})_2$ and c5) $\text{Ca}_{10}(\text{PO}_4)_6(\text{OH})_2$. From larger to smaller clusters, we have chosen the six phosphate groups which are closer to the axis of the hexagonal channel formed by Ca atoms. The OH groups are located in this axis [1]. In each cluster, they are retained only those Ca atoms which remain closer to the six phosphate groups. For each aggregate, a complete optimization of the geometry is performed before the calculation of the electronic and vibrational densities of states. The clusters considered have always an inversion centre, so the calculation clearly separates infrared modes from the Raman active frequencies.

Charge population analysis, including Mulliken, Hirshfeld and Voronoi charges, and the study of the geometrical parameters allow for the comparison of the structure of the phosphate groups in the different clusters considered, and also with the free, neutral and charged, phosphate. The results indicate that, as expected, the structure is quite stable and rather

independent of the actual environment in the finite cluster. However, some distortions and differences are found when compared with the free phosphate structure.

The structure of the calculated electronic DOS for all the clusters resembles that of the HA crystal (Ca and phosphate dominated bands of electronic states). However, finite size effects show up at the Fermi level, producing a smaller band gap.

The calculated infrared vibrational spectra of all the clusters show the two bands associated to the normal modes of the free phosphate: One band around $\nu=1000\text{ cm}^{-1}$, associated to the asymmetric stretching mode, and another one at $\nu=500\text{ cm}^{-1}$, corresponding to the bending mode. Furthermore, the high frequency stretching mode of the OH group is also obtained at $\nu=3500\text{ cm}^{-1}$. The infrared spectrum of the smaller cluster c5 is given in Figure 1.

The biological processes induce the substitution of some phosphate groups of the HA by carbonate CO_3 groups. Alternatively, the carbonate group can also substitute the OH group. The influence of these two substitutions in the vibrational infrared spectrum of the HA has been analyzed in our case using the smaller cluster c5, and the infrared spectrum is given in Figure 2.

Acknowledgments: Work supported by MEC of Spain (Grants MAT2008-06483-C03-01 and -03) and Junta de Castilla y León (Grants VA017A08 and GR23). IC acknowledges support from MEC-FSE through the Ramón y Cajal Program.

References:

- [1] L. Calderín, M. J. Stott, and A. Rubio, *Phys. Rev. B* **67** (2003) 134106.
- [2] L. Calderín, D. Dunfield, and M. J. Stott, *Phys. Rev. B*, **72** (2005) 224304.
- [3] J.A. Alonso, *“Structure and Properties of Atomic Clusters”*, Imperial College Press (2005) Chap. 12.
- [4] G. te Velde et al., *J. Comp. Chem.* **22** (2001) 931; C. Fonseca Guerra et al., *Th. Chem. Acc.* **99** (1998) 391; <http://www.scm.com>

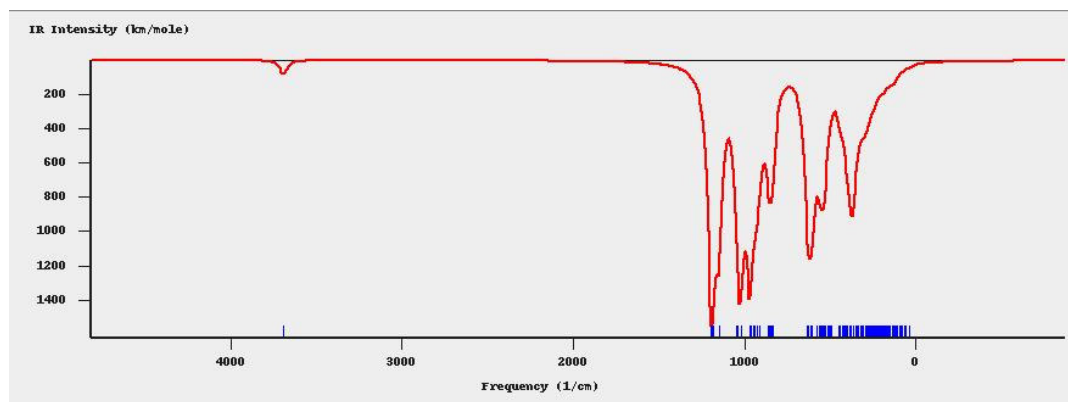


Figure 1: Calculated infrared spectrum for the cluster c5 $\text{Ca}_{10}(\text{PO}_4)_6(\text{OH})_2$.

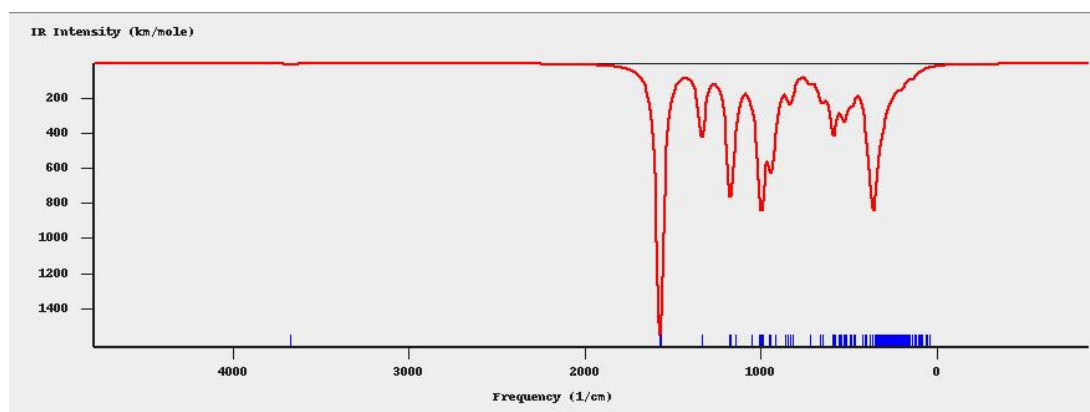


Figure 2: Calculated infrared spectrum for the cluster $\text{Ca}_{10}(\text{PO}_4)_4(\text{CO}_3)_2(\text{OH})_2$.

THE USE OF PHOTOLABILE OLIGONUCLEOTIDES TO FABRICATE PATTERNED SURFACES

Brendan Manning¹, Roger Ramos¹, Simon Leigh², Jon Preece², Ramon Eritja¹

¹*Institute for Research in Biomedicine, Institute for Advanced Chemistry of Catalonia (IQAC), CIBER-BBN Networking Centre on Bioengineering, Biomaterials and Nanomedicine. Helix Building, Baldiri Reixac 15, E-08028 Barcelona, Spain.*

²*Nanoscale Chemistry Laboratory. School of Chemistry. The University of Birmingham, B15 2TT, United Kingdom.*

brendan.manning@gmail.com

There is a large interest in the use of the self-assembling properties of biomolecules in nanotechnology. Biomolecules are seen as the ideal candidate to build next generation biosensors and for the fabrication of a variety of 'bottom up' nanoscale devices.

Among biomolecules, oligonucleotides have captured a large part of this interest¹⁻³. The facile synthesis and modification of oligonucleotides make it easy to graft to surfaces and the relatively high physiochemical stability allows easy handling under ambient conditions. The sequence specific hydrogen bonding allows programming of structures with a simple four letter alphabet; C, G, T, A.

For the fabrication of biosensors and nanoscale devices the precision engineering and positioning of nanoscale building blocks, such as oligonucleotides, will be required. Photolithography is currently the most popular method for the fabrication of micro and nano-electronics, recently having being used to engineer 32nm sized features⁴. Recently it has been shown that short oligonucleotides can be synthesized on a silicon substrate using modern photolithographic techniques. These high density DNA chips have been successfully used for rapid DNA sequence analysis.^{5,6}

In the present communication we study the use of oligonucleotides carrying photolabile groups in their sequence as a new kind of biological resist to form patterns on surfaces. To this end, a method for the fabrication of patterned surfaces using hairpin oligonucleotides carrying photolabile groups is described. A photolabile group has been introduced at the loop of an intramolecular oligonucleotide hairpin. The photolabile oligonucleotide was immobilized on glass and SiO₂ surfaces. Photolysis results on the formation of areas carrying single-stranded DNA sequences that direct the deposition of the complementary sequence at the photolyzed sites, fig 1.

References:

- (1) Aldaye, F. A.; Palmer, A. L.; Sleiman, H. F. *Science* 2008, *321*, 1795-9.
- (2) Gothelf, K. V.; LaBean, T. H. *Org Biomol Chem* 2005, *3*, 4023-37.
- (3) Seeman, N. C. *Mol Biotechnol* 2007, *37*, 246-57.
- (4) Lai, K.; Burns, S.; Halle, S.; Zhuang, L.; Colburn, M.; Allen, S.; Babcock, C.; Baum, Z.; Burkhardt, M.; Dai, V.; Dunn, D.; Geiss, E.; Haffner, H.; Han, G.; Lawson, P.; Mansfield, S.; Meiring, J.; Morgenfeld, B.; Tabery, C.; Zou, Y.; Sarma, C.; Tsou, L.; Yan, W.; Zhuang, H.; Gil, D.; Medeiros, D.; Harry, J. L., Mircea, V. D., Eds.; SPIE: 2008; Vol. 6924, p 69243C.
- (5) Fodor, S. P.; Read, J. L.; Pirrung, M. C.; Stryer, L.; Lu, A. T.; Solas, D. *Science* 1991, *251*, 767-73.

(6) Lipshutz, R. J.; Fodor, S. P.; Gingeras, T. R.; Lockhart, D. J. *Nat Genet* 1999, 21, 20-4.

Figures:

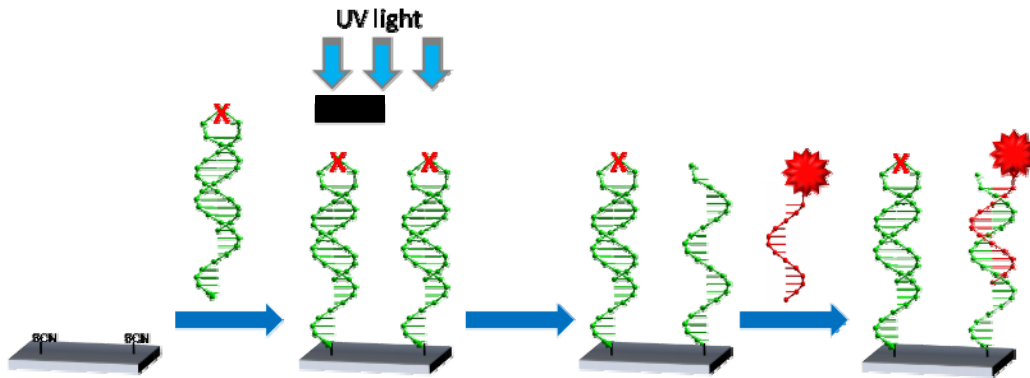


Figure 1 Scheme for the immobilization and patterning of hairpin oligonucleotides

SELF-ASSEMBLING OF MAGNETIC NANOPARTICLE ONTO TECHNOLOGICAL SUBSTRATES

Luís Peña, Lluís Balcells, and Benjamín Martínez

Institut de Ciència de Materials de Barcelona (ICMAB-CSIC) Campus UAB, 08193 Bellaterra, Spain.

Mirian Baron and Victor F. Puntes

Institut Català de Nanotecnologia, Campus UAB, 08193 Bellaterra, Spain.

ben.martinez@icamab.es

Obtaining monolayers of highly ordered magnetic nanoparticles (NPs) onto technological substrates is a very interesting issue from both basic research and technological points of view. Long range ordered arrays of magnetic NPs have a great potential for applications in magnetic and electronic devices, thus making this field of research a very active one in the past few years. An ordered array of such NPs can be used in novel tunnel magnetoresistance device or spin-torque nano-oscillators. Nevertheless, obtaining highly ordered monolayers of magnetic NPs on top of on technological substrates has revealed to be a hard attainable issue. The common method to produce ordered two-dimensional arrays of NPs is self-assembling. Self-assembling is a complex process in which several interactions between NPs, substrate, and solvent are involved. As a result of the complexity of the process, a mixture of mono- and bi-layers with order in the few nanometres range is usually obtained when dealing with substrates with technological interest, such as complex oxides. In this work we report on self-assembly processes of Co NPs (10 nm in diameter) on top of silicon substrates by using different techniques. Samples have been prepared by using drop-casting, spin coating and Langmuir-Blodgett techniques. The influence of different parameters such as substrate temperature, evaporation time, NPs concentration, etc., are analyzed. By using the two first techniques self-assembled monolayers of Co nanoparticles in the micrometric range have been obtained (see Fig. 1). The Langmuir-Blodgett technique has also been used to study self-assembly processes of silica NPs of about 70 nm in diameter on Silicon and glass substrates. Preliminary results on this latter issue will also be discussed

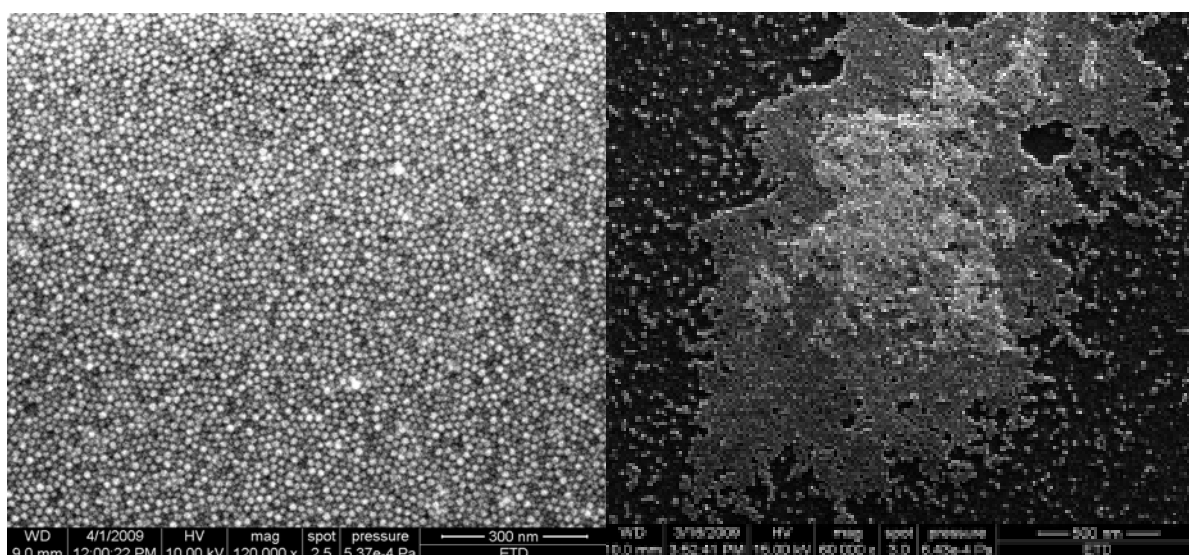


Figure 1: SEM micrograph of a self-assembled monolayer of Co nanoparticles (left). Detail of an area with transition from a single to double layer assembly.

A DNA CHIP FOR THE DETECTION OF MICROORGANISMS IN WATER SAMPLES – DESIGN AND PRELIMINARY RESULTS

Nelson Martins^a, Filipa F. Vale^a, Maria J. Vale,^a Helena Vieira^b

^aFaculdade de Engenharia, Universidade Católica Portuguesa, Rio de Mouro, Portugal.

*^bBIOALVO SA, Edifício ICAT, Campus da FCUL, Lisbon, Portugal
nelson.e.v.martins@gmail.com*

Waterborne pathogens are responsible for several diseases, either due to the consumption of contaminated drinking water or due to the contact with polluted recreational waters. There is an increasing awareness that emergent and viral pathogens should also be monitored for determining water quality. Conventional detection methodologies present several shortcomings, such as reliance in indicator species, low throughput and increasing resources as more species are to be detected. DNA chips have the potential to serve as surveillance systems for the simultaneous detection of pathogens, overcoming these limitations. In the present study, a rapid method for the detection of multiple waterborne pathogens (bacteria and viruses) was developed, using a DNA chip (AQUACHIP®). Species and group specific probes were implemented on a DNA chip, both for mandatory and non-mandatory microorganisms. Considerations regarding the AQUACHIP® design (probe layout, replicates and dilutions), DNA labeling and amplification, and preliminary results of the application of the chip are presented.

The probes which were previously developed and validated were cloned into pBS KS for sequencing and to develop an accessible source of the DNA for implementation on the AQUACHIP®. Probe identity and target microorganisms are described in detail elsewhere [1], and are divided in three main groups: probes for the detection of the groups and species of microorganisms that are currently enforced by the Portuguese and European legislation (the coliform bacteria group, *Escherichia coli*, Enterococci and *Clostridium perfringens*); a group of probes for non-mandatory microorganisms, selected according to their impact on public health (*Pseudomonas aeruginosa*, *Staphylococcus aureus*, *Legionella pneumophila*, *E. coli* O157, *Campylobacter coli* and *C. jejuni*, *Salmonella* spp. and *Shigella* spp.); and two probes for pathogenic virus detection (Hepatitis A virus and Norovirus genogroup I).

The chip was designed in order to maximize the cost-effectiveness, replicability of the results, and to allow the determination of the sensitivity limits of the technology. Additionally, the chip was designed to accommodate future expansion to a greater number of species. Each AQUACHIP® was printed in quadruplicate in glass slides, allowing for the processing of a maximum of four water samples simultaneously; in each AQUACHIP®, three dilutions of nine replicates of each probe were distributed semi-randomly in different zones, to avoid probe location biases.

Before hybridization, sample DNA was labeled and amplified in a single step using the Roche-Nimblegen One-Color DNA kit, to increase the detection sensitivity [2] and reduce processing time.

Preliminary results show the detection capabilities of the AQUACHIP® for *E.coli* DNA.

Future work will include the validation of the AQUACHIP® with all the target species, alone and in combination, with DNA extracted from pure cultures and from artificially contaminated water samples, and finally with DNA extracted from complex environmental water samples.

This work was funded by Fundação Calouste Gulbenkian, program Environment and Health 2005.

References:

[1] Vale, F.F., Silva, A.M., Granja, A.T., Vale, M.J. and Vieira, H. *Physica Status Solidi (c)* **in press** (2009) doi: 10.1002/pssc.200881703

[2] Lee, D.Y., Shannon, K. and Beaudette, L.A., *J Microbiol Methods*, **65** (2006) 453-467.

SELF-ASSEMBLY OF POLYCARBOXYLIC ACIDS INTO TWO-DIMENSIONAL MOLECULAR NETWORKS: A THEORETICAL STUDY

N. Martsinovich, A. Troisi

Department of Chemistry, University of Warwick, UK

The phenomenon of self-assembly of molecular superstructures is attracting an increasing interest in nanotechnology due to possible applications in materials science and molecular electronics [1]. Self-assembly of molecules is controlled by specific intermolecular interactions. In particular, hydrogen bonds (H-bonds) are among the strongest intermolecular interactions, they are directional and give rise to complex supramolecular networks on a variety of substrates [1-4].

This abstract presents our theoretical studies of self-assembly of benzenedicarboxylic acids into hydrogen-bonded supramolecular structures. Experimental scanning tunnelling microscopy studies of self-assembly of these molecules [4] revealed the network structures based on closely packed H-bonded chains of molecules. Here we model the process of aggregation of isolated molecules into ordered two-dimensional (2D) networks, using a combination of force field molecular dynamics and Monte Carlo calculations, with the aim to investigate the emergence and evolution of ordered supramolecular structures.

Our results show the initial rapid formation of short H-bonded molecular chains, which, in some conditions, may then assemble parallel to each other into 2D sheets due to van der Waals interactions between the chains. We find that a high density of molecules leads to compact and highly ordered structures consisting of close-packed molecular chains, similar to the experimental images [4], whereas a low concentration of molecules leads to long chains which do not assemble into compact 2D structures.

1. J. A. Theobald, N. S. Oxtoby, M. A. Phillips, N. R. Champness, P. H. Beton, *Nature* 424, 1029 (2003).
2. N. Martsinovich, L. Kantorovich, *J. Phys. Chem. C* 112, 17240 (2008).
3. M. Mura, N. Martsinovich, L. Kantorovich, *Nanotechnology* 49, 465704 (2008).
4. M. Lackinger, S. Griessl, T. Markert et al., *J. Phys. Chem. B* 108, 13652 (2004).

Temperature Dependence of the Optical Transitions in Single-walled Carbon Nanotubes

*Patrick May*¹, *Hagen Telg*¹, *Christian Thomsen*¹, *John Robertson*², and *Janina Maultzsch*¹

¹*Institut für Festkörperphysik, Technische Universität Berlin, Hardenbergstrasse 36, D-10623 Berlin, Germany*

²*Department of Engineering, University of Cambridge, Cambridge CB3 0FA, United Kingdom*

pmay@physik.tu-berlin.de

Single-walled carbon nanotubes (SWCNTs) are promising candidates for a variety of electronic and optical applications. Optical transitions play a central role in the understanding of carbon nanotubes [1]. Both theoretical and experimental studies revealed that light absorption excites strongly correlated electron-hole pairs in semiconducting nanotubes, known as excitons, with binding energies of several hundred meV [2,3].

There is a strong debate on how much optical transitions are dominated by excitons in metallic SWCNTs as well. In general, binding energies are higher in nanotubes due to their one-dimensional character in comparison to bulk semiconductors. Theoretical calculations show that excitons exist even in metallic SWCNTs with binding energies predicted around 50 meV, depending on the nanotube chiral index (n,m) and the transition energy E_{ii} [4,5].

Here we present results on the temperature dependence of the transition energies E_{ii} of SWCNTs. Tunable Raman spectroscopy has been used to investigate the radial breathing mode (RBM).

We performed measurements of the optical transition energy E_{ii} at different temperatures for both metallic and semiconducting SWCNTs in the range of 300 K and 873 K.

In case of semiconducting SWCNTs, we observe a monotonic decrease of E_{ii} with increasing temperature. Metallic SWCNTs show a different behavior, which can be divided into three parts. First we observe a downshift of E_{ii} as a function of temperature. At higher temperatures, we observe an upshift in the transition energy (blueshift) at approximately 573 K. At even higher temperatures there is again a downshift similar to the first one.

We suggest that this behavior can be interpreted in terms of excitons in metallic nanotubes, which are dissociated into free electron-hole pairs at temperatures related to the exciton binding energies.

References:

- [1] S. Reich, C. Thomsen, J. Maultzsch, *Carbon Nanotubes*, Wiley-VCH, Weinheim (2004).
- [2] J. Maultzsch, R. Pomraenke, S. Reich, E. Chang, D. Prezzi, A. Ruini, E. Molinari, M. S. Strano, C. Thomsen, and C. Lienau, *Phys. Rev. B* **72**, 241402, (2005).
- [3] F. Wang, G. Dukovic, L. E. Brus, and T. F. Heinz, *Science* **308**, 838, (2005).
- [4] J. Deslippe, C.D. Spataru, D. Prendergast, and S.G. Louie, *Nano Letters* **7**, 1626 (2007).
- [5] C. D. Spataru, S. Ismail-Beigi, L. X. Benedict, and S. G. Louie, *Phys. Rev. Lett.* **92**, 077402 (2004).

TUNNEL CURRENTS ACROSS SILANE DIAMINES/DITHIOLS AND ALKANE DIAMINES/DITHIOLS

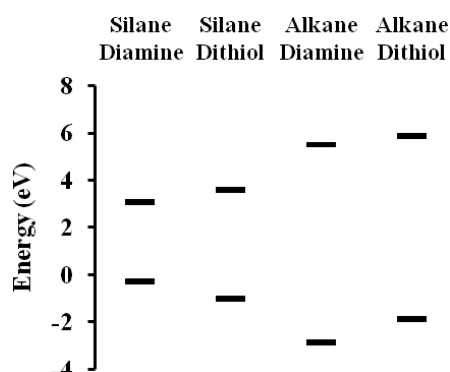
Shane McDermott¹, Christopher B. George², Giorgos Fagas¹,
James C. Greer¹, and Mark A. Ratner²

¹Tyndall National Institute, Cork, Ireland

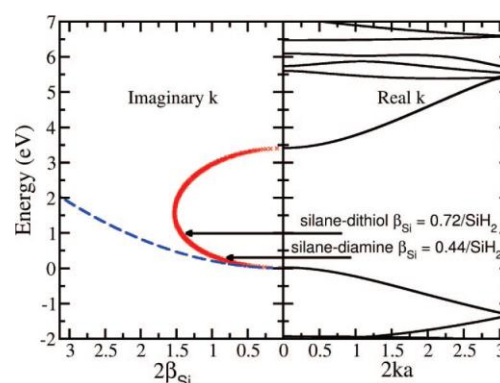
²Northwestern University, Evanston, IL, USA

shane.mcdermott@tyndall.ie

This presentation focuses on the theoretical treatment of the electronic current across alkane and silane oligomers with amine end groups used to bond to metallic electrodes [1]. We use both a non-equilibrium Green's function (NEGF) method and a many-electron correlated scattering (MECS) methods to calculate electron transport. The low voltage conductance for these molecular systems decays exponentially with increasing length and our calculations reproduced this behaviour. Smaller conductance values and steeper decay in the alkane-bridged junctions are consistently found compared with the silane-bridged junctions, but quantitative differences in the decay constants obtained from the two formalisms arise. End group effects for both oligomers are also studied and analysed using a simple tunnel barrier model and complex band structure calculations.



Molecular frontier energy levels for the hexane and hexasilane bonded to gold clusters via amine and thiol end groups. Energies levels are approximated by the Kohn-Sham eigenvalues from the DFT B3LYP calculations. The zero of energy is taken to be the Fermi level approximated as the work function of gold (-5.1 eV).



Complex band structure for silicon hydride chains and silane-based tunnel junctions with amine or thiol linkers. The decreased HOMO-LUMO gap size in the silanes, compared to the alkanes, makes the values decay constant for silanes more sensitive to small differences in the Fermi-level alignment compared to alkanes.

The trend observed in the reduction of the decay constants for the silanes relative to the alkanes is consistent with a simple tunnel barrier model and a more rigorous complex band-structure analysis. However, the analysis also points out that the exact decay values for the silanes are sensitive to small errors in the energy level alignments. Of the four systems studied, the alkane diamine junctions seem to have the most tolerance for error in band alignment, partly due to the large HOMO-LUMO gap and partly due to the nature of the charge transfer between the gold electrode and amine linker. Because the silanes have smaller HOMO-LUMO gaps, errors in the band alignment for these systems are magnified and the inverse decay length is found to be extremely dependent on the exact Fermi-energy position. Nevertheless, the silane inverse decay length is found to be lower than that of the alkane decay value, indicating that σ -bond delocalization may be another means by which to tailor molecular electronic properties, serving

as an intermediate between π -conjugated and nonconjugated systems. This could serve as another potential tool in the tool kit of molecular transport engineering.

[1] A Comparative Study for the Calculation of Tunnel Currents Across Silane Diamines/Dithiols and Alkane Diamines/Dithiols, Shane McDermott, Chris George, Giorgos Fagas, J. C. Greer, and M. A. Ratner, *Journal of Physical Chemistry C* **113**, pp. 744-750 (2009)

SPIN POLARISATION OF ELECTRONS USING CHIRAL MOLECULAR POTENTIALS

S. Yeganeh¹, M. A. Ratner¹, E. Medina², and V. Mujica^{1,3}

¹Department of Chemistry and Center for Nanofabrication and Molecular Self Assembly, Northwestern University, Illinois 60208-3113, USA.

²Laboratorio de Física Estadística de Sistemas Desordenados, Centro de Física, IVIC, Apartado 21827, Caracas 1020A, Venezuela.

³Argonne National Laboratory, Center for Nanoscale Materials, Argonne, Illinois 60439-4831, USA.

We present a model for the transmission of spin-polarized electrons through oriented chiral molecules, where the chiral structure is represented by a helix. The scattering potential contains a confining term and a spin-orbit contribution that is responsible for the spin-dependent scattering of the electrons by the molecular target. The differential scattering cross-section is calculated for right- and left-handed helices and for arbitrary electron spin polarizations. We apply our model to explain chiral effects in the intensity of photo-emitted polarized electrons transmitted through thin organic layers. These are spin-active molecular interfaces that exhibit electron dichroism and a number of remarkable magnetic properties. In our model, differences in intensity are generated by the preferential transmission of electron beams whose polarization is oriented in the same direction as the sense of advance of the helix. This model can be easily extended to the Landauer regime of conductance, where conductance is due to elastic scattering, so that we can consider the conductance of chiral molecular junctions. Further experiments that probe the effects of chirality in electron transport are suggested.

Synthesis and characterization of europium-doped La₂O₃ nanoparticles

M. Méndez^{1,4,5}, J.J. Carvajal¹, F. Díaz¹, M. Aguiló¹, A. Guiguere², D. Drouin², E. Martínez-Ferrero³, P. Salagre⁴, Y. Cesteros⁴, R. Palacios⁵, J. Pallarès⁵, L.F. Marsal⁵

¹*Física i Cristal·lografia de Materials (FiCMA), Universitat Rovira i Virgili (URV), c/ Marcel·lí Domingo s/n, Campus Sescelades, E-43007, Tarragona, Spain.*

²*Dept. Electrical and Computer Engineering, Université de Sherbrooke, Sherbrooke, PQ, J1K 2R1, Canada.*

³*Institute of Chemical Research of Catalonia (ICIQ), Avd. Països Catalans 16, 43007 Tarragona, Spain*

⁴*Departament de Química Física i Inorgànica, Universitat Rovira i Virgili (URV), c/Marcel·lí Domingo s/n, Campus Sescelades, E-43007, Tarragona, Spain*

⁵*Nano-Electronic and Photonic Systems, Departament d'Enginyeria Electrònica, Elèctrica i Automàtica, Universitat Rovira i Virgili, Av. Països Catalans 26, 43007 Tarragona, Spain*

maria.mendez@urv.cat, joanjosep.carvajal@urv.cat

Rare-earth sesquioxides (Y₂O₃, La₂O₃, Lu₂O₃, etc.) have been extensively studied as host matrices for lanthanide (Ln) ions in the field of luminescence. Furthermore, Ln doped sesquioxides in the form of thin films have been investigated for their potential applications in luminescent displays [1]. Lanthanum oxide is a semiconductor material with the largest band gap among rare earth sesquioxides with a value of 4.3eV. This compound has numerous applications in various fields of industry: as a component of catalyst supports, particularly in methanol production, and as a component of ceramics. Its synthesis in a form of fine dispersion represents now an exciting area of research [2].

When doping La₂O₃ with luminescent active Ln ions, such as Eu³⁺, will allow combining the semiconductor properties of La₂O₃ with the red emission of Eu³⁺. Such red phosphors have been previously investigated under the form of bulk and nanoparticle materials [3,4]. Due to quantum confinement effect and surface effect, nanosized materials with particle sizes of 100 nm or less may show electrical, optical and luminescent properties more efficient than the corresponding bulk materials. Up to now, nanoparticles of Eu-doped La₂O₃ have been synthesized by means of solution combustion synthesis [3], and nitrate decomposition procedures [4]. Such nanoparticles showed emissions centered in the red region of the electromagnetic spectrum, at around 626 nm.

Among organic-inorganic hybrid materials, polymer nanocomposites attract strong interest because of the combination of both the properties of the nanoparticles (optical, electronic or mechanical) and those of the polymer (solubility, film formation, and chemical activity) [5].

In the present work we developed the synthesis of Eu doped La₂O₃ nanoparticles by several synthesis methods such as: the modified Pechini method, which is an alternative to the conventional sol-gel method, the precipitation method and a hydrothermal process.

The nanoparticles obtained have been characterized by differential thermal analysis-thermogravimetric analysis (DTA-TG) in the temperature range from 300 K to 1100 K, infrared spectroscopy (FTIR), and by X-ray diffraction (XRD) to determine their crystalline structure and average grain sizes. Their morphology, homogeneity, distribution and particle size have been investigated by electronic microscopy such as scanning electron microscopy (SEM) and transmission electron microscopy (TEM). The sizes of these nanoparticles range between 10 and 300 nm, depending on the synthesis method. Figure 1 shows some of the smaller particles obtained by the hydrothermal method, and the nanoparticles obtained by the

modified Pechini method after calcination at 1073K. Finally, the photoluminescence (PL) and cathodoluminescence (CL) properties of the Eu doped La_2O_3 nanoparticles obtained have been analyzed. Photoluminescence is shown in Figure 2, after excitation of the nanocrystalline La_2O_3 doped with 5% Eu^{3+} at 250 nm. In this figure, the strongest emission peak is centered at 626 nm corresponding to the $^5\text{D}_0 \rightarrow ^7\text{F}_2$ transition of Eu^{3+} , indicating that Eu^{3+} ions have been successfully incorporated in the structure of La_2O_3 .

Acknowledgements. This project has been supported by the Spanish Government under projects TEC2006-06531, MAT2008-06729-C02-02/NAN, and CONSOLIDER HOPE CSD2007-00007 and AECID-A/016246/08, by the Catalan Authority under project 2005SGR658, and by the Research Center on Engineering of Materials and Systems (EMaS) of the URV. J.J. Carvajal is supported by the Education and Science Ministry of Spain and European Social Fund under the Ramón y Cajal program RYC2006-858.

References:

- [1] C. Martinet, A. Pillonnet, J. Lancok, C. Garapon, J. of Luminescence, **126** (2007) 807-816.
- [2] S. Mentus, Dijana Jelić, Veselinka Grudić, J. of Thermal Analysis and Calorimetry, **90** (2007) 2, 393-397.
- [3] HuangQing Liu, LingLing Wang, Weiqing Huang, ZhiWei Peng, Materials Letters, **61** (2007) 1968-1970.
- [4] J.K. Park, S.M. Park, C. H. Kim, H. D. Park, J. of Materials Science Letters, **20** (2001) 2231-2232.
- [5] Jinming Kuang, Jinying Yuan, Mi Zhou, Weizhong Yuan, Xiaofeng Sui, Zhaolong Li, Materials Letters, **62** (2008) 4078-4080.

Figures:

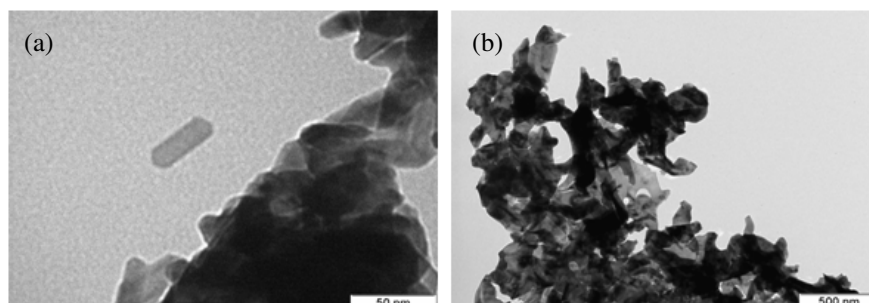


Figure 1. TEM image of nanoparticles obtained by (a) hydrothermal process and calcination at 873K; and (b) modified Pechini method and calcination at 1073 K.

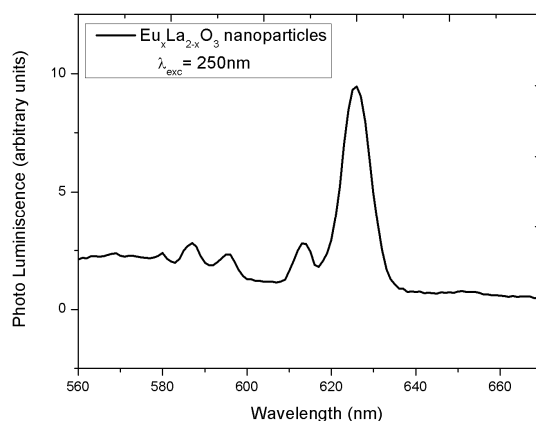


Figure 2. Emission spectra of nanocrystalline La_2O_3 doped with 5% Eu^{3+} ions under 250 nm excitation.

White-light up-conversion emission in transparent sol-gel derived glass-ceramics containing rare-earth doped YF₃ nano-crystals

A.C. Yanes¹, A. Santana-Alonso¹, J. Méndez-Ramos^{2,*}, J. del-Castillo¹ and V.D. Rodríguez²

¹Dpto. Física Básica, Universidad de La Laguna, 38206 La Laguna, Tenerife, Spain

²Dpto. Física Fundamental y Experimental, Electrónica y Sistemas, Universidad de La Laguna, 38206 La Laguna, Tenerife, Spain

jmendezr@ull.es

Transparent nano-glass-ceramics containing YF₃ nanocrystals doped with luminescent rare-earth ions, such as Yb³⁺, Er³⁺ and Tm³⁺ and combinations of those ions, were obtained under adequate heat treatment of precursor glasses synthesized by room-temperature sol-gel processing. Thus, precursor silica glasses with composition 90SiO₂-10YF₃ co-doped with 0.3 Yb³⁺- 0.1 Er³⁺, with 0.3 Yb³⁺- 0.1 Tm³⁺, and triply-doped with 0.3 Yb³⁺, x Er³⁺ and 0.1 Tm³⁺ with x ranging from 0.025 to 0.1 (in mol%), were obtained by sol-gel method as described in [1,2] and subsequently heat-treated to achieve controlled precipitation of YF₃ nano-crystallites. Hence we report the sol-gel route for obtaining rare-earth doped YF₃ nanoparticles dissolved in silica glasses, alternative to reported conventional high-temperature melting techniques for these nano-composites [3,4]. Upconversion luminescence features confirm the effective partition of luminescent ions into precipitated nano-crystals. The dependence of the overall emitting colour has been analyzed, as a function of doping ions and respective concentration and heat treatment temperature of precursor glasses, and quantified in the CIE standard chromaticity diagram. Moreover, tuneability colour has been achieved with varying rare-earth ions concentration. In particular, very bright and efficient upconversion emission, almost matching the standard equal energy white light illumination point of the CIE diagram, was obtained in the 675 °C-treated 0.3 Yb³⁺- 0.05 Er³⁺-0.1 Tm³⁺ nano-glass-ceramics, showing up as promising candidate materials for potential applications in photonic integrated devices and infrared tuneable phosphors.

References:

- [1] S. Fujihara, C. Mochizuki and T. Kimura, *J. Non-Cryst. Solids*, **244** (1999) 267.
- [2] A. C. Yanes, A. Santana-Alonso, J. Méndez-Ramos, J. del-Castillo and V. D. Rodríguez, **480** *J. Alloys Compd.* (2009) 706.
- [3] D. Chen, Y. Wang, Y. Yu, P. Huang and F. Weng, *J. Solid State Chem.*, **181** (2008) 2763.
- [4] F. Weng, D. Chen, Y. Wang, Y. Yu, P. Huang and H. Lin, *Ceramics International*, **35** (2009) 2619.

Acknowledgments:

The authors would like to thank Gobierno Autónomo de Canarias (PI042005/039), Consejería de Industria, Comercio y Nuevas Tecnologías (IDT-TF-07/077) and Ministerio de Ciencia y Tecnología of Spain Government (FIS 2006-02980) for financial support.

Figures:

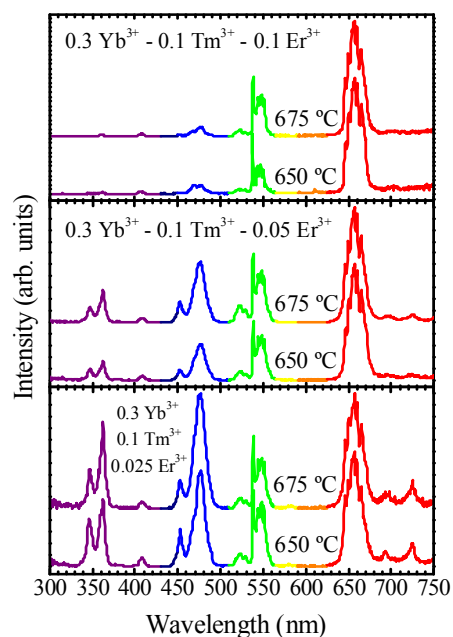


Figure 1. Up-conversion emission spectra in $90\text{SiO}_2\text{-}10\text{YF}_3$ triply-doped with 0.3 Yb^{3+} , $x \text{ Er}^{3+}$ and 0.1 Tm^{3+} (in mol%), where a) $x = 0.1$, b) $x = 0.05$, c) $x = 0.025$, under 980 nm excitation at 200 mW pump power as function of heat treatment temperature of the samples in the range $650\text{-}675 \text{ }^\circ\text{C}$. Spectra have been normalized to the maximum of the 660 nm emission band.

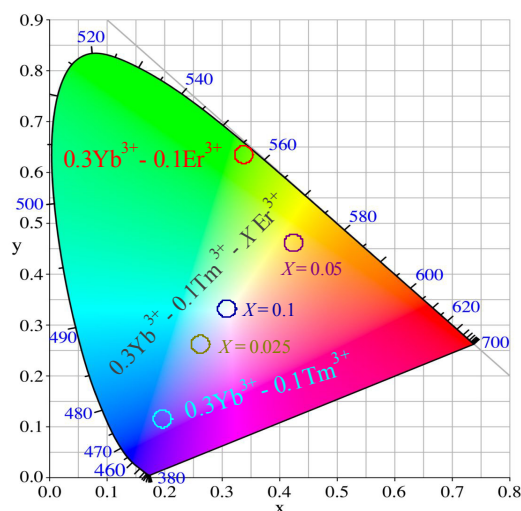


Figure 2. CIE standard chromaticity diagram including coordinates of $90\text{SiO}_2\text{-}10\text{YF}_3$ co-doped with $0.3 \text{ Yb}^{3+} - 0.1 \text{ Er}^{3+}$, $0.3 \text{ Yb}^{3+} - 0.1 \text{ Tm}^{3+}$, and $0.3 \text{ Yb}^{3+} - X \text{ Er}^{3+}$, 0.1 Tm^{3+} (in mol%) with $X = 0.05, 0.025$, respectively, heat-treated at $675 \text{ }^\circ\text{C}$ under 980 nm excitation at 200 mW pump power.

Up-conversion in Yb³⁺-Ho³⁺-Tm³⁺ co-doped NaYF₄ nano-crystals embedded in a silica glass synthesized by sol-gel route

A. Santana-Alonso¹, J. Méndez-Ramos^{2,*}, A.C. Yanes¹, J. del-Castillo¹ and V.D. Rodríguez²

¹Dpto. Física Básica, Universidad de La Laguna, 38206 La Laguna, Tenerife, Spain

²Dpto. Física Fundamental y Experimental, Electrónica y Sistemas, Universidad de La Laguna, 38206 La Laguna, Tenerife, Spain

jmendezr@ull.es

NaYF₄ is an excellent host material for rare earth ions presenting very high efficiencies in up-conversion processes. Nano-glass-ceramics containing NaYF₄ nano-crystals emerge as promising candidates for general lighting appliances and integrated optical devices [1, 2]. Here we report highly transparent nano-glass-ceramics comprising rare-earth doped NaYF₄ nano-crystals prepared by adequate heat treatment of precursor glasses synthesized by the sol-gel technique. Thus, silica glasses with composition 95SiO₂-5NaYF₄ co-doped with 0.3 Yb³⁺ and 0.1 Ho³⁺ and tri-doped with 0.3 Yb³⁺-x Ho³⁺-0.1 Tm³⁺ with x = 0.1, 0.05 and 0.025 (mol%) were obtained by sol-gel method as described in [3,4]. Subsequently, these sol-gel glasses were heat-treated in air at different temperatures ranging from 500 to 650 °C in order to achieve controlled precipitation of nano-crystallites, giving rise to transparent glass-ceramics. A structural analysis by means of X-ray diffraction measurements confirmed the formation of NaYF₄ nano-crystals analyzing the crystallization degree of nano-glass-ceramics as function of the heat treatment temperature. Luminescence features have been also related to the crystallinity degree of the samples. Red, green and blue up-conversion emissions were obtained under infrared excitation at 980 nm and corresponding mechanisms involved have been analyzed in terms of excited state absorption and energy transfer processes. A comparison between co-doped and tri-doped samples reveals that the introduction of Tm³⁺ ions, with appropriate heat treatment and doping levels, results in the addition of the blue up-conversion emission that along with the green and red ones, gives rise to an efficient white light generation that could be seen by the naked eye. High energetic up-conversion emissions and well-resolved Stark structure of emission bands support the conclusion of crystalline-like environment for the rare-earth ions into the precipitated nano-crystals. The total visible up-conversion emissions have been quantified in the CIE standard chromaticity diagram. Finally, bright white light generation has been achieved in Yb³⁺-Ho³⁺-Tm³⁺ tri-doped samples with appropriate choice of heat treatment temperature and adequate relative rare-earth doping level.

References:

- [1] J. F. Suyver, J. Grimm, M. K. Van Veen, D. Biner, K. W. Krämer, H. U. Güdel, *J. Lumin.*, **1** (2006) 117.
- [2] F. Liu, E. Ma, D. Chen, Y. Yu, Y. Wang, *J. Phys. Chem. B* **110** (2006) 20843.
- [3] S. Fujihara, C. Mochizuki and T. Kimura, *J. Non-Cryst. Solids*, **244** (1999) 267.
- [4] A. C. Yanes, A. Santana-Alonso, J. Méndez-Ramos, J. del-Castillo and V. D. Rodríguez, **480** *J. Alloys Compd.* (2009) 706.

Acknowledgments:

The authors would like to thank Gobierno Autónomo de Canarias (PI042005/039), Consejería de Industria, Comercio y Nuevas Tecnologías (IDT-TF-07/077) and Ministerio de Ciencia y Tecnología of Spain Government (FIS 2006-02980) for financial support.

Figures:

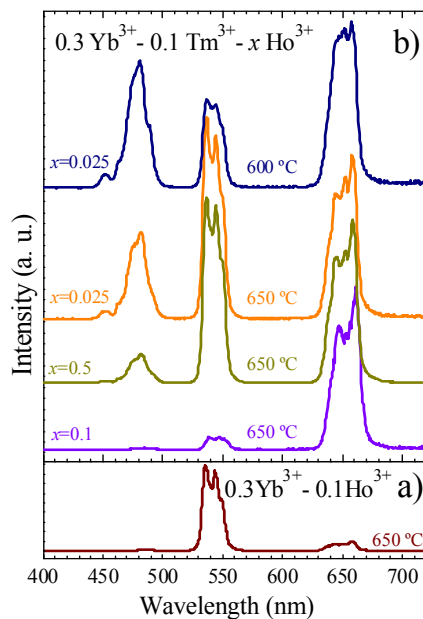


Figure 1. Up-conversion emission spectra under 980 nm excitation at 200 mW pump power corresponding to (a) 95SiO₂-5NaYF₄: 0.3 Yb³⁺, 0.1 Ho³⁺ (mol %); and (b) 95SiO₂-5NaYF₄: 0.3 Yb³⁺, x Ho³⁺ and 0.1 Tm³⁺ (mol %), with $x = 0.1, 0.05$ and 0.025 , heat-treated at indicated temperatures. Spectra in (b) have been normalized to the 640-660 nm band.

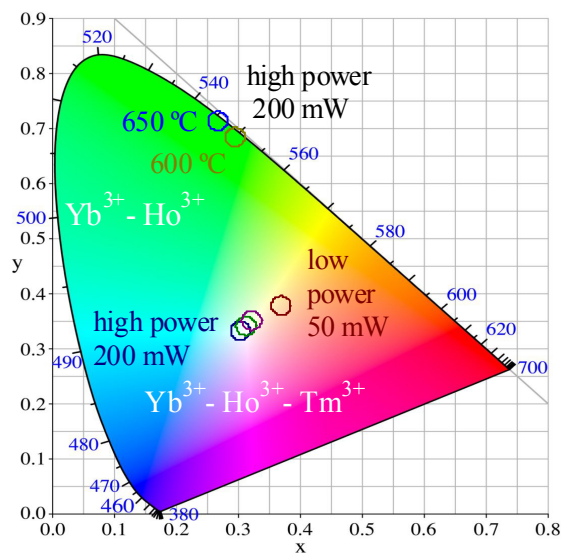
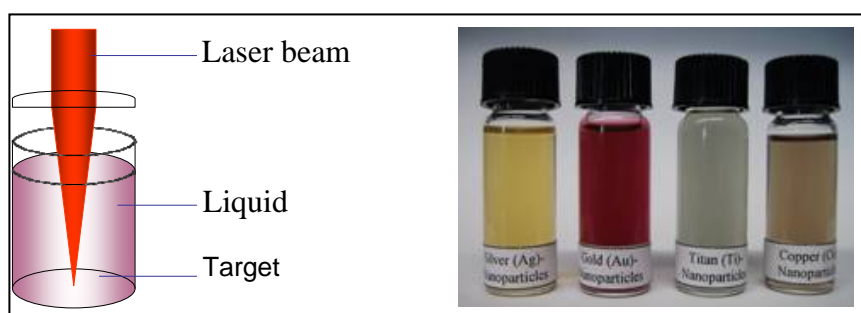


Figure 2. CIE standard chromaticity diagram with corresponding colour coordinates of total visible up-conversion emission under 980 nm pump power at 200 mW of 95SiO₂-5NaYF₄ doped with 0.3 Yb³⁺ and 0.1 Ho³⁺ (mol %) nano-glass-ceramics heat-treated at 600 and 650 °C, respectively. Additionally, colour coordinates of the 95SiO₂-5NaYF₄ nano-glass-ceramics tri-doped with 0.3 Yb³⁺, 0.025 Ho³⁺ and 0.1 Tm³⁺ (mol %) heat-treated at 600 °C for different pump powers ranging from 50 to 200 mW are also presented.

Nanoparticle and nanocomposite generated by laser ablation in liquids-tuning the process towards applications

Ana Menéndez-Manjón, Stephan Barcikowski
Laser Zentrum Hannover, Hollerithallee 8, Hannover, Germany
a.menendez@lzh.de

In recent years laser ablation in liquids has proven to be a suitable technique for the generation of nanoparticles¹, nanocomposites² and nanomarkers³. After focussing the laser beam on a solid target, immersed in liquid, matter is removed from the target. The ablated material is trapped and dispersed in the liquid environment. The simplified experimental set-up and some laser-based colloids are shown in the figure. The characteristics of the resulting colloid are controlled by ablation parameters and liquid properties. Metal, alloys and magnetic nanoparticles have been successfully generated by this technique in different solvents and with very diverse laser parameters.



In this talk, an overview and latest findings of laser ablation in solvents and the most decisive parameters for controlling particle size distribution and productivity will be given. Laser parameters (pulse length, pulse energy and repetition rate) or ablation procedure (focussing conditions, liquid dynamics and temperature) have been investigated and their influence in the colloid properties will be presented.

Additives in the solvent, such as polymers, anionic surfactants or biomolecules help to control the size and stability of the particles, and coating or functionalization is possible in one-step process. This enables the production of nanoparticulated systems like nanocomposites, and multiple applications as DNA-targeting.

This work was supported by the German Federal Ministry of Education and Research (FKZ 13N9799) and the *Deutsche Forschungsgemeinschaft* (CH:197-8-1) for kinetic studies.

References:

- [1] S. Barcikowski, A. Menendez-Manjon, B. Chichkov, M. Brikas, G. Raciukaitis, *Appl. Phys. Lett.*, **91** (2007), 8.
- [2] S. Barcikowski, M. Hustedt, B. Chichkov. *Polimery*, **53** (2008), 657 – 662.
- [3] S. Petersen, S. Barcikowski, *Ad. Func. Mat.*, **8** (2009), 1197-1172.

A New Pyramidal Quantum Dots System: achieving high optical quality in an uniform, site-controlled system

Lorenzo O. Mereni, Valeria Dimastrodonato, Robert J. Young, Emanuele Pelucchi
 Tyndall National Institute, University College of Cork, Cork, Ireland
lorenzo.mereni@tyndall.ie

A reliable site controlled in a Quantum Dots (QD) system is highly desirable for many emerging technologies and has thus garnered significant effort from the scientific community. Many techniques have been proposed recently aiming to develop a method to controllably seed the nucleation of individual quantum dots^{1,2}. A large number of these techniques have been successful and it is now possible to produce ordered arrays of dots with nanometer accuracy in their position. Nonetheless none of these techniques, so far, have achieved this goal while maintaining an optical quality, in terms of spectral purity and intensity, comparable to that achieved by self assembled, i.e. non site controlled, grown QDs.

Pyramidal Quantum Dots grown by MOVPE in pre-patterned tetrahedral recesses on GaAs (111)B substrates –Fig.a-, a technique that matured at the Ecole Polytechnique in Lausanne, are one of the most intriguing solutions to address the site control problem³. They have been used to demonstrate single photon emission with both optical or electrical excitation and are among the most uniform systems shown to date^{4,5}. Conjugating the characteristics of Pyramidal QDs with the optical quality of Stranski-Krastanov grown dots is a major step which remains to be taken towards the realisation of an “ideal” QD source which is sufficiently reliable and robust for applications.

We will present a new Pyramidal QD system in which it has been possible to achieve both high uniformity and record narrowness of the linewidth from the neutral exciton emission (the best linewidth measured being just 18 μeV –Fig. d- but almost all the dots showed linewidths narrower than 30 μeV): this is an unprecedented result for any site controlled or MOVPE grown dots. Two factors have made this achievement possible: an extremely clean growth process and the replacement of AlGaAs, the traditional barrier material for this kind of dots, with GaAs. The latter not only makes the structure more simple –Fig.b-, all the vertical quantum structures that formed in previous schemes due to alloy segregation no longer exist, but it also reduces impurity incorporations associated with the presence of Aluminium, thus eliminating one of the principal causes of diminished optical quality.

Many parameters in our system are easily tuned: investigations are ongoing to understand how far the wavelength of the quantum dot emission can be pushed towards the red, but wavelengths as long as 1100 nm have been achieved by simply changing the dot size and the Indium content in the $\text{In}_x\text{Ga}_{1-x}\text{As}$ alloy of the dot layer. This opens interesting possibilities keeping in mind the 1300/1500nm goal for optical communications.

The uniformity of the neutral exciton emission (Fig. c), which was identified by mean of power dependant measurements and, where possible, of fine structure splitting measurements, was probed on our best sample (the dot layer was nominally 0.5 nm of $\text{In}_{0.25}\text{Ga}_{0.75}\text{As}$). The standard deviation from the average value of 1463.5 nm was found to be just 1.2 meV, the best reported to date to our knowledge, corresponding to a FWHM of the Gaussian distribution of 2.8 meV.

The fine structure splitting of the neutral exciton was measured and found to be very small ($< 7 \mu\text{eV}$ for some dots): this encourages further investigation to realise a novel highly uniform site-controlled source of both single and entangled photons⁶.

- [1] S. Kiravittaya et al., *Applied Physics Letters*, **89** (2006) 233102
 [2] R. Mark Stevenson, Robert J. Young, Patrick See, Carl E. Norman, Andrew J. Shields, Paola Atkinson and David Ritchie, *Physica E* **25**, (2004) 288 – 297
 [3] Arno Hartmann et al., *Appl. Phys. Lett.*, **73** (1998) 2322-2324
 [4] M. H. Baier, C. Constantin, E. Pelucchi and E. Kapon, *Appl. Phys. Lett.*, **84** (2004) 1967-1969
 [5] K. Leifer, E. Pelucchi, S. Watanabe, F. Michelini, B. Dwir and E. Kapon, *Appl. Phys. Lett.* **91**, (2007) 081106
 [6] R. M. Stevenson, R. J. Young, P. Atkinson, K. Cooper, D. A. Ritchie and A. J. Shields, *Nature* **439** (2006) 179-182

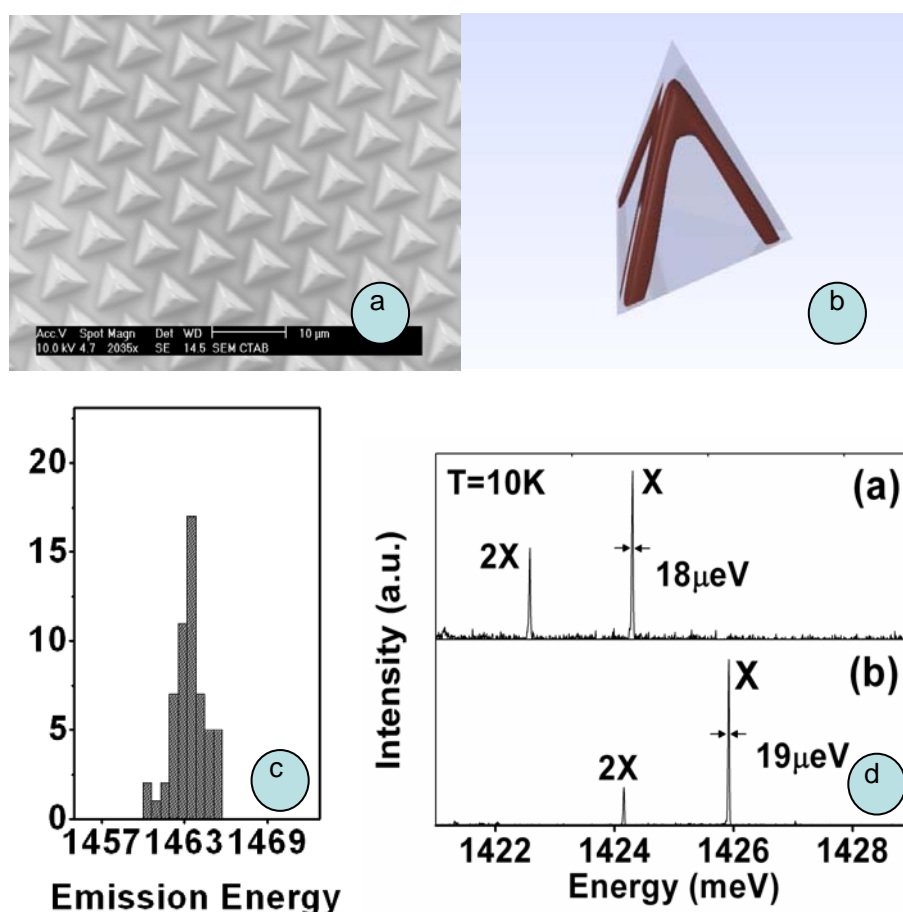


Figure: a) An SEM image of an ordered matrix of Pyramidal Quantum Dots in back etched geometry; b) A schematic drawing of the inner structure of one QD: in particular it is possible to see the lateral quantum wires. Between each couple of wires lies a lateral quantum well (not shown); c) Statistical distribution of the 60 pyramids investigated for the uniformity study. The inhomogeneous broadening due to size variations is only 2.8 meV (FWHM); d) PL spectra of two quantum dots on our best sample: the PL was made at 10K and in a very low excitation regime, the two integration times were different, but the longest (b) was 5 sec demonstrating the good quantum efficiency of these dots. The neutral exciton lines were well fitted with Lorentzian lineshapes of respectively 18 and 19 μeV FWHM.

OPTIMIZATION AND SCALED-UP OF A METHOD FOR THE PREPARATION OF DISPERSIONS FORMED BY ISOLATED MAGNETIC NANOPARTICLES FOR BIOMEDICAL APPLICATIONS

N. Miguel, A G. Roca, O. Bomati-Miguel, J. Santamaría

Dpto. Ingeniería Química y TMA, Centro de Investigación Biomédica en Red (CIBER-BBN),

C/ P. Cerbuna, 12 50009 numiguel@unizar.es.

Superparamagnetic Fe₃O₄ magnetic nanoparticles (MNPs) have been shown as a suitable MRI contrast agent. Because of their larger magnetic moment in comparison to paramagnetic ions, particulate contrast agents produce enhanced proton relaxation rates in the tissue microenvironment at significantly lower doses. In addition, MNPs show long blood half-life time that depends of coating and the aggregate size particles [1]. The principal limitations of the commercial contrast agents in NMR are their lack of crystallinity and the broad size distribution of the particles obtained by conventional synthesis methods. Recently, these problems were overcome by the use of the thermal decomposition where iron organic compounds generate magnetic nanoparticles at high temperatures in high boiling point organic solvents in the presence of oleic acid. However, the as-synthesized particles are hydrophobic in nature; therefore, these particles are incompatible with the physiological medium.

In this study monodisperse iron oxide magnetic nanoparticles were obtained with a precise control of size, high crystallinity and good magnetic properties by optimized “one-pot” synthetic route. The synthesis has been scaled-up in order to produce large amounts. This synthesis method is based on the thermal decomposition of iron organic compounds in presence of triethylene glycol (TREG) [2, 3]. The role of TREG is to provide a biocompatible, water-dispersible coating, which also acts during the synthesis process as a reagent, reducing partially the iron precursor. Furthermore, TREG is absorbed on the magnetic nanoparticles surface forming a hydrophilic coating, retards oxidation of the particle surface, reduce toxicity, and delays detection by the immune system.

In a typical preparation a TREG solution (30 mL) containing Fe(acac)₃ (2 mmol) was prepared. After being purged with argon, the reaction mixture was kept at 180 °C for 30 min followed by 30 min at 280 °C. Finally, Fe₃O₄ nanocrystals were obtained after a posttreatment that included precipitation, decantation and washing in water. The process has been optimized controlling diverse parameters as mechanical stirrer, heating rates and time of reaction. The process of scaled has been realized TREG solution (90 mL) containing Fe(acac)₃ (6 mmol).

The morphology of the so-obtained products were quite different in function of the heating rate of this process. Thus, for heating rate under 10 °C/min, individual and uniform magnetic nanoparticles have already formed, however these nanoparticles were agglomerated forming nanorod-like structures. In contrast, when heating rates were increased over 10 °C/min non-agglomerated magnetic particles with uniform shape and narrow size distribution were observed.

Fig.1 presents a representative TEM image of scale-up synthesis Fe₃O₄ nanocrystals finally obtained in a PBS buffer solution which has the same pH values and ionic strength as physiological conditions. The non-aggregated nature of the particles in a physiological buffer was confirmed by TEM. The mean size of particles is 7.0 nm ($\sigma= 0.18$). Hydrodynamic size is around 11 nm in PBS.

The magnetic properties of the optimized magnetite nanoparticles were investigated with a Superconducting Quantum Interference Devices (SQUID). Figure 2 shows the room-temperature magnetization of as-prepared magnetite nanocrystals. The nanocrystal exhibited the superparamagnetic characteristics. Their saturation magnetization was 56 emu/g. Magnetic size calculated by Chantrell equation is 5.1 nm showing that all the magnetic moments of the particles rotate coherently inside the particles.

Their potential MRI agents contrast was investigated in vitro and ex vivo. In vitro, the r_1 and r_2 relaxivities of as-synthesized magnetite nanoparticles were found to be 15 (Fe) $\text{mM}^{-1}\text{s}^{-1}$ and 49 (Fe) $\text{mM}^{-1}\text{s}^{-1}$ respectively. Such values for r_1 and r_2 suggest that as-synthesized magnetite nanoparticles can act as both T_1 and T_2 contrast agent taking into account their ultra-small size, but seem to be more favourable as T_2 contrast agents due to their much larger r_2 value.

In summary, we have demonstrated that the synthesis of magnetic nanoparticles from $\text{Fe}(\text{acac})_3$ precursors in a TREG environment can be tailored to obtain non-aggregated nanoparticles, which form a stable dispersion in water and PBS buffer solution. The control of the rate of heating and the concentration of the iron precursor species seem to be the key parameter in the balance of nucleation/growth processes and therefore in the production rates of this process, as well as in the control of the final morphology of the so-obtained particles. In vitro experiments have shown that these MNPs have an excellent enhancement T_2 contrast in MRI imaging. Therefore, this optimized synthesis is a good candidate to prepare contrast agents for NMR imaging.

References:

- [1] R.N. Low. *Mag. Reson. Imag. Clin. N.Am.* **9** (2001) 717-743.
- [2] F. Fievet, J.P Lagier, *Solid State Ionics*, **32-33** (1989) 198
- [3] J. Wan, W. Cai, *Chem. Commun.* **47** 5004-5006 (2007)

Figures:

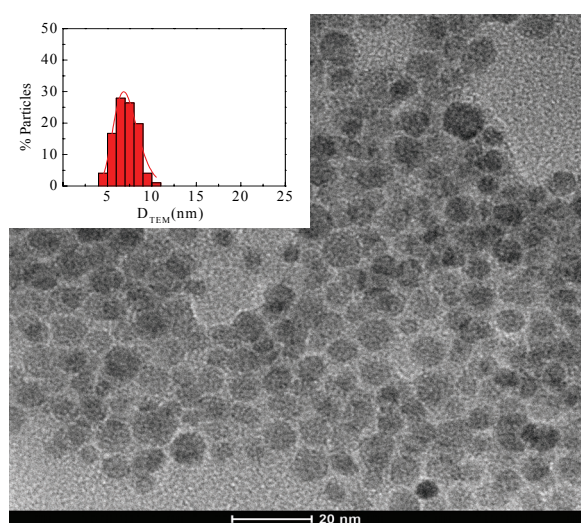


Fig.1 TEM image of the scaled-up Fe_3O_4 nanoparticles dispersed in a PBS buffer solution

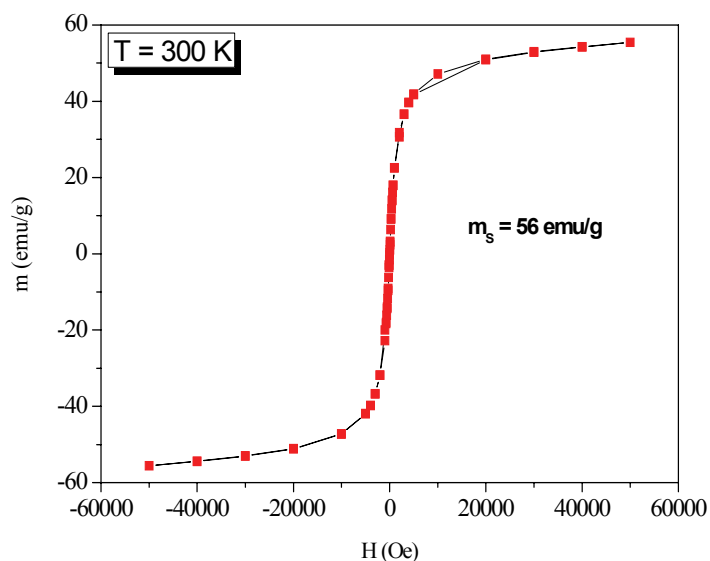


Fig.2. SQUID for the optimized nanoparticles

**MID-INFRARED LIGHT EMITTING DIODES AND HIGH-SPEED PHOTODIODES
BASED ON TYPE II HETEROSTRUCTURES WITH DEEP AlSb/InAsSb/AlSb
QUANTUM WELLS IN ACTIVE LAYERS**

M.P. Mikhailova¹, K.D. Moiseev¹, E.V. Ivanov¹, I.A. Andreev¹, M.Yu. Mikhailov¹,
Yu.P. Yakovlev¹

E. Hulicius², A. Hospodkova², J. Pangrac², T. Simecek²

1) Ioffe Institute RAS, St. Petersburg, Russia.

2) Institute of Physics AS CR, v.v.i, Prague, Czech Republic.

E-mail: mikh@iropt1.ioffe.rssi.ru

We report the first study of positive and negative luminescence in light-emitting diodes (LEDs) and photoelectrical properties of type II p-InAs/AlSb/InAsSb/AlSb/p(n)-GaSb(InAs) heterostructures with deep single and triple quantum wells (QW) incorporated at the heterointerface. Recently negative electroluminescence (EL) has been studied in the narrow-gap InAs, InSb, CdHgTe, InAsSb bulks, p-n junctions and superlattices [1,2]. The structures were grown on p-InAs: Mn (100) substrate by metal-organic vapor phase epitaxy and consist of 20 nm-AlSb/5 nm-InAs_{0.84}Sb_{0.16}/20 nm-AlSb QW and 0.5 μm p(n)-GaSb(InAs) capped layer. Mesa-diodes of 300 μm in diameter were prepared by standard photolithography. EL spectra were measured both at forward and reverse bias at 77 K and in higher temperature range 300-380 K. Low-temperature spectra at the forward bias (“+” is at the p-InAs substrate) consist of two positive EL bands with photon energy $h\nu_{max} = 0.407$ eV and 0.376 eV ($\lambda_{max} = 3.05$ μm and 3.3 μm, respectively), which can be written to band-to-band radiative recombination transitions in InAs and from Mn acceptor level ($E_a = 31$ meV). Full width at a half maximum (FWHM) was about 21 meV for the both bands. High-intensive negative EL was found in temperature range 300-380 K at the reverse bias. Negative EL spectra were situated in the range 0.3-0.4 eV (3-4 μm) and their shape was similar to ones of positive EL (Fig.1). Dependence of negative EL intensity on drive current value in the range of 25-200 mA, photon energy and temperature was studied. It was established that at high temperature (> 75 °C) and drive current up to 100-150 mA the negative EL intensity exceeds the positive one by 60 %. High efficiency of the negative EL was due to the suppression of Auger recombination at temperature increase.

Proposed heterostructures can operate as LEDs or as photodiodes with switching positive-to-negative luminescence in the spectral range 3-4 μm. Their applications include gas sensing, ecological monitoring, testing of thermal imagers etc.

Last years a great attention have been paid to creation new type QW photodiodes for mid-infrared spectral range. GaAs/AlGaAs and InGaAs/InP QW photodiodes operated in the spectral range 3-5 μm were reported [3]. Recently high-speed photodiodes based on GaSb heterostructures were designed by us [4]. In the frame of this work we studied also electrical and photoelectrical properties of the nanostructures p-InAs/p(n)GaSb(InAs) with a single and triple QWs in active layer which demonstrated high luminescence efficiency. Current-voltage (I-V) characteristics, capacitance-voltage and spectra of photoresponse were first studied at 77 and 300 K for the samples with QW at the interface. Experimental results have shown rectifying I-V characteristics at low bias. The differential resistance R_0 was evaluated from I-V characteristics at zero bias. We found $R_0=258$ kOhm and $R_0 \times A=120$ Ohm \times cm² (77 K). Fig. 2 demonstrates the spectral response for photodiode based on p-InAs/AlSb/InAsSb/AlSb/p-GaSb single QW heterostructure measured at 77 and 300 K. The spectra are located in the range of 1.0-3.4 μm at 77 K and in the range 1.2-3.8 μm at 300 K. At T=77 K a weak additional peak was observed at around of 4.3 μm. High quantum efficiency $\eta=0.6-0.7$ and detectivity $D_\lambda^* = 10^{10} - 3.5 \times 10^{11}$ cmHz^{1/2}W⁻¹ at T=200-77 K were evaluated in the photovoltaic mode. Surprising sharp fall of capacitance versus reverse bias was observed in the samples with 3 QWs in an active layer

(fig.3). Capacitance decreased from 200 pF ($V=0$ V) up to 1.5 pF ($V=-1$ V) at room temperature. It correspond to $\tau=R_L C=75$ ps where $R_L=50$ Ohm. It is evidence that charge depletion layer is situated in the quantum size region of the structure. This value corresponds to high frequency bandwidth about 10 GHz. Such superfast QW photodiodes are suitable for heterodyne detection of quantum cascade lasers, ecological monitoring, medical diagnostics.

Work was supported in part by RFBR grant #09-02-0063, Program of the Presidium of RAS, GAAV of the Czech Republic Grant no. A100100719 and Project of Institute of Physics AV0210100521.

References:

- [1] V.I. Ivanov-Omskii, B.A. Matveev, Semiconductors, **41** (2002) 247.
- [2] T.Ashley, G.R. Nash, in: Mid-Infrared Optoelectronics (Springer Series in Optical Science) ed. By A. Krier, London, Springer-Verlag, (2006).
- [3] S. Haywood and M. Missous, *ibid.*, p. 429.
- [4] Yu.P. Yakovlev, I.A. Andreev, E. Kunitsyna, M.P. Mikhailova, SPIE, **vol. 4320**(2006) 120.

Figures:

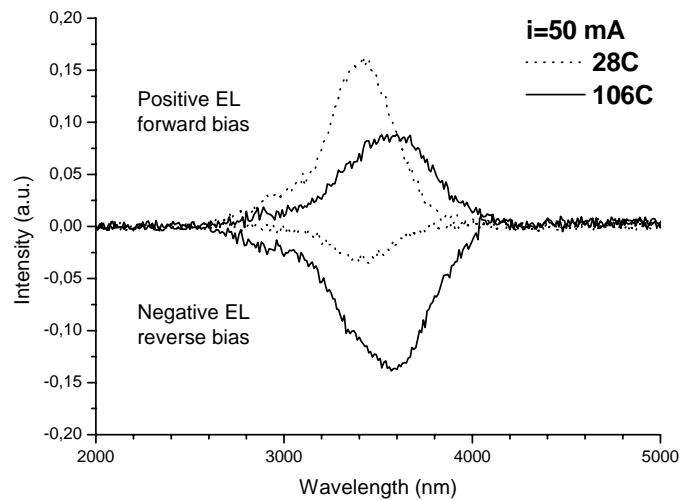


Fig. 1. EL spectra of InAs/AlSb/InAsSb/AlSb/GaSb SQW heterostructure under forward and reverse bias at two temperatures.

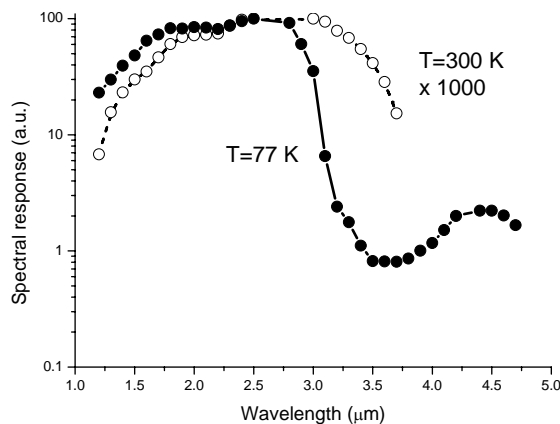


Fig. 2. Normalised spectra of photoresponse of the InAs/

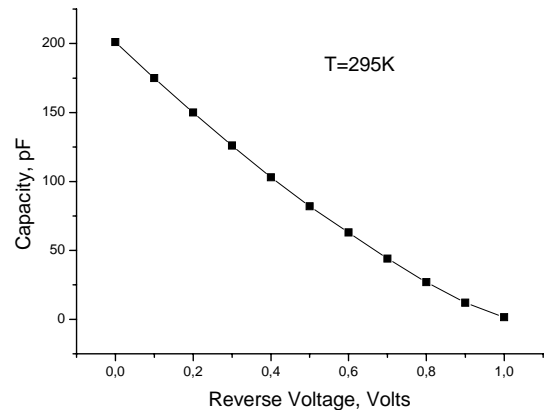


Fig.3. Capacitance versus reverse bias for the

AlSb/InAsSb/AlSb/GaSb single QW heterostructure.

triple AlSb/InAsSb/AlSb QWs heterostructure.

SURFACE-ENHANCED RAMAN SCATTERING BY CdS QUANTUM DOTS

A. Milekhin¹, L. Sveshnikova¹, T. Duda¹, N. Surovtsev², S. Adichtchev², D. R. T. Zahn³

¹*Institute of Semiconductor Physics, 630090 Novosibirsk, Russia*

²*Institute of Automation and Electrometry, 630090, Novosibirsk, Russia*

³*Institut für Physik, Technische Universität Chemnitz, 09126 Chemnitz, Germany*

milekhin@thermo.isp.nsc.ru

Semiconductor quantum dots (QDs) having promising optical and electronic properties optoelectronic applications are the subject of numerous investigations. The study of their phonon spectrum is equally important because it determines the processes of carrier relaxation. Most of the published data related to phonons in QDs were obtained in Raman scattering experiments and refer to QD arrays such as Ge/Si, A³B⁵ etc. A small spatial volume and thus small Raman cross-section leads to extremely low Raman efficiency of a single QD making the information on phonon spectrum of a single QD not available today. Surface-enhanced Raman scattering (SERS) consists in dramatical increase of the signal (typically factor of 10⁵÷10⁶) by molecules adsorbed on a rough surface of some metals or their clusters due to surface plasmons. In this paper, we report on observation of SERS effect in CdS QDs deposited on a solid substrate. Strong enhancement of intensity (at least factor of 150) of Raman scattering by quantum dots is observed by deposition of silver clusters onto the nanostructure surfaces.

CdS QDs in a behenic matrix of various thicknesses (10-440 monolayers) were formed by Langmuir-Blodgett (LB) method on a quartz and Si substrates, covered by Au layers. After that the matrix of behenic acid was removed by annealing and free QDs CdS QDs having spherical shape and average size of 5÷6 nm were obtained. Ag nanoclusters on the surface of CdS QD films were also formed by using the LB technology by depositing of 30 monolayers of behenic acid. The samples containing behenic acid matrix were set in AgNO₃ solution. As a result of reaction of the behenic acid film with AgNO₃ solution the silver behenate films were obtained. After the second annealing of the structures Ag nanoclusters were formed on the QD surface. The Raman spectra were recorded at T = 20 K using a Dilor XY800 triple spectrometer in the non-polarized backscattering configuration. Several lines of Ar⁺ and HeCd lasers in the spectral range of 441.6÷528.7 nm were used for excitation.

Figure 1 shows the Raman spectra of the structures containing free CdS QDs with and without Ag nanoclusters. The Raman spectrum of CdS QDs without Ag nanoclusters reveals the only weak feature near 300 cm⁻¹ associated with the LO phonons in the QDs.

Deposition of Ag nanoclusters on the surface of QD layers leads to strong enhancement (150-fold) of Raman intensity. Raman spectrum of free CdS QDs with Ag nanoclusters (Fig. 1) exhibits several intensive peaks related to the first-Raman scattering by LO phonons from CdS QDs at 304 cm⁻¹ and their overtones up to 5th order with spacings approximately equal to the LO phonon energy in CdS QDs. The shape asymmetry of the LO phonon line is due to surface optical phonons in the QDs occurring at about 280 cm⁻¹. The comparison of the LO phonon line shape for samples 440f and 440Ag is shown in the inset to Fig. 1. As one can see, the frequency positions of the Raman features in both spectra coincide while their full widths at half maximum differ in four times.

The enhancement factor of SERS has a resonance dependence on the laser excitation energy with a maximum at 2.6 eV (Fig. 2). That is close to the energy of absorption maximum which is observed in absorption spectrum of silver nanoclusters associated with the surface plasmon resonance (SPR) in the nanoclusters.

At least two effects can be responsible for the LO phonon line narrowing.

First, SERS is selective with respect to the QD size. Indeed, CdS QDs formed by LB technique have a relatively broad distribution of QD size (about 20 %). Large QDs having relatively lower energies of electronic interband transitions contribute mostly to Raman spectra at lower excitation energies (below 2.9 eV). This leads to increasing their relative contribution to the Raman spectra at lower excitation energies close to the SPR energy due the SERS effect.

Confinement effect of optical phonons in the large QDs is negligible, therefore, the energy position of the peaks due to LO phonons localized in CdS QDs observed in the SERS spectra shows no dependence on the excitation wavelength. As a result, no spreading of the line shape due to the size fluctuation in the QD array is expected in the SERS spectra.

Second, SERS effect is selective with respect to the quantum number of the phonon mode confined in QDs. According to the surface selection rules the A_1 -type modes are to be active in SERS spectra measured in the experimental geometry applied. Therefore, only the most pronounced mode fundamental mode with $l=0, n=1$ (which is the A_1 mode) is enhanced by SERS effect while the others are suppressed by selection rules or have much lower intensity.

In conclusion, surface-enhanced Raman scattering by confined LO phonons and their overtones in CdS QDs is observed. The narrowing of the FWHM of LO peak in SERS spectra with respect to the ordinary Raman scattering is explained by size- and mode-selective nature of SERS in the QDs.

This work was supported by the Russian Foundation for Basic Research (grants 08-02-90441 Ukr a and 09-02-00458 a) and the International Research Training Group (Internationales Graduiertenkolleg, GRK 1215) "Materials and Concepts for Advanced Interconnects".

Figures:

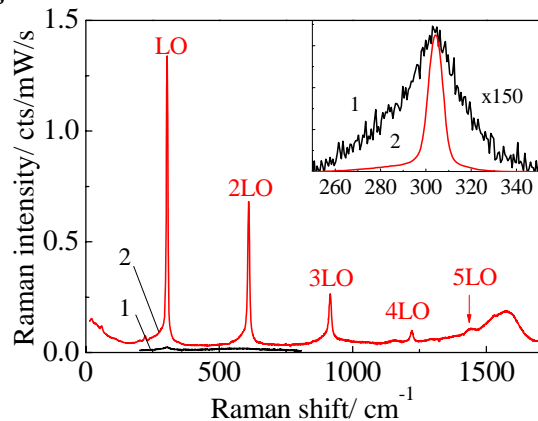


Fig.1. Raman spectra of free CdS QDs without and with Ag clusters (curves 1 and 2, respectively) excited with the 476.5 nm laser line.

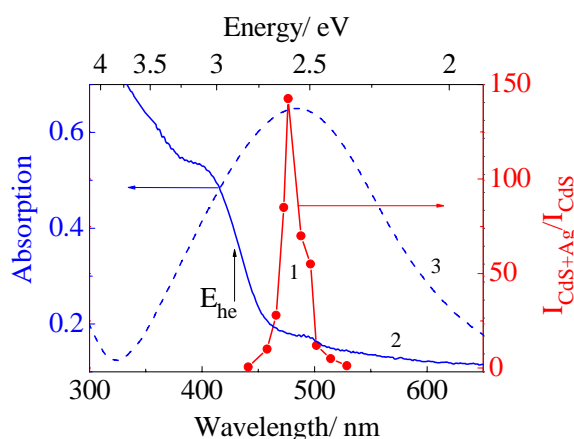


Fig.2. Enhancement factor of SERS by LO phonons in CdS QDs as a function of laser excitation energy -(curve 1); and experimental absorption spectra of the structures with free QDs- (curve 2); and with Ag clusters and without CdS QDs- (curve 3).

Molecular doping in Silicon Nanowires: an ab-initio study

Alvaro Miranda^{1,2*}, Xavier Cartoixà¹, Miguel Cruz-Irisson², and Riccardo Rurali¹

¹Departament d'Enginyeria Electrònica, Universitat Autònoma de Barcelona,
08193 Bellaterra, Barcelona, Spain

²Instituto Politécnico Nacional, ESIME-Culhuacan, Av. Santa Ana 1000,
04430 México D.F., México

*amirandad9700@ipn.mx

We present *ab-initio* calculations based on density functional theory (DFT) of the effects on the electronic bands structure, total and projected density of states of surface molecular adsorption onto hexagonal cross-section silicon nanowires (SiNWs) grown along the $\langle 111 \rangle$ direction.

Continuous miniaturization of microelectronic devices requires a corresponding reduction in feature size, and low-dimensional materials have become one of the most active research topics in recent years. In particular, SiNWs have attracted much attention due to their compatibility with conventional silicon-based integrated circuit technology allowing potential applications as building blocks in a variety of nano-scale devices such as field-effect transistors (FETs) [1], sensors [2], etc. Thus, advances in doping techniques are required that will allow the introduction of controlled amounts of dopants into nanowires (NWs) without degrading their electronic properties or morphology. Electrical doping for Si NWs has been achieved primarily through *in situ* doping, with the dopant introduced in the gaseous phase for incorporation during vapor-liquid-solid (VLS) growth, with metallic nanoparticles such as Au used as the catalytic growth seeds [3]. However, this *in situ* approach does not always give favorable results [4]. Enhanced surface doping during growth, for instance, competes with dopant introduction at the liquid-solid growth interface and can cause non-uniform doping along the NW length, with higher doping closer to the NW base. Electrical doping of NWs by *ex situ* techniques separates the doping step from the NW growth process and thus does not lead to sidewall-enhanced dopant variations along the NWs or changes in NW morphology [5]. *Ex situ* doping in a batch process also potentially allows for more uniform and controlled dopant concentrations over a large NW array, with the added possibility of spatial selectivity.

On the other hand, Fernández-Serra *et al.* [6] showed that in passivated NWs as large as few nanometers in diameter, a large proportion of dopants will be trapped and electrically neutralized at surface dangling bond defects, significantly reducing the carrier density. This inconvenience is shared by both conventional *in-situ* and *ex-situ* approaches. Here we explore the possibility of obtaining molecular doping of Si NWs. We show that a molecular-based *ex-situ* doping, where molecules are adsorbed at the sidewall of the NW, can be an alternative path to doping. We discuss the cases of both donors and acceptors.

We present some preliminary results for a Si NW doped with tetracyanoethylene [Fig. 1(c)], whose band structure is shown in Fig. 1(a). It can be seen that the adsorbed molecule contributes with a localized state (no dispersion) close to the conduction band edge, pinning the Fermi level. The molecular nature of this state is further supported by the total electronic density of states (DOS) and the projected DOS, where projections are made on every element [Fig.1(b)]. There it can be seen that the localized states is almost exclusively made up of C and N contribution, thus it is localized at the molecule adsorption site.

Finally in Figs. 1 (d-f) where the representation in real space of the corresponding wave functions iso-surfaces is shown; (d-e) and (f) iso-surfaces corresponding to top valence band two states and bottom conduction band one state respectively.

In larger nanowires, where the band gap is smaller due to a reduced quantum confinement, this state is expected to be shallow enough to be an active electron donor.

References:

- [1] Y. Cui, Z.H. Zhong, D.L. Wang, W.U. Wang and C.M. Lieber, *Nano Lett.*, **3** (2003) 149.
 [2] Y. Cui, Q.Q. Wei, H.K. Park and C.M. Lieber, *Science*, **293** (2001) 1289.
 [3] Y. Wang, K. K. Lew, T. T. Ho, L. Pan, S. W. Novak, E. C. Dickey, J. M. Redwing, and T. S. Mayer, *Nano Lett.*, **5** (2005) 2139.
 [4] L. Pan, K.-K. Lew, J. M. Redwing, and E. C. Dickey, *J. Cryst. Growth*, **277** (2005) 428.
 [5] K. Byon, D. Tham, J. E. Fischer, and A. T. Johnson, *Appl. Phys. Lett.*, **87** (2005) 193104.
 [6] M.V. Fernández-Serra, Ch. Adessi, and X. Blase, *Phys. Rev. Lett.*, **96** (2006) 166805.

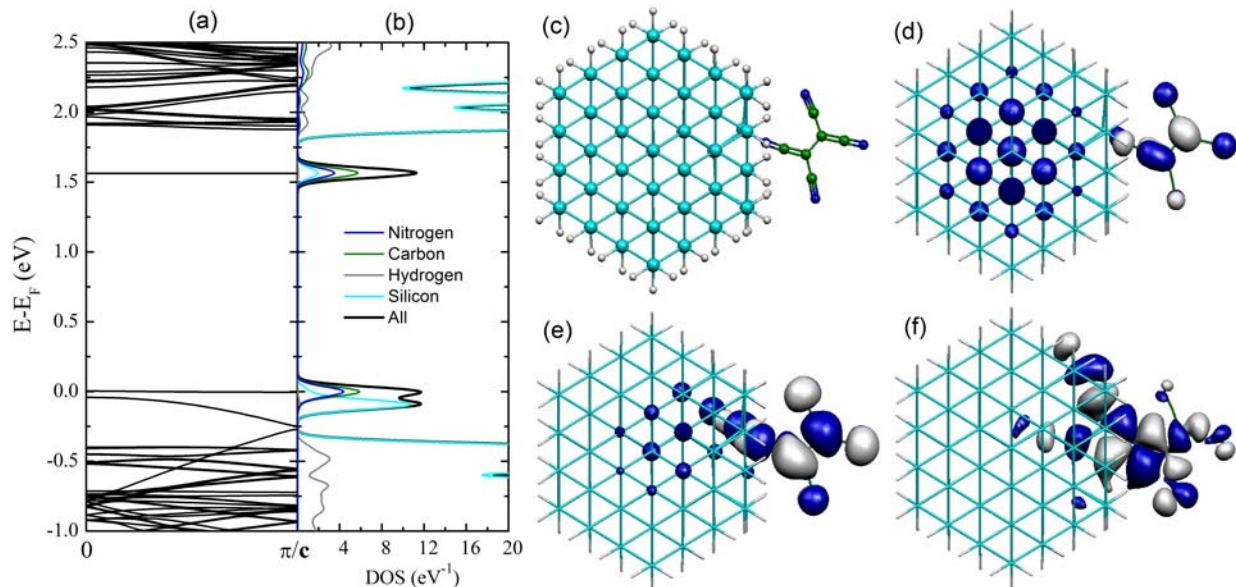


Figure 1. (a) The electronic band structure of the SiNW. One state have the Fermi level, the wave vector k in the first half of the Brillouin zone. (b) The total and projected electronic density of states of the SiNW, (c) Tetracyanoethylene doped on Silicon nanowire. The wave function iso-surfaces of the three states (d-f) of the SiNW.

Preparation and Derivatization of wsCNTs -Their applications as Super-absorbents

Hemant Mittal, R. Jindal and B.S. Kaith
Dr. B. R. Ambedkar National Institute of Technology,
Jalandhar, Punjab, INDIA
e-mail: mittal.hemant5@gmail.com

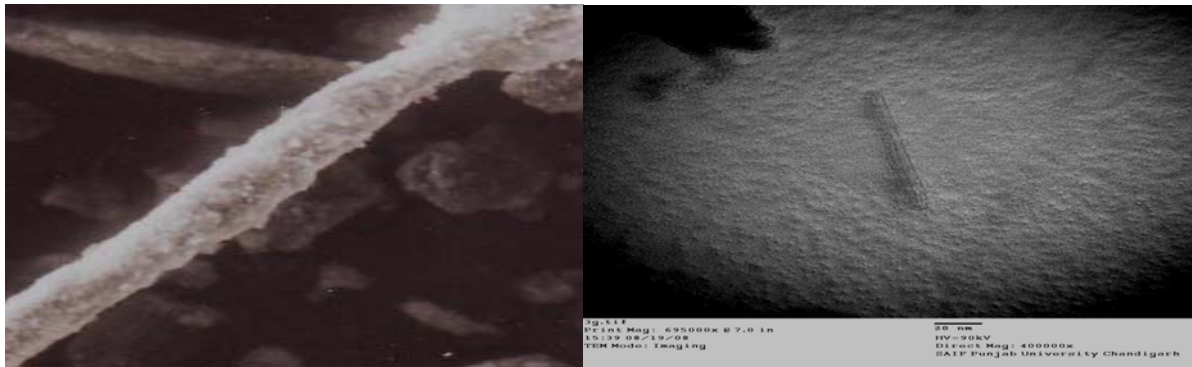
Since the discovery of carbon nanotubes (CNTs) in 1993 by Iijima [1], the field of research centered around the different modes of their synthesis, properties and end applications. Work on CNTs has experienced a fast-paced growth because of their remarkable structure dependent properties. With unique chemical, mechanical, optical, electronics and electrical properties, carbon nanotubes (CNTs) find their way as attractive building blocks for the fabrication of advanced materials with improved performance or even with new properties [2]. The utility of nanotubes in each of its application, including sustained drug delivery devices, field emission and storage devices, electronics [3,4], nano-composites, sensors as well as tools for high resolution and biomedical imaging depends on one or more of their unique fundamental properties like high aspect ratio, high mechanical strength and excellent thermal and electrical conductivity at different temperatures.

Low cost synthesis has a marked effect on the potential use of CNTs in varied fields. Since lack of solubility poses a significant impediment to their exploitation in many potential commercial applications, therefore, it is most desirable to improve its hydrophilic properties, so that it can be made water soluble and could be derivatized further for its wide use of spectrum [5]. In our present research work, we have developed a novel, low-cost method for the synthesis of water soluble multiwalled carbon nanotubes (wsCNTs) from petroleum waste using cold percolation technique. Hydrophilic functionality is introduced by refluxing with dilute nitric acid (2.6M). These water soluble carbon nanotubes were characterized by using different techniques like SEM, TEM and FTIR. Synthesized CNTs were further derivatized with acrylamide, potassium persulphate-ferrous ammonium sulphate as an initiator system and N,N'-methylenebisacrylamide as a crosslinker so that it could be used as a super-absorbent for its application in petroleum sector. The resultant derivatized CNT has been found to be an efficient super-absorbent.

References:

- [1] S. Iijima and T. Ichihashi, *Nature*, **363** (1993) 603.
- [2] P.M. Ajayan, *Chem. Rev.*, **99** (1999) 1787.
- [3] H. Ago, K. Petritsch, M.S.P. Shaffer, A.H. Windle and R.H.Friend, *Adv. Mater.*, **11** (1999) 1281.
- [4] A. Kasumov, R. Deblock, M. Kociak, B. Reulet, H. Bouchiat, I. Khodos., Y Gorbатов, V. Volkov, C. Journet and M. Burghard, *Science*, **284** (1999) 1508.
- [5] V. N. Khabashesku and J. L. Margrave, **1** (2004) 849.

Figures:



REVISED STATISTICAL THERMODYNAMICS FORMALISM FOR CALCULATION OF THERMODYNAMIC PROPERTIES OF SMALL SYSTEMS

M. Mohsen-Nia*, F. S. Mohammad Doulabi

Thermodynamic Research Laboratory, University of Kashan, Kashan, Iran

Abstract

The effect of size and dimension decreasing of materials to a nanometer scale on the physical and chemical properties has been caused strong research efforts to study on experimental and theoretical methods for evaluation of size reduction [1, 2]. Due to their properties, nano-structured materials have received increasing attention in various fields of science and technology [3, 4].

Although there are different experimental methods for nano-structured materials fabrication in the literature, but the theoretical research works on these topics are given as a motivation to introduce a generic theory. Statistical mechanics provides an exact interpretation of intermolecular force effect on properties of bulk state of materials. The evaluation of the macroscopic properties based on microscopic characteristic of materials, is the main advantage of statistical mechanics over classical thermodynamics. In the statistical mechanics based on an averaging procedure in imaginable ensembles, a large number of systems with different microscopic characteristics but similar macroscopic characteristics may be expected. This idea is developed by Gibbs, Maxwell, and Boltzmann [5].

The ensemble concept states that macroscopic properties can be calculated by performing averages over the systems in the ensemble. For a typical macroscopic system with a large number of particles, the relative deviations from the mean are extremely small and can be ignored. Therefore, the probability distribution of the properties such as energy or pressure in canonical ensembles can be considered as a Gaussian distribution which is practically a delta function. Thus, to evaluate the probability distribution for determining the ensemble average, a simplified assumption can be considered. According to the basic assumptions in the statistical thermodynamics, the ensemble average of a property can be equated to the corresponding thermodynamic property [7].

However, the probability distribution of the properties in canonical ensembles for the small systems can not be regarded as a delta function. Thus, the simplified assumptions for the large systems must be reconsidered for calculating the small system properties. An early discussion of the suitable modification of this theory was developed by Hill [8].

For the small systems, the absence of quantitative models for accurate calculating the thermodynamic properties and predicting the observed phenomena is a serious limitation in progress of this field of science. Although in the recent years many research works have been done on the experimental studies of the small systems but without new theoretical models for the quantitative description of structure and dynamics of the small systems, the research community might miss many important scientific opportunities in this field of research [9, 10].

Therefore, for the more accurate description of such system by wide intuition of the important role of size and the number of the particles in the properties of the studied systems, the modified statistical models should be employed [6].

In this work, in order to calculate the energy of the small system based on the basic concept of statistical mechanical ensemble theory, a realistic distribution function is considered. The obtained relation for energy of the small system is consistent with that obtained for the large systems. This will enable us to extend the general method of statistical mechanical ensemble theory to description of small-systems in a transparent way.

REFERENCES:

- [1] H. Feshbach , Physics Today, 40 (1987) 9.
- [2] T. C. P. Chui , D. R. Swanson , M. J. Adriaans , J. A. Nissen , and J. A. Lipa , Phys.Rev. Lett. 69 (1992) 3005.
- [3] L. Tosheva, V.P. Valtchev, Chem. Mater. 17 (2005) 2494.
- [4] Mao-Sung Wu, Pin-Chi J. Chiang, Jyh-Tsung Lee, Jung-Cheng Lin, J. Phys. Chem. B 109 (2005) 23279.
- [5] T. L. Hill, "statistical Thermodynamics", Addison_Wesley, reading, Mass.,1960.
- [6] A. Reif, Fundamentals of Statistical and Thermal Physics, New York (1976)
- [7] Mc quarrie D. A., Statistical Thermodynamics, Hrper's Chemistry series & Row,publishers, New York,1976
- [8] T. L. Hill, Nano Letters 1 (2001) 273.
- [9] G. Gallavotti and E. G. D. Cohen, Phys. Rev. Letts., 74 (1995) 2694.
- [10] V. García-Morales, J. Cervera, J. Pellicer, Physics Letters A, 336 (2005) 82.

SELECTIVE SYNTHESIS OF SMALL GOLD CLUSTERS WITH ODD OR EVEN SIZES

L. M. Molina¹, M. C. Blanco², J. A. Alonso¹, M. J. Rodríguez-Vázquez²,
C. Vázquez-Vázquez², J. Rivas² and M. A. López-Quintela²

¹*Department of Theoretical, Atomic and Optical Physics,
University of Valladolid, Valladolid, Spain*

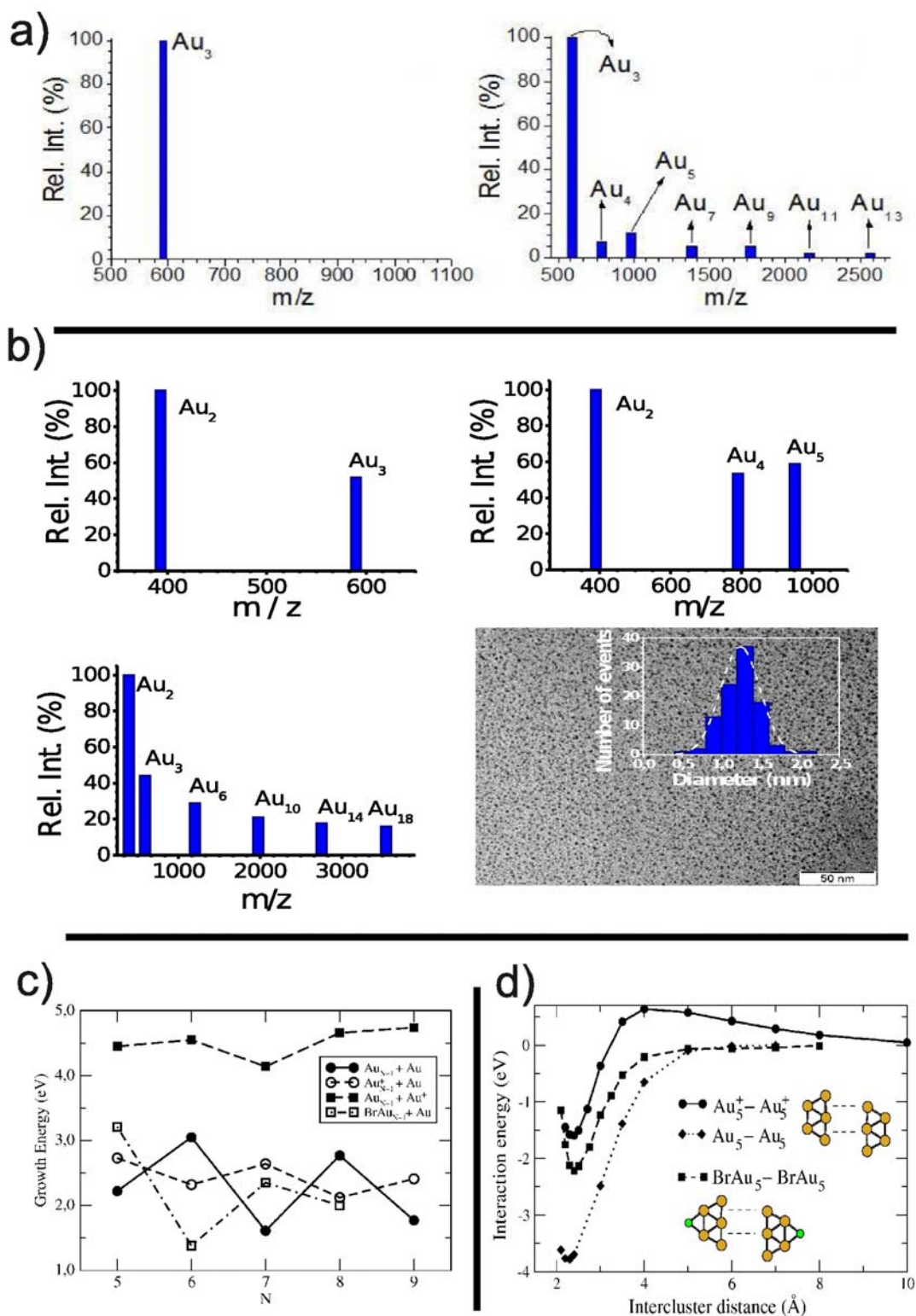
²*Laboratory of Magnetism and Nanotechnology, Institute of Technological Research,
University of Santiago de Compostela, Santiago de Compostela, Spain*
lmolina@fta.uva.es

Gold clusters are highly interesting for their unique physical and chemical properties, having attractive applications as highly selective nanocatalysts, active sites in chemical sensors, etc... Their properties vary strongly atom-by-atom, and even- or odd-numbered clusters have qualitatively different features due to the change in the number of valence electrons. However, for practical applications it is necessary to develop new production techniques beyond the standard mass-selection techniques which provide too low yields. In a recent work, we have reported the synthesis in solution (with a procedure based in the two-phase method) of small gold clusters (Au_N , with $2 \leq N \leq 18$) in large quantities, selecting only the odd-numbered ones [1] (see Fig. 1a). We now report an easy procedure of selecting the parity of the clusters produced, by a change in the type of capping agent during the solution synthesis, which results in preferential formation of even-numbered clusters (see Fig. 1b). In parallel to the experiments, we have also performed DFT simulations of the stability, charge state and mutual interaction of small gold clusters. The simulations show that the qualitatively different cluster-counterion interaction leads to different cluster charge states during growth, which linked to the intrinsic differences between odd- and even-numbered clusters results in selective production of a given cluster parity (see Fig. 1c). Also, we find different growth mechanisms, atom-by-atom in the cationic case, and by coalescence in the neutral case (see Fig. 1d). The simplicity of the synthesis procedure and the ability to easily control a key cluster feature as the open-shell character (which has a direct relationship to the cluster reactivity), opens new possibilities for the mass production of these clusters and their extensive use in novel industrial applications. Work supported by Spanish MEC, JCyL and the European Union.

References:

[1] M. J. Rodríguez-Vázquez, C. Vázquez-Vázquez, J. Rivas and M. A. López-Quintela, *Eur. Phys. J. D*, 52 (2009) 23.

Figure 1: a) Mass spectra (positive ions) of gold clusters synthesized by the two-phase method at increasing amounts of reducing agent. b) The same spectra using a different type of capping agent. c) Growth energies for neutral, cationic and bromine-capped gold clusters. Growth energies for capture of Au^+ cations are also shown (solid squares). d) Interaction energy (with respect to separate fragments) as a function of mutual cluster distance for the coalescence process of Au_5 , Au_5^+ and BrAu_5 clusters.



Analysis by ATR-FTIR of the curing process in epoxy resins modified with two different Polyhedral Oligomeric Silsesquioxanes (POSS).

B. Montero, C. Ramírez, M. Rico, A. Torres, L. Arboleda.

Grupo de Polímeros. Universidad de A Coruña. E. U. P. Av. 19 de Febrero s/n, 15405. Ferrol. Spain

labpolim@udc.es

Polyhedral Oligomeric Silsesquioxanes (POSS) can be dispersed in thermosetting resins at nanometric scale to form inorganic/organic hybrid nanocomposites. In contrast to conventional inorganic fillers, POSS have the advantages of monodispersed size, low density, high thermal stability and controlled functionalities. [1]

In the present work, the mechanism of polymerization of an epoxy-diamine system, when it is modified with several percentages in weight of two different POSS, was studied by Attenuated Total Reflection Fourier Transform Infrared, ATR-FTIR. The epoxy-diamine system was formed by diglycidylether of bisphenol A (DGEBA), as epoxy resin and 4,4'-(1,3-phenylene diisopropylidene) bisaniline (BSA), as hardener. The two selected POSS were the octaepoxy-cyclohexyldimethylsilyl-POSS (OECh) and the epoxy-cyclohexylcyclohexyl-POSS (EChCh). Both of them contain eight and one epoxy groups in their structure, respectively, which can take part into the curing reaction so that, the POSS remains chemically connected in the final product. The figure 1 shows the structures of all materials.

A curing process optimized by differential scanning calorimetry analysis, DSC, was applied to the modified samples, which consists on an initial heating during 3h at 130 °C and a post-curing process during 4h at 150 °C, in a conventional oven. At designated time intervals, small portions of the sample were withdrawn from the oven and the reaction was suddenly stopped by freezing, in order to be tested by ATR-FTIR.

In the figure 2, the results of the ATR-FTIR analysis for the two epoxy-diamine samples modified with a 2,5 wt% of both POSS can be seen. As the cure reaction advances, the diamine reacts with the two epoxy groups present in the mixture, the epoxy from the thermosetting resin (DGEBA) and the epoxy from the POSS (EChCh/OECh), until the secondary amine groups are generated. It can be observed that the reaction with the thermosetting resin is more favourable than with the epoxy POSS, because the absorbance of the band corresponding to the bending of epoxy from DGEBA, at 917 cm^{-1} , disappears along the curing process, contrary to the bending band of epoxies belonging to POSS molecules, at 745 cm^{-1} for OECh and 743 cm^{-1} for EChCh. Moreover, the diamine reacts in a mayor proportion with the monofunctional POSS, EChCh, than with the octafunctional, OECh. This can be explained by means of steric hindrance, as more voluminous the epoxy containing molecule is, more difficult will be the approaching of the amine. [2, 3]

As the primary amine groups have been consumed, polyetherification reactions begin to appear as a result of the reaction between the hydroxyl groups, resulting of the opening of the oxirane rings, and the epoxy groups remaining. This phenomenon is confirmed by the presence of the stretching band of aliphatic ether groups around the 1100 cm^{-1} . So, competition phenomena exist between both kind of polymerization, the reaction with the hardener and the homopolymerization.

Financial support: MAT2007-61677.

References:

- [1] J. J. Schwab, J. D. Lichtenhan, *Appl. Organometal. Chem.*, **12**(1998)707.
 [2] G. Rajagopalan, K. M. Immordino, J. W. Gillespie Jr., S. H. McKnight, *Polymer*, **41**(2000)67.
 [3] C. Ramírez, M. Rico, A. Torres, L. Barral, J. López, B. Montero, *European Polymer Journal*, **44**(2008)3035.

Figures:

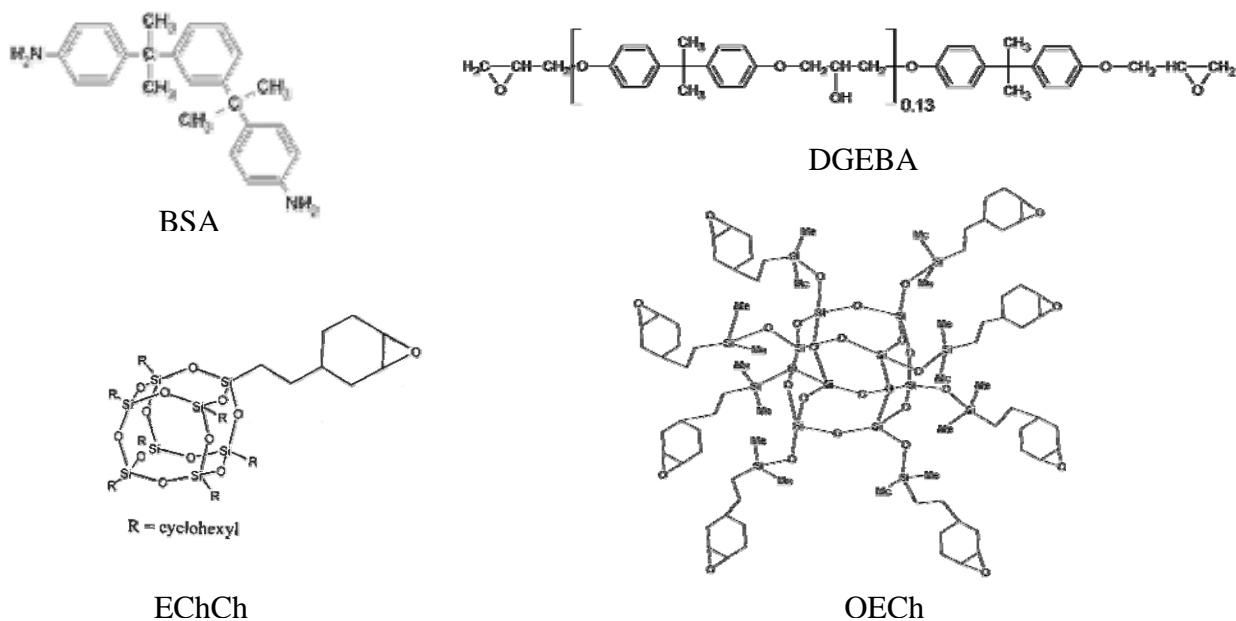


Figure 1. Structures of different materials forming the final nanocomposite.

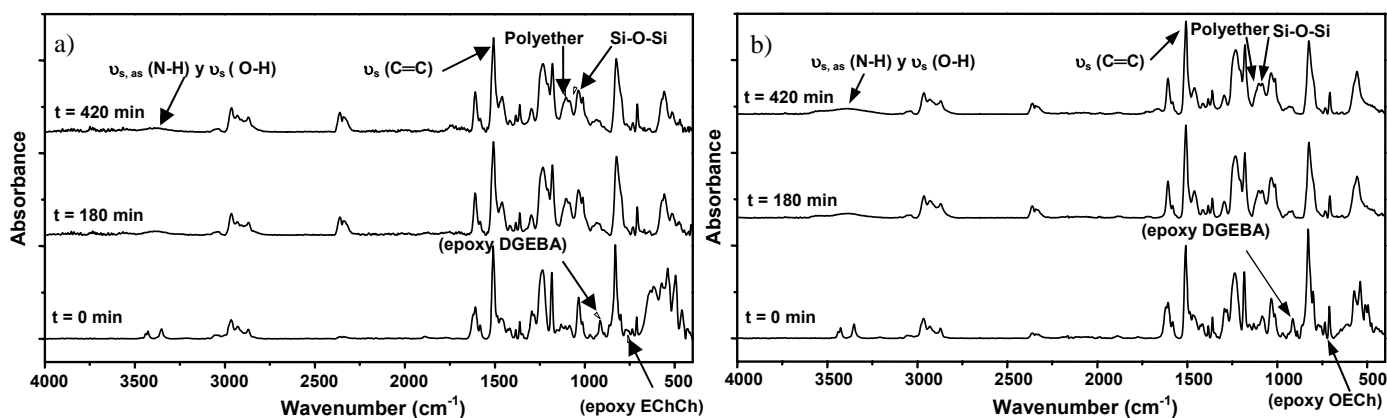


Figure 2. ATR-FTIR spectra obtained for samples with 2,5 wt % of a) EChCh and b) OECh.

UNDERSTANDING THE PHYSICS OF CONDUCTANCE SWITCHES

M. Morales-Masis and J.M. van Ruitenbeek

*Kamerlingh Onnes Laboratorium, Universiteit Leiden, PO Box 9504, 2300 RA Leiden,
The Netherlands*

[*morales@physics.leidenuniv.nl*](mailto:morales@physics.leidenuniv.nl)

With the ever decreasing size of electronic components, there is a continuous necessity to make ever smaller electronic switches. One of the approaches towards very small components lies in the use of solid electrolytes, which exhibit 'memristive' (memory resistive) properties.

In the correct configuration, these materials with highly mobile ions can form very small or even atomic contacts under the influence of an applied voltage. For example, the Ag₂S-based 'atomic switch' reported by Terabe et al. [1].

Using Ag₂S as the model material for such solid electrolyte devices, we have developed a method to grow Ag₂S thin films and to measure its memory resistive properties, in order to study the fundamental mechanism involved in resistance switching [2].

In different experiments, the Ag₂S thin films are contacted to electrodes: a Ag or Pt thin film as the bottom electrode and a Pt wire or Pt-coated AFM tip as the top electrode. Measurements at low bias voltages indicate semiconductor behavior, whereas they exhibit reproducible bipolar resistance switching at higher bias voltages (figure 1, left panel). In the fully bipolar conductance switching regime, the device shows in the high conductance state several multiples of quantum conductance (figure 1, right panel). We have found this conductance to be proportional to the applied bias voltage and to the size of the top electrode. By using a sharp, conductive AFM or STM tip, a few atoms contact can be achieved resulting in the observation of few multiples of the quantum conductance.

As a second approach to form atomic contacts with this solid electrolyte, we propose to use Ag₂S single crystalline whiskers. Under specific conditions, these whiskers are formed as a bi-product of our process to form Ag₂S thin films (figure 2).

By contacting and applying a voltage to these single crystalline wires, one should be able to directly observe material transport and deformation of the crystal due to Ag⁺-ion diffusion, in the transition from high to low resistance states.

These observations will help us to have a complete understanding of the mechanism of conductance switching and possibly allow the direct observation of the formation of a single atomic contact.

References:

- [1] K. Terabe, T. Hasegawa, T. Nakayama and M. Aono M, *Nature* **433** (2005) 47-50.
- [2] M. Morales-Masis, S.J. van der Molen, W.T. Fu, M.B. Hesselberth and J.M. van Ruitenbeek, *Nanotechnology* **20** (2009) 095710.

Figures:

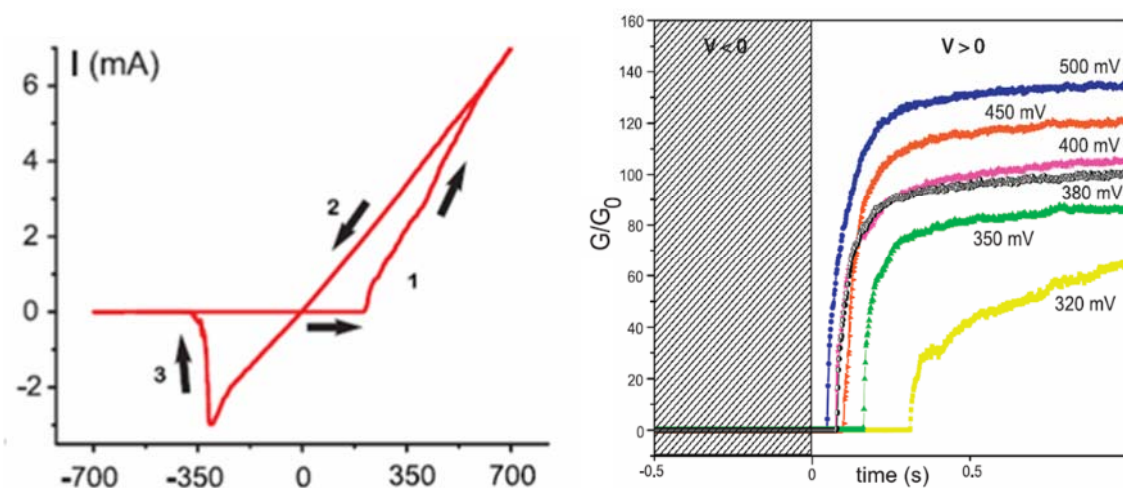


Figure 1 Left panel: IV characteristics of bipolar switching observed in Ag_2S thin films. The numbers 1 and 3 indicate the 'off' state (low conductance) and 2 indicates the 'on' state (high conductance). Right panel: Increase in the conductance as a function of time when different voltage steps are applied to the Ag_2S device.

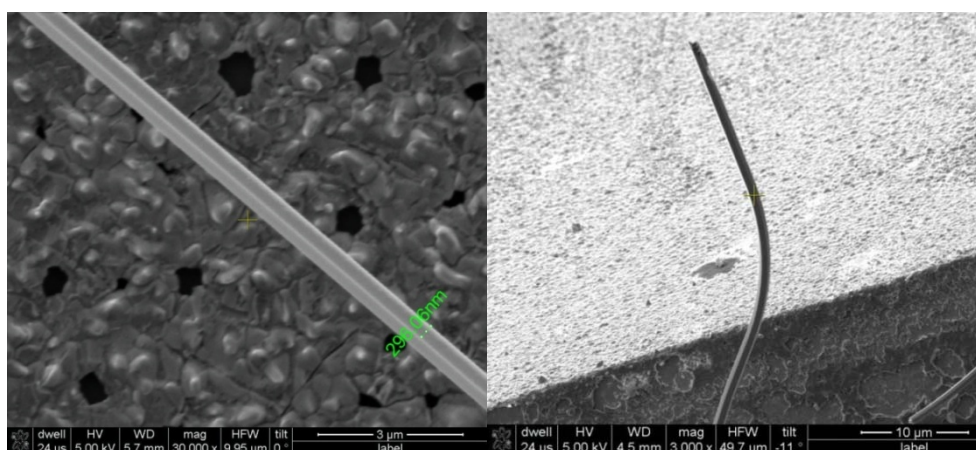


Figure 2 Single crystalline whiskers of Ag_2S . SEM images indicate the formation of wires with diameters in the range of 0.1 up to 1 μm and several microns long.

Fe₃O₄ nanoparticles-Loaded Cellulose Sponge: Novel system for the Arsenic removal from aqueous solution

D. Morillo, M. Avila, G. Perez M. Valiente

Grup de Tècniques de Separació, Universitat Autònoma de Barcelona, 08193 Bellaterra, Barcelona, Spain

Diego.Morillo@campus.uab.es

Magnetic properties provide certain nanoparticles, such as those of iron oxides, an interesting solution for separation purposes [1]. When a magnetic field is applied, the particles acquire a certain magnetization but, the long range order is lost when the field is removed. However, during magnetic separation particles interact with each other generating aggregates. To overcome this situation, we have developed the magnetite nanoparticles fixation on a sponge of cellulose which helps to decrease the aggregation state and increase the adsorption of pollutants from aqueous effluents. We have applied this system to the adsorption of arsenic, both arsenate and arsenite, from aqueous solutions.

Synthesis, characterization and application of magnetite nanoparticles to treat arsenic contaminated aqueous solution through a batch process were carried out. The experimental conditions effects over the arsenic adsorption capacity of magnetite nanoparticles are assessed. Magnetite nanoparticles have been synthesized by stocks solution of iron (III) and iron (II) in chloride media [2, 1]. Characterization was carried out by Transmission Electron Microscopy (TEM) determining particle size as shown in Fig.1a and X-Ray Diffraction (XRD) in order to certificate magnetite as the principal component of nanoparticles, Fig. 1b. Fixation of magnetite nanoparticles was performed over an Open-Celled Cellulose and Polyamide Sponge support (Forager Sponge, Dynaphore) using a spray of magnetite nanoparticles as present in Fig. 2a, 2b.

Observed adsorption capacity is higher for sponge systems than for magnetic nanoparticles, maintaining their overall nanoproperties and demonstrating that sponge system is a suitable solution for the aggregation problem on magnetic nanoparticles. A comparison with the adsorption of Arsenic by ferric ion loaded sponge [3] will be presented.

References:

- [1] A. Uheida, G. Salazar-Alvarez, E. Björkman, Y. Zhang, M. Muhammed, J. Colloid Interface Sci., **298**, (2006) 501-507.
- [2] A. Uheida, G. Salazar-Alvarez, E. Björkman, Y. Zhang, M. Muhammed, J. Colloid Interface Sci., **301** (2006) 402-408.
- [3] J.A. Muñoz, A. Gonzalo, M. Valiente, Environ. Sci. Technol., **26**, (2002) 3405-3411.

Figures:

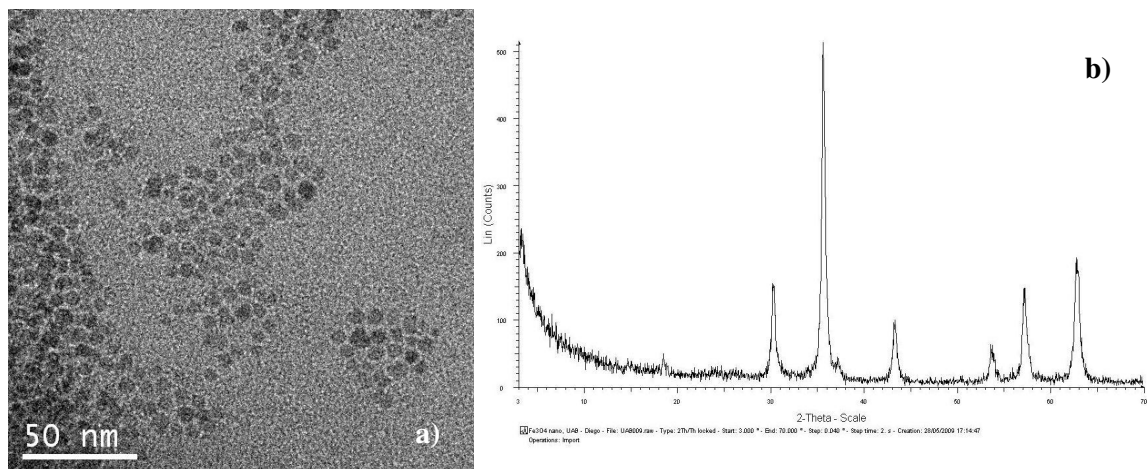


Fig 1. TEM images of Magnetite nanoparticles synthesized in this work and the distribution of size (a), X-ray diffractogram who shows the magnetite characteristics picks and its corresponding atomic planes (b)

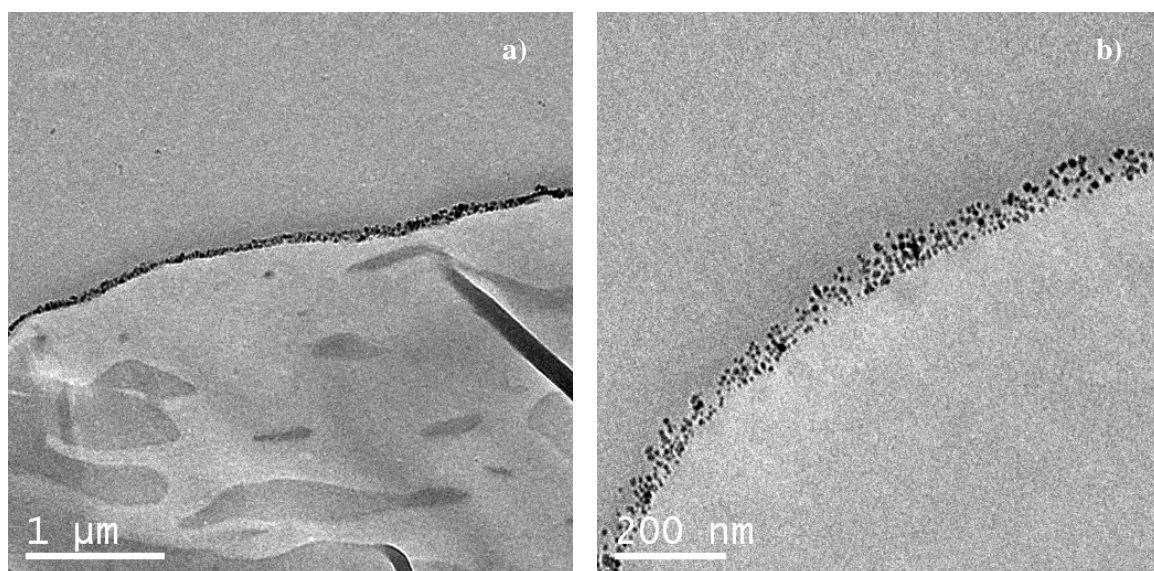


Fig. 2. TEM images of Magnetite nanoparticles loaded sponge (a, b).

COMPACT X-RAY SOURCES FOR NANOTECHNOLOGY

A. Mozelev

Small Scale Research and Production Company RADICAL

X-ray portable diffractometer for stress and strain measurement (XRD) permits the measurement of stress and strain in large objects. Residual can be measured in order to avoid faults, damages and accidents. The essential part of this arrangement is the source of X-ray radiation. Many current portable X-ray unit use different radioisotopes sources. Environmentalists consider isotopes to be dangerous. Now days the ecological purity requirement for the geophysical devices with radioisotopes sources stimulates researches of other kinds of sources. For this reason other sources of X-ray radiation represent an attractive alternative. Electron and ions acquire a high energy and produce X-rays with a relatively high efficiency by interaction with different materials. In this work, a principally new source using a radiation generator is proposed (1).

Preliminary calculations and mathematical simulation have revealed that an X-ray generator has advantages over the traditional radioisotope sources. The remote control of physical parameters (intensity, energy of gamma quants, etc.) makes it possible to use a gamma quant generator in various applications. A generator was designed for deep borehole with high temperatures and high pressure. It was necessary to have a small size, high power generator in order to produce high count rates. Several variants of vacuum tubes were evaluated. We constructed a unit with a tube D=90 mm.; kinetic energy of electron E=1 Mev.; D=70 mm., E=700 Kev.; D=60 mm., E=500 Kev.; D=45 mm., E=150 Kev. In the course of investigation a model generator was constructed. Studies with this unit revealed the more investigation to confirm our theoretical calculations. As a result of this work we made the following changes: diameter less than 70 mm; length less than 300 mm; weight less than 2 kg, electron source specification: kinetic energy 500 KeV; pulse duration 10 ns; impulse frequency 0.5 -- 50 Hz.

Our primary data collecting and processing software combined with the unique X-ray source allowed fast stress and strain analysis. Numerous stress/strain studies of high-pressure vessels, welded joints, elements of rockets and aircraft engines, parts of structures, mechanisms, etc. The XRD reliability in diagnostics of such objects. In order to obtain a high intensity of radiation and short pulse duration (10 ns) required the formulation of a new measuring method and special equipment. The generator required source of 24 V, 50 W. Using a new high - speed detector and X-ray generator can be usefuul in hydrology, geophysical assessment of potential sites for the disposal of high-level radioactive wastes investigations nanotechnology and rock density measure, etc. (2)

1. Mozelev A. High Voltage Discharge and Vacuum Insulation at the Minimissing Volume, Int. Symp. Electrical Discharge and Vacuum In sulation. Berkeley, California, 1996.
2. Mozelev A. et al. Probe for Radiologically Determing the Density of Rock In a Drilled Well, United States Paten Number 5,736,636. Date of Patent: Apr. 7, 1998.

In vitro mammalian cytotoxicological study of PAMAM dendrimers –towards quantitative structure activity relationships

Sourav Prasanna Mukerjee^{a,b}, Maria Davoren^{a,b}, Hugh J. Byrne^b

^aRadiation and Environmental Science Centre, Focas Research Institute, Dublin Institute of Technology, Kevin Street, Dublin 8, Ireland.

^bNanolab, Focas Research Institute, Dublin Institute of Technology, Kevin Street, Dublin 8, Ireland.

sourav.mukherjee@dit.ie

The *in vitro* cytotoxic response of mammalian dermal and colon cell-lines to full generation dendritic polyamidoamine (PAMAM) nanoparticles was investigated. Given the wide range of proposed applications for PAMAM dendrimers, such as drug ^[1], DNA ^[2] and siRNA ^[3] delivery systems, MRI probes ^[4] etc., it is important to know whether the particles themselves can cause any health hazards. Dendrimers of generations G4, G5, G6 were chosen for this study. Cytotoxicity parameters, including metabolic, lysosomal and mitochondrial activity, were evaluated after 24 h exposure. In addition, long term toxicity was evaluated by means of the clonogenic assay. G4 dendrimers were found to be the least toxic, G6 the most. Physicochemical characterization in terms of particle size and zeta potential in all media was performed. A linear correlation was found between the change in zeta potential of the dendrimers in media and their surface area measured in phosphate buffer saline. The interaction of the dendrimer nanoparticles with 5% FBS supplemented media was also studied using UV/visible absorption spectroscopy. The data suggest significant interaction of nanoparticles with FBS protein and media components which increases with the generation of the dendrimers. The toxic response also correlated linearly with the zeta potential and notably the change in zeta potential of the dendrimers in the media, further pointing towards indirect or secondary toxic mechanisms. With the increasing generation of PAMAM dendrimers more intra-cellular reactive oxygen species production was observed. Preliminary data also suggest a structure dependant apoptotic response of the cells. In all cases a trend of generation dependant toxic response and interaction of the dendrimers with the cell culture media is observed which may lay the basis of structure activity relationships.

References:

1. C. Yiyun, X. Tongwen, F. Rongqiang, European Journal of Medicinal Chemistry, 40, 1390 (2005).
2. M. Guillot-Nieckowski, S. Eisler, F. Diederich, New J. Chem., 31, 1111 (2007).

3. J. Zhou, J. Wu, N. Hafdi, J. P. Behr, P. Erbacher, L. Peng, *Chemical communications* (Cambridge, England), 2362 (2006).
4. S.D. Swanson, J.F. Kukowska-Latallo, A.K. Patri, C. Chen, S. Ge, Z. Cao, A. Kotlyar, A.T. East, J.R. Baker, *International journal of nanomedicine*, 3, 201 (2008).

Raman Study of Electronic Properties of Propylamin-functionalized Single-walled Carbon Nanotubes

Matthias Müller¹, Janina Maultzsch¹, Zois Syrgiannis^{2,3}, Frank Hauke^{2,3}, Andreas Hirsch^{2,3}, Christian Thomsen¹

¹Technische Universität Berlin, Hardenbergstr. 36, 10623 Berlin, Germany

²Zentralinstitut für Neue Materialien und Prozesstechnik, Universität Erlangen-Nürnberg, Dr.-Mack-Str. 81, 90762 Fürth, Germany

³Institut für Organische Chemie, Universität Erlangen-Nürnberg, Henkestr. 42, 91054 Erlangen, Germany

mueller@physik.tu-berlin.de

Covalent sidewall functionalization of carbon nanotubes has become a keystone to a variety of nanotube applications and therefore the chemical reaction sequences have been reviewed in many related articles. To attack the tubes framework, quite harsh reaction conditions are necessary [1]. A major task of synthesis and characterization is a well-defined increase of the solubility of carbon nanotubes in certain media.

The understanding of how a functional group influences the tube framework and its electronic structure is an important topic on the road to versatile application. Raman spectroscopy is a very powerful and non-destructive technique for both the investigation of structural changes in the tube lattice and changes of the electronic structure of nanotubes [2].

In our work a direct nucleophilic addition reaction based on *in situ* generated primary amides which are used for attaching *n*-propylamine addends to the sidewalls of single-walled carbon nanotubes (SWCNTs) is introduced. A reoxidation by air of a negatively charged $(n\text{PrNH})_n\text{-SWCNT}^{n-}$ intermediate leads to a covalently bound amino functionality. From the chemist's view this causes a drastic increase of the solubility of the SWCNT-derivative in organic solvents [3]. The influence of the amino functionalities on the electronic structure of the nanotubes is investigated by means of resonant Raman scattering. From the extracted resonance profiles of the radial breathing modes (RBMs) the chiral indices of the corresponding tubes are assigned following the procedure of Ref. [4]. We observe significant changes in the transition energies and the widths of the resonance windows due to chemical modification of SWCNTs. The relative Raman intensities of the decorated samples indicate a diameter dependence of the reactivity as it has been observed for other moieties [5]. From analysis of the defect-induced *D* mode in combination with thermogravimetric analysis (TGA) we observe a considerable degree of functionalization accompanied by an almost unharmed tube structure, which ensures that the observed effects are mainly driven by changes of the electronic structure. We discuss our findings in the context of a possible selectivity of certain tube species to the chemical reaction.

References:

[1] A. Hirsch, O. Vostrowsky, *Top Curr Chem* **245**, 193–237 (2005).

[2] S. Reich, C. Thomsen, J. Maultzsch, *Carbon Nanotubes*, Wiley-VCH, Weinheim (2004).

- [3] Z. Syrgiannis, F. Hauke, J. Röhl, M. Hundhausen, R. Graupner, Y. Elemen, A. Hirsch, Eur. J. Org. Chem. 2544-2550 (2008).
- [4] J. Maultzsch, H. Telg, S. Reich, C. Thomsen, Phys. Rev. B **72**, 205438 (2005).
- [5] M. Müller, J. Maultzsch, D. Wunderlich, A. Hirsch, C. Thomsen, phys. stat. sol.(b) **245** No. 10, 1957 (2008).

Figures:

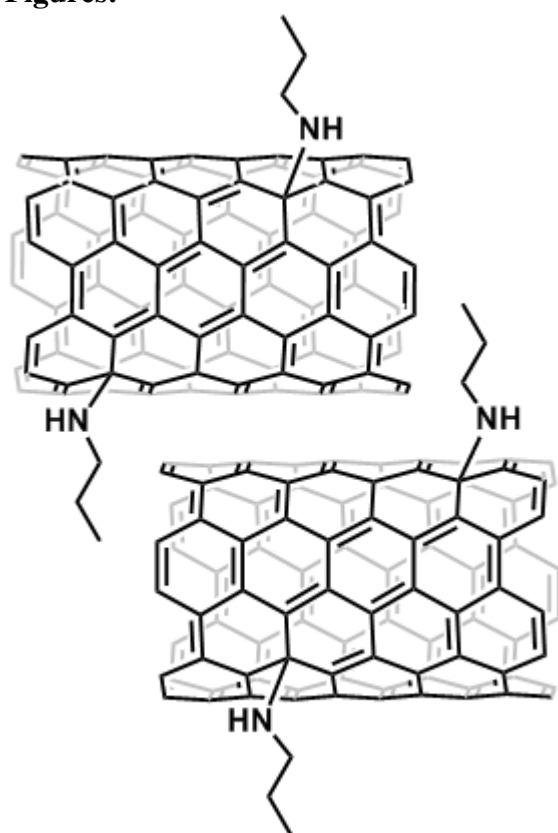


Figure 1: (nPrNH)_n-SWCNT

APPLICATION OF CONVERGENT TECHNOLOGIES (NANO-BIO-INFO-COGNO) IN HEALTH: THE IBERO-NBIC NETWORK

A. Pazos¹, F. Martin-Sanchez², J. Dorado¹, C.R. Munteanu¹, I. Hermosilla², V. López-Alonso²,
G. López-Campos²

¹University of A Coruña (UDC), Campus de Elviña, S/N 15071, A Coruña, Spain

²Carlos III Health Institute (ISCIII), Ctra. Majadahonda a Pozuelo, Km. 2, 28220
Majadahonda, Madrid, Spain

muntisa@gmail.com

In the last decades, several technologies with sound scientific basis have reached a high degree of development and have a strong impact in various areas of the society. These fields are: nanotechnology, biotechnology, information technologies and cognitive technologies (NBIC). The convergence between them is expected to produce innovative advances in technologies that may contribute to the improvement of citizen's health and welfare. The Ibero-American scientific and technological communities might face important challenges but also opportunities for innovation and development.

Healthcare is one of the fields where this convergence is already taking place. However, NBIC convergence is still growing in the Ibero-American region and new research projects and collaborative networks are being funded in order to facilitate the interaction between groups that work within the different fields or within their intersections (Nano-Bio, Nano-Info, Nano-Cogno).

The Ibero-American network (Ibero-NBIC) has recently been funded by the CYTED (Ibero-American Program for Science and Development) for the period 2009-2012. Ibero-NBIC has eleven nodes from seven countries (Spain, Portugal, Venezuela, Brazil, Uruguay, Argentina and Chile) with complementary expertise in all of the four areas. The network is coordinated by the University of A Coruña (Spain). This project aims to gather a broad community of scientists from the Ibero-American region that know, develop and assess applications of Convergent Technologies in Healthcare from an integrative and multidisciplinary perspective. The network will promote synergies among countries, disciplines and methods, and it will pay special attention to the related ethical, legal and social aspects. Training and mobility of researchers and knowledge management in the field are also issues to be addressed by this project. Finally, specific network groups will model concrete scenarios of application in healthcare (colorectal cancer diagnosis, therapy and prevention with specific nanoparticles) that will be used in prospective studies.

In summary, the activity of the Ibero-NBIC network aims to contribute to the CYTED objectives through the elaboration of a research Roadmap for Nanomedicine and Convergent Technologies in Health, taking into account the specifics of the region and the state of play in other parts of the world (EU, USA, Japan). It is expected that this exercise will generate new programs and grants and give a better view of the benefits of these research avenues and their consequences on society. This program will be the key to exposing the young scientists to the convergence of these technologies at the very beginning of their professional careers, giving them a broader vision on the scientific basis and expected impact on health and society.

NEW NANOSIZED CATALYTIC SYSTEM FOR BIGINELLI REACTION

D. Prodius^a, F. Macaev^a, V. Mereacre^a, S. Shova^{b,e}, Yu. Lutsenco^{a,b}, E. Styngach^a, P. Ruiz^c, J. Lipkowski^d, Yu. A. Simonov^e, C. Turta^a and D.N. Muraviev^c.

^a*Institute of Chemistry, Academy of Sciences of Moldova, Chisinau, Moldova*

^b*State University of Moldova, Department of Chemistry, Chisinau, Moldova*

^c*Analytical Chemistry Division, Department of Chemistry, Autonomous University of Barcelona, Barcelona, Spain*

^d*Institute of Physical Chemistry, Polish Academy of Sciences, Warszawa, Poland*

^e*Institute of Applied Physics, Academy of Sciences of Moldova, Chisinau, Moldova*

Dimitri.Muraviev@uab.es

During the last decade, the multicomponent reactions have become increasingly important in the organic and medicinal chemistry as efficient and low-cost tool for the combinatorial synthesis. The Biginelli reaction is typically a Lewis acid-catalyzed three-component cyclocondensation of an aldehyde, a β -ketoester and urea, which results in the formation of various dihydropyrimidones (see Scheme 1). These compounds are widely used in the pharmaceutical industry as calcium channel blockers, antihypertensive agents, mitotic kinase inhibitors and antiviral agents among applications.

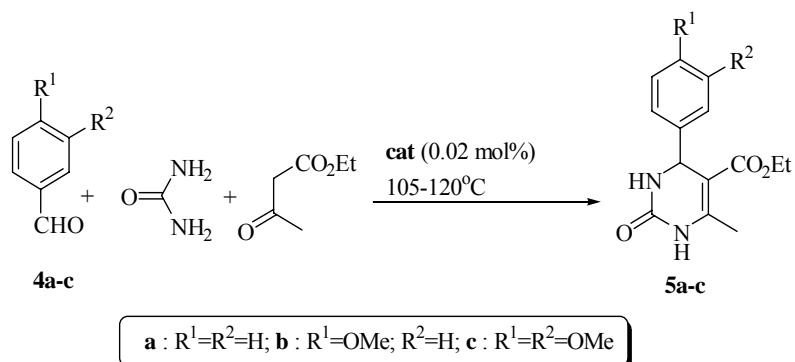
In this presentation we report the results obtained by the synthesis and characterization of μ_3 -oxo-bridged clusters containing $\{\text{Fe}_2\text{CuO}\}$ core as precursors for the preparation of more efficient nanosized catalytic systems for the Biginelli reactions operating at a lower catalyst concentration. The monodisperse nanoparticles of iron and copper oxides soluble in the organic solvents were obtained by the thermal decomposition of clusters $[\text{Fe}_2\text{CuO}(\text{CCl}_3\text{COO})_6(\text{THF})_3]$ and $[\text{Fe}_2\text{CuO}(\text{CCl}_3\text{COO})_6(4\text{-DMAP})_3]$ in 1-hexadecylamine (HDA) under argon atmosphere (THF = tetrahydrofuran, and 4-DMAP = 4-dimethylaminopyridine).

The TEM analysis of the decomposition products showed that the best results were obtained in the case of $[\text{Fe}_2\text{CuO}(\text{CCl}_3\text{COO})_6(4\text{-DMAP})_3]$ decomposition. The nanoparticles of the resulting product are round shaped and are homogeneously distributed by sizes and with particle diameters ranging from 4 to 7 nm (see Fig. 1). As follows from the particle distribution histogram, an average particle diameter is about 5.65 nm.

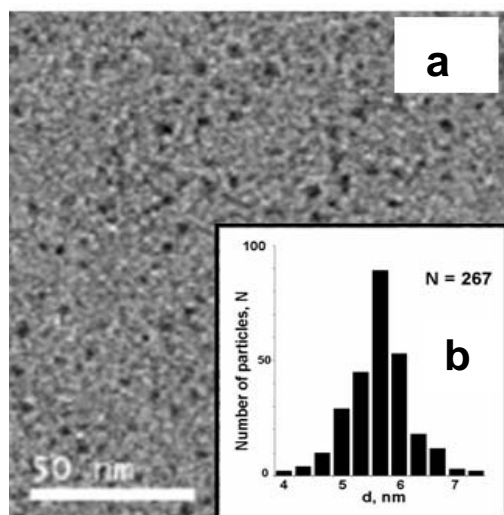
We examined the Biginelli solvent-free reaction of ethyl acetoacetate with aromatic aldehydes and urea in the presence of $\gamma\text{-Fe}_2\text{O}_3\text{-CuO}$ catalyst nanoparticles at 105-120°C (Scheme 1). The reaction led to the formation of 3,4-dihydropyrimidin-2-(1*H*)-ones **5a-c** which were formed at different yields. It has been shown that the nature of the catalyst and that of the initial aldehyde significantly influence the reaction rate and the product yield. Under these novel conditions, the reaction time was significantly shortened from 18 h of the classical Biginelli method to 2 h, and the concentration of catalyst was decreased by more than 30 times: from 0.6–5.0 mol% to 0.02 mol%.

Acknowledgements: The authors acknowledge INTAS programme (Project No.05-1000008-7834), CSSDT (08.819.05.01F), Grant 09.836.05.2A and Ministerio de Ciencia e Innovación of Spain (Project MAT 2006-03745) for the financial support of this work.

Figures:



Scheme 1. Schematics of Biginelli reaction.

Fig. 1. TEM image of $\gamma\text{-Fe}_2\text{O}_3/\text{CuO}$ (**a**) and particle sizes distribution histogram (**b**).

STUDY OF THE SUPERCAPACITIVE BEHAVIOR OF CARBON-NANOTUBES BASED ELECTRODES PREPARED BY CVD AND PECVD

Toygan Mutlu, Burak Caglar, Eric Jover, Roger Amade, Enric Bertran
FEMAN Group, IN2UB, Department of Applied Physics and Optics, Universitat de Barcelona,
c/Martí i Franquès 1, E-08028, Barcelona
ebertran@ub.edu

Supercapacitors store electrical energy through double-layer charging and/or faradaic processes. They fill the gap between batteries (low specific power and high specific energy) and conventional capacitors (high specific power and low specific energy), i.e. they have a specific power as high as conventional capacitors and a specific energy close to that of batteries [1].

Due to their outstanding properties (mechanical, electrical, thermal...), carbon nanotubes (CNTs) have been used in an increasing range of applications. In fact, applications related to supercapacitors have already been reported [2-4]. However, the influence of the morphological (CNTs length, diameter and alignment) and functionalization properties of the CNTs has not been studied yet.

In this work, we have prepared CNTs by means of Chemical Vapour Deposition (CVD) and Plasma Enhanced Chemical Vapour Deposition (PECVD) in order to control their alignment (see Figure 1). Other parameters such as catalyst thickness layer, temperature, deposition time have been optimised to tune CNTs length and diameter. Obtained electrodes were further modified to enhance their response by means of plasma techniques. As a dielectric layer of the supercapacitor MnO_2 was added to the surface of the CNTs.

Obtained electrodes were characterized by means of Cyclic Voltametry, Chronopotentiometry and SEM measurements. The two electrochemical methods permit to evaluate the efficiency of the developed electrodes and the SEM results are used to assess the morphology of the CNTs. In this way, we will be able to correlate the CNTs characteristics with the efficiency of the electrodes.

References:

- [1] Peng, C., Zhang, S., Jewell, D., Chen, G.Z., Progress in Natural Science, **18** (2008) 777-788.
- [2] Chen, J.H., Li, W.Z., Wang, D.Z., Yang, S.X., Wen, J.G., Ren, Z.F., Carbon, **40** (2002) 1193-1197.
- [3] Li, C.S., Wang, D.Z., Liang, T.X., Wang, X.F., Ji, L., Materials Letters, **58** (2004) 3774-3777.
- [4] Lee, C.Y., Tsai, H.M., Chuang, H.J., Li, S.Y., Lin, P., Tseng, T.Y., Journal of the Electrochemical Society, **152** (2005) A716-A720.

Figures:

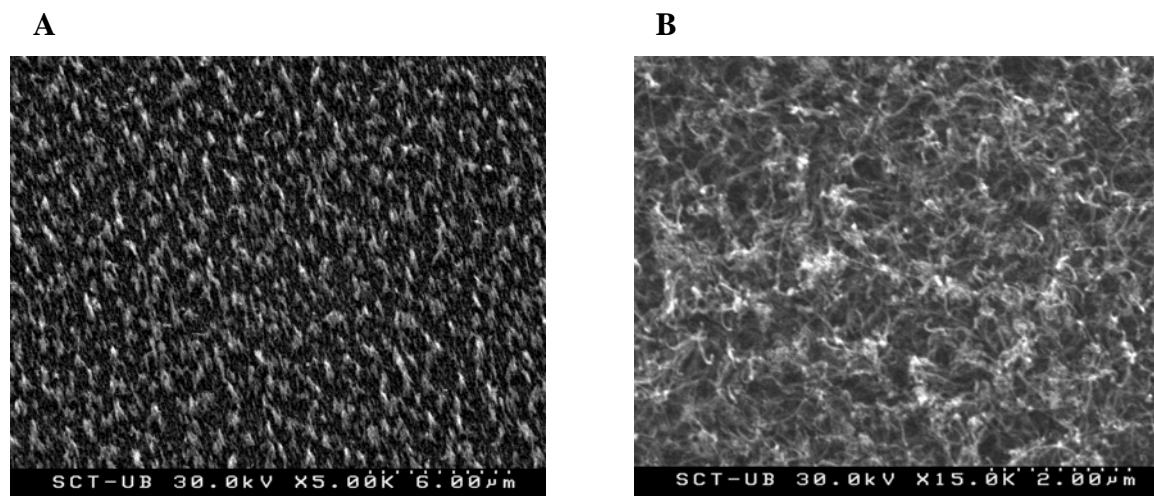


Figure 1. A: Electrode based on aligned CNTs grown by PECVD. B: Electrode based on CNTs grown by CVD.

EXPERIMENTS REGARDING THE ROLE OF MAGNETIC/NON-MAGNETIC STIRRING IN THE PROCESS OF FERROPHASE PREPARATION FOR STABLE MAGNETIC FLUIDS

Claudia Nadejde¹, D. Creanga¹, L. Almasy^{2,3}, M. Ursache-Oprisan¹, N. Apetroaie¹, V. Badescu⁴

¹*“Al.I. Cuza” University, 11A Carol I Blvd., 700506, Iasi, Romania*

²*Laboratory for Neutron Scattering, PSI and ETH Zürich, CH-5232 Villigen, Switzerland*

³*Adolphe Merkle Institute, University of Fribourg, CH-1700 Fribourg, Switzerland*

⁴*Institute of Technical Physics, 700506, Iasi, Romania*

dorinacreanga@yahoo.com

This study is focused on the optimization of oil-based magnetic fluid preparation. Soft magnetic materials in the form of colloidal suspensions of iron oxides have been prepared based on magnetite nanoparticles and hydrocarbons aiming to obtain raw materials suitable for wide range technical uses, as well as for peculiar biological applications. The ferrophase was dispersed in kerosene and sterically stabilized with oleic acid surfactant, magnetic and non magnetic stirring being applied in the frame of several preparation protocols.

Small particle size, as well as narrow size distribution represent a “sine qua non” condition of magnetic fluid utilization [1-2]. The stability of magnetic colloidal suspensions is strongly dependent on the solid phase granularity, as summarized by Rosensweig [3]. Stable magnetic suspensions can be produced consisting in magnetite nanoparticles coated with surfactant layer, when the diameter of the ferrophase core is lower than about 10 nm. Several synthesis methods of preparation and stabilization of nanoparticles of appropriate size have been developed, the most classical methods being the co-precipitation of iron salts, and the mechanical grinding of larger, micron sized particles. Size reduction by “wet” milling allows one to obtain small and rather uniform ferrophase particles [4-6], however the long time duration of this procedure may appear as a significant disadvantage.

Ferrophase particles were synthesized by the Massart method [7], consisting in the co-precipitation of ferric and ferrous oxides in alkali medium - magnetite and possibly maghemite being precipitated from auto-catalysis reactions between ferric and ferrous salts, namely $\text{FeCl}_3 \cdot 6\text{H}_2\text{O}$ and $\text{FeSO}_4 \cdot 7\text{H}_2\text{O}$. Magnetic stirring was applied to favor chemical processes during ferrophase precipitation and subsequent coating. After the solid phase separation by filtration and rinsing with distilled water, the water traces were removed by repeated rinsing with acetone and ethanol. Ferrophase particles were coated with oleic acid at high temperature (over 80°C) in hexane under continuous, vigorous stirring kerosene being further added as carrier liquid after hexane vaporization. Magnetic stirring was applied to favor chemical processes during ferrophase precipitation and respectively ferrophase coating for equal durations of sixty minutes (S1 sample).

Second type of nanoparticles was obtained by non magnetic processing (wet milling) of micron size magnetite particles of industrial provenance at room temperature, in the presence of oleic acid and kerosene (for thousands of hours). Consequently, two types of samples resulted:

Sample	Stirring during ferrophase precipitation	Stirring during ferrophase dispersion
S1	Magnetic	Magnetic
S2	-	Non-magnetic

Structural properties of these magnetic fluids were investigated by transmission electron microscopy (TEM – Fig. 1), atomic force microscopy (AFM – Fig. 2), X-ray diffraction and small-angle neutron scattering and magnetization measurements (Fig. 3). The influences of the two types of mixing (magnetic and non-magnetic) on the microstructural and magnetic features

are compared and discussed. Ferrophase particles with an average diameter of about 10 nm were identified as preponderant in the prepared magnetic fluid samples, the narrowest histogram being revealed in the case of totally non-magnetic stirring (S2). Rare aggregates having quasi-spherical shape were also observed. Also, it was shown that short chains of particles were predominant among the particle aggregates.

These results showed the feasibility of both routes of preparing magnetite nanoparticles of comparable sizes and size distributions. Under the applied conditions, wet milling resulted in a ferrofluid batch with better granularity – smaller average physical diameter, smaller crystallite size and lower frequency of particle aggregates – evident advantages overrunning the disadvantage of long time processing. Further improvement of preparation protocol is planned to include combined methods of final fluid extraction from the bulk sample by magnetic filtration and controlled concentration in order to optimize the practical procedure. Variations in certain parameters of preparation (e.g. milling time, liquid medium) will be explored aiming to control the properties and quality of the final product.

References:

- [1] S. Mornet, S. Vasseur, F. Grasset, E. Duguet, *J. Mater. Chem.*, 14 (2004) 2161
- [2] M. Zborovski, et al., *J. Magn. Magn. Mater.*, 194 (1999) 224
- [3] R.E. Rosensweig, *Ferrohydrodynamics*, Cambridge University Press, Cambridge, (1985)
- [4] C. Cotae, D.E. Creanga, *Balkan Phys. Lett.*, 4 (1998) 281,
- [5] D.E. Creanga, C. Cotae, *Ind. J. Pure Appl. Phys.*, 34 (1996) 957
- [6] D.E. Creanga, Gh. Calugaru, *J. Magn. Magn. Mater.* 289 (2005) 81
- [7] R. Massart, *IEEE Trans. Magn.*, MAG-17 (1981) 1247

Figures:

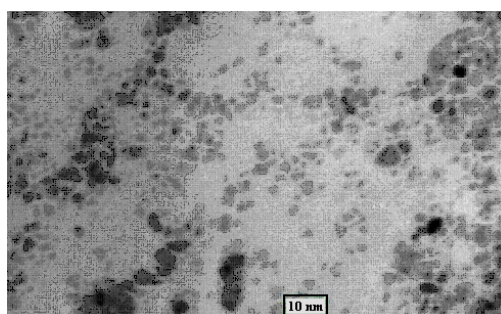


Fig. 1. Ferrophase particles revealed by TEM investigation

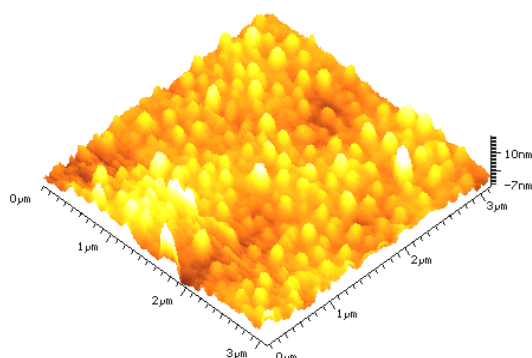


Fig. 2. AFM 3-D image recorded for S2 magnetic fluid sample (3x3 nm)

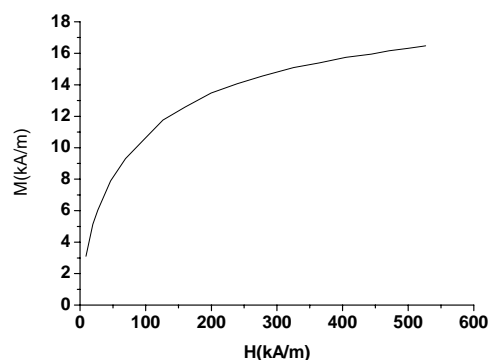


Fig. 3. Magnetization curve of magnetic fluid

Carbon Nanotube Reinforced Rod-Rigid Polyimide Composite

Minoo Naebe, Tong Lin, Xungai Wang

Centre for Material and Fibre Innovation, Deakin University, VIC3217, Australia
minoo.naebe@deakin.edu.au

Rigid rod-like polymers have excellent thermal stability, chemical resistance, mechanical strength and electric insulation because of the highly rigid backbone and highly ordered molecular arrangement [1]. Among the rigid rod-like polymers that have been developed the rigid rod-like polyimides are most common used ones because of the excellent properties-price-processability balance [2]. In electronic industry, the polyimide has been broadly used for interlayer insulation and alignment for liquid crystal displays. The aromatic polyimide has also been known as one of the most important super engineering plastics. Poly (*p*-phenylene biphenyltetracarboximide (BPDA-PDA) is the most widely used rigid rod-like polyimide, especially in microelectronic and aerospace industries. BPDA-PDA has many unique features such as low thermal expansion coefficient (CTE) and high modulus.

It is known that the mechanical properties of a polymer can be improved by incorporation of nano-sized fillers into the polymer matrix. The most common nanofillers for reinforcement are nanoparticles nanotubes/fibres, and nanoplatelets (e.g. clay). The extent of improvement was highly depended on the dimension of fillers, their dispersion and interaction with the hosting polymer matrix. Most work in the polyimide composite used clay as fillers to improve the gas barrier and thermal expansion properties as well as mechanical strength of film-based samples [3-4]. There are very limited works devoted to carbon nanotube-based rod-like polyimide composite. Carbon nanotubes (CNTs) have been incorporated in various polymers to improve mechanical, electronic and thermal properties. The presence of CNTs in rigid rod-like polymer could alter the molecular orientation lead to changes in mechanical and thermal properties, which has not been evident to date.

In this study, we report on how CNTs influence the morphology, mechanical strength and thermal stability of a polyimide; BPDA-PDA. It has been observed that the presence of 1 wt% multi-walled carbon nanotubes (MWNT) in the polymer matrix can considerably improve the tensile strength yet decrease the elongation at break (Figure 1). However, higher MWNT composition did not further increase the tensile strength. The presence of nanotubes also led to increase in the thermal stability and shrinkage properties (Table 1).

References:

- [1] Ree M, Park Y-H, Kim K, Kim SI, Cho CK, and Park CE. *Polymer*, **8** (1997) 6333.
- [2] Hergenrother PM, Watson KA, Smith JG, Connell JW, and Yokota R. *Polymer* **43**(2002) 5077.
- [3] Herminghaus S, Boese D, Yoon DY, and Smith BA. *Applied Physics Letters* **59** (1991)1043.

[4] Yano K, Usuki A, and Okada A. Journal of Polymer Science A:Polymer Chemistry 35 (1997) 2289.

Figures:

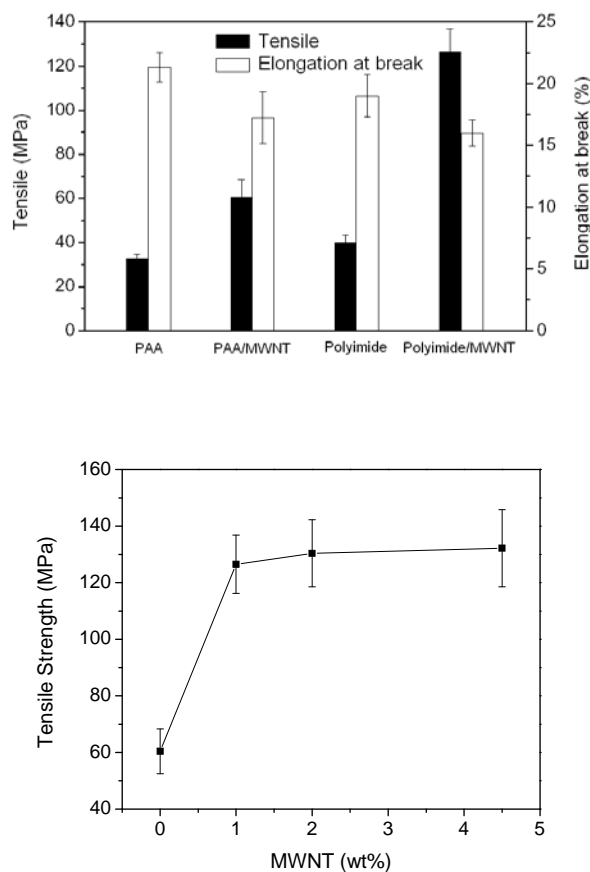


Figure 1: (top) Tensile strength and elongation at break of PAA and BPDA-PDA polyimide films with and without containing MWNT (1.0wt%), (bottom) Tensile strength of BPDA-PDA containing different composition of MWNT.

Table 1: Data for onsets and peaks of weight loss, T_g and CTE values (below T_g)

Samples	1st Peak		2nd Peak		3rd Peak		T_g (°C)	CTE (10^{-6}cm^{-1})
	Onset (°C)	Peak (°C)	Onset (°C)	Peak (°C)	Onset (°C)	Peak(°C)		
PAA	139	173	278	367	475	616	157	-584
Polyimide	100	165	394	417	475	619	340	-224
MWNT/PAA	139	170	278	309	520	615	158	-837
MWNT/polyimide	100	135	533	623	-----	-----	333	-391

A Comparative Study of Metal Incorporated (Ag, Au and Cu) Titania as Antibacterial System

Manaswita Nag¹, Ch. Subbalakshmi² and Sunkara V Manorama¹

¹Nanomaterials Laboratory, Indian Institute of Chemical Technology, Hyderabad 500607, India

²Centre for Cellular and Molecular Biology, Uppal Road, Hyderabad 500007, India
manorama@iict.res.in

The metallic nanoparticles, such as silver, copper and gold are known to have antimicrobial properties and are potential alternative systems for water and air purification.^{1,2} The functionality of nanoparticles can be improved by combining a wide range of materials such as, metal, semiconductors, polymers etc.³ The resulting nanocomposites, generally exhibit high activity, low toxicity, selectivity, long lasting action period, easy handling, chemical stability and thermal resistance compared to organic agents which can be easily scaled-up for industrial applications. Owing to all these advantages, these supported nanoparticles can be used in a variety of public sectors and for domestic purposes.^{4,5}

The present work is a comparative study of metal loaded (Ag, Au and Cu) titania as antibacterial system. Although the antibacterial activity of silver nanoparticles is known, Au and Cu are less studied in this regard. Earlier we have reported a Ag-TiO₂-Polymer antibacterial system.⁶ In line with our previous study here we have explored antibacterial activity of metals other than silver. In the present study we have adopted a simple and convenient method to synthesize linker-free metal/TiO₂ composite nanoparticles via *in situ* photoreduction of metal salts on the surface of TiO₂ nanoparticles. The materials are characterized by XRD, TEM, UV-DRS, Raman and XPS analysis. The amount of metal in the samples are determined by Scanning Electron Microscopy (SEM) and Energy Dispersive X-ray Analysis (EDAX).

The metal-doped titania (M-TiO₂) particles are demonstrated to be useful and effective in antibacterial applications and present a reasonable alternative for the development of new antibacterial agents. Both solution and agar-plate studies conclude that pure titania had no antibacterial effect and the metal-doped samples are effective. The antimicrobial activities of the synthesized M-TiO₂ nanocomposite materials are assayed under aerobic conditions.⁷ Microbial growth was determined by the increase in (optical density at $\lambda = 600$ nm) OD₆₀₀ by UltraViolet (UV) absorption studies after incubation of the samples. The M-TiO₂ nanocomposites showed almost complete killing of bacterial colonies for both the Gram positive and Gram negative bacteria. All the M-TiO₂ samples showed appreciable antibacterial effect compared to standard antibiotic Gentamycin.

Conclusions

The major contribution of the present study is as follows:

1. The present work reports the synthesis, characterization and effective use of metal deposited titania nanoparticles as antibacterial system.
2. Metal-doped titania nanoparticles are synthesized via a photodeposition technique. The synthesis process involves the photocatalytic activity of the support titania only.
3. These nanocomposites are characterized by XRD, Raman, TEM, UVDRS, SEM-EDAX and XPS. XRD shows presence of metallic Au however no peaks for Ag or Cu are observed. The presence of all metals (Ag, Au and Cu) is confirmed unambiguously by SEM-EDAX and XPS.

4. Metal-doped titania nanoparticles with metal doping concentrations from 0.1 to 0.3 atom% are studied against both Gram positive and Gram negative bacteria in order to gain an understanding of their antibacterial properties.
5. Both solution and agar-plate studies conclude that pure titania had no antibacterial effect and the metal-doped samples are effective as antibacterial agents. It is observed that with concentrations as low as 10 mg/mL of the Ag-TiO₂ nanocomposite samples are active. However the Cu-TiO₂ and Au-TiO₂ show activity at 15 mg/mL and ~ 20 mg/mL respectively.

The studies prove that these metal-titania nanocomposites are a reasonable alternative for the development of new antibacterial agents.

References:

- [1] Acharya, V.; Prabha, C. R.; Narayanamurthy, C.; *Biomaterials*, **25** (2004) 4555.
- [2] Cioffi, N.; Ditaranto, N.; Torsi, L.; Picca, R. A.; De Giglio, E.; Sabbatini, L.; Novello, L.; Tantillo, G.; Bleve-Zacheo, T.; Zambonin, P. G.; *Anal Bioanal Chem.*, **382** (2005) 1912.
- [3] Hornebecq, V.; Antonietti, M.; Cardinal, T.; Delapierre, M. T. *Chem. Mater.*, **15** (2003) 1993.
- [4] Kim, Y. H.; Lee, D. K.; Cha, H. G.; Kim, C. W. and Kang, Y. S.; *J. Phys. Chem. C*, **111** (2007) 3629.
- [5] Jana, N. R.; Gearheart, L.; Murphy, C. J. *J. Phys. Chem. B*, **105** (2001) 4065.
- [6] Sher Shah, M. S. A.; Nag, M.; Kalagara, T.; Singh, S.; Manorama, S. V. *Chem. Mater.*, **20** (2008) 2455.
- [7] Sitaram, N.; Subbalakshmi, C.; Krishnakumari, V. and Nagaraj, R. *FEBS Letters*, **400** (1997) 289.

Figures:

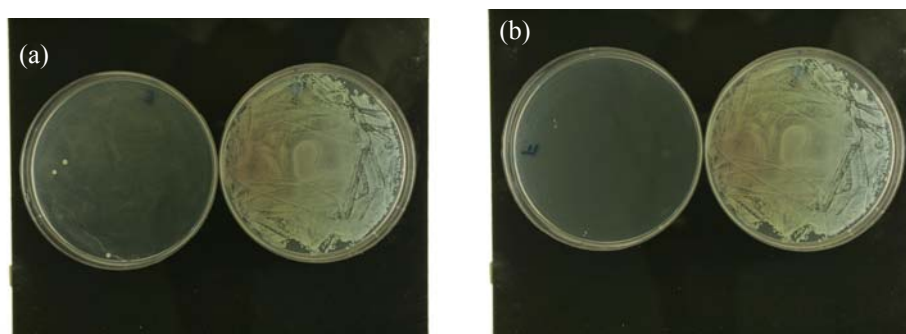


Figure. Visual image of the bacterial culture in presence of (a) synthesized Cu-TiO₂ compared to (b) standard antibiotic (Gentamycin) for *P. aeruginosa* (Gram negative bacteria).

Design of High-speed low power Reversible Logic BCD Adder Using HNG gate

A.Nageswararao
Dept.of ECE, RMK engineering college
Anna University, India
naga.alvaru@gmail.com

Prof.D.Rukmani Devi
Dept.of ECE, RMK engineering college
Anna University, India
rdrukmani319@gmail.com

Abstract - Reversibility plays a fundamental role when computations with minimal energy dissipation are considered. In recent years, reversible logic has emerged as one of the most important approaches for power optimization with its application in low power CMOS, optical information processing, quantum computing and nanotechnology. This research proposes a new implementation of Binary Coded Decimal (BCD) adder in reversible logic. The design reduces the number of gate operations compared to the existing BCD adder reversible logic implementations. So, this design gives rise to an implementation with a reduced area and delay. We can use it to construct more complex systems in nanotechnology.

Keywords: BCD adder, decimal arithmetic, reversible logic, garbage output, HNG gate.

I. INTRODUCTION

Energy loss during computation is an important consideration in low power digital design. Landauer's principle states that a heat equivalent to $kT \ln 2$ is generated for every bit of information lost, where 'k' is the Boltzmann's constant and 'T' is the temperature [1]. At room temperature, though the amount of heat generated may be small it cannot be neglected for low power designs. The amount of energy dissipated in a system bears a direct relationship to the number of bits erased during computation. Bennett showed that energy dissipation would not occur if the computations were carried out using reversible circuits [2] since these circuits do not lose information. A reversible logic gate is an n-input, n-output (denoted as n*n) device that maps each possible input pattern to a unique output pattern. There is a significant difference in the synthesis of logic circuits using conventional gates and reversible gates. While constructing reversible circuits with the help of reversible gates fan-out of each output must be 1 without feedback loops. As the number of inputs and outputs are made equal there may be a number of unutilized outputs called garbage in certain reversible implementations. This is the number of outputs added to make an n-input k-output function reversible.

For example, a single output function of 'n' variables will require at least n-1 garbage outputs. Classical logic gates such as AND, OR, and XOR are not reversible. Hence, these gates dissipate heat and may reduce the life of the circuit. So, reversible logic is in demand in power aware circuits.

A reversible conventional BCD adder was proposed in [4] using conventional reversible gates. In [4], a full adder design using two types of reversible gates - NG (New Gate) and NTG (New Toffoli Gate) with 2 garbage outputs was implemented. The BCD adder was then designed using such full adders. Even though the implementation was improved in [5] using TSG reversible gates, this approach was not taking care of the fanout restriction of reversible circuits, and hence it was only a near-reversible implementation. An improved reversible implementation of decimal adder with reduced number of garbage outputs is proposed in [6]. Another improved reversible implementation of decimal adder using reversible gates which results in further reduction in number of gates and garbage outputs with a fanout of 1 is proposed in [7]. The present work proposes a modified version of decimal addition using reversible gates which results in reduction in number of gate operations in full adder reversible gates with a fanout of 1. The design is done using 3 types of reversible gates.

The organization of this paper is as follows: Initially, necessary background on reversible logic gates that are used for the design is given. Then the proposed BCD adder is implemented using reversible gates. Finally, the paper concludes with a comparison of the proposed design with different types of reversible BCD adders available in literature, in terms of delay, number of gates and garbage outputs.

II. REVERSIBLE LOGIC GATES

This section describes reversible gates that are used for the implementation of the proposed BCD adder.

Figure 1 shows a 3*3 New Gate [7]. New Gate can be used as a gate that generates an AND gate, an OR gate or an XOR gate. If $B=0$, then $Q=C$ and $R=(A'C)+I=A+C$.

Similarly, when $C=0$, then $Q=AB$ and $R=A+B$ which are the carry and sum outputs of a half adder. Figure 2 shows a Feynman Gate [8]. Feynman Gate (FG) can be used as a copying gate. Since a fanout greater than one is not allowed, this gate is useful for duplication of the required outputs.

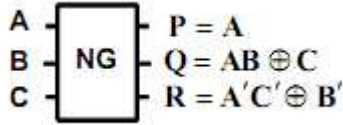


Figure 1: 3*3 New Gate (NG)

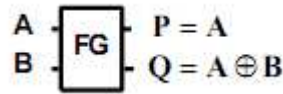


Figure 2: 2*2 Feynman Gate (FG)

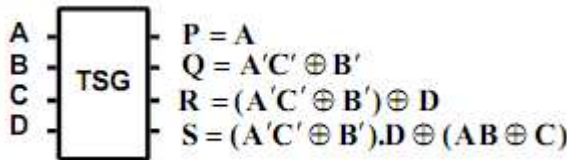


Figure 3: 4*4 TS Gate (TSG)

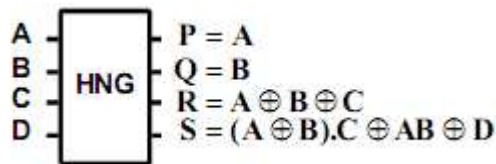


Figure 4: 4*4 HN Gate (HNG)

If $B=0$, then $P=A$ and $Q=A$. Figure 3 shows a TS Gate (TSG) [9]. A full adder circuit can be realized by a TSG with $C=0$ and A , B and C_{in} at A , B , D inputs of TSG. Then Sum and C_{out} are realized at R and S outputs of TSG. A full adder circuit can also be realized by a HN gate (HNG)[3] shown in figure 4 with $D=0$ and A , B and C_{in} at A , B , C inputs of HNG. Then Sum and C_{out} are realized at R and S outputs of HNG.

III. REVERSIBLE LOGIC IMPLEMENTATION OF DECIMAL ADDER

The BCD adder shown in Figure 5 has three blocks - 4-bit binary adder, 6-correction circuit and a modified special adder. 4-bit full adder adds the BCD inputs and generates a binary sum, S ($S_{3,0}$). This output is checked for a value greater than '9' or for a carry out, by the 6-correction circuit which generates a '6-correction' bit, 'L' using Equation (1).

$$L = C_{out} + S_3 (S_1 + S_2) \quad (1)$$

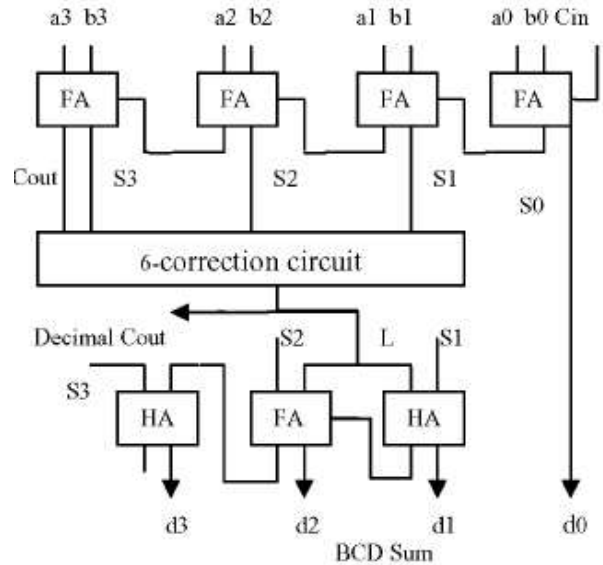


Figure 5: BCD Adder

The inputs to the second adder stage are S ($S_{3,0}$) and 4-bit number N ($N_{3,0}$) whose value is 6 (0110_2) or 0 (0000_2) depending on 'L' bit. So, N_0 and N_3 are always zero, and N_1 and N_2 is 'L' bit. To reduce the hardware and to increase the speed of the circuit, the final adder stage (special adder) is a modified version of the 4-bit binary adder with two half adders and one full adder.

Recently, reversible implementations of conventional BCD adders were proposed by Hafiz [4] Thapliyal [5] and James [6]. Implementation by Hafiz [4] makes use of 23 reversible gates and produces 22 garbage outputs whereas the implementation of Thapliyal [5] uses 11 reversible gates and produces 22 garbage outputs without taking care of fanout. There are 4 outputs in which the fanout is more than one in the implementation of [5], of which 3 are having fanout of 2 and the other having 3. If the fanout points were replaced by copying gates FG then the total number of gates would be increased to 16. Reversible implementation of BCD adder in [6] reduces the number of gates to 11 and garbage outputs to 13 with fanout restrictions. Reversible implementation of the BCD adder [10] uses the reversible gates such as TSG, FG and NG shown in Figure 5 takes care of the fanout restriction of reversible circuits and reduces the number of reversible gates. The proposed reversible implementation of the BCD adder done using the reversible gates such as HNG, FG and NG shown in Figure 7 also takes care of the fanout restriction of reversible circuits and reduces the number of reversible gate operations.

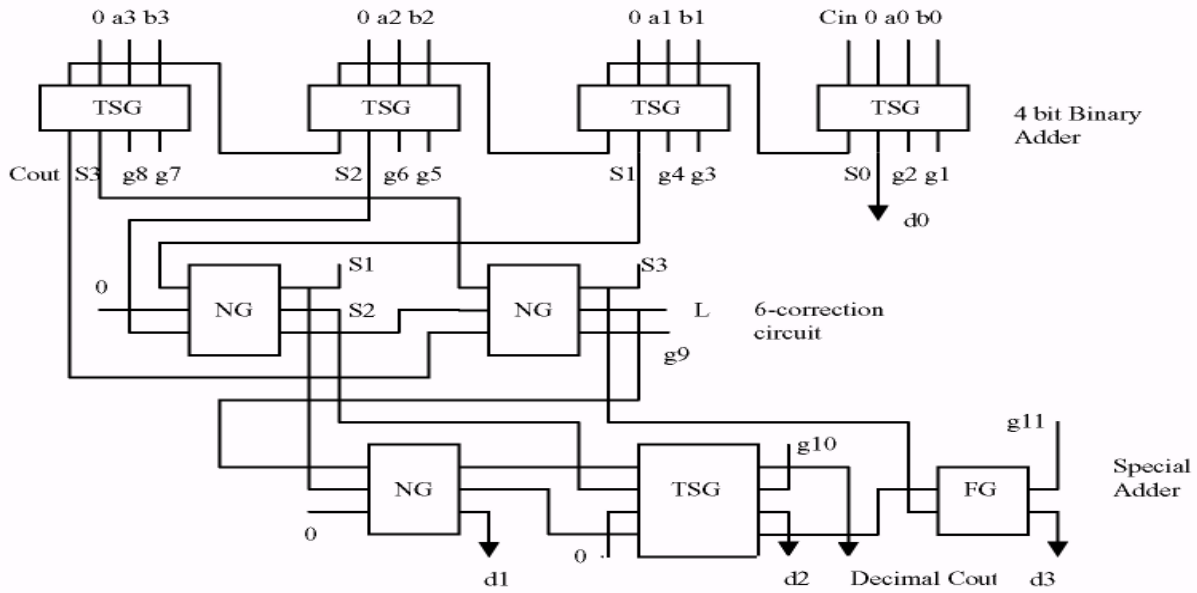


Figure 6: Reversible Implementation of BCD Adder in [10].

A 4-bit binary adder is implemented using 4 full adders. A full adder has 3 inputs and 2 outputs. To make a full adder reversible some garbage outputs are to be added. A reversible full-adder circuit can be realized with at least two garbage outputs. In full-adder circuit, there are three input combinations (0, 0, 1), (0, 1, 0) and (1, 0, 0) for which the output is same (1, 0). So, at least two garbage bits are required to make a unique output combination for each input combination. A number of reversible full adders are available in literature [7, 9]. But the implementation of a full adder using TSG [5] takes least number of gates, and produces least number of garbage outputs. Since a full adder can be implemented using one TSG, a 4-bit binary reversible adder implementation requires 4 TSGs and produces 8 garbage outputs. For reducing the number of gates, the 6-correction circuit output 'L' can be modified as in Equation (2).

$$L = \text{Cout} + S_3 (S_1 + S_2) = \text{Cout} \oplus S_3 (S_1 + S_2) \quad (2)$$

It can be seen that the implementation requires 2 gates (2 NGs) to produce the 6-correction output, 'L', and the sum outputs (S_{3-1}) with only one garbage output. The S_1 , S_2 and S_3 outputs produced without using any copying gate (FG) can be used as inputs for the next stage. This gives a reduction of 3 gates and 4 garbage outputs compared to the implementation in [4].

Special adder is implemented using 3 gates (NG, HNG, FG). It is already seen that a 3*3 NG can implement a half adder, and a 4*4 HNG can implement a full adder. An FG replaces the final half adder in the special adder.

This is because only the sum bit (d_3) is required as decimal sum output and the carry is discarded from the final addition. So, using an NG will give rise to 2 garbage outputs while an FG will produce only one garbage output. The BCD sum is indicated as d_{3-0} carryout from the stage as 'Decimal C_{out} ' in Figure 6. This implementation uses 9 reversible gates, and produces 11 garbage outputs. Further, it is noted that the implementation in [4] can be used only as a single digit BCD adder since a carryout (Decimal C_{out}) is not produced. This may be resolved by the addition of one more copying gate. The proposed design shown in Fig 7 can be used for cascading BCD adders for multidigit BCD addition with the help of the carry out (Decimal C_{out}) produced.

An N-digit BCD adder will have a total (worst case) delay (d_{sum}) equal to the sum of the 'carry delay' ($T_{d_{cout}}$) through N digits and 'sum delay' through the last digit ($T_{sum-digit}$). this is given in equation (3).

$$T_{d_{sum}} = NT_{d_{cout}} + T_{special\ adder} \quad (3)$$

$$\text{Where } T_{d_{out}} = (T_{bin-adder} + T_{6-correction}).$$

$T_{bin-adder}$ is the delay of 4-bit binary adder.

$T_{6-correction}$ is the delay in generating decimal $C_{out}(d_{cout})$ after $T_{bin-adder}$.

$T_{special-adder}$ is the additional delay of the final adder stage (special adder) of the last digit after generating Decimal $C_{out}(d_{cout})$.

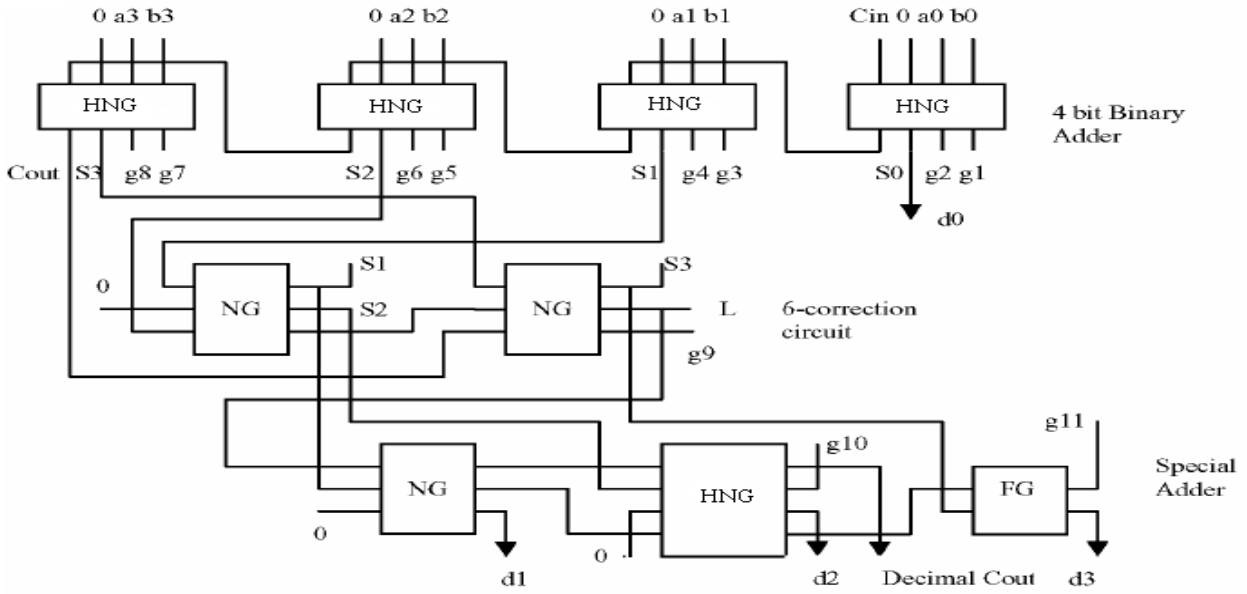


Figure 7: Proposed Reversible Implementation of BCD Adder.

TABLE 1. COMPARATIVE ANALYSIS OF REVERSIBLE BCD ADDERS

Reversible BCD Adders	4 bit Adder		6 -correction circuit		Correction/ Special Adder		Complete Circuit			
	No: of gates	No: of garbage o/p	No: of gates	No: of garbage o/p	No: of gates	No: of garbage o/p	No: of gates	No: of garbage o/p	Delay of Decimal Cout for N-digit BCD adder	Delay of BCD Sum for N-digit BCD adder
BCD Adder in [4]	NG-4 NTG-4 Total-8	8	FG-3 NG-3 Total-6	6	NG-4 NTG-4 Total-8	8	NG-11 NTG-8 FG-3 Total-22	22	12N	12N+7
BCD Adder using TSG [5] (fanout>1)	TSG-4	8	NG-3	6	TSG-4	8	TSG-8 NG-3 Total-11	22	7N	7N+3
BCD Adder using TSG [5] (fanout=1)	TSG-4	8	FG-3 NG-3 Total-6	6	TSG-4 FG-2 Total-6	8	TSG-8 NG-3 FG-5 Total-16	22	9N	9N+4
BCD Adder in [6] (fanout=1)	TSG-4	8	NG-2 FG-1 Total-3	2	FG-2 NG-1 TSG-1 Total-4	3	TSG-5 NG-3 FG-3 Total-11	13	7N	7N+3
BCD Adder In(10) (fanout=1)	TSG-4	8	NG-2	1	FG-1 NG-1 TSG-1 Total-3	2	TSG-5 NG-3 FG-1 Total-9	11	7N	7N+1
Proposed BCD Adder (fanout=1)	HNG-4	8	NG-2	1	FG-1 NG-1 HNG-1 Total-3	2	HNG-5 NG-3 FG-1 Total-9	11	7N	7N+1

For a reversible implementation this is given as

$$T_{\text{rev-dsum}}=7N+1 \quad (4)$$

Where $T_{\text{rev-dout}}=T_{\text{rev-bin-adder}}+T_{\text{rev-6-correction}}$

$$T_{\text{rev-bin-adder}} = 4 \text{ gate delays (4HNG)}$$

$$T_{\text{rev-6-correction}} = 3 \text{ gate delays (2NG+1HNG)}$$

$$T_{\text{rev-bin-adder}} = 1 \text{ gate delay (1FG)}$$

Similar analysis done on reversible implementations of BCD adders in [4], [5] and [6] are tabulated in Table 1. Even though this delay analysis will not give exact results because of the difference in complexity of the gates used, it gives a good estimate of the delay reduction attained by reversible implementation of proposed BCD adder. The Table also shows a comparison in terms of number of reversible gates and garbage outputs at different levels and for the complete circuit. It is clear that the proposed implementation uses least number of gate operations and gives least delay compared to all other implementations. The reduction in number of gate operations (area) required will lead to reduced power consumption.

IV. RESULTS AND DISCUSSION

Evaluation of the proposed reversible BCD adder circuit is: the proposed reversible adder circuit is more efficient than existing circuit presented in [10] evaluation of proposed circuit can be comprehended easily with the help of the comparative analysis in Table 2.

Table2: comparative experimental results of existing and proposed reversible adder circuits.

Reversible BCD adder circuit	Total logical calculation (T)
Design in [10]	$27a+21b+24c$
Proposed Design	$27a+16b+9c$

The only difference between proposed design with the existing design in [10] is the use of HNG gate instead of TSG gate. We use it because the HNG gates have less logical calculation than the TSG gates. One of the main factors of the circuit is its hardware complexity.

We can prove that our proposed circuit is better than the existing approaches in terms of hardware complexity.

Let

a=A two input EX-OR gate calculation

b=A two input AND gate calculation

c=A NOT gate calculation

T=Total logical calculation

For [10] the total logical calculation is:

$$27a+21b+24c$$

For our proposed design logical calculation is:

$$27a+16b+9c$$

Therefore, the proposed reversible adder circuit is better than the existing circuits in terms of complexity.

V. CONCLUSION AND FUTURE WORK

A modified reversible BCD adder implementation is presented. The architecture is specially designed to make it suitable for reversible logic implementation. It is demonstrated that the proposed design is highly optimized in terms of number of reversible gate operations.

The design strategy is chosen in such a way to reduce the most important factor of the reversible circuit cost: the number of reversible gate operations. This work forms an initial step in the building of complex reversible systems, which can execute more complicated operations. The reversible circuit proposed here forms the basis of a Decimal ALU for a reversible CPU. VLSI implementations using only one type of modular building block can decrease system design and manufacturing cost. Characterization of new families of 'n-input' - 'n-output' reversible gates that can be used for regular structures is an area which can be explored further. In this research, a known traditional logic implementation for BCD adder was modified to get a delay reduction for multi-digit addition, and then each of the internal elements was replaced with reversible equivalents. Further investigation into determining alternate implementations can be done using logic synthesis methods.

REFERENCES

1. R. Landauer, "Irreversibility and Heat Generation in the Computational Process", IBM Journal of Research Development, 5, 1961, 183-191.
2. Bennett, C., "Logical Reversibility of Computation," IBM Journal of Research and Development, 17, 1973, 525-532.
3. Majid haghparast, Keivan Navi "Design of a novel multiplier circuit Using HNG in Nanotechnology" ISSN 18181-4952-2008.
4. Hafiz Md. Hasan Babu and A. R. Chowdhury, "Design of a Reversible Binary Coded Decimal Adder by Using Reversible 4-bit Parallel Adder", VLSI Design 2005, pp-255-260, Kolkata, India, Jan 2005.
5. Himanshu. Thapliyal, S. Kotiyal and M.B Srinivas, "Novel BCD Adders and their Reversible Logic Implementation for IEEE 754r Format", VLSI Design 2006, Hyderabad, India, Jan 4-7, 2006, pp. 387-392.
6. R. James, T. K. Shahana, K. P. Jacob and S. Sasi, "Improved Reversible Logic Implementation of Decimal Adder", IEEE 11th VDAT Symposium Aug 8-11, 2007.
7. Md. M. H. Azad Khan, "Design of Full-adder With Reversible Gates", International Conference on Computer and Information Technology, Bangladesh, 2002, pp. 515-519.
8. R. Feynman, "Quantum Mechanical Computers", Optical News, 1985, pp. 11-20.
9. H. Thapliyal and M.B Srinivas, "A Novel Reversible TSG Gate and Its Application for Designing Reversible Carry Look-Ahead and Other Adder Architectures", Tenth Asia-Pacific Computer Systems Architecture Conference, Singapore, Oct 24 - 26, 2005
10. Rekha K.james, Shahana T.K, T.Poulose Jacob, Sreela Sasi "A new look at Reversible logic implementation of Decimal adder", IEEE 1-4244-1368-0/07.

SIZE TUNING AND OXYGEN PLASMA INDUCED PORE FORMATION ON SILICA NANOPARTICLES

Remya Nair, Y. Yoshida, T. Maekawa, D. Sakthi Kumar

Bio Nano Electronics Research Center,
Graduate School of Interdisciplinary New Science, Toyo University
Kawagoe-shi, Saitama – 350-8585, Japan.
remya.d.nair@gmail.com

Silica nanoparticles (SNPs) occupy a prominent position in scientific research because of their easiness in preparation and enormous uses in various applications [1]. Porous silica nanoparticles have a promising role in various drug delivery applications [2, 3]. Significant research progress has been made in controlling and modifying the properties of mesoporous silica materials since its discovery [4-6]. In contrast to the earlier reports of tuning the particle size by adjusting atleast four different parameters [7, 8], here we are reporting about our attempt to control the nanoparticle size by making variations in a single parameter; the concentration of ammonia solution. Silica nanoparticles of size ranging from 5 nm to 250 nm have been successfully synthesized by controlling only the concentration of ammonia solution keeping all other parameters (concentration of TEOS, ethanol and water) constant [Fig 1]. Oxygen plasma was found to be a successful direct tool for generating pores on silica nanoparticles without the use of any structure directing agent and our method proved to be very easy and time saving one [Fig 2]. The nature and morphology of nanoparticles were investigated by scanning electron microscopy, transmission electron microscopy, dynamic light scattering, energy dispersive X-ray spectroscopy and Fourier transformed infrared spectroscopy.

References:

- [1] K.S. Rao et al., *J. Colloid Interface Sci.*, **289** (2005) 125-131.
- [2] I.I. Slowing et al., *Adv. Drug Del. Rev.*, **60** (2008) 1278-1288.
- [3] F. Torney et al., *Nat. Nanotech.*, **2** (2007) 295-300.
- [4] G. Bogush et al., *J. Non-Cryst. Solids*, **104** (1988) 95-106.
- [5] T. Yokoi et al., *J. Am. Chem. Soc.*, **128** (2006) 13664-13665.
- [6] J. Guo et al., *J. Colloid Interface Sci.*, **326** (2008) 138-142.
- [7] S. K. Park et al., *Colloids Surf. A.*, **197** (2002) 7-17.
- [8] Davies G-L et al., *Chem. Phy. Lett.*, **468** (2009) 239-244.

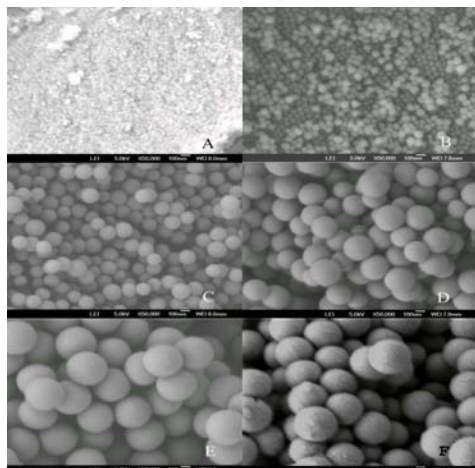
Figures:

Fig 1: SEM images of silica nanoparticles at different concentrations of ammonia solution

A: Silica nanoparticles at 6% NH_3 solution (Average diameter: 9.16 nm)

B: Silica nanoparticles at 8% NH_3 solution (Average diameter: 67.81 nm)

C: Silica nanoparticles at 12% NH_3 solution (Average diameter: 137.66 nm)

D: Silica nanoparticles at 16% NH_3 solution (Average diameter: 216.62 nm)

E: Silica nanoparticles at 20% NH_3 solution (Average diameter: 242.07 nm)

F: Silica nanoparticles at 24% NH_3 solution (Average diameter: 257.03 nm)

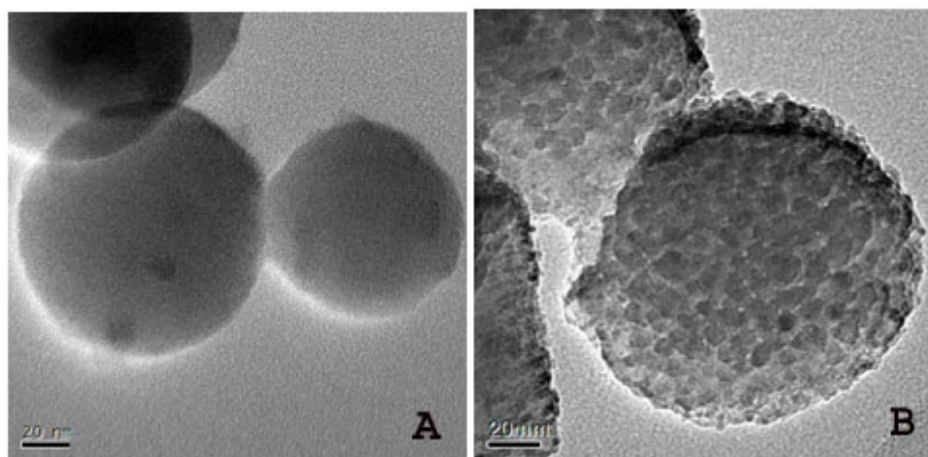


Fig 2: TEM image of silica nanoparticles with and without plasma treatment

PHYSICS-BASED COMPACT MODEL FOR SCHOTTKY BARRIER CARBON NANOTUBE FET

M. Najari^{1,2}, *S.Frégonèse*¹, *C. Maneux*¹, *T. Zimmer*¹, *H. Mnif*², *N. Masmoudi*²

¹ *Université de BORDEAUX, CNRS, UMR 5218, FRANCE,* ² *National School of Engineering of Sfax – LETI Laboratory - Sfax, TUNISIA, montassar.najari@ims-bordeaux.fr*

Introduction:

For not highly doped or undoped source/drain regions, CNTFET Schottky barriers (**SB**) are formed between the metal contacts and the semiconducting carbon nanotube at source/drain (S/D). Under these conditions, the source and drain current is affected by tunnelling mechanisms through these barriers. By changing the gate voltage (figure 1), energy bands are shifted which modulates the SB transmission function and subsequently the transistor current. In this work, we focus on the self-consistent analytical modeling of SB-CNTFET. Self-consistent means that the effect of the injected charge (current) in the channel on the band bending and consequently on the drain current is taken into account. In section II, the physics-based analytical model for the channel charge in the SB-CNTFET is presented. Section III gives the drain-source current formulation and finally, a comparison between the Current-Voltage characteristics of the SB model and a MOS-like simulated CNTFET is performed.

Formulation of the intrinsic nanotube charge:

In the SB-CNTFET, the linear charge density n_{CNT} results from the product of the Fermi-Dirac (FD) distribution $f(E)$ times the density of states $g(E)$ times the source-drain transmission function $T_T(E)$. This later describes the transparency of the SB at the source/CNT or CNT/Drain interfaces, over the carrier energy range:

$$n_{CNT} = e \int_{E_0}^{+\infty} \frac{g(E)}{2} \times T_T(E) \times [f(E - \mu_S) + f(E - \mu_D)] dE \quad (1)$$

with E_0 being the mid-gap energy of the intrinsic region. The integral (1) has no direct analytical solution. Hence, an approximation of the transmission function is proposed in this work according to the assumption published in [1]. This approximation consists in solving analytically the 1D modified Poisson equation for the channel potential which leads to calculate an effective SB height. Hence, considering the approximations on the effective SB height and assuming a 1D density of states relation, the linear density of charge in the source writes as:

$$n_{CNT,S} = eD_0 \int_0^{+\infty} \frac{1}{\sqrt{E + \Phi_{SB}^{eff} - sbbd_{[p]}}} \times \frac{1}{1 + \exp\left(\frac{E + \Phi_{SB}^{eff} - eV}{k_B T}\right)} dE \quad (2)$$

Since this integral has no analytical solution over the whole potential V and carrier energy E ranges, partial solutions have been considered according to the Fermi distribution and the density of state relative variation.

Partial analytical solutions calculation

At low gate bias conditions, the FD distribution is considered as an exponential function in the energy range of interest which leads to the following analytical solution of the integral [2].

$$n_1 = eD_0 \sqrt{\pi k_B T} \exp\left(\frac{eV - sbbd_{[p]}}{k_B T}\right) \left[1 - \text{Erf}\left(\sqrt{\frac{\Phi_{SB}^{eff} - sbbd_{[p]}}{k_B T}}\right)\right], \text{ where Erf}(x) \text{ is the error function.}$$

At high bias, an additional energy bound Δ is required to solve (2) in order to separate the energy range where the FD distribution is nearly constant and the energy range where the FD distribution behaves as an exponential function. Then, the linear charge density is written:

$$n_2 = eD_0 \left[\int_{\Phi_{SB}^{eff}}^{\Delta} g(E)f(E)dE + \int_{\Delta}^{+\infty} g(E)f(E)dE \right]$$

i) *Low energy*: For an energy range from Φ_{SB}^{eff} to Δ , the FD distribution variation evolves weakly compared with $g(E)$. Thus, it can be expanded in a Taylor series around $E=sbbd_{[p]}$ and the linear density of charge becomes:

$$n_{2a} = 2eD_0 \times \left[\sqrt{\Phi_{SB}^{eff} - sbbd_{[p]}} \left(a_0 + \frac{a_1}{3} (\Phi_{SB}^{eff} + sbbd_{[p]}) \right) + \sqrt{\Delta + \Phi_{SB}^{eff} - sbbd_{[p]}} \left(a_0 - \frac{1}{3} a_1 (sbbd_{[p]} - \Phi_{SB}^{eff} - \Delta) \right) \right]$$

ii) *High energy*: For an energy range from Δ to $+\infty$, $g(E)$ is considered as constant and equal to $g(\Delta)$ and the exponential approximation is used for the Fermi distribution. The analytical expression of the linear density of charge is then straightforwardly obtained as:

$$n_{2b} = eD_0 \frac{\alpha}{\sqrt{\Delta + \Phi_{SB}^{eff} - sbbd_{[p]}}} k_B T \exp\left(-\frac{\Delta + \Phi_{SB}^{eff} - sbbd_{[p]}}{k_B T}\right)$$

Finally, for model convergence issues, a smoothing function, f_{SMO} is used to obtain a complete solution [3]. Figure 2 shows the good agreement between the complete analytical charge model result and the numerical solution over a wide range of the SB height and gate voltage.

Formulation of the drain current:

The current through the structure is calculated by means of the Landauer–Buttiker formula assuming a one dimensional ballistic channel in between the SB. Hence, after integration over energy and for all the energy sub-bands, the drain-source current is expressed as [4]:

$$I = \frac{4ek_B T}{h} \sum_{p=1}^{+\infty} \left[\ln\left(1 + \exp\frac{eV_S + \Phi_{SB}^{eff} - sbbd_{[p]}}{k_B T}\right) - \ln\left(1 + \exp\frac{eV_D + \Phi_{SB}^{eff} - sbbd_{[p]}}{k_B T}\right) \right]$$

where the calculation of $sbbd[p]$ is consistent with the general expression of energy dispersion. Figure 3 shows the IV-characteristics of the SB-CNTFET model ($\Phi_{SB}=0.5eV$) in comparison with simulation results for a MOS like CNTFET according to drain voltage: (i) SB’s limit by a factor of 2 the drain-to-source current and (ii) shift the gate threshold voltage. Further developments are in progress to evaluate SB’s impact on dynamic performances.

Conclusion

An analytical physics based compact model for Schottky barrier CNTFET has been developed and implemented in a SPICE like simulation environment. It has been shown the SB affect strongly the I(V) characteristics of the transistor. Small signal simulation will be performed to benchmark SB-CNTFET with respect high frequency performance.

References:

- [1] J. Appenzeller al, phys. stat. sol. (a) 205, No. 4, (2008), pp.679–694
- [2] I. S. Gradshteyn and al., Table of Integrals, Series, and Products, 1994, ch. 3, p. 363.
- [3] M.Najari and al. in Proc. IEEE Int. Conf. DTIS (2008), pp.1-6
- [4] S. Fregonese and al. IEEE TED, Vol. 55, NO. 6, June (2008)

Figures:

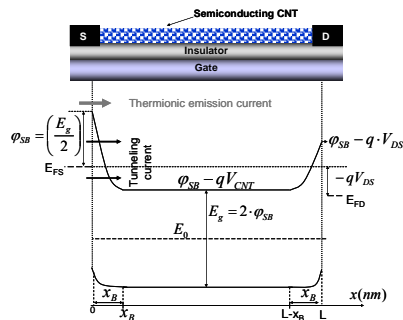


Fig 1. SB-CNTFET structure in back gate configuration with first conduction and valence sub-energy band profiles for $V_{GS} > V_{DS}$

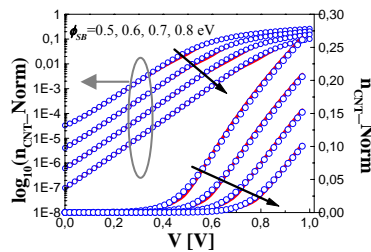


Fig 2. Linear channel charge density [normalized by $eD_0=8e/(3\pi bV_{pp\Gamma})$] at 300K, as a function of the potential V for different Φ_{SB} . Dots are numerical calculation and lines are analytical solution.

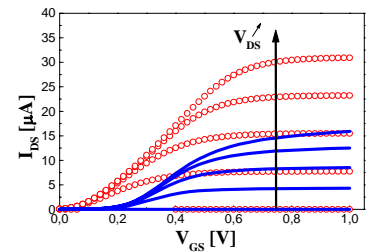


Fig 3. I_{DS} as a function of the V_{GS} bias for 5 drain biases ranging from 0 to 0.2V by a step of 25mV. Dots are for MOS-like CNTFET and lines are for SB-CNTFET analytical model with $\Phi_{SB}=0.5eV$.

A NOVEL APPROACH TO CREATE STRONG AND CONDUCTIVE CONSTRUCTION MATERIALS

Larisa I Nasibulina¹, Ilya Anoshkin¹, Andrzej Cwirzen³, Karin Habermehl-Cwirzen³, Ying Tian¹, Sergey D Shandakov^{1,2}, Albert G Nasibulin¹, Vesa Pentala³, and Esko I Kauppinen^{1,4}

¹ Department of Applied Physics and Center for New Materials, Helsinki University of Technology, Espoo, PO Box 5100, FIN-02150, Finland

² Laboratory of Carbon NanoMaterials, Department of Physics, Kemerovo State University, Kemerovo 650043, Russia

³ Laboratory of Building Materials Technology, Faculty of Engineering and Architecture, Helsinki University of Technology, Espoo, PO Box 5100, FIN-02150, Finland

⁴ VTT Biotechnology, Biologinkuja 7, 02044, Espoo, Finland

e-mail: laran@cc.hut.fi

Carbon nanotubes (CNTs) and carbon nanofibers (CNFs) are known to possess exceptional tensile strength, elastic modulus and electrical and thermal conductivity. They are promising candidates for the next-generation high-performance structural and multi-functional composite materials. However, one of the largest obstacles to creating strong, electrically or thermally conductive CNT/CNF composites is the difficulty of getting a good dispersion of the carbon nanomaterials in a matrix. Typically, time-consuming steps of purification and functionalization of the carbon nanomaterial are required. We propose a new approach to grow CNTs/CNFs directly on the surface of matrix particles.

As the matrix we selected cement, the most important construction material. We synthesized in a simple one-step process a novel cement hybrid material (CHM), wherein CNTs and CNFs are attached to the cement particles. The CHM has been proven to increase 2 times the compressive strength and 40 times the electrical conductivity of the hardened paste, i.e. concrete without sand ^[1].

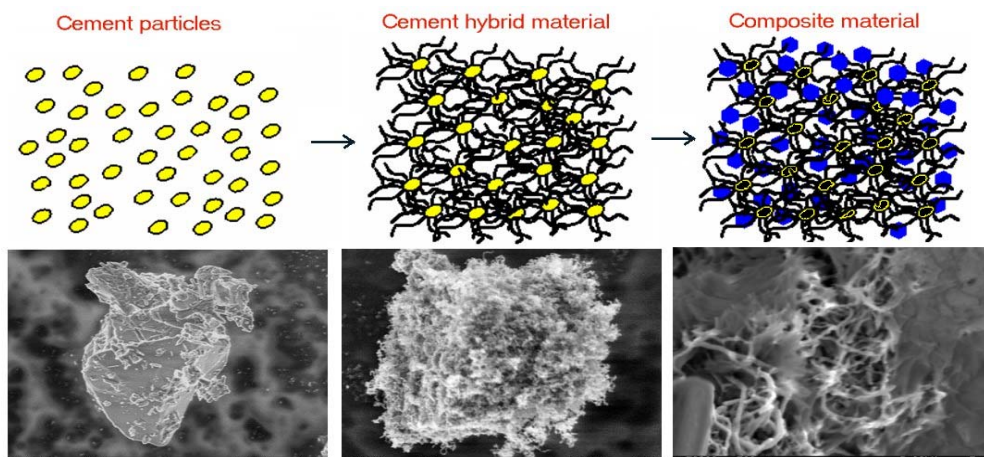


Figure Schematic representation of general concept of the incorporation of CNTs/CNFs into composite material by their direct growth on the surface of matrix particles.

[1] A. G Nasibulin *et al.* A novel cement-based hybrid material. 2009 *New J. Phys.* **11**, 023013.

Inconsistent behavior of electrical conductivity in Pd thin film as a function of film thickness

S. Nazarpour, F. Afshar, A. Cirera

Department of Electronics, University of Barcelona, Spain, 08028
nazarpour@ub.edu

The electrical conductivity of thin metal films has become a problem of increasing importance because of their widespread use in electronic devices. Generally, the resistivity of thin films is described in terms of scattering of the conduction electrons at the external surfaces. The theoretical basis for this phenomenon was given by Thomson [1]. The standard theory for calculation the electrical conductivity of thin films is commonly described by Fuchs [2] whose work was later extended and corrected by Sondheimer [3]. More attention into the microstructure of thin films has led to appreciation of the fact that not only the external surfaces, but also the grain boundaries will modify the resistivity [4]. The aim of the work is to investigate the effect of thickness variation in Pd thin films on interfacial properties, surface topography and electrical conductivity.

Pd was evaporated on top of the SrTiO₃ (STO) by means of electron beam physical vapor deposition (EBPVD). Different thicknesses of Pd were obtained with increasing distance between evaporation source and substrates. Deposition was conducted with 1.6 KV potential, 200 mA emission intensity, and the pressure better than 4×10^{-6} mbar. Substrate temperature was set at 300° C to increase the crystallinity of the film. The crystalline structure has been determined by X-Ray Diffraction (XRD) analysis in θ -2 θ scan by means of a 4-circle X-ray diffractometer with Cu-K α radiation. Atomic force microscopy (AFM) was utilized to clarify the growth mode of the Pd on top of the STO. Electrical conductivity was measured by means of two conductive tips and amperage - voltage plot (I-V) was attained. Besides, X-ray Photoelectron Spectroscopy (XPS) was used in depth analysis mode to elucidate the interfacial phenomena.

XRD results of Pd showed the growth of Pd on (111) crystallographic direction. Furthermore, it is reported that all metals with FCC structures such as Au and Pd, tend to have a natural preference in (111) orientation during the growth which is strongly due to the low number of the bonds with neighboring atoms in these low dense plans. Indeed, low lattice mismatch between Pd and STO could be the main reason for inconceivable adhesion properties [15]. Fig (1) dedicated to AFM topographic imaged for hillocks which appear in the different thickness of Pd thin film. As shown in Fig 1 (a), same height of hillock has been seen in 25 nm and 45 nm thin film of Pd while the hillock height decreased in 65 nm thickness. However, 100 nm Pd thin film showed the coarse and height hillocks. Indeed, the total area of the hillocks is minimum in 45 nm film in compare with the other thin films. This might roughly illustrate the lower surface roughness of 45 nm Pd film in compare with three other samples. In fact, the surface roughness introduce an extra degree of electron scattering called surface scattering which the decrease dramatically the electrical conductivity of the thin films. Therefore, the numerical amount has been used to measure the surface roughness of Pd thin film with 45nm thickness meanwhile Root-Mean-Square (RMS) roughness of the film was calculated around 4.6 nm roughness that could be subjected as a smooth film with respect to evaporation method. Fig 2 shows the electrical conductivity of different thicknesses of Palladium and consists of four selected thickness means 25nm, 45nm, 65nm, and 100nm. As shown in fig 2, it seems that Pd with 25nm thickness wasn't conductive due to partly growth of the film that happened because of low thickness. Basically, it is well-established that with increasing the thickness, resistance of the thin films will decrease. Thus, it was expected that electrical resistance of 45nm thickness film is more than 65nm thickness Pd film but it quashed, just in case. Indeed, Pd thin film with 100nm thickness was showed the lowest electrical resistance as was expected.

Fig 3 (a-c) showed the XPS signals of 45 nm thickness of Palladium thin film. As shown in Fig 3 (a), displays the corresponding Pd 3d features in as annealed sample. Appeared signal in 336.2 eV consists of Pd 3d_{3/2} which its intensity decreased with increasing sputtering time. Fig 3 (b) showed the Oxygen behavior in the interface of Pd and SrTiO₃. As shown in fig 3 (b), low concentration of Oxygen has been seen in the layer while raised with increasing the sputtering time which has been shown clearly in fig 3 (c). This phenomenon could be because of relaxation process due to breaking the bonds between oxygen and Sr, happened on the interface of Pd-STO. It seems, porosity of Pd magnified oxygen penetration and an unknown composition of Palladium oxide was appeared. Mainly, Palladium oxide acts as an insulator and increase the resistance of the films, dramatically. It would be a competition between the increasing the thickness and increasing the stress in the interface to govern the electrical resistance. It seems, existed stress governed to electrical conductivity in the thickness range between 30nm to 70nm.

[1] J. J. Thomson, Proc. Camb. Phil. Soc. 2 (1901) 119.
 [2] K. Fuchs, Proc. Camb. Phil. Soc. 34 (1938) 100.
 [3] E. H. Sondheimer, Adv. Phys. 1 (1952) 1.
 [4] A. F. Mayadas, M. Shatzkes, and J. F. Janak, Appl. Phys. Lett. 14 (1969) 345.

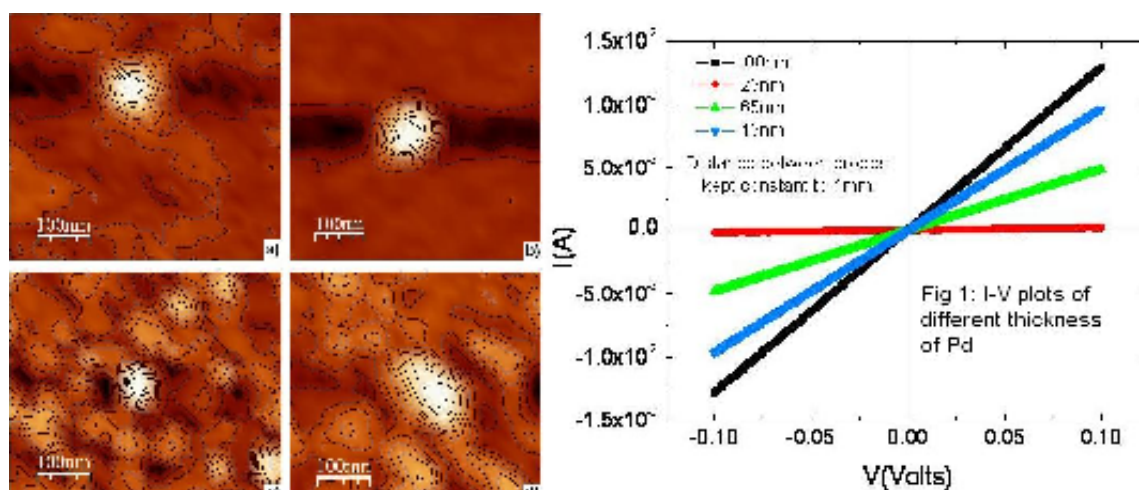


Fig 1: AFM 3D image of different thickness of Pd

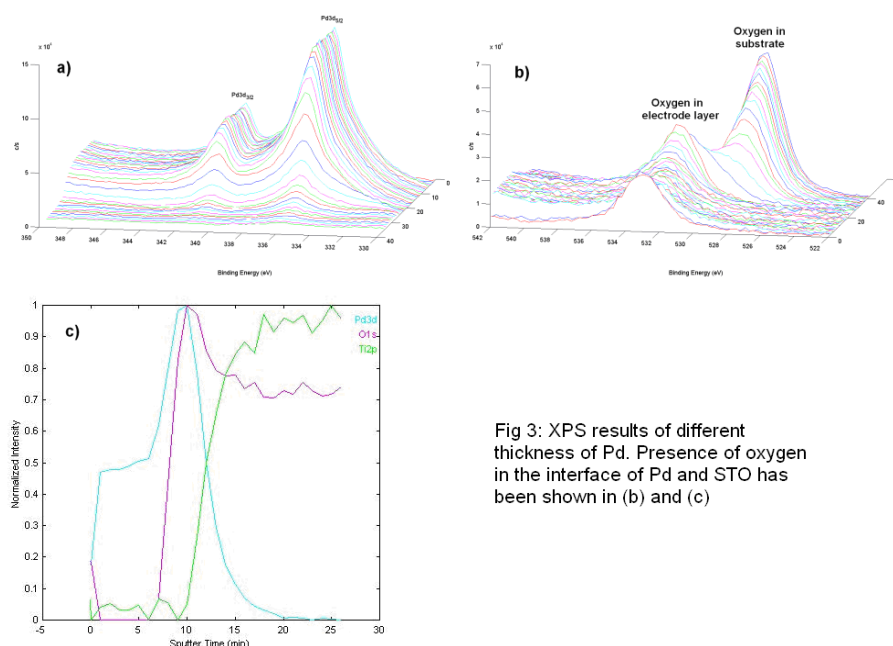


Fig 3: XPS results of different thickness of Pd. Presence of oxygen in the interface of Pd and STO has been shown in (b) and (c)

REALIZING A CRYSTALLOGRAPHIC ORIENTATION DEPENDENT CHEMICAL ETCHING OF GRAPHENE

P. Nemes – Incze¹, M. Gábor², K. Kamarás³, L.P. Biró¹

1 Research Institute for Technical Physics and Materials Science, H-1525 Budapest, PO. Box 49, Hungary, www.nanotechnology.hu

2 Technical University Budapest, Hungary, H-1521 Budapest, PO Box 91

*3 Research Institute for Solid State Physics and Optics, Hungarian Academy of Sciences, H-1525 Budapest, PO Box 49, Hungary
nemes@mfa.kfki.hu*

The excellent electrical properties of graphene, like very high electron mobility, long coherence length of charge carriers, etc. has brought this exiting 2D crystal into the spotlight of nanomaterials research [1]. Graphene may well turn out to be a key material in shaping post silicon nanoelectronics, with demonstration devices of graphene based field effect transistors having already been realized.

For the large scale implementation of graphene based electronics two major obstacles have to be overcome: preparing large scale graphene layers and patterning these into the desired component architectures. Graphene nanostructures especially nanoribbons are very sensitive to the crystallographic orientation of the nanostructure edges, for example it is predicted that graphene nanoribbons having zig-zag edges are always metallic, while ribbons with armchair edges may be semiconducting. A controlled crystallographic orientation dependent etching of these structures would be a great tool in achieving the kinds of applications dreamt up for graphene. One way to achieve this goal is to use STM lithography [2]. On the other hand we have developed an etching technique, which is subtle enough to differentiate between the slightly different stability of zig-zag and armchair edges in graphene, thus obtaining selective etching. We used graphene samples prepared by micromechanical cleavage deposited onto Si wafers, having a 300 nm thick SiO₂ layer. We present a detailed scanning probe microscopy (STM, AFM) investigation into the nature of the etched graphene layers. It is important to note that contrary to the oxidation of graphene [3], carbon removal only occurs at the sample edges or at previously introduced oxidation holes [3] (see the right Figure) and grain boundaries (see the left Figure) leaving the rest of the graphene layer unharmed, as evidenced by Raman spectroscopy.

Using our etching method we can produce crystallographically oriented structures in graphene samples, opening up new opportunities for device fabrication.

Acknowledgement

Support by OTKA-NKTH grants 67793 and 67851 is acknowledged.

References:

- [1] A.K. Geim, et al., Nature Materials, **6** (2007) 183.
- [2] L. Tapasztó, et al., Nature Nanotechnology **4** (2008) 937.
- [3] Li Liu, et al., Nano Letters, **8** (7) (2008) 1965–1970.

Figures:

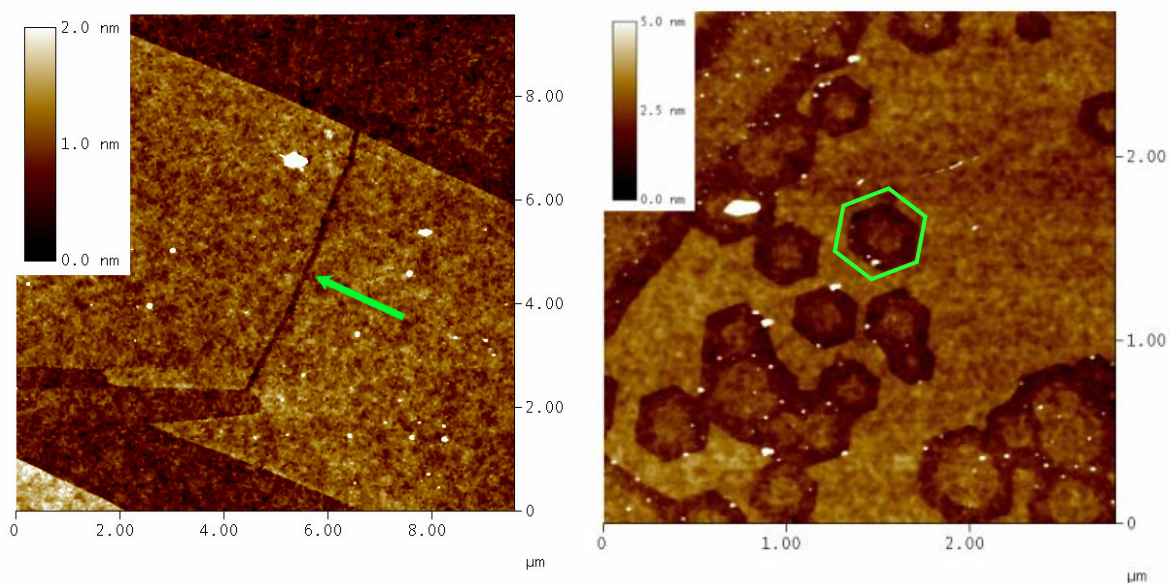


Figure. Etched graphene layers supported on SiO₂ substrates. **Left image:** etching of a grain boundary in graphene. In the position of the grain boundary the graphene has been etched away revealing a trench, as shown by the green arrow. **Right image:** Enlarging of previously introduced oxidation pits in the graphene surface. The pits are hexagonal in nature which proves that anisotropic etching has occurred.

SPIN DEPENDENT TUNNELING IN FERROMAGNET/INSULATOR/PARAMAGNET JUNCTIONS

Ingmar Neumann^{1,}, Marius Costache¹, Sergio O. Valenzuela^{1,2}*

¹*Centre d'Investigació en Nanociència i Nanotecnologia (CIN2, CSIC – ICN), Campus UAB, E-08913 Bellaterra, Spain*

²*Institució Catalana de Recerca i Estudis Avançats (ICREA)*

**Ingmar.Neumann.Icn@uab.cat*

One of the main challenges of the field of spintronics [1] is the controlled injection of spin polarized currents from ferromagnetic into nonmagnetic materials by means of an insulating tunnel barrier. In order to get a better understanding of the involved tunnelling process, novel devices have been developed that, in contrast to the widely studied magnetic tunnel junctions, allow one to distinguish between tunnelling out-of or into a ferromagnetic electrode by inverting the applied voltage bias [2]. The obtained data with such devices show a strong asymmetry about zero bias, which we analyze with a theoretical approach based on an analytical free-electron model. Our simple model is unable to render all of the complexity inherent to nonideal interfaces, scattering, or complex band structures. However, it qualitatively explains the experimental observations and shows that complex behaviour of the polarization as a function of voltage is intrinsic to spin tunnelling and is highly sensitive to the ratio between the electron wave numbers inside and outside the barrier region.

References:

[1] Zutic, I.; Fabian, J. & Sarma, S., *Reviews of Modern Physics*, **76** (2004) 323.

[2] Valenzuela, S. O.; *Int. J. Mod. Phys. B*, **23**, (2009) 2413; Valenzuela, S. O.; Monsma, D. J.; Marcus, C. M.; Narayanamurti, V. & Tinkham, M., *Phys. Rev. Lett.*, **94** (2005) 196601.

IN SITU OBSERVATIONS OF THE DYNAMICS AT NANOSCALE BY ULTRAFAST TRANSMISSION ELECTRON MICROSCOPY

Liliya Nikolova, Federico Rosei and Jean-Claude Kieffer

Institut National de la Recherche Scientifique, Montréal, Québec, Canada

Shona McGowan and Bradley Siwick

McGill University, Montréal, Québec, Canada

James Evans, Thomas LaGrange and Nigel Browning

Lawrence Livermore National Laboratory, Livermore, California, USA

As a continuous solid crystal is reduced in scale to a system of small number of atoms, its behavior often changes considerably. This can lead to interesting optical, electronic, magnetic, and catalytic properties. A significant amount of effort has been expended, particularly over the last two decades, on characterizing the size-, quantum- or surface states-effects to which these changes are generally attributed (1-4). The possibility of tailoring the properties of nanomaterials has lead to some interesting discoveries and potential applications in medicine, energy conversion and storage, catalysis, sensing, electronics, etc. To harness the properties of such novel systems, however, a better understanding needs to be developed on their structure and the effect on the nanomaterials' properties.

The equilibrium states of most materials are well known and have been probed by large variety of techniques. Information on the intermediate states, however, is not complete. To reveal the process of structural transformation and to understand the dynamics, a description of the states during a structural transition is need with temporal resolution in the nanosecond to femtosecond range. At present, there is no well-developed general method for the atomic-level structural determination of short-lived transient states.

For ultrafast studies of structural transition, X-ray and electron diffraction are generally employed. Despite their high spatial resolution, they visualise the reciprocal space, thus giving information on presence or absence of periodical structure. As shown in figure 1, however, a combination of high temporal resolution and real space imaging are required for the study of processes such as nucleation, interphase boundary motion, shock propagation, radiation damage, solid state chemical reactions (5-9). This prompts the necessity of a new method that can provide real space imaging with high temporal and spatial resolution.

The transmission electron microscope (TEM) is a powerful and versatile tool for characterisation of the materials offering high spatial resolution (as low as 0.5\AA (10; 11)); but due to the poor temporal resolution, it is rarely used for in situ direct imaging of structural transitions. Limited by the video capture rate of the camera, the images are usually acquired in seconds-scale. In this presentation, we will outline recent work on the modification of a TEM to obtain a Dynamic TEM (DTEM). By improving the temporal resolution we can reveal the dynamics of non-reversible processes of structural transitions (12-14). Challenges and advantages of such modification will be described in the context of our initial results on amorphous Silicon and Germanium nucleation. The TEM modified at INRS is the first DTEM in Canada.

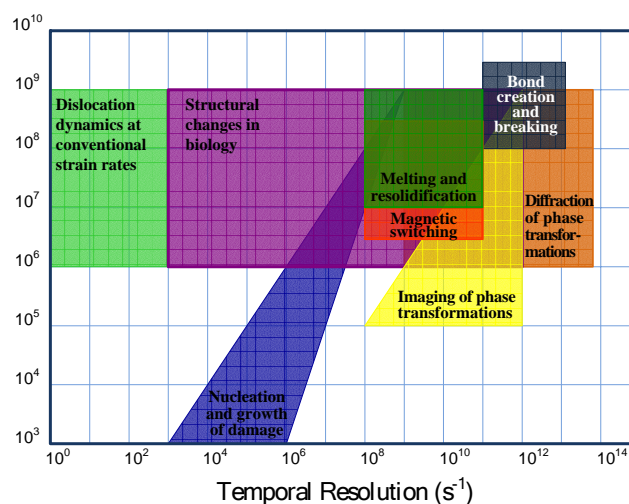


Figure 1 (5)

Bibliography

1. **F. Rosei.** Nanostructured surfaces: challenges and frontiers in nanotechnology. *Journal of Physics: Condensed Matter*. 2004, Vol. 16, pp. S1373–S1436.
2. **J.W. Reiner, F.J. Walker and C.H. Ahn.** Atomically Engineered Oxide Interfaces. *Science*. 2009, Vol. 323, pp. 1018-1019.
3. **L. Nikolova, R.G. Saint-Jacques, C. Dahmoune, and G.G. Ross.** Silicon nanoparticle formation in SiO₂ by Si ion implantation : effect of energy and fluence on size distribution and on SiO_x composition. *Surface and Coatings Technology*. 2009. Accepted article. To be published in Special issue on SMMIB15. Available online Ref #SCT14881.
4. **G. Schmid and B. Corain.** Nanoparticulated gold: Syntheses, structures, electronics, and reactivities. *European Journal of Inorganic Chemistry*. 2003, Vol. 17, pp. 3081-3098.
5. **W.E. King, G.H. Campbell, A. Frank, B. Reed, J.F. Schmerge, B.J. Siwick, B.C. Stuart, and P.M. Weber.** *Journal of Applied Physics*. 2005, Vol. 97, 11, p. 111101.
6. **J.S. Kim, T. LaGrange, B.W. Reed, M.L. Taheri, M.R. Armstrong.** Imaging of Transient Structures Using Nanosecond In Situ TEM. *Science*. 2008, Vol. 321, pp. 1472-1475.
7. **J.M. Thomas.** A Revolution in Electron Microscopy. *Angewandte Chemie*. 2005, Vol. 44, pp. 5563 – 5566.
8. **O.-H. Kwon, B. Barwick, H.S. Park, J.S. Baskin, and A.H. Zewail.** 4D visualization of embryonic, structural crystallization by single-pulse microscopy. *PNAS*. 2008, Vol. 105, 25, pp. 8519–8524.
9. **M.L. Taheri, B.W. Reed, T.B. LaGrange, and N.D. Browning.** In situ laser synthesis of Si nanowires in the dynamic TEM. *Small*. 2009, Vol. 4, 12, pp. 2187-2190.
10. **C. Kisielowski, B. Freitag, M. Bischoff, H. van Lin, S. Lazar, G. Knippels, P. Tiemeijer, M. van der Stam, S. von Harrach, M. Stekelenburg, M. Haider, S. Uhlemann, H. Müller, P. Hartel, B. Kabius, D. Miller, I. Petrov, E.A. Olson, T. Donchev, E.A. Kenik, A.R. Lupini, J. Bentley, S.J. Pennycook, I.M. Anderson, A.M. Minor, A.K. Schmid, T. Duden, V. Radmilovic, Q.M. Ramasse, M. Watanabe, R. Erni, E.A. Stach, P. Denes and U. Dahmen.** Detection of Single Atoms and Buried Defects in Three Dimensions by Aberration-Corrected Electron Microscope with 0.5-Å Information Limit. *Microscopy and Microanalysis*. 2008, Vol. 14, pp. 469-477.
11. **D. J. Smith.** Development of Aberration-Corrected Electron Microscopy. *Microscopy and Microanalysis*. 2008, Vol. 14, pp. 2-15.
12. **O. Bostanjoglo, R. Elschner, Z. Mao, T. Nink, and M. Weingärtner.** Nanosecond electron microscope. *Ultramicroscopy*. 2000, Vol. 81, pp. 141-147.
13. **M.R. Armstrong, K. Boyden, N.D. Browning, G.H. Campbell, J.D. Colvin, W.J. DeHope, A.M. Frank, D.J. Gibson, F. Hartemann, J.S. Kim, W.E. King, T.B. LaGrange, B.J. Pyke, B.W. Reed, R.M. Shuttlesworth, B.C. Stuart, and B.R. Torralva.** Practical considerations for high spatial and temporal resolution dynamic transmission electron microscopy. *Ultramicroscopy*. 2007, Vol. 107, pp. 356-367.
14. **T. LaGrange, K. Boyden, C.G. Brown, G.H. Campbell, J.D. Colvin, W.J. DeHope, A.M. Frank, D.J. Gibson, V.F. Hartemann, J.S. Kim, W.E. King, P.J. Pyke, B.W. Reed, M.D. Shirk, R.M. Shuttlesworth, B.C. Stuart, B.R. Torralva, and N.D. Browning.** Single-shot dynamic transmission electron microscopy. *Applied Physics Letters*. 2006, Vol. 89, pp. 044105-044107.

Conductance of Au-BDT-Au molecular wires: A quantitative analysis

Zhanyu Ning¹, Wei Ji¹ and Hong Guo¹

¹ *Centre for the Physics of Materials and Department of Physics,
McGill University, Montreal,
QC, Canada H3A 2T8
ningz@physics.mcgill.ca*

The conductance of gold-benzenedithiol(BDT)-gold molecular junctions has been extensively studied since 1997¹. However, the difference between the experimental measurements and theoretical calculation are still within 1 or 2 orders of magnitudes. Even the theoretical investigations themselves have hardly been able to reach a consensus. The calculated results vary by 1 or 2 orders of magnitudes, depending on the adopted atomic models and/or *ab initio* methods⁶⁻¹⁸. This controversial situation persisted for more than ten years so far, although the non-equilibrium green's function combined with density functional theory(NEGF+DFT) method has achieved many successes in quantitative modeling of transport problems in many other molecular systems¹⁹⁻²². Some straight-forward questions might be raised: What makes the gold-BDT-gold system so special? Is our current *ab initio* technique lacking of some basic ingredients for this particular system? In this work, we attempt to resolve these issues.

First of all, using NEGF+DFT method(Generalized Gradient Approximation with Perdew-Burke-Ernzerhof 96 functional (GGA-PBE) is adopted), we calculated the transmission coefficient following the atomic model widely assumed in literatures^{1,4}. The result($0.4G_0$), which is consistent with the previous calculation^{11,16,18}, is found to be much higher than the experimental value($0.01G_0$)⁴. According to the analysis of density of states, it appears that the electronic hybridization between gold and BDT in this commonly adopted atomic model is overestimated, which results in the calculated high conductance through the junctions. It was reported that the conductance is very sensitive to the atomic geometry in molecular junctions²⁵. However, the detailed local geometry in this junction has not been well investigated so far. We thus performed a very careful surface calculation using standard PAW-PBE method as implemented in VASP. It was discovered that the $S-H$ bond is non-dissociative when BDT molecules attach to the gold surface via a gold ad-atom. After considering a plenty of representative atomic configurations, the non-dissociative structures are found to be always more stable than the H-dissociated structures by at least $0.2eV$. This non-dissociative adsorption is also supported by the previous experimental and theoretical work^{23,24}

Afterward, a further transport calculation based on the new atomic model with non-

dissociative $S-H$ bond has been carried out with the NEGF+PBE method. The calculated conductance of Au-BDT-Au junctions is found to be about $0.02G_0$, which is comparable with the experimental data of $0.011G_0$ ⁴. Our results strongly suggest that the non-dissociative $S-H$ bond plays an important role in describing the Au-BDT electronic coupling.

Finally, since the experiment was done in some solutions, it is considerably important to introduce the solvent effects, as discussed in this work.

-
- ¹ M. A. Reed, *et al.*, Science **278**, 252 (1997).
 - ² M. Tsutsui, *et al.*, Appl. Phys. Lett. **89**, 163111 (2006).
 - ³ E. Lörtscher, *et al.*, Phys. Rev. Lett. **98**, 176807 (2007).
 - ⁴ X. Y. Xiao, *et al.*, Nano. Lett. **4**, 267 (2004).
 - ⁵ M. Kiguchi, *et al.*, Appl. Phys. Lett. **89**, 213104 (2006).
 - ⁶ M. Di Ventra, *et al.*, Appl. Phys. Lett. **76**, 3448 (2000).
 - ⁷ K. Stokbro, *et al.*, Comp. Mat. Sci. **27**, 151 (2003).
 - ⁸ S. W. Huang, *et al.*, J. Chem. Phys. **121**, 6485 (2004).
 - ⁹ T. Tada, *et al.*, J. Chem. Phys. **121**, 8050 (2004).
 - ¹⁰ P. Delaney and J. C. Greer, Phys. Rev. Lett. **93**, 036805 (2004).
 - ¹¹ S. H. Ke, *et al.*, J. Chem. Phys. **123**, 114701 (2005). S. H. Ke, *et al.*, J. Am. Chem. Soc. **126**, 15897 (2004). S. H. Ke, *et al.*, J. Chem. Phys. **127**, 144107 (2007).
 - ¹² G. C. Solomon, *et al.*, J. Chem. Phys. **122**, 224502 (2005).
 - ¹³ R. B. Pontes, *et al.*, J. Am. Chem. Soc. **128**, 8996 (2006).
 - ¹⁴ J. Jiang, *et al.*, J. Chem. Phys. **124**, 34708 (2006).
 - ¹⁵ D. Q. Andrews, *et al.*, J. Chem. Phys. **125**, 174718 (2006).
 - ¹⁶ C. Toher and S. Sanvito, Phys. Rev. Lett. **99**, 56801 (2007). Phys. Rev. B **77**, 155402 (2008).
 - ¹⁷ D. Q. Andrews, *et al.*, Nano. Lett. **8**, 1120 (2008).
 - ¹⁸ M. Strange, *et al.*, J. Chem. Phys. **128**, 114701(2008).
 - ¹⁹ C. C. Kaun, *et al.*, Phys. Rev. B **67**, 121411(R) (2003).
 - ²⁰ C. C. Kaun and H. Guo, Nano Lett. **3**, 1521 (2003).
 - ²¹ T. Frederiksen, *et al.*, Phys. Rev. Lett. **93**, 256601 (2004).
 - ²² Z. Ning, *et al.*, Phys. Rev. Lett. **100**, 056803 (2008).
 - ²³ I. I. Rzeznicka, *et al.*, J. Phys. Chem. B **109**, 15992 (2005).
 - ²⁴ J. G. Zhou and F. Hagelberg, Phys. Rev. Lett. **97**, 045505 (2006).
 - ²⁵ M. Kamenetska, *et al.*, Phys. Rev. Lett. **102**, 126803 (2009).

FABRICATION, ASSEMBLY AND CHARACTERISATION OF GOLD ON-CHIP NANOWIRE ELECTRODES FOR ELECTROCHEMICAL APPLICATIONS

*Karen Nolan, John MacHale, Aidan J. Quinn, Alan O’Riordan
Tyndall National Institute, Lee Maltings, Prospect Row, Cork, Ireland*

Compared to traditional macroelectrodes, nanoscale electrodes have tremendous potential when employed in electrochemical studies; due to enhanced sensitivity arising from increased mass transport to the electrode (convergent, 3D, diffusion) and low background charging currents (due to reduced surface area)^[1,2]. Future electrochemically-based diagnostic products, such as sensors, will require sensing elements with greatly enhanced performance. Nanoelectrodes offer a viable route to attaining this performance improvement. However, a critical challenge in the development of nanoelectrodes is developing a low cost, robust and reproducible fabrication process for the fabrication of on-chip nanowire electrodes with critical dimensions 200 nm down to 50 nm and to electrically contact them in order to attain high measurable currents (nA - μ A).

In this talk I will be present a novel route, we have recently developed, for fabrication and integration of gold nanowires, ranging in length from tens to hundreds of microns, with typical a heights and widths of \sim 250 nm and \sim 250 nm, respectively. The structural and electrical properties of these nanowire electrodes were characterised using SEM, AFM, and their electrical characterisation (two-point and four-point) and electrochemical performance characterised using ferrocene, as a model redox analyte. To fabricate nanowires, thin metal film of gold \sim 200 nm, was evaporated onto a smooth facet of an epoxy block and further encapsulated in epoxy. Ultramicrotomy was employed to section an epoxy block (normal to the gold film surface) to form nanomembranes bearing nanowires. Figure 1 (a) displays a schematic representation of this process.

Following fabrication, the nanowires were assembled at silicon chip substrates comprising of arrays (32 x 32) of unique binary alignment markers. Electrical contacts were deposited onto nanowires using standard lithography metal evaporation and lift-off techniques, employing the binary markers for alignment. Electrical contacts were designed with pitches ranging from 10 μ m to 200 μ m, to define the active length of the nanowire electrode. An example of a nanowire electrically contacted is shown in Figure 1(b); below. Room temperature electrical characterization of nanowires demonstrated Ohmic behaviour, e.g. a typical gold nanowire \sim 125 μ m in length had an average resistance of \sim 52 Ω correlating well to theoretical models, thus showing that nanowires prepared and integrated in this manner displayed low contact resistance. For electrochemical characterisation, a further passivation layer was deposited on a chip surface and an opening etched in this layer to expose the underlying nanowire. This enabled direct interaction between the nanowire and the local environment. Cyclic

voltammograms obtained using nanowire electrodes exhibited sigmoidal profile consistent with work previously reported using the ferrocene as a validation model^[3].

References:

[1] Compton, R. G.; Wildgoose, G. G.; Rees, N. V.; Streeter, I.; Baron, R., Design, fabrication, characterisation and application of nanoelectrode arrays. *Chemical Physics Letters* 2008, 458, (1-6), 1-17.

[2] Murray, R. W., Nanoelectrochemistry: Metal nanoparticles, nanoelectrodes, and nanopores. *Chemical Reviews* 2008, 108, (7), 2688-2720.

[3] Lanyon, Y. H., De Marzi, G., Watson, Y. E., Quinn, A. J., Gleeson, J. P., Redmond, G., Arrigan, D. W. M., *Anal. Chem.*, 2007, 79, 3048-3055.

Figures:

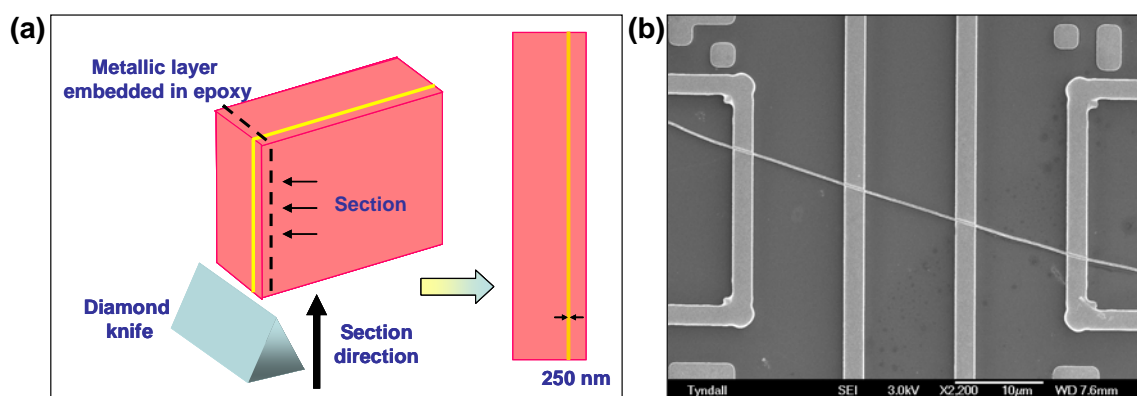


Figure 1(a): a schematic representation of the fabrication of nanowires **(b):** A Scanning Electron Micrograph of an assembled and electrically contacted gold nanowire (approx 10 µm pitch).

Crystalline Structure of Electrospun Peptide

Wiwat Nuansing, Alexander Bittner

CIC nanoGUNE, Tolosa Hiribidea, 76, 20018 Donostia – Sansebastian, Spain

w.nuansing@nanogune.eu

We demonstrate the ability to fabricate a small peptide modified with a large aromatic group into fiber form with diameters ranging in micrometers by using the electrospinning technique [1, 2].

Fmoc-Phenylalanyl-Glycine (Fmoc is based on the 6-5-6 ring system of fluorene) was dissolved in a highly polar solvent (hexafluoro-2-propanol) and a droplet was polarized to up to 15 kV in a electrospinning system. The resulting peptide fibers were studied using confocal Raman spectroscopy and compared to known IR spectra of Fmoc-Phe.

An optical microscopic image of electrospun Fmoc-Phe-Gly and a micro-Raman confocal image are shown in Fig 1. The Raman spectra (Fig 2.) feature mainly vibrations of the fluorenyl group. Scanning electron microscopy (SEM) (Fig 3), micrometer-sized fibers are composed of rod-like crystallites of ~350 nm diameters.

We suggest the formation of peptide fibers because the aromatic residues in the peptide (fluorenyl and phenyl) cause π -stacking of the molecules [3]. Hence molecules assemble into fibers when electrospinning assists the molecular alignment.

References:

- [1] D. Li, Y. Xia, *Adv. Mater.*, **16** (2004) 1151-1170.
- [2] T.J Sill, H.A Recum, *Biomater.*, **29** (2008) 1989-2006.
- [3] G. Singh, A.M Bittner, S. Loscher, N. Malinowski, K. Kern, *Adv. Mater.*, **20** (2008) 2332.

Figures:

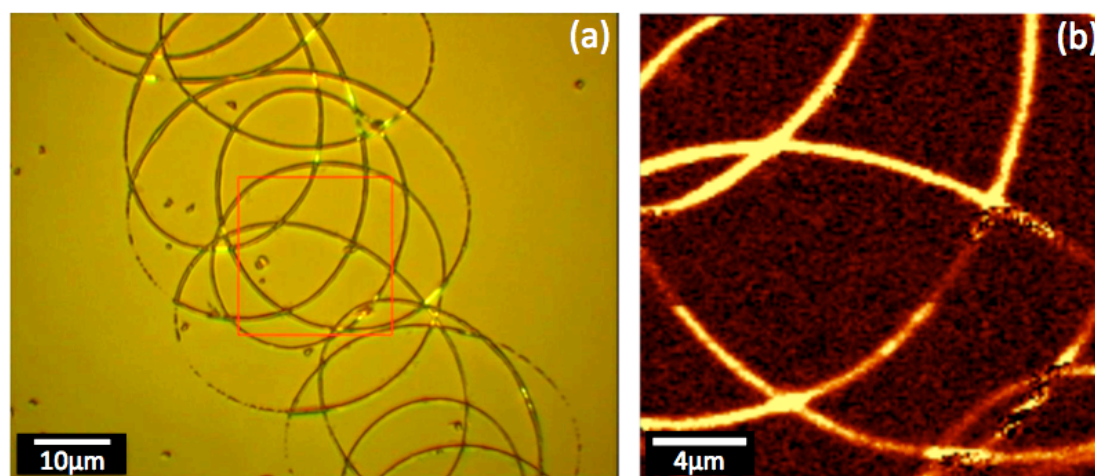


Fig 1. (a) Optical microscopic image of electrospun Fmoc-Phe-Gly on glass substrates (b) Micro-Raman confocal image at the red by used the filter at $1594.6 - 1631.4 \text{ cm}^{-1}$.

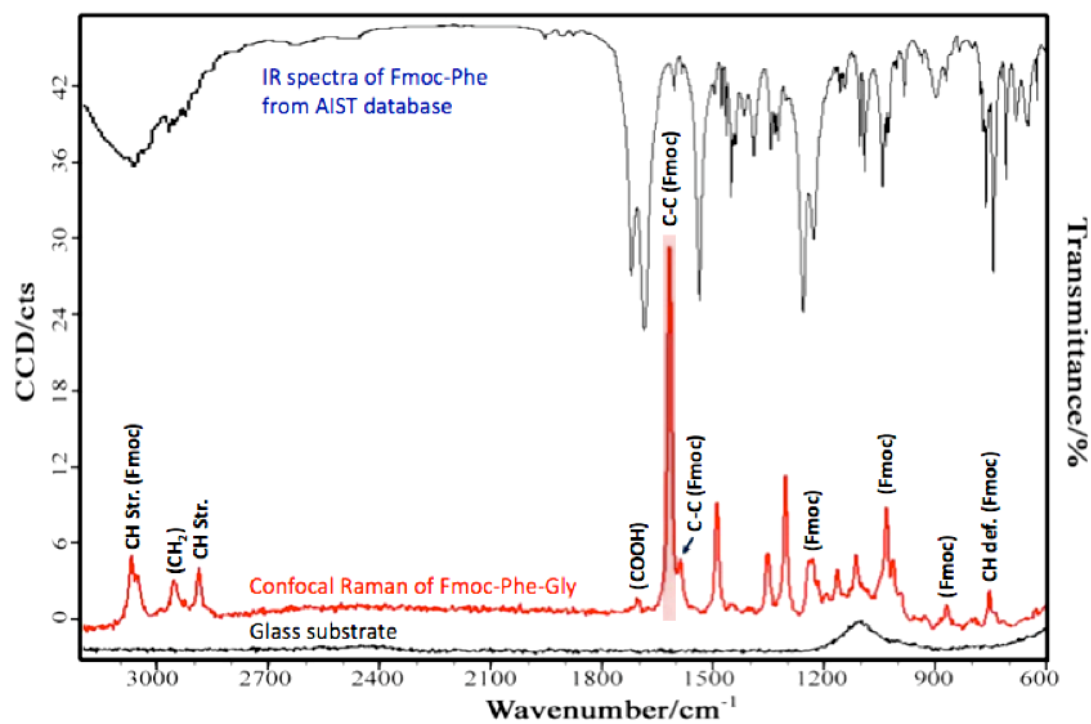


Fig 2. Confocal Raman spectra of the electrospun Fmoc-Phe-Gly fibers on glass substrates compared to IR spectra of Fmoc-Phe from AIST database.

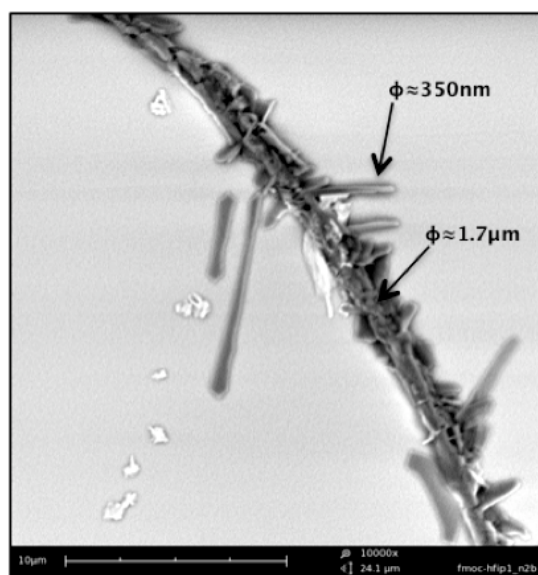


Fig 3. SEM micrograph of the electrospun Fmoc-Phe-Gly.

High Power Durable Nano Resonators with Epitaxial Aluminum Electrodes

R. Nüssl, D. Beckmeier, T. Sulima, I. Eisele and W. Hansch
Institute of Physics, University of the Federal Armed Forces, Werner-Heisenberg-Weg,
85579 Neubiberg, Germany
rudolf.nuessl@unibw.de

Highly textured aluminum films have been grown on mono-crystalline lithiumtantalate (LiTaO₃) using ultra thin titanium films as adhesion layers for pure aluminum. Texture measurements by means of EBSD (Electron Backscatter Diffraction) show that the thickness of the intermediate titanium layer significantly influences texture and grain structure of the overlying 400nm aluminum film. Increasing the thickness of the titanium layer from 0 nm to 20 nm leads to a change of aluminums texture from unoriented polycrystalline over highly oriented in single direction to highly oriented in twin structure.

Highly textured or epitaxial thin aluminum films on piezoelectric single-crystalline substrates like LiTaO₃ have attracted much interest due to their high stress durability at ultra high frequencies since these films improve the performance of surface acoustic wave (SAW) devices significantly [1]. On a blank LiTaO₃ substrate aluminum forms a polycrystalline film with random crystal orientations. To overcome this problem an ultra thin adhesion layer of pure titanium has been used allowing aluminum to grow with a smooth surface and highly textured with crystal axis $\langle 111 \rangle$ parallel to the sample normal. Electron Backscatter Diffraction (EBSD) technique supported by Atomic Force Microscopy (AFM) has been applied to obtain information about films microstructure. In our experiment we have found that the surface roughness can be minimized while the collective alignment of grains in one single direction is maximized, if an optimized thickness of the titanium underlayer is chosen.

Starting with a piezoelectric substrate (LiTaO₃, 42° Y-X-Cut) six samples have been prepared by deposition of an ultra thin titanium adhesion layer (0, 1, 2, 5, 10, 20 nm) followed by the main metallization comprising of 400 nm pure aluminum. Sequential deposition of titanium and aluminum has been performed by electron beam evaporation in an ultra-high-vacuum environment.

Results of EBSD and AFM analysis are shown in Fig. 1 to Fig. 3. AFM images (Fig. 1-3b) show the surface topography of the samples and the determined average surface roughness (Ra). Different grey scales in the EBSD maps (Fig. 1-3a) indicate different out of plane grain orientations, while white-colored grains represent grains in the major crystal orientation. The pole plots (Fig. 1-3c) show the in-plane textures and the inverse pole plots (Fig. 1-3d) show the out-of-plane textures of the aluminum films.

The first two samples (without titanium and with 1 nm titanium) in Fig. 1 show polycrystalline growth of aluminum with random in-plane orientations (see grain maps and pole plots). AFM measurements demonstrate rough surfaces (Ra > 25 nm).

In contrast, samples with 2 nm and 5 nm titanium adhesion layer show very smooth surfaces (Ra < 3 nm), as depicted in Fig. 2b, and a highly oriented crystal growth with a strong $\langle 111 \rangle$ out-of-plane texture, as shown in the inverse pole plot in Fig. 2d. The triple of dark spots in the pole plot (Fig. 2c) indicates one single in-plane orientation, what motivates us to call these films quasi-epitaxial.

The samples formed with 10 nm and 20 nm titanium (Fig. 3) show a strong growth of $\langle 111 \rangle$ Al as well. These samples exhibit the same main crystal orientation as the samples with 2 nm and 5 nm, but the aluminum films tend to develop a second in-plane orientation, that is rotated 180° round the samples normal relative to the main crystal orientation, as revealed by the pole plot. The black areas in the EBSD map (Fig. 3a) illustrate these 180° rotated grains.

Fig. 4 shows the orientation of the aluminum lattice on the monocrystalline substrate from the topview, which has been reconstructed from EBSD data. To confirm the crystal direction of

aluminum, found by our EBSD measurements, we fabricated SAW devices. We applied heavy load and visualized the degradation of the electrodes by means of scanning electron microscopy (SEM), as shown in Fig. 5. The SEM measurements indicate triangular grains sunk in the electrode fingers due to material migration of aluminum. The grains show the same crystal direction which is revealed by EBSD.

Our results show that titanium as an intermediate layer can strongly enhance the $\langle 111 \rangle$ out-of-plane texture of the overlying aluminum film. These results agree well to the results of other work groups [1, 2].

The appearance of a second in-plane Al texture (see Fig. 3) can be explained if one takes into account that titanium develops its own $\langle 0001 \rangle$ texture as its layer thickness is increased [2]. With its hexagonal atomic arrangement towards the surface $\langle 0001 \rangle$ titanium offers two energetically equal states for the growth of $\langle 111 \rangle$ aluminum, which are rotated by 180° compared to each other, as shown in Fig. 6. This atomic arrangement might explain the appearance of Al twin-grains as thickness of the titanium adhesion layer is increased.

References:

[1] O. Nakagawara, "High power durable SAW antenna duplexers for W-CDMA with epitaxially grown aluminum electrodes," 2002 IEEE Ultrasonics Symposium, Proc. (2002), 43.
 [2] A. Kamijo, "A highly oriented Al[111] texture developed on ultrathin metal underlayers," J. Appl. Phys. Vol. 77, No. 8, 1995.

Figures:

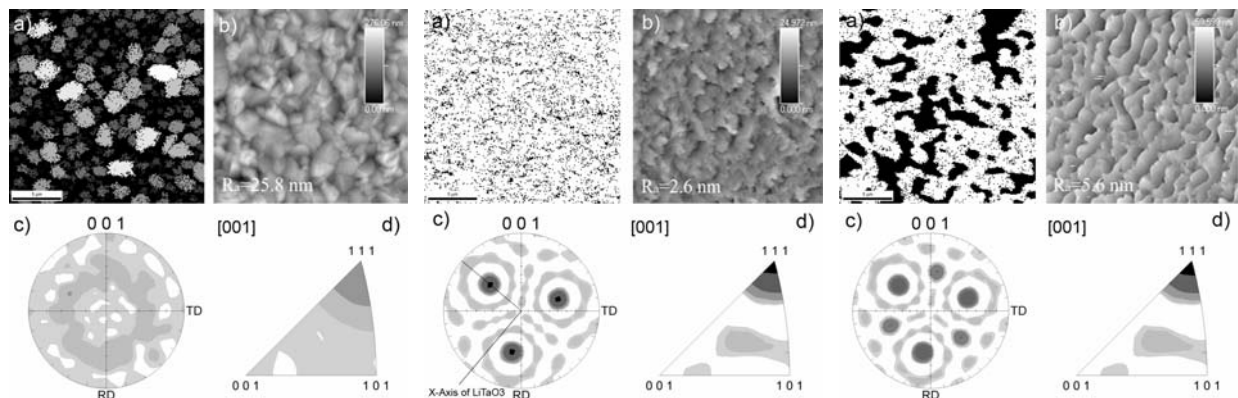


Fig. 1. Grain structure and texture of 400 nm Al with 0 nm or 1 nm titanium underlayer

Fig. 2. Grain structure and texture of 400 nm Al with 2 nm or 5 nm titanium underlayer

Fig. 3. Grain structure and texture of 400 nm Al with 10 nm or 20 nm titanium underlayer

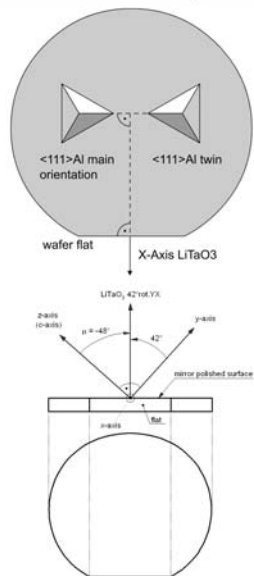


Fig. 4. In-plane-orientation of $\langle 111 \rangle$ Al on LiTaO₃

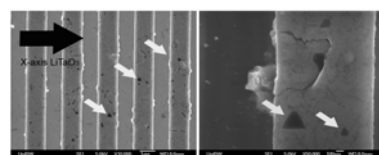


Fig. 5. Triangular grains sunk in the electrodes due to material migration in heavily loaded SAW devices

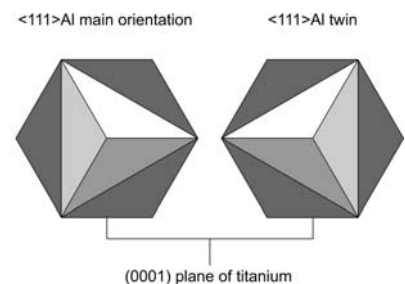


Fig.6. Alternatives of $\langle 111 \rangle$ Al to grow on titaniums (0001) plane

COMPUTER BASED METHODS FOR ACCURATE BACKGROUND REMOVAL IN SPM METROLOGY APPLICATIONS.

J. O'Mahony¹, L McDonnell²

¹ Pharmaceutical and Molecular Biotechnology Research Centre, Waterford Institute of Technology, Cork Road, Waterford, Ireland.

²Centre for Surface & Interface Analysis, Department of Applied Physics & Instrumentation, Cork Institute of Technology, Rossa Avenue, Cork, Ireland
jomahony@wit.ie

Scanning probe microscopy (SPM) images contain contrast information derived from the superposition of a true surface on a curved and tilted background. This background component comprises of the additional trajectory of the SPM scanner due to the sample tilt and the scan range. Polynomial approximation routines employing either least squares or interpolation and extrapolation methods are considered appropriate for the estimation and removal of this background. Many approximation methods require the sampling of a fixed set of data points that may include surface “peaks” and “troughs” resulting in an erroneous estimation of the scanner induced background. This error introduces an artificial “hollow” around topographic “peaks” limiting the ability of the SPM to consistently provide true information over larger scan ranges. Some algorithms address this problem by offering the user the option of removing specified portions of the image from the background data set. Such an approach can introduce other artifacts and can involve excessive user interaction.

In a previous paper we have shown that selecting points from each image linescan that best approximate the background and interpolating a polynomial through these background points provides a high quality fit to the scanner background [1]. A simple background selection procedure based on the selection of the minimum values within different regions of the line profile is the quickest way to obtain the data points that best represent the scanner curvature. This method of background selection is subject to error from negative going outliers that may be present in the data set and a more rigid background selection criterion using a median value provides a solution to this problem. Modifications to the basic interpolation algorithms for an improved quality of fit will be discussed. Least squares polynomial fitting will always provide the most accurate determination of the scanner background provided that the polynomial is estimated using only background data points. Figure 1 compares the quality of our estimation method with that of a commercial algorithm.

We will discuss appropriate methods for background selection that will provide the best possible fit for surfaces comprising of specifically bound particles, the bias in the background estimate only being limited in theory by the roughness of the substrate. In addition we will show how predictor corrector methods can be employed as a true on-line method of background extraction. These methods provide the fastest possible means of removing the scanner background and may have applications in high speed AFM, but due to the indeterminate nature of the occurrence of binding events, there is no way of guaranteeing the sampling of background data points only. The use of forgetting factors allow the effects of foreground events to be minimised.

In this paper we report on the development of these background estimation methods for the automatic removal of scanner background that can allow the unambiguous measurement of 3 nm sized particles on a surface of 1 nm roughness. We further discuss the merits of each method with respect to their application for the measurement of ferritin/anti-ferritin binding events occurring on activated biological surfaces.

References

[1] L.McDonnell, J.O'Mahony and G.Roe, Physikalische-Technische Bundensanstalt, Braunschweig, **vol.F-44**, (2002), pp.22-28.

Figures

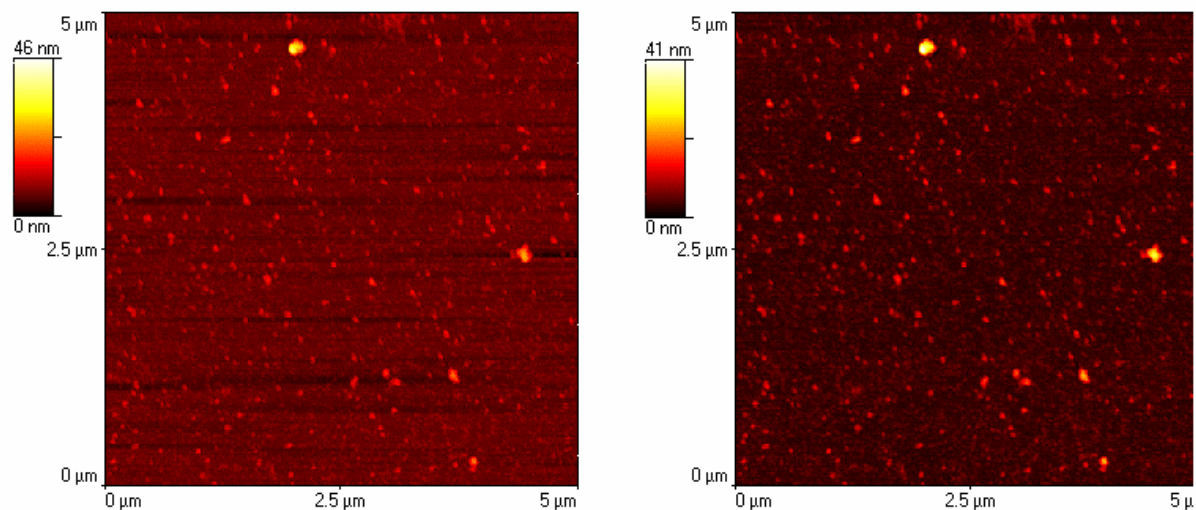


Figure 1. Comparison of the quality of fit provided by the Least Squares Algorithm with background selection (RHS) and the quality of fit provided by a commercial leveling algorithm (LHS).

Integration Process of Carbon Nanotube Piezoresistive Elements into Microsensors

Naoki Oda¹, Takahito Ono¹, Masayoshi Esashi²

¹Graduate School of Engineering, Tohoku University, 6-6-01 Aza-Aoba, Aramaki, Aobaku, Sendai 980-8579, Japan

²The World Premier International Research Center Initiative for Atom Molecule Materials, Tohoku University, , 6-6-01 Aza-Aoba, Aramaki, Aobaku, Sendai 980-8579, Japan
ono@nme.mech.tohoku.ac.jp

Carbon nanotubes (CNTs) are very attractive materials owing to its large gage factor as a piezoresistive element. Thus, CNTs have high potential abilities as a strain gage for various sensor applications. However, batch-fabrication process for integrating CNTs is generally difficult because CNTs are flexible and easily deformed during microfabrication process, in addition adhesion force to substrate is very weak. In this paper, we report the batch-fabrication process of integration of carbon nanotubes piezoresistive elements into microstructures based on chemical vapour deposition of carbon nanotubes, and deposition of SiO₂ onto the CNTs.

It has been reported that semiconductive CNTs exhibit a gage factor of over 1000 [1,2], also metallic CNTs exhibits a gage factor of ~200 [3]. In generally, a gage factor of silicon piezoresistor is ~100, depending on its dopant concentration, thus, CNTs are very useful for gaining the sensitivity of piezoresistive microsensors.

In order to demonstrate the integration of CNTs into microstructure, a cantilevered structure shown in Fig. 1 is fabricated in this research. At the support part of the freely-suspended SiO₂ cantilever, the strain gage of CNTs, which are buried into SiO₂, is formed. This CNTs buried into SiO₂ are regarded as a composite of CNTs and SiO₂ (CNTs-SiO₂), where the CNTs are directed into the longitudinal direction of the cantilever. The CNTs-SiO₂ resistive elements as a strain gage are electrically connected by Cr-Au wires. The bending of the cantilevered structure will produce the strain in the longitudinal direction of CNTs and change their resistance.

Figure 2 shows the schematic of the fabrication process. Starting material is Si wafer, and SiO₂ is deposited on the surface by plasma enhanced chemical vapour deposition (PECVD) using TEOS (Si(OC₂H₅)₄) as a gas source. CNTs are grown from a 1 nm-thick Fe pattern using PECVD (shown in upper figure of Fig. 3). We employed a CNTs alignment technique in order to form aligned CNTs as reported in Ref. [3]. In this method, the substrate with CNTs is dipped into ethanol and taken out from the solution. The CNTs can be well aligned into in-plane direction on the surface as shown in the lower figure of Fig. 3. Next, the CNTs are buried into SiO₂ using ozone-TEOS CVD, and this process can form the CNTs-SiO₂ composite as shown in Fig. 4. After photolithography, the CNTs-SiO₂ are patterned by reactive ion etching (RIE) using a mixture of SF₆ and Xe gases. Figure 5 shows the SEM image after the patterning. Next, Cr-Au pattern are formed for making electrical wires and pads. Then, cantilever structures are formed by patterning the SiO₂ using RIE. Finally, the cantilevers with a total thickness of 4 μm are released by etching the Si substrate from the backside using resist as a mask.

Figure 6 shows SEM images of the completed microstructures. On the surface of the support part, piezoresistors of CNTs-SiO₂ is formed. We believe that this integration process of the piezoresistive elements of CNTs can applied to various sensor applications.

References:

- [1] R. J. Grow et al., Appl. Phys. Lett., **86** (2005) 093104.
- [2] C. Stampfer et al., Nano Lett., **6** (2006) 1449.
- [3] C. Stampfer et al., Nano Lett., **6** (2006) 233.
- [4] Y. Hayamizu et al., Nature Nanotechnology, **3** (2008) 289.

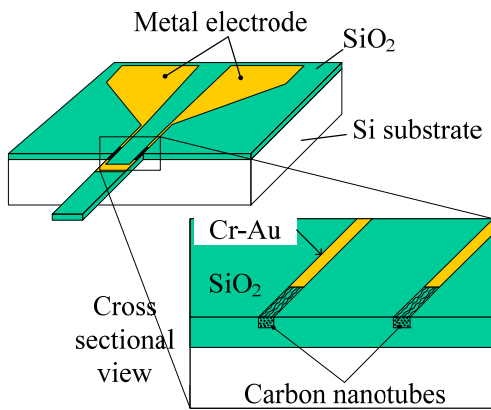


Figure 1. Schematic of fabricated microstructure with carbon nanotube piezoresistive elements as a strain gage.

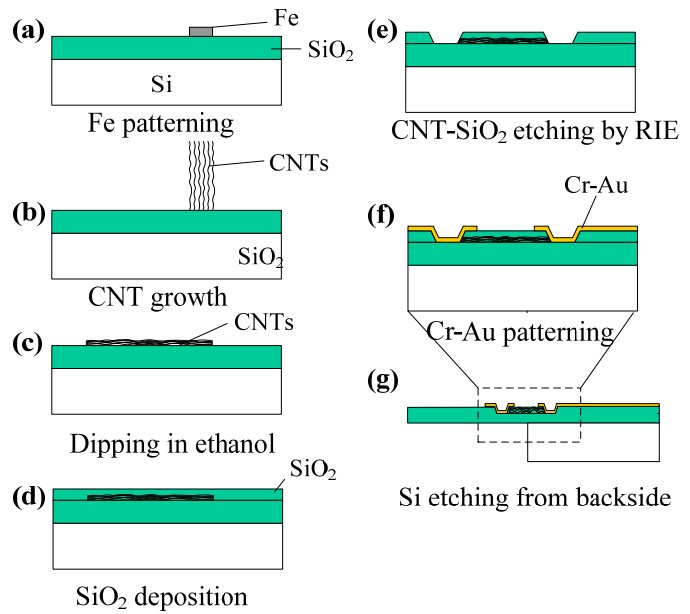


Figure 2. Microfabrication process of the integration of carbon nanotube piezoresistive elements.

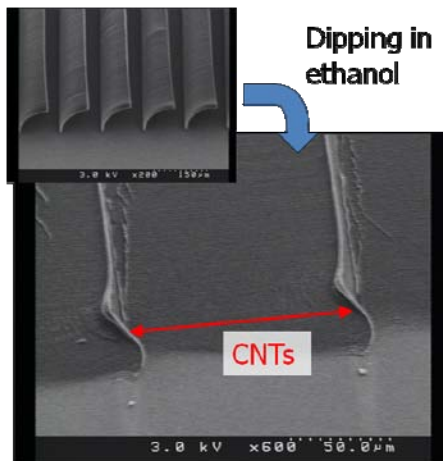


Figure 3. SEM image carbon nanotubes aligned on the SiO₂ surface.



Figure 4. SEM image of CNTs-SiO₂. The CNTs aligned on the SiO₂ surface are buried into SiO₂ using ozone-TEOS CVD.

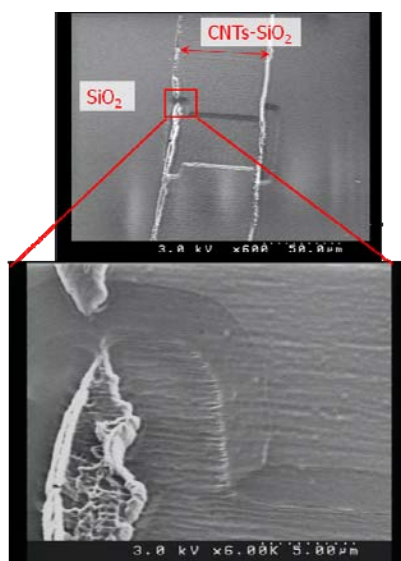


Figure 5. SEM image of the patterned CNTs-SiO₂ using reactive ion etching.

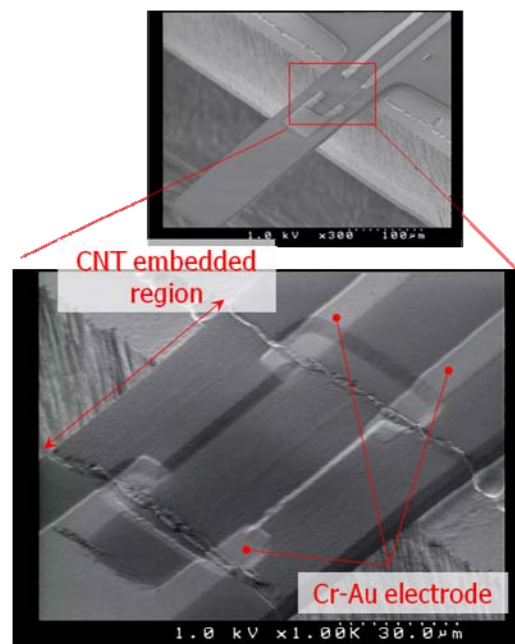


Figure 6. SEM image of completed microcantilever. At the support part, carbon nanotube piezoresistors are formed, and the piezoresistors are electrically connected via Cr-Au electrical wires.

An array of quantum dots as a spin filter device by using Dicke and Fano effects

Pedro A. Orellana¹, Judith Ojeda², Monica Pacheco²

¹*Departamento de Física, Universidad Católica del Norte,
Avenida Angamos 0610, Antofagasta, Chile*

²*Departamento de Física, Universidad Técnica Federico Santa María,
Casilla 110-V, Valparaiso Chile*

orellana@ucn.cl

Recently, there has been much interest in understanding the manner in which the unique properties of nanostructures may be exploited in spintronics devices, which utilize the spin degree of freedom of the electron as the basis of their operation [1-2]. A natural feature of these devices is the direct connection between their conductance and their quantum-mechanical transmission properties, which may allow their use as an all-electrical means for generating and detecting spin polarized distributions of carriers.

Quantum dots are man-made nanostructures in which electrons are confined in all space dimensions [3]. Energy and charge quantization results from this confinement. As both features are present in real atomic systems, useful analogies between *real* and *artificial* atomic systems have been exploited recently. Enforcing this analogy, Fano [4-5] and Dicke effects [6] were also found to be present in quantum dot configurations. On the other hand, Song *et al.* [2] described how a spin filter may be achieved in open quantum dot systems, by exploiting the Fano resonances that occur in their transmission characteristic. In a quantum dot in which the spin degeneracy of carrier is lifted they showed that the Fano effect may be used as an effective means to generate spin polarization of transmitted carriers and that electrical detection of the resulting polarization should be possible.

In a previous work [7], we showed that in side-coupled double quantum-dot system the transmission shows a large peak-to-valley ratio. Moreover, the difference of energy between the resonances and antiresonances can be controlled adjusting the difference between the energy levels of the two quantum dots by gate voltages due to the Dicke effect. The Dicke effect in optics takes place in the spontaneous emission of a pair of atoms radiating a photon with a wavelength much larger than the separation between them [6]. The luminescence spectrum is characterized by a narrow and a broad peak, associated with long and short-lived states, respectively. The former state, coupled weakly to the electromagnetic field, is called subradiant, and the latter, strongly coupled, a superradiant state. In the present work, we show that the above properties can be used to design an efficient spin filter with a quantum dot array system. We show that by controlling the Fano and Dicke effects this system can be used as an efficient spin filter even for small values of the magnetic field.

In this work we propose a new design of a spin-dependent polarizer. The device consists of a quantum dot array coupled to leads, as shown schematically in Fig1. By lifting the spin degeneracy of the carriers in a quantum dot by means of a magnetic field, Fano and Dicke effects are used as effective means to generate spin polarization of the electrical current. A detailed analysis of the spin-dependent transmission and polarized current is carried out. For instance, in Fig. 2 we show a contour plot with the weighted spin polarization for a fixed magnetic field of as a function of the Fermi energy and Δ the asymmetric parameter. The region of maximum of polarization is centered on the Zeeman energy and it grows with Δ .

References:

- [1] S. Datta and B. Das, Appl. Phys. Lett. **56**, (1990) 665.
 [2] J. F. Song, Y. Ochiai and J. P. Bird, Appl. Phys. Lett. **82** (2003) 4561.
 [3] L. Jacak, P. Hawrylak and A. Wojs, Quantum Dots (Springer--Verlag, Berlin, 1998).
 [4] U. Fano, Phys. Rev. **124**, (1961) 1866.
 [5] K. Kobayashi, H. Aikawa, A. Sano, S. Katsumoto and Y. Iye, Phys. Rev. B **70**, (2004) 035319.
 [6] Dicke R H, Phys. Rev. **89** (1953) 472.
 [7] P. A. Orellana and F. Domínguez-Adame, phys.stat. sol. (a) **203**, (2006) 1178.

Figures:

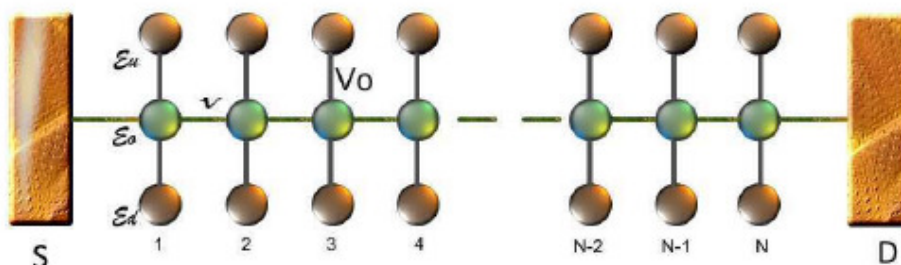


Fig 1: Schematic view of a quantum dot array coupling to leads.

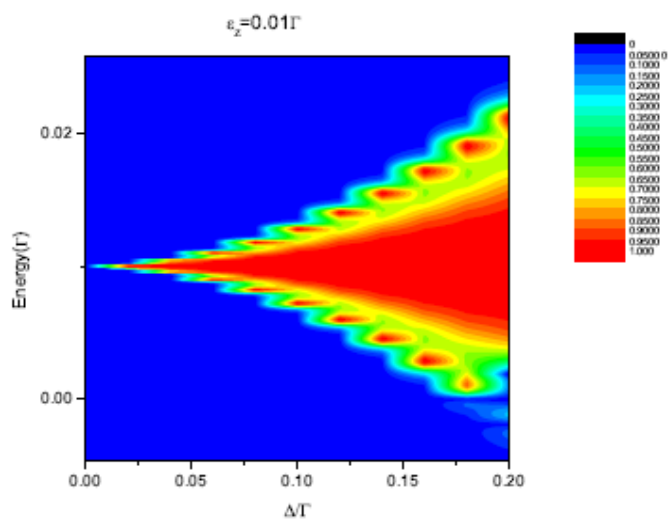


Fig 2: Contour plot of weighted spin polarization for the quantum dot array as a function of the Fermi energy and Δ for fixed magnetic field.

TWO-DIMENSIONAL BANDS OF RARE EARTH/GOLD SURFACE ALLOYS MEASURED WITH ARPES

M. Ormaza¹, M. Corso², L. Fernández², F. Schiller³, J. E. Ortega^{1,2,3}, Mathieu Verstraete⁴ and Angel Rubio^{2,3,4}

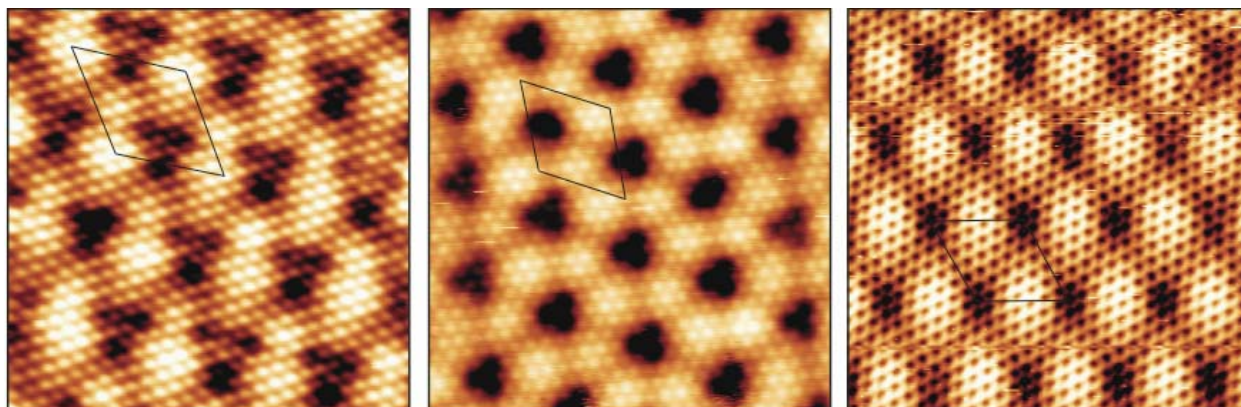
¹*Departamento de Física Aplicada I, Universidad del País Vasco, San Sebastián, Spain*

²*Donostia International Physics Center DIPC, San Sebastián, Spain*

³*Centro de Física de Materiales, Centro Mixto CSIC/UPV-EHU, San Sebastián, Spain*

⁴*Dpto. de Física de Materiales, Universidad del País Vasco, Centro Joxe Mari Korta, Av. de Tolosa 72, E-20018 San Sebastián, Spain*

The high temperature reactive deposition of rare earths (RE) on Au(111) has been thoroughly investigated combining STM and Angle Resolved Photoemission (ARPES) experiments. These materials are attractive for their possible exploitation in several fields as magnetic recording or hydrogen storage. We have focused on the reactive epitaxy of Gd, La, and Ce, where we have found that, under specific growth parameters, one can obtain RE/Au alloyed monolayers and bilayers with extraordinary crystalline perfection (see the Figure below). In the three metals the optimum surface structure, namely the one exhibiting homogeneous alloying over the whole surface, corresponds to the REAu₂ stoichiometry. Moreover, the lattice mismatch between the REAu₂ layers and the Au (1×1) substrate gives rise to long-range periodic Moiré patterns, whose lattice constant varies from 32±2 Å in La to 33±2 Å in Ce and to 38±2 Å in Gd (see the Figure below). The latter has been successfully tested as a growth template for magnetic Co nanodot arrays. By means of ARPES we have studied the two-dimensional band structure of such surface alloys. ARPES experiments have been carried out at the Synchrotron Radiation Center in Wisconsin. The band structure is similar in all cases with minor spectral intensity and energy variations. The results have been compared with band structure calculations performed by M. Verstraete and A. Rubio within the European Theoretical Spectroscopy Facility (ETSF) project. Theoretical calculations and experimental bands basically agree to explain the band dispersion, energy position, and orbital nature of the bands. Fine variations among the different RE compounds are explained in qualitative terms.



STM images (14.3×14.3 nm²) showing the atomic structure of the Gd-Au (left), the La-Au (center), and the Ce-Au (right) surface alloys grown by reactive epitaxy on Au(111). The Moiré pattern, whose unit cell is pictured in all cases, arises due to the mismatch with the Au(111) lattice underneath.

Quantum transport in carbon-based nanostructures perturbed by time-dependent potentials.

M. Pacheco, A. Latgé, C. G. Rocha

Universidad Santa María, Physics Department, Avda. España 1680, Valparaíso, Chile
monica.pacheco@usm.cl

Novel quantum transport phenomena rise when nanoscale materials are perturbed by external time-dependent fields [1-2]. Comparing with stationary fields, a time-varying one can effectively modulates the quantum phase of the electronic wave functions, bringing new possibilities of technological applications [3]. However, most experimental and theoretical studies on carbon-based nanomaterials have been made for dc transport properties and more extensive studies are still lacking to take advantage to this useful technique for novel nanodevices applications.

In this work we study transport properties of carbon nanotubes and graphene nanoribbons under time-dependent perturbations, external magnetic fields and electrostatic gates. In particular we investigate nanostructures which can confine electronic states realizing a carbon-based double quantum-dot (CDQD). These structures are fabricated by forming tunnel barriers within the nanotube by means of topological defects or obtained by bending or kinking mechanically the tube using an AFM [4]. CDQD are also obtained by patterning a single-layer graphene by electron-beam lithography [5]. In a CDQD the conductance as a function of the gate voltage presents resonances which will be modified due to the time-varying potential [6]. We will study the feasibility that the conductance of carbon-based CDQDs devices can be controlled by tuning the frequency and radiation field intensity (AC parameters) and by applying gate or source-drain voltages.

The combination of both external magnetic fields and time-dependent potentials provides alternative schemes to modulate the Fabry-Perot conductance oscillations [7]. We will study the conductance of driven three-terminal carbon-based systems in the Fabry-Perot interference regime in the presence of a magnetic field and external time-dependent fields applied on the gate plate or as a bias voltage.

We solve the problem using standard non-equilibrium Green's function (NGF) techniques. The conductance is calculated by the Landauer-type formula in terms of the transmission function which is obtained from the retarded and advanced Green's function of the carbon-based system in the presence of the field, and its coupling to the leads.

References:

- [1] G. Platero and R. Aguado, Phys. Rep. **395** (2004) 1
- [2] P. A. Orellana, and M. Pacheco, Phys. Rev. B **75** (2007) 115427
- [3] B. L. Altshuler, and L. I. Glazman, Science **283** (1999)1864; C. Kocabas, H-sik Kim, T. Sanks, J. A. Rogers, A. A. Pesetski, J. E. Baumgardner, S. V. Krishnaswamy, and H. Zhang, PNAS **105** (2008)1405
- [4] P. Jarillo-Herrero et al. Phys. Rev. Lett. **94** (2005)156802; S. Sapmaz et al. Nano Lett. **6** (2006)1350 ; M. J. Biercuk et al. Nano lett. **4** (2005)2499.
- [5] C. Stampfer, E. Schurtenberger, F. Molitor, J. Güttinger, T. Ihn, and K. Ensslin, Nano Lett. **8** (2008) 2378.
- [6] L. E. F. Foa Torres, and G. Cuniberti, App. Phys. Lett. **94** (2009) 222103
- [7] B. Raquet, R. Avriller, B. Lassagne, S. Nanot, W. Escoffier, J-M Broto, and S. Roche, Phys. Rev. Lett. **101** (2008) 046803.

Sensing Properties of Oxide Core-Shell Nanofibers Synthesized by a Novel Two-Step Method

Jae Young Park, Sun-Woo Choi and Sang Sub Kim

School of Materials Science and Engineering, Inha University, Incheon 402-751, Korea

sangsub@inha.ac.kr

Core-shell nanomaterials, a type of heterostructured nanomaterial, are expected to be widely used in the areas of catalysis, drug delivery, chemical and bio sensors, etc. As the demand for fabricating various core-shell nanomaterials and nanostructures increases, it is becoming important to develop new methods of synthesizing a wide variety of core-shell nanomaterials in order to modify or improve the properties of monolithic nanomaterials [1-3].

In this work, we propose a novel method of synthesizing oxide core-shell nanofibers by employing electrospinning and atomic layer deposition (ALD) in sequence. Electrospinning is known to be a simple, inexpensive technique to synthesize nanofibers or nanowires in a highly reproducible manner from polymer solutions or melts [4]. ALD is a technique that allows for the growth of smooth and conformal films on the underlying surface with atomic-scale thickness control at low temperatures [5].

The preparation of some different kinds of oxide core-shell nanofibers including TiO₂-ZnO and SnO₂-ZnO core-shell nanofibers using the method will be presented, as an example of its effectiveness. Then, the hybrids in the form of oxide core-shell nanofibers were tested as platform to detect various gas species. Good sensitivity and dynamic repeatability were observed for the sensor, demonstrating that the core-shell nanofibers hold promise for the realization of sensitive and reliable chemical sensors. The methodology proposed in this work is expected to be one of most suitable methods for preparing various kinds of oxide core-shell nanofibers or nanowires.

References:

- [1] B. Tian, X. Zheng, T. J. Kempa, Y. Fang, N. Yu, G. Yu, J. Huang and C. M. Lieber, *Nature*, **449** (2007) 885.
- [2] O. Hayden, A. B. Greytak and D. C. Bell, *Adv. Mater.*, **17** (2005) 701.
- [3] Q. Kuang, Z. Y. Jiang, Z. X. Xie, S. C. Lin, Z. W. Lin, S. Y. Xie, R. B. Huang and L. S. Zheng, *J. Am. Chem. Soc.*, **127** (2005) 11777.
- [4] S. Ramakrishna, K. Fujihara, W. E. Teo, T. C. Lim and Z. Ma, "An Introduction to *Electrospinning and Nanofibers*," ; World Scientific Pub. Co. Inc., Singapore (2005).
- [5] S. M. George, A. W. Ott and J. W. Klaus, *J. Phys. Chem.*, **100** (1996) 13121.

Acknowledgement:

This work was financially supported by Korea Science and Engineering Foundation (KOSEF) grant funded by Ministry of Education Science and Technology (MEST) (M2AN01).

Figure :

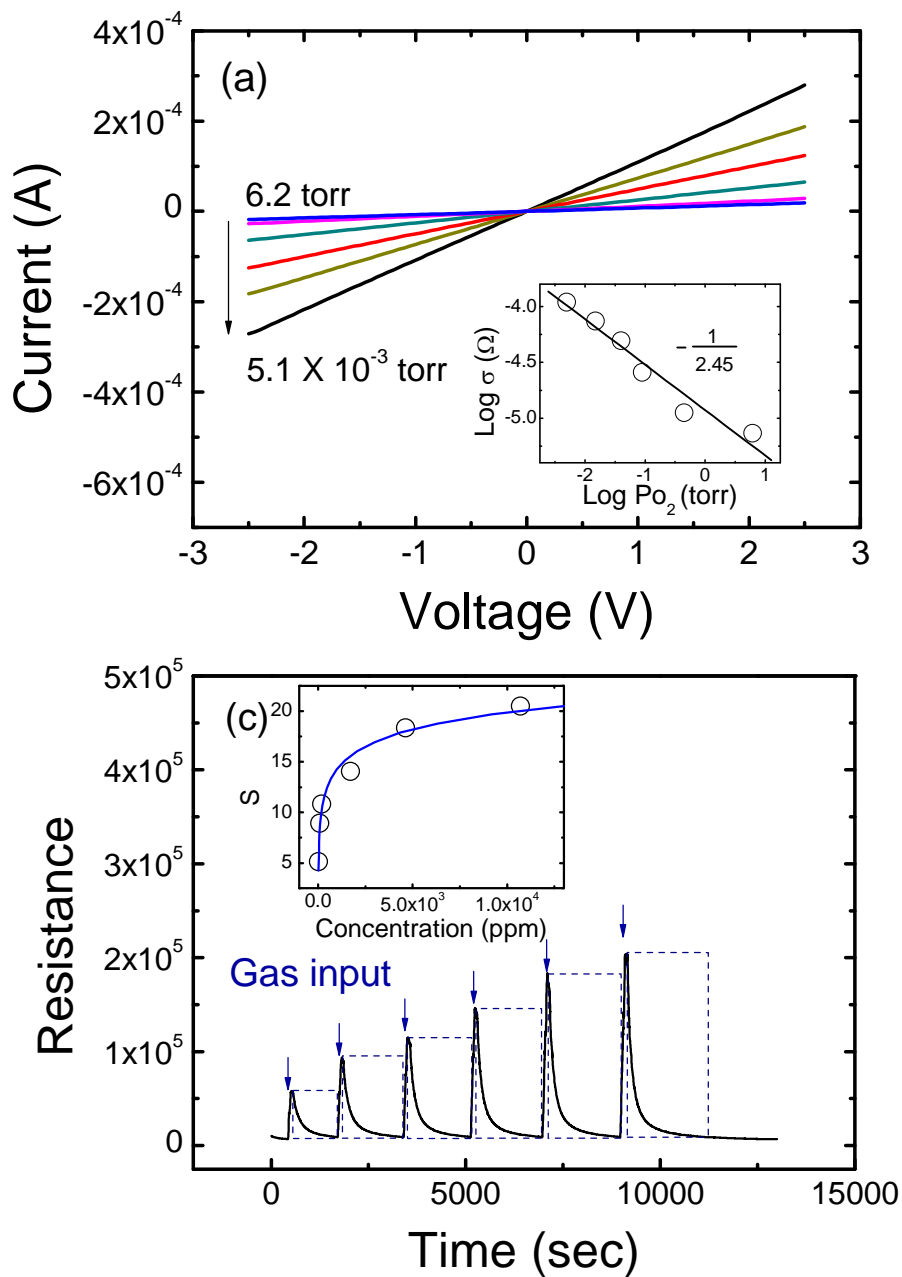


Figure 1 : (a) I-V behavior of the TiO₂-ZnO core-shell nanofiber sensor at various O₂ pressures at 573 K. The inset represents $\log \sigma$ versus $\log P_{O_2}$. The slope is $-1/2.45$, indicating *n-type* conduction is operating in the sensor. (b) Dynamic response of the sensor to oxygen pressure. The inset represents the variation of sensitivity as a function of oxygen pressure.

Initial growth stages of AlF_3 on $Cu(100)$: an STM study

M.G.G. Passeggi, Jr.,^a *J.C. Moreno-López*,^a *G. Ruano*,^a *R.A. Vidal*,^a *J. Ferrón*^{a,b}

^a *Laboratorio de Superficies e Interfaces, Instituto de Desarrollo Tecnológico para la Industria Química (CONICET-UNL), Güemes 3450, (S3000GLN) Santa Fe, Argentina*

^b *Departamento de Materiales, Facultad de Ingeniería Química, Universidad Nacional del Litoral, Santiago del Estero 2829, (S3000AOM) Santa Fe, Argentina*

mpggih@intec.unl.edu.ar

The composition, growth mechanism and structure of thin films of insulators deposited on several metal surfaces are topics that have attracted widespread interest in recent years. Work in this field has been motivated by the quality requirements of the thin films needed to develop advanced microelectronic, optical, and magnetic devices, as well as nanometer-scale structures [1]. Aluminium fluoride (AlF_3) films are of particular interest, for their potential applications in nanometer-scale patterning through electron beam lithography [2], due to under electron irradiation it shows radiolysis, i.e. the desorption of the fluoride with consequent formation of an aluminium metallic layer [3].

Recently, AlF_3 growth over different substrates has been characterized by means of electron and ion spectroscopies. Thus, Sánchez *et al.* reported a layer by layer growth of AlF_3 thin films on $Al(111)$ surfaces studied by means of Auger electron spectroscopy and electron energy loss spectroscopy [4]. Vergara *et al.*, characterized the growth process of AlF_3 films on $GaAs(110)$ from sub-monolayer coverages up to several layers, by means of AES, ion sputter depth profiling and time of flight-direct recoil spectroscopy [5]. In spite of this, nothing has been reported concerning with the initial stages of AlF_3 growth on metal surfaces by means of scanning tunnelling microscopy (STM). So, in this work we present a STM study of the initial growth stages of AlF_3 on $Cu(100)$ at room temperature, as well as the response of the insulating film to annealing treatments.

At very low coverages, AlF_3 molecules decorate both sides of the substrate step-edges (Fig. 1a). Once the step-edges are saturated compact islands start to nucleate on terraces (Fig. 1b). Around coverages of 0.1 ML, the terrace islands display a shape evolution from a compact to a fractal-like form (Fig. 1a and 1b). Upon further evaporation the fractal-like islands grow in size. Although, they do not show a complete coalescence, they form a sort of lateral 2D film, which covers the substrate with a single monolayer until 0.8 ML (Fig. 1c). With further deposition the covered surface area is still 80 % but some black patches appear over some islands (Fig. 2a). We interpret these dark areas as bi-layer, or even thicker islands of AlF_3 . So, at coverages beyond 0.8 ML the 2D growth turns into a 3D islands mode growth. This is supported by the fact that the dark areas increase with further depositions of AlF_3 , becoming impossible to acquire STM images at coverages close to 1.5 ML and beyond. On the other hand, a post-annealing treatment of the $AlF_3/Cu(100)$ surface above 625 K leads to the formation of square islands with a specific azimuthal relation with the high symmetry directions of the $Cu(100)$ surface, which show a metallic-like behaviour (Fig. 2b and 2c).

This work was financially supported by CONICET, UNL, and ANPCyT from Argentina.

References:

- [1] Z. Zhang and M.G. Lagally, *Science* **276** (1997) 377.
 [2] A. Murray *et al.*, *J. Vac. Sci. Technol. B* **3** (1985) 367; G.S. Chen, *J. Vac. Sci. Technol. A* **17** (1999) 403; W. Langheinrich *et al.*, *J. Vac. Sci. Technol. B* **10** (1992) 2868; H. Watanabe *et al.*, *Jpn. J. Appl. Phys.* **34** (1995) 6950.
 [3] A. Murray *et al.*, *Appl. Phys. Lett.* **45** (1984) 589; V.I. Nikolaichik, *Philos. Mag. A* **68** (1993) 227; G.S. Chen *et al.*, *J. Vac. Sci. Technol. B* **15** (1997) 1954; L.I. Vergara *et al.*, *Appl. Surf. Sci.* **229** (2004) 301.
 [4] E.A. Sánchez *et al.*, *Nucl. Instr. and Meth. B* **203** (2003) 41.
 [5] L.I. Vergara *et al.*, *Surf. Sci.* **482-485** (2001) 854.

Figures:

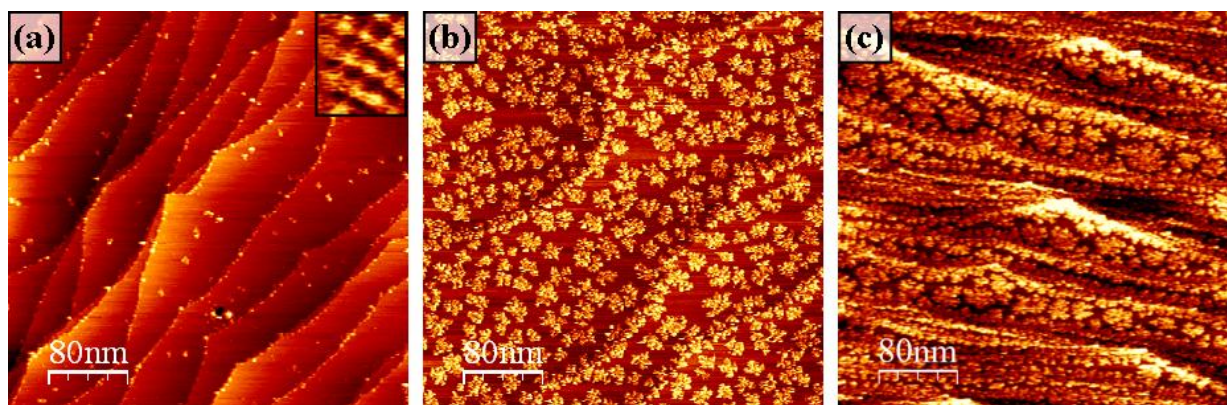


Figure 1: STM images ($400 \text{ nm} \times 400 \text{ nm}$) of AlF_3 deposited on $\text{Cu}(100)$ at 300 K, (a) 0.05, (b) 0.5 and (c) 0.8 ML. They were acquired with a sample bias voltage of $V_s = +2.5 \text{ V}$ and tunnel currents of $I_t = 0.1\text{-}0.15 \text{ nA}$. The inset in (a) shows a STM image ($0.8 \text{ nm} \times 0.9 \text{ nm}$) recorded between the AlF_3 islands displaying atomic resolution on $\text{Cu}(100)$. The image was acquired at $V_s = +0.2 \text{ V}$ and $I_t = 0.1 \text{ nA}$.

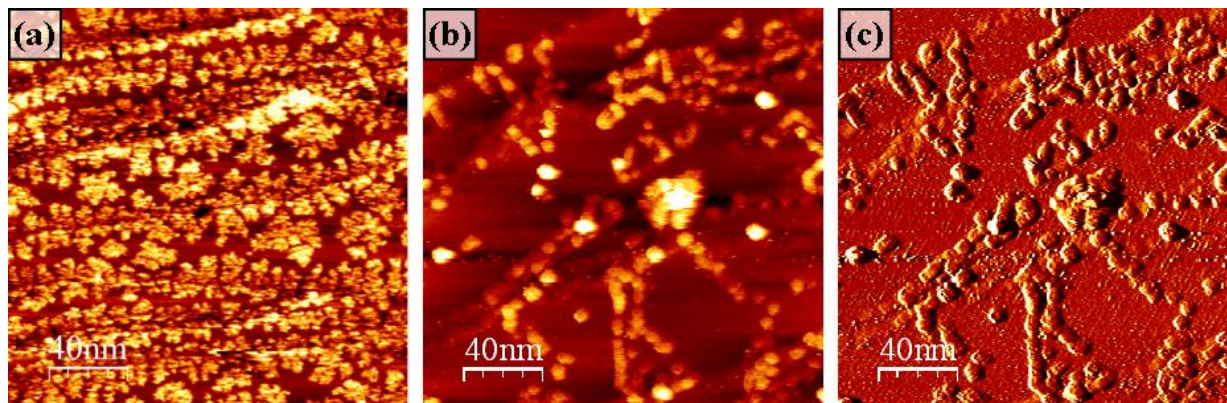


Figure 2: STM images ($200 \text{ nm} \times 200 \text{ nm}$) of 0.85 ML of AlF_3 deposited on $\text{Cu}(100)$ at 300 K. Topographic images acquired before (a) and after (b) a post-annealing treatment at 735 K was done. (c) Current STM image acquired simultaneously with the topographic one presented in (b). The images were acquired at $V_s = +2.5 \text{ V}$ and $I_t = 0.10\text{-}0.15 \text{ nA}$.

Gold Nanoparticle-Amino acid Assembly: A Nanomedicinal Approach to Cancer Therapy

Hirak K Patra, Anjan K Dasgupta

Department of Biochemistry, University of Calcutta, Kolkata, 700019, India

hirakpatra@gmail.com

- The gold nanoparticles is being used since ancient time for its various empirical therapeutic applications and now been recognized as most potent delivery nanosystem because of its metallic inertness and the biocompatibility. The reports also support the entry and localization of the nanoparticles within the cells. But this is the first time we are reporting that the gold nanoassembly with the amino acids can explore the potentiality of the gold nanoparticles after its apparant inert chemistry. We are reporting that gold nanoparticles synthesized with the most biocompatible molecules like amino acids to produce its unique credential to act as nanomedicine by severe response of the cancer cells and by restricting the tumor growth in vivo. The gold nanoparticles synthesized in presence of arginine can efficiently kill the Human Skin Fibroblast cancerous cells A375 and Human Lung Epithelial Cancer Cell Line A549. The extent of its efficiency in terms of killing of cancer cells is much more than the reported till date. The molecular cross-talk in cell cycle perspective investigated to locate the target module where the said component can act as anticancer agent. The carcinoma induced by EAC cells in the peritoneal cavity of swiss albino mice can be restricted to some extend by means of treatment with the Arg-gnp.

References:

[1] Hirak K. Patra, Shuvojit Banerjee Utpal Chaudhuri, Prabir Lahiri and Anjan Kr. Dasgupta, *Nanomedicine*, **3**, 111-119 (2007).

[2] Turkevich, J., Stevenson, P. C., Hiller, J. Discuss. *Faraday Soc.* **11**, 55(1951)

Figures:

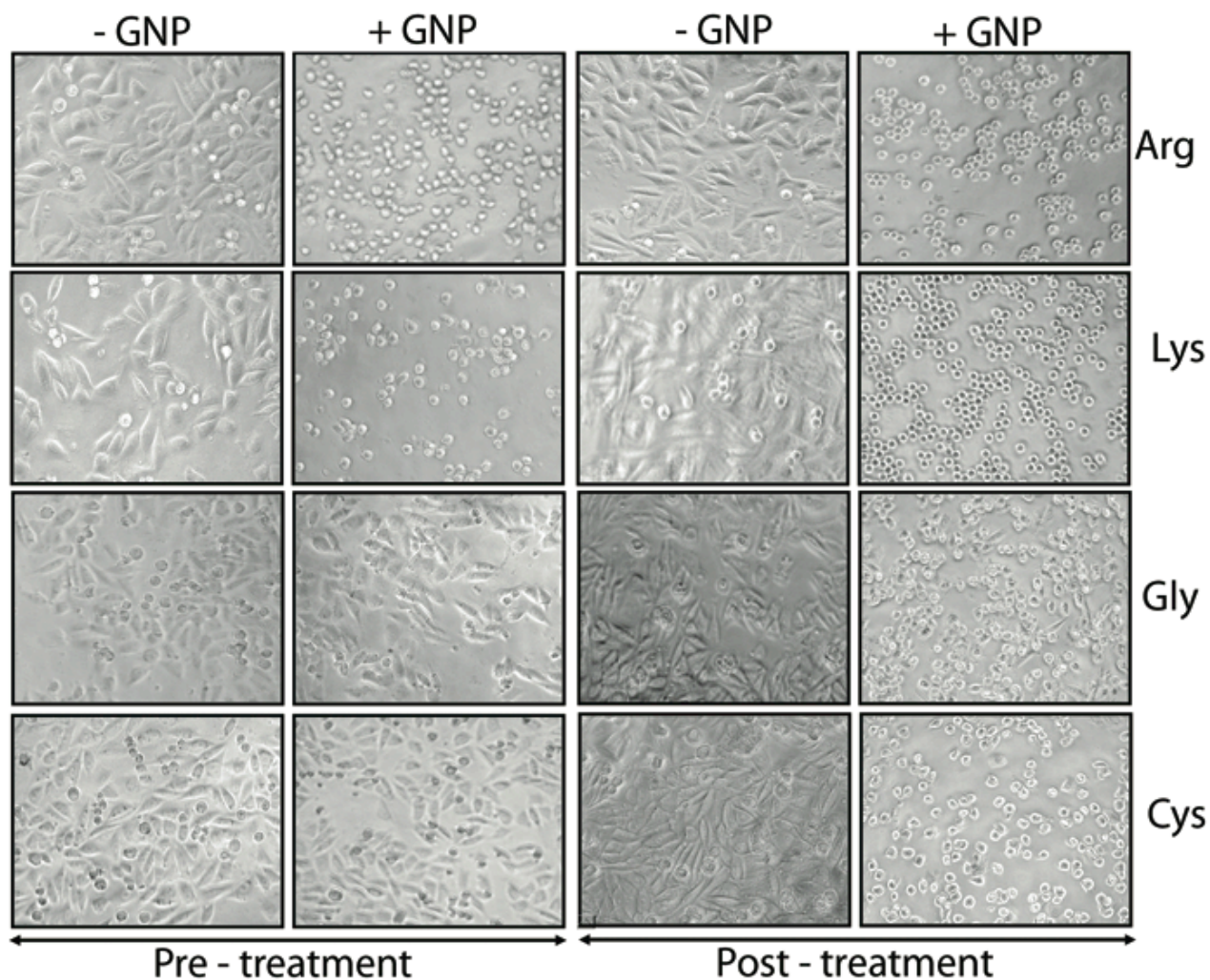


Fig. 1 The table of content of the response of Skin carcinoma A375 cancerous cell to the gold nanoparticles. The panel are showing the phase contrast images of the differential response to the surface modified gold nanoparticles [Right side molecules are indicating as the surface capping/modifying agent]

ROLE OF LABILE BONDING IN STOCHASTIC SWITCHING OF MOLECULAR CONDUCTANCE STUDIED BY STM

Lionel Patrone¹, Jérémie Soullier¹, Pascal Martin¹, Bruno Jousselme², Fabrice Moggia²

¹ *Institut Matériaux Microélectronique Nanosciences de Provence, CNRS IM2NP UMR 6242 ISEN-Toulon, Maison des Technologies, Place Georges Pompidou, F-83000 Toulon, France*

² *CEA/DSM/IRAMIS/SPCSI, Bât. 466, CEA/Saclay, F-91191 Gif-sur-Yvette cedex, France*

lionel.patrone@im2np.fr

Due to miniaturization of CMOS devices new memory cells with high density and low-power consumption are investigated. Molecular switches are likely to be among the most basic and important components of future molecule-based electronic devices. In the literature, on-off switching effect has been reported with phenylene-ethynylene oligomers bonded to gold via S-Au, using nanopore junctions [1] and scanning tunneling microscopy (STM). In these STM studies, molecules of interest have been inserted in an alkylthiol self-assembled monolayer (SAM). The observed stochastic conductance switching has been explained by conformational changes through aromatic ring rotation [2] or molecular hybridization changes at the interface with gold [3]. However, independent STM studies on SAMs on gold have reported similar stochastic switching effects for thiol molecules which cannot exhibit any conformational changes [4]. A thiol bond breaking/reforming mechanism was invoked, due to the labile nature of thiol bonding. Potential use of such conductance switching for molecular memory cells requires determining whether it is intrinsic to specific molecules or due to a bond fluctuation mechanism. For this purpose, comparative experiments need to be carried out on molecules more strongly bonded to the substrate. In this work, we compare the influence of S-Au labile bond versus C-Si stronger covalent one in obtaining a stochastic conductance switching of terthiophene molecules (3T). First we prepared binary SAMs of small bundles of 3T dispersed in dodecyl (DD) matrix, both on Au(111) using thiol-ended molecules and on hydrogenated silicon surface H-Si(111) with molecules bearing a vinyl reactive head. For this purpose, terthiophene-thiol and terthiophene-allyl molecules were synthesized. If obtaining binary SAMs on Au(111) is well known [5], growth of binary SAMs on H-Si(111) was studied using ellipsometry, contact angle measurements and scanning probe microscopy in order to obtain the right conditions giving isolated 3T molecules in DD. Then, we performed STM experiments on these binary SAMs, using the apparent molecular height of 3T above DD matrix as a measure of electronic conductance. We observed stochastic switching events for S-Au bond as reported in the literature. A statistical analysis of molecular blinking was carried out. However we show that stochastic switching is hindered in the case of C-Si bond. These results allow attributing the origin of published stochastic switching observations to a bond fluctuation mechanism. Moreover this work shows that silicon is a suitable substrate for developing molecular memory cells both avoiding stochastic switching and being compatible with microelectronics technology.

[1] J. Chen et al., *Science* 1999, 286, 1550

[2] Z.J. Donhauser et al. *Science* 2001, 292, 2303

[3] A.M. Moore et al., *J. Am. Chem. Soc.* 2006, 128, 1959 ; *Measurements and Mechanisms of Single-Molecule Conductance Switching*, *Frontiers in Materials Research* Vol. 10, p. 29, edited by Springer, Berlin - Heidelberg, 2008

[4] G.K. Ramachandran et al., *Science* 2003, 300, 1413

[5] L. Patrone et al., *Chem. Phys.* 2002, 281, 325

MECHANICAL PROPERTIES OF METALLIC PENTAGONAL NANOWIRES: TEMPERATURE DEPENDENCE

*S. Peláez**, *P. A. Serena*
Consejo Superior de Investigaciones Científicas
Instituto de Ciencia de Materiales de Madrid
c/Sor Juana Inés de la Cruz 3, Cantoblanco 28049-Madrid
**email: spelaez@icmm.csic.es*

Nanotechnology covers a broad variety of basic and applied studies aiming at the control of different properties at the nanometer level for their use in promising applications. In particular, metallic nanowires are very interesting systems from a basic physics point of view as well as within the context of future nanoelectronics and sensors industry. However, suspended ultra-thin metallic nanowires are rather weak and hardly reproducible structures. Only monatomic chains have been obtained experimentally in a reproducible way, but they are only stable under extremely controlled conditions and at very low temperatures[1].

Nevertheless, recent theoretical and experimental studies have pointed towards the possibility of obtaining pentagonal (icosahedral) nanowires consistently from the breaking of metallic nanocontacts in certain conditions [2-5]. These icosahedral or pentagonal nanowires are formed by subsequent staggered parallel pentagonal rings (with a relative rotation of $\pi/5$) connected with single atoms, showing a characteristic -5-1-5-1- ordering (see an example in Fig. 1a). The atomic sequence -1-5-1-5- presents a fivefold symmetry with respect the nanowire axis. This symmetry does not correspond to any crystallographic FCC nor BCC structures. The -1-5-1-5- staggered nanowire configuration may be understood in terms of a sequence of interpenetrated icosahedra. This icosahedral symmetry is very common in very small systems due to the large stability and high coordination characterizing such geometry [6]. Contrary to monatomic chains, icosahedral nanowires are rather robust structures at relatively high temperatures[4] and, therefore, they may be considered as promising candidates for being used as components in nanodevices [5]. For this reason, there is a need to study the mechanical response of these pentagonal nanowires, focussing on its temperature dependence.

In this work we perform Molecular Dynamics (MD) simulations of the elastic properties of Al, Ni and Cu pentagonal nanowires at different temperatures. The Embedded Atom Method (EAM) interatomic potential [7] is used to describe the energetics of the nanowires. Periodic boundary conditions along the nanowire axis are used to simulate infinite nanowires. For each nanowire under study we have carried out a constant temperature MD simulation using a Nose-Hover thermostat. Once thermal and mechanical equilibrium is achieved, the periodic unit cell is strained along the direction of the nanowire axis to simulate the compression or tension of the system. At each strained situation, the system evolves in a NVT ensemble until it reaches equilibrium. Then the virial stress is calculated. At the end of the simulation a stress vs. strain curve is obtained (see Fig 1b), from which the Young's modulus can be extracted. We have considered pentagonal Al, Ni and Cu nanowires formed by 96 atoms (i.e., 16 x -5-1- units). The stress strain curves have all been obtained for temperatures ranging from 0.1 to 0.6 times the bulk melting temperature of the corresponding metallic species.

For all the nanowires and temperatures simulated we show their mechanical response to tension and compression. We present results of the Young's moduli (see Fig 2) and yielding points of these nanowires. We also show that when subject to a low compression, these nanowires prefer to bend forming an 'S' like nanowire, still maintaining their pentagonal structure, instead of collapsing directly into a cluster.

In general we observe that the Young's modulus of these pentagonal nanowires is much higher than that of the bulk metal or other FCC nanowires. This trend has also been observed in previous works [8]. This fact, added to the high temperature stability of these nanowires and the recently proposed possibility of obtaining these nanowires in the laboratory from nanocontact ruptures, opens a window to their potential use in future nanoscale devices.

FIGURES:

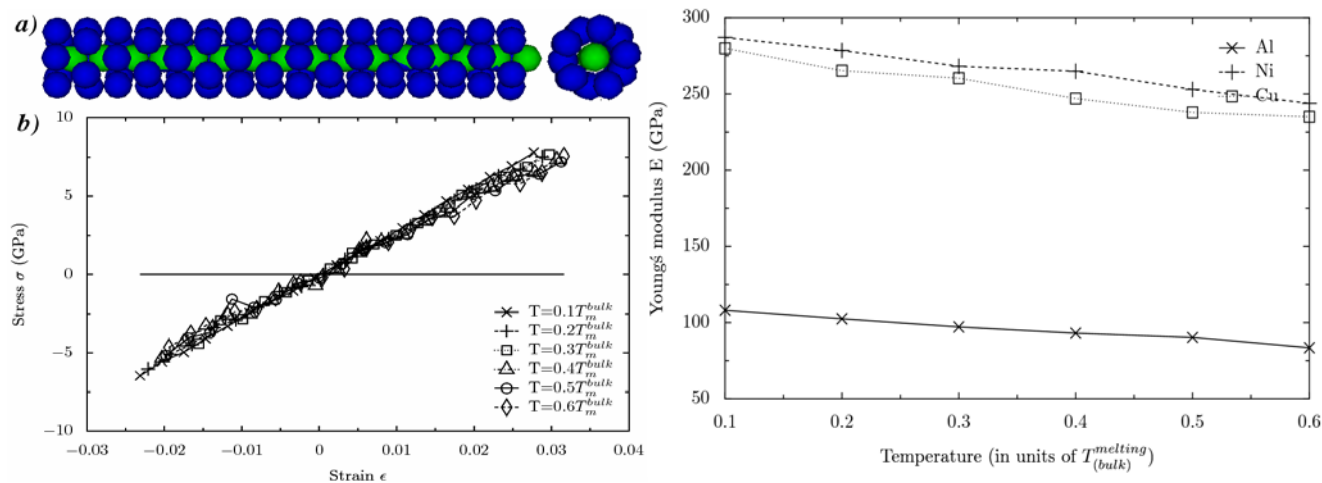


Fig 1: (a) Schematic representation of the pentagonal nanowires under study. Subsequent pentagonal rings are rotated $\pi/5$ and joined by a central (axial) atom. Color (green for axial atoms) is only shown for visualization purposes. (b) Stress vs Strain curves for Cu nanowires at the different temperatures under study.

Fig 2: Temperature dependence of the Young's modulus for the three metallic species under study.

REFERENCES:

- [1] N. Agraït, A. Levy-Yeyati and J.-M. van Ruitenbeek, *Phys. Rep.* **277**, 81 (2002).
- [2] J. C. González, V. Rodrigues, J. Bettini, L. G. C. Rego, A. R. Rocha, P. Z. Coura, S. O. Dantas, F. Sato, and D. S. Galvao, and D. Ugarte, *Phys. Rev. Lett.* **92**, 126102 (2004).
- [3] P. García-Mochales, R.Paredes, S. Peláez and P.A. Serena, *Journal of Nanomaterials* **2008**, 361464 (2008).
- [4] P. García-Mochales, R.Paredes, S. Peláez and P.A. Serena, *Phys. Stat. Sol. (a)* **205**, 1317 (2008).
- [5] V.K. Sutrar and D.R. Mahapatra, *J. Phys.: Condens. Matter* **20**, 335205 (2008).
- [6] N.A. Bulienkov and D.L. Tytik, *Russ. Chem. Bull. Int. Ed.* **50**, 1 (2001)
- [7] Y. Mishin, D. Farkas, M. J. Mehl, and D. A. Papaconstantopoulos, *Phys. Rev. B* **59**, 2292 (1999).
- [8] L. Wang, C. Peng and J. Gong, *Eur. Jour. Mech. A/Solids.* **28**, 877 (2009)

MAGNETIC PROPERTIES OF SELF-ASSEMBLED COBALT NANOPARTICLES CRYSTAL SUPERLATTICES

L. Peña¹, M. Varón², Ll. Balcells¹, V. Puntès² and B. Martínez¹

¹*Institut de Ciència de Materials de Barcelona(ICMAB-CSIC) Campus UAB, 08193 Bellaterra, Spain.*

²*Institut Català de Nanotecnologia (ICN-ICREA), Campus UAB, 08193 Bellaterra, Spain.*

Colloidal dispersed nanoparticles (NP) could self assemble into complex structures when segregated from the solvent either by evaporation or precipitation in adequate conditions. Thus, different micro and macroscopic structures like opals, fractals, anisotropic structures and others formed by nanoparticles can be obtained as a result of the balance between electrostatic forces, surface tension, entropy, substrate topography and affinity, among others, and evidently, the size, shape and concentration of the particles. In addition, in ferromagnetic materials, the dipolar magnetic interactions, add a new term in the interactions balance.

High anisotropic structures obtained by self-assembly of ferromagnetic NPs reveal the strong dipolar interaction even with soft magnetic materials like cobalt. Additionally, superlattices self-assembled without applied magnetic field are of fundamental interest to understand the magnetic interaction, because a partial orientation of easy axes of the NP is not induced. On the another hand, these mesoscopic structures that bridge the gap between the microscopic atomic level and the macroscopic state can contribute to understanding magnetism in both regimes.

In this work we report on the important role of dipolar magnetic interactions on the formation of self-assembled structures of magnetic NPs in the absence of applied magnetic field. We used a 6 nm spherical Co NPs synthesized by thermal decomposition in a mixture of organic solvent (dichlorobenzene) and two surfactants (oleic acid and trioctyl phosphine oxide). The self-assembly process is realized onto high ordered pyrolytic graphite (HOPG). The rice-grain like structures was observed when the colloid, deposited by drop casting technique, is evaporated at room temperature.

Self-assembled structures on graphite have been characterized by optical microscopy and SEM (see Fig. 1). Atomic force microscopy images of the nanoobjects are shown in Fig.2 (left), together with magnetic force microscopy images (see Fig.2 right), making evident the magnetic character of these self-assembled structures. Basic magnetic characterization of the self-assembled samples is shown in Fig. 3

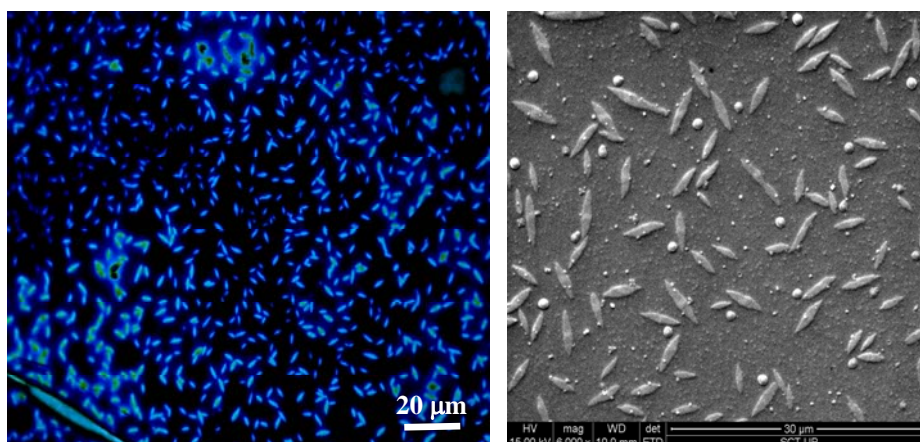
FIGURES

Figure 1. Left: Optical Image of self-assembly structures (5-9 μm) of cobalt nanoparticles after its deposition onto HOPG substrate. Right: SEM Image of self-assembly structures (5-9 μm) of cobalt nanoparticles after its deposition onto HOPG substrate.

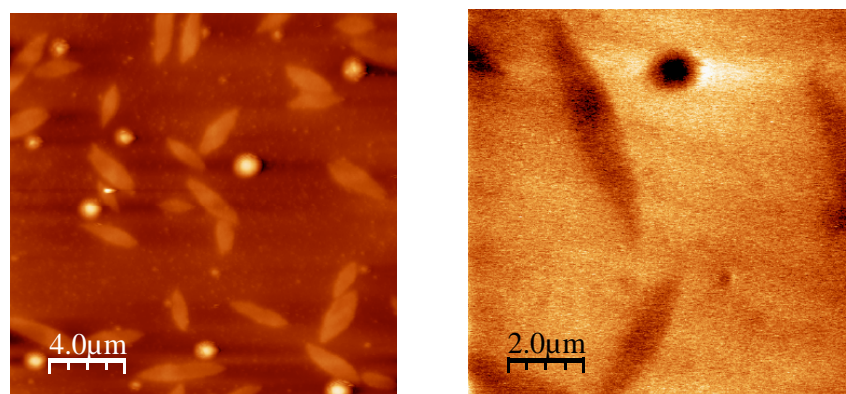


Figure 2. Left) Atomic force microscopy image of self-assemble structures integrated by cobalt nanoparticles. Right) MFM image of some of these structures showing the magnetic character at room temperature.

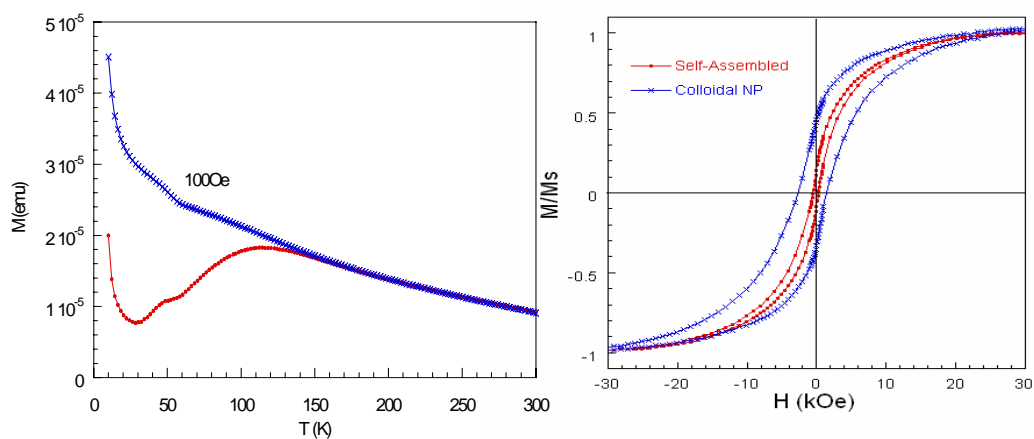


Figure 3. ZFC (red) and FC (blue) magnetization curve of self-assembled NPs onto HOPG (Left). Low temperature ($T=10$ K) hysteresis loop for colloidal and self-assembled Co NPs (Right).

Synthesis and magnetic properties of monodisperse mixt ferrite nanoparticles.

Leonardo Pérez-Mirabel^a, Fernando Martínez-Julián^b, Susagna Ricart^b, Alberto Pomar^b
Ramón Yáñez^a and Josep Ros^{a*}

^aDepartament de Química Universitat Autònoma de Barcelona,

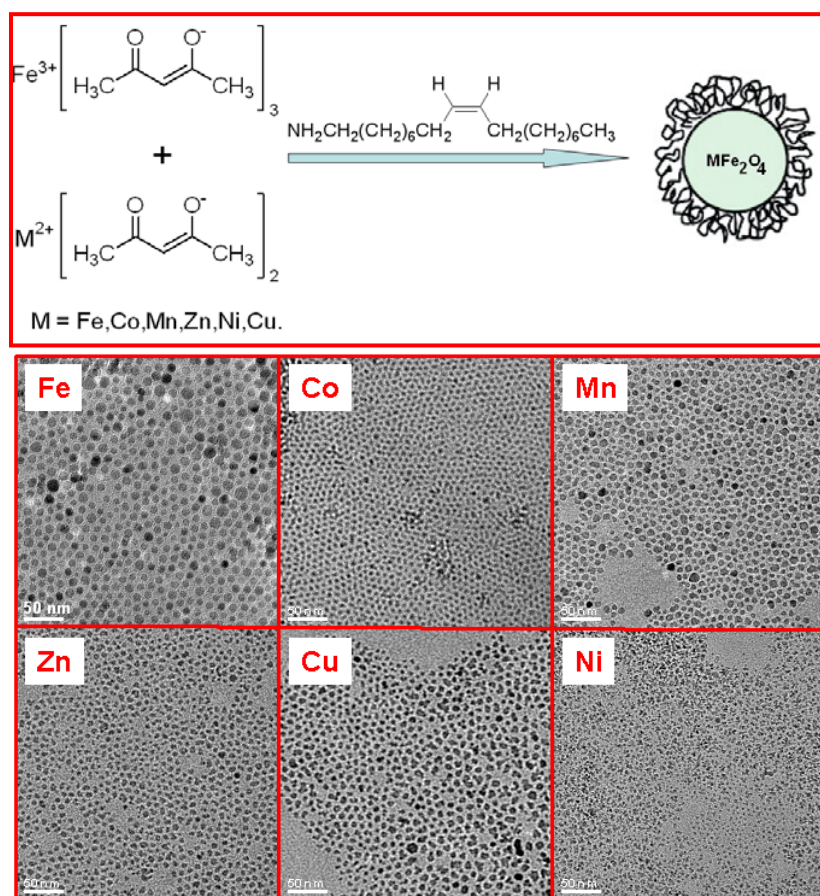
^bInstituto Ciencias de Materiales de Barcelona (CSIC), Campus UAB, 08193

Bellaterra, Spain

08193 Bellaterra, Spain

josep.ros@uab.es

Six different types of ferrite MFe_2O_4 nanoparticles (M: Mn, Co, Ni, Fe, Zn or Cu) have been synthesized by using a simple “one-step” reaction, boiling in oleylamine a mixture of the corresponding metal acetylacetonates. The oleylamine plays both, the role of solvent and coating species. In order to investigate the nanoparticles properties, these have been fully characterized by X-ray diffraction, TEM and SQUID magnetometry.



S. Sun, H. Zeng, D. B. Robinson, S. Raoux, P. M. Rice, S. X. Wang, and G. Li *J. Am. Chem. Soc.*, **2004**, 126 (1), 273-279

D. Caruntu, Y. Remond, N. H. Chou, M. Jun, G. Caruntu, J. He, G. Goloverda, C. O'Connor, V. Kolesnichenko. *Inorg. Chem.*, **2002**, 41 (23), 6137-6146•

Effects of molecular π -stacking on the conductance of nanographene-gold junctions

Ángel J. Pérez-Jiménez, Juan C. Sancho-García
Departamento de Química-Física,
Universidad de Alicante, E-03080, Alicante, Spain
aj.perez@ua.es

First-principles calculations on several gold-acene-gold nanojunctions indicate that their low-bias conductance is due to the onset of a HOMO-derived resonance, thus being quite sensitive to the detailed interaction between the molecule and the gold leads. It is also found that such interaction is dominated by the electrophilic binding of Au to the acene, explaining the increase of the conductance as the ionization potential and the hardness of the molecular arrangement diminish. Both quantities are inversely proportional to the molecular length and the number of molecules present on a π stack, being also lower for circumacenes than for oligoacenes of the same size, opening a way to adjust the conductance by appropriate selection of the acene and control of its π -stacking. It is also found that the conductance depends dramatically on the amount of π overlap between the molecules in the stack, as well as on the particular disposition of the metallic tips with respect to the molecule. Calculations on charged nanojunctions of this type reveal their potential use as field-effect transistors. The conclusions reached point towards π -stacked arrangements of large circumacenes as potential candidates to build useful nanodevices for molecular electronics made out of nanographene-based materials.

NANOPATTERNING ON LIGHT-EMITTING NANOCOMPOSITES

L. Persano, S. Molle, S. Girardo, A. A. R. Neves, A. Camposeo, R. Stabile, R. Cingolani and D. Pisignano

National Nanotechnology Laboratory of CNR-INFM, Distretto Tecnologico, Scuola Superiore ISUFI, Università di Lecce, via Arnesano I-73100, Lecce, Italy

The incorporation of inorganic particles in organic polymers strongly affects the native properties of the polymer materials. In particular, the combination of the wide tunability, easy of processing and structural flexibility of conjugated polymers, with the optical and thermal stability of inorganic light emitting fillers, allows one to specifically design optically active systems whose emitting properties can be tailored over a wide emission range by the prediction of the energy interaction among the organic and inorganic phases. Nanopatterning of nanocomposite still represents a challenge. In this work we present a platform of soft lithographic methods for micro- and nano-structuring of hybrid organic/inorganic composite materials consisting of Zinc oxide nanoparticles (Fig. 1) embedded in several light emitting conjugated polymers, from PPV to PFO derivatives. The nanocomposite pattern exhibit a resolution up to the 100-nm scale. The photoluminescence properties together with the rheological behaviour of the nanocomposites films have been carefully investigated both before and after nanopatterning.

References

L. Persano, et al. *Advanced Functional Materials* **18**, 2692 (2008).

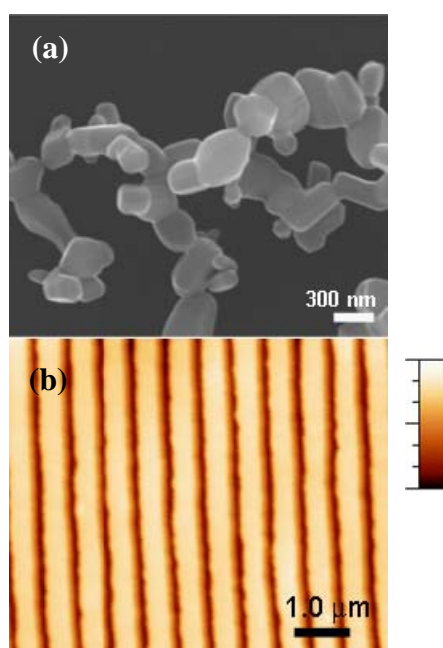


Fig. 1 Employed ZnO nanoparticles imaged by SEM (a); AFM view of a patterned nanocomposite surface (vertical scale from zero to 200 nm) (b).

Polyol synthesis of Carbon coated lithium nickel Phosphate and lithium Cobalt Phosphate Nano particles.

P. Ramesh kumar^a, N. Satyanarayana^{a*}

^a Department of Physics, Pondicherry University, Puducherry - 605 014, India.

Abstract:

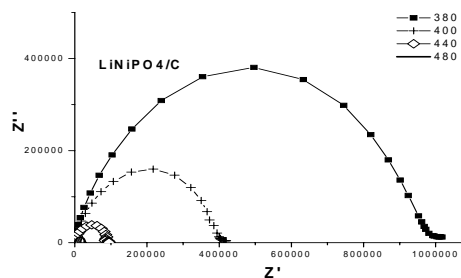
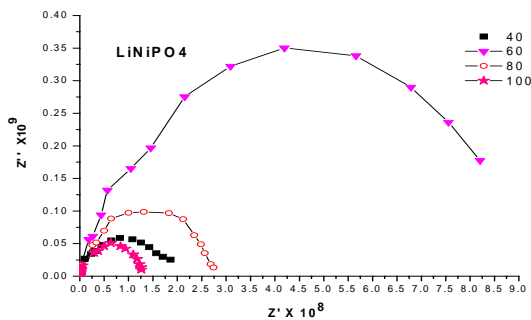
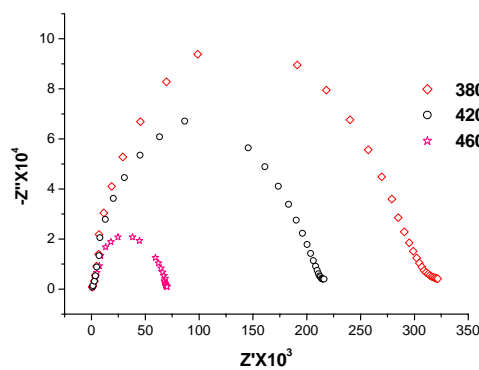
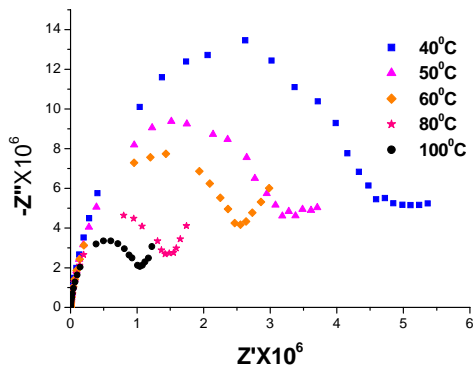
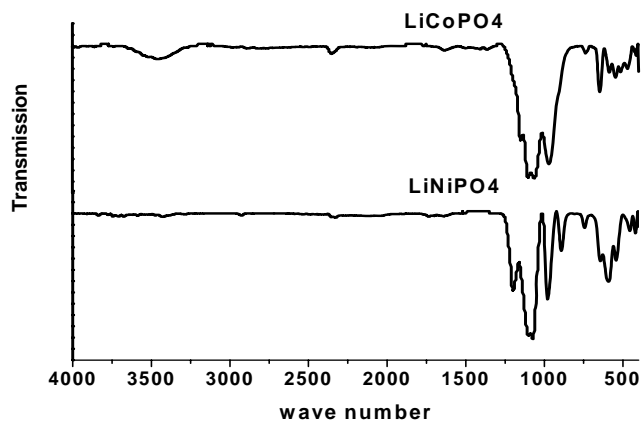
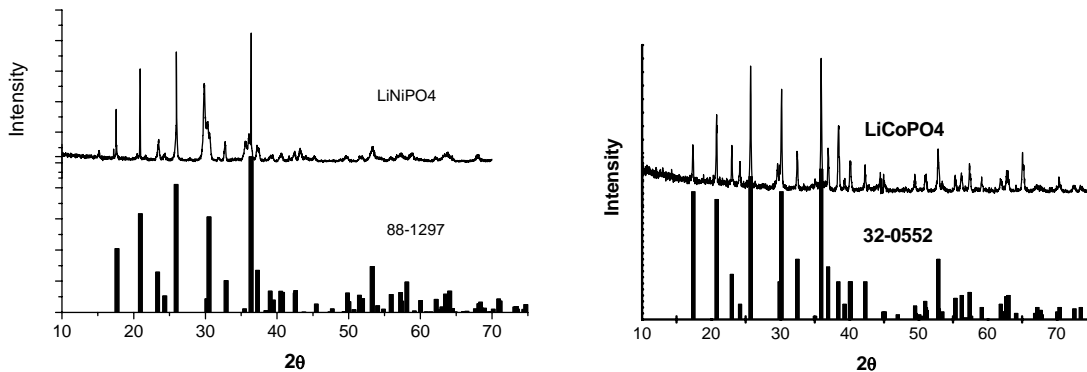
The large family of compounds of the $ABPO_4$ type (A and B are mono and divalent cations, respectively) exhibits different frameworks depending on the relative size of the A and B ions. These phosphates exhibit variety of structural features. The most prominent of one is the existence of tunnels, in which small ions moves freely, a property that makes them potential hosts for the insertion and de-insertion of ions. As a result, they will have high capacity, good thermal stability and environmental benignity and Hence, these compounds have been proposed as an alternative electrode materials for rechargeable lithium ion batteries. Thus the advancement in lithium battery technology is envisaged on the basis of lithium metal phosphate materials as an active cathode material. Hence, present work focuses on the polyol synthesis of Carbon coated lithium nickel Phosphate and lithium Cobalt Phosphate Nano particles. PVP used as a surfactant to avoid the agglomeration and controlling the particle size of $LiNiPO_4$, $LiCoPO_4$ nano particles.

Lithium acetate, nickel acetate, Cobalt acetate, ammonium dihydrogen phosphate are taken as precursor materials and PVP as stabilizer (plasticizer). and polyacrylic acid and EG are used as carbon source for Carbon coated Lithium metal phosphates. And the Synthesized samples are characterized and conformed the Structure, phase purity, microstructure and conductivity by the XRD, FTIR, SEM-EDX. Impedance spectroscopy techniques. Further the newly developed compounds will be used for the fabrication of Li-ion batteries. The detailed result will be presented and discussed.

Acknowledgments: Authors are gratefully Acknowledged CSIR, DRDO and DST for utilizing the research facilities available from the major research projects.

Keywords: Olivine structure, $LiNiPO_4$, $LiCoPO_4$ Cathode material, XRD, FT-IR, SEM, EDX, Impedance.

*Corresponding author E-mail: nallanis2000@yahoo.com
(Prof. N. Satyanarayana) Phone: +91413-2654404



SEM-EDX images are we unable to include because of restrictions in size of file.

Phase separation in $\text{La}_{1-x}\text{Ca}_x\text{MnO}_3$ via nanoscale doping inhomogeneities.

A. Piñeiro^{1,2}, V. Pardo^{1,2}, D. Baldomir^{1,2}, F. Rivadulla³, A. Rodríguez⁴, A. Gómez⁴, J. E. Arias²
and J. Rivas¹

¹ Departamento de Física Aplicada, Facultad de Física, Universidad de Santiago de Compostela, E-15782 Campus Sur s/n, Santiago de Compostela, Spain.

² Instituto de Investigaciones Tecnológicas, Universidad de Santiago de Compostela, E-15782 Campus Sur s/n, Santiago de Compostela, Spain.

³ Departamento de Química-Física, Universidad de Santiago de Compostela, 15782 Santiago de Compostela, Spain.

⁴ CESGA, Avda. de Vigo s/n, 15705 Santiago de Compostela, Spain.

alberto.pineiro2@rai.usc.es

Colossal Magnetoresistance has been studied extensively for the past 20 years, and those investigations have shown it is intimately related to the phenomenon of electronic/magnetic *phase separation*. Understanding the origin of this effect is a prerequisite to the understanding of the physics of strongly correlated electron systems.

One paradigmatic system exhibiting phase separation is $\text{La}_{1-x}\text{Ca}_x\text{MnO}_3$ compound. This material has been deeply studied and there are plenty of experimental evidences of a dynamic magnetic phase separation at low temperature near $x \sim 0.2$ and $x \sim 0.5$. [1]

We have taken into account a structure with Ca doping levels close to $x \sim 0.2$ (exactly $x = 0.1875$) from a computational point of view via "*ab initio*" calculations for the first time in order to study the magnetic phase separation on the nanoscale. We use density functional theory (DFT) and calculations were carried out with the WIEN2k package [2] using the LSDA+U [3] approximation, exploring typical values of U for this compound (from 3 eV to 6 eV).

We have elaborated several large superstructures based on the unit cell $\text{La}_{0.8125}\text{Ca}_{0.1875}\text{MnO}_3$ that represent the experimentally observed situation of a magnetic phase (antiferromagnetic (AF), in this case) completely surrounded by a magnetically different phase (ferromagnetic (FM), in this case). We want to simulate a magnetically phase separated state by embedding one of these magnetic phases into the other.

We have calculated many of these phase separated superstructures introducing different magnetic configurations (one dimensional AF (FM) chains surrounded by a FM (AF) guide and two cases with an AF (FM) nanometric region completely surrounded by a FM (AF) region). For comparing their relative stability with respect to the phase-separated cases, we have calculated an entirely ferromagnetic superstructure and also an entirely antiferromagnetic superstructure. Our calculations show that the purely FM structure is the most stable one, and the AF structure is the more unstable. Magnetism alone cannot explain the observations. Initially, we have assumed that the La and Ca atoms (the dopants) are distributed in a perfectly homogeneous manner throughout the crystal. But, experimentally, we know that this might not be the case; nano-sized chemical inhomogeneities in the structure can happen and will not be detected by standard diffraction measurements.

We construct 4 different structures, depending on how these Ca atoms are distributed. We can

define $\langle r \rangle$ as the average distance between Ca atoms in the lattice $\langle r \rangle = \frac{\sum_i^n r_i}{n}$, where r_i is the distance between nearest Ca atoms and n is the number of nearest Ca atoms.

We calculated the energy of these new structures and, after a structural relaxation, obtained that the most stable structure corresponds to an intermediate case between a homogeneous and a totally inhomogeneous case. These small chemical inhomogeneities will be accompanied of magnetic homogeneities, leading to a nanoscale magnetic phase separation that could be observed experimentally.

We have constructed also four different possible Ca-dopant configurations in the $\text{La}_{0.625}\text{Ca}_{0.375}\text{MnO}_3$. In this concentration the material does not show phase separation experimentally. Our calculations show that chemical inhomogeneities that occur at this concentration are smaller in magnitude, not enough to lead to a phase separated state, then the picture is consistent.

Our results show important evidences about the origin of the chemical magnetic phase separation close to a magnetic phase transition. We have calculated that magnetism alone cannot drive phase separation. Instead, dopant inhomogeneities on the nanoscale are the driving force of the phase separation phenomenon in manganites.

References:

- [1] S. W. Cheong and H. Y. Hwang: *Ferromagnetism vs Charge/Orbital Ordering in Mixed-Valent Manganites*, in *Colossal Magnetoresistance Oxides*, edited by Y. Tokura (Gordon & Breache, Monographs in Condensed Matter Science, London 1999)
- [2] P. Blaha, K. Schwarz, G. K. Madsen, D. Kvasnicka and J. Luitz, *WIEN2k, An Augmented Plane Wave Plus Local Orbitals Program for Calculating Crystal Properties*. ISBN 3-9501031-1-2, Vienna University of Technology, Austria (2001).
- [3] A. I. Liechtenstein, V. I. Asinimov, and J. Zaanen, *Phys. Rev. B* **52** (1995) R5467.

Figures:

STM Study of Magnetic Polyoxometalates on HOPG Surfaces

E. Pinilla-Cienfuegos⁽¹⁾, A. Forment-Aliaga⁽¹⁾, E. Coronado⁽¹⁾,
G. Sáenz-Arce⁽²⁾ and C. Untiedt⁽²⁾

⁽¹⁾ Instituto de Ciencia Molecular, Universidad de Valencia,
PO Box 22085, E-46071 Valencia, Spain

⁽²⁾ LT-NanoLab Departamento de Física Aplicada, Facultad de Ciencias
(Fase II), Universidad de Alicante, San Vicente del Raspeig, E-03790
Alicante, Spain.

elena.pinilla@uv.es

Polyoxometalates (POMs) are a large class of discrete oxides composed of early transition elements (especially vanadium, molybdenum, and tungsten) exhibiting extensive applications in diverse fields such as catalysis, electronics, magnetism and medicine⁽¹⁾. From a magnetic point of view the heteropolynuclear complexes of W and Mo form diamagnetic frameworks that can coordinate paramagnetic metal ions while keeping them well isolated from the neighbouring magnetic clusters. In fact, mononuclear lanthanide-based POMs have recently demonstrated the occurrence of Single Molecule Magnet (SMM)-like relaxation in this sort of compounds⁽²⁾.

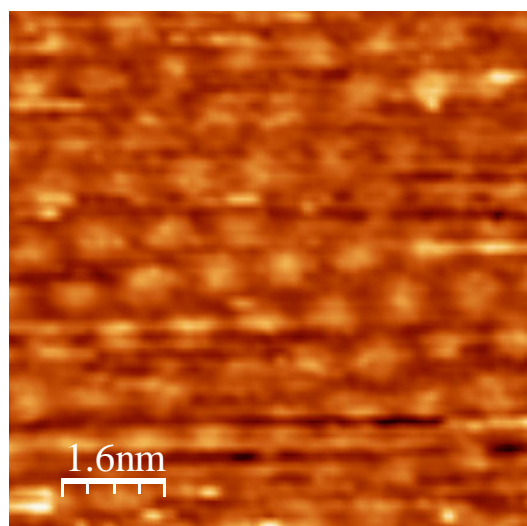
In these metal-oxide molecular clusters, a variety of physical techniques including the spectroscopic technique of inelastic neutron scattering (INS), can be used to determine the energies and wave functions of the different spin state of the cluster^(3,4). However, all these measurements are performed on bulk samples. In order to obtain information about the low energy levels from a single polyoxometalate, scanning tunneling spectroscopy (STS) at low temperatures can be used when the molecules are deposited on a conducting substrate. Therefore the interaction of the metal-oxide cluster with the surface has to be taken in consideration.

Herein we will describe the controlled deposition of magnetic POMs onto High Oriented Pyrolytic Graphite (HOPG) with two different examples: the Preyssler-type $K_{12}[DyP_5W_{30}O_{110}]$ (SMM) and the Kegging-type $K_{10}[Co_4(H_2O)_2(PW_9O_{34})_2]$. Scanning Tunneling Microscopy (STM) was used to image the shapes, packing, and orientation of the two molecules at room temperature.

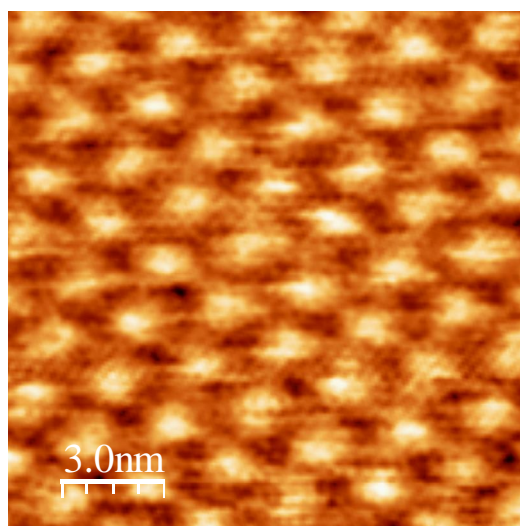
STM images show the formation of highly regular 1D and 2D molecular arrangements. Therefore it is possible to find single molecules to perform spectroscopy experiments as a preliminary step for the development of the study of the lowest electronic levels of magnetic molecules by STM and to determine the molecule-substrate interaction complementing the INS studies.

References:

- [1] Special thematic issue of Chem.Rev. , **98** (1998), 1-390.
- [2] Murad A. AlDamen, Juan M. Clemente-Juan, Eugenio Coronado, Carlos Martí-Gastaldo, and Alejandro Gaita-Ariño, J. AM. CHEM. SOC., **130**, (2008), 8874–8875.
- [3] Juan M. Clemente-Juan, Hanspeter Andres, Juan J. Borrás-Almenar, Eugenio Coronado, Hans U. Gu1del, Michael Aebersold, Gordon Kearly, Herma Bulttner, and Markus Zolliker, J. Am. Chem. Soc., **121** (1999), 10021-10027.
- [4] Hanspeter Andres Juan, M. Clemente-Juan, Michael Aebersold, Hans U. Gu1del, Eugenio Coronado, Herma Bulttner, Gordon Kearly, Julio Melero and Ramón Burriel, J. Am. Chem. Soc., **121** (1999), 10028-10034.

Figures:

STM Image of $K_{12}DyP_5W_{30}O_{110}$.
8 nm x 8 nm



STM image of $K_{10} [CO_4 (H_2O)_2 (PW_9O_{34})_2]$.
15 nm x 15 nm

COLLOIDAL NANOCRYSTALS FOR QUANTUM INFORMATION TECHNOLOGY

Ferruccio Pisanello^{1,2,*}, *Luigi Martiradonna*², *Piernicola Spinicelli*¹, *Godefroy Lemenager*¹,
*Angela Fiore*¹, *Jean-Pierre Hermier*³, *Liberato Manna*², *Elisabeth Giacobino*¹, *Roberto Cingolani*², *Massimo De Vittorio*² and *Alberto Bramati*¹

¹ *Laboratoire Kastler Brossel, CNRS UMR8552, Université Pierre et Marie Curie, Ecole Normale Supérieure, 4 place Jussieu, 75252 Paris Cedex 05, France*

² *National Nanotechnology Laboratory, CNR/INFM, Scuola superiore ISUFI, Università del Salento, 16 Via Arnesano, Lecce 73100, Italy*

³ *Groupe d'étude de la Matière Condensée, CNRS UMR8635, Université de Versailles, Saint-Quentin-en-Yvelines, 45 avenue de Etas-Unis, 78035 Versailles Cedex, France*

* pisanello@spectro.jussieu.fr

Efficient single photon sources (SPSs) are now catching the scientific community attention. Quantum information technology algorithms are based on antibunched photon fluxes and on the fine control of their quantum states and polarization properties. Among the proposed approaches for SPSs based devices, actually two technologies are in competitions: the Stranski-Krastanov epitaxial quantum dots (QDs) and wet-chemically synthesized colloidal nanocrystals (NCs). Epitaxial QDs have been deeply studied in past years and antibunched photon fluxes up to a temperature of ~ 200 K have been achieved by using either GaN QDs [1] or a single QD embedded in a single quantum wire [2]. In spite of the possibility to simply achieve electrical injection [3] and positioning inside photonic crystals nanocavities [4], room temperature single photon emission in epitaxial nanostructures has not been demonstrated so far. On the other hand, colloidal core/shell NCs are efficient sources of antibunched photons at room temperature [5] and show several advantages which let us envision their application to final devices. It has been demonstrated that the shape and size of the NCs can be tailored to overcome the drawbacks which so far limited the nanocrystals applications, such as blinking [6] and unpolarized emission [7]. Beside the characterization of their physical properties [8,9], the compatibility with the nano-engineering techniques has been recently demonstrated [10] and the first evidence of SPSs based on single nanocrystal coupled to a cavity mode has been demonstrated [11].

In this work we report on efficient SPSs based on a particular type of nanocrystals, in which a CdSe rod-like shell surround a CdS spherical core (Fig.1(a)). The polarization properties of these nanoparticles make them suitable for the implementation of quantum information technology algorithms based on photon polarization, such as BB84 and B92 for private cryptography keys distribution [12][13]. The CdSe/CdS core/shell dot-in-rod (DR) nanocrystals have been synthesized with a seeded growth approach [14], which yields nanorods with narrow distributions of both lengths and diameters. A DR mono-molar solution (in toluene) was dropcasted on a microscope glass coverslip and excited using a picosecond pulsed laser. By means of a high sensitivity Hanbury-Brown and Twiss setup, based on two avalanche photodiodes, we performed time and polarization resolved measurements. In order to proof the non classical behavior of the light emitted from the single DR, the coincidence histogram (proportional to the autocorrelation function $g^{(2)}(\tau)$) was measured for several nanocrystals, showing a near perfect antibunching (see Fig.1(b)): the few coincidences near zero delay mean that the probability to detect more than one photon at the same time is extremely low and the sharp periodic peaks indicate that two photons are usually spaced of a multiple of the period of the laser pulses.

The photoluminescence mean value, excluding the time intervals in which the single nanocrystal was not emitting due to the blinking, was computed for several values of the polarization-detection angle (θ); the obtained values, reported in Fig.1(c), follow the function $\cos^2(\theta)$, achieving a degree of linear polarization of $\sim 75\%$. By measuring the distances between every received photon and the laser pulses (used as a trigger) we computed the mean lifetime of the electron-hole pair excited in the nanoparticles (ideally one for each laser pulse) obtaining $\tau_r \sim 11$ ns. In conclusion, in this work we have shown that single colloidal DRs, by virtue of their relatively short lifetime, good antibunching and a high degree of linear polarization ($\sim 75\%$), represent a key building block for the realization of high rate and efficient single photon sources for quantum cryptography applications.

References:

- [1] C. Santori *et al.*, *Nat. Mat.*, **5** (2006) 887.
- [2] A. Tribu *et al.*, *Nano Lett.*, **8** (2008) 4326.
- [3] Z Yuan *et al.*, *Science*, **295** (2002) 102.
- [4] T. Yoshie *et al.*, *Nature*, **432** (2004) 200.
- [5] P. Michler *et al.*, *Nature*, **406** (2000) 968.
- [6] B. Mahler *et al.*, *Nat. Mat.*, **7** (2008) 659.
- [7] J. Hu *et al.*, *Science*, **292** (2001) 260.
- [8] G. Morello *et al.*, *Phys. Rev. B*, **78** (2008) 195313.
- [9] D. Steiner *et al.*, *Nano Lett.*, **8** (2008) 2954.
- [10] A. Quattieri *et al.*, *Microelectron. Eng.*, in press (2008), doi:10.1016/j.mee.2008.11.073.
- [11] A. Quattieri *et al.*, *New J. Phys.*, **11** (2009) 033052.
- [12] C. H. Bennet and G. Brassard, in *Proc. of the IEEE International Conference on Computers, Systems, and Signal Processing, Bangalore, India*, (1984) 175.
- [13] C. H. Bennet, *Phys. Rev. Lett.*, **68** (1992) 3121.
- [14] L. Carbone *et al.*, *Nano Lett.*, **7** (2007) 2942.

Figures:

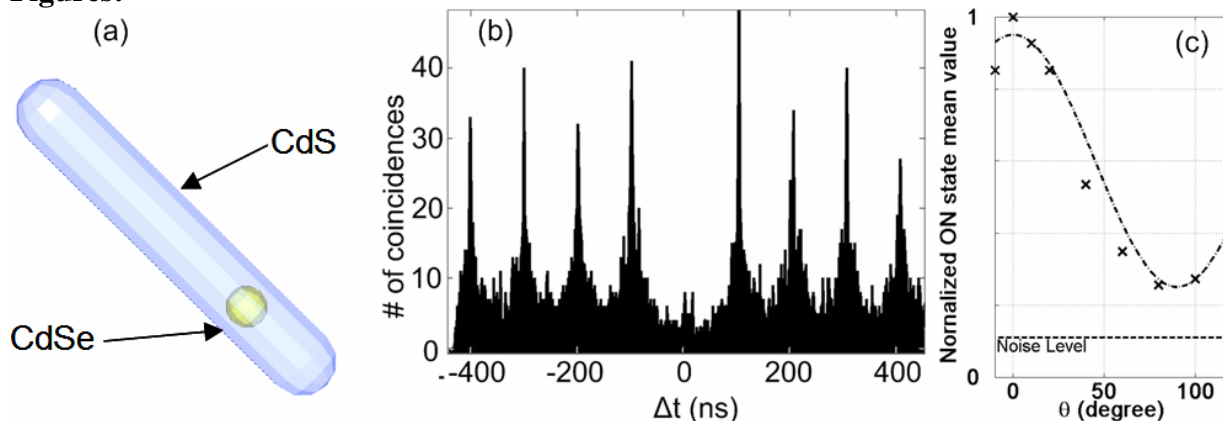


Fig. 1 (a) Schematic representation of the analyzed dot-in-rod. (b) Typical coincidences histogram obtained from a single and isolated dot-in-rod. (c) Normalized intensity for several polarization angles computed by excluding the time intervals in which the nanocrystal was not emitting.

CHARACTERIZATION OF CARBON NANOTUBE FIBERS PREPARED BY DIELECTROPHORESIS

Margo Plaado¹, Kristjan Saal¹, Rünno Lõhmus¹, Uno Mäeorg², Ants Lõhmus¹

¹Institute of Physics, University of Tartu, Riia 142, 51014, Tartu, Estonia

²Institute of Organic and Bioorganic Chemistry, University of Tartu, Jakobi 2, 51014, Tartu, Estonia

plaado@fi.tartu.ee

Carbon nanotubes (CNT's) are extraordinary materials due to their several superior properties like ultra-high strength (~150 GPa), Young's modulus (~1 TPa), chemical stability, thermal and electrical conductivity [1,2]. The technologies to produce the materials with high aspect ratio (up to 10^6) make CNT-s very promising for wide variety of technological applications like nanoelectronics, nanooptics, NEMS, advanced materials etc.

Being a part of numerous technical solutions, many drawbacks still exists on CNT's way for real applications. For example, the preparation of very promising CNT organic and inorganic composites usually met difficulties related to dissolving of the tubes in desired matrix material. Single nanotube based applications are limited due to problems in preparing the tubes one by one. Chemical modification of the tubes is also difficult task.

Still in some cases lucky and smart investigators have found tricks to easy handle of these materials. For example dielectrophoresis method is suggested for preparing long aligned CNT's based fibers [3,4].

Here we report mechanical and electrical properties of CNT fibers prepared by dielectrophoresis method. Our experimental set-up enables us to vary essential preparation parameters like concentration of CNT solution, drawing speed, operational voltage and frequency. Different precursor properties are varied and tested from fibers drawing point of view. Obtained fibers are tested in terms of important characteristics like: density, tensile strength, Young's modulus and conductivity. Typical as-grown fibers shows the following characteristics: diameter 1–200 μm , length up to 10 cm, density 0.2 - 0.5 g/cm^3 , tensile strength up to 150 MPa, Young's modulus 5,5 GPa, and conductivity $\sim 10^3$ S/m. We also show that slight alterations of the fibers like heat- and specific chemical treatment can considerably improve the above-mentioned characteristics.

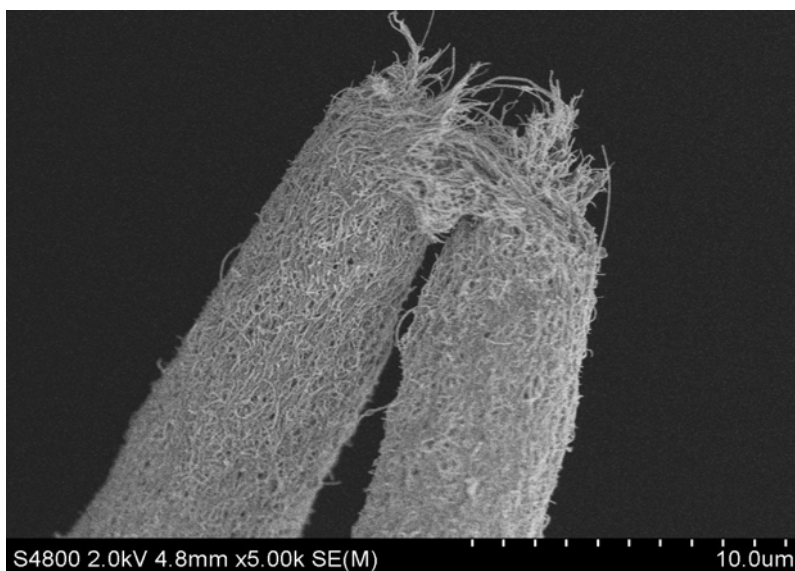


Figure 1. SEM image of broken dielectrophoresis grown carbon nanotube fiber.

Acknowledgements

This work was supported by the Estonian Science Foundation grant no 7102 and by the Estonian Nanotechnology Competence Center.

References:

- [1] B. G. Demczyk, Y. M. Wang, J. Cunnings, M. Hetman, W. Han, A. Zettl, R.O. Richie, *Mater. Sci. Eng. A* 2000, 334, 173-178.
- [2] M. F. Yu, B. S. Files, S. Arepalli, R. S. Ruoff, *Phys. Rev. Lett.* 2000, 84, 5552-5555.
- [3] H. W. Lee, S. H. Kim, Y. K. Kwak, C. S. Han, *Rev. Sci. Instrum.* 2005, 76, 046108.
- [4] J. Tang, B. Gao, H. Z. Geng, O. D. Velev, L. C. Qin, O. Zhou, *Adv. Mater.* 2003, 15, 1352-1355.

Edge-enhanced Raman scattering in Si nanostructures: Single nanowire Raman detection at ~ 1 nW laser excitation power

Vladimir Poborchii, Tetsuya Tada and Toshihiko Kanayama

MIRAI Nanodevice Innovation Research Center, National Institute of Advanced Industrial Science and Technology, AIST Tsukuba Central 4, Higashi, Tsukuba 305-8562, Japan

Vladimir.P@aist.go.jp

Specific optical properties of high-refractive-index nanostructures provide interesting experimental opportunities for studying their Raman spectra and, therefore, stress, phonon confinement and other important characteristics. Here, we report about recently discovered edge-enhanced Raman scattering (EERS) in Si nanostructures [1] and give further details related to this phenomenon. EERS takes place at the 363.8 nm excitation wavelength corresponding to very high Si refractive index $N_{Si} \sim 6.5$ (at the wavelength 370.8 nm corresponding to the Raman band of Si it is even higher $N_{Si} \sim 7.0$). In combination with well-known Si resonant-Raman enhancement in near-UV, the enhancement considered in this work makes possible Raman measurements of tiny Si structures at extremely low laser excitation power.

We studied following Si nanostructures: 1) nanostripes (rectangular cross-section with the thickness and width > 100 nm); 2) nanowires (rectangular cross-section with the thickness ~ 10 nm and width 10 - 40 nm); 3) nanopillars (circular cross-section with the diameters in the range 10 – 20 nm). In our experiments, we used 300 nm thick Si nanostripes in the shallow-trench-isolated (STI) device structures. Nanowires oriented along the [110] or [100] axes of Si wafer were fabricated from 10 nm thick semiconductor-on-insulator (SOI) structure by the electron beam lithography. High-aspect-ratio nanopillars oriented along the [001] axis of Si wafer were prepared by the same method from bulk Si. Measurements were done using confocal Raman microscope Nanofinder-30 (Tokyo Instruments Inc.) equipped with the 363.8 nm wavelength Ar laser. 1.4 numerical aperture oil-immersion lens allowed focusing light in ~ 150 nm. Diffraction grating and mirrors were optimized for the near-UV spectral range.

Our finite-difference-time-domain (FDTD) simulation showed that the electric field of the 363.8 nm light is highly concentrated at the edges of Si nanostripe when the light is polarized parallel to it. Light localization area appeared to be less than 20 nm. With decrease in the nanostripe cross-section, in the case of the nanowire, the 364 nm light electric field enhancement is observed in all volume of the nanowire. Change of the nanowire cross-section shape from rectangular to circular did not influence the effect. For the visible light, the enhancement effect is much weaker because the refractive index of Si in the visible is lower than that in UV.

In agreement with the FDTD simulation, we observed Raman enhancement at the edges of the Si nanostripes in the configuration with both incident and scattered lights polarized parallel to the stripes. EERS allowed us to obtain Raman signal from < 20 nm wide area at the stripe edge and then to determine type and value of the stress in this area with the spatial resolution much better than ~ 150 nm provided by our objective lens.

Raman measurement of nanowires required very low excitation power (~ 100 nW) in order to avoid laser-induced heating. However, even at such low excitation power, Raman signal of single Si nanowires was not weak (Fig. 1) due to EERS (we use this term even for nanowires despite the enhancement takes place in the total volume of the nanowires). Fig. 1 shows that the

nanowire spectra taken at 8 and 85 nW display the same Raman shift 520.15 cm^{-1} and FWHM 3.2 cm^{-1} , while the spectrum taken at 9500 nW excitation display slight downshift 520.05 cm^{-1} and significant band broadening up to 4.9 cm^{-1} caused by the inhomogeneous laser-induced heating [2]. We should note that the illuminated area of a 20 nm wide nanowire is 7-8 times smaller than the area of the laser spot with $\sim 150\text{ nm}$ diameter. Therefore, actual excitation power for 20 nm wide nanowire is only $\sim 1\text{ nW}$ at the $\sim 8\text{ nW}$ excitation. Taking this into account, we have found that the Raman signal of Si nanowire with the $10\text{ nm} \times 15\text{-}20\text{ nm}$ cross section displays $\sim 10^2$ enhancement compared to Si wafer or SOI the nanowires were made of.

Paradoxical increase in the Raman intensity of Si nanowire with the decrease in its width (in certain range of widths) was experimentally observed (Fig. 2) and confirmed by FDTD simulation. Phonon confinement effect was clearly detected in the Raman spectra of both nanowires and nanopillars. Si nanowire Raman band broadening and downshift (compared to the Si standard FWHM $\sim 2.8\text{ cm}^{-1}$ and Raman shift $\sim 520.5\text{ cm}^{-1}$) with decrease in their width was found to be in reasonable agreement with theoretical calculations.

This work was partly supported by NEDO.

References:

- [1] V. Poborchii, T. Tada, T. Kanayama, *Appl.Phys.Lett.* **94** (2009) 131907,
 [2] S. Piscanec, M. Cantoro, A.C. Ferrari, J.A. Zapien, Y. Lifshitz, S.T. Lee, S. Hofmann and J. Robertson, *Phys.Rev.B*, **68** (2003) 241312(R)

Figures:

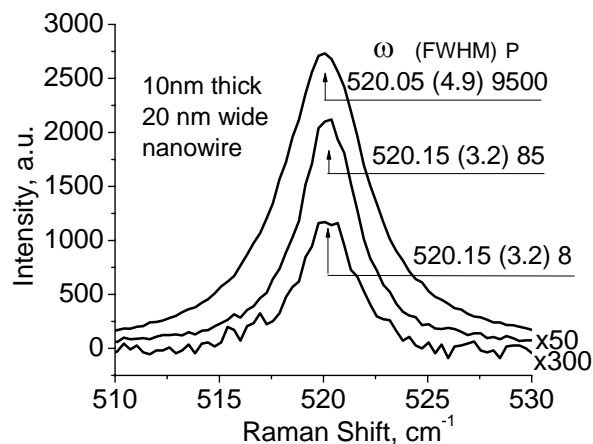


Fig. 1. Dependence of the Si nanowire Raman spectrum on the laser excitation power. ω stands for the Raman shift while P stands for the power.

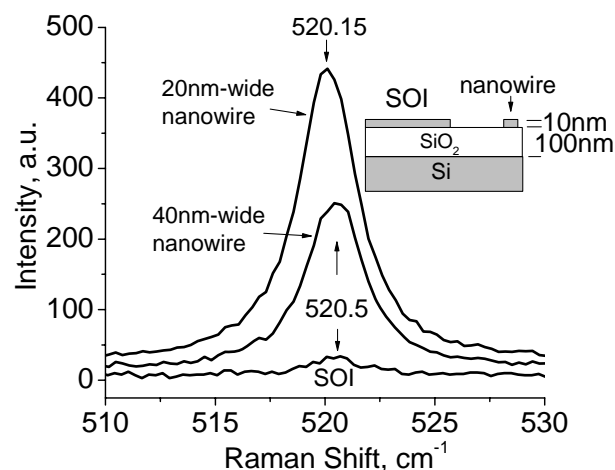


Fig. 2. Single Si nanowire Raman spectra taken in the configuration with both incident and scattered lights polarized parallel to the nanowire at the excitation power of 85 nW; and SOI Raman spectrum taken at the same condition. Cross-section of the sample with SOI and nanowire is schematically shown in the inset. (Raman signal from the Si substrate was just 1.5 times stronger than that from SOI. Therefore, one can neglect its contribution to the nanowire spectra.)

ALUMINA NANOPOWDER AND EUROPIUM Co-DOPED SILICA OPTICAL FIBERS

Ondrej Podrazky, Ivan Kasik, Marie Pospisilova, Vlastimil Matejec
Institute of Photonics and Electronics AS CR, v.v.i.,
Chaberska 57, 182 51 Prague, Czech Republic
podrazky@ufe.cz

Rare-earth doped optical fibers are important for telecommunications, where they are used in fiber lasers and fiber amplifiers. In our previous work¹ we demonstrated that doping optical fibers with nanopowders of aluminium and erbium oxides can improve their performance. While the doping of fibers with erbium is suitable for use in telecommunications because of its emission at approx. 1550 nm, the doping of fibers with europium and measurement of its emission spectra in visible range provides information about europium ions local environment, i.e. crystallinity of the fiber cores and it can help us to optimize parameters for preparation of other rare-earth doped fibers.

Two types of silica-based preforms co-doped with aluminium and europium were prepared by the methods described before¹. One type of preforms was prepared using solution of aluminium chloride while the other type was prepared using dispersion of alumina nanopowder. A solution of europium chloride was used for doping of preforms by europium.

In this work, we will present a comparison of “conventionally” and “nanoparticle” doped optical fibers and preforms using fluorescence emission spectra, AFM analysis and confocal microscopy.

This work was supported by the Czech Science Foundation, contract No.102/07/P507.

References:

- [1] Podrazky O., Kasik I., Pospisilova M., Matejec M.: Use of nanoparticles for preparation of rare-earth doped silica fibers, *Phys. Status Solidi A* (Proceedings of TNT 2008 "Trends in Nanotechnology"), accepted for publishing in 2009.

NANOPOWDERS OF MUTUAL SYSTEMS FeNi AND FeCo

Zaharov Yu.A., Popova A.N.

Kemerovo department of ICSSM SD RAS;

SEE HPE «Kemerovo State University»

650043, Kemerovo, Krasnaya st., 6 – 1331

zaharov@kemsu.ru

In order to study dependence of nanoparticles properties (such as distribution of nanoparticles sizes (narrow particle size distribution), shape and morphology, phase structure, state of particles surface, dispersiveness, porosity, electric conductivity, magnetic susceptibility) on its preparation conditions it has been researched various reaction conditions (mixture, reagents concentrations and its introduction velocity, temperature, pH medium, shaking conditions, influence of magnetic fields and so on). The preparation technique is chosen as it has a number of features and technological availability.

X-ray (phase and structural) analysis, and also X-ray fluorescence analysis have allowed considering a structure of double systems in triad Fe-Co-Ni. For system FeCo in the field of structures from 50 up to 70 weight % of cobalt there is only body-centered cubic (BCC) phase of a firm solution. Behind borders of the specified range alongside with this phase there are others, but dependence of parameter of a lattice of the BCC-phase on a weight share of cobalt is well approximated by linear function in the field of structures from 35 up to 90 %. At warming up of system before sintering (≈ 700 °C) parameters of a lattice do not vary. The phase structure and nanocomposite structures outside firm solutions – complex hydroxide iron-cobalt phase, Co(OH)_2 , FCC- and hexagonal cobalt phases is studied. In system FeNi in the field of 55–100 weight % Ni firm solutions on the basis of a nickel phase without bottom on iron border miscibility which is observed in case of the solution iron-cobalt constructed on the basis of an iron crystal lattice are realized, but the border of miscibility is observed bottom on nickel. Warming up of structures FeNi in an inert atmosphere up to 700°C leads to expansion of limits of solubility.

The X-ray phase analysis showed that the ratios of components (Fe and Ni, Fe and Co) in the region of solid solutions correspond to the calculated ones (proof of solutions formation) but deviate from them for compositions containing oxide-hydroxide phases, RFA also showed the admixture of oxygen-bearing phases in the nanosize metal (NSM) (1-6 per cent by weight depending on mode of synthesis) and high degree of purity regarding others analyzed elements (less than 0.05 per cent by weight). In connection with the above and with the purpose of investigation of NSM surface and of the character of thermo-induced transformations taking place in these materials the DTA for all systems was performed. The qualitative similarity of the composition of adsorbed gases and nanofragmental surface compounds is established for all of considered NSM – sorption of H_2O , O_2 , CO_2 ; oxides, hydroxides, carbonates. The dependence of their amounts on synthesis conditions is investigated. The general character of reactions proceeding by heating of NSM is also qualitatively defined – desorption, thermal decomposition of the surface hydroxides, carbonates, oxides, secondary oxidation of NSM by remaining oxygen traces. The temperature ranges of the proceeding of these reactions for NSM of various compositions is established. The ranges of temperature are rather close for desorption processes (80-120 °C) and differ more appreciably for reactions of thermal decomposition of hydroxide (230-280 °C), carbonates (300-320 °C) and oxides (360-400 °C) nanofragments.

The most important properties of examined NSM for practical use are their magnetic properties. Our efforts – synthesis of pure (without diamagnetic admixtures), mono-shape,

rather monodispersed, with crystalline sizes close to expected dimensions of magnetic domains, corrosion-resistant nickel, cobalt and especially solid solutions FeNi and FeCo – were pointed towards production of magnetically soft materials with high values of saturation induction in low magnetic fields. The analysis of whole experimental data shows. The systems FeNi and FeCo in the range of solid solutions are particularly magnetically soft materials with no dependence of magnetic properties on temperature in the range 5-300 °K. The saturation of magnetization is realized in low magnetic fields is about 7500 Oe for FeNi and 10400 Oe for FeCo and reaches 120 G cm³/g for FeNi and 200 G cm³/g for FeCo that is higher than the magnitudes for FeCo systems earlier obtained by other scientists.

NANO SURFACE GENERATION OF GRINDING PROCESS USING ELECTROLYTIC IN-PROCESS DRESSING (ELID) TECHNIQUES WITH SINGLE WALL CARBON NANO TUBES

S. Prabhu*, B.K. Vinayagam

School of Mechanical Engineering,
S.R.M. University, Chennai 603 203
Tamil Nadu, India

E-mail: prabhume@yahoo.co.in, bkvei23@yahoo.com

*Corresponding author

Abstract: Recent developments in grinding have opened up new avenues for finishing of hard and brittle materials with Nano-surface finish, high tolerance and accuracy. Grinding with super abrasive diamond wheels is an excellent way to produce ultra precision surface finish. However, super abrasive diamond grits need higher bonding strength while grinding, which metal-bonded grinding wheels can offer. Truing and dressing of the wheels are major problems and they tend to glaze because of wheel loading. When grinding with super abrasive wheels, wheel loading can be avoided by dressing periodically to obtain continuous grinding. Electrolytic in-process dressing (ELID) is the most suitable process for dressing metal-bonded grinding wheels during the grinding process. Nano-surface finish can be achieved only when chip removal is done at the atomic level. ELID is one of the processes used for atomic level metal removal and Nano-surface finish. However, no proper and detailed studies have been carried out to clarify the fundamental characteristics for making this process a robust one. Consequently, an attempt has been made in this study to understand the fundamental characteristics of ELID grinding and their influence on surface finish using single wall carbon nano tubes.

Keywords: Single wall carbon nanotube, Grinding process, surface roughness, ELID Process, Surface roughness tester.

References

- [1] Bandyopadhyay, B.P., Ohmori, H. and Takahashi, I. (1996) 'Ductile regime mirror finish grinding of ceramics with electrolytic in-process dressing (ELID) grinding', *Materials Manufacturing Process*, Vol. 11, No. 5, pp.789–801.
 - [2] Gomes de Oliveria, J. and Dornfeld, D.A. (2001) 'Application of AE contact sensing in reliable grinding monitoring', *Annual CIRP*, Vol. 50, No. 1, pp.217–220.
 - [3] Hassui, A., Diniz, A.E., Oliveira, J.F.G., Felipe, J. and Gomes. J.J.F. (1998) 'Experimental evaluation on grinding wheel wear through vibration and acoustic emission', *Wear*, Vol. 217, pp.7–14.
- Itoh, N. and Ohmori, H. (1996) 'Grinding characteristics of hard and brittle materials by fine grain lapping wheels with ELID', *Journal of Materials Processing Technology*, Vol. 62, No. 4, pp.315–320.

Figures:



Photographic view of the Experimental setup

Surface Roughness Using Elid Technique with SWCNT

③

Prüfer
Datum
Nr.
Filter	M1
LT	4.80 mm
LC	0.80 mm
LM/n	5
MB	80 μm
CAL	DIN
Rz	11.03 μm
Ra	1.88 μm
Rk	4.30 μm

Synthesis and characterization of highly ordered Fe_xPd_{100-x} nanowire arrays by template assisted electrodeposition

V. Vega^{1,2}, V.M. Prida², M. Ilyn³, J.J. Suñol⁴, J. Gonzalez³, B. Hernando²

¹SCTs, Universidad de Oviedo, Edificio Severo Ochoa, 33006, Oviedo, Asturias, Spain

²Depto. Física, Universidad de Oviedo, Calvo Sotelo s/n, 33007 Oviedo, Asturias, Spain

³Dept. of Material Physics, Chemistry Faculty, Universidad del País Vasco
UPV/EHU, 20080 San Sebastian, Guipuzcoa, Spain.

⁴ Universidad de Girona, Campus Montilivi, Lluís Santaló s/n, 17003 Girona, Spain
vmpp@uniovi.es

Iron-Palladium Alloys are of great scientific and technological interest due to its potential applications as sensors and microactuators [1], in hydrogen separation and membrane hydrogenation reactions [2, 3] and in environmental remediation [4].

Among the most exciting properties of Iron-Palladium alloys it is the magnetic shape memory (MSM) behavior, related to the structural Austenite-to-Martensite reversible phase transitions that can be driven by either varying temperature or applied magnetic field [5]. This implies that Fe-Pd alloys can be used as intelligent/smart thermo-elastic materials for their application in devices based on Giant-Magnetostriction, Magnetoresistance (MR) and Magnetocaloric (MCE) effects [1].

However, bulk thermo-elastic Shape Memory Alloys are not suitable for their use in rapid actuation devices because their response speed is significantly limited by the heat conduction of the material itself. One possibility for overcoming this disadvantage consists of fabricating nanostructured MSM alloys in the form of thin films [6], or as arrays of self-ordered nanowires embedded into nanoporous anodic alumina membranes (NAAM) [7], where high uniaxial shape anisotropy enables FePd nanowires to overcome thermal fluctuations even in very small sizes. Electrochemical deposition has proved its feasibility for synthesizing various functional nanostructured materials [8], whilst up to date, it is so difficult to prepare stable and effective deposition electrolytes of these FePd alloys [6].

In this work, we report on the fabrication process as well as on morphological and magnetic properties of highly ordered Fe_xPd_{100-x} ($11 \leq x \leq 75$) nanowire arrays synthesized by template assisted electrochemical deposition into the pores of NAAMs. Self-assembled nanoporous alumina membranes showing a high-ordering degree were produced by two step anodization process as reported elsewhere [9]. Electrochemical deposition of Fe-Pd nanowire arrays was performed from an aqueous ammonium citrate complex bath [4, 10] keeping the pH value around 9. Structural phases study has been carried out by X-Ray Diffraction measurements. Morphological and compositional characterization was performed by using Scanning Electron Microscopy (SEM) and Electron Dispersive X-ray spectroscopy (EDX), as it can be seen in Fig. 1 a) and b), respectively. Fig. 2 shows the in-plane and out of-plane hysteresis loops measured in a Vibrating Sample Magnetometer (PPMS-9 T). We search the optimal composition that allows obtaining best MCE effect for magnetic refrigerant devices.

References:

- [1] D.Vokoun, C.T.Hu, Scripta Mater. **47** (2002) 453.
- [2] K. J. Bryden, J. Y. Ying, J. Membrane Sci. **203** (2002) 29.
- [3] K.J. Bryden, J.Y. Ying, Nanostructured Mater. **9** (1997) 485.

- [4] B.-Y. Yoo, S.C. Hernandez, B. Yoo, Y. Rheem, N.V. Myung, *Water Sci. & Technol.* **55** (2007) 149.
- [5] H. Uchida, Y. Matsumura, H. Uchida, H. Kaneko, *J. Magn. Magn. Mater.* **239** (2002) 540.
- [6] F. Wang, S. Doi, K. Hosoiri, H. Yoshida, T. Kuzushima, M. Sasadaira, T. Watanabe, *Electrochim. Acta* **51** (2006) 4250.
- [7] X.L. Fei, S.L. Tang, R.L. Wang, H.L. Su, Y.W. Du, *Solid State Comm.* **141** (2007) 25
- [8] V. Fleury, W.A. Watters, L. Allam, T. Devers, *Nature* **416** (2002) 719.
- [9] H. Masuda, K. Fukuda, *Science* **268**, (1995) 1466.
- [10] V.M. Prida, V. Vega, V. Franco, J.L. Sánchez-Llamazares, M.J. Pérez, J.D. Santos, Ll. Escoda, J.J. Suñol, B. Hernando, *J. Magn. Magn. Mater.* **321** (2009) 790.

Figures:

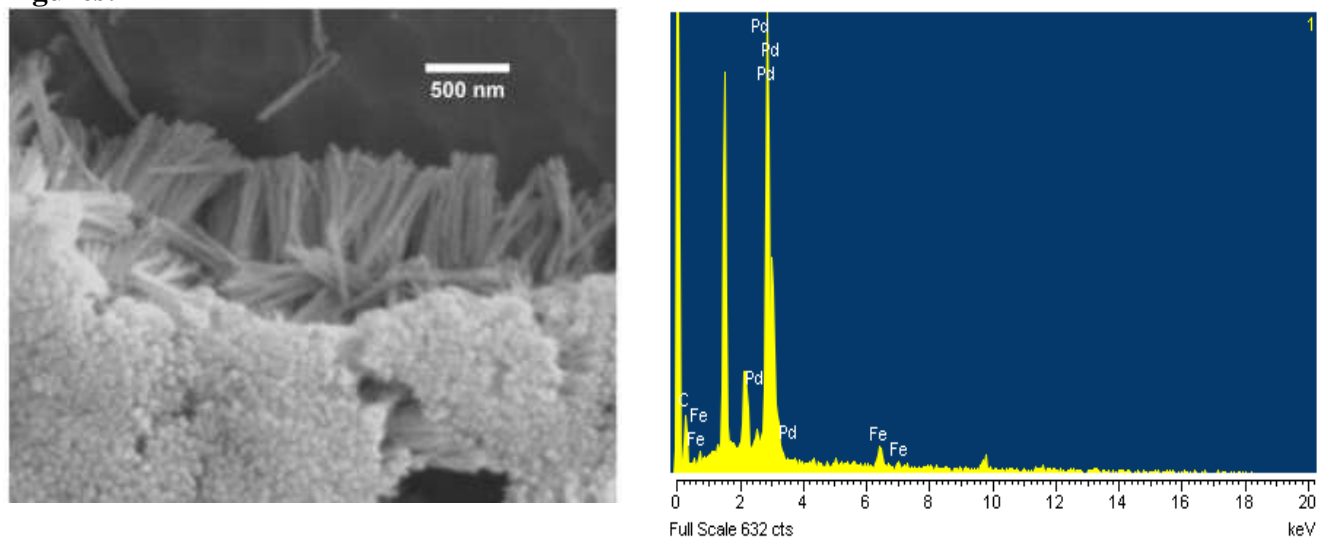


Figure 1: a) SEM Image of Fe-Pd nanowires after removing the AAO template by chemical etching. b) EDX spectrum showing the Iron and Palladium composition of nanowires.

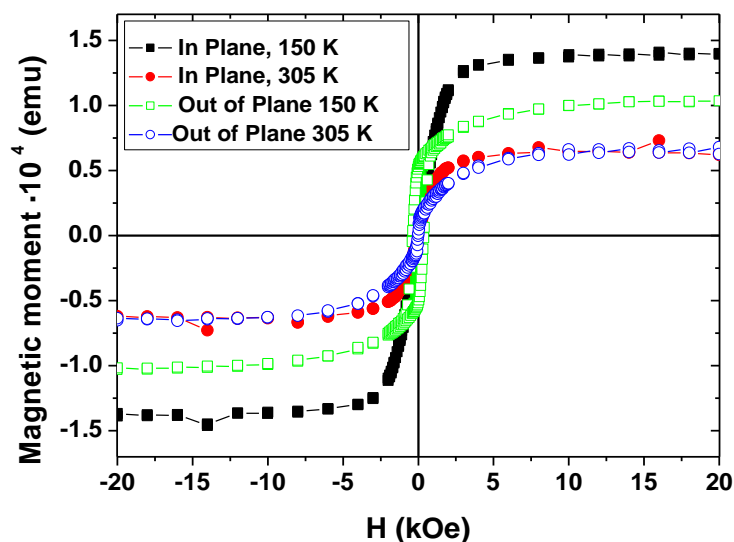


Figure 2: In plane (full symbols) and out of plane (open symbols) hysteresis loops of Fe-Pd nanowire arrays measured at 150 K and 305 K.

Topics: *Low dimensional materials; Nanomagnetism.*

QUANTITATIVE DETERMINATION OF THE MOBILITY AND SLIDING FRICTION FORCE OF GAS PHASE DEPOSITED NANOPARTICLES FROM THEIR AGGLOMERATION BEHAVIOR

Ute Queitsch¹, Alfred Hucht², Bernd Rellinghaus¹ and Ludwig Schultz¹

1 Organization, Address, City, Country

¹IFW Dresden, P.O. Box 270116 D-01171, Germany

²Universität Duisburg-Essen, Lotharstr. 1, 47057 Duisburg

u.queitsch@ifw-dresden.de

As combined efforts of industrial and basic research push the dimensions of future devices, machines and concepts down to the nanoscale a fundamental understanding and a molecular-level control of the involved mechanisms and interactions is crucial for the ultimate realization of these technological advancements. As the dimensions are reduced, surface forces increasingly gain importance for the overall system behaviour and tribological properties as friction, wear and lubrication limit the reachable degree of miniaturization for moving nanocomponents as for example in nano-electromechanical systems (NEMS). Due to the small dimensions direct measurements of e.g. included forces or surface potentials are challenging and either afford extensive experimental setups [1,2] which only allow for quantitative information when complex contact mechanics are included, or research is restricted to MD simulations which are limited in terms of complexity of the treated problems and to the confined computing resources [3,4].

We have developed a fast and easy method for the quantitative determination of the mobility and sliding friction force of gas phase deposited nanoparticles on amorphous carbon by simple image analysis. This is done by a combination of experimental studies on the agglomeration behaviour of gas phase deposited nanoparticles on surfaces with simulations on the Brownian diffusion of these particles.

Nanoparticles tend to agglomerate. Here 5nm sized FePt nanoparticles are deposited from the gas phase on aC substrates. As shown in Figure 1 (a) the fraction of agglomerated particles increases with increasing particle density. This is partly due to the statistical arrival of the particles. The according fraction is simulated and depicted as a blue curve. The experimentally derived agglomeration (plotted as symbols) is clearly higher than this purely random agglomeration. This means, the nanoparticles have to be mobile after deposition. In order to determine the nanoparticle mobility we assumed Brownian particle diffusion in two dimensions, described by

$$\langle r(t)^2 \rangle = 4Dt$$

with the diffusion constant $D=10^{-12} \text{m}^2/\text{s}$, taken from the literature [5,6]. With a constant rate of $F_d = 10^6/\text{s}$ we randomly deposited particles on a substrate with dimensions $L \times L$ and periodic boundary conditions. After deposition, the particles are allowed to move randomly on the surface for a limited time t_d , after which they are assumed to have exhausted their initial kinetic energy by friction effects. Furthermore, the particles are blocked immediately when they agglomerate with another particle. Adjusting the unknown diffusion time t_d to the experimentally observed agglomeration rates revealed, that the particles diffuse for about $10 \mu\text{s}$ (equivalent to 40 nm) after deposition (Figure 1b). Assuming, the initial kinetic energy (in the order of 3eV/ particle) is completely transferred to frictional effects, which is realistic at this low kinetic energy (soft landing), we determine the sliding friction force F to be in the order of 10^{-1}nN which is in well agreement with previous results of SFA or FFM studies.

The presented method is applicable for all mobile nanostructures on arbitrary substrates.

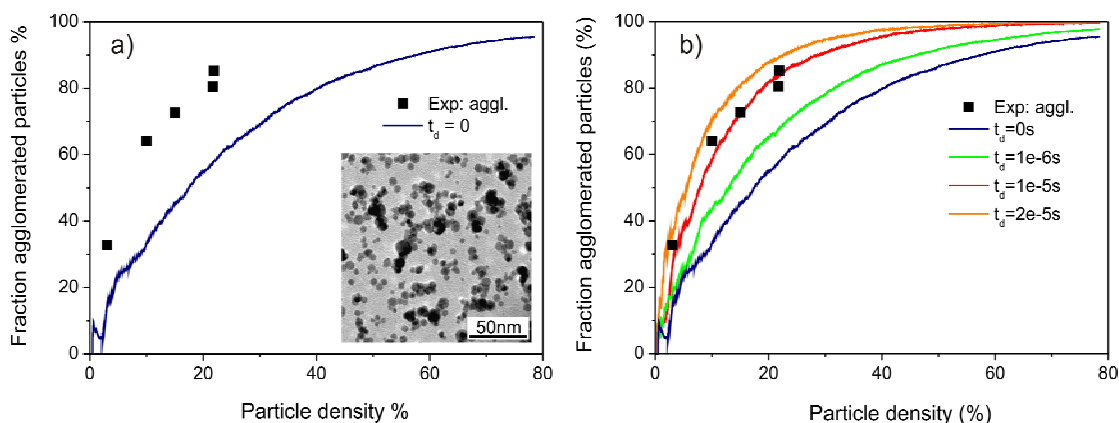


Figure 1: *a)*: Fraction of agglomeration vs. the nanoparticle density as derived from experiment and simulation. *b)*: Calculated agglomeration vs. density curves for particles which are deposited at random positions at the substrate and are then allowed to diffuse on the surface by a limited time t_a .

References:

- [1] CM. Mate, GM. McClellan, R. Erlandson and S. Chiang, *Phys. Rev. Lett.*, **59**, (1987), 1942
- [2] UD. Schwarz, O. Zwörner, P. Köster and R. Wiesendanger, *Phys. Rev. B*, **56**, (1997), 6987
- [3] U. Landmann, WD. Luedtke, NA. Burnham and RJ. Colton, *Science*, **248**, (1990), 454
- [4] P. Deltour, JL. Barrat and P. Jensen, *Phys. Rev. Lett.*, **78**, (1997), 4597
- [5] L. Bardotti, P. Jensen, A. Hoareau, M. Treilleux and B. Cabaud, *Phys. Rev. Lett.*, **73**, (1995), 4694
- [6] J. Chen and KY., Chan, *Molecular Simulation*, **31**, (2005), 527

Optical anisotropy of self-aligned Ag nanoparticles and nanowires on pre-rippled Si surfaces

M. Ranjan, S. Facsko, W. Möller

Institute of Ion-Beam Physics and Materials Research,
Forschungszentrum Dresden-Rossendorf, Dresden, Germany
m.ranjan@fzd.de

Nobel metal nanoparticles exhibit special optical properties due to their localized Surface-Plasmon-Resonance (SPR). The SPR frequency and strength depend on particle size, shape, surrounding medium, and alignment of the particles. In recent years many studies have been conducted in which metal nanoparticles were grown in a controlled and ordered way on pre-structured substrates. In this way the optical properties could be tuned and a strong optical anisotropy was achieved [1-4]. One way to make the pre-patterned substrates and to align particles is to use lithography. However, in order to reach patterns with dimensions similar to the particle size e-beam lithography has to be used which is not economic for large area patterning.

In the present study ion beam sputtering has been used for pre-structuring of the substrate followed by e-beam evaporation for deposition of the metal. First a low energy ion beam (Ar^+ , 500 eV) is incident on the substrate surface (Si in our case) at an angle of 67° to the surface normal to produce well ordered (20-50 nm) ripple patterns [5]. An atomic force microscopy image of such a patterned Si surface is shown in Fig. 1a. Then physically vaporized Ag atoms are deposited at grazing angle of 70° to the surface normal and perpendicular to the ripples direction. Varying different deposition parameters, i.e. ripple periodicity, substrate temperature and atomic flux, we were able to produce well ordered Ag nanoparticles and nanowires. A very high degree of alignment not reported so far using the present technique has been achieved. Fig. 1b and 1c show the aligned Ag particles and nanowires, respectively, self-aligned on pre-patterned Si.

The effect of temperature was also investigated for three cases: 1) deposition on a heated substrate; 2) post annealing in vacuum after deposition; and 3) post annealing after deposition and exposing to atmosphere. In all three cases the temperature has different influence on the alignment of the particles.

The aligned Ag nanoparticles and nanowires were characterized using ellipsometric spectroscopy in the photon energy range of 1.2-3.3 eV. Angle dependent change in the ellipsometric parameters Ψ and Δ show a strong anisotropic behavior (Fig. 2a), which is not observed on a bare Si rippled surface or for non-aligned Ag particles on a flat Si substrate. Dielectric functions extracted from the ellipsometric measurements using Lorentz oscillator model also confirm a strong angle dependency. Fig. 2b shows the real and imaginary part of the dielectric function for three different ripples orientation of 0° , 45° , and 90° with respect to the incoming light. We will report how this optical anisotropy depends on the shape, size, and alignment of the Ag nanoparticles and nanowires, respectively.

References:

- [1] T.W.H. Oates, A. Keller, S. Facsko, A. Mücklich, *Plasmonics* **2** (2007) 47.
- [2] S. Camelio, D. Babonneau, D. Lantiat, L. Simonot, *EPL* **79** (2007) 47002.
- [3] T.W. H.Oates, A.Keller, S.Noda, S.Facsko, *Appl. Phys. Lett.* **93** (2008) 063106.
- [4] A. Toma, D. Chiappe, D. Massabo, C. Boragno, F. B. de Mongeot, *Appl. Phys. Lett.* **93** (2008) 163104.
- [5] A. Keller, S. Facsko, and W. Möller, *New J. Phys.* **10** (2008) 063004.

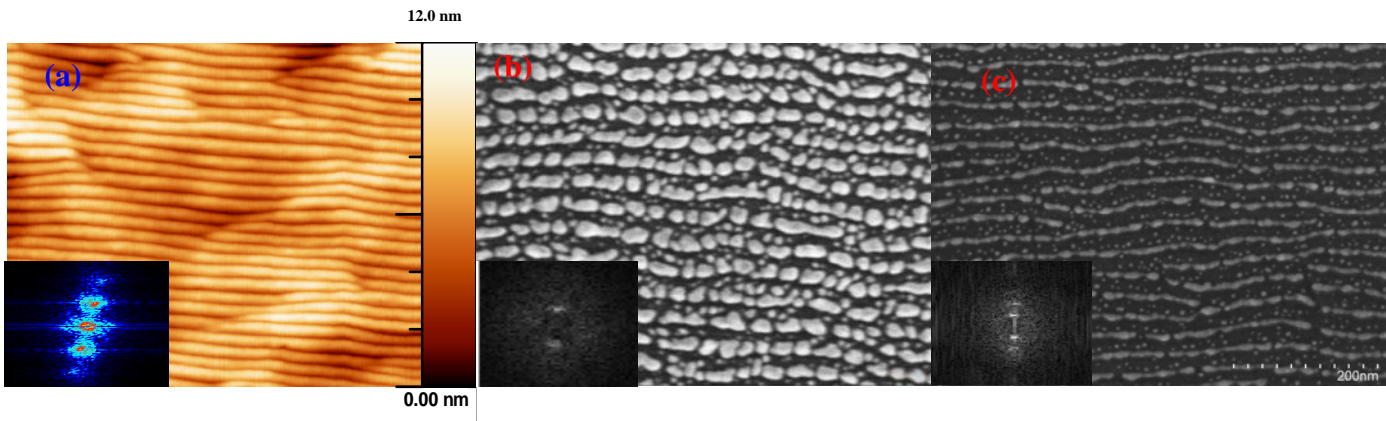


Figure 1: (a) Atomic force microscopy image of pre-rippled Si substrate, (b) Scanning electron microscopy image of aligned Ag nanoparticles and (c) of nanowires on pre-patterned Si templates with a periodicity of 32 nm. Insets show the Fourier transforms of the images.

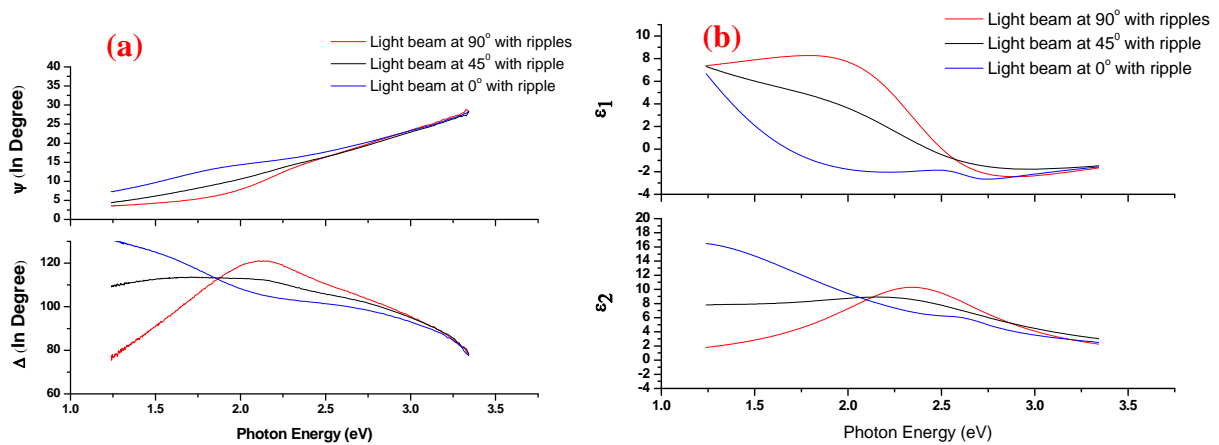


Figure 2: (a) (Ψ, Δ) capture using ellipsometry. The light beam is incident at three different angles of 0° , 45° and 90° with respect to the ripples orientation. (b) Dielectric function (ϵ_1, ϵ_2) extracted using Lorentz oscillator model.

EFFECT OF SILVER NITRATE CONCENTRATION, TEMPERATURE AND TIME ON BIOSYNTHESIS OF SILVER NANOPARTICLES USING '*ASPERGILLUS FUMIGATES*'

Zahra Ranjbar Navazi, Mohammad Pazouki, Farah Sadat Halek
Energy Division, Materials & Energy Research Center, Karaj, Iran
Corresponding Author Email: mpazouki@merc.ac.ir

Abstract

Research on synthesizing nanoparticles with desirable shape, size and composition has increased due to unusual physicochemical and optoelectronic properties of nanoparticles. By using the method of microbial biosynthesis, nanoparticles of different chemical composition, well-defined size and distinct morphology is possible [1].

In this study silver nanoparticles have been synthesized using '*Aspergillus fumigatus*' [2] with different silver nitrate concentrations including 0.5, 1, 1.5 and 2mM. Also the effect of temperature and time lapse on the value and size of the synthesized silver nanoparticles has been investigated. Four samples in the same conditions were agitated in different temperatures including 25°C, 30°C, 35°C, 40°C, 45°C and the optimized one was withdrawn in different time intervals to measure the absorbance using UV-visible spectrophotometer. Actually silver nanoparticles formation has been confirmed spectrophotometrically in which, a peak around 420 nm in UV-visible spectrum corresponds to the Plasmon absorbance of silver nanoparticles [3,4]. The size and morphology of the particles have been investigated using transmission electron microscopy (TEM).

According to the UV-visible spectrums shown in Figure1, the optimized silver nitrate concentration was 1.5mM because of the high absorbance around 420nm and smoother shape in the spectrum of this sample in compared with other spectrums.

Also as indicated in Figure 3, samples in 40°C and 45°C had the highest absorbance around 420nm but UV-visible spectrum of the sample in 40°C is smoother than the one belonged to the sample in 45°C, demonstrating more monotonous size distribution in this sample.

According to the TEM micrographs in Figures 2 and 4, the size of the synthesized nanoparticles in 25°C and 40°C was sequentially in the range of 5-15nm and 10-60nm. Consequently choosing the appropriate temperature has depended on the preference of the reduction rate of the silver ions or the desirable size of the silver nanoparticles.

Keywords: silver nanoparticles, biosynthesis, fungus, *Aspergillus fumigatus*.

References:

- [1] Bhattacharya D, Rajinder G (2005) Nanotechnology and potential of microorganisms. *Crit Rev Biotechnol* 25:199– 204.
- [2] Kuber C. Bhainsa, S.F. D'Souza, Extracellular biosynthesis of silver nanoparticles using the fungus *Aspergillus fumigatus*, *Colloids and Surfaces B: Biointerfaces* 47 (2006) 160–164.
- [3] T.J. Beveridge, M.N. Hughes, H. Lee, K.T. Leung, R.K. Poole, I. Savvaiddis, S. Silver, J.T. Trevors, Metal–microbe interactions: Contemporary approaches, *Adv. Microb. Physiol.* 38 (1997) 177–243.
- [4] J.D. Holmes, P.R. Smith, R. Evans-Gowing, D.J. Richardson, D.A. Russel, J.R. Sodeau, Energy-dispersive-X-ray analysis of the extracellular cadmium sulfide crystallites of *Klebsiella aerogenes*, *Arch. Microbiol.* 163 (1995) 143–147.

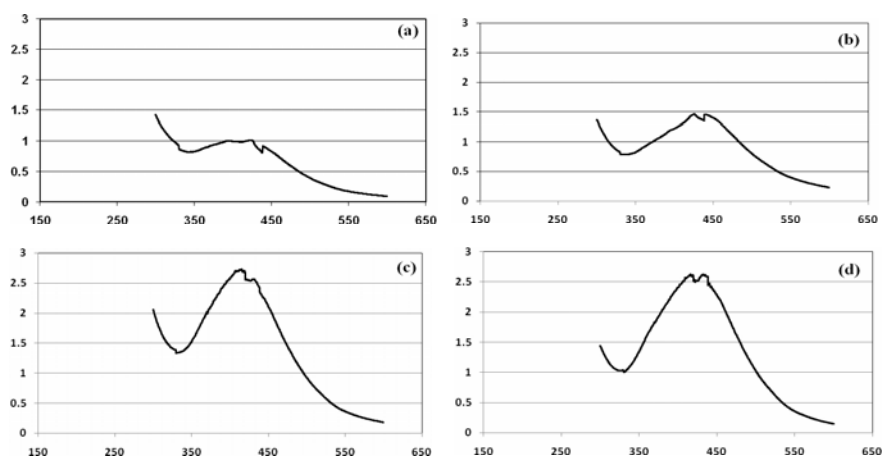


Figure1: UV-visible spectrum of samples with: (a)0.5, (b)1, (c)1.5 and (d)2mM silver nitrate.

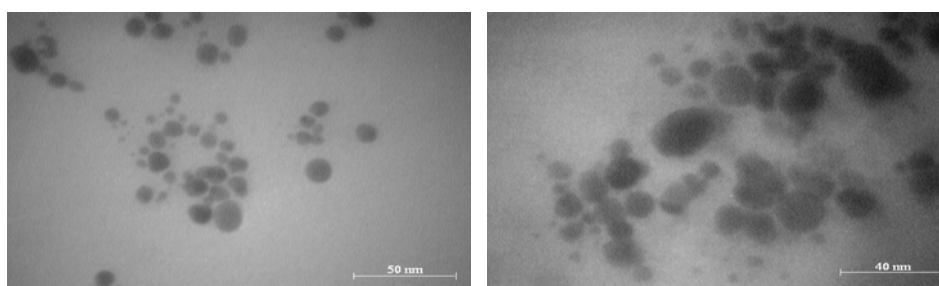


Figure2: TEM micrographs of samples with: (a)1.5, (b)2mM silver nitrate.

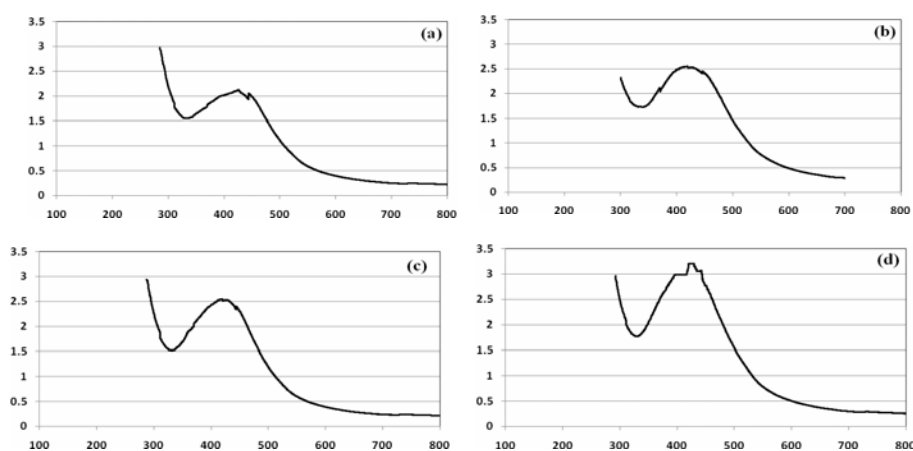


Figure3: UV-visible spectrums of the samples in: (a)30, (b)35, (c)40 and (d)45°C.

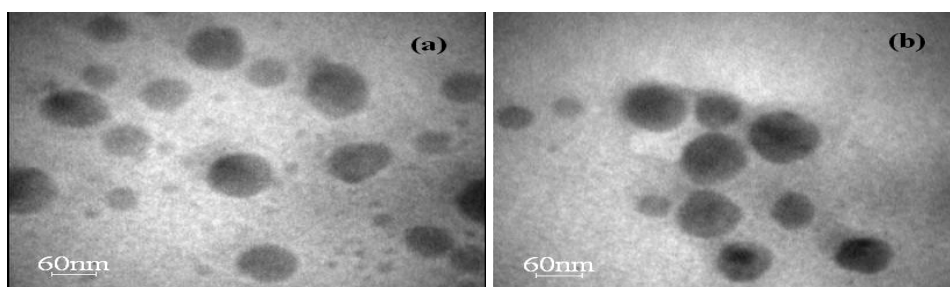


Figure4: TEM micrographs of samples in: (a)35°C, (b)40°C

Nanostructured Surface Preparation for Enhancement of Sensitivity of Electrochemical DNA Sensors

Tesfaye Refera Soreta¹, Jorg Strutwolf², Olivier Y.F. Henry¹ and Ciara K. O'Sullivan^{1,3}

¹*Nanobiotechnology and Bioanalysis Group, Department of Chemical Engineering, Universitat Rovira I Virgili, Av. Països Catalans, 26, 43007, Tarragona, Spain*

²*Tyndall National Institute, Lee Maltings, Cork, Ireland*

³*Institució Catalana de Recerca i Estudis Avançats, Passeig Lluís Companys 23, 08010 Barcelona, Spain.*

tesfaye.refera@urv.cat, ciara.osullivan@urv.cat

Biosensor signals can be enhanced by specifically designed transducer surfaces for anchoring the recognition molecules. For electrochemical DNA biosensors, the spacing and orientation of immobilized DNA probes is critical for maximal hybridization with target and to achieve low detection limit [1-3]. We have developed a nanostructured electrode surface preparation method that can create a favorable environment for DNA probe molecule attachment to electrode surface and creates suitable orientation for maximal hybridization with the complementary target. The approach is based on sequential gold nanoparticles electrochemical nucleation on glassy carbon surface [4]. Briefly, the first stage of gold nanoparticles are nucleated on clean glassy carbon electrode by applying a potential pulse. The nucleated nanoparticles are then insulated by forming self assembled monolayer (SAM) of thiolated probe DNA. For effective insulation of the nanoparticles, 2-mercaptoethanol is used as a back filler SAM. Then, the second stage of gold nanoparticles nucleation is made on glassy carbon area that was not covered with gold nanoparticles in the first deposition stage. The method enables an increase of the number density of nanoparticles deposited by preventing them from aggregation as well as to create isolated domains for probe molecule for effective hybridization with target molecules there by eliminating problems associated with steric hindrance. For 10 nM target nucleotide consisting of 63 bases detected by sandwich assay using HRP labeled marker probe, hydrogen peroxide as a substrate and hydroquinone redox mediator. A 15 fold higher signal was observed with the nanostructured electrode than planar polycrystalline gold electrode. Currently the work is in progress to further optimize the system in order to determine the lowest detection limit.

References:

- [1] Southern, E., Mir K., Shchepinov M., Nature Genetics, **21** (1999): p. 5-9.
- [2] Sanchez-Pomales, G., Santiago-Rodriguez L., Rivera-Velez N.E., Cabrera C.R., Journal of Electroanalytical Chemistry,. 611 (2007): page. 80-86.
- [3] Satjapipat, M., Sanedrin, R., Zhou, F., Langmuir, 17 (2001), page 7637-7644
- [4] Soreta, T.R., Strutwolf, J., O'Sullivan, C.K., ChemPhysChem. 9 (2008) page 920-927

Figures:

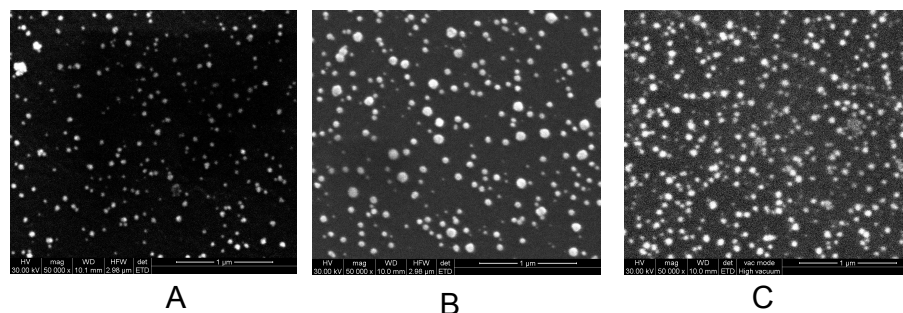


Figure 1. Scanning electron microscopy images of gold nanoparticles electrochemically deposited on glassy carbon electrode at 0V versus Ag/AgCl from 0.1 mM KAuCl₄ in 0.5 M H₂SO₄

- (A) first deposition stage (5 seconds),
- (B) Three deposition rounds of 5 s each with out SAM protection
- (C) Three deposition rounds of 5 s each with SAM of 2-mercaptoethanol protection. The increase in particle number density due to protection of the particles with a SAM in

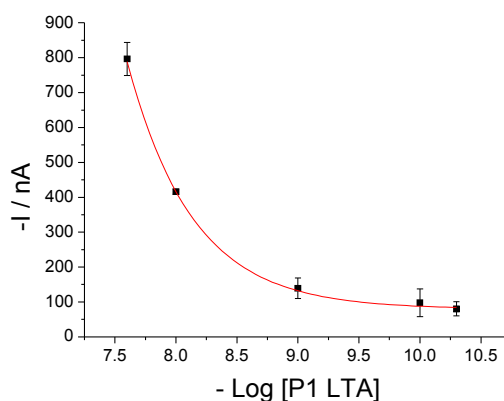


Figure 2. Preliminary result

Calibration curve for determination of P1-LTA (63 bases long) single strand target DNA by sandwich assay using horseradish peroxidase conjugated marker probe. Optimization of the procedure is in progress in order to achieve detection of even lower concentration of target. (error bar standard deviation for triplicate determinations)

Catalyst Oxidation for Silicon nanowire VSS growth

Vincent T. Renard, Michael Jublot, Denis Rouchon, Patrice Gergaud, Amal Chabli & Vincent Jousseume

CEA, LETI, MINATEC, F38054 Grenoble, France

vincent.renard@cea.fr

The lack of a CMOS compatible synthesis catalogue prevents successful transfer to industry of potential applications of silicon nanowires (NW). Here, Gold and high temperatures are prohibited. Unfortunately, growing nanowires with CMOS friendly catalyst (like Copper) at low temperature is in general not possible with standard Vapour-liquid-Solid mechanism. Indeed, these metals form an eutectic with silicon only at elevated temperatures. It was very recently discovered that the metal catalyst may remain in the solid state during growth allowing for the so-called Vapour-Solid-Solid growth (VSS) [1-4]. Soon after this discovery, diffusion during incubation (catalyst preparation) has been identified as setting a fundamental lower limit on the VSS growth temperature using Copper ($T > 500^\circ\text{C}$) [5]. We demonstrate here that this limitation can be circumvented by chemical activation. Our approach is based on oxidation of the catalyst before growth. It is opposite to common practice since the presence of oxygen is usually thought of as poisoning the growth. On the contrary, taking advantage of the high reactivity of cuprous oxide, it circumvents the limitations when incubation relies on the diffusion of silicon in copper.

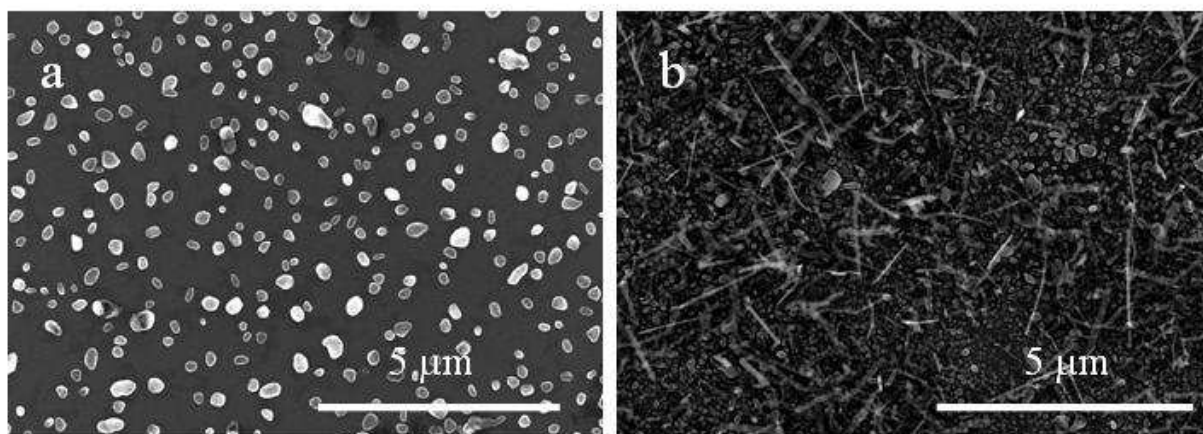


Figure: a) Silicon nanowire yield with oxide free Copper. b) Silicon nanowire yield with oxidized Copper.

Figure 1 shows that at 400°C , silicon nanowires grow only if Copper is oxidized by flowing O_2 prior to growth. It is well documented that thermally oxidizing Copper forms cuprous oxide Cu_2O . The interest for this very reactive compound was recently renewed since it may have interesting applications in photovoltaics and chemistry [6]. We propose that upon introduction of Silane (SiH_4) Cuprous oxide chemically activate the formation of Cu_3Si according to the following reaction: $2\text{SiH}_4 + 3\text{Cu}_2\text{O} \rightarrow 2\text{Cu}_3\text{Si} + 3\text{H}_2\text{O} + \text{H}_2$ ($\Delta G = -43.8$ kJ as determined with FactSage® package). Previously, Kalache *et al.* had measured an activation energy for the growth of Si nanowires with Cu with a mechanism based on diffusion. Impressively, this activation energy corresponds to the formation of Cu_3Si by diffusion of silicon in copper and sets a lower synthesis temperature to 500°C by this method. Together with the experiments of Kalache *et al.* [5] our result therefore demonstrates that for the growth to occur, the main energy barrier to overcome is the formation of Cu_3Si from which the nanowires precipitate. At least down to 400°C , the growth is not limited by the usual steps (gas-phase transport of the Si-

containing gas to the wire, precursor decomposition, surface/volume diffusion of Si in the silicide or incorporation of Si to the growing wire) but by catalyst preparation.

We will discuss the structural and chemical quality of the nanowires obtained by this new method of chemical activation of the growth which opens up new possibilities in view of CMOS compatibility.

References:

- [1] T. I., Kamins, Stanley *et al*, J. Appl. Phys. **89**, (2001)1008-1016
- [2] Y. Wang *et al*, Nature Nanotech. **1**, (2006) 186-189
- [3] Y. Yao, S. Fan, Materials Letters **61**, (2007) 177–181
- [4]. J. Arbiol *et al*, Nanotechnology **18**, (2007) 305606
- [5] B. Kalache, P.R. Cabarrocas, A. F. Morral, *Inn. J. Appl. Phys., Part 2* **45** (2006) L190
- [6] M. Lampimäki *et al*. J. Chem. Phys. **126**, (2007) 034703

THERMAL TRANSPORT THROUGH MESOSCOPIC DIELECTRIC PARTICLES AT LOW TEMPERATURES

D. Reyes, A. Ávila

Universidad de los Andes, Carrera 1 N° 18A 10, Bogotá D. C., Colombia

di-reyes@uniandes.edu.co, a-avila@uniandes.edu.co

Research on phonon propagation through nanostructures is expected to allow the exploration of thermal transport narrowing the degrees of freedom just to one dimension. Studies have shown that, although electrons and phonons obey different statistics, the thermal conductance in one-dimensional systems under low temperature conditions is also quantized [1]. Deviations from the exact thermal quantization have been reported as functions of the wire geometry and wire-to-reservoirs coupling [1]–[4]. Estimations of the thermal conductivity have been carried out following the Landauer formalism in which the thermal conductance of one-dimensional channels depends of the transmission coefficient for each propagating mode [1].

On dielectric channels, at low temperatures (0.3 – 1 K), modes having a close-to-zero cutoff frequency make a major contribution to thermal conductance [3]. In this article, we only take into account the longitudinal mode. By means of numerical methods (Finite Differences Method), the transmission probability between reservoirs is obtained for straight, catenoidal and spherical channel structures as function of phonon wave number. The accuracy of numerical method was verified for simple channel structures whose analytical results were available [1].

Transmission probability proved to be dependent of the thermal dielectric channel's cross sectional area. The obtained transmission probabilities show peaks associated to phonon scattering which depends on (a) the relation between the contact area at the interface and minimum channel area; (b) the channel length; and (c) phonon wavelength. These three parameters seem to control the dispersion relation more than the channel's shape itself.

Thermal transmission through spherical particles has not been verified back from experimental data; however, the work proposes the experimental conditions that should be fulfilled. Results show that it is possible to control thermal conductance at low temperatures by means of geometrical parameters of the channel.

References:

- [1] K. Schwab, E. A. Henriksen, J. M. Worlock, M. L. Roukes, Measurement of the quantum of thermal conductance, *Nature* 404, 974, April 27, 2000.
- [2] L. Rego, G. Kirczenow, Quantized Thermal Conductance of Dielectric Quantum Wires, *Phys. Rev. Lett.* 81, 232, 1998.
- [3] D. H. Santamore, M. C. Cross., Effect of phonon scattering by surface roughness on the universal thermal conductance, *Phys. Rev. Lett.* 87, 115502, 2001.
- [4] D. E. Angelescu, M. C. Cross, M. L. Roukes, Heat transport in mesoscopic systems, *Superlatt. Microstruct.* 23, 673, 1998.

CYSTEINE GOLD NANOPARTICLES IN OPEN-TUBULAR CAPILLARY ELECTROCHROMATOGRAPHY

Pavel Řezanka, Kamil Záruba, Magda Vosmanská, David Sýkora, Vladimír Král
Dept. of Analytical Chemistry, Institute of Chemical Technology Prague, Technická 5, 166 28
Prague 6, Czech Republic
pavel.rezanka@vscht.cz

Gold nanoparticles which are known for thousands years started their progress in 19th century. Nowadays gold nanoparticles are used in several fields of chemistry, physics, materials, medicine, and optics due to their unique physical and chemical properties (ref. 1). However, their applications in the separation science are still relatively rare. Nanoparticles have been successfully used to enhance optical and electrochemical detection and separation (ref. 2).

Gold nanoparticles usable in separation techniques can be prepared by several means. The most frequent approaches are: first, citrate reduction of aqueous solution of a gold(III) salt; second, borohydride reduction of aqueous solution of a gold(III) salt; and third, two phase (water-toluene) reduction using borohydride as reducing agent and tetraoctylammonium bromide as transfer agent of gold(III) salt. Each method provides different concentration and size of the generated nanoparticles as well as the different potential for their subsequent modification (ref. 3). Most of the applications are related to capillary electrochromatography where nanoparticles have been added to the run buffer or coated to the walls of a capillary (ref. 3). The immobilization of the gold nanoparticles onto the inner surface of a fused-silica capillary can be carried out applying layer-by layer technique (ref. 4) or covalent modification *via* (3-mercaptopropyl)trimethoxysilane (ref. 5).

The functionality of biological compounds is based on chirality. The chirality of compounds is crucial factor in living organisms, therefore enantiospecific analysis is very important in the separation techniques. Although Wang et al. reported use of chiral molecule cysteine modified gold nanoparticles in capillary electrophoresis, they only used this system for separation different compounds, not enantiomers (ref. 4).

In this work the gold nanoparticles were prepared by citrate reduction of a gold(III) salt. In the next step, the citrate stabilized nanoparticles were modified with cysteine at different concentrations. The resulting nanoparticles were characterized by absorption spectroscopy and transmission electron spectroscopy and used for the immobilization into the capillaries. The fused-silica capillaries were pre-derivatized by (3-mercaptopropyl)trimethoxysilane that allows a covalent modification of the capillary walls with the modified gold nanoparticles (Fig. 1). These capillaries were used to separate the enantiomers of selected aminoacids and the effect of the concentration of immobilized cysteine, concentration of the immobilized nanoparticles, pH of the running buffer, and other factors is discussed.

Acknowledgement: Financial support from The Ministry of Education, Youth and Sport of the Czech Republic, no. MSMT6046137307, and from The Czech Science Foundation, no. 203/09/0675, are gratefully acknowledged.

References:

- [1] M.-C. Daniel, D. Astruc, Chem. Rev., **104** (2004) 293-346.
- [2] P. Řezanka, K. Záruba, V. Král, Chem. Listy, **101** (2007) 881-885.
- [3] C. Nilsson, S. Birnbaum, S. Nilsson, J. Chrom. A, **1168** (2007) 212-224.
- [4] W. Wang, L. Zhao, F. Zhou, J.-J. Zhu, J.-R. Zhang, Talanta, **73** (2007) 534-539
- [5] L. Yang, E. Guihen, J. D. Glennon, J. Sep. Sci., **28** (2005) 757-766.

Figures:

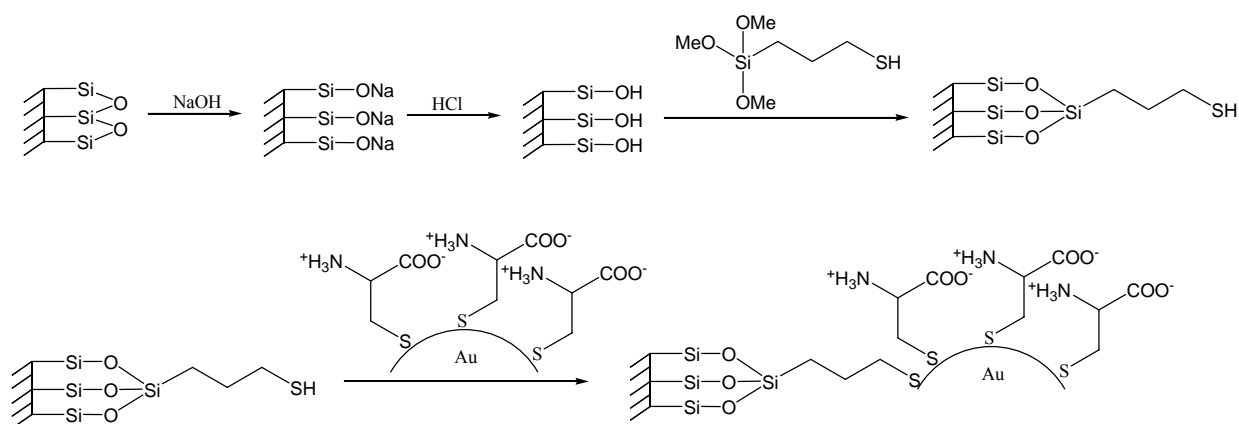


Figure 1. Schematic preparation of capillary modified by gold nanoparticles

FIELD EMISSION CHARACTERIZATION OF INDIVIDUAL MOLECULES AND ATOMIC STRUCTURES

Moh'd Rezeq^{a*}, Ma Han Lwin^a, Christian Joachim^{a, b}

a) Institute of Materials Research and Engineering (IMRE), 3 Research Link, Singapore 117602 (Singapore).

b) CEMES-CNRS, 29 rue J. Marvig, PO Box 4347, F-31055 Toulouse Cedex, France.

* Corresponding author: Email: rezeqm@imre.a-star.edu.sg

It is quite common that atomic and molecular entities can be readily identified and studied in scanning probe microscopy, particularly in scanning tunneling microscope (STM). In such powerful machines a well defined STM tip allows the manipulation and the spectroscopic investigations of atoms or molecules on a flat substrate [1-3]. Here, we introduce a new approach for selecting, viewing and analyzing atomic and molecular configurations on the apex of sharp tips. The field ion microscope (FIM) is an ideal instrument where a typical STM like tip can be characterized and sharpened with atomic precision [4-7]. We demonstrate that when the tip radius is reduced to < 1 nm new field emission characteristics emerge [8]. Unlike conventional tips, in this regime the field electron emission is confined to the location of the most protruding atoms on the apex surface, as illustrated in Fig 1.

For further analysis, two double atom tip cases have been selected with different atom-atom separations, as in Fig. 2. The Field emission microscopy (FEM) revealed a reasonable match between FEM maxima and the atom positions for relatively distant atoms. Whereas a larger apparent spacing between FEM peaks compared to the corresponding atom positions have been noticed for closely spaced pair of atoms, Fig. 2. In the latter case the field emission intensity has also been observed to alternate between both atomic channels at an increasing applied tip voltage. This alternation phenomenon is evident in Fig. 3 and indicates a field emission competition between the two electron atomic channels that are created due to the existence of local surface bands.

Another promising application of nano-tips will be presented which is pertaining to the selection and characterization of individual molecules. In fact several papers have showed FEM images of Cu-phthalocyanine (Cu-Pc) molecules deposited on blunt tips [9,10]. When the tip apex is reduced to ~ 1 nm radius, in the range of the molecular size, we show that a single molecule can be selectively deposited and imaged, as shown in Fig 4. This process permits the electronic characterization of a single molecule in the FEM [11].

References:

1. D. M. Eigler and E. K. Schweizer, *Nature* **344** (1990) 524.
2. C. Joachim, J. Gimzewski, R. Schlittler and C. Chavy, *Phys. Rev. Lett.* **74** (1995) 2102.
3. P. G. Piva, G. Dilabio, J. L. Pitters, J. Zikovsky, M. Rezeq, S. Dogel, W. A. Hofer and R. A. Wolkow, *Nature* **435** (2005) 658.
4. M. Rezeq, J. Pitters and R. Wolkow, *J. Chem. Phys.* **124** (2006) 204716.
5. V. T. Binh, S. T. Purcell, V. Semet and F. Feschet, *Appl. Surf. Sci.* **130-132** (1998) 803.
6. H. W. Fink, *IBM J. Res. Develop* **30** (1986) 461.
7. T. Y. Fu, L. C. Cheng, C. H. Nien and T. T. Tsong, *Phys. Rev. B* **64** (2001) 113401.
8. M. Rezeq, C. Joachim and N. Chandra, *Surf. Sci.* **603** (2009) 697.
9. A. Melmed and E. W. Muller, *J. Chem. Phys.* **29** (1958) 1037.
10. H. Morikawa and K. Okamoto, *Jpn. J. Appl. Phys.* **35** (1996) 4486.
11. Moh'd Rezeq, Ma Han Lwin and Christian Joachim, in progress.

Figures:

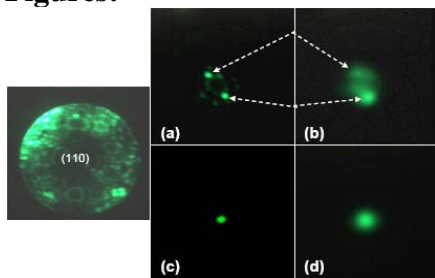


Fig. 1. A FIM of a (110) W blunt tip, left. (a) a nanotip with with an atomic scale apex at 4.5 kV, (b) FE confined to the most protruding atoms at -380V. (c) and (d) FIM and FEM of a single atom apex, at 2.9 kV and -260 V respectively

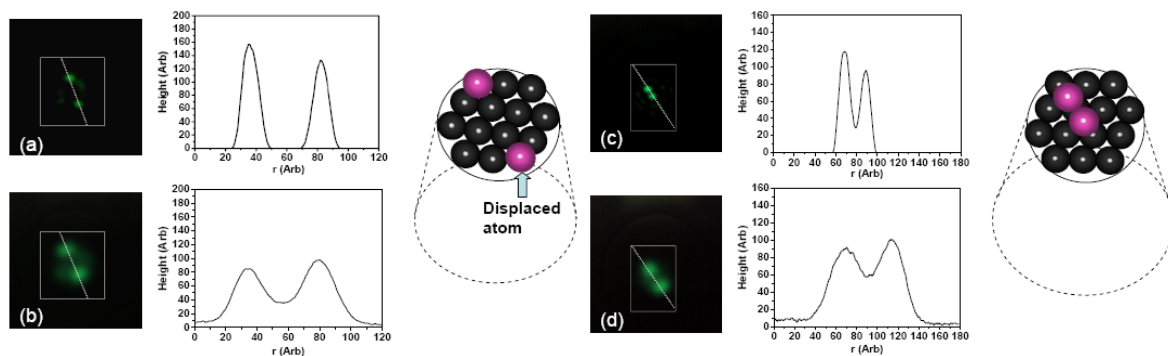


Fig. 2. (a) and (b) FIM and FEM of two distant protruding atoms with their line profiles and representing ball models. (c) and (d) FIM and FEM of two close atoms with the their line profiles and representing ball models.

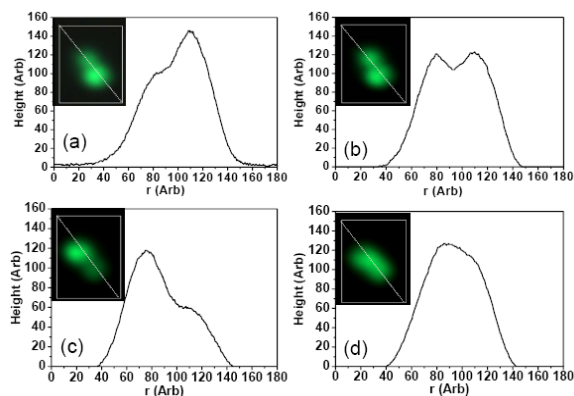


Fig. 3. Field emission alternation at elevated applied voltages, -(380 to 420 V)

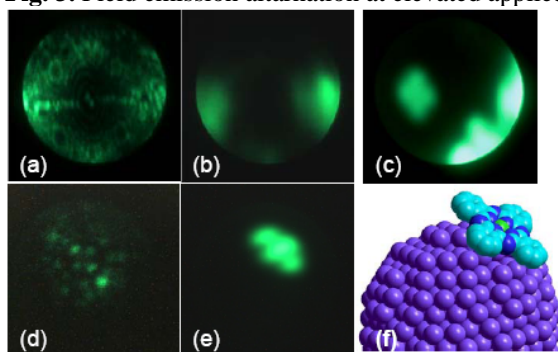


Fig 4. (a & b) FIM and FEM of a clean and blunt tip. (c) a cluster of Cu-Pc deposited, bottom right along with an individual molecule around the centre of the apex with well resolved 4 lobes. (d) a FIM of an ultra sharp tip, (e) a single Cu-Pc molecule deposited on the tip pex as illustrated in the next model in (f).

Formation and characterization of electrically induced nanodiodes in thin oxide films

M. Ricoma, E. Miranda and J. Suñé

Departament d'Enginyeria, Universitat Autònoma de Barcelona, 08193 Bellaterra, Spain
enrique.miranda@uab.es

The application of a high voltage to the gate electrode of a MOS structure generates traps or defects within the insulating material that eventually leads to its dielectric breakdown. This final state consists in the formation of localized leakage current paths between the electrodes which exhibit conductance levels close to the quantum conductance unit $G_0=2e^2/h$, where e is the electron charge and h the Planck's constant. In this work, we extend a previous model for the I-V characteristic of a single spot [1] to the case of multiple parallel leakage paths. The model is based on the so-called generalized diode equation (diode + series resistance) and is solved in terms of the Lambert W function, *i.e.* the solution of the transcendental equation $we^w=x$. Within this framework, the diode-like behavior is ascribed to the formation of the band bending at the semiconductor electrode and the series resistance to the constriction effect. We show that by means of electrical stress, we are able to control the conductance level of the device simply by adding intentionally generated leakage sites.

For the experiments we used MOS capacitors grown on n-type Si (10^{15} cm^{-3}), with 3 nm-thick SiO₂, poly-Si gate and area of $1.96 \times 10^{-5} \text{ cm}^2$. Initially, the spots are generated using a high voltage sweep from 5V to 13V as shown in Fig. 2. The curves were measured in different samples. The considered region of the I-Vs corresponds to the linear conduction regime (also known as hard breakdown) and each jump in the characteristic can be associated with the creation of a new spot in a different location over the device area. For one of the I-Vs plotted in Fig. 1, Fig. 2 reveals that the conductance of the whole characteristic spans over a few quantum units. If instead of a complete sweep, the measurement is stopped after each jump and a low voltage I-V is performed (this time from 0V to 4V) a set of I-Vs like the one shown in Fig. 3 (linear axis) and Fig. 4 (log axis) is obtained. After the low voltage I-V, the high voltage stress is resumed until the detection of a new jump. Fig. 5 shows the differential conductance of such curves in units of G_0 . Notice that at least the first six curves exhibit conductance levels close to integer values of G_0 . These features are indicative of the mesoscopic nature of electron transport after dielectric breakdown.

In what follows, the model proposed to account for the conduction in the nanodiodes system is described. According to [1], the current flowing through one of the nanodiodes can be modeled using the expression:

$$I_i = I_{0i} \{ \exp[\alpha_i (V - I_i R_i)] - 1 \} \quad (1)$$

where I_{0i} , α_i and R_i are fitting constants. Considering the equivalent circuit model depicted in Fig. 6, the total current that flows through the structure reads:

$$I = \sum_i I_i = \sum_i \left(\frac{1}{\alpha_i R_i} W \{ \alpha_i I_{0i} R_i \exp[\alpha_i (V + I_{0i} R_i)] \} - I_{0i} \right) \quad (2)$$

Figures 3 and 4 show the same experimental data (symbols) and simulation results (red lines) in two representations. Notice that the model is able to capture the behavior of the experimental I-Vs both for low (exponential increase) and high (linear regime) applied voltages. A thorough analysis of the model parameters will be presented in the final submission.

[1] E. Miranda, IEEE Electron Dev Lett 26, 673 (2005)

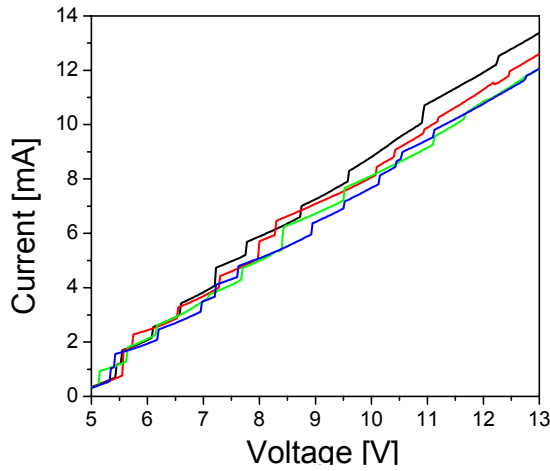


FIG. 1. FORMATION OF BREAKDOWN SPOTS BY MEANS OF A HIGH VOLTAGE SWEEP. EACH CURVE WAS MEASURED IN A DIFFERENT DEVICE.

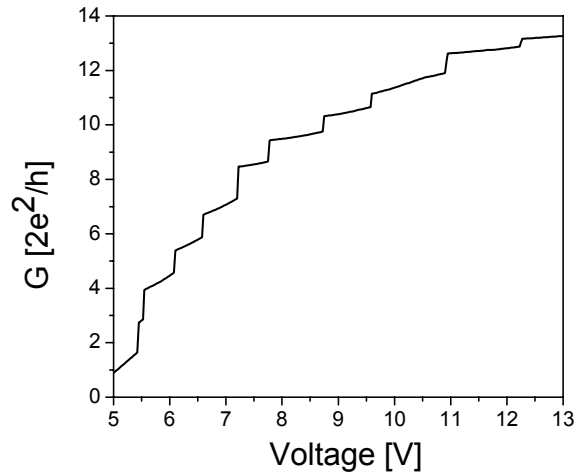


FIG. 2. EVOLUTION OF THE CONDUCTANCE-VOLTAGE CHARACTERISTIC DURING THE GENERATION OF SPOTS.

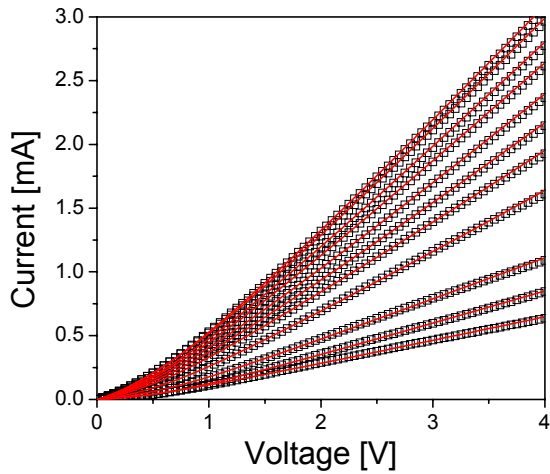


FIG. 3. CURRENT-VOLTAGE CHARACTERISTICS AFTER THE DETECTION OF MULTIPLE BREAKDOWN EVENTS. (LINEAR AXIS TO EMPHASIZE THE HIGH VOLTAGE REGION)

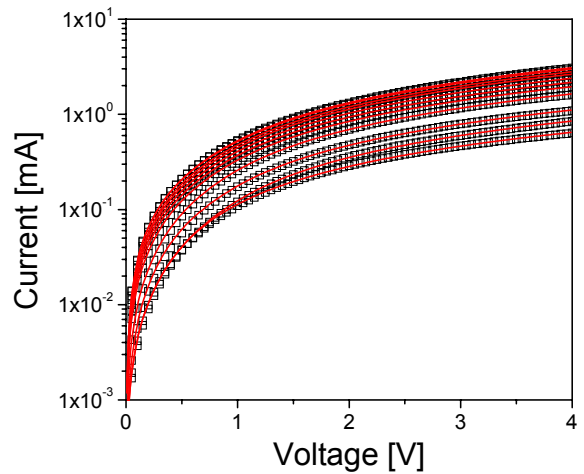


FIG. 4. CURRENT-VOLTAGE CHARACTERISTICS AFTER THE DETECTION OF MULTIPLE BREAKDOWN EVENTS. (LOG AXIS TO EMPHASIZE THE LOW VOLTAGE REGION)

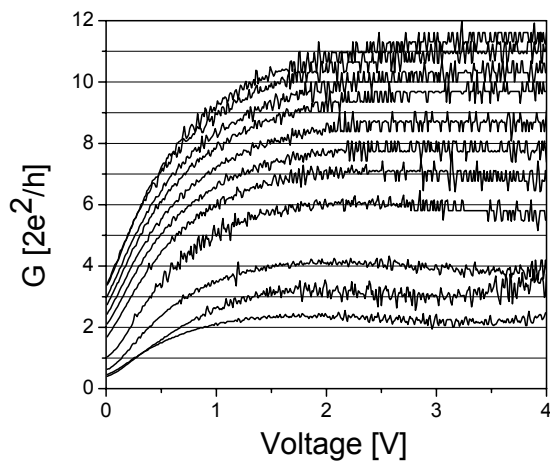


FIG. 5. CONDUCTANCE-VOLTAGE CHARACTERISTICS ASSOCIATED WITH THE I-VS SHOWN IN FIGS. 3 AND 4.

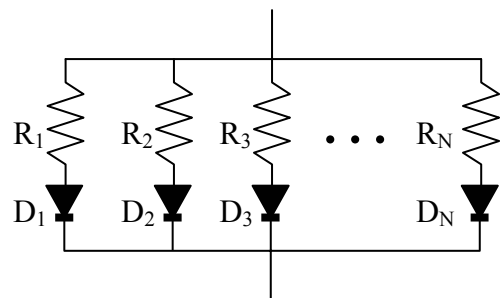


FIG. 6. EQUIVALENT CIRCUIT MODEL FOR THE LEAKAGE CURRENT FLOWING THROUGH THE BROKEN DOWN STRUCTURE.

SPAGS-STM, a true high performance tool for in-silico imaging*Alain Rochefort**École Polytechnique de Montréal, Département de génie physique and Regroupement québécois sur les matériaux de pointe (RQMP), Montréal, Canada.**and**CEA-INAC/SPrAM, Grenoble, France.*alain.rochefort@polymtl.ca

The production of numerical STM images of large-scale molecular systems is often limited to the use of low-level theory such as the Tersoff-Hamann (TH) approach [1]. A significant amount of STM features are revealed by such a representation of surface states that are obtained from electronic structure calculations, except that the influence of the tip is totally excluded. Electron scattering approach such as the Laudauer-Buttiker formula (LBF) [2] considers the influence of the tip, but can also considers electron-electron, electron-phonon, and several other inelastic scattering events [3]. Due to all these features, the LBF approach represents one of the most accurate models for generating STM images.

Despite the high accuracy of such scattering approach, the associated computational complexity and effort needed to obtain STM images still constitute the major drawbacks of the LBF technique. Nevertheless, our recent development in parallel computing [4] and space discretization [5] in STM simulations open a route toward a next generation of real-time STM imaging. In addition, we are presently developing new software features where chemical and physical intrusions within the model framework can be performed. Following this chemical intrusion scheme, the composition of the molecular specie studied by STM can be modified, and the resulting STM image be rapidly computed and visualized. For example, it costs nearly 16 sec to evaluate a STM image of a (5,5) nanotube model containing 250 carbon atoms within TH limits, while around 1 sec is needed to evaluate a new STM image in which a carbon atom has been replaced by a nitrogen atom (see Figure 1) in the original model [6]. This improvement in rate of producing STM images was possible through a judicious use of matrix refreshment and iterative techniques for matrix diagonalization. This intrusive mode opens an efficient route for exploring the role of functional groups or heteroatoms on the origin of STM contrasts of adsorbed molecules.

In this presentation, a brief overview of our most recent contributions in the rapid production of accurate STM images will be given. In addition, several convincing examples related to electron confinement nearby nanostructures, to surface reshaping induced by adsorbates, and to more subtle molecular interactions such as π - π interactions will be discussed. Finally, I will show that quantitative analysis of STM contrasts can be used to understand, and in some cases to discriminate between possible surface mechanisms.

References:

- [1] J. Tersoff, D.R. Hamann, *Phys. Rev. B* **31** (1985) 805.
- [2] M. Buttiker, Y. Imry, R. Landauer, S. Pinhas, *Phys. Rev. B* **31** (1985) 6207.
- [3] C. J. Chen, "Introduction to Scanning Tunneling Microscopy", Oxford Science Publications, 2nd edition, New York, (2008).
- [4] B.A. Janta-Polczynski, J.I. Cerdá, G. Éthier-Majcher, K. Piyakis, A. Rochefort, *J. Appl. Phys.*, **104** (2008) 023702.
- [5] S. Bedwani, F. Guibault, A. Rochefort, *J. Comput. Phys.* **227** (2008) 6720.

[6] N. Boulanger-Lewandowski, S. Bedwani, F. Guibault, J.I. Cerdá, A. Rochefort, to be published.

Figures:

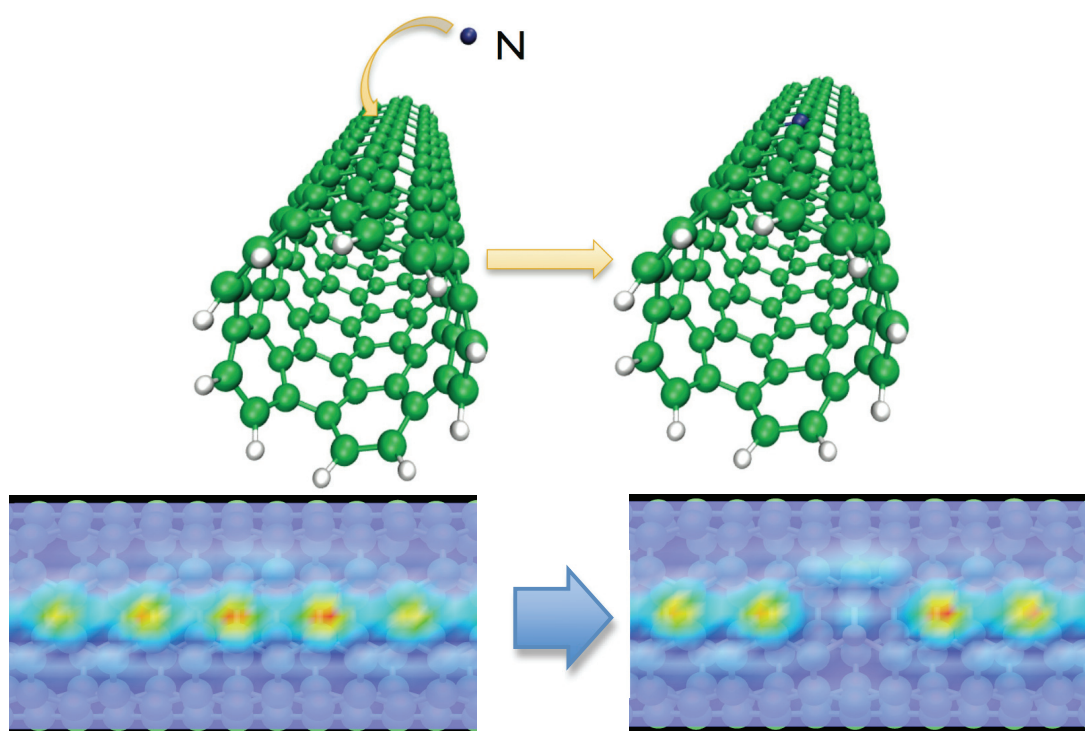


Figure 1. Representation of the chemical intrusion (top) in the evaluation of STM images (bottom) of a (5,5) carbon nanotube (left side) in which a carbon atom is replaced by a nitrogen atom (right side).

Extension of the Source-Sink Potential (SSP) approach for multiple channels conductance calculations

Philippe Rocheleau and Matthias Ernzerhof

Département de Chimie, Université de Montréal, Montréal, Québec, Canada

philippe.rocheleau@umontreal.ca

In molecular electronics, molecules are connected to macroscopic contacts and the current passing through is studied as a function of the applied voltage. We focus on modeling the transmission of electrons through such a molecular electronic device (MED). Based on a simple Hückel Hamiltonian to describe the π electrons in conjugated systems, the SSP method [1] employs complex potentials to replace the wavefunction of the infinite contacts in a rigorous way. This method takes advantage of the known asymptotic form of the wavefunction in the contacts and yields a simple expression for the electron transmission probability [2,3]. The initial SSP approach [4] was limited to two one-dimensional contacts, here we extend the approach to multiple channels, i.e., to two-dimensional contacts including transverse modes. We describe the development of the method and illustrate it with applications.

References:

- [1] F. Goyer, M. Ernzerhof and M. Zhuang, J. Chem. Phys., **126**, (2007) 144104.
- [2] M. Ernzerhof, J. Chem. Phys., **127**, (2007) 204709.
- [3] B.T. Pickup and P.W. Fowler, Chem. Phys. Lett., **459**, (2008) 198-202.
- [4] P. Rocheleau and M. Ernzerhof, J. Chem. Phys., **130** (17) (2009).

Low temperature STM/STS study of silicon nanowires grown on the Ag(110) surface

*F. Ronci*¹, *S. Colonna*¹, *A. Cricenti*¹, *P. De Padova*¹, *C. Ottaviani*¹, *C. Quaresima*¹, *C. Carbone*², *B. Aufray*³, *G. Le Lay*³

¹*ISM-CNR, via del Fosso del Cavaliere, 00133 Roma, Italy*

²*ISM-CNR, Trieste, S. S. Km163.5, I-34012 Basovizza (TS), Italy*

³*CRMCN-CNRS, Campus de Luminy, Case 913, 13288 Marseille Cedex 9, France*

ronci@ism.cnr.it

The production of low-dimensional nanostructures and the study of their peculiar electronic and optical properties is a hot topic attracting growing interest in the scientific community. In particular, monodimensional (1D) nanowires are under investigation for their potential use for the achievement of nanosized electronic devices. One method for realizing such nanostructures is the so-called bottom-up approach. In our case, silicon nanowires are obtained by self assembly of silicon deposited on the Ag(110) surface. The immiscibility of silicon and silver ensures that no silicides are formed at the surface, while the anisotropy of the substrate acts as a template for the formation of such monodimensional nanostructures.

A partially covered surface shows isolated nanowires all oriented in the same [-110] direction with an internal periodicity of about 0.58 nm along the wire (2 times the substrate periodicity in the [-110] direction), and characterized by well defined widths of about 0.8 and 1.6 nm (2 or 4 times the substrate periodicity in the [001] direction). The fully covered surface shows a very highly ordered crystallographic structure in which 1.6 nm wide parallel nanowires are packed in a 5x periodicity in the [001] direction (perpendicular to the wire). [1-3]

Synchrotron radiation Photoemission Spectroscopy results confirm the highly ordered internal structure of the wires with the presence of two very sharp components of the Si-2p core levels, while valence band spectra suggest a highly metallic behavior for the silicon nanowires. [1-2]

Here, we report a Scanning Tunneling Microscopy (STM) and Spectroscopy (STS) study as a function of temperature (ranging from room to liquid helium temperature) of the Si/Ag(110) surface with different silicon coverage, namely a) the bare silver surface, b) the partially covered surface and c) the fully covered one.

The internal wire structure will be discussed by examining high-resolution STM images acquired at low temperature and the electronic properties studied by STS, showing a clear metallic behavior, will be reported as well.

References

- [1] C. Léandri et al., Surface Sci. **574**(2005) L9.
- [2] P. De Padova et al., Nano Lett. **8** (2008) 271.
- [3] H. Sahaf et al., Applied Physics Letters, **90** (2007) 263110.

Transport properties of graphene ribbons with a random distribution of side attached benzene-like molecules.

Luis Rosales¹ and *Sebastián Reyes*²

¹*Instituto de Física, Pontificia Universidad Católica de Valparaíso, Casilla 4059, Valparaíso, Chile,*

²*Departamento de Física, Pontificia Universidad Católica de Chile, Casilla 306-Santiago22, Santiago, Chile,*
luis.rosales@ucv.cl

In the last years graphene and graphene nanoribbons (GNRs) have attracted a lot of scientific attention. The special and novel electronic properties together with the mechanical stability of this structures, even at room temperature, have suggested many possible applications in science and technology [1]. One of these applications is related with the capability of graphene layers to detect molecules absorbed or attached to the systems. There are several experimental reports concerning with the detection of different types of absorbed molecules in the system, such as nitrogen dioxide, nitrogen trioxide, water, etc. [2, 3]. An interesting experimental evidence is the detection of aromatic molecules in graphene layers. By measurements of the transport properties of a single layer graphene-based field effect transistor, it has been studied the effects of these aromatic molecules in the systems. It has been shown that these molecules are strong binding to graphene through π - π bonds between the molecular aromatic rings and the graphene, and therefore, are easily detected by the device [4].

In previous works, we have studied the effects of a single and a finite number of side attached molecules to graphene ribbons. We have found that the energy spectrum of a single molecule is reflected as a series of Fano antiresonances in the conductance curves of the system [5]. Besides, we have studied the effects of attach two molecules of different length to armchair GNRs. We have found that it is possible to identify the corresponding spectrum of each molecule from the Fano antiresonances of the conductance of the systems [6]. Finally, we have studied the effects on the transport properties of zigzag and armchair GNRs at which a finite number of molecules are side-attached in a periodic sequence. We have studied the conductance gap modulation as a function of the length of the molecules, the relative distance between them, and the number of attached molecules [7].

In this work we show a theoretical study of the electronic transport properties of GNRs at which linear benzene-like molecules have been side-attached at the ribbons edges in a random distribution. All the considered systems have been described using a single band tight binding hamiltonian. Based on the Green's function matching formalism within a real-space renormalization technique, we have calculated the local density of states and the electronic conductance of these systems.

We have considered two different systems: i) a long pristine graphene ribbon with molecules attached in both edges, and ii) two finite graphene ribbons parallel between each other, connected to metallic leads. In the latter system the molecules are attached between these parallel ribbons as molecular "bridges".

We have considered different scenarios taking into account different lengths and molecular concentrations. The random distribution imposes a disorder potential to electrons in the system. This extra potential produces a localization of the electronic wavefunction inside of the conductor which is characterized by a localization length. We have focused in the study of the

dependence of the localization length with the type of molecule, and on the concentration of this external perturbation [8].

References:

- [1] A. Geim, A.H. MacDonald *Physics Today* 60, 2007, 35-41; A. Geim, P.Kim, *Scientific American*, 2008, 90-97
- [2] F. Schedin, A. Geim, S. Morozov, E. Hill, P. Blake, M. Katsnelson, K. Novoselov, *Nature Materials* 6, 2007, 652
- [3] T. Wehling, K. Novoselov, S. Morozov, E. Vdovin, M. Katsnelson, A. Geim, A. Lichtenstein, *Nano Lett.* 8, 2008, 173
- [4] X. Dong , D. Fu, W. Fang, Y. Shi, P. Chen, L. Li, *Small*, 2009 in press, DOI: 10.1002/sml.200801711
- [5] L. Rosales, A. Latgé, Z. Barticevic, M. Pacheco and P. Orellana, *Nanotechnology* 19, 2008, 065402
- [6] L. Rosales, P. Orellana, Z. Barticevic and M. Pacheco, *Microelectronics* 39, 2008, 1233
- [7] L. Rosales, A. Latgé, P. Orellana, Z. Barticevic and M. Pacheco, *Nanotechnology* 20, 2009, 095705
- [8] L. Rosales and S. Reyes, unpublished (2009)

MULTI-SOLVENT ZnO STABLE COLLOIDAL DISPERSIONS VIA ORGANOMETALLIC METHOD

Rubio Garcia Javier^{1,2}, Kahn Myrtil¹, Chaudret Bruno¹, Mingotaud Christophe², Gauffre Fabienne²

¹Laboratoire de Chimie de Coordination, 205 rte de Narbonne, 31000 Toulouse, France, myrtil.kahn@lcc-toulouse.fr

²laboratoire des IMRCP, Université de Toulouse, 118 rte de Narbonne, 31000 Toulouse, France, gauffre@chimie.ups-tlse.fr

Metal oxide nanoparticles with tunable morphologies are desirable for many applications including energy conversion, electronics and optics. ZnO nanoparticles are among the most widely used metal oxides nanoparticles. Indeed, ZnO is a wide band gap semi-conductor that displays luminescent properties in the near ultraviolet and visible regions. These properties are translated into a wide range of applications such as gas sensors,¹ optoelectronics,² field-emission devices,³ photo-anodes or dye-sensitized solar cells,⁴ and bio-imaging.⁵ We are interested in designing water-soluble ZnO nanoparticles, with well defined structure and properties.

Recently we reported a very simple synthetic method for the preparation of zinc oxide nanoparticles based on decomposition of an organometallic precursor⁶ in organic media. The growth and final morphology were controlled by the use of long alkyl chain ligands. However these particles were redispersible in some organic solvent but not in water or protic solvents.

Here we present a modification of our previously reported procedure based on the think-wise selection of the stabilizing agent. This new methodology enables the dispersion of the obtained particles in both organic and protic solvents without further modifications. The dispersion of the particles in water is especially noteworthy due to potential environmentally friendly applications. The size and shape of the particles can be tuned (spheres or rods between 3-20nm) by changing the experimental conditions.

The fluorescent properties of ZnO oxide nanoparticles depend on the defects present in the lattice: emissions in red⁷, green⁸, yellow⁹ or blue¹⁰ regions are reported.

In the present study particles synthesized using carboxylic acids or amines as stabilizing functional groups were investigated. Changes in the particle defects are related to the selection of the stabilizing agent. Therefore using carboxylic acid only yellow emission is observed. However yellow or blue emissions resulted in the case of amines. The emissions can be tuned by varying the excitation energy (**Figure 1**). These observations keep unchanged regardless to the solvent in which the particles dispersed.

Figures:

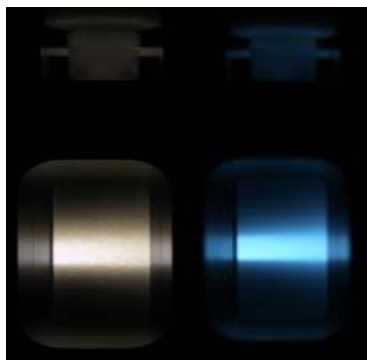


Figure 1.

References:

- [1] X. Chu, D. Jiang, A. B. Djuricic and H. L. Yu, *Chem. Phys. Lett.*, 2005, **401**, 426
- [2] J. C. Johnson, H. Q. Yan, R. D. Schaller, L. H. Haber, R. J. Saykally and P. D. Yang, *J. Phys. Chem. B*, 2001, **105**, 11387.
- [3] O. G. Schmidt and K. Eberl, *Nature*, 2001, **410**, 168.
- [4] K. Keis, L. Vayssieres, S.-E. Lindquist and A. Hagfeldt, *Nanostruct. Mater.*, 1999, **12**, 487.
- [5] Y. L. Wu, C. S. Lim, S. Fu, A. I. Y. Tok, H. M. Lau, F. Y. C. Boey and X. T. Zeng, *Nanotechnology*, 2007, **18**, 215614.
- [6] M. Monge, M. L. Kahn, A. Maisonnat, B. Chaudret, *Angew. Chem.* 2003, **115**, 5479-5482.
- [7] Wang, X.; Kong, Xianggui; Y., Yi; Zhang, H. *Journal of Physical Chemistry C* (2007), 111(10), 3836-3841.
- [8] Bang, Jungsik; Yang, Heesun; Holloway, Paul H. *Nanotechnology* (2006), 17(4), 973-978.
- [9] Kahn, M. L.; Cardinal, T.; Bousquet, B.; Monge, M.; Jubera, V.; Chaudret, B. . *ChemPhysChem* (2006), 7(11), 2392-2397.
- [10] Zeng, H.; Li, Z.; Cai, W.; Liu, P.. *Journal of Applied Physics* (2007), 102(10), 104307/1-104307/4.

Optical Fiber pH Sensor based on Surface Plasmon Resonance in the Infra-red Region

C. R. Zamarreño, M. Hernández, I. R. Matías, F. J. Arregui

Public University of Navarra (UPNA), Campus Arrosadia S/N, Pamplona, NA, SPAIN

carlos.ruiz@unavarra.es

In this work, we present the fabrication of novel optical fiber pH sensors based on surface plasmon spectroscopy detection technique in the infra-red region. Surface plasmon resonance (SPR) spectroscopy has originated numerous works in the area of chemical, biochemical and biological sensors within the last decades [1]. However, the utilization of noble metals, such as gold and silver, as the SPR supporting layer has often limited the development of further applications. Here, we propose the utilization of indium tin oxide (ITO) coated optical fibers as the SPR supporting devices [2], which shift the SPR wavelength to the infra-red region [3]. Then, these new optical fiber SPR supporting devices are used as substrates to deposit a polymeric pH sensitive coating, which varies its thickness with the pH of the surrounding medium.

The fabrication of these devices was structured in two differentiated parts. Firstly, ITO was deposited over a 200 μm diameter fused silica fiber using a sol-gel dip coating process as previously described by R. Ota et al. [4]. Then, Layer-by-Layer deposition technique was used to fabricate a thin homogeneous polymeric coating onto the ITO coated optical fiber formed by the sequentially adsorption of the poly-acrylic acid (PAA) and poly-allylamin hydrochloride (PAH) films up to 50 bilayers [5]. In Figure 1 it is shown a scanning electron microscope image of a transversal section of the pH sensitive device where it can be appreciated the ITO film and the polymeric coating of approximately 300 nm and 150 nm respectively.

The deposited [PAH/PAA]₅₀ coating has been already proven to be sensitive to variations in the pH of the surrounding media, which originates variations in the thickness of the coating, known as the swelling/deswelling phenomenon. Hence, these variations can be detected by monitoring the shifts in the surface plasmon resonance wavelength using a typical optical transmission setup as it is represented in Figure 2. The sensor response was characterized when the sensitive region was immersed in different pH buffer solutions. In Figure 3 are shown the absorbance spectra obtained when the sensor was immersed alternately in pH 5, pH 6 and pH 7, where it can be clearly appreciated the variation in absorbance for the different pH values. Finally, the maximum absorbance wavelengths were obtained by using a peak detection algorithm and are represented in Figure 4 showing fast response time and high repeatability with a maximum variation of 35 nm in the studied range.

References:

- [1] R. Slavík, J. Homola, E. Brynda, *Biosensors and Bioelectronics*, **17** (2002) 591-595.
- [2] R. C. Jorgenson, S. S. Yee, *Sens. & Actuators B*, **12** (1993) 213-220.
- [3] C. Rhodes, S. Franzen, JP. Maria, M. Losego, D. N. Leonard, B. Laughlin, G. Duscher y S. Weibel, *J. App. Phys.*, **100** (2006) 054905.
- [4] R. Ota, S. Seki, M. Ogawa, T. Nishide, A. Shida, M. Ide, Y. Sawada, *Thin Solid Films*, **411** (2002) 42-45.
- [5] J. Goicoechea, C.R. Zamarreño, I.R. Matias, F.J. Arregui, *Sens. & Actuators B*, **138** (2009) 613-618.

Figures:

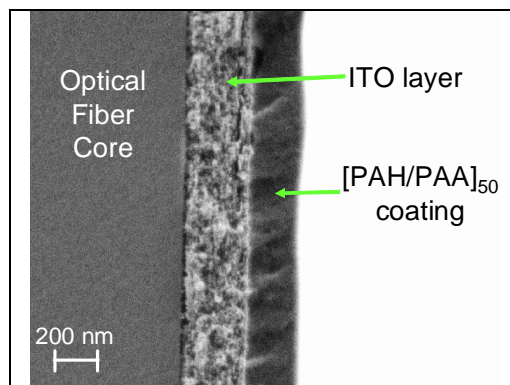


Figure 1. SEM image of the structure formed onto the optical fiber.

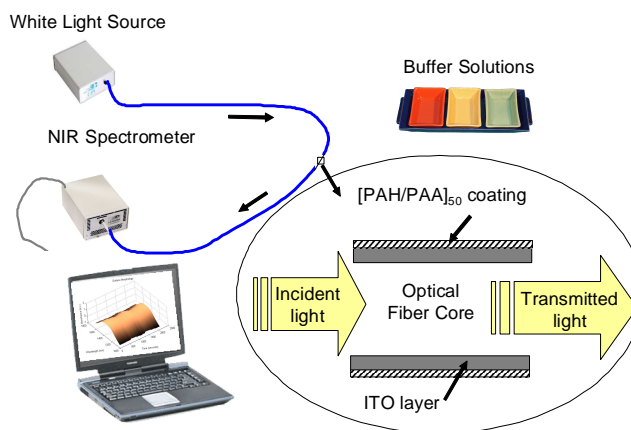


Figure 2. Experimental transmission setup

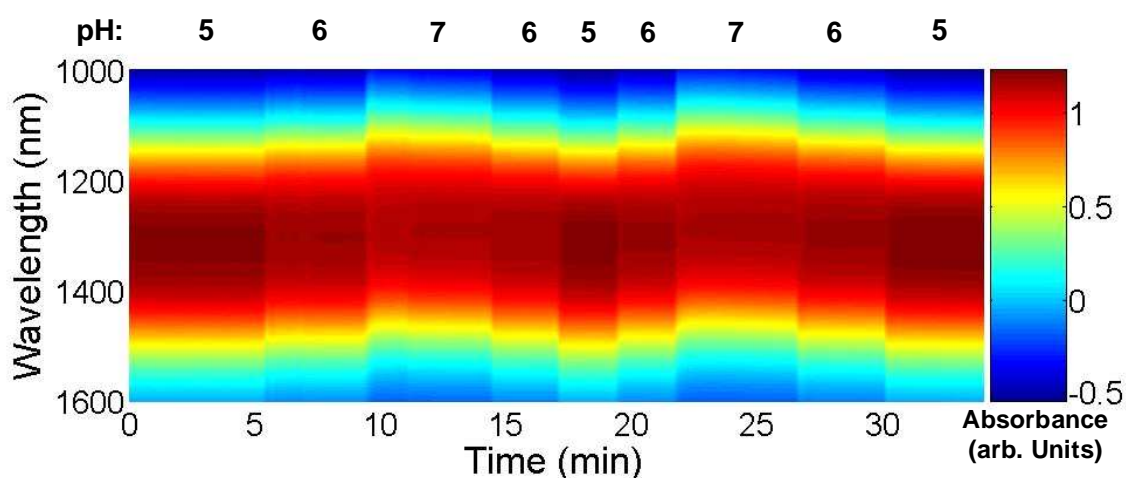


Figure 3. Dynamical response in absorbance when the sensitive region is immersed in different pH buffer solutions.

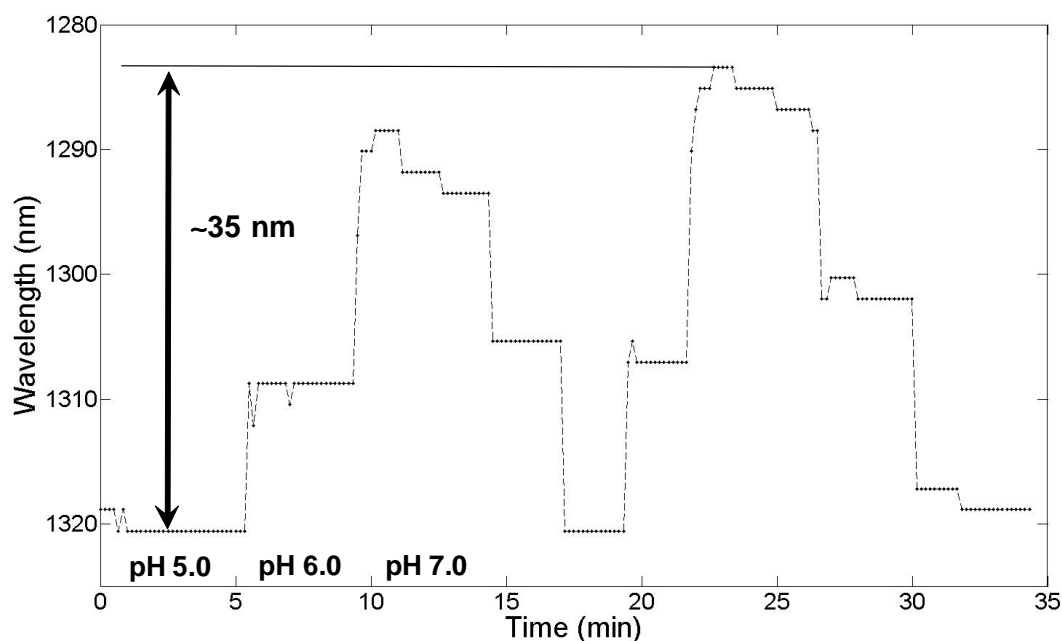


Figure 4. Variation of the wavelength at maximum absorbance when the sensor is immersed in different pH buffer solutions.

Synthesis of Polymer Stabilized Palladium Nanoparticles by Wet Chemical and Electrochemical Routes

P. Ruiz, J. Macanás, M. Muñoz and D.N. Muraviev

Analytical Chemistry Division, Department of Chemistry, Autonomous University of Barcelona, 08193 Bellaterra, Barcelona, Spain.

Patricia.Ruiz.Nicolas@uab.cat

Synthesis and Characterization of Metal nanoparticles (MNPs) attract great interest of scientists and technologists due to their special physical and chemical properties. A high trend for aggregation is considered to be the main drawback of MNPs, as their coalescence results in the loss of their special shape and properties. The development of Polymer-Stabilized MNPs (PSMNPs) is considered to be one of the most promising solutions to the MNPs stability problem [1, 2]. In many instances the electrochemical applications of MNPs are based on the use of noble metals (Pd, Pt, etc.) due to their well-known unique electrocatalytic properties. The synthesis of PSMNPs can be successfully carried out by using InterMatrix Synthesis (IMS) technique, which consists in sequential loading of the functional groups of the polymer (sulfonated poly(etherether ketone), SPEEK in our case) with the desired metal ions followed by their chemical reduction inside the membrane, what results in the formation of PSMNPs.

In this presentation we report the results obtained by the development of an electrochemical version of IMS technique in the synthesis of Pd-PSMNPs and their comparison with those obtained by using the usual wet chemical route. In the first case Pd-PSMNPs were synthesized by electrochemical reduction of palladium ions inside a SPEEK-membrane deposited onto the surface of an electrode, while in the second case the reduction of palladium ions inside the membrane was carried out by a chemical method (e.g. reduction by a sodium borohydride solution). A third method can be done by successive electrochemical and chemical reduction. All three versions of IMS technique can be classified as “in situ-IMS” method. In all cases the SPEEK-MNP-nanocomposites were characterized by using microscopic and electrochemical techniques in order to evaluate MNPs size and electrocatalytic response of the MNPs-modified electrodes.

Typical TEM images of Pd-MNPs obtained by different versions of IMS method are shown in Fig. 1. As it is clearly seen, the size of Pd-MNPs is higher in the case of chemical reduction (see Fig. 1a). The use of the coupled electrochemical-chemical reduction results in the formation of smaller nanoparticles (see Fig. 1b) what increases the performance of the catalytic material. An additional improvement could be considered if MNPs were formed on both sides of the membrane, thus, enhancing the response of doubly modified electrodes (electrochemical-chemical) in comparison with those obtained when using solely chemical reduction.

In general terms we propose that the electrochemical reduction results in the predominant formation of Pd-PSMNPs on the internal side of the membrane (located on the electrode-membrane interface) whereas the chemical reduction leads to the formation of palladium MNPs mainly on the outer side of the membrane (membrane-solution interface). In the case when using both chemical and electrochemical reduction the formation of Pd-MNPs might proceed by both sides of the membrane.

The results of the amperometric detection of H_2O_2 with Pd-PSMNPs synthesized by different in situ IMS methods (see Fig. 2.) clearly testify to the validity of above hypothesis.

References:

- [1] A.D. Pomogailo, G.I. Dzhardimalieva, A.S. Rozenberg, D.N. Muraviev, *J. Nanoparticle Res.*, **5** (2003) 497-519.
- [2]. D.N. Muraviev, *Contribut. Sci.* 3(1) (2005) 19-32.

- [3] D.N. Muraviev, J. Macanás, M. Farre, M. Muñoz, S. Alegret, *Sens. Actuators B*, **118(1-2)** (2006) 408-417.
- [4] J. Macanas, M. Farre, M. Muñoz, S. Alegret, D. N. Muraviev, *Phys. Stat. Sol. (a)*, **203, 6**, (2006) 1194-1200.
- [5] D.N.Muraviev, J. Macanás, P. Ruiz, M. Muñoz, *Phys. Stat. Sol. (a)*, **205, 6**, (2008) 1460-1464.
- [6] D.N.Muraviev, P. Ruiz, M. Muñoz, J. Macanás, *Pure Appl. Chem.*, **80, 11** (2008) 2425-2437.

Figures:

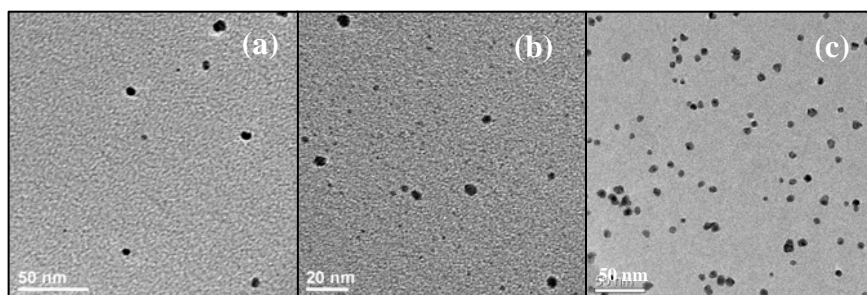


Fig. 1 Typical TEM images of Pd-PSMNPs-SPEEK nanocomposite inks synthesized by “in situ-IMS” (a,b) and “ex situ-IMS” (c), where (a) corresponds to chemical reduction and (b) electrochemical-chemical reduction.

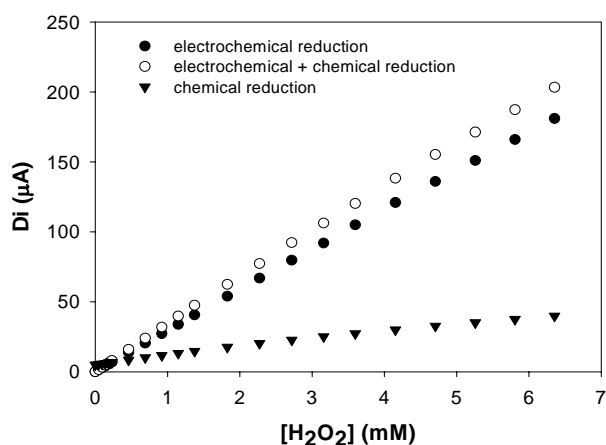


Fig. 2 Calibration curves of electrochemical detection of H₂O₂ concentration with Pd -PSMNP-based amperometric sensors. These PSMNPs have been obtained by using different ways to do the reduction process. Experimental conditions: potential: -250 mV; 0.1 M acetate buffer, pH = 5.0.

Eykes: a new software application for analyzing Transmission Electron Microscopy images of nanoparticles

P. Ruiz¹, F. Courteille^{2,3}, J. Macanás¹.

¹ *Analytical Chemistry Division, Department of Chemistry, Autonomous University of Barcelona, 08193 Bellaterra, Barcelona, Spain.*

² *Laboratoire Génie Chimique, Université de Toulouse, INPT, UPS, Toulouse (France)*

³ *Laboratoire Génie Chimique, CNRS, Toulouse (France)*

Jorge.Macanas@uab.cat

Synthesis and characterization of metal nanoparticles (MNPs) are topics of interest in many applications such as device fabrication, quantum computing, catalysis and sensing due to their special physical and chemical properties which are directly related to their size [1].

Further advancement of Nanotechnology needs a better understanding of nanomaterial properties and implies a better characterization of key parameters such as nanoparticle size and size distribution which are frequently evaluated by using Transmission Electron Microscopy (TEM), a well known microscopy technique, capable of imaging at a significantly higher resolution than light microscopes [2]. Unfortunately, in practice, TEM images are particularly noisy and low contrasted, making their processing a challenging task to accomplish. Thus, results from TEM images have been often obtained by manually measuring and counting many nanoparticles, a task that is highly subjective and labor intensive.

During these last years, several computer imaging particle analysis software tools have been conceived for extracting automatically (or semi-automatically) useful information contained in images what may allow for a more accurate assessment of the size and frequency (size distribution) of nanoparticles. However, sometimes these tools are included in very expensive software packages impossible to be afford by many research groups. In addition, some of these tools are not easy to be used by non-experts mainly because of the subjectivity of the thresholding step [3,4,5,6,7,8,9].

In this work, we report the development of a new software solution for nanoparticles counting (Eykes) and compare it with manually obtained data. The main characteristics of this software application are its ease in performance and its compatibility with many images difficultly analyzed by standard software.

Concretely, for the image analysis, we consider only two phases (solid objects and void) and, therefore, the image processing algorithm is very simple. After enhancing contrast, we perform an image denoising by applying smooth filters (gaussian and median filters). Then, we split the image in several sub-images, and for each sub-image, we apply a simple threshold by using the Otsu algorithm. In the final image each particle is identified, numbered and characterized. In **Figure 1** a typical set of images is shown demonstrating the excellent nanoparticle recognition provided by the software.

The statistical treatment of data (for histogram representation and so on) is not included in the software package since each researcher has its own preferences for data representation but all the extracted information is written in a file which can be imported in any other statistics software tools.

References:

[1] J. Da Ponte, T Sadowski, C.C. Broadbridge, D. Day, A.H. Lehman, D. Krishna, L. Marinella, P. Munhutu, M. Sawicki, Proceedings of the SPIE, 6575, 65750H (2007).

- [2] G. Van Tendeloo, P. Geuens, J.-F. Colomer, O. L. Lebedev, Proceedings, 6th Multinational Congress on Microscopy - European Extension - 2003, Pula (Croatie), 21-26 (2003)
- [3] J. DaPonte, T. Sadowski, C.C. Broadbridge, D. Day, A. Lehman, D. Krishna, L. Marinella, P. Munhutu, M. Sawicki, *Proceedings of the SPIE*, 6575, 65750L (2007).
- [4] W.D. Pyrz, D.J. Buttrey, *Langmuir*, 24, 11350-11360 (2008).
- [5] I. Srnová-Sloufová, F. Lednicky, A. Gemperle, J. Gemperlova, *Langmuir*, 16, 9928-9935 (2000).
- [6] A. Weibel, R. Bouchet, F. Boulc, P. Knauth, *Chemistry of Materials*, 17, 2378-2385, (2005).
- [7] L-C. Chen, C.C. Ho, *Rev. Adv. Mater. Sci*, 18, 677-684 (2008).
- [8] M.T. Reetz, M. Maase, T. Schilling, B. Tesche, *J. Phys. Chem. B*, 104, 8779-8781 (2000).
- [9] G.H. Woehrle, J.E. Hutchison, S.Özkar, R.G. Finke, *Turk. J. Chem*, 30, 1-13 (2006).

Figures:

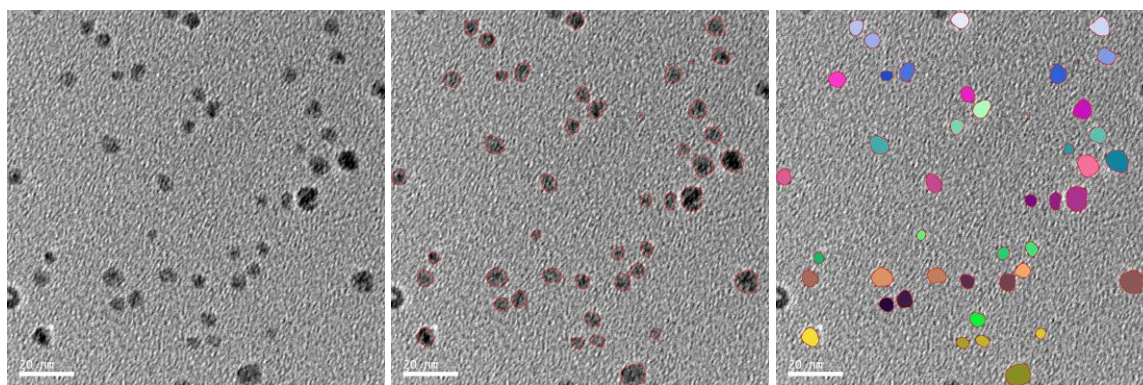


Fig. 1 Typical TEM images of polymer stabilized Cu nanoparticles. Original image (left) and analyzed images (center and right).

EXPERIMENTAL DESIGN FOR DETERMINATION OF EFFECTIVE PARAMETERS IN HYDROTHERMAL SYNTHESIS OF TiO₂-DERIVED NANOTUBES

M. Safaei^{1, 2}, *R. Sarraf-Mamoory*¹, *M. Rashidzadeh*², *M. Manteghian*³

¹ *Materials Engineering Department, Tarbiat Modares University, Jalal Ale Ahmad Avenu., Tehran, Iran*

² *Catalyst Research Center, Research Institute of Petroleum Industry, West Blvd. Azadi Sport Complex, Tehran, Iran*

³ *Chemical Engineering Department, Tarbiat Modares University, Tehran, Iran*
safaei@modares.ac.ir

The synthesis of titanate nanotubes (TNT) which offers a very high specific surface area, high aspect ratio, better electrical contact, and transport of charge carrier has attracted particular interests in creating as a new kind of nanostructure materials due to various applications of photocatalysts, high effect solar cell, gas sensor, semiconductor devices, and new generation electrodes for lithium batteries [1-4]. Currently, there are developed methods for synthesis of titanate nanotubes including chemical synthesis with template, electrochemical synthesis, and alkaline hydrothermal synthesis. Among the aforementioned synthesis approaches, hydrothermal treatment received wide investigations, owing to their cost-effective, easy route to obtain nanotubes, the feasibility and availability of widespread applications [5-7].

Statistical experimental design methodology is an established and proven methodology for product and process improvements. The Plackett-Burman design was demonstrated to be powerful tools for identifying significant process parameters with relatively few experiments. A Plackett-Burman design can examine up to $N-1$ parameters ($f \leq N-1$) in N experiments, with N being a multiple of 4 [8]. Therefore, in this work, a screening approach, involving the use of Plackett-Burman experimental design, permitted the evaluation of the effects of 8 parameters from hydrothermal synthesis of TiO₂-derived nanotubes such as raw material surface area, m_{TiO_2} , filling factor, temperature, time, aging, stirring, and HCl concentration on surface area of synthesized samples. The selection of levels of the different parameters was carried out based on preliminary experiments results. A matrix with 11 parameters (eight real parameters A-H and three fictitious parameters I-K) was used. Each synthesis was performed based on the conditions generated from Plackett-Burman design to obtain twelve different products.

The initial TiO₂ powders have the purity of >99.5 % and a BET surface area of 50 and 10 m²/g, respectively. Pore structure of the TiO₂-derived nanomaterials was characterized by N₂ adsorption at -196 °C using an adsorption apparatus (Micrometrics, ASAP2010). The external features and morphology of the TiO₂ were analyzed by using a high-resolution transmission electron microscope (HR-TEM, Philips CM 200 FEG). In preparation, a commercial TiO₂ powder was dispersed in an aqueous solution of NaOH (10N) under vigorous magnetically stirring for about 1 hr to form a white suspension, followed by placing into a Teflon container. After hydrothermal processing, in each case the mixture was allowed to cool then aged at room temperature without stirring. The precipitate was repeatedly centrifuge and rinsed with distilled water and HCl solution until ~pH =6-7. The powder was dried in air at 100 °C for 24 hrs to give the as-synthesized product.

Since all the parameters were coded on a +1 to -1 scale, the absolute magnitude of the resulting coefficients (t_{obs}) can be used to rate the relative importance of the parameters. A parameter is considered significant if the value of the t-test is above a tabulated student's t-value (t_{tab}). The number of degrees of freedom and the applied significance level, α , will determine t_{tab} . A tabulated student's t-value around ± 4.3 is a guide to predict the important reveal effects. Standardized Pareto plot (Fig. 1) represents the absolute value of t_{obs} on surface area. For each

parameter, give rapid visual information on the magnitude of t_{obs} . The length of the bar is proportional to the significant of parameter. If the magnitude of bar is more than the t_{tab} value, parameter is significant. Regarding to $t_{obs} < t_{tab}$, the most significant parameter is filling factor that enhanced their amounts. In addition to, temperature, stirring, raw materials surface area, and time are of relative significance parameters on surface area of synthesized samples, respectively but other parameters have little effects on these responses in the ranges tested. The last three lowest surface area responses related to the higher surface area raw material and stirring condition. TEM micrographs (Fig. 2) showed that the morphology for high, medium, and low surface areas of products is nanotubes, nanowires, and nanospheres, respectively.

References:

- [1] G.K. Mor, O.K. Varghese, M.Paulose, K. Shankar , C.A. Grimes, *Sol. Energy Mater. Sol. Cells* **90** (2006) 2011.
- [2] H.H. Ou, S. L. Lo, *Sep. Purif. Technol.* **58** (2007) 179.
- [3] D. V. Bavykin, J. M. Friedrich, F. C. Walsh, *Adv. Mater.* **18** (2006) 2807.
- [4] Q. Chen, L.M. Peng, *Int. J. Nanotechnol.* **4** (2007) 44.
- [5] J.H. Jung, H. Kobayashi, Kjeld J. C. van Bommel, S. Shinkai, , T. Shimizu, *Chem. Mater.* **14** (2002) 1445.
- [6] P. Hoyer, *Adv. Mater.* **8** (1996) 857.
- [7] D. Eder, M.S. Motta, I.A. Kinloch, A.H. Windle, *Phys. E* **37** (2007) 245.
- [8] R.L. Plackett , J.P. Burman, *Biometrika* **33** (1946) 305.

Figures:

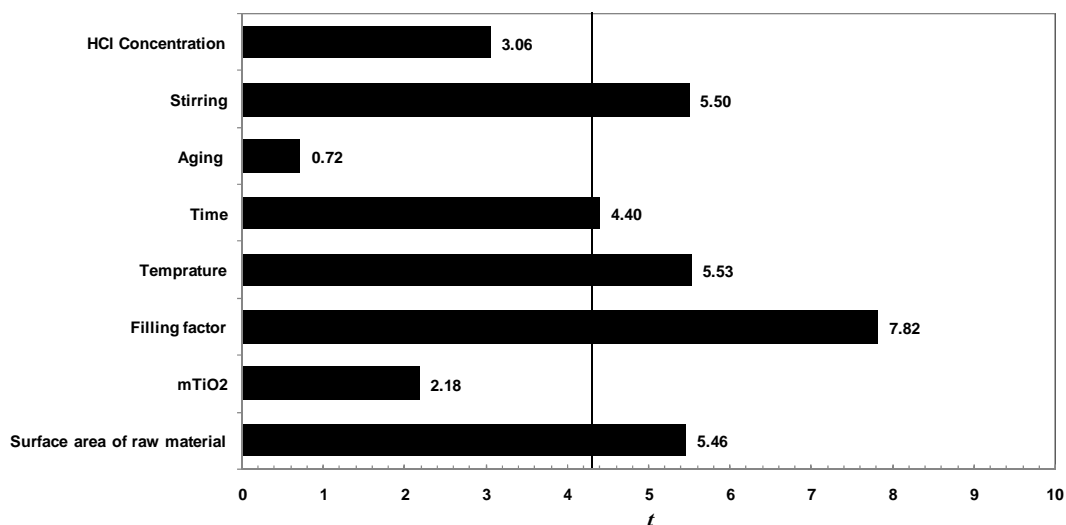


Fig. 1: Standardized Pareto chart of effects on surface area of synthesized samples ($\alpha=0.05$)

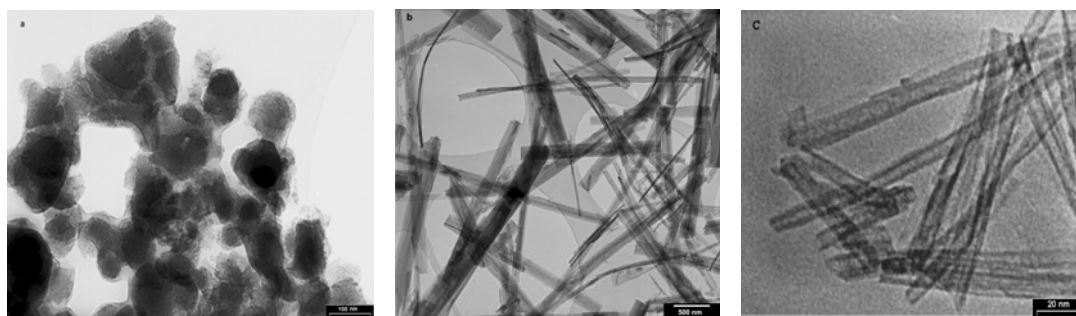


Fig. 2: TEM images of synthesized samples (a) nanospheres (b) nanowires (c) nanotubes

Study on Nanoparticles Dispersion Sodium - Atomic Interaction and Fundamental Property -

Jun-ichi SAITO

Japan Atomic Energy Agency, 4002 Narita, Oarai, Ibaraki, JAPAN
saito.junichi78@jaea.go.jp

Introduction

Liquid sodium is used as a coolant in fast breeder reactors (FBR) because of its superior thermal conductivity and wide liquid phase temperature region. However, it shows the high chemical reactivity of the sodium itself. If the high chemical reactivity of sodium can be suppressed, the safety of the FBR plant improves. Therefore, technology for the suppression of the chemical reactivity of liquid sodium is desired.

It is well known that nanoparticles exhibit unique characteristics compared with bulk material. There are many studies applying the properties of nanoparticles[1]. Recently, there has been research aimed at improving the thermal conductivity of the coolant by dispersing nanoparticles into water. In this study, our attention is paid to the atomic interaction between nanoparticles and sodium atoms. The concept of chemical reactivity control of sodium dispersing nanoparticles (hereafter called “Nanofluid”) was described and the relation between an atomic interaction and the fundamental property of Nanofluid was investigated.

Concept of Nanofluid

An conceptual image of the dispersion of nanoparticles in liquid sodium is shown in Fig.1(a)[2]. Dispersing the nanoparticles into liquid sodium, the nanoparticle forms a cluster with the surrounding sodium atoms. The nanoparticle attracts the surrounding sodium atoms by atomic bonding. It is expected that the clusters are dispersed in liquid sodium. An image of the reaction between Nanofluid and water is shown in Fig.1(b). The reaction of sodium atoms which have been attracted with nanoparticle will delay because the sodium atoms have to be pulled off from the nanoparticle. Hence, it is thought that the chemical reactivity is suppressed by dispersing nanoparticles.

The specific surface of the nanoparticle becomes larger by the minimization of its diameter. The effect of reducing reactivity is in proportion to the area of the contact surface between the nanoparticle and the sodium. Therefore, it is enhanced by decreasing the diameter of nanoparticle and even a small amount of nanoparticles can obtain a larger effect.

Atomic Interaction between Nanoparticle and Sodium

An atomic interaction between nanoparticle and sodium was calculated using the density functional theory (DFT). The models using the calculation consist of many nanoparticle atoms and sodium atom. 3d transition elements were chosen for the nanoparticle atom, because of their strong atomic bonding.

From the calculation result, the atomic bonding between nanoparticle atom and sodium atoms was larger than that between sodium atoms. It means that the nanoparticle catches many sodium atoms at the surface and a stable cluster is formed with the nanoparticle and the surrounding sodium atoms. It is expected that the fundamental property of Nanofluid changes by atomic bonding.

Furthermore, forming the cluster, charge transfer takes place from sodium atom to the nanoparticle atom. This charge transfer is caused by the difference of electronegativity between transition element and sodium. This means that the surface of nanoparticle becomes positively charged and that the clusters repulse mutually. Hence, it is expected that the clusters are dispersed in liquid sodium.

Fundamental Property of Nanofluid

According to the theoretical calculation the atomic bonding between nanoparticle and sodium is larger than that between sodium atoms. In order to investigate the atomic interaction between nanoparticle and sodium, the surface tension which related to the atomic interaction was measured. It is expected that the surface tension of Nanofluid becomes larger than that of sodium because atomic bonding of Nanofluid is larger than that of sodium. The surface tension of Nanofluid was larger than that of sodium. The measured result is shown in Fig.2. This result means that the surface tension of Nanofluid became large by enhancing the chemical bonding. It is expected from this result that the change of atomic bonding affects the reactivity behavior of Nanofluid.

On the other hand, it was confirmed that viscosity of Nanofluid was similar to sodium because of small amount of nanoparticles. Furthermore the melting temperature of Nanofluid was same as that of sodium.

Acknowledgement

Present study is the result of "Development of chemical reactivity reduction technology of liquid sodium metal based on Nanotechnology" entrusted to Japan Atomic Energy Agency by the Ministry of Education, Culture, Sports, Science and Technology of Japan (MEXT).

References:

- [1] Fissan, H. J., and J. Schoonman: Vapor-phase synthesis and processing of nanoparticle materials (nano): -a European Science Foundation (ESF) program, *J. Aerosol Sci.*, 29: (1998) 755-757.
- [2] Ara, K., Ohira, H., Saito, J., Konomura, M. and Toda, M., Abstracts of 2005 Annual Meeting of Atomic Energy Society of Japan, (2005) C1.

Figures:

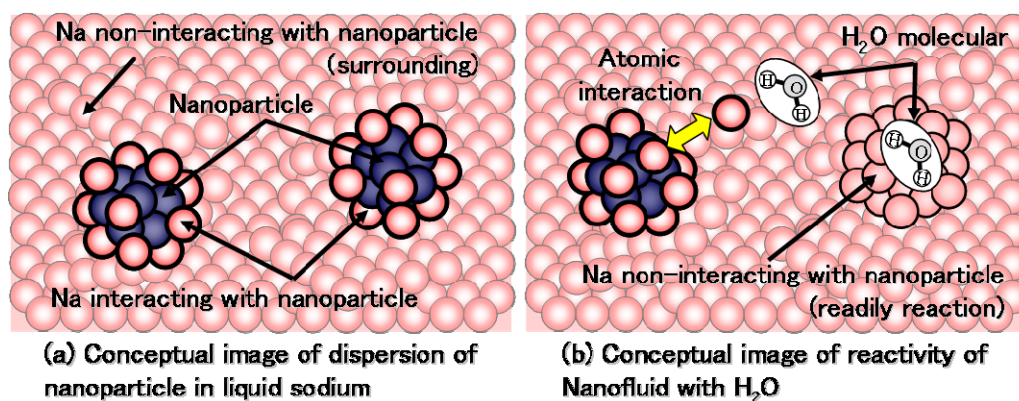


Fig. 1 Conceptual images of Nanofluid and its chemical reactivity

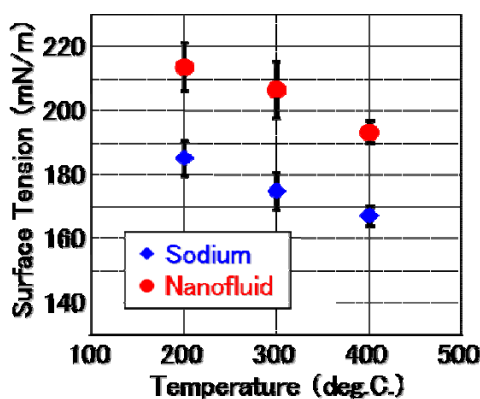


Fig.2 Surface tension of Nanofluid and sodium

**APPLICATION OF CONVERGENT TECHNOLOGIES
(NANO-BIO-INFO-COGNO) IN HEALTH:
THE IBERO-NBIC NETWORK**

A. Pazos¹, F. Martin-Sanchez², J. Dorado¹, C.R. Munteanu¹, I. Hermosilla², V. López-Alonso²,
G. López-Campos²

¹University of A Coruña (UDC), Campus de Elviña, S/N 15071, A Coruña, Spain

²Carlos III Health Institute (ISCIII), Ctra. Majadahonda a Pozuelo, Km. 2, 28220
Majadahonda, Madrid, Spain

muntisa@gmail.com

In the last decades, several technologies with sound scientific basis have reached a high degree of development and have a strong impact in various areas of the society. These fields are: nanotechnology, biotechnology, information technologies and cognitive technologies (NBIC). The convergence between them is expected to produce innovative advances in technologies that may contribute to the improvement of citizen's health and welfare. The Ibero-American scientific and technological communities might face important challenges but also opportunities for innovation and development.

Healthcare is one of the fields where this convergence is already taking place. However, NBIC convergence is still growing in the Ibero-American region and new research projects and collaborative networks are being funded in order to facilitate the interaction between groups that work within the different fields or within their intersections (Nano-Bio, Nano-Info, Nano-Cogno).

The Ibero-American network (Ibero-NBIC) has recently been funded by the CYTED (Ibero-American Program for Science and Development) for the period 2009-2012. Ibero-NBIC has eleven nodes from seven countries (Spain, Portugal, Venezuela, Brazil, Uruguay, Argentina and Chile) with complementary expertise in all of the four areas. The network is coordinated by the University of A Coruña (Spain). This project aims to gather a broad community of scientists from the Ibero-American region that know, develop and assess applications of Convergent Technologies in Healthcare from an integrative and multidisciplinary perspective. The network will promote synergies among countries, disciplines and methods, and it will pay special attention to the related ethical, legal and social aspects. Training and mobility of researchers and knowledge management in the field are also issues to be addressed by this project. Finally, specific network groups will model concrete scenarios of application in healthcare (colorectal cancer diagnosis, therapy and prevention with specific nanoparticles) that will be used in prospective studies.

In summary, the activity of the Ibero-NBIC network aims to contribute to the CYTED objectives through the elaboration of a research Roadmap for Nanomedicine and Convergent Technologies in Health, taking into account the specifics of the region and the state of play in other parts of the world (EU, USA, Japan). It is expected that this exercise will generate new programs and grants and give a better view of the benefits of these research avenues and their consequences on society. This program will be the key to exposing the young scientists to the convergence of these technologies at the very beginning of their professional careers, giving them a broader vision on the scientific basis and expected impact on health and society.

ALKOXIDE GEL NANOFILM CRACKING PROCESSES FOR CREATING OF NOVEL STRUCTURES

Aigi Salundi¹, Jakob Jõgi¹, Valter Reedo¹, Martin Järvekülg¹, Jaan Kalda² and Ants Lõhmus¹

¹Institute of Physics, University of Tartu, Riia 142, 51014 Tartu, Estonia

²Institute of Cybernetics, Tallinn University of Technology, Tallinn Ehitajate tee 5, 19086, Tallinn, Estonia
aigi.salundi@ut.ee

Low-dimensional IVB group metal oxide materials are of great interest due to the applications in photocatalysis, electronics, high temperature isolation and solar cells industry. The elaboration of different strategies for the synthesis of micro- and nano-scale oxide materials is essential for improving the properties and finding new applications for these materials.

We have reported a novel phenomenon and mechanism of low-dimensional tubular oxide structure formation [1]. This discovery provides a new methodology for direct, non-template method for preparing microtubular structures of HfO₂, ZrO₂ and TiO₂. Deposition of solvent free metal alkoxide polymer layer on glass substrate and exposing it with controlled amount of humid atmosphere leads to self-formation of gel film segments that have a tendency for spontaneous rolling upon adding a proper solvent that dissolves the sol under the gel layer.

The purpose of our work is to explain the formation phenomenon of above-mentioned tubular oxide structures, to visualize it in real time in order to reach a better understanding of the processes and control the shape and size of obtained microstructures. The character of gel nanofilm cracking is influenced by various parameters like temperature, ambient humidity, rate of solvent evaporation and presence of nano- and micro-scale defects. Current work includes:

- Achieving control over solvent evaporation rate, temperature and ambient humidity.
- Visualization of crack propagation in alkoxide gel films resulting formation of film segments by optical microscope and scanning electron microscope. Videoclips of the process will be demonstrated.
- Preliminary modelling of the process.

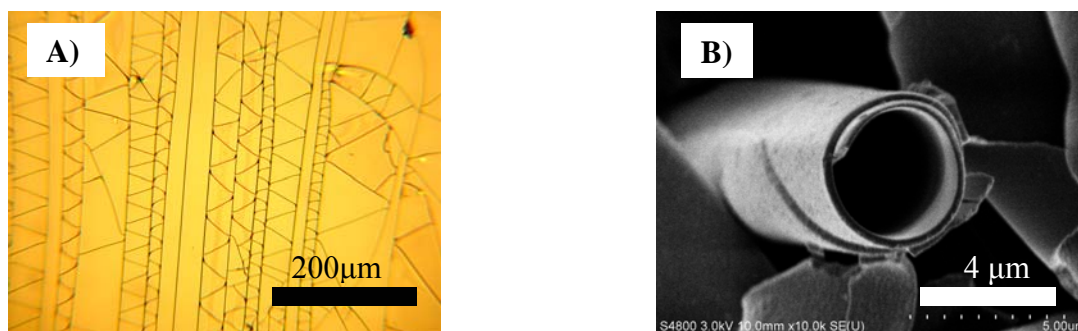


Fig.1 Metal alkoxide gel film cracking: A) optical microscope image of cracking of gel segments, B) SEM image of rolled up gel-segments.

[1] V. Reedo, M. Järvekülg, A. Lõhmus, U. Mäeorg, Novel route for preparation of tubular TiO₂ microstructures, *phys. stat. sol. (a)* 2008, 205, 6, 1511-1514.

CHEMICAL SYNTHESIS OF ZINC OXIDE MONOPODS AND BIPODS: EFFECT OF SUBSTRATE

P. K. Samanta^{a, b}, S. Basak^a and P. Roy Chaudhuri^a

^a*Department of Physics & Meteorology, Indian Institute of Technology,
Kharagpur-721302, India*

^b*Department of Physics, Ghatal R. S. Mahavidyalaya, Paschim Medinipur,
Ghatal-721212, India*

pjush.samanta@gmail.com

Introduction

Zinc Oxide (ZnO) is a very well known multifunctional material being studied since the last decades due to its versatile properties that make it useful in various nanophotonic and optoelectronic devices. Due to its wide band gap of ~3.37 eV and large exciton binding energy, it shows UV and visible photoluminescence, short wavelength light emission, optical transparency and many more [1-4]. Various types of ZnO nanostructures have been reported so far and different methods have been used in their fabrications. Here we report a simple chemical reaction process at low cost towards the fabrication of ZnO monopods and bipods and effect of substrate on the morphology and photoluminescence.

Experimental

All reagents used were of analytical grade and need no further purification. In our typical synthesis process Zinc nitrate solution (0.5M) was prepared by dissolving 14.8g of ZnNO₃ (MERC) in water to prepare 100ml solution. NaOH (1M) solution was prepared by dissolving 4g of NaOH (MERC) in water to prepare 100ml solution. Under constant stirring of NaOH solution the above zinc nitrate solution was added drop wise for 15 minutes. After 30min constant stirring the solution was heated so that it starts boiling. Now different substrates (glass, and quartz) were dipped in the solution by a simple clamp stand arrangement. The boiling was continued to 45 minutes. After cooling the solution to room temperature, the substrates were taken out of the solution. A white film was deposited on the substrates. The substrates were then cleaned several times by distilled water and dried at 40^oC for further characterizations. A white precipitate was also collected from the bottom. The powder is then dried in an ordinary oven for further characterizations through Grazing incidence X-ray diffraction (GIXRD), field emission scanning electron microscope (FESEM) and photoluminescence (PL).

Results and Discussions

Figure 1 (A, B) shows the X-ray diffraction pattern of the thin films on different substrates (glass, quartz and he precipitated powder). The pattern was indexed with hexagonal unit-cell structure consistent with the JCPDS card no-36-1451. In few cases some small peaks are appeared (marked with *) due to the formation of zinc hydroxide upon absorption of moisture from atmosphere.

Figure 2 (A, B) show the prism-like monopods as observed in the case of the precipitated powder samples. Zinc nitrate on reaction with NaOH at room temperature, produces ZnO nanorods. On increasing reaction temperature up to the boiling the solution the rods are transformed into prism-like monopods (fig-2A). The sizes of the monopods are about 150 nm. But in the same reaction process while different substrates (glass/quartz) are dipped in the solution, a thin film was deposited in which the particles are like bipods (fig-3A, B). The particles are uniformly distributed in the thin film which is evident from the FESEM images. The particles are ~100-150 nm in length and the waist size is about 80- 100 nm. It is noteworthy to mention that the size of the monopods and bipods are nearly same but the bipods consist of two monopods which have size half of the monopods in earlier case. Also no preferential growth was observed for these structures. So in our case the substrates have no effect on the preferential orientation of the grown ZnO nanostructures but the shape and size of the nanostructures strongly depend on the substrates. No differences in size of the bipods were observed in case of glass and quartz substrate.

Transmission electron microscopic study was also carried out for further study of the fabricated nanostructures. Inset of figure-3A shows a TEM image of the nano bipods grown on glass substrate. The spindles are about 100-150 nm in length and the waist diameter is about 80-100 nm. The bipods are actually consisting of two prism joined base to base which can be clearly observed from figure-1e.

Conclusions

In conclusion a simple wet chemical method has been established for the fabrication of ZnO monopods and bipods. The fabricated structures show photoluminescence in violet and UV region due to the change of microstructure from monopods to bipods. We also observe the substrate affect the morphology of the nanostructure.

References

- [1] M. H. Huang, S. Mao, H. Feick, H. Yan, Y. Wu, H. Kind, E. Weber, R. Russo, and P. Yang, *Science*, **292**(2001)1897.
- [2] X. Wang, J. Zhang and Z. Zhu, *Applied Surface Science*, **252**(2006)2404.
- [3] Jih-Jen Wu and Sai-Chang Liu, *Adv. Mater.*, **14**(2002)215.
- [4] Hanmei Hu et al, *Materials Chemistry and Physics*, **106** (2007) 58.

Figures

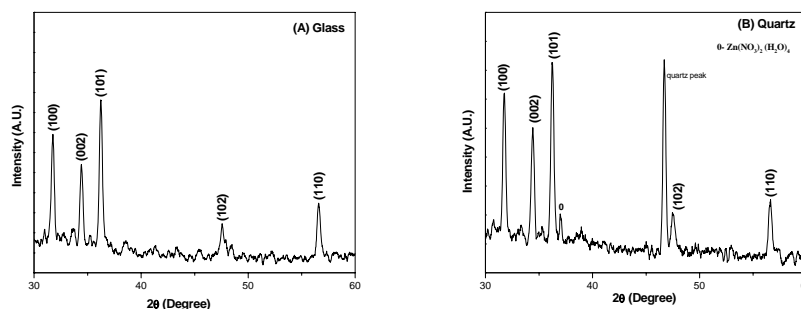


Figure-1: GIXRD pattern of ZnO bipods on (A) glass and (B) quartz substrate.

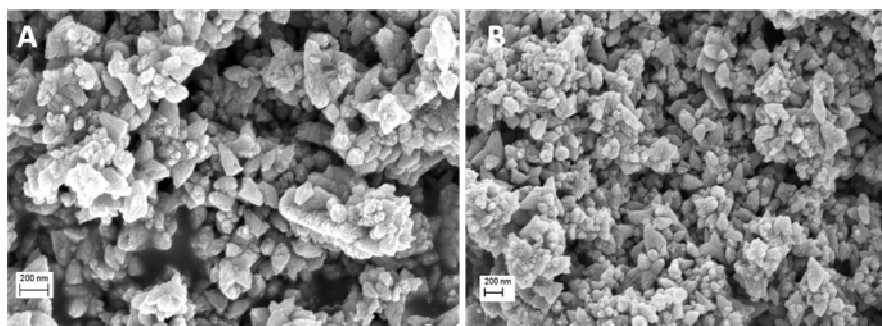


Figure-2; FESEM images of ZnO monopods grown without any substrate.

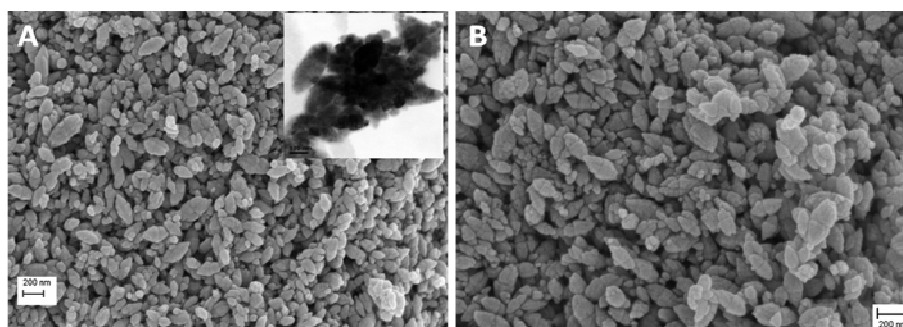


Figure-3: ZnO bipods grown on (A) glass and (B) quartz substrate. Inset shows the TEM image of the bipods for glass substrate

A structural study of the superparamagnetic behavior of $\text{Sr}_{0.5}\text{Ba}_{0.5}\text{CoO}_3$

A.S. Botana^{1,2}, A. Pineiro^{1,2}, V.Pardo^{1,2}, D. Baldomir^{1,2}, P. M. Botta⁴, C. de la Calle⁵, J.E. Arias^{1,2} and J. Rivas¹.

¹ *Departamento de Física Aplicada, Facultad de Física, Universidad de Santiago de Compostela, E-15782 Campus Sur s/n, Santiago de Compostela, Spain.*

² *Instituto de Investigaciones Tecnológicas, Universidad de Santiago de Compostela, E-15782 Campus Sur s/n, Santiago de Compostela, Spain.*

⁴ *Instituto de Investigaciones en Ciencia y Tecnología de Materiales (INTEMA), CONICET-UNMdP, J.B. Justo 4302 B7608FDQ Mar del Plata, Argentina.*

⁵ *Instituto de Ciencia de Materiales de Madrid (ICMM), CSIC, Cantoblanco, 28049 Madrid, Spain*

antia.sanchez1@rai.usc.es

Systems formed by magnetic nanostructures have been deeply studied in the last few years, showing some interesting technological applications, in fields such as magnetic recording, sensors, magnetic memory and magnetoelectronics. One of the main problems associated to these nanostructures is their fabrication and manipulation at so low atomic scale.

Curiously, it was found that the cobaltite serie $\text{Sr}_x\text{Ba}_{1-x}\text{CoO}_3$ exhibits a superparamagnetic behavior [1], suggesting the existence of magnetic clusters [2] suitable to be size controlled through the doping Sr concentration.

Despite the effort in understanding this phase separation phenomenon at the nanoscale in complex oxides, it is not understood today. Our work will analyze this cluster-like-behavior in a crystalline structure and we will present some results on the half-doped compound $\text{Sr}_{0.5}\text{Ba}_{0.5}\text{CoO}_3$. We shall concentrate on exploring the proper space group and structure via ab initio calculations from experimental structural data that cannot elucidate the ordering of oxygen vacancies. A structural relaxation will be carried out for the possible space groups to obtain the ground state geometry of the system. In addition, the effects of oxygen vacancies and its influence on the phase separation will be studied.

References:

- [1] K. Yamaura, H. Zandbergen, K. Abe and R. Cava, *J. Solid State Chem.*, **146** (1999) 96.
- [2] V. Pardo, J. Rivas and D. Baldomir, *Appl. Phys. Lett.*, **86** (2005) 202507.

Self-nanostructuring of the chemical termination of SrTiO₃(001) substrates: templates for fabrication of functional oxide nanostructures

R. Bachelet⁽¹⁾, F. Sanchez⁽¹⁾, J. Santiso⁽²⁾, F. J. Palomares⁽³⁾, M. Paradinas⁽¹⁾, C. Ocal⁽¹⁾,
and J. Fontcuberta⁽¹⁾

⁽¹⁾ Institut de Ciència de Materials de Barcelona, ICMA-B-CSIC,
Campus UAB, 08193 Bellaterra, Spain

⁽²⁾ Centro de Investigación en Nanociencia y Nanotecnología, CIN2, ICN-CSIC,
Campus UAB, 08193 Bellaterra, Spain

⁽³⁾ Instituto de Ciencia de Materiales de Madrid (CSIC),
Cantoblanco, E-28049 Madrid, Spain

fsanchez@icmab.es

Low-dimensional structures of complex oxides with a wide range of functional properties, from ferroic to catalytic properties, hold the promise to lead to a new generation of materials with unrivalled properties compared to their bulk counterparts. However, nanostructure fabrication of complex oxides is not as well-established as these of metals or semiconductors, which is partly due to the complexity of lattices and the numerous chemical elements. Moreover, the long-range order in self-assembling methods is very challenging. Therefore, new strategies are required for cost-effective fabrication of ordered oxide nanostructures. Here we report a method to fabricate functional oxide nanostructures ordered over the centimeter scale. The method is based in tailoring the chemical termination of SrTiO₃(001) substrates and exploiting the selective nucleation of functional oxides on SrO(001) and TiO₂(001) surfaces.

We have studied in detail the morphological and chemical evolution of the topmost surface of STO substrates with annealing. We recently reported that annealing of STO substrates at 1100-1200 °C causes surface diffusion of the two existing chemical terminations. As a result, TiO₂-terminated terraces separated by SrO-terminated quasi one-dimensional regions are formed [1]. Now we will show that proper annealing at higher temperature (1300 °C) under oxidizing conditions causes Sr diffusion from the bulk, resulting in atomically flat surfaces, perovskite-layered SrO terminated. Moreover, we will show that the progressive surface enrichment of SrO allows to obtain surfaces with chemical-termination separated at the nanoscale (Figure 1). Such large-area nanopatterned surfaces, stable at relatively high temperature, can be used as template to grow functional ordered nanostructures, exploiting the termination-dependent nucleation.

We will show how the intermediate chemically-organized surfaces occurring during the progressive SrO enrichment can be used as template for nanostructure fabrication of ferromagnetic oxides by chemically-driven selective nucleation. First we prove it with SrRuO₃, which is known to nucleate distinctly and preferentially on TiO₂ rather than on SrO termination of SrTiO₃(001) surfaces [1,2]. The topographic atomic force microscopy images of a treated substrate and a deposited film in Figure 2 show that SrRuO₃ nucleates exclusively on the TiO₂-termination, and thus it replicates any nanostructuring of a treated substrate.

We have also investigated the selective growth of the ferromagnetic oxides La_{2/3}Sr_{1/3}MnO₃ and CoFe₂O₄ on nanostructured substrates. The results confirm the selective growth and indicate that the method here presented offer new opportunities for the fabrication of functional low-dimension structures of complex oxides.

References:

- [1] R. Bachelet, F. Sánchez, J. Santiso, C. Munuera, C. Ocal, J. Fontcuberta, *Self-organization of the SrTiO₃(001) chemical terminations: a route for oxide nanostructure fabrication by selective growth*, Chemistry of Materials, in press (published online)
- [2] R. Bachelet, F. Sánchez, J. Santiso, J. Fontcuberta, *Reversible growth mode transition in SrRuO₃ epitaxy*, Applied Physics Letters **93**, 151916 (2008)

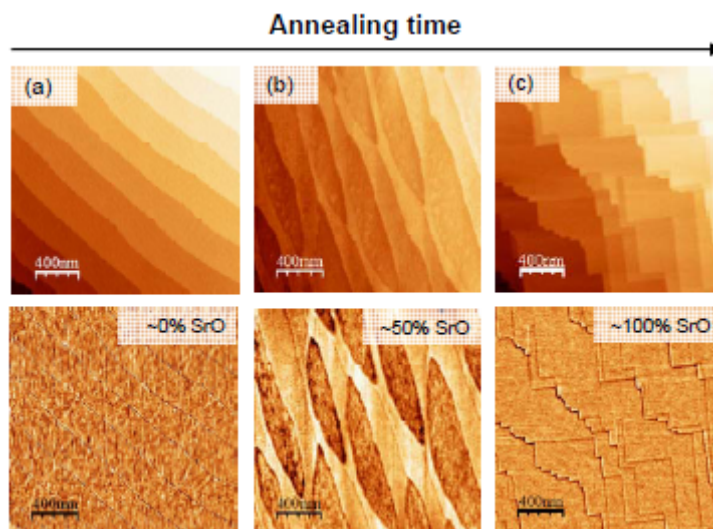
Figures:

Figure 1: AFM topographic (top panels) and phase-lag (bottom panels) images of a chemically-treated SrTiO₃(001) substrate after annealing at 1300 °C for (a) 2h, (b) 12h, and (c) 72h.

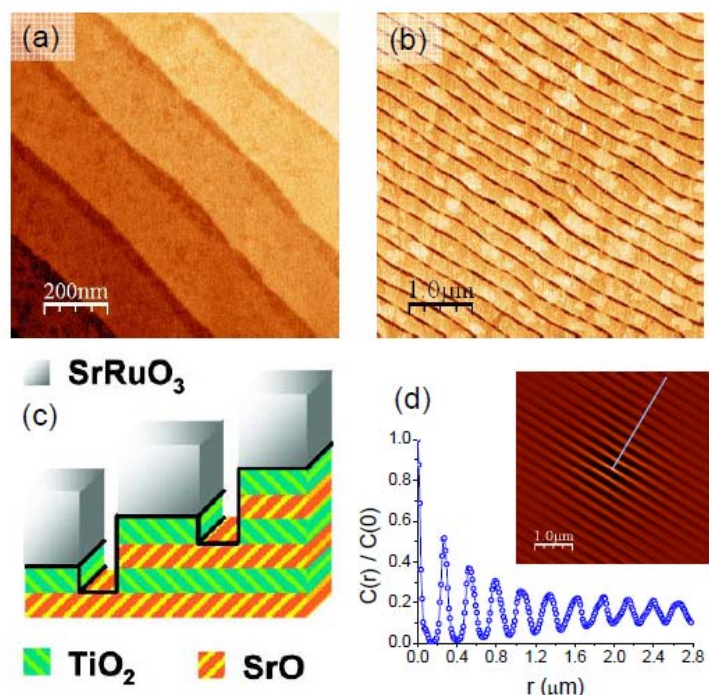


Figure 2: AFM topographic images: (a) 1 x 1 μm² area of bare SrTiO₃(001) substrate after annealing at 1200 °C for 2h, and (b) 5 x 5 μm² area of a SrRuO₃ film, 7 monolayer thick, deposited on (a). (c) Sketch of the substrate nanostructuration and the selective growth. (d) Self-correlation of (b) and the corresponding profile taken perpendicular to the steps signalling the long-range spatial order.

ON THE MAGNETISM OF SUBSTITUTIONAL TRANSITION-METAL IMPURITIES IN GRAPHENIC NANOSTRUCTURES

E. J. G. Santos, A. Ayuela, D. Sánchez-Portal

Centro de Física de Materiales, Centro Mixto CSIC-UPV/EHU and Donostia International Physics Center (DIPC), Apdo. 1072, 2080 San Sebastián, Spain

We report a theoretical study of substitutional Ni, Co and Fe impurities in graphene. Only Co_{sub} defect is magnetic with a magnetic moment of $\sim 1\mu_B$ for the isolated impurity. However, when the Co substitution takes place in more than one site, the total magnetic moment of the system exhibits a strong dependency on the relative position of the Co_{sub} impurities. More precisely the magnetic moment depends on the number of Co substitutions in A and B sublattices. This behaviour is better understood when we realize that the electronic structure of a substitutional Co impurity nearby the Fermi energy is equivalent to that of a carbon vacancy in a simple π -tight-binding model of graphene. Therefore, we can expect the Lieb's [1] theorem to apply to this situation and the total magnetic moment to behave as $|C_{O_A} - C_{O_B}|$, where C_{O_A} and C_{O_B} are, respectively, the number Co substitutions in the A and B graphene sublattices [2].

In contrast to Co impurities, Ni_{sub} defects, which have been recently detected in carbon nanotubes by Ushiro *et al.* [3] using extended x-ray absorption fine structure (EXAFS) and x-ray absorption near edge structure (XANES) data, show a zero magnetic moment in flat graphene. However, Ni_{sub} impurities develop a non-zero magnetic moment in metallic carbon nanotubes [4]. This surprising behavior stems from the peculiar curvature dependence of the electronic structure of Ni_{sub}. A similar magnetic/non-magnetic transition of Ni_{sub} can be expected by applying other kinds of anisotropic strain to a flat graphene layer [5].

In general, we have found that we can draw an analogy between the electronic structure in the neighborhood of the Fermi energy, and its strain dependence, of substitutional Co, Ni and Fe atoms in graphenic systems and that of an unreconstructed carbon vacancy in graphene with different charge states. With this analogy at hand we can easily understand and predict many complex and interesting phenomena for graphenic nanostructures substitutionally doped with transition metals.

[1] E. H. Lieb, Phys. Rev. Lett. **62**, 1201 (1989).

[2] E. J. G. Santos, D. Sánchez-Portal and A. Ayuela, in preparation.

[3] M. Ushiro, K. Uno, T. Fujikawa, Y. Sato, K. Tohji, F. Watari, W. J. Chun, Y. Koike, and K. Asakura, Phys. Rev. B **73**, 144103 (2006).

[4] E. J. G. Santos, A. Ayuela, S. B. Fagan, J. Mendes Filho, D. L. Azevedo, A. G. Souza Filho and D. Sánchez-Portal, Phys. Rev. B **78**, 195420 (2008).

[5] D. Sánchez-Portal, E. J. G. Santos and A. Ayuela, in preparation.

Synthesis and fluorescent properties of gold atomic clusters

B. Santiago-González and M. A. López-Quintela

*Laboratory of Nanomaterials and Magnetism (NANOMAG). Institute of Technological Research. Depart. of Physical Chemistry and Applied Physics. University of Santiago de Compostela. E-15782 Santiago de Compostela. Spain
beatriz.santiago@usc.es*

Small metal clusters typically consist of several to tens of atoms, with sizes below 2 nm. These atomic clusters behave like molecules and exhibit enhanced catalytic activity, luminescence, and unique charging properties. In particular, the fluorescent properties make them potential labels for biological applications.

In this work, we have synthesized alkenethiol-protected gold clusters by introducing alkenethiol ligands onto the surfaces of gold nanoparticles. This strategy offers an interesting approach to create metal clusters from nanomaterials. [1,2] Photoluminescence spectra of gold clusters produced using this method, excited at 400 nm, exhibit a maximum emission around 520 nm.

A novel templating procedure using nanosomes, made of bola-hydroxyl and mercaptopalmitic acids acting as capping agents, was also used for the direct production of clusters. [3]

Characterization of samples was carried out by UV-vis and Fluorescence spectroscopy, TEM and AFM.

References:

- [1] D. G. Duff and A. Baiker. "A new hydrosol of gold clusters. 1. Formation and particle size variation.", *Langmuir*, **9**,(1993), 2301-2309.
- [2] C-C. Huang, C-K. Chiang, Z-H. Lin, K-H. Lee, and H-T. Chang. "Bioconjugated gold nanodots and nanoparticles for protein assays based on photoluminescence quenching." *Anal. Chem.*, **80**, (2008), 1497-1504.
- [3] J-P. Douliez, B. Novales, C. Gaillard. "Synthesising gold nanoparticles within bola fatty acid nanosomes." *Journal of Colloid and Interface Science*. (unpublished).

Ferromagnetic resonance in nanometric epitaxial Fe₃Si films on (111)Ge

Nuno M. Santos¹, Evgeny R. Zhitoytsev¹, Kohei Hamaya²,
Taizoh Sadoh², Masanobu Miyao², and Nikolai A. Sobolev¹

¹ *IN3 – Institute for Nanostructures, Nanomodelling and Nanomanufacturing, Departamento de Física, Universidade de Aveiro, 3810-193 Aveiro, Portugal*

² *Department of Electronics, Kyushu University, 744 Motoooka, Fukuoka 819-0395, Japan*

Nsantos@ua.pt

The epitaxial growth of ferromagnetic thin films on semiconductor substrates is the base of a new technology applied to the spintronic devices. The ferromagnetic silicide Fe₃Si is a promising material for a spin injector. Usually the Fe₃Si thin films are grown on (001) substrates (GaAs, MgO). However, it has recently been shown that the low-temperature molecular beam epitaxy (MBE) growth of Fe₃Si on (111)Ge provides atomically flat interfaces and good magnetic properties, e.g., Curie temperature as high as 840 K [1]. Furthermore, an unexpected uniaxial magnetic anisotropy was observed in the film plane, and the direction of the uniaxial easy axis was different for each of the as-grown samples. By postgrowth annealing, surprisingly, the random orientation of the uniaxial easy axis was aligned to a direction along about [0–11]. An enhancement of the ordering of the magnetic DO3 phase was suggested. In the present work, we apply the ferromagnetic resonance (FMR) spectroscopy to further study this in-plane anisotropy.

Fe₃Si epilayers were grown on n-type (111)Ge substrates by low-temperature (130°C) MBE. The thickness of the epilayers was about 50 and 100 nm. The post-growth annealing was carried out at temperatures up to 375°C for 30–120 min. FMR spectra were obtained using an X-band spectrometer (~9.8 GHz). Measurements of the angular dependences of the FMR signal were performed at room temperature for the in-plane and out-of-plane field orientations. The angular dependences of the FMR line position were analyzed in the framework of the well-established theory [2]. In order to analyze the angular dependence of the linewidth, a phenomenological model considering intrinsic (homogeneous) and inhomogeneous contributions was adopted [3].

We have observed a very strong difference of the FMR linewidth for the 100 nm and 50 nm thick as-grown samples. The lines in the latter are several times narrower. Simulations of the angular dependence of the line width indicated an effective magnetization dispersion $\Delta(4\pi M_{eff}) = 390$ G in the 100 nm thick and 60 G in the 50 nm thick samples. This means a much higher homogeneity of the thinner films. Thus, in the follow-up work we investigated only the latter ones. In the as-grown sample, the simulations give a Gilbert damping factor $\alpha = 0.004$ and the dispersion of the effective magnetization orientation $\Delta\theta_H = 0.1^\circ$. There is very weak uniaxial in-plane anisotropy of the resonance line position. Annealing at 350°C enhances this anisotropy without significantly changing the linewidth parameters. This means, there is probably no ordering of the DO3 magnetic phase. After increasing the anneal temperature to 375°C, we observed the appearance of a six-fold anisotropy, as expected for the (111) plane of the DO3-type Fe₃Si, still superimposed with a uniaxial anisotropy. Our results confirm that no second phase is formed as a result of the annealing at temperatures up to 375°C, as no additional FMR line appears in the samples. The annealing-induced changes of the magnetic anisotropy parameters are discussed in detail.

References:

- [1] Y. Ando, K. Hamaya, K. Kasahara, et al., *J. Appl. Phys.* **105**, 07B102 (2009).
- [2] S.V. Vonsovskii, ed. *Ferromagnetic Resonance*. Pergamon, Oxford (1966).
- [3] S. Mizukami, Y. Ando and T. Miyazaki. *Phys. Rev. B* **66**, 104413 (2002).

SYNTHESIS AND MAGNETIC PROPERTIES OF DIMERS OF WEAKLY MAGNETICALLY COUPLED MOLECULES

E. Carolina Sañudo,^{a,*} T. Cauchy,^b R. H. Laye,^c S. J. Teat,^d O. Roubeau,^e E. Ruiz,^b G. Aromi^b

^a Institut de Nanociència i Nanotecnologia Universitat de Barcelona, Diagonal 647, 08028 Barcelona, SPAIN. ^b Departament de Química Inorgànica, Universitat de Barcelona, Diagonal 647, 08028, Barcelona, SPAIN. ^c Department of Chemistry, University of Manchester, M13 9PL Manchester, UK. ^d Advanced Light Source, Lawrence Berkeley Laboratory, 1 Cyclotron Road, MS2-400, Berkeley, California 94720 USA. ^e Université' Bordeaux I, CNRS-CRPP, 115 av. Dr. A. Schweitzer, 33600 Pessac, France.

Email: carolina.sanudo@qi.ub.es

It has been proposed that a two qu-bit quantum gate could be built from two spin clusters held together by a linker [1]; to function, the two units must interact, i. e. magnetic exchange, and the interaction should be switchable from the 'on' state to the 'off' state. Right now there are not any examples of molecules that fulfill all of the requirements and the synthesis of a suitable system is a challenge. We focus our efforts in new synthetic routes to dimers of molecules that can fulfill the abovementioned requirements by two means: ligand design and serendipitous assembly. New examples of dimers of molecules are presented, obtained by either method and their magnetic properties studied. Following the ligand design approach, the use of the ligand 1,3-bis-(3-oxo-3-(2-hydroxyphenyl)-propionyl)-2-methoxybenzene alone or in combination with pyrazine has resulted in the isolation of a series of dimers of tetranuclear and trinuclear. The dimers with a pyrazine bridge are shown to display the weak magnetic coupling expected. By serendipitous assembly, dimers of tetranuclear Ni cluster and trinuclear Fe complexes are presented.

[1] *Phys. Rev. Lett.* **2003**, *90*, 47901.

GROWN AND CHARACTERIZATION OF SEMICONDUCTOR NANOSTRUCTURES BY LASER ABLATION

M. Sanz^{1}, M. Walczak¹, M. Oujja¹, R. de Nalda¹, J. G. Izquierdo², L. Bañares² and M. Castillejo¹*

¹*Instituto de Química Física Rocasolano, CSIC, Serrano 119, 28006 Madrid, Spain*

²*Departamento de Química Física I, Facultad de Ciencias Químicas, Universidad Complutense de Madrid, 28040 Madrid, Spain*
mikel.sanz@iqfr.csic.es

Pulsed lasers can be used to generate clusters in laser ablation processes and to deposit nanoparticles on different substrates; this process is known as Pulsed Laser Deposition (PLD). In PLD a pulsed laser beam is focused onto the surface of a solid target and the ejected material in the plume is collected in a substrate placed nearby. Laser sources emitting at UV, VIS and IR wavelengths and delivering short pulses, in the nanosecond (ns) and the femtosecond (fs) domain, with controlled fluence, are used to ablate the targets. The main drawback of this deposition method is the presence of microscopic particulates on the surfaces of the films which are present with high densities when the optical absorption coefficient of the target is small at the wavelength used for ablation [1]. The use of fs laser pulses offers high material removal efficiency and high deposition rates of nanometer scale particles free of microscopic particulates and therefore fs PLD constitutes an attractive procedure for the fabrication of nanostructured deposits [2].

In this work we present the obtained nanostructured deposits of semiconductors with exceptional optical and electronic properties widely used in photovoltaic devices, sensors, optical coatings and in photocatalysis such as TiO₂ [3], CdS [4], ZnS and ZnO. The deposition processes takes place inside a PLD chamber in vacuum or under oxygen at different pressures. The effects of the pulse duration (ns or fs pulses), laser wavelength (532, 355 and 266 nm using ns pulses and 800, 400 and 266 nm with fs pulses), the temperature of the substrate and the atmosphere of deposition that are suitable for obtaining nanostructured deposits were investigated.

The deposits are characterized by X-ray photoelectron spectroscopy (XPS) to determine their composition, by X-Ray diffraction (XRD) to examine their crystallinity and by environmental scanning electron microscopy (ESEM) and atomic force microscopy (AFM) to observe the surface structure. As an example, Figure 1 shows an AFM image of a TiO₂ deposit grown by ablating the target with fs pulses from a Ti:Sapphire laser at 266 nm in vacuum at room temperature.. The size of the deposited nanostructures is found to increase with laser wavelength (Fig.2) and the presence of micro-particulates can be avoided using ultrashort pulses. The smallest nanoparticles (30 nm), with a narrower size distribution are obtained by fs PLD upon UV irradiation.

References:

- [1] M. Sanz, M. Walczak, M. Oujja, A. Cuesta and M. Castillejo, *Thin Solid Films* (2009), doi:10.1016/j.tsf.2009.04.026.
- [2] M. Sanz, M. Walczak, R. de Nalda, M. Oujja, J.F. Marco, J. Rodríguez, J.G. Izquierdo, L. Bañares, M. Castillejo, *Appl. Surf. Sci.* **255** (2009) 5206.
- [3] X. Chen and S. S. Mao, *Chem. Rev.* **107** (2007) 2891.
- [4] N.V.Hullavarad, S.S Hullavarad, P.C. Karulkar, *J. Nanosci. Nanotechnol.* **8** (2008) 3272.

Figures:

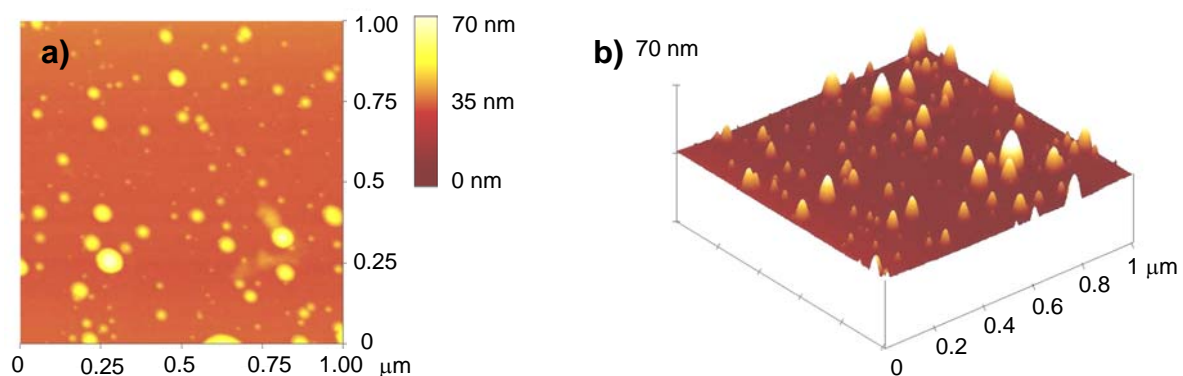


Figure 1. AFM images of the TiO_2 nanostructures deposited by fs PLD under vacuum, at RT and 266 nm: a) topography image and b) 3D topography image.

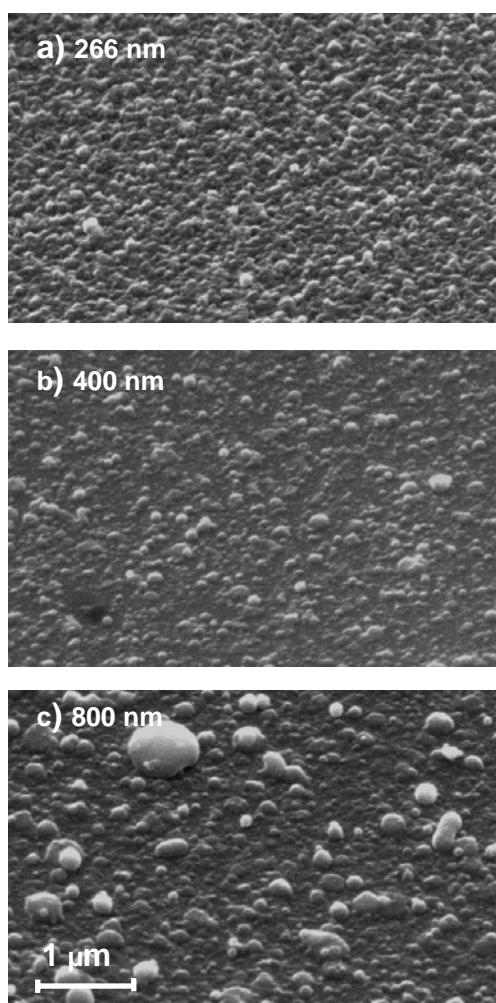


Figure 2. ESEM images of the surfaces of TiO_2 thin films grown by fs PLD at RT in vacuum at the indicated deposition wavelengths. The bar size is 1 μm in all images.

**SYNTHESIS OF SILVER NANOPARTICLES AND STABILIZATION
IN DIFFERENT LIQUID AND SOLID SOL-GEL MATRICES.
OPTICAL AND STRUCTURAL CHARACTERIZATION.**

Saraidarov Tsiala, Levchenko Viktoria, Reisfeld Renata

*The Hebrew University of Jerusalem, Inorganic Chemistry Department,
Givat-Ram, 91904 Jerusalem, Israel,
Contact e-mail: tsiala@cc.huji.ac.il*

Nano-sized clusters of noble metals in a dielectric media have attracted much attention due to their potential applications in many areas including nonlinear optical devices, surface-enhanced Raman spectroscopy, near-field scanning optical microscopy, biological sensing, heterogeneous catalysis, anti-reflective films, solar cells, light-emitting diodes and integrated optics. Metal nanoparticles dispersed in dielectric materials exhibit a strong characteristic extinction peak, due to plasmon resonance occurring nearly at 420nm in the visible region of optical spectrum. Surface plasmons are collective oscillations of the electrons of conductors leading to a resonant interaction between incident light and the conductor. Metal nanoparticles can result in strong scattering of incident light and greatly enhanced local fields, and can also lead to enhanced fluorescence [1].

Nanoparticle clusters of noble metals can be introduced into a various dielectric matrix, in polymers and sol-gel glasses. In recent years, sol-gel synthesis of nano-composites containing ultra fine particles of noble metals in silica and titania matrices has developed rapidly. The sol-gel technology has advantages in the formation of films with controllable thickness, three dimensional protection of the NCs, prevention of NCs growth, aggregation and oxidation.

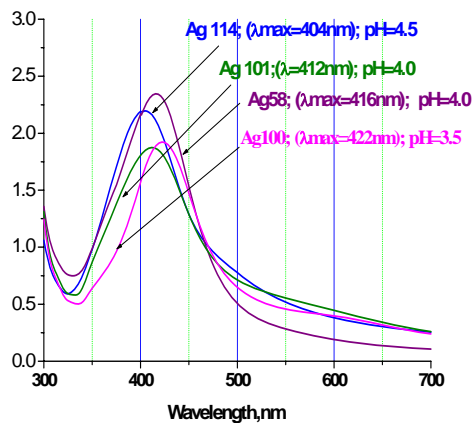
In this work we present simple procedures for the synthesis of various size Silver nanoparticles (NPs) and experimental results about influences of surrounding sol-gel materials on optical and structural properties of synthesized silver nanoparticles (NPs). Various size of silver NPs were obtained in water using citric acid, ammonium hydroxide and/or ascorbic acid at various pH, and stabilized in different sol-gel colloidal solutions. As host sol-gel materials we choose ormosils composite matrices such as: Silica-Polyurethane (SiPU), Zirconia-Glymo (ZrGl) and Glymo- Phenylsiloxane-Polyurethane (GPSPU).

Recently was shown [2] that, in suspension of silver colloids made with well-defined sizes and low heterogeneity, the resonance peak shifts to longer wavelengths when the particle size increases. In this work we estimate the silver NPs size and shape in various sol-gel solutions and solid films from measured absorption spectra and SEM measurements. Absorption spectra of silver NPs obtained in various pH and using different reducing conditions show the above mentioned resonance shifts which correspond to the increase of the particles size (Figures 1-2). SEM structural characterization of ormosils solid films included silver NPs show homogeneous and well-dispersed silver NPs. Maximum size of the silver grains that could be accommodated in the amorphous matrix were observed to be 62-64 nm. In all matrices particles size obtained by SEM were identical to those which were estimated from the corresponding absorption spectra. Finally, we conclude that it is possible to control silver NPs size at various pH and reducing conditions. Obtained silver NPs can be stabilized in appropriated sol-gel ormosils solution and solid films without changing their optical properties for a long time.

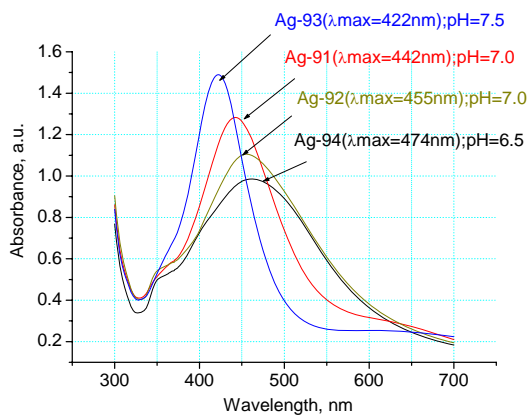
References:

- [1] R. Reisfeld \, Ts. Saraidarov \, V. Levchenko, J Sol-Gel Sci Technol, 50 (2009)194–200.
 [2] Lakowicz Joseph R, Krishanu Ray, Mustafa Chowdhury, Henryk Szmanski, Yi Fu, Jian Zhang, Kazimierz Nowaczyk, R Soc Chem Anal, 133 (2008)1308–1346.

Figures1: Absorbance spectra of silver NPs obtained with ascorbic acid at various pH (3.5-4.5).



Figures 2: Absorbance spectra of silver NPs obtained with citric acid at various pH (6.5-7.5).



Temperature dependence of the ground-state exciton in PbSe core, and relevant core-shell colloidal quantum dot structures

A. Sashchiuk, G. I. Maikov, A. Kigel, R. Vaxenburg, D. Yanover, E. Lifshitz
Schulich Faculty of Chemistry and Solid State Institute, Technion, Haifa, Israel
chaldona@techunix.technion.ac.il

PbSe and PbS colloidal quantum dots (CQDs) are the focus of widespread interest due to their unique electronic and optical properties, with feasibility of applications in near infra-red (NIR) lasers, biological markers, photovoltaic solar cells, Q-switches and nano-electronic devices [1,2]. These semiconductors have a simple cubic crystal structure with nearly identical lattice constants 5.93 Å and 6.12 Å at 300 K, respectively, which facilitates the formation of heterostructures. Recently, [3] high quality PbSe/PbS core-shell and completely original PbSe/PbSe_xS_{1-x} core-alloyed shell CQDs structures produced using a single injection process, offering the potential to tailor the crystallographic and dielectric mismatch between the core and the shell, forming a perfect crystalline hetero-structure. These structures present a tunability of the band-edge offset with variation of the shell thickness and composition, eventually controlling the electronic properties of the CQDs.

The present study describes a thorough investigation of the temperature influence on luminescence spectra and their decay processes in the PbSe/PbS core-shell (CS) (produced using two injection process) and PbSe/PbSe_xS_{1-x} core-alloyed shell CQDs (with $0 \leq x < 1$ produced using a single injection process with an initial Pb/Se/S molar ratios of 1/1/1.5 and 1/0.6/0.8) in comparison with luminescence spectra of the PbSe core CQDs dispersed in glass solution. The compositional and crystallographic structural properties of the studied samples were confirmed by a high-resolution transmission electron microscopy, and energy dispersive analysis of x-ray. The ground-state exciton lifetime was measured and recorded at laser fluence ~ 0.2 mJ/cm², ensuring the formation of a single exciton per a single CQD.

Figure (A) and (B) shows the representative continuous-wave (cw) photoluminescence (PL) spectra of PbSe with a radius (R) of 2 nm and of PbSe/PbS CS CQDs with R=1.65 nm and shell thickness (Th) of 0.55 nm, measured at various temperatures as indicated in the legend. The absorbance first exciton transition (1.03 eV) at room temperature (RT) is the same for these structures. Figure (C) presents the plots of the PL peak energy versus the temperature (see legends) of PbSe/PbS CS CQDs and of PbSe/PbSe_{0.3}S_{0.7} core-alloyed shell CQDs structures produced with an initial Pb/Se/S molar ratio of 1/0.6/0.8, in comparison with the PL spectra of PbSe core CQDs as indicated in legends. Figure (D) demonstrates the transient PL curves of CQDs shown in Figure (C) according to the legend notations and measured at RT.

PL spectroscopy analyses of these nanostructures, electronic band-gaps and photo-emission demonstrate that compositional, and phonon-electron interactions properties play important roles in these structures. The influence of a dark-bright states thermal activation on the energy and dynamics of a ground-state exciton of PbSe/PbS CS and PbSe/PbSe_xS_{1-x} core-alloyed shell CQDs respect to these of PbSe core CQDs [4] would be discussed.

PL-decay time investigations shows that PL decay process of PbSe/PbS CS CQDs differ from that of PbSe core CQDs, which shows only single exponent behavior. The ground-state lifetimes of the core-shell structures presented in Figure D, in particular the PbSe/PbS CS CQDs, showed substantially longer lifetime on the microsecond time scale at RT, both with respect to their corresponding cores and with respect to that of a PbSe core with a similar overall size. The significant difference in lifetimes between cores and CS CQDs (particular

with smallest core) is a demonstration of the excellent passivation of the shell which prevents non-radiative quenching of the excitons by the Auger effect and is responsible of PL quantum efficiency increasing in core-shell CQDs. This may be beneficial in gain and solar cell devices.

References:

- [1] V. I. Klimov, J. Phys. Chem. B 110 (2006)16827.
- [2] M. D. Fischbein, M. Drndic, Appl. Phys. Lett. 88 (2006) 063116.
- [3] E. Lifshitz, M. Brumer, A. Kigel, A. Sashchiuk, M. Bashouti, M. Sirota, E. Galun, Z. Burshtein, A.Q. Le Quang, I. Ledoux-Rak, J. Zyss, J. Phys. Chem. B 110 (2006) 25356.
- [4] A. Kigel, M. Brumer, G.I. Maikov, A. Sashchiuk, E.Lifshitz, Small (2009) in press.

Figures:

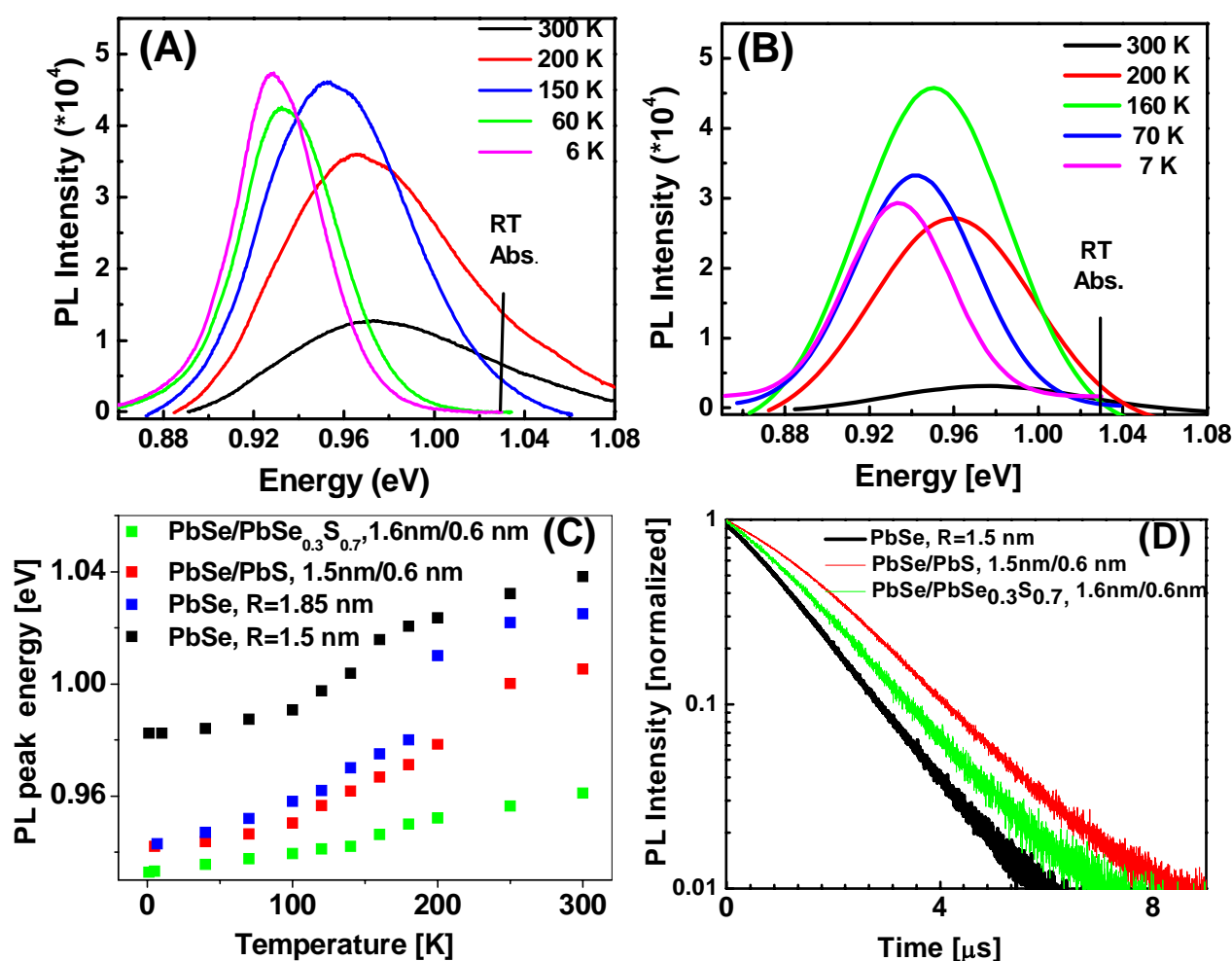


Figure (A) Representative cw-PL spectra of PbSe CQDs; with R= 2 nm; **(B)** Representative cw-PL spectra of PbSe/PbS CS CQDs with R=1.65 nm and Th =0.55 nm, measured at various temperatures as indicated in the legend; Absorbance first exciton transition (1.03eV) at RT is labeled; **(C)** Plots of the PL peak energy versus the temperature, according to the legend notation. (■) PbSe core CQDs with R=1.5 nm, (■) PbSe CQDs with R=1.85 nm; (■) PbSe/PbS CS CQDs with R=1.5 nm and Th =0.6 nm (■) PbSe/PbSe_{0.3}S_{0.7} CQDs with a R=1.6 nm and Th =0.6 nm prepared with a initial Pb/Se/S molar ratio of 1.0/0.6/1.8.; **(D)** The transient PL curves of CQDs shown in (C) according to the legend notations.

Modeling of Nanocrystal-Molecule Nanostructure Formation

Nicolas Sassi, Claire Barrett, Aidan J. Quinn

Nanotechnology Group, Tyndall National Institute, Lee Maltings, Prospect Row, Cork, Ireland.

nicolas.sassiat@tyndall.ie

Self-assembled nanocrystal-molecule nanostructures have generated significant research interest in recent years with potential applications in molecular electronics, plasmonics and biosensing. Recently we have developed solution-based processes for assembly of plasmonic nanostructures through controlled mixing of citrate-stabilised gold nanocrystals and molecular linkers with isothiocyanate end groups; see Figure 1a. We term these nanostructures “ n -mers”, where n denotes the number of nanocrystals in the structure. Figure 1b shows high-resolution Scanning Electron Microscopy (SEM) images of individual n -mers deposited from solution. Analysis of several hundred SEM images acquired across multiple substrates yields quantitative distributions for monomers ($n = 1$), dimers ($n = 2$) and higher order n -mer nanostructures; see Figure 2a.

Here we report on development of complementary random-walk and rate-equation simulation routes to gain insight into the influences of the key processes underlying nanostructure formation. These processes include (i) adsorption of linker molecules at the nanocrystal surface; (ii) coalescence of molecule-bearing nanocrystals to form dimers, trimers and higher-order n -mer nanostructures; (iii) desorption of linker molecules (possibly leading to n -mer dissociation).

For experiments with durations up to several hours, 3-dimensional random-walk algorithms were developed to model n -mer formation. Values for the nanocrystal diffusivity were estimated using the Stokes-Einstein equation and show good agreement with experimental data^{1,2} even at the nanometre scale. “Coarse-grain” step sizes in the micron range were chosen for nanocrystals executing random walks, i.e., on the order of the mean separations between nanocrystals in solution; with corresponding time steps ~ 10 ms. Similar “fine-grain” algorithms were employed to model collision efficiencies, e.g., the likelihood of two nanocrystals or a nanocrystal and a molecule located within the same micron-scale cell “meeting” during one time step of the coarse-grain model. For the fine-grain simulations, length-scales ~ 20 -40 nm and time-scales ~ 1 -10 μ s were employed.

Figure 2a shows the measured distribution of nanostructures from a typical experiment, acquired following controlled mixing of citrate-stabilised Au nanocrystals (core diameter $d = 20$ nm) with bi-functional linker molecules over a 2 hour period. More than 2500 nanostructures were counted across multiple substrates (error bars show the 95% confidence interval). Figure 2b shows two limiting cases for the random-walk model based on the data shown in Figure 2a. One solution corresponds to a dynamic equilibrium situation, where the n -mer populations rapidly approach limiting values, which are maintained by a balance between nanostructure formation and dissociation. The second solution corresponds to a slower evolution of the n -mer distribution with a correspondingly smaller value for the ratio of the probabilities for dissociation and formation.

As the random-walk method is computationally expensive for modelling experiments over longer time scales (days to weeks), a coupled rate-equation model was also developed, based on approaches used by Venables and co-workers to model island growth at surfaces.³ This approach yields the rates of change of the monomer, dimer and higher order n -mer populations as a function of time. Good agreement with experimental data has been achieved for a time series experiment, where the evolution of the n -mer distribution for a nanocrystal-molecule solution was monitored over 7 days. Linker molecules were added at regular intervals while mixing and small aliquots of the solution were removed and diluted to quantify the

nanostructure distribution using SEM. Interestingly, the rate constants which best describe this week-long experiment are in reasonable agreement with the values extracted for dynamic equilibrium case of the random walk model described above for shorter experimental time scales (hours).

Reconciliation of the random-walk and rate-equation models is currently underway in order to extract the rate constants and corresponding activation energies for nanostructure formation and dissociation. Comparisons are also being undertaken with the results of simulations of the optical properties of monomer and dimer nanostructures since the optical properties of the nanostructure solutions reported here are measured in (almost) real-time, thus providing a potential experimental probe of the n -mer distribution evolution at the time scales at or below 1 second.

References:

- [1] Wuelfing et al., *Anal. Chem.*, **71**, (1999), 4069-4074
- [2] Xu et al., *J. Phys. Chem. C*, **111**, (2007) 32-35
- [3] Venables et al., *Rep. Prog. Phys.*, **47**, (1984), 399-459

Figures:

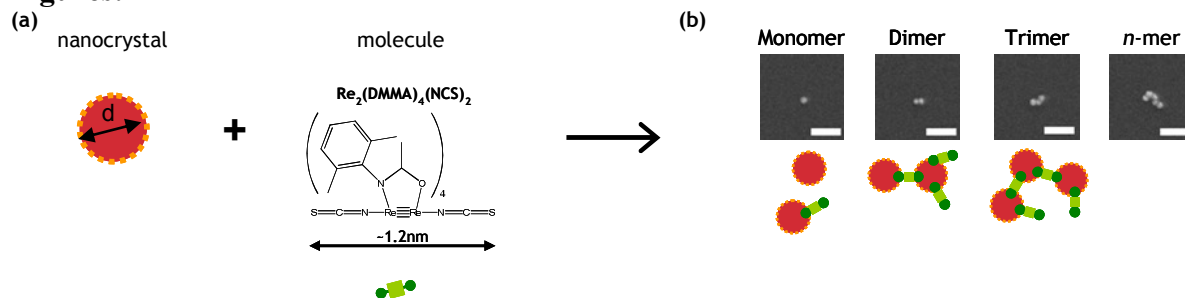


Figure 1 (a) Schematic (not to scale) of nanocrystal-molecule nanostructures formed by mixing citrate-stabilised Au nanocrystals (core diameter $d = 20$ nm) with bi-functional Re linker molecules. (b) SEM images and schematics of nanocrystal-molecule " n -mer" nanostructures: Monomer ($n = 1$), dimer ($n = 2$), trimer ($n = 3$), etc. Scale bars: 100 nm.

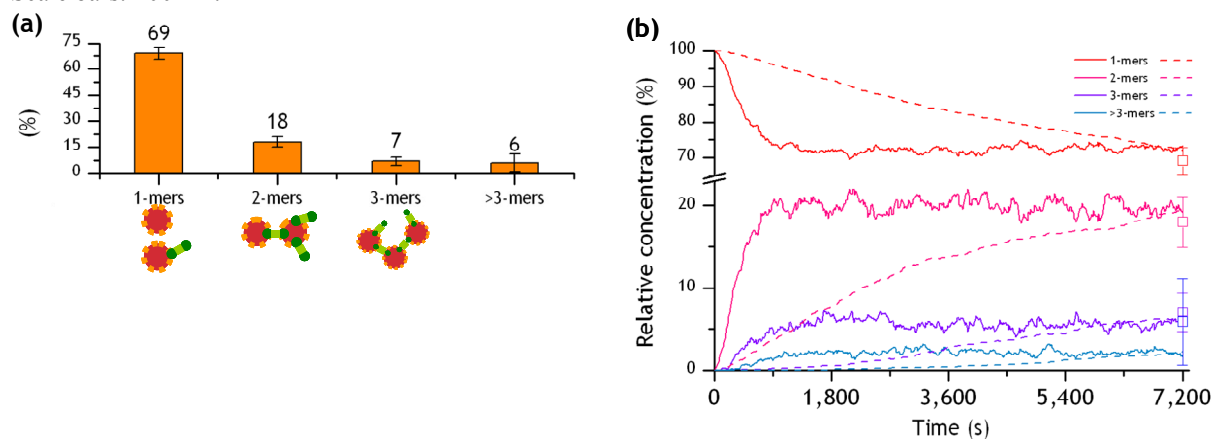


Figure 2 (a) Histogram showing the distribution of n -mer nanostructures extracted from measured SEM data: More than 2200 nanostructures were counted from 272 locations across 21 separate substrates. The error bars show the 95% confidence interval (b) Two limiting cases of the random walk model are shown which agree (after 2 hours) with the data in (a): One corresponds to a dynamic equilibrium (solid curves), where the n -mer populations rapidly approach limiting values, which are maintained by a balance between nanostructure formation and dissociation. The second case corresponds to a slower evolution of the n -mer distribution with a correspondingly smaller ratio of the probabilities for dissociation and formation.

MONTE CARLO MODELLING OF ELECTRON TRANSPORT IN SI QUANTUM-WIRE DOUBLE-GATE MOSFETs IN PRESENCE OF ATOMISTIC IMPURITIES

G. Albareda, X. Saura, X. Oriols, R. Rurali and J. Suñé

Departament d'Enginyeria Electrònica,

Universitat Autònoma de Barcelona, 08193, Bellaterra, SPAIN

Contact E-mail: Guillem.Albareda@uab.es

Silicon nanowire multiple-gate MOSFETs are now-a-days accepted as one of the most promising candidates to achieve with success the next future CMOS technology requirements. In one hand, the addition of multiple-gate structures to the near vicinity of the extremely thin nanowire channels offers an exceptional electrostatic robustness that prevents from the jeopardizing short-channel effects. On the other hand, multiple-gate MOSFETs do not require channel doping to operate, and in this sense, such structures are inherently more resistant to random dopant fluctuation effects than conventional single-gate MOSFETs [1]. Nevertheless, with regard to this second point, even “undoped” channels can contain doping atoms arising from contamination or from Source/Drain implantation processes. Due to the random nature of such processes, the number and position of doping atoms are subject to stochastic variations, and consequently, differences between particular members of a same technology appear [2].

The origin of random doping fluctuations effects is fundamentally electrostatic. In this sense, the importance of properly treating the short-range Coulomb forces is particularly relevant when the channel of nanoscale MOSFETs is reduced to a few nanometres. Although the electron-impurity interaction has been treated more or less accurately in previous works devoted to investigate this topic, electron-electron interactions are usually approximated or simply ignored [3,4]. In the present work we take up again this topic describing the electrostatics by means of a classical many-particle electron transport formalism (Monte Carlo like) that goes beyond the standard “mean field” approximation [5]. In particular, we compute the electron dynamics by solving a different 3D Poisson equation for each particular *i*-electron (with a particular charge density and boundary conditions for each electron) that avoids the consideration of its own charge and considers, without any approximation, not only the electron-impurity interaction, but also the electro-electron correlations.

Here we evaluate the relevance of the random doping fluctuation effects within the main characteristics of a double-gate quantum-wire MOSFET (see fig. 1) by placing single ionized impurities, positive or negative, in three different places along its channel (centred in lateral directions). Fig. 2 shows the mean current through the active region of the nanowire as a function of the applied gate voltage, V_{Gate} , in the saturation region ($V_{\text{Drain}}=0.5\text{V}$). Caused by the potential barrier associated to a negative dopant within the channel and the potential well associated to a positive one, negative impurities present higher threshold voltages than positive ones. It can be also observed that negative ions are more effective in blocking current when they are closer to the source contact (and vice versa for positive impurities). Fig. 3 shows the current density distribution in a particular slice located at the position of the positive/negative impurity (which is situated at the source-channel interface). Notice that while the positive impurity does not cause any relevant deformation on the current density distribution (fig. 3.a), the negative one produces not only a reduction on the maximum value of the current density, but also an important deformation of its spatial distribution, pushing carrier dynamics away its location (fig. 3.b). It is important to remark that, due to lateral confinement, the injection of carriers obeys a sinusoidal spatial distribution centred on “y” and “z” dimensions that causes volume inversion along the channel. Finally, the probability of an electron injected from the source contact to achieve the drain contact (i.e. transmission) is presented in figure 4 as a

function of its injection energy (i.e. the kinetic energy of the electron when it is situated at the source-channel interface) for $V_{Gate}=0$ and $V_{Drain}=0.5V$. In particular, the transmission is computed in presence of a negative impurity at different positions along the channel. Although the transmission is increased as the dopant is moved from source to drain at low energies, this order is lost for higher energies. This interesting effect is a particular characteristic of the many-particle systems, which allow energy interchange between particles as they move along the channel. As the ionized impurity is moved from source to drain, the time elapsed between the injection of an electron at the source and the achievement of the impurity position is increased. Therefore, such an electron will interact more and more with the rest of carriers as the ionized atom is moved toward the drain contact.

References:

[1] J.P. Colinge, Solid State Electron, 48 (2004) 897–905.
 [2] R. Yan et al., Solid State Electron, 52 (2008) 1872–1876.
 [3] R. Rurali et al., Nano Lett., 8 (9) (2008) 2825–2828.
 [4] W.J. Gross, IEEE Trans. Electron Dev., 47 (10) (2000) 1831-1837.
 [5] G. Albareda et al., Phys. Rev. B, 79 (2009) 075315

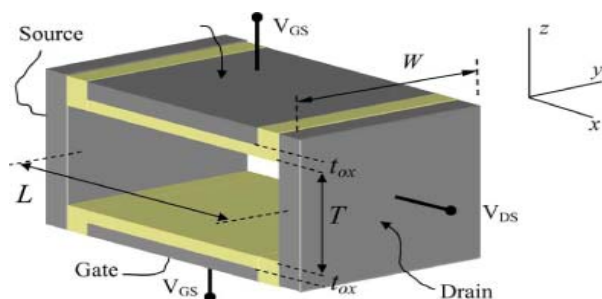


Fig. 1. Schematic representation of the quantum wire double gate FET. Electron transport in the “x” direction (from source to drain) takes place along a Silicon (100) orientation channel, at room temperature. The channel (nanowire) of the FET has lateral dimensions, $W=5nm$ and $T=2nm$, that determine the electron confinement. The minimum energy of the first sub-band for one of the six equivalent ellipsoidal constant energy valleys is $E_{1D}^q = 0.182eV$. Due to the lateral electron confinement, the velocities in the “y” and “z” directions are zero.

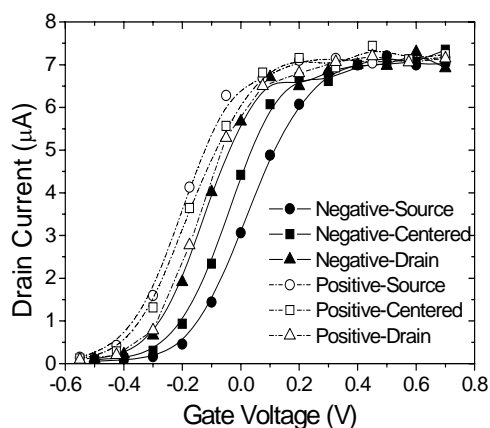


Fig. 2. Average drain current at $V_{Drain}=1V$ as a function of the gate voltage for positive/negative impurities located at different places along the channel.

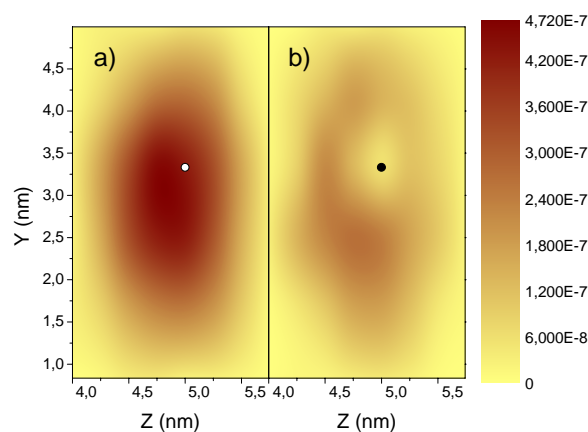


Fig. 3. Current density distribution for a particular slice of the quantum wire situated at the position of a positive, a), or negative, b), impurity situated at the source-channel interface.

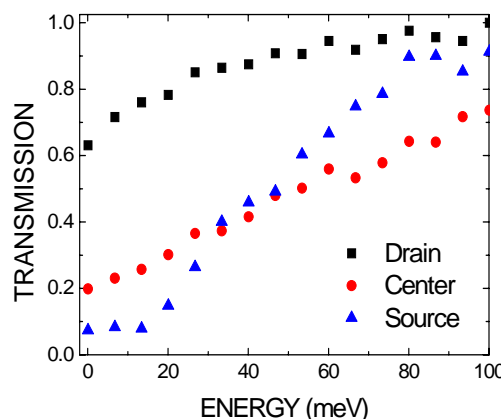


Fig. 4. Transmission as a function of the injection energy for a negative dopant located at different places along the nanowire.

Phosphorus delta-doping and scanning probe nanolithography: a new tool kit for atomically-precise germanium transistors.

G. Scappucci^{1,2}, G. Capellini³, W. C. T. Lee¹, and M. Y. Simmons¹

¹School of Physics, University of New South Wales, Sydney, NSW 2052, Australia.

²Australian Research Council Centre of Excellence for Quantum Computer Technology, University of New South Wales, Sydney, NSW 2052, Australia.

³Dipartimento di Fisica, Università di Roma Tre, Via della Vasca Navale 84, 00146 Roma, Italy.

giordano.scappucci@unsw.edu.au

In the early days of the semiconductor industry the first transistor and integrated circuits were both fabricated in germanium due to its higher electrical performance compared to silicon. Further progress in Ge based transistors was hampered by the lack of a stable oxide that could be employed as a high quality gate dielectric. The recent development on high- κ dielectrics has renewed the interest in Ge as a replacement of Si in the next generation of high mobility nanoscale transistors. However, a further major roadblock has been the difficulty in obtaining reliable doping within the thermal budget allowed by high- κ dielectrics ($T < 400$ °C) due to the enhanced diffusion of n-type dopants in Ge compared with Si [1].

Here we present a low thermal budget technique [schematics in Fig.1(a)] for the fabrication of P delta-doped layers in Ge based upon the adsorption and subsequent incorporation of PH₃ molecules onto a Ge(001) surface, followed by the encapsulation of the P atoms under a MBE-deposited Ge layer [2]. The doping process has been investigated *in-situ* by means of the STM/STS techniques. The structural, compositional and electrical properties of the delta layers have been characterized ex-situ by TEM, SIMS and Hall bars magnetotransport measurements, respectively.

The SIMS ³¹P depth profile [Fig. 1(b)] shows a sharp and isolated peak below the surface with a full width at half maximum ~ 2 nm, smaller than the average ~ 5 nm Bohr radius for P donors in Ge, demonstrating the effectiveness of the doping technique in confining a two-dimensional (2D) sheet of P atoms on the starting Ge surface. Magnetotransport measurements at 4 K are reported in Fig1(c). From the linear slope of the transverse Hall resistance vs. magnetic field we calculate an electrically-active carrier concentration of 7.2×10^{13} cm⁻² at 4.2 K which extrapolates to a 3D bulk concentration of 6.1×10^{20} cm⁻³. This is a record value for n-type doping of Ge, one order of magnitude higher than other electrically active concentration reported previously for P-doped Ge layers. The inverted peak at zero magnetic field in the longitudinal magnetoconductance is due to the weak localization, a clear signature of the 2D nature of transport in these systems, associated with the strong confinement of the carriers in the delta-doped layer. From the weak localization theory for a disordered 2D system of non interacting electrons we estimate a phase coherence length of ~ 96 nm, higher than phase coherence values reported in Si:P δ -layers with comparable carrier densities.[3]

Similarly to what has been recently demonstrated on Si [4], the achievement of phosphorus delta-layers in Ge opens up the possibility of a scanning-probe hydrogen lithography approach to the fabrication of nanoscale planar doped devices in Ge. In particular we intend to combine the P delta-doping and H-lithography techniques to create ultra-sharp n-doping profiles to use as source/drain regions for high-mobility atomically-precise Ge transistors.

To this purpose, we have achieved, by optimizing the H dose and process temperature, an atomically flat, monohydride-saturated Ge(001) surface, as demonstrated by STM/STS characterization. On such surface, by using the STM tip to stimulate the desorption of the hydrogen atoms, we demonstrate controlled nanolithography. We show how using different lithographic parameters we achieve a minimum line width of ~ 2 nm (Fig. 2).[5]

References:

- [1] Y. Kamata, *Materials Today*, **11** (2008) 30.
 [2] G. Scappucci, G. Capellini, W. C. T. Lee, and M. Y. Simmons, *Appl. Phys. Lett.*, **94** (2009) 162106.
 [3] K. E. J. Goh, L. Oberbeck, M. Y. Simmons, A. R. Hamilton, and M. J. Butcher, *Phys. Rev. B*, **73** (2006) 035401.
 [4] M. Y. Simmons, F. J. Ruess, K. E. J. Goh, W. Pok, T. Hallam, M. J. Butcher, T. C. G. Reusch, G. Scappucci, *Int. J. Nanotechnol.*, **5** (2008) 352.
 [5] G. Scappucci, G. Capellini, W. C. T. Lee, and M. Y. Simmons, in preparation (2009).

Figures:

Fig. 1: (a) Schematic diagrams of the fabrication process for a Ge:P delta-doped layer; (b) Phosphorus depth profile determined by SIMS; (c) Magnetotransport measurements at 4K.

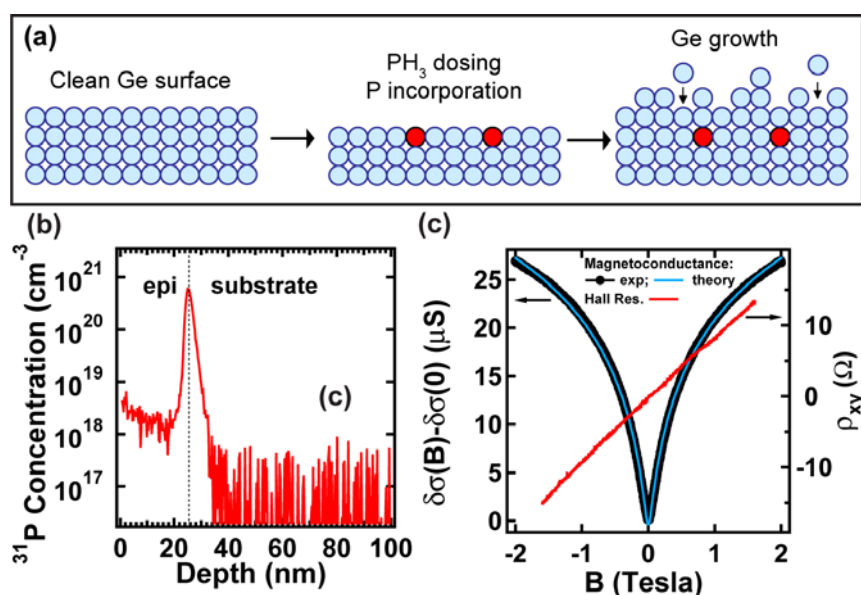
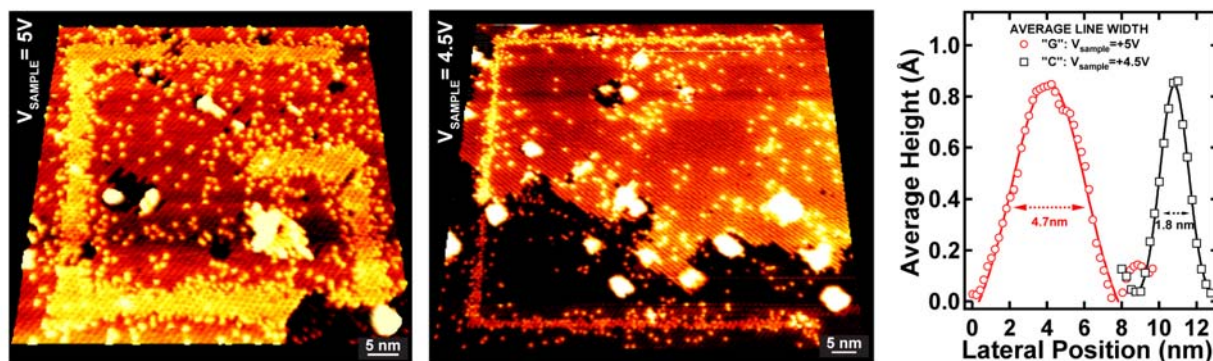


Fig. 2: Scanning probe nanolithography on H-terminated Ge(001). Decreasing the sample to STM tip bias, the average line width of the letters “G” and “C” is reduced from ~ 5 nm to ~ 2 nm respectively.



Shedding light on the crystallographic etching of graphene at the atomic scale

Franziska Schäßel¹, Jamie H. Warner², Alicja Bachmatiuk¹, Bernd Rellinghaus¹, Bernd Büchner¹, Ludwig Schultz¹, Mark H. Rümmeli¹

¹IFW Dresden, P. O. Box 270116, D-01171 Dresden, Germany

*²Department of Materials, University of Oxford, Parks Rd, Oxford, OX1 3PH, United Kingdom
f.schaeffel@ifw-dresden.de*

Owing to the unique electronic properties of graphene, as for example the high intrinsic carrier mobility, the interest in this novel sp² carbon material has rapidly expanded since it was first isolated [1]. However the gapless band structure of truly two-dimensional graphene makes it unsuitable for direct use in graphene-based field effect transistors. Thus, the integration of graphene into semiconducting nanoelectronics necessitates the fabrication of graphene nanoribbons (GNRs) where the lateral quantum confinement opens a band gap. The fabrication of GNRs with a well-defined and regular edge structure without defects is a prerequisite to reduce edge effects [2, 3]. Conventional methods for GNR fabrication, e.g. electron beam lithography, produce GNRs with significant edge roughness. GNR with desired shapes may be produced via chemical routes [4, 5] or scanning tunnelling microscope lithography [3].

Recent research into the channelling of few layer graphene via catalytic hydrogenation using metallic catalyst nanoparticles shows that this technique is potentially a key engineering route for the fabrication of GNRs with atomic precision [6, 7]. In this technique metal catalyst particles are deposited onto a graphite or graphene sheet and exposed to hydrogen at elevated temperatures. The catalyst particles help to dissociate hydrogen, which then reacts with carbon from a graphite step edge forming methane. Thus the catalyst particle takes up carbon from a graphite step and an etch channel is produced.

We have studied the catalytic hydrogenation utilizing gas phase prepared cobalt nanoparticles as catalyst for carbon gasification and etch channel formation in hydrogen atmosphere. The onset temperature for cobalt catalyzed carbon gasification in hydrogen atmosphere was found to be 600°C, i.e. much lower than that reported for iron (900°C, [6]) and nickel (700°C, [7]). Aberration corrected high resolution transmission electron microscopy (HRTEM) studies were performed to directly determine the etch direction(s) and to investigate the catalyst particles before and after the hydrogenation reaction. The development of aberration corrected microscopes enables researchers to investigate samples that are sensitive to high energy electron radiation damage, so called “knock-on damage”, at lower accelerating voltages without the loss of resolution. In our studies the HRTEM investigations were performed at 80 kV accelerating voltage.

It is known that the removal of one carbon atom from an armchair edge costs less energy than from a zigzag edge during carbon gasification reactions. Thus zigzag channels, i.e. channels along the $\langle 11\bar{2}0 \rangle$ directions, are preferred and also experimentally observed in most cases after the catalytic etching, since an armchair site will be etched away more easily [7, 8]. Typical bending angles of 60° and 120° are expected. 30° bends are observed less frequently, since this would involve a change from a $\langle 11\bar{2}0 \rangle$ to a $\langle 10\bar{1}0 \rangle$ direction or vice versa. However, in our experiments etching along armchair edges is observed more frequently for small nanoparticles. An example is given in Figure 1 showing a HRTEM micrograph of two etch tracks formed by Co nanoparticles at 600°C. Fourier enhancement of the micrograph allows one to identify the

graphene structure and determine the etch direction to be along armchair edges (Figs. 1b and 1c). Figure 1d shows a magnified image of the marked area in Figure 1b to illustrate the graphite structure. The graphite unit cell (green rhombus) and the main crystallographic directions of graphite, i.e. zigzag and armchair edges, are highlighted in yellow and orange, respectively. Recently a change of the “preferred” etching direction was suggested to occur for very small nickel particles (e.g. below 10 nm) [7]. Therefore tailoring of graphene nanostructures, e.g. GNRs, with well-defined armchair edges via the adjustment of nanoparticle size in catalytic hydrogenation may indeed be possible.

References:

- [1] K. S. Novoselov, A. K. Geim, S. V. Morozov, D. Jiang, Y. Zhang, S. V. Dubonos, I. V. Grigorieva, A. A. Firsov, *Science* **306** (2004) 666.
- [2] Y. Kobayashi, K.-I. Fukui, T. Enoki, K. Kusakabe, Y. Kaburagi, *Phys. Rev. B* **71** (2005) 193406.
- [3] L. Tapasztó, G. Dobrik, P. Lampin, L. P. Biró, *Nature Nanotech.* **3** (2008) 397.
- [4] A. Yu, P. Ramesh, M. E. Itkis, E. Bekyarova, R. C. Haddon, *J. Phys. Chem. C* **111** (2007) 7565.
- [5] X. Li, X. Wang, L. Zhang, S. Lee, H. Dai, *Science* **319** (2008) 1229.
- [6] S. S. Datta, D. R. Strachan, S. M. Kharnis, A. T. C. Johnson, *Nano Lett.* **8** (2008) 1912.
- [7] L. Ci, Z. Xu, L. Wang, W. Gao, F. Ding, K. F. Kelly, B. I. Yacobson, P. M. Ajayan, *Nano Res.* **1** (2008) 116.
- [8] A. Tomita, Y. Tamai, *J. Phys. Chem.* **78** (1974) 2254.

Figures:

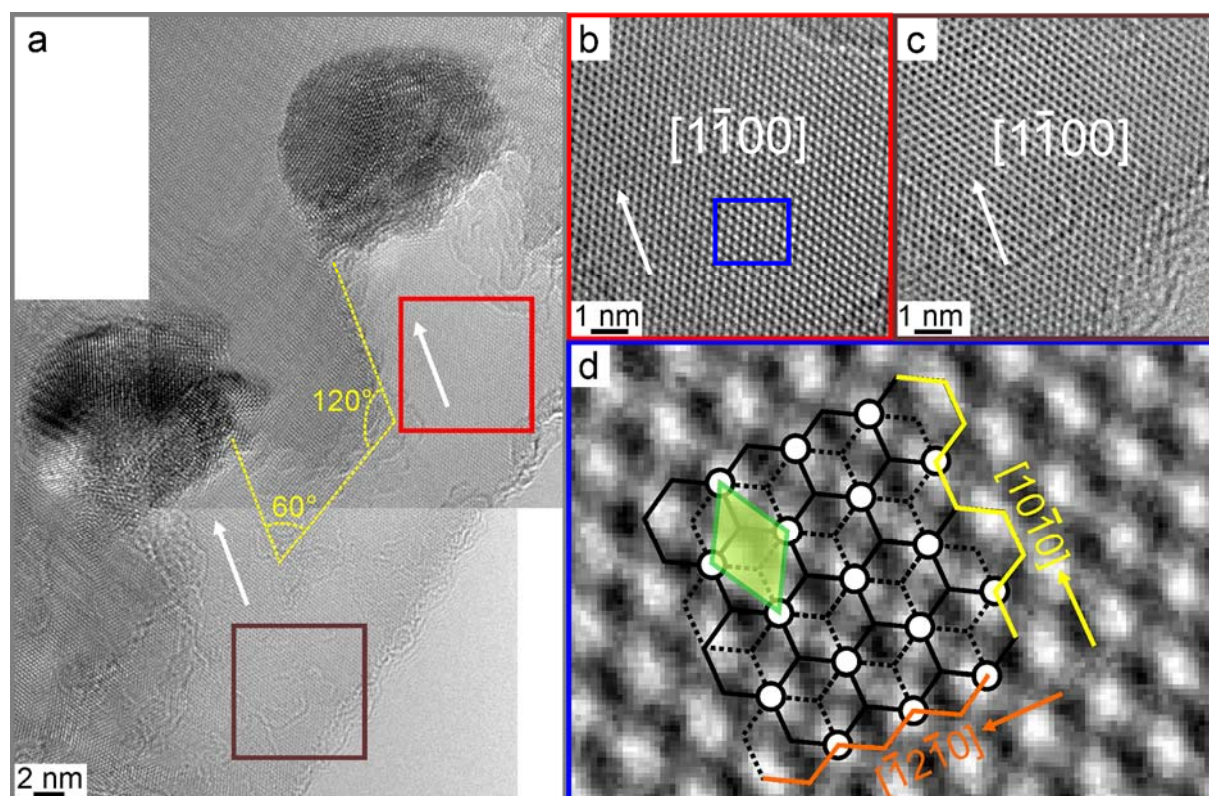


Figure 1: a) HRTEM micrograph of Co nanoparticles etching graphene/graphite. b, c) Fourier enhanced micrographs of the marked areas in a) revealing the graphite structure and etching direction. d) Magnified image of the marked area in b) and illustration of the graphite structure including unit cell (green rhombus) and the main crystallographic directions.

Tuning of metallic vs semiconducting selectivity in the reaction of diazonium with SWNT to enhance CNTFETs performances

*Grégory Schmidt, Salomé Gallon, Stéphane Esnouf,
Jean-Philippe Bourgoin and Pascale Chenevier*

*Service de Physique de l'Etat Condensé (CNRS URA 2464)
CEA Institute Radiation Matter of Saclay
91191 Gif sur Yvette (France)
gregory.schmidt@cea.fr*

Nanoelectronics applications of single wall carbon nanotubes are strongly impeded by the fact that synthesized carbon nanotubes (NT) have heterogeneous electronic properties (metallic and semiconducting). It is possible to separate metallic and semiconducting (m- and sc-) NT by a number of methods among which chemical functionalization with diazoniums. Despite the importance of the diazonium coupling route, the mechanism is still mostly unknown and has been the subject of very few studies [1,2]. Indeed, diazonium reactivity has proved rich and complex, which renders the mechanism elucidation difficult. Nevertheless, only a proper mechanistic understanding of the reaction can bring tools to fine tune the reaction, hence allowing the necessary fine balance between functionalization yield and preserved conductivity [3], or an increase in m- vs sc-NT selectivity up to high enough levels for separation purposes.

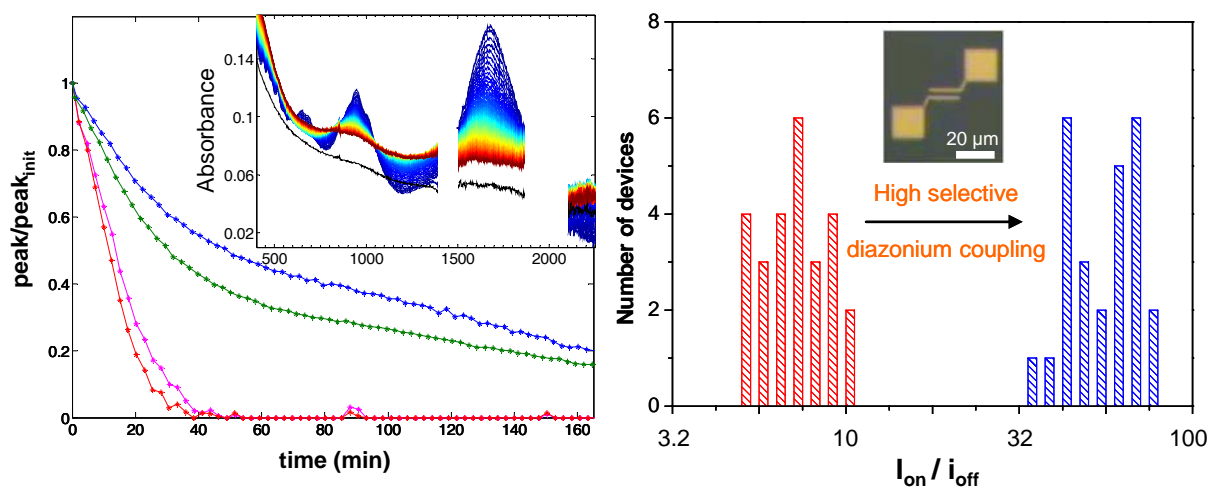
We investigated the mechanism of the reaction [4] using kinetic follow up by spectroscopy and electron spin resonance (ESR). A free radical chain reaction is evidenced without ambiguity. Metallic NT are shown to play an unexpected catalytic role. The step determining the selectivity toward metallic NT is identified by a Hammett correlation. A mechanistic model is proposed that predicts reactivity and selectivity as a function of diazonium electrophilicity and metallic to semiconducting CNT ratio.

Thanks to the detailed understanding of the mechanism, we propose a method to significantly increase the selectivity of diazonium coupling to metallic NT. We increase the selectivity from **4** with the best electrophilic diazonium to **13** with our method [5]. This improved method impacts dramatically the electrical performances of carbon nanotube field effect transistors (CNTFETs). Indeed, the fine tuning of the reaction parameters allows achieving NT transistors with preserved high on state current and high current modulation even for reduced channel lengths.

References:

- [1] C. A. Dyke, M. P. Stewart, F. Maya, J. M. Tour, *Synlett*. **2004**, 155.
- [2] M. L. Usrey, E. S. Lippmann, M. S. Strano, *J. Am. Chem. Soc.* **2005**, 127, 16129.
- [3] L. An, Q. A. Fu, C. G. Lu, J. Liu, *J. Am. Chem. Soc.* **2004**, 126, 10520.
- [4] G. Schmidt, P. Chenevier, et al. *Chemistry A Eur. J.* **2009**, 15, 2101-2110.
- [5] G. Schmidt, P. Chenevier, French Patent n°0950757, **2009**.

Figures:



Kinetics (left) of absorption peak decrease (m-NT at 688nm, red, and sc-NT at 940nm, blue) for the reaction of SWNT with Bromo-benzenediazonium (Br-BDT) in aqueous solution. The inset (left) shows absorption peak decrease during the reaction performed with intervals of 1 min. Compared the statistic of modulation on several devices for unreacted and high selective functionalized NT (right).

**PHOTOSENSITIZATION OF CARBON NANOTUBES USING PHOTOSYNTHETIC
PROTEINS TO OPTOELECTRONIC APPLICATIONS**

*Grégory Schmidt, Bernard Lagoutte, Winfried Leibl,
Jean-Philippe Bourgoïn and Pascale Chenevier*

*Service de Physique de l'Etat Condensé (CNRS URA 2464)
CEA Institute Radiation Matter of Saclay
91191 Gif sur Yvette (France)
gregory.schmidt@cea.fr*

To face up the challenge of climate change and environmental issues, the applied renewable energy research field is rapidly expanding. Hence, during the last ten years, the organic photovoltaic cells performances have made significant progresses. The current limits of these systems are mainly due to the low quantum yield of dyes and the speed of charge transport towards electrodes. To raise the power conversion yield of organic photocells to the level of silicon technology, an innovative bio-hybrid using carbon nanotubes and a photosynthetic protein as “super dye” has been assessed. Indeed this protein optimized by nature during millions of years has exceptional optical properties (quantum yield of 1) that may prove to enhance dramatically performances of optoelectronic and photovoltaic devices. To validate the potential of this protein, we perform a carbon nanotubes field-effect transistor optically controlled by photosynthetic proteins.

The NanoSost project: towards to a sustainable, responsible and safe nanotechnology

*Sempere, J.¹, Nomen R.¹, Serra, E.¹, Grillo M.¹, López de Ipiña, J.², Vaquero C.²,
Balas F.³, Arruebo M.³ and Santamaría J.³*

(1) IQS-Universitat Ramon Llull, Via Augusta, 390, 08017 Barcelona, Spain

(2) LEIA, Centro de Desarrollo Tecnológico, Leonardo Da Vinci, 11, 01510 Miñano, Spain

*(3) Universidad de Zaragoza – Instituto de Nanociencia de Aragón (INA), Pedro Cerbuna 12,
50009 Zaragoza, Spain*

julia.sempere@iqs.url.edu

Nanotechnology is in total expansion, and every week hundreds of new nanostructured materials are prepared. Most of them are nonexistent in the nature. It is usually not known which can be the effects of those new materials on the human health or the environment. In the same way, not very often legal regulations or norms exist on the controls that must be applied on technological processes in order to allow the use of nanomaterials in safe form. It is urgent to acquire knowledge in the indicated areas.

The great hopes put by the scientific community and the industry in the use of nanotechnology are beginning to take shape in new materials of innovating and, in many cases, surprising characteristics. It is enough with watching the public funds devoted to R&D in the nanotechnology field which are investing the different EU states and the European Commission to understand the relevance that they hope that nanotechnology products will acquire. Spain is not an exception, having created diverse options of financing of projects in the area of the nanotechnology defined in its national plan of investigation. Nanotechnology is no more a scientific promise to become a mercantile reality. In 2007 the market of nanotechnology products was of 135,000 million of dollars (*Lux Research*). The same source estimates a 2014-15 market above the trillion (10^{12}) of dollars, and that the nanotechnology products will represent the 15% of the manufacturing industry with sales up to 10 times greater than biotechnological products. The *nano* number of products grows to a vertiginous rate. If in November of 2006 about 300 products *nano* were available in the market (Maynard, *Nature*, 444, 2006), that number practically duplicated only 8 months later (*estimation of the Woodrow Wilson International Center*).

It is necessary to create the knowledge bases for the development of new technologies that allow that expected sustainable development of nanotechnology, guarantying new clean and safe productive processes, preserving the occupational health and safety and the health of consumers and environment. This constitutes an unavoidable requirement to assure that the immense effort in R&D that is being carried out not sees frustrated by unknown emergent or little valued risks.

The **NanoSost** project persecutes as general objective creating the knowledge and establishing the scientific bases necessary to guarantee as possible the safe use of nanoparticles (metallic, ceramics, polymeric, etc.) and nanostructured materials in general, and its behaviour both in isolated form or as ingredients in the production of end goods. The whole life cycle of the material from its production until its elimination is taken into account with the purpose of favouring a sustainable industrial development corresponding to the social expectations and providing guarantees to the health and safety of workers and consumers.

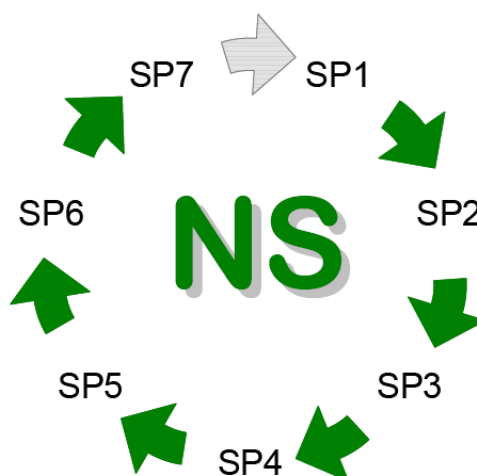
NanoSost is organized in seven subprojects oriented to the next objectives:

1. (*Standards*) Preparing, selecting and characterising references and standards of different engineered nanoparticles, measuring them under conditions which mimic those of the industrial processes.
2. (*Chemical Risk*) Adapting the existing or developing new measurement techniques for the determination of the chemical safety of nanomaterials and the materials including them.
3. (*Biological Risk*) Using techniques, fundamentally *in vitro*, for the test of effects of nanoparticles on people and the environment.
4. (*Environmental Measurement*) Preparing methods for the evaluation of the risk, including suitable technologies of simulation for the design of systems of prevention and protection for the manipulation of nanoparticles and establishing their dispersion in the working place and the environment. With preference, the work will be oriented to measurement techniques that can be applied in movable equipment.
5. (*Risk Control*) Development of advanced techniques of measurement allowing the design of systems of protection, both collective and individual.
6. (*Barrier Materials*) Preparing new barrier materials and evaluating the effectiveness of existing materials to guarantee the prevention and protection against hazards produced by nanomaterials in all the stages of their processing.
7. (*Risk management*) To establish what types of tests and which are the techniques of measurement more adapted to audit and certificate the safety of manipulation, use and elimination of nanomaterials and of compounds containing them.

The **NanoSost** consortium is formed by 21 Spanish organisations drawn from universities, technological centres, and industrial companies.

The **NanoSost** project (PSE-420000-2008-3) is being funded by the Spanish Ministry of Science and Innovation.

Figures:



The study of self-sensing semiconducting nanowire based electromechanical resonators

Shamashis Sengupta^[1], Hari S. Solanki^[1], Sajal Dhara^[1], Vibhor Singh^[1], Rohan Dhal^[1], Jeevak Parpia^[2], Arnab Bhattacharya^[1], Mandar. M. Deshmukh^[1]

1 Dept. of Condensed Matter Physics and Materials Science, Tata Institute of Fundamental Research, Homi Bhabha Road, Mumbai 400 005, India

2 LASSP, Cornell University, Ithaca NY 14853

shamashis@tifr.res.in

Introduction: Nanoelectromechanical (NEMS) resonators have generated sufficient interest and are being used extensively to study small displacements, mass sensing, spin-torque effect, charge sensing and Casimir force. We present^[1] the study of electromechanical resonators made from nanowires of semiconducting material InAs using electrostatic actuation.

Device fabrication: The InAs nanowires have been prepared^[2] by metal organic vapor phase epitaxy (MOVPE). The devices are fabricated by suspending InAs nanowires above a Si wafer coated with 300 nm of SiO₂ using electron beam lithography. In a typical device, the gap between the nanowire and the substrate is about 200 nm, and the nanowires are clamped at both ends by Cr/Au electrodes (see Fig. 1(a). for a typical device of length 2.9 microns and diameter ~ 100 nm).

Measurement technique: The Si substrate behaves like a back gate when a bias voltage is applied between this and the nanowire. The system then acts like a capacitor and consequently, charges are induced on the nanowire. A radio frequency signal V_g^ω at frequency ω and DC voltage V_g^{DC} are simultaneously applied to the back gate using a bias-tee. V_g^{DC} (in the experiments ranging from -50V to +50V) determines the overall tension in the wire. Due to the application of V_g^ω (amplitude~100mV), the nanowire feels a driving force at the frequency ω to which it responds. RF voltage $V_{SD}^{\omega+\Delta\omega}$ is applied between the source and drain at a frequency $(\omega+\Delta\omega)$ slightly shifted from the gate excitation. Using a lock-in, the current through the device (also called the mixing current, denoted by $I^{\Delta\omega}$) at the difference frequency $\Delta\omega$ is monitored. Due to the oscillatory motion of the nanowire, its capacitance is also modulated at the same frequency and this shows up in the mixing current^[3].

$$I^{\Delta\omega} = \frac{1}{2} \frac{dG}{dq} \left(\frac{dC_g}{dz} z(\omega) V_g^{DC} + C_g V_g^\omega \right) V_{SD}^{\omega+\Delta\omega}$$

where G is the conductance of the nanowire, q is the charge induced by the gate, C_g is the gate capacitance, $z(\omega)$ is the amplitude at drive frequency ω and z -axis is perpendicular to the substrate. At resonance, the mixing current shows a sharp change (a peak or a dip) against a slowly changing background.

Observations: Fig.1(b) shows the colourscale plot of the mixing current as the gate voltage and driving frequency are varied. (This is room temperature data). We see a non-monotonic W-shaped dispersion of resonant frequency as a function of V_g^{DC} . The system is effectively like a harmonic oscillator, and the spatially

varying electric field leads to a softening of the spring constant for lower values of V_g^{DC} , thereby causing a negative dispersion. At higher V_g^{DC} , the increase in tension due to applied V_g^{DC} dominates and the behaviour switches to positive dispersion.

We have observed other mechanical modes near the fundamental as well as the presence of avoided level crossings. These arise from motion in the transverse direction y which is perpendicular to z . Due to slight asymmetry in the physical structure of the nanowire, the two modes of oscillation are coupled. The asymmetry in the amplitudes of the two modes in the mixing current data is also explained by this model.

By driving the oscillator at higher amplitude gate excitations, we have observed the hysteretic response which is characteristic of non-linear oscillators.

A few measurements have recently been conducted on these resonators at lower temperatures, in the range of 150-300K. It has been observed that the resonant frequency increases with a decrease in temperature. Further experiments will be conducted in this direction in the near future.

References

[1] H. Solanki et al, *Semiconducting nanowire FET based electromechanical resonator*, submitted (2009)

[2] S. Dhara et al, *Phys. Rev. B* 79 (2009), 121311 (R)

[3] V. Sazonova et al, *Nature*, 431 (2004), 284

Figures

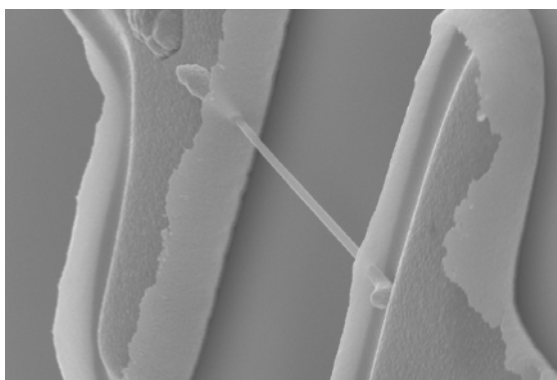


Fig.1(a)

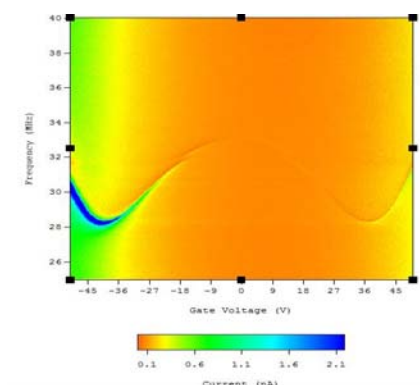


Fig.1(b)

Figure 1. (a) SEM image of a suspended nanowire of length 2.9 microns. (b) Colourscale plot of mixing current as a function of frequency and gate voltage.

CHEMICAL DESIGN FOR THE TAILORED PRODUCTION OF METAL-DOPED NANOSTRUCTURED CARBON FOAM BY LASER ABLATION

A. Seral-Ascaso,¹ E. Muñoz,^{2,} M. L. Ruiz-González,³ M. L. Sanjuán,¹ J. M. González-Calbet,³ M. Laguna¹, and G. F. de la Fuente¹*

¹ *Instituto de Ciencia de Materiales de Aragón (Universidad de Zaragoza-CSIC), Zaragoza, Spain.*

² *Instituto de Carboquímica (CSIC), Miguel Luesma Castán 4, 50018 Zaragoza, Spain*

³ *Departamento de Química Inorgánica I, Facultad de Ciencias Químicas, Universidad Complutense, 28040 Madrid, Spain.*

edgar@icb.csic.es

Carbon nanostructured materials such as nanofoams [1], single-walled nanotubes [2,3], and nanohorns [3] can be efficiently produced by laser ablation of carbon-containing targets. Relevant laser parameters such as wavelength, pulse repetition rate, laser fluence (pulsed- or cw mode) or irradiance, as well as other experimental conditions (mainly atmosphere composition and pressure, target composition, and external or laser-generated heating) strongly affect the recombination of the evaporated species and, therefore, the nature and properties of the produced materials [4,5].

The present work thus pretends to illustrate the potential of using selected organometallic precursors for the tailored production of metal-doped nanostructured carbon foams. Laser ablation of the employed organometallic precursors leads to the formation of soot exhibiting a spongy texture. High-resolution transmission electron microscopy studies reveal that these materials consist of metal nanoparticles embedded in carbon matrices comprising both amorphous carbon and graphitic nanostructures. The results reported here suggest that the nature and properties of the produced materials can be tailored at the molecular level by conveniently choosing the metals and ligands of the ablated targets. A new family of carbon nanostructured materials can be thus envisioned by employing the simple, versatile laser ablation technique described in this work [6].

This work has been supported by the regional Government of Aragón (Spain, Project PM028/2007) and the Spanish Government (CEN-20072014).

References:

- [1] A.V. Rode, S.T. Hyde, E.G. Gamaly, R.G. Elliman, D.R. McKenzie, S. Bulcock, *Appl. Phys. A*, **69** (1999) S755.
- [2] W.K. Maser, E. Muñoz, A.M. Benito, M.T. Martínez, G.F. de la Fuente, Y. Maniette, E. Anglaret, J.L. Sauvajol, *Chem. Phys. Lett.*, **292** (1998) 587.
- [3] A.A. Puzosky, D.J. Styers-Barnett, C.M. Rouleau, H. Hu, B. Zhao, I.N. Ivanov, D.B. Geohegan, *Appl. Phys. A*, **93** (2008) 849.
- [4] E. Muñoz, W.K. Maser, A.M. Benito, M.T. Martínez, G.F. de la Fuente, A. Righi, J.L. Sauvajol, E. Anglaret, Y. Maniette, *Appl. Phys. A*, **70** (2000) 145.
- [5] E.G. Gamaly, A.V. Rode, W.K. Maser, E. Muñoz, A.M. Benito, M.T. Martínez, G.F. de la Fuente, *Appl. Phys. A*, **70** (2000) 161.
- [6] E. Muñoz, M. de Val, M.L. Ruiz-González, C. López-Gascón, M.L. Sanjuán, M.T. Martínez, J.M. González-Calbet, G.F. de la Fuente, M. Laguna, *Chem. Phys. Lett.*, **420** (2006) 86.

INFLUENCE OF A MAGNETIC FIELD ON PROPERTIES TUNNELING SUPERCONDUCTIVITY WITH ANHARMONIC DEPENDENCE OF A CURRENT - PHASE

Sergeyev D.M.

*Military Institute of Air Defense Forces, avenue Moldagulova 16, Aktobe, Kazakhstan
serdau@rambler.ru*

Recently tunneling superconductivity Josephson of a type of steel by one of perspective materials nanoelectronics. Nowadays attracts attention creation of the quantum computer, which basic is quantum bits - "q-bit", representing two-level quantum systems. A fundamental problem on ways of creation of the quantum computer is the realization q-bit with the large time decohere. The most perspective method of realization q-bit are - solid-state Josephson q-bit [1,2]. A not soluble problem Josephson q-bit is the small time decohere. The creations "passive" on an external electromagnetic field solid-state q-bit are necessary for "improvement" of time decohere and new materials and methods of their realization.

One of the materials for realization solid-state q-bit should be superconducting nanosystems on Josephson junction (JJ) with anharmonic by current - phase dependence [3, 4]. The deviation (rejection) of meanings (importance) of a ratio a current - phase is observed in JJ at reduction of thickness antiferromagnetic of a layer [5]. The sine not wave current - phase ratio is inherent and for JJ on the basic of high-temperature superconductors (HTSC) in metallic oxide films HTSC $\text{YBa}_2\text{Cu}_3\text{O}_7$. Anharmonicity parities (ratio) the current - phase of different Josephson's structures has a different nature and character [6]. In work [7] anharmonic character superconducting current is explained by introduction of own inductance JJ:

$$j(\varphi) = \sin(\varphi - l j(\varphi)), \quad (2)$$

where $l = 2\pi\hat{O}/\hat{O}_0 = 2\pi LI_c/\hat{O}_0$. The small meaning (importance) l enables approximate the equation (2) (fig. 1 a):

$$j(\varphi) = \sin \varphi - l \sin(2\varphi)/2. \quad (3)$$

From the analysis of expressions (1), (2) deviations of a current-phase ratio from the sine wave forms are described by expression:

$$j(\varphi) = \sin \varphi - \frac{1}{k} \sin(k\varphi), \quad (4)$$

where $k > 1$ – factor (degree) anharmonicity of current-phase dependence JJ also is directly proportional $k \propto l$. For different whole meanings $k=2,3,4,5$ dependence of a ratio the current - phase is given in figure 1.

Dependence of the maximal superconducting current on a magnetic field in JJ with anharmonic by current-phase dependence:

$$I_{\max} = I_c \left| \frac{\sin(\pi\hat{O}/\hat{O}_0)}{\pi\hat{O}/\hat{O}_0} - \frac{1}{2k} \frac{\sin(k\pi\hat{O}/\hat{O}_0)}{\pi\hat{O}/\hat{O}_0} \right|. \quad (6)$$

For meanings $k = 2, 3, 4, 5$ the dependence of the maximal superconducting current on a magnetic field is given in figure 2. From a fig. 2 it is visible, that dependence feature of a superconducting current from a magnetic flow in «anharmonic» JJ, as against «harmonic», is formations of two maxima of a current, and also $\hat{O}/\hat{O}_0 = 0$ at with increase of factor anharmonicity aspiration of meanings of a supercurrent to zero $I_{\max} \Rightarrow 0$.

In such Josephson's nanosystems the microwhirlwinds superconducting current connected by heterogeneity can be formed. Probably, one of the reasons of occurrence of heterogeneity is varying anharmonic weak links of a ratio the current - phase JJ.

In «anharmonic» JJ it is possible to operate the maximal meaning (importance) of a superconducting current under influence of a magnetic flow changing factor anharmonicity of a

current-phase ratio. Thus, influence of a magnetic field on weak links Josephson type as with anharmonic by current-phase dependence essentially differs from «usual» JJ: formations of two maxima of a current instead of one; at aspiration of meanings $\hat{O}/\hat{O}_0 = 0$ of a superconducting current to zero, which amplifies with increase of factor anharmonicity; increase of the maximal meaning of a current with increase of factor anharmonicity. Not trivial response on influence of a magnetic field, than «usual» JJ gives an opportunity to receive a new magnetic nanomaterials on JJ with anharmonic by a ratio a current - phase.

References:

- [1] Pashkin U.A., Astafiev O.V., Yamamoto T., Nakamura Y., Tsai J.S. Progress in Physical Science (Physics Uspekhi) Vol. 174, №9 (2004) p. 1011-1012.
 [2] Mooij J. E., Orlando T. P., Levitov L., Tian L., Caspar H. van der Wal, Lloyd S. Science 285 (1999) p. 1036.
 [3] Sergeev D.M. The thesis of the reports IX of a seminar on problems of physics of the condensed state of matter, Ekaterinburg (2008) p. 166–167.
 [4] Sergeev D.M. The collection of works of the international conference «The young scientists - science, technologies and vocational training», Moscow (2008) p. 110–113.
 [5] Askerzade I.N. Pis'ma v Zhurnal Tekhnicheskoi Fiziki. Vol. 33, №17. (2007) p. 10-15.
 [6] Sergeev D.M., Shunkeyev K.Sh. The collection of works of the international conference «Fundamental problems of high-temperature superconductivity FPS'08», Zvenigorod (2008) p. 344.
 [7] Askerzade I.N. Journal of Technical Physics. Vol. 73, №11 (2003) p. 140-142.

Figures:

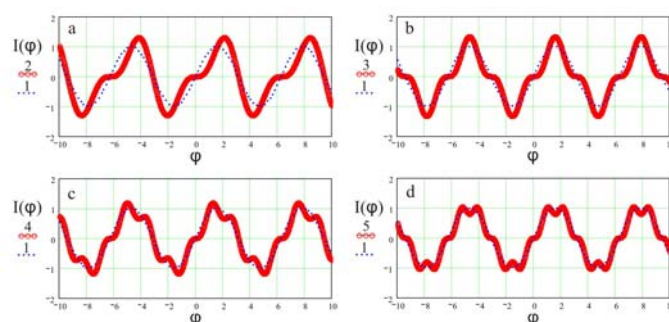


Figure 1 - Dependence superconducting current from a phase

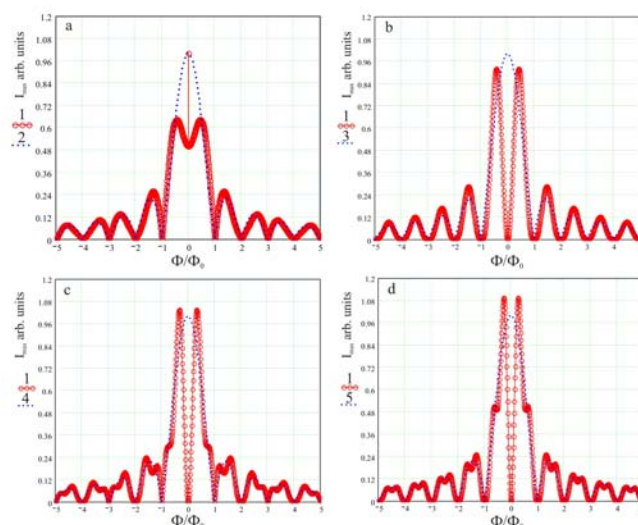


Figure 2 - Dependence maximal superconducting current from a magnetic field

ENGINEERING SPIN STRUCTURES ON THE ATOMIC SCALE

D. Serrate^{1,2}, Y. Yoshida², P. Ferriani², A. Kubetzka², S.-W. Hla³, M. Menzel², K. von Bergmann², S. Heinze^{2,4} and R. Wiesendanger²

¹*Institute of Materials Science of Aragon, CSIC-Univ. Zaragoza, Pedro Cerbuna 12, 50009 Spain*

²*Institute of Applied Physics, Hamburg Universität, Jungiusstrasse 11, 20359 Germany*

³*Department of Physics & Astronomy, Ohio University, Athens, Ohio, USA*

⁴*Institute of Theoretical Physics and Astrophysics, Christian-Albrechts-Universität zu Kiel, Leibnizstraße 15, 24098 Kiel, Germany*

serrate@unizar.es

In practice, the smallest entity which can portray a well defined magnetic moment over time is a single magnetic atom, which can be viewed as the building block of functional magnetic nanostructures. Apart from the profound implications in magnetic data storage, the structural design and the control of the magnetic properties down to the atomic level is a prerequisite to address the new Physics emerging on the nanoscale. Spin-polarized scanning tunneling microscopy (SP-STM) has proven a powerful tool to perform real space magnetic imaging with atomic resolution [1,2]. On the other hand, STM facilities have the unique ability to precisely manipulate adatoms and molecules on surfaces [3,4]. The combination of both techniques would be the paradigm for experiments on artificially built spin structures. In this work we perform for the first time simultaneous atomic manipulation and SP-STM to achieve absolute control of the magnetization direction of transition metal atoms on a well established reference magnetic template. We used an iron coated tungsten tip to precisely move individual magnetic atoms on a magnetic substrate. Direct exchange interaction couples ferromagnetically the atom magnetization to the substrate nearest neighbors. Thus, positioning the atoms on template sites having different local spin direction allows setting the adatom magnetization by means of lateral manipulation. SP-STM performed with the same tip on several atomically engineered magnetic nanostructures reveals clear spin contrast, which can be understood on the basis of density functional theory within the generalized gradient approximation. The magnetic contrast is explained in terms of spin-resolved imaging of atomic orbitals, and it can be used to univocally determine an arbitrary atom magnetization direction. This work opens up an appealing research opportunity on the field of magnetic interactions in atomically tailored nanostructures.

References:

- [1] F. Meier, L. Zhou, J. Wiebe, and R. Wiesendanger, *Science*, **320**, (2008) 32
- [2] A. Kubetzka, P. Ferriani, M. Bode, S. Heinze, G. Bihlmayer, K. von Bergmann, O. Pietzsch, S. Blügel, and R. Wiesendanger, *Phys. Rev. Lett.*, **94** (2005) 087204
- [3] D.M. Eigler and E.K. Schweizer, *Nature*, **344** (1990) 524.
- [4] S.-W. Hla, L. Bartels, G. Meyer, and K.H. Rieder, *Phys. Rev. Lett.*, **85** (2000) 2777

Design of a Taguchi statistical experiment for Optimization and in Vitro Evaluation of Nano-Hydrogel prepared by ionotropic gelation method

M. A. Shahbazi¹, M. Hamidi^{1,2}

1- Department of pharmaceutics, Faculty of pharmacy, Shiraz University of medical sciences, Shiraz, P.O.BOX 71345-1583, Iran

2- Department of pharmaceutics, Faculty of pharmacy, Zanjan University of medical sciences, Zanjan, Iran

Introduction

Preparation of nanoparticle is a well-known method used to modify/control the drug release. In this study, chitosan, the deacetylated derivative of chitin, was used as a natural polymer with approved pharmaceutical applications [1] due to its biodegradability and biocompatibility [2], and low toxicity [3]. The preparation of chitosan-heparin nanoparticles was accomplished using the ionotropic gelation method in order to improvement of heparin efficacy. This technique was selected due to its simplicity and production of nanoparticles with relatively high drug loading. Heparin was selected as a model drug as its short biological half life and side effects makes it a good candidate for sustained release nanoparticulate preparation.

Materials & Method

Sodium Acetate, acetic Acid, heparin, chitosan and other chemicals and solvents used in this study were of analytical grade and were purchased locally. Generally, ionotropic gelation method is used for preparation of hydrogel nanoparticles. Polymer was dissolved in acetate buffer and then the drug was added in this solution while being stirred vigorously. For achievement to desired particle size, a fractional factorial design was used to establish optimum combination of chitosan concentration, heparin concentration, pH of buffer, addition rate of heparin to chitosan solution, temperature and mixer rate. Also effect of these parameters on particle size when one of the parameters is changed and other parameters are fixed was evaluated. The unique qualities and performance of nanoparticles as devices of drug delivery arise directly from their physicochemical properties. Hence, determining such characteristics is essential in achieving a mechanistic understanding of their behavior. Therefore, hydrogel nanoparticles were characterized by evaluation of particle size, morphology, zeta potential, drug encapsulation efficiency, stability, and subsequent release kinetics. Also using chitosan with different molecular weights, the cross-linked nanoparticles was made and evaluated in size, volume, and morphology as well as release kinetics.

Results and Discussion

The ionotropic gelation method was successfully used for production of chitosan-heparin nanoparticles. Morphology of the prepared hydrogels was studied by transition electronic microscope (TEM) technique and results showed spherical and dense shape (Figure 1). Additionally, FTIR spectra of chitosan, heparin, and chitosan-heparin nanoparticles exhibited interactions between carboxyl groups of heparin and amino groups of chitosan. Drug entrapment efficiency was more than $73.44 \pm 2.31\%$ which confirmed the suitability of the method for production of nanoparticles with high drug loading. Also, in vitro release behavior of heparin, from hydrogels was studied (Figure 2). Particle size analysis

showed that nanoparticles were in a narrow size distribution with mean particle size of 63 ± 4 nm (Figure 3).

Conclusions

In this study we developed a novel, positively charged and colloidal chitosan nanoparticulate system as a vehicle for delivery of heparin. The finding of this study showed the applicability of this method for delivery of anionic drugs. Further studies such as in vivo toxicity tests and in vivo release should be performed to evaluate the applicability of these nanoparticles as a novel drug delivery system.

References

- [1] L. Illum, Pharm Res, 15 (1998) 1326.
- [2] G. Borchard, H.E. Junginger, Adv Drug Del Rev, 52 (2001) 103.
- [3] J. Karlsen, O. Skaugrud, Manuf Chem, 62, (1991) 18.



Fig. 1. Transition electron microscopy (TEM) image of Chitosan-Heparin nanoparticles.

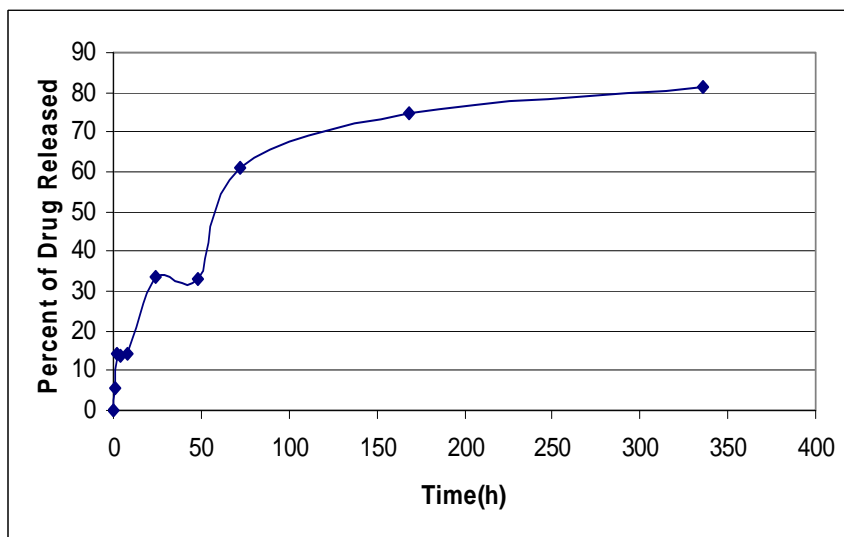


Fig. 2. Release of heparin from chitosan-heparin nanoparticles

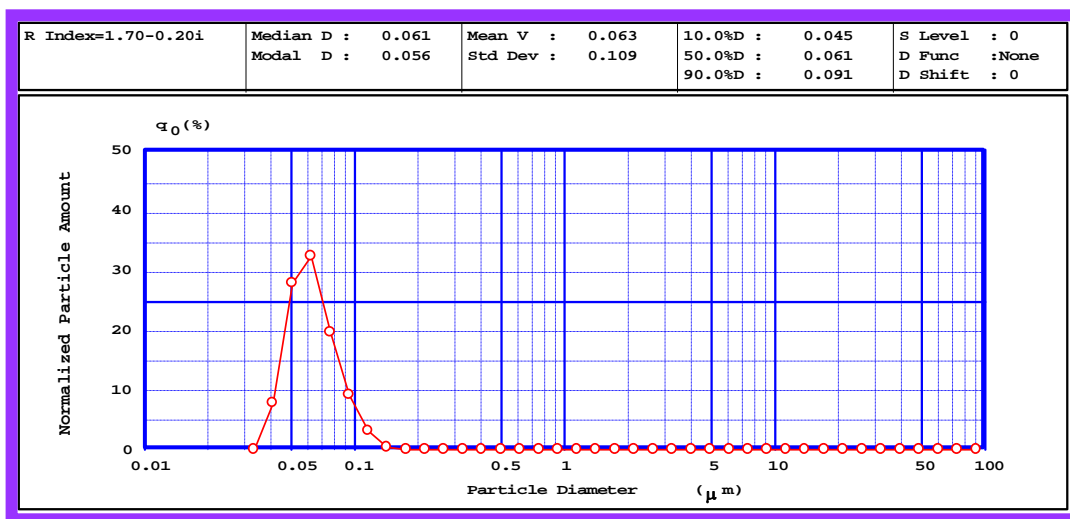


Fig.3. Nanoparticles size distribution

ENHANCED ABSORPTION OF N719 DYE IN THE PRESENCE OF PLASMONIC NANO-ISLANDS

Nafiseh Sharifi *, Nima Taghavinia***

* Institute for Nanoscience and Nanotechnology, Sharif University of Technology, Tehran 14588, Iran

** Physics Department, Sharif University of Technology, Tehran 14588, Iran

sharifi@ncl.sharif.edu

Abstract: Dye-sensitized solar cells (DSSCs) are a relatively low cost solar cell technology when compared to traditional solid-state silicon solar cells and they have achieved overall light-to-electricity conversion efficiencies of over 10.6% [1]. Low absorption of sensitizers is one of the limiting factors in the performance of these devices, hindering progress in achieving higher efficiencies. Molecular engineering of sensitizer is prevailing research to enhance light-harvesting capability of the dye adsorbed onto the film surface. But in this study, more interesting approach, which uses surface plasmon resonance (SPR) has been utilized and the effect of SPR on the absorption of N719 dye has been investigated. The optimal size of silver nanoparticles as a surface plasmon source and also the optimum concentration of dye have been studied. It is revealed that the control of the structure and quantity of Ag particles is important to apply the surface plasmon resonance effect to dye-sensitized solar cells. Enhancement of absorption is attributed to the electric-field augmentation via SPR between nanoparticles and the coupling of plasmon modes with the electronic excitation in dyes. Discrete dipole approximation (DDA) method was employed, which justifies the experimental results.

[1] O'Regan, B.; Gratzel, M. "A low-cost, high-efficiency solar cell based on dye-sensitized colloidal TiO₂ films", *Nature*, 353, 737-740, (1991).

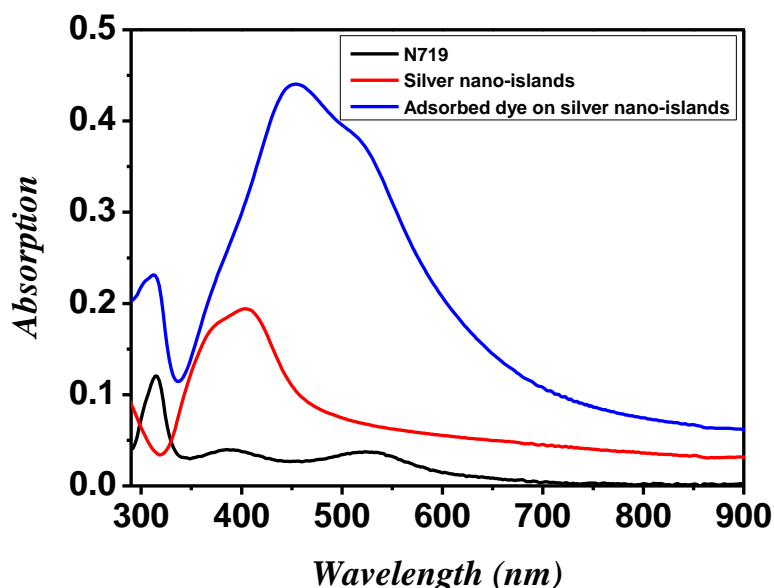


Fig. 1. Absorption of N719 (black), silver nano-islands (red) and adsorbed dye on silver nano-islands (blue).

Synthesis and Characterization of Zinc Oxide Nanostructures Under Different Reaction Conditions

Deepali Sharma*, Jaspreet Rajput and B.S. Kaith
Department of Chemistry
Dr. B.R. Ambedkar National Institute of Technology
Jalandhar 144011, India

E-mail*: dps_chem@yahoo.co.in

Abstract

Over the past decade, the synthesis of inorganic nanostructures has become an active area of research due to significant potential applications in catalysis, optoelectronics, microelectronics, magnetic and biology. Among these, zinc oxide is of wide interest as it has many potential applications in electronics, structural and biomaterials. Moreover, it possesses unique properties such as, direct band gap semiconductor (3.37 eV), large exciton binding energy (60meV), piezoelectric property, bio-safe and bio-compatible. In the nano -range, zinc oxide structures are expected to possess interesting properties that are quite different from their bulk counterpart. Up to now, numbers of synthetic approaches have been developed to prepare zinc oxide nanostructures of different morphologies, for instance, solution- based, vapour-based and template-assisted synthesis. [1-5]

In this paper, authors have made the efforts to synthesize zinc oxide nanostructures of diverse morphologies under different reaction conditions using surfactants which were synthesized under ambient conditions. Role of the surfactants in deciding the morphology of the zinc oxide nanostructures was established through Scanning electron microscopy (SEM), Transmission electron microscopy (TEM) and X-ray diffraction (XRD) techniques. Zinc oxide nanostructures synthesized were found to possess the size ranging from 20 nm to 35 nm. These nanostructures have further been used as reinforcing materials for the preparation of green nanocomposites.

References

- [1] H. Zang, D. Yang, Y. Ji, X. Ma, J. Xu and D. Que, *J.Phys. Chem. B* 2009, **108**(13), 3955-3958.
- [2] M. P. Manoharan, A. V. Desai, G. Neely and M. A. Haque, *J. Nanotechnology* 2008. (in press)
- [3] J. Huang, C. Xia, L. Cao and X. Zeng, *Mat. Sci. Engg. B* 2008, **150**, 187-1934.
- [4] Z. L. Wang, X. Y. Kong and Y. Ding, *Adv. Mater.* 2005, **17**, 2562-2567.
- [5] B. D. Yuhas, D. O. Zitoun, P. J. Pauzausjje, R. He and P. Yang, *Angew. Chem. Int. Ed.* 2006, **45**, 420-423.

MAGNETISM OF NANOCARBONS: FULLERENE C₆₀ AND GRAPHENE

E.F.Sheka

Peoples' Friendship University of Russia, Moscow 117198, Russia

sheka@icp.ac.ru

Odd electrons are a characteristic feature of nanocarbons. The term naturally covers terms “ π electrons”, “magnetic electrons”, and “dangling bonds” [1] and indicates that the number of valence electrons of each carbon atom of the species is larger by one than that of interatomic bonds formed by the atom. Due to enlarging length of the valence bonds of the species in comparison to the ones of classic π electron systems such as benzene or ethylene molecules a considerable weakening of the electron interaction occurs which causes a partial exclusion of odd electrons from the covalent bonding so that odd electrons, covalently bound in the classic molecules, become effectively unpaired in more complicated nanocarbons. These effectively unpaired electrons provide a partial radicalization of the species which results in a considerable enhancement of their chemical reactivity and magnetism.

Molecular magnetism of odd-electron systems is considered in terms of the Heisenberg Hamiltonian via the total spin S and the exchange integral J or the magnetic coupling constant. The constant determination is the central point of the magnetism study that crucially depends on the appropriate mapping between the Heisenberg spin eigenstates and the computationally determined electronic states.

Once being a perfect alternative to many-body configurational interaction, one-determinant unrestricted broken-symmetry Hartree-Fock approach applied to weakly interacting odd electrons provides a reliable determination of both pure-spin state energies and the relevant J value from the spin-contaminated eigenvalues of the UBS HF solutions [2]. In the case of even

number of “magnetic” (odd) electrons J is determined as $J = \frac{E_{S=0}^{UBS HF} - E_{S_{max}}^{PS}}{S_{max}^2}$. Here

$E_{S=0}^{UBS HF}$ and $E_{S_{max}}^{PS}$ are the energy of the UBS HF singlet state and the pure-spin state with maximal spin S_{max} that is the exact pure-spin single-determinant solution, respectively. Oppositely to the case, both magnetic coupling constant J and pure-spin states cannot be straightforwardly obtained within the one-determinant UBS DFT scope. Usually, additional particular procedures are needed to reach the goal.

The magnetization proceeds when J absolute value is small. This is of a particular importance for the systems with the singlet ground state due to the second-order character of the magnetic phenomenon in this case [3]. The performed UBS HF computations revealed that magnetic response of singlet nanocarbons was provided by a collective action of odd electrons and was size-dependent. The above criterion concerning the smallness of the J value is met when fullerene molecules are joined in carpet oligomers of a few nm in linear size [4] and when graphene is split into nm -size nanopanes [5]. The size-dependent origin of magnetism is well supported by experimental findings related to nanostructured polymerized fullerene crystals and activated carbon fibers consisting of nanographite domains. The explanation of disappearing magnetic response in single polymerized fullerene crystals and micro-size graphene is suggested.

1. E.F. Sheka, Int. Journ. Quant. Chem. **107**, 2932 (2007).
2. L.Noodleman, J Chem Phys. **74**, 5737 (1981).
3. A.K.Zvezdin, V.M.Matveev, A.A. Mukhin, et al. Rear Earth Ions in Magnetically Ordered Crystals (Russ). Nauka: Moskva (1985).
4. E.F. Sheka, V.A.Zayets, and I.Ya.Ginzburg, JETP **103** 728, (2006)
5. E.F. Sheka and L.A. Chernozatonskii, arXiv:0901.3229v1 (2009).

Reactive oxygen species photosensitized in the presence of carbon- and TiO₂-based nanostructured materials: ESR spin-trapping and AFM assays

A. Sienkiewicz¹, K. Pierzchała¹, B. Vilenó^{1,2}, A. J. Kulik¹, A. Magrez¹, M. Lekka³, and L. Forró¹

¹*Laboratory of Nanostructures and Novel Electronic Materials, Institute of Physics of Condensed Matter, Faculty of Basic Sciences, Ecole Polytechnique Fédérale de Lausanne, Station 3, CH-1015 Lausanne, Switzerland*

²*Institute of Molecular Biophysics, Florida State University, Tallahassee, FL-32306, USA*

³*The Henryk Niewodniczański Institute of Nuclear Physics, Polish Academy of Sciences, ul. Radzikowskiego 152, PL-31-342 Krakow, Poland*

andrzej.sienkiewicz@epfl.ch

Carbon- and TiO₂-based nanomaterials are increasingly attracting a lot of attention because of their existing and potential applications in numerous areas. Here, we report on photocatalytic properties of water-soluble derivatives of fullerene C₆₀ (fullerols) and commercially available and custom-synthesized nanoTiO₂. Electron spin resonance (ESR) in combination with spin-trapping technique was used to characterize the capability of the studied nanostructured materials to photosensitize reactive oxygen species (ROS). Atomic force microscopy (AFM), optical microscopy and AFM force-mode spectroscopy were also used to assess the photo-oxidative damage induced to individual living cells in the presence of the studied nanomaterials under exposure to visible/UVA light illuminations.

For aqueous solutions of fullerols, C₆₀(OH)_n, with n=18–24, and C₆₀(OH)₁₉(ONa)₁₇×18H₂O, illuminated with visible light, ESR reactive scavenging with TMP-OH and near infrared (NIR) detection at 1270 nm revealed photosensitization of singlet oxygen (¹Δ_g).^{1,2} For aqueous suspensions of nanoTiO₂ illuminated with UV-A light, ESR spin-trapping with DMPO in combination with selective ROS inhibitors revealed the formation of superoxide (O₂^{•-}) and hydroxyl (OH[•]) radicals. The generation efficiency of ROS was found to be particle size- and shape-dependent. NanoTiO₂ anatase with the primary particle size of 20-30 nm revealed the highest efficiency of ROS formation. The custom-made TiO₂ nanotubes and nanowires also efficiently generated ROS, with the relative quantum yield of ~30% as compared to a reference photocatalyst, P25 Degussa.

AFM phototoxicity assays of fullerols and nanoTiO₂ were performed for various types of human cells, including: neurons, fibroblasts, glioblastoma, melanoma and bladder cells. The experimental AFM setup enabled us to generate the oxidative stress on living cells *in situ*, in a ‘liquid-cell’ of the AFM probe, directly before the measurements [3]. For cells exposed to the oxidative stress, the AFM force spectroscopy revealed a marked drop in cell stiffness, which scaled with exposure to the deleterious action of ROS. The observed cell elasticity changes were nanoparticle type-dependent. P25 Degussa was found to be the most phototoxic system against living cells from all the TiO₂-based nano-catalysts in this study.

Changes in the cell stiffness were associated to the ROS-mediated cytoskeleton reorganization and/or to the oxidative damage to focal adhesions [4]. These findings were also supported by the optical images of cells with specifically stained (FITC-phalloidin) actin fibers, which drastically decayed for cells exposed to the photo-oxidative stress generated in the presence of nanoparticulate materials [5].

References:

- [1] A. Sienkiewicz, B. Vilen, K. Pierzchała, M. Czuba, P.R. Marcoux, A. Graczyk, P.G. Fajer, and L. Forró, *J. Phys.: Condens. Matter*, **19** (2007), 285201.
- [2] B. Vilen, P.R. Marcoux, M. Lekka, A. Sienkiewicz, T. Feher, and L. Forró, *Adv. Funct. Mat.*, **16** (2006) 120-128.
- [3] B. Vilen, A. Sienkiewicz, M. Lekka, P.R. Marcoux, and L. Forró, *Supramolecular Structure and Function*, **9** (2008) 153.
- [4] B. Vilen, M. Lekka, A.Sienkiewicz, S. Jeney, G. Stoessel, J. Lekki, L. Forró, and Z. Stachura, *Environ. Sci. Technol.*, **41** (2007) 5149.
- [5] K. Pierzchała, M. Lekka, A.J. Kulik, P. Laidler, A. Sienkiewicz, and L. Forró, to be published.

CARBON NANOTUBES (CNTs): A MODIFIED COMPUTATIONAL MODEL FOR STUDY OF ELECTRONIC PROPERTIES

Katya Marinova Simeonova,
Associate Professor, (PhD),
Civil Engineer, Engineer-mathematician,
Institute of Mechanics, Bulgarian Academy of Sciences,
Acad. G. Bonchev, str., Bl. 4,
1113 Sofia, Bulgaria
Phone: +359 2 979 6460,
E-mail: katyas@bas.bg
katyageorge@abv.bg

Recent advancements of nanoscience (nanomaterials and nanotechnologies), has been attracted many scientists and researchers from the world. Discovering of carbon nanotubes (CNTs) in 1991, by S. Iijima[1], was a revolution not only in science, but also in smart materials science. (CNTs) possess extraordinary physico-mechanical properties (high elasticity moduli, high stiffness, high strength), transport, electrical, optical, electronic, etc. properties. Moreover these nanomaterials have small nanoscale sizes (about 50-100nm in diameter and some microns in length). These nanostructured materials find application in many fields of technique, electronics, optoelectronics, semiconductors, nanomedicine, molecular and cellular biology, [2].

The aim of the work, presented could be formulated as follows: to give a modified (numerical) model for study of the effects of different parameters (tube's diameter, magnetization, temperature, fitting constants etc.) on the electronic properties of (CNTs). Theoretical predictions and experimental data in literature have been used for that purpose.

Numerical algorithms and numerical FORTRAN programs, designed by author, have been presented also in the work. Numerical simulations, conducted give an opportunity for obtaining graphics, reflecting dependencies between fundamental gaps, versus tube's diameter, magnetization versus time and fitting parameters.

Comparison between these numerical (computational) results and experimental data in literature shows a very good agreement.

Key words: carbon nanotubes (CNTs), modified model, electronic, tube's diameter [1]. S. Iijima, Nature 395, 1991

[2]. Katya Simonova, Ganka Milanova, ISCOM2007, Book of Abstracts, p. 136, ISCOM 2007, 24-30 September 2007, Peniscola, Spain, (poster with financial support of ISCOM2007)

NANOWIRES, NANORODS AND NANOTUBES: COMPUTATIONAL MODELS AND METHODS FOR STUDY OF PROPERTIES, SYNTHESIS, CHARACTERIZATION AND FABRICATION.

Katya Marinova Simeonova
PhD, Civil engineer, Engineer-mathematician,
Associate Professor,
Institute of Mechanics, Bulgarian Academy of Sciences,
Acad. G. Bonchev, str., Bl. 4
1113 Sofia, Bulgaria,
Ph. +359 2 979 6460
E-mail: katyas@bas.bg
katyageorge@abv.bg

Nanoscale materials have exceptional physico-mechanical, electronic, optical, electrical, chemical etc. properties. Applications of nanowires, nanorods, nanotubes and nanoshells in different fields of technique, industry, electronics, etc, have important role also. Synthesis, characterization and assembly of nanowires and nanotubes as building systems, have been studied from many researchers, [1]. The aim of the work, presented could be formulated as follows: to give recent results, on modeling of nanowires, nanorods, nanotubes for purposes of electronic detection. SEM (scanning electron microscopy, TEM (tunneling electron microscopy) and Raman spectroscopy have been discussed in [2]. Structural, mechanical, electrical, sensing, optical and magnetic properties of nanoscale materials have been reviewed in the paper [3]. A computational model, based on the site binding model for zinc oxide nanorods and experimental studies have been presented in [4]. MEMS micro- fluidic platforms, have been given too. Nanoshells for cancer therapy, modeling and simulations by nanotube-metal contact resistance, multifunctional nanorods for gene delivery, applications have been discussed also. Some novel studies, conducted by NASA have been analyzed too. Future plans, for computational studies and models for nanoscale materials behavior have been given as well.

Key words: nanoscale materials, nanotubes, nanowires, nanorods, nanoshells

References

- [1] C. Ma and Z. L. Wang, Adv. Mat., 17, 2635 (2005)
- [2] D. M. Whang, J. Song, Y. Mu and C. M. Liebei, NanoLetters 3, 1255 (2003)
- [3] G. X. Wang et al, Prep. of cadm. Sel. Nanow. and nanot., 2007
- [4] Z. Fan and J. G. Lu, Nanostr. ZnO: Build. Blocks for Nanosc. Dev., Int. J. of High Speed Electr. and Syst., vol. 16, N4 (2006), 883

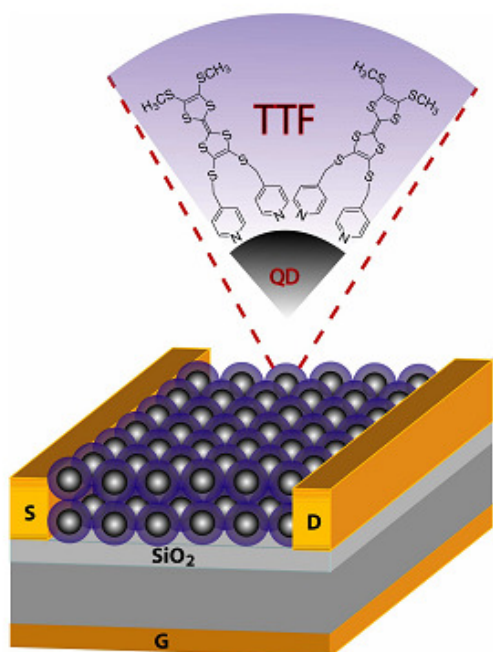
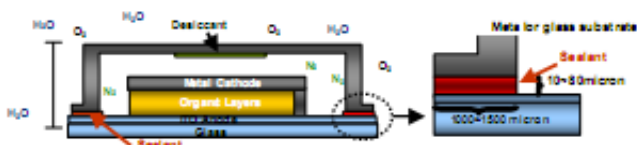
A Study on Application of Polymers and Nanoscale Materials in Organic Electronics Devices

K. Simeonova^a, G. Milanova^b

^a Ph.D, Civil Engineer, Engineer-mathematician, Associate Professor,
Institute of Mechanics, Bulgarian Academy of Sciences,
e-mail: katyas@mech.bas.bg

^b Ph.D, Civil Engineer, Komstroi'94, Pancharevo, Sofia, Bulgaria,
e-mail: katyageorge@abv.bg

The organic electronics, is a very useful tool for engineers, technicians, and scientists for creating of measuring instruments: digital multimeter (DMM), organic light – emitting diode (OLED), ¹. The aim of the work, presented could be formulated as follows: to analyze, and to discuss recent organic electronics devices, mentioned above, ²; Polymer nanowires; Semiconductor industry; Organic Solar Cells. Integration of organic electronic materials with semiconductor nanoparticles has been discussed in ². Organic electronics materials and devices have been shown in Fig.1 and Fig.2. The future problems of organic electronics, devices, materials and applications have been given in ³. Some computational models for study of problems mentioned above will be presented as well.



Integration of organic electronic materials with semiconductor nanoparticles has been discussed in ². Organic electronics materials and devices have been shown in Fig.1 and Fig.2. The future problems of organic electronics, devices, materials and applications have been given in ³. Some computational models for study of problems mentioned above will be presented as well.

Key words: organic electronics, (DMM); (OLED); materials

¹ S. Gillissen, K. Severyns, **2002**, <http://SealantsforOrganicElectronicDevices.url>

² Tongxiang Lu, A thesis, Sept. **2007**, <http://viewcontent.url>

³ J. Movva, B. Spearin et al, **2006**, Volume 3, 13

DYNAMICS OF DILUTE MAGNETIC NANOPARTICLE SUSPENSIONS

Authors—Vanchna Singh¹, Varsha Banerjee¹, Manish Sharma²

¹Department of Physics, Indian institute of Technology, Hauz Khas, New Delhi -110016,INDIA. (email- vanchna.s@rediffmail.com)

²Centre for Applied research In Electronics, Indian Institute of Technology, Hauz Khas, New Delhi -110016, INDIA.

Dilute suspensions of magnetic nanoparticles (MNP) have attracted a lot of attention due to their immense technological and biological applications. These MNP suspensions can be used as labels for sensing applications [1]. The main reason behind their wide applicability is the ease with which these can be detected and manipulated. Biological applications such as magnetic resonance imaging, targeted drug delivery, biomarkers and biosensors rely on transport and manipulation of individual particles with size ranging from few nanometers to tens of nanometers [2]. This size range enables them to interact or bind with biological entities like proteins, genes, viruses and cells. Thus, these MNP's provide a means of tagging biological entities and eventually be driven and manipulated by external fields. It is hence crucial to understand the dynamics of single domain magnetic nanoparticles.

When analysing the dynamics of such nanoparticle suspensions, several factors play competing roles. The system behavior is governed by the mutual strengths of the various interaction energies present, which include magnetic dipolar and vanderwaal's (attractive) as well as steric and thermal (repulsive) interactions. This leads to competing aggregation and fragmentation processes within the system leading to cluster formation (refer figure 1). We present a simple model incorporating aggregation and fragmentation process (as ratio D/w) by appropriately writing down the rate equations for these processes. We wish to mention here that most of the earlier studies are based on irreversible aggregation process. By including fragmentation, the cluster aggregation process becomes self-limiting. The average cluster size in the initial stages exhibits power law dependence similar to irreversible aggregation based models. However it converges to a time independent value at later times. This behavior for various ratios of aggregation to fragmentation strengths exhibits scaling as shown in figure 2. The simulation results are compared with experimental data on a variety of MNP suspensions [3]. The comparisons are satisfactory.

Further the relaxation mechanism of single domain magnetic nanoparticles within the suspensions can either be dominated by either Neel and or Brownian relaxation [4]. The response times of the particles are altered by magnetic volume, enhanced volume due to surfactant coatings, anisotropy constant and temperature. Also, all experimental samples have an inherent particle size distribution leading to polydispersity. Polydispersity considerably alters the response functions. This is demonstrated in figure 3 where we plot the AC susceptibility $\chi(\omega)$ vs ω for monodisperse and polydisperse samples. In this study, we systematically analyse the effect of polydispersity on $\chi(\omega)$. We also provide a procedure to extract particle size distribution from $\chi(\omega)$ if the later is unavailable in experiments using Cole-Cole plot analysis [5].

To conclude, the study is an attempt to understand—

- (i) factors which affect single particle relaxation and polydispersity which is ubiquitous in experimental samples.
- (ii) clustering of MNP and its effect on response functions.

The two are important in distinct physical settings.

References:

1. Q.A. Pankhurst, J. Connolly, S.K. Jones, J. Dobson, J. Phys. D. 36, R167 (2003)
2. P.C. Fannin, T. Relihan, S.W. Charles, Phys. Rev B, 55, 14423 1997
3. D. Eberbeck, F. Wiekhorst, U. Steinhoff, L. Trahms, J. Phys. Cond. Matt., 18, S2829 (2006).
4. W.F. Brown, J. Appl. Phys., 34, 1319 (1963).
5. D.W. Davidson, R.H. Cole, J. Chem. Phys., 19, 1484 (1951).

Figures:

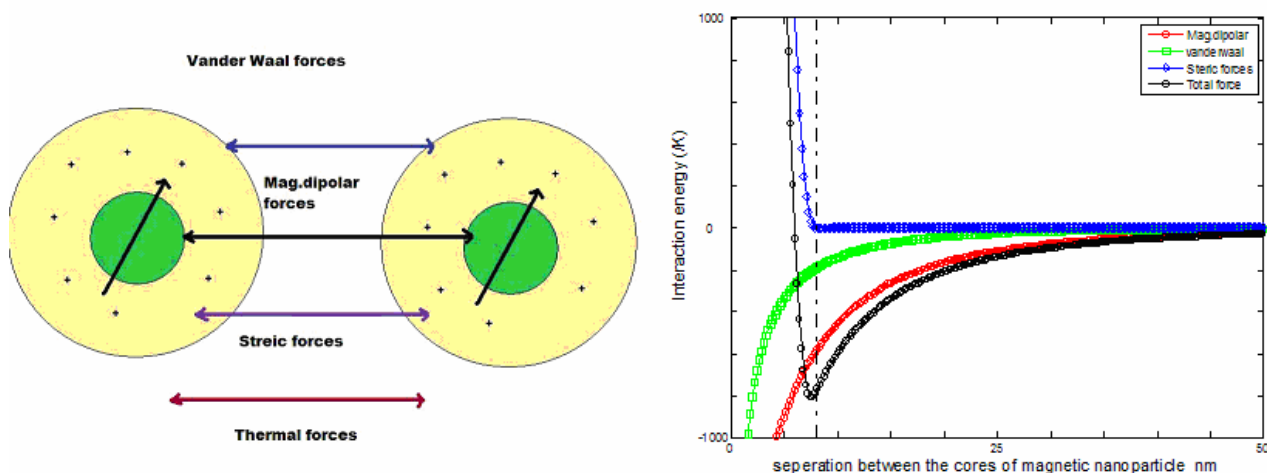


Figure1: Interaction energies between two nanoparticles

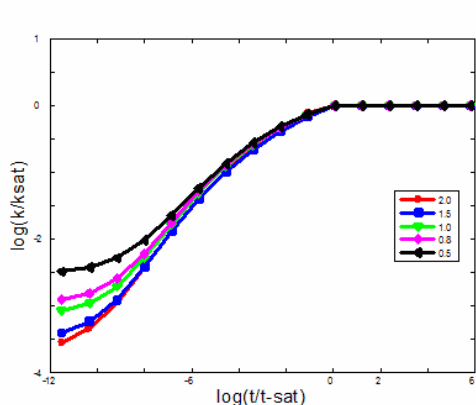


Figure 2: Variation of K_{avg} vs time for different ratios of aggregation and fragmentation depicting (i) Power law behavior initially (ii) steady state behavior at later times (iii) scaling at all ratios.

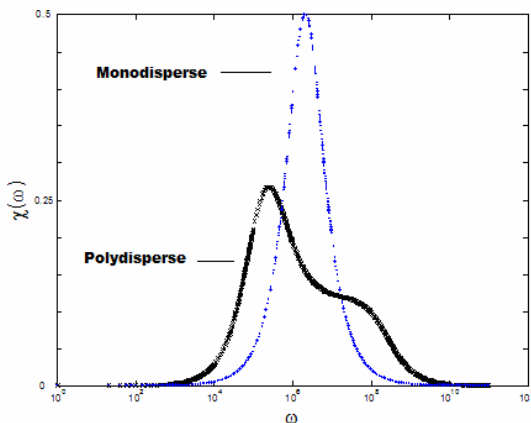


Figure 3: Effect of polydispersity on response function (lognormal distribution with $r_m=7.5$ nm , std.dev=0.35 respectively)

THE NANO MODIFICATION OF HARD COATINGS WITH NITROGEN ION IMPLANTATION

B. Skoric, D. Kaks, A. Miletic and G. Favaro
University of Novi Sad, Trg D. Obradovica 6, Novi Sad, Serbia
CSM Instruments, Peseux, Switzerland
skoricb@uns.ns.ac.yu

Thin hard coatings deposited by physical vapour deposition (PVD), e.g. titanium nitride (TiN) are frequently used to improve performance in many engineering applications

In this paper, we present the results of a study of TiN films which are deposited by a Physical Vapor Deposition and Ion Beam Assisted Deposition. In the present investigation the samples with duplex coating was studied, and subsequent ion implantation was provided with N^{5+} ions. The ion implantation was applied to enhance the mechanical properties of surface. The most successful and widespread model for nanoindentation data analysis is one in which the unloading data are assumed to arise from a purely elastic contact. The form most often used is known as the Oliver and Pharr method.

This paper describes the successful use of the nanoindentation technique for determination of hardness and elastic modulus. In the nanoindentation technique, hardness and Young's modulus can be determined by the Oliver and Pharr method, where hardness (H) can be defined as: $H = P_{max}/A$, where P_{max} is maximum applied load, and A is contact area at maximum load. In nanoindentation, the Young's Modulus, E, can be obtained from: $1/E_r = (1-\nu_i^2)/E + (1-\nu_r^2)/E_r$, where ν_i = Poisson ratio of the diamond indenter (0.07) and E_i = Young's modulus of the diamond indenter. Therefore, in recent years, a number of measurements have been made in which nanoindentation and AFM have been combined.

Indentation was performed with CSM Nanohardness Tester. The results are analyzed in terms of load-displacement curves, hardness, Young's modulus, unloading stiffness and elastic recovery. The nanohardness of coating measured by Berkovich indenter is about 42.4 GPa. The analysis of the indents was performed by Atomic Force Microscope. The stress determination follows the conventional $\sin^2\psi$ method, using a X-ray diffractometer. The analyzed AE signal was obtained by a scratching test designed for adherence evaluation. AE permits an earlier detection, because the shear stress is a maximum at certain depth beneath the surface, where a subsurface crack starts. The critical load L_{c2} corresponds to the load inducing the partial delamination of the coating.

Coating is often in tensile stress with greater microhardness. The film deposition process exerts a number of effects such as crystallographic orientation, morphology, topography, densification of the films. The evolution of the microstructure from porous and columnar grains to densel packed grains is accompanied by changes in mechanical and physical properties. A variety of analytic techniques were used for characterization, such as scratch test, calo test, SEM, AFM, XRD and EDAX. Therefore, by properly selecting the processing parameters, well-adherent TiN films with high hardness can be obtained on engineering steel substrates, and show a potential for engineering applications.

The experimental results indicated that the mechanical hardness is elevated by penetration of nitrogen, whereas the Young's modulus is significantly elevated.

The deposition process and the resulting coating properties depend strongly on the additional ion bombardment.

References:

[1] K. Mogensen, N. Thomsen, S. Esikilden, C. Mathiasen and J.Bottiger, Surface and Coatings Technology 99 (1998) 140.

[2] W. Ensinger, Surface and Coatings Technology 99 (1998) 1.

[3] J.C.A. Batista, C. Godoy, A. Matthews, A. Leyland, Surface Engineering, 9 (2003) 37.

Figures:

Table 1. Surface microhardness ($HV_{0.03}$) and nanohardness (load-10mN).

	Unit	pn/IBAD	PVD	pn/PVD/II	Fused Silica
Average	Vickers	2007	3028	3927	943
Average	GPa	21.6	32.6	42.6	10,1

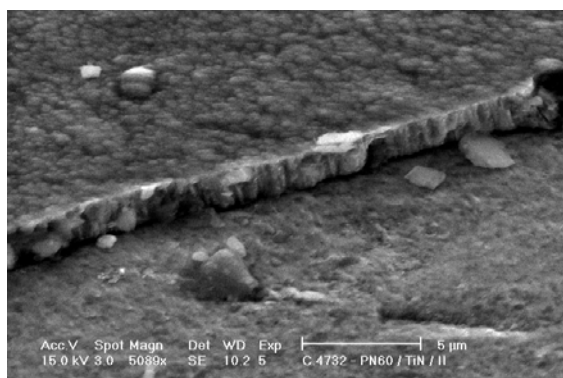


Figure 1. Surface morphologies of coating.

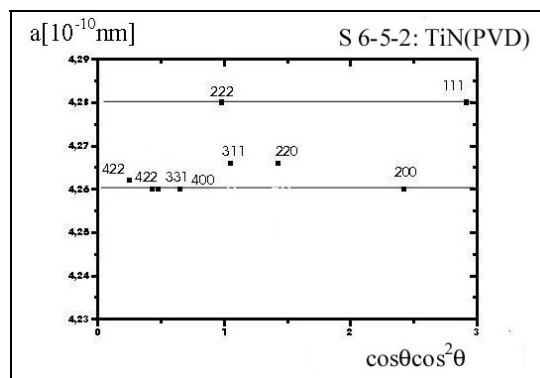


Figure 2. The Cohen-Wagner plot, lattice parameters a_{hkl} vs. $\cos\theta\cot^2\theta$.

MAGNETIC PROPERTIES OF Co, Al AND Mn, AL Co-DOPED ZnO FILMS

A.O. Ankiewicz¹, Q. Xu², H. Schmidt², M. Lorenz³, M. Grundmann³, N. Franco⁴, E. Alves⁴, M.C.Carmo¹, and N.A. Sobolev¹

¹ I3N and Departamento de Física, Universidade de Aveiro, 3810-193 Aveiro, Portugal

² Institut für Ionenstrahlphysik und Materialforschung, FZ Dresden-Rossendorf, 01328 Dresden, Germany,

³ Institut für Experimentelle Physik II, Universität Leipzig, 04103 Leipzig, Germany

⁴ Ion Beam Laboratory, Instituto Tecnológico e Nuclear, 2686-953 Sacavém, Portugal

ZnO films, co-doped with Co and Al or Mn, Al, were grown from $\text{Zn}_{0.945}\text{Mn}_{0.05}\text{Al}_{0.005}\text{O}$ or $\text{Zn}_{0.945}\text{Co}_{0.05}\text{Al}_{0.005}\text{O}$ ceramic targets, respectively, on a-plane sapphire substrates by means of pulsed laser deposition (PLD) using a KrF excimer laser. The growth and sample parameters are given in the table.

Sample	Target composition	$p(\text{O}_2)$ [mbar]	Substrate T [°C]	No. of pulses	t [nm]	n (5 K) [cm ⁻³]
TF1	$\text{Zn}_{0.945}\text{Mn}_{0.05}\text{Al}_{0.005}\text{O}$	4×10^{-5}	343	1500	36	2.13×10^{20}
TF2	$\text{Zn}_{0.945}\text{Mn}_{0.05}\text{Al}_{0.005}\text{O}$	0.005	726	30300	782	9.96×10^{18}
TF3	$\text{Zn}_{0.945}\text{Co}_{0.05}\text{Al}_{0.005}\text{O}$	4×10^{-5}	450	1800	43	1.42×10^{20}
TF4	$\text{Zn}_{0.945}\text{Co}_{0.05}\text{Al}_{0.005}\text{O}$	0.001	726	30300	685	4.35×10^{18}

The composition of the films was measured by combined Rutherford backscattering spectrometry (RBS) and particle induced X-ray emission (PIXE). The Al content in the films could not be determined, due to the underlying Al_2O_3 substrate. The Co and Mn contents in the films turned out to be larger than in the corresponding PLD targets and amounted to about 9 at.%. The crystal structure of the films was characterized by X-ray diffraction (XRD) and reciprocal space mapping (RSM), which indicated the highly c-axis-oriented ZnO films. No second phases, especially, no Co nanocrystals were detected even for a very long signal accumulation. No magnetic resonance trace of Co nanocrystals [2] was detected, either.

The critical electron concentration, at which the metal to insulator transition occurs, was estimated for a Co doped film to be $n_c = 4 \times 10^{19} \text{ cm}^{-3}$ [1]. Thus, we have a film with $n < n_c$ and another one with $n > n_c$ for each type of doping. A possible ferromagnetic response of charge carriers in ferromagnetic semiconductors is the anomalous Hall effect (AHE). The Mn doped films and the Co doped film with the larger n show no AHE. However, TF4 shows an AHE at 5 K. TF4 also exhibits weak ferromagnetism at 5 K in SQUID measurements.

The magnetic resonance (EPR and FMR) and SQUID magnetization measurements revealed that the Mn doped ZnO samples were clearly paramagnetic, the Mn ions being substitutional on Zn sites. On the other hand, the EPR signature of substitutional Co^{2+} on Zn sites was not found in the Co doped samples. Instead, a broad resonance signal with $g_{\text{eff}} > 2$ was recorded, which behaves as FMR of a magnetic film in the case of non-aligned magnetization. Also, the magnetoresistivity (MR), Hall effect, and SQUID measurements point to some kind of ferromagnetic order in the Co doped samples. However, there is no evidence of carrier mediated ferromagnetism, since the sample exhibiting larger magnetic order (TF4) is the one with lower carrier concentration and the Co is not mainly incorporated as substitutional Co^{2+} in the ZnO lattice. We believe that the formation of small precipitates or spinodal decomposition is more likely to be the origin of the observed weak ferromagnetism.

[1] Q. Xu et al., Phys. Rev. B **73**, 205342 (2006).

[2] H.J. von Bardeleben et al., Appl. Phys. Lett. **93**, 142505 (2008).

Surface modified $\text{Li}_{1.05}\text{Ni}_{0.35}\text{Co}_{0.25}\text{Mn}_{0.4}\text{O}_2$ cathode material by using nano particle coating for lithium secondary battery

J.T. Son

Department of Nano Polymer Science and Engineering, Chungju National University, Chungju 380-702, Republic of Korea

Jt1234@cjnu.ac.kr

In this study, nano-crystallized LiCoO_2 was coated on the surface of $\text{Li}_{1.05}\text{Ni}_{0.35}\text{Co}_{0.25}\text{Mn}_{0.4}\text{O}_2$ powders via sol-gel method. The influence of coated $\text{Li}_{1.05}\text{Ni}_{0.35}\text{Co}_{0.25}\text{Mn}_{0.4}\text{O}_2$ about electrochemical behavior was discussed. The surface morphology characterization was achieved by transmission electron microscopy (TEM). Nano-crystallized LiCoO_2 was clearly observed on the surfaces of $\text{Li}_{1.05}\text{Ni}_{0.35}\text{Co}_{0.25}\text{Mn}_{0.4}\text{O}_2$. The phase and structural change of the cathode materials before and after coating were revealed by X-ray diffraction spectroscopy (XRD). It showed that LiCoO_2 coated $\text{Li}_{1.05}\text{Ni}_{0.35}\text{Co}_{0.25}\text{Mn}_{0.4}\text{O}_2$ cathode exhibited distinct surface morphology and lattice constants. Fig.1. of Cyclic voltammetry (2.8-4.6 V) shows that the characteristic voltage transition on cycling exhibited by the bare compound are suppressed by 7 wt% LiCoO_2 coating. This behavior implies that LiCoO_2 prevent structural change of $\text{Li}_{1.05}\text{Ni}_{0.35}\text{Co}_{0.25}\text{Mn}_{0.4}\text{O}_2$ or reaction with electrolyte on cycling. In addition, LiCoO_2 coated $\text{Li}_{1.05}\text{Ni}_{0.35}\text{Co}_{0.25}\text{Mn}_{0.4}\text{O}_2$ compound highly improves rate capability, one of the important battery performances, by varying discharge current at 0.1 - 4.0C rate. From the correlation between these characteristics of bare and coated $\text{Li}_{1.05}\text{Ni}_{0.35}\text{Co}_{0.25}\text{Mn}_{0.4}\text{O}_2$, the role of LiCoO_2 coating played on the electrochemical performance of $\text{Li}_{1.05}\text{Ni}_{0.35}\text{Co}_{0.25}\text{Mn}_{0.4}\text{O}_2$ was probed.

Key words: Cathode material; $\text{Li}_{1.05}\text{Ni}_{0.35}\text{Co}_{0.25}\text{Mn}_{0.4}\text{O}_2$; sol-gel coating; LiCoO_2 ; Lithium ion battery

*Corresponding author; jt1234@cjnu.ac.kr (Jong-Tae. Son)

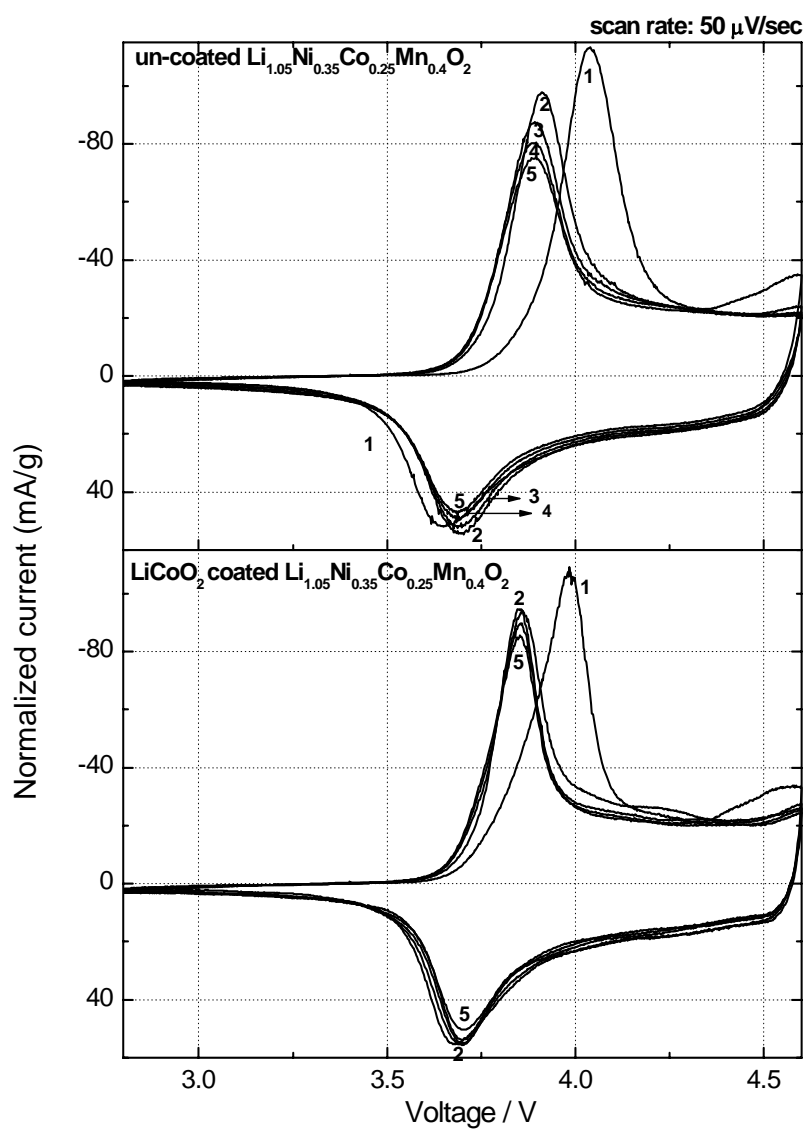


Fig. 1. Cyclic voltammetry of the bare and 7.0 wt. % LiCoO_2 oxide(nanoparticle) coated $\text{Li}_{1.05}\text{Ni}_{0.35}\text{Co}_{0.25}\text{Mn}_{0.4}\text{O}_2$ cell between 2.8 and 4.6 V at a scan rate of 50 s^{-1} .

MOLECULAR ORIENTATIONS OF NEMATIC LIQUID CRYSTALS IN BAR COATING PROCESS.

Hyejin Ko and Kigook Song
Materials Research Center for Information Display
Kyung Hee University, Youngin, Gyeonggi-do 446-701, Korea,
ksong@khu.ac.kr

Although spin coating is the most popular method used to form a polymeric thin film for various electronic devices, its use is very limited for applications in large area samples. We formed thin liquid crystal(LC) films using a bar coating method and studied LC orientation changes in the film prepared by this coating method. In the present study, photo-curable liquid crystalline di-acrylate (BASF LC242) which shows a nematic mesophase between 80 ~ 120 °C was used. The nematic LC was bar-coated at various temperatures and then cured to a thin film by UV exposure. The orientation of LC molecules in the film was investigated using polarized FTIR spectroscopy and a birefringence measurement. We found that LC molecules in the film are oriented in a normal direction to the bar coating direction when coated near crystallization temperature while oriented along the coating direction with increasing coating temperature. It is known for liquid crystal polymers that LC flows show various shear induced orientation mode, i.e., the LC director tumbling (rotational) at low shear rate, wagging (oscillatory) at intermediate shear rates, and alingning (stationary) modes at high shear rates. To understand such effects in the thin film coating process of nematic liquid crystals, we investigated effects of coating conditions, such as coating speed, film thickness, and temperature, on LC molecular orientations in the film. The effect of bar coating conditions on LC orientations was studied for nematic liquid crystalline di-acrylate using polarized FTIR spectroscopy. It is quite surprising that LC molecules align perpendicular to the coating direction during a bar coating process, that is, the LC orientation direction is normal to a shear flow direction at slow coating speed or low coating temperature. LC molecules are aligned perpendicular to the flow direction at a low coating speed and change the orientation direction to parallel with increasing coating speed as shown in Figure 1 where the order parameter S changes its sign from negative to positive with the bar coating rate. Using ATR-FTIR spectroscopic technique, it was also found that LC molecules near the top layer are inclined to orient parallel to the coating direction whereas perpendicular at the bottom layer.

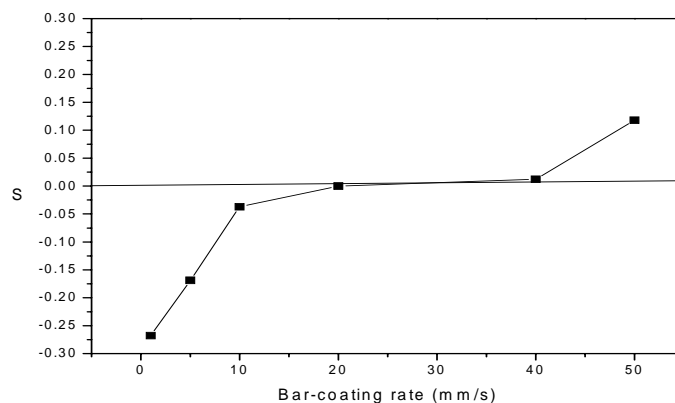


Figure 1. Order parameter of liquid crystal molecules in the film bar-coated at various coating speed.

Magnetic zigzag graphene nanoribbons from carbon nanotubes

D. Soriano, F. Muñoz Rojas, J. Fernandez Rossier, J. J. Palacios
Universidad de Alicante, San Vicente del Raspeig E03690, Alicante, Spain
David.Soriano@ua.es

Recently, zigzag graphene nanoribbons (ZGNR) has been proposed as a new type of carbon based magnetoresistive device due to their remarkable electronic properties[1]. The appearance of flat bands at the Fermi energy associated with edge states leads to magnetic moments localized at the edges[2,3]. The resistance of the whole structure strongly depends on the relative orientation of these magnetic moments and usually decreases when this orientation goes from antiparallel to parallel by applying an external magnetic field.

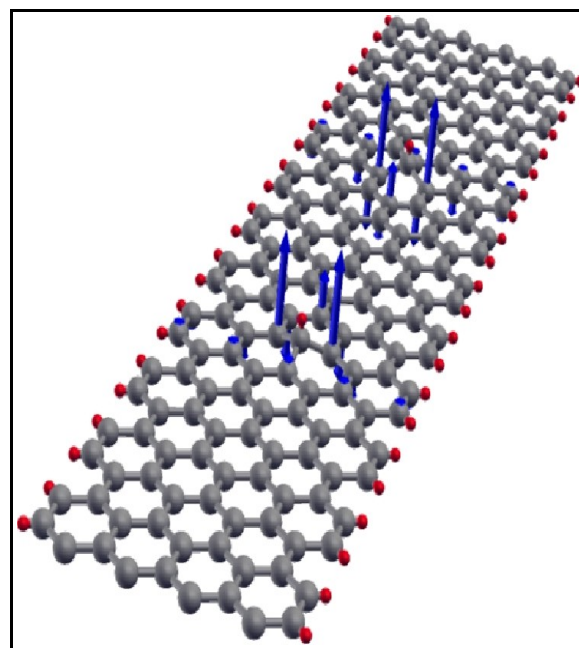
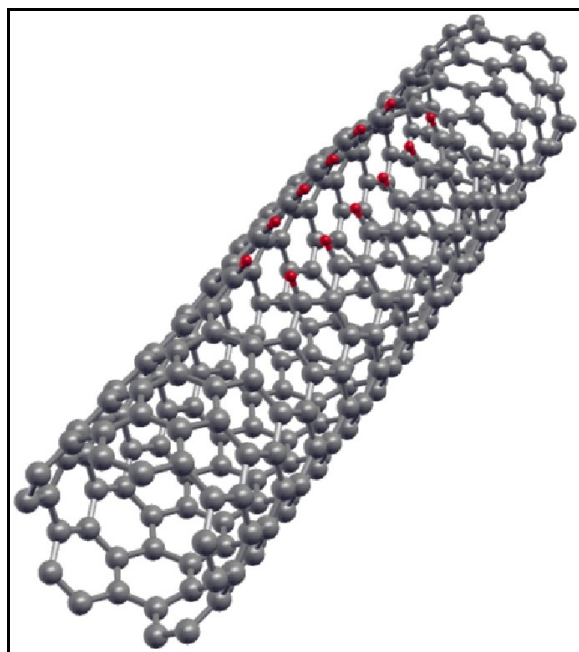
So far, experimental research on ZGNRs has been hampered due to difficulties in the fabrication of ribbons with well-defined and controlled edges. Recent work [4,5] shows the possibility of fabrication of these nanodevices by chemically unzipping metallic (n,n) carbon nanotubes (CNTs) (see figure). Here we study the emergence of magnetism and the relation between conductance and spin order for these unzipped CNT's using density functional theory (DFT) calculations and compare with results obtained with the Hubbard model[6]. It is, however, an open question whether or not magnetism survives since this is dependent on the specific chemical saturation of the open edges. We address this question for both hydrogen and oxygen saturated edges. We use the Landauer formalism with the Green's function approach for the conductance calculation.

We also explore the magnetoresistive properties of CNT's and ribbons with non-magnetic edges after doping with hydrogen. It is known that a single hydrogen atom on top of a carbon atom in graphene has a magnetic moment. In the case of a low concentration of hydrogen dopants, it is believed that the ground state features local moments with zero total spin. We show that an application of a strong enough magnetic field can spin polarize the system and reduce the resistance.

References:

- [1] F. Muñoz-Rojas, J. Fernandez-Rossier, J. J. Palacios. Phys. Rev. Lett. **102**, (2009) 136810
- [2] J. Fernandez-Rossier. Phys. Rev. B **77**, (2008) 045301
- [3] J. Fernandez-Rossier, J. J. Palacios. Phys. Rev. Lett. **99**, (2007) 177204
- [4] Dmitry V. Kosynkin *et al.* Nature **458**, (2009) 872-876
- [5] Liying Jiao *et al.* Nature **458**, (2009) 877-880
- [6] H. Santos, L. Chico, L. Brey. [ArXiv:0904.4400](https://arxiv.org/abs/0904.4400)

Figures:



The theoretical study of the atomic and electronic structure of graphene biribbons*L.A. Chernozatonskii*, P.B. Sorokin*,*****Institute of Biochemical Physics RAS, 119334 Moscow, Russia****Siberian Federal University, Krasnoyarsk, 660041 Russia**PBSorokin@gmail.com*

The emergence of graphene as a stable pure two-dimensional system has been one of the most important events in electronic condensed matter physics over the last years [1]. Until recently, the 2D paradigm was limited mostly to electrons confined to quantum wells or inversion layers in semiconductor heterostructures. The situation changed when it was found that individual atomic planes could be pulled from a graphite crystal.

One of many interesting properties of graphene is the Dirac type of electronic band structure and the drastic changes of the conductivity of graphene-based structures with electron confinement. Thus, two possibilities for the realization of this effect have been proposed: carbon nanotubes (periodic boundary conditions for the wave-vector of the electron) and graphene ribbons (finite-width graphene strips - zero boundary conditions).

Shortly after the isolation of graphene it was found that the electronic structure of few layered graphene strongly depends from the number of layers. Here we raise the question: how the electronic structure of the graphene ribbons changes with increasing number of the layers?

We studied the different compositions of the biribbons. The electronic structure of AGR+AGR, ZGR+ZGR and AGR+ZGR biribbons was obtained. The parallel and perpendicular relative orientations of the ribbons were studied. In the case of the non-parallel orientation of the ribbons the appearance of the quantum dot was found. A possible application of the biribbons in the nanoelectronics was discussed.

References:

- [1] K. S. Novoselov, A. K. Geim, S. V. Morozov, D. Jiang, Y. Zhang, S. V. Dubonos, I. V. Grigorieva, and A. A. Firsov, *Science* **306** (2004) 666.

The investigation of two-dimensional semiconducting nanostructures based on single graphene sheets with "lines" of adsorbed hydrogen

L.A. Chernozatonskii*, P.B. Sorokin**

*Institute of Biochemical Physics RAS, 119334 Moscow, Russia

**Siberian Federal University, Krasnoyarsk, 660041 Russia

PBSorokin@gmail.com

The emergence of graphene as a stable pure two-dimensional system has been one of the most important events in electronic condensed matter physics over the last three years [1]

We systematically studied graphene based superlattices with periodically adsorbed hydrogen pairs [2].

It is shown that lines of adsorbed hydrogen pair atoms divide a graphene into electronically independent strips and form an electron waveguide or 2H-line graphene-based superlattice (2HG-SL). The electronic spectra of a "zigzag" $(n,0)$ 2HG-SL are similar to those of armchair graphene ribbons and have similar oscillation of the band gap with the width between adjacent 2H-lines (number n). The composite dual-periodic $(n,0)+(m,0)$ 2HG-SLs of "zigzag" strips are analyzed, with the conclusion that they may be treated as quasi-two-dimensional heterostructures (Fig. 1). The induced strain with the direction perpendicular to the hydrogen pair "lines" significantly changes the electronic structure of 2HG-SL. For example, in the case of the 2HG-SL $(3n,0)$ ($n > 2$) we observed the semiconductor-metal transition. Superlattices of the (n,n) type with a "staircase" of adsorbed pairs of H atoms are semiconductors with nearly linear decreasing of the band gap with increasing n . We found that the configuration with the opposite spin (antiferromagnetic) orientation between ferromagnetically ordered edge states of the (n,n) 2HG-SL is energy favorable. We studied possible existence of the hydrogen lined waveguide junction. Finally, we suggested an experimental way of fabricating of 2HG-SL.

This work was supported by Russian Fund of Basic Research (grant 08-02-01096).

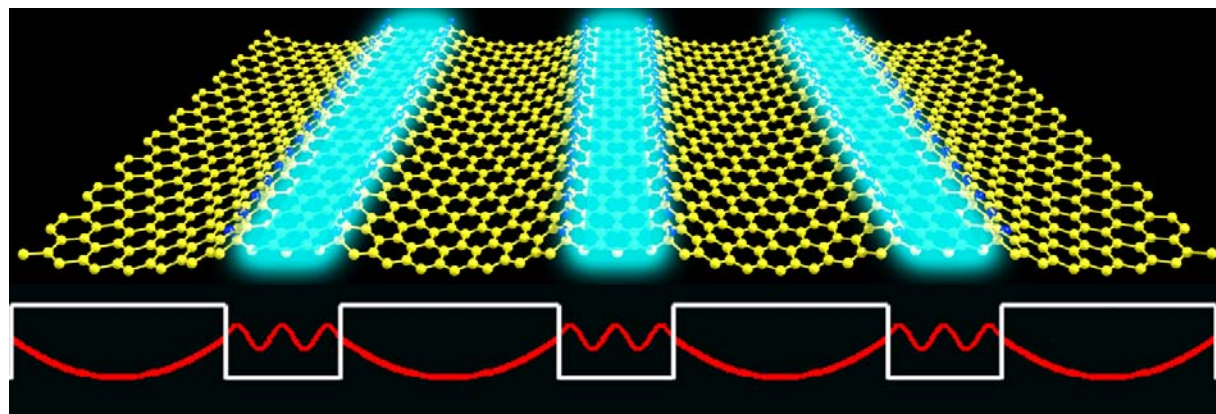


Fig. 1. $(3,0)+(7,0)$ 2HG-SL scheme, where $(3,0)$ strips (highlighted) are electronic waveguides.

References:

[1] K. S. Novoselov, A. K. Geim, S. V. Morozov, D. Jiang, Y. Zhang, S. V. Dubonos, I. V. Grigorieva, and A. A. Firsov, *Science* **306** (2004) 666.

[2] L. A. Chernozatonskii, P.B. Sorokin and J. Brünig, *Appl. Phys. Lett.* **91**, (2007) 183103

Derivation of a kinematic-like hardening behaviour of CNT – polymer composites based on stick-slip.

V. Spitas^{*1}, E. Zouridaki^{*1}, C. Spitas^{*2}, P. Michelis^{*3}

^{*1} Laboratory of Applied Mechanics, Technical University of Crete,
Chania GREECE, vspitas@science.tuc.gr

^{*2} School of Industrial Design Engineering, Technical University of Delft
Delft, THE NETHERLANDS, cspitas@geartech.net

^{*3} Institute of Mechanics of Materials and Geostrutures S.A.,
Penteli, GREECE, immg@otenet.gr

Abstract

The ability of nanocomposites containing stretched and aligned CNTs in the direction of loading to absorb high amounts of energy in cyclic loading is well-known and has been established experimentally in a number of contemporary works [1-8]. This very ability of CNT-reinforced nanocomposites is particularly important from a technological point of view since it may lead to the development of new-concept lightweight structural engineering materials with exceptional passive damping capacity. More specifically, Koratkar et al. (2005) [1] reports an increase for the loss modulus of the polymer more than 10 times with only 2% CNTs content in epoxies and Suhr et al (2005) [2] measured an increase by two orders of magnitude for well-aligned CNTs for 50% volume fraction. According to Ajayan et al. (2006) [3] interfacial slippage between the CNT and the polymer matrix can prove helpful for damping. Rajoria and Jalili (2005) [4] reported a marked increase in both the elastic modulus using MWCNTs. Zhou et al. (2004) [5] modeled the dynamical behavior of CNT nanocomposites using a four-phased composite, composed of a resin, voids and bonded and debonded nanotubes following a Weibull statistical distribution.

Until now, modeling of the damping capacity of CNTs due to the reported stick-slip in a nanocomposite has been mostly phenomenological without any connection to the intrinsic interfacial shear stress between the CNT and the matrix and the other geometry-related (i.e. CNT diameter and length, CNT volume content) and material-related properties (i.e. elastic moduli and Poisson's ratios for the CNT and the matrix). In this work the full-stress-strain response of a representative volume element (RVE) containing a single CNT aligned with the direction of loading is derived (Fig. 1), based on a continuum-mechanics approach involving energy transfer between the CNT and the matrix as well as energy dissipation during sliding in a single loading-unloading cycle using Finite Elements.

When the RVE is loaded axially, both CNT and matrix absorb elastic strain energy up to the point when the maximum shear stress at the CNT-matrix interface exceeds the interfacial shear strength causing slippage of the CNT inside the matrix. During nanosliding (Fig. 2), which starts at the ends of the CNT where interfacial shear stresses reach their maximum (Young et al. (2004) [6]) and progress towards the center as the external load is increased, the interface energy (Barber et al. (2006) [7], Qian et al. (2000) [8]) is released. After load-reversal, the mechanism is repeated in an opposite way causing hysteretic stress-strain behaviour of the nanocomposite, in which the dissipated energy per cycle depends on the interfacial strength, the geometry, the relative elastic properties of the CNT and the matrix and the volume fraction of the CNTs. Simulation results with varying volume fraction of CNTs indicate that exceptionally high energy dissipation is attainable in nanocomposites particularly when aligned and straightened long CNTs are used presenting high interfacial shear strength.

Using the above analysis, the damping properties of a nanocomposite containing aligned CNTs along the axis of loading are predicted numerically. The stick-slip process and the way that this relates to energy loss as the nanocomposite is subjected to cyclic loading is explained in detail and an energy-based analysis is carried out to calculate the dissipated energy per cycle introducing the concept of energy transfer to the inactive polymer material zones around the CNT through slip zones developed at the ends of the nanotube. Stress-strain charts are plotted from the FEA results and it is demonstrated that high CNT content is not in general linked with

increased damping capacity. Finally, the existence of natural constraints and internal stress thresholds for the initiation of the stick-slip mechanism are recognized and a mixed vibration attenuation mechanism based partly on the intrinsic viscous behavior of the polymeric matrix and the stick-slip behavior of the embedded CNTs is proposed and demonstrated on a single DOF vibrating system in tension-compression.

References

[1] Koratkar N., Suhr, J., *Appl. Phys. Lett.*, **87**, (2005), 63-102.
 [2] Suhr, J., Koratkar N., Keblinski P., Ajayan P., *Nature Materials*, **4**, (2005), 134
 [3] Ajayan P., Suhr J., Koratkar N., *J. Mater. Sci.*, **41**, (2006), 7824
 [4] Rajoria H., Jalili N., *Comp. Sci. Tech.*, **65**, (2005), 2079
 [5] Zhou X., Shin E., Wang K., Bakis C., *Comp. Sci. Tech.*, **64**, (2004), 2425
 [6] Young R., Eichhorn S., Shyng Y., Davies R., *Macromolecules*, **37**, (2004), 9503
 [7] Barber A., Cohen S., Eitan A., Schadler L., Wagner H., *Adv. Mater.*, **18**(1), (2006), 83
 [8] Qian D., Dickey E., Andrews R., Rantell T., *Appl. Phys. Lett.*, **76**(20), (2000), 2868

Figures

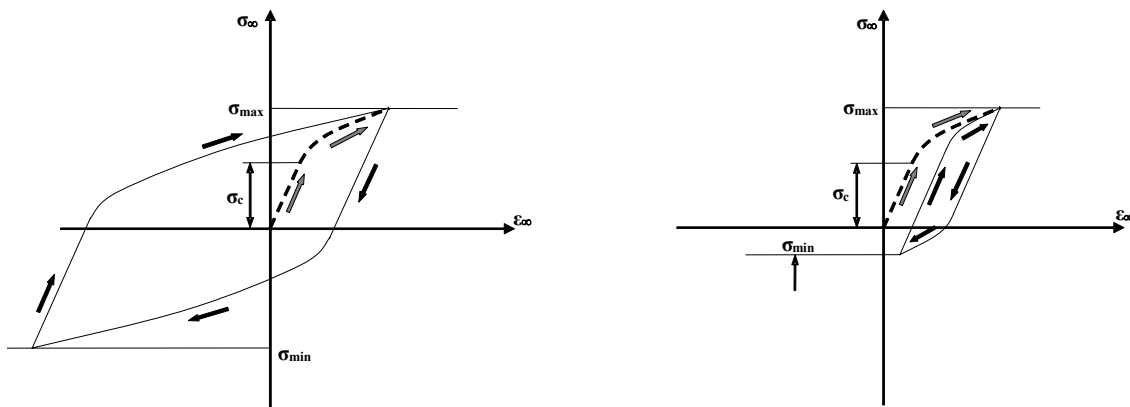


Fig. 1: Symmetrical ($|\sigma_{\max}| = |\sigma_{\min}|$) (left) and unsymmetrical ($|\sigma_{\max}| \neq |\sigma_{\min}|$) (right) loading-unloading cycle of a nanocomposite based on the stick-slip RVE model

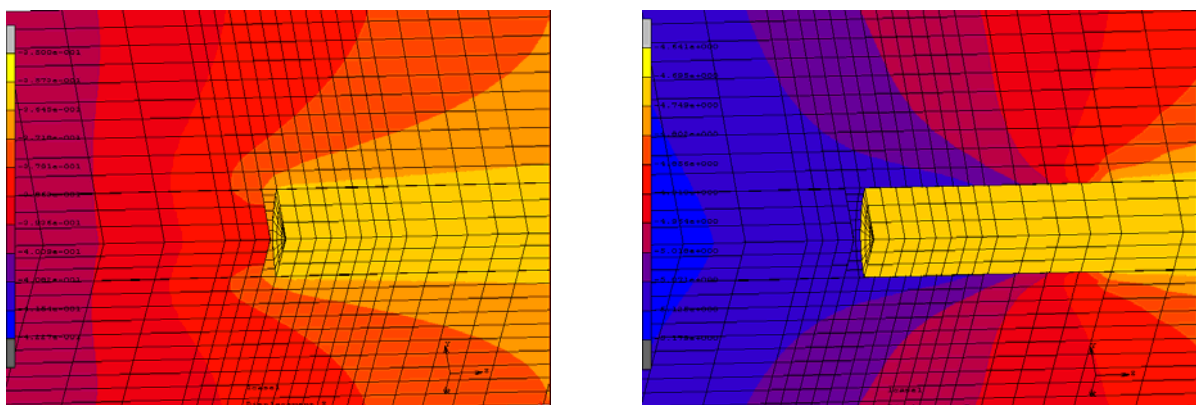


Fig. 2: Quarter-symmetrical FEA displacement plots of a CNT (yellow) inside a plastic matrix. On the left the CNT is firmly connected with the matrix ($|\sigma_{\infty}| < |\sigma_c|$), whereas on the right the CNT has slipped in the matrix ($|\sigma_{\infty}| > |\sigma_c|$)

CHANGES IN THE EQUILIBRIUM COMPONENT COMPOSITION AND SPATIAL REORIENTATION OF THE MOLECULAR COMPONENTS OF POLYMETHINE DYE LAYERS INDUCED BY PHOTO AND THERMAL EXCITATION

Anton A. Starovoytov, Elena N. Kaliteevskaya, Valentina P. Krutyakova, Tatyana K. Razumova
Saint-Petersburg State University of Information Technologies, Mechanics, and Optics,
Kronverkskiy pr., 49, St. Petersburg, Russia
Starovoytov.Anton@Gmail.com

Layers of di- and tricarbocyanine polymethine dyes were studied to evaluate the effect exerted by the molecular structure and thickness of a layer on its component composition. It was shown that the number of aggregated forms and the relative equilibrium concentration of the monomeric stereoisomers of various structures depend on the layer thickness [1], length of polymethine chain, and electron-donating ability of heterocyclic end groups (EGs). Thin layers contain cis-monomers of different structure as major form (fig. 1). The number of types of cis-isomers decreases and the relative concentration of the all-trans isomers increases with increasing thickness. As the electron-donating ability of EGs and the chain length grow, the width of the layer absorption spectrum increases owing to the increase in the number of stereoisomers of different types (fig. 2).

We studied reversible and irreversible changes in the isomer composition, change of the number of aggregated forms, and irreversible spatial reorientation of the layer components under heating and resonance photoexcitation of layer components by laser radiation [2]. The atomic force microscopy revealed surface inhomogeneities of lesser size and more smooth surface relief in the irradiated layer. The emission-excitation fluorescence spectra were studied. The stereoisomerization mechanisms at photoexcitation and heating were ascertained. The stereoisomerization rates were measured. The kinetic and energy parameters and the stereoisomerization yields of the ground- and excited-state components were estimated.

It was concluded that the equilibrium stereoisomeric composition of the layer is determined by degree of asymmetry, which is induced in the intramolecular electron density distribution by the interaction with substrate. Thermally-induced reversible changes in the component composition are due to the reversible cis \leftrightarrow all-trans stereoisomerization upon rotation of a molecule fragment around the second polymethine chain bond [3] and irreversible changes, due to the change in the asymmetry of the electron density distribution owing to irreversible spatial reorientation of layer components. The spatial reorientation of layer components is determined by all-trans \rightarrow cis stereoisomerization upon rotations around the central bonds.

We developed the energy model for rearrangement of layer by heating and photoexcitation and suggested the mathematical model for calculating changes in spatial orientation angles. To do this, we allowed for the excited-state photostereoisomerization, ground-state thermal isomerization, radiationless heating, nonlinear bleaching under the action of power radiation, and heat-conductivity processes. The model calculations of thermally- and photoinduced spatial reorientation of all-trans isomer are close to experimental values (fig. 3). It was shown that in the case of photoexcitation, the degree of rearrangement and the run of the orientation angle vs. the total excitation energy curve essentially depend on both the excited-state population and the temperature to which a layer is heated by absorbed radiation energy.

References:

[1] E. N. Kaliteevskaya, V. P. Krutyakova, T. K. Razumova, *Optics and Spectroscopy*, **97** (2004) 901–908.

[2] E. N. Kaliteevskaya, V. P. Krutyakova, T. K. Razumova, A. A. Starovoytov, Proceedings of SPIE, **6728** (2007) 68.

[3] E. N. Kaliteevskaya, V. P. Krutyakova, T. K. Razumova, Optics and Spectroscopy, **100** (2006) 300–306.

Figures:

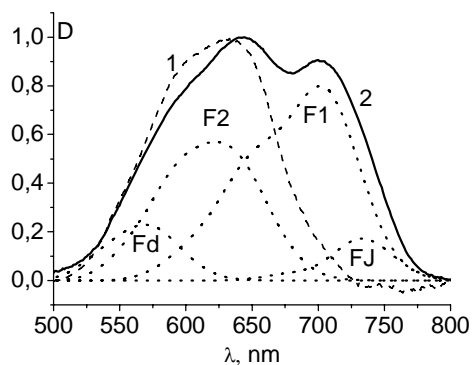


Fig 1. Normalized absorption spectra and spectra of molecular components (F1 and F2 – all-trans and cis-isomers, Fd – dimers, FJ – J-aggregates) of dicarbocyanine dye layers ($\Phi_0 = 45^\circ$). Maximum optical absorption density D_{\max} : 0.00357 (1), 0.04071 (2).

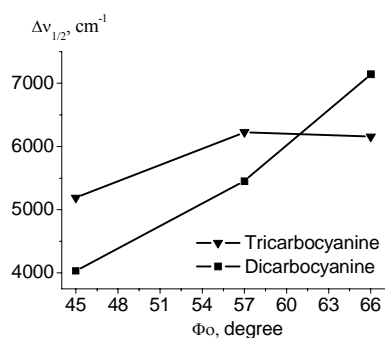


Fig 2. Half-widths of absorption spectra of molecular layer ($D_{\max} > 0.035$) vs. electron-donating ability of EGs.

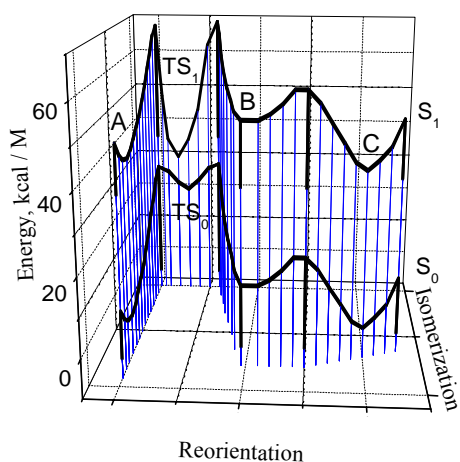


Fig. 3. The S_1 and S_0 energy level scheme for all-trans isomer at photo- and thermally induced reorientations of the angles of orientation of the layer components.

Scanning probe measurements and electromigration of metallic nanostructures under ultra-high vacuum conditions

Dominik Stöffler¹, Shawn Fostner², Peter Grütter², and Regina Hoffmann¹

1 Physikalisches Institut and DFG Center for Functional Nanostructures (CFN), Universität Karlsruhe, D-76128 Karlsruhe, Germany

2 Physics Department, McGill University, H3A-2T8 Montreal, Canada

dominik.stoeffler@pi.uka.de

With the ongoing process of miniaturization of electronic circuits, there is a growing interest to analyze the quantum effects which play an important role in metal contacts of nanometer size. Due to the small size it is desirable to characterize such nanostructures by scanning probe techniques. We use e-beam lithography as well as shadow evaporation through a stencil mask to fabricate nanobridges made of gold and other metals. The bridges are then thinned by a controlled cyclic electromigration process in ultra-high vacuum (UHV). While investigating e-beam lithography fabricated platinum structures with the scanning tunneling microscope (STM) in UHV we have discovered a tunneling voltage-dependent deposition of additional material, possibly carbon, of up to 10 nm thickness. We imaged the deposited material both with STM and with scanning electron microscopy (SEM).

To avoid such a deposition on the metallic bridges we have used scanning force microscopy in amplitude modulation mode to investigate the structures in UHV. While platinum wires need a larger voltage to start the electromigration process compared to gold, the gold wires show no fundamental difference of electromigration in UHV compared to electromigration under ambient conditions. We have obtained images with up to 3nm resolution. A slit is formed during the first thinning cycles and hillocks build up on one of the electrodes. By observing the additional modifications during further electromigration cycles we were able to determine the area where a nanocontact remains. Additionally, below $10 G_0$ ($G_0=2e^2/h$), we have observed discrete jumps of the conductance as well as telegraph noise. In conductance histograms generated from five samples, oscillations with a period slightly smaller than $1 G_0$ are observed [1]. The positions of the peaks correspond well to expected values of work-hardened gold junctions taken from literature [2] and are related to the atomic structure of the resulting gold nanocontacts. We believe that controlled electromigration enhances the probability to obtain equilibrium atomic positions compared to the mechanically controlled break junctions, because the junctions are heated to approximately 350 K.

References:

[1] R. Hoffmann et al., Appl. Phys. Lett. 93, (2008) 043118.

[2] I. K. Yanson et al., Phys. Rev. Lett. 95, (2005) 256806.

Figures:

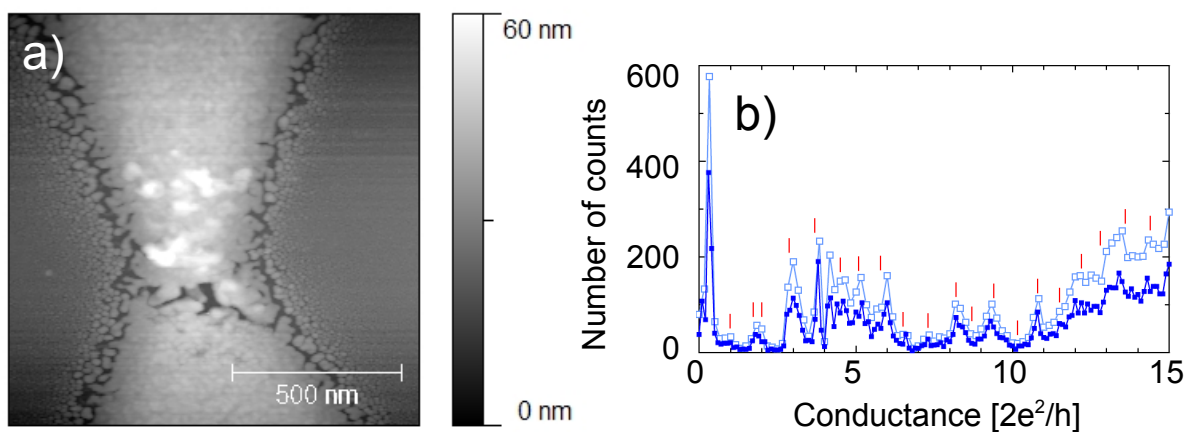


Fig. 1: a) Scanning force microscopy image of a Au nanostructure on an oxidized Si substrate after feed-back controlled electromigration. A slit has developed through the thinning process and hillocks have build up on one electrode. b) Conductance histogram obtained from five samples. Red lines mark the positions of the peaks taken from literature [2].

HIGH POWER DURABLE RESONATORS FABRICATED WITH ALUMINUM-SCANDIUM-ALLOYS

T. Sulima, R. Nuessl, I. Eisele and W. Hansch

*Institute of Physics, University of the Federal Armed Forces, Werner-Heisenberg-Weg,
85579 Neubiberg, Germany
rudolf.nuessl@unibw.de*

To investigate fatigue of aluminum-scandium (AlSc) alloys in thin films under cyclic mechanical stress, 860 MHz nano resonators with AlSc electrodes have been fabricated. The Sc content in the alloy has been varied from 0 % to 2,5 %. The resonators have been operated with heavy load at high frequencies and power durability has been determined. Devices with AlSc electrodes exhibit an increased power durability compared to conventional aluminum metallized devices. All films have been investigated by means of electron backscatter diffraction (EBSD) and atomic force microscopy (AFM) to obtain texture and grain structure. Degradation of electrodes has been visualized by scanning electron microscopy (SEM). The enhanced mechanical stress durability of electrodes fabricated with AlSc alloys is contributed to the refined grain structure in these alloys.

With higher operation frequencies and shrunked device dimensions the requirements for the power durability of SAW devices have increased rapidly. Although these devices are driven electrically they may fail mechanically. Surface acoustic waves propagating perpendicular to the electrodes of the device induce heavy cyclic stress in the metal. Thus, material fatigue depending on applied load occurs with operation time. A decrease of resonance frequency reveals a loss of electrodes stiffness which leads to device failure.

Scandium is a light metal with a density of 2,985 g/cm³. This is close to the density of aluminum (2,7 g/cm³), which makes it preferable for SAW applications. Scandium is known for improving the mechanical properties of Al, if alloyed in small concentrations. Due to its high price its use as an alloying element is limited to a small sector of applications, e.g. bicycle frames and baseball bats.

Starting with a piezoelectric substrate (LiTaO₃, 42° Y-X-Cut) four samples have been prepared with lift off technique. After a short pre-clean with O₂ plasma sample metallization has been deposited by co-evaporation of Al and Sc at ultra high vacuum conditions ($p < 10^{-9}$ mbar). Al has been evaporated by means of electron beam and Sc has been evaporated out of a high temperature effusion cell. Sc sublimates at approximately 1525 °C with a stable rate, thus flux and scandium content in the alloy have been controlled via the temperature of the cell. Sample preparation ended with a lift off step in an ultrasonic bath of acetone solution.

A measurement setup, which kept the electrical load constant while the resonance frequency decreases, has been used to determine power durability (PD). In our experiments the device failure criterion was fulfilled when the original resonance frequency was shifted by 1000 ppm, i. e. 860 kHz for our 860 MHz test devices. PD has been quantified in dB units. Pure aluminum (0 % Sc) has been defined as reference value (0 dB). This value represents the input power a device can endure until its failure criterion is reached after one hour of loading.

Results of thin film analysis by AFM and EBSD are shown in Fig. 1 and Fig. 2. The sample without scandium exhibits a grain size of 200 nm in average, as shown by the AFM measurement in Fig. 1a. Since a vertical $\langle 111 \rangle$ axis is energetically advantageous, aluminums out of plane texture is close to $\langle 111 \rangle$, as shown by the large blue areas in the EBSD map in Fig. 1b and by the inverse pole figure in Fig. 1d.

With increasing Sc content the Al grains get more refined, as shown by AFM measurements and EBSD maps in Fig. 2a and b. The orientation of the refined grains changes from $\langle 111 \rangle$

axis vertical to randomly oriented grains. AFM measurements demonstrate small grains in the samples with AlSc. The refinement of grains in AlSc alloys is contributed to the formation of Al₃Sc particles. A scandium content of 2,5 % increases PD by approximately 10 dB, as illustrated in Fig. 3. This represents an input power increase by one order of magnitude.

The decrease in resonance frequency for the AlSc devices is lower than for the pure Al devices, if the same electrical load is applied. This indicates a slower loss of electrode stiffness, i.e. a higher resistivity to mechanical stress. We contribute this to the enhanced material properties of the AlSc alloy. The improved PD, as shown in Fig. 3, can be explained by the refined grain structure of AlSc alloys. Measuring power durability we observed long aluminum extrusions out of the AlSc electrodes as operation power exceeded a certain value. These extrusions can span the gap between two electrodes (Fig. 5) and thus may lead to a short circuit. This would explain the sudden drop of resonance frequency, as shown in Fig. 4. As a result the entire device can be destroyed, as illustrated in Fig. 5d.

References:

[1] J. Roynet, "Scandium in aluminum alloys," International Material Reviews Vol. 50, 2005, pp. 19-44.
 [2] Y. Leipikh, "Strain effects in surface acoustic wave elements with a piezoelectric acoustic line and sensors based on this effect," Semiconductor Physics, Quantum electronics and optoelectronics, Vol. 3, No. 1, 2000, pp. 91-93.

Figures:

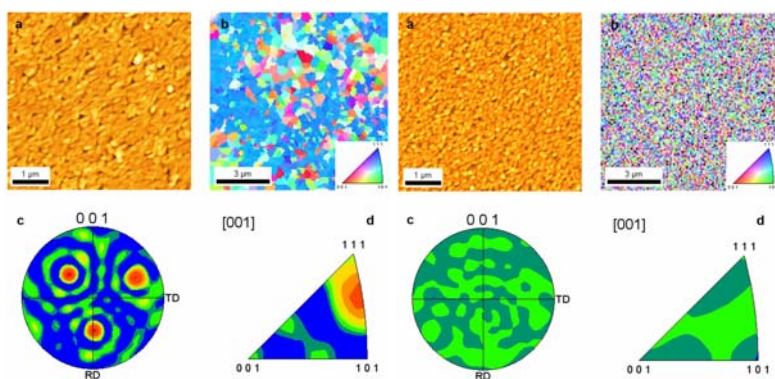


Fig. 1. Surface morphology (a), out of plane grain orientations (b) and texture (c and d) of aluminum film with no scandium deposited on blank LiTaO₃.

Fig. 2. Surface morphology (a), out of plane grain orientations (b) and texture (c and d) of aluminum film with 2,5% scandium deposited on blank LiTaO₃.

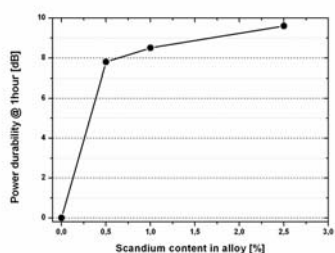


Fig. 3. Power durability versus scandium content of the test devices.

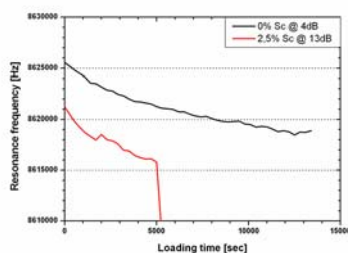


Fig. 4. Drop of resonance frequency in devices under heavy load with no scandium (black curve) and with 2,5% scandium (red curve).

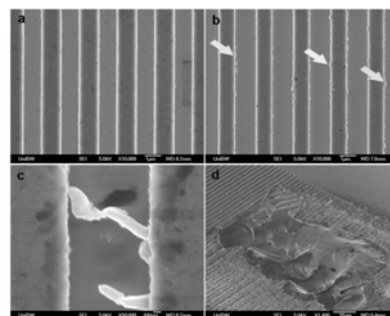


Fig. 5. Unstressed electrodes (a), formation of small hillocks at low load on pure Al electrodes (b), formation of long extrusions at high load on AlSc electrodes (c) and destroyed device after shortcircuit of electrodes (d).

A General Route to Efficient Near-Infrared Emission of Optically Active Nanozeolites

Hong-Tao Sun, Minoru Fujii

Department of Electrical and Electronic Engineering, Graduate School of Engineering, Kobe University, Rokkodai, Nada, Kobe 657-8501, Japan

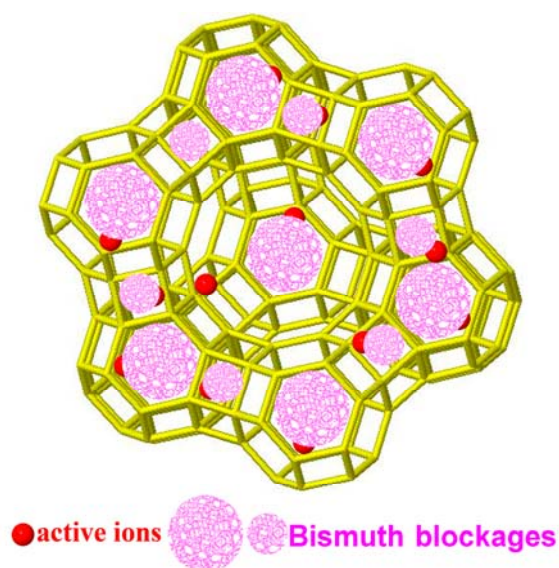
timothyhsun@gmail.com

Here we report on a facile and novel strategy to realize strong, air-stable, long-lived, near-infrared (NIR) photoluminescence (PL) from rare-earth ions and bismuth compounds embedded zeolites. This method consists of a simple ion-exchange process and subsequent high-temperature annealing under a controlled atmospheric condition. We demonstrate that `blocking` the small pores of zeolites by using bismuth compounds with low melting points is an excellent approach to realize efficient NIR emission from active centres [1] (**Figure 1**). Moreover, we found that bismuth not only acts as blocks of selectively closing down the `in-out windows` of water molecules, but as ultrabroad NIR luminescence centres if we annealed the samples in an inert atmosphere. The advantages of this finding can be summarized as follows: (i) the PL from these annealed zeolites is strong and air-stable; (ii) the quantum efficiencies of NIR emission are high in these nanomaterials; (iii) the PL displays spectral tunability by tailoring preparation parameters; (IV) The broad NIR PL with a FWHM more than 160 nm covers the whole telecommunication windows, which is much broader than those of rare-earth ions. Most importantly, herein we demonstrate that even in samples containing a large amount of water, it is possible to realize efficient NIR emission if we can effectively separate active ions from coordinated water. Owing to the peculiar optical properties of these activated zeolites and mature zeolites assembly techniques developed, we believe that it is promising for their wide applications as active media of broadly tunable micro or nano optical sources and devices.

References:

[1] H-T. Sun, T. Hasegawa, M. Fujii, F. Shimaoka, Z. Bai, M. Mizuhata, S. Hayashi, S. Deki, *Applied Physics Letters*, 94 (2009) 141106.

Figure 1: Schematic illustration of the structure of rare-earth and bismuth ions codoped zeolites annealed at high temperatures.



NANOSTRUCTURED MATERIALS DEVELOPED BY CONTROLLED ANNEALING

J. Bonastre, L. Escoda, B. Hernando, J.L. Sánchez-Llamazares*, J.J. Suñol*

P II, EPS, Campus Montilivi s/n, Girona University 17071 Girona, Spain

**Dept. Física, Univ. Oviedo, Calvo Sotelo s/n 33007 Oviedo, Spain.*

joan josep.sunyol@udg.edu

The knowledge of the crystallization kinetics of nanomaterials is important to control their structure and properties. Several authors deal with calculating the amount of transformed material during crystallization. They have led to the determination of temperature-time transformation, T-T-T, curves for the description of the isothermal crystallization reaction since the work of Uhlmann [1]. Other transformation diagram has been introduced [2] to describe non-equilibrium crystallization under continuous heating regime, namely the T-HR-T (temperature-heating rate- transformation) diagram.

Several techniques have been utilized to investigate the kinetics of crystallization processes. In particular, differential scanning calorimetry (DSC) is one of the most often applied to assess crystallization kinetics. From DSC data, several models have been developed to analyze experimental data under isothermal or continuous rate conditions. In this work, we analyze the crystallization process of several Co rich alloys by applying different models, including isoconversional methods. Once a model has been determined, one can construct the transformation diagrams [3]. Transformation diagrams permits us the selection of annealing treatments in order to develop materials with the desired nanostructure. Structural analysis is also performed by X-Ray diffraction (XRD).

Co and Fe rich alloys were investigated for applications in magnetic devices as generators, sensors, actuators and power transformers [4, 5]. The mechanical alloying is a technique that involves the synthesis of materials by high-energy ball milling and has been reported to be capable of producing non-equilibrium structures including amorphous alloys, nanostructured materials and extended solid solutions [6, 7]. The mechanical alloying of rapidly solidified flakes of metallic ribbons is a two-step procedure necessary to obtain powdered samples prior to the consolidation of complicated shape materials. For it, the mechanical alloying of melt – spun flakes of ribbons is applied as an alternative route to develop powdered alloys [8, 9]. In this work, Co rich melt-spun alloys were obtained and mechanically alloyed in low energy milling conditions, and their structure and thermal behaviour was analyzed.

A detailed knowledge of the temperature dependence of nucleation and crystalline growth results essential for nanomaterials design and to control their microstructure. In technical applications, the thermal stability of nanocrystalline alloys is a problem of fundamental interest to determine the useful working temperature ranges. The kinetics of transformation gives information relative to the stability and applicability of these materials.

Financial support from MCYT (MAT2006-13925-C02-02 and 01) and DURSI (2005-SGR00201) is acknowledged. J.B. agrees a FPI MICYT Spanish grant.

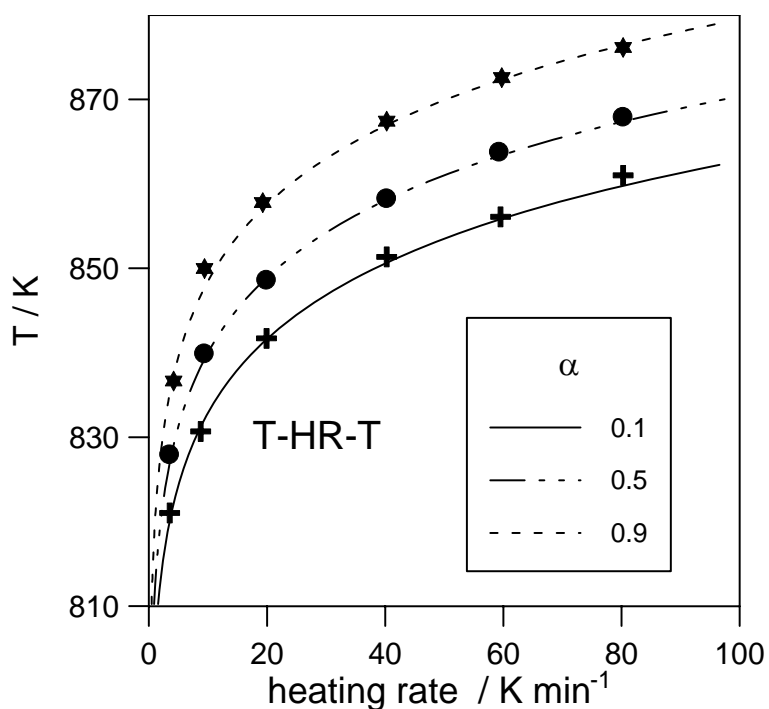
References:

[1] D.R. Uhlmann, *J. Non-Cryst. Solids*, **7** (1972) 337.

[2] S. Suriñach, M.D. Baró, J.A. Diego, N. Clavaguera, M.T. Clavaguera-Mora, *Acta Metall. Mater.* **40** (1992) 37.

- [3] J.J. Suñol, R. Berlanga, M.T. Clavaguera-Mora, N. Clavaguera, *Acta Materialia*, **50** (2002) 4783.
- [4] M.E. McHenry, M.A. Willard and D.E. Laughlin, *Progress in Materials Science* **44** (1999) 291.
- [5] R.B. Schwarz, T.D. Shen, U. Harms and T. Lillo, *J. Magn. and Magn. Mater.*, **283** (2004) 223.
- [6] C.C. Koch, *Nanostruct. Mater.* **2** (1993) 109.
- [7] J.J. Suñol, A. Gonzalez, L. Escoda, T. Pradell, M.T. Mora, N. Clavaguera, *Mater. Sci. Eng. A* **375**, 881 (2004).
- [8] B.S. Murty and S. Ranganathan, *Intern. Mater. Reviews* **43**, (1998) 101.
- [9] J. Bonastre, L. Escoda, J. Saurina, J.J. Suñol, J.D. Santos, M.L. Sánchez, B. Hernando, *J. Non-Cryst. Solids* **354** (2008) 5126.

Figure: T-HR-T diagram of the crystallization process of a Co based metallic glass. Experimental data (symbols) and isoconversional calculated curves (lines) for transformed fractions (0.1, 0.5 and 0.9).



PREPARATION OF DIFFERENT SHAPE METAL OXIDE MICRO- AND NANOSTRUCTURES BY GELATION OF OLIGOMERIC METAL ALKOXIDE CONCENTRATES

Tanel Tättē¹, Marko Part¹, Kelli Hanschmidt¹, Madis Paalo¹, Glen Kelp¹, Uno Mäeorg², Alexei E. Romanov³, Marco Natali⁴, Jonas Gurauskis⁵, Ants Lõhmus¹

¹*Institute of Physics, University of Tartu, Riia 142, 51014, Tartu, Estonia*

²*Institute of Organic and Bioorganic Chemistry, University of Tartu, Jakobi 2, 51014, Tartu, Estonia*

³*Ioffe Physico-Technical Institute, Polytechnicheskaya 26, 194021, St. Petersburg, Russia*

⁴*ICIS-CNR, Corso Stati Uniti 4, 35127 Padova, Italy*

⁵*Instituto de Ciencia de Materiales de Aragón C.S.I.C., University of Zaragoza Fac. de Ciencias, c/Pedro Cerbuna 12, 50009, Zaragoza, Spain*

tanelt@fi.tartu.ee

Metal oxide ceramics are applied in wide range of high-tech applications like temperature resistant layers, high refractive index materials, photonics, transparent electrodes, abrasives, constructing materials etc. These applications are possible due to unique extreme properties of the materials. However, complications to prepare these materials in desired shape often limit their applicability. The problems are related to nature of these materials in bulk as they rather decompose at elevated temperatures than transform to moldable melts. The problems are usually overcome by using sintering of compressed powders. The technology has found wide industrial use as it enables to prepare complicated structures at rather low cost. Unfortunately, based on microcrystalline raw materials, that method is almost useless in order to prepare defined shape microstructures.

To overcome the limitations, metal alkoxide based sol-gel technology has been taken into use. Desired final shape structures are obtained as a result of gelation of sols in suitable molds as thin films or as jets pulled into air [1]. The method has many advantages like much lower heat treatment temperatures compared to powder sintering. In addition it is easy to dope the materials with different additives. Sol-gel process is also attractive as it is easy to scale it up.

Current presentation introduces the possibilities to use novel alkoxide based oligomeric precursors in order to prepare metal oxide structures. Precursor structure is clarified by IR, NMR, SAXS, AFM and other techniques. Analyses have proved that precursors contain short sterically stabilised oligomeric particles, which define elasto-viscos flow behaviour.

Combining the chemical processing like hydrolysis and polycondensation with mechanical manipulations like jet pulling, tape casting, micromolding etc, enables us to prepare the materials in wide range of shapes in nano and micro scale like nanofibres, nanosharp needles, microstrips on the surface, microtubes, self-standing membranes and others (Figure 1) [2-3].

AFM imaging revealed that obtained structures have surface roughness no more than 1-2 nm. Microtubular structures have gas resistance up to at least 200 atm. of He pressure applied inside the tube. At least down to 2-3 μm thickness (diameter), the structures have significant waveguiding properties [4].

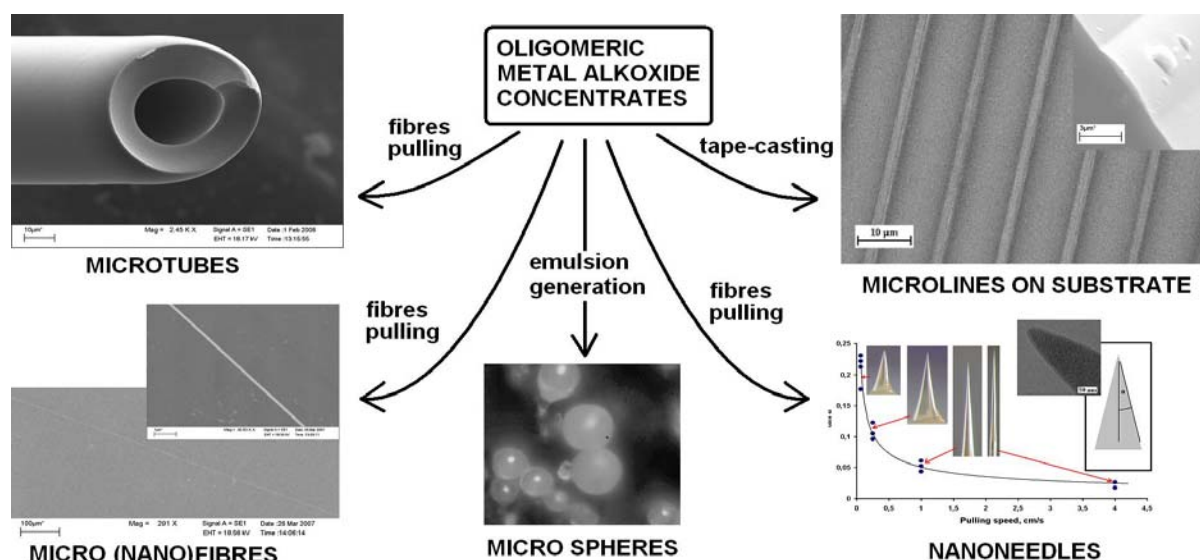


Figure 1. Different shape metal oxide structures prepared from metal alkoxide oligomeric concentrates.

This work was supported by the Estonian Science Foundation grants no 7456, 7612 and by the Estonian Nanotechnology Competence Centre.

References:

- [1] S. Sakka (Ed.), Handbook of Sol-Gel Science and Technology I-III, 2005, Springer
- [2] T. Tätte, M. Paalo, V. Kisand, V. Reedo, A. Kartushinsky, K. Saal, U. Mäeorg, A. Lõhmus, I. Kink, *Nanotechnology*, vol. **18**, p. 124501, 2007.
- [3] T. Tätte, R. Talviste, M. Paalo, A. Vorobjov, M. Part, V. Kiisk, K. Saal, A. Lõhmus, I. Kink, *NSTI Nanotech 2008*, 3 (June 1-5, 2008) 109-111.
- [4] paper in preparation

EPOXY BASED HYBRID MATERIALS USING FUNCTIONALISED ALKOXYSILANES.

J. Tenas¹, Y. R. de Miguel¹, L. Irusta², M. J. Fernández-Berridi²

*1LABEIN-Tecnalia, Centre for Nanomaterials Applications in Construction and Nanostructured and Eco-efficient Materials for Construction Unit, Associated Unit LABEIN-Tecnalia/CSIC,
Parque Tecnológico de Bizkaia. Edificio 700. C/Geldo. Derio. Spain*

*2Department of Polymer Science and Technology, University of Basque Country
Centro Joxe Mari Korta. Avda. Tolosa 72. Donostia-San Sebastián. Spain*

jtenas@labein.es

The hybridisation of epoxy resins using functionalised alkoxy silanes is an area of vast academic and industrial interest [1-3]. Previous studies [4, 5] have shown that hybridisation, in some cases, can lead to highly homogeneous materials with superior properties. However, there is still a lack of understanding of the relationship between the structure, composition, method of preparation and final material properties.

The aim of our work is to study the effect of the use of different alkoxy silane functionalities, such as amine, epoxy, phenyl, etc. upon the final properties of the materials.

In this poster, we will present selected results from DSC, TGA, DMTA, SEM and IR analysis of hybrids prepared from the following alkoxy silanes (Figure 1).

The thermal, mechanical, morphological and structural properties and the method of preparation of these materials will be discussed with reference to the functionalities used in each case.

References:

- [1] Judeinstein, P; Sanchez, C. J. Mater. Chem., **6** (1996), 511 – 525
- [2] Lu, S; Zhang, H.; Zhao, C.; Wang, X. J Mater. Sci., **40** (2005), 1079-1085
- [3] Matejka, L; Dušek, K; Pleštil, J; Kříž, J; Lednický, F. Polymer , **40** (1998), 171-181
- [4] Prezzi, L.; Mascia, L. Adv. Polym Tech, **24** (2005), 91-102
- [5] Ochi, M; Takahashi, R. J. Polym. Sci. Pol. Phys, **39** (2001), 1071-1084

Figures:

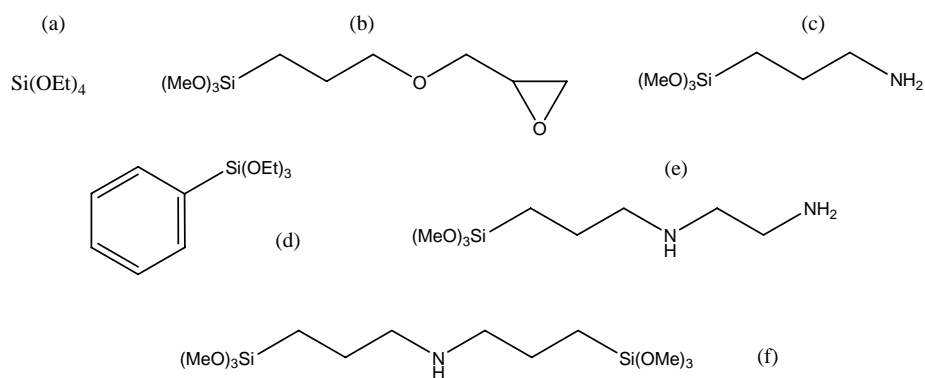


Figure 1: a) TEOS; b) (3-Glycidyloxypropyl)trimethoxysilane; c) (3-Aminopropyl)triethoxysilane; d) Phenyltriethoxysilane; e) N-[3-(Trimethoxysilyl)propyl]ethylenediamine; f) Bis[3-(trimethoxysilyl)propyl]amine

CNT Forest Growth on Tungsten Wire for X-Ray Cathode to enhance electron emission capabilities.

Bernat Terrés-Güerri^{*, a, b}, Hye Jin Park^{a, b}, Núria Ferrer-Anglada^{a, c}, Viera Skakalova^{a, b},
Siegmar Roth^{a, b}

^a *Max-Planck-Institut für Festkörperforschung, Heisenbergstraße 1, D-70569 Stuttgart, Germany*

^b *SinEurop Nanotech GmbH, Kernerstr. 34, 70182 Stuttgart, Germany*

^c *Applied Physics Dept. U. Politècnica de Catalunya, J. Girona 3-5, 08034 Barcelona, Spain*

* *Corresponding author: bernat.terres@gmail.com*

Keywords: carbon nanotubes, electron emission, cathode, X-Ray, CNT growth, Tungsten.

Abstract

The benefit of using Carbon Nanotube field emission properties is an attractive feature for several electronic devices. This research focuses on the use of Carbon Nanotubes to improve the electron emission properties of the Tungsten (W) wires commonly used in X-Ray diffraction devices. Grown by CVD along the Tungsten cathode, forest formations of Carbon Nanotubes lead to a better thermionic electron emission and even allow the cold extraction of the electrons. We have tested and discussed different concentrations as well as different orientations of the CNT over the Tungsten wires. All cathodes were systematically evaluated and conditioned in a vacuum chamber. The CNT growth mechanism and the measurements are provided.

References

1. W. Wongwiriyan, S. Honda, T. Mizuta, T. Ohmori, Japanese Journal of Applied Physics Vol. 45, No. 3A, pp. 1880–1882 (2006).
2. H. Sato, K. Hata, K. Kajiwara and Y. Saito, IEEE, 10.1109/IVNC.2007.4480989 (2007).

**NANOSCALE MECHANISMS FOR MONOLAYER SELF-HEALING VIA
EXCESS INK TRAPPING IN MICROCONTACT PRINTING**

Greg Gannon, J Andreas Larsson, James C Greer and Damien Thompson

Tyndall National Institute, University College Cork
Cork (Ireland)

The control and fine-tuning of surface diffusion is of considerable interest in the nanotechnology community and is a key parameter in the further development of nanopatterning techniques including dip pen nanolithography, high-speed microcontact printing (μ CP), edge spreading lithography and microdisplacement printing. We focus on characterizing the influence of naturally-occurring surface defects on the diffusion, or “spreading”, of hexadecanethiol “ink” molecules in μ CP using hexadecanethiol self-assembled monolayers (SAMs) on gold. Our massively-parallelized molecular simulations permit long ten nanosecond-plus simulations, yielding steady state structures and statistics for system sizes on the order of 10^6 atoms. Simulations reveal how the molecular assembly prerequisite for monolayer healing and growth can occur via “trapping” of excess ink molecules by interfacial domain boundary regions in the self-assembling monolayer; these naturally-occurring domain boundaries act as diffusion barriers. This new data on the nanoscale mechanisms of SAM self-healing and self-limiting ink spreading will aid the identification of optimum processing conditions for μ CP and serves as a further illustration of the power of large-scale molecular simulations to complement and deepen experimental knowledge for directed “bottom up” molecular assembly, specifically the optimization of nanopatterning using self-assembly and molecular recognition.

Elaboration and growth study of epitaxial SnO₂ thin films deposited on (0001) Al₂O₃ substrates by sol-gel process

E. Thune, W. Hamd, A. Boule, R. Guinebretière

Laboratoire Sciences des Procédés Céramiques et de Traitements de Surface
SPCTS, UMR CNRS 6638
ENSCI, 47 Avenue Albert Thomas, 87065 Limoges Cedex, France

In the form of thin films, SnO₂ finds applications as gas sensors, solar cells and transparent electrodes. The application of SnO₂ for functional wide bandgap semiconductors requires highly crystalline epitaxial films [1]. Since SnO₂ is unstable at high temperatures, the preparation of epitaxial SnO₂ thin layers requires a careful optimisation of processing temperature. Moreover, in the case of sol-gel processing of thin films, post-deposition thermal annealing induces the film islanding and the exaggerated growth of those islands having the lowest interfacial energy [2].

In this communication, we present the elaboration and the microstructural characterization of SnO₂ films prepared from two different tin oxide precursor solutions: tin (IV) isopropoxide Sn(OC₃H₇)₄ in a mixed solvent (toluene + isopropanol) and an alcoholic solution of modified SnCl₂·2H₂O. The thin films were grown by dip-coating on (0001) sapphire substrates. After drying, a first thermal treatment at medium temperature induces the crystallization of tin oxide. High temperature treatment induces grain growth and the formation of textured films. The microstructure of both polycrystalline and textured films has been studied by conventional and high resolution XRD, AFM and TEM.

[1] L.C. Tien, D.P. Norton, J.D. Budai, *Mat Res Bul*, **2009**, 44, 6-10.

[2] R. Bachelet, S. Cottrino, G. Nahélou, V. Coudert, A. Boule, B. Soulestin, F. Rossignol, R. Guinebretière, *Nanotechnology*, **2007**, 18, 015301 (9 pages).

NANOSTRUCTURED SAPPHIRE VICINAL SURFACES AS TEMPLATES FOR THE GROWTH OF SELF-ORGANIZED OXIDE NANOSTRUCTURES

E. Thune, A. Boulle, W. Hamd, D. Babonneau, A. Fakih, C. Moquin, R. Guinebretière

Laboratoire Sciences des Procédés Céramiques et de Traitements de Surface
SPCTS, UMR CNRS 6638
ENSCI, 47-73 Avenue Albert Thomas, 87065 Limoges Cedex, France

Nanostructured systems based on heteroepitaxial islands (noble metals, transition magnetic metals, functional oxides, etc.) grown onto oxide surfaces (MgO, ZnO, Al₂O₃, etc.) are attracting intensive interest due to both the fundamental significance and potential application in optics, electronics, spintronics, and magnetic data storage. In such nanosystems, the control of the atomic structure, the shape, and the size of the islands is of prime importance in determining the overall physical properties. In addition, many of the applications so far envisaged also require precise arrangement of these structures into ordered arrays.

In the present work, we aim at producing self-organized nanostructures in a two-step process. The first step consists in the preparation of suitable templates by thermally activated surface diffusion on vicinal surface of oxide single-crystals. Such templates should be chemically and structurally stable over long periods of time and in various environments (air, vacuum, high temperatures...) so as to be compatible with various deposition processes. In the second step, nanoparticles will be grown on these templates using different techniques (sol-gel, chemical vapor deposition (CVD) and sputtering).

Vicinal substrates of sapphire with miscut angle of 5 and 10° from the (001) planes towards the [110] direction have been annealed in air or in Ar atmosphere in the range from 1000 to 1500 °C. The behaviour of these surfaces has been characterized as a function of the temperature, the thermal treatment time, and the thermal annealing atmosphere by Atomic Force Microscopy observations.

A thermal treatment at 1250 °C allows to stabilize a surface made of periodically spaced nanosized step-bunches. Such stepped surfaces were used as template to grow self-patterned epitaxial oxide nanoparticles by thermal annealing of yttria-stabilized zirconia thin films produced by sol-gel dip-coating. Grazing Incidence Small Angle X-ray Scattering and High-Resolution Transmission Electron Microscopy were used to study the morphology of the nanoparticles and their epitaxial relationships with the substrate.

Effect of Zn addition on optical properties and microstructure of Y₂O₃:Eu nanopowders by solution combustion method

Esmail Tohidlou¹, Yadolah Ganjkanlou², Mahmood Kazemzad², Mehdi Shafii¹
 1-University of Sistan and Baluchestan, P.O.BOX: 9816745563-161, Zahedan, Iran
 2-Materials and Energy Research Center, P.O. BOX: 31787- 316, Tehran, Iran
etohidloo@yahoo.com, yadolah1@gmail.com, kazemzad@gmail.com,
shafieeafarani@gmail.com

Eu doped Y₂O₃ phosphors have been studied as potential red phosphors for applications in field emission displays, cathode ray tube phosphors, three color lamps and etc [1]. The chemical and thermal stability of Y₂O₃:Eu are higher than sulfide based phosphors such as Y₂O₂SO₄:Eu [2-4]. It has also higher quantum efficiency and stability against high current densities, but unfavorable chromaticity and conductivity of this compound decrease the cathodoluminescence intensity and result in limited application for this compound [3]. These limitations can be overcome by addition of zinc to the Y₂O₃:Eu phosphor. Zinc is usually added to the surface of phosphors (dead layer) in order to increase their conductivity and cathodoluminescence intensity [2]. But results of this study showed that doping Zn at the structure improves the chromaticity and photoluminescence intensity [2, 3].

In this work, three samples with chemical composition of Y₂O₃:Eu(3%) [Sample A], Y₂O₃:Eu(3%),Zn(2.5%) [Sample B], Y₂O₃:Eu(3%),Zn(2.5%) (Zn was added only at surface) [Sample C] were synthesized by multistep urea solution combustion method.

Investigation of these samples by XRD (Fig. 1) and photoluminescence analysis methods (Fig. 2) showed that, addition of zinc at the structure of phosphors instead of surface, enhances the photoluminescence intensity as well as red color chromaticity (Fig. 3). Moreover, SEM images (Fig. 4) and micro-structural and crystallographic parameters, determined by Rietveld refinement method, revealed that sample C has lower crystallinity. This confirms that doping of Zn in Structure of Y₂O₃:Eu (Sample B) is more effective than addition of Zn only at the surface. It is originated from grain growth inhibition caused by zinc oxide accumulated on the surface (sample C).

References:

- [1] S. Ekambaram, K.C. Patil, M. Maaza, Journal of Alloys and Compounds, **393** (2005) 81-92.
- [2] S.H. Shin, J.H. Kang, D.Y. Jeon, S.H. Choi, S.H. Lee, Y.C. You, D.S. Zang, Solid State Communications, **135** (2005) 30-33.
- [3] S. Sakumaa, H. Kominami, Y. Neob, T. Aoki, Y. Nakanishi, H. Mimura, Applied Surface Science, **244** (2005) 458-460.
- [4] K.Y. Jung, K.H. Han, Y.S. Ko, Journal of Luminescence, **127** (2007) 391-396.

Figures:

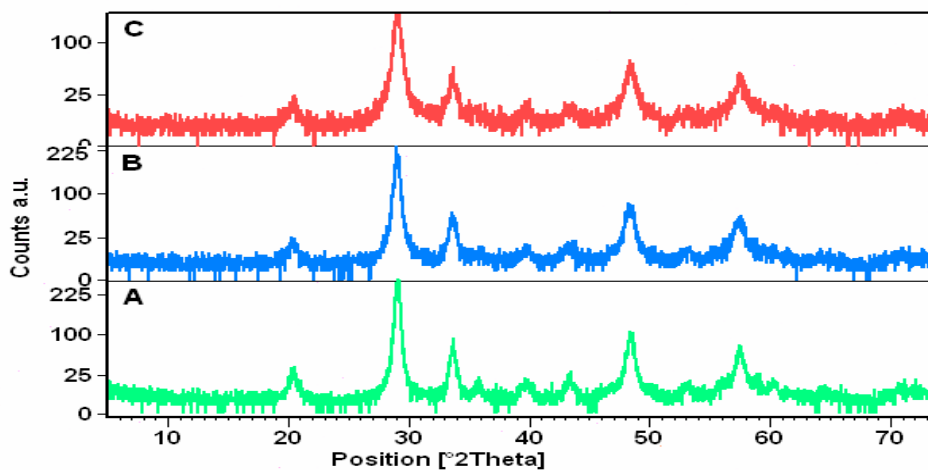


Fig.1 XRD of all samples

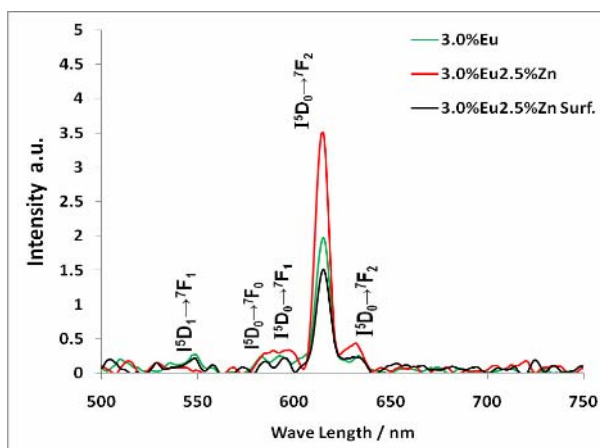


Fig.2 photoluminescence spectra of all samples

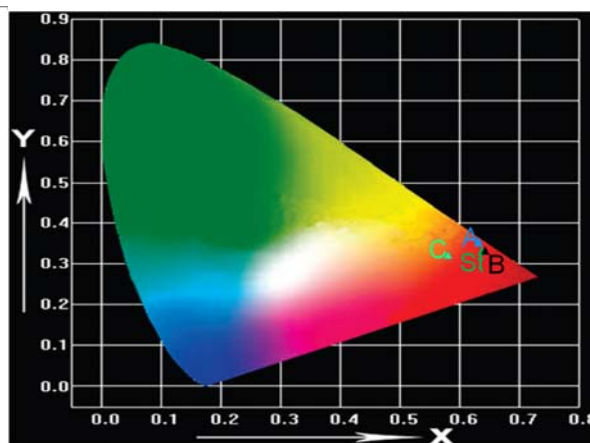


Fig.3 Chromaticity of various sample

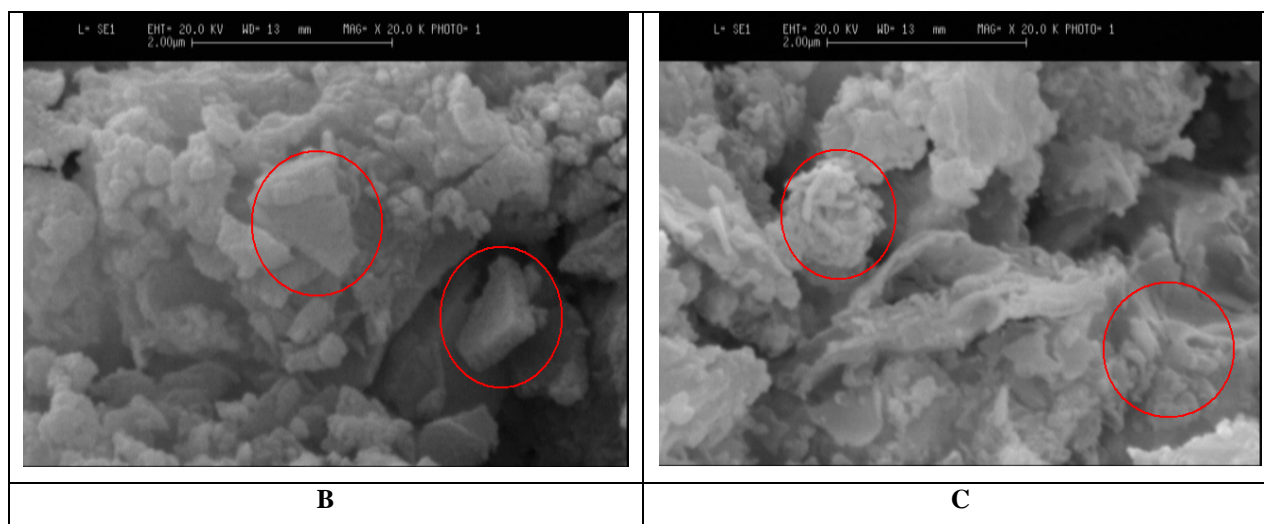


Fig.4 SEM image of sample B and C

PROPERTIES OF FULLERITE AND OTHER SYMMETRIC FORMS OF CARBON

Francisco Torrens, Gloria Castellano

Institut Universitari de Ciència Molecular, Universitat de València, Edifici d'Instituts de Paterna, P. O. Box 22085, 46071, and Instituto Universitario de Medio Ambiente y Ciencias Marinas, Universidad Católica de Valencia San Vicente Mártir, 46003, València, Spain

Country

francisco.torrens@uv.es

Fullerene–nanotube peculiarities show up in that these systems represent the only soluble forms of carbon, what is related to their molecular structures. The phenomena are explained in the *bundlet* model, in which the free energy of a nanotube in a cluster is combined from two components: a volume one proportional to the number of molecules n in a cluster and a surface one to $n^{1/2}$. Growth mechanisms of fractal clusters in fullerene solutions are analyzed with similarity laws, determining the thermodynamic characteristics of fullerite crystals, in accordance with which the dimensionless Debye temperatures for all crystals belonging to the considered class should be close. Debye temperatures are determined by a similarity relation from experiments–estimations. Fullerite Debye temperature is twice that for inert-gas crystals because, near the Debye temperature, the fullerite crystal is orientationally ordered so that its structure is dissimilar to face-centred cubic. A fullerene molecule, whose thermal rotation is frozen, cannot be considered as a spherically symmetric particle. The fulfilment of the similarity laws, which are valuable for particles with spherically symmetric interaction potential, would hardly be expected. The *hierarchical splits graph* (HSG) for {Ne,Ar,Kr,Xe,C₆₀} (Fig. 1) reveals conflicting relations between pairs Ne–Ar, Ne–Kr, Ne–C₆₀, Ar–Kr and Ar–C₆₀ because of interdependences, indicating spurious relations resulting from base-composition effects. The HSG is in general agreement with the partial correlation diagram, dendrogram, radial tree, splits graph and their hierarchical versions. In *hierarchical principal component analysis* (HPCA) similar properties are replaced by their corresponding PCA factor. The F_1 explains 99.97% of the variance, F_{1-2} 100.00%, *etc.* The most important result is that Ne (class 1, $0 > F_1 > F_2$, Fig. 2 *left*) is detached from Ar ($F_1 \gg F_2$, *bottom*), which joins {Kr,Xe} in class 2 in agreement with hierarchical correlation analysis, HCA and splits graph. Provisional conclusions follow. (1) Many open questions remain regarding the behaviour of the electronic structural quantities (HOMO, LUMO, electronic density, electronic correlation and exchange, aromaticity, *etc.*), as well as developing the more intimate relation between the nanotube bonding and their symmetry in their growth, as well as in their diffusion process. (2) Experimental exploration is necessary for establishing a cluster nature of SWNT solubility. The infrared absorption spectra of an SWNT solution at various temperatures can be analyzed; the dependence will indicate the presence of SWNT clusters. According to Raoult's law, the saturation vapour pressure of a solvent above solution differs from the one above a pure solvent, by value proportional to concentration of solute particles. Solvent vapour flow, determined by pressure difference, enables dependence of solute particle concentration: a nonlinear dependence will indicate SWNT clusters in solution. (3) In accordance with the similarity laws, the dimensionless Debye temperatures for all crystals belonging to the considered class should be close. Debye temperatures are determined by similarity relation from experiments–estimations. Fullerite Debye temperature is twice that for inert-gas crystals because, near the Debye temperature, the crystal is orientationally ordered, so that its structure is dissimilar to face-centred cubic.

References:

- [1] F. Torrens and G. Castellano, *Comput. Lett.*, **1** (2005) 331.
- [2] F. Torrens and G. Castellano, *Curr. Res. Nanotechn.*, **1** (2007) 1.
- [3] F. Torrens and G. Castellano, *Microelectron. J.*, **38** (2007) 1109.
- [4] F. Torrens and G. Castellano, *J. Comput. Theor. Nanosci.*, **4** (2007) 588.
- [5] F. Torrens and G. Castellano, *Nanoscale Res. Lett.*, **2** (2007) 337.

Figures:

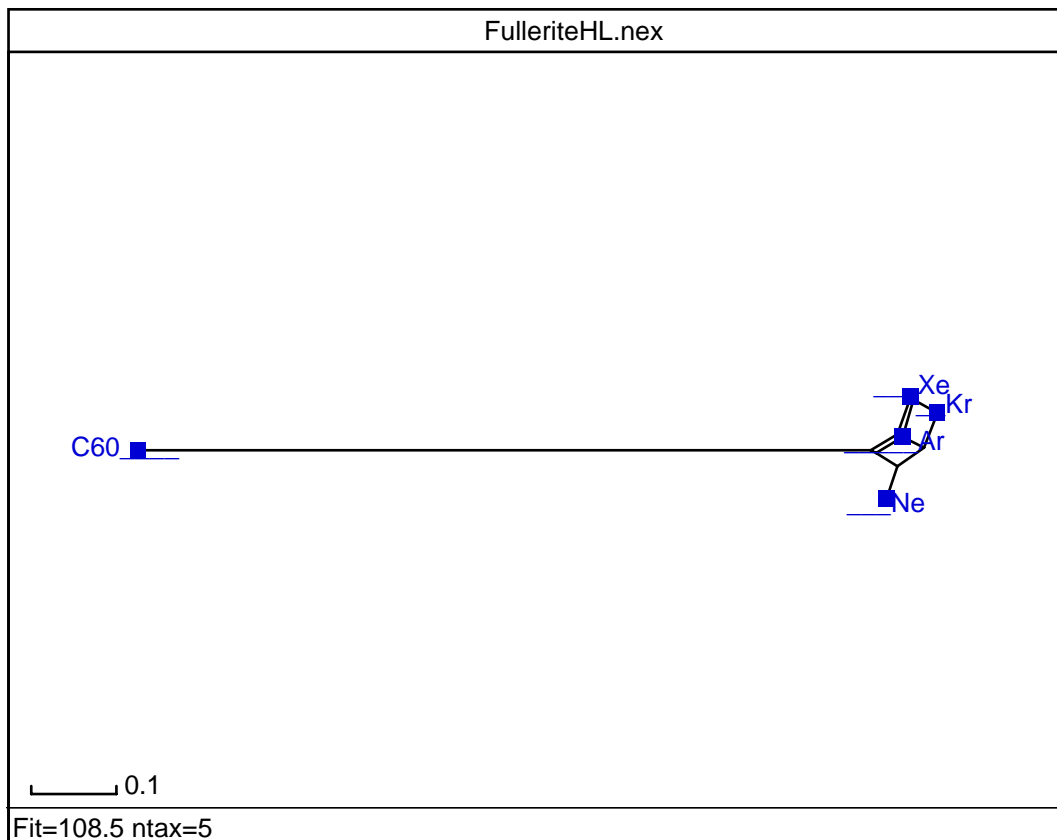


Fig. 1. Hierarchical splits graph for inert-gas/ C_{60} crystals with regard to properties.

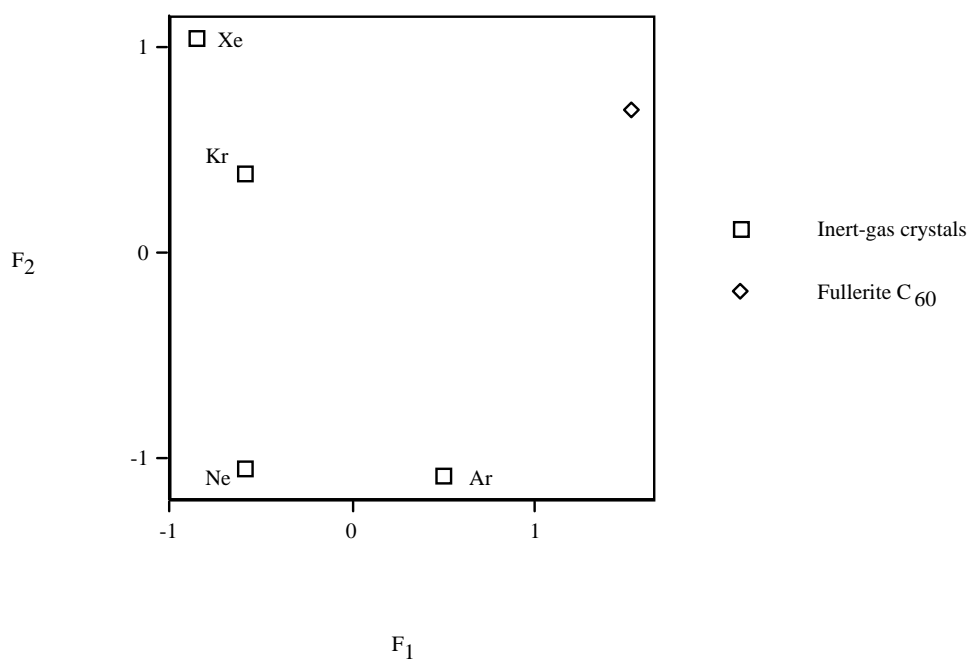


Fig. 2. Hierarchical PCA F_2 - F_1 plot for properties of inert-gas/fullerite crystals.

FABRICATION AND CHARACTERIZATION OF WELL-ORDERED MONO AND MULTILAYER LANGMUIR-BLODGETT FILMS INCORPORATING ZINC PHTHALOCYANINES

J. Torrent-Burgués^{1,3}, P. Cea², I. Giner², E. Guaus¹

¹*Departamento de Ingeniería Química, Universitat Politècnica de Catalunya, 08222 Terrassa (Barcelona), Spain*

²*Departamento de Química Orgánica-Química Física, e Instituto de Nanociencia de Aragón (INA) Universidad de Zaragoza, 50009, Zaragoza, Spain.*

³*Institut de Bioenginyeria de Catalunya (IBEC), 08028 Barcelona, Spain.*

juan.torrent@upc.edu

Phthalocyanines (Pc) and metallo-phthalocyanines (MPc) have been used for many years as blue and green dyes, but recently they have also been investigated due to their applications as catalysts, chemical sensors, photosensitizers, and in electronic and photonic technologies. In particular, zinc phthalocyanines (ZnPc) had initially received less attention but recent investigations target on their use in photodynamic therapy. These applications usually require a thin film deposited on a solid substrate. Studies in Langmuir-Blodgett (LB) films of MPc are important in understanding of interfacial spectroscopic processes occurring in organic solid materials deposited on inorganic solid substrates for further developing of photovoltaics and optoelectronic devices.

In this work we report the fabrication of Langmuir and LB films of a substituted ZnPc (octakis(oxyoctyl)phthalocyanine of zinc, Figure 1B), and their characterization by means of several techniques including surface pressure (π -A) and surface potential (ΔV -A) isotherms as well as UV-Vis Reflection spectroscopy and Brewster Angle Microscopy (BAM) for the films at the air-water interface together with UV-Vis absorption and FTIR spectroscopies, Atomic Force Microscopy (AFM) and cyclic voltammetry for the LB films.

The π -A and ΔV -A isotherms and BAM images indicate a phase transition at a surface pressure of ca. 9 mN/m, a multilayer formation at surface pressures around 19-20 mN/m, and at a surface pressure around 27 mN/m a disordered collapse of the film occurs. In addition, AFM images of LB films at $\pi=10$ and $\pi=20$ show a monomolecular and multilayer film, respectively. The comparison of the UV-Vis spectra of ZnPc in solution, the reflection spectra of the Langmuir films and UV-Vis spectra of LB films reveals a significant reduction in the Q band intensity for the films (Figure 1A), indicative of a preferential orientation of ZnPc in the Langmuir and LB films versus the random distribution in solution. The LB films of this substituted ZnPc show different reduction and oxidation waves as is shown in Figure 2. The oxidation and reduction peaks I_o and I_r , respectively, are correlated with the redox process Pc^2/Pc^{-1} . The reduction peaks II_r and III_r and the oxidation peak II_o , are correlated with the processes Pc^{-2}/Pc^{-3} and Pc^{-3}/Pc^{-4} . The different processes show an irreversible behaviour.

Acknowledgements

The authors are grateful for financial assistance from Ministerio de Educación y Ciencia (MEC) from Spain and fondos FEDER in the framework of the projects CTQ2006-05236 and CTQ2007-68101-C02-02 as well as to DGA for its support through the interdisciplinary project PM079/2006. I.G. acknowledges his DGA pre-doctoral grant.

Figures:

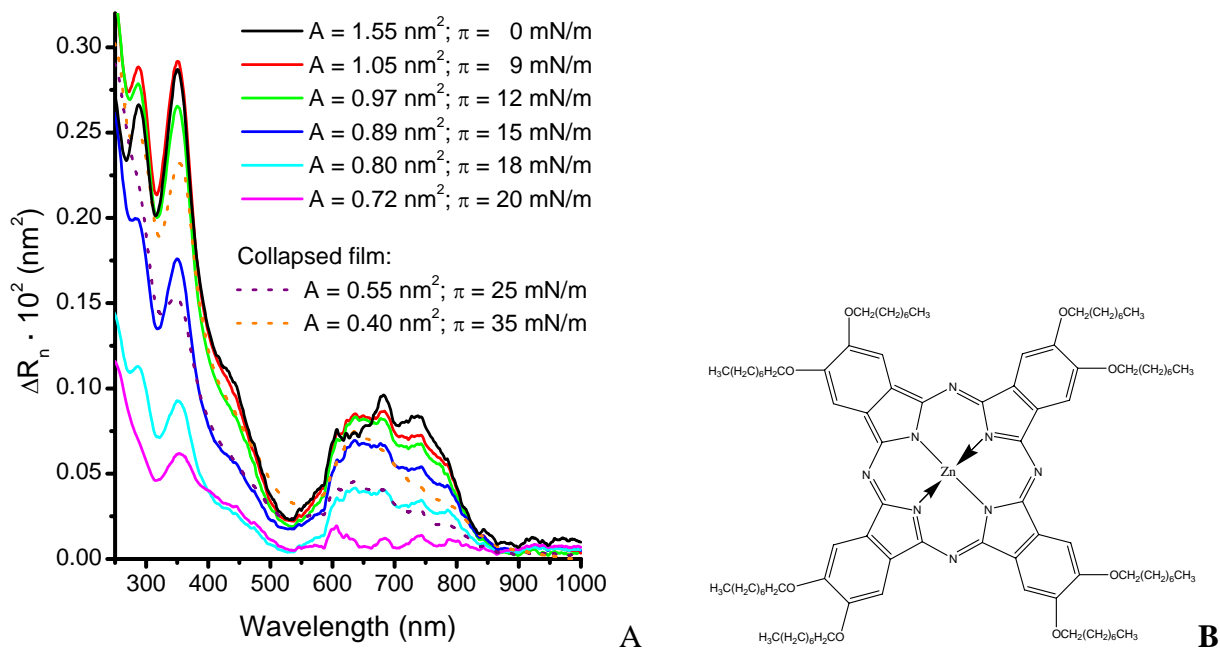


Figure 1. A) Normalized UV-vis Reflection spectra of ZnPc Langmuir films recorded upon the compression process at the indicated areas per molecule and surface pressures. B) Chemical structure of octakis(oxyoctyl)phthalocyanine of zinc, abbreviated as ZnPc in this contribution.

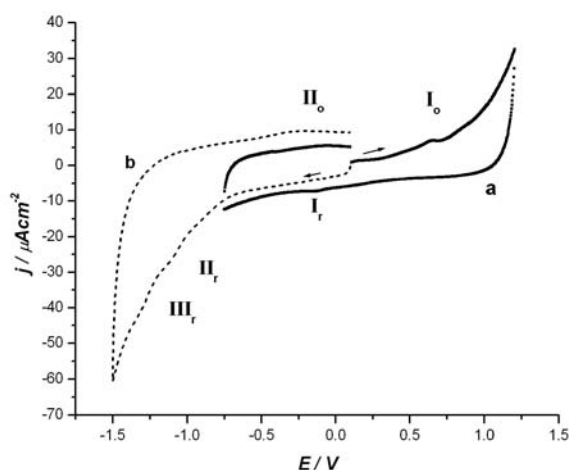


Figure 2. Cyclic voltammograms of a GCE modified with a LB film of ZnPc in a 0.1 M NaClO_4 solution, scanning toward: a) anodic potentials; b) cathodic potentials.

Silicon microcantilevers with MOSFET detection

Giordano Tosolini^a, Guillermo Villanueva^b, Francesc Perez-Murano^a, Joan Bausells^a

^aInsto. de Microelectronica de Barcelona,IMB-CNM (CSIC), 08193 Bellaterra, Spain

^bCalifornia Institute of Technology, 91125 Pasadena, CA, USA

joan.bausells@imb-cnm.csic.es

Silicon microcantilevers, originally developed for atomic force microscopy, are increasingly used in biochemical sensing [1]. Commonly, the detection of the cantilever deflection involves optical transduction which presents a very low noise but has some associated problems, e.g. integration, parallel detection and use in opaque fluids. One alternative is piezoresistive transduction that can be achieved either by embedding a resistor [2] or a MOSFET [3] as transducing element. Historically, resistors have been more used than MOSFET mainly because their simpler fabrication, but MOSFET-based stress detectors offer improved performances, compared to the piezoresistance-based ones, due to their sensitivity to local stress at the channel surface and their better noise properties.

MOSFET-based cantilevers have long been used in MEMS, and only very recently for biomolecular sensing [4] to detect surface stress caused by molecular binding to the cantilever surface. We choose a different approach for the biomolecule detection, based on the detection of intermolecular binding forces between a functionalized cantilever tip and a functionalized surface [5], and therefore propose a novel device design. In our case the cantilevers are supported by two legs to reduce the stiffness, and are oriented in the non standard $\langle 100 \rangle$ direction to optimize the piezoresistive properties improving these ways the force sensitivity.

The devices have been fabricated on (100) SOI wafers with the active layer thickness of 340 nm. The procedure uses common micromachining techniques, DRIE to free the cantilever and counts 6 photolithographic steps (Fig. 1). Two MOSFETs in series are fabricated using As implantation for source and drain with the channel and the cantilever aligned on $\langle 100 \rangle$ direction, i.e. rotated 45° respect to the wafer flat. The $\langle 100 \rangle$ longitudinal piezoresistive coefficient for N-type conduction is higher than the normally used $\langle 110 \rangle$ orientation for P-type [6]. This also results in a lower spring constant due to the lower Young modulus of silicon in this direction. Every chip consists of a couple of identical cantilevers (Fig. 2), with a width of 24 μm and a leg width of 10 μm (channel length $L_{\text{CH}}=10$ or 20 μm and width $W_{\text{CH}}=4$ μm , cantilever length $L=200$ or 400 μm and theoretical spring constant of around 4 and 0.4 mN/m respectively).

We report the electrical characteristics, I_D/V_D , of the transistors ($L_{\text{CH}}=10$ μm) for different gate voltages V_G (Fig. 3). For this purpose a semiautomatic probe system Karl Suss PA200 and a semiconductor parameter analyzer HP4155 were used. The transistor characteristics present small deviations inside the chip and a standard deviation between 6% and 12% on wafer. The electromechanical characteristics of the cantilevers ($L=200$ μm) were obtained by using an AFM probe to deflect them, as described in [7]. The output voltage, V_0 , (Fig. 4) was recorded continuously as a function of the cantilever deflection, Δz , for both movements downwards and upwards after amplification and one filter stage. The results (Fig. 5) are the average of 25 measurements. The measured displacement sensitivity is $\Delta V/\Delta z = 2.46$ V/ μm and the relative estimated force sensitivity for an applied force, F , at the end of the cantilever is $\Delta V/F = 25$ $\mu\text{V/pN}$. The total noise of the circuit was calculated integrating the power spectral density measured, between 0.1 Hz and 10 kHz, by a dynamic signal analyzer (SR785) yielding a value of 1.4 mV. With these values the minimum detectable force is 56 pN ($F_{\text{min}}=V_{\text{noise}}/(\Delta V/F)$). This result is very promising and suggests that it is possible to achieve a resolution of around 20 pN for the system for an optimized thickness ($V_G=3\text{V}$, $V_D=5\text{V}$, $V_S=1\text{V}$).

References:

- [1] N.V. Lavrik, M.J. Sepaniak, P.G. Datskos, Review of Scientific Instruments 75 (2004) 2229-2253
- [2] M. Tortonese, R.C. Barrett, C.F. Quate, Appl. Phys. Letters 62 (1993) 834-836
- [3] Akiyama et al, J.Vac. Sci. Technol. B 18(6) (2000) 2669-2675
- [4] G. Shekawat, S.-H. Tark, V.P. Dravid, Science 311 (2006) 1592-1595.
- [5] M. Rief, F. Oesterhelt, B. Heymann, H.E. Gaub, Science 275 (1997) 1295-1297.
- [6] Y. Kanda, Sensors and Actuators A 28 (1991) 83-91.
- [7] G. Villanueva, J. Montserrat, F. Pérez-Murano, G. Rius, J. Bausells, Microelec. Eng. 73-74 (2004) 480-486.

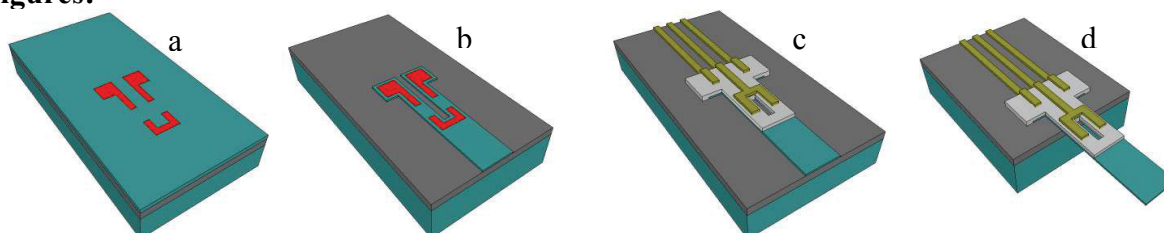
Figures:

Figure 1: Different steps of the technological process: a) implantation, b) definition of the cantilever, c) windows and gates definition, d) metallization, DRIE and cantilever release.

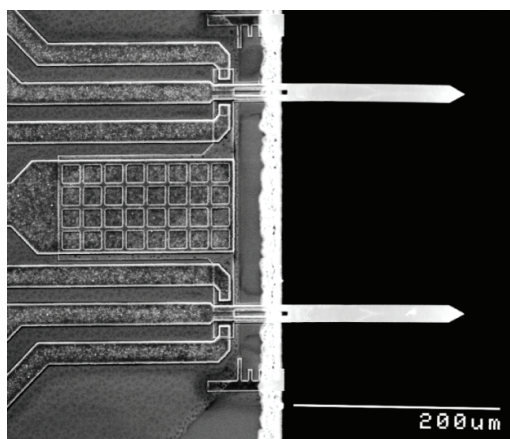


Figure 2: SEM image of a part of the chip with a pair of identical MOSFET cantilevers

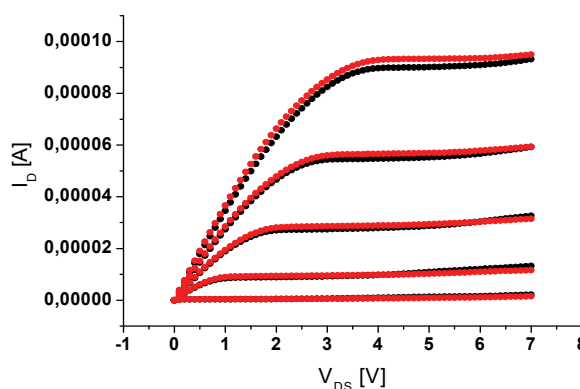


Figure 3: Electrical characteristics of the two MOSFETs on a chip ($V_G = 0V \div 4V$)

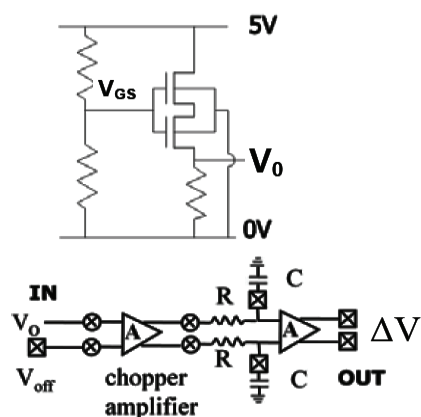


Figure 4: Electronic setup used for the measurement of the electromechanical behaviour of the cantilevers (ampl. = 630)

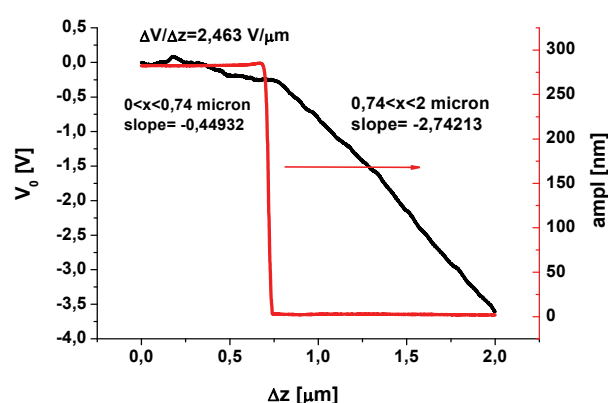


Figure 5: Electromechanical response (ΔV) of the cantilever against cantilever deflection (black) produced by a stiff AFM probe (20 N/m). In red the oscillation amplitude of the AFM probe used to determine the contact point.

EPITAXIAL GROWTH OF ORGANIC NANOCRYSTALS WITH ANTIFERROELECTRICAL STACKING

Marta Trelka¹, Anais Medina¹, David Écija¹, Christian Urban¹, Christian Claessens¹, Roberto Otero^{1,3}, JoseMaria Gallego², Tomas Torres¹ and Rodolfo Miranda^{1,3}

¹Universidad Autonoma de Madrid, Facultad de Ciencias Cantoblanco 28049, Madrid, Spain
²ICMM-CSIC, Madrid, Spain, ³IMDEA Nanociencia, Madrid, Spain

marta.trelka@uam.es

Organic nanoparticles display size-dependent absorption and fluorescence bands and single photon emission. The detailed understanding of these effects is hindered by the difficulty in the synthesis of organic nanocrystals, i.e. organic nanoparticles with an ordered molecular arrangement. A possibility that remains mostly unexplored is the synthesis of such nanocrystals on solid surfaces. In the same way in which crystalline inorganic nanodots can be epitaxially grown on suitable substrates under conditions in which 3D Volmer-Weber growth takes place, an organic system could in principle be devised such that the growth of crystalline 3D islands sets in before the completion of the first monolayer. In practice, however, for organic adsorbates deposited on inorganic substrates intermolecular interactions are much weaker than molecule-substrate interactions, thus promoting a layer-by-layer mode, and preventing the fabrication of isolated 3D nanocrystal.

Here we show that, upon deposition of cone-shaped subphthalocyanine (SubPc) molecule (See Figure 1) on Cu(111), isolated triangular nanocrystallites up to 3 ML appear on the surface before the completion of the first monolayer (See Figure 2). The different molecular layers show an alternating or antiferroelectric (AF) stacking of the molecular dipole moments. The structure of such nanocrystals can be explained by the joint effect of electrostatic (dipole-dipole) and dispersive (J_I-J_I) interactions. Although 1 ML-thick islands can also be found on the surface, the molecular arrangement in these areas is different from the geometry of the first layer molecules in the crystallites. We suggest that the formation mechanism of the organic nanocrystals is related to the existence of two different adsorption geometries, cone-up and cone-down, each of which sits on different molecular layers placed at different distances from the surface upon crystallite formation.

References:

- [1] Alivisatos, A. P. Semiconductor Clusters, Nanocrystals, and Quantum Dots *Science* **271**, 933-937 (1996).
- [2] Lounis B. & Orrit M. Single-photon sources *Reports on Progress in Physics* **68**, 1129-1179 (2005).
- [3] Murray, C. B., Kagan, C. R. & Bawendi, M. G. Synthesis and characterization of monodisperse nanocrystals and close-packed nanocrystal assemblies *Annu. Rev. Mater. Res.* **30**, 545-610 (2000).
- [4] Xiao, D. *et al.* Size-tunable emission from 1,3-diphenyl-5-(2-anthryl)-2-pyrazoline nanoparticles *J. Am. Chem. Soc.* **125**, 6740-6745 (2003).

Figure 1. a) Chemical structure of the chlorosubphthalocyanine molecules and side view of its 3D structure showing the dipole moment. The molecules will be sketched as gray triangles with green circles at the outermost benzene rings. They will display a white dot at the centre when the Cl atoms points up (sticking out of the surface); the lack of such a white dot indicates that the Cl atoms points towards the surface. b) $33.4 \times 26.5 \text{ nm}^2$ STM image of 0.2 ML SubPc/Cu(111) ($I_t = -0,380 \text{ nA}$; $V_{\text{bias}} = -2,1 \text{ V}$). c) Zoom-in ($10.8 \times 5.5 \text{ nm}^2$) showing the two types of STM images associated with the adsorption of SubPc: a bright protrusion and a trefoil shape. We interpret these features as corresponding to the coexistence of Cl-up and Cl-down adsorption geometries.

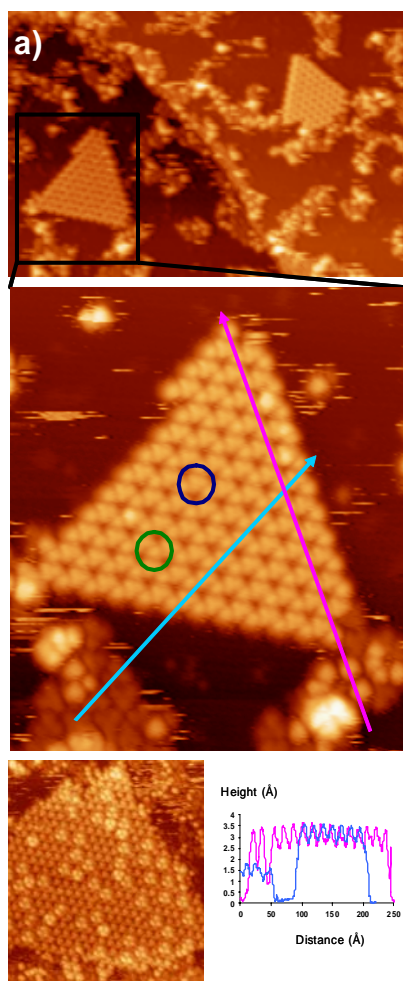
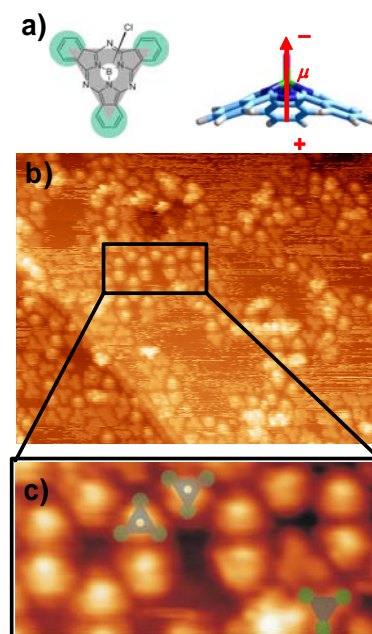


Figure 2. a) $62.4 \times 41.6 \text{ nm}^2$ STM image of 0.4 ML SubPc/Cu(111) ($I = -0,8 \text{ nA}$; $V = -2,9 \text{ V}$). Two triangular islands can be found. As for the 1 ML thick islands, high resolution STM images such as (b, $22.3 \times 26.1 \text{ nm}^2$) show two different molecular features, bright protrusions (green circles) and trefoil shapes (blue circles). The bright protrusions are identical in shape and size to the Cl-up molecules identified in Figure 2, but the trefoil features are 0.2 nm higher (c). Even thicker islands can be found upon further deposition (d, $33.4 \times 39.2 \text{ nm}^2$).

Development and Characterization of EGFR-targeted Iron-oxide Nanoparticles for Improved Magnetic Resonance Imaging of Brain Tumors.

U. Trojahn^{*}, M. Jaramillo[§], J. Baardsnes[§], A. Bell^{**}, B. Blasiak^{§§}, U. Iqbal^{**}, J. Zhang^{**}, R. MacKenzie^{**}, B. Tomanek^{§§}, D. Stanimirovic^{**}, and M. O'Connor-McCourt^{*§}.

^{*}McGill University, Department of Biochemistry, Montreal, QC, Canada,

[§]Biotechnology Research Institute, National Research Council, Montreal, QC, Canada,

^{**}Institute for Biological Sciences, National Research Council, Ottawa, ON, Canada

^{§§}Institute for Biodiagnostics, National Research Council, Calgary, AB, Canada

Ulrike.Trojahn@mail.mcgill.ca

Magnetic resonance imaging (MRI) is a prevailing medical imaging technique for solid tumors, because of its non-invasive nature and high soft-tissue contrast. In the clinics, contrast agents, such as iron oxides or gadolinium chelates, are administered to enhance the MRI signal by increasing the proton relaxation times of tissue water [1]. These agents passively accumulate at the tumor site due to the altered vessel architecture commonly observed in cancerous tissue; a phenomenon referred to as enhanced permeability and retention (EPR) effect.

Glioblastoma multiforme (GBM), also named fourth grade astrocytoma, is the most abundant and severe type of primary brain neoplasm with a mean patient survival of 14 months. At the present, surgical resection in combination with adjuvant radio- and chemotherapy (temozolomide) is the standard GBM therapy applied in the clinics [2]. Patient outcome is expected to improve with efficacious removal of the tumor mass; therefore precise delineation of tumor outlines is of key importance to the brain surgeon.

The epidermal growth factor receptor (EGFR) is overexpressed by gene amplification in half of GBM patients; herein, the expression of a constitutively active mutant receptor subtype (EGFRvIII) is observed in 40% of the cases and has shown to correlate with poor prognosis (*Figure 1*) [3]. EGFR belongs to the ErbB family of receptor tyrosine kinases, whose members are crucially involved in signaling pathways that regulate cell proliferation, differentiation, survival and angiogenesis. In particular, the highly invasive cells at the tumor boundaries display increased levels of EGF receptors on their surface [4].

In this study we developed an EGFR-specific superparamagnetic iron oxide nanoparticle, which is anticipated to improve the visualization of tumor outlines by MR imaging. The small size of the nanoprobe may improve tissue penetration and allow for the detection of infiltrating cancer cells in the surrounding brain. Furthermore, receptor-mediated internalization of the contrast agent into the cells is expected to improve accumulation and retention at the tumor site, resulting in prolonged high T2-contrast in brain lesions.

Novel anti-EGFR camelid antibody fragments were generated to target the nanoparticulate contrast agent to the tumor site [5]. Here, we demonstrate the tumor cell targeting ability of these 15 kDa antibody fragments linked to commercially available iron oxide nanoparticles in a glioblastoma cell line model (*Figure 2*). Furthermore, we carried out a thorough characterization of the conjugated nanoparticles, investigating its stability, toxicity, magnetic properties, blood circulation times and *in vitro* and *in vivo* targeting ability.

This nanoparticulate contrast agent could later on be exploited as multi-modal imaging agent, combining the benefits of MR imaging and fluorescence labeling for intra-operative visualization of tumor cells.

References:

- [1] Sorensen AG. J Clin Oncol. 2006 Jul 10;24(20):3274-81. Review.
- [2] Lefranc F, Rynkowski M, DeWitte O, Kiss R. Adv Tech Stand Neurosurg. 2009;34:3-35. Review.
- [3] Frederick L, Wang X-Y, Eley G, James CD. Cancer Res. 2000 Mar 1;60(5):1383-7
- [4] Okada Y, Hurwitz EE, Esposito JM, Brower MA, Nutt CL, Louis DN. Cancer Res. 2003 Jan 15, 63:413-16.
- [5] Zhang J, Tanha J, Hiram T, Khieu NH, To R, Tong-Sevinc H, Stone E, Brisson JR, MacKenzie CR. J Mol Biol. 2004 Jan 2;335(1):49-56.

Figures:

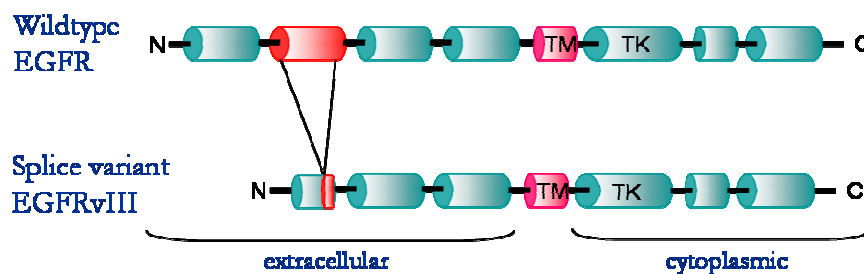


Figure 1. Schematic representation of the extra- and intracellular domains of the epidermal growth factor receptor (EGFR) and the mutant receptor (EGFRvIII).

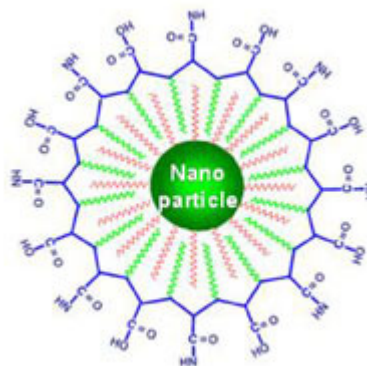


Figure 2. Schematic representation of the surface modifications on superparamagnetic iron oxide nanoparticle obtained from Ocean NanoTech, Springdale, AR, USA.

NANOPOROUS BIOSILICA PRODUCED BY DIATOM CELLS CULTURED IN THE PRESENCE OF METALS.

*Kazuo Umemura*¹, *Taku Yamazaki*¹, *Takashi Sasanuma*², *Shigeki Mayama*³

¹*Tokyo University of Science, 1-3 Kagurazaka, Shinjuku, Tokyo 1628601, Japan,* ²*Musashi Institute of Technology, 1-28-1 Tamazutsumi, Setagaya, Tokyo 158-8557, Japan,* ³*Tokyo Gakugei University, Koganei, Tokyo 184-8511, Japan*

meicun2006@163.com

Nanoporous biosilica produced by living diatom cells is one of the most unique architectures in nature. The size of frustules is varied from several microns to several hundred microns. The size of nanopores is varied from several nm to several hundred nm size. Although the nanoporous silica called frustules have been widely used for industrial applications such as water filters, building materials, etc, several research groups have started combining diatom frustules and nanotechnology as a new approach. For example, preparation of metal/carbon replica using a frustule, use of frustules as templates for nanoimprint, and fabrication of single frustule NO_x sensor were reported these several years. [1]-[5] Furthermore, in order to functionalized frustules, injection of nickel and titanium into frustules by culturing living diatom cells with the specific metals. [6]-[7]

In this paper, we demonstrated introducing platinum and titanium into diatom frustules of *Navicula* sp. and *Melosira nummuloides* by cultivation in the presence of those metals. The diatom cells were well grown in the medium when concentration of metals was less than 05 mg/L. After the cultivation, frustules were purified and characterized by scanning electron microscopy (SEM) and X-ray photoelectron spectroscopy (XPS). SEM images clearly showed that the shape of the obtained frustules was not significantly different from that of wild frustules.

Figure 1 shows typical example of SEM images of diatom frustules that were grown in the presence of platinum. Enough amounts of frustules were obtained during usual cultivation period (Fig.1A). Nanoporous structures were confirmed on frustule surfaces (Fig.1B). The SEM images suggested that complete structures of nanoporous biosilica were well produced even in the presence of metals.

This works was supported by Grant-in-Aid for Advanced Research, Tokyo University of Science.

References:

- [1] M.W. Anderson, S.M. Holmes, N. Hanif, C.S. Cundy, *Angew. Chem. Int. Ed. Engl.* 39(15), 2707–2710(2000).
- [2] M.W. Anderson, S.M. Holmes, N. Hanif, C.S. Cundy, *Angew. Chem. Int. Ed.* 39(15), 2707–2710(2000).
- [3] M.R. Weatherspoon, M.B. Dickerson, G. Wang, Y. Cai, S. Shian, S.C. Jones, S.R. Marder, K.H. Sandhage, *Angew. Chem. Int. Ed.* 46(30), 5724–5727(2007).
- [4] D. Losic, J.G. Mitchell, N.H. Voelcker, *Chem. Commun. (Camb.)* 39, 4905–4907(2005).
- [5] Z. Bao, M.R. Weatherspoon, S. Shian, Y. Cai, P.D. Graham, S.M. Allan, G. Ahmad, M.B. Dickerson, B.C. Church, Z. Kang, H.W. 3rd. Abernathy, C.J. Summers, M. Liu, K.H. Sandhage, *Nature* 446(7132), 172–175(2007).
- [6] S.M. Kang, K.-B. Lee, D. JinKim, I.S. Choi, *Nanotechnology* 17, 4719–4725(2006).
- [7] C. Jeffryes, T. Gutu, J. Jiao, G.L. Rorrer, *ACS Nano.* 2(10), 2103–2112(2008).

Figures:

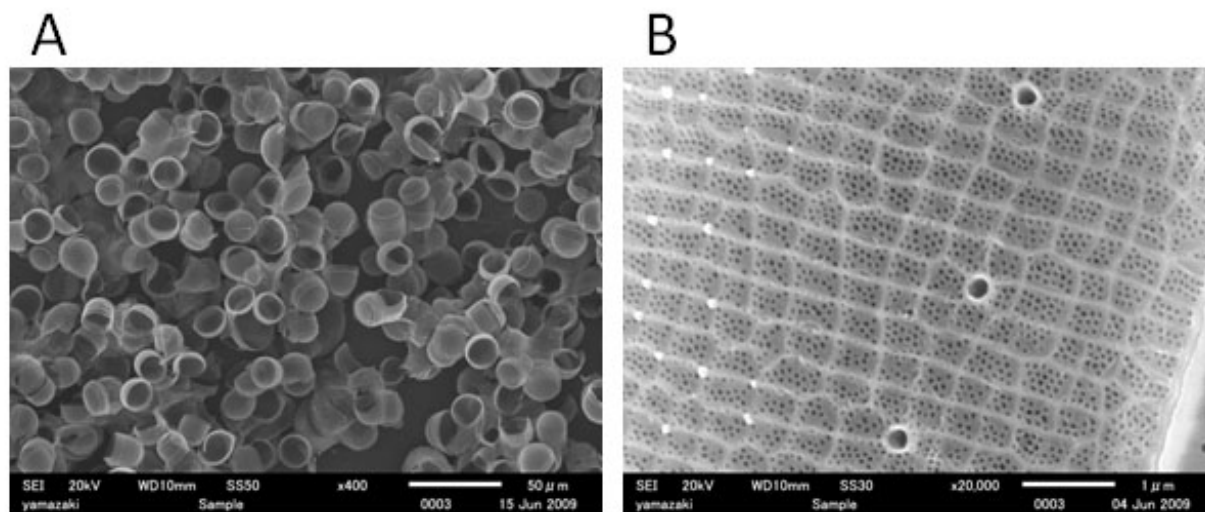


Figure 1 SEM images of purified frustules that were grown in the presence of metals. (A) Scale bar is 50 μm . (B) Scale bar is 1 μm .

CHARGE-TRANSFER-INDUCED STRUCTURAL REARRANGEMENTS AT BOTH SIDES OF ORGANIC ACCEPTOR/METAL INTERFACES

C. Urban¹, J. M. Gallego², Y. Wang³, T-C. Tseng⁴, D. Écija¹, M. Trelka¹, R. Otero^{1,5}, Steve L. Tait⁴, Nian Lin⁴, Mitsuharu Konuma⁴, Alexei Nefedov⁷, Christof Wöll⁷, María Ángeles Herranz⁵, U. Starke⁴, M. Alcamí³, F. Martín³, N. Martín^{5,6}, K. Kern⁴ and R. Miranda^{2,6}

¹Dpto. Física de la Materia Condensada, Univ. Autónoma de Madrid. Madrid, Spain

²Instituto de Ciencia de Materiales de Madrid, CSIC. Madrid, Spain

³Dpto, Química, Univ. Autónoma de Madrid. Madrid, Spain

⁴Max Planck Institute für Festkörperforschung, Stuttgart, Germany

⁵Dpto, Química Orgánica, Univ. Complutense de Madrid. Madrid, Spain

⁶IMDEA-Nanociencia, Madrid, Spain

⁷Lehrstuhl für Physikalische Chemie, Ruhr-Universität Bochum, Germany

Christian.Urban@uam.es

Since the discovery of the first organic conductor in the charge transfer complex TTF-TCNQ, organic heterostructures based on blends of donor and acceptor molecules have displayed exciting electrical and optical properties with promising technological applications, which requires understanding the alignment of the energy levels and the corresponding charge transfer processes at metal/organic interfaces. Charge transfer, however, leads not only to modifications in the alignment of energy levels, but also to *structural* transformations. Such charge transfer-induced structural rearrangements might have significant effects on the subsequent growth and structure of organic films and, thereby, on device performance.

Here we report on the self-assembly under UHV of the strong organic acceptor TCNQ (tetracyanoquinodimethane) on Cu(100) by STM, LEED, XPS, XAS and DFT calculations. STM images rectangular TCNQ islands whose structure is determined by LEED. DFT and STM reveal that the adsorbed molecules are strongly deformed with respect to their gas phase configuration. Furthermore, while the molecular arrangement along the shortest side of the islands can be modelled by simple direct intermolecular interactions, the DFT simulations show that the inter-adsorbate interactions along the fast-growth direction of the rectangular islands arise from stress-relief induced by TCNQ molecules sitting in neighbouring sites. This is due to the strong charge transfer (confirmed by XPS and XAS) resulting in an adsorbate-induced reconstruction of Cu (100). The mechanism might be general for strong organic-acceptor/metal interfaces.

[1] Forrest, S. R. The path to ubiquitous and low-cost organic electronic appliances on plastic. *Nature* **428**, 911-918 (2004).

[2] Moons, E. Conjugated polymer blends: linking film morphology to performance of light emitting diodes and photodiodes. *J. Phys. Cond. Matter.* **14**, 12235-12260 (2002).

[3] Blom, P. W. M., Mihailetschi, V. D., Koster, L. J. A., Markov, D. E. Device Physics of Polymer:Fullerene Bulk Heterojunction Solar Cells. *Adv. Mater.* **19**, 1551-1566 (2007).

[4] Brabec, C. J., Sariciftci, N. S., Hummelen, J. C. Plastic Solar Cells. *Adv. Funct. Mater.* **11**, 15-26 (2001).

[5] Jerome, D. Organic Conductors: From Charge Density Wave TTF-TCNQ to Superconducting (TMTSF)2PF6. *Chem. Rev.* **104**, 5565-5591 (2004).

[6] Manriquez, J. M., Yee, G. T., Scott McLean, R., Epstein, A. J., Miller, J. S. A Room-Temperature Molecular/Organic-Based Magnet. *Science* **252**, 1415-1417 (1991).

[7] Jain, R. *et al.* High-temperature metalorganic magnets. *Nature* **445**, 291-294 (2007).

[8] Gambardella, P. *et al.* Supramolecular control of the magnetic anisotropy in two-dimensional high-spin Fe arrays at a metal interface. *Nat. Mater.* **104**, 189-193 (2009).

[9] Stöhr, J., Outka, D. A. Determination of molecular orientations on surfaces from the angular dependence of near-edge x-ray-absorption fine-structure spectra. *Phys. Rev. B* **36**, 7891-1905 (1987).

[10] Stöhr, J., *NEXAFS Spectroscopy* (Springer-Verlag, Berlin, 2003).

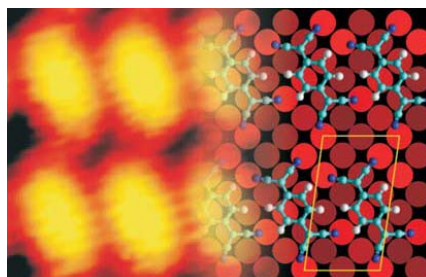
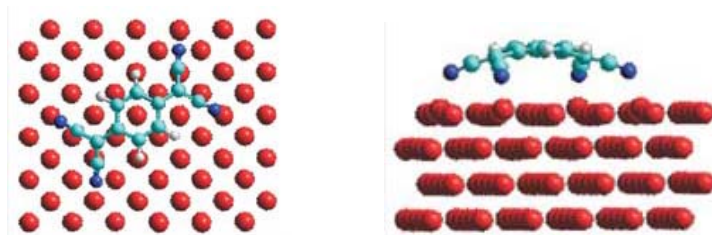
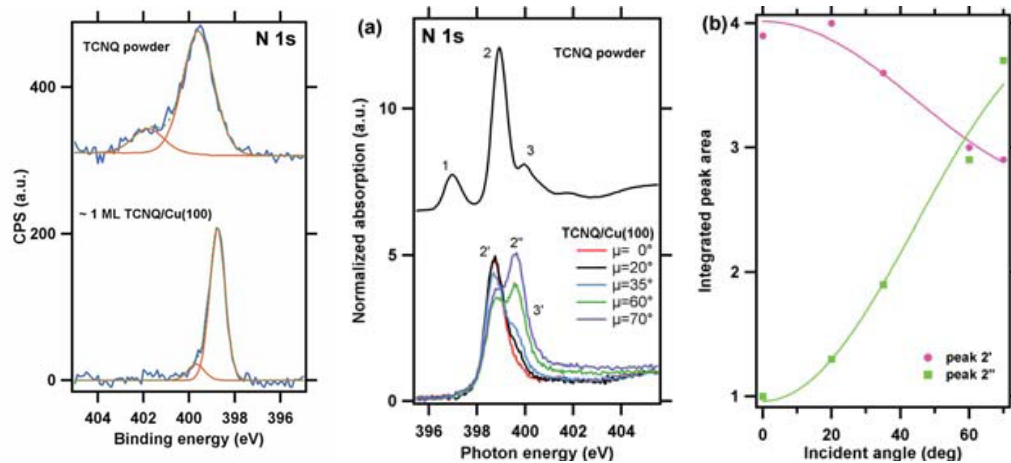
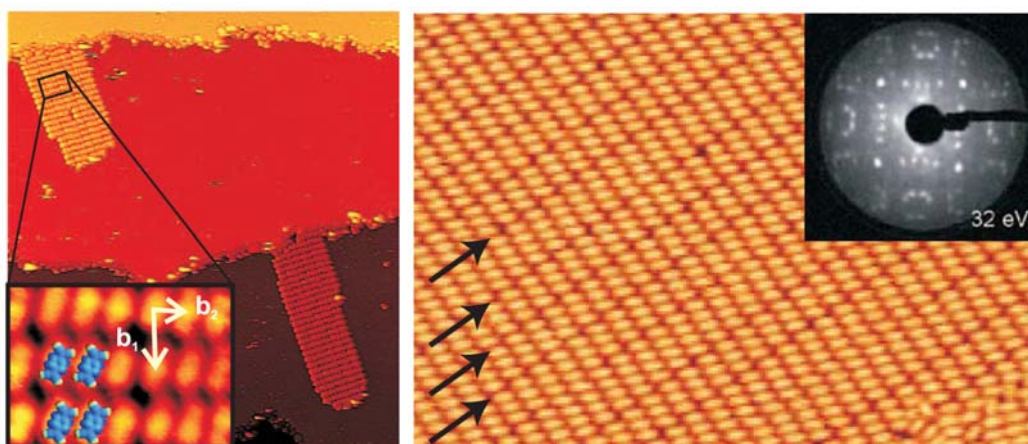
[11] Bässler, *et al.* Near Edge X-ray Absorption Fine Structure Resonances of Quinoid Molecules. *Langmuir* **16**, 6674-6681 (2000).

[12] Sing, M. *et al.* Structural vs electronic origin of renormalized band widths in TTF-TCNQ: An angular dependent NEXAFS study. *Phys. Rev. B* **76**, 245119 (2007).

[13] Fraxedas, J. *et al.* Characterization of the unoccupied and partially occupied states of TTF-TCNQ by XANES and first-principles calculations. *Phys. Rev. B* **68**, 195115 (2003).

[14] Otero, R. *et al.* An Organic Donor/Acceptor Lateral Superlattice at the Nanoscale. *Nano Lett.* **7**, 2602-2607 (2007).

Figures:



An antibacterial surface coating composed of PAH/SiO₂ nanostructured films by Layer by Layer

A. Urrutia, P. Rivero, L. Ruete, J. Goicoechea, I.R. Matías, F.J. Arregui.
Public University of Navarra (UPNA), Campus Arrosadía S/N, Pamplona, Spain
aitor.urrutia@unavarra.es

In this article we propose a novel antibacterial coating composed of SiO₂ and the polymer Poly(allylamine hydrochloride) (PAH) on glass slides by the technique Layer-by-Layer (LbL), see Figure1. This technique has already used in previous works [1-4], and it has the advantage that it allows to control the construction of nanosized and well organized multilayer films. In other works, it has been studied the antibacterial behaviour of the silica [5]. In this work, the new nanotexturized LbL SiO₂ surface acts as antibacterial agent. The fabricated coatings have been tested in bacterial cultures of genus *Lactobacillus* to observe their antibacterial properties.

LbL coatings were performed by dipping the substrates (glass slides) into alternatively charged solutions, PAH as polycation and SiO₂ as polyanion. This dipping cycle was repeated until a total of 50 (PAH/SiO₂) bilayers were constructed. AFM images were obtained from the substrates (see Figure2) in order to characterize the thickness and the surface morphology of the LbL coatings.

Those new surfaces were tested in *Lactobacillus Delbrueckii* bacteria culture to observe their antibacterial activities. *L. Delbrueckii* was inoculated in a “MRS Broth” aqueous medium and incubated at 37° C for 24 hours. The obtained bacterial suspension was shaken and diluted 100000 times. “MRS Agar” was autoclaved at 121° C for 30 min and cooled in sterile Petri-dishes to form a 3mm thick slab. Then 0.1ml bacterial dilution suspension was spread uniformly on the surface of the nutrient agar slab. The substrates coated with PAH/SiO₂ were then placed on the agar slab. Also, clean glass slides like reference were placed (disinfected by dipping in isopropanol and treated by contact flame). Then Petri-dishes were introduced into an incubator for 24 hours at 37°C.

The antibacterial activities against *L. Delbrueckii* of the multilayer (PAH/SiO₂) were carefully measured using an optical method. Figure 3 shows the results in two substrates placed on agar slabs after 24 h. The first one shows one reference substrate where we can observe lots of *L. Delbrueckii* colonies that grow up randomly in the whole agar slab surface. The second one shows one substrate coated with PAH/SiO₂. Here it is possible to see a clear difference between the coated area (there is not growth colonies) and the uncoated area and the rest of the slab (there is growth colonies).

All the experiments were performed in triplicate. The results were analyzed and are represented in average, taking the error as the standard deviation. The treated surfaces reach $90,5 \pm 5\%$ of inhibition effect on the growth of *L. Delbrueckii* after 24 hours. In conclusion, it has been demonstrated these PAH/SiO₂ coating films have a very good antibacterial behaviour against *Lactobacillus Delbrueckii*.

References:

- [1] G. Decher. **277**, (1997), 1232-1237.
- [2] N. I. Kovtyukhova, B. R. Martin, J. K. N. Mbindyo, T. E. Mallouk, M. Cabassi and T. S. Mayer. **19**, (2002), 255-262.
- [3] P. Bertrand, A. Jonas, A. Laschewsky and R. Legras. **21**, (2000), 319-348.
- [4] J. W. Ostrander, A. A. Mamedov and N. A. Kotov. **123**, (2001), 1101-1110.
- [5] Z. Li, D. Lee, X. Sheng, R. E. Cohen and M. F. Rubner. **22**, (2006), 9820-9823.

Figures:

Figure 1: The electrostatic self-assembly or Layer-by-Layer technique

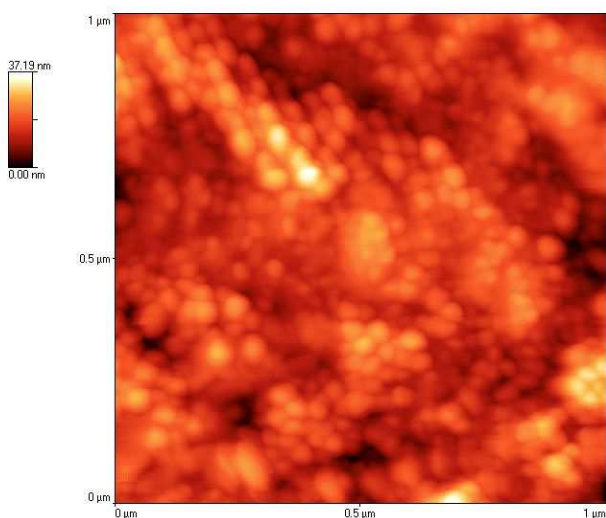
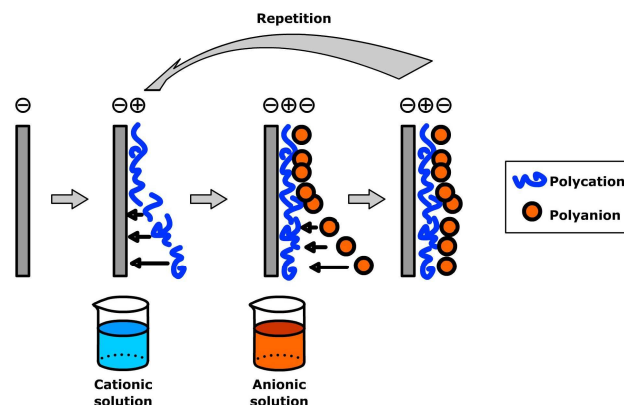
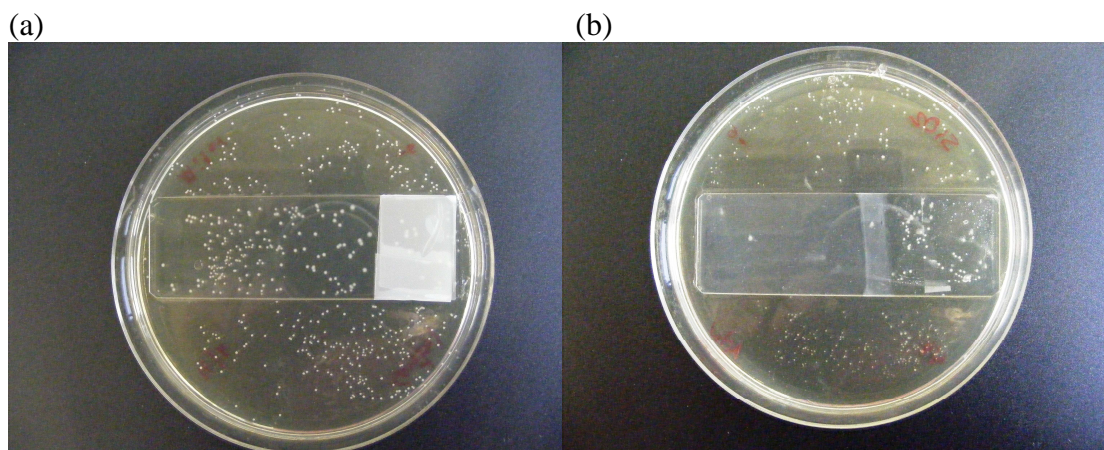


Figure 2: 1x1μm AFM image of the PAH/SiO₂ multilayer.

Figure 3: *L. Delbrueckii* cultures after 24 hours in: (a) reference substrate and (b) coated substrate.



Yttria totally stabilized zirconia nanoparticles obtained through the pyrosol method

*B.S. Vasile**, *Otilia-Ruxandra Vasile***, *Cristina Ghitulica**, *Ecaterina Andronescu**, *Raluca Dobranis*, *Elena Dinu**, *Roxana Trusca****

**University POLITEHNICA from Bucharest, Faculty of Applied Chemistry and Material Science, No. 1-7 Polizu Street, Postal Code 011061, Bucharest, Romania*

*** National Research Institute for Electrochemistry and Condensed Matter, No. 202 Splaiul Independentei street, Postal Code 060021, Bucharest, Romania*

**** Metav C.D., No. 31 C.A. Rosesti Street, Postal Code 020015, Bucharest, Romania*
bogdan.vasile@upb.ro

It is well known that zirconia based ceramics, partially or totally stabilised, have a wide use in many fields, such as biomedical, sensors, catalysts, cutting tools and abrasives, components with high thermo-mechanical properties, filters or solid oxide fuel cells technologies. The use of totally stabilised zirconia in fuel cells technologies is due mainly to the very good ionic conductivity of cubic zirconia at medium and high temperature [1, 2, 3].

The pyrosol method consists in the formation of an aerosol from a diluted solution of precursors, using a high frequency ultrasounds generator. The formed aerosol is carried through a furnace, in a quartz tube, by a carrier gas. During the passage of the aerosol through the furnace, some reactions occur such as evaporation, calcination and densification of the powder. At the end of the tube, a high voltage wire collects the powder.

In this work, 10 mole percent yttria stabilised cubic zirconia is obtained through the pyrosol method, starting from a diluted solution of zirconia nitrate ($\text{N}_2\text{O}_7\text{Zr} \times 6\text{H}_2\text{O}$) and yttrium nitrate ($\text{Y}(\text{NO}_3)_3 \times 4\text{H}_2\text{O}$) [1]. The pyrosol method was used in order to obtain reactive powders, with dimensions in the nanometers range.

The main factors which are influencing the parameters of the obtained powders are concentration of the precursors' solutions, soluble salts type, synthesis temperature, vibration frequency, etc. In the present paper, it was investigated the influence of the concentration of solutions (5×10^{-2} M, 2.5×10^{-2} M and 1.25×10^{-2} M) and of the thermal treatment temperature (700, 800 and 900°C) on the dimensions, morphology and composition of powders.

The analyses used to characterise the obtained powders were X-ray diffraction, scanning electron microscopy (SEM), atomic force microscopy (AFM) and high resolution transmission electron microscopy (HRTEM).

The only crystallographic phase identified through X-ray diffraction, for powders prepared at 800°C and higher and for all concentrations, is cubic zirconia.

From SEM images it was observed that there were obtained perfect spherical particles. By increasing the thermal treatment temperature the particle sizes increases, reaching 0.6 microns, but by decreasing the concentration of the precursors' solutions, the particle size reaches a medium size of approximately 85 nm.

The profiles extraction of topography images from AFM reveal that more than 90 % of particles are below 90 nm.

From HRTEM images it can be seen that the spherical particles are formed from an agglomeration of nanocrystalites, reaching even a mean dimension of 4 nm for 1.25×10^{-2} M concentration of the starting solutions, which is the lowest concentration used, synthesized at 800°C . The maximum size of nanocrystalites is of approximately 9 nm, for the 5×10^{-2} M starting solutions, treated at 900°C .

We may conclude that the pyrosol process is a relatively simple method, which is allowing the preparation of reactive cubic zirconia powders, with dimensions in the nano domain and spherical morphology, with valuable application in main industrial fields.

References:

- [1] Chih-Wei Kuo, Yueh-Hsun Lee, Kuan-Zong Fung, Moo-Chin Wang, *Journal of Non-Crystalline Solids*, 2005, 304–311;
 [2] Christel Laberty-Robert, Florence Ansart, Simone Castillo, Guillaume Richard, *Solid State Sciences*, 4 (2002), 1053–1059;
 [3] Yueh-Hsun Lee, Chih-Wei Kuo, I-Ming Hung, Kuan-Zong Fung, Moo-Chin Wang, *Journal of Non-Crystalline Solids*, 351 (2005), 3709–3715.
 [4] Manuel Gaudona, Elisabeth Djurado, Norbert H. Menzler, Morphology and sintering behaviour of yttria stabilised zirconia (8-YSZ) powders synthesised by spray pyrolysis, *Ceramics International* 30 (2004) 2295–2303.

Figures:

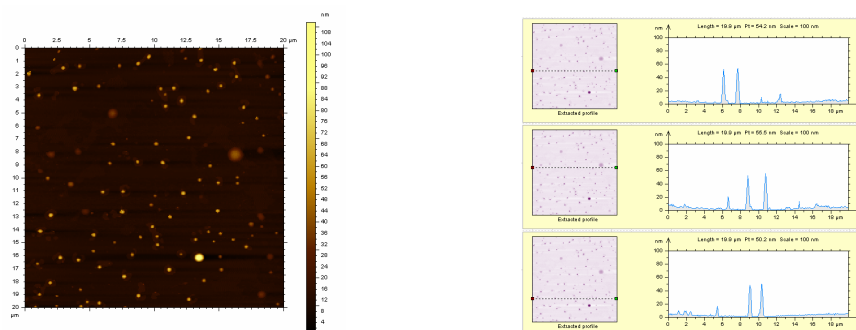


Figure 1 – A topography AFM image of 20µm and the extracted profile obtained on cubic yttria stabilised zirconia synthesised from the concentration of precursor solution of $1.25 \times 10^{-2} \text{M}$ at 800°C

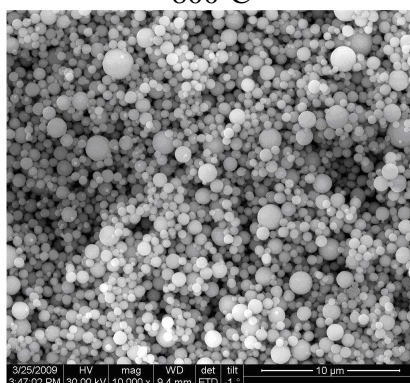


Figure 2 – SEM image on cubic yttria stabilised zirconia synthesised from the concentration of precursor solution of $1.25 \times 10^{-2} \text{M}$ at 800°C

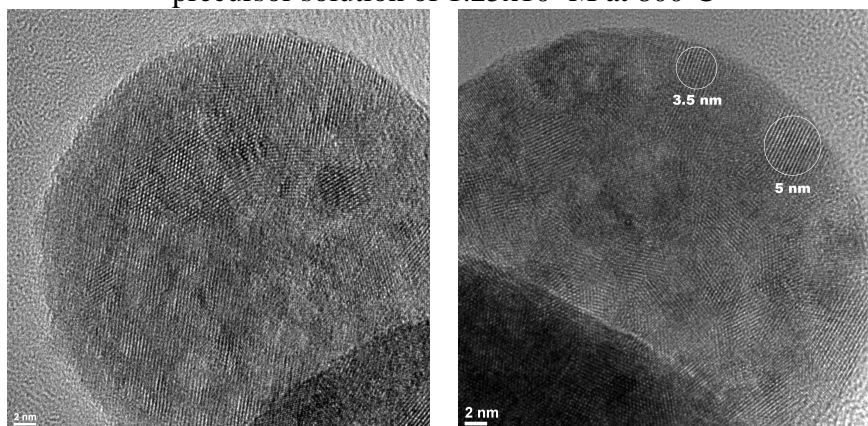


Figure 3 – TEM (HRTEM) image obtained on cubic yttria stabilised zirconia synthesised from the concentration of precursor solution of $1.25 \times 10^{-2} \text{M}$ at 800°C

NEW NANOSTRUCTURED MATERIALS BASED ELECTROCHEMICAL MICROSENSORS

*Otilia-Ruxandra Vasile¹, Raluca-Ioana van Staden¹, Jacobus Frederick van Staden¹,
Simona-Cornelia Bălăsoiu¹, Bogdan Ștefan Vasile²*

¹ *Laboratory of Electrochemistry & PATLAB Bucharest, National Institute of Research for
Electrochemistry and Condensed Matter, Splaiul Independentei street, no 202,
Postal Code 060021, Bucharest-6, ROMANIA*

² *University POLITEHNICA from Bucharest, Faculty of Applied Chemistry and Material
Science, Polizu Street, No. 1-7, Postal Code 011061, Bucharest, Romania*

E-mail: otiliaradacina@yahoo.com

New nanostructured materials based on porphyrins are proposed for the design of microsensors. The porphyrins are forming molecular aggregates which favour the formation of nanochannels. The nanostructure of the porphyrins aggregates is shown using the atomic force microscopy. The size of the active surface of the microsensor proposed was determined using scanning electron microscopy.

The design of the proposed microelectrodes is simple and reliable. The porphyrin is the active compound which is physically immobilized in the diamond or carbon paste. The diamond paste electrodes are well known for their reliability, high S/N ratio and their high sensitivity [1-3].

The response characteristics of the microelectrodes were evaluated using DPV. The proposed microelectrodes were successfully used for the assay of dopamine and vitamin C in samples such as biological fluids, pharmaceutical compounds and beverages.

References:

- [1] R.I. Stefan, S.G. Bairu, J.F. van Staden, *Anal.Lett.*, 36 (2003) 1493.
- [2] R.I. Stefan, S.G. Bairu, J.F. van Staden, *Anal.Bioanal.Chem.*, 375 (2003) 844.
- [3] R.I. Stefan, S.G. Bairu, *Anal.Chem.*, 75 (2003) 5394.

Relation between Macroscopic and Microscopic Hyperpolarizability of Er(III) complexes with organic mixed ligands

Cristina Vasiliu¹, Ana Emandi², N. Jula³, Marilena Vasilescu⁴

¹*National Institute for Optoelectronics INOE 2000, 1 Atomistilor Blvd.,
PO Box MG 5, RO-077125, Magurele, Bucharest, Romania icvasiliu@inoe.inoe.ro*

²*University of Bucharest, Faculty of Chemistry, Department of Inorganic Chemistry,
23 Dumbrova Rosie St., RO-010184, Bucharest, Romania, ancae@b.astral.ro*

³*Military Technical Academy, 81-83, G. Cosbuc street, Bucharest, Romania, njula@mta.ro*

⁴*Institute of Physical Chemistry, Romanian Academy, Splaiul Independentei 202, 060021
Bucharest, Romania.*

Photonics concerns the generation, transport, processing and detection of light. The field has received a powerful impetus recently with the introduction of nano-scale concepts. Moreover, organic materials now appear as key components in photonic devices such as light-emitting diodes, integrated lasers, or photovoltaic cells. Organic molecular systems offer unique opportunities in nano-photonics since both top-down and bottom-up strategies can be pursued towards the nano-scale.

The emerging fields of biophotonics, nonlinear microscopy, nanofabrication, optical sensing, optical memory and information storage require knowledge of nonlinear optical parameters of materials and design strategies to synthesise materials with NLO effects applicable in the technologies.

Aiming at developing new types of hybrid NLO materials with enhanced properties (for instance with stronger ionic bond) we have synthesized and investigated Er(III) cation coordinated with organic ligands with coordinative groups (OH, COOH) and Donor D and respective Acceptor A in 4,4' related to COOH donor group. L is a neutral ligand. The coordinative anion complexes were precipitated with a bulk cation of tetra-alkyl ammonium. The general formula is presented in Figure.1

Organic molecules coordinated to a cation represent a great potential for applications in electro-optic and all optical devices. This is due to different factors such as large molecular hyperpolarizability, fast electronic response time, versatility, easy thin films or single crystals processing and low cost. One of the simplest and most precise methods of second order nonlinear optical property characterization is the electric field induced second harmonic generation technique EFISH. This technique provides directly the sum of second hyperpolarizability and orientationally induced part of the first molecular hyperpolarizability.

In this paper we deal with the molecular dipole moment determination in solution by the effect of solvents on the absorption and fluorescence characteristics of organic compounds. Dipole moments of short-lived species are of considerable interest because they provide information on electronic and geometrical structure of these transient species. Knowledge of dipole moment of electronically excited species is often useful in the design of non-linear optical materials and elucidation of the nature of the excited state, as well as the course of any photochemical transformation. Experimental data on excited states are useful in the parameterizations of semi-empirical quantum chemical procedures for these states.

Among the techniques available for the determination of excited state dipole moments, the most popular is that based on the Lippert–Mataga equation [1]. In this technique, absorption and fluorescence shift followed using the solvent polarity, described by dielectric constant ϵ and refractive index n . The increase in the dipole moment value in the excited state, $\Delta\mu$, was estimated using the dependence of either the fluorescence wavenumber, ν_F , or the Stokes shift, $\Delta\nu$, on some solvent polarisation functions, the Lippert-Mataga [1,2] model and the E_T^N solvent parameter given by Reichardt. [3,4,5]

The dipole moment values in fundamental and excited states, calculated from absorption and emission fluorescence spectra of the above mentioned organic complexes in solvents with different dielectric constant ϵ and refractive indices are presented. The dipole moments in fundamental states were also determined by Guggenheim method. [6]

References:

- [1] Lippert, E. *Z. Naturforsch.* 10a, (1955) 541.
 [2] Mataga, N., Kaifu, Y. and Koizumi, M. *Bull. Chem. Soc. Jap.* 29, (1956)465.
 [3] Ravi, M., Samanta, A. and Radhakrishnan, T.P. *J. Phys. Chem.* 98, (1994)9133-9136.
 [4] Kumar, S., Jain, S.K. and Rastogi, R.C. *Spectrochimica Acta part A* 57, (2001) 291-298.
 [5] Reichardt, C. *Angew. Chemie, Int. Edn. Engl.* 18, (1979) 98-110.
 [6] B. Thompson, *J. Chem. Educ.*, 43, (1996),66.

Figures:

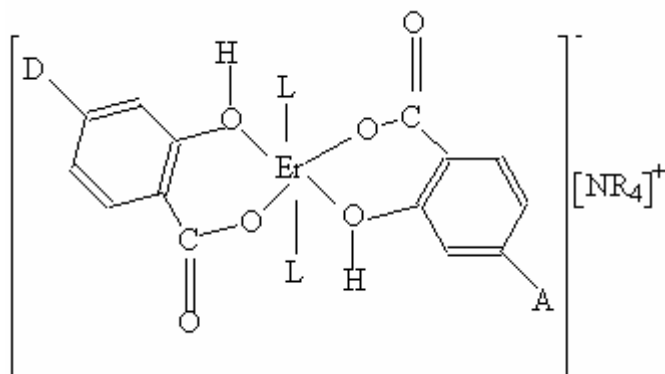


Figure 1. General formula of organic complexes : Er(III) cation coordinated with organic ligands with coordinative groups (OH, COOH) and Donor D and respective Acceptor A in 4,4' related to COOH donor group, L

Impact of dimerization and stretching on the transport properties of molybdenum atomic wires

A. Vega,¹ A. García-Fuente,¹ V. M. García-Suárez² and J. Ferrer³

¹*Departamento de Física Teórica, Atómica y Óptica, Universidad de Valladolid, Spain*

²*Department of Physics, Lancaster University, United Kingdom*

³*Departamento de Física, Universidad de Oviedo, Spain*

vega@phenix.fam.cie.uva.es

We study the electrical and transport properties of monoatomic Mo wires with different structural characteristics. Mo is an interesting metal element as regards its ability to form one-dimensional structures. Recent ab-initio calculations of free-standing Mo atomic clusters have shown that linear atomic chains containing up to four atoms are more stable than two- and three- dimensional structures.¹ On the other hand, individual molybdenum chains have been produced and controlled by encapsulating them inside carbon nanotubes very recently.²

Our calculations have been performed within the DFT formalism with the generalized gradient approximation for the exchange and correlation potential. We have used the SMEAGOL code³ to compute the transmission coefficients and the current using the Landauer formalism:

$$I(V) = \frac{2e}{h} \int dE T(E, V) (f_L(E, V) - f_R(E, V))$$

As a consequence of Mo having an exact half band filling, the ground state of the Mo wire is formed by tightly bound dimers. We consider first periodic wires with inter-atomic distances ranging between the dimerized wire to that formed by equidistant atoms. The ground state of all the chains is non magnetic. As all these chains are periodic, the transmission coefficients $T(E)$ in units of G_0 will just count the number of bands at energy E , being $G_0 = 2e^2/h$ the conductance quantum unit. We find that the dimerized case has a gap in the electronic structure which makes it insulating. As we move to the equidistant case, many occupied and unoccupied bands move gradually towards the Fermi level, and for equidistant chains, as well as for slightly dimerized chains, we have a metallic behaviour (Fig 1).

We also simulate two conducting equidistant one-dimensional Mo electrodes separated by a scattering region which contains a number of dimers between 1 and 6. Even with only 1 dimer, the transmission at the Fermi level falls from 6 to only 1 G_0 . As we increase the number of dimers in the scattering region, the transmission at the Fermi level decreases in an exponential way (Fig 2). This means that the transport must be in the tunnelling regime. The I-V characteristics strongly depend on the number of dimers and vary from ohmic to tunnelling, with the presence of different gaps.

The interatomic distances recently measured between Mo atoms in individual monoatomic chains encapsulated inside carbon nanotubes² ranged from 3.2 to 3.8 Å. Those wires are then far from being dimerized, but their distances are longer than the distances in the equidistant wire that we have studied. These stretched chains are ferromagnetic, with a full spin polarization, where the magnetic moment is saturated to its maximum possible value of 6 μ_B . This makes the chain an insulator, due to the magnetic splitting that leaves all the majority spin s- and d-states below the Fermi level and all the minority spin s- and d-states above the Fermi level.

References:

- [1] F.Aguilera-Granja, A. Vega, L. J. Gallego, *Nanotechnology*, **19** (2008) 145704.
- [2] H. Muramatsu, T. Hayashi, Y. Ahm Kim, D. Shimamoto, M. Endo, M. Terrones, M. Dresselhaus, *Nano Letters*, **8** (2008) 237.
- [3] A. R. Rocha, V. M. García-Suárez, S. W. Bailey, C. J. Lambert, J. Ferrer, S. Sanvito, *Physical Review B* **73** (2006) 085414.

Figures:

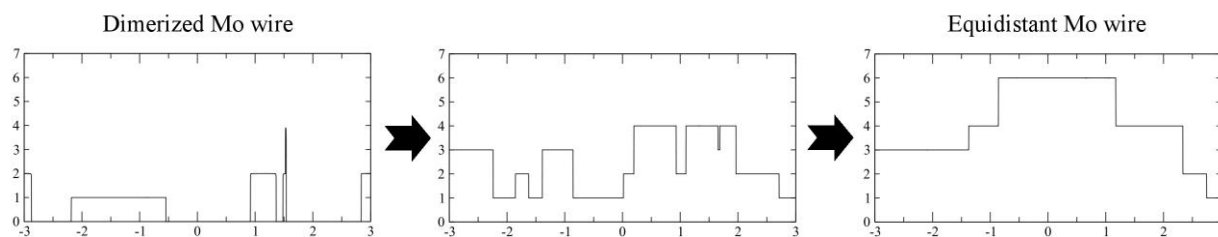


Figure 1: Transmission (G_0) as a function of the energy referred to the Fermi energy (eV) for a Mo atomic wire with the interatomic distance going from the dimerized to the equidistant case.

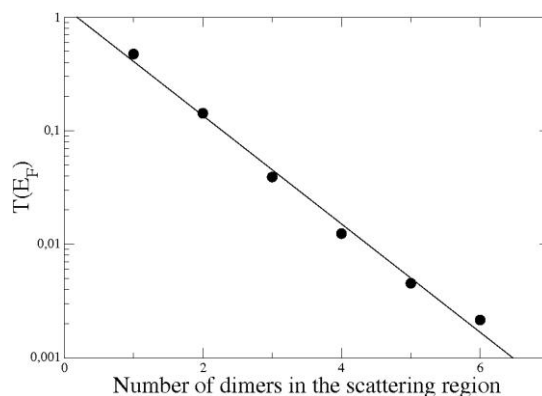


Figure 2: Logarithm of the transmission at the Fermi level as a function of the number of dimers in the scattering region.

Halloysite Clay Nanotubes: Characterization, Biocompatibility and Use as Drug Carriers

Viviana Vergaro^{1*}, *Elshad Abdullayev*², *David Mills*², *Giovanna Giovinazzo*³, *Angelo Santino*³
*Roberto Cingolani*¹, *Yuri M. Lvov*² and *Stefano Leporatti*¹

¹*National Nanotechnology Laboratory of CNR-INFM, University of Salento, ISUFI, Lecce, 73100, Italy*

²*Institute for Micromanufacturing, Louisiana Tech University, 911 Hergot Ave, Ruston, LA 71272, USA*

³*Institute of Sciences of Food Production C.N.R. Section of Lecce, via Monteroni, 73100, Lecce, Italy*

[email: viviana.vergaro@live.it](mailto:viviana.vergaro@live.it)

One way to utilize the high functionality and stability of bio-related materials is to create hybrids consisting of materials of biological origin and inorganic materials. Halloysite is defined as a 1:1 layered aluminosilicate, chemically similar to kaolin, which has predominantly hollow tubular structure in the submicron range [1-3]. Halloysite is an economically viable raw material that can be mined as a raw mineral. As for most natural materials, the size of halloysite particle varies within 1-2 microns of length and 15-100 nm of inner diameter depending on the deposits or even within different locations in a specific deposit. Halloysite nanotubes (HNTs) are efficient nano-containers capable of entrapping a range of active agents [2] within the inner lumen, followed by their retention and slow release [3]. Halloysite is a green environmentally friendly object available in commercial quantities. The lumen of the halloysite tube accommodates globular protein diameters, allowing their entrapment within the inner lumen of the halloysite while retaining their activity for use in biocatalysis. In this work a combination of high resolution imaging technique such as TEM, SEM and SFM have been employed to elucidate the structure. We have investigated their visco-elastic properties by force-indentation measurements (Young Modulus (E) between 180 and 230 kPa, in Contact Mode) and performed cytotoxicity tests (viability preserved until HNTs concentration of 50 μ g/ml and maximal incubation time of 72 hours) utilizing neoplastic cell lines (breast and cervical cancer cells). Furthermore their uptake has been confirmed by Confocal Laser Scanning Microscopy (CLSM) after their functionalisation with fluorescence molecules. The results indicate that halloysite nanotubes have been readily uptaken by neoplastic cells and exhibit a high level of biocompatibility. To confirm their possible biomedical use as a therapeutic nanocarrier we have successfully encapsulated bioactive compounds (e.g. resveratrol) and studied their anti-neoplastic effect into model cancer cell lines. Research on use of the clay nanotube for sustain drug delivery for dermatological treatment and bone repair is in progress. A typical drug release time from these biocompatible nanotubes was 20-50 hours (e.g. for anticancer dexamethasone) and for proteins 50-200 hours.

References:

- [1] R. Price, B. Gaber, Y. Lvov J. Microencapsulation **18**, (2001) 713.
- [2] Y. Lvov, D. Shchukin, H. Mohwald, R. Price ACS Nano Journal **2**, (2008) 814.
- [3] N. Veerabadran, Y. Lvov, R. Price Macromolecular Rapid Commun. **30**, (2009) 99.

Figures:

- 1) (a) and (b) TEM images of HNTs (scale bar 200 nm); (c) Three-dimensional topographic Tapping Mode SFM view of HNTs; (d) Tapping Mode Amplitude image of HNTs and corresponding height profile (inset).
- 2) CLSM images of HNTs uptake by cancer cells. HNTs appear green since they are FITC-marked and became yellow after internalisation into cancer cells. Nuclei are Hoechst stained (blue).

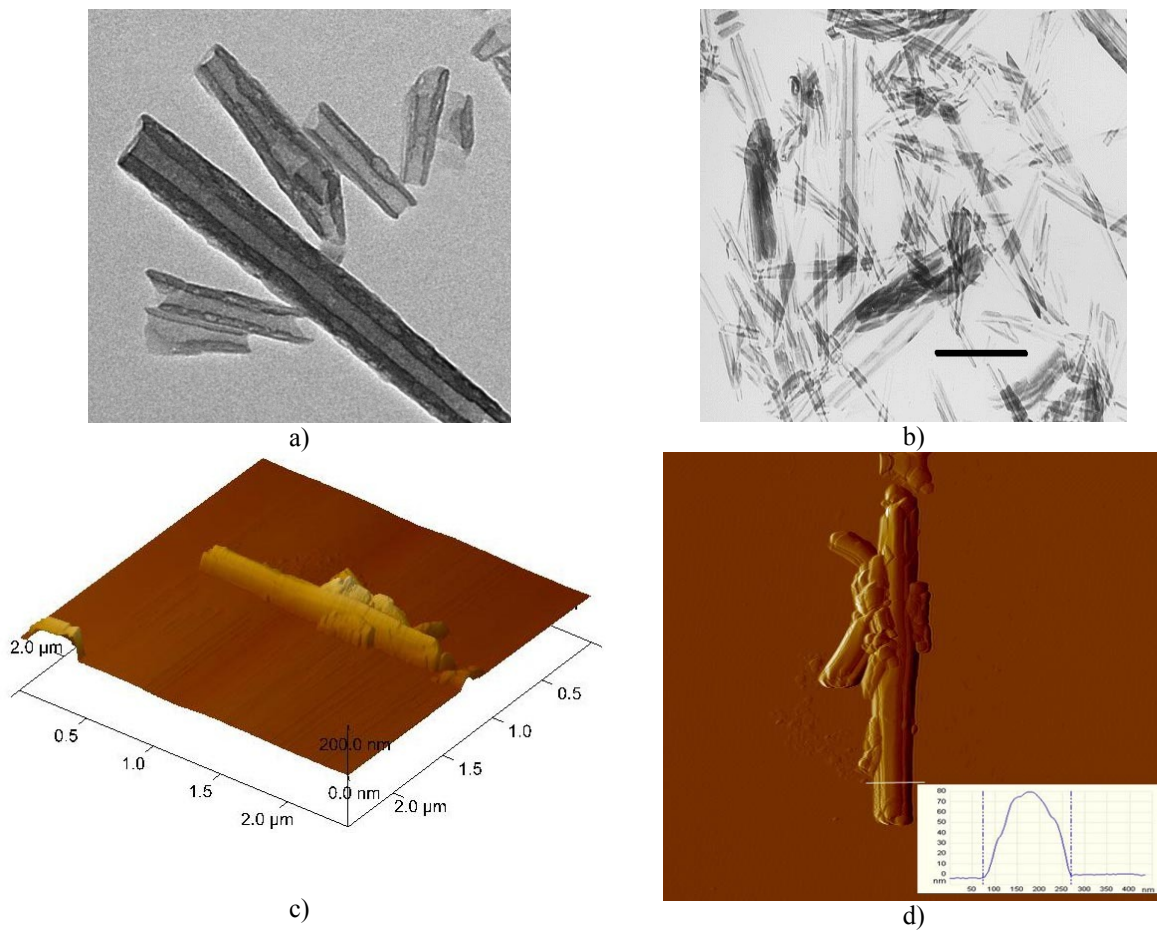


Figure 1

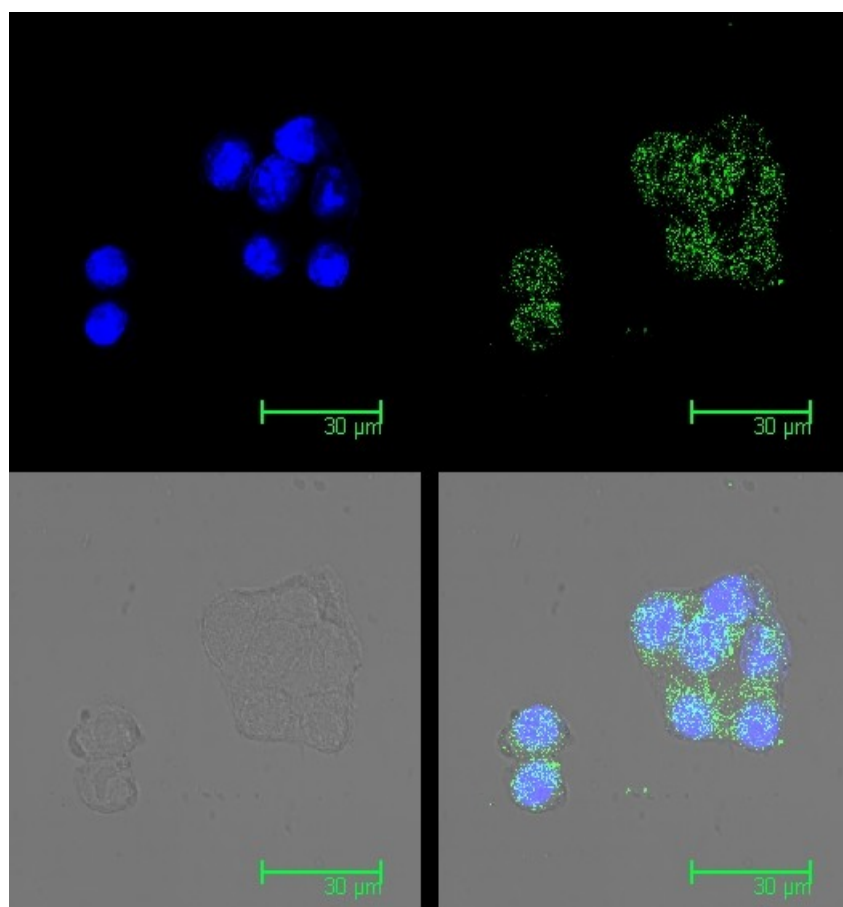


Figure 2

INTERACTION OF OXOANIONS WITH GOLD NANOPARTICLES MODIFIED BY PORPHYRIN-BRUCINE CONJUGATE STUDIED BY ECD SPECTROSCOPY

*Lenka Veverková, Ondřej Julínek, Pavlína Novotná, Kamil Záruba, Vladimír Král
Institute of Chemical Technology, Department of Analytical Chemistry,
Technická 5, 166 28 Prague 6, Czech Republic,
Lenka.Veverkova@vscht.cz*

The development of molecular sensors for detecting selectively chemically and biologically important anionic species has become a major research project in supramolecular chemistry. It is still a challenge to find and study materials capable of recognizing and sensing anions in aqueous media [1]. The possible use of modified porphyrins as selector is based on formation of non-covalent π - π complexes between porphyrins core and planar analyte together with additional binding modes, like H-bonding, coulombic interaction [2]. Immobilization of porphyrin derivative on surface of nanoparticles allows studying interaction in environment in which selector is insoluble [3].

The goal of this work was to study the interaction between oxoanions and porphyrin-brucine conjugates [4] in methanol-water solution and water, the influence of gold nanoparticles on the interactions was also studied.

Nowadays, gold nanoparticles are often prepared by chemical reduction of Au(III) [5]. Sodium citrate belongs to the most usable reducing agents [6] to prepare citrate stabilized gold nanoparticles. Mercapto-derivatives have been commonly used as modifiers of gold nanoparticles in recent years. 3-Mercaptopropionic acid (3-MPA) represents such a compound. At basic pH nanoparticles modified by 3-MPA have negative charge on the surface due to carboxylate groups. This allowed immobilization of porphyrin conjugates which have positive charge due to quaternary nitrogen atoms by ionic bond. Ionic this immobilization of porphyrine can be. Also carried out by direct immobilization of porphyrin conjugates on non-modified gold nanoparticles because of their negative surface charge.

The method based on the reduction of $K[AuCl_4]$ by citrate was used to prepare 15 nm average size gold nanoparticles (ref. 5). The immobilization of porphyrin conjugates was carried out by two different ways of ionic interaction. First, direct immobilization of conjugate on nanoparticles, second, immobilization of conjugate on 3-MPA premodified gold nanoparticles. Such prepared nanoparticles were purified by centrifugation and characterized. Interactions of oxoanions (NO_3^- , $H_2PO_4^{2-}$, SO_4^{2-} , ClO_3^- , ClO_4^- , HCO_3^- , ReO_4^-) with porphyrin-brucine conjugates in methanol-water solution and water were studied by ECD spectroscopy. Stability constants for complexes of porphyrin-brucine conjugates with oxoanions were calculated and the effect of gold nanoparticles will be described.

The financial support from the MSMT6046137307, FRVS, LC512, KAN200100801 and KAN200200651 is gratefully acknowledged.

References:

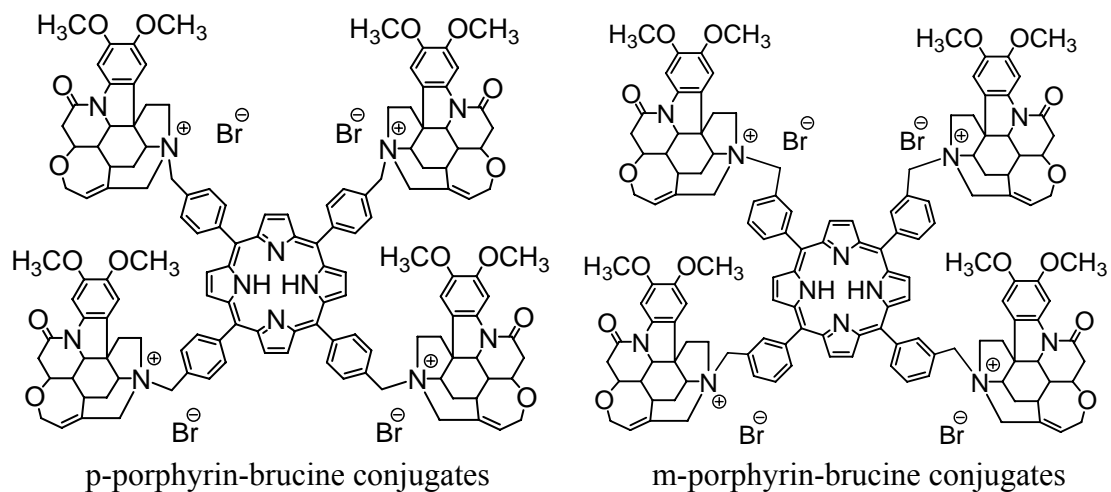
- [1] Boldyrev, A. I.; Gutowski, M.; J. Acc. Chem. Res., **29** (1996) 497.
- [2] Záruba K., Setnička V., Charvátová J., Rusin O., Tománková Z., Hrdlička J., Sýkora D., Král V., Collect. Czech. Chem. Commun., **66** (2001) 693.
- [3] Řezanka P., Záruba K., Král V., Tetrahedron Lett., **49** (2008) 644.

[4] Král V., Pataridis S., Setnička V., Záruba K., Urbanová M., Volka K., *Tetrahedron*, **61** (2005) 5506.

[5] Shipway N. A., Katz E., Willner I., *Chem. Phys. Chem.*, **1** (2000) 1655.

[6] Turkevitch J., Stevenson P. C., Hillier J., *Discuss. Faraday Soc.*, **11** (1951) 55.

Figures:



Measurement of Repulsive Casimir Forces Using Silicon Membranes.

G. Vidal, J. Agustí, F. Torres, G. Abadal and N. Barniol.

Universitat Autònoma de Barcelona, ETSE, edifici Q, 08193 Bellaterra, Spain

Gabriel.Vidal@uab.cat

In this work we present an attempt to measure repulsive Casimir force. The Casimir force is a direct manifestation of boundary dependence of quantum vacuum due to the alteration by the boundaries of the zero-point electromagnetic energy. This phenomena was first described by H.B.G. Casimir in 1948 [1] with an explanation of retarded Van-der-Waals interactions. Casimir found an expression of a finite and attractive force between two infinite and neutral planes. This positive Casimir force has been measured several times, between a sphere and a plane, using different methodologies [2, 3].

Few years ago the existence of a repulsive Casimir force was also predicted [4]. The Casimir effect is strong dependent on boundary. Size, geometry, topology and materials that compose the boundary can switch the force from attractive to repulsive. Kenneth and co-workers [4] predicted the repulsive Casimir force between element 1 and 2 immersed in a medium 3, with the relation between their permittivities as $\epsilon_1 > \epsilon_3 > \epsilon_2$. Gold, bromobenzene and silica fulfill this relation, and have been used by Capasso and co-workers [5] to measure, for the first time, the repulsive Casimir force.

On the other hand, repulsive Casimir force due to the geometry of the boundary was predicted by many authors, as Gusso and co-workers [6]. This work predicts the existence of a repulsive component of the Casimir force between two plates if one of them has a set of rectangular cavities.

One of the main problems of MEMS (MicroElectromechanical Systems) is the sticktion, the collapse of the resonant structures on the electrodes or substrate. The existence of the repulsive Casimir forces could solve, or diminish, this problem, extending the life of MEMS. The aim of our work is focused on measuring the repulsive Casimir forces on MEMS, particularly between a silicon membrane and an electrode.

We have calculated the Casimir forces between a silicon membrane and an electrode which is engraved with a set of rectangular cavities. Our attempt of measurement is based on the ACO model (Anharmonic Casimir Oscillator) [7] which predicts a shift of the resonance frequency of MEMS due to the presence of the Casimir force. We have calculated this shift on the resonance frequency of a silicon membrane (thermal excited) with the distance between membrane and electrode (engraved with rectangular cavities). For an attractive force, the shift is negative (spring softening) and for a pure repulsive force the shift is positive (spring hardening).

To measure the frequency shift we have fabricated a demonstrator: on a SOI wafer, with 300 nm thick crystal silicon, we have opened a window at the back side of the wafer and we have performed a wet etching (KOH etching) of the silicon (around 500 μm thick) until the oxide layer. Then we have etched the oxide, obtaining a crystal silicon membrane of 300 nm of thickness. We have fabricated a set of these membranes with different areas (different resonant frequencies): 500 μm^2 , 700 μm^2 and 1000 μm^2 . On the other hand, in a silicon wafer, we have fabricated the electrode, making a hollow 1 μm deep and circular shape at the center of the wafer. Finally, using electron beam lithography, we have engraved the set of rectangular cavities of sides 100 nm wide, 1 μm deep and 100 μm long. A gold layer, 20 nm thick, was deposited both on the wafer with the membranes and the wafer with electrode (in order to enlarge the Casimir effect). Finally, the two wafers were sealed (between them) forming a cavity 1 μm deep between membranes and electrodes.

In order to measure the frequency response of the membrane we have design a measurement system based on Fabry-Perot interference method. The demonstrator will be mounted in a

vacuum chamber (in order to reduce the damping effect of the air) forming a Fabry-Perot cavity with a red-light filter. Outside the vacuum chamber there are a 632.8 nm He-Ne laser and an optical system designed for detecting the membrane vibration on a photodetector (1 GHz bandwidth) connected to a spectrum analyzer (see figure 3). The measurement system is now in the test stage.

References:

- [1] H.B.G. Casimir, Proc. K. Ned. Akad. Wet. **51** (1948) 793.
- [2] S.K. Lamoreaux, Physical Review Letters **78** (1997) 5.
- [3] U. Mohideen, A. Roy, Physical Review Letters **81** (1998) 4549.
- [4] O. Kenneth, I. Klich, A. Mann, M. Revzen, Physical Review Letters **89** (2002) 033001-1.
- [5] J.N. Munday *et al.*, Nature Letters **457** (2009) 170.
- [6] A. Gusso, A.G.M. Schmidt, Brazilian Journal of Physics **36** (2006) 168.
- [7] F.M. Serry, D. Walliser, G. J. Maclay, Journ. Microelectrom. syst. **4** (1995) 193.

Figures:

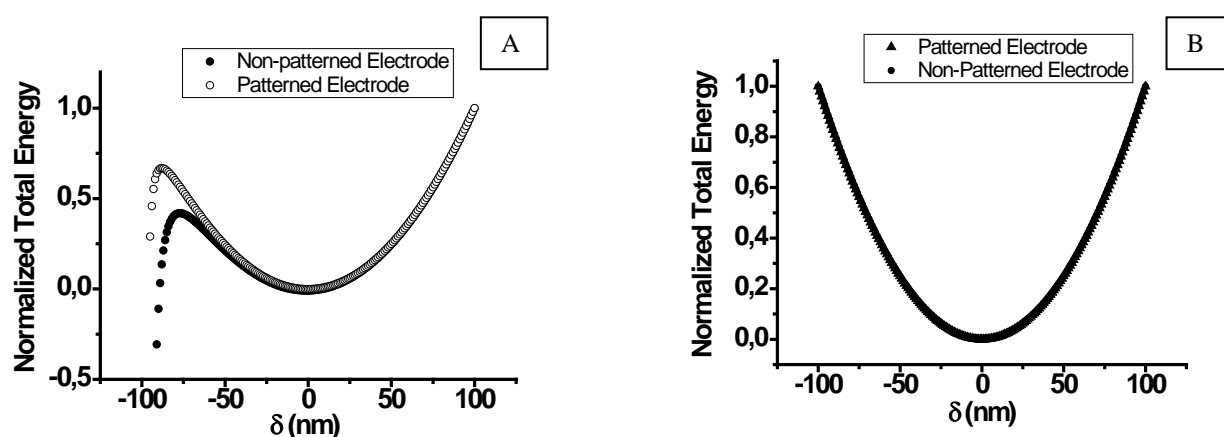


Figure 1: Normalized total membrane energy (Total Energy/Maximum Elastic Energy) versus membrane displacement. **A:** The membrane in his equilibrium position is at $L=100$ nm from the fixed electrode. **B:** Membrane is at $L=800$ nm from the fixed electrode. At that distance the total membrane energy is barely modified by the Casimir effect and the membrane vibrates harmonically.

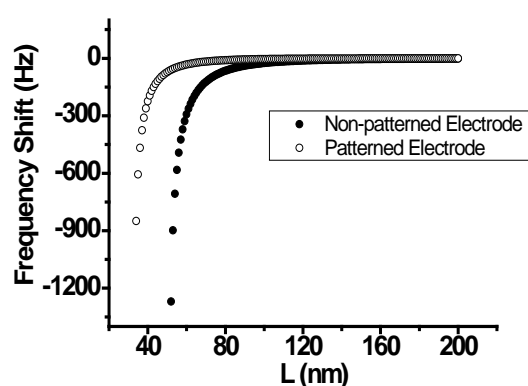


Figure 2: Frequency shift of the membrane resonator frequency due the presence of the electrode at distance L . With the patterned electrode the frequency shift is reduced respect the non-patterned electrode.

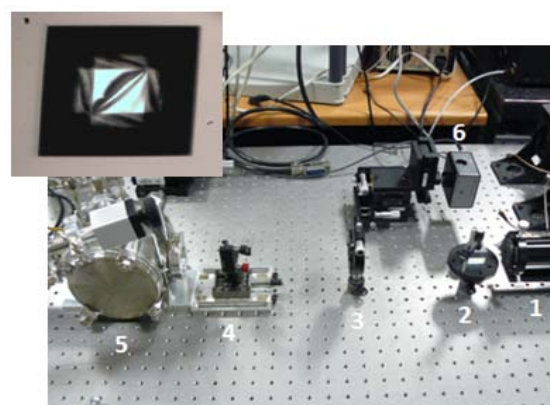


Figure 3: Experimental Set-up and membrane (inset). Laser (1), beamsplitter (2), retarder (3), focusing lens (4), vacuum chamber where the bonded wafers and the filter forming the Fabry-Perot cavity are introduced (5) and photodetector (6).

STUDY OF CHARACTERISTICS OF GIZO BASED TFT DEVICES IN THE SUB-MICRON SCALE

Antonis Olziersky^a, Anna Vilà^a, Juan-Ramon Morante^a, Pedro Barquinha^b, Luis Pereira^b, Rodrigo Martins^b, Elvira Fortunato^b

^a Materials for Electronics and Energy-M2E/IN2UB/XaRMAE, Electronics Department, University of Barcelona, Marti i Franques 1, 08028 Barcelona, Spain

^b Department of Materials Science/CENIMAT/IN3, Faculty of Science and Technology, New University of Lisbon and CEMOP-UNINOVA, Campus Caparica, 2829-516, Caparica, Portugal
aolziersky@el.uib.es

Multi-component metal oxide semiconductors have gained a great deal of attention in the recent years due to a unique combination of several advantages both electronically and technologically. Among the many kinds of oxide semiconductors, which have been studied thus far, $\text{Ga}_2\text{O}_3\text{-In}_2\text{O}_3\text{-ZnO}$ (GIZO) combines high mobility, controlled resistivity, steady amorphous phase and low processing temperature. The implementation of this semiconductor in thin film transistors (TFTs) has delivered devices with low off currents, high on/off ratio and very good overall performance [1].

Usually the fabricated TFTs are based in optical lithography and scaling down of such devices is limited. With this paper an investigation of the performance of GIZO-based devices in the sub-micron scale is presented with the fabrication bottom gate staggered TFTs (fig. 1) by incorporating electron beam lithography (EBL) for the realization of source and drain electrodes. The width (W) and length (L) of the transistor's gate are determined by the width of the electrodes and the distance between them respectively. For this work, several different W/L ratios were realized. TFTs were characterized electrically (transfer characteristic presented in fig. 2) and we have found that the produced devices had a mobility of around $50 \text{ m}^2/\text{Vs}$, low off current in the range of 10^{-11} A and a sub-threshold voltage slope of $0.35 \text{ V}/\text{dec}$.

References:

[1] P. Barquinha, A. Vilà, G. Gonçalves, L. Pereira, R. Martins, J.R. Morante, E. Fortunato, IEEE Trans. Elec. Devices 55 (2008) 954-960.

Figures:

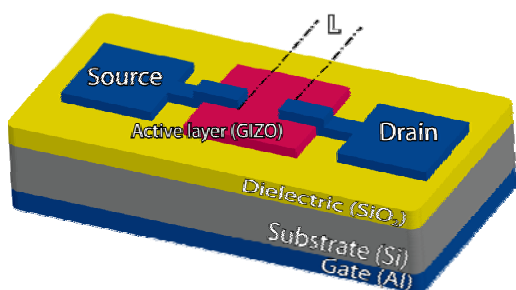


Fig. 1 Bottom staggered TFT

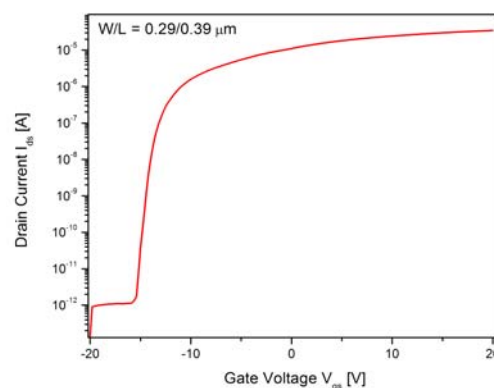


Fig. 2 Transfer characteristic of submicron TFT device

Synthesis of fluorescent copper clusters

Noelia Vilar, M. Carmen Blanco, Arturo López-Quintela, and José Rivas

*Laboratory of Nanomaterials and Magnetism (NANOMAG). Institute of technological Research-Department of Physical Chemistry and Applied Physics. University of Santiago de Compostela. E-15782. Santiago de Compostela. (A Coruña). Spain.
noelia.vilar@usc.es*

Metal clusters are groups of a small number of atoms with sizes (≈ 1 nm) similar to the electron Fermi wavelength, resulting in molecule-like behavior including discrete electronic states and size dependent fluorescence. It has been recently shown that transition metal zero-valence clusters having small number of atoms, Mn ($n \leq 20$, n = number of atoms), can be synthesized by simple electrochemical techniques [1]. In this work we will show the synthesis of copper clusters (CuCLs) by an electrochemical method. These copper clusters are stable in acetonitrile and aqueous solutions displaying different photoemission ranges, which can be tuned in the UV and visible region depending on the solvent. These results can be useful to achieve a fine tuning of the fluorescence properties, which is needed for their use in important practical applications, like integrated optical devices, bio-labeling and sensors.

Cu clusters were characterized using UV-Vis and fluorescence spectroscopy, X-ray photoelectron spectroscopy (XPS) and atomic force microscopy (AFM). The obtained results reveal the possibility of tuning the emission range changing the post-treatment conditions.

References:

- [1] M.A. López Quintela and J. Rivas. "Procedure for the preparation of atomic quantum clusters". Spanish patent application N°. P200402041, 2005.PCT/ES2006/070121,2006.

Figures:

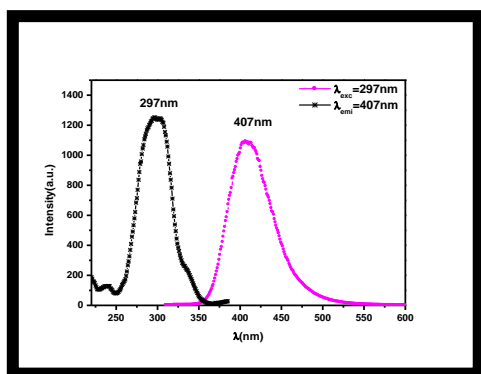


Fig. 1: Excitation/Emission spectra of CuCLs in water.

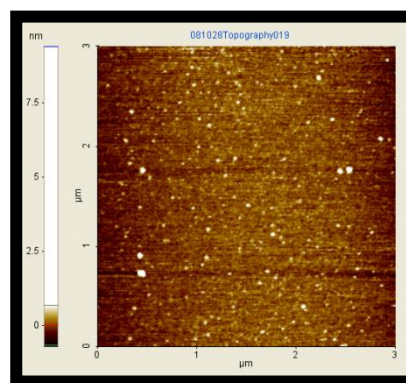


Fig. 2: AFM image of CuCLs deposited on a mica surface showing an average height of 0.6nm.

PREPARATION OF MAGNETIC POLYSTYRENE-DIVINYLBENZENE HYBRID NANOCOMPOSITES

A. Vilchez¹, C. Rodríguez-Abreu¹, P.M. Botta², C.E. Hoppe² and R.J.J. Williams²

¹ *Instituto de Química Avanzada de Cataluña. Consejo Superior de Investigaciones Científicas (IQAC-CSIC) and CIBER de Bioingeniería, Biomateriales y Nanomedicina (CIBER-BBN), Spain*

² *Institute of Materials Science and Technology (INTEMA), University of Mar del Plata and National Research Council (CONICET), J. B. Justo 4302, 7600 Mar del Plata, Argentina.*

avvqst@cid.csic.es

Hybrid nanocomposites consist of an organic (or inorganic) nanomaterial dispersed in a continuous inorganic (or organic) matrix. There is a growing interest on such nanocomposites[1], due to their enhanced properties derived from the synergistic contributions of the dispersed and the continuous components, that have found applications in high density storage media, sensors, optical filters, electronic materials, coatings, delivery systems and so on.

Herein, we present results on the preparation of rigid and transparent polystyrene-divinylbenzene (PS-DVB) transparent monoliths containing well dispersed magnetic iron oxide nanoparticles. The nanoparticles were synthesized using reverse microemulsions and were capped with a molecule which is compatible with the polymer matrix. Particulate and porous hybrid materials with characteristic dimensions in both the nano and micro scale have also been obtained via colloidal systems such as emulsions and high internal phase ratio emulsions (HIPREs)

References:

[1] A. C Balazs, T. Emrick, T.P. Russell, *Science* **314** (2006) 1107

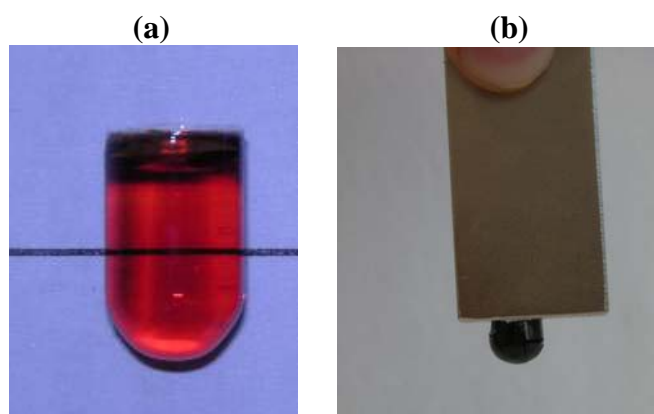


Figure 1: Images showing a PS-DVB monolith with low (a) and high (b) concentrations of embedded iron oxide nanoparticles. Note that the monolith is strongly attracted by a magnet in (b)

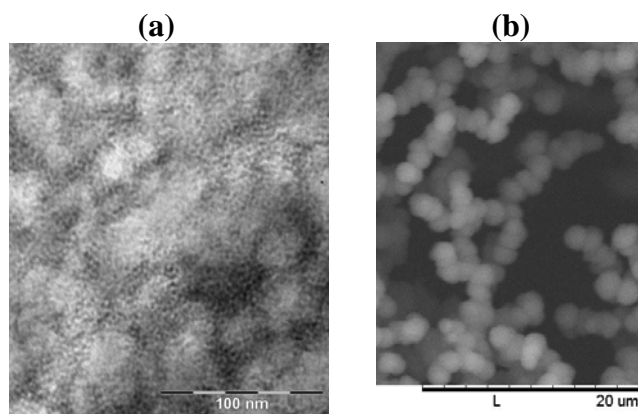


Figure 2: Microscopic images of iron oxide nanoparticles embedded in a PS-DVB matrix (a) and nanocomposite microparticles prepared using emulsions as templates (b)

PREPARATION OF MAGNETIC POLYSTYRENE-DIVINYLBENZENE HYBRID NANOCOMPOSITES

A. Vilchez¹, C. Rodríguez-Abreu¹, P.M. Botta², C.E. Hoppe² and R.J.J. Williams²

¹ *Instituto de Química Avanzada de Cataluña. Consejo Superior de Investigaciones Científicas (IQAC-CSIC) and CIBER de Bioingeniería, Biomateriales y Nanomedicina (CIBER-BBN), Spain*

² *Institute of Materials Science and Technology (INTEMA), University of Mar del Plata and National Research Council (CONICET), J. B. Justo 4302, 7600 Mar del Plata, Argentina.*

avvqst@cid.csic.es

Hybrid nanocomposites consist of an organic (or inorganic) nanomaterial dispersed in a continuous inorganic (or organic) matrix. There is a growing interest on such nanocomposites[1], due to their enhanced properties derived from the synergistic contributions of the dispersed and the continuous components, that have found applications in high density storage media, sensors, optical filters, electronic materials, coatings, delivery systems and so on.

Herein, we present results on the preparation of rigid and transparent polystyrene-divinylbenzene (PS-DVB) transparent monoliths containing well dispersed magnetic iron oxide nanoparticles. The nanoparticles were synthesized using reverse microemulsions and were capped with a molecule which is compatible with the polymer matrix. Particulate and porous hybrid materials with characteristic dimensions in both the nano and micro scale have also been obtained via colloidal systems such as emulsions and high internal phase ratio emulsions (HIPREs)

References:

[1] A. C Balazs, T. Emrick, T.P. Russell, *Science* **314** (2006) 1107

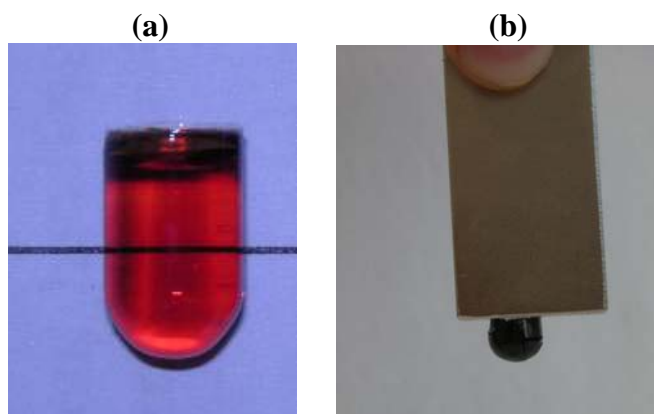


Figure 1: Images showing a PS-DVB monolith with low (a) and high (b) concentrations of embedded iron oxide nanoparticles. Note that the monolith is strongly attracted by a magnet in (b)

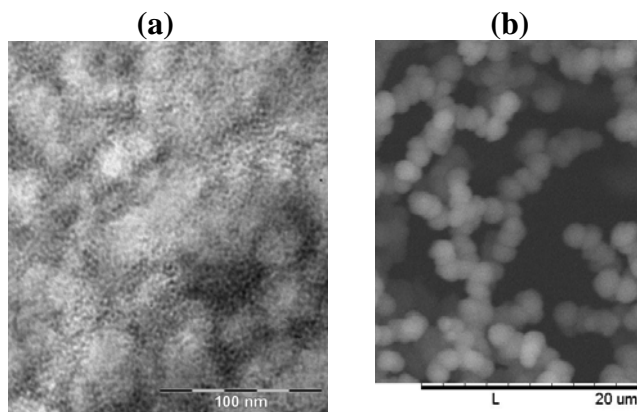


Figure 2: Microscopic images of iron oxide nanoparticles embedded in a PS-DVB matrix (a) and nanocomposite microparticles prepared using emulsions as templates (b)

THEORETICAL ANALYSIS OF ACOUSTICAL MICROSENSORS RESPONSE IN NANOBIOLOGY APPLICATIONS

M.V.Voinova and M.Jonson

Department of Physics, University of Gothenburg,
412 96, Göteborg Sweden

We present new results in physical analysis of acoustical SAW- based (Love- wave) resonators and magnetoelastic microsensors in biofluidic applications where the negligible amount of biomolecular material can be monitored *in situ* in a liquid phase. We reported the exact solution of the dispersion equation of surface acoustic waves (SAW) of Love type for the first type of resonators and demonstrate the importance of size effects in magnetoelastic resonators never taken into account before in such systems. Our results can readily be applied to the correct interpretation of resonance frequency and quality factor changes measured in various biofluidic applications.

Our choice of the resonators has been motivated by the following. SAW-based microsensors operate at high frequency (up to GHz) which is a great benefit for monitoring of mass since the measurable signal, the shift in phase velocity $\Delta V/V$, is $\sim \omega^2$. The Love wave polarization corresponds to the no-slip conditions for example, when the biomolecular coating material is covalently bound to the substrate. Magnetoelastic sensors is a type of acoustic resonance devices considered as the magnetic analog of SAW sensors. Besides of simple design, miniaturization and low cost of the magnetoelastic materials, the advantage of magnetoelastic resonators is a possibility of wireless remote measurements [1,2]. Their working principle is based on a usage of magnetostrictive ribbon-shaped elements of a few mm in size as transducers that mechanically oscillate at a fundamental frequency f_0 when placed in *ac* magnetic field. Viscous- or mass loads cause a variation in the resonance frequency $\Delta f = f - f_0$ of the resonator. Simultaneous monitoring of the dissipation factor $D \equiv 1/Q$ allows to measure fluid viscosity [1]. Both characteristics can be measured with high precision comparable with the SAW sensors. Since polymer coated magnetoelastic resonators are used for biosensors operating mainly in fluids [3,4], it is a crucial to connect the material parameters of coating and biofluid with the experimentally accessible damping coefficient and resonance frequency shifts of the oscillator. Another physical phenomenon that can influence these characteristics is the size effect due to the specific geometry of the resonator. In the present work we take into account both these effects by studying the dynamics of coated resonators oscillating in a longitudinal mode and immersed in biofluid. Comparison of our results with other types of microsensors such as bulk acoustic waves (BAW) devices and thin-film bulk resonators in nanobiology applications [5] is presented as a short survey.

References

- [1] M.K.Jain and C.A.Grimes. Sens.Actuators A 100 (2002) pp.63-69.
- [2] 2a.Pengfei Pang, Wenyue Yang, Sijing Huang, Qingyun Cai, Shouzhao Yao. Analytical Letters, 40 (2007) pp.897-906.
- [3] Jiehui Wan, Huihua Shu, Shichu Huang, Ben Fiebor, I-Hsuan Chen, Valery A.Petrenko, and Bryan A.Chin. IEEE Sensors J. 7 (2007) pp. 470-477.
- [4] Chuanmin Ruan, Kefeng Zeng, Oomman K.Varghese and Craig A.Grimes. Biosens.Bioelectronics 19 (2004) pp.1695-1701.
- [5] M.V. Voinova, J. Sensors, 2009 (in press).

IN-SITU MECHANICAL TESTING OF NANOWIRES AND NANODOTS

*J. Michler, L. Philippe, D. Zhang, Z. Wang, W. Mook, V. Friedli, I. Utke,
EMPA, Materials Science and Technology, Thun, Switzerland
zhao.wang@empa.ch*

Nanowires are among the most exciting one-dimensional nanomaterials because of their potential use as building blocks for future nanoelectronic devices or as nanoelectromechanical systems in artificial human nose and ear implants. These applications require an in depth understanding of mechanical integrity issues like the dependence of electronic and optical properties under mechanical strain or a precise knowledge of mechanical material properties for device design, respectively. The integration of nanomechanical testing equipment inside a scanning electron microscope allows for the handling of nanowires and to observe failure mechanisms under load.

We developed recently several instruments for nanomechanical testing of nanowires in the SEM: an atomic force microscope (AFM) in SEM for resonance testing and nanobending experiments, a MEMS-based nanotensile testing device, a nanoindentation device for nanocompression and nanoindentation experiments, and a femptogramm mass sensor to measure density. These instruments were used to measure mechanical properties of metal and semiconductor nanowires.

The fracture strength of epitaxial silicon nanowires grown on a [111] silicon substrate by the vapor-liquid-solid process was measured by AFM. The average strength calculated from the maximum nanowire deflection before fracture was around 12 GPa, which is 6% of the Young's modulus of silicon along the nanowire direction. This value is close to the theoretical fracture strength, which indicates that surface or volume defects, if present, play only a minor role in fracture initiation. Similarly, the fracture strength of ZnO nanowires vertically grown on sapphire substrates was measured in tensile and bending experiments. The fracture strain of 7.7 % measured in the bending test was found to be close to the theoretical limit of 10% and revealed a strength about twice as high as in the tensile test. From the tensile experiments, the Young's modulus could be measured to be within 30% of that of bulk ZnO, contrary to the lower values found in the literature.

Electrodeposited nanocrystalline cobalt nanowires were loaded in tension and revealed surprisingly low Young's modulus values of 64 GPa. An independent measure of the Young's modulus by nanoindentation along the wire axis revealed similar values. Coupling these values with a resonance excitation technique revealed the low nanowire modulus was due to a low mass density.

Nanocompression tests on single crystal gold nanodots will also be presented. These structures yielded in a stochastic manner which was followed by repeatable plastic flow which, very similar to nanoindentation results of flat single crystals. However yielding of these freestanding structures was accompanied by large displacement bursts between 5-50% engineering strain which were analysed by in-situ SEM observations.

ELECTROSTATICS OF CARBON NANOTUBES AND GRAPHENE: ELECTRIC CHARGES AND DEFORMATION.

Z. Wang, R. W. Scharstein, M. Zdrojek, Th. Mélin, M. Devel and L. Philippe

EMPA (Swiss Federal Laboratories for Materials Testing and Research), Thun, Switzerland. Electrical Engineering Department, University of Alabama, AL, USA. Faculty of Physics, Warsaw University of Technology, Warsaw, Poland. Departement ISEN, Institut d'Electronique de Microélectronique et de Nanotechnologie, Villeneuve d'Ascq, France. Institute UTINAM, University of Franche-Comté, Besancon, France.

wzzhao@yahoo.fr

We present a detailed study of the static enhancement effects of the electric charges in carbon nanotubes (CNTs), by using theoretically an atomic charge-dipole model and experimentally electrostatic force microscopy. Our studies reveal that the charge enhancement ratio decreases with the tube length and increases with the tube radius. Quantitative agreement is obtained between theory and experiment [1,2].

The distribution of net electric charge in graphene is also investigated, using both a constitutive atomic charge-dipole interaction model and an approximate analytical solution to Laplace's equation. We demonstrate a strong size dependence of the charge distributions in finite-size, infinitely-long and multi-layered rectangular graphene sheets, respectively. It is found that the edge charge enhancement effect becomes more significant when the length, the width or the number of layer of graphene increases [3].

We demonstrate the strong dependence of the electrostatic deformation of CNTs on the field strength and the tube length, using molecular simulations. Metallic nanotubes are found to be more sensitive to an electric field than semiconducting ones of the same size. For a given field, the induced deformation increases with tube length but decreases with tube radius. Furthermore, it is found that nanotubes can be more efficiently bent in a center-oriented transverse electric field [4].

References:

- [1] Z. Wang, M. Zdrojek, Th. Mélin, and M. Devel, Phys. Rev. B **78** (2008) 085425.
- [2] Z. Wang, Phys. Rev. B **79** (2009) 155407.
- [3] Z. Wang and R. W. Scharstein, *to be published*.
- [4] Z. Wang and L. Philippe, Phys. Rev. Lett. **102** (2009) 215501.

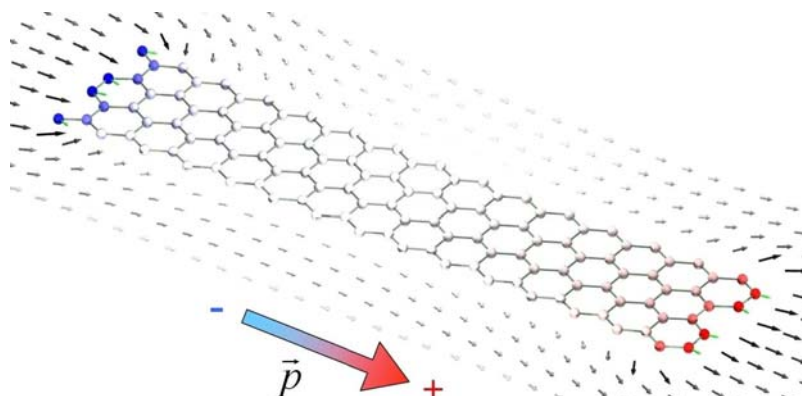


Figure 1: When an electric field is applied through a graphene.

QPLUS AFM WITH SMALL OSCILLATION AMPLITUDES AND HIGH FREQUENCIES AT 5 K

A. Bettac, J. Koeble, M. Maier, K. Winkler, B. Uder, A. Feltz

¹ *Omicron NanoTechnology GmbH, Germany*

(corresponding author: K. Winkler, e-mail: k.winkler@omicron.de)

The creation and investigation of nano-structures, molecules or atomic structures on insulating surfaces is a key approach for electronic decoupling from the substrate. It pushes AFM as a complementary imaging and spectroscopy technique to STM. Ideally, the used AFM probe should simultaneously or alternatively work in STM/STS modes without performance compromises on the latter. Based on a proven low temperature (5K) LT STM platform, we have integrated a QPlus sensor [1], which employs a quartz tuning fork for force detection in non-contact AFM. For combined STM operation, this sensor has key advantages over conventional cantilevers: (i) a solid metal tip for optimal STM/STS and (ii) high stiffness and high stability, i.e. low vibrational noise due to small self-resonance amplitudes.

For quantitative force spectroscopy on insulating thin films or semiconductors, decoupling of tunneling current and piezo-electrically induced AFM signal is important. By measurements on Si(111) and Au(111) we prove that a dedicated pre-amplification technique avoids cross-talk. In addition, extremely low signals require the first amplification stage to be very close to the sensor, i.e. to be compatible with low temperatures. STS measurements using a Niobium tunneling tip reveal the superconducting gap with a FWHM of approx. 2.5 meV and prove a probe temperature of approx. 5K.

The high stiffness (1800 N/m) of the sensor allows for operation with extremely small amplitudes to (i) more precisely keep the sensor with a certain force interaction regime, (ii) increase sensitivity especially for short range forces and (iii) allow for force measurements during atom manipulation experiments without disturbing the manipulation event as such [2].

As benchmark measurements, we present (1) atomic resolution imaging on single crystal NaCl with oscillation amplitudes down 72pm (peak-to-peak) in constant df imaging feedback (fig. 1) and, (2) operation at higher flexural modes in constant df imaging feedback with frequencies above 300 kHz (fig. 2). We also present atomic resolution measurements on MgO(100), Au(111), and first evaluation measurements of the QPlus sensor in Kelvin Probe (KPM) mode operation on Si(111) 7x7.

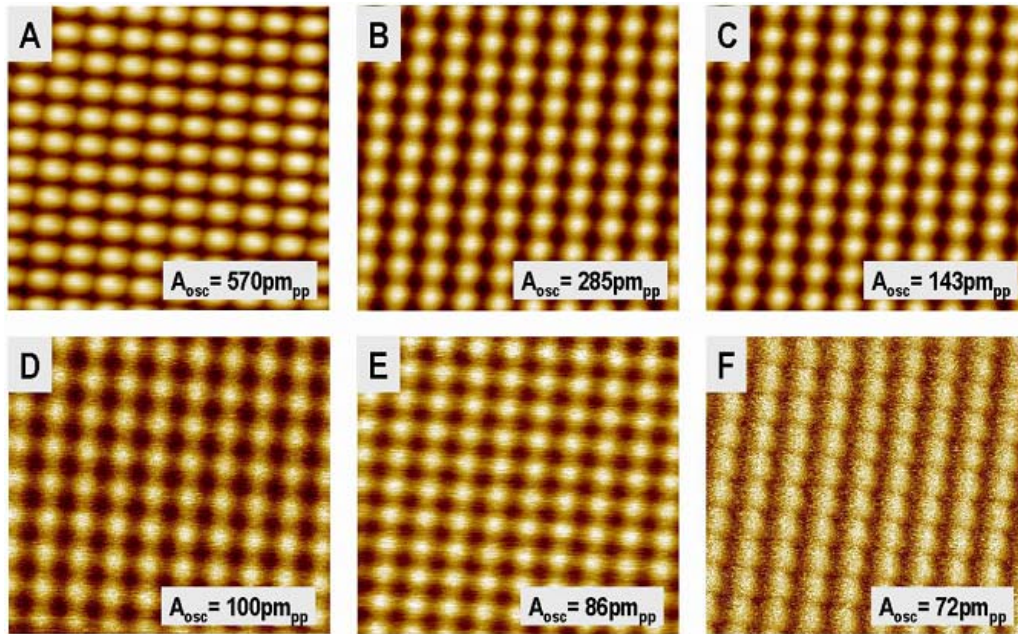
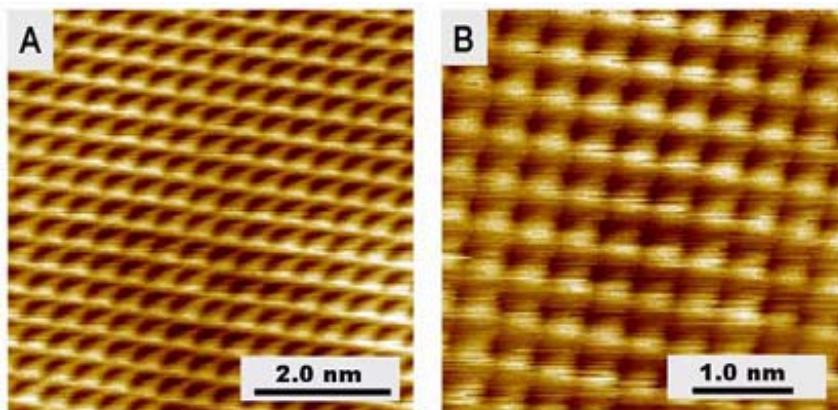


Fig.1: QPlus AFM on single crystal NaCl(100) in df feedback at low oscillation amplitudes down to 72 pm_{pp}. Raw data, line-by-line background correction, no filtering. 4 nm x 4 nm, T = 5 K, $f_0 = 47874$ Hz, $Q = 90000$, $U_{\text{gap}} = +500$ mV (a to c) and $U_{\text{gap}} = -400$ mV (d to f), $df = -$



10.8 Hz, -16.5 Hz, -22.3 Hz, -17.5 Hz, -19.3 Hz, -40.75 Hz (a to f).

Fig. 2: QPlus AFM on NaCl(100) using a flexural mode at T = 5 K. Sensor operated at a frequency of $f_0 = 318534$ Hz for df feedback. Base frequency is 47 kHz. $U_{\text{gap}} = 450$ mV, $Q = 9300$. (a) $df = -2.37$ Hz, $A_{\text{OSC}} = 1.5$ nm_{pp}. (b) $df = -4.45$ Hz, $A_{\text{OSC}} = 0.5$ nm_{pp} Raw data, line-by-line background correction, no filtering.

[1] F. J. Giessibl, et al., Appl. Phys. Lett. 73, 3956 (1998)

[2] M. Ternes, et al., Science 319, 1066 (2008)

SURFACE NANOSTRUCTURATION TO INCREASE POLYPYRROLE ADHESION DEPOSITED BY PECVD

Jose Luis Yagüe^{1,2}, Núria Agulló¹, Zineb Mekhalif², Salvador Borrós¹

¹*Grup d'Enginyeria de Materials (GEMAT), Institut Químic de Sarrià-Universitat Ramon Llull, Via Augusta 390, 08017 Barcelona*

²*Laboratory of Chemistry and Electrochemistry of Surfaces, University of Namur (FUNDP), Rue de Bruxelles 61, B-5000 Namur, Belgium
salvador.borros@iqs.url.edu*

Conducting polymers are gaining increasing attention for micro and nanoelectronic applications[1]. One of the most important efforts is being focused on the developing of gas sensors. In comparison with other materials, conducting polymer can offer a higher sensitivity, a shorter response time or a lower cost fabrication. However, sometimes these polymers present a lack of adhesion with the substrate. Thus, to prevent this unwanted effect is necessary to modify the surface. The use of self-assembled monolayers (SAMs) has become a very common technique to nanostructure surfaces. Choosing a proper terminated group of the monolayer can lead to the design of the surface with the properties required in each work. For instance, Willicut[2] et al reported that a pyrrole-terminated group enhances the deposition and growing of polypyrrole by electrochemical synthesis. According to this, previous investigations in our research group have demonstrated that the same effect can be observed in the deposition of polypyrrole by plasma enhanced chemical vapor deposition (PECVD)[3]. PECVD is a solventless technique through which the desired material layer can be achieved from the vapor phase. In addition, this technique allows an absolute control in the deposition rate to obtain very thin films. Regarding earlier work, the effect of alkanethiols monolayers assembled on a gold surface have been widely studied. Nevertheless, the use of copper in microelectronics for the fabrication of almost any electronic device makes necessary a deeper study in this kind of surface. Moreover, not only a thiol group can be assembled on copper, but a selenol group can become an alternative for this purpose[4]. In this work we describe and compare the employ of ω -(pyrrolyl)alkanethiol and selenol molecules with different chain length to modify a copper substrate. The quality and the ordering of the monolayer have been studied by XPS and electrochemical experiments. Further plasma polymerization has been carried out on the different modified substrates to study the deposition-growth mechanism, adhesion and electrical properties of these films.

References:

- [1] M. Angelopoulos, *Ibm Journal of Research and Development* 45 (2001) 57
- [2] R. J. Willicut and R. L. Mccarley, *J.Am.Chem.Soc.* 116 (1994) 10823
- [3] J. L. Yagüe, N. Agulló, S. Borrós, *Plasma Processes and Polymers* 5 (2008) 433
- [4] Z. Mekhalif, G. Fonder, D. Auguste, F. Laffineur, J. Delhalle, *Journal of Electroanalytical Chemistry* 618 (2008) 24

Figures:

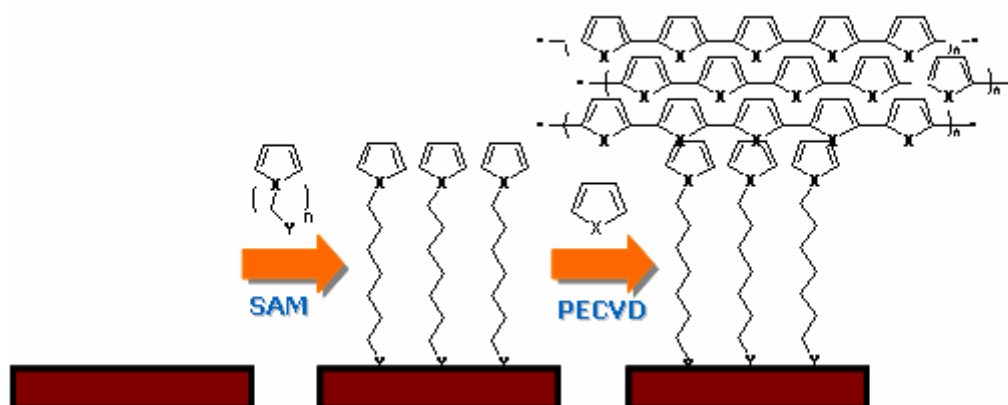


Figure 1. Scheme of the surface modification using self-assembly and the posterior plasma polymerization.

Study of the dielectric properties of $\text{La}_{0.67}\text{Ca}_{0.33}\text{MnO}_3$ nanoparticles and $\text{La}_{0.67}\text{Ca}_{0.33}\text{MnO}_3@ \text{SiO}_2$ nanocomposites

S. Yáñez-Vilar¹, M. Sánchez-Andújar¹, S. Castro-García¹, J. Mira², J. Rivas², M. A. Señarís-Rodríguez¹

¹Dept. Química Fundamental, Univ. da Coruña, A Zapateira s/n, 15071 A Coruña, España

²Dept. Física Aplicada, Univ. Santiago de Compostela, 15781 Santiago de Compostela, España
syanez@udc.es

The search of materials with high dielectric constant has been a field of interest due to the important applications of this property in many electronic devices, like high-performance capacitors [1]. In this materials group, oxides with the perovskite structure are well known for their ability to produce high dielectric constants.

In this context, in a previous work, our investigation group have studied the dielectric properties of a polycrystalline sample of the manganese perovskite $\text{La}_{0.67}\text{Ca}_{0.33}\text{MnO}_3$ with particle size $\sim 10 \mu\text{m}$ [2]. We have found that, at room temperature, it shows, high values of dielectric constant ($\epsilon'_r > 10^4$) in a wide frequency range ($10^2 < \nu < 10^5$ Hz). Nevertheless, despite this attracting high ϵ'_r , it also shows high dielectric losses, associated to a relatively high conductivity of the sample, a serious drawback for potential technological applications.

In this work, and with the aim to reduce the dielectric losses, we have reduced the particle size of the polycrystalline material to the nanometric scale, and have prepared core-shell composites growing nanolayers of an insulating material (SiO_2) over the obtained $\text{La}_{0.67}\text{Ca}_{0.33}\text{MnO}_3$ nanoparticles.

For this purpose, nanometric particles of $\text{La}_{0.67}\text{Ca}_{0.33}\text{MnO}_3$, with $\phi \sim 100$ nm, were synthesized by the sol-gel method described in [3] with a final heat treatment at $700^\circ\text{C}/3$ hours. $\text{La}_{0.67}\text{Ca}_{0.33}\text{MnO}_3@ \text{SiO}_2$ core-shell nanocomposites with different thickness of SiO_2 shell (Figure 1) were prepared using the Stöber method [4]. The obtained samples were morphologically and structurally characterized by means of X-ray powder diffraction and transmission electron microscopy. Its complex dielectric permittivity, $\epsilon_r = \epsilon'_r - i\epsilon''_r$, was measured as a function of frequency ($20 \leq \nu$ (Hz) $\leq 10^6$) and temperature ($200 \leq T$ (K) ≤ 300).

The room temperature frequency dependent dielectric behavior of the so obtained materials is compared in Figure 2. As it can be seen, the dielectric constant of the $\text{La}_{0.67}\text{Ca}_{0.33}\text{MnO}_3$ nanoparticles is higher than in the case of the nanocomposites (Figure 2a). Nevertheless and most interestingly, in the coated samples the loss tangent has decreased by a factor of ~ 10 , as compared to the uncoated sample (Figure 2b). From the practical point of view, the best dielectric behaviour is found in the $\text{La}_{0.67}\text{Ca}_{0.33}\text{MnO}_3@ \text{SiO}_2$ ($\phi_{\text{SiO}_2} \sim 3$ nm) nanocomposite: it still shows a rather high dielectric constant ($\epsilon'_r > 10^2$), while its dielectric losses have decreased ($\tan\delta < 10$ for $\nu > 10^4$ Hz).

Acknowledgments:

The authors are grateful for financial support from Xunta de Galicia under project PGIDIT06PXB103298PR. S. Yáñez-Vilar want to thank to MEC of Spain for her FPI fellowship.

References:

- [1] R. J. Cava, *J. Mater. Chem.*, **11** (2001) 54-62.
- [2] B. Rivas-Murias, Tesis Doctoral, Universidade da Coruña **2006**.
- [3] C. Vázquez-Vázquez, M. C. Blanco, M. A. López-Quintela, R. D. Sánchez, J. Rivas, S. B. Oseroff, *J. Mater. Chem.*, **8** (1998) 991-1000.
- [4] W. Stöber, A. Fink, E. Bohn, *J. Colloid Interface Sci.*, **26** (1968) 62.

Figures:

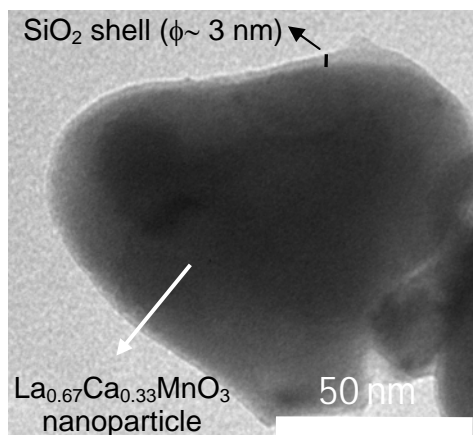


Figure 1. TEM micrograph of $\text{La}_{0.67}\text{Ca}_{0.33}\text{MnO}_3@SiO_2$ core-shell composite. The thickness of the SiO_2 nanocoating is ~ 3 nm.

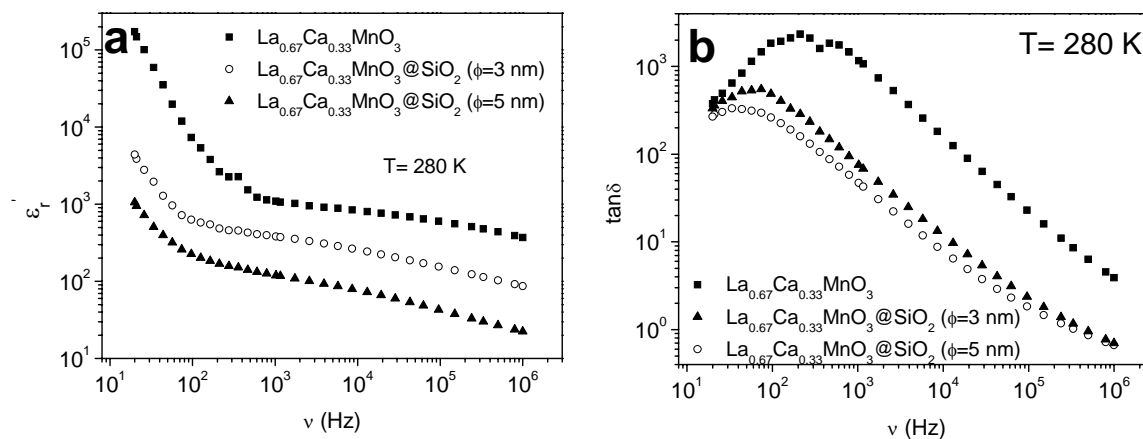


Figure 2. Frequency (ν) dependence of a) the dielectric constant (ϵ'_r) and b) the loss tangent ($\tan\delta$) for the $\text{La}_{0.67}\text{Ca}_{0.33}\text{MnO}_3$ nanoparticles and the $\text{La}_{0.67}\text{Ca}_{0.33}\text{MnO}_3@SiO_2$ nanocomposites measured at $T=280$ K.

Preparation and characteristics of solution-processable organic thin film transistors on a PES substrate

Yong Suk Yang, Seong Hyun Kim, Sang Chul Lim, Doo-Hyeb Youn, In-Kyu You, and Seong Youl Kang

*IT Convergence and Components & Materials Research Laboratory, Electronics and Telecommunications Research Institute 138, Gajeongno, Yuseong-gu, Daejeon 305-700, Korea
jullios@etri.re.kr*

In recent years, flexible-formed organic thin-film transistors (OTFTs) have been intensely investigated due to their low cost and lightweight for potential use in applications such as flexible displays and low-cost flexible integrated circuits (ICs).[1,2] Polymer OTFTs with poly-4-vinylphenol(PVP) gate dielectrics were integrated onto flexible polyethersulfone (PES) substrates by spin-coating and inkjet printing methods. The active materials used were poly(9,9-dioctylfluorene-co-bithiophene) (F8T2) and poly(3-hexylthiophene) (P3HT) polymers, which were functionalized with biotin hydrazide. The relationship between the chemoresistive change and the binding of avidin-biotin moieties in the polymers was observed in the output and on/off characteristics of OTFTs. The exposure of OTFTs to avidin caused a lowering of the I_D at $V_D = -40$ V, $V_G = -40$ V of nearly five orders of magnitude, and the results were very applicable to a biosensor.

References:

- [1] F. Mouffouk, S. J. Brown, A. M. Demetriou, S. J. Higgins, R. J. Nichols, R. M. G. Rajapakse, and S. Reeman, *J. Mater. Chem.*, **15** (2005) 1186.
- [2] W. Liang, Y. Huang, Y. Xu, R. K. Lee, and A. Yariv, *Appl. Phys. Lett.*, **86** (2005) 151122.

Figures:

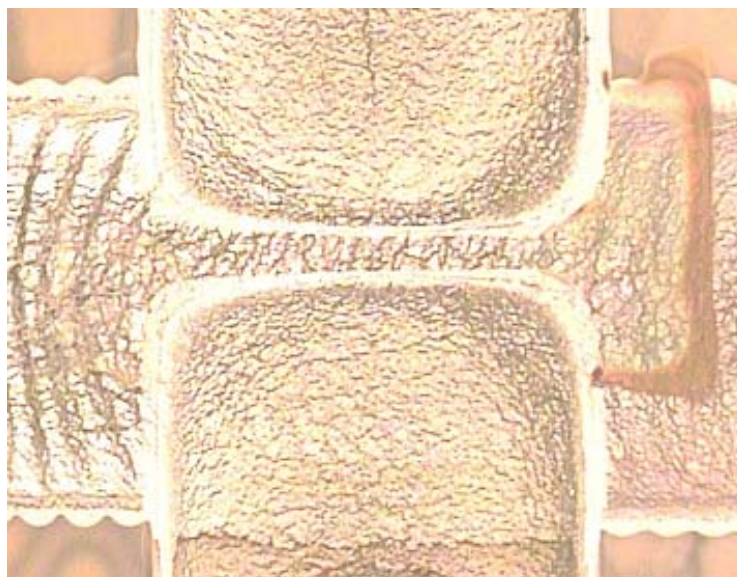


FIG. 1. Photograph of a solution-processable organic thin film transistor on PES by a inkjet printing.

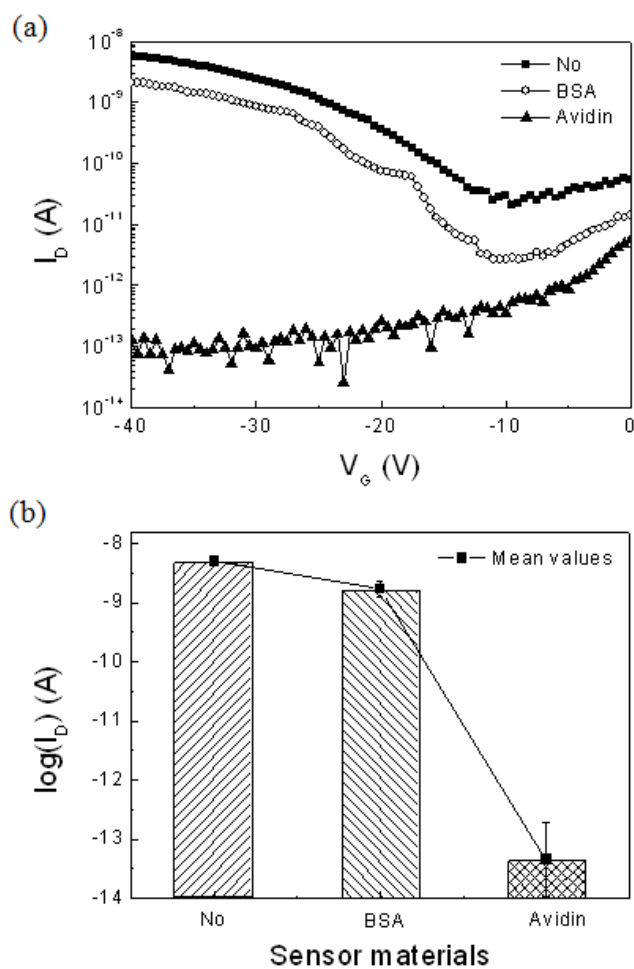


FIG. 2. (a) I_D - V_G characteristics of biotinylated F8T2 TFTs before and after exposure the antigen containing solutions. (b) Mean value and error bar of the I_D results at $V_D = -40$ V, $V_G = -40$ V obtained from ten independent measurements.

CHARACTERIZATION OF CU NANO-COLLOID PREPARED BY WIRE ELECTRIC EXPLOSION PROCESS IN LIQUID

Sangsun Yang, Jae-Cheol Yoon and Ji-Hoon Yu

Powder Technology Group, Functional Materials Division, Korea Institute of Materials Science, 531 Changwon-daero Changwon, KOREA
nanoyang@kims.re.kr

Wire electric explosion process has been found about two hundred years ago and developed for the synthesis of nanoparticles from several ten years ago. It can be seen that energy deposited in the wire in the ohmic heating stage is larger in a dense medium. When a wire is exploded in a condensed medium, the resistance of discharge gap is higher than in air. For example, ohmic heating stage in water is almost twice as large as that in air. Wire electric explosion in liquid (WEEL) is possible to control the energy deposition in wire by changing the electrical breakdown, atomization enthalpy and expanding plasma, etc. Various kinds of liquids with different density are possible to use for medium in WEEL. Therefore, the properties of nanoparticles can be controlled by WEEL.

Ink-jet printing is a kind of noncontact and direct process as a pattern on demand type. It is also possible to make a conductive metal nanoparticles pattern simply, continuously and economically. Therefore, there are many kinds of merits on ink-jet printing process considering the application field like TFT, PCB, FPD, RFID, Solar cell, etc. To apply nanoparticles to electrical printing technology, long time stability of nanoparticles without contamination in liquid is indispensable. Wire explosion process in liquid is a kind of new process to prepare stable nanoparticle colloids with high purity.

Cu nano-colloid was prepared by wire electric explosion in de-mineralized water and anhydrous ethanol. Experimental instrument is composed of a high voltage power supply, a capacitor, continuous wire feeding system and an explosion chamber which is possible to contain various kinds of liquids. To control the properties of Cu nano-colloid, experimental conditions such as thickness of Cu wire and applied voltage are changed.

As shown in figure 1, Cu nano-colloids were successfully prepared by wire electric explosion in anhydrous ethanol with different concentration. The size of Cu nanoparticles in colloid is about 20 nm (figure 2). Dispersion stability of Cu nano-colloid was measured by transmittance of laser light. Ink-jetting property of Cu nano-colloid will be presented.

References:

- [1] J. R. Greer and R. A. Street, *Acta Mat.* **55** (2007) 6345.
- [2] R. Sarathi, T.K. Sindhu and S.R. Chakravarthy, *Mater. Lett.* **61** (2007) 1823.
- [3] A.E. Ter-Oganesyan, S.I. Tkachenko, V.M. Romanova, A.R. Mingaleev, T.A. Shelkovenko and S.A. Pikuz, *Plasma Phys. Rep.*, **31** (2005) 919.
- [4] A. Grinenko, Y.E. Krasik, S. Efimov, V.T. Gurovich and V.I. Oreshkin, *Physics of Plasma* **13** (2006) 042701.

Figures:

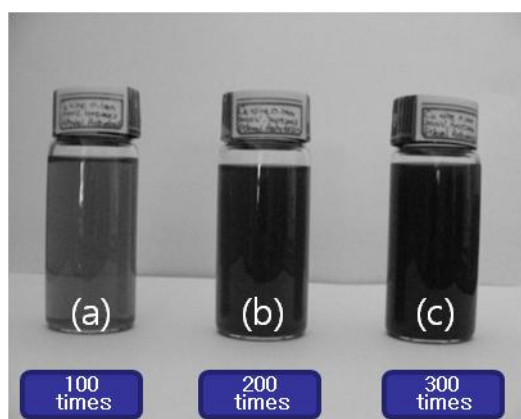


FIG. 1. Picture of Cu nano-colloids prepared by wire electric explosion process in anhydrous ethanol. (a) 100 times explosion, (b) 200 times explosion and (c) 300 times explosion.

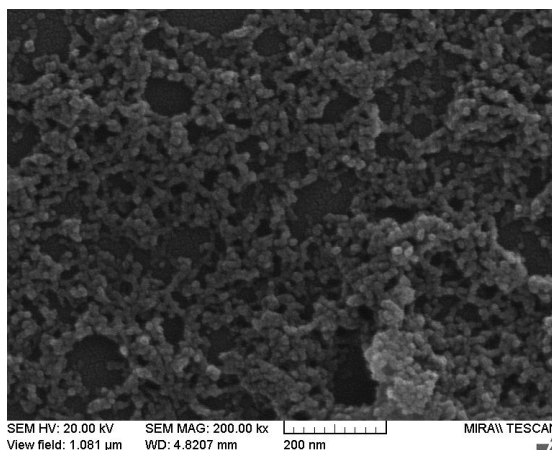


FIG. 2. SEM image of Cu nanoparticles. 2,500 V applied on 0.1 mm Cu wire.

Nanocomposite a-C:Cr coatings deposited by shielded cathodic vacuum arc

L. Yate, L. Martinez-de-Olcoz, J. Esteve, A. Lousa

*Departament de Física Aplicada i Òptica, Universitat de Barcelona. Martí i Franquès 1,
Planta 5^a, 08028 Barcelona, Spain*

l.yate@ub.edu

Chromium incorporated amorphous carbon (a-C:Cr) coatings were deposited onto silicon substrates by cathodic vacuum arc deposition using a Cr target in an Ar/C₂H₂ gas mixture atmosphere. A linear magnetic shield was employed to reduce the macroparticles density in the films. Various negative bias voltages ranging from 50 to 450 V were applied to the substrates. X-ray diffraction (XRD) analysis shows that amorphous structures are formed in all cases. X-ray photoelectron spectroscopy (XPS) analysis was used to quantify the sp³/sp² ratio bonding in the films. Raman spectroscopy was used to study the presence of different forms of free amorphous carbon. The Raman spectra were decomposed into four single Gaussians and the results are discussed in terms of the ratio of the areas of the two D bands to the areas of the two G bands, I(D)/I(G), and the position and width of the peaks. The results showed that the sp³ fraction is inversely proportional to the negative bias voltage and to the I(D)/I(G) ratio. The higher the sp³ fraction, the lower the positions of the Raman peaks.

**EFFECTS OF ANTIMICROBIAL NANOPARTICLES TO MEDICAL TEXTILES
FOR PERMANENT ANTIMICROBIAL ACTIVITY**

Nilüfer Yıldız VARAN, Nevin Çiğdem GÜRSOY

Istanbul Technical University, Textile Technologies and Design Faculty, Department of
Textile Engineering, TURKEY

Antimicrobial textiles are classified as those textile and fibrous materials subjected to various finishing techniques to afford protection for both the user of textile materials (against bacteria, yeast, dermatophytic fungi and other related microorganisms for aesthetic, hygienic or medical purposes) and the textile itself (biodeterioration caused by mould, mildew and rot producing fungi) without negatively affecting the other important characteristics of the textiles. Conventional antimicrobial agents provide only a limited antimicrobial effect to textiles. Application of nanoparticles can provide high durability for fabrics, because nanoparticles have a large surface area-to-volume ratio and high surface energy, thus presenting better affinity for fabrics and leading to an increase in durability of the function.

In this research, at first antimicrobial nanoparticles such as silver, chitin, etc. were synthesised then applied to various medical textile fabric samples by using wet treatment, etc. Their antimicrobial activities were tested and compared with the untreated medical textile fabric samples. And also washing durabilities were tested in order to see the permanent antimicrobial effects of nanoparticles to textiles. It was observed that permanent antimicrobial effects to medical textiles were achieved by the increasing of wash durabilities.

Synthesis and spectroscopic properties of silver:dye composite nanoparticles with a double-shell structure

Akihito Yoshida, Noritsugu Kometani

Department of Applied Chemistry, Graduate School of Engineering,

Osaka City University, Osaka, Japan

yoshida@a-chem.eng.osaka-cu.ac.jp

Noble metal nanoparticles (NPs), such as Au, Ag and Cu NPs, are currently one of the most attractive nanomaterials. They have a wide variety of applications including catalysis, printable conductor, antibacterial agent, and so on. In particular, there has been a large interest in the optical and spectroscopic properties because of the ability to couple with the electromagnetic wave in the visible or near-infrared region, called localized surface plasmon resonance (LSPR). The LSPRs induce a large extinction of light and generate the enhanced electromagnetic fields in the vicinity of the metal surfaces. More importantly, the enhanced fields lead to several intriguing phenomena such as surface-enhanced Raman scattering (SERS), enhanced photoluminescence (PL), and enhanced Förster resonance energy transfer. Manipulating and controlling the surface-enhanced effects are therefore considered to be an essential issue for the development in the area of imaging, diagnostics, photonics, plasmonics, etc.

Cyanine dye J-aggregates (JAs), a kind of molecular assemblies, have been known to form on the solid surfaces, LB films, etc., and have several interesting spectroscopic properties which cannot be observed in the form of monomer. For example, they show a sharp absorption band (J-band) red-shifted with respect to the monomer band and the resonance fluorescence with a small Stokes shift. Those properties have been extensively studied for many years and explained in terms of the delocalization of Frenkel exciton, resulting from the strong coupling between transition dipole moments of dyes.

Considering the unique properties of the surface plasmon and exciton, it is reasonable to expect that the hybrid materials composed of the noble metal NPs and the JAs exhibit certain novel properties useful for the optical or optoelectronic materials. In this sense, our group has been interested in such hybrid systems [1-3].

In this study, to examine the spectroscopic properties of the exciton–plasmon hybrid systems, we have synthesized double-shell-type composite NPs, consisting of the following three components; spherical Ag core, spacer layer (inner shell), and cyanine dye JA layer (outer shell) (see Figure 1a). The spacer layer is made of the self-assembled monolayer of *N, N, N*-trimethyl(11-mercaptoundecyl)ammonium chloride (TMA) and plays a significant role in the formation of JA shell. Two kinds of cyanine dyes, 3,3'-disulfopropyl-5,5'-dichloro-thiacyanine sodium salt (TC) and 3,3'-disulfopropyl-5,5'-dichloro-oxacyanine triethylammonium salt (OC) (Figure 1b) were used as an ingredient of the JA shell. In Figure 2, the absorption spectra of colloidal solution containing Ag/TMA/TC and Ag/TMA/OC composite NPs are shown. The spectrum of the Ag/TMA/TC NPs (Figure 2a) is characterized by two peaks at 398 nm and 470 nm. The former peak can be ascribed to the LSPR band of Ag NPs, and the latter peak to the J-band of TC JAs, supporting the ability of TMA layer to facilitate the J-aggregation. On the other hand, the spectrum of the Ag/TMA/OC NPs (Figure 2b) shows an anomalous “dip” at 409 nm, instead of a “peak” of OC J-band ($\lambda_{J,OC} = 410$ nm [4]). The appearance of the dip-type absorption suggests the presence of a strong *exciton–plasmon coupling* between the Ag NP core and the OC JA shell.

Acknowledgment:

This work is a part of the Osaka Central Area Industry-Government-Academia Collaboration Project on "City Area Program" sponsored by MEXT (Ministry of Education, Culture, Sports, Science & Technology, Japan), 2007–2009. This work is also partially supported by KAKENHI (20510079), MEXT.

References:

- [1] N. Kometani, M. Tsubonishi, T. Fujita, K. Asami, Y. Yonezawa, *Langmuir*, **17** (2001) 578.
 [2] A. Yoshida, N. Kometani, Y. Yonezawa, *Colloids Surf., A*, **313/314** (2008) 581.
 [3] A. Yoshida, Y. Yonezawa, N. Kometani, *Langmuir*, **25** (2009) 6683.
 [4] K. Tani et al. *J. Photochem. Photobiol., A*, **199** (2008) 150.

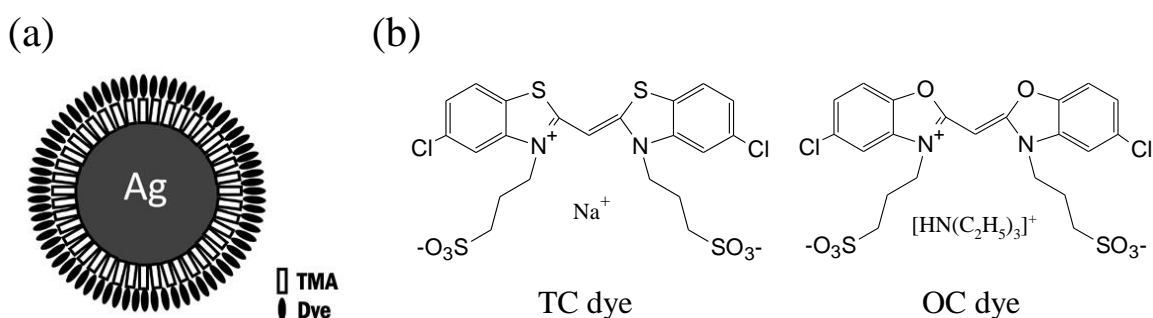
Figures:

Figure 1. (a) Schematic illustration of an Ag/TMA/Dye composite NP. (b) Molecular structure of the cyanine dyes used in this study.

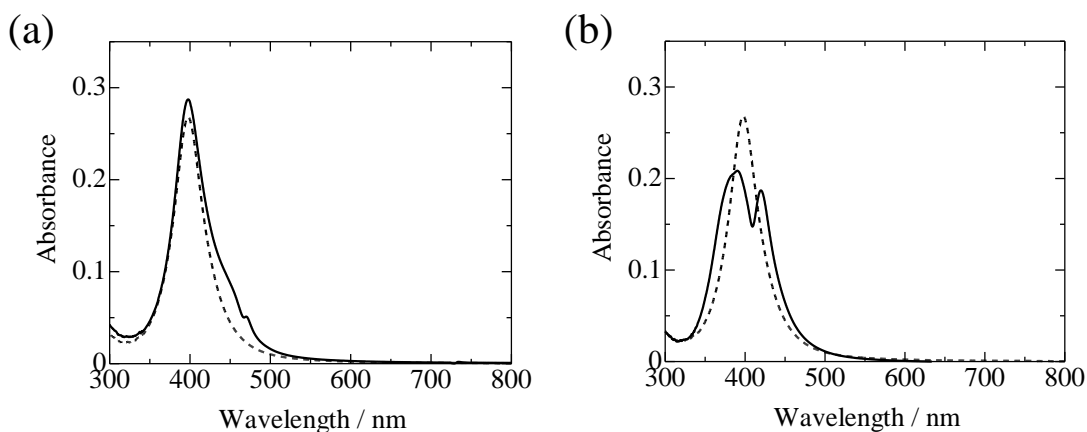


Figure 2. Absorption spectra of colloidal solutions containing (a) Ag/TMA/TC NPs and (b) Ag/TMA/OC NPs. The spectra depicted in broken line in each spectrum correspond to the Ag/TMA NPs (without dye layer).

Manipulation of WO₃ nanoparticles using AC electric fields

Elham Kamali Heidari¹, Ehsan Maezbanrad¹, Babak Raissi¹, Seyed Reza Mahmoodi¹,
Cyrus Zamani²

¹ *Materials and Energy Research Center, P.O. Box 14155-4777, Tehran, Iran*

² *Department of Nano Electronics, University of Barcelona, Barcelon , Spain
czamani@el.ub.es*

Abstract

Tungsten oxide WO₃ is an *n*-type semiconductor with interesting physical and chemical properties that make it suitable for various technological applications such as catalysts, electrochromic devices or gas sensors. In the field of sensor fabrication the particles shall be located between two conductive electrodes. Among various approaches for the manipulation of nanostructures, AC electrophoresis (ACEP) is an attractive technique for the effective, inexpensive, and parallel manipulation of semiconductor nanostructures [1-2].

In this research, Alternative electric field was applied to align WO₃ nanoparticles between two Au electrodes with a 100µm gap. For this purpose suspensions with different concentrations were prepared and deposition was carried out applying various voltages and frequencies. The results showed that, controlling the value of applied voltage, frequency and suspension concentration, would lead to the particles migration and deposition into desired locations (Fig.1). Moreover, the SEM results showed that the particles bridge the gap between the two electrodes forming parallel patterns (Fig.2) which can result in higher responses with an improved stability if used as a gas sensor. This study reveals that the AC electrophoretic techniques have the potentiality for precise manipulation of nanoparticles which would be useful in making micro/nano electronic devices.

References:

- [1] N G Green, A Ramos, and H Morgan, J. Phys. D: Appl. Phys. 33 (2000) 632–641.
- [2] Seung-Yong Lee , Ahmad Umar, Duk-II Suh, Ji-Eun Park, Yoon-Bong Hahn, Jeong-Yong Ahnc, Sang-Kwon Leea ;Physica E 40 (2008) 866–872

Figures:

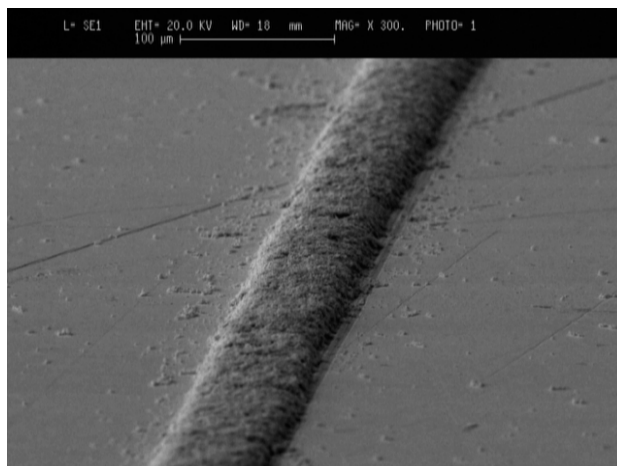


Fig.1. WO₃ nanoparticles deposited in the gap between the electrodes, at 30V, frequency of 10KHz and suspension concentration of 0.1gr/lit WO₃/Acetone

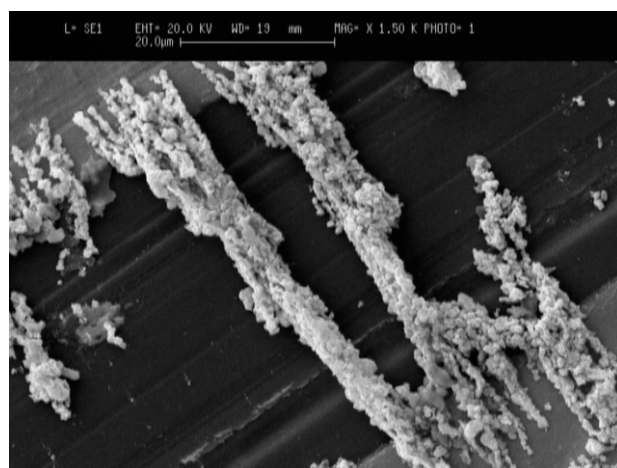


Fig.2. WO₃ nanoparticles bridging the gap at 50V and a frequency of 10 KHz

Synthesis of mesoporous anatase TiO₂ nanoparticles, using nanocasting method

Seyed Reza Mahmoodi¹, Babak raissi¹, Ehsan Marzbanrad¹, Elham Kamali Heidari¹, Cyrus Zamani²

¹Materials and Energy Research Center, P.O. Box 14155-4777, Tehran, Iran

²Department of Electronics, University of Barcelona, Spain

czamani@el.uib.es

Abstract:

The optical and electronic properties of semiconductor nanoparticles are largely attributed to quantum confinement or surface effects. Over the past 10 years, mesoporous titania has attracted much attention because of its high surface area and large pores[1-2], which are of great importance in photocatalysis, highly specific chemical sensors, luminescence, and solar cells.

In this research we applied a nanocasting route to prepare mesostructured material for CO sensing. Mesoporous TiO₂ was synthesized by nanocasting route, using SiO₂ as a template. For this purpose, in the first step, mesoporous SiO₂ was prepared using polyethylene oxide /polypropylene oxide block copolymer as soft template, and TEOS as silica source. In the second phase TTIP and mesoporous SiO₂ were dissolved in isopropanol and stirred vigorously for 1 hour, dried at room temperature at air atmosphere and heated at 550°C with heating rate of 10°C/min for 4h. At last the SiO₂ hard template was removed by HF. BET measurements showed a specific surface area of 700m²/gr for synthesized SiO₂ while after impregnation and template removal, this area is reduced for TiO₂ nanoparticles. HRTEM and XRD results, in a good agreement, showed single crystalline nanoparticles possessing anatase structure which is the favorite crystal structure for gas sensing or photocatalytic applications.

References:

[1] Li Zhao, Jianguo Yu, Journal of Colloid and Interface Science 304 (2006) 84–91

[2] Chao Wang, Qin Li, Ruo-Ding Wang, Materials Letters 58 (2004) 1424– 1426

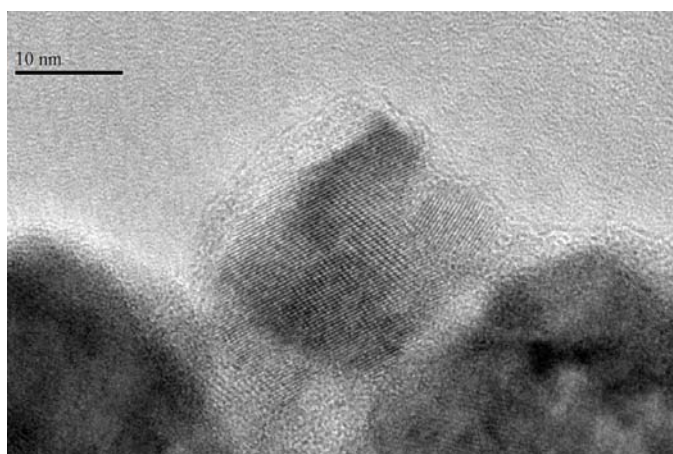
Figures:

Fig.1. TEM image of TiO_2 nanoparticles, with d-spacing of about 3.5\AA belonging to (101) planes in anatase TiO_2

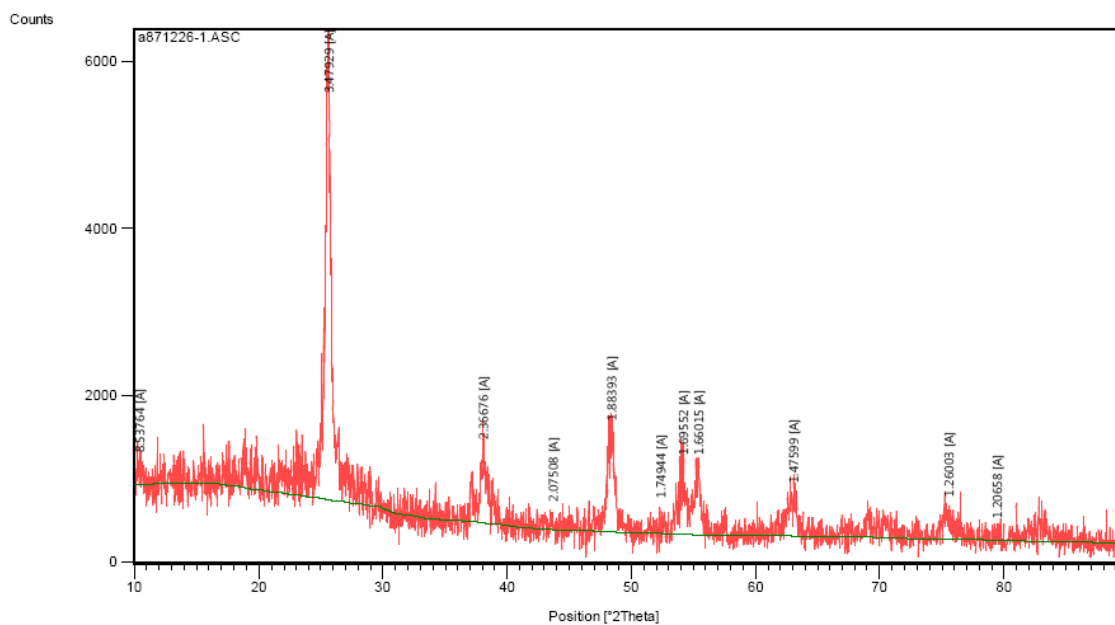


Fig. 2. XRD pattern of TiO_2 nanoparticles

Nanowire formation by means of coalescence of small gold clusters encapsulated inside carbon nanotubes

B. Zhu^{1,2}, M. Hou¹, Y. Wang², Z. Pan²

¹*Physique des Solides Irradiés et des Nanostructures CP234, Faculté des Sciences, Université Libre de Bruxelles, Bd du Triomphe, B-1050 Brussels, Belgium*

²*Applied Ion Beam Physics Laboratory, Institute of Physics, Fudan University, 225, Handan Road, Shanghai, China*

bzhu@ulb.ac.be, beien_zhu@fudan.edu.cn

We report the atomistic molecular dynamics study of the stable configurations of small icosahedral Au clusters (Au₁₃, Au₅₅, and Au₁₄₇) encapsulated inside single wall carbon nanotubes (CNTs). The interactions between carbon atoms and between Au atoms were described by the many-body Brenner potential and the Finnis-Sinclair potential, respectively. A Lennard-Jones (L-J) potential was used to describe the C-Au interaction.

In the first step, the stability of single clusters in CNTs was examined and the binding energies of Au₁₃ and Au₅₅ clusters to CNTs with different radii were estimated. The results are given in Table I.

Table I: Binding energies (in eV) of Au₁₃ and Au₅₅ clusters in CNTs with different radii

Tube	(7,7)	(8,8)	(9,9)	(12,12)	(13,13)	(15,15)
Au ₁₃	Unstable	3.35	3.28	3.25	3.22	3.18
Au ₅₅	-----	-----	-----	7.35	7.30	7.27

All binding energies shown are positive. In this case, the filling of SWNTs with clusters is an exothermic process. Moreover we found that the largest binding energies appear in the cases of (8,8) CNTs for Au₁₃ and (12,12) CNTs for Au₅₅. In these cases, as well as for Au₁₄₇ cluster in (15,15) CNTs, the distances between tubes and cluster surfaces are close to the equilibrium distance of the L-J potential, 0.3nm.

In the second step, the coalescence of two clusters in CNTs was studied. Two Au₁₃ clusters in a (8,8) CNTs coalesce spontaneously and form a nanowire segment at room temperature. The initial 5-fold icosahedral symmetry turns into a 7-fold symmetrical wire as shown in fig. 1.



Fig.1. Snapshot of a 7-fold nanowire segment resulting from the coalescence of two Au₁₃ clusters. Views parallel and perpendicular to the axis of the (8,8) CNTs are displayed. The CNTs is not shown.

Two Au₅₅ clusters in a (12,12) CNTs were also found to coalesce spontaneously at room temperature. In contrast with the case of Au₁₃ coalescence, the nanowire segment has two 5-fold symmetric caps. However after raising the temperature up to more than 600K the caps disappear and the symmetry changes to 6-fold (fig. 2).

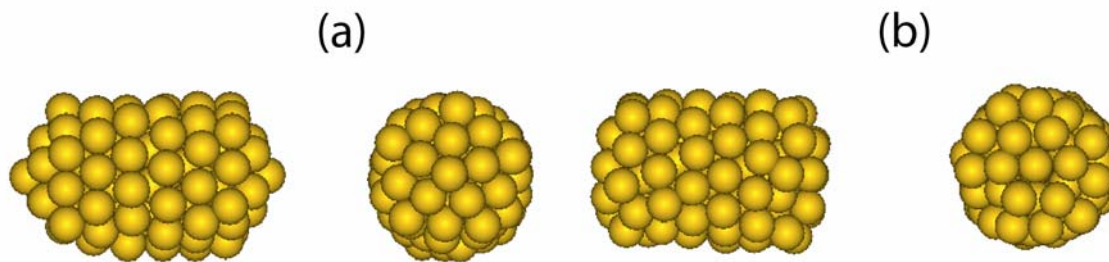


Fig.2: Snapshots of a nanowire segment resulting from the coalescence between two Au_{55} clusters in a (12,12) CNTs. a) 5-fold segment at room temperature; b) 6-fold segment after heating at 600K.

This structure was found better stable than 5-fold by a quenched annealing method. Like the smaller clusters, two Au_{147} clusters were also found to coalesce spontaneously at 300K. Similarly to Au_{55} , they also formed a nanowire segment with two icosahedral caps. After heating and cooling down the system, the caps disappeared also, but the wire segment turned fcc.

These results illustrate that, similarly to filling, coalescence is also exothermic.

In order to identify the main factors governing structural evolution, we analyzed the change in potential energies. It was found that the energy changes are mainly taken over by Au-Au interactions. On the other hand, the disappearing of caps minimizes the surface to volume ratio of the wires, which are not constrained to 5-fold symmetry anymore. This allows the fcc character to appear in the Au_{147} case. The effect of CNTs with appropriate radii is to make coalescence a one dimensional process. The Au system evolves to its minimal energy configuration with this constraint. Indeed, in large tubes, coalescence was found to become three dimensional and a competition between the formation of wires and the deformation of tubes occurs. Finally we encapsulated Au_{13} and Au_{55} clusters one by one into CNTs with different radii. This allowed to show that inserting a set of Au_{55} clusters induces a deformation of the larger than (12,12) CNTs. When inserting Au_{13} clusters in larger than (8,8) tubes, then latter are no deformed but the clusters form a nanowire which matches the confined inner space of CNTs. In this case, a nanowire with the same 6-fold structure as with Au_{55} clusters is formed at room temperature without the use of an annealing treatment. These results suggest that a viable way to fabricate nanowires with controlled diameters and structure is to encapsulate small metal clusters inside the appropriate CNTs.

REVEALING THE ROLE OF ANCHORING GROUPS IN THE ELECTRICAL CONDUCTION THROUGH SINGLE-MOLECULE JUNCTIONS

L.A.Zotti¹, J.C.Cuevas¹, T. Kirchner², T. Huhn², E. Scheer², A. Erbe², F. Pauly³

¹Departamento de Física Teórica de la Materia Condensada, Universidad Autónoma de Madrid, E-28049 Madrid, Spain

²Physik Bereich, Universität Konstanz, D-78457 Konstanz, Germany

³Institu für Theoretische Festkörperphysik, Universität Karlsruhe, D- 76131 Karlsruhe, Germany

linda.zotti@uam.es

Recent advances in nanofabrication techniques have made possible to contact individual molecules between metallic electrodes and to measure their electronic transport properties. This fact has triggered the hope that single molecules could be used as electronically active elements in a variety of applications. This has given rise to the birth of a new interdisciplinary field already known as *Molecular Electronics*. Although the initial results are promising, the future of this field still depends crucially on our ability to understand the basic transport mechanisms that determine the electrical current at the single-molecule scale.

With this idea in mind, a great effort has been devoted recently to understand how the transport properties of molecular junctions can be tuned by modifying chemically the molecules under study [1]. In this sense, one of the main problems that have been addressed is the role of anchoring groups in the transport through single-molecule junctions [2,3]. However, these studies have been largely based on the analysis of the low-bias conductance, which does not allow to elucidate the exact influence of the terminal groups in both the electronic structure and transport characteristics of the junctions.

In this work we present a combined theoretical and experimental study of the transport properties of ethyne single molecules chemically modified by the introducing thiol, nitro and cyano terminal groups. The measurements were performed using the mechanically controllable break-junction (MCBJ) technique. The advantage of this experimental approach is that it allows us to record the current-voltage (I-V) characteristics, which provide valuable information not contained in the linear conductance. We show that the observed I-V curves can be accurately fitted with a single-level resonant tunneling model. From the fits, we are able to extract both the width of the resonant level that dominates the transport, which is a measure of the strength of the metal-molecule coupling, and the position of this level. Thus, we are able for the first time to establish quantitatively how different end groups determine the metal-molecule coupling and to show these groups affect the internal electronic structure of the molecules.

In order to support the previous conclusions, we have performed first principles calculations of the transport properties of these molecules using a combination of density functional theory and non-equilibrium Green's function techniques [4]. Our computational results show that for all molecules the conductance is dominated by a single level, the closest one to the gold Fermi level. The strength of the coupling and the molecular level energy position were extracted from the first principles calculations and they were found to be in good agreement with our experimental results. We find that the coupling strength is similar for thiol, amino [5] and nitro ending groups, while it is much lower for the cyano group. Moreover, for thiol- and amino-terminated molecules the current proceeds through the highest occupied molecular orbital (HOMO), while in the case of nitro- and cyano-terminated molecules, the conductance was found to be dominated by the lowest unoccupied molecular orbital (LUMO), in agreement with the findings of recent thermopower experiments [6]. These results demonstrate that end groups

not only determine the metal-molecule coupling, but they also strongly modified the internal electronic structure of the molecules, changing in turn the nature of the electrical conduction.

The ensemble of our results constitutes an important step forward in the understanding of the relation between the electronic structure of single molecules and the transport properties of the junctions in which they are embedded.

References:

- [1] L. Venkataraman, J.E. Klare, C. Nuckolls, M.S. Hybertsen and M. L. Steigerwald, *Nature* **442**, (2006) 904
 [2] X. Li, J. He, J. Hihath, B. Xu, S. M. Lindsay, and N. Tao, *J. Am. Chem. Soc.* **128**, (2006) 2135
 [3] Y. S. Park, A. C. Whalley, M. Kamenetska, M.L. Steigerwald, M. S. Hybertsen, C. Nuckolls, L. Venkataraman, *J. Am. Chem. Soc.* **129**, (2007) 15768
 [4] F. Pauly, J.K. Viljas, U. Huniar, M. Häfner, S. Wohlthat, M. Bürkle, J.C. Cuevas, Gerd Schön, *New J. Phys.* **10**, (2008) 125019.
 [5] M.S.Hybertsen, L.Venkataraman, J.E.Klare, A.C.Whalley, M.L.Steigerwald, C.Nuckolls, *J. Phys. Condens.Matter* **20**, (2008) 374115
 [6] K. Baheti, J.A. Malen, P. Doak, P. Reddy, S-Y. Jang, T.D. Tilley, A. Majumdar, R.A. Segalman, *Nano Letters* **8**, (2008) 715

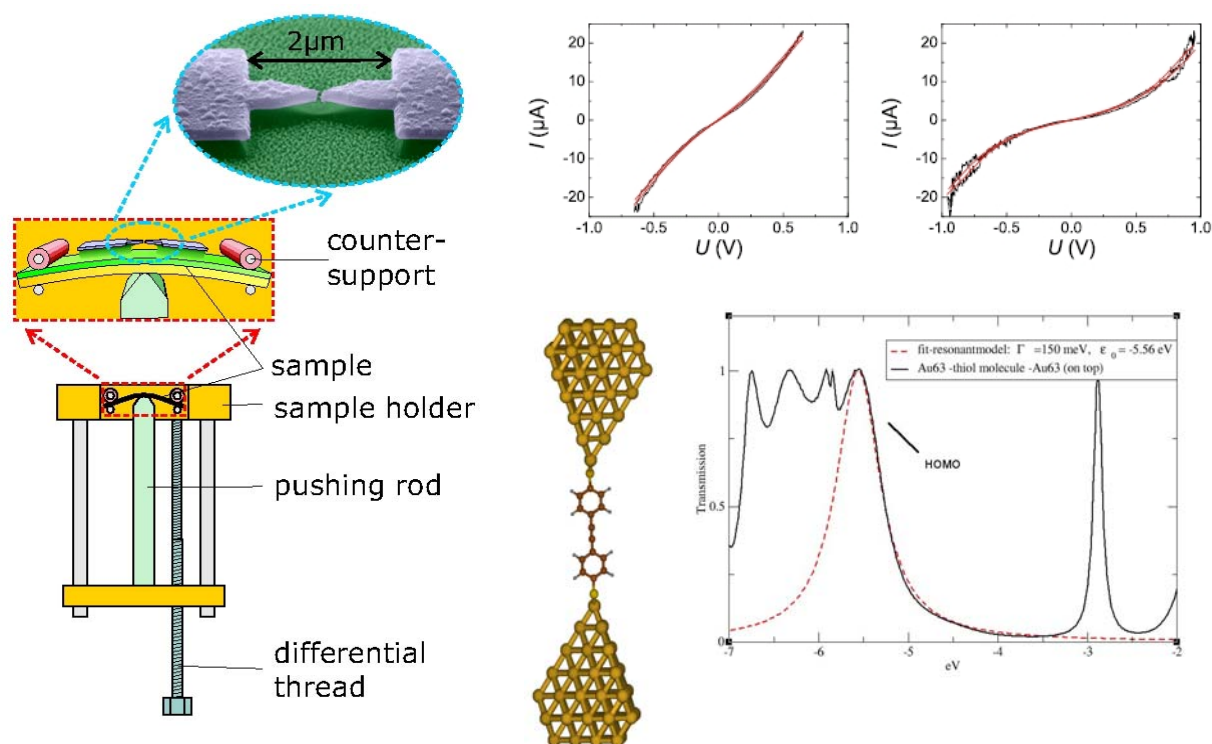


Figure 1: Left: Microfabricated mechanically controllable break-junction set-up. Upper right: Experimental I-V curves of Au |1,2-bis(4-thiolphenyl)ethyne|Au junctions. Lower right: First principle calculations of the transmission through this junction.

First-principles linewidths of quantum-well states in Pb(111) thin films.

X. Zubizarreta^{1,2}, I. Yu. Sklyadneva^{1,3}, V. M. Silkin^{1,2} and E. V. Chulkov^{1,2}

¹ Donostia International Physics Center (DIPC), Paseo de Manuel Lardizabal, 4, 2018, San Sebastián/Donostia, Basque Country, Spain

² Departamento de Física de Materiales and Centro Mixto CSIC-UPV/EHU, Facultad de Ciencias Químicas, UPV/EHU, Apdo.1072, 20080 San Sebastián/Donostia, Basque Country, Spain

³Institute of Strength Physics and Materials Science, pr. Akademicheski 2/1, 634021, Tomsk, Russia

Contact e-mail: xzubizarreta001@ikasle.ehu.es

First-principles calculations of the linewidth of quantum-well states (QWS) in Pb(111) thin films are presented. Damping rates are obtained as the sum of electron-phonon and inelastic electron-electron scattering contributions, $\Gamma = \Gamma_{e-ph} + \Gamma_{e-e}$. Layer-dependent *ab initio* calculations of Γ_{e-ph} were performed for 4-10 monolayers thick free-standing Pb(111) films, whereas the electron-electron scattering contribution was estimated from first-principles calculations of Γ_{e-e} for the parent bulk band dispersing along $\Gamma - L$. As expected, scaling of the linewidth with the square of the quasiparticle energy is found. The effect of spin-orbit coupling on the band energies and on Γ_{e-e} is analyzed and found to be small in the studied energy range.

BORONIC ACID MODIFIED SILVER NANOPARTICLES FOR SACCHARIDE RECOGNITION

Pavel Žvátora, Pavel Řezanka, Kamil Záruba, Vladimír Král

*Dept. of Analytical Chemistry, Institute of Chemical Technology Prague, Technická 5, 166 28
Prague 6, Czech Republic
pavel.zvatora@vscht.cz*

Determination of saccharides is important in many respects. Glucose plays a pivotal role in various metabolic processes. The boronic acid moiety represents a widely used recognition element for the determination of saccharides. Boronic acids have been known for over 100 years, but the interaction between boronic acids and diols has not been recognized until the 1950s (ref. 1).

This work deals with preparation of silver nanoparticles modified by 4-mercaptophenylboronic acids (Fig.1) and their interactions with selected saccharides (D(+)-glucose, D(+)-saccharose, D(+)-fructose, D(+)-lactose) (Fig.2). Metal nanoparticles have attracted considerable attention both fundamentally and technologically because of their unique physical and chemical properties. One of the most fascinating aspects is the manner how they interact with light.

Nanoparticles were prepared by reduction of AgNO_3 by EDTA (ref. 2) and they were characterized by variety of techniques including electron microscopy, absorption spectroscopy and surface enhanced Raman spectroscopy (SERS). The latter method is based on collective plasmon oscillation of a metal surface electrons that causes enormous amplification of Raman scattered light intensity.

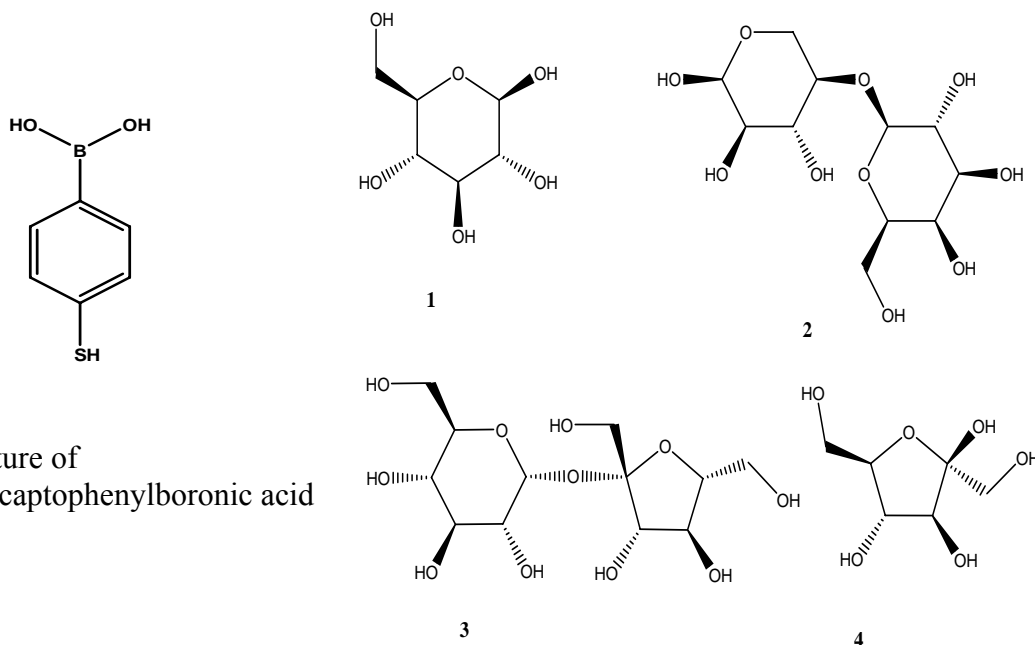


Fig. 1: Structure of 4-mercaptophenylboronic acid

Fig. 2: Structure of used saccharides.

An influence of increasing ionic strength (ref. 3) of the silver nanoparticles solution on SERS intensity was studied. Partial aggregation of nanoparticles led to increasing absorbance at about 785 nm and consequently to increasing of SERS intensity (measured using laser excitation at 785 nm). Ionic strength was increased by $1 \text{ mol}\cdot\text{L}^{-1}$ calcium chloride and UV/Vis

absorption spectra and SERS spectra of 3-mercaptopropanoic acid immobilized on the silver surface were recorded and evaluated.

Direct immobilization of 4-mercaptophenylboronic acid was confirmed by SERS spectroscopy after aggregation of silver solution nanoparticles as mentioned above. Signals of 4-mercaptophenylboronic acid SERS spectrum were assigned by *ab initio* calculation and wavenumbers of B-OH vibrations were confirmed by experiment with deuterated water. Optimal pH for interaction of modified nanoparticles was tested. Interactions of modified nanoparticles with saccharides were monitored by Raman spectroscopy. Signal of γ (C-B) vibration at 635 cm^{-1} disappeared with increasing molar ratio of glucose (Fig. 3).

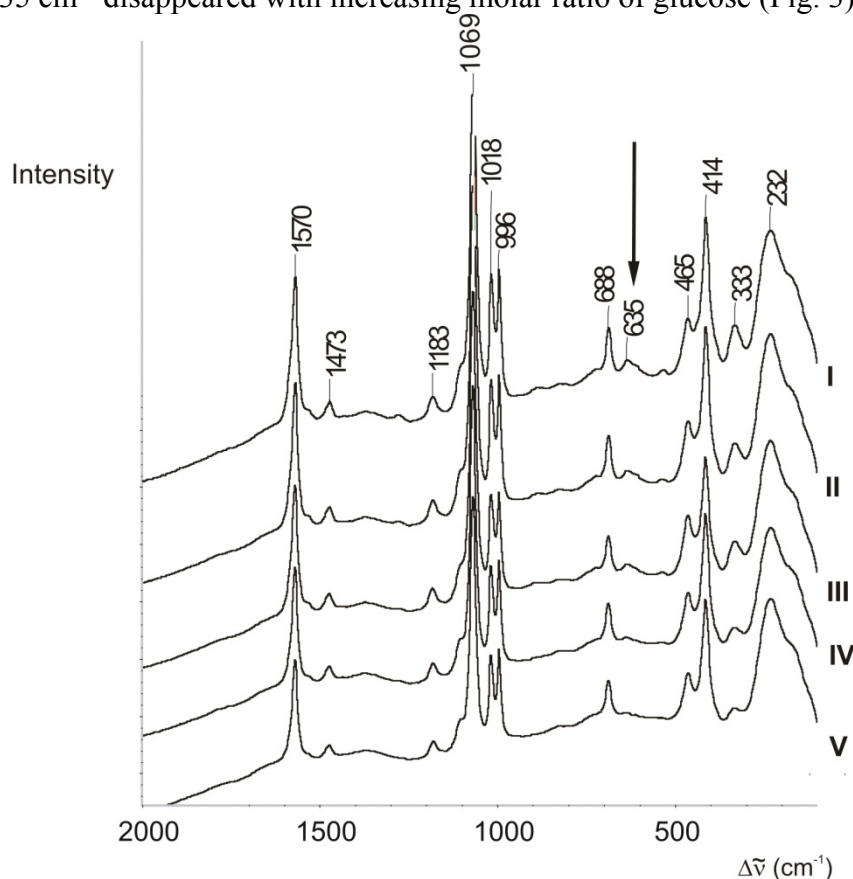


Fig. 3: SERS spectra modified nanoparticles with D(+)-glucose. Molar ratio of the 4-mercaptophenyl boronic acid towards glucose was 0 (spectrum I), 50 (spectrum II), 100 (spectrum III), 250 (spectrum IV), and 500 (spectrum V).

Spectra showed no selectivity of saccharides interaction with modified nanoparticles. In the next step, we would like to focus on better reproducibility this complicated measurements and use to obtain data for estimating stability constants for complex modified silver nanoparticles and saccharides.

References:

- [1] Mader S. H., Wolfbeis O. O.: *Microchim. Acta*, **162** (2008) 1.
- [2] Heard S. M., Grieser F., Barraclough C. G., Sanders J. V.: *J. Colloid Interface Sci.*, **93** (1983) 545.
- [3] Cañamares M. V., Garcia-Ramos J. V., Sanchez-Cortes S., Castillejo M., Oujja M.: *J. Colloid Interface Sci.*, **326** (2008) 103.

nanoICT School 2009 San Sebastian - Spain / October 26-30, 2009



	Monday 26/10/2009	Tuesday 27/10/2009	Wednesday 28/10/2009	Thursday 29/10/2009	Friday 30/10/2009
AM	Courses	Courses	Invited Talks	Courses	Courses
	Lunch	Lunch	Lunch	Lunch	Lunch
PM	Courses	Courses	Invited Talks	Courses	Courses
	School 1 NanoOptics and NanoPhotonics		nanoICT only-day Workshop	School 2 NanoICT modelling issues	

Confirmed Professors

School 1: NanoOptics and NanoPhotonics (October 26-27, 2009)

- Remi Carminati (ESPCI, France)
- Rainer Hillenbrand (CIC nanoGUNE Consolider, Spain)
- Luis Froufe (ICMM-CSIC, Spain)
- Juan Jose Saenz (Universidad Autonoma de Madrid, Spain)
- Niek van Hulst (ICFO, Spain)

School 2: nanoICT modelling issues (October 29-30, 2009)

- Javier Aizpurua (DIPC, Spain)
- Uzi Landman (Georgia Tech, USA)
- Massimo Macucci (Pisa University, Italy)
- Pablo Ordejon (ICMAB, Spain)
- Stephan Roche (CEA-INAC, France)
- Daniel Sanchez-Portal (CSIC - UPV - DIPC, Spain)

Participation of approximately 40 young scientists is planned (20 per school).
Grants covering registration fee, travel and accommodation will be available.

Organisers



Sponsors

